



ECIO 2022

4th May – 6th May

Milan, Italy

23rd European Conference on
Integrated Optics



POLITECNICO
MILANO 1863





WELCOME TO ECIO 2022

Dear participants,

it is a great pleasure for us to welcome you to the 23rd edition of the European Conference on Integrated Optics - ECIO 2022.

Our pleasure is made particularly deep by the fact that, three years after the 2019 edition in Ghent, ECIO is back as a full-in-presence conference. We made the decision to go with this traditional format well aware of the possible risks, but fully supported by the entire Steering Committee and strongly motivated by the honor of hosting this first post-pandemic edition. At the end we are here, so we share with you our happiness in saying "Welcome to Milano!".

We would like to thank you all for the great participation, far beyond our best expectations. The number of ECIO 2022 attendants is in line with pre-pandemic editions, meaning that our community was really waiting for a return to live events with face-to-face interactions. The conference program is very rich with 8 plenary and keynote speakers, 14 invited speakers, 52 oral contributions, 67 posters and 14 exhibitors. A shared opinion by the Steering Committee is that the technical level of the contributions is very high. This means that scientific research has not slowed down, despite all the difficulties and limitations we have had to face in recent years. Browsing through the conference program you will see how much integrated optics has progressed and penetrated into new fields of application, such as photonic computing and neural networks, quantum communications and processing, advanced sensing and spectroscopy, extending also to new wavelength ranges (from extreme UV to Terahertz). This evolution guided our choice to organize the conference program according to "application-oriented" technical sessions.

The conference will be held at the Politecnico di Milano, the largest technical university in Italy, with more than 40,000 students. We hope you will find here a pleasant and lively environment, where to spend three days full of science, culture and social events (without ever forgetting the health regulations).

We warmly thank the sponsors for their support and all the members of the Local Organizing Committee who have given a fundamental contribution to make all this possible.

Enjoy ECIO 2022, enjoy Milano,

Andrea and Francesco

Steering Committee

Conference Chairs

Andrea Melloni, Politecnico di Milano, Italy

Francesco Morichetti, Politecnico di Milano, Italy

Committee Members

Mohand Achouche, 3-5 Labs, France

Imran Akca, Vrije Universiteit, Amsterdam, The Netherlands

Pavel Cheben, National Research Council, Canada

Qixiang Cheng, Cambridge University, United Kingdom

Daoxin Dai, Zhejiang University, China

Wolfgang Freude, Karlsruhe Institute of Technology, Germany

Dominic Gallagher, Photon Design, United Kingdom

Sonia Garcia Blanco, University of Twente, The Netherlands

Kiichi Hamamoto, Kyushu University, Japan

Johnatan Klamkin, University of California Santa Barbara, USA

Di Liang, Hewlett Packard Labs, USA

Arnan Mitchell, RMIT University, Australia

Pascual Muñoz, Universitat Politècnica de València, Spain

Richard Penty, University of Cambridge, United Kingdom

Ryszard Piramidowicz, Warsaw University of Technology, Poland

Joyce Poon, Max Planck Institute, Germany

Carlos Alonso Ramos, Université Paris-Saclay, France

Günther Roelkens, Ghent University, Belgium

Patrick Runge, Fraunhofer HHI, Germany

Pablo Sanchis, Universitat Politècnica de València, Spain

Sébastien Tanzilli, Institut de Physics de Nice, France

Hon Ki Tsang, Chinese University of Hong Kong, Hong Kong

Gonzalo Wangüemert Pérez, Universidad de Málaga, Spain

Kevin Williams, Eindhoven University of Technology, The Netherlands



POLITECNICO
MILANO 1863

Local Organizing Committee

Andrea Melloni

Francesco Morichetti

Christian De Vita

Matteo Petrini

Andrés Martínez

Oscar Jimenez

Syedmohammad Seyedinnavadeh

Piero Borga

Gabriele Cavicchioli

Claudio Somaschini

Laura Brambilla



POLITECNICO
MILANO 1863

Piazza Leonardo da Vinci, 32
20133, Milano, Italy



polifab
POLITECNICO DI MILANO

Via Giuseppe Colombo, 81,
20133, Milano, Italy



Promoest S.r.l.
Via G.B. Moroni 33
20146 Milano, Italy
Tel +39 0243912468
ecio2022@promoest.com

Invited Speakers ECIO 2022

Plenary Speakers

Volker Sorger, George Washington University, USA
Photonic Black-box Modules for Machine Intelligence

Paul Prucnal, Princeton University, USA
Prospects and Applications of photonic neural networks

Keynote Speakers

David Marpaung, Twente University, *Brillouin scattering in silicon nitride photonic circuits*

Haisheng Rong, Intel, *Recent advances in silicon integrated photonics for high-bandwidth and energy-efficient optical interconnects*

Laurent Vivien, CNRS and Univ. Paris Saclay, *Advances and trends of Si photonics*

Meint Smit, TU/e Eindhoven University, *History and perspectives of an InP-based generic foundry approach*

Rajeev Ram, EECS MIT, *High-Performance CMOS Photonic Interfaces: From AI to IoT and Everywhere Between*

Thomas Krauss, York University, *What to do, and what not to do, to get published in OPTICA*

Invited Speakers

Antonella Bogoni, SSSA and Inphotec, *Integrated microwave photonics*

Christine Silberhorn, University of Paderborn, *Quantum photonics based on nonlinear integrated optics*

De Angelis Costantino, Università di Brescia, *Integrated THz-photonics transceivers by all-dielectric phonon-polariton nonlinear nanoantennas*

Fredric Boeuf, STm, *Beyond Interconnects Applications using a 300mm Silicon Photonics Technology*

Helene Debregeas, Almae Technologies, *Towards passive hybridization of high-power and high-speed InP transmitters*

Hugh Podmore, Honeywell Aerospace, *Waveguide Fourier Transform Spectrometers for Remote Sensing and Raman Spectroscopy*

Jaime Garcia, Nanophotonics Technology Center - UPV, *High performance photonic devices based on photonic crystal bimodal interferometers*

Lorenzo Pavesi, Università di Trento, *Silicon photonics neural networks in optical communications*

Nathalie Picqué, Max-Planck Institute of Quantum Optics, *On-chip frequency comb interferometry*

Paolo Villorosi, Università di Padova, *Quantum Communications protocols enhanced by Integrated Optics*

Peter Banzer, University of Graz, *Rethinking Sensing – Developing Next Generation Camera Technology*

Renato Lombardi, Huawei, *Advances on 5G, research directions and role of optical technologies - An industry view*

Tian Gu, MIT, *Integrated optical interfacing using a freeform 3-D coupling platform*

Wim Bogaerts, Ghent University - IMEC, *Does the world need general-purpose programmable photonics?*



POLITECNICO
MILANO 1863

Program at a glance

	Umanitaria	Politecnico di Milano		
	Wednesday May 4 th	Thursday May 5 th		
08:30		Registration		08:30
09:00		Keynote T.K.1		09:00
09:30	Registration	T.A PICs for quantum optics	T.B Sensing & ranging	09:45
		Coffee Break		11:15
		T.C Comb & supercontinuum generation	T.D Periodic structures & Meta-Devices	11:45
12:30	Lunch	Lunch		13:15
14:00	Opening Ceremony	Lunch, Poster T.P & Exhibitors Session		13:45
14:30	Plenary P1 & P2			
16:00	Coffee Break	Keynote T.K.2 & T.K.3		15:45
16:30	High Score Session	T.E Laser Integration	T.F Spectroscopy & MID-IR	16:45
18:00	OPTICA			
18:30	Poster W.P			
19:15	Welcome cocktail	Gala Dinner		19:15

Program at a glance

Politecnico di Milano		
Friday May 6 th		
Registration		08:30
Keynote F.K.1		09:00
F.A Microwave photonics & Terahertz	F.B Waveguide technology & coupling	09:45
Coffee Break		11:15
F.C Advances in silicon photonics	F.D Neural networks & quantum sources	11:45
Lunch		13:15
F.D Programmable photonics	F.F Integrated platforms for visible & XUV	14:30
Coffee Break		16:00
Keynote F.K.2 & F.K.3		16:30
Closing Ceremony & Awards		17:30

		Room: 3.0.3
		Room: De Donato
		Chiosstro & Room: 3.0.2



POLITECNICO
MILANO 1863

Scientific Program

Wednesday, 4th May 2022

Umanitaria

09:30 to 12:30 REGISTRATION

12:30 to 14:00 LIGHT LUNCH

14:00 to 14:30 OPENING CEREMONY

14:30 to 16:00 PLENARY

Session Chair: Andrea Melloni, Politecnico di Milano

- P.1 Photonic Black-box Modules for Machine Intelligence**
Volker Sorger, George Washington University, USA
- P.2 Prospects and Applications of photonic neural networks**
Paul Prucnal, Princeton University, USA

16:00 to 16:30 COFFEE BREAK

16:30 to 18:00 HIGH SCORE SESSION

Session Chair: Wolfgang Freude, Karlsruhe Institute of Technology

- W.B.1 Monolithically Integrated Electronics in Zero-Change Silicon Photonics**
Francesco Zanetto, Politecnico di Milano, Italy
- W.B.2 Multi-channel optical coherence tomography with a CMOS silicon nitride photonic integrated circuit**
Stefan Nevlacsil, AIT Austrian Institute of Technology GmbH, Austria
- W.B.3 Hybridly Integrated Photonic Integrated Circuit for Wavelength and Polarization Determination**
Axel Schoenau, Fraunhofer-Institut für Nachrichtentechnik, Germany
- W.B.4 Generation of high-frequency phonons in silicon optomechanical crystal**
Jianhao Zhang, Centre de Nanosciences et de Nanotechnologies, France

18:00 to 18:30 What to do, and what not to do, to get published in OPTICA
Thomas Krauss, York University, UK

18:30 to 20:00 POSTER SESSION (The Chiostro)

- W.P.1 A Hybrid Optical Waveguide Platform for High-Performance Integrated Photonic Devices**
Hamed Nikbakht, Bob van Someren, Chunyu Lu, B. Imran Avci

- W.P.2 Thermal and wiring optimizations of dense SOA arrays on an adhesively bonded InP membrane**
Yi Wang, Jorn van Engelen, Victor Dolores-Calzadilla, Kevin Williams, Meint Smit, Yuqing Jiao
- W.P.3 Practical characterization of InP Waveguides and MMI couplers using Mach-Zehnder interferometers**
Amer Bassal, Guillaume Binet, Wouter Diels, Axel Schönau, Oliver Abdeen, Moritz Baier, Martin Schell
- W.P.4 Compact ring resonator at 8 μm wavelength**
Natnicha Koompai, Thi Hao Nhi Nguyen, Jacopo Frigerio, Andrea Ballabio, Virginia Falcone, Xavier Le Roux, Carlos Alonso-Ramos, Laurent Vivien, Adel Bousseksou, Giovanni Isella, Delphine Marris-Morini
- W.P.5 Subwavelength engineered silicon Bragg gratings for on-chip filtering with high optical rejection and narrow bandwidth**
Dorian Oser, David E. Medina Quiroz, Diego Perez Galacho, Xavier Le Roux, Sebastien Tanzilli, Laurent Vivien, Laurent Labonte, Eric Cassan, Carlos Alonso Ramos
- W.P.6 Performance tradeoffs in low-loss Si₃N₄ waveguides for linear and nonlinear applications**
Marcello Girardi, Victor Torres-Company, Anders Larsson
- W.P.7 Mitigating Polarization Rotation Effects in Thin-Film Lithium Niobate Waveguides**
Gabriele Cavicchioli, Maziyar Milanizadeh, Giuseppe Cusmai, Roberto Longone, Francesco Morichetti, Andrea Melloni
- W.P.8 Minimisation of Parasitic Capacitance in Electro-Absorption Modulators for High-Speed Operation**
Jack Mulcahy, Xing Dai, John McCarthy, Frank Peters
- W.P.9 New and efficient sacrificial layer for transfer printing technology**
Hemalatha Muthuganesan, Fatih Bilge Atar, Agnieszka Gocalinska, Emanuele Pelucchi, Brian Corbett
- W.P.10 Fabrication and characterization of symmetric Au-nanostructures with SERS activity**
M. Lafuente, E.J.W. Berenschot, R.M. Tiggelaar, A. Susarrey-Arce, R. Mallada, M.P. Pina, S.M. García-Blanco, N.R. Tas
- W.P.11 Comparison of Gaussian Process Kernels for Surface Roughness Modelling**
Samuel Hörmann, Jakob Wilhelm Hinum-Wagner, Jürgen Sattelkow, Desiree Rist
- W.P.12 Designing a GaN photonic platform for near-IR applications**
Megan O'Brien, Nicola Maraviglia, Vitaly Zubialevich, Brian Corbett
- W.P.13 Micro-Transfer-Printed O-band GaAs QD III-V-on-Si DFB Laser**
Jing Zhang, Igor Krestnikov, Ruggero Loi, Peter Ossieur, Guy Lepage, Peter Verheyen, Joris Van Campenhout, Gunther Roelkens
- W.P.14 Iron Doping for Transfer Printed High Speed EAM**
Shengtai Shi, Jack Mulcahy, Xing Dai, Frank H. Peters
- W.P.15 Monolithic integration of photonic integrated circuits with silicon photodiodes**
Martino Bernard, Fabio Acerbi, Mher Ghulinyan
- W.P.16 Photonic flip-chip assembly of InP on TriPleX with laser soldering**
Wenjing Tian, Lucas Beste, Alexander Khachikyan, Christoph Mittelstädt, Ronald Dekker, Kerstin Wörhoff, Joost van Kerkhof, Rui Santos, Kevin Williams, Xaveer Leijten



- W.P.17 Low-stress Si₃N₄ waveguides on sapphire substrate**
Kai Wang, E.J.W. Berenschot, M. Dijkstra, R.M. Tiggelaar, S.M. Martinussen, L. Chang, W.A.P.M. Hendriks, B.T.H. Borgelink, R.N. Frentrop, V.V. Tkachuk, N. Tas, S.M. Garcia-Blanco
- W.P.18 A thick silicon photonics platform for quantum technologies**
Matteo Cherchi, Arijit Bera, Antti Kemppinen, Jaani Nissilä, Kirsi Tappura, Marco Caputo, Lauri Lehtimäki, Janne Lehtinen, Joonas Govenius, Mika Prunnila, Timo Aalto
- W.P.19 Low Limit of Detection in Bulk Liquids Using a Fibre-Packaged Waveguide-Enhanced Raman Sensor**
Jérôme Michon, Priscille Bonnassies, Derek Kita, Carlos Alonso-Ramos, Laurent Vivien, Juejun Hu
- W.P.20 Wideband and large optical throughput Fourier-transform spectrometer implemented on a silicon nitride chip**
David González-Andrade, Thi Thuy Duong Dinh, Sylvain Guerber, Nathalie Vulliet, Sébastien Cremer, Stephane Monfray, Eric Cassan, Delphine Marris-Morini, Frédéric Boeuf, Pavel Cheben, Laurent Vivien, Aitor V. Velasco, Carlos Alonso-Ramos
- W.P.21 Deep-learning algorithms for resilience to fabrication imperfections in integrated Fourier-transform spectrometer**
Zindine Mokeddem, Daniele Melati, David González-Andrade, Thi Thuy Duong Dinh, Eric Cassan, Yuri Grinberg, Pavel Cheben, Dan-Xia Xu, Jens Schmid, Laurent Vivien, Delphine Marris-Morini, Aitor V. Velasco, Carlos Alonso-Ramos
- W.P.22 On-chip silicon nitride ring resonator for background suppression in Brillouin spectroscopy**
Giuseppe Antonacci, Kareem Elsayad, Dario Polli
- W.P.23 Performance comparison of polarization rotator designs on 800 nm thick silicon nitride platform**
Georgios Patsamanis, Dimitra Ketzaki, Dimitrios Chatzitheocharis, Konstantinos Vyrsoinos
- W.P.24 Photonic chip based biosensing system with fully automatic alignment and parallel detection capability**
L. Chang, W.A.P.M. Hendriks, I. Hegeman, R.N. Frentrop, M. Dijkstra, J.P. Korterik, N.A. Schilder, H.A. Seubers, S.M. García-Blanco
- W.P.25 Integrated optical readout layer for ultrafast real-time delay reservoir computing**
Tigers Jonuzi, Mirko Goldmann, Apostolos Argyris, Ingo Fischer, Miguel C. Soriano, David Domenéch
- W.P.26 Dynamic labelling for enhanced biosensing with microring resonators**
Piero Borga, Francesca Milesi, Nicola Peserico, Chiara Groppi, Antonio Fincato, Riccardo Bertacco, Andrea Melloni
- W.P.27 Towards an integrated optic-electronic-optic interferometer**
Alexander Schindler, Felix Ganzer, Patrick Runge, Md Salek Mahmud, Sebastian Randel, Martin Schell
- W.P.28 Enhancing Sensitivity and Reducing Temperature Dependence of Contactless Light Sensors**
Vittorio Grimaldi, Francesco Zanetto, Fabio Toso, Francesco Morichetti, Andrea Melloni, Giorgio Ferrari, Marco Sampietro

W.P.29 Photonic time-delay reservoir computing based on an asymmetric Mach-Zehnder interferometer with reconfigurable memory capacity

Mohab Abdalla, Clément Zrounba, Raphael Cardoso, Guanghui Ren, Andreas Boes, Arnan Mitchell, Alberto Bosio, Ian O'Connor, Fabio Pavanello

W.P.30 Experimental Characterization of sub-THz Wireless Communications Building Blocks on a Silicon Platform

Kalliopi Spanidou, Robinson Guzmán, Luis Orbe, Luis González Guerrero, Guillermo Carpintero

W.P.31 Design of a modular and scalable photonic-integrated WSS for multi-band applications

Lorenzo Tunesi, Ihtesham Khan, Muhammad Umar Madood, Enrico Ghillino, Andrea Carena, Vittorio Curri, Paolo Bardella

W.P.32 Programmable Integrated Photonic Circuits: applications for 5G, Computing, Data Center and Sensing

Daniel Pérez López

19:15 WELCOME COCKTAIL & POSTER



POLITECNICO
MILANO 1863

Thursday, 5th May 2022

Politecnico di Milano

From 08:30 REGISTRATION

09:00 to 09:30 PLENARY (Room: 3.0.3)

Session Chair: Andrea Melloni, Politecnico di Milano

T.K.1 High-Performance CMOS Photonic Interfaces: From AI to IoT and Everywhere Between

Rajeev Ram, EECS MIT, USA

09:45 to 11:15 PICS FOR QUANTUM OPTICS (Room: 3.0.3)

Session Chair: Roberto Osellame, Politecnico di Milano

T.A.1 Quantum Communications protocols enhanced by Integrated Optics - INVITED

Paolo Villorosi, Università di Padova, Italy

T.A.2 PIC Technologies for Quantum Secure Communications

Taofiq Paraiso, Thomas Roger, Davide Marangon, Innocenzo De Marco, Mirko Sanzarp, Robert Woodward, James Dynes, Zhiliang Yuan, Andrew Shields

T.A.3 Mid-infrared Ghost spectroscopy application using an entangled photons source in silicon

Matteo Sanna, Davide Rizzotti, Stefano Signorini, Lorenzo Pavesi

T.A.4 Quantum photonics based on nonlinear integrated optics - INVITED

Christine Silberhorn, University of Paderborn, Germany

09:45 to 11:15 SENSING AND RANGING (Room: De Donato)

Session Chair: Marc Sorel, University of Glasgow

T.B.1 Rethinking Sensing – Developing Next Generation Camera Technology - INVITED

Peter Banzer, University of Gratz, Austria

T.B.2 Integrated Computer Generated Waveguide Hologram for Versatile Free-Space Beam Projection

David De Vocht, Tianran Liu, Yuqing Jiao, Erwin Bente

T.B.3 Broadband optical beam steering over a wide field of view with a silicon quadratic metalens

Yang Liu, Jianhao Zhang, Xavier Le Roux, Cedric Villebasse, Eric Cassan, Delphine Marris-Morini, Laurent Vivien, Carlos Alonso-Ramos, Daniele Melati

T.B.4 Carbon Dioxide Sensing with a Photonic Integrated Differential Absorption LiDAR Transmitter

Antonio Perez-Serrano, Clara Quevedo-Galan, Victor R. Aguilera-Sanchez, Jose Manuel G. Tijero, Ignacio Esquivias

T.B.5 Low-noise frequency-agile photonic integrated lasers for coherent ranging

Grigory Lihachev, Johann Riemensberger, Wenle Weng, Junqiu Liu, Hao Tian, Anat Siddhart, Viacheslav Snigirev, Vladimir Shadymov, Andrey Voloshin, Rui Ning Wang, Jijun He, Sunil A. Bhave, Tobias J. Kippenberg

11:15 to 11:45 COFFEE BREAK

11:45 to 13:00 **COMB AND SUPERCONTINUUM GENERATION (Room: 3.0.3)**

Session Chair: Mariangela Gioannini, Politecnico di Torino

- T.C.1 On-chip frequency comb interferometr - INVITED**
Nathalie Picqué, Max-Planck Institute of Quantum Optics, Germany
- T.C.2 Impact of the saturable absorber on the linewidth enhancement factor of hybrid silicon quantum dot comb lasers**
Thibaut Renaud, Heming Huang, Geza Kurczveil, Raymond G. Beausoleil, Frédéric Grillot
- T.C.3 Low Noise 2.6 to 26 GHz Tenfold Frequency Multiplication by an InP Broadly Tunable Optical Comb**
Nicola Andriolli, Eduardo Saia Lima, Evandro Conforti, Giampiero Contestabile, Arismar Cerqueira Sodr  Junior
- T.C.4 Heterogeneously integrated low-loss lithium niobate photonic platform**
Mikhail Churaev, Annina Riedhauser, Rui N. Wang, Charles M hl, Terence Bl sin, Miles H. Anderson, Viacheslav Snigirev, Anat Siddharth, Youri Popoff, Ute Drechsler, Danilele Caimi, Simon H nl, Johann Riemensberger, Junqiu Liu, Paul Seidler, Tobias J. Kippenberg
- T.C.5 Mid-Infrared Supercontinuum Generation in a Tapered SiGe/Si Waveguide for Multi-Species Gas Spectroscopy**
Alberto Della Torre, R mi Armand, Milan Sinobad, Kokou Firmin-Fiaboe, Barry Luther-Davies, Stephen Madden, Arnan Mitchell, Thach Nguyen, David J. Moss, Jean-Michel Hartmann, Vincent Reboud, Jean-Marc Fedeli, Christelle Monat, Christian Grillet

11:45 to 13:00 **PERIODIC STRUCTURES AND META-DEVICES (Room: De Donato)**

Session Chair: Gonzalo Wanguemert Perez, Universidad de M laga

- T.D.1 High performance photonic devices based on photonic crystal bimodal interferometer - INVITED**
Jaime Garcia, Nanophotonics Technology Center - UPV, Spain
- T.D.2 Curved waveguide grating demultiplexer (CWG) with a flattened response via bimodal output waveguides**
Abdelfettah Hadij-ElHouati, Robert Halir, Alejandro Ortega-Mo ux, J. Gonzalo Wang emert-P, Jens H. Schmid, Pavel Cheben, I igo Molina-Fernandez
- T.D.3 Subwavelength metamaterials for broadband mode multiplexing and power splitting in silicon waveguides**
Aitor V. Velasco, David Gonz lez-Andrade, Raquel Fern ndez de Cabo, Jaime Vilas, Irene Olivares, Antonio Dias, Jos  Manuel Luque-Gonz lez, J. Gonzalo Wang emert-P rez, Alejandro Ortega-Mo ux, I igo Molina-Fern ndez, Robert Halir, Pavel Cheben
- T.D.4 Metamaterial-engineered silicon devices fabricated with deep UV immersion lithography**
Daniele Melati, Vladyslav Vakarin, Thi Thuy Duong Dinh, Xavier Le Roux, Warren Kut King Kan, C cilia Dupr , Bertrand Szelag, St phane Monfray, Fr d ric Boeuf, Pavel Cheben, Eric Cassan, Delphine Marris-Morini, Laurent Vivien, Carlos Alonso-Ramos
- T.D.5 Design of autocorrective interferometers using the Bloch sphere**
Matteo Cherchi



POLITECNICO
MILANO 1863

13:15 LUNCH

13:45 to 15:45 POSTER SESSION (Garden)

- T.P.1 Topological control of light spectrum using dynamically modulated optical waveguides**
Francesco S. Piccioli, Alexander Szameit, Jacopo Carusotto
- T.P.2 Bound States in the Continuum in LiNbO₃ Waveguides: An Assessment**
Jiří Čtyroký, Jiří Petráček, Vladimír Kuzmiak, Ivan Richter
- T.P.3 Spontaneous polarization reversal induced in α -phase lithium niobate channel waveguides by proton exchange**
Alicia Petronela Rambu, Vasile Tiron, Eugen Oniciuc, Sorin Tascu
- T.P.4 Optimization of Brillouin Gain in Subwavelength Silicon Membrane Waveguides using a Genetic Algorithm**
Paula Nuño Ruano, Jianhao Zhang, Daniele Melati, David González Andrade, Xavier Le Roux, Eric Cassan, Delphine Marris-Morini, Laurent Vivien, Norberto Daniel Lanzillotti-Kimura, Carlos Alonso Ramos
- T.P.5 Nonlocal Fourier modal method**
Pavel Kwiecien, Milan Burda, Ivan Richter
- T.P.6 Nonlocal interactions in planar metal layers**
Milan Burda, Pavel Kwiecien, Ivan Richter
- T.P.7 Comparative performance evaluation of transparent conducting oxides with moderate mobility for all-optical switching in silicon**
Juan Navarro-Arenas, Jorge Parra, Pablo Sanchis
- T.P.8 Supercontinuum generation in ultra-low loss silicon nitride waveguides**
Yijun YANG, Christian Lafforgue, Quentin Wilmart, Thibaut Sylvestre, Sylvain Guerber, Xavier Le Roux, Eric Cassan, Delphine Marris-Morini, Carlos Alonso-Ramos, Bertrand Szelag, Laurent Vivien
- T.P.9 Intersubband Absorption in p-type Ge Multiple Quantum Wells for Mid-IR Sensing Applications**
Andrea Barzaghi, Virginia Falcone, Stefano Calcaterra, Raffaele Giani, Andrea Ballabio, Daniel Chrastina, Giovanni Isella, Jacopo Frigerio
- T.P.10 Static and Dynamic Nonlinear Effects in Silicon Micro-Rings: Impact of Trap Assisted Shockley Read Hall Carrier Recombination**
Marco Novarese, Stefania Cucco, Sebastian Garcia Romero, Jock Bovington, Rongqing Hui, Mariangela Giannini
- T.P.11 Integrated electro-optical modulator operating in the long-wave infrared spectral range**
Thi Hao Nhi Nguyen, Natnicha Koopai, Miguel Montesinos-Ballester, Lucas Deniel, Jacopo Frigerio, Andrea Ballabio, Virginia Falcone, Xavier Le Roux, Carlos Alonso-Ramos, Laurent Vivien, Adel Bousseksou, Giovanni Isella, Delphine Marris-Morini
- T.P.12 1x5 reconfigurable optical wireless routers for on-chip interconnection**
Loredana Gabriele, Gaetano Bellanca, Jacopo Nanni, Marina Barbiroli, Franco Fuschini, Velio Tralli, Davide Bertozzi, Giovanni Serafino, Vincenzo Petruzzelli, Giovanna Calò

- T.P.13 Compact and Alignment-Tolerant Vertical Coupler for Heterogeneous Photonic Integration**
Chunhui Yao, Qixiang Cheng, Richard V. Penty
- T.P.14 Lithium-niobate-based frequency-agile integrated laser sources**
V. Snigirev, A. Riedhauser, G. Likhachev, J. Riemensberger, R. N. Wang, C. Moehl, M. Churaev, A. Siddharth, G. Huang, Y. Popoff, U. Drechsler, D. Caimi, S. Hoenl, J. Liu, P. Seidler, T. J. Kippenberg
- T.P.15 A Monolithically Integrated Tunable Comb Source and Filter**
John McCarthy, Maryam Shayesteh, Frank H. Peters
- T.P.16 Silicon photonic mode demultiplexer enabled by on-chip beamforming**
David González-Andrade, Xavier Le Roux, Thi Thuy Duong Dinh, Dorian Oser, Diego Pérez-Galacho, Eric Cassan, Delphine Marris-Morini, Laurent Vivien, Carlos Alonso-Ramos
- T.P.17 Plasmonic slot ferroelectric MZIR modulator on Si₃N₄ in the O-band**
Dimitrios Chatzitheocharis, Dimitra Ketzaki, Georgios Patsamanis, Konstantinos Vyrsoinos
- T.P.18 Integrated Wavelength Filter on thin-film Lithium Niobate for a Photonic-enabled Radiometer**
Jessica César Cuello, Robinson C. Guzmán, Alberto Zarzuelo, Jeffrey Holzgrafe, Marko Lončar, Gabriel Santamaria, Luis E. García, Guillermo Carpintero
- T.P.19 Thermally tunable Silicon polarization rotator based on mode hybridization**
Theoni Prousalidi, Giannis Pouloupoulos, Carmelo Scarcella, Harry Zervos, Daisy Bergin, Anthony Bulling, Stéphane Detraz, Milana Lalović, Leonardo Marcon, Lauri Olanterä, Ulrik Sandven, Christophe Sigaud, Csaba Soos, Jan Troska, Hercules Avramopoulos
- T.P.20 Demonstration of self-spiking neuron behavior in a monolithically integrated two-section laser**
Lukas Puts, Kevin Williams, Daan Lenstra and Weiming Yao
- T.P.21 Compact, spatial-mode-interaction-free, ultralow-loss, nonlinear photonic integrated circuits**
Xinru Ji, Junqiu Liu, Jijun He, Rui Ning Wang, Zheru Qiu, Johann Riemensberger, Tobias J. Kippenberg
- T.P.22 Ultra-broadband polarization beam splitter with a gradual anisotropy engineered subwavelength metamaterial**
José Manuel Luque-González, Robert Halir, J. Gonzalo Wangüemert-Pérez, Pavel Cheben, Íñigo Molina-Fernández, Alejandro Ortega-Moñux
- T.P.23 Stokes-vector receivers on an indium phosphide membrane**
Sander Reniers, Jos van der Tol, Kevin Williams, Yuqing Jiao
- T.P.24 Ge/Si Electrically Tunable VIS/SWIR Photodetector**
Andrea Ballabio, Andrea De Iacovo, Jacopo Frigerio, Andrea Fabbri, Giovanni Isella, Lorenzo Colace
- T.P.25 Mode Overlap Simulations for Quantification of Bend Loss in Silicon Nitride Strip Waveguides for Sensing**
Anton Buchberger, Desiree Rist, Jakob Hinum-Wagner, Samuel Hörmann, Jochen Kraft, Alexander Bergmann
- T.P.26 In-line photo-thermal plasmonic detectors integrated in TiO₂ optical waveguides**
Andres Martinez, Vittorio Grimaldi, Deepak Kumar Sharma, Christian De Vita, Francesco Morichetti, Alexandre Bouhelier, Marco Sampietro



- T.P.27 Numerical Analysis of Digital Pulse Modulation of Strongly Injection-Locked Whistle-Geometry Microring Lasers**
Gennady A. Smolyakov, Marek Osiński
- T.P.28 Characterization of Passively Mode-Locked Lasers and Saturable Absorbers based on an InP quantum well amplifier suitable for active-passive integration at 1300 nm**
Joel Hazan, Aser Nassar, Steven Kleijn, Kevin Williams, Erwin Bente
- T.P.29 Freeform optical arrays for free-space coupling into photonic integrated circuits**
Rakan E. Alsaigh, Martin P.J. Lavery
- T.P.30 Inverse Design of Nanophotonic Circuitry Components based on Reinforcement Learning**
Marco Butz, Alexander Leifhelm, Marlon Becker, Benjamin Risse, Carsten Schuck
- T.P.31 Polarization mode converter based on hybrid integration of nanowires on a silicon waveguide**
Ali Emre Kaplan, Valerio Vitali, Francesco Rossella, Valeria Demontis, Andrea Fontana, Periklis Petropoulos, Vittorio Bellani, Cosimo Lacava, Ilaria Cristiani
- T.P.32 Numerical calculation of active waveguide Bragg gratings amplification dependences**
Ángel Sanz-Felipe, Manuel Macias-Montero, Rocío Ariza, Juan A. Vallés, Javier Solís
- T.P.33 SiP Waveguide-Embedded Electronic Devices controlled by Substrate/Gate Potential Tuning**
Alessandro Perino, Francesco Zanetto, Matteo Petrini, Francesco Morichetti, Andrea Melloni, Giorgio Ferrari, Marco Sampietro
- T.P.34 Low loss SiN optical modulator for kHz-rate switching applications**
Alessandro Brugnoli, Ali Emre Kaplan, Michele Re, Cosimo Lacava, Ilaria Cristiani
- T.P.35 Miniaturization of 90-degree hybrid optical couplers**
Alessio Miranda, Weiming Yao, Jos van der Tol, Kevin Williams

13:45 to 15:35 EXHIBITORS SESSION (Room: 3.0.2)

Note: See pag. 27 for the complete program

15:45 to 16:30 INDUSTRIAL KEYNOTES (Room: 3.0.3)

Session Chair: Francesco Morichetti, Politecnico di Milano

- 15:45 T.K.2 Recent advances in silicon integrated photonics for high-bandwidth and energy-efficient optical interconnects**
Haisheng Rong, Intel, USA
- 16:15 T.K.3 Advances on 5G, research directions and role of optical technologies - An industry view**
Renato Lombardi, Huawei, Italy

16:45 to 18:30 LASER INTEGRATION (Room: 3.0.3)

Session Chair: Kevin Williams, Eindhoven University of Technology

- T.E.1 Towards passive hybridization of high-power and high-speed InP transmitters**
INVITED
Helene Debregeas, Almae Technologies, France

- T.E.2 Micro-Transfer-Printed III-V-on-Si Laser with 120nm tuning range**
Emadreza Soltanian, Grigorij Muliuk, Sarah Uvin, Dongbo Wang, Guy Lepage, Peter Verheyen,, Joris Van Campenhout, Stefan Ertl, Johanna Rimböck, Nicolas Vaissiere, Delphine Néel, Joan Ramirez, Jing Zhang, Gunther Roelkens
- T.E.3 CW emission and self-pulsing in III/V SiN hybrid laser with narrowband mirror**
Cristina Rimoldi, Lorenzo Columbo, Sebastian Romero-García, Jock Bovington, Mariangela Gioannini
- T.E.4 Integration of Quantum Dot Lasers with SOI Waveguides using Micro-Transfer Printing**
Ali Uzun, Fatih Atar, John Justice, Brian Corbett, Ruggero Loi, Alex Farrell, Peter Ossieur, Jing Zhang, Gunther Roelkens, Igor Krestnikov, Johanna Rimböck, Stefan Ertl, Marianna Pantouvaki, Guy Lepage, Joris Van Campenhout
- T.E.5 Long cavity hybrid mode-locked laser with improved modulation efficiency**
Yasmine Ibrahim, Sylvain Boust, Quentin Wilmart, Jean-François Paret, Alexandre Garreau, Karim Mekhazni, Catherin Fortin, François Duport, Ghaya Baili, Corrado Sciancalepore, Stéphanie Garcia, Laurent Vivien, Frédéric van Dijk
- T.E.6 GaSb/SOI flip-chip integrated DBR laser at 2 μ m wavelength region**
Nouman Zia, Jukka Viheriala, Heidi Tuorila, Samu-Pekka Ojanen, Eero Koivusalo, Joonas Hilska, Mircea Guina

16:45 to 18:30 SPECTROSCOPY AND MID-IR (Room: De Donato)

Session Chair: Sonia Garcia Blanco, University of Twente

- T.F.1 Waveguide Fourier Transform Spectrometers for Remote Sensing and Raman Spectroscopy - INVITED**
Hugh Podmore, Honeywell Aerospace, Canada
- T.F.2 Mid-infrared Fourier-transform spectrometer based on suspended silicon metamaterial waveguides**
Thi Thuy Duong Dinh, Xavier Le Roux, Natnicha Koompai, Daniele Melati, Miguel Montesinos-Ballester, David González-Andrade, Pavel Cheben, Aitor V. Velasco, Eric Cassan, Delphine Marris-Morini, Laurent Vivien, Carlos Alonso-Ramos
- T.F.3 Germanium quantum wells for mid-infrared integrated photonics**
Andrea Barzagli, Virginia Falcone, Stefano Calcaterra, Raffaele Giani, Andrea Ballabio, Giovanni Isella, Daniel Chrastina, Michele Ortolani, Michele Virgilio, Jacopo Frigerio
- T.F.4 Mid-Infrared High Q Factor Silicon-Germanium Ring Resonator**
Marko Perestjuk, Rémi Armand, Alberto Della Torre, Milan Sinobad, Arnan Mitchell, Andreas Boes, Jean-Michel Hartmann, Jean-Marc Fedeli, Vincent Reboud, Christelle Monat, Christian Grillet
- T.F.5 Ge micro-crystals photodetectors with enhanced infrared responsivity**
Virginia Falcone, Andrea Ballabio, Andrea Barzagli, Carlo Zucchetti, Luca Anzi, Federico Bottegoni, Jacopo Frigerio, Roman Sordan, Paolo Biagioni, Giovanni Isella
- T.F.6 Etchless Pedestal Chalcogenide Waveguides for Mid-IR On-Chip Sensing and Spectroscopy Applications**
Vasileios Mourgelas, Ben Rowlinson, James Wilkinson, Ganapathy Senthil Murugan

18:30 & 19:15 CASTELLO VISIT
19:30 GALA DINNER



POLITECNICO
MILANO 1863

Friday, 6th May 2022
Politecnico di Milano

08:00 to 09:00 REGISTRATION

09:00 to 09:30 KEYNOTE (Room: 3.0.3)

Session Chair: Delphine Marris-Morini, Université Paris-Sud

F.K.1 Brillouin Scattering in Silicon Nitride Photonic Circuits
David Marpaung, Twente University, Netherlands

09:45 to 11:15 MICROWAVE PHOTONICS AND TERAHERTZ (Room: 3.0.3)

Session Chair: Delphine Marris-Morini, Université Paris-Sud

F.A.1 Photonic integration for microwave photonics systems - INVITED
Antonella Bogoni, SSSA and Inphotec, Italy

F.A.2 Microwave-optical transduction using high overtone bulk acoustic resonances
Terence Blésin, Anat Siddharth, Hao Tian, Rui Ning Wang, Alaina Attanasio, Sunil A. Bhave, Tobias J. Kippenberg

F.A.3 Widely Tunable Flat-Top Integrated Microwave Photonic Passband Filter
Claudio Porzi, Manuel Reza, Paolo Ghelfi, Marc Sorel, Antonella Bogoni

F.A.4 Integrated THz-photonics transceivers by all-dielectric phonon-polariton non-linear nanoantennas - INVITED
De Angelis Costantino, Università di Brescia, Italy

09:45 to 11:15 WAVEGUIDE TECHNOLOGY AND COUPLING (Room: De Donato)

Session Chair: Carlos Alonso Ramos, Université Paris-Saclay

F.B.1 Integrated optical interfacing using a freeform 3-D coupling platform - INVITED
Tian Gu, MIT, USA

F.B.2 3D printed on-chip parabolic mirror for chip-to-fiber and chip-to-chip coupling
Yujia Kong, Herman Offerhaus, Meindert Dijkstra, Sonia García Blanco, Lantian Chang

F.B.3 Demonstration of an on-chip optical circulator for TE mode light
Rui Ma, Sander Reniers, Yuya Shoji, Tetsuya Mizumoto, Kevin Williams, Yuqing Jiao, Jos Van Der Tol

F.B.4 Assessment of electro- and thermo-optics response of thin film lithium niobate with phase shifted Bragg gratings
Alessandro Prencipe, Katia Gallo

F.B.5 Enhanced all-optical reading of subwavelength magnetic bits on a photonic integrated device using magneto-plasmonic effects
Hamed Pezeshki, Figen Ece Demirer, Reinoud Lavrijsen, Jos van der Tol, and Bert Koopmans

11:15 to 11:45 COFFEE BREAK

11:45 to 13:15 **ADVANCES IN SILICON PHOTONICS (Room: 3.0.3)**

Session Chair: Pablo Sanchis, Universitat Politècnica de València

F.C.1 Beyond Interconnects Applications using a 300mm Silicon Photonics Technology
INVITED

Fredric Boeuf, STm, France

F.C.2 Automatic Testing of Silicon Photonic Add/Drop Multiplexer

Matteo Petrini, Rita Baldi, Moritz Seyfried, Francesco Morichetti, Andrea Melloni

F.C.3 Micro transfer printing of electronic integrated circuits on Silicon photonics substrates

Ruggero Loi, Prasanna Ramaswamy, Alex Farrell, Antonio Jose Trindade, Alin Fecioru, Johanna Rimböck, Stefan Eartl, Marianna Pantouvaki, Guy Lepage, Joris Van Campenhout, Tinus Pannier, Ye Gu, David Gomez, Patrick Steglich, Peter Ossieur

F.C.4 Integrated Electronic Control of Silicon Mach-Zehnder Interferometers

Fabio Toso, Francesco Zanetto, Maziyar Milanizadeh, Andrea Melloni, Marco Sampietro, Francesco Morichetti, Giorgio Ferrari

F.C.5 Optical modulation based on DC Kerr effect in silicon waveguide

Jonathan Peltier, Léopold Viroth, Christian Lafforgue, Lucas Deniel, Delphine Marris-Morini, Guy Aubin, Farah Amar, Dehn Tran, Callum G. Littlejohns, David J. Thomson, Weiwei Zhang, Laurent Vivien

11:45 to 13:15 **NEURAL NETWORKS AND QUANTUM SOURCES (Room: De Donato)**

Session Chair: Taofiq Paraíso, Toshiba

F.D.1 Silicon photonics neural networks in optical communications - INVITED

Lorenzo Pavesi, Università di Trento, Italy

F.D.2 Quantifying Hidden Noise in Integrated Nonlinear Sources

Ben M. Burridge, Imad I. Faruque, John G. Rarity, Jorge Barreto

F.D.3 Strong Pump Rejection Filter for Polarization-Diverse Silicon Platforms

Jérôme Michon, Xavier Le Roux, Alexandre Huot de Saint-Albin, Dorian Oser, Sébastien Tanzilli, Laurent Labonté, Eric Cassan, Laurent Vivien, Carlos Alonso-Ramos

F.D.4 Fully Integrated, Scalable Quantum Entropy Source at 1 Gbps

Miquel Rudé, Domenico Tulli, Waldimar Amaya, Carlos Abellán

F.D.5 Sub-milliwatt and tunable optical power limiters using vanadium dioxide in ultra-compact silicon waveguides

Jorge Parra, Juan Navarro-Arenas, Jean Pierre-Locquet, Pablo Sanchis

13:15 to 14:30 LUNCH

14:30 to 16:00 **PROGRAMMABLE PHOTONICS (Room: 3.0.3)**

Session Chair: David Marpaung, University of Twente

F.E.1 Does the world need general-purpose programmable photonics - INVITED

Wim Bogaerts, Ghent University - IMEC, Belgium



- F.E.2 Multi-channel free-space optical communication between self-configuring silicon photonics meshes**
SeyedMohammad SeyedinNavadeh, Maziyar Milanizadeh, Francesco Zanetto, Vittorio Grimaldi, Christian De Vita, Giorgio Ferrari, David A.B. Miller, Andrea Melloni, Francesco Morichetti
- F.E.3 6-mode Universal Photonic Processor fabricated by Femtosecond Laser Writing**
Ciro Pentangelo, Francesco Ceccarelli, Simone Piacentini, Riccardo Albiero, Simone Atzeni, Andrea Crespi, Roberto Osellame
- F.E.4 A high-index SiON integrated photonic-electronic platform for quantum technologies**
Mher Ghulinyan, Martino Bernard, Gioele Piccoli, Matteo Sanna, Massimo Borghi, Stefano Azzini, Fabio Acerbi, Giovanni Paternoster, Alberto Gola, Lorenzo Pavesi, Georg Pucker
- F.E.5 A Universal 20-mode Quantum Photonic Processor**
Caterina Taballione, Malaquias Correa Anguita, Michiel de Goede, Pim Venderbosch, Ben Kassenberg, Henk Snijders, Narasimhan Kannan, Devin Smith, Jorn Epping, Reinier van der Meer, Pepijn W. H. Pinkse, Hans van den Vlekkert, Jelmer J. Renema

14:30 to 16:00 INTEGRATED PLATFORMS FOR VISIBLE & XUV (Room: De Donato)

Session Chair: Giuseppe Cusmai, Advanced Fiber Resources

- F.F.1 Integrated distributed feedback (DFB) perovskite lasers in SiN waveguide platform**
Federico Fabrizio| Piotr Cegielski, Manuel Runkel, Saeed Goudarzi, Cedric Kreuzel, Bartos Chmielak, Lyudmila Staroduptceva, Dmitry Dirin, Viktoriia Morad, Maksym Kovalenko, Thomas Riedl, Max Lemme
- F.F.2 TiO₂ channel waveguides with 0.5 dB/cm propagation losses**
Alvaro Aguirre Fontenla, Ward .A.P.M. Hendriks, Meindert Dijkstra, Sonia M. Garcia-Blanco
- F.F.3 Integrated Amorphous-Silicon Photodetector on Silicon Nitride Waveguide**
Christian De Vita, Fabio Toso, Natale Giovanni Pruiti, Charalambos Klitis, Giorgio Ferrari, Marc Sorel, Andrea Melloni, Francesco Morichetti
- F.F.4 Low-noise near-ultraviolet photonic integrated lasers**
Anat Siddharth, Thomas Wunderer, Grigory Lihachev, Andrey S. Voloshin, Camille Haller, Rui Ning Wang, Mark Teepe, Zhihong Yang, Junqiu Liu, Johann Riemensberger, Nicolas Grandjean, Noble Johnson, Tobias J. Kippenberg
- F.F.5 Low-loss chemical mechanically polished Al₂O₃ thin films for UV integrated photonics**
Soheila Mardani, M. Dijkstra, W.A.P.M. Hendriks, M.P. Nijhuis - Groen, S.M. Garcia-Blanco
- F.F.6 Femtosecond Laser Micromachining of Integrated Hollow-core Waveguides for High-order Harmonic Generation and XUV Filtering**
Pasquale Barbato, Gabriele Crippa, Anna Gabriella Ciriolo, Michele Devetta, Caterina Vozzi, Salvatore Stagira, Valer Tosa, Roberto Osellame, Rebeca Martinez Vazquez

16:00 to 16:30 COFFEE BREAK



16:30 to 17:30 KEYNOTES F.K.2 (Room: 3.0.3)

Session Chair: Charles Baudot, Ciena Corporation

F.K.2 Advances and trends of Si photonics

Laurent Vivien, isheng Rong, CNRS and Univ. Paris Saclay, France

F.K.3 History and perspectives of an InP-based generic foundry approach

Meint Smit, TU/e Eindhoven University, Netherlands

17:30 to 18:00 CLOSING CEREMONY & AWARDS

Exhibitors

Thursday & Friday

Room 3.0.1, 09:00 to 18:00



Télefo S.p.A. was founded in 1986 with the purpose of representing and distributing components and instrument to the Italian optical and telecommunication markets. The activity is based on an agreement between the manufacturer and the company, entitling the latter to act on an exclusive basis throughout Italy. The company's goals are: to bring the best products onto the Italian market, to serve as a vehicle for updating technology and to be available to all its Italian customers as a reference for all kinds of information. In order to succeed we are particularly aiming on knowledge, service and product quality.



As the pioneer and market leader in high-precision additive manufacturing, we are your reliable partner for microfabrication systems, software, and solutions. We are a vibrant, award-winning company and a BICO company since June 2021. More than 3,000 system users are driving future-shaping applications with over 1,300 peer-reviewed journal publications. Our latest innovation is the Quantum X align – Best-in-class 3D printer with nano-precision alignment system and the first 3D printer with advanced 3D alignment capabilities that enables the printing of freeform microoptical elements directly onto optical fibers and photonic chips, setting new standards in the design and fabrication of microoptical elements. Auto-aligned 3D printing significantly reduces complex chip-level mode field tuning, eliminates active alignment and enables novel and unprecedented use of freeform microoptics at optical interfaces.



The Synopsys Optical Solutions Group provides design tools that model all aspects of light propagation for high-accuracy optical product simulations and visualizations. With intelligent, easy-to-use solutions and an expert support team anchored by optical engineers, Synopsys helps organizations deliver superior optics to market faster. Learn more at our website. Our Products: Optical Design Solutions: LightTools, Code V, LucidShape, RSoft, Scattering Measurements, Engineering Services



AFR Milan is part of AFR, a leading provider of optical components, designed mainly for telecommunication, fiber laser, data center, autonomous vehicle, fiber sensor and bio-medical equipment applications. AFR Milan is dedicated to design, develop and manufacture bulk and Thin Film Lithium Niobate components and modulators. AFR Milan facility, including R&D labs, state of the art wafer fab and module line is situated in San Donato Milanese, Italy.



sm-optics invests in technology development to create and deliver value based solution consolidating today's network into a solid base to build upon. sm-optics liaises over the consolidated Software capabilities and over 20 years experience to facilitate customer vision of the future into today's network reality.



LIGENTEC is a Swiss based manufacturing partner, offering low loss SiN Photonic Integrated Circuits (PICs) for industries such as Quantum technologies, LiDAR, Communications, Space and Sensors. Due to its high confinement, the thick nitride waveguides and resonators have low bending losses and excel even in high power applications from the visible to the mid-IR. The main application areas for this advanced silicon photonics low loss technology include coherent telecommunication, LiDAR, metrology, supercontinuum generation, spectroscopy, sensing and microwave photonics. LIGENTEC's All Nitride Core Technology platform is fully CMOS compatible, thus allowing us to offer ramping up to high volumes benefiting from the scale of the semiconductor industry.



VLC Photonics is a world leading engineering company offering full range of services for the development of Photonic Integrated Circuits (PICs), with a focus in design in testing. Current service portfolio includes: techno-economic feasibility studies and consultancy, in-house PIC design, characterization and test, and full PIC prototyping through external manufacturing and packaging/assembly partners. VLC Photonics, as a pure-play fabless design house, works with multiple foundries embracing the generic integration model. VLC Photonics has expertise in all the main Photonic integration technologies, including Silicon-on-insulator, Silica/PLC, SiN/TripleX, InP/GaAs. VLC Photonics also works closely with foundries to contribute to the building of their Process Design Kits (PDKs), allowing external users to easily access their manufacturing capabilities. Since 2020, VLC Photonics is part of Hitachi, Ltd.



**POLITECNICO
MILANO 1863**

At VPIphotonics, we believe in empowering you to define the cutting edge. We do this by providing software that is integrated, interoperable and industry-leading. We provide professional simulation software for photonic devices and waveguides, optoelectronics, integrated photonics and fiber optics applications, optical transmission system and network applications. We also deliver comprehensive training courses and provide consulting services addressing customer-specific design and configuration requirements. VPIphotonics partners actively with leading international companies and institutions in various private and publicly funded research projects. Our University Partner Program supports research and education at hundreds of universities worldwide. We offer award-winning simulation tools that are cited in over 1550 technical conference and journal papers. Visit our website and contact us today for a free software demo and evaluation



Raith is a leading precision technology manufacturer for nanofabrication, electron beam lithography, FIB SEM nanofabrication, nanoengineering, and reverse engineering applications. Customers include universities and other organizations involved in various fields of nanotechnology research and materials science – as well as industrial and medium-sized enterprises that use nanotechnology for specific product applications or produce compound semiconductors. Founded in 1980 and headquartered in Dortmund, Germany, Raith employs more than 250 people. The company works as closely as possible with customers in the most important global markets through subsidiaries in the Netherlands, the USA, and Asia and through an extensive partner and service network.



CORNERSTONE is an open source, license free silicon photonics rapid prototyping foundry based in the UK. The prototyping platform utilises industrially-compatible deep-UV projection lithography to enable seamless scaling-up of production volumes, but also retains device level innovation capability using high-resolution e-beam lithography and flexibility in its process flows. This process versatility and open source, license free model is what differentiates CORNERSTONE from other foundries. Currently CORNERSTONE offers three different silicon-on-insulator platforms, a silicon nitride platform, as well as suspended-silicon and germanium-on-silicon platforms for mid-infrared applications, all via a multi-project-wafer service.



ficonTEC is a recognized market leader for automated assembly and testing systems for high-end optoelectronic components, photonic devices and photonics integrated circuits. Considerable process capability and dedicated technologies have been accumulated in serving the needs of a broad selection of industry segments – including telecom, datacom & 5G, high-power diode laser assembly, sensing from bio-med to automotive lidar, micro-optics, and much more. ficonTEC's flexible and scalable automation options enable customized assembly and test solutions suitable for early device development, for new product introduction (NPI), and all the way up to high-volume production facilities for contract manufacturing or for in-house corporate R&D and production. Today, with a global installation base totaling some 1000 machines, each one is the automated and optimized embodiment of a customer-defined process.



LioniX International is a leading global provider of customized microsystem solutions. We have driven technological and commercial development in our specialist fields—photonic integrated circuits and MEMS—since 2001. As a vertically integrated company, we work across all stages of the production process from design to delivery of a finished module. And with world-class fabrication facilities, we scale production volumes as your requirements grow. Our strength lies in the service we provide as well as the creativity of our problem solving. By building a project team with you at the center and by asking the right questions, we make sure to deliver solutions that not only solve a problem, but drive your business.



Thorlabs, a vertically integrated photonics products manufacturer, was founded in 1989 to serve the laser and electro-optics research market. As that market has spawned a multitude of technical innovations, Thorlabs has extended its core competencies in an effort to play an ever increasing role serving the Photonics Industry at the research end, as well as the industrial, life science, medical, and defense segments. The organization's highly integrated and diverse manufacturing assets include semiconductor fabrication of Fabry-Perot, DFB, and VCSEL lasers; fiber towers for drawing both silica and fluoride glass optical fibers; MBE/MOCVD epitaxial wafer growth reactors; extensive glass and metal fabrication facilities; advanced thin film deposition capabilities; and optomechanical and optoelectronic shops.

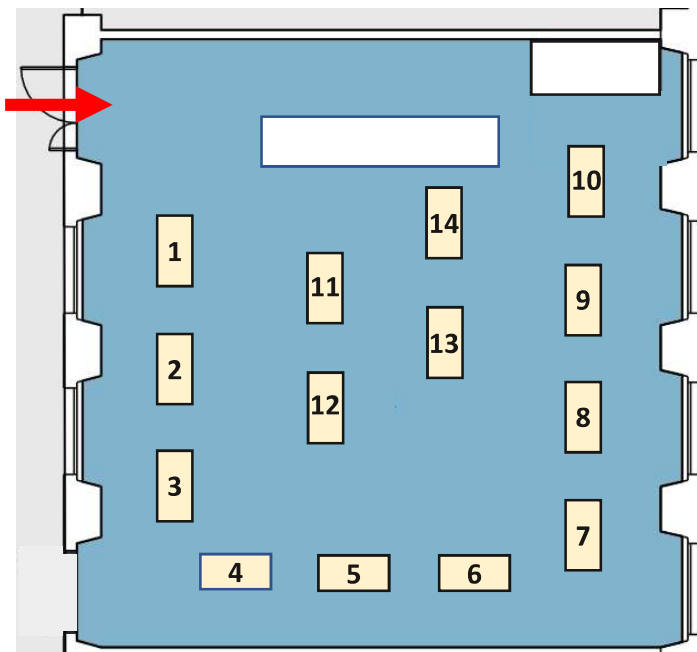


Universitat Politècnica de València (UPV) is a leading Spanish university with world-wide reputed groups in: tele/datacom, instrumentation, environmental sensing, chemistry, bio/life sciences, food & drug analysis among other. Former solar cell manufacturing company Siliken established a 500 square meters class 100-10000 (ISO-5/7) 6" MEMS pilot line clean room at Ciudad Politécnica de la Innovación – UPV. After Siliken stopped operations, UPV owns the clean room which was operated by industrial agents since 2015. From 2018, the clean room is operated by UPV personnel as UPVfab. The cleanroom facility is current part of the research infrastructure by the Institute for Telecommunications and Multimedia Applications (iTEAM) and the Instituto de Tecnología Química (ITQ).



iPronics, Programmable Photonics is a spinoff company from the Universitat Politècnica de València, Spain. iPronics develops the innovative concept of Field Programmable Photonic Gate Arrays (FPPGAs), which are based on a common optical hardware configurable through software to perform multiple functions. iPronics contributes to the development of future information processing systems where electronics and photonics work cooperatively by synergistically exploiting the best capabilities of each technology. It brings the added value of optical reconfigurability to products with broad fields of application including 5 and 6G telecommunications, data center interconnection, artificial intelligence, signal processing, sensing and quantum information.

Exhibition Room 3.0.1



1. Telefo
2. Nanoscribe
3. Synopsys
4. AFR Milan
5. smOptics
6. Ligentec
7. VLC
8. VPIphotonics
9. Raith
10. Cornerstone
11. ficonTEC
12. LioniX
13. Thorlabs
14. UPVfab

Exhibitors Session

Thursday, 5th May 2022

Room 3.0.2, 13:45 to 15:45

13:45 InSpek

13:55 LIGENTEC

14:05 LioniX

14:15 CORNERSTONE

14:25 AFR Milan

14:35 ficonTEC

14:45 Nanoscribe

14:55 RAITH

15:05 iPronix

15:15 VPIphotonics

15:25 VLC PHOTONICS

15:35 SYNOPSYS

Sponsors



ficonteC
micro assembly machines



smoptics
siae microelettronica group

Supported by



JePPiX
Platform for Photonic Integration



POLITECNICO
MILANO 1863



Milano



Comune
di Milano



EUROPEAN
CONFERENCE ON
INTEGRATED OPTICS

The proceedings of this conference will be archived at:
<https://www.ecio-conference.org/previous-editions/>

High-density Integrated Photonic Tensor Processing Unit with a Matrix Multiply Compiler

(Plenary Speaker)

Xiaoxuan Ma¹, Nicola Peserico¹, Ahmed Khaled³, Zhimo Guo³, Bhavin J. Shastri³, Volker J. Sorger^{1,2*}

¹Department of Electrical and Computer Engineering, 800 22nd St. N.W. George Washington University, USA

²Optelligence Company, 10703 Marlboro Pike, Upper Marlboro, 20702, USA

³Department of Physics, Engineering Physics Astronomy, Queen's University, Kingston, ON K7L 3N6, Canada

* corresponding author e-mail: sorger@gwu.edu

The explosion of artificial intelligence and machine-learning algorithms, connected to the exponential growing of the exchanged data, is driving a search for novel application-specific hardware. Among the many, the photonics field appears to be in the perfect spotlight for this global data explosion, thanks to its almost infinite bandwidth capacity associated with limited energy consumption. In particular, Photonic Integrated Circuits (PICs) capable of performing Matrix-Vector Multiplication (MVM) operations have been shown as a tangible alternative to the common electronic CMOS processors. These PICs integrate several hundreds of optical components in a single chip, operating at GHz speed. In this paper, after an initial review of the main types of PIC architectures for artificial intelligence, we present our microring-based solution, that allows performing MVM with tunable weight matrix, and its use as processor for image filtering.

Keywords: Silicon Photonics, Matrix-Vector Multiplication, Photonics, PICs, Tensor Core

1. INTRODUCTION

The increasing amount of data processing in recent years has pushed the processing performances to the limit of actual microprocessor architectures [1]. As the limit of Moore's Law is approaching, capping the number of transistors per area, the limitations on the actual architecture would lead to larger and larger data centers, raising concern about safety and energy consumption [2]. The increased use of Artificial Intelligent (AI) and Machine-Learning algorithms [3], [4], in particular Deep Neural Networks (DNNs) [5], puts pressure on the current CPU with tasks whereby they are not designed for, like the Matrix-Vector Multiplication (MVM) [6]. In a typical DNN algorithm, each neuron receive inputs from every neuron of the previous layer, and weight them before passing through an activation function [7]. This weighting is performed as a dot-product between input and weights vectors, and by so, could be generalized into a MVM for all the neurons of a layer, making this MVM task crucial for the performance of the AI algorithm [8]. New solutions, called Tensor Cores, are rising, proposing new paradigms to achieve higher performances in terms of speed, throughput, and energy efficiency [9]–[12]. Among many, photonics solutions have been raised as one of the major candidates thanks to the intrinsic behavior of electromagnetic waves [13], which allow performing inference at zero energy cost, as well as the high bandwidth, and the possibility to integrate all the components into a single chip, known as Photonic Integrated Circuits (PICs) [14]–[17]. In the recent years, several different PICs have been proposed to perform the MVM task, known as Photonic Tensor Cores (PTCs) [13], [18]–[23]. Implementations with different approaches and components have taken the stage and shown better results than corresponding electrical counterparts, in terms of speed and energy efficiency [24]. Moreover, taking advantage of the flexibility on the fabrication side, PICs have been integrated with various materials to support either higher speed (using high speed Si-Ge photodiode for example [25]), or nonvolatile memories using Phase Change Materials [26]–[29]. In this paper, we will present an overview of the main approaches on performing the MVM task on PICs, comparing the implementations and architectures that have appeared in the latest years. We will then present our configuration [13], showing the main advantages and the integration level achieved by the silicon photonics PIC. By using the General Matrix Multiply (GeMM) compiler to subdivide matrices into smaller ones that are compatible with our fabricated device, we will show image processing result using our PIC.

2. RESULTS

Photonic Integrated Circuit for MVM

As mentioned previously, the light has been one of the main candidates for performing the MVM function on future

4 - 6 May 2022 - Milano, Italy - 23rd European Conference on Integrated Optics

computing architectures. In particular, considering the MVM main function, the multiply and accumulate (MAC) function benefits from the coherent electromagnetic nature of the light, implying the possibility to perform multiplication by lossless interference, while the accumulation is performed directly on the photodiode once light signals are collected. By allowing manipulation of light employing nanoscale waveguides, PIC can integrate a large number of MAC operations on small scale, employing a high number of inputs, high-speed modulators, and photodetectors. To perform the MAC function, several different approaches have been proposed during the latest years, by varying the basic components elements, as well as the input and output configurations. Those different architectures show different performances, in terms of actual speed (measured as MAC operations per second), footprint, energy consumption, and etc. By reviewing these approaches in PICs, we focus on the main difference among the architectures of the PICs. However, most of the most used parameters that are used to compare the PTC processor (such as MAC operations per second or footprint) are not included, as they depend mainly on both the modulators (for input vectors) and the photodiodes (for output vectors) technologies for each implementation, rather than from architecture choices. In a similar sense, it is more interesting to focus on common limitations, such as the number of controllers that each circuit requires, the footprint scaling, and the possibility to implement nonvolatile memory elements to further reduce energy consumption.

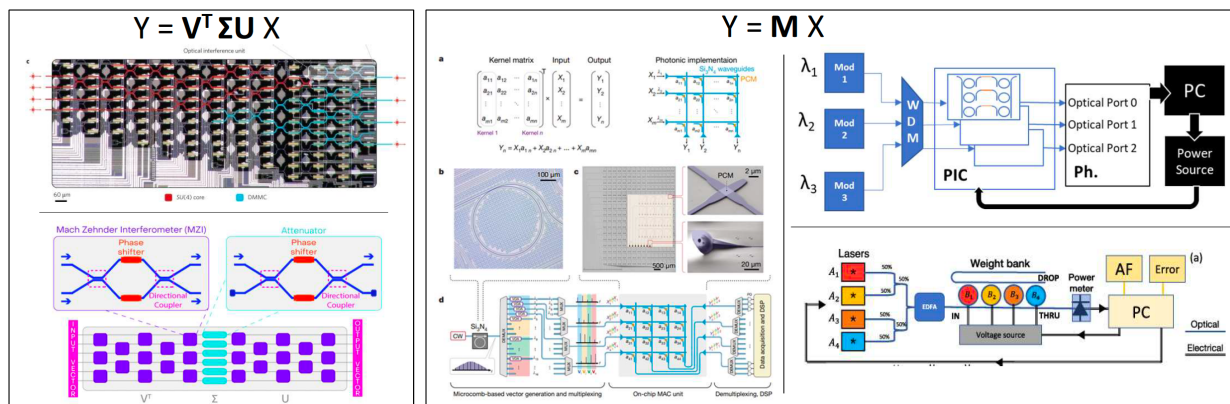


Fig. 1. Comparison of PTC hardware implementations. (Left) Exploiting the mathematical properties of the matrix singularization by dividing the main matrix into sub-matrices (e.g. 3) via of singular value decomposition [24]. (Right) Photonic algebra approaches leveraging parallelization (i.e. WDM) and incoherent accumulation (i.e. photodetection) [13], [21], [30]

A. Matrix-Vector Multiplication Approaches

As the first step, we divided the PIC into two main categories, based on the mathematical approaches for MAC operation: the first one relies on the singularization, where the main matrix is divided by the meaning of singular value decomposition into 3 matrices; the second approach avoids this decomposition, by implementing schemes that directly implements the main matrix. In fig. 1 examples of both approaches are shown, while a comparison of the major parameters is made in table I.

1) $Y = V^T \Sigma U X$: Exploiting the mathematical proprieties of the matrix single value decomposition (SVD), the implementation of this approach has focused on using cascaded Mach-Zender Interferometers (MZIs) [18], [31], [32]. In particular, the external matrices V and U are unitary matrices, and by so implementation is straightforward by using inter- connected MZIs, while the diagonal matrix Σ is implemented by a series of attenuators, usually implemented by MZI. This approach has seen many results over the years, from mode demultiplexing [33], to proper larger networks [18], and final market-ready products [24]. The use of MZI networks comes with several advantages, like the ideality of the MZI response, even without perfect components [34], the coherent scheme that requires just one single laser to work, and the speed of reconfigurability allowed by the pull-down PN junction configuration of the MZI. Thanks to the reliability of the configuration and the single laser source, this approach already showed promising results and startups hit the market with solutions based on it. Moreover, even the bit resolution achieved takes advantage of this advanced state- of-the-art, reaching a high bit resolution, up to 10 bit. On the other side, this configuration comes with some limits, mainly due to the higher complexity behind SVD and the footprint required to fulfill this operation. Dividing the matrix requires a pre-computational step, as well as more components integrated into the PIC, increasing the complexity of the whole architecture.

2) $Y = MX$: Many architectures that are based on this approach appeared in the latest years, mostly exploiting multiple input lasers sources and their WDM combinations at the photodiodes. In particular, all the implementations rely on an attenuation mechanism to implement the multiplication part, while the combination of multiple wavelengths at the photodiode returns the sum of incoming light beams. One implementation exploits PCM-actuated couplers between rows and columns of an optical waveguide grid [21]. Each wave-length coming from a unique Comb laser source is modulated and fed into a certain row. The tunable couplers bend a certain amount of the incoming light toward the selected column. The photodiode at the end of the column collects the composition of the different light beams, whose amplitude is determined by the couplers. This scheme relies on the simplicity of the implementation that reduce the number of controllers to the minimum (equal to the size of the matrix), and implementing them with PCM allows having almost 0 energy cost, but limits the speed of reconfiguration.

A. Architecture Comparison

As seen, many different architectures could be used to implement MVM, as summarized in table I. In the table, actual Figure-of-Merit MAC/s nor MAC/J is not reported, as for all the architectures, it will mainly rely on the inputs modulator

Type of Operation	$Y = V^T \Sigma U X$ 		$Y = MX$ 	 [This work]
Input	1 Laser, N Modulators	1 Comb Laser, N Modulators	N Lasers, N Modulators	N Lasers, N Modulators
Outputs	M(=N) Photodiodes	M Photodiodes	M or 2*M Photodiodes	M Photodiodes
Area/Basic Element Area	$N^2 + N$	$N \times M$	$N \times M$	$N \times M$
Controllers	$2N^2 + N$	$N \times M$	$2(N \times M)$	$N \times M$
Parallelization	No	WDM Off Chip	WDM On Chip	WDM On Chip
Weight Bit Resolution	8/10	5	>5	5
P-RAM	No	Yes	No	Yes

Table I. SCALING COMPARISON OF VARIOUS APPROACHES ON PERFORMING GeMM AND MAC OPERATIONS USING PHOTONIC CHIP-BASED COMPONENTS. N = SIZE OF INPUT VECTOR; M = SIZE OUTPUT VECTOR; P-RAM = PHOTONIC RANDOM ACCESS MEMORY, ALLOWING FOR ZERO-STATIC POWER CONSUMPTION, ONCE THE WEIGHTS ARE SET.

The second implementation uses the add-drop microring resonators as the element to perform the multiplication as attenuation of the incoming light beam [19], [22], [30]. Microrings permit the use of the same elements as WDM combiner by simply cascading them. The use of microrings allows for an important footprint reduction (microring using SiPh could be downsized to a $10 \mu\text{m}$ radius) while having high-speed reconfiguration thanks to the internal pn junction, that nowadays could reach more than 25 GHz. Moreover, thanks to the add-drop configuration, the architecture could have both positive and negative sign weights in the matrix, without the need for post-processing to correct the data. The main disadvantage is coming from the control perspective, as microring tends to be asensitive element towards noise sources, such as temperature variation, stress, and so on. By so, besides the modulation controlling the pn junction, another signal must be applied to the heater to assure a perfect alignment between microring's resonance and laser's wavelength, doubling the number of controls. Moreover, due to this high integration and need for resonance stabilization, PCM elements could not be placed in the ring itself, making this architecture not suitable for low-energy applications, such as edge computing. The last architecture is the one used in this paper and combines a different placement of microring elements [13]. This architecture takes advantage of the add-drop microring as the element to fan-out the WDM inputs and recombine them after attenuation is applied in the waveguide link between them. This architecture has the advantage to be able to use both PCM, slow-speed heater-based components, and high-speed pn junction to achieve the required attenuation, by so fulfill the requirement of both edge computing application and data centers one. The number of controls could be high in principle (up to 3 controllers for each element of the matrix), however, by relying on the fabrication quality and accepting a reduction of the resolution, the control could be reduced to just an attenuator per element of the matrix. More details will be given later in the paper. and output photodiodes, whose characteristics are coming from the fabrication process rather than the component used to perform the MAC operation. One parameter that influences the choice for the architecture is the chip footprint. The basic $Y = MX$ architecture seems to take advantage of the more direct equation, as scaling is proportional to the matrix size, while the MZM approach suffers from the decomposition matrices. For the number of controls, the best solutions appear to the one based on couplers and coupled microrings, even if this last one might be affected by the detuning of the microrings, as we discuss later in the paper. The architecture based on single add-drop microrings could either have the same $M \times N$ controllers, if just one tuning method is used (for example employing heaters as tuning element and weight), but to support high-speed reconfiguration each microring needs to integrate both a trimming method (i.e. heaters) and a high-speed tuning (i.e. the pn junction), doubling the number of controls. The lack of need of tuning for the coupler architecture comes at the cost of a more complex input that requires a comb laser and a WDM mux, and demux external to the chip for the output, increasing the complexity of the overall system. Bit resolution shows a strong point for the architectures based on MZM, for mainly two reasons: the more straightforward capability on controlling the phase difference in the MZM, resulting in a larger ER, and so larger bit resolution; the

advanced stage of the products based on this technology that already reached the market, so having passed the optimization process. The last piece of confrontation is regarding the possibility to implement P-RAM on the circuits, by using Phase Change Materials (PCMs) for example. In a larger view, as more and more MVM circuits will be used to implement DNN, having the possibility to integrate photonic memory elements would have a crucial benefit in terms of energy efficiency. That would allow targeting edge computing applications, rather than just cloud application in data centers. Up to our knowledge, just two architectures allow integrating the PCMs, placing those materials either in the couplers or between coupled rings. The architecture based on MZM could benefit in case a phase- only PCM would be presented, as most of the materials are now affecting adsorption too, such as GSST, GSSE, or GST. Integration of PCMs into microring resonator might be challenging for the same reason, adding also a problem of cross-heating interference, as tuning element could affect the phase of the material, resulting in an unwanted switching.

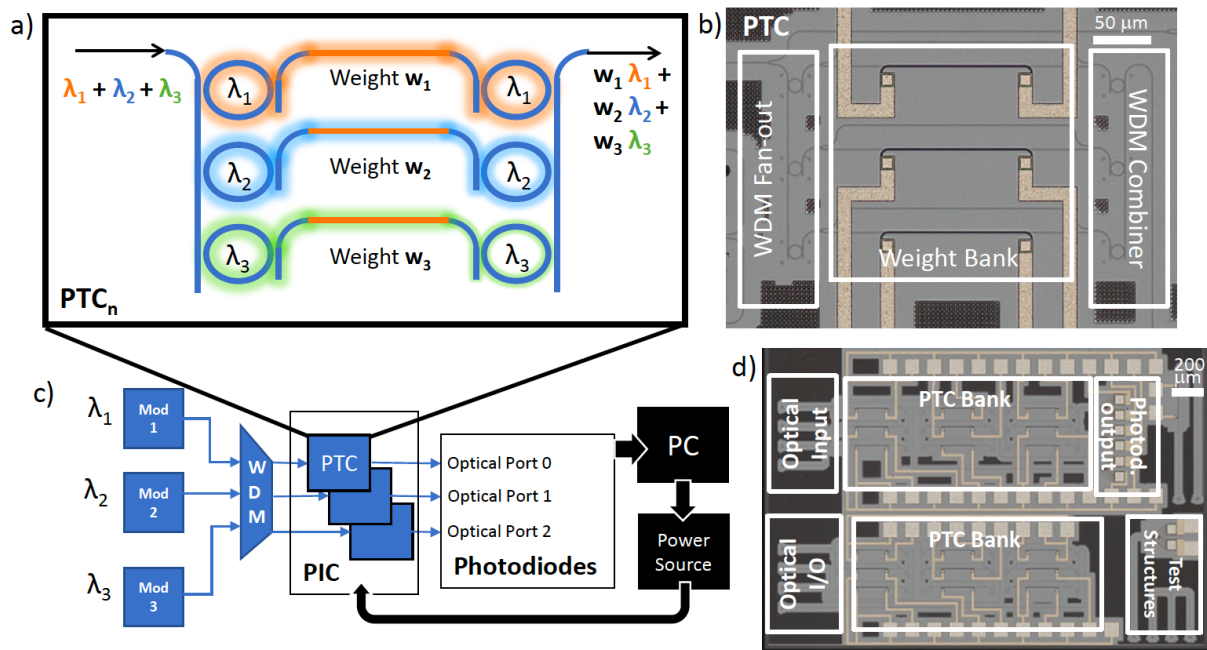


Fig. 2. a) Schematic of silicon photonic tensor core. b) Microscope image of the photonic tensor core, which includes WDM fan-out, weight bank, WDM combiner. c) Schematic of testing setup. d) Microscope image of the photonic tensor core chip, which including PTC without on-chip photodiode version and PTC with on-chip photodiode version.

3. INCREASING MAC DENSITY: COUPLED-RINGS, INTEGRATED DETECTORS PIC SOLUTION FOR GEMM COMPILER

The architecture presented in this paper is based on coupled add-drop microring resonators. The structure is modular, as one PTC can perform a dot-product, and so MVM can be achieved by parallelization of the single module. An array of lasers is modulated with the input vector values, combined by a WDM mux, and fed into the silicon photonic chip. The input is then distributed to every single PTC module by a series of splitters. In each module, the first series of microring act as WDM demux, each arm followed by an optical attenuator, implemented with adsorption PCM, MZI, or VOA, acting as the multiplication part of the dot product. The recombination is performed by the second series of microring, as a WDM combiner, so the output is the accumulation of the different wavelength sources scaled by the weights, as shown in figure 2a-c, performing the MAC operation we expect. The modularity of the structure allows to size the circuit based on the need, having a PTC bank, reducing the number of components and complexity for edge computing applications if needed.

A. Photonic Integrated Circuit

The PIC presented has been fabricated using an active silicon photonics process by AMF [35]. The waveguide is 220 nm height, 500 nm width channel waveguide. WDM fan-outs and combiners are made by a series of three passive microring resonators, whose radii are around 10 μm , with minimal variations to avoid overlapping in the resonance. The weights are implemented by MZIs, each having a heater element on one of the two arms. To minimize thermal crosstalk between weights, the MZIs are placed more than 100 μm apart. The choice of using MZI was due to compactness, high Extinction

Ratio (ER, >20 dB), and yet simplicity: using VOA would result in a larger footprint, while MRR or PCMs would have smaller ER (<5 dB) and would increase the complexity. Each PTC is formed by three PTC modules to implement a full 3x3 MVM. The PTC has been repeated 2 times, having optical outputs for the first one, and integrated photodiodes for the second one. The spectrum of one PTC is shown in figure 3a, while figure 3b shows a section with the 3 peaks for each output port. Outputs from one optical port while changing the heating power at the arm of MZI are shown in figure 3c, reaching more than 20 dB ER for each weight. The choice of not using any tunable element on the microring resonators responsible for the WDM fan-out and combiner leads to a simpler and more compact circuit, having fewer elements to pilot and a lower number of electrical pads. On the other hand, the cost is a lower ER for the system. Even if the microring is placed nearby, and so reducing the fabrication variability, a slight mismatch of resonance can be seen in the optical power spectrum, for example for the Optical Port 1 at λ_1 in figure 3b. This manifests as a reduction of the ER usable for the weights, comparing to the initial values provided by the MZI, as all the paths must have the same maximum and minimum power output. In figure 3c, the usable ER is then reduced to around 15dB, from the more than 25 dB provided by the MZI. The reduction of ER is directly translated into a reduction of bit resolution, limiting the performance of this architecture for high-bit resolution applications.

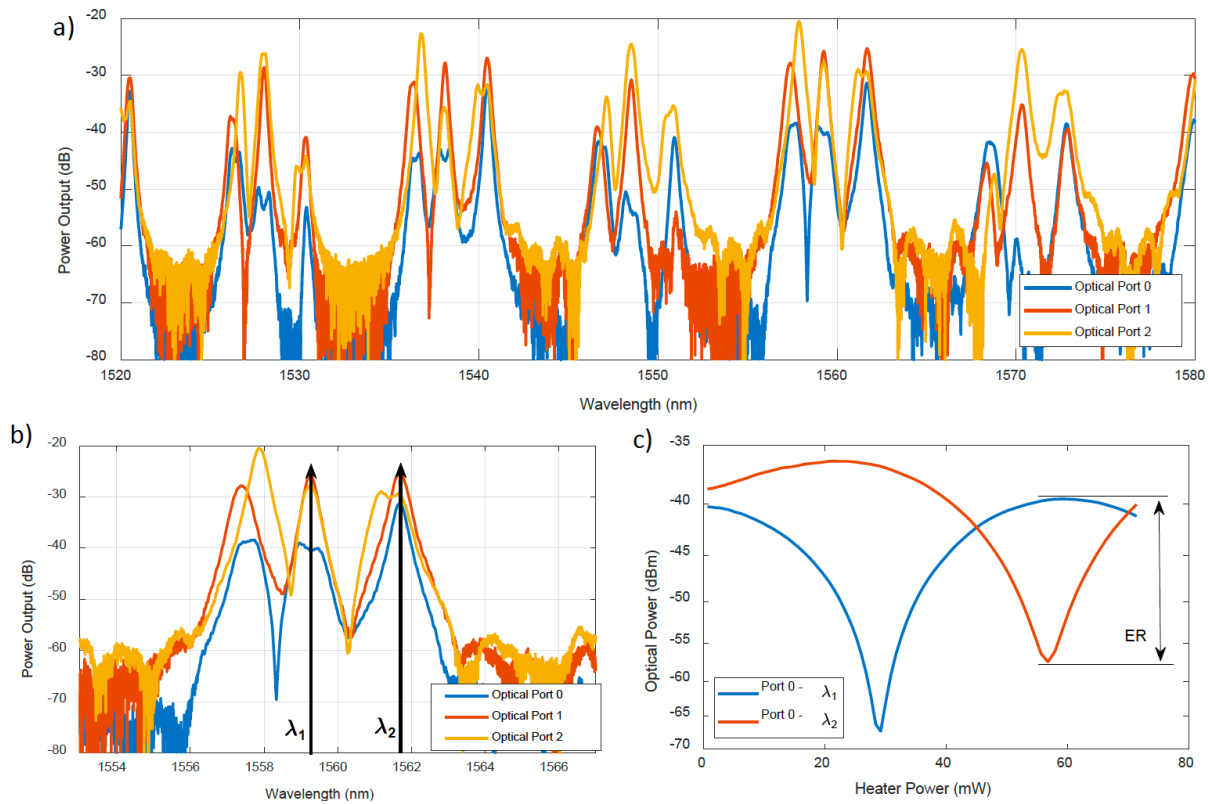


Fig. 3. a) Optical spectrum of the SiPh tensor core. b) Detail of the spectrum and the wavelength of the lasers. c) The performance of two thermo-optical MZI modulators used in Port 0 as weights. The selected ER is the operative range for that particular port, with a range suitable for both wavelengths.

A. Power Maps: Optical Output

For our experiment setup, we measure the circuit using 2 different lasers and varying the power dissipated by the heaters, as shown in figure 4a, providing an output that is the linear sum of the 2 modulated inputs multiplied by their weights. In particular, we use a fiber array to inject the combined laser sources into the PIC by a grating coupler and collecting the outputs by grating couplers. The output beams are then transformed into an electrical signal by a series of photodiodes, and send to a control PC. The PC is controlling the voltage sources to control the heater components of the PIC. In this framework, we expect the output power to look like the ideal power map in figure 4b when both inputs are modulated at their maximum power. This ideal map would result in perfect MAC operation, by so a perfect MVM from our PTC. In Figure 4c-e, we show the power maps obtained by one PTC having 3 modules. Since each weight is performed by an MZI, it is possible to see the non-ideal response of the map while varying the heaters' powers. In this case, to perform the proper mathematical function, we select a subset of the map that would mimic the ideal response.

As discussed before, due to the passive microring resonator used in our circuit and the non-linearity response of the MZI as attenuator, the ER is limited, while each heater span over a different range of power, limiting the resolution. Considering for example the map from port 0, the selection that better mimics the ideal response would have the λ_1 weight span from 55 to 20 mW, while the range of the second weight would be from 30 to 55 mW, causing a different resolution from the DAC that would provide the signal. Moreover, the round shape of the contours reflects the round shape of the MZI responses, by so creating a fixed error from the ideal mathematical response.

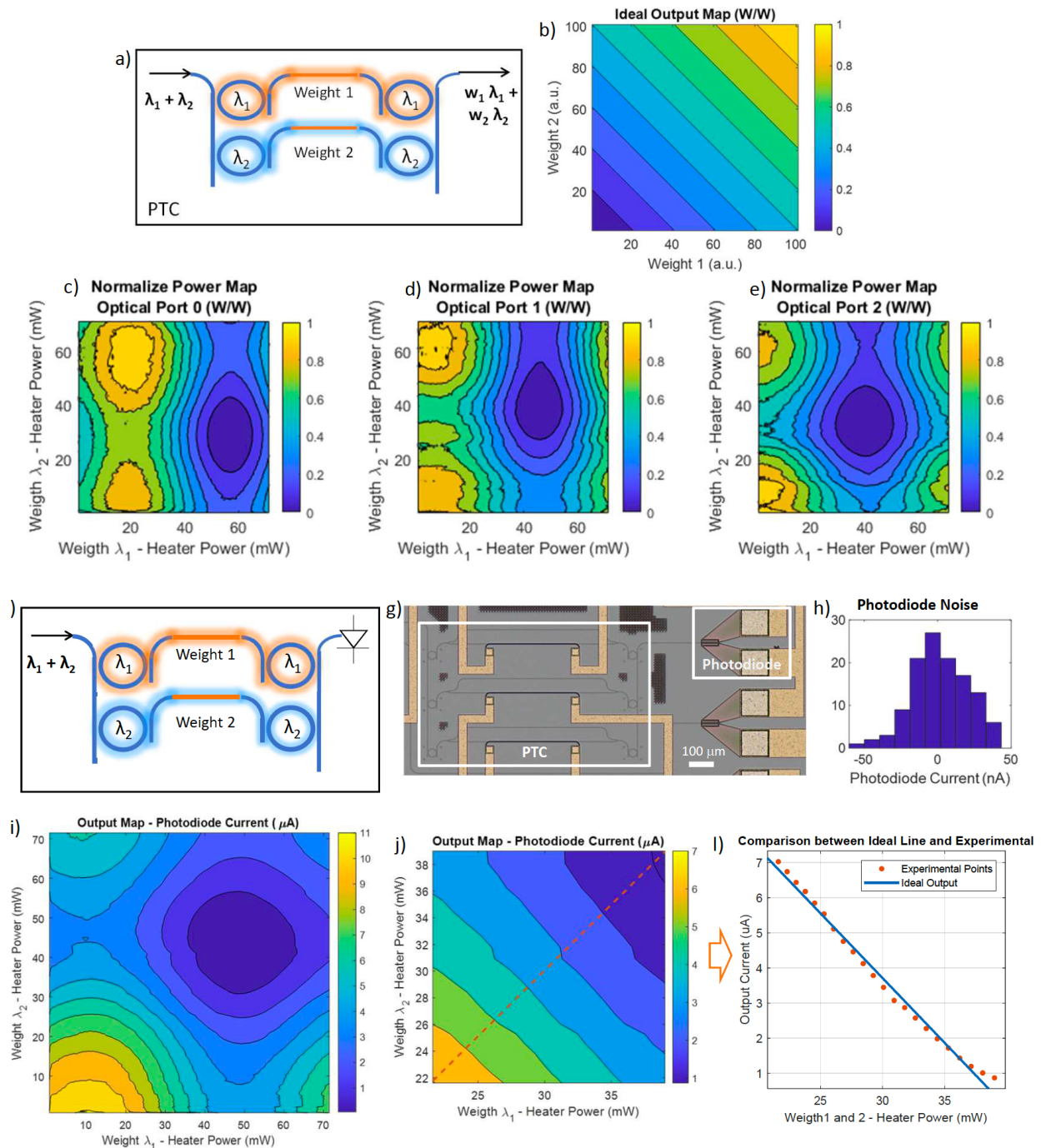


Fig. 4. a) Schematic of the SiPh tensor core without on-chip photodiode. b) Ideal output power map. c-e) The normalized output power map of port 0, port 1, and port 2. f) Schematic of the SiPh tensor core with on-chip photodiode. g) The detailed microscope image of SiPh tensor core with on-chip photodiode. h) Noise analysis of on-chip photodiode. i) Power map of one photodiode. j,l) The detailed power map of photodiode, which shows more linear performance.

In the same chip, we placed also a 3×3 PTC with integrated photodiodes as outputs of each PTC module. Figures 4f,g show the scheme and photo of the tested PTC, employing two of the three wavelengths inputs available. Having the integration of the photodiode reduces the noise due to the misalignment of the fiber array and provides more power, as coupling loss between the waveguide and integrated photodiodes is almost null. We measure one power map employing the photodiode at the output of the PTC module, as shown in figure 4i. In particular, the ER in terms of current is about 11 μA , while the shape is not so distorted compared to the previous power maps. In this case, it is easy to set a subset of the map that mimics the proper ideal power map. In figure 4j we select a subset spanning the power for around 20 mW on each weight. The result looks similar to the ideal map, having less distortion on the contour. However, by doing this we reduce the ER to 9 dB, losing half of the maximum ER achievable by the circuit. Given this ER and the noise of the photodiode, we can compute the maximum resolution achievable in terms of the number of levels, reaching a bit resolution of 5.9-bits. The linearity of the response is shown in figure 4l, as we extract the diagonal values of the selected subset of the power map and compared them with the ideal linear response. The result is showing a good overlapping of the two, with a variation that reflects the photodiode noise.

GeMM Compiler: Most of the tasks a PTC will execute will require a number of matrix elements that exceed the physical number of available matrix weights of the PTC itself. This is, incidentally, the case also for electronic counterparts, such as GPU or TPU etc. For example, for image processing, the typical 4K HD image could reach 3840×2160 pixels, exceeding the size all the possible Tensor core processors. To overcome the limitation, a mathematical approach can be used, called GeMM compiler [36], to reduce the size of the matrices by subdividing them. For example, for the Hadamard product, we can see the splitting of the main matrix and vectors into smaller ones in figure 5. By so, even our 3×3 PTC could compute larger MVM.

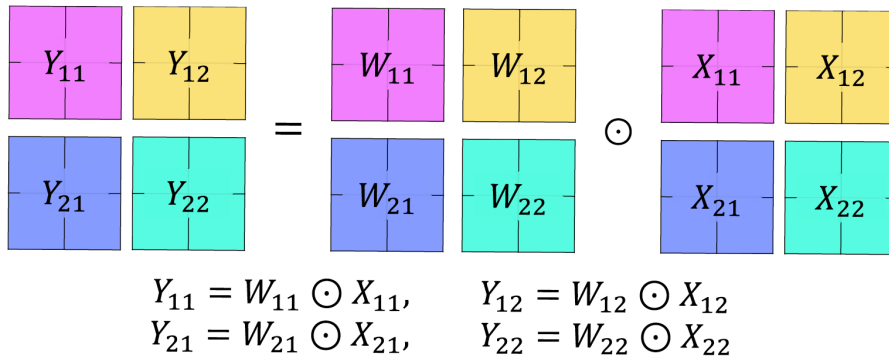


Fig. 5. GeMM Compilers offer virtualization to process input data matrices that are larger (i.e. more matrix entries) than the physical hardware (i.e. PTC) provides. The example illustrated here shows the Hadamard product approach.

GEMM Emulation Results: To test our PTC, we employ GeMM compiler for image processing, applying edge filters to B&W images. In the first set of results, we use the power map obtained with the PTC with the photodiode to emulate two different image filters: a 3-bit one for all-direction edge detection, and a 5-bit blur filter, starting from the B&W logo of GWU (threshold at 0.8) with dimension 316×183 pixels. The results for both filters are shown in figure 6, showing the ideal results computed by Matlab and the emulated results computed by the PTC. By counting all the pixels with wrong values comparing to the ideal one, we can estimate an error rate of 1.1% for the edge detection, and 5.05% for the blur filter.

GEMM Experimental Results: We proceed then to the experimental result by performing edge detection on a smaller version of the GW signature and a smaller section of GW image. To perform these measurements, we set the 2 wavelengths as shown in figure 3, extract the power map, and set the boundaries to minimize the difference between the experimental map and the ideal one. The input is defined as a 1-bit image, while the edge filter is a 3-bit matrix with negative values. To perform the computation, for each pixel the PTC computed the Hadamard product of the 3×3 filter and a 3×3 subset of the input image, using the GeMM compiler to fit the 2×1 PTC matrix. Since the filter has negative values, we divide the computation into two parts by adding an offset to the filter matrix and subtracting the same offset afterward. Both parts of the computation are done by the PTC to perform the correct procedure. For the first image (GW initials), we show the results with and without integrated photodiodes in figure 7c,d). Both experimental results demonstrate good agreement with the ideal one computed by Matlab. In this case, the error rate

for the PTC without the photodiode is about 5.9%, while the error rate for the PTC with integrated photodiode is 2.5%. For the GW logo, we show the raw data from the experimental results (figure 7g) and the one after threshold function is applied (figure 7h). This last one returns an error rate of 3.41%. As we have seen in the power map, the integration of the photodiodes improves the response of the overall PTC system, mainly thanks to the reduction of the noise, and the higher and more stable optical power reaching the photodiodes, as we avoid the losses and instability of the optical grating couplers as output couplers to the fibers. This is interesting because one might be tempted to believe that the solution with components of the shelf (COTS) and individually packaged dedicated hardware would be performing higher than micrometer-small chip-integrated solutions. While the raw performance of the COTS detector may still outperform that of the PIC counterpart, demonstrating a PTC is a system-level challenge rather than a component-level design optimization only. Indeed, future designs should take the system-level aspect into the foreground towards improving performance, reliability, and cost.

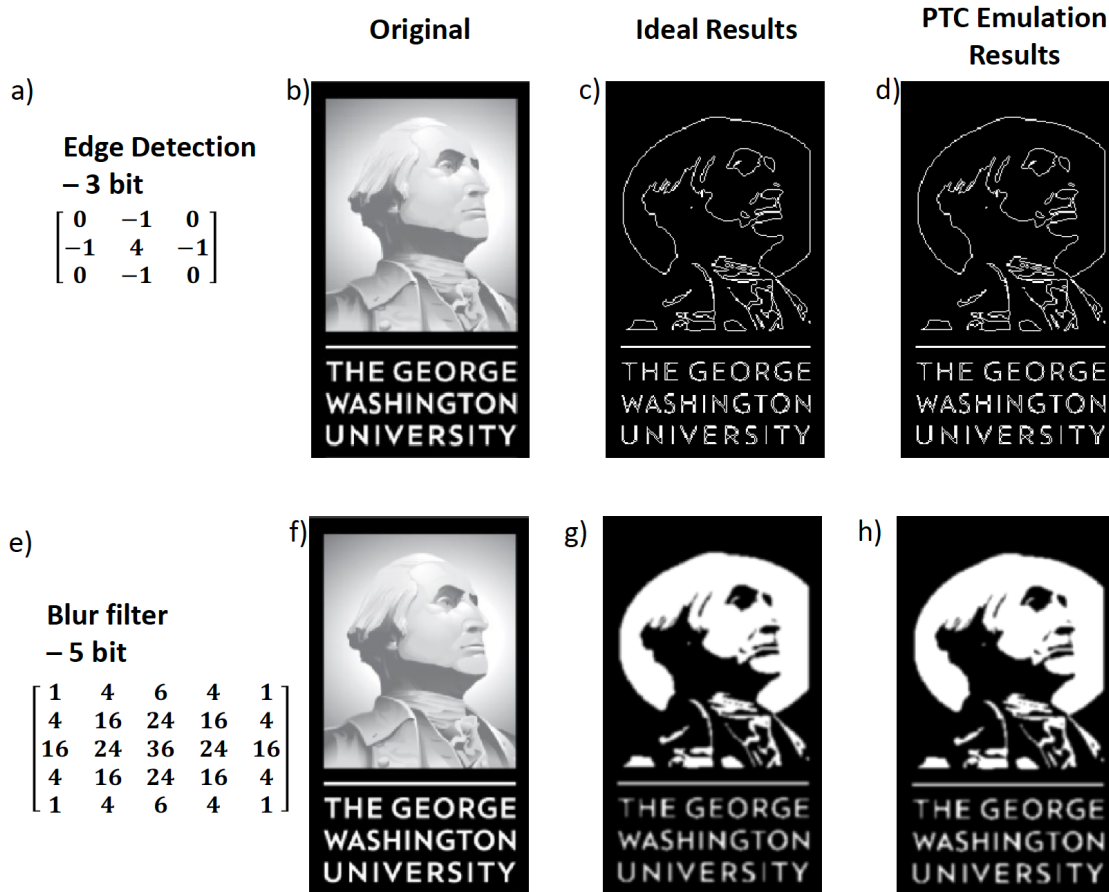


Fig. 6. 3-bit Edge detection (a) on a PTC for an input image (b) comparing an ideal result (i.e. mathematical edge filter) (c) with an emulated PTC results using the MAC performance from Fig. 4, obtaining an error rate of 1.1%. Similarly, a 5-bit blur filter (e) along with idea (g) and PTC-emulated (h) results showing, overall, a low error rate (5.05%).

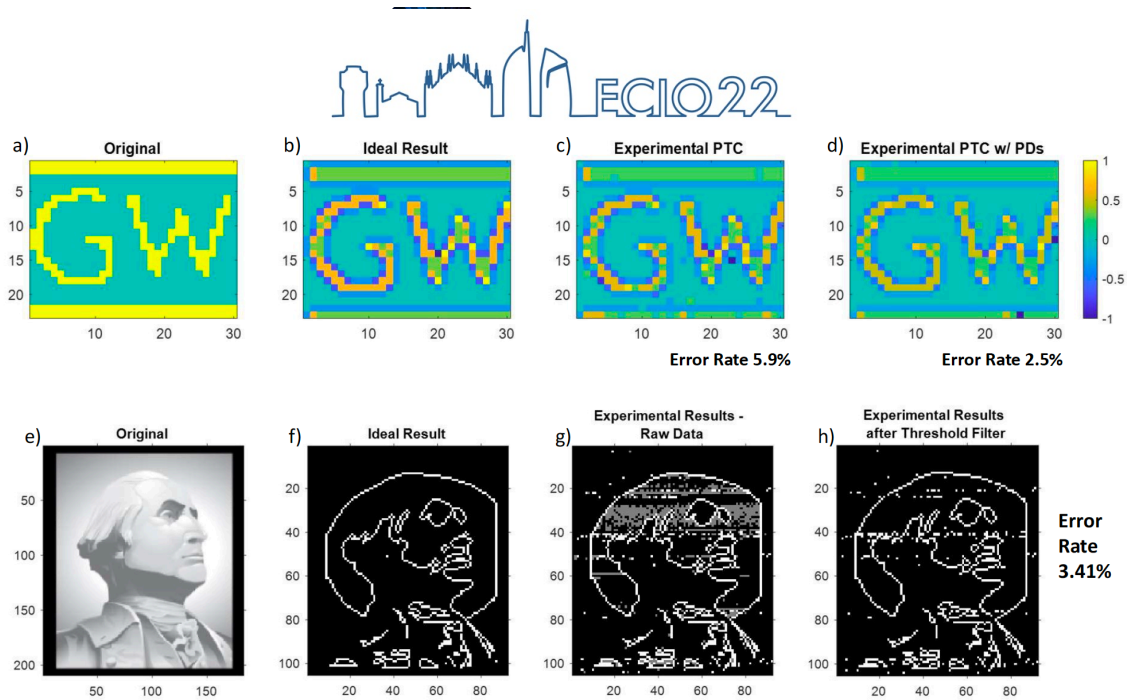


Fig. 7. On-PIC image filtering demonstration using a 3x3 photonic tensor core (PTC) processor and a GeMM compiler based on implementing the Hadamard product approach. (a)-(d): edge detection of the GW logo showing an about 2x improved error rate when the on-chip photodetectors are used on the PIC as compared to utilizing off-chip COTS components. (e)-(h) edge detection of the GW image showing good agreement for PTC with photodiodes also for larger and more complex images, with an error rate of less than 3.5%.

Conclusions

Similar to CMOS processors, machine learning accelerators also improve performance with integration density, and faster results can be achieved by adopting the photonics approach. Here we designed, manufactured, packaged and tested a photonic tensor core (PTC) to perform general matrix multiplication (GeMM) operations. Our approach utilized channel parallelization implemented via wavelength division multiplexing (WDM). The architecture and design exploits linear amplitude opto-electronic multiplication and on-chip analog accumulation to perform the on-chip MAC operation in the optical domain. This enables full-bit precision summation prior to the ADC digitization. To bring this novel design into context, performance improves significantly with chip integration, as indeed expected. By using a GeMM compiler performing the Hadamard product operation, we experimentally demonstrate the performance of the PTC with image processing, showing up to 5-bit resolution, and an error rate of about 3.41%. By implementing a faster weight update, the same architecture can be used for on-chip training for Machine Learning, taking advantage of the high-speed response of photonics performing the tasks required.

In summary, photonic chips can accelerate matrix-vector multiplications and hence machine learning or signal processing function directly on analog and/or light signals in the optical domain leading to an energy-efficient propagation-based multiplication operation, and full bit-precision summation operations. In addition, given the short time-of-flight and we present a comparison between various integrated photonic architectures performing Matrix-Vector Multiplication, highlighting scaling laws concerning the component complexity, footprint, bit resolution, and integration with photonic memory elements. We then present our architecture based on coupled add-drop microring resonators, having the flexibility to integrate high-speed weights as well as low-speed zero-energy consuming ones. The silicon photonic chip implementing this architecture has been presented in two variations, with grating couplers, and with integrated photodiodes as outputs. Interestingly, the PTC performance, tracked by the image filtering error rate, is higher using on-chip photodiodes as compared to dedicated stand-alone detectors off-chip; that is, despite a higher component performance, the noise from the electronic I/O is impacting the error rate. This suggests that system-level the 50GHz fast electro-optic modulation and photodetection speeds of integrated photonic components today, the latency and throughput for such electronic-photonic GeMM accelerators can be significant. The low latency, especially, can open new technological horizons on tracking rapid-moving objects at nanosecond delays. Our future work will include applications and system-level demonstrations of processing and filtering mixed signals, along with integrating this PTC into robotics, drones, or small form-factor satellites such as CubeSats for reducing cluster-scale AI to chip-scale for demonstrating high-SWAP network-edge AI.

Acknowledgment

V.J.S. is supported by the PECASE Award under the AFOSR grant (FAA9550-20-1-0193)

References

- [1] G. Batra, Z. Jacobson, S. Madhav, A. Queirolo, and N. Santhanam, "Artificial-intelligence hardware: New opportunities for semiconductor companies," *McKinsey and Company, January*, vol. 2, 2019.
- [2] D. A. Miller, "Attojoule optoelectronics for low-energy information processing and communications," *Journal of Lightwave Technology*, vol. 35, no. 3, pp. 346–396, 2017.
- [3] M. I. Jordan and T. M. Mitchell, "Machine learning: Trends, perspectives, and prospects," *Science*, vol. 349, pp. 255–260, 7 2015.
- [4] G. Batra, Z. Jacobson, S. Madhav, A. Queirolo, and N. Santhanam, "Artificial-intelligence hardware: New opportunities for semiconductor companies artificial intelligence is opening the best opportunities for semiconductor companies in decades. how can they capture this value?"
- [5] W. Samek, G. Montavon, S. Lapuschkin, C. J. Anders, and K. R. Müller, "Explaining deep neural networks and beyond: A review of methods and applications," *Proceedings of the IEEE*, vol. 109, pp. 247–278, 3 2021.
- [6] H. Zhou, J. Dong, J. Cheng, W. Dong, C. Huang, Y. Shen, Q. Zhang, M. Gu, C. Qian, H. Chen *et al.*, "Photonic matrix multiplication lights up photonic accelerator and beyond," *Light: Science & Applications*, vol. 11, no. 1, pp. 1–21, 2022.
- [7] I. Goodfellow, Y. Bengio, and A. Courville, *Deep learning*. MIT press, 2016.
- [8] O. Russakovsky, J. Deng, H. Su, J. Krause, S. Satheesh, S. Ma, Z. Huang, A. Karpathy, A. Khosla, M. Bernstein *et al.*, "Imagenet large scale visual recognition challenge," *International journal of computer vision*, vol. 115, no. 3, pp. 211–252, 2015.
- [9] C. Zhang, P. Li, G. Sun, Y. Guan, B. Xiao, and J. Cong, "Optimizing fpga-based accelerator design for deep convolutional neural networks," in *Proceedings of the 2015 ACM/SIGDA international symposium on field-programmable gate arrays*, 2015, pp. 161–170.
- [10] N. P. Jouppi, C. Young, N. Patil, D. Patterson, G. Agrawal, R. Bajwa, S. Bates, S. Bhatia, N. Boden, A. Borchers *et al.*, "In-datacenter performance analysis of a tensor processing unit," in *Proceedings of the 44th annual international symposium on computer architecture*, 2017, pp. 1–12.
- [11] J. Peng, Y. Alkabani, S. Sun, V. J. Sorger, and T. El-Ghazawi, "Dnnara: A deep neural network accelerator using residue arithmetic and integrated photonics," in *49th International Conference on Parallel Processing-ICPP*, 2020, pp. 1–11.
- [12] P.-S. Wang, Y. Liu, Y.-X. Guo, C.-Y. Sun, and X. Tong, "O-cnn: Octree-based convolutional neural networks for 3d shape analysis," *ACM Transactions On Graphics (TOG)*, vol. 36, no. 4, pp. 1–11, 2017.
- [13] M. Miscuglio and V. J. Sorger, "Photonic tensor cores for machine learning," *Applied Physics Reviews*, vol. 7, p. 031404, 2 2020. [Online]. Available: <http://arxiv.org/abs/2002.03780>
<http://dx.doi.org/10.1063/5.0001942>
- [14] B. J. Shastri, A. N. Tait, T. F. de Lima, W. H. Pernice, H. Bhaskaran, C. D. Wright, and P. R. Prucnal, "Photonics for artificial intelligence and neuromorphic computing," *Nature Photonics*, vol. 15, pp. 102–114, 2 2021.
- [15] C. Huang, V. J. Sorger, M. Miscuglio, M. Al-Qadasi, A. Mukherjee, L. Lampe, M. Nichols, A. N. Tait, T. F. D. Lima, B. A. Marquez, J. Wang, L. Chrostowski, M. P. Fok, D. Brunner, S. Fan, S. Shekhar, P. R. Prucnal, and B. J. Shastri, "Prospects and applications of photonic neural networks," 2022. [Online]. Available: [https://www.tandfonline.com/action/journalInformation?journalCode=tapx20\[35\]](https://www.tandfonline.com/action/journalInformation?journalCode=tapx20[35]) "Amf-qp-rnd-011 amf pdk3.1 user manual v1,"
- [16] N. Peserico, T. F. de Lima, T. F. de Lima, P. Prucnal, and V. J. Sorger, "Emerging devices and packaging strategies for electronic- photonic ai accelerators: opinion," *Optical Materials Express*, Vol. 12, Issue 4, pp. 1347-1351, vol. 12, pp. 1347–1351, 4 2022. [Online]. Available: <https://opg.optica.org/viewmedia.cfm?uri=ome-12-4-1347seq=0html=true>
<https://opg.optica.org/abstract.cfm?uri=ome-12-4-1347> <https://opg.optica.org/ome/abstract.cfm?uri=ome-12-4-1347>
- [17] W. Bogaerts, D. Pérez, J. Capmany, D. A. Miller, J. Poon, D. Englund, F. Morichetti, and A. Melloni, "Programmable photonic circuits," *Nature*, vol. 586, no. 7828, pp. 207–216, 2020.
- [18] Y. Shen, N. C. Harris, S. Skirlo, M. Prabhu, T. Baehr-Jones, M. Hochberg, X. Sun, S. Zhao, H. Larochelle, D. Englund, and M. Sol-jacic, "Deep learning with coherent nanophotonic circuits," *Nature Photonics*, vol. 11, pp. 441–446, 6 2017.
- [19] A. N. Tait, T. F. De Lima, M. A. Nahmias, H. B. Miller, H.-T. Peng, B. J. Shastri, and P. R. Prucnal, "Silicon photonic modulator neuron," *Physical Review Applied*, vol. 11, no. 6, p. 064043, 2019.
- [20] D. Pérez, I. Gasulla, L. Crudgington, D. J. Thomson, A. Z. Khokhar, K. Li, W. Cao, G. Z. Mashanovich, and J. Capmany, "Multipurpose silicon photonics signal processor core," *Nature communications*, vol. 8, no. 1, pp. 1–9, 2017.
- [21] J. Feldmann, N. Youngblood, M. Karpov, H. Gehring, X. Li, M. Stappers, M. L. Gallo, X. Fu, A. Lukashchuk, A. S. Raja, J. Liu, D. Wright, A. Sebastian, T. J. Kippenberg, W. H. P. Pernice, and H. Bhaskaran, "Parallel convolutional processing using an integrated photonic tensor core," *Nature*, vol. 589, 2021. [Online]. Available: <https://doi.org/10.1038/s41586-020-03070-1>
- [22] C. Huang, S. Fujisawa, T. F. de Lima, A. N. Tait, E. C. Blow, Y. Tian, S. Bilodeau, A. Jha, F. Yaman, H.-T. Peng *et al.*, "A silicon photonic– electronic neural network for fibre nonlinearity compensation," *Nature Electronics*, vol. 4, no. 11, pp. 837–844, 2021.
- [23] X. Xu, M. Tan, B. Corcoran, J. Wu, A. Boes, T. G. Nguyen, S. T. Chu, B. E. Little, D. G. Hicks, R. Morandotti *et al.*, "11 tops photonic convolutional accelerator for optical neural networks," *Nature*, vol. 589, no. 7840, pp. 44–51, 2021.
- [24] C. Demirkiran, F. Eris, G. Wang, J. Elmhurst, N. Moore, N. C. Harris, A. Basumallik, V. J. Reddi, A. Joshi, and D. Bunandar, "An electro-photonic system for accelerating deep neural networks," 9 2021. [Online]. Available:

- <http://arxiv.org/abs/2109.01126>
- [25] S. Lischke, A. Peczek, J. Morgan, K. Sun, D. Steckler, Y. Yamamoto, F. Korndörfer, C. Mai, S. Marschmeyer, M. Fraschke *et al.*, “Ultra- fast germanium photodiode with 3-db bandwidth of 265 ghz,” *Nature Photonics*, vol. 15, no. 12, pp. 925–931, 2021.
 - [26] C. R’ios, N. Youngblood, Z. Cheng, M. Le Gallo, W. H. Pernice, C. D. Wright, A. Sebastian, and H. Bhaskaran, “In-memory computing on a photonic platform,” *Science advances*, vol. 5, no. 2, p. eaau5759, 2019.
 - [27] J. Meng, M. Miscuglio, N. Peserico, X. Ma, Y. Zhang, C.-C. Popescu, M. Kang, K. Richardson, J. Hu, and V. J. Sorger, “Electrical pulse driven multi-level nonvolatile photonic memories using broadband transparent phase change materials,” *arXiv preprint arXiv:2203.13337*, 2022.
 - [28] Y. Zhang, J. B. Chou, J. Li, H. Li, Q. Du, A. Yadav, S. Zhou, M. Y. Sha-laginov, Z. Fang, H. Zhong, and et al., “Broadband transparent optical phase change materials for high-performance nonvolatile photonics,” *Nature Communications*, vol. 10, no. 1, 2019.
 - [29] J. Feldmann, N. Youngblood, C. D. Wright, H. Bhaskaran, and W. H. Pernice, “All-optical spiking neurosynaptic networks with self-learning capabilities,” *Nature*, vol. 569, no. 7755, pp. 208–214, 2019.
 - [30] G. Liu, W.-P. Ma, H. Cao, al, R. Zhu, T. Qiu, J. Wang, B. A. Marquez, Z. Guo, H. Morison, S. Shekhar, L. Chrostowski, P. Prucnal, and B. J. Shastri, “Photonic pattern reconstruction enabled by on-chip online learning and inference,” *Journal of Physics: Photonics*, vol. 3, p. 024006, 2 2021. [Online]. Available: <https://iopscience.iop.org/article/10.1088/2515-7647/abe3d9> <https://iopscience.iop.org/article/10.1088/2515-7647/abe3d9/meta>
 - [31] D. A. Miller, “Self-configuring universal linear optical component,” *Photonics Research*, vol. 1, no. 1, pp. 1–15, 2013.
 - [32] T. W. Hughes, M. Minkov, Y. Shi, and S. Fan, “Training of photonic neural networks through in situ backpropagation and gradient measure- ment,” *Optica*, vol. 5, no. 7, pp. 864–871, 2018.
 - [33] A. Annoni, E. Guglielmi, M. Carminati, G. Ferrari, M. Sampi- etro, D. A. Miller, A. Melloni, and F. Morichetti, “Unscrambling light—automatically undoing strong mixing between modes,” *Light: Science & Applications*, vol. 6, no. 12, pp. e17110–e17110, 2017.
 - [34] D. A. Miller, “Perfect optics with imperfect components,” *Optica*, vol. 2, no. 8, pp. 747–750, 2015.
 - [35] <http://www.advmf.com/>, 2020.
 - [36] H. Zhang, X. Cheng, H. Zang, and D. H. Park, “Compiler-level matrix multiplication optimization for deep learning,” *arXiv preprint arXiv:1909.10616*, 2019.

Photonics for Neuromorphic Computing

Paul R. Prucnal⁽¹⁾, Thomas Ferreira de Lima^(1,3), Joshua C. Lederman⁽¹⁾, Weipeng Zhang⁽¹⁾, Eli Doris⁽¹⁾, Chaoran Huang^(1,4), Alexander N. Tait⁽²⁾, Bhavin J. Shastri^(1,2)

⁽¹⁾ Department of Electrical Engineering, Princeton University, Princeton, NJ 08544, USA, prucnal@princeton.edu

⁽²⁾ Department of Physics, Engineering Physics & Astronomy, Queen's University, Kingston, ON K7L 3N6, Canada, shastri@ieee.org

⁽³⁾ NEC Laboratories America, Princeton, NJ 08540, USA, thomas@nec-labs.com

⁽⁴⁾ Department of Electronic Engineering, the Chinese University of Hong Kong, Hong Kong, China SAR, crhuang@ee.cuhk.edu.hk

Abstract *Photonic systems have unique characteristics that make them well-suited for the implementation of neural networks. These neuromorphic photonic systems imitate the human process of neural decision making while operating many times faster than biological or even conventional electrical processors. We have harnessed the wide bandwidth, wavelength multiplexing, and large number of interconnects of photonic systems to achieve high performance on a wide number of neuromorphic processing tasks.*

Introduction

Neuromorphic photonics represents the intersection of three academic fields that have been around for many decades: neural networks, optical signal processing, and silicon photonics. Initial innovators in these fields include John McCarthy on artificial intelligence (AI), Joe Goodman on Fourier optics, and Richard Soref on the electro-optic effect in silicon [1-3]. More recently, others have bridged these fields, such as Dmitri Psaltis with free space optics and neural networks in the 1980s [4]. In the 2000s, seminal work by Capmany and Novak and later Marpaung and Capmany drove the development of integrated RF photonic systems [5].

Over the past decade, there has been increasing demand for improved AI processors as AI models increase exponentially in size and complexity. At the same time, the consistent transistor size improvement described by Moore's Law has slowed, and conventional electronic processors face fundamental physical barriers preventing further performance improvement. The need for a new model of AI computation is great. Neuromorphic photonics, built off of decades of prior research but with newfound relevance, has grown to fill that gap.

Anticipating the potential of the field of photonics when applied to AI, in the 2010s the Lightwave Lab at Princeton University began implementing neural networks on silicon photonic chips [6, 7]. We have continued to develop and refine integrated photonic neural networks up until the present day, working both in the continuous-time and spiking domain. This work has led to successful experimental demonstrations of integrated silicon photonic neural networks in application to diverse information processing tasks [8-11].

Leveraging Optical Processing for Neural Networks

Analog optical data processing offers several key advantages over conventional digital signal processing. The much greater bandwidth of optical carriers over RF carriers allows the entire RF spectrum to be modulated simultaneously onto a single narrowband optical signal. This signal faces no ADC bottlenecks and minimal frequency-dependent distortion. Furthermore, multiple independent signals may be combined onto a single waveguide or fiber-optic cable using different carrier wavelengths (wavelength multiplexing). These signals may be distributed and processed in parallel using few physical interconnects and without the need for switching. Finally, the optical filters and electro-optic conversion that may be integrated into optical processors operate at very short time scales, enabling ultra-low latency processing and operating frequencies in the tens of gigahertz.

These characteristics of optical systems make them uniquely suited to neural network processing. Neural networks require large series of sequential calculations, very large numbers of interconnections, and nonlinearity to perform decision-making. Optical processors meet those needs with ultra-low-latency processing, high-bandwidth, wavelength-multiplexed interconnects, and fast nonlinearities implemented with optoelectronic devices.

Integration of Neural Networks on Silicon

Neural networks emulate biological neural systems to achieve intelligent decision-making. Biological neurons perform three key data-processing operation. They first accept many distinct input signals and apply weights to them,

multiplying the signal by a coefficient to determine the “importance” of that signal to the desired decision. Second, they sum the weighted signal, integrating the different data sources into a single quantity. Finally, they apply a nonlinear thresholding function, determining if the input data is sufficient to pass forward to further neurons in the network. This output signal serves as the input signal to the next set of neurons.

We implement neural networks on monolithic integrated silicon photonic chips using a “Broadcast and Weight” architecture. Data signals in this architecture are modulated on distinct wavelengths of light. The signals are multiplexed onto a single waveguide, then broadcast to all target neurons, requiring no switching or routing protocols. Each photonic neuron implements the three key operations described previously. Weighting may be performed in the optical domain using micro-ring resonators (MRRs). These modulators act as tunable wavelength-specific filters, transferring a designated portion of a particular input wavelength to a secondary waveguide. Summing is performed by photodetectors, which collect all input light across wavelengths, converting photons to an electric current. Dual balanced photodetectors connected to the primary and secondary waveguide enable the full range of positive (excitatory) and negative (inhibitory) photocurrents. Finally, the electrical signal is converted back into the optical domain with a nonlinear optical modulator.

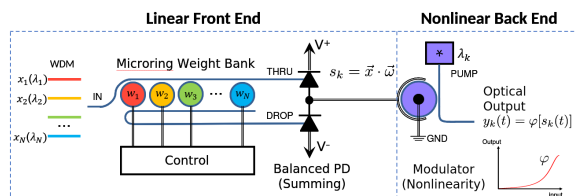


Fig. 1: Simplified schematic of a photonic neuron. Micro-ring modulators tuned by an electronic control system apply weights. A pair of balanced photodetectors (PDs) perform summing. A nonlinear modulator converts the signal back to the optical domain while executing the key decision-making function [9].

Accurate and tunable MRR weighting represents a key challenge in silicon photonic neural networks. The resonance of MRRs may be shifted with the application of heat through embedded n-doped heaters (the thermo-optic effect) [12]. This technique has the additional advantage of enabling feedback control, as the buildup of light in the resonator shifts the resistance of the heater. Alternatively, electro-optic effects may be applied for tuning. This effect operates extremely quickly, with demonstrated performance of 1.5-10 GHz using a forward-bias PIN junction and 45 GHz with a

reverse-bias junction, making it preferable when implementing the final, nonlinear modulation step of the neuron [13, 14]. We have demonstrated state-of-the-art electro-optic MRR tuning with 8.5-bit accuracy and 9-bit precision [15].

Recent developments in photonic packaging have propelled photonic neural networks further toward practical application. We have successfully integrated full weight control on a single board copackaged with a silicon photonic chip [15]. Sensitive vertical or edge optical alignment has been required until recent days to couple signals on and off chip, but photonic wirebonds represent a promising technology that should enable robust fiber-optic connections to silicon chips, eliminating a key packaging barrier.

MRR-based weight control has been demonstrated in a large variety of spaces, including optical switching [16], data interconnection [17], RF beamforming [18], spiking networks [19], and LIDAR [20].

Our lab has demonstrated complete neuromorphic system integration on silicon with foundry-compatible components, and we have created open-source design tools that enable quick, in-house optical and electrical design [21].

Neuromorphic Photonics Demonstrations

We have successfully applied silicon photonic neuromorphic systems to a range of important applications.

Model Predictive Control (MPC) [9]. MPC is a control technique wherein each time step involves computing an optimal path to a target based on constraints. Its control equation can be formulated as a constrained quadratic program. The latency of the program determines the achievable sampling rate and the control horizon. The quadratic program may be mapped onto a recurrent neural network to implement MPC, enabling ultra-low-latency computation. We demonstrated a 15 ns convergence time, as compared to the 12 ms convergence achieved by a Lockheed Martin FPGA controller, a six order-of-magnitude improvement.

Blind Source Separation (BSS) [10, 22]. BSS involves the recovery of multiple independent input signals from multiple arbitrary but distinct unknown mixtures of those signals. It employs independent component analysis, adjusting the weights of a demixing matrix to maximize kurtosis, resulting in output signals that are maximally non-Gaussian and most likely to match the unknown original signals. Performing BSS on RF signals in the optical domain allows us to harness the extremely wide bandwidth of

optical signals relative to RF signals. We have demonstrated fast, accurate BSS with minimal digital-signal-processing by implementing the demixing matrix using a neuromorphic silicon photonic system, successfully demixing signals ranging from 1 to 13.8 GHz with 85% separability.

Nonlinearity Dispersion Compensation [11]. Undersea fiber-optic cables represent the backbone of the international internet. Signals in these cables are distorted by nonlinear optical effects, requiring digital-signal-processing compensation prior to demodulation. An integrated photonic solution that reduces the digital processing burden is therefore in high demand. We have demonstrated a fully-integrated photonic neural network that achieved real-time nonlinearity compensation using captured long-haul fiber optic communication data with 0.60 dB real photonic improvement.

RF Fingerprinting [23]. There are increasing demands on our wireless communications systems and limited bandwidth with which to fulfill them. Cognitive networks represent one solution, but they present severe security challenges. RF Fingerprinting identifies transmitters by unique, difficult-to-spoof physical characteristics in their signals, enabling physical-level security for cognitive networks. Artificial intelligence may be applied to identify these signals. We developed a hybrid photonic-electronic architecture comprised of a silicon photonic system and an FPGA that can successfully classify between 30 identical transmitters in real time with over 96% accuracy.

Roadmap for Neuromorphic Photonics

Further development in neuromorphic photonic systems requires better integration of photonic chips, CMOS ASICs, microcontrollers, lasers, and both digital and analog memory within a single package (see Fig 2). This vision of a general-purpose hybrid photonic-electronic architecture has inspired the creation of a number of companies in neuromorphic photonics, including Luminous, Lighton, LightMatter, Optalysys, Lightelligence, Optius, and Optelligence, as well as the work of many researchers at universities across the world.

Conclusion

Modern technological development has led to a vast increase in the demand for fast, performant artificial intelligence. Neuromorphic photonics has a unique capacity to meet this need, as the high-bandwidth interconnections and

wavelength-based networking available in the optical domain match closely to the requirements of neural networks. We have developed photonic neural networks on silicon chips, with fully-integrated optical weighting, nonlinearity, and interconnections. These chips have been successfully packaged with control electronics, resulting in small form-factor general-purpose processors. Our processors have been applied successfully to a variety of tasks in which they can exploit the key strengths of neuromorphic photonics.

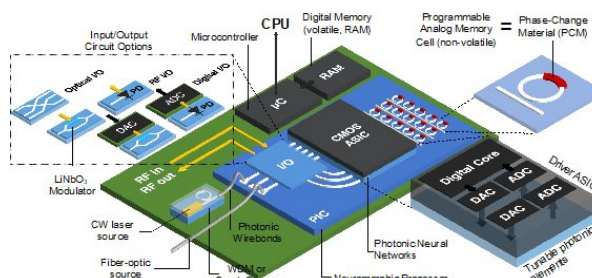


Fig. 2: Roadmap for a future hybrid photonic/electronic general-purpose computing architecture. A silicon chip with phase-change-material weights controlled by a tightly integrated CMOS ASIC that includes DACs and ADCs. Lasers and fiber optic sources are wirebonded to the chip. A microcontroller with external RAM performs operations not feasible on photonic systems [24].

References

- [1] Goodman. Introduction to Fourier Optics. (Roberts and Company, 1968).
- [2] Soref and Bennet. IEEE JQE 23, 123 (1987).
- [3] McCarthy. Dartmouth Workshop on AI (1956).
- [4] Farhat and Psaltis. Appl. Opt. 24, 1469-1475 (1985).
- [5] Marpaung et. al. Laser & Photonics Rev. 7, 506 (2013).
- [6] Tait, Prucnal et. al. JLT 32, 3427-3439 (2014).
- [7] Tait, Prucnal et. al. Sci. Rep. 7, 7430 (2017).
- [8] Peng, Prucnal et. al. IEEE JQE 26, 5100209 (2020).
- [9] Lima, Prucnal et. al. IEEE JLT 37, 1515-1534, (2019).
- [10] Ma, Prucnal et. al. Opt. Letters 45, 6494-6497 (2020).
- [11] Huang, Prucnal et. al. Nat. Electr. 4, 837-844 (2021).
- [12] Huang, Shastri, Prucnal et al. APL Photonics 5 (2020).
- [13] Manipatruni et al. Opt. Exp. 18, 18235-18242 (2010).
- [14] Novack Proc. SPIE, 8781 (2013).
- [15] Zhang, Prucnal, et al, arXiv:2104.01164 (2021).
- [16] Jayatileka et al. Optica 6, 84-91 (2019).
- [17] Liang et al. OFC (2020).
- [18] Xiang et al. JSTQE 24, (2018).
- [19] Feldman et al. Nature 569, (2019).
- [20] Larocque et al. Opt. Express 27 (2019).
- [21] <https://github.com/lightwave-lab/zeropdk>
- [22] Zhang, Prucnal, et al, arXiv:2104.01164 (2021).
- [23] Peng, Shastri, Prucnal, et. al. ArXiv:2106.13865 (2021).
- [24] Shastri, Tait, Prucnal et al. Nature Photonics 15 (2021).

Monolithically Integrated Electronics in Zero-Change Silicon Photonics

Francesco Zanetto, Fabio Toso, Vittorio Grimaldi, Matteo Petrini, Mazyar Milanizadeh, Alessandro Perino, Paola Piedimonte, Francesco Morichetti, Andrea Melloni, Giorgio Ferrari, Marco Sampietro

Department of Electronics, Information and Bioengineering, Politecnico di Milano, piazza Leonardo da Vinci 32, Milano, Italy
* email: francesco.zanetto@polimi.it

Monolithic cointegration of electronic and photonic devices is expected to enable a new realm of applications and high-performance chips. This work presents the integration of electronic circuits in a zero-change commercial Silicon Photonics technology and, as a first application, reports on the time-multiplexed control of a 16-to-1 optical router enabled by this approach.

Keywords: *electronic-photonic cointegration, zero-change technology, MOS transistors*

INTRODUCTION

Monolithic electronic-photonic integrated chips (EPICs) are envisioned as the natural evolution of solid-state optics, enabling a new realm of high-performance systems for telecommunications, automotive and datacenters [1,2]. In Silicon Photonics, on-chip electronics can be exploited to counteract the sensitivity of optical devices to temperature variations and ensure reliable photonic functionality. The control circuitry is normally implemented off-chip [3,4], requiring several connections to access each photonic device. As the number of elements to be controlled increases, this approach becomes rapidly unfeasible due to space limitations and wirebonding issues. The possibility of integrating part of the electronics directly on the photonic chip is therefore of great advantage.

The commercially available EPIC technologies try to add photonic components to mature electronic nodes [5,6], with drawbacks in terms of optical performance and production costs, especially considering the large footprint of photonic devices. To solve this limitation, in this work we demonstrate the opposite approach and show that electronic circuits can be integrated in commercial Silicon Photonics technologies without changing the standard processing steps. As a first application of this solution, we demonstrate the use of an on-chip analog multiplexer to feedback-control the functionality of a 16-to-1 optical router transmitting a 10-Gbps modulated signal.

MOSFET TRANSISTORS IN SILICON PHOTONICS

The implementation of electronic circuits in Silicon Photonics is made difficult by the Silicon-On-Insulator (SOI) stack, that is not conceived to implement vertical structures like MOSFETs. The available metal layers are usually at least 700 nm away from the silicon to ensure minimum interaction with the propagating light and are therefore too distant to be used as transistors gates. To overcome this limitation, we managed to design fully functional lateral transistors (Fig. 1a). The native SOI layer, lightly p-doped, is used as the substrate of n-type MOSFETs. A p+ doped silicon lateral gate is then lithographed as close as possible to the transistor body, at a distance of 200 nm. The transistor channel width W is therefore set by the 220 nm thickness of the SOI layer. The Drain (D) and Source (S) contacts are created by locally n-doping the transistor body, while a p-type diffusion provides the bulk contact. The channel length L of 4 μm has been chosen with the aid of numerical simulations. The final MOSFET is a symmetric cell obtained by mirroring the single geometry along the D-S axis and by connecting the two side Gates with a common top metal. Fig. 1b shows the scanning electron microscope photograph of the fabricated device, while its measured characteristic curve is reported in Fig. 1c, showing a threshold voltage of 1.84 V, a gain factor $\mu_n C_{\text{ox}} W/L$ of 4 $\mu\text{A}/\text{V}^2$ and an Early voltage of 35 V. Being the transistors realized without changing neither the processing steps nor the design rules of the photonic technology (zero-change paradigm), the approach is completely technology-transparent and therefore it can be implemented in any Silicon Photonics platform, even in multi-project wafer (MPW) runs as in this demonstration.

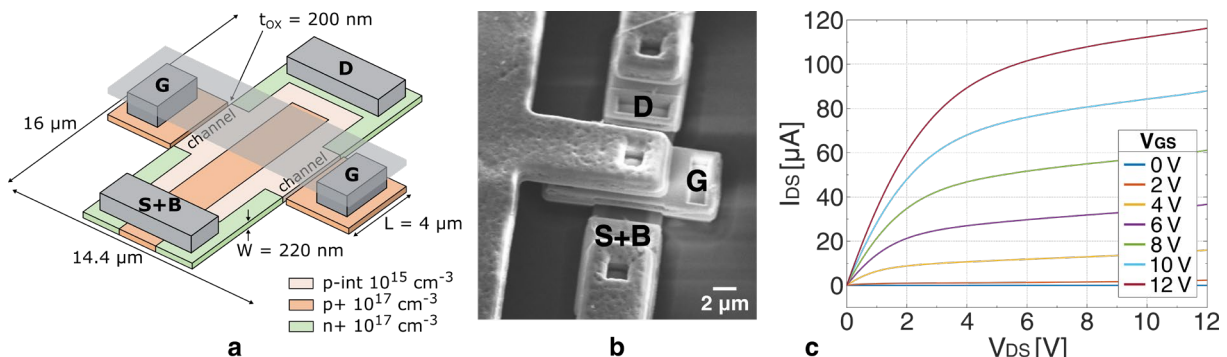


Fig. 1. a) 3D view, b) SEM photograph and c) measured characteristic curve of the designed MOSFET in Silicon Photonics.

INTEGRATED MULTIPLEXER FOR THE REDUCTION OF ELECTRICAL I/Os IN PHOTONIC CHIPS

The single MOSFET is the main building block of any electronic circuit. By using 596 transistors and 36 resistors, we monolithically integrated on the photonic chip a 16-to-1 analog multiplexer. A multiplexer can be a key enabling component for the control of high-density photonic systems, where a large number of sensors and actuators is required to counteract the sensitivity of optical devices to temperature variations and fabrication tolerances. Indeed, as the photonic complexity grows, the number of electrical connections towards the external control electronics increases dramatically, causing problems of routing and area occupation. Time-multiplexing of the sensors readout can be envisioned as an effective way to reduce the number of these connections, since each detector can be usually interrogated at a relatively low frequency of few kHz. The designed 16-to-1 MUX is the key component that enables this operation, allowing to sequentially connect 16 photodiodes to a single external readout by using just 8 pads. The number of pads required to operate the MUX can be computed as $N_{PADS, MUX} = \log_2(N_{SENSORS}) + 4$, since 1 output, 2 power supplies and 1 reference voltage are needed in addition to the digital address bits. This number should be compared with $N_{PADS, NO MUX} = N_{SENSORS}$ needed in the normal case. Therefore, the use of the MUX is advantageous when more than 8 sensors are read. The advantage becomes more evident as the number of sensors increases, since doubling the multiplexer channels requires only adding a digital bit.

The schematic of the designed multiplexer, made of digital gates and single-pole double-throw switches, is shown in Fig. 3a connected to 16 photodiodes (PD). The overall footprint of the circuit is $250 \mu\text{m} \times 1200 \mu\text{m}$ (Fig. 3b) and the static power consumption is 3.6 mW with a supply voltage of 12 V. The switching transient of the MUX when changing the configuration of the digital bits is reported in Fig. 3c, showing a settling time of 500 ns. If, for instance, a readout rate of 10 kHz is targeted, this speed allows to potentially perform time-multiplexing of up to 200 detectors interrogated in sequence using just 12 pads. The MUX signal bandwidth is instead reported in Fig. 3d, highlighting that signals up to around 100 MHz can be routed without relevant penalties by the device.

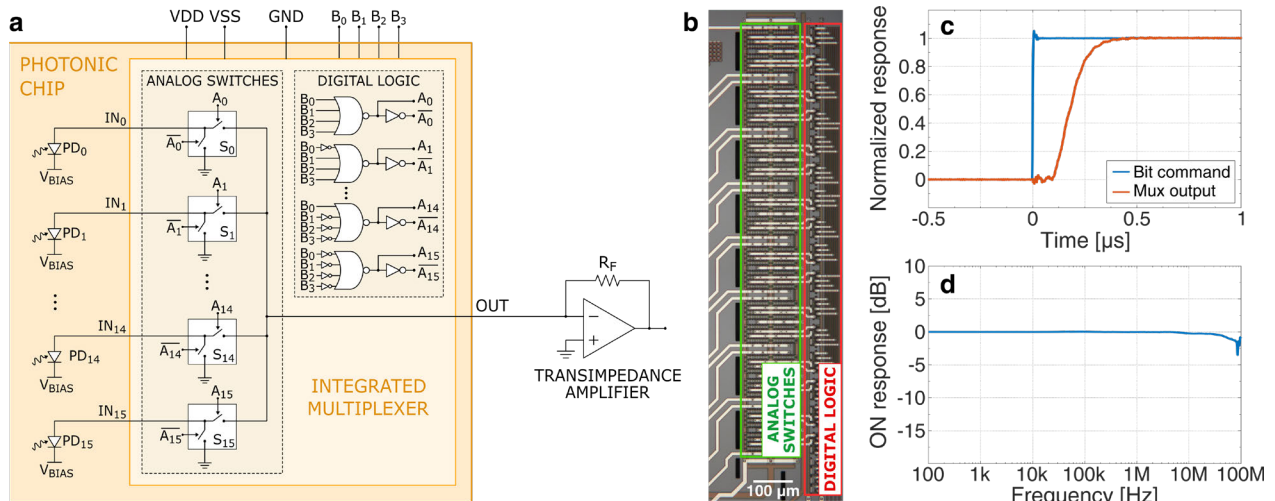


Fig. 2. a) Schematic view and b) microscope photograph of analog multiplexer in Silicon Photonics, connected to integrated photodiodes. c) Measured switching transient and d) signal bandwidth of the device, demonstrating its correct functionality.

TIME-MULTIPLEXED CONTROL OF A 16-TO-1 OPTICAL ROUTER

The presented analog multiplexer has been used to feedback-control a 16-to-1 optical router, whose complexity and functional scaling is currently limited by the need of external control electronics [7]. The optical router is made with a 4-layer binary tree of Mach-Zehnder interferometers (MZI) (Fig. 6a), that steer the light from one of the 16 inputs of the circuit to a single optical output. The state of each MZI is monitored with germanium PDs, while their working point is set with thermal actuators. Fig. 6b shows the microscope photograph of the EPIC, where the compact size of the electronic MUX with respect to the photonic router can be appreciated.

To control the optical circuit, a time-multiplexed feedback logic was implemented. The dithering technique in combination with integral controllers has been used to tune each MZI [8]. We set the dithering frequency to 2 kHz and the MUX switching to 80 kHz, allowing to read the 4 sensors along each path at 20 kHz and avoid aliasing phenomena. Differently from the standard technique, deserialization of the readout is needed in this case to extract 4 data sequences from a single ADC bit stream and to apply the generated voltages to the correct heaters. The deserializer, dithering extraction block, integral controllers and management logic were implemented with an FPGA on the external control electronic board.

To verify the correct operations of the proposed system, we performed optical measurements assessing the input-output routing and transmission performance. A laser at 1550 nm, modulated at 10 Gbps with a PRBS31 on-off keying scheme and amplified with an erbium-doped fiber amplifier, has been injected into the EPIC with a power of 5 dBm. After on-chip routing, the output signal has been monitored with a high-speed receiver. Eye diagrams and bit-error-rate (BER) measurements have been performed to quantify the degradation in the transmission quality induced by the time-multiplexed control. Fig. 4c shows the BER measurements performed for 8 input-output configurations, requiring to interrogate all the PDs in the chip. An average power penalty of just 0.3 dB with respect to the back-to-back (B2B) case and a penalty variation of around 0.2 dB among the different configurations are observed, confirming the correct operation of the MUX and of the time-multiplexed control strategy regardless of the interrogated photodiodes. The same is also certified by the eye diagrams (Fig. 4d) that remain clearly open in all the conditions, with an average extinction ratio of 9 dB and a variation of 0.1 dB among the selected light paths.

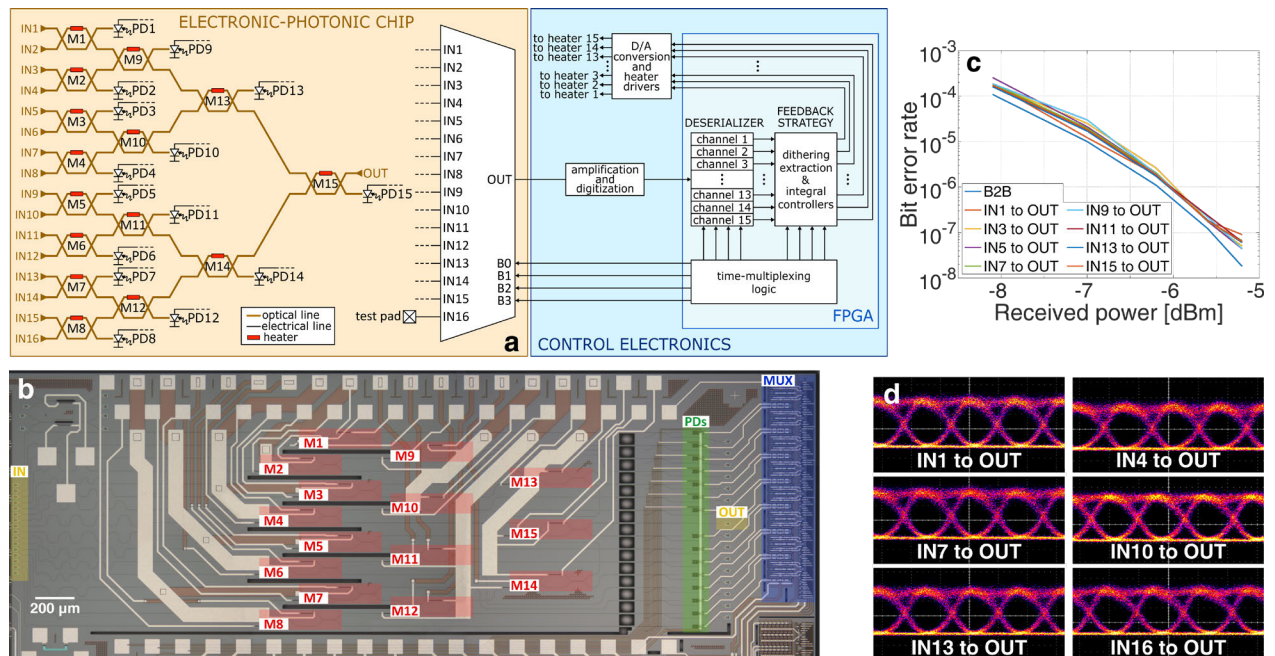


Fig. 3. a) Schematic view of the electro-optical system. b) Microscope photograph of the EPIC. c) BER measurements and d) eye diagrams at 10 Gbps for several I/O configurations, demonstrating the successful operation of the time-multiplexed control.

CONCLUSIONS

We demonstrated that electronic circuits can be integrated in Silicon Photonics without changing the standard processing steps. To prove the advantages of this approach, an integrated analog MUX has been successfully used to feedback-control a 16-to-1 optical router. We envision that the cointegration of electronics inside photonic chips can really boost the performance of integrated optics and enable new relevant applications and architectures.

Acknowledgements: part of the work was carried out at PoliFab, the nanofabrication facility of Politecnico di Milano.

References

- [1] D. Thomson et al., "Roadmap on silicon photonics," *Journal of Optics*, vol. 18, no. 7, pp. 073003, 2016.
- [2] N. Margalit et al., "Perspective on the future of silicon photonics and electronics," *Applied Physics Letters*, vol. 118, no. 22, pp. 220501, 2021.
- [3] K. Padmaraju and K. Bergman, "Resolving the thermal challenges for silicon microring resonator devices," *Nanophotonics*, vol. 3, no. 4-5, pp. 269-281, 2014.
- [4] F. Zanetto et al., "WDM-based silicon photonic multi-socket interconnect architecture with automated wavelength and thermal drift compensation," *IEEE Journal of Lightwave Technology*, vol. 38, no. 21, pp. 6000-6006, 2020.
- [5] J. S. Orcutt et al., "Open foundry platform for high-performance electronic-photonics integration," *Optics express*, vol. 20, no. 11, pp. 12222-12232, 2012.
- [6] K. Giewont et al., "300-mm monolithic silicon photonics foundry technology," *IEEE Journal of Selected Topics in Quantum Electronics*, vol. 25, no. 5, pp. 1-11, 2019.
- [7] A. Ribeiro, et al., "Column-row addressing of thermo-optic phase shifters for controlling large silicon photonic circuits," *IEEE Journal of Selected Topics in Quantum Electronics*, vol. 26, n. 5, pp. 1-8, 2020.
- [8] F. Zanetto et al., "Dithering-based real-time control of cascaded silicon photonic devices by means of non-invasive detectors," *IET Optoelectronics*, vol. 15, no. 2, pp. 111-120, 2021.

Generation of high-frequency phonons in silicon optomechanical crystal

Jianhao Zhang¹, Xavier Le Roux¹, Paula Nuño-Ruano¹, Daniele Melati¹, Miguel Motesinos-Ballester¹, Eric Cassan¹, Delphine Marris-Morini, Laurent Vivien¹, Norberto Daniel Lanzillotti-Kimura¹, and Carlos Alonso-Ramos^{1,*}

¹Centre de Nanosciences et de Nanotechnologies, Université Paris-Saclay, CNRS, 91120 Palaiseau, France
*carlos.ramos@c2n.upsaclay.fr

We report the optomechanical excitation and readout of X-band phonons in a silicon optomechanical crystal. Bloch mode engineering is used to implement optomechanical cavity confining 10-GHz phonons with measured quality factor up to 3000. This result illustrates the potential of the proposed optomechanical Bloch mode engineering in silicon, for applications in communications, sensing and quantum-state control.

Keywords: *micro-wave, subwavelength, radiation pressure, Brillouin*

INTRODUCTION

Optomechanical resonators allowed remarkable demonstrations of coupling between photons and phonons in the context of cavity optomechanics [1] and Brillouin scattering [2]. Silicon photonics provides low production cost and seamless compatibility with the state-of-art optoelectronic circuitry. However, silicon has a higher stiffness and acoustic velocity than the silica commonly used as substrate, hindering phonon confinement in structures realized using the silicon-on-insulator (SOI) technology. Nevertheless, silicon membrane optomechanical resonators [3-5] have recently enabled a myriad of optomechanical demonstrations, including Brillouin lasing [6] and phonon lasing [7]. Optomechanical crystals feature small optical volume and high confinement for photons, being of particular interest for the optomechanical transduction. To optically excite and readout these devices, the optical mode profile has to be optimized to maximize the overlap with the mechanical mode, which is generally confined within the silicon [8]. Concurrently, the frequency of the mechanical modes is mainly governed by waveguide width. Hence, due to trade-offs in optical confinement and optomechanical interaction, most demonstrations relied on phonons with frequencies below 5 GHz.

Here, we propose and demonstrate a silicon membrane optomechanical cavity interfacing X-band phonons (frequency near 10 GHz) and C-band photons (wavelength near 1550 nm). Engineering of Bloch modes for photons and phonons in periodic silicon optomechanical crystal leads to the confinement of high-frequency phonons that can be optically driven and readout with guided optical modes. This design is experimentally confirmed by the optical probing of 10-GHz phonons, with high mechanical quality factor up to 3000. The optical control of X-band phonons shown here opens intriguing opportunities for applications in microwave signal generation and processing, radar, and quantum transduction [9,10].

RESULTS

Figure 1(a) shows a schematic overview of the proposed silicon membrane structure. The periodic waveguide comprises a core with a width of $W = 340$ nm and a thickness of $t_{Si} = 220$ nm. The period of the corrugation is $\Lambda = 420$ nm, while the teeth have a width of $W_T = 400$ nm and length of $L_T = 100$ nm. This waveguide grating supports several mechanical modes with frequencies above 8 GHz, as shown in Fig. 1 (b). As an example, in Fig. 1(c) we show the displacement profile of six selected modes, including in-plane flexural mode (I), out-of-plane flexural mode (II), transversely-strained/stressed modes (mode III and V), and flexion-strain/stress combined modes (mode IV and VI). For the modes IV and V the maximum of the displacement is localized within the waveguide core.

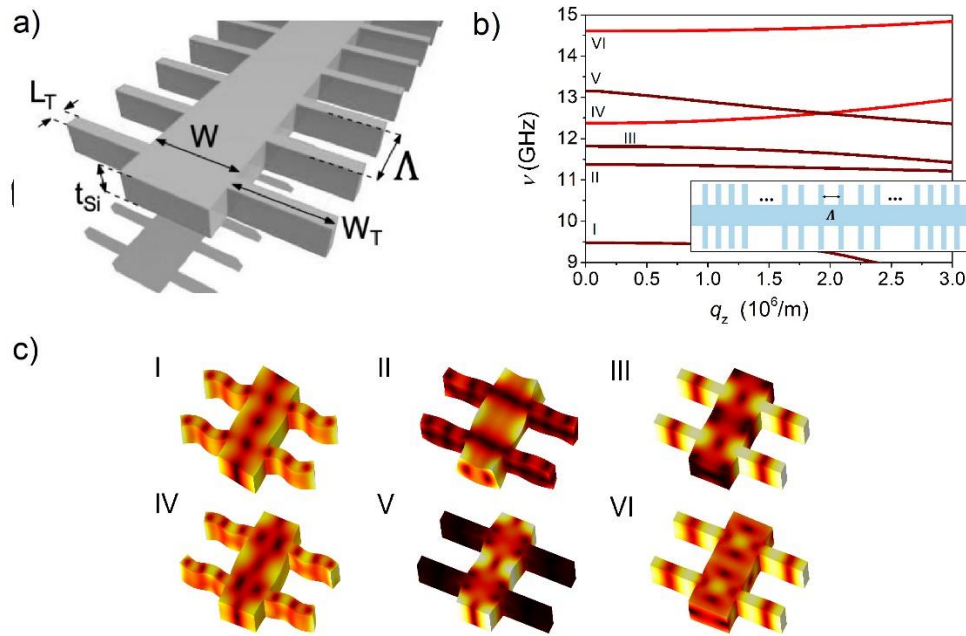


Fig. 1. (a) Schematic view of the proposed optomechanical Si grating. (b) Band diagram of the mechanical modes supported by the proposed structure (c) Normalized displacement profiles of six different optomechanical modes.

To co-localize the phonons and photons, an optomechanical crystal cavity is formed by reducing the lattice period from 420 nm in the center down to 380 nm at the lateral mirrors, for a total length of 72 periods. Figure 2 shows the calculated field distribution for the optical mode, Fig. 2a, and the mechanical mode, Fig. 2b. Optical and mechanical modes exhibit a good spatial overlap.

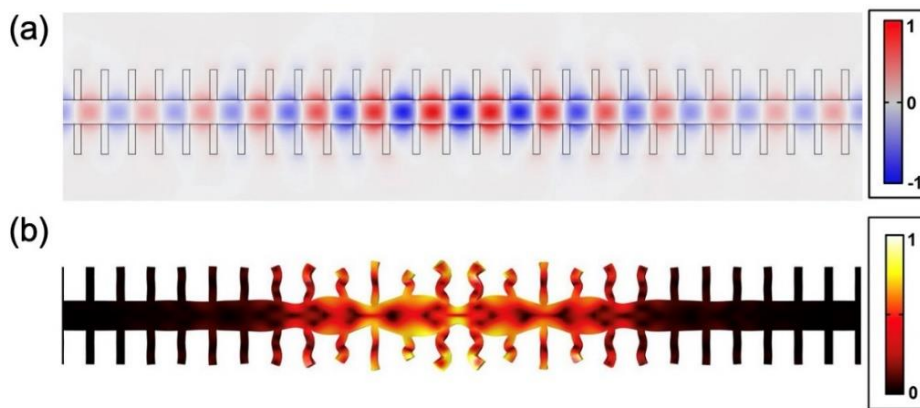


Fig. 2. (a) The fundamental optical resonant mode at 1550 nm wavelength, with transverse-electric polarization. (b) The fundamental mechanical resonant mode with a frequency of 11.649 GHz.

The fabricated optomechanical cavity is shown Fig. 3 (a). Subwavelength-cladded silicon waveguides (Fig 3(a), right bottom panel) are used at the input and output of the cavity, alongside with the focused grating couplers for light interfacing with the cleaved SMF-28 fibers. The cavity is thermally populated by an optical pump at 1547 nm wavelength. This generation of phonons is monitored via the beating between the pump and generated optical harmonic sidebands, collected by a high-speed photodetector. Figure 3 (b) shows the radio-frequency signature of mechanical motions at 10.2 GHz, in good agreement with the frequency of the calculated mechanical mode. The detail of the radio-frequency spectrum is presented in Fig 3 (c), showing a remarkable quality factor of 2920, from which we deduce a phonon decay rate of 3.49 MHz.

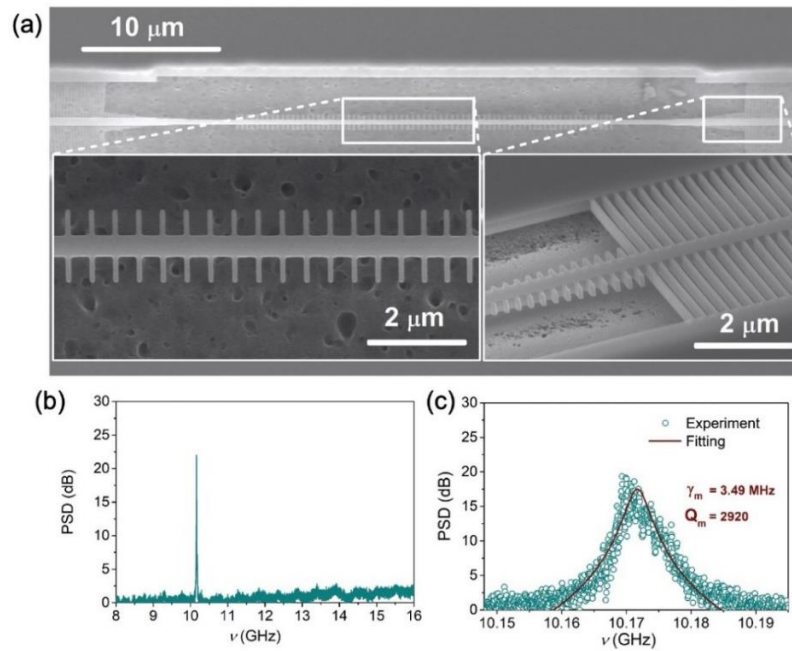


Fig. 3. (a) Scanning electron microscope images of the fabricated optomechanical micro-resonator, showing general view and detail of the cavity center and access subwavelength waveguides. Radio-frequency spectrum of the optomechanical cavity in: (b) wide range and (c) zoomed-in view near 10.17 GHz.

DISCUSSION

We have proposed and developed a novel optomechanical scheme for the generation of X-band acoustic phonons. Bloch-mode engineering is used to control the field distribution of the photonic and phononic modes. This proposed design yields high overlap between near-IR optical mode and X-band mechanical mode. This design is experimentally demonstrated, showing optomechanical excitation and readout using an optical mode with a wavelength near 1550 nm to probe a mechanical mode with mechanical quality factor of 3000, at the state-of-the-art for ambient, room-temperature conditions. The proposed approach has a great potential for applications in communications, sensing, and quantum technologies.

Acknowledgements: Agence Nationale de la Recherche is acknowledged for supporting this work through BRIGHT ANR-18-CE24-0023-01 and MIRSPEC ANR-17-CE09-0041.

References

- [1] M. Aspelmeyer, T. J. Kippenberg, and F. Marquardt, *Cavity optomechanics*, Rev. Mod. Phys., vol. 86, pp. 1391-1452, 2014.
- [2] B. J. Eggleton, C. G. Poulton, P. T. Rakich, M. J. Steel and G. Bahl, *Brillouin integrated photonics*, Nat. Photon., vol. 13, pp. 664-677, 2019.
- [3] E. A. Kittlaus, H. Shin and P. T. Rakich, *Large Brillouin amplification in silicon*, Nat. Photon., vol. 10, pp. 463-468, 2015.
- [4] R. Laer et al., *Interaction between light and highly confined hypersound in a silicon photonic nanowire*, Nat. Photon., vol. 9, pp. 199-203, 2015.
- [5] M. Eichenfield, J. Chan, R. M. Camacho, K. J. Vahala, and O. Painter, *Optomechanical crystals*, Nature, vol. 462, pp. 78-82, 2009.
- [6] N. T. Otterstrom, R. O. Behunin, E. A. Kittlaus, Z. Wang and P. T. Rakich, *A silicon Brillouin laser*, Science, vol. 360, pp. 1113-1116, 2016.
- [7] L. Mercade, K. Pelka, R. Burgwal, A. Xuereb, A. Martjnez and E. Verhagen. *Floquet phonon lasing in multimode optomechanical systems*. Phys. Rev. Lett., vol. 127, pp. 073601, 2021.
- [8] A. H. Safavi-Naeini, D. Van Thourhout, R. Baets and R. V. Laer, *Controlling phonons and photons at the wavelength scale: integrated photonics meets integrated phononics*, Optica, vol. 6, pp. 213-231. 2019.
- [9] S. Barzanjeh, A. Xuereb, S. Grolacher, M. Paternostro, C. A. Regal and E. M. Weig, *Optomechanics for quantum technologies*, Nat. Phys., vol. 18, pp. 15-24, 2022.
- [10] M. Mirhosseini, A. Sipahigil, M. Kalae and O. Painter, *Superconducting qubit to optical photon transduction*, Nature, vol. 588, pp. 24-31, 2020.

Hybridly Integrated Photonic Integrated Circuit for Wavelength and Polarization Determination

(Student paper)

Axel Schoenau, Tianwen Qian, Peer Liebermann, Christian Kastner, Hauke Conradi, Martin Kresse,
David de Felipe, Moritz Baier, Norbert Keil, Martin Schell

Fraunhofer-Institut für Nachrichtentechnik, Heinrich-Hertz-Institut, 10587 Berlin, Germany
axel.schoenau@hhi.fraunhofer.de

We propose a hybridly integrated, polymer- and InP-based photonic integrated circuit (PIC). The wavelength accuracy is 0.1 nm over almost the entire C-band, and polarization accuracy is 1.7° across the entire Poincaré sphere. The technologies used allow for easy scaling.

Keywords: photonic integrated circuits, hybrid integration, polarization, fiber-coupling

INTRODUCTION

Application specific photonic integrated circuits (ASPICs) state an appealing solution for products where low-weight, small footprint and low-price are crucial for commercial success. Indium phosphide based platforms such as [1] enable integration of several hundred optical building blocks, e.g., lasers, modulators, amplifiers and detectors on less than a square centimeter area. Those ASPICs are already deployed in telecommunication, sensing, biophotonics and signal-processing applications. HHI's polymer waveguide platform PolyBoard [2] adds the integration of, e.g., optical isolators, free-space sections with nonlinear elements, and thin film elements [3-5]. For emerging fields in photonic integration, such as quantum technology, these functionalities are essential. Merging both technologies forming hybridly integrated fiber-coupled polymer- and InP-based ASPICs attracts the exploration of new fields in photonic integration.

In this paper, we present a hybridly integrated PIC for wavelength and polarization detection of the incoming light. The wavelength determination is mainly realized on a polymer-based wavelength meter (PolyBoard). Polarization state detection is accomplished with an indium phosphide (InP) based polarimeter [6] directly butt-coupled and fixed to the PolyBoard. Additionally, U-grooves on the PolyBoard allow for adjustment-free fiber-to-chip coupling [4], thus reducing the assembly and packaging efforts.

THEORY AND METHODOLOGY

Fig. 1 shows the PIC layouts and a photo of the entire assembly. Light is coupled with an optical fiber simply clicked into an etched U-groove on the polymer-based wavelength meter (PolyBoard) and is split by consecutive 1x2 MMIs

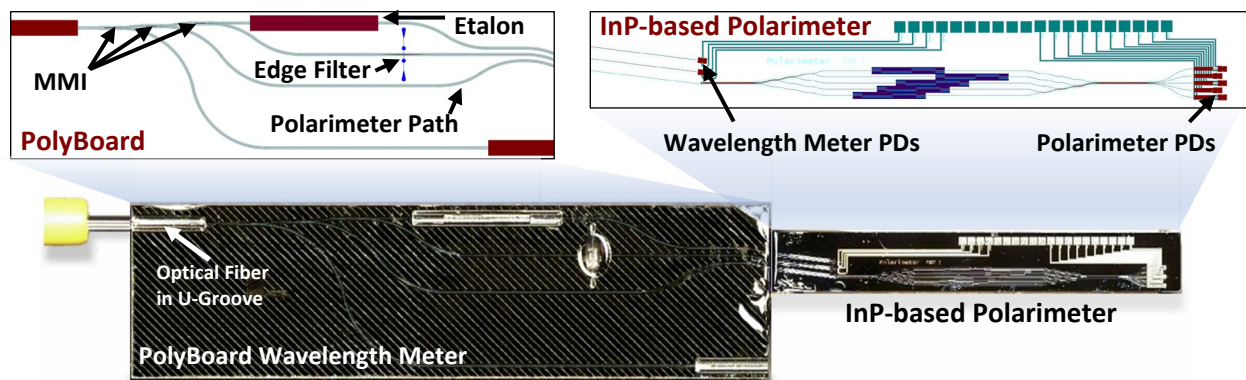


Fig. 1. Fiber-coupled polymer-based wavelength meter (PolyBoard) containing optical filters butt-coupled to the InP-based polarimeter PIC

into several paths. The top path of the wavelength meter contains a free-space 67 GHz etalon based on a graded-index (GRIN) lens with a reflectively coated facet inserted in a PolyBoard free-space section, whereas in the lower path a thin-film edge filter is inserted into the optical path by means of an etched slot. Each of the two paths is terminated by a photodiode (PD) on the attached InP PIC. A third polymer waveguide directly guides the light to

the polarimeter PIC where it is finally detected by a PD array. Angled spot size converters on each PIC provide low-loss butt-coupling with index-matched epoxy.

The working principle of the monolithically integrated polarimeter is based on interferometry and allows retrieving the input polarization of the light by measuring device output powers. The sampled output powers uniquely correspond to the input polarization, expressed by the Stokes vector and can be displayed on the Poincaré sphere [7]. An initial polarization calibration with four distinct polarizations at various wavelengths as described in [6] is necessary.

Fig. 2 shows the working principle of the wavelength meter. During initial calibration, the photocurrents of the etalon and edge filter path are recorded at defined wavelengths across the entire C-band and serve as reference signal at every particular wavelength. As a result, each measured tuple of photocurrents uniquely corresponds to a wavelength. In general, an etalon is used since its steeper rising and falling slope compared to the edge filter path enhances the accuracy of wavelength determination. Nevertheless, the accuracy is reduced around the maxima and minima.

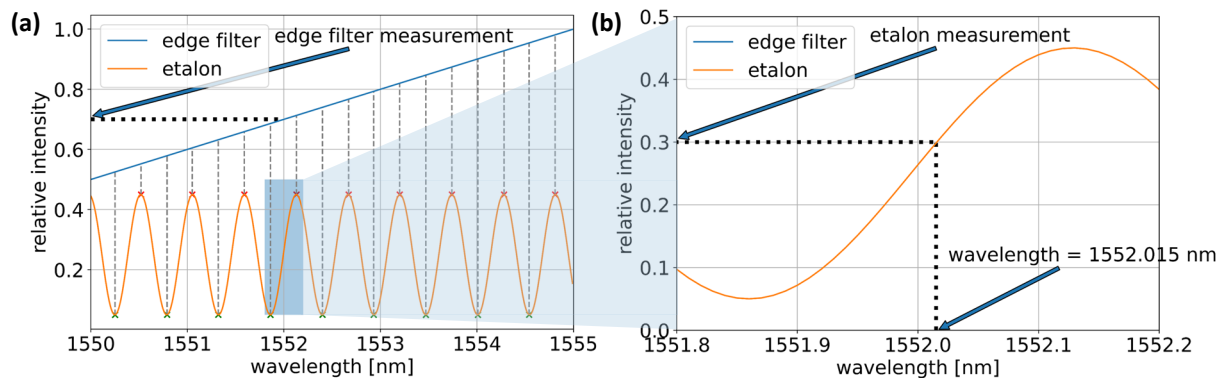


Fig. 2. Exemplary relative intensities detected after the edge filter and etalon. (a) For coarse wavelength determination, the edge filter path is used whereas for fine wavelength determination (b), the etalon path is evaluated.

RESULTS AND ANALYSIS

A multi-contact probe and commercially available sourcemeters are used for detecting the photocurrents while applying a bias voltage of -2 V. After polarization calibration, 465 distinct polarizations are launched into the fiber at different wavelengths across the C-band. Using the information from the polarization calibration, the recorded photocurrents can be expressed by Stokes vectors on a Poincaré sphere. Fig. 3 exemplarily shows the mapping results at 1545 nm. The input polarizations are treated as target polarizations and are represented by blue circles. The sampled powers are then converted to Stokes vectors (red dots) which should ideally match the target polarizations leading to an error (great-circle distance $\Delta\xi$) of 0° between both. The great-circle distance returns the minimum distance of two points on a sphere's surface [8]. Here, the input power independent measurement of the assembly reveals a mean error of 1.64° and a maximum error of 5.30° at 1545 nm.

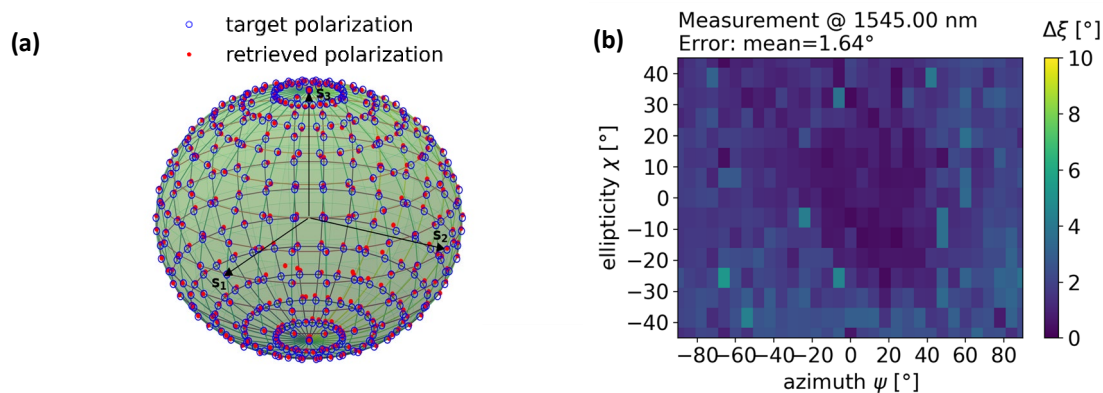


Fig. 3. Experimental results at 1545 nm. (a) 465 target (blue circles) and retrieved (red dots) polarizations are visualized on the Poincaré sphere. The corresponding heatmap (b) shows the error $\Delta\xi$ between the measured and launched state of polarizations.

The reference measurements for wavelength meter operation are shown in Fig. 4 (a). For better visualization, a limited wavelength range in the C-band of 15 nm is presented. After calibration, defined wavelengths with 25 pm spacing are launched into the fiber. The measured photocurrent at the wavelength meter PDs are converted to wavelengths as displayed in Fig. 4 (b) revealing an average deviation of below 0.1 nm. Improvements in the resolution can be potentially achieved by means of increasing the slope in the flanks of the spectral response of the etalon. This can be done by means of decreasing the free-spectral range of the filter function, which corresponds to increasing the length of the free-space section, or increasing the extinction ratio, which can be achieved by increasing the reflectivity in the coated facet of the GRIN lenses. Furthermore, the addition of a second etalon featuring its spectral rising and falling edges at the maxima and minima of the already integrated etalon would enhance the wavelength determination.

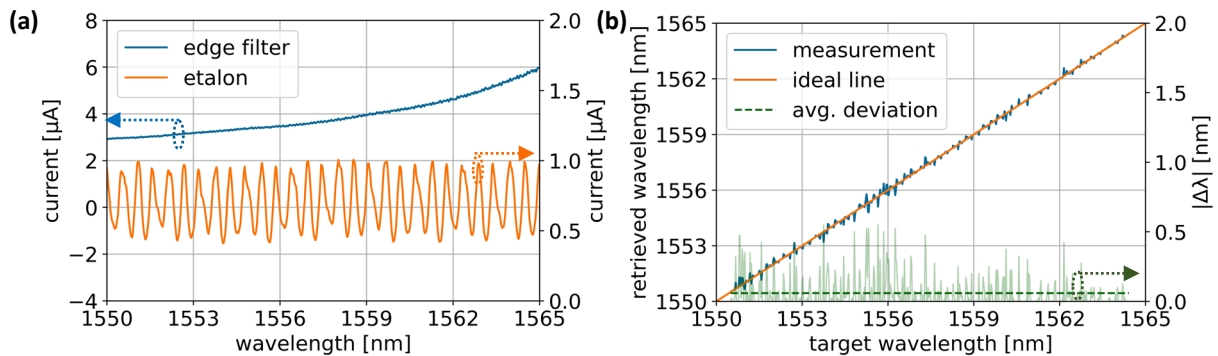


Fig. 4. (a) Edge filter and etalon reference measurement. (b) Target and retrieved wavelength with absolute wavelength deviation $|\Delta\lambda|$.

CONCLUSION

We successfully demonstrated a compact fiber-coupled hybridly integrated wavelength meter plus polarimeter with an accuracy of 0.1 nm over almost the entire C-band and 1.7° across the entire Poincaré sphere. Beyond the above demonstrated application, the PolyBoard as well as the InP-based PIC enable more complex designs. Scalable fiber-chip-coupling in etched U-grooves overcomes time and labor consuming alignment of single fibers or even fiber arrays and allows multi-channel applications without adapting the assembly approach. We paved the way for further applications based on the proposed assembly technology.

References

- [1] F. M. Soares et al., "InP-Based Foundry PICs for Optical Interconnects," *Applied Sciences*, vol. 9, no. 8, p. 1588, Apr. 2019, doi: 10.3390/app9081588.
- [2] M. Kleinert et al., "Hybrid Polymer Integration for Communications, Sensing and Quantum Technologies from the Visible to the Infrared," 2021 European Conference on Optical Communication (ECOC), 2021, pp. 1-4, doi: 10.1109/ECOC52684.2021.9605865.
- [3] D. de Felipe et al., "Recent Developments in Polymer-Based Photonic Components for Disruptive Capacity Upgrade in Data Centers," in *Journal of Lightwave Technology*, vol. 35, no. 4, pp. 683-689, 15 Feb. 15, 2017, doi: 10.1109/JLT.2016.2611240.
- [4] M. Kleinert et al., "A platform approach towards hybrid photonic integration and assembly for communications, sensing, and quantum technologies based on a polymer waveguide technology," 2019 IEEE CPMT Symposium Japan (ICSJ), 2019, pp. 25-30, doi: 10.1109/ICSJ47124.2019.8998655.
- [5] H. Conradi et al., "High Isolation Optical Isolator: A new Building Block for PolyBoard Photonic Integrated Circuits," 2018 European Conference on Optical Communication (ECOC), 2018, pp. 1-3, doi: 10.1109/ECOC.2018.8535472.
- [6] M. Baier et al., "Fully Integrated Stokes Vector Receiver for 400 Gbit/s," 2019 Optical Fiber Communications Conference and Exhibition (OFC), 2019, pp. 1-3.
- [7] Huard, Serge: *Polarization of Light*. Wiley, (1997). – ISBN 978-0-471-96536-7
- [8] L. M. Kells et al.: *Plane And Spherical Trigonometry*. McGraw Hill Book Company, Inc., (1940). pp. 323-326.

Multi-channel optical coherence tomography with a CMOS silicon nitride photonic integrated circuit

Stefan Nevlacsil^{1*}, Paul Muellner¹, Martin Sagmeister², Gerald Meinhardt², Desiree Rist², Jochen Kraft², Nanko Verwaal³, Leonhard Klein³, Moises Jezzini⁴, Sean Collins⁴, Padraic Morrissey⁴, Stefan Gloor⁵, Marcus Duelk⁵, Stefan Richter⁶, Michael Kempe⁶, Elisabeth Rank⁷, Wolfgang Drexler⁷, and Rainer Hainberger¹

¹AIT Austrian Institute of Technology GmbH, Giefinggasse 4, 1210 Vienna, Austria

²ams-OSRAM AG, Tobelbaderstrasse 30, 8141 Premstaetten, Austria

³Fraunhofer Institute for Integrated Circuits IIS, Am Wolfsmantel 33, 91058 Erlangen, Germany

⁴Tyndall National Institute, Lee Maltings Dyke Parade, Cork, T12 R5CP, Ireland

⁵EXALOS AG, Wagistrasse 21, 8952 Schlieren, Switzerland

⁶Carl Zeiss AG, Carl-Zeiss-Promenade 10, 07745 Jena, Germany

⁷Center for Medical Physics and Biomedical Engineering, Waehringer Guertel 18-20/4L, 1090 Vienna, Austria

* stefan.nevlacsil@ait.ac.at

Parallelization of acquisition beams in optical coherence tomography (OCT) provides a significant speed advantage for volumetric measurements but is not commercially viable with current system architectures. We report the development of a four-channel OCT system employing a silicon nitride CMOS photonic integrated circuit. First OCT measurement results indicate that this system achieves a signal-to-noise ratio close to state-of-the-art systems with a four-fold increase in imaging speed.

Keywords: Photonic integrated circuit, silicon nitride, optical coherence tomography

INTRODUCTION

Optical coherence tomography (OCT) is the gold standard in retinal diagnostics, providing non-invasive real-time in-vivo volumetric images of the human retina [1]. However, the high costs and large dimensions of state-of-the-art systems prevent its use for a wider range of applications, e.g., for point-of-care diagnostics. Therefore, miniaturization of OCT systems attracts increasing interest. Photonic integrated circuits (PICs) represent a promising approach to achieve not only more compact but also cheaper OCT systems [2]. However, the performance of previous PIC-based OCT systems was worse than state-of-the-art systems and potential cost and/or size advantages were insufficient to result in wider application. To a large degree this is the result of a direct translation of conventional design approaches used in fiber/bulk optical-based systems to PIC-based systems. By utilizing PIC intrinsic advantages, the drawbacks of these systems, in particular higher overall losses, can be compensated making PIC-based approaches a viable option for miniaturized and cost-efficient high-performance OCT systems.

In state-of-the-art OCT systems a single laser beam is scanned over the sample. The returning light from the sample with low power is then brought to interference with a high-power light from a reference mirror resulting in a boost of the signal-to-noise ratio. For retinal diagnostics, a fast acquisition rate is required, otherwise, the image quality suffers due to the combination of the stepwise scanning with the involuntary eye movements of the patients. A straightforward way to increase the acquisition rate is using multiple probing beams that image different parts of the retina in parallel. However, from a practical point of view multi-channel systems made of conventional fiber and bulk optical components are not commercially viable due to the associated costs, packaging requirements, and maintenance issues caused by the large number of discrete optical components. These limiting factors can be addressed by employing PICs. Increasing the number of photonic building blocks to realize multiple channels does not significantly impact the cost of a PIC and due to its monolithic nature, packaging and maintenance of photonic building blocks within the PIC is not required. In addition, PICs can be combined with CMOS opto-electronic and electronic components, allowing optical detection and electronic signal processing within a single monolithic CMOS PIC. This further reduces the need for packaging. In this work, we present a four-channel OCT system based on a silicon nitride waveguide-based CMOS PIC.

DESIGN OF PHOTONIC INTEGRATED CIRCUIT FOR MULTI-CHANNEL OCT

Two modalities of OCT are predominant, spectral-domain (SD) and swept-source (SS) OCT [3]. In both, spectrally resolved interferograms are acquired comprising the spatial information of the sample accessible via Fourier transformation. In SS-OCT the interferogram is acquired with a pair of balanced photodiodes, which is synchronized to a wavelength sweeping laser source, while in SD-OCT a broadband light source is used, and a spectrometer resolves the wavelengths. For parallelization, SS-OCT is the modality of choice because it requires only multiple synchronized photodiodes instead of multiple spectrometers. For the wavelength region $840 \text{ nm} \pm 50 \text{ nm}$ was chosen, which is commonly used in OCT systems for retinal diagnostics. Silicon nitride (SiN) was selected as

waveguide material because of its transparency in this wavelength region. In addition, fabrication of the SiN waveguides with plasma-enhanced chemical vapor deposition (PECVD) ensured CMOS-compatibility and allowed the monolithic co-integration of photodetectors and read-out electronics [4].

A critical aspect with respect to the overall performance of a multi-channel OCT system is the routing of light. The light probing the retina and the returning light from the retina share a common path, therefore, routing light towards the photodiodes used for detection can result in a significant loss of signal. In a single-channel system high loss of the signal light can be avoided by using an asymmetric power splitter. By selecting the splitting ratio in such a way that most of the source light is sacrificed, e.g., for a 90/10 splitter only 10% is used to probe the retina, most of the returning light (i.e., 90%) is routed towards the detection rather than back to the light source. Due to the overall higher power demand this option is not viable for multi-channel systems. To address this issue, we devised a novel system architecture employing a polarization-based path routing scheme [5], in which a broadband polarization beam splitter (PBS) is used to achieve a low-loss path separation between the probing light and the returning light. An according system architecture is outlined in Fig. 1(a).

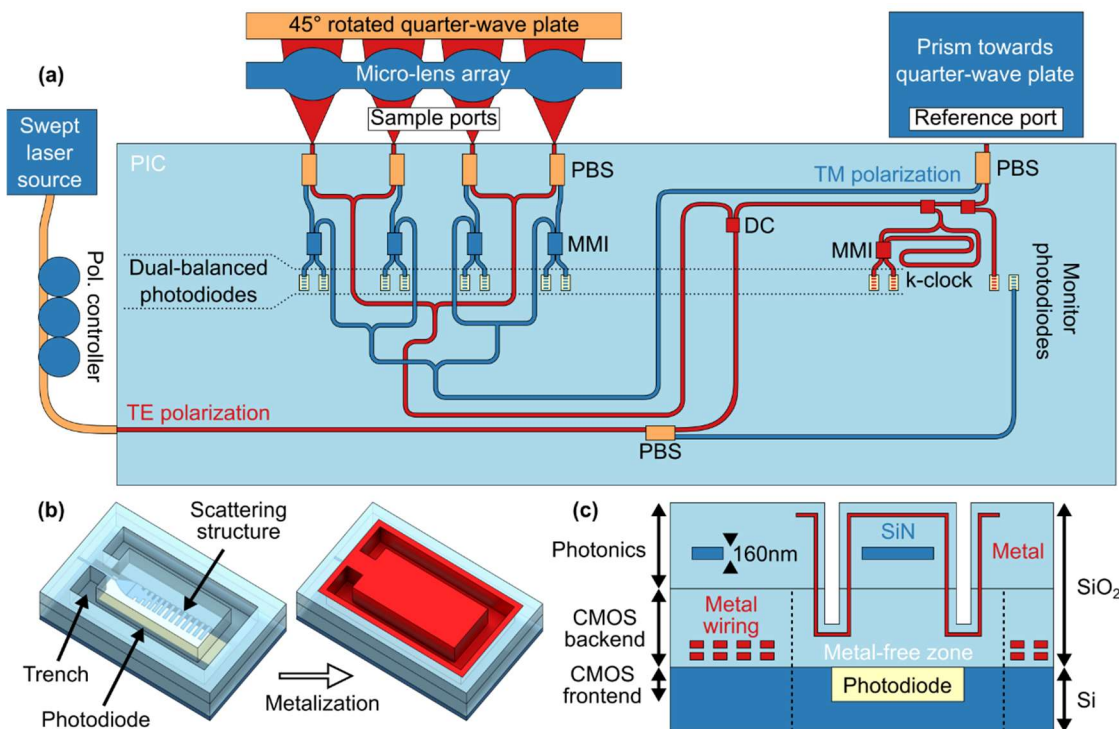


Fig. 1. (a) Schematic of the layout of the CMOS PIC used to realize the four-channel OCT system. The co-integrated electronic components are not shown. TE polarized light coming from a swept laser source is coupled to the PIC at the west side via an optical fiber. It passes a polarization beam splitter (PBS), where the monitor photodiode at the cross port provides a feedback for the external polarization controller. At the through port, a directional coupler (DC) separates the power into reference and sample power (30/70). In the sample path the light is split into four channels before it exits the PIC at the north side through a micro-lens array to reduce the divergence. In the reference path a small amount of the power is tapped towards a power monitor photodiode and a k-clock, which is used for linearization of the wavelength sweep in the post-processing. A prism at the reference port exit reflects the light upwards. On the way towards the sample and reference mirror the light passes a 45° rotated quarter-wave plate resulting in circular polarized light. The returning light passes the quarter-wave plate again resulting in light with TM polarization being coupled back to the PIC where it is routed via the PBS towards the multi-mode interferometer (MMI). The interfered light is coupled to a pair of photodiodes used for balanced detection. (b) Schematic of the novel concept used to couple light from the waveguide to the monolithically co-integrated photodiode several micrometers underneath: A scattering structure deflects the light out of the waveguide and a metal cage structure enclosing the scattering structure ensures that most of the light is redirected towards the photodiode. The cage is formed by a trench etch of the cladding followed by metal deposition. (c) Layer stack of the chip allowing monolithic co-integration of CMOS opto-electronics, electronics, and silicon nitride waveguides.

Another challenge which had to be overcome was the efficient coupling of the light from the waveguides to the photodiodes. Using a standalone waveguide grating, light is lost in lateral direction with multiple micrometers of SiO₂ between the waveguide material and the doped silicon of the substrate acting as active area of the photodiode. To avoid this issue a novel waveguide-to-photodiode coupling structure was developed (see Fig. 1(b)). A scattering structure is utilized which is encapsulated by metal in all directions except towards the photodiode. This ensures that most of the light is redirected towards the active area.

Fig. 1(c) depicts a schematic of the layer stack used for the CMOS PIC. The photonic components were processed at the back end of line on top of a CMOS chip. Significant effort had to be put into optimizing the fabrication process to allow waveguides with sufficiently low propagation losses on top of underlying metal layers. Due to the metal layers in the CMOS backend elevations of tens of nanometers were present in the SiO₂ after standard CMOS processing. Therefore, multiple steps of chemical-mechanical polishing had to be applied to achieve a sufficiently smooth surface for waveguide processing. Propagation losses of 1.3 (1.1) dB/cm were observed for TE (TM) polarization, respectively, for a wavelength of 840 nm. A penalty of few tenths of dB/cm was observed in comparison with waveguides processed with the same PECVD without underlying metal layers.

RESULTS

The fabricated CMOS PIC was optically and electronically packaged (see Fig. 2(a)). The PIC-based OCT module was then included in a modified Zeiss OCT system. For the measurements an EXALOS prototype swept source laser source was used with a central wavelength of 840 nm, a FWHM bandwidth of 60 nm, a total optical output power of up to 50 mW (17 dBm), and a repetition rate of 100 kHz. The sensitivity, i.e., the signal-to-noise ratio of a measurement with a mirror as sample, was determined to be 88-91 dB. The power exiting the PIC per channel was 0.52 mW (-3 dBm), a factor of ~11 dB results from the selected splitting ratios alone. Fig. 2(b) shows non-averaged tomograms of different sections of an eye model with similar optical properties as the human retina. The tomograms were acquired in parallel with a scanning rate of 100 kHz per channel (4x100 kHz in total).

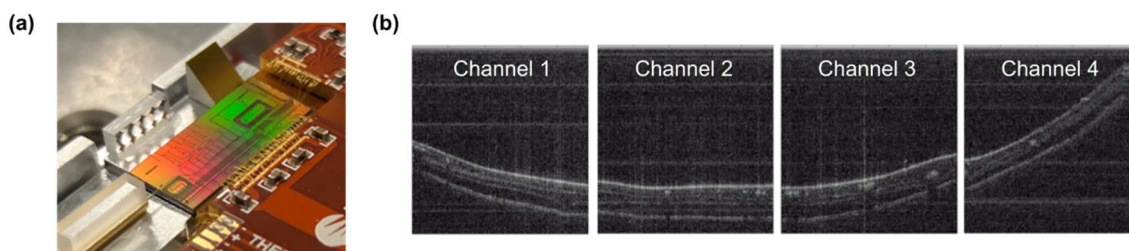


Fig. 2. (a) Photo of the packaged CMOS PIC. (b) First measurement results of the PIC-based four-channel OCT system using an eye model as sample. Each of the four measurement channels scans a different part of the retina with a small overlap of the area to facilitate stitching of the individual images into a combined one.

DISCUSSION & OUTLOOK

We have shown that co-integration of SiN photonic, opto-electronic, and electronic components within a single monolithic chip without a significant loss penalty is possible with the developed fabrication process flow. In addition, the established polarization-based routing scheme and library of photonic building blocks provides sufficient performance for OCT measurement. This was shown with a CMOS PIC-based OCT system with a total acquisition rate of 400 kHz with sensitivities close to 90 dB in a first measurement. More in-depth characterization is however still required to determine the full performance specifications, especially, the tomograms do not fully reflect the measured sensitivities. Furthermore, in-vivo measurements are necessary to test the system in a more realistic scenario.

Acknowledgements: This research has received funding from the European Union's Horizon 2020 research and innovation program under grant agreement No 688173 (OCTCHIP) and No 871312 (HandheldOCT).

References

- [1] W. Drexler, J.G. Fujimoto, *Optical Coherence Tomography*, Springer, Cham, 2015
- [2] E. A. Rank, A. Agneter, T. Schmoll, R. A. Leitgeb, W. Drexler, *Miniaturizing optical coherence tomography*, *Translational Biophotonics*, 2021
- [3] J. F. de Boer, R. A. Leitgeb, M. Wojtkowski, *Twenty-five years of optical coherence tomography: the paradigm shift in sensitivity and speed provided by Fourier domain OCT*, *Biomed. Opt. Express* 8(7), 3248–3280, 2017
- [4] M. Sagmeister, G. Koppitsch, P. Muellner, S. Nevlacsil, A. Maese-Novo, R. Hainberger, D. Seyringer, J. Kraft, *Monolithically integrated, CMOS-compatible SiN photonics for sensing applications*. in *Proceedings of EUROSENSORS*, 2(13), 1023, 2018
- [5] S. Nevlacsil, P. Muellner, A. Maese-Novo, M. Eggeling, F. Vogelbacher, M. Sagmeister, J. Kraft, E. Rank, W. Drexler, and R. Hainberger, *Multi-channel swept source optical coherence tomography concept based on photonic integrated circuits*, *Opt. Express* 28, 32468-32482, pp. 121-127, 2020

A Hybrid Optical Waveguide Platform for High-Performance Integrated Photonic Devices

(Student paper)

Hamed Nikbakht¹, Bob van Someren², Chunyu Lu¹ and B. Imran Avci¹

¹LaserLaB, Department of Physics and Astronomy, VU University Amsterdam, De Boelelaan 1081, 1081 HV Amsterdam, The Netherlands

²Elf Software, 3061 WS Rotterdam, The Netherlands

* b.i.avci@vu.nl

Here, we report the initial results of our etch-free hybrid optical waveguide platform and the novel photonic integrated circuits (PICs) fabricated using this platform. Our waveguide technology is based on a thin layer of silicon nitride and low-loss polymer. It is a simple, rapid, cost-effective, and low-loss platform that can be used to fabricate various high-performance PIC devices.

Keywords: *hybrid waveguide, single-mode, high-performance, photonic integrated circuits (PICs)*

INTRODUCTION

Photonic integrated circuits (PICs) hold great promise for future applications such as quantum computers, neuromorphic networks, portable imaging systems, and disposable sensors. The current technology for fabricating such devices is based on patterning materials such as silicon, silicon nitride, silicon carbide, etc., which requires several fabrication steps [1,2]. Processing of these materials needs to be done in a cleanroom environment and usually, several iterations are needed to optimize the design. Direct access to such fab facilities is limited, and researchers who do not have such access need to get this service from commercial companies, which is expensive and has a long lead-time. Such a lengthy process also makes debugging the design almost meaningless. Multi-project wafer run services have been started as an alternative solution [3]. However, the cost/mm² is still high (~ 10k Euros) and the lead-time is even longer.

Two main challenges force one to utilize such an expensive and sophisticated fabrication process. Due to the high refractive index of mentioned materials, the waveguides must be small to remain single-mode. Therefore, it seems that using a lower refractive index (RI) material with a more straightforward patterning process is the solution. However, another challenge arises with a low RI. Reducing the RI contrast between the core and the cladding increases the bending loss [4,5]. Therefore, the bending radius of the waveguides in a device with low RI contrast must be large; making the overall footprint of the PIC is also big. In addition to big device size, large PICs suffer from propagation loss as well.

We designed and demonstrated a material stack that can be used to make high-performance PICs at a very low cost and considerably short time. In this method, we pattern photoresist and do not etch the high index material (silicon nitride, Si₃N₄ in this case) which simplifies the fabrication dramatically. Due to the small RI contrast, pushing the resolution to the sub-micron regime is not required and simple photolithography techniques can be used to make these devices. In addition to being cost-effective and fast, the material stack that we designed also allows us to make relatively sharp bends with a minimum bending radius of 100 μm, which is a big challenge for strip-loaded waveguides. We found out that these sharp bends can only be achieved for certain mode volume ratios between the polymer and the high-index layer [6]. This paper will discuss the material stack and demonstrate some of the devices that we fabricated and characterized by using this fabrication approach.

DESIGN AND EXPERIMENTAL RESULTS

This platform utilizes strip-loaded waveguides with a high index layer as the core and a patterned low index UV-curable polymer custom photoresist layer as the guiding cladding (**Error! Reference source not found.a**). A mode calculation of this structure shows that the power is distributed between Si_3N_4 and polymer layers and the interaction of the mode with the sidewalls of the polymer is relatively small (**Error! Reference source not found.b**). The thickness of the polymer layer is 1200 nm and its refractive index at 1.5 μm wavelength range is 1.56. In this work, Si_3N_4 is used as the high index material. Fig. 1 demonstrates the simulation, fabrication, and measurement results of the optical waveguides and microring resonators. The full-width-at-half-maximum (FWHM) of the resonance peaks of the elliptical ring resonator was measured as $\text{FWHM} = 3.3 \text{ pm}$, which corresponds to a quality factor of $Q = 4.7 \times 10^5$. The propagation loss value is calculated to be $\sim 0.9 \text{ dB/cm}$ based on the measured Q values.

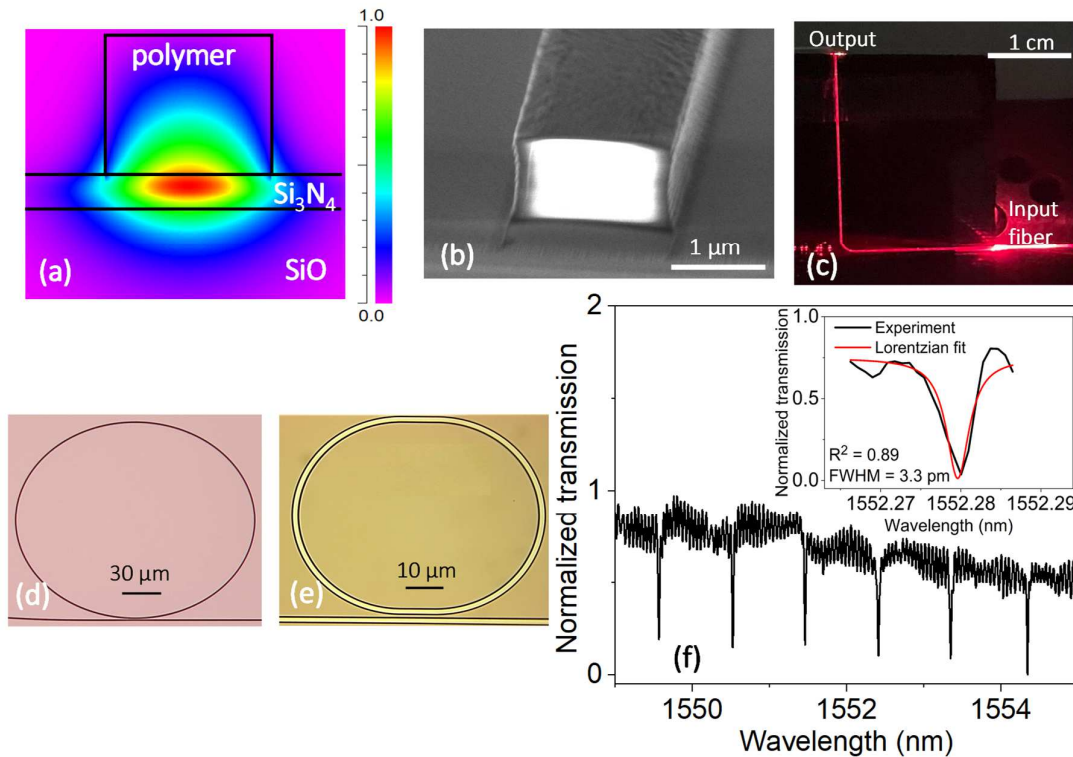


Fig. 1. (a) Beam propagation simulation result of the optical waveguide. (b) SEM image of the cross-section of the optical waveguide. (c) Red light propagation in these waveguides. Fabricated microcavity devices (d) elliptical (e) race track resonators. (f) Measurement results of the elliptical ring resonator.

The width of the patterned polymer strip is in the range of 1-2 μm , which makes it possible to fabricate by contact mask photolithography or other diffraction-limited UV photolithography techniques, which is the most widely available equipment in the cleanrooms. Another advantage of this platform is the possibility of reducing roughness in the patterned polymer layer by heating it to its glass transition temperature. At that temperature, the surface tension of the polymer reduces the roughness resulting in smaller scattering loss of the waveguides. The use of polymer photoresists also enables us to reuse the substrates. Most of the polymer photoresists are soluble in acetone or their specific remover. Considering that the pattern is only transferred to the polymer photoresist, one can reuse the substrate by washing the polymer layer.

We designed several PIC components (broadband non-uniform directional couplers, Sagnac loop mirrors, two different types of coupled-cavity systems, elliptical ring resonators, race track resonators, arrayed waveguide gratings, and so on) to test the performance of our platform. In Fig. 2, some of the experimental results are given. With the coupled cavity system demonstrated in Fig.2a, we achieved Fano-like asymmetric resonance peaks. The structure is formed by using Sagnac loop mirrors and a pulley-type microring resonator. The ultra-broadband 3dB coupled given in Fig. 2c is a novel concept [7]. It is a vertically shifted non-uniform coupler that operates over a very

large bandwidth (1300-1600 nm). Different waveguide widths (w_1 , w_2 , w_3) and vertical shift values (L_{shift}) were investigated and the optimum values were obtained through beam propagation simulations.

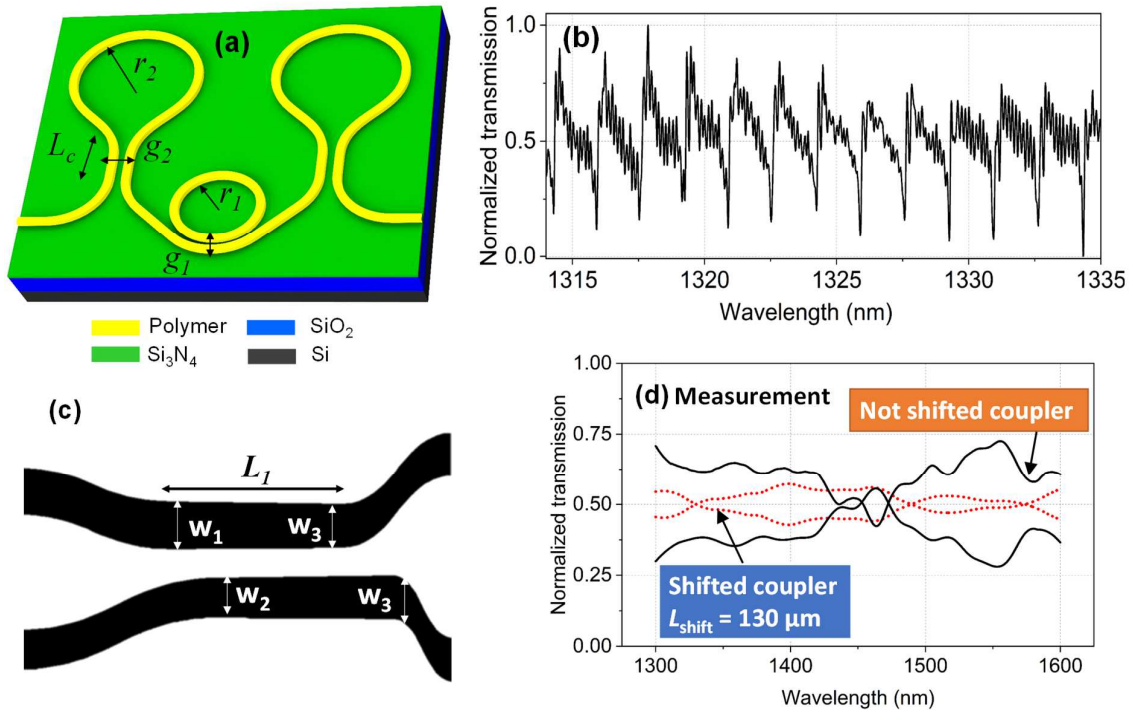


Fig. 2. (a) Schematic of the coupled cavity system and (b) its transmission response. (c) Schematic ultra-broadband coupler design and (d) its transmission response.

CONCLUSIONS

In short, we demonstrated that our new fabrication platform that can provide PICs with low bending and propagation losses in a very short time for a small budget. This will change the way we prototype PIC devices. We have already tested several new ideas and demonstrated very high performance. We believe this new approach will be an enabler for the researchers and companies that are working in the field of integrated photonics.

References

- [1] W. Bogaerts, D. Taillaert, B. Luyssaert, P. Dumon, J. Van Campenhout, P. Bienstman, D. Van Thourhout, R. Baets, V. Wiaux, and S. Beckx, Basic structures for photonic integrated circuits in Silicon-on-insulator, *Opt. Express* vol. 12, pp. 1583-1591, 2004.
- [2] S. K. Selvaraja, P. Jaenen, W. Bogaerts, D. Van Thourhout, P. Dumon, and R. Baets, Fabrication of Photonic Wire and Crystal Circuits in Silicon-on-Insulator Using 193-nm Optical Lithography, *J. Light. Technol.* vol. 27, no. 18, pp. 4076-4083, 2009.
- [3] N. M. Fahrenkopf, C. McDonough, G. L. Leake, Z. Su, E. Timurdogan and D. D. Coolbaugh, The AIM Photonics MPW: A Highly Accessible Cutting Edge Technology for Rapid Prototyping of Photonic Integrated Circuits, *IEEE J. Select. Top. Quantum Electron.* vol. 25, no. 5, pp. 1-6, 2019.
- [4] K. Shang, S. Pathak, C. Qin, and S. J. B. Yoo, Low-Loss Compact Silicon Nitride Arrayed Waveguide Gratings for Photonic Integrated Circuits, *IEEE Photonics J.*, vol. 9, no. 5, pp. 1-5, 2017.
- [5] Katsunari Okamoto, Chapter 2 - Planar optical waveguides, *Fundamentals of Optical Waveguides (Second Edition)*, Academic Press, 2006, Pages 13-55.
- [6] A. Boes, B. Corcoran, L. Chang, J. Bowers, and A. Mitchell, Status and Potential of Lithium Niobate on Insulator (LNOI) for Photonic Integrated Circuits, *Laser Photon. Rev.* vol. 12, pp. 1700256, 2018.
- [7] Akca B. I. and van Someren B. 2020. Waveguide. UK Patent Application, filed June 26, 2020. No: GB2009731.7
- [8] Akca, B. I. 2019. Broadband optical coupler and switch. Dutch Patent Application, filed September 25, 2019. No: 2023901 International Patent Application No. PCT/NL2020/050588.

Thermal and wiring optimizations of dense SOA arrays on an adhesively bonded InP membrane

(Student paper)

Yi Wang^{1*}, Jorn van Engelen¹, Victor Dolores-Calzadilla^{1,2}, Kevin Williams¹, Meint Smit¹, and Yuqing Jiao¹

¹Eindhoven Hendrik Casimir Institute (EHCI), Eindhoven University of Technology, Eindhoven, 5600MB, the Netherlands

²Photonic Integration Technology Center (PITC), Eindhoven University of Technology, Eindhoven, 5600MB, the Netherlands

*y.wang10@tue.nl

InP membrane on Si can empower dense monolithic photonic circuits. However, densely integrated SOA arrays on this platform face the challenge of poor heat sinking and injection non-uniformity. In this paper, we propose to tackle these two problems simultaneously by conducting thermal shunts connecting to the Si heatsink, which also serves as an interposer for dense electrical wirings. An electrical-thermal model is established numerically for the SOAs. With the presence of thermal shunts, a 10- μm viable pitch is achieved at room temperature, without forced convective cooling. This array allows a relatively high injection current density of 5.6 kA cm^{-2} before reaching failure temperatures. The injection-nonuniformity is numerically solved to be 2 %.

Keywords: InP, Membrane, Dense integration, SOA

INTRODUCTION

Indium phosphide membrane on silicon (IMOS) [1] is a promising technology to enhance the integration density of InP-based photonic integrated circuits (PIC), since it offers nanophotonic waveguides via the high-contrast InP-benzocyclobutene (BCB)-Si layer structure, in which BCB is the adhesive bonding layer. Although a route to high-density SOA arrays has already been indicated on this platform [2], two challenges remained unsolved: Efficient heat sinking through the thermally isolating BCB [3], [4] and dense electrical wirings. In this paper, we aim to solve these two challenges at the same time by introducing thermal shunts that can act as conduction wires connecting to the Si heatsink and interposer. Electrical-thermal simulation is conducted to obtain the thermal performance under different conditions, including current density, SOA array pitch and the presence of the thermal shunt. Injection nonuniformity of narrow accessing wires necessary for dense arrays is also analyzed numerically by segmenting the SOA along the length.

RESULTS

The structure of the membrane SOA is depicted in Fig. 1(a). The 2-D thermal profile of the SOA in a plane perpendicular to the light propagation direction is obtained by numerically solving the electric drift-diffusion equations for the electrons and holes in the full layer stack, and then calculating the total heat generation of Joule heating and recombination heating. Contact resistance is not included, since it's not a fundamentally limiting factor. As a result, a direct relation between current injection and heat generation is established. This device-level detail is needed to analyze the local heat generation of the SOA and design for efficient heat sinking.

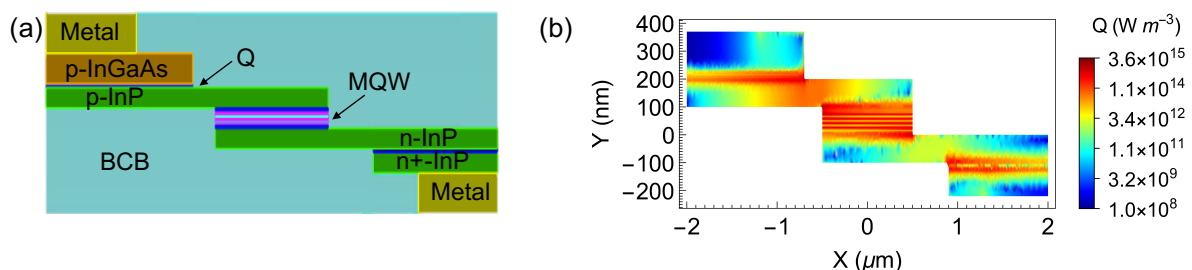


Fig. 1. Thermal profile of the membrane SOA. (a): Schematics showing the layer structure of the SOA. (b): Logarithmic plot of the heat generation Q at 2.3 kA cm^{-2} injected current density, which theoretically provides 23dB mm^{-1} modal gain at 300 K.

4 hotspots are visible in Fig. 1 (b), namely in the Q layer between p-InGaAs contacting layer and p-InP cladding, the center of the p-InP cladding, the multi-quantum well (MQW) core, and the Q layer between the n-InP cladding and n+-InP contacting layer. The hotspots in Q layers are due to band discontinuities at the Q/InP interfaces, while in

the p-InP cladding and the MQW core they are due to higher material resistivity, i.e. lower mobility of holes compared to electrons, and stronger carrier recombination, respectively. Note that Fig. 1(b) is plotted in logarithmic scale. As can be observed, the hotspots are more aggregated near the p-side. Besides, for suppression of Zinc diffusion, an epitaxy direction from n-side to p-side is desired in the fabrication of membrane SOAs [5], which leads to the p-side being beneath the n-side after wafer bonding and substrate removal. Therefore, it is more efficient to place thermal shunts made of Ti-Pt-Au connecting to the bottom heatsink (substrate) at the p-side.

After obtaining the maps of heat generation for the single SOA, 2-D heat transfer simulation is performed in the plane orthogonal to the waveguide direction for arrays of SOAs of different pitches and at varying injected current densities, in order to quantify the effect of the thermal shunt. In simulation, infinite arrays are considered, which is the worst-case scenario as there is no lateral heat dissipation. This condition is simulated by one SOA with periodic boundary conditions on the left and right, as seen in Fig. 2(a). The bottom of the 500 μm Si substrate which is in contact with the heatsink, is set to a constant temperature of 300 K. All other external boundaries are set to convective with a heat transfer coefficient $h = 5 \text{ W m}^{-2} \text{ K}^{-1}$ to emulate a natural air environment without forced cooling. Parameter sweep is done on the thickness, length and angle of the thermal shunt, and we have found that a shunt thickness of 200 nm is already sufficient to drastically reduce the core temperature. As seen in Fig. 2 (a) and Fig. 2 (c), for an extraordinarily dense 10 μm SOA pitch and 2.3 kA cm^{-2} current density, the heat originally blocked by the BCB layer is now successfully dissipated through the thermal shunt made of metal, and a 23 K decrease in the core temperature is achieved. As seen in Fig. 2 (b), if we aim for a higher injected current at such 10 μm pitch, the scheme without thermal shunt will be unfeasible because the temperature inside the core will quickly reach 370 K ($\sim 100^\circ\text{C}$) and beyond. At this temperature, most of the lasers/SOAs start to fail. In contrast, with the thermal shunt, the SOA array can withstand 5.6 kA cm^{-2} current density before reaching 370 K. At a large 200 μm pitch, which is close to the situation of standalone SOAs, the scheme with thermal shunt still has more than 10 K decrease in core temperature compared to the scheme without.

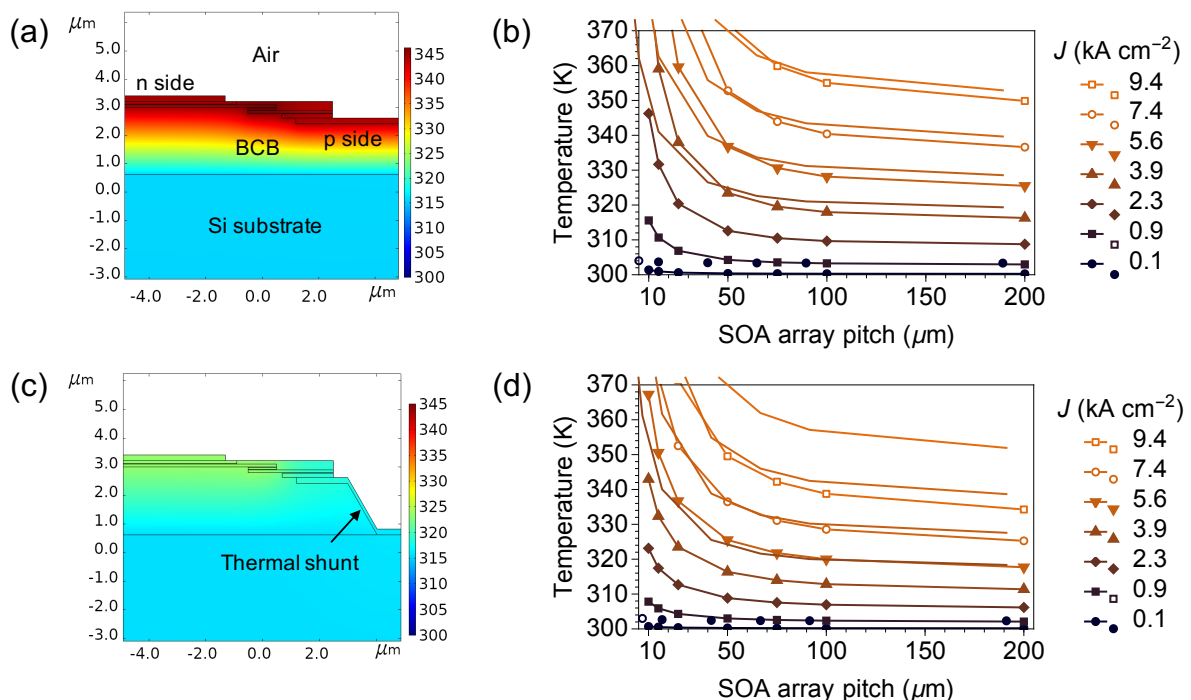


Fig. 2. Heat transfer simulation of the SOA. (a), (c): Temperature distributions without/with shunts at 2.3 kA cm^{-2} and 10 μm SOA pitch. Note that the bottom of the Si substrate extends outside of the plot window and is not shown. (b), (d): Temperature in the core without/with shunts at varying SOA pitches and current densities.

Since the thermal shunts at the p-side are made of metal, they can be naturally used as wirings. The Si substrate can be utilized as an electrical interposer with low-resistance, electroplated gold wires. In this way, the n-side can be connected together to form a common anode, which can serve as a large thermal dissipator enabling double-side cooling without the need for flip-chip bonding, as seen in Fig. 3(a). Therefore, even better heat sinking can be

achieved. However, at high integration density, narrow wires are physically needed, and therefore the injection nonuniformity due to an electric potential drop in the wiring itself cannot be ignored. Considering fabrication tolerance, gold wires with a width w_{Au} of $8\ \mu\text{m}$ can be used for the $10\ \mu\text{m}$ pitch, as seen in Fig. 3(a). The relation between wire thickness h_{Au} and injection nonuniformity needs to be investigated. This is done by segmenting the SOA along the light propagation direction, and solving for the electric potential for each segment using Ohm's law. The bias voltage V_0 is applied at one end of the SOAs, and the electrical potentials at the other end of the SOAs with a function of SOA lengths, under different wire thickness and bias voltages are plotted in Fig. 3 (b) and Fig. 3(c), respectively. As can be seen, for a typical $500\ \mu\text{m}$ long SOA, $1\ \mu\text{m}$ -thick wires on the Si interposer are sufficient to provide $< 2\%$ nonuniformity in electric potential at a high $1.5\ \text{V}$ bias voltage. This configuration could be further extended to support SOAs as long as $1\ \text{mm}$ with $2\ \mu\text{m}$ -thick wires on the interposer, which is readily achievable.

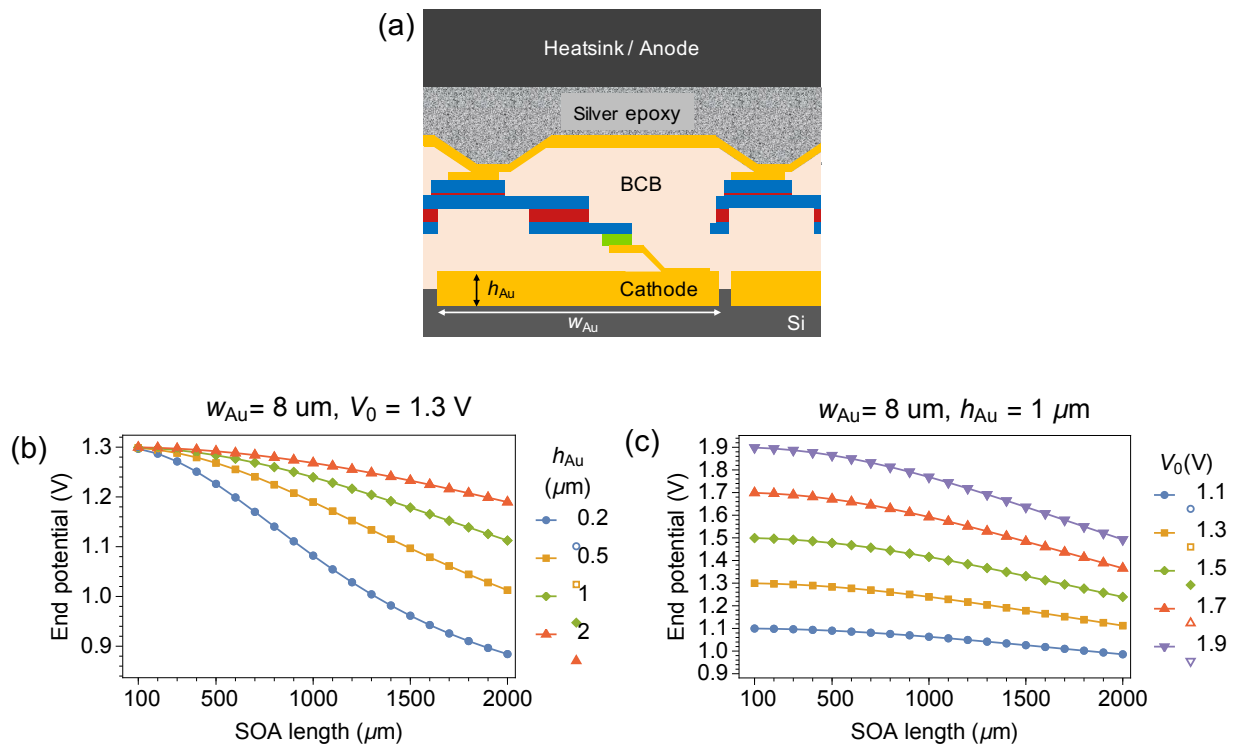


Fig. 3. Injection nonuniformity of the SOAs. (a) Schematics showing the dense wiring solution. (b): Electric potential at the far-end of the SOA with varying wire thickness at a $1.3\ \text{V}$ bias voltage. (c): Electric potential at the far-end of the SOA with $1\ \mu\text{m}$ -thick access wire at varying bias voltages V_0 .

CONCLUSION

In this paper, we propose to use metal thermal shunts and a full heat spreader to improve the thermal performance of SOA arrays on a membrane platform. With such thermal shunts, $10\ \mu\text{m}$ pitch can be realized within the $370\ \text{K}$ thermal cap at a high current density of $5.6\ \text{kA cm}^{-2}$. Together with a Si interposer, the $200\ \text{nm}$ -thick thermal shunts can also be used as dense wiring solutions with $< 2\%$ injection nonuniformity for $500\ \mu\text{m}$ long SOAs.

References

- [1] Y. Jiao *et al.*, "Indium Phosphide Membrane Nanophotonic Integrated Circuits on Silicon," *Phys. Status Solidi A*, vol. 217, no. 3, p. 1900606, Feb. 2020, doi: 10.1002/pssa.201900606.
- [2] Y. Wang *et al.*, "Versatile butt-joint regrowth for dense photonic integration," *Opt. Mater. Express*, vol. 11, no. 8, p. 2478, Aug. 2021, doi: 10.1364/OME.431963.
- [3] C. Zhang, D. Liang, G. Kurczveil, J. E. Bowers, and R. G. Beausoleil, "Thermal Management of Hybrid Silicon Ring Lasers for High Temperature Operation," *IEEE J. Select. Topics Quantum Electron.*, vol. 21, no. 6, pp. 385–391, Nov. 2015, doi: 10.1109/JSTQE.2015.2428057.
- [4] W. Yao *et al.*, "Towards the Integration of InP Photonics With Silicon Electronics: Design and Technology Challenges," *J. Lightwave Technol.*, vol. 39, no. 4, pp. 999–1009, Feb. 2021, doi: 10.1109/JLT.2020.3043799.
- [5] J. J. G. M. van der Tol *et al.*, "Indium Phosphide Integrated Photonics in Membranes," *IEEE J. Select. Topics Quantum Electron.*, vol. 24, no. 1, pp. 1–9, Jan. 2018, doi: 10.1109/JSTQE.2017.2772786.

Practical characterization of InP Waveguides and MMI couplers using Mach-Zehnder interferometers

(Student paper)

Amer Bassal, Guillaume Binet, Wouter Diels, Axel Schönau, Oliver Abdeen, Moritz Baier, Martin Schell

Fraunhofer-Institut für Nachrichtentechnik, Heinrich-Hertz-Institut, 10587 Berlin, Germany
 amer.bassal@hhi.fraunhofer.de

We present, with Mach-Zehnder structures, a simplified method using one fiber coupling, rather than two, to simultaneously characterize waveguide group index, dispersion, and losses along with the imbalance of multimode interference couplers in InP.

Keywords: Mach-Zehnder interferometers, group index, propagation loss, dispersion

INTRODUCTION

One fundamental component of photonic integrated circuits (PICs) is the passive waveguide (WG). Its spectral properties are especially important for purposes beyond simple routing, e.g. in ring lasers and long cavity mode locked lasers. Several techniques have been adopted to obtain the wavelength dependent group index and propagation loss of WGs. The propagation loss can be obtained from the input and output optical spectra. This requires a precise calibration of the setup to compensate for coupling and instrument losses, which is difficult to achieve.

For the group index, one method is to use the free spectral range (FSR) of the interference spectrum from a Fabry-Perot cavity [1]. This, however, requires an accurate determination of the cavity length which is difficult due to the inaccuracy of facet cleaving. An alternative method for an accurate group index measurement consists of using a broad band source, fed into a Mach-Zehnder interferometer (MZI) with one arm containing the device under test and the other being a free space path. Analyzing the MZI output with an optical spectrum analyzer (OSA), it is possible to derive the wavelength dependent group index and hence chromatic dispersion [2, 3]. Similarly in PICs, MZI structures built using multimode interference (MMI) couplers are used to measure the index [4]. Using multiple MZI structures, one can get the losses and the MMI couplers branching ratios from the interference spectrum [5], where the values become independent of the fiber coupling losses. This method, however, still requires fiber coupling to both input and output waveguides, which complicates (semi)automated measurements significantly.

Here, we propose an MZI based method, requiring only a single fiber coupling, to simultaneously obtain the group index, losses and imbalance of MMI couplers. Indium Phosphide (InP) integrated MZI structures with different arm length differences ($730.4 \mu\text{m}$ & $210.4 \mu\text{m}$) are coupled into monolithically integrated DC photodiodes (PDs), so the dispersion, losses and imbalance can be derived from photocurrents rather than optical intensities.

THEORY AND METHODOLOGY

Fig. 1(a) shows the layout of the integrated MZI structures. Light is coupled with a fiber through the spot size converter (SSC), split using 1×2 MMIs into different MZI structures with various arm length differences ΔL , two with $\Delta L = 210.4 \mu\text{m}$ and one with $\Delta L = 730.4 \mu\text{m}$, recombined in 2×1 MMIs, and finally absorbed by PDs. For an MZI with arm lengths L and $L + \Delta L$, the output intensity I_{out} for varying input wavelengths can be expressed as follows,

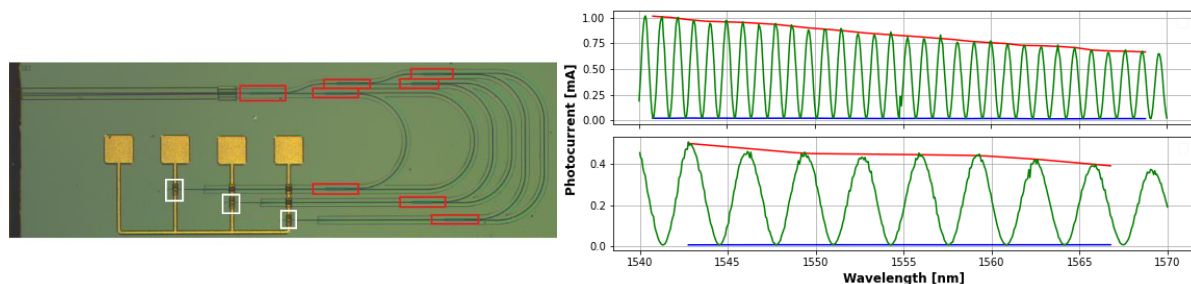


Fig. 1. (a) Photograph of the MZI structure, and (b) the Photocurrent spectrum.

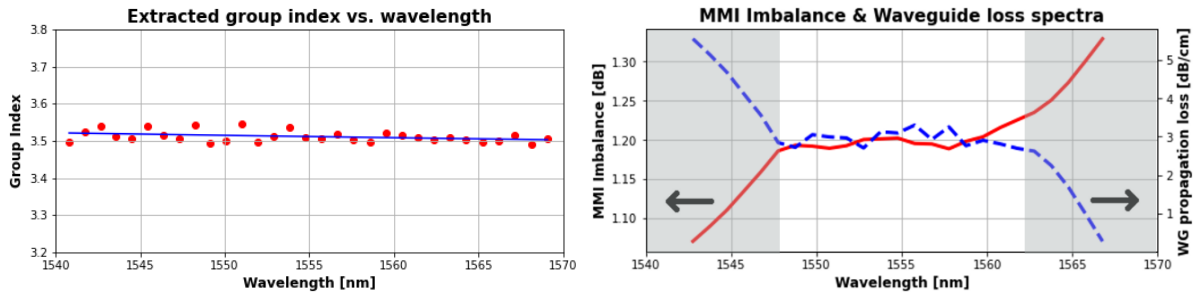


Fig. 2. (a) The extracted group index and (b) the propagation losses and MMI imbalance, all in TE mode.

$$I_{out} = I_{in} e^{-\alpha L} \left[e^{-2\alpha \Delta L} S_1^2 + S_2^2 + 2e^{-\alpha \Delta L} S_1 S_2 \cos\left(\frac{2\pi n_g(\lambda)}{\lambda} \Delta L\right) \right] \quad (1)$$

where I_{in} is the input intensity, α is the propagation loss in [Np/m], S_1 and S_2 are the MMI intensity splitting ratios, and $n_g(\lambda)$ is the group index. The I_{out} spectrum shows fringes due to interference as expected from the cosine argument.

Given ΔL , at each wavelength the group index is obtained from the FSR, which is expressed as $\Delta\lambda = \lambda^2 / n_g \Delta L$. Having the group index, the chromatic dispersion is obtained as $D(\lambda) = dn_g(\lambda) / cd\lambda$, where c is the light speed. From Eq. 1, the losses are obtained from the photocurrent extrema in the interferogram using the parameter defined below,

$$I_d \equiv \frac{I_{max} + I_{min}}{I_{max} - I_{min}} = \frac{e^{-2\alpha \Delta L} S_1^2 + S_2^2}{2S_1 S_2 e^{-\alpha \Delta L}} \quad (2)$$

where the PD responsivity cancels out. Writing the equation in the dB scale, converting the propagation losses from [Np/m] to [dB/m], and with the help of the quadratic formula, we get the following linear equation,

$$\pm dB\left(\frac{S_2}{S_1}\right) + \frac{\alpha}{2} \Delta L = dB\left(I_d \pm \sqrt{I_d^2 - 1}\right) \quad (3)$$

where the WG loss α and the MMI Imbalance, $dB(S1/S2)$, can be obtained using two equations with two values of ΔL .

RESULTS AND ANALYSIS

The chip was fiber coupled in a setup calibrated for the Transverse Electric (TE) mode with the input wavelength swept with 0.6 pm steps. For each wavelength, the photocurrent of the PD, biased at -1 V, was recorded to obtain the interferogram shown in Fig. 1 (b). The FSR was then obtained by fitting a parabola around each peak yielding the group index spectrum in Fig. 2 (a). Around 1550 nm, a group index of 3.51 and $D = -2250$ ps/(nm.km) can be observed for the WG under test with an Fe doped InGaAsP core. Similar values have previously been reported around 1550 nm as $n_g = 3.49$ for InGaAsP WGs [6] and $D = -1700$ ps/(nm.km) for a pure InP sample [7].

The peak and dip envelopes of the interferograms, smoothed with a window of 15 and 3 points respectively, are interpolated as shown in Fig.1 (b), and Eq. 3 was used to estimate the WG losses and MMI imbalance shown in Fig. 2 (b). The minimum values (~ 7 μ A) are well above the PD dark current (~ 2 nA). Propagation losses fluctuate around 3 dB/cm compared to values ~ 2 dB/cm from conventional transmission measurements of the same WG type. The curves in Fig. 2 (b) deviate near the edges, in the shaded areas, which is possibly due to the low number of fringes in the 210 nm interferogram, and due to the sensitivity of Eq. 2 resulting from the subtraction in the denominator. This method is nevertheless a fast way of simultaneously obtaining the WG losses and MMI imbalance.

References

- [1] Z. Li, D. Lu, Y. He, *A waveguide loss measurement method based on the reflected interferometric pattern of a Fabry-Perot cavity*, Integrated Optics: Devices, Materials, and Technologies XXII, 2018
- [2] J. Lee, D. Kim, *Versatile chromatic dispersion measurement of a single mode fiber using spectral white light interferometry*, Optics Express, vol. 14, no. 24, 11608, 2006
- [3] F. Leo, U. Dave, S. Keyvaninia, B. Kuyken, G. Roelkens, *Measurement and tuning of the chromatic dispersion of a silicon photonic wire around the half band gap spectral region*, Optics Letters, vol. 39, no. 3, p. 711, 2014
- [4] S. Dwivedi, T. Van Vaerenbergh, A. Ruocco, T. Spuesens, P. Bienstman, P. Dumon, W. Bogaerts, *Measurements of Effective Refractive Index of SOI Waveguides using Interferometers*, Advanced Photonics, 2015
- [5] A. Gutierrez, A. Brimont, M. Aamer, P. Sanchis, *Method for measuring waveguide propagation losses by means of a Mach-Zehnder Interferometer structure*, Optics Communications, vol. 285, no. 6, pp. 1144-1147, 2012
- [6] D. Rabus, M. Hamacher, *MMI-coupled ring resonators in GaInAsP-InP*, IEEE Photonics Technology Letters, vol. 13, no. 8, pp. 812-814, 2001
- [7] G. Pettit, W. Turner, *Refractive Index of InP*, Journal of Applied Physics, vol. 36, pp. 2081-2081, 1965

Compact ring resonator at 8 μm wavelength

(Student paper)

Natnicha Koompai¹, Thi Hao Nhi Nguyen¹, Jacopo Frigerio², Andrea Ballabio², Virginia Falcone², Xavier Le Roux¹,
 Carlos Alonso-Ramos¹, Laurent Vivien¹, Adel Bousseksou¹,
 Giovanni Isella², and Delphine Marris-Morini¹

¹ Centre de Nanosciences et de Nanotechnologies, Université Paris-Saclay, CNRS, 91120 Palaiseau, France

² L-NESS, Dipartimento di Fisica, Politecnico di Milano, Polo di Como, Via Anzani 42, 22100 Como, Italy

e-mail: natnicha.koompai@universite-paris-saclay.fr

Abstract: High quality factor and compact integrated ring resonator are important building blocks still missing in the long wave infrared region. In this work we report the design of ring resonators exploiting conformal couplers in a Ge-rich graded-index SiGe platform. Q-factor of 1300 is already obtained experimentally, while devices are under improvements, targeting values up to 10^5 .

Keywords: ring resonator, silicon photonics, mid-IR wavelength, silicon, germanium

INTRODUCTION

Chemical sensing based on mid-infrared spectroscopy is an extremely versatile technique to identify chemical substances, as most of the molecules have their fundamental vibrational and rotational resonances in this spectral range. This wavelength range can thus be exploited to detect small traces of environmental and toxic vapors in a variety of applications including environment, health care, or industrial monitoring [1-3]. In terms of photonics platform, silicon (Si) photonics can provide a major impact in mid-IR photonics in terms of compactness, reliability, and high-volume fabrication. In this context, it has been shown in previous years that germanium (Ge)-rich graded Silicon Germanium (SiGe) platform, relying on a graded SiGe layer epitaxially grown on Si, can be used with low propagation losses up to 11 μm wavelength, for both TE and TM polarization. A whole set of passive devices have then been developed, while the first active devices based on non-linear optics [4] and electro-optic [5] effects have been demonstrated recently. Despite preliminary works on integrated resonators [6], high quality factor (Q-factor) and compact ring resonator are important building blocks still missing in the long wave infrared region. In this work, we report the design, fabrication and characterization of ring resonators operating at a wavelength around 8 μm . While current characterization indicate that Q factor is of at least 10^3 , improvements are expected in the future, targeting Q-factor up to 10^5 .

RESULTS

a. Waveguide geometry and ring resonator design

A 6 μm thick graded-index SiGe waveguides grown on top of Si is employed. Within the SiGe layer, the concentration of Ge linearly increases from Si up to pure Ge. Therefore, light is confined in the upper part of the waveguide. Further information regarding this platform can be found in our previous work [7]. Waveguides are designed using rib-like geometry with a width of 4 μm , and an etching depth around 6 μm as shown in Fig.1a. Previous demonstration of integrated resonator operating around 8 μm wavelength were based on racetrack resonators. However, it is known that each interface between straight and bend waveguide can be responsible for optical losses in the resonator. To achieve high Q factor cavities, it is important to reduce all origin of losses. Therefore, in this work conformal couplers are employed, to achieve appropriate coupling between the bus waveguide and the resonator, keeping a single bend waveguide geometry inside the resonator. As a second advantage, more compact cavities are thus obtained leading to an increased Free Spectral Range (FSR) when compared with racetrack resonators. The schematic view of the resonator is thus shown in the fig.1b.

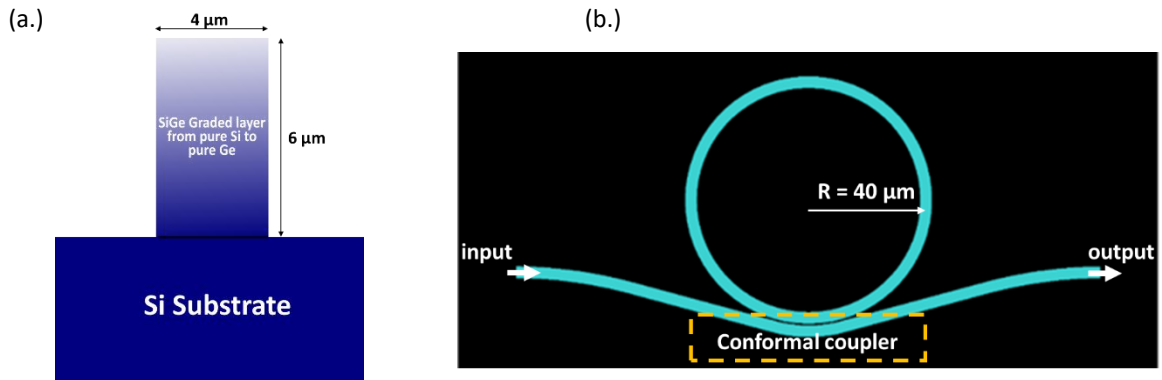


Fig.1. Schematic view of (a) cross section of the SiGe waveguide: on top of the Si wafer the epitaxial stack is formed by 6 μm graded layer, in which the concentration of Ge is increased linearly from 0 – 100%; (b) top view of the ring resonator design: the use of a conformal coupler has been proposed as a key to increase the coupling between the ring and bus waveguide

Numerical simulations have been performed to evaluate the resonator minimum radius. Interestingly, thanks to the high index within the SiGe waveguide, bend radius as low as 40 μm are expected to provide negligible contribution on the resonator loss when compared to the typical waveguide propagation loss of 1-2 dB/cm. The ring radius has thus been chosen to be 40 μm, while the gap distance between the ring resonator and the bus waveguide has been fixed to 500 nm. The length of the conformal coupler is 20 μm, targeting a power coupling factor (k^2) of a few percents.

b. Device fabrication

Epitaxial growth of the SiGe layer is performed by Low Energy Plasma Enhanced Chemical Vapour Deposition (LEPECVD). The fabrication of the ring resonator has then been done by using standard cleanroom techniques, including electron beam lithography (EBL), followed by inductively coupled plasma (ICP) etching. Fig.2. presents the top view image of the device using the optical microscope. Waveguides facets were diced obtaining a smooth facet to facilitate butt-coupling of the free-space laser beam.



Fig.2. Optical microscope image of the ring resonator and bus waveguide design after EBL lithography

c. Characterization of the resonator

The measurement has been performed using an external cavity quantum cascade laser operating in TM polarization. The wavelength scan has been performed between $\lambda = 7.41 \mu\text{m}$ and $9.3 \mu\text{m}$ with a central wavelength of $8 \mu\text{m}$, and in steps of 1 nm. The input/output signals were coupled in and out of the chip by means of ZnSe aspheric lenses. The collected signal was sent either to a microbolometer beam profiler to ensure that light is coming coupled on the optical waveguide, or to a HgCdTe (MCT) detector to scan the transmission spectrum. The transmission spectrum of the ring resonator is shown in the Fig.3a. Clear characteristic interferometric pattern of a ring resonator is observed with a FSR of 63.8 nm which is compatible with a group index inside the ring of 3.99. Figure 3(b) shows a zoomed-in view of a resonance at $8.07 \mu\text{m}$. From this figure, it can be seen that the measurement is currently limited by the

set-up resolution. Using the Lorentzian fit, we obtained a full width at half-maximum (FWHM) of $\Delta\lambda \sim 6$ nm, which corresponds to a Q-factor of 1300.

$$Q = \frac{\lambda_{\text{central}}}{FWHM} \quad (1)$$

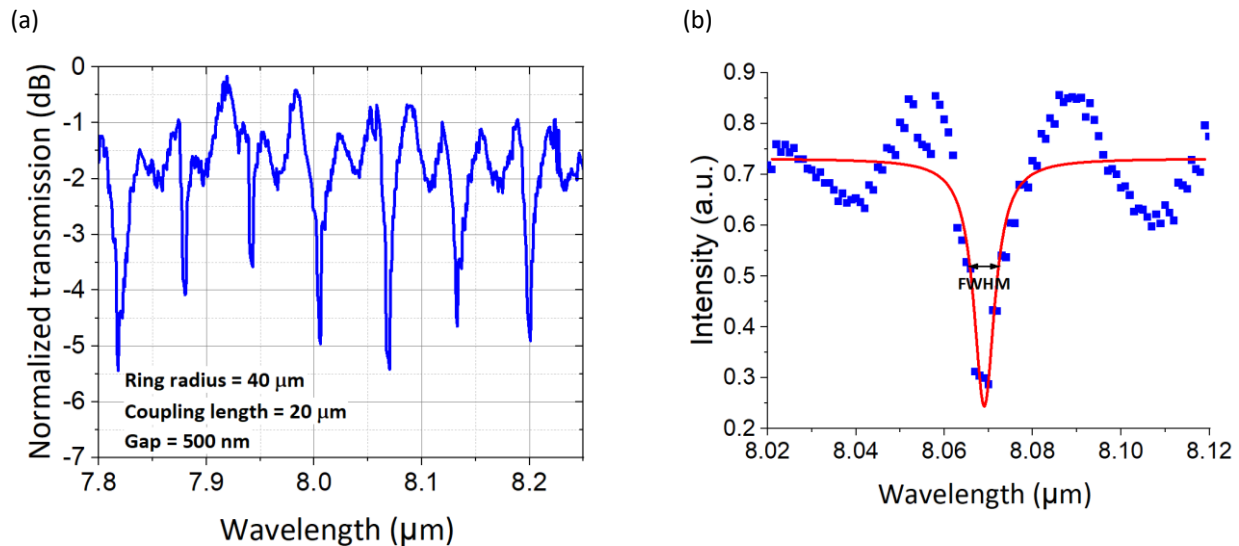


Fig.3. (a) Experimental transmission spectra of ring resonator operating in the TM-polarization. The ring radius is $40 \mu\text{m}$ with the coupling length of $20 \mu\text{m}$. (b.) Zoomed-in view of a single resonance (blue squares) of the left-side graph, showing the Lorentzian fit (red curve).

DISCUSSION

A compact ring resonator, operating at $8\mu\text{m}$ wavelength and using a conformal coupler in Ge-rich graded SiGe platform has been reported. From the experimental results, the Q-factor has been approximated around 1300, for a ring radius of $40 \mu\text{m}$ and a coupling length of $20 \mu\text{m}$. The structure is currently under improvement to optimize the coupling coefficient, targeting Q factors of more than 10^5 .

Acknowledgements

This work was supported by Light-up Project (ANR-19-CE24-0002-01). This work was partly supported by the French RENATECH network.

References

- [1.] Baehr-Jones, T., et al., *Silicon-on-sapphire integrated waveguides for the mid-infrared*. Optics Express, 2010. **18**(12): p. 12127-12135.
- [2.] Hu, J., et al., *Feature issue introduction: mid-IR photonic materials*. Optical Materials Express, 2013. **3**(9): p. 1571-1575.
- [3.] Lin, H., et al., *Mid-infrared integrated photonics on silicon: a perspective*. Nanophotonics, 2018. **7**(2): p. 393-420.
- [4.] Montesinos-Ballester, M., et al., *On-Chip Mid-Infrared Supercontinuum Generation from 3 to 13 μm Wavelength*. ACS Photonics, 2020. **7**(12): p. 3423-3429.
- [5.] Montesinos-Ballester, M., et al., *Mid-infrared Integrated Electro-optic Modulator Operating up to 225 MHz between 6.4 and 10.7 μm Wavelength*. ACS Photonics, 2022. **9**(1): p. 249-255.
- [6.] Ramirez, J.M., et al., *Broadband integrated racetrack ring resonators for long-wave infrared photonics*. Optics Letters, 2019. **44**(2): p. 407-410.
- [7.] Ramirez, J.M., et al., *Graded SiGe waveguides with broadband low-loss propagation in the mid infrared*. Optics Express, 2018. **26**(2): p. 870-877.

Subwavelength engineered silicon Bragg gratings for on-chip filtering with high optical rejection and narrow bandwidth

Dorian Oser^{1,2}, David E. Medina-Quiroz^{1,*}, Diego Pérez-Galacho³, Xavier Le Roux¹, Sébastien Tanzilli⁴, Laurent Vivien¹, Laurent Labonté⁴, Éric Cassan¹ and Carlos Alonso-Ramos¹

¹Université Paris-Saclay, CNRS, Centre de Nanosciences et de Nanotechnologies, 91120, Palaiseau, France

²QuTech, Delft Technical University, Delft, The Netherlands

³ITEAM research institute, Universitat Politècnica de València, Camino de Vera s/n, 46022, Valencia, Spain

⁴Université Côte d'Azur, CNRS, Institut de Physique de Nice (INPHYNI), Parc Valrose, 06108 Nice Cedex 2, France

* corresponding author: david.medina@universite-paris-saclay.fr

Emerging nonlinear and optomechanic applications in silicon photonics demand for on-chip optical filtering with high rejection and narrow bandwidth. Here, we report a novel geometry for Bragg filters exploiting modal and subwavelength engineering to achieve narrowband filtering with high optical rejection. Based on this approach, we experimentally demonstrate Bragg filters with null-null bandwidths down to 1.8 nm and 60 dB of rejection.

Keywords: Subwavelength, Bragg, narrowband, high rejection, multi-modal.

INTRODUCTION

The existing industrial facilities for electronics are a great advantage for the development of efficient and functional photonic circuits in the silicon on insulator (SOI) platform. However, several key functionalities remain a challenge to implement, that is the case for filters with high optical rejection and narrow bandwidth. This filter implementation is required for applications requiring comparatively high pumping powers to exploit nonlinear phenomena based on Kerr or Brillouin effects. One typical example are photon-pair sources that make use of spontaneous four wave mixing (SFWM) in silicon resonators [2-4]. These applications range from quantum key distribution [5] to optical quantum computing [6]. These integrated photon-pair sources have a huge power difference between the pump and the photon-pairs leading to the necessity of high-rejection of the pump, up to 100 dBs [7-8].

There have been different approaches for obtaining optical filtering in silicon. Bragg filters have been widely investigated and implemented [9,10] due to their simplicity (passive elements) and notable performance. Furthermore, there have been important improvements in the selectivity of the filtering wavelength, both decreasing the bandwidth down to 1 nm [9-13] and achieving rejection strengths up to 80 dBs [14] in different instances. Subwavelength metamaterial engineering of the Bragg lattice allows the implementation of weak perturbations that in turn, yield the narrowband notch responses. However, the rejection level is not high (~ 40 dBs) due the necessity of large filtering sections that enhance the detrimental effect of phase errors produced by fabrication defects. A recent approach has been demonstrated that utilises non-coherent cascading filters enabling efficient rejection up to 80 dBs even in presence of fabrication defects [14]. In this approach, several filter sections are connected with single-mode waveguides. In each Bragg section, the fundamental mode propagating through the waveguide is reflected into a higher order mode and then, the higher mode is radiated out. There are similar approaches in which contra-directional gratings were implemented [15-17]. Nevertheless, it has not been possible to attain rejection up to 80 dBs with narrow bandwidth down to 1 nm in a Bragg filter system.

Here, we propose and experimentally demonstrate an innovative Bragg grating geometry that exploits both, subwavelength modal engineering and non-coherent cascading to achieve the desired narrowband response while maintaining the ultra-high optical rejection (>>40dB). The Bragg lattice proposed comprises two different subwavelength sub-periods that are shifted by half period, as showed in Fig. 1(a). Thus, weak perturbations can be implemented even if the corrugation width is large. At the same time, the shifting by half a period in the left and right hand sides of the grating enables the coupling of the anti-symmetric first order mode when the fundamental mode is reflected [18]. On the other hand, the interconnection of the filters by single mode waveguides ensures the non-coherent cascading. The main advantage of this geometry is that the coupling strength is determined by the two subwavelength corrugations difference, so there is freedom to choose the minimum corrugation (dW) [14].

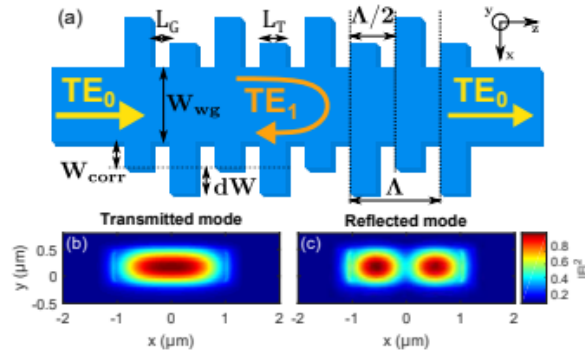


Fig. 1. (a) Proposed geometry of a single section of the Bragg grating. (b) Transmitted mode profile. (c) Reflected mode profile.

RESULTS

The Bragg grating was designed to operate using transverse-electric (TE) polarized light at a wavelength near 1550 nm in a Si platform of 220 nm thickness and air as upper-cladding. As a first approach, the transmission of the guided modes was simulated using 3D finite difference in the time domain (FDTD) method. The distribution of the fields is shown in Fig. 1(b) for the transmitted mode and Fig. 1(c) for the reflected one. Reflected light propagates in the first-order waveguide mode. Further simulations were carried out to compare the performance of the proposed subwavelength engineered grating with a simple Bragg grating with rectangular corrugation. The transmission spectra, shown in Fig. 2(a), implies a reduction of the bandwidth as of the rejection of the filter. Thus, simulation of the null-to-null bandwidth in relation with the filter length were needed to have a clearer idea of the bandwidth reduction, as seen in Fig. 2(b).

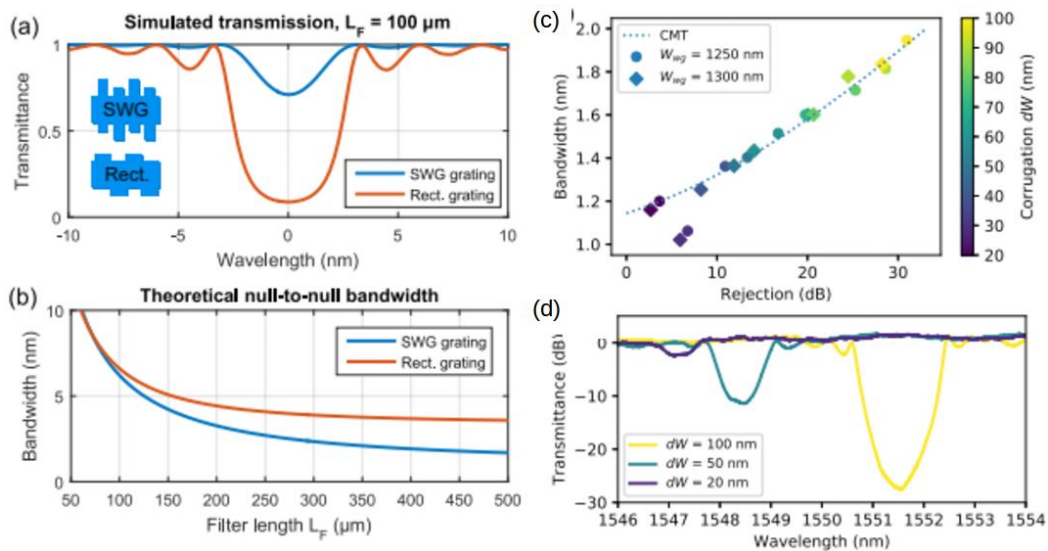


Fig. 2. (a) Simulated transmission for comparison of Bragg geometries. (b) Null-to-null bandwidth vs the filter length. (c) Experimental dependency of the bandwidth and rejection with dW for two different waveguide widths. (d) Transmittance for three different dW with fixed length.

The overall performance of the filters was assessed by fabricating the desired Bragg geometry in a SOI platform of 220 nm thickness and an oxide cladding of $3 \mu\text{m}$ as it is observable in Fig. 3(a) and Fig. 3(b). The main feature to investigate was the corrugation difference (dW) so the several filters fabricated had a fixed length of $500 \mu\text{m}$ with a varying dW between 20 nm and 100 nm. The bandwidth and rejection relative to dW were measured and plotted in Fig. 2(c) for two different waveguide widths. Furthermore, the transmittance for three dW was plotted in Fig. 2(d). From these two experiments it is apparent that the bandwidth can be tuned by changing the dW , which in part, is correlated with the decrease of rejection.

Finally, a more complex photonic circuit was developed for testing the cascading of the new geometry. The proposed geometry, depicted in Fig. 3(c), comprises a modal coupler to recover the reflected light from the filters and 9 Bragg sections connected with single-mode waveguides in S-bend configuration. The transmittance measured for both, the output through the filters and of the drop output was plotted in Fig. 3(d). The measured bandwidth is 1.8 nm. The cascaded filter exhibits a rejection of at least 60 dBs (which is the threshold for the detection limit), which is 35 dBs higher than the single-section filter.

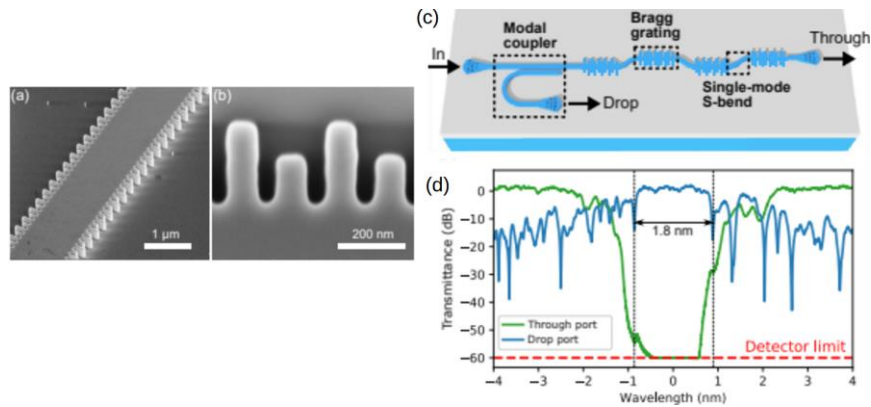


Fig. 3. (a) Scanning electron microscope images of the subwavelength-engineered Bragg filter and (b) detailed image of the corrugation. (c) Schematic of the cascading multi-filter photonic circuit. (d) Measured transmittance of both the through port and the drop port.

DISCUSSION

The proposed geometry for the Bragg filter was successfully characterized and implemented in a multi-stage circuit. The application of subwavelength engineering for multi-modal coalescence within the filter proves to be a useful tool for controlling the null-to-null bandwidth, achieving narrowband responses down to 2 nm. The non-coherent cascading provides a remarkably high optical rejection, higher than 60 dBs. The subwavelength engineered Bragg filter's corrugation is designed to yield weak perturbations by taking advantage of difference in corrugations of sub-periods. The implementation was done in a SOI platform of 220 nm thickness and with a single-etch step. These results are promising for further developments of high-performance Si Bragg filters that take advantage of subwavelength and modal engineering and will be applied to various on-chip applications.

Acknowledgements: This work was partially funded by the Agence Nationale de la Recherche (ANR-MIRSPEC-17-CE09-0041, ANR-BRIGHT-18-CE24-0023-01) and the French RENATECH network. The fabrication of the photonic circuits was carried out at the Plateforme de Micro-NanoTechnologie/C2N, partially funded by the Conseil Général de l'Essonne.

References

- [1] Dorian Oser, Diego Pérez-Galacho, Xavier Le Roux, Sébastien Tanzilli, Laurent Vivien, Laurent Labonté, Éric Cassan, and Carlos Alonso-Ramos, "Silicon subwavelength modal Bragg grating filters with narrow bandwidth and high optical rejection," *Opt. Lett.* **45**, 5784-5787 (2020)
- [2] S. Azzini, D. Grassani, M. J. Strain, M. Sorel, L. Helt, J. Sipe, M. Liscidini, M. Galli, and D. Bajoni, *Opt. express* **20**, 23100 (2012).
- [3] W. C. Jiang, X. Lu, J. Zhang, O. Painter, and Q. Lin, *Opt. Express* **23**, 20884 (2015).
- [4] F. Mazeas, M. Traetta, M. Bentivegna, F. Kaiser, D. Aktas, W. Zhang, C. Ramos, L. Ngah, T. Lunghi, E. Picholle et al., *Opt. Express* **24**, 28731 (2016).
- [5] N. Gisin, G. Ribordy, W. Tittel, and H. Zbinden, *Rev. modern physics* **74**, 145 (2002).
- [6] E. Knill, R. Laflamme, and G. J. Milburn, *Nature* **409**, 46 (2001).
- [7] M. Piekarek, D. Bonneau, S. Miki, T. Yamashita, M. Fujiwara, M. Sasaki, H. Terai, M. G. Tanner, C. M. Natarajan, R. H. Hadfield et al., *Opt. Letters* **42**, 815 (2017).
- [8] D. Oser, S. Tanzilli, F. Mazeas, C. Alonso-Ramos, X. Le Roux, G. Sauder, X. Hua, O. Alibart, L. Vivien, É. Cassan et al., *npj Quantum Inf.* **6**, 1 (2020).
- [9] D. Pérez-Galacho, C. Alonso-Ramos, F. Mazeas, X. Le Roux, D. Oser, W. Zhang, D. Marris-Morini, L. Labonté, S. Tanzilli, E. Cassan et al., *Opt. letters* **42**, 1468 (2017).
- [10] C. Klitis, G. Cantarella, M. J. Strain, and M. Sorel, *Opt. Letters* **42**, 3040 (2017).
- [11] J. Wang, I. Glesk, and L. Chen, *Electron. Lett.* **51**, 712 (2015).
- [12] Z. Zou, L. Zhou, M. Wang, K. Wu, and J. Chen, *Opt. Express* **24**, 12831 (2016).
- [13] P. Cheben, J. Ctyroky, J. H. Schmid, S. Wang, J. Lapointe, J. G. Wangüemert-Pérez, Í. Molina-Fernández, A. Ortega-Moñux, R. Halir, D. Melati et al., *Opt. letters* **44**, 1043 (2019).
- [14] D. Oser, F. Mazeas, X. Le Roux, D. Pérez-Galacho, O. Alibart, S. Tanzilli, L. Labonté, D. Marris-Morini, L. Vivien, É. Cassan et al., *Laser & Photonics Rev.* p. 1800226 (2019).
- [15] X. Nie, N. Turk, Y. Li, Z. Liu, and R. Baets, *Opt. letters* **44**, 2310 (2019).
- [16] M. Hammood, A. Mistry, M. Ma, H. Yun, L. Chrostowski, and N. A. Jaeger, *Opt. letters* **44**, 439 (2019).
- [17] W. Shi, X. Wang, W. Zhang, L. Chrostowski, and N. Jaeger, *Opt. letters* **36**, 3999 (2011).
- [18] H. Qiu, J. Jiang, P. Yu, T. Dai, J. Yang, H. Yu, and X. Jiang, *Opt. letters* **41**, 2450 (2016).

Performance tradeoffs in low-loss Si₃N₄ waveguides for linear and nonlinear applications

(Student paper)

Marcello Girardi^{1*}, Anders Larsson¹, and Victor Torres-Company¹

¹Department of Microtechnology and Nanoscience, Chalmers University of Technology, SE-41296, Sweden
* girardi@chalmers.se

We experimentally analyze tradeoffs in terms of waveguide losses, dispersion engineering and single-mode behaviour for different waveguide geometries. Our results suggests that photonic integrated circuits relying on nonlinear waveguides benefit from including a dedicated waveguide geometry via multi-layer integration to yield a seven-fold improvement in terms of loss.

Keywords: silicon nitride, waveguide, nonlinear, low-loss, photonic integrated circuits

INTRODUCTION

Silicon nitride (Si₃N₄) is a versatile material platform for photonic integration thanks to its wide transparency window, strong Kerr nonlinearity, high refractive index, and absence of two-photon absorption [1], [2]. This allowed the development of waveguides with ultralow loss, in the order of 1dB/m or lower [2]–[4], which proved to be crucial for Si₃N₄-based nonlinear optics applications, e.g., frequency comb generation [5] and generation of squeezed quantum states [6]. Nonlinear applications require a careful design of the waveguide geometry to attain the desired dispersion. These waveguides feature strong confinement but unfortunately are multimode (MM), which represents a potential problem when assembled together with other linear components to build complex photonic integrated circuits, e.g., in programmable photonic circuits [7] and quantum photonics [6].

Linear optics requires a single-mode (SM)-waveguide design to avoid parasitic coupling to higher order modes [8]. Starting from a dispersion-engineered strong-confinement design, the only way to achieve SM operation in Si₃N₄ is to reduce the waveguide width. However, this results in a mode with stronger interaction with the sidewalls and increased radiation loss due to roughness [9]. As a result, there is a fundamental tradeoff between single-mode behaviour, dispersion-engineering and losses in strong-confinement Si₃N₄ waveguides.

Advances in multi-layer integration [10] would allow bridging between Si₃N₄ layers featuring different thicknesses, hence effectively overcoming the aforementioned tradeoff. One could envision e.g. to attain dispersion-engineered nonlinear waveguides in a thick Si₃N₄-layer featuring strong optical field confinement and with the aid of interposers, enable an adiabatic transition to a low-confinement waveguide geometry with SM operation for linear processing [11], [12]. Before resorting to implement such a dual-layer platform, it is crucial to evaluate quantitatively the potential gains in improved losses. That is exactly the objective of this work. Here we present the

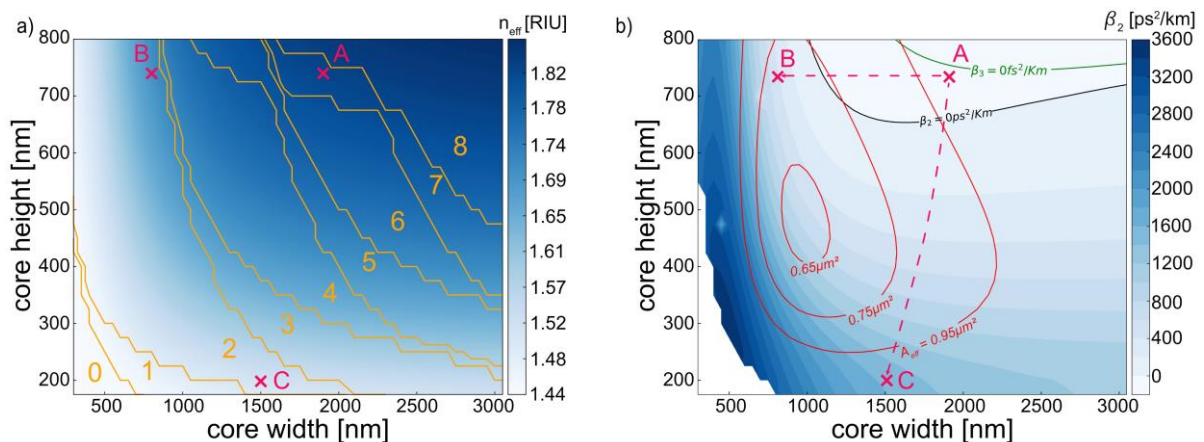


Fig. 1. a) Effective refractive index of the fundamental TE mode and number guided modes (orange lines). b) Color map of the dispersion (β_2) with the zero-dispersion line (black), the zero third order dispersion line (green) and the effective area (A_{eff}) of the fundamental TE mode (red). The magenta crosses represent the three geometries tested and the arrows show the two strategies considered to attain single mode operation.

first comprehensive experimental analysis of the trade-offs in optical losses between using a dispersion-engineered platform and a dedicated platform for single-mode operation. A crucial aspect of this analysis is that the assessment is done with minimum changes in the etching process, thus allowing for a meaningful and fair comparison between waveguide geometries.

RESULTS

The three waveguide geometries selected for this study are a dispersion-engineered waveguide with thickness 740nm and width 1900nm (A), a SM waveguide 800nm wide with the same thickness (B), and a SM waveguide with reduced thickness, i.e. 200nm thick and 1500nm wide (C). The three geometries are represented by the magenta crosses in figure 1a. The dispersion-engineered waveguide geometry was selected to attain anomalous dispersion and a third-order dispersion coefficient close to zero (see figure 1b). These parameters are crucial to the generation of Kerr soliton frequency combs but, as showed in figure 1a, the waveguide supports six modes, three in the TE and three in the TM polarization. From figure 1a, one can observe that pure SM operation is not possible with a thickness of 740nm, but a waveguide with width <850nm is SM with two supported polarizations, hence our choice of the second waveguide geometry B. In figure 1b we can see that in this condition the mode effective area (A_{eff}) is small, i.e., the interaction with the sidewalls is strong. To decrease the interaction with the sidewalls, we opted for a larger A_{eff} , maintaining the SM condition, i.e., the thin waveguide geometry C. Moreover, this geometry maintains a simulated critical bending radius of $\sim 100\mu\text{m}$, as showed in figure 2f. This allows the development of more compact devices compared to ultrathin waveguides, which feature a critical bending radius ten times larger [3].

To test the three geometries, we fabricated two different samples, one for each thickness. The samples were fabricated on 100mm wafers with a subtractive fabrication approach. The 740nm thick sample followed the fabrication flow reported in our previous work [13]. The fabrication of the 200nm thick sample followed a simplified processing since stress release trenches are not necessary for this thickness. As shown in the SEM pictures reported in figure 2d and 2e, the fabrication process yields waveguides with ultra-smooth sidewalls, believed to be in the sub nm scale, i.e. below the resolution of our SEM.

To evaluate the loss of the waveguides we designed ring resonators with point coupling and bending radius of $227\mu\text{m}$. The bending radius was selected to minimize the bending loss and achieve an FSR of $\sim 100\text{GHz}$. The rings were characterized via sweep wavelength interferometry in the range 1500-1600nm following the procedure described in [14]. From the measurement, we obtained the intrinsic linewidth of the cavities (k_0). The histograms

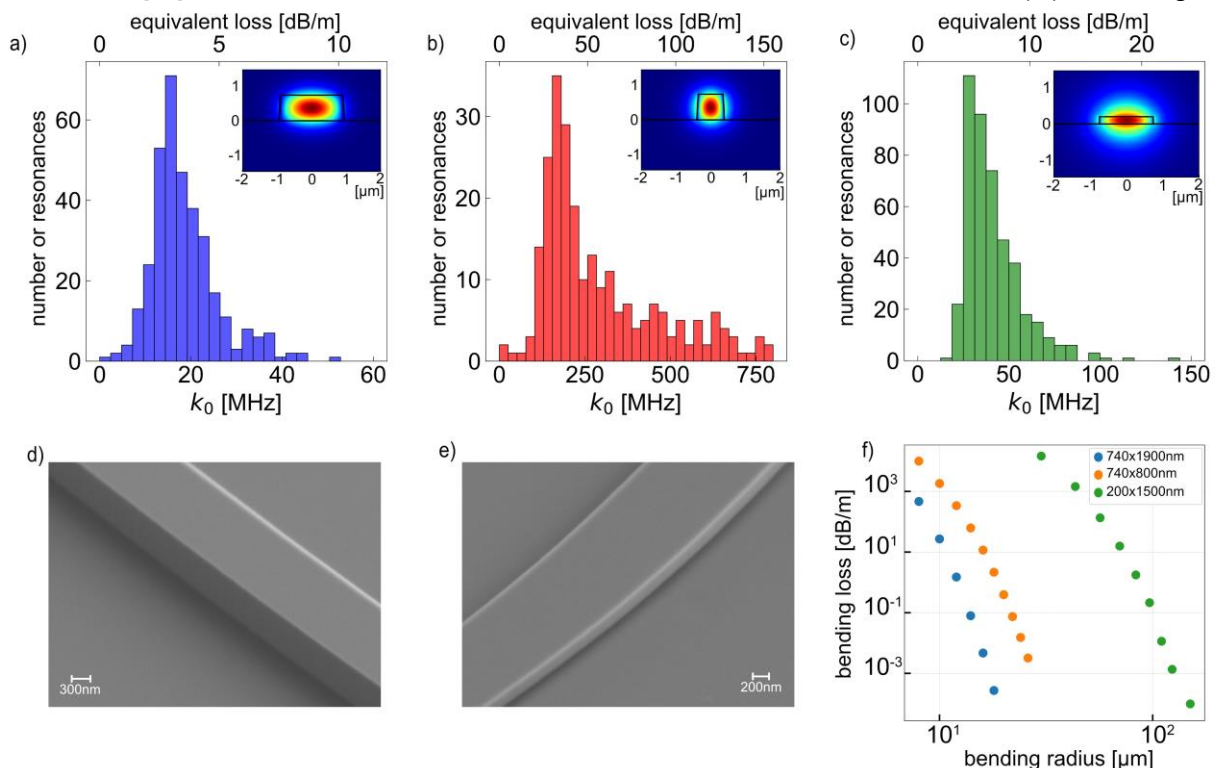


Fig. 2. a), b), c) Histograms of the intrinsic linewidths and equivalent propagation loss measured for the three different geometries, respectively (A) 740x1900nm, (B) 740x800nm and (C) 200x1500nm and mode field distributions (insets). d), e) SEM picture of the 740x800nm and 200x1500nm waveguides in tilted view to show the sidewalls. f) Simulated bending loss for the three geometries considered.

of k_0 for the three different geometries are reported in figure 2a, 2b and 2c, with the equivalent propagation loss on the upper axis. As expected, increasing the confinement factor from a multimode to a single mode waveguide, without changing the thickness leads to an increase of the equivalent propagation loss. The most probable value raises from 2.7 dB/m of the multimode waveguide (A) to 30.0 dB/m of the single mode waveguide (B). This is explained by the stronger interaction of the mode with the sidewalls [15], as clearly showed by the smaller A_{eff} in figure 1b, and the mode field distribution in the inset of figure 2b. The most probable equivalent propagation loss for the thin Si_3N_4 geometry (C) is 4.1 dB/m which is a more than a seven-fold improvement of the propagation loss for single mode application. This type of geometry will prove beneficial in large devices, e.g., arrayed waveguide grating multiplexers or long delay lines, where it is paramount to avoid modal dispersion and long propagation length are necessary.

CONCLUSION

We experimentally benchmarked in terms of losses two different waveguide thicknesses to show the trade-off for SM operation. We demonstrated that a thinner SM waveguide with moderate confinement has seven times better loss compared to a strong confinement SM waveguide. This suggests that integrating multiple dedicated platforms via 3D integration will be beneficial for complex photonic integrated circuits, e.g., quantum photonic circuits.

Acknowledgements: This work was performed in part at Myfab Chalmers. We acknowledge support from the European Research Council (GA 771410) and the Swedish Research Council (2016-06077 and 2020-00453).

References

- [1] P. Muñoz *et al.*, "Silicon nitride photonic integration platforms for visible, near-infrared and mid-infrared applications," *Sensors (Switzerland)*, vol. 17, no. 9, p. 2088, 2017.
- [2] J. Liu *et al.*, "High-yield, wafer-scale fabrication of ultralow-loss, dispersion-engineered silicon nitride photonic circuits," *Nat. Commun.*, vol. 12, 2021.
- [3] M. W. Puckett *et al.*, "422 Million intrinsic quality factor planar integrated all-waveguide resonator with sub-MHz linewidth," *Nat. Commun.*, vol. 12, 2021.
- [4] Z. Ye, P. Zhao, K. Twayana, M. Karlsson, V. Torres-Company, and P. A. Andrekson, "Overcoming the quantum limit of optical amplification in monolithic waveguides," *Sci. Adv.*, vol. 7, no. 38, pp. 8150–8165, 2021.
- [5] B. Shen *et al.*, "Integrated turnkey soliton microcombs," *Nature*, vol. 582, no. 7812, pp. 365–369, 2020.
- [6] J. Wang, F. Sciarrino, A. Laing, and M. G. Thompson, "Integrated photonic quantum technologies," *Nature Photonics*, vol. 14, no. 5, pp. 273–284, 2020.
- [7] W. Bogaerts *et al.*, "Programmable photonic circuits," *Nature*, vol. 586, no. 7828, pp. 207–216, 2020.
- [8] C. R. Pollock and M. Lipson, *Integrated photonics*, 2003.
- [9] S. Roberts, X. Ji, J. Cardenas, M. Corato-Zanarella, and M. Lipson, "Measurements and modeling of atomic-scale sidewall roughness and losses in integrated photonic devices," *arXiv Prepr. arXiv2105.11477*, 2021.
- [10] N. Bai, X. Zhu, Y. Zhu, W. Hong, and X. Sun, "Tri-layer gradient and polarization-selective vertical couplers for interlayer transition," *Opt. Express*, vol. 28, no. 15, p. 23048, 2020.
- [11] W. D. Sacher, Y. Huang, G. Q. Lo, and J. K. S. Poon, "Multilayer silicon nitride-on-silicon integrated photonic platforms and devices," *J. Light. Technol.*, vol. 33, no. 4, pp. 901–910, 2015.
- [12] W. D. Sacher *et al.*, "Tri-layer silicon nitride-on-silicon photonic platform for ultra-low-loss crossings and interlayer transitions," *Opt. Express*, vol. 25, no. 25, p. 30862, 2017.
- [13] Z. Ye, K. Twayana, P. A. Andrekson, and V. Torres-Company, "High-Q Si_3N_4 microresonators based on a subtractive processing for Kerr nonlinear optics," *Opt. Express*, vol. 27, no. 24, pp. 35719–35727, 2019.
- [14] K. Twayana, Z. Ye, Ó. B. Helgason, K. Vijayan, M. Karlsson, and V. Torres-Company, "Frequency-comb-calibrated swept-wavelength interferometry," *Opt. Express*, vol. 29, no. 15, p. 24363, 2021.
- [15] D. Melati, A. Melloni, and F. Morichetti, "Real photonic waveguides: guiding light through imperfections," *Adv. Opt. Photonics*, vol. 6, no. 2, p. 156, 2014.

Mitigating Polarization Rotation Effects in Thin-Film Lithium Niobate Waveguides

(Student paper)

Gabriele Cavicchioli¹, Maziyar Milanizadeh¹, Giuseppe Cusmai², Roberto Longone², Francesco Morichetti¹, Andrea Melloni¹

¹Dipartimento di Elettronica, Informazione e Bioingegneria - Politecnico di Milano, Milano, 20133 Italy.

²Advanced Fiber Resourced – San Donato Milanese, 20097 Italy

* gabriele.cavicchioli@polimi.it

Lithium niobate on insulator (LNOI) technology enables the integration of a new generation of electro-optical devices in complex photonic architectures, but it requires a fine control of polarization rotation effects induced by waveguide bending. In this work we present the design and the experimental characterization of a polarization maintaining LNOI waveguide, and we investigate the influence of the waveguide birefringence on the polarization crosstalk.

Keywords: LNOI, polarization, lithium niobate, optical waveguides

INTRODUCTION

Lithium niobate on insulator (LNOI) has emerged as a promising platform for the integration of fast electro-optical devices, such as modulators and switches, in complex photonic integrated circuits (PICs). In this technology the electro-optic effects are enhanced by the strong field confinement in high-index-contrast waveguides with a small effective area; furthermore, tight waveguide bending enables the realization of compact devices, such as microring resonators, which are not allowed in classical Ti-diffused lithium niobate technology. LNOI waveguides are typically rib-shaped and may have tilted sidewall due to the etching process; these features, together with the high-index-contrast, make LNOI waveguides sensitive to polarization rotation effects due to waveguide bending [1]. Polarization coupling can occur when the waveguide modes are hybrid [2]. In bent waveguides mode hybridness increases with the curvature, so bends can act as polarization rotators. Moreover, if along the propagation path the TE and TM orthogonal modes degenerate, the coupling between them is enhanced [1]. Since lithium niobate (LN) is an anisotropic material, the birefringence of a LNOI waveguide strongly depends on the orientation of the waveguide with respect to the LN crystal axes. Waveguides able to maintain the polarization are therefore of main importance to avoid polarization rotation effects.

In this work we investigate the polarization behaviour of LNOI waveguides, focusing on the polarization rotation induced by bent sections. We optimize the geometry of a buried rib-shaped LNOI waveguide to mitigate polarization rotation effects and we validate experimentally the effectiveness of the proposed design.

DESIGN OF POLARIZATION MAINTAINING LNOI WAVEGUIDES

Polarization coupling in bent waveguides can be treated in the framework of coupled mode theory and the following expression provides the TE-TM power conversion efficiency [1]

$$K = \frac{k_p^2}{k_p^2 + \frac{(\beta_{TE} - \beta_{TM})^2}{4}} \sin^2 \left(\left(k_p^2 + \frac{(\beta_{TE} - \beta_{TM})^2}{4} \right)^{1/2} L \right), \quad (1)$$

where L is the length of the bend β_{TE} and β_{TM} are the propagation constants of the fundamental TE and TM modes, respectively, and k_p is the polarization coupling coefficient that depends on the modal fields, on the refractive index profile of the waveguide and on the bending radius [1, 2]. In general, both propagation constants and k_p depend on propagation direction. To mitigate polarization coupling, k_p should be reduced. This is possible by decreasing the waveguide index contrast, by choosing waveguide geometries which are symmetrical with respect to the horizontal axis or by increasing the bending radius [2]. Alternatively, the phase mismatch term $\beta_{TE} - \beta_{TM}$, which depends on the waveguide birefringence, can be increased. Both strategies reduce the TE-TM polarization crosstalk K .

The waveguides considered in this work are realized on a X-cut LNOI wafer, so the extraordinary axis Z ($n_e = 2.138$) lies in-plane, and the ordinary axes X and Y ($n_o = 2.211$) are out-of-plane and in-plane respectively. For this cut, there are two relevant waveguide orientations: Y-propagation and Z-propagation. In the former the propagation direction is parallel to the Y-axis, while in the second one is parallel to the Z-axis. The waveguide has a rib-shaped cross-section (Fig. 1.a) and, after the etching of the LN films, the rib has a trapezoidal shape with sidewalls slope of about 30°, as shown in the SEM photograph of Fig. 1.b. Moreover, a shallow etching reduces propagation losses. Test

patterns including bent waveguides with different radii were fabricated to experimentally investigate polarization rotation effects (Fig. 1.c).

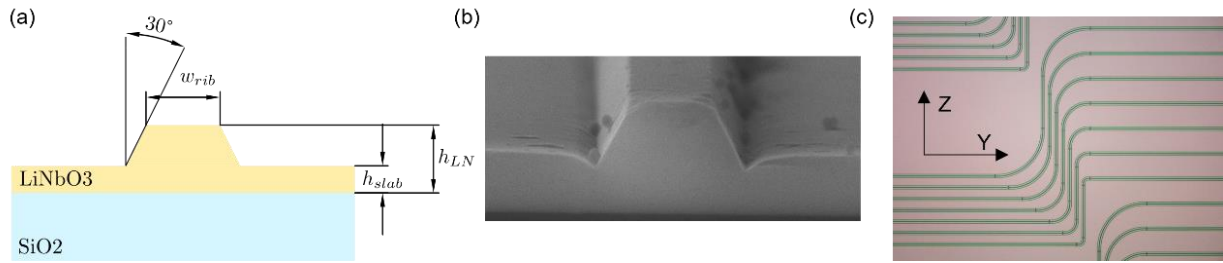


Figure 1. (a) Schematic of the waveguide geometry. (b) SEM picture of a LNOI waveguide. (c) Top view of an S-bend waveguide pattern. The straight sections are aligned with the crystal axis.

The parameters for the optimization of the waveguide design are then the slab height (h_{slab}), the thickness of the LN film (h_{LN}), the cladding refractive index and the waveguide width (w_{rib}). Figure 2.a shows the effective indices of the first three guided modes for a 700-nm-thick rib waveguide with $h_{slab} = 400$ nm and air cladding for different values of w_{rib} . In Y-propagation the effective indices of the fundamental TE₀₀ and TM₀₀ modes are almost the same for any waveguide width, meaning that the structural birefringence is compensated by material birefringence [3]. As a result, for this crystal orientation, the fundamental modes are almost degenerate and even a small perturbation of the waveguide profile, including sidewall roughness and bends, can induce a coupling between the TE and TM polarization. On the other hand, in Z-propagation, the birefringence is one order of magnitude higher ($B \sim 0.18$) and the waveguide shows almost a degeneration for the TM₀₀ and TE₁₀ modes around $w_{rib} = 1.6$ μm , which could be exploited to realize polarization splitter rotators [4]. Considering Fig. 2, we designed the waveguide cross section to maximize the birefringence in Y-propagation using a FEM mode solver. The optimized geometry has $h_{LN} = 550$ nm, $h_{slab} = 250$ nm. The birefringence in Y-propagation is about 0.017 and it is almost independent from the rib width (Fig 2.b) while a value of 0.22 is observed in Z propagation. The waveguides are single mode up to a rib width of 1.0 μm .

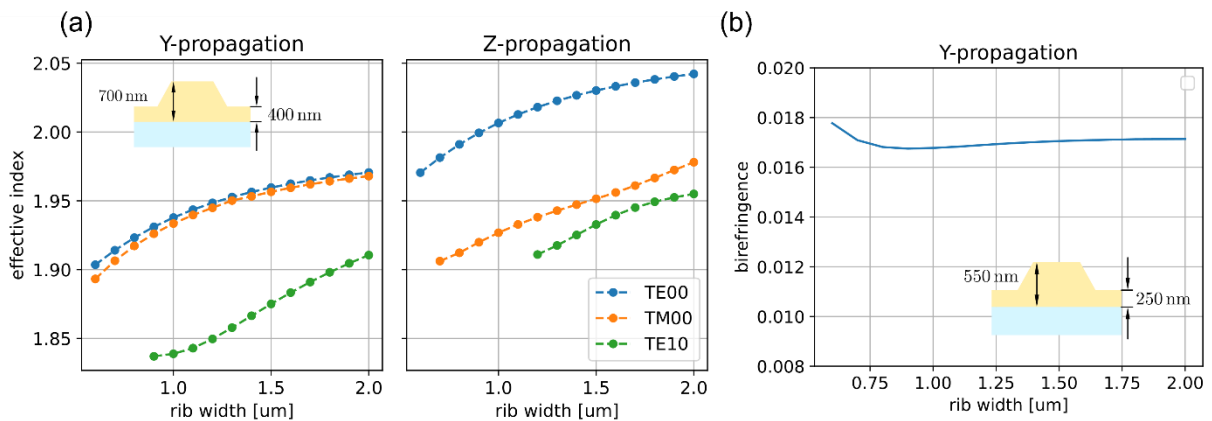


Figure 2. (a) Effective index of a LNOI waveguide with $h_{LN} = 700$ nm, $h_{slab} = 400$ nm and air cladding for the Y and Z propagation directions. (b) Birefringence for different rib widths of the optimized waveguide.

EXPERIMENTAL RESULTS

Two waveguide designs have been compared experimentally to evaluate their polarization behaviour. The first one is the 700-nm-thick rib waveguide of Fig. 2.a, the second one is the optimized 550-nm-thick waveguide of Fig. 2.b. The thicker waveguide shows a much weaker birefringence ($B \sim 0.007$) in Y propagation. To assess the polarization rotation, the 90° S-bends shown in Fig. 1.c, with radius R from 50 μm to 250 μm were used. The input/output straight waveguide sections are oriented along Y-propagation, while the inner straight waveguide section within the 90° S-bend is oriented along Z-propagation; in the latter section, polarization coupling is negligible because of the high waveguide birefringence. Fig. 3 shows the evolution of the polarization state (SOP) at the output of the S-bend over a wavelength range of 10 nm centered at 1550 nm when a TE mode is injected into the input waveguide. In the first low-birefringence waveguide the SOP wraps all around the Poincaré sphere (Fig 3.a) because of a strong polarization coupling. On the optimized waveguide, the higher birefringence keeps the SOP almost stable around the TE input polarization point (Fig. 3.b).

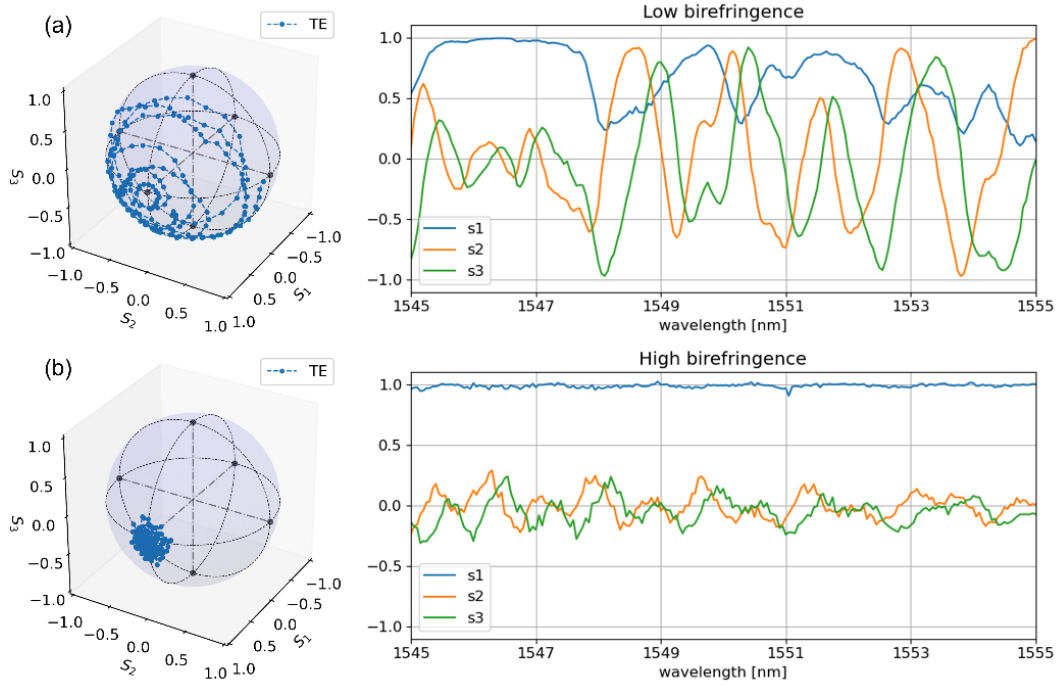


Figure 3. Evolution of the SOP on the Poincaré sphere and Stokes parameters at the output of an S-bend with rib width $w_{rib} = 0.7 \mu\text{m}$ for waveguides with different birefringence: (a) 700-nm-thick, $B = 0.007$; (b) 550-nm-thick, $B = 0.017$.

For weak polarization coupling, the polarization crosstalk K can be approximated as

$$K = \max\left(\frac{1-s_1}{2}\right) \sim k_p^2 L^2, \quad (2)$$

where s_1 is the first normalized Stokes parameter. In Table 1 the polarization crosstalk of the 500-nm-thick waveguide is reported for different bending radii. For sharp bends the crosstalk decreases by increasing the bending radius R . However, for large R the crosstalk increases because the overall length of the S-bend increases. The estimated value of k_p derived from eq. (2), does not increase linearly with $1/R$ so the polarization crosstalk K depends on both the length of the bend and its bending radius. Hence, to realize a bend with defined angle θ , an optimum value of bending radius exists, which for $\theta = 90^\circ$ is $140 \mu\text{m}$. This means that to mitigate polarization crosstalk it is not enough to increase the bending radius, but it is necessary to carefully design the geometry of the whole bend.

$R [\mu\text{m}]$	$K [\text{dB}]$	$k_p [\mu\text{m}^{-1}]$
50	-11.46	5346.01
110	-14.29	1754.31
140	-15.24	1235.58
170	-14.51	1106.75
200	-13.49	1057.96

Table 1: Polarization crosstalk introduced by a $90^\circ+90^\circ$ S-bend (Fig. 1c) with rib width of $0.7 \mu\text{m}$ and variable bending radii.

CONCLUSIONS

In this work we investigated the polarization coupling phenomena in LNOI bent waveguides. An optimal waveguide cross section that guarantees single mode operation and high birefringence is found. An experimental analysis demonstrated that in bent waveguides exists an optimal bending radius R that minimizes the polarization crosstalk.

REFERENCES

- [1] F. Morichetti, A. Melloni, and M. Martinelli, "Effects of polarization rotation in optical ring-resonator-based devices," *Journal of Lightwave Technology*, vol. 24, Art. no. 1, Jan. 2006.
- [2] B. E. Little and S. T. Chu, "Theory of polarization rotation and conversion in vertically coupled microresonators," *IEEE Photonics Technology Letters*, vol. 12, Art. no. 4, Apr. 2000.
- [3] A. Pan, C. Hu, C. Zeng, and J. Xia, "Fundamental mode hybridization in a thin film lithium niobate ridge waveguide," *Optics Express*, vol. 27, Art. no. 24, Nov. 2019.
- [4] Z. Chen, Y. Pan, X. Liu, H. Lin, X. Zhong, and X. Cai, "Single-step Etching Polarization Splitter-rotator based on Lithium Niobate Ridge Waveguide," in *Asia Communications and Photonics Conference (ACPC) 2019*, 2019, p. M4A.

Minimisation of Parasitic Capacitance in Electro-Absorption Modulators for High-Speed Operation

(Student paper)

Jack Mulcahy^{1,2}, Xing Dai^{1,2}, John McCarthy^{1,2}, and Frank H. Peters^{1,2}

¹University College Cork, College Road, Cork, T12 K8AF, Ireland

²Tyndall National Institute, Lee Maltings Complex, Dyke Parade, Cork, T12 R5CP, Ireland

* jack.mulcahy@tyndall.ie

A lumped element electro-absorption modulator (EAM) with ultra-low parasitic capacitance contacts is presented. The device uses a carefully designed contact pillars and semiconductor etches to minimise the capacitance of the EAM in order to facilitate high speed operation. With parasitic capacitances minimised to $\approx 15\text{fF}$, S21 simulations extracted from experimental S11 measurements predict a $50\mu\text{m}$ long EAM with speeds of up to 80GHz.

Keywords: *Electro-absorption Modulators, III-V Materials, High Speed Devices*

INTRODUCTION

Photonic integrated circuits (PICs) have been evolving over the past 10 years to progress from the research to the commercial stage. Market studies predict a market volume of 3.3bn USD by the year 2027. [1] Photonic integration has already been a subject of research since the 1980s using optically passive waveguide materials, with particular interest in InP along with the related compound semiconductor materials; InGaAsP and InGaAlAs. Their natural wavelength range of operation of about 1300–1650nm perfectly matches the optimal spectral range of optical fibres used for fibre optic communications. Beyond passive-optical functionalities, this class of material is also capable of providing active optical functions, namely laser light generation and detection, making it a perfect choice for full monolithic integration.

Electro-absorption modulators (EAMs) based on the Quantum Confined Stark Effect (QCSE), have a low driving voltage, high extinction ratio, are easier to integrate with single mode lasers, and are relatively short ($<150\mu\text{m}$). [2] The robust design and operation of EAMs allow them to be integrated monolithically to form effective optical components. In this work, we will highlight a novel flexible RF electrical contact scheme, showing parasitic capacitance as low as 15fF. The design and fabrication process of an EAM utilising this contact scheme will be detailed, and shown to operate with a bandwidth of up to 80GHz.

DEVICE DESIGN

The lumped EAM device was fabricated on two different in-house grown InP based materials which were designed to modulate wavelengths surrounding 1310nm. The first material was optimised for lumped EAM fabrication and made use of 12 quantum wells with a width of 9nm. The second material was designed with the monolithic integration of lasers in mind and thus uses 6 quantum wells each with a width of 9nm for use in fabricating externally modulated lasers (EMLs). EAMs of varying lengths were fabricated ranging from 50 to $175\mu\text{m}$. As shown in Fig. 1 the modulating section of the EAM is electrically isolated from a surrounding pseudo-passive section by etching away the contact layers on the waveguide between these sections. This technique resulted in a measured isolation resistance of $>10\text{ k}\Omega$. The term pseudo-passive is used here to describe how the section surrounding the EAM is absorptive to 1310nm light if unbiased, but will become passive if sufficiently forward biased.

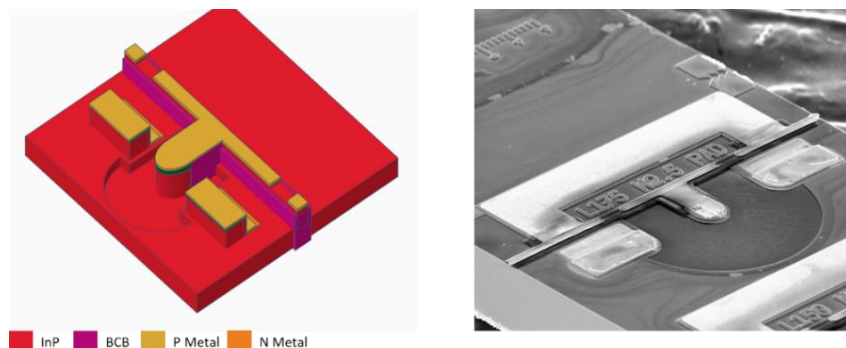


Figure 1 - On the left is a 3D model of the EAM device showing the main EAM waveguide connected to the signal contact and two accompanying ground contacts suitable for a GSG probe. On the right is a SEM image of the fabricated device.

In the ideal case the EAM is a lumped element with differential resistance R_j and capacitance C_j . Thus, the response time of this circuit goes as $R_j C_j$, which determines the bandwidth. The EAM is dependent on the electric field across the quantum well region to induce the QCSE. When reverse biased, the resistance of the EAM is high, thus a load resistance, R_l is typically placed in parallel to terminate the device and minimise electrical reflections back to the source. [3]

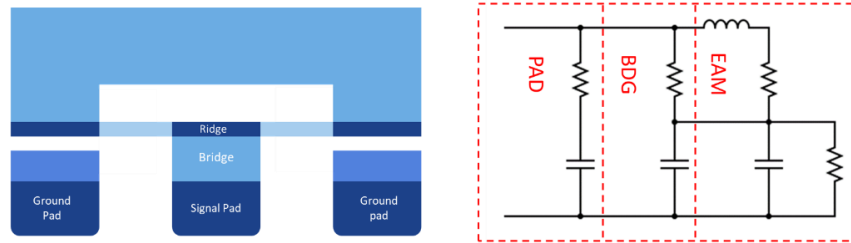


Figure 2 – Electrically, the EAM device can be broken down into 3 distinct sections; the contact pad, the metal bridge connecting the contact pad to the EAM, and the EAM itself.

As seen in Fig. 2, the EAM can be separated into three distinct electrical sections; the GSG contacts, the metal bridge suspended on a polymer connecting the signal contact to the EAM, and the EAM itself. The contact pads and the bridge are part of the contact scheme to deliver the RF signal to the EAM as the width of the waveguide forming the EAM is on the order of $2.5\mu\text{m}$ which makes direct probing or wire-bonding the device significantly more difficult. These contacts give rise to parasitic impedance to the microwave signal delivery. As the bandwidth of the EAM; $f_{3\text{dB}}$ is inversely related to the impedance of the circuit, minimising these parasitic impedances maximises the EAM's speed.

CONTACT PAD OPTIMISATION

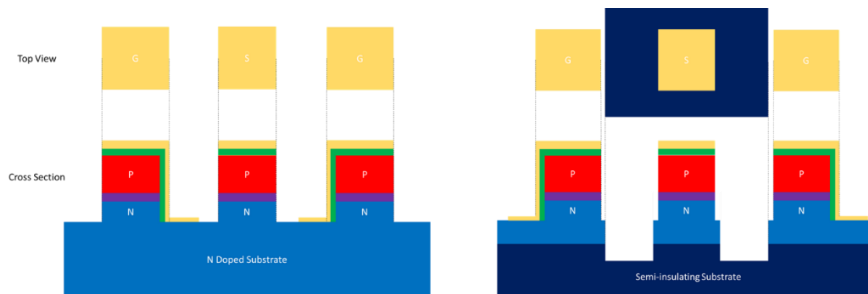


Figure 3 - On the left is a DC device with GSG contacts on an n-doped substrate. On the right is a modified contact scheme designed to minimise the influence of the signal pad's capacitance.

In the fabrication of DC devices ($<10\text{GHz}$ operation), an n-doped substrate is often used as shown in Fig. 3. This is unsuitable for high-speed performance as the signal contact pillar's parasitic capacitance is large which limits the devices overall speed. In the structure optimised for high-speed performance a semi-insulating substrate is used and the contact pillars are isolated via a deep etch into the semi-insulating substrate. This isolation prevents charge buildup below the signal contact, eliminating the capacitance between the signal contact and the n-doped layers.

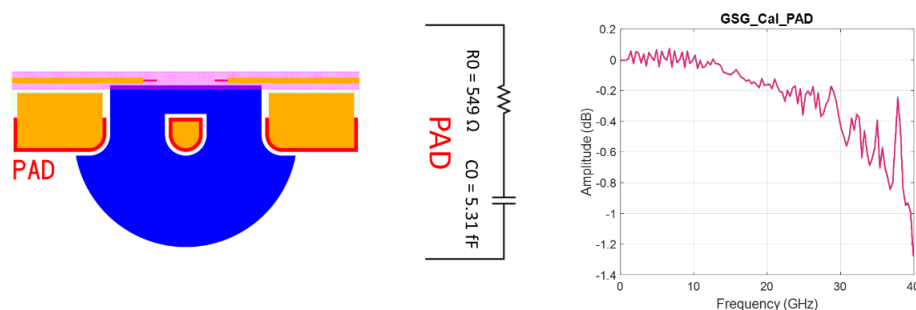


Figure 4 – On the left is the test structure fabricated to perform an isolated measurement of the parasitic capacitance of the pads. In the centre is a fitted model of the experimental data. On the right is the S_{11} measured.

While the capacitance of the signal contact with the substrate directly beneath it has been eliminated, there is an associated capacitance between the signal contact and ground contact. A test structure based on Fig 3 was fabricated in order to test the resultant parasitic capacitance of the isolated pillar contacts. This test structure was

characterised by measuring the S11 scattering matrix from 0-40GHz using a vector network analyser (VNA). The measured complex impedance values were then fitted to an LRC circuit model by applying a least squares minimisation to the magnitude and phase data, with the extracted capacitance being $\approx 5\text{fF}$ for the device.

BRIDGE OPTIMISATION

With the impedances of the contact pillars known the additional impedance of the metal bridge connecting the pillars to the ridge waveguide was quantified using a test structure as shown in Fig. 5. The metal bridge forms a pair of capacitor plates with the lower n region remaining following the deep isolation etch as shown in the figure below. By characterising the S11 data of the test structure shown and accounting for the impedances of the pillars, the parasitic capacitance of the bridge was experimentally verified from S11 analysis to be $\approx 10\text{fF}$.

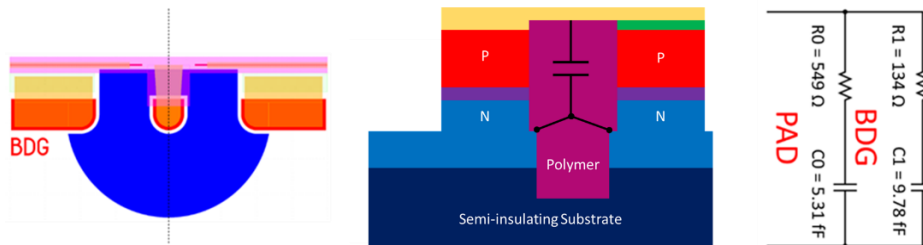


Figure 5 - On the left is the test structure used to determine the metal bridge's contribution to the EAM's parasitic capacitance. In the centre is a cross section schematic of the source of the bridge's capacitance. On the right is the fitted model of the experimental data measured.

EAM MEASUREMENTS

Through experimental characterisation of the previous test structures, the characteristics of the EAM were able to be isolated through S11 measurements of the device. This process was applied to EAMs of lengths varying from 50 to 175 μm . Fig. 6 shows the simulated S21 graph based on these experimental results which shows a $f_{3\text{dB}}$ of up to 80GHz for a termination resistance of 25 Ω .

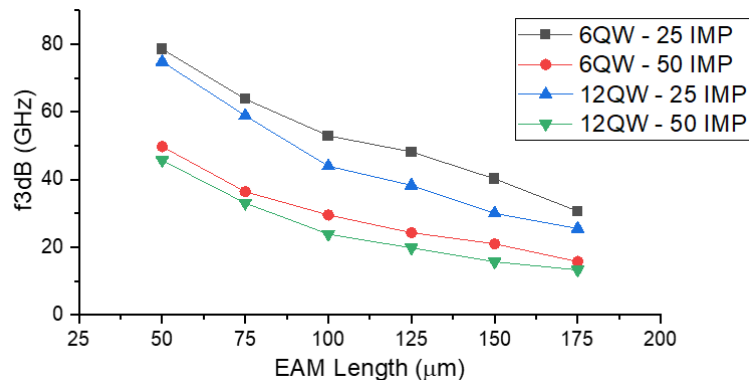


Figure 6 – Over 60 devices were experimentally characterised. By isolating the parasitic capacitance measured before, simulated S21s were generated and $f_{3\text{dB}}$ were extracted for devices of varying length. The average value for each material is presented above for impedances of 25 Ω and 50 Ω

Acknowledgements: This research was funded by Science Foundation Ireland (SFI) through the Irish Photonic Integration Centre (IPIC) under SFI-12/RC/2276_P2.

CONCLUSION

A lumped element electro-absorption modulator (EAM) with ultra-low parasitic capacitance contacts has been shown with parasitic capacitances minimised to $\approx 15\text{fF}$. S21 simulations extracted from experimental S11 measurements predict a 50 μm with average $f_{3\text{dB}}$ speeds of up to 80GHz based on experimental data.

References

- [1] Photonic Integrated Circuits Market to Reach \$3.3 Billion by 2027. 2019. https://www.novuslight.com/photonicintegrated-circuits-market-to-reach-3-3-billion-by-2027_N9494.html
- [2] C. R. Doerr, L. Zhang, P. J. Winzer, J. H. Sinsky, A. L. Adamiecki, N. J. Sauer, and G. Raybon, "Compact High-Speed InP DQPSK Modulator," IEEE Photonics Technology Letters, vol. 19, no. 15, pp. 1184–1186, 2007.
- [3] W. Han, C. Daunt, H. Yang, M. Rensing, X. Wang, P. O'Brien, and F. Peters, "Development of a broadband matching network for electro-absorption

New and efficient sacrificial layer for transfer printing technology

Student paper

Hemalatha Muthuganesan¹, Fatih Bilge Atar¹, Agnieszka Gocalinska¹, Emanuele Pelucchi¹ and Brian Corbett¹

¹Tyndall National Institute, Lee Maltings Complex Dyke Parade, Cork, T12R5CP, Ireland

*hemalatha.m@tyndall.ie

We introduce a novel dual sacrificial layer, comprising of InGaAs plus AlInAs, for releasing InP-based devices in the transfer printing process. We double the etch rate compared to either AlInAs or InGaAs alone, along with enhanced selectivity to InP, including at room temperature release. Extremely smooth surfaces are obtained for improved adhesion with transfer printing.

Keywords: *Transfer printing, Photonic Integrated Circuits, release layer, AlInAs, InGaAs, Coupon*

INTRODUCTION

Photonic integrated circuits (PIC) are the need of the hour to satisfy the demand for ever-increasing data rates. Silicon is the leading material for PIC, due to its high refractive index contrast in SOI platforms, facilitating small footprint devices and mass production via existing CMOS foundries. However, it is an indirect bandgap semiconductor, which demands integration with compound semiconductors to realise active components. There are multiple ways for integration such as a 3 μm SOI platform with Ge photodiodes [1], InP based generic integration [2], epitaxially grown III-V on InP/SOI [3], wafer bonding of III-V on Si [4] and transfer printing of III-V on Si [5]. Among all these techniques, transfer printing (TP) is considered here for its salient features such as efficient reuse of expensive substrate wafers, high throughput and room temperature integration, taking less than 40 s for single printing [6]. To perform TP, the devices (also called as coupons) made on the source wafer are released from its substrate using a sacrificial layer. These released coupons are mechanically held in place via tethers, which are picked using a PDMS stamp and then printed to target wafers.

Thus far, InP-based epistacks have used either AlInAs or InGaAs as the sacrificial layers, which are wet etched using dilute FeCl_3 . In [7], InP ridge lasers are released using 1 μm of n-doped InGaAs, where the lasers coupons are oriented along 45° to the major axis i.e. along $\langle 010 \rangle$, due to the anisotropic etching property of InGaAs in FeCl_3 . An etch rate of 1.3 $\mu\text{m}/\text{min}$ at 18 $^\circ\text{C}$, along with smooth coupon interface was obtained. However, there are two drawbacks, firstly, undercut takes a long duration and during the wet etch the surrounding InP layers are slowly etched vertically creating a ‘dish’ profile. Thus, the selectivity of InGaAs/InP is an important parameter, which is low at 735. Secondly, the density of coupons on a wafer is reduced, due to the requirement of $\langle 010 \rangle$ alignment. In [8], a comparative study between 500 nm of n-doped InGaAs and AlInAs layers as sacrificial layers is done, in which AlInAs has isotropic and faster etch rate compared to InGaAs in same FeCl_3 mixture. In this work, we combine both AlInAs and InGaAs release layers, via which we have achieved enhanced benefits in comparison to earlier works.

The two most important requirements of a sacrificial layer are the etch rate and selectivity to InP. Here we have achieved almost twice higher etch rate both at 4 $^\circ\text{C}$ and at room temperature. Generally, as the etch rate increases (e.g. room temperature process) the selectivity decreases. However, we could achieve, 1.3 and 3 times greater selectivity compared to [8], [7] at around room temperature, along with higher etch rates. Due to this combined effect, the undercut process can be carried out at room temperature itself saving the time of reducing the temperature to 4 $^\circ\text{C}$. Along with faster etch rates wider coupons could be released quickly. We also achieved extremely smooth coupon interface for adhesive-less transfer printing. This is achieved by growing InGaAs on top of AlInAs, where InGaAs is etched both laterally as well as from the bottom, which speeds up the release, and makes the etch profile more isotropic.

FABRICATION PROCESS

The epitaxial stack consists of 1 micron of n-doped InP on the sacrificial layers consisting of 400 nm of InGaAs and 100 nm of AlInAs on an (100) oriented InP wafer. Using a silicon nitride hardmask a range of rectangular, square and circular mesas, with widths varying from 40 μm to 400 μm and diameter from 50 μm to 500 μm , oriented along 0°, 45° and 90° to the major axis $\langle 011 \rangle$, as shown in Fig. 1A, are etched into the substrate, exposing the sacrificial layers. The sacrificial layers are etched using a wet chemistry of $\text{FeCl}_3:\text{H}_2\text{O}$ (1g per 2 mL) at 4 °C and 22 °C \pm 0.1 °C. Three different etch rates are involved, R1-lateral etch rate along $\langle 011 \rangle$ for AlInAs, which is 55 nm/s, taken from [8] at 20 °C. R2-etch rate of $\langle 010 \rangle$ plane for InGaAs, obtained from [7] at 18 °C is 22 nm/s. R3 is the vertical etch rate along $\langle \bar{1}00 \rangle$ for InGaAs, at room temperature is measured to be greater than 110 nm/s. Though there is a slight difference in temperature and doping between reference and this work, we take $R_3 > R_1 > R_2$. At the start of wet etch, only the $\langle 011 \rangle$ and $\langle 01\bar{1} \rangle$ planes are accessible. The etch rate of AlInAs is higher than InGaAs and is isotropic, so AlInAs starts being undercut (R1). Once AlInAs is etched then InGaAs can also be accessed from beneath along $\langle \bar{1}00 \rangle$ (R3), which has a rapid etch rate. Thus, having a 100 nm of AlInAs layer below InGaAs, facilitates the ingress of the etchant in vertical direction, thus etching InGaAs faster matching that of AlInAs.

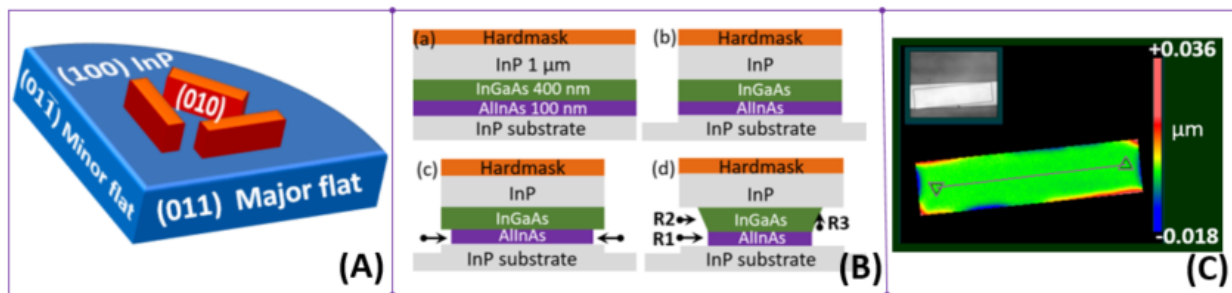


Fig. 1A, Schematic of crystal orientations shown with coupons along 0°, 45° and 90° to the major axis. B, schematic of the coupon fabrication process. C, The inset shows the microscope image of the coupon interface. White Light Interferometry gives a roughness of 2 nm on the bottom side of the 150 μm x 50 μm coupon.

RESULT AND ANALYSIS

The coupon surface is examined with Scanning Electron Microscopy (SEM), Atomic Force Microscopy (AFM) and White Light Interferometry (WLI). The interface is highly smooth as measured by WLI (Fig. 1C) and confirmed again by AFM, giving roughness of the order of 0.2 nm over 10 μm x 10 μm . Fig. 2 shows a comparison between this dual release with InGaAs [7] and AlInAs release layers [8]. Figure 2(A) is a plot of etch depth as a function of time, for coupons oriented along $\langle 011 \rangle$, $\langle 010 \rangle$ and $\langle 01\bar{1} \rangle$ at 6 °C. With the dual release we succeed in obtaining similar etch rate irrespective of coupon orientation. This confirms that anisotropic nature of InGaAs etch has been overcome by using the AlInAs layer below. This enhances vertical chemical access along $\langle \bar{1}00 \rangle$ plane to InGaAs with rapid etch rate. Figure 2(B) shows the etch rates as a function of bath temperatures. It can be seen that the dual release has a higher etch rate of 2 $\mu\text{m}/\text{min}$ and 4.85 $\mu\text{m}/\text{min}$ at 4 °C and 22 °C, respectively, which is an improvement over earlier works. Figure 2(C) is a plot of the selectivity, which is defined as the ratio of lateral etch rate along $\langle 011 \rangle$ direction of release layer to vertical etch rate of InP along $\langle 100 \rangle$ direction. From [7,8] the selectivity is shown to decrease with temperature. For AlInAs/InP at 20 °C the selectivity is 1620, and for InGaAs/InP at 18 °C the selectivity is 735. With the dual release structure the selectivity of (InGaAs+AlInAs)/InP at 22 °C is 2127. By comparing plot B and C, we can say this dual release stack has higher etch rate as well as higher selectivity at 22 °C. It is a room temperature process with faster etch rate and increased selectivity.

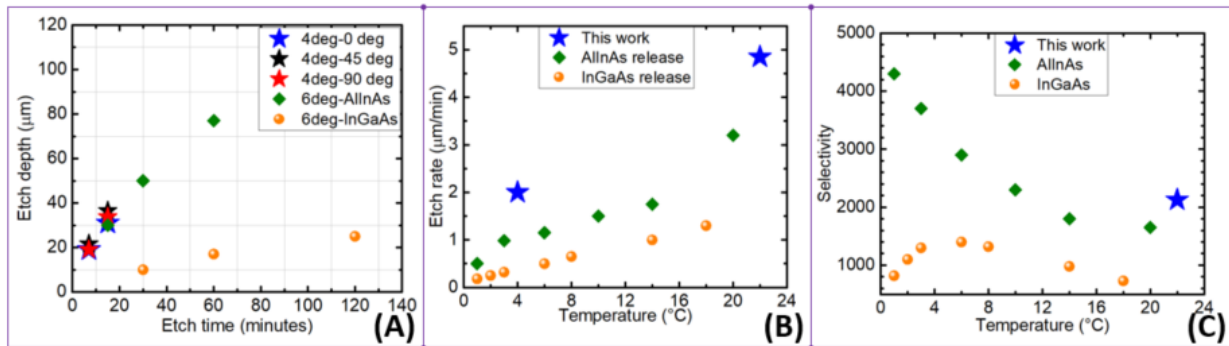


Fig. 2: A, shows the etch depths for coupons of different orientations in this work along with InGaAs[7] and AllnAs[8], B, C, are a comparison of etch rates and selectivity between dual release layers and [7,8].

CONCLUSION

This work presents the result of combined sacrificial layer of InGaAs plus AllnAs for InP based devices, used in transfer printing. We could achieve rapid release with higher selectivity to InP even at room temperature compared to separate individual release layers. The entire release process is faster and easier because of not having to cool the bath temperature to 4 °C, in order to get better selectivity. The etch rate is almost the same along all planes $\langle 011 \rangle$, $\langle 010 \rangle$ and $\langle 01\bar{1} \rangle$ unlike InGaAs, thus enabling device alignment along $\langle 011 \rangle$ plane. We also obtain an extremely smooth interface, enabling good adhesion during transfer printing in comparison to only AllnAs sacrificial layer. In future, optimizing the thickness of each release layer could be considered to improve the etch rate and surface quality.

Acknowledgements: This work was supported by Science Foundation of Ireland through 12/RC/2276_P2.

References

- [1] T. Aalto *et al.*, *Open-Access 3-μm SOI Waveguide Platform for Dense Photonic Integrated Circuits*, IEEE journal of selected topics in quantum electronics, vol. 25, no. 5, Sept/Oct 2019.
- [2] M. Smit *et al.*, *An introduction to InP- based generic integration technology*, Semiconductor Science and Technology, vol. 29, June 2014.
- [3] Y. Han *et al.*, *Selectively grown III-V Lasers for Integrated Si-Photonics*, Journal of Lightwave Technology, vol. 39, no. 4, Feb 2021.
- [4] D. Liang *et al.*, *Recent progress in Heterogeneous III-V-on-Silicon Photonic Integration*, Light: Advance Manufacturing, 2021.
- [5] J. Zhang *et al.*, *III-V-on-Si photonic integrated circuits realized using micro-transfer-printing*, APL Photonics, vol. 4, Nov 2019.
- [6] B. Corbett *et al.*, *Transfer printing for silicon photonics*, Semiconductors and Semimetals, vol. 99, pp. 43-70, 2018.
- [7] R. Loi, *Transfer printing of AlGaInAs/InP etched facet lasers to Si substrate*, IEEE Photonics Journal, vol. 8, no. 6, Dec 2016.
- [8] J. O'Callaghan, *Comparison of InGaAs and InAlAs sacrificial layers for release of InP-based devices*, Optical Materials Express, vol. 7, no. 12, Dec 2017.

Fabrication and characterization of symmetric Au-nanostructures with SERS activity

(Student paper)

M. Lafuente,^{1,2,4,*} E.J.W. Berenschot,¹ R.M. Tiggelaar,³ A. Susarrey-Arce,¹ R. Mallada,⁴ M.P. Pina,⁴ S.M. García-Blanco,² N.R. Tas¹

¹ Mesoscale Chemical Systems, University of Twente, 7500 AE Enschede, The Netherlands

² Integrated Optical Systems Group, University of Twente, 7500 AE Enschede, The Netherlands

³ Nanolab cleanroom, MESA+ Institute, University of Twente, 7500 AE Enschede, The Netherlands

⁴ Instituto de Nanociencia y Materiales de Aragón (INMA), CSIC-Universidad de Zaragoza, 50009, Zaragoza, Spain.

* m.lafuenteadiego@utwente.nl

In this work, ordered symmetric Surface-Enhanced Raman Scattering (SERS) gold nanostructures were fabricated and characterized. The fabrication protocol is divided into (i) nano-wedges process and (ii) Au-shaping process. The SERS activity was analyzed by calculating the analytical enhancement factor (AEF) and interpreted by finite-difference time-domain (FDTD) simulation.

Keywords: wafer-scale, ordered Au nanostructures, nano-wedges, SERS, FDTD simulations.

INTRODUCTION

The Surface-Enhanced Raman scattering (SERS) effect is produced by the resonant oscillation of conducting electrons at the interface of metallic nanostructures under light irradiation, which greatly increases the Raman signal of the molecules in contact with the metallic surfaces. In this way, SERS overcome the main drawback of Raman spectroscopy, i.e., its lack of sensitivity, while keeping its selectivity, i.e., recording the fingerprint of the absorbed molecules. The regions with the highest local electric field are called “hot spots,” and, generally, they are located in small gaps between metallic nanostructures. This signal enhancement allows using SERS as an analytical tool in multiple applications, such as biomedicine, security, healthcare, environmental monitoring, and the agro-food industry.

The SERS enhancement effect is produced by combining an electromagnetic mechanism and a chemical mechanism [1]. The electromagnetic SERS enhancement depends on the dimensions of the nanostructures, and can be predicted by finite-difference-time-domain (FDTD)-simulations, allowing to generate a better understanding of this SERS mechanism and to improve the interpretation of the experimental data.

Top-down fabrication offers many options for fabrication of well-controlled nanostructures with a wide selection of sizes and geometries, excellent reproducibility, and wafer-scale uniformity [2,3]. Among others, displacement Talbot lithography (DTL) is an emerging patterning technique by means of which ordered nanostructures can be produced with a monochromatic beam over large areas [4].

In this work, symmetric gold (Au)-nanostructures have been fabricated, and its SERS activity was studied (Fig. 1). The fabrication protocol is divided into (i) nano-wedges process and (ii) Au-shaping process. The analytical enhancement factor (AEF) was measured using rhodamine 6G (R6G) as an analyte. The comparison of the experimental results with FDTD-simulations allowed us to understand the electric field distribution over the various Au-nanostructure configurations [5].

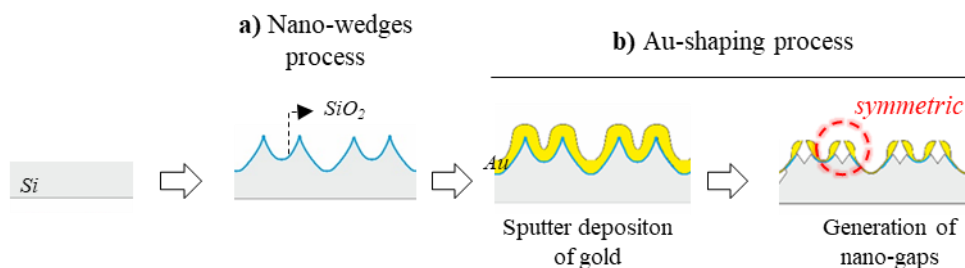


Figure 1. Schematic overview of the process for creating symmetric Au-nanostructures.

EXPERIMENTAL SECTION

The main step in the nanofabrication of these SERS substrates is the sputtering of Au films onto silicon etched nano-wedges. Briefly, the first step, named the “nano-wedges process,” produced a template for the realization of well-defined Au-nanostructures with highly reproducible nanogaps (Fig. 1a). Here, a combination of three techniques was employed: (i) DTL, (ii) reactive ion etching (RIE), (iii) and anisotropic wet etching of silicon. The second step, referred to as “Au-shaping process” (Fig. 1b), consisted of a sputter deposition of Au onto these nano-wedges and further nanomachining (among others ion beam etching (IBE)) into gold nanostructures with defined nanogaps, i.e., symmetric Au-nanostructures. Note that the thickness of the sputtered Au film, in combination with the time length of IBE, determined the remaining Au-pattern around a nano-wedge was symmetric.

The plasmonic effect was simulated using the FDTD method by means of a commercial software package (Lumerical Solutions Inc, FDTD solutions). An Alpha 300 Raman spectrometer was used with a confocal optical microscope. Excitation of the samples was carried out with a 633 nm laser at room temperature, a laser power of 3 mW, and an acquisition time of 1 s. SERS substrates were incubated overnight in R6G 1 μM ; then rinsed in distilled water and air-dried. Subsequently, on the specimen, three different maps of $50 \times 50 \mu\text{m}^2$ containing 100 measurement locations were measured. The Raman intensity of the C-C stretching vibrational mode of R6G at 1510 cm^{-1} was used as a mapping signal. The AEF was calculated according to equation (1):

$$AEF = (I_{SERS}/C_{SERS}) / (I_{Raman}/C_{Raman}) \quad (1)$$

Where: C_{Raman} and C_{SERS} are the R6G concentrations during the Raman measurements and SERS conditions, respectively. I_{SERS} is the intensity of the R6G molecules on the SERS substrates, and I_{Raman} corresponds to the intensity of the R6G molecules measured in the liquid phase (1 mM concentration).

RESULTS and DISCUSSION

The dimensions and characteristics of the fabricated SERS substrates are summarized in Table 1, and Fig. 2a shows the SEM images. In a SERS substrate, the most important requirements are large-scale uniformity, reproducibility during nanofabrication, and robust SERS signal intensity. These parameters are studied by evaluating SERS intensity mappings at three different locations on the same SERS substrate. From averaging the mapping results, the AEF was calculated using equation 1.

FDTD-simulations help to understand the possible origin of such enhancement. The electrical field intensity distribution for symmetric Au-nanostructures is shown in Fig. 2b, in which the color scale represents the normalized amplitude of the enhanced electric field intensity $|E|$ with respect to the amplitude of the incoming electric field $|E_0|$ with a value of 1. It can be seen that the SERS arises mainly at the gap between the Au-flaps, as could be expected based on the surface plasmon coupling effect between Au-flaps [1].

Table 1. Dimensions and characteristics of SERS substrates studied in this work.

Sample I.D.	Gap (G) [nm]	Etched silicon depth (SiD) [nm]	Au flap width [nm]	Measured AEF
sym	6 ± 2	40 ± 3	67 ± 7	1.8×10^5

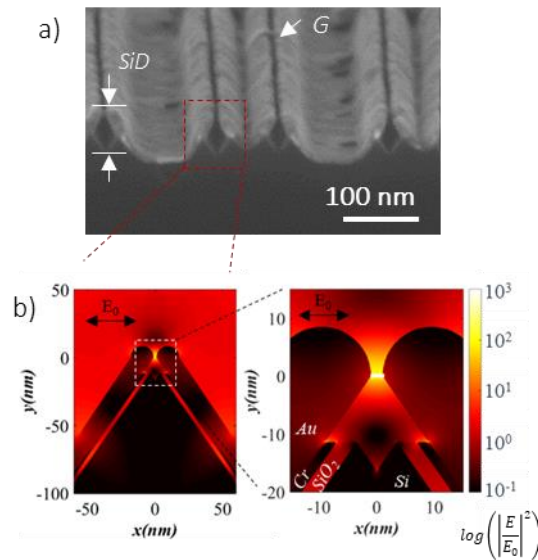


Figure 2. (a) Cross-sectional HR-SEM images of the symmetric and Au-nanostructures. (b) FDTD simulated distribution of the local field intensity enhancement factor at a wavelength of 633 nm for symmetric and Au-nanostructures.

CONCLUSIONS

The ordered Au nanostructures surrounding the tip of nano-wedges are highly tuneable by varying the thickness of the sputtered Au layer. FDTD simulations, validated by experimental results, in the case of symmetric Au nanogaps, the SERS effects arise mainly at the gap between the Au-flaps.

References

- [1] P. L. Stiles et al., *Surface-enhanced Raman spectroscopy*, Annual Review of Analytical Chemistry, vol. 1, pp. 601–626, 2008.
- [2] A. Shiohara et al., *Recent approaches toward creation of hot spots for SERS detection*, Journal of Photochemistry & Photobiology, C: Photochemistry Reviews, vol. 21, pp. 2–25, 2014.
- [3] D. Jonker et al., *A wafer-scale fabrication method for three-dimensional plasmonic hollow nanopillars*, Nanoscale Advances, vol. 3, pp. 4926–4939, 2021.
- [4] H. Le-The et al., *Wafer-scale fabrication of high-quality tuneable gold nanogap arrays for surface-enhanced Raman scattering*, Nanoscale, vol. 11, no. 25, pp. 12152–12160, 2019.

Comparison of Gaussian Process Kernels for Surface Roughness Modelling

Student paper

Samuel Hörmann^{1,2,*}, Jakob Wilhelm Hinum-Wagner^{1,2}, Jürgen Sattelkow¹, Desiree Rist¹,

Alexander Bergmann²

¹ams OSRAM, Tobelbader Straße 30, 8141 Unterpremstätten, Austria

²Institute of Electrical Measurement and Sensor Systems, Graz University of Technology, Inffeldgasse 33/I, 8010 Graz, Austria

*samuel.hoermann@ams-osram.com

Waveguide losses are a crucial factor for high performance integrated photonic devices. However, a rigorous description of the surface roughness remains lacking, even though this critically affects the induced scattering losses. We propose Gaussian processes as a suitable framework and compare various kernels for the regression of the measured sidewall roughness of a state-of-the-art PECVD silicon nitride process.

Keywords: Surface roughness, Gaussian process regression, silicon photonics, silicon nitride

INTRODUCTION

Integrated photonics is a flourishing field of research with applications in telecom and sensing. Raman spectroscopy, optical coherence tomography and biosensors are just examples of its vast potential. The waveguide losses pose fundamental limitations on the performance. In previous studies, it has been found that the main contribution to the propagation losses is sidewall roughness induced scattering.[1] We investigate a plasma enhanced chemical vapor deposition (PECVD) silicon nitride technology highly beneficial for sensing, since silicon nitride exhibits a high transparency for wavelength in the visible and the near-infrared (NIR) region in comparison to the established silicon-on-insulator (SOI) technology. Since PECVD thin films are usually deposited at working temperatures between 200 °C and 500 °C, the process is CMOS compatible.[2] An example of such a sensing architecture in side view is depicted in Fig. 1 b).

In the fabrication of the waveguides on wafer-level, several process steps can have a huge impact on the line edge- and the sidewall roughness. During the lithography step, the photoresist type and thickness, the bake temperature, and the O₂ plasma descum can affect the sidewall roughness.[3],[4] During plasma etching, roughness is introduced by ion bombardment resulting in typical striations as shown in Fig. 1 a). It can be minimized e.g. by the type and ratio of used gases. For silicon nitride, mainly CF-based gases (CF₄ and CHF₃) are used with admixed O₂ that balances the residual fluoride polymer on the surface. A low-polymer etch recipe with nitrogen and an increased oxygen concentration (CHF₃/O₂/N₂) is used to enhance the removal of polymers from the sidewalls.[5]

The conceptual model for surface roughness has not been explored rigorously, although this critically affects the caused scattering via the Wiener-Khinchin-Theorem.[6] Hence, we propose Gaussian process regression (GPR) as a suitable framework. The theoretical link between surface roughness as a Gaussian process and scattering losses will be explored in a future publication, currently in preparation. A zero-mean Gaussian process is fully described by its auto-covariance function, the kernel.[7] It quantifies how similar neighboring points of the processes are in average.

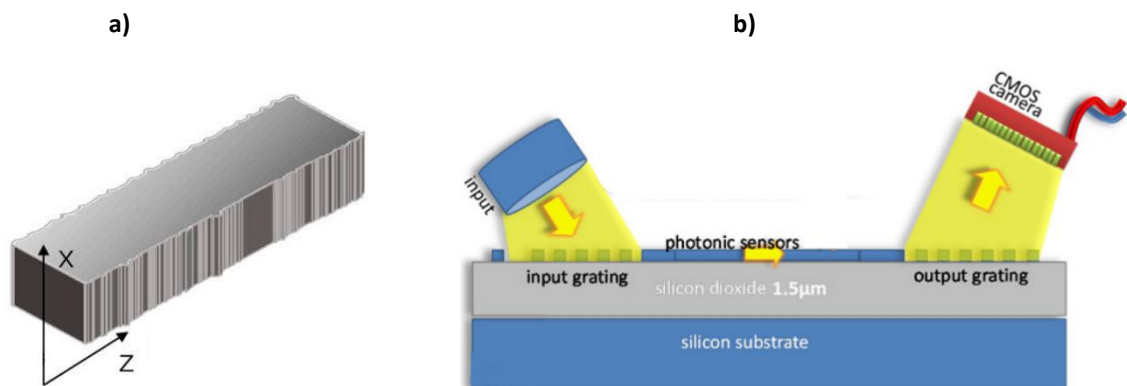


Fig. 1. a) Sidewall roughness of an arbitrary waveguide in x- and z-direction. b) Side view of silicon nitride Silicon nitride sensing platform with incoupling and outcoupling approach. [8],[2], edited

The auto-covariance was investigated before, but not tied to a Gaussian process.[1],[9] For this purpose, an exponential kernel was used, that is,

$$\kappa(z) = \sigma^2 e^{-\frac{|z|}{l}} \quad (1)$$

where z is the distance between the points on the surface of the waveguide, σ is the RMS roughness and l is the correlation length. In the context of Gaussian processes, σ and l are hyperparameters. The exponential kernel is the only one with Markov properties and its sample functions are non-continuously differentiable. Hence, it is doubtful if the exponential kernel is the right choice to model a physical process. Smoother processes can e.g. be found in the Matérn class with the kernel [7]

$$\kappa_\nu(z) = \frac{\sigma^2}{\Gamma(\nu)2^{\nu-1}} \left(\frac{\sqrt{2\nu}}{L_c} |z|\right)^\nu K_\nu \left(\frac{\sqrt{2\nu}}{l} |z|\right) \quad (2)$$

where Γ is the gamma function, K_ν is a modified Bessel function and ν determines the differentiability, that is, the process is $\nu - 1$ times continuously differentiable. To be precise, the exponential kernel is also of the Matérn class with $\nu = 1/2$. Other popular choices are $\nu = 3/2$ and $\nu = 5/2$. Another possible kernel frequently utilized in machine learning is the Gaussian or squared-exponential (SE) kernel (corresponding to $\nu \rightarrow \infty$), which is infinitely often continuously differentiable, contrary to the exponential kernel.

RESULTS

For the experimental determination of the sidewall roughness, a stack of silicon dioxide and silicon nitride was deposited. After a photolithography and etch step, the wafer with the structured silicon nitride atop was dissected. The surface roughness of the sidewall was measured with an atomic force microscope (AFM) in tilt operation. A processed AFM height image of the sidewall roughness can be seen in Fig. 2. The method, is currently scientifically investigated by our team and planned to be published later this year. In this work, we are primarily interested in the features of the surface roughness along the waveguide axis (z).

Comparing different kernels is known as model selection in machine learning. It encompasses both the choice of kernel and the values of its hyperparameters θ . The regression objective in this work is to estimate the posterior distribution over θ given the data $D: p(\theta|D)$. However, this problem is analytically intractable. Instead, we choose a batched approach and divide the 2D surface data of the roughness of Fig. 2 into 12 surface areas along the waveguide height, corresponding to areas with a height of approx. 35 nm. The GPR is performed on each and the maximum likelihood (ML) parameters $\arg\max_{\theta} p(D|\theta)$ are evaluated.

The mean and standard deviation of the hyperparameters can then be trivially evaluated over the ensemble of batches. This assumes a multivariate normal distribution for $p(\theta|D)$ and ignores the off-diagonal elements of its covariance matrix. Further, correlations between batches are also neglected. To analyse the surface data of Fig. 2, we formulate 2D, multivariate versions of the kernels. This follows the generalization to multi-dimension regression described by Rasmussen et al. [7] and leads to anisotropic kernels, which feature dedicated correlation lengths for each dimension. Hence, we have the set of hyperparameters $\theta = \{\lambda, \sigma, l_x, l_z\}$ with an estimation for the uncorrelated measurement noise λ , the RMS roughness σ and the length scales l_x and l_z . Due to the distortion of the data along the height x , we ignore l_x . Each kernel under consideration has the set of hyperparameters θ in the same form as defined above.

In this fashion, we applied the freely available Python GPR library “George” and arrive at the resulting maximum likelihood hyperparameters and marginal likelihoods for the kernels listed in Table 1. The median logarithmic marginal likelihood is the decisive measure for the descriptive precision of the kernel for the surface roughness data. We notice, that indeed the prevalent exponential and SE auto-covariances are inferior to the Matérn forms. Whether the 3/2 or 5/2 version is better suited, cannot be assessed in this work, as that would require a more detailed analysis with bigger dataset. Beyond the above mentioned influence on the scattered loss, we also see that the chosen form of the kernel leads to significant differences in the correlation length, which for the exponential kernel is 220(150) nm and for the Matérn 3/2 kernel is 36(16) nm.



Fig. 2. Height image of a $2.5 \mu\text{m} \times 0.2 \mu\text{m}$ cut-out of the sidewall.

Table 1: Statistically analysed maximum likelihood hyperparameters and maximum likelihood of 2D Gaussian process kernels for the description of the sidewall roughness of PECVD silicon nitride waveguides for integrated photonics. The statistics was arrived at by dividing the waveguide into 12 height batches. The brackets denote the standard deviations.

Kernel	λ in nm	σ in nm	l_z in nm	Median log. marginal likelihood
Exponential	0.03(10)	3.5(8)	220(150)	-602
Matérn 3/2	0.52(10)	3.3(6)	36(16)	-581
Matérn 5/2	0.57(6)	2.9(5)	24(11)	-582
SE	0.61(7)	2.5(4)	16(8)	-596

DISCUSSION

For a holistic analysis of the posterior distribution of the hyperparameters $p(\theta|D)$, there exist more sophisticated methods, which do not assume it as Gaussian and instead employ the Monte Carlo algorithm and its variations to sample from this distribution.[11] By knowing the posterior distribution in detail, the error bounds of the hyperparameters can be estimated with higher confidence. Moreover, it is easier computationally tractable for larger datasets. When the present analysis routine was applied to the complete dataset, i.e. the whole measured sidewall area, this issue was already encountered and the computation was not feasible on a common computer anymore. With our simplified method, it is likely that the error bounds of the hyperparameters are underestimated. That is partly due to the neglected covariances between batches, the assumption of a Gaussian $p(\theta|D)$, and the hyperparameter prior $p(\theta)$, which wasn't considered yet and corresponds to assuming it as constant. Moreover, statistical analysis of the batches is possibly enhanced by using the achieved likelihood as corresponding weights.

The above evaluation approach also estimates RMS roughness along x , which is distorted due to the AFM measurement and not yet properly corrected. That further implies, that the RMS roughness parameter gets skewed too. However, 1D regressions at multiple waveguide heights, which leads to cross sectional profiles, were conducted and showed the Matérn kernel to be preferable as well.

Another observation is that our investigated surface roughness does not show the distinct striations which typically are assumed.[1] This complicates the theoretical description, since for a given sidewall the perturbation due to the roughness is then not constant anymore along the waveguide height. Therefore, it must be treated with a dependence on z and x .

Finally, we want to highlight the two important conclusions that a different auto-covariance function entails, which seems indicated by the higher marginal likelihood of the Matérn kernels. First, according to the Wiener-Khinchin-theorem, the spectrum of the kernel is altered and subsequently also the scattered light, leading to lower or higher losses. Secondly, the maximum likelihood hyperparameters can also change, with evidently high magnitude.

REFERENCES

- [1] A. Melloni, D. Melati, F. Morichetti, *Real photonic waveguides: guiding light through imperfections*, Advances in Optics and Photonics, vol. 6, issue 2, pp. 156-224, 2014
- [2] P. Muellner, E. Melnik, G. Koppitsch, J. Kraft, F. Schrank, R. Hainberger, *CMOS-compatible Si₃N₄ waveguides for optical biosensing*, Procedia Engineering, vol. 120, pp. 578-581, 2015
- [3] C. Bellegarde, E. Pargona, C. Sciancalepored, C. Petit-Etienne, V. Hughesd, J. Hartmann, P. Lyand, *Improvement of Sidewall Roughness of Sub-Micron Silicon-on-Insulator Waveguides for Low-Loss On-Chip Links*, in proceedings of the Conference Silicon Photonics XII, SPIE OPTO, vol. 10108, 2017
- [4] T. Suligoj, K.L. Wang, P. Biljanovi, *Minimization of Sidewall Roughness in Si Pillar-like Structures by Photolithography Optimization*, in proceedings of the 11th IEEE Mediterranean Electrotechnical Conference, 2002
- [5] S. P. Roberts, X. Ji, J. Cardenas, A. Bryant, M. Lipson, *Sidewall Roughness in Si₃N₄ Waveguides Directly Measured by Atomic Force Microscopy*, In Proceedings of the Conference on Lasers and Electro-Optics, 2017[10]
- [6] Yates, Roy D., and David J. Goodman. *Probability and stochastic processes: a friendly introduction for electrical and computer engineers*. John Wiley & Sons, 2014.
- [7] C. E. Rasmussen, C. K. I. Williams, *Gaussian Processes for Machine Learning*, the MIT Press, 2006.
- [8] H Shang, P. Yu, B. Wang, T. Yu, T. Li and H. Jiang, *Investigation for Sidewall Roughness Caused Optical Scattering Loss of Silicon-on-Insulator Waveguide with Confocal Laser Scanning Microscopy*, Coatings, vol. 10, art. num. 236, 2020
- [9] D. M. Kita, J. Michon, S. G. Johnson, J. Hu, *Are slot and subwavelength grating waveguides better than strip waveguides for sensing?*, Optica, vol. 5, issue 9, pp. 1046-1054, 2018
- [10] R. D. Yates, D. J. Goodman, *Probability and stochastic processes: a friendly introduction for electrical and computer engineers*, John Wiley & Sons, 2014.
- [11] A. Svensson, J. Dahlin, T. B. Schön, *Marginalizing Gaussian process hyperparameters using sequential Monte Carlo*, in proceedings of the 6th IEEE International Workshop on Computational Advances in Multi-Sensor Adaptive Processing, pp. 477-480, 2015

Designing a GaN photonic platform for near-IR applications

(Student paper)

Megan O'Brien^{1,2}, Nicola Maraviglia¹, Vitaly Zubialevich¹, and Brian Corbett¹

¹Tyndall National Institute, Lee Maltings, Cork, Ireland

²Physics Department, University College Cork, College Road, Cork, Ireland

* megan.obrien@tyndall.ie

We simulate an AlGaIn/GaN waveguide structure that allows for efficient edge coupling of 1300 nm-emitting lasers. An optimum coupling loss of 0.6 dB is simulated for a quantum dot laser, and 1 dB for a quantum well laser. By using a double-etched mode converter with > 98 % conversion efficiency, waveguide bend losses < 0.04 dB can be achieved for 90° waveguide bend radii > 70 μm for both polarizations.

Keywords: Gallium nitride waveguides, photonic integration, micro-transfer printing

INTRODUCTION

Gallium nitride (GaN) is an interesting alternative waveguide material to Si and SiN for integrated photonics. It has a broad transmission window combined with useful linear and nonlinear optical properties [1,2], with high speed optical modulation demonstrated [3]. In order to exploit the full potential, the active device needs to be integrated which we proposed to do via micro-transfer printing (μTP) and end-fire coupling.

In this paper, we design a waveguiding platform based on a GaN core layer surrounded by AlGaIn cladding layers on a sapphire substrate [4]. The coupling efficiency between the transferred lasers and the waveguide facet is optimised through matching modes while also calculating the misalignment tolerance that can occur as a result of μTP. We design a double-etched taper structure to transition from a shallow etched ridge waveguide, optimised to couple to the laser mode, to a partially etched waveguide designed for efficient light routing.

EDGE COUPLING

The waveguide structure was chosen in order to best match the lasing mode size in the lateral and transverse directions, Fig. 1(a). As GaN is a positive uniaxial material, there is a significant difference in the effective indices for both polarizations, with the TM modes generally being higher in effective index than the TE modes. The birefringent GaN and AlGaIn refractive indices were extrapolated to 1300 nm using the Sellmeier formula [5]. The small index difference between Al_xGa_{1-x}N cladding layers and a GaN core allows a large mode size to be achieved. The ridge height and width are carefully selected to obtain single mode operation, with the total height of the AlGaIn upper cladding layer fixed at 0.5 μm. Fig. 1 (b) and (c) shows the regions where the structure is single-mode for the TE and TM polarization.

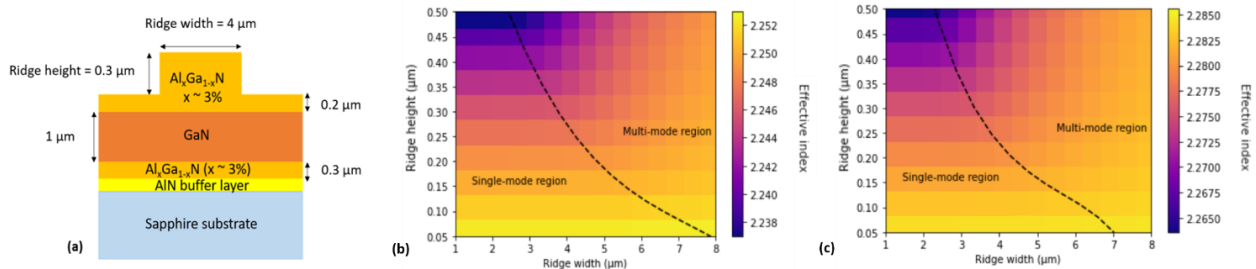


Fig. 1. (a) AlGaIn/GaN waveguide structure, (b) single-mode and multi-mode regions of the waveguide as a function of ridge height and ridge width for TE polarization and (c) TM polarization. The colour in Fig 3 (b) and (c) graphs represent the varying effective indices for both polarizations.

For efficient edge-coupling, the lasing mode needs to be aligned carefully with the waveguide mode in both transverse, lateral and longitudinal directions. We examine the edge-coupling efficiency of (i) a TE-polarized quantum dot (QD) laser, and (ii) a TM-polarized quantum well (QW) laser in both the transverse and lateral directions, assuming no gap and reflections between the laser facet and waveguide facet in the longitudinal direction. The waveguide ridge width is fixed at 4 μm, while both laser ridge widths are varied between 2- 5 μm. Beyond 5 μm, the laser structures became multi-modal. In Fig. 2 we can see that for a ridge width of 5 μm for both lasing

structures, an optimum coupling loss of 1 dB for the QW laser and 0.6 dB for the QD laser can be obtained. The alignment tolerance in the lateral direction is more relaxed than in the transverse direction for both structures. The difference between coupling loss can be attributed to larger mode size mismatch in the transverse direction, which is more significant for the QW laser as can be seen from the asymmetry in the graphs.

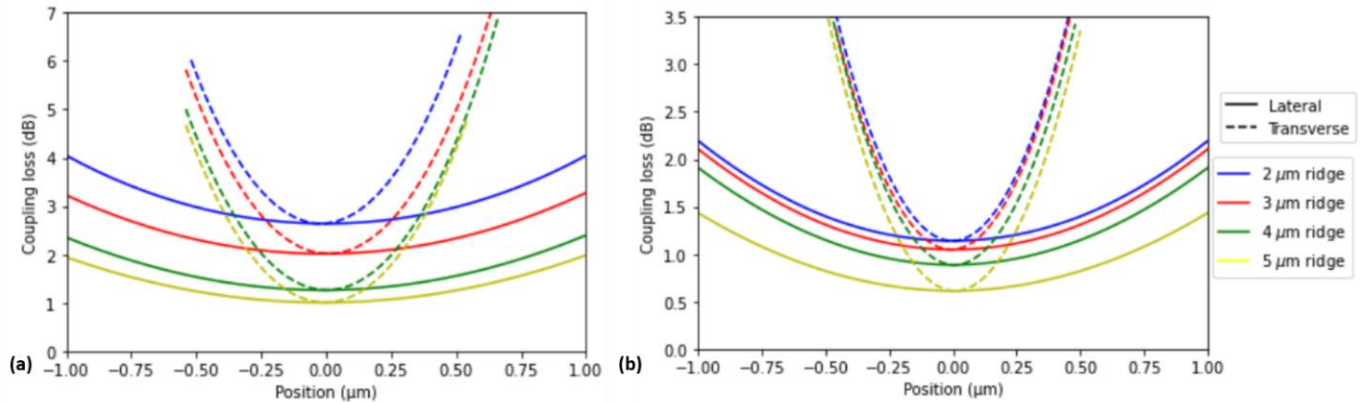


Fig. 2. Coupling loss in both the lateral (solid lines) and transverse (dashed lines) directions for (a) a QD laser structure, and (b) a QW laser structure, for lasing ridge widths between 2-5 μm . Overall the QD laser is better at coupling in both directions than the QW structure.

MODE CONVERSION

While advantageous for edge coupling, a wide waveguide for an integrated photonic circuit requires bends with large radii for low excess loss. Therefore, an inverse taper design is needed to convert the waveguide to a structure better suited for bends. Such a low-loss converter between waveguide sections of different sizes has been demonstrated before on the silicon-on-insulator (SOI) platform by using a double etch [6]. A similar structure on the GaN platform is shown in Fig. 3(a), with a top-down view provided in Fig. 3 (b).

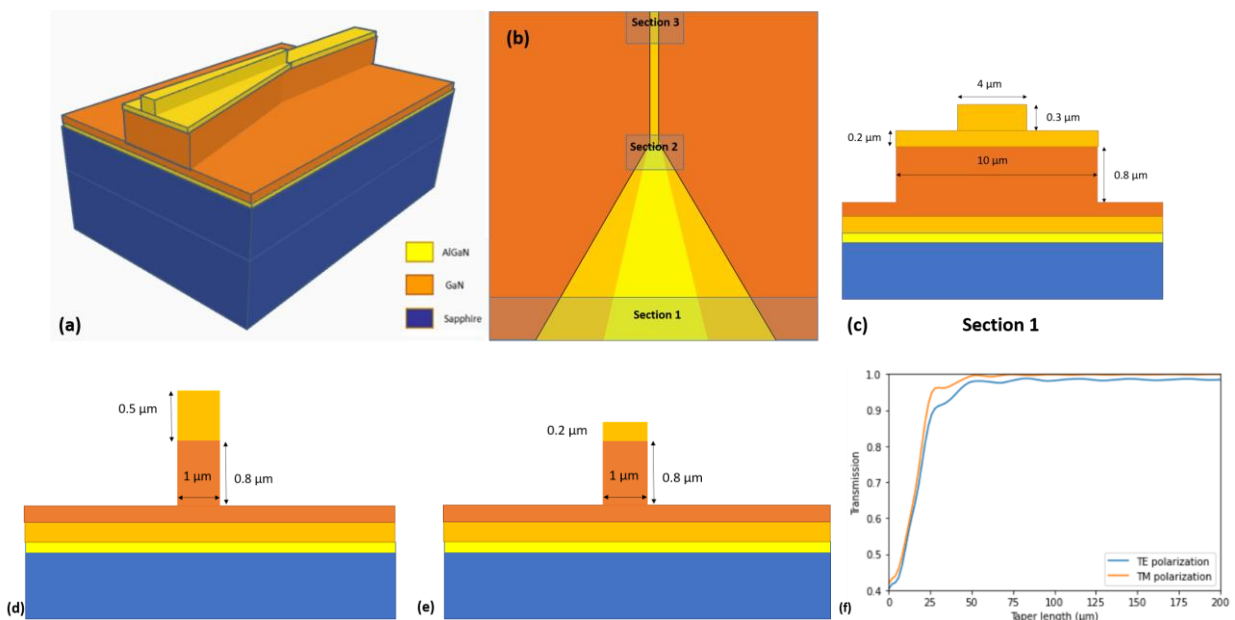


Fig.3. (a) Schematic of the double etched mode converter design, (b) top-down view of the structure with highlighted regions, (c) cross section of Section 1 where both tapers start, (d) Section 2 where the shallow-etched AlGaIn taper ends, and (e) Section 3 where the structure continues on, and (f) transmission through the structure as a function of taper length for both TE and TM polarizations.

The structure is sectioned into 3 parts in order to explain the structure dimensions. The structure was simulated with a deep etch of 0.8 μm into the 1 μm thick GaN core. The starting width of the etched section of the GaN core was set to be 10 μm , while the shallow etched AlGaIn ridge waveguide was 4 μm as seen in Fig 3 (c). The taper tip width of both tapers was fixed to 1 μm as seen in Fig 3 (d), with both the AlGaIn and GaN tapers set to be the same taper length. In Fig. 3 (e), the AlGaIn taper terminates, and the structure successfully converts to dimensions suitable

for bends. It can be seen that a taper length $> 50 \mu\text{m}$ results in a transmission $> 98 \%$ for both polarizations. The short taper lengths needed to achieve successful mode conversion, compared to the long taper lengths needed in previous demonstrations [6], is as a result of the width dimensions being on the same scale.

The TE_0 and TM_0 mode profiles of the deeply etched GaN waveguide structure from Fig. 3 (e) is shown in Fig 4 (a) and (b). The etch depth into the GaN was selected to minimize the radiation losses as the mode propagates around the bend. It can be seen that before the bend commences, the TE_0 mode is less confined than the TM_0 mode. Increasing the ridge width improves the confinement, but higher order modes are supported as a result. The loss was calculated for a 90° waveguide bend for varying bend radii with both polarizations. In Fig. 4(c), it can be seen that bend losses $< 0.02 \text{ dB}$ can be achieved for the TM polarization at a bend radius $> 70 \mu\text{m}$, while for the TE polarization bend losses $< 0.04 \text{ dB}$ is obtained at a bend radius $> 100 \mu\text{m}$. At a bending radius of $200 \mu\text{m}$, the bending losses are $< 0.01 \text{ dB}$ for both polarizations.

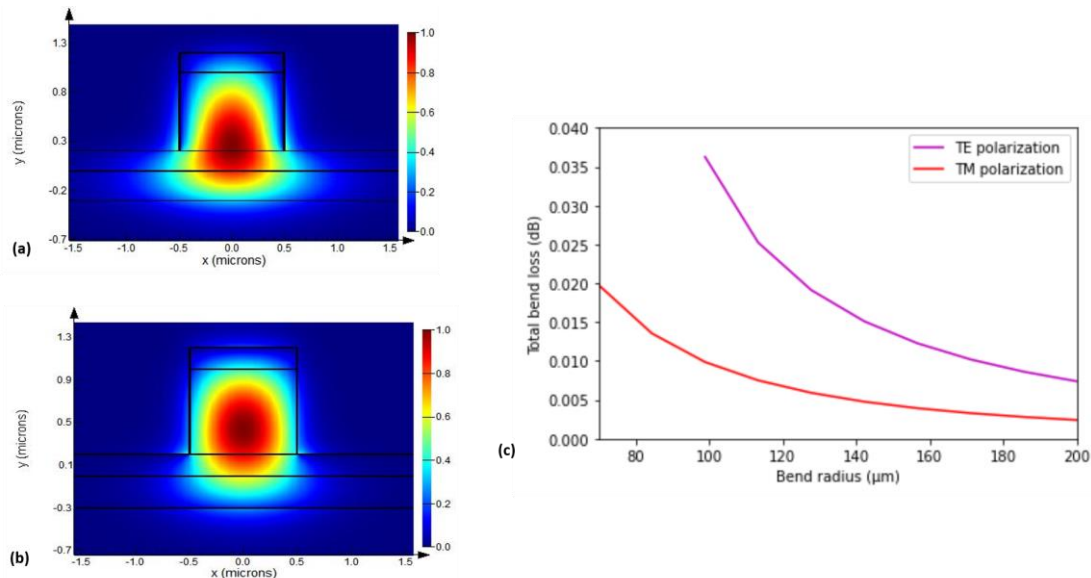


Fig.4. (a) E_x component of the TE_0 mode and (b) E_y component of the TM_0 mode after tapering, and (c) total bend loss for a 90° bend with varying bend radii.

CONCLUSION

The results in this paper demonstrate that by carefully designing the waveguide structure to minimize coupling loss and bend loss, GaN shows promise as a suitable platform for integrated photonics. Future work includes fabricating and characterizing the waveguides, transfer printing the laser devices to the waveguide platform, and further investigating the platform for electro-optic applications.

ACKNOWLEDGEMENT

This work was supported by Science Foundation Ireland through grant no. 12/RC/2276_P2.

References

- [1] D. Munk, M. Katzman, O. Westreich, Moran Bin Nun, Y. Lior, N. Sicron, Y. Paltiel, A. Zadok, *Four-wave mixing and nonlinear parameter measurement in a gallium-nitride ridge waveguide*, Optical Materials Express, vol. 8, no.1, pp. 66-72, 2018
- [2] E. Stassen, M. Pu, E. Semenova, E. Zavarin, W. Lundin, K. Yvind, *High-confinement gallium nitride-on-sapphire waveguides for integrated nonlinear photonics*, Optics Letters, vol. 44, no.5, pp. 1064-1067, 2019
- [3] P. Das, T.L. Wu, S.Tallur, *Design and analysis of high electron mobility transistor inspired: III-V electro-optic modulator topologies*, Semiconductor Science and Technology, 35(9), 095028. 2020
- [4] O. Westreich, M. Katz, Y. Paltiel, O. Ternyak, N. Sicron, *Low Propagation loss in GaN/AlGaIn-based ridge waveguides*, Physica Status Solidi (A) Applications and Materials, vol 212, no. 5, pp. 1043-1048, 2015
- [5] Ü. Özgür, G. Webb-Wood, H. O. Everitt, *Systematic measurement of $\text{Al}_x\text{Ga}_{1-x}\text{N}$ refractive indices*, Applied Physics Letters, vol. 79, no.25, pp. 4103-4105, 2001
- [6] T. Aalto, K. Solehmainen, M. Harjanne, M. Kapulainen, P. Heimala, *Low-loss converters between optical silicon waveguides of different sizes and types*, IEEE Photonics Technology Letters, vol. 18, no.5, pp. 709-711, 200

Micro-Transfer-Printed O-band GaAs QD III-V-on-Si DFB Laser

Jing Zhang^{1,2*}, Igor Krestnikov³, Ruggero Loi⁴, Peter Ossieur⁵, Guy Lepage⁶, Peter Verheyen⁶, Joris Van Campenhout⁶, and Gunther Roelkens^{1,2}

¹Photonics Research Group, INTEC, Ghent University - IMEC, Ghent, Belgium

²Center for Nano- and Biophotonics, Ghent University - IMEC, Ghent, Belgium

³Innolume GmbH, Konrad-Adenauer-Allee 11, 44263 Dortmund, Germany

⁴X-Celeprint Ltd, Lee Maltings, Dyke Parade, Cork, Ireland

⁵IDLab, INTEC, Ghent University – IMEC, Ghent, Belgium

⁶IMEC, Kapeldreef 75, 3001 Heverlee, Belgium

* jingzhan.Zhang@ugent.be

We present an array of GaAs QD III-V-on-Si DFB lasers integrated by micro-transfer printing. An alignment tolerant III-V/Si taper structure is used to evanescently couple light from the laser cavity to the underlying 400 nm thick rib waveguide. Single mode operation around 1300 nm with 48 dB side mode suppression ratio and a waveguide-coupled power of 0.5 mW is demonstrated.

Keywords: Silicon Photonics, Distributed Feedback Laser, Micro-Transfer Printing, Heterogeneous Integration

INTRODUCTION

Driven by the ever-increasing data traffic, giant data centers have been built in the past few years. In order to connect the servers in these data centers, significant volumes of optical transceivers with high reliability, low-power consumption and low-cost are heavily demanded. Silicon photonics (SiPh) is the most promising contender to meet this demand due to its high-index contrast and CMOS compatibility, which allows for the realization of compact photonic integrated circuits (PICs) on 200 mm or 300 mm wafers in a high-volume and at low cost. Yet, the absence of integrated laser sources is a significant obstacle in reducing the cost. Different approaches have been explored to cope with this challenge by combining the advantages of III-V materials and SiPh. Amongst these approaches, die/wafer-to-wafer bonding has been developed as a commercial solution [1], however it requires the development of dedicated III-V processes in a CMOS fab. Hetero-epitaxial growth is acknowledged as an ultimate solution and experienced significant progress in recent years, but advances in material quality are still needed and similarly III-V processing in a CMOS fab needs to be developed[2]. An alternative is the use of micro transfer printing, which decoupled the processing of the III-V semiconductors and that of the silicon photonics and allows for the integration of device coupons released from the native substrate onto a target substrate in a massively parallel way. Quantum dot lasers (QD lasers) have attracted intense interest in recent years due to their superior characteristics, such as low linewidth enhancement factor, temperature stability, high flexibility in gain bandwidth and emission wavelength engineering etc. [3]. In this work, we developed a process flow for the integration of GaAs QD laser devices on a SiPh platform using micro-transfer printing. Following this process flow we demonstrate an array of evanescently coupled O-band GaAs QD on Si DFB lasers.

DESIGN and FABRICATION

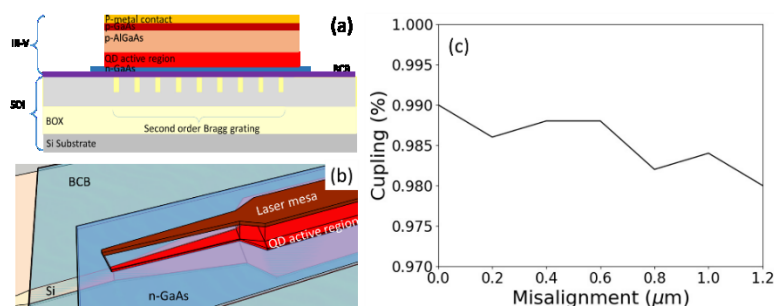


Fig. 1. (a) Schematic of the GaAs QD-on-Si DFB laser, (b) Schematic of the alignment-tolerant III-V/Si taper structure, (c) Simulated coupling efficiency as a function of lateral misalignment.

The Si waveguide circuits used in this work were fabricated at imec, by 193nm Deep-UV lithography and a 180 nm single-step etch into a 400nm thick Si device layer. Fig. 1(a) shows the schematic of the GaAs QD/Si DFB laser cavity, which has a hybrid waveguide structure where a III-V waveguide is overlaid on a uniform second-order Bragg grating

with a thin layer of DVS-BCB in between. The Bragg grating is patterned on a 9 μm wide rib waveguide and the length, period and duty cycle of it are 700 μm , 390 nm and 75%, respectively. The overall length of the GaAs QD structure is 1660 μm long, which consists of a straight III-V rib waveguide with a 2 μm wide p-mesa and a 6 μm wide QD active region, and a pair of two-level III-V/Si taper structures at each side to couple the optical power to the underlying Si waveguides, as shown in Figure 1(b). This taper structure shows excellent lateral alignment tolerance as shown in Fig.1(c), for the case of a 30 nm thick DVS-BCB bonding layer, which is able to accommodate the alignment accuracy that a state-of-the-art micro-transfer printing tool can obtain ($<1 \mu\text{m}$ @ 3σ). As a trade-off, its overall length is 310 μm .

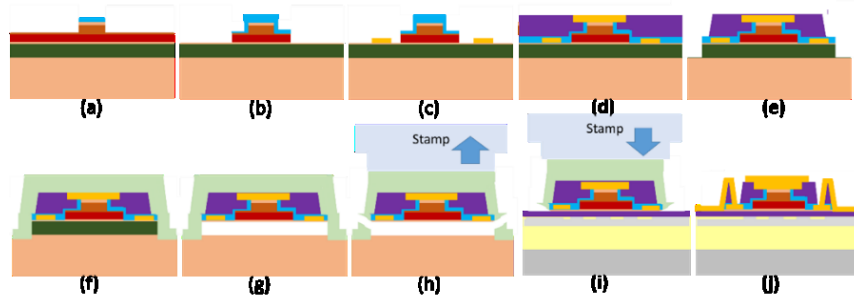


Fig. 2. Process flow for the definition of the GaAs QD SOA structures on the native GaAs substrate. (a-b) Rib waveguide definition, (c) n-contact metal deposition, (d) BCB planarization and p-contact metal deposition, (e) coupon mesa definition, (f) photoresist encapsulation and tether definition, (g) release etch, (h-i) Micro-transfer printing of GaAs QD device coupons, (j) final metallization.

The GaAs QD epitaxial structure used in this work was grown by Innolume. It consists of 11 QD layers interleaved with GaAs spacer layers, a 200 nm thick p-GaAs contact layer, a 670 nm thick p- $\text{Al}_{0.8}\text{Ga}_{0.2}\text{As}$ cladding and, a 250 nm thick n-GaAs contact layer and a 1 μm thick $\text{Al}_{0.95}\text{Ga}_{0.05}\text{As}$ release layer. The dimensions of the GaAs device coupons are 40 μm by 1700 μm . The process flow of the fabrication and release of the GaAs QD device coupons and their micro-transfer printing on the target SiPh substrate is described in Fig. 2. The p-cladding mesa is defined by electron beam lithography with a hydrogen silsesquioxane (HSQ) resist and ICP dry etching (Fig.2(a)), followed by the other ICP dry etching with a SiN hard mask to pattern the QD active layers (Fig.2(b)). Then the n-contact metal stack layer is deposited (Fig.2(c)). After planarising the III-V waveguide structures using a thick BCB layer and p-contact metal deposition (Fig.2(d)), the coupon is defined by a combination of RIE etch and ICP etch into the GaAs substrate (Fig.2(e)). The coupon is then encapsulated with a thick photoresist layer (Fig.2(f)) and ready for release etching. A room temperature 1:1 37% HCl:DI solution is used to selectively etch the release layer (Fig.2(g)). On the SiPh substrate a thin BCB layer is spin-coated and is then baked at 150 $^{\circ}\text{C}$ for 15 minutes. Next, a PDMS stamp with a post size similar to that of the device is used in the micro-transfer printing process to pick-up the device up from the donor III-V substrate and to transfer print it onto the SiPh substrate (Fig.2(h,i)). Finally, a few simple steps of photoresist encapsulation layer removal, BCB curing and metal deposition are performed to allow electrical contact of the device (Fig.2(j)).

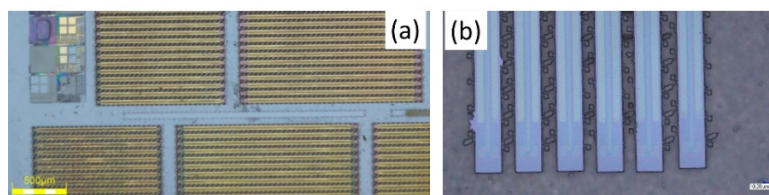


Fig. 3. (a) Microscope image of the released GaAs device coupons, (b) Bottom surface of the released coupons.

Fig. 3(a) shows a microscope image of the GaAs device coupon arrays after release etching, where a dummy coupon without tether structures was detached from the substrate, indicating the completion of the undercut of the coupons. Before the micro-transfer printing process, an array of coupons was picked up manually using a piece of scotch tape. It reveals a flat and smooth bottom surface as shown in Fig.3(b), which ensures a high yield micro-transfer printing. An X-Celeprint $\mu\text{TTP-100}$ lab-scale tool was used for the transfer printing process. 5 out of 6 coupons were successfully printed on a SiPh substrate and the only failure was caused by a local particle contamination. Fig. 4(a) shows the transfer-printed GaAs QD devices after removing the photoresist encapsulation using an RIE oxygen plasma. Fig. 4(b) shows the fabricated DFB lasers with metal contact pads and Fig. 4(c) shows the cross-section of the III-V/Si hybrid waveguide structure with a 2 μm wide p-AlGaAs mesa, a 6 μm wide QDs waveguide and a 9 μm wide underlying Si rib waveguide. The thickness of the resulting BCB bonding layer is less than 20 nm and the

alignment accuracy for each coupon is $<1 \mu\text{m}$. Unfortunately, the p-AlGaAs was attacked in the taper section during a wet etching step (Fig.4(d)), which introduces optical loss in the structure.

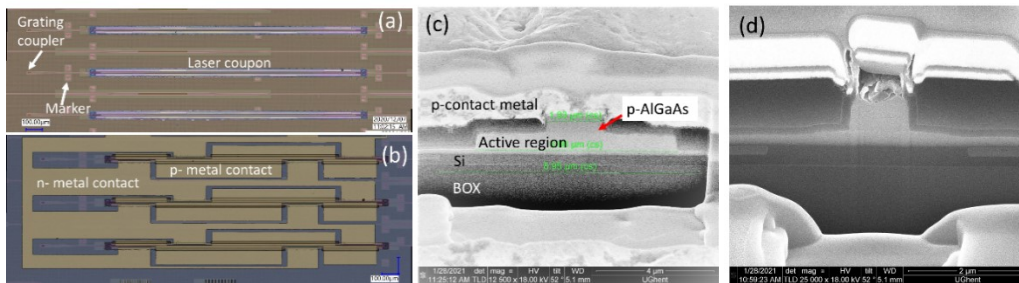


Fig. 4. Microscope image of (a) a Si PIC with micro-transfer-printed GaAs device coupons and (b) the resulting DFB lasers; (c) Focused Ion Beam cross section of the hybrid waveguide, (d) Focused Ion Beam cross section at the taper section, showing a perfect alignment but a damage in the p-AlGaAs cladding layer.

CHARACTERIZATION

The characterization of the fabricated devices was carried out on a temperature-controlled stage at 20°C . A Keithley current source with a pair of DC probes was used to apply the bias current onto the devices. A standard single mode fiber was used to collect the output power from a grating coupler. It is then connected to a fiber splitter with one channel feeding into a power meter and the other connected to an optical spectral analyzer. Fig. 5(a) shows the measured I-V response and the calculated differential resistance, which reduces with the increase of bias current and reaches 5Ω at 140 mA . As shown in Fig.5(b), the maximum single-side waveguide-coupled output power is above 0.5 mW , which is obtained by calibrating out the loss of the fiber grating coupler and fiber links. The threshold current is below 40 mA . The relatively low power is caused by the imperfect III-V taper structure, where the p-AlGaAs was attacked in the fabrication, as shown in Fig.4(d). Single mode operation at 1300 nm with a maximum side mode suppression ratio (SMSR) of 48 dB was demonstrated, as the superposed spectra show in Fig.5(c).

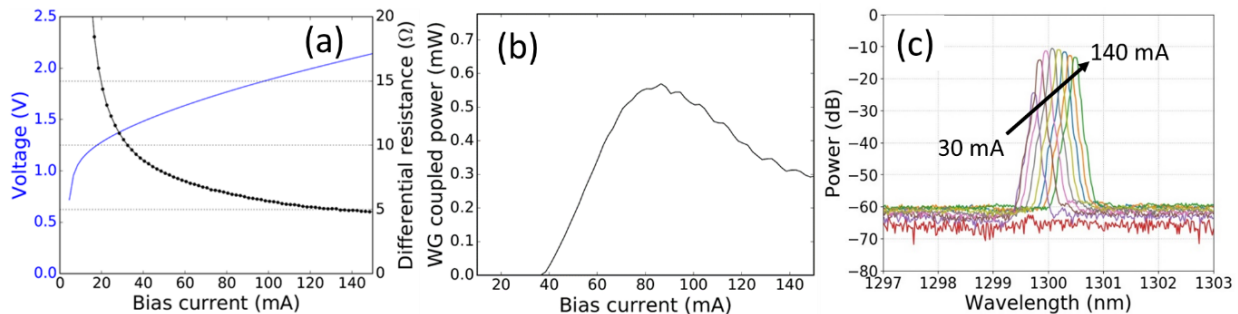


Fig. 5. Performance of a representative GaAs QD on Si DFB laser at 20°C . (a) V-I curve and differential resistance, (b) P-I curve (c) Superposition of the output spectra with the increase of the applied bias current.

CONCLUSION

We developed the process flow for the fabrication and release of GaAs QD device coupons on a GaAs source wafer. These device coupons were successfully transfer-printed on a SiPh substrate. The demonstrated DFB lasers show single mode operation at 1300 nm with 48 dB side mode suppression ratio. Although the output power of the fabricated device is not ideal, this demonstration verified the feasibility of the integration of GaAs QD lasers on a SiPh platform using micro-transfer printing.

Acknowledgements: This work was supported by the European Union's Horizon 2020 research and innovation programs under agreement 825453 (CALADAN).

References

- [1] R. Jones et al., "Heterogeneously Integrated InP-Silicon Photonics: Fabricating Fully Functional Transceivers," IEEE Nanotechnology Magazine, vol. 13, no. 2, pp. 17-26, April 2019.
- [2] Y. Shi et al., "GaAs Nano-Ridge Lasers Epitaxially Grown on Silicon," Ph.D thesis, Ghent University, 2020.
- [3] G. Frédéric et al., "Physics and applications of quantum dot lasers for silicon photonics," Nanophotonics, vol. 9, no. 6, pp. 1271-1286, 2020.
- [4] B. Corbett et al., "Transfer Printing for Silicon Photonics", Semiconductors and Semimetals, vol. 99, pp.43-70, 2018

Iron Doping for Transfer Printed High Speed EAM

(Student paper for poster session)

Shengtai Shi^{1,2,*}, Jack Mulcahy^{1,2}, Xing Dai^{1,2}, Frank H. Peters^{1,2}

¹ Integrated Photonics Group, Tyndall National Institute, Lee Maltings, T12 R5CP, Cork, Ireland

² Physics Department, University College Cork, T12 XF62, Cork, Ireland

* Correspondence: shengtai.shi@tyndall.ie

In this paper, a method of using an iron doped InP layer to achieve a micro transfer printing (MTP) compatible high-speed electro-absorption modulator (EAM) is proposed. An equivalent circuit model analysis of the transfer printed EAM is presented with a simulated speed up to 45.6GHz. In addition, discussion on the fabrication process for such high speed MTP EAM is provided. Finally, test results on the adopted iron doped InP material is presented to demonstrate latest progress which paves way to realize high-speed photonics integration via micro transfer printing.

Keywords: *Electro-absorption Modulator, Micro-transfer printing, Iron doping InP, Silicon Photonics; Photonics integration;*

INTRODUCTION

The increasing need for next generation communication technology has put forth a rapid development trajectory for silicon photonics and photonic integration technology. Statistic suggests the amount of data that was created, consumed, and stored within global network would have increased by nearly 50 times from 2010 – 2022 [1]. Behind this tremendous phenomenon a key point to notice is the ever increasing capability for photonic integrated circuits (PICs) to process data with higher and higher speeds. Industry reports from Yole forecast the market of silicon photonics from 2019 – 2025 growing at 40% every year on average [2]. Besides, recent developments on promising large scale heterogeneous integration technology such as micro-transfer printing (MTP) has emerged to the surface, enabling silicon photonics and matured III-V compound semiconductor material and its technology platform, such as InP, InGaAs, InGaAlAs etc, to achieve more cost-effective and high performance PICs to be made.

Compared to mature photonic integration technology such as flip chip bonding or die to wafer bonding, MTP stands out with advantages in high integration density, high efficiency of material use, high throughput and low cost [3]. Using transfer printing, noteworthy results have been reported to achieve different components such as lasers, photodetectors and amplifiers to be integrated with silicon photonic circuits [4-6]. Beyond the current scope of presented research, an electro-absorption modulator (EAM) based on the Quantum Confined Stark Effect (QCSE) with optimized ultra-low capacitance is ideal for demonstrating the potential in high speed applications using MTP as a large scale photonic integration solution [7]. A QCSE based EAM has high extinction ratio and low driving voltage and could be integrated to make complex PICs like external-modulated lasers. Due to the nature of incompatibility between transfer printing and standard high speed device processing steps, adopting an iron doping layer in the standard high speed EAM is proposed as a solution to overcome integration challenges. Details on the device design, fabrication process will be discussed in the following sections, with a focus to examine the high speed performance comparisons through equivalent circuit simulations.

Device Design and Fabrication

The high speed EAM utilizes a customized in-house InP based epitaxy with 12 quantum wells of each 9nm width. The designed working wavelength is 1310nm for monolithic integration purposes and the speed performance is optimized by a high speed contact pad scheme which helps minimize parasitic capacitance. As Figure 1 shows below, the non-MTP EAM is fabricated on a semi insulating substrate to minimize device parasitic capacitance. A bridge section is created to connect the EAM ridge section with the RF signal pad. The pad is electrically isolated from the waveguide sections. The configuration of this EAM design with GSG contact pads for RF signals has been tested experimentally, given a parasitic capacitance as low as 15fF and yielding a working bandwidth predicted to be 47GHz in a 50Ω system.

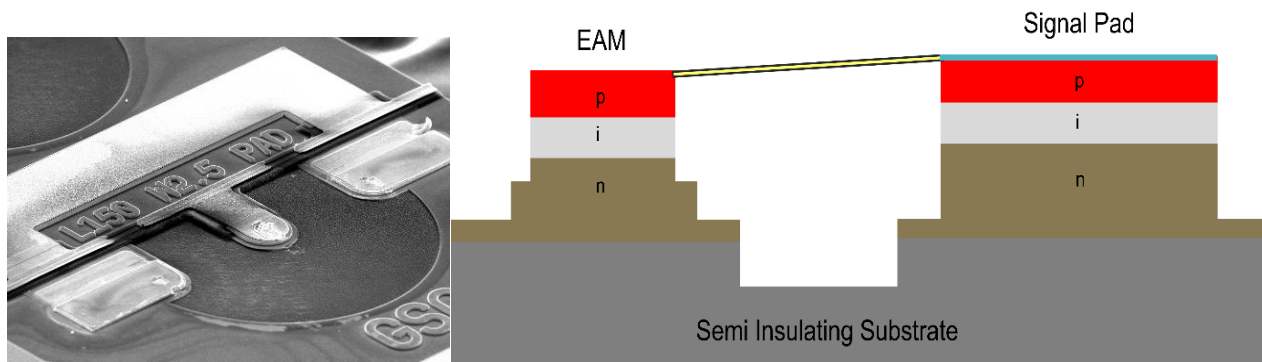


Fig. 1. (a) SEM of a fabricated high speed EAM Structure and (b) schematic of a cross-section from the structure

To allow successful MTP photonic integration using the high speed EAM, the device fabrication needs to incorporate necessary changes for making transfer printing compatible without sacrificing the device performance. In a current state-of-the-art MTP device integration process as indicated in Fig 2(a), the III-V source wafer and silicon photonics target wafer are processed separately before the transfer [5]. Device coupons on a source wafer are released beforehand and can be individually inspected and tested prior to the integration. On an InP based source wafer, the releasing of coupons involves a chemical selective undercut processing of usually an InGaAs layer using $\text{FeCl}_3:\text{H}_2\text{O}$ (1:2) solution [8]. Once the release is completed, the coupons are ready to be transfer-printed. The entire transfer print cycle is summarized as steps shown in Fig 2(b) below [4].

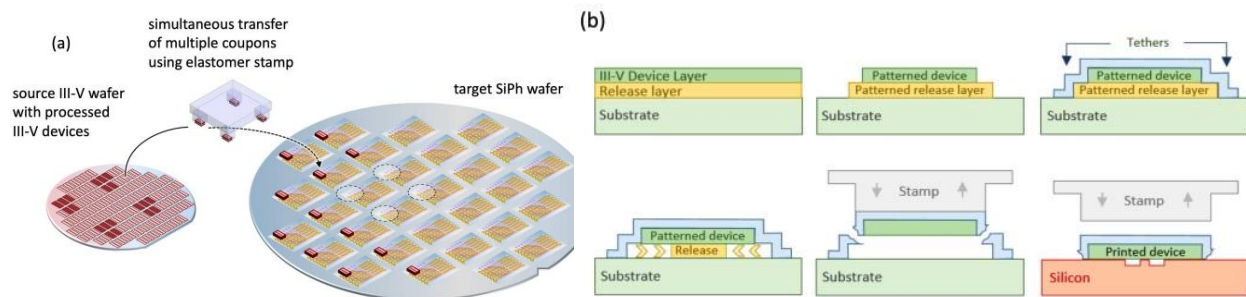


Fig. 2. (a) Schematic of a MTP integration process between III-V source and SiPh target and (b) schematic of MTP process steps

In order to make sure the speed from a heterogeneous integrated high speed EAM via MTP works on par with a monolithically optimized and fabricated device, the parasitic capacitance of the transfer printed EAM also has to be minimized, namely keeping the overall influence of the potential extra parasitic capacitance generated from MTP processing as small as possible. In the next section, different sources of parasitic capacitance are identified in the equivalent circuit model of the high speed EAM, and the solution of using an iron doped layer to minimize the MTP influence will be explained and presented via simulation and details based on experimental results.

Equivalent Circuit Model Analysis

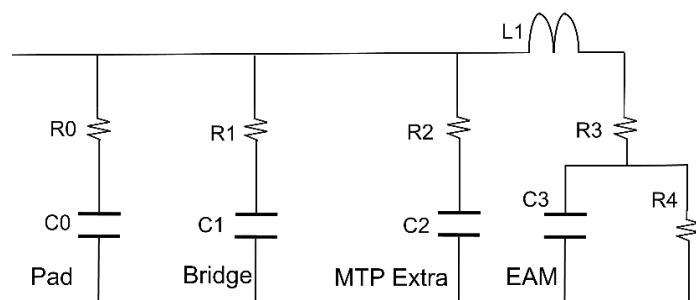


Fig. 3. Equivalent circuit of a high speed EAM device with MTP processing

The equivalent circuit model in Fig 3 is extracted based on the structure of the EAM as indicated by Fig 1. In the high speed EAM structure there are three sections which will impact the speed of the final device, namely, the big contact pad, the metal bridge connecting ridge and signal pad, and finally the EAM section itself. Based on optimized designs, each section has its minimized RC value in a lumped element configuration of the EAM, and they will determine the overall impedance of the EAM when a RF signal is fed through the GSG contacts. Previous works have been dedicated to minimizing the overall impedance of the device, and based on experimental data, the RC value of each section is for instance as indicated in Table 1 below.

	Pad		Bridge		MTP Extra		EAM		Simulation Default	
	R0	C0	R1	C1	R2	C2	R3	C3	R4	L0
No iron doping	67Ω	15fF	56Ω	9.3fF	150Ω	90fF	107Ω	14.6fF	5.7Ω	300fH
With iron doping	67Ω	15fF	56Ω	9.3fF	5000Ω	90fF	107Ω	14.6fF	5.7Ω	300fH

Table.1. Parameters in an equivalent circuit model with and without the iron doping layer

With MTP fabrication the coupon is undercut away from its intrinsic semi-insulating substrate. As a result the bonding pad can no longer be isolated from the EAM using a deep etch. Instead, the current could go through the thin n-doped layer in the epitaxy connecting the signal pad to the EAM, thus increasing the effect of the parasitic capacitance and limiting the bandwidth of the device. The iron doping layer is added to maintain a high resistivity which will help to minimize the effect of MTP added impedance to the overall device. Based on calculations, the MTP added capacitance from the signal pad is about 90fF. In the case without using an iron doped layer in the MTP EAM, as shown in Table 1 and Figure 3, the MTP added resistance R2 is 150Ω, consisted of 100Ω from the signal pad and 50Ω from coupling through the thin n-doped layer. When an iron doping layer is present, because the resistivity of the tested iron doping InP material is over $10^8 \Omega\text{cm}$, which is on average 100 times larger than the resistivity of n-doped InP, R2 will be boosted to be over 5kΩ. Using a proprietary software from our group for high-speed performance simulations, a comparison of the simulated S21 performance for transfer printed MTP with and without the iron doped layer is presented in Figure 4 below. It is evident that, without iron doping, the bandwidth of the device drops to 21.6GHz, and with an iron doped layer present, the bandwidth of the device is maintained at 45.6GHz, showing only about 1.5GHz bandwidth lost by using transfer printing.

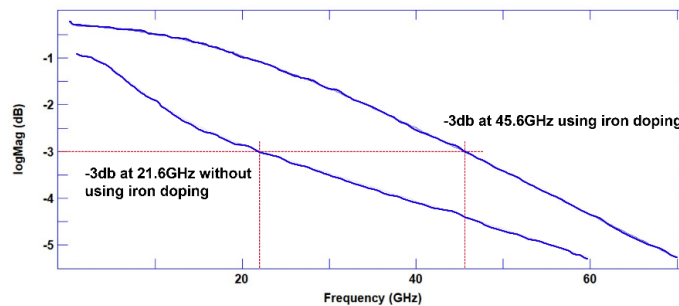


Fig. 4. Simulated S21 for MTP EAM with and without iron doping layer

Conclusion

In this paper, using an iron doped layer for transfer printed high speed EAMs is presented as a promising solution to mitigate the performance loss due to MTP processing. Simulated S21 results indicates that by adding iron doping the speed of the device could be maintained at a level over 45GHz, showcasing possibilities to achieve high speed applications for future PICs using transfer printing for photonic integration.

Acknowledgements: This research was funded by Science Foundation Ireland (SFI) through the Irish Photonic Integration Centre (IPIC) under SFI-12/RC/2276_P2. This research is also supported by ESPRC and SFI Centre for Doctoral Training in Photonic Integration and Advanced Data Storage.

References

- [1] Statista. Amount of data created., *consumed and stored 2010-2025*, by Arne Holst D. Jones, *Title of publication*, Journal name, vol. 1, no. 2, pp. 121-127, 2012
- [2] <https://optics.org/news/11/5/12>
- [3] J. Zhang *et al*, "III-V-on-Si photonic integrated circuits realized using micro-transfer-printing," *APL Photonics*, vol. 4, (11), pp. 110803-110803-10, 2019.
- [4] J. Zhang *et al*, *Transfer-printing-based integration of a III-V-on-silicon distributed feedback laser*, *Optics Express*, vol. 6, no.7, pp. 8821-8830, 2018.
- [5] B.Haq *et al*, *Micro-Transfer-Printed III-V-On-Silicon*, C-Band Semiconductor Optical Amplifiers, *Laser Photonics Review*, vol. 14, no.7, 1900364, 2020.
- [6] J. Zhang *et al*, *Silicon photonics fiber-to-the-home transceiver array based on transfer-printing-based integration of III-V photodetectors*, *Optics Express*, vol. 25, no.13, pp. 14290-14299, 2017.
- [7] J. Mulcahy *et al*, *Modulators in Silicon Photonics---Heterogenous Integration & and Beyond*, *Photonics 2022*, vol.9, no.40, 2022
- [8] J. O'Callaghan *et al*, *Comparison of InGaAs and InAlAs sacrificial layers for release of InP-based devices*, *Optical Materials Express*, vol.7, no.12, pp. 4408-4414, 2017

Monolithic integration of photonic integrated circuits with silicon photodiodes

Paper/Poster

Martino Bernard¹, Fabio Acerbi¹, Mher Ghulinyan¹

¹Sensor & Devices, Fondazione Bruno Kessler, Via Sommarive 18, Trento, 38123, Italy

* bernard@fbk.eu

We report on the monolithic integration of a photonic integrated circuit with silicon photodetectors embedded in the substrate. We characterized photodiodes as linear detectors in inverse bias regime and investigated the implementation of avalanche photodiodes as room-temperature single-photon detectors around 850nm of wavelength using the same technology.

Keywords: *Integrated Photonics, Single Photon Detectors, Optoelectronics.*

INTRODUCTION

Quantum-Photonic Integrated Circuits (Q-PICs) exploit the exceptionally low sensitivity of photons to external disturbances to realize robust quantum systems. While this resilience is particularly interesting in the perspective of room-temperature quantum systems, the main methods of detection remain either bulk off-chip photon counters or integrated cryogenic detectors, such as superconducting nanowires and edge detectors, which bind Q-PICs experiments to a cryostat.

Single Photon Avalanche Diodes (SPADs) could offer a valid integrated, room-temperature alternative for single photon detection in the near infrared region, which can be homogeneously integrated with the QPIC inside the substrate.

RESULTS

We show novel methods of PIC-detector coupling that allows for the monolithic fabrication of substrate-integrated photodiodes and a silicon nitride PIC on the same chip. With the use of an engineered wet-etching process [1], we can shape either the waveguide or the cladding below the waveguide in the vertical dimension to realize off-plane coupling.

In the first case, sketched in Fig. 1a, we shape the waveguide itself, realizing a vertical tapering down to a weakly guiding structure that leaks the light into the detector, realized in the silicon substrate as a p-n junction. The figure shows a FEM simulation of the electrical field of a Silicon Nitride waveguide that is tapered down from its single mode condition to a strongly substrate-coupled thin waveguide. Fig 1b shows an optical image of the structure during measurements. In the figure, light at 850nm of wavelength is injected from the left. The single-mode waveguide is well visible due to its consistent surface scattering, that makes the waveguide appear as bright in the image. At the centre of the image, the inverse tapering occurs, and the light leaks rapidly into the detector.

The second method instead consists into shaping the bottom cladding of the photonic layer into a basin with shallow wedge borders on top of the region of the detectors. A FEM simulation of the coupling region is shown in Fig.1c, where a silicon oxynitride single-mode waveguide follows the wedge formation of the bottom cladding. In this way, the waveguide itself is gently laid right on top of the detector, allowing for a strong waveguide-detector optical coupling. Fig. 1d shows an optical image of the structure, where the shallow wedge borders are emphasized by the formation of characteristic newton rings. Fig. 1e shows a bird-view image of the fabricated chip during characterization. On the left the input waveguide is visible. Light propagates inside the waveguide and reaches the coupling region, where the optical power is transduced into a photocurrent, which is measured at -1V bias. The characterization of these last devices, summarized in Fig. 1f, demonstrate a PIC-diode coupling with a total efficiency exceeding 40% [2].

Analogous devices were realized with p-n junction to be used in avalanche mode, as SPADs. Next, will be the first promising results concerning the coupling with SPADs paving the way for on-chip, room-temperature, single photon detection.

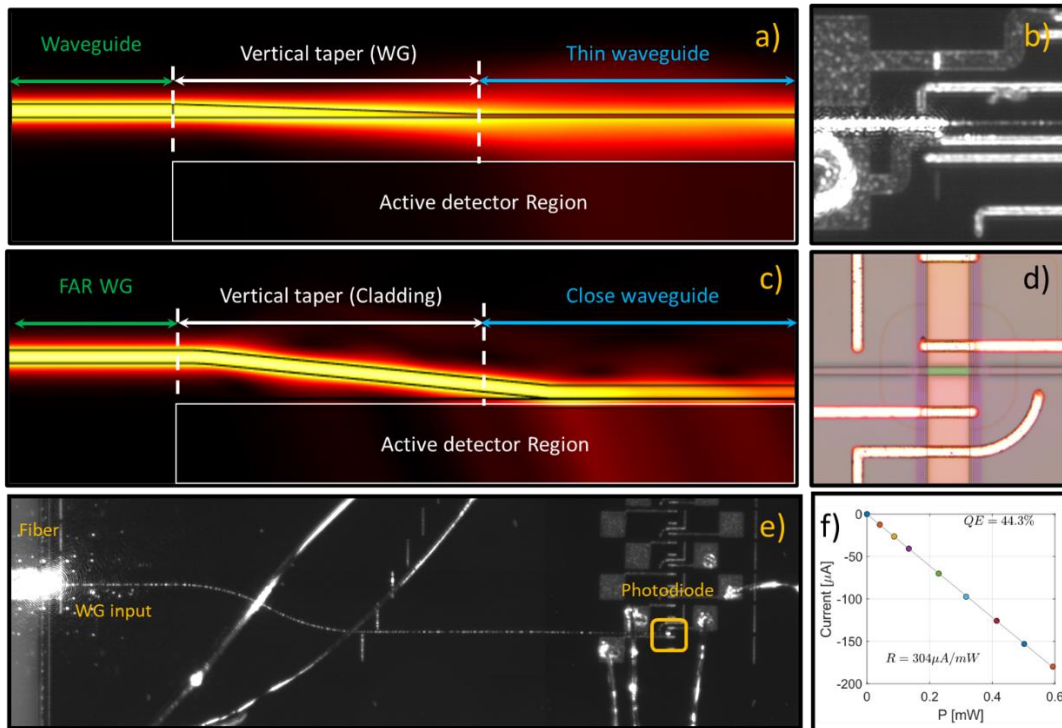


Fig. 1. (a) FEM simulation of the optical field around the vertically inverse tapered waveguide
 (b) Optical micrograph of the fabricated device during characterization, with light injected from the left.
 (c) FEM simulation of the optical field in the waveguide near the wedge-cladding coupling region
 (d) Optical micrograph of the fabricated device in the region of the waveguide-detector coupling.
 (e) Bird-view image of the device during characterization. On the left is visible the input fiber, where light is injected into the waveguide. Light travels into the waveguide to the detector region, where it is coupled to the photodiode.
 (f) Experimental characterization of the detector responsivity, which is above 44%.

Acknowledgements: we acknowledge the support of the MNF Laboratory staff of FBK during sample fabrication. We wish to thank G. Paternoster, L. Pancheri and G. Pucker for useful discussion. We acknowledge financial support from the Autonomous Province of Trento, under the initiative "Quantum at Trento - Q@TN", projects Q-PIXPAD and CoSiQuP. We also acknowledge funding from the European Union's Horizon 2020 research and innovation programme under grant agreements No 777222, ATTRACT INPEQuT and No 899368, EPIQUS.

References

- [1] M. Ghulinyan, M. Bernard R. Bartali, G. Pucker, *Formation of Mach Angle Profiles during Wet Etching of Silica and Silicon Nitride Materials*, Applied Surface Science, vol 359, pp 679-686, 2016
- [2] M. Bernard, F. Acerbi, G. Paternoster, G. Piccoli, L. Gemma, D. Brunelli, A. Gola, G. Pucker, L. Pancheri, M. Ghulinyan, *Top-down Convergence of NIR Photonics with Silicon Substrate-Integrated Electronics*, Optica, vol. 8, n0. 11, pp 1363-1367, 2021

Photonic flip-chip assembly of InP on TriPleX with laser soldering

Wenjing Tian^{1*}, Lucas Beste², Alexander Khachikyan³, Christoph Mittelstädt³, Ronald Dekker⁴, Kerstin Wörhoff⁴, Joost van Kerkhof⁵, Rui Santos¹, Kevin Williams¹ and Xaveer Leijts¹

¹The Eindhoven Hendrik Casimir Institute, Eindhoven University of Technology, 5600 MB Eindhoven, The Netherlands

²Weytronik GmbH, Im Bruch 62-64, 28844 Weyhe, Germany

³Research & Development, ficonTEC Service GmbH, Rehland 8, Achim, 28832, Germany

⁴LioniX International, Hengelosestraat 500, 7521 AN Enschede, The Netherlands

⁵PHIX Photonics Assembly, De Veldmaat 17, 7522 NM, Enschede, The Netherlands

* w.tian1@tue.nl

We present a photonic flip-chip assembly for a 4 mm × 4.6 mm InP die with 58 electrical connections on a 16 mm × 8 mm TriPleX die by using laser soldering. Two laser soldering schemes are investigated and show reliable contacts with a 6 N shear force: (1) using a laser wavelength where silicon is highly transmissive (through-silicon laser soldering) and (2) using a laser wavelength where silicon is not transmissive (heat-conduction laser soldering).

Keywords: Photonic assembly and packaging, Flip-chip bonding, laser soldering.

INTRODUCTION

Assembly and packaging for photonic integrated circuits (PICs) have been attracting considerable research interests over the years, in particular towards a combination of III-V and Si-based PICs [1]. However, many challenges remain, such as cost-efficient and high-density interconnects. In addition, current packaging for III-V on Si devices is often limited to small component levels, such as semiconductor optical amplifiers or laser diodes. Flip-chip bonding is a well-established technology in the integrated circuits (IC) industry [2] and is favorable for the assembly of die-level PICs with high-density interconnects. Unlike electronic ICs, PICs require more accurate positioning and precise power dissipation. When flip-chip bonding different materials, for example, InP on Si, the difference in thermal expansion results in significant stress when cooling down after soldering, especially for larger dies. Laser soldering is suited for flip-chip bonding of complex PICs assemblies because of non-tactile heating, highly localized thermal energy, good accessibility, and short soldering times allowing a high-throughput process [3].

In this work, we propose a photonic flip-chip assembly concept for an InP (Indium Phosphide) PIC on a TriPleX (silicon oxide-nitride)[4] carrier using passive alignment and laser soldering in an automated fashion. A self-aligned structure is utilized for multiport optical inputs and outputs [5, 6]. Two laser soldering schemes are investigated for flip-chip bonding: through-silicon laser soldering and heat conduction laser soldering. Eutectic gold-tin (AuSn with 80/20 wt-%) solder pads were used which is the state-of-the-art solder metal composition. They are widely used for fluxless flip-chip assembly in optoelectronics packaging [7]. We experimentally demonstrate a 4 mm × 4.6 mm InP die with 58 electrical pads assembled onto a 16 mm × 8 mm TriPleX die based on this concept. Results are promising and provide a high-density, reliable interconnect assembly of InP on TriPleX.

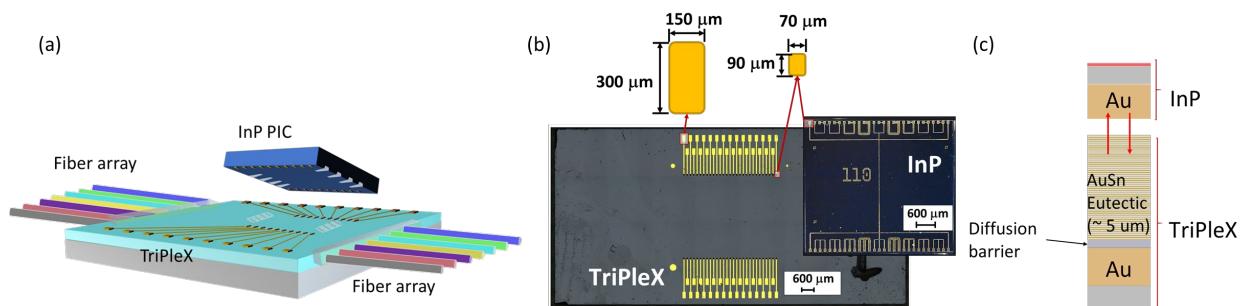


Fig. 1. Concept: (a) Schematic of a flip-chip assembled InP PIC on a TriPleX carrier that connects to fiber arrays; (b) Microscope images of TriPleX and InP test chips, the enlarged view is a schematic of a probing pad (150 μm × 300 μm) and a bonding pad (70 μm × 90 μm); (c) schematic of the metal stack of the bonding pad and solder pad.

CONCEPT

The photonic flip-chip assembly concept for an InP PIC on a TriPleX carrier is shown schematically in Fig.1 (a). Light is coupled from fiber arrays to waveguides on the TriPleX carrier, and vice versa. This is a standard technology on the TriPleX platform that is well-suited for fiber-to-chip coupling [4]. A passive self-alignment method is utilized for

coupling light from the TriPleX chip into the InP chip as reported in [5]. This self-alignment is done simultaneously and as a result of the flip-chip soldering process. This technique has been demonstrated to achieve interconnect density of 40 channels per mm and provides $\pm 2 \mu\text{m}$ alignment tolerance within 0.5 dB [6].

Electrical connections are required to drive the InP PIC. They also provide the mechanical connection between InP and TriPleX. A set of test chips are designed and fabricated to investigate the difference between the two soldering methods, as shown in Fig. 1 (b). The InP PIC is positioned and bonded onto the TriPleX carrier through subsequent laser soldering. We standardize chip layouts and interconnects using open standards [8], to use the same soldering scheme for different PIC designs. The InP chips measure $4 \text{ mm} \times 4.6 \text{ mm}$, with a thickness of $200 \mu\text{m} \pm 20 \mu\text{m}$. On the P-side of the chip, on two opposite sides, there are each 29 electrical pads (bonding pads) with a size of $70 \mu\text{m} \times 90 \mu\text{m}$ at $150 \mu\text{m}$ pitch. For the test chips, these are electrically interconnected in triplets, as can be seen in Fig. 1 (b). The TriPleX test chip measures $16 \text{ mm} \times 8 \text{ mm}$, with a thickness of $525 \mu\text{m} \pm 25 \mu\text{m}$. On the TriPleX chip, bonding pads that match the size and location of their InP-chip counterparts are arranged on the top side of the TriPleX chip. Eutectic AuSn solder, about $5 \mu\text{m}$ thick, is applied on top of each bonding pad on TriPleX during fabrication, as shown schematically in Fig.1 (c). The bonding pads of the TriPleX chip are routed to larger probing pads at the outer edges for electrical testing and driving after assembly.

TECHNOLOGY AND SETUP

Two types of laser soldering schemes were used for reflowing the eutectic AuSn solder pads, as shown schematically in Fig.2 (a, b). The eutectic AuSn-pads have a melting temperature of $278 \text{ }^\circ\text{C}$. One laser soldering scheme is through-silicon laser soldering using a 1475 nm central wavelength (CWL) laser source, the other scheme is heat-conduction laser soldering using a 975 nm CWL laser source. Regarding the first scheme, most of the laser power is transmitted through the TriPleX chip, and a smaller part is reflected or scattered, which is mostly determined by the refractive index contrasts between air, silicon, and silica and by the surface roughness. Taking the multiple reflections into account, we calculated that an average of $\sim 60\%$ of the laser power is transmitted through the TriPleX chip, which matches with experiments. As a result, the metal bonding pads directly absorb the thermal energy from the soldering laser. Notably, AuSn solder pads are heated up and melted in a laser-on-time of less than 1 ms. Due to the localized thermal energy, minimal thermal stress is inflicted on the PICs. The second soldering scheme is a standard laser soldering technique that is widely used in industrial applications [3]. Here, most of the laser power is absorbed by the TriPleX chip, and less part is reflected. Up to 70% of laser power is absorbed by the TriPleX chip. Heat is transferred from the thermal energy of the soldering laser, through the TriPleX chip, to the metal bonding interfaces. Multiple solder pads can be melted in a laser-on-time from a few hundred milliseconds to a few seconds.

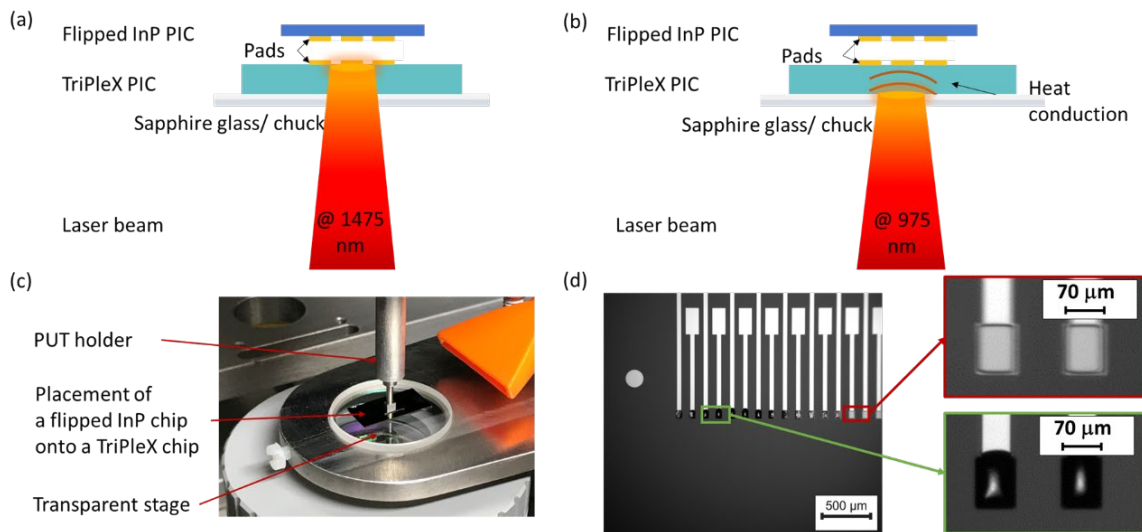


Fig. 2. Technology, setup, and assembly process: (a, b) Schematic of through-silicon laser soldering and heat conduction laser soldering; (c) Image of a flipped InP chip held by a pick-up-tool (PUT) and placed on top of the TriPleX chip on a transparent stage; (d) Microscope image of 16 bonding pads with eutectic AuSn solders on a TriPleX chip; the top enlarged view shows two bonding pads with original solders, the bottom one shows two bonding pads with reflowed solders after laser illumination.

RESULTS AND DISCUSSION

We conducted flip-chip bonding experiments for the test chips shown in Fig. 1 (b) with both types of soldering lasers. Fig. 2 (c) shows the laser-soldering-assisted assembly process based on an automated machine vision[9]. First, the TriPleX carrier is placed on a transparent sapphire glass chuck. Then, an automated pick-and-place tool

picks the flipped InP chip and moves it onto the pre-defined location of the TriPleX carrier. Fig. 2 (d) is a microscope image that shows wetted solders on the bonding pads and an alignment marker on the TriPleX carrier. This research machine integrates the two soldering laser sources to compare the two schemes. The laser beam is guided by a focusing optics system to the bottom side of the chip and melts the AuSn solder pads on the TriPleX chip, joining both chips.

As for the 1475 nm laser source, its spot diameter on the backside surface of the TriPleX chip has a size of $\sim 340 \mu\text{m}$. A pad-by-pad reflow scheme requires a laser-on-time of 0.3 ms. Regarding the 975 nm laser source, its spot diameter on the backside surface of the TriPleX chip has a size of $\sim 330 \mu\text{m}$. It sufficiently heats an area of about 1 mm at the location of solder pads in a laser-on-time of 3 s. The mechanical strength was checked by shear force testing as shown in Fig. 3. The measured shear force is $\sim 6 \text{ N}$ for both schemes, which meets the 2X MIL-STD 883 standards [10].

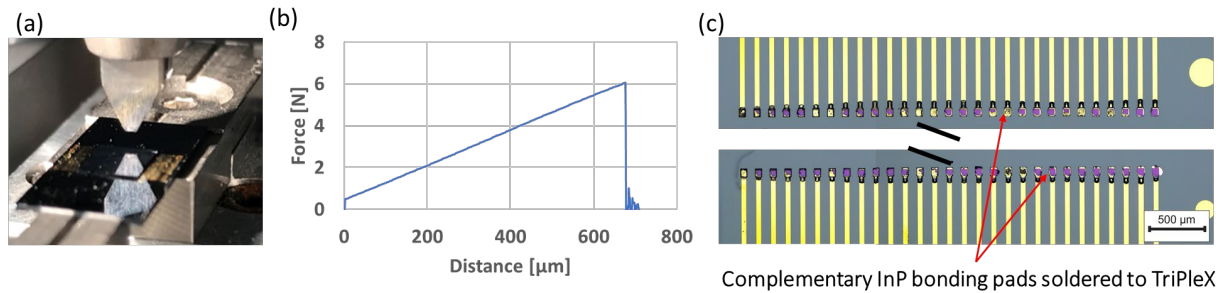


Fig. 3. Experiment results: (a). Image of an assembled InP on TriPleX chip under shear force test; (b). Shear force results; (c). Microscope image of two rows of 29 bonding pads each on TriPleX with complementary InP bonding pads after the shear test.

We presented a photonic flip-chip assembly concept for InP on TriPleX using two laser soldering schemes. The through-silicon soldering shows fast soldering time, lower power for solder reflow, and less thermal impact on PICs which is preferred over heat-conduction soldering, especially for large InP dies. These results indicate a significant step forward towards reliable photonic packaging for complex devices with high-density interconnects.

Acknowledgments: Authors acknowledge Tjibbe de Vries, Tim de Visser, and Patrick Bax for processing the InP test chips. The authors thank SMART Photonics for InP wafer thinning and polishing. This work has received funding from Eurostars through FLEXFIX project under grant agreement No. E12495.

References

- [1] L. Carroll, J.-S. Lee, C. Scarcella, K. Gradkowski, M. Duperron, H. Lu, Y. Zhao, C. Eason, P. Morrissey, M. Rensing, S. Collins, H. Hwang, and P. O'Brien, "Photonic Packaging: Transforming Silicon Photonic Integrated Circuits into Photonic Devices," *Applied Sciences*, vol. 6, no. 12, 2016.
- [2] E. Davis, W. E. Harding, R. S. Schwartz, and J. J. Corning, "Solid logic technology: versatile, high-performance microelectronics," *IBM Journal of Research and Development*, vol. 8, no. 2, pp. 102-114, 1964.
- [3] W. Horn, "Welding and Soldering with High Power Diode Lasers," 2009.
- [4] K. Wörhoff, R. G. Heideman, A. Leinse, and M. Hoekman, "TriPleX: a versatile dielectric photonic platform," *Advanced Optical Technologies*, vol. 4, no. 2, 2015.
- [5] W. Tian, K. Wörhoff, R. Dekker, A. Khachikyan, C. Mittelstädt, J. v. Kerkhof, Y. Ren, R. Santos, K. Williams, and X. J. M. Leijtens, "Self-aligned flexible waveguides for interfacing flip-chip assembled InP photonic integrated circuits on SiN," in *IEEE Benelux Chapter Annual Symposium 2021, Mons, Belgium, 2021*.
- [6] X. Leijtens, R. Santos, and K. Williams, "High Density Multi-Channel Passively Aligned Optical Probe for Testing of Photonic Integrated Circuits," *IEEE Photonics Journal*, vol. 13, no. 1, pp. 1-15, 2021.
- [7] M. Hutter, H. Oppermann, G. Engelmann, L. Dietrich, and H. Reichl, "Precise Flip Chip Assembly Using Electroplated AuSn20 and SnAg3.5 Solder," in *56th Electronic Components and Technology Conference 2006, 2006*, pp. 1087-1094.
- [8] S. Latkowski, D. Pustakhod, M. Chatzimichailidis, W. Yao, and X. J. M. Leijtens, "Open Standards for Automation of Testing of Photonic Integrated Circuits," *IEEE Journal of Selected Topics in Quantum Electronics*, vol. 25, no. 5, pp. 1-8, 2019.
- [9] "ficonTEC Service GmbH"; <https://www.ficontec.com/>.
- [10] "MIL-STD-883," <https://landandmaritimeapps.dla.mil/Downloads/MilSpec/Docs/MIL-STD-883/std883.pdf>.

Low-stress Si₃N₄ waveguides on sapphire substrate

(Student paper)

K. Wang¹, E.J.W. Berenschot², M. Dijkstra¹, R.M. Tiggelaar³, S.M. Martinussen¹, L. Chang¹, W.A.P.M. Hendriks¹, B.T.H. Borgelink², R.N. Frentrop¹, V.V. Tkachuk¹, Niels Tas², S.M. García Blanco^{1*}

¹Integrated Optical Systems, University of Twente, P.O. 217, 7550 AE, Enschede, Netherlands

²Mesoscale Chemical Systems, MESA+ Institute, University of Twente, 7500 AE Enschede, The Netherlands

³NanoLab cleanroom, MESA+ Institute, University of Twente, 7500 AE Enschede, The Netherlands

* s.m.garciablanca@utwente.nl

In this work, we present a new platform, Si₃N₄-on-sapphire, in which 1.35 μm thick Si₃N₄ layers can be deposited in a single low pressure chemical vapor deposition (LPCVD) step with very low residual tensile stress (<50 MPa). The residual stress in the deposited Si₃N₄ layers, as well as the stress gradient, were characterized by means of suspended stress diagnostic structures. Details of the design, fabrication, and characterization of the stress diagnostic structures will be presented. A thick (1.35 μm) suspended spiral waveguide was fabricated using a specially designed poly-crystalline silicon (poly-Si) sacrificial layer. No buckling of the suspended waveguide structure was observed upon removal of this sacrificial layer, further confirming the low stress of the Si₃N₄ layer.

Keywords: Thick silicon nitride, sapphire, stress, cracks

INTRODUCTION

Silicon nitride is one of the most promising materials for integrated optics due to its very low losses (less than 1 dB/m), nonlinearity, and transparency over a wide wavelength range (0.4 μm to 6.7 μm) [1], [2]. However, Si₃N₄ films deposited by low pressure chemical vapor deposition (LPCVD) on silicon substrates have a strong residual tensile stress of more than 1 GPa, which makes Si₃N₄ structures thicker than 300 nm prone to fracture [3].

In this paper, we present a new optics platform, Si₃N₄-on-sapphire, which solves the problem of high residual stress in the LPCVD Si₃N₄ layer upon deposition on silicon substrates. Various suspended stress diagnostic structures are designed and fabricated. A tensile residual stress of ~45 MPa and a stress gradient of 150 MPa/μm (in the thickness direction) in the Si₃N₄ layer are determined by means of these stress diagnostic structures. Finally, a 1.35 μm thick suspended Si₃N₄ spiral waveguide is fabricated on a sapphire substrate by a single LPCVD run over pre-patterned poly-crystalline silicon (poly-Si) film that is afterward selectively removed.

DESIGN AND FABRICATION OF SUSPENDED STRESS DIAGNOSTIC STRUCTURES

In order to study the stress in the LPCVD Si₃N₄ on sapphire layer, two types of stress diagnosis structures are designed, namely a cantilever and a strain gauge. Cantilevers and strain gauges are used to study stress gradient and stress value respectively. The cross-sectional configuration of both suspended structures are shown in Fig.1(a). The Si₃N₄ directly on the sapphire acts as an anchor, and the suspended Si₃N₄ is the functional part of the device.

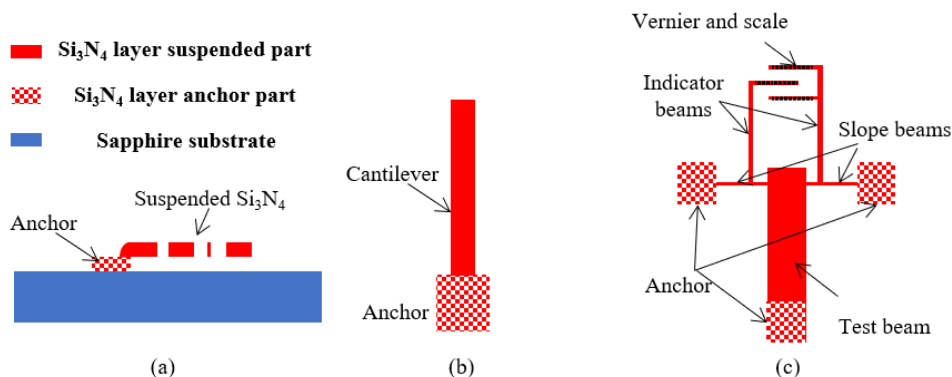


Fig. 1 (a) Cross-sectional view of the suspended stress diagnostic structure. (b) Top view of the cantilever structure. (c) Top view of the strain gauge structure.

The top view design of the cantilever is shown in Fig.1(b). After the suspended Si₃N₄ is released, a difference in stress that may exist throughout the layer thickness of the suspended Si₃N₄ film will cause the cantilever to deflect.

Cantilever beams of different lengths and widths are designed to measure the stress gradient in the Si_3N_4 suspended layer.

Strain gauges are used to measure the stress in the Si_3N_4 layer. The design of the strain gauge is shown in Fig.1(c). The wide test beam of the structure has one end connected to a fixed anchor point, and the other end suspended in the air. When the suspended Si_3N_4 is released, the test beam will be strained under the action of the residual stress of the Si_3N_4 layer. The deformation of the test beam caused by the residual stress will bend the slope beam and causes a large displacement at the tip of the indicator beam and the displacement of the tips can be read at the Vernier scale. The stress in the structural layer can be calculated through the displacement of the tip measured by the optical microscope and the derived strain gauge conversion factor.

Fig. 2 shows a schematic diagram of the fabrication process of the designed suspended stress diagnostic structures. First, $1\ \mu\text{m}$ thick poly-Si sacrificial layer is deposited on a sapphire substrate by means of LPCVD at 590°C (Fig. 2(b)). Then, using contact lithography and subsequent pattern transfer via directional reactive ion etching (RIE), this poly-Si sacrificial layer is patterned as shown in Fig. 2(c). Next, $1.35\ \mu\text{m}$ thick LPCVD Si_3N_4 is deposited on the patterned poly-Si at 800°C , followed by contact lithography and directional RIE to pattern the Si_3N_4 layer to obtain the configuration of the stress diagnostic structure. Finally, aqueous tetramethylammonium hydroxide (TMAH) wet etching is performed to release the Si_3N_4 structural layer, yielding suspended diagnostic structures (Fig. 2(f)).

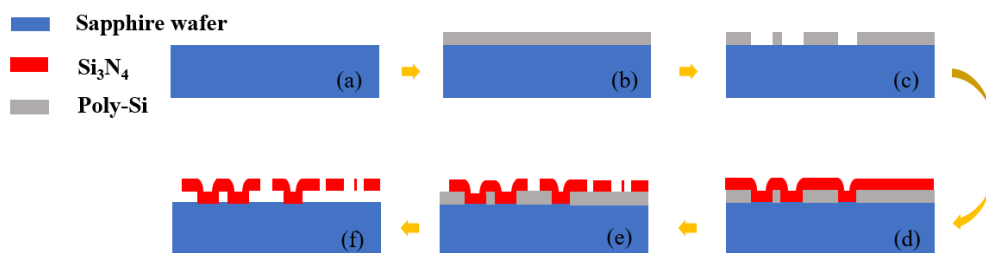


Fig. 2 Schematic diagrams of the fabrication sequence of suspended stress diagnostic structures.

Fig. 3 (a) and (c) show the fabricated cantilever and strain gauge. The brightness changes in the figure indicate that the suspended structures bends away from the sapphire substrate. In Fig 3.(b), an SEM photo shows two sets of cantilevers of different lengths. The left side of the cantilevers is anchored to the sapphire substrate, and the right side is suspended. All the cantilevers bend upwards. Fig. 3 (d) shows an SEM photo of three different sizes of strain gauges.

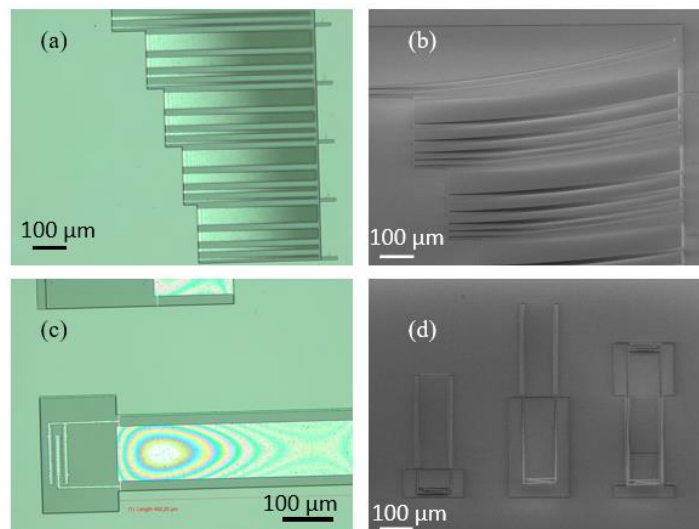


Fig. 3 (a) Optical and (b) scanning electron microscope (SEM) images of cantilevers. (c) Optical and (d) SEM images of strain gauges. The scale bar in all photos is 100 microns.

STRESS GRADIENT AND STRESS MEASUREMENT RESULTS

The deflection of the end of the cantilever beam is measured with an optical microscope, and the stress gradient is calculated subsequently. Measuring results are shown in Fig. 4. The longer the cantilever shows the smaller the stress gradient. Due to gravity, a larger torque is exerted on larger cantilevers, which offsets its deflection. By

calculating the average of the stress gradients obtained by eight sets of different cantilever beam lengths, we obtain that the stress gradient in the LPCVD Si_3N_4 layer is approximate $\sim 150 \text{ MPa}/\mu\text{m}$.

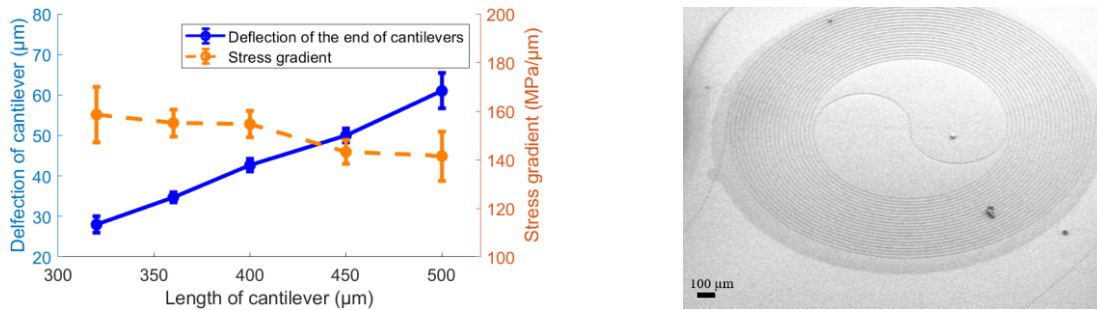


Fig. 4. (a) Measured deflection value of the end of the fabricated cantilever beams and corresponding calculated stress gradient. The error bar sizes are the standard deviation of the three sets of measurement data; (b) SEM image of the fabricated suspended $1.35 \mu\text{m}$ thick Si_3N_4 spiral waveguide on sapphire.

The deflection of the strain gauge could be read on the Vernier scale through the optical microscope. Subsequently, the stress values in the Si_3N_4 suspended layer were obtained. The measurement structures from two different wafers showed consistent measurement results, verifying the repeatability of the results of the measurement structure. The measured stress value in LPCVD Si_3N_4 is $40\sim 50 \text{ MPa}$.

SUSPENDED SPIRAL WAVEGUIDE

A suspended spiral waveguide is fabricated by means of an advanced fabrication process. A poly-Si mesa with sloped edges was utilized as a sacrificial layer to ensure an adiabatic transition from the non-suspended to the suspended waveguide structure. The fabricated suspended spiral waveguide is shown in Fig. 4(b).

CONCLUSIONS

By designing and fabricating stress diagnostic structures, we measured residual tensile stress of $\sim 45 \text{ MPa}$ in a $1.35 \mu\text{m}$ thick LPCVD Si_3N_4 layer deposited on a sapphire substrate. The measured value is approximately twenty times lower than the residual stress value of Si_3N_4 on silicon [4], which explains why Si_3N_4 layers with a thickness of $1.35 \mu\text{m}$ can be deposited by single-run LPCVD without cracking. The stress gradient normal to the Si_3N_4 surface in suspended Si_3N_4 was found to be $\sim 150 \text{ MPa}/\mu\text{m}$. The designed stress diagnostic structures can be used to study the influence of the fabrication process on stress and stress gradient in future layers. A suspended $1.35 \mu\text{m}$ thick Si_3N_4 spiral waveguide was fabricated, exhibiting no signs of buckling.

References

- [1] C. G. H. Roeloffzen, M. Hoekman, E. J. Klein, L. S. Wevers, R. B. Timens, D. Marchenko, D. Geskus, R. Dekker, A. Alippi, R. Grootjans, A. Van Rees, R. M. Oldenbeuving, J. P. Epping, R. G. Heideman, K. Worhoff, A. Leinse, D. Geuzebroek, E. Schreuder, P. W. L. Van Dijk, I. Visscher, C. Taddei, Y. Fan, C. Taballione, Y. Liu, D. Marpaung, L. Zhuang, M. Benelajla, and K. J. Boller, "Low-loss Si_3N_4 triplex optical waveguides: technology and applications overview," *IEEE J. Sel. Top. Quantum Electron.* 24, 1–21 (2018).
- [2] J. Liu, G. Huang, R.N. Wang, et al. "High-yield, wafer-scale fabrication of ultralow-loss, dispersion-engineered silicon nitride photonic circuits," *Nat Commun* 12, 2236 (2021).
- [3] A. Dutt, C. B. Poitras, K. Luke, and M. Lipson, "Overcoming Si_3N_4 film stress limitations for high quality factor ring resonators," *Opt. Express* 21, 22829–22833 (2013).
- [4] Habermehl, S. "Coefficient of Thermal Expansion and Biaxial Young's Modulus in Si-Rich Silicon Nitride Thin Films," *J. Vac. Sci. Technol. A* 36 (2), 021517 (2018).

A thick silicon photonics platform for quantum technologies

Matteo Cherchi, Arijit Bera, Antti Kemppinen, Jaani Nissilä, Kirsi Tappura, Marco Caputo, Lauri Lehtimäki, Janne Lehtinen, Joonas Govenius, Mika Prunnila, and Timo Aalto

VTT – Technical Research Centre of Finland
matteo.cherchi@vtt.fi

We have developed an ultra-low-loss silicon photonics platform that can significantly contribute to the second quantum revolution, supporting not only quantum photonics but also solid-state quantum systems. We will present two examples: the development of next generation quantum key distribution systems and the scaling-up of superconducting quantum computers using cryogenic optical transceivers.

***Keywords:** silicon photonics, quantum key distribution, quantum computers, cryogenic photonics, superconducting nanowire single photon detectors, quantum technologies*

INTRODUCTION

We are leaving in the so-called second quantum revolution, which is aiming to exploit phenomena like quantum superposition and entanglement for real-life applications. Photonic technologies are expected to have a major role, not only to implement quantum photonic circuits, but also using classical light for solid-state quantum systems. In particular, photonic integrated circuits (PICs) can support several different quantum technologies, contributing to scale up system complexity and integration density, while providing unmatched performance and stability. In this regard, our micron-scale silicon photonics platform [1] comes with unique features including low propagation losses (down to 4 dB/m demonstrated to date [2]), broadband and low-loss coupling to fibres (≈ 0.5 dB), fast (> 40 GHz) and responsive (≈ 1 A/W) integrated germanium photodetectors [3], up-reflecting mirrors for broadband and low-loss coupling to arrays of single photon detectors, tight bends [4] enabling high integration density, efficient phase shifters, low-loss Mach-Zehnder interferometers, multi-million Q ring resonators [5], polarization insensitive operation, polarization splitters and rotators, including all-silicon Faraday rotators [6]. An example of quantum photonics application is large-scale deployment of quantum key distribution (QKD) and, in particular, efficient multiplexed receivers. A second interesting case is the use of PIC technology to scale-up superconducting quantum computers, by connecting the hosting cryostat using classical optical links. In this case the main challenge is the development of suitable electrical-to-optical converters (EOC) and optical-to-electrical converters (OEC) operating at cryogenic temperatures.

NEXT GENERATION QKD

A first example application that can be enabled by the thick SOI platform is quantum key distribution (QKD) networks [7] with higher key rates and/or longer working distance. In fact, PIC solutions are in the roadmap of major QKD players [8], because of their unmatched stability, and scalability. We briefly present here how our platform could support the development and the large-scale deployment of high-performance QKD systems, both based on discrete variable (DV) and on continuous variable (CV).

In the DV-QKD implementations most suitable for long distances, the key rate scales linearly with the link transmission probability η , i.e., the probability of a transmitted photon to be detected at the receiver. This is in clear contrast with classical optical communications. Considering that longest links are operated even in excess of 70 dB loss, there is in general a large mismatch between the transmission and detection speeds. This provides a unique opportunity to combine the fastest optical modulators ever achieved with the most efficient single photon detectors demonstrated to date, namely plasmonic modulators and SNSPDs. Transmitter speeds of present QKD systems are in the order of a few GHz, meaning that plasmonic phase and amplitude modulators could be used to boost the key rate by at least two orders of magnitude, while being still well matched by SNSPDs on the receiver side. Even though high losses of plasmonic modulators, are not at all a problem for practical DV-QKD transmitters (which rely on strongly attenuated light sources), they are clearly not tolerable on the receiver side. Still, this is not a strong limitation, given that the many robust protocols for practical DV-QKD rely on “passive” receivers, that require no modulators [9–11]. The combination of plasmonic modulators and SNSPDs becomes even more attractive when considering that some of the most promising DV-QKD protocols, including measurement device independent (MDI) QKD [12] and twin-field (TF) QKD [13], connect the users through a central unit (completely untrusted) where all the photon detections occur (Fig. 1(a)). Large scale deployment of these systems can be achieved by providing all users with low-cost transmitters (achievable with plasmonic chips) while deploying a central detection unit – owned by the operator – to host a table-top closed-cycle cryostat where thousands of SNSPD can be economically cooled down and operated in parallel. In this vision, the cryostat would be connected with tens to hundreds of fibres, and each fibre should carry tens to hundreds of wavelength division multiplexed

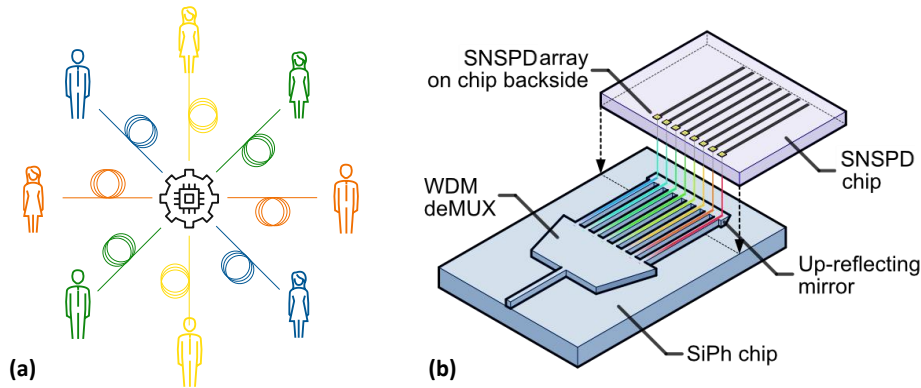


Fig. 1 (a) Schematic representation of QKD implementations based on a central node for photon detection; (b) 3D sketch of a SNSPD array flip-chip bonded on a low-loss demultiplexing PIC.

(WDM) signals. With this goal in mind, we are presently fabricating at VTT low loss AWGs to demultiplex the WDM signals coming from a single fibre and then couple them to flip-chip-bonded arrays of SNSPDs designed and fabricated by our partner company Single Quantum that match the PIC layout (see Fig. 1(b)).

An alternative approach is CV-QKD, relying on Gaussian states instead of single photons. The main advantage is that they require only standard telecom components [14] used for classical coherent optical communication and, in particular, there is no need for single photon detectors. The main drawback is that secure implementations scale quadratically with the transmission probability η , which limits the operation range to links with about 10 dB loss (i.e. about 50 km assuming standard 0.2 dB/km fibre loss). Furthermore, unlike DV-QKD, the receiver speed must match the transmitter speed. On the transmitter side, plasmonic modulators are again the perfect choice, given that their losses are not at all an issue, and they can easily achieve both phase and amplitude ultrafast modulation at the same time [15]. Ultrafast phase modulation would be needed also on the receiver side, but luckily on the local oscillator only and not on the quantum signals [14], meaning that some modulator losses are acceptable. Detection is typically made using shot-noise-limited balanced pulsed homodyne detectors [14], which operation speed and stability can greatly benefit from PIC integration and dedicated electronics [16]. We therefore plan to exploit the fast Ge PDs in our platform in combination with our in-house expertise in ultra-fast electronics. In our vision, the CV-QKD receiver will be monolithically integrated on our thick SOI platform, to include the ultrafast plasmonic phase modulator and the balanced photodiode. Also in this case, the PIC will ensure much better and stable control of relative phase and time jitter compared to realisations based on optical fibres, therefore leading to improved overall performance of the whole QKD system.

SCALING UP QUANTUM COMPUTERS

A second example application is the use of optical fibres to transfer data to and from superconducting quantum computers aiming to scale-up the number of qubits and achieve useful universal quantum computing. It is generally agreed that universally useful quantum computers will require about one million qubits [17]. To date, most advanced universal quantum computers are based on superconducting qubits operated at temperatures around 100 mK, and electrical transmission lines are used to carry the electrical signals driving and reading the qubits inside the cryostat. Such approach will become more and more challenging for thousands of qubits and beyond, due to the limited bandwidth, high crosstalk, and high thermal conductivity of electrical cables.

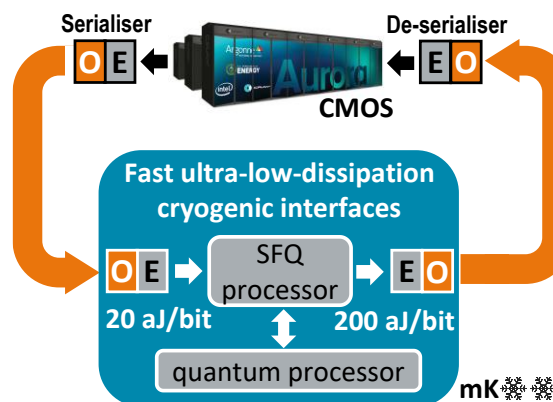


Fig. 2 Optical fibre links will help scaling up cryogenic quantum computers and interfacing them with supercomputers.

To overcome these limitations, we are pioneering the next generation of communication interfaces for cryogenic qubits, using optical fibres and suitable OECs and EOCs. We are developing this technology in parallel with the development of the Finnish quantum computer, which has recently achieved the first milestone of five qubits [18], and now targeting fifty qubits by 2024.

Our vision is summarised in Fig. 2, where a large amount of data from a supercomputer is serialised by a suitable EOC and sent through an optical fibre to a cryogenic OEC to drive a cryogenic classical co-processor based on fast and energy efficient single flux quantum (SFQ) logic [19]. After inputting the data into the quantum processor, the SFQ co-processors use the calculation output to drive a suitable cryogenic EOC that, through another optical fibre, sends the results to a de-serialising OEC communicating back to the supercomputer. As part of this vision, we are presently developing, together with our partners, several PIC solutions for different building blocks, including the serialiser and the cryogenic OEC and EOC.

Acknowledgements: We acknowledge support by the European Union's Horizon 2020 through the project [aCryComm](#), Grant Agreement N. 899558, by the Academy of Finland Flagship Programme, Photonics Research and Innovation ([PREIN](#)), decision number 320168.

References

1. T. Aalto, M. Cherchi, M. Harjanne, S. Bhat, P. Heimala, F. Sun, M. Kapulainen, T. Hassinen, and T. Vehmas, "Open-Access 3- μm SOI Waveguide Platform for Dense Photonic Integrated Circuits," *IEEE J. Sel. Top. Quantum Electron.* **25**, 1–9 (2019).
2. A. Bera, Y. Marin, M. Harjanne, M. Cherchi, and T. Aalto, "Ultra-low loss waveguide platform in silicon photonics," in (*SPIE*, 2022), Vol. 12006, pp. 12006–4.
3. T. Vehmas, M. Kapulainen, P. Heimala, G. Delrosso, F. Sun, F. Gao, and T. Aalto, "Monolithic integration of up to 40 GHz Ge photodetectors in 3 μm SOI," in *Silicon Photonics XV* (International Society for Optics and Photonics, 2020), Vol. 11285, p. 112850V.
4. M. Cherchi, S. Ylinen, M. Harjanne, M. Kapulainen, and T. Aalto, "Dramatic size reduction of waveguide bends on a micron-scale silicon photonic platform," *Opt. Express* **21**, 17814–17823 (2013).
5. B. Zhang, K. A. Qubaisi, M. Cherchi, M. Harjanne, Y. Ehrlichman, A. N. Khilo, and M. A. Popović, "Compact multi-million Q resonators and 100 MHz passband filter bank in a thick-SOI photonics platform," *Opt. Lett.* **45**, 3005–3008 (2020).
6. D. Jalas, N. Hakemi, M. Cherchi, M. Harjanne, A. Petrov, and M. Eich, "Faraday rotation in silicon waveguides," in *14th International Conference on Group IV Photonics* (IEEE, 2017), pp. 141–142.
7. E. Diamanti, H.-K. Lo, B. Qi, and Z. Yuan, "Practical challenges in quantum key distribution," *Npj Quantum Inf.* **2**, npjq201625 (2016).
8. T. K. Paraíso, I. De Marco, T. Roger, D. G. Marangon, J. F. Dynes, M. Lucamarini, Z. Yuan, and A. J. Shields, "A modulator-free quantum key distribution transmitter chip," *Npj Quantum Inf.* **5**, 1–6 (2019).
9. A. Boaron, G. Boso, D. Rusca, C. Vulliez, C. Autebert, M. Caloz, M. Perrenoud, G. Gras, F. Bussi eres, M.-J. Li, D. Nolan, A. Martin, and H. Zbinden, "Secure Quantum Key Distribution over 421 km of Optical Fiber," *Phys. Rev. Lett.* **121**, 190502 (2018).
10. D. Stucki, N. Brunner, N. Gisin, V. Scarani, and H. Zbinden, "Fast and simple one-way quantum key distribution," *Appl. Phys. Lett.* **87**, 194108 (2005).
11. A. Boaron, B. Korzh, R. Houlmann, G. Boso, D. Rusca, S. Gray, M.-J. Li, D. Nolan, A. Martin, and H. Zbinden, "Simple 2.5 GHz time-bin quantum key distribution," *Appl. Phys. Lett.* **112**, 171108 (2018).
12. L. C. Comandar, M. Lucamarini, B. Fr ohlich, J. F. Dynes, A. W. Sharpe, S. W.-B. Tam, Z. L. Yuan, R. V. Pentyl, and A. J. Shields, "Quantum key distribution without detector vulnerabilities using optically seeded lasers," *Nat. Photonics* **10**, 312–315 (2016).
13. M. Pittaluga, M. Minder, M. Lucamarini, M. Sanzaro, R. I. Woodward, M.-J. Li, Z. Yuan, and A. J. Shields, "600-km repeater-like quantum communications with dual-band stabilization," *Nat. Photonics* **15**, 530–535 (2021).
14. P. Jouguet, S. Kunz-Jacques, A. Leverrier, P. Grangier, and E. Diamanti, "Experimental demonstration of long-distance continuous-variable quantum key distribution," *Nat. Photonics* **7**, 378–381 (2013).
15. W. Heni, Y. Fedoryshyn, B. Baeuerle, A. Josten, C. B. Hoessbacher, A. Messner, C. Haffner, T. Watanabe, Y. Salamin, U. Koch, D. L. Elder, L. R. Dalton, and J. Leuthold, "Plasmonic IQ modulators with attojoule per bit electrical energy consumption," *Nat. Commun.* **10**, 1–8 (2019).
16. C. Bruynsteem, M. Vanhooeke, J. Bauwelinck, and X. Yin, "Integrated balanced homodyne photonic–electronic detector for beyond 20 GHz shot-noise-limited measurements," *Optica* **8**, 1146–1152 (2021).
17. "A Preview of Bristlecone, Google's New Quantum Processor," *Google AI Blog* (n.d.).
18. "Finland's first 5-qubit quantum computer is now operational," <https://www.vttresearch.com/en/news-and-ideas/finlands-first-5-qubit-quantum-computer-now-operational>.
19. D. S. Holmes, A. L. Ripple, and M. A. Manheimer, "Energy-Efficient Superconducting Computing—Power Budgets and Requirements," *IEEE Trans. Appl. Supercond.* **23**, 1701610–1701610 (2013).

Low Limit of Detection in Bulk Liquids Using a Fibre-Packaged Waveguide-Enhanced Raman Sensor

Jérôme Michon^{1,2,3,*}, Priscille Bonnassies¹, Derek Kita², Carlos Alonso-Ramos³, Laurent Vivien³, Juejun Hu²

¹InSpek SAS, 73 Rue Léon Bourgeois, 91120 Palaiseau, France

²Department of Materials Science and Engineering, Massachusetts Institute of Technology, 77 Massachusetts Avenue, Cambridge MA 02139, USA

³Centre de Nanosciences et de Nanotechnologies (C2N), Université Paris-Saclay, UMR CNRS 9001, 10 Boulevard Thomas Gobert, 91120 Palaiseau, France

*Corresponding author e-mail: jerome@inspek-solutions.com

We present a fibre-packaged waveguide-enhanced Raman spectroscopic sensor with an adiabatic directional coupler enabling the collection of the backscattered signal and the removal of any signal from the fibres. Its limit of detection (LoD) is the lowest reported to date for a WERS sensor without surface enhancing mechanism.

Keywords: Raman spectroscopy, chemical sensing, SiN

INTRODUCTION

Waveguide-enhanced Raman spectroscopy (WERS) has attracted significant interest as a method leveraging the performance, size, and cost benefits of integrated photonics for Raman spectroscopic sensing of chemical and biological species [1]. While all the components of a full WERS system (light source, filters, interaction region, spectrometer) may eventually be integrated on a single chip, current limitations mandate using a source and spectrometer that are off-chip. The coupling of light to and from the WERS chip is most practically done using optical fibres, which can be bonded to the chip to remove the vibration sensitivity and need for expensive alignment stages inherent to lens coupling. Fiber-coupling however requires additional components to avoid the background from the fibres, notably a coupler separating the forward- and backward-propagating signals. Our initial demonstration of fibre-coupled WERS relied on a conventional directional coupler [2].

A limitation of conventional directional couplers however lies in their small bandwidth around the optimal wavelength where they function as a 50-50 splitter, whereas a Raman spectrum typically spans over a hundred nanometers: a spectrum ranging from 500cm^{-1} to 3000cm^{-1} with a pump at 800nm corresponds to wavelengths from 840 to 1100 nm. Deviations from the 50-50 splitting ratio result in losses and thus to a degraded SNR in the spectral ranges where they occur. Lattice filters were recently demonstrated as a broadband coupler that can simultaneously filter out the pump signal, enabling fibre-coupled interrogation of the WERS chip without any contribution from the fibres [3]. These filters however suffer from a large footprint and a complex, fabrication-sensitive design. While multi-mode interferometers (MMI) offer another broadband, small-footprint, easy-to-design way of implementing the coupler required to collect the backscattered Raman signal [4], they do not act as a filter, which leads to residual pump signal propagating (and thereby generating background Raman signal) in the output waveguide and fibre. It has not been shown whether such a non-filtering coupler was sufficient to fully remove the contribution from the fibres. Here, we explore this question using adiabatic directional couplers.

RESULTS

Adiabatic directional couplers use adiabatic mode evolution to ensure broadband operation. We designed and implemented an adiabatic coupler [5] in a simple WERS circuit comprising edge couplers, the adiabatic coupler, and two spirals in a region with the cladding removed to expose the waveguides. The chips were fabricated by Lionix BV (Netherlands) on a 100 nm silicon nitride (SiN) platform and bonded to fiber arrays for easy interrogation. They were then integrated in a flow cell to allow for reliable measurements of solutions with arbitrary integration time.

The 360 μm -long adiabatic directional couplers showed a splitting ratio of $50\% \pm 10\%$ between 800 nm and 1000 nm [Fig. 1(a)], which corresponds to a difference in loss of less than 0.2 dB over the entire 200 nm wavelength range considered. To quantify the contribution of the fibres to the background of the collected Raman spectrum, spectra were acquired for varying fibre lengths and a linear regression performed to obtain the spectrum of the device with zero fiber length. As can be seen on Fig. 1(b), the contribution from 5 meters of fibre is much smaller than the contribution of the chip itself. The adiabatic coupler is therefore sufficient to remove the fibre signal.

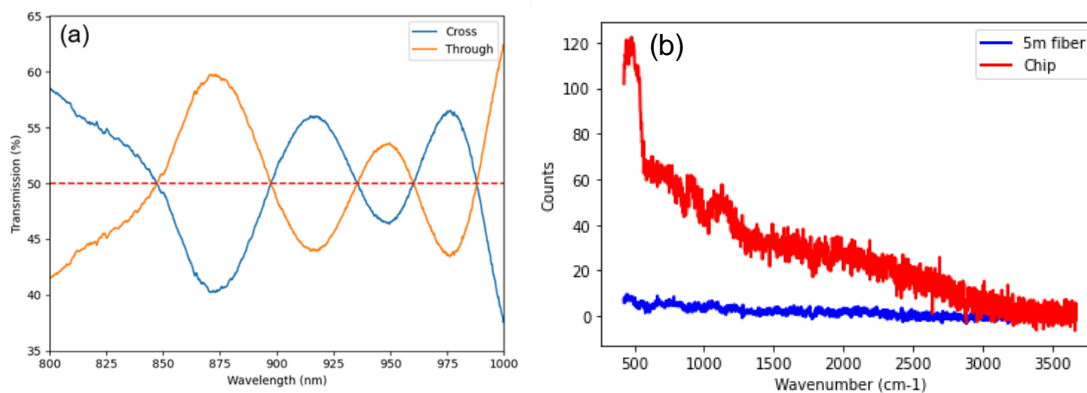


Fig. 1. (a) Measured transmission of the adiabatic coupler. (b) Measured Raman spectra with the contributions from the chip and the fibres separated by linear regression on the fibre length.

To quantify the LoD of the sensor, Raman spectra were obtained for varying concentrations of isopropyl alcohol (IPA) in water. The signal-to-noise ratio (SNR) was calculated for each spectrum by normalizing the spectrum, subtracting a reference measurement of deionized water, and applying a penalized least squares algorithm to remove the baseline [6]. We focused on the 818 cm^{-1} characteristic peak of IPA to measure and plot the SNR. We note that the treatment used to extract the noise makes no assumption about the signal, notably the positions and linewidths of the Raman peaks of the analyte. The evolution of the SNR with the concentration (Fig. 2) can then be used to determine the LoD by finding the concentration that verifies $\text{SNR} = 3$. Although the lowest concentration for which a spectrum was obtained is $0.33\text{ mol}\cdot\text{L}^{-1}$, a fit of the evolution of the SNR with concentration suggests that the sensor's LoD for IPA lies at $0.03\text{ mol}\cdot\text{L}^{-1}$ (0.2 wt% in water).

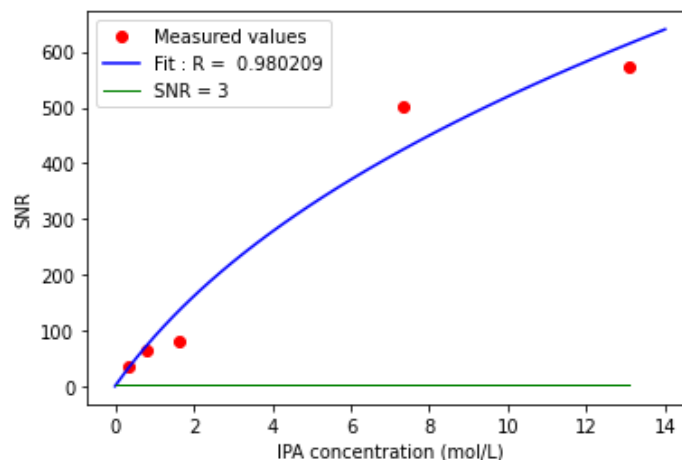


Fig. 2. SNR as a function of the IPA concentration. A fit function following the theoretical form $\text{SNR} = a \frac{c}{\sqrt{c+B}}$ with c the concentration and a, b constants, was used.

DISCUSSION

We have experimentally demonstrated that a simple 50-50 splitter such as an adiabatic directional coupler is sufficient to fully remove the fibre background from the collected backscattered Raman signal in WERS sensors. Without any further on-chip filtering, the integration of an adiabatic coupler alongside broadband edge couplers and a WERS sensing region on a fibre-coupled chip allows for chemical sensing in bulk liquids. This device exhibits the lowest LoD reported to date for a WERS sensor without surface enhancing mechanism. Such a coupler offers a small-footprint, easy-to-design alternative to lattice filters.

Acknowledgements: The authors acknowledge fabrication support from the Plateforme de Micro-Nano-Technologie/C2N, which is partially funded by the Conseil Général de l'Essonne. The chips were fabricated by Lionix BV (Netherlands) as part of a multi-project wafer (MPW) run. The authors thank Claire Poujouly and Jean Gamby for help with the microfluidic setup.

References

- [1] M. Ettabib, A. Marti, Z. Liu, B. Bowden, M. Zervas, P. Bartlett, and J. Wilkinson, "Waveguide Enhanced Raman Spectroscopy for Biosensing: A Review", *ACS Sensors*, vol. 6, pp. 2025-2045, 2021.
- [2] D. Kita, J. Michon, and J. Hu, "A packaged, fiber-coupled waveguide-enhanced Raman spectroscopic sensor," *Optics Express*, vol. 28, pp. 14 963–14 972, 2020.
- [3] N. Tyndall, T. Stievater, D. Kozak, M. Pruessner, and W. Rabinovich, "Passive photonic integration of lattice filters for waveguide-enhanced Raman spectroscopy," *Optics Express*, vol. 28, pp. 34927-34934, 2020.
- [4] K. Reynkens, S. Clemmen, A. Raza, H. Zhao, J. Peñaranda, C. Detavernier, and R. Baets, "Mitigation of photon background in nanoplasmonic all-on-chip Raman sensors," *Optics Express*, vol. 28, pp. 33564, 2020.
- [5] L. Cao, A. Elshaari, A. Aboketaf, and S. Preble, "Adiabatic couplers in SOI waveguides," in *Conference on Lasers and Electro-Optics 2010*, paper CThAA2, 2010.
- [6] J. Ye et al. "Baseline correction method based on improved asymmetrically reweighted penalized least squares for Raman spectrum", *Applied Optics*, vol. 59, pp. 10933-10943, 2020.

Wideband and large optical throughput Fourier-transform spectrometer implemented on a silicon nitride chip

David González-Andrade^{1,*}, Thi Thuy Duong Dinh¹, Sylvain Guerber^{1,2}, Nathalie Vulliet², Sébastien Cremer², Stéphane Monfray², Eric Cassan¹, Delphine Marris-Morini¹, Frédéric Boeuf², Pavel Cheben^{3,4}, Laurent Vivien¹, Aitor V. Velasco⁵ and Carlos Alonso-Ramos¹

¹Centre de Nanosciences et de Nanotechnologies, CNRS, Université Paris-Saclay, 10 Bd. Thomas Gobert, Palaiseau, 91120, France

²STMicroelectronics SAS, 850 rue Jean Monnet, Crolles, 38920, France

³National Research Council Canada, 1200 Montreal Road, Bldg. M50, Ottawa, Ontario K1A 0R6, Canada

⁴Center for Research in Photonics, University of Ottawa, 25 Templeton St., Ottawa, Ontario K1N 6N5, Canada

⁵Instituto de Óptica Daza de Valdés, Consejo Superior de Investigaciones Científicas (CSIC), 121 Serrano St., Madrid, 28006, Spain

* david.gonzalez-andrade@c2n.upsaclay.fr

On-chip spectrometers are important devices for applications in medical diagnostics, and atmospheric research. However, the performance of state-of-the-art on-chip spectrometers is hampered either by narrow operating bandwidths, limited optical throughput or low spectral resolution. In this work, we present a wideband silicon nitride spectrometer with a wide-area multiaperture input which substantially increases the optical throughput.

Keywords: *silicon photonics, silicon nitride, spatial heterodyne, Fourier-transform spectrometer, wideband, optical throughput, étendue*

INTRODUCTION

The presence and concentration of different substances in a sample can be determined by analyzing the interaction of electromagnetic fields with matter. Optical spectroscopy studies the vibrational and rotational motions of the molecules when the light is emitted, scattered, or absorbed and covers the electromagnetic spectrum from 100 nm to 20 μm [1]. Optical spectrometers are typically classified into benchtop and miniaturized spectrometers. Benchtop systems are bulky but offer a high spectral resolution over a wide wavelength range, making them suitable for multi-target applications (e.g., food industry, astrophysics, and biochemical analysis). Miniaturized spectroscopic systems have been proposed with great prospects for remote sensing, *in situ* environmental monitoring and health care [2].

Silicon photonics has enabled the development of compact, robust, and high-performance optical components at low cost, showing a great potential for the implementation of miniaturized spectrometers. Different approaches have been proposed based on light dispersion, wavelength-dependent speckle patterns or light interference and reconstruction through the Fourier transform (FT). Dispersive devices comprise arrayed waveguide gratings, echelle gratings and microring resonators, among others. Although these devices yield spectral resolutions on the order of several hundreds of picometers, they are sensitive to fabrication imperfections and have a single input aperture that limits the optical throughput. Similarly, the signal-to-noise ratio in speckle-based spectrometers is limited due to their single input aperture and the losses intrinsically associated with their principle of operation, i.e., scattering, leakage, and evanescent coupling. Conversely, Fourier-transform spectrometers exploit the Jacquinot's advantage to increase the optical throughput. The key concept is to optimize the light collection at the input to implement a large area input based on multiple apertures. This input area can be enlarged by increasing the number of apertures, benefiting from wider solid angles and thus an inherently large optical throughput (i.e., the optical throughput is the product of the solid angle and the input area) A convenient architecture for on-chip implementations is the spatial heterodyne Fourier-transform (SHFT) spectrometer, which employs an array of Mach-Zehnder interferometers (MZI) with different optical path differences and obviates the need for moving or active components [3,4]. In addition, SHFT spectrometers allow for multiaperture input configurations and compensation of fabrication deviations due to independent access to each interferometer input and output [3]. However, SHFT spectrometers demonstrated to date only show narrowband operation near 1.55 μm and it is only recently that the Jacquinot's advantage was exploited in this type of spectrometers [5].

Here, we demonstrate a wideband silicon nitride (SiN) SHFT spectrometer with a wide-area multiaperture input to increase the optical throughput. Our experimental results show a high resolution of 49 pm (worst case) within the 1260–1600 nm wavelength range, while the optical throughput is increased by 13 dB compared to a single-aperture device [6].

RESULTS

A three-dimensional (3D) schematic and a two-dimensional (2D) side view of the proposed multiaperture input are depicted in Fig. 1. We consider a silicon nitride film with a thickness of $T_{SiN} = 600$ nm surrounded by a SiO_2 upper cladding and a buried oxide (BOX) layer with thicknesses of $1.5 \mu m$ and $1.4 \mu m$ (T_{BOX}), respectively. The device was designed for transverse-electric (TE) polarization. The diffractive section of the input grating composes a periodic array of shallow-etched and unetched SiN segments with a period of $\Lambda = 1025$ nm, a duty cycle of $DC = a/\Lambda = 61.5\%$, and an etch depth of $T_E = 300$ nm. The design of the width (W_{GC}) and length (L_{GC}) of the original 3D structure can be treated separately because of the large difference between grating width and thickness [7]. Thus, we optimized transversal (x direction) and longitudinal (z direction) geometries to maximize the overlap between the Gaussian field with a $500 \mu m$ beam waist of the pigtailed gradient-index (GRIN) fiber collimator and the field radiated by the grating. The grating coupler comprises 16 inputs of $20 \mu m$ each. As the coupler length is determined by the grating radiation strength (i.e. the lower the grating radiation strength the longer the grating length), we exploited the low refractive index contrast of the SiN waveguides in combination with the shallow-etched geometry to substantially reduce the radiation strength and achieve a grating length of $L_{GC} = 410 \mu m$. Note that increasing the grating length reduces the angular aperture in the longitudinal direction. However, it consists of a total of 16 small grating couplers in the transversal direction, which does not reduce the angular aperture along this direction. Finally, the grating section was connected to each MZI input by means of $500\text{-}\mu m$ -long tapers (L_T).

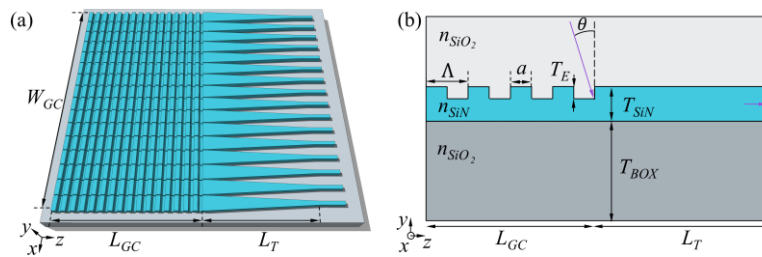


Fig. 1. Schematic representation of the wide-area multiaperture input grating coupler in (a) 3D and (b) 2D (side view).

The SHFT spectrometer comprises an array of 16 MZIs with a reference arm of constant length and a spiral arm with increasing length. A maximum length difference of 22.8 mm was implemented between the reference and spiral arms. In order to overcome the performance limitations of state-of-the-art beam splitters, we utilized ultra-wideband SiN beam splitters based on modal engineered slot waveguides. These splitters have low losses and low power imbalance within a wavelength range spanning from 1260 nm to 1680 nm [8].

The fabrication of the device was carried out using the 300 mm silicon photonics R&D platform at STMicroelectronics. Patterns were defined using 248 nm deep-ultraviolet (deep-UV) lithography and transferred to the SiN layer through a dry etching process. Finally, the SiO_2 cladding was deposited. An optical image of the fabricated SHFT spectrometer is shown in Fig. 2a, while scanning electron microscope (SEM) images of the input grating coupler, an MZI and an output grating coupler are shown in Figs. 2b, 2c, and 2d, respectively.

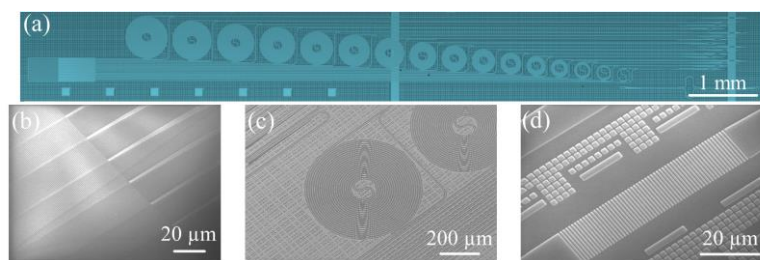


Fig. 2. Optical images of (a) the SHFT spectrometer. SEM images of (b) the input grating coupler, (c) the most unbalanced Mach-Zehnder interferometer and (d) an output grating coupler.

The device characterization was performed using a GRIN fiber collimator to illuminate the wide-area input grating coupler and a cleaved single-mode optical fiber (SMF-28) to collect the light from each MZI output. To assess the optical throughput improvement, we measured the transmittance of each MZI at 1563 nm and we normalized it with respect to the transmission of a reference structure with conventional grating couplers (see Fig. 3a). A 13 dB increase in the total collected power is achieved compared with a conventional input grating coupler (single aperture). Measurements in a total of 18 different spectral regions were also carried out within the $1260 - 1600$

nm wavelength range by adjusting the tilt angle of the GRIN collimator and the SMF-28 fiber independently. Figure 3b shows the retrieved spectrum of a monochromatic input and a doublet in three different spectral regions. The wavelength resolution, measured at full width at half maximum, is about 30 pm near 1260 nm and 50 pm near 1600 nm, while the free spectral range (FSR) varies from 260 nm to 470 nm within the same bandwidth.

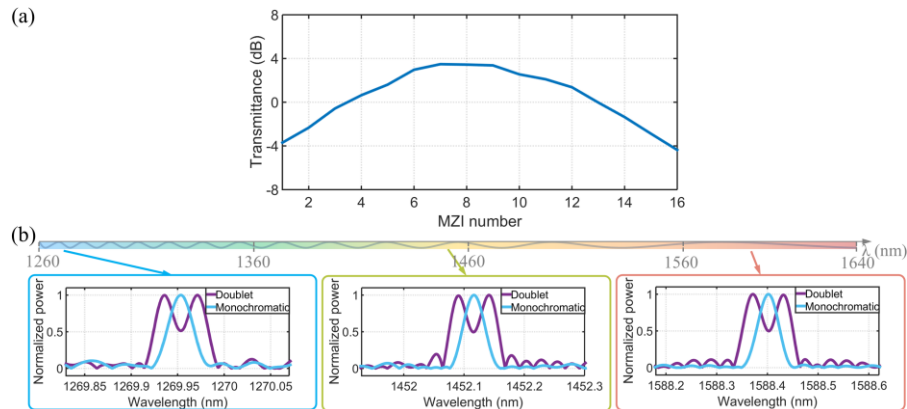


Fig. 3. (a) Transmittance of the Mach-Zehnder interferometers at 1563 nm normalized with respect to the transmission of two conventional grating couplers in back-to-back configuration. (b) Retrieved spectrum of a monochromatic input and a doublet.

DISCUSSION

In this work, we demonstrated the first wideband SHFT spectrometer with large optical throughput. The device was fabricated using 248 nm deep-UV lithography in an industrial SiN platform. It comprises an array of 16 MZI with a maximum imbalance of 22.8 mm. To achieve wideband operation, high-performance SiN beam splitters were used in each MZI. Specifically, beam splitters enabled a wide operation over a 340 nm bandwidth (1260 – 1600 nm). Furthermore, the chip input interface was designed to cover a large light collecting surface of $320 \times 410 \mu\text{m}^2$, leveraging the multiple surface grating couplers to increase the optical throughput by 13 dB compared to a single-aperture device. A worst-case spectral resolution of ~ 50 pm in a 470 nm FSR was experimentally demonstrated within the 1260 – 1600 nm wavelength range. We believe that these results open promising prospects for the development of miniaturized spectrometers aimed at multi-target applications in the near-infrared.

Acknowledgements: This work has been funded in part by the Spanish Ministry of Science and Innovation (MICINN) under grants RTI2018-097957-B-C33, PID2020-115353RA-I00 and RED2018-102768-T; and the Community of Madrid - FEDER funds (S2018/NMT-4326). This project has received funding from the Horizon 2020 Research and Innovation Program under the Marie Skłodowska-Curie grant No. 734331. This work has been partially funded by the French Industry Ministry (Nano2022 project under IPCEI program); and the Agence Nationale de la Recherche (ANR-MIRSPEC-17-CE09-0041).

References

- [1] P. Worsfold, C. Poole, A. Townshend, M. Miró, *Encyclopedia of Analytical Science*, Elsevier, 2019.
- [2] A. Zilkie, *Si photonics for wearable health sensors*, in IEEE 17th International Conference on Group IV Photonics (GFP), pp. WD2, 2021.
- [3] P. Cheben, S. Janz, M. Florjańczyk, D.-X. Xu, *Planar waveguide wavelength dispersive devices with multiple waveguide input aperture*, U.S. patent 8,351,043, 2009.
- [4] M. Florjańczyk, P. Cheben, S. Janz, A. Scott, B. Solheim, D.-X. Xu, *Multiaperture planar waveguide spectrometer formed by arrayed Mach-Zehnder interferometers*, *Opt. Express*, vol. 15, no. 26, pp. 18176-18189, 2007.
- [5] T. T. D. Dinh, D. González-Andrade, M. Montesinos-Ballester, L. Deniel, B. Szlag, X. Le Roux, E. Cassan, D. Marris-Morini, L. Vivien, P. Cheben, A. V. Velasco, C. Alonso-Ramos, *Silicon photonic on-chip spatial heterodyne Fourier transform spectrometer exploiting the Jacquinot's advantage*, *Opt. Lett.*, vol. 46, no. 6, pp. 1341-1344, 2021.
- [6] D. González-Andrade, T. T. D. Dinh, S. Guerber, N. Vulliet, S. Cremer, S. Monfray, E. Cassan, D. Marris-Morini, F. Boeuf, P. Cheben, L. Vivien, A. V. Velasco, C. Alonso-Ramos, *Broadband Fourier-transform silicon nitride spectrometer with wide-area multiaperture input*, *Opt. Lett.*, vol. 46, no. 16, pp. 4021-4024, 2021.
- [7] D. Taillaert, P. Bienstman, R. Baets, *Compact efficient broadband grating coupler for silicon-on-insulator waveguides*, *Opt. Lett.*, vol. 29, no. 23, pp. 2749-2751, 2004.
- [8] D. González-Andrade, S. Guerber, E. Durán-Valdeiglesias, D. Pérez-Galacho, X. Le Roux, N. Vulliet, S. Cremer, S. Monfray, E. Cassan, D. Marris-Morini, F. Boeuf, P. Cheben, L. Vivien, A. V. Velasco, C. Alonso-Ramos, *Ultra-wideband dual-polarization silicon nitride power splitter based on modal engineered slot waveguides*, *Opt. Lett.*, vol. 45, no. 2 pp. 527-530, 2020.

Deep-learning algorithms for resilience to fabrication imperfections in integrated Fourier-transform spectrometers

(Student paper)

Zindine Mokeddem^{1,*}, Daniele Melati¹, David González-Andrade¹, Thi Thuy Duong Dinh¹, Eric Cassan¹, Yuri Grinberg², Pavel Cheben^{2,3}, Dan-Xia Xu², Jens Schmid², Laurent Vivien¹, Delphine Marris-Morini¹, Aitor V. Velasco⁴, Carlos Alonso-Ramos¹

¹Centre de Nanosciences et de Nanotechnologies, CNRS, Université Paris-Saclay, Palaiseau 91120, France

²National Research Council Canada, 1200 Montreal Road, Bldg. M50, Ottawa, Ontario K1A 0R6, Canada

³Center for Research in Photonics, University of Ottawa, Ottawa, Ontario K1N 6N5, Canada

⁴Instituto de Óptica Daza de Valdés, Consejo Superior de Investigaciones Científicas (CSIC), Madrid 28006, Spain

*zindine.mokeddem@c2n.upsaclay.fr

Silicon photonic spectrometers have a great potential for applications in medicine, environmental monitoring and hazard detection. One of the major limitations of silicon spectrometers is their high sensitivity to fabrication imperfections and variations of environmental conditions. We exploit the ability of deep-learning algorithms to detect and classify specific patterns, even in the presence of noise, to improve the resilience of silicon Fourier-transform spectrometers.

Keywords: Miniaturized Spectrometer, Silicon Photonics, Fourier-Transform, Deep Learning

INTRODUCTION

Silicon photonic spectrometers have a great potential for applications in medicine, environmental science, astrophysics and hazard detection. Amongst other approaches such as arrayed waveguide gratings (AWGs) [2], waveguide echelle gratings [3], or cascaded micro-ring resonators [4], spatial heterodyne Fourier-transform (SHFT) architectures provide high optical throughput and increased signal to noise ratio [5]. SHFT spectrometers are generally implemented with an array of Mach-Zehnder interferometer (MZIs) with linearly increasing optical path length differences. The resulting spatial interferogram allows retrieving the input spectrum, while enabling passive calibration to correct fabrication imperfections [5]. However, temperature fluctuations during SHFT operation induce phase errors in the spatial interferogram that can severely distort the retrieved spectrum through wavelength shifts, sidelobe level increments, and other artifacts [6].

Machine learning algorithms have been proposed to substantially mitigate temperature sensitivity of silicon SHFTs, level [7]. This approach was applied to the detection of specific absorption features directly from the output interferogram of the SHFT, without the need to analytically retrieve the input spectrum. This approach yielded a 100-fold improvement of tolerances against temperature variations. However, machine learning algorithms were trained with the same SHFT chip used later for measurements, hence limiting their accuracy to the specific fabrication imperfections of the particular chip. That is, the machine learning algorithm has to be trained for each individual SHFT chip, hampering the scalability of the approach.

Here, we propose a new technique for creating a generalized deep-learning model capable of handling random and unknown fabrication imperfections, as well as variations in environmental conditions. This approach circumvents the need to re-train a model for each individual SHFT chip, opening new perspectives for large-volume realization of robust SHFT spectrometers in silicon photonics. The first results on simulated SHFT models show a detection accuracy exceeding 90 % for random unknown waveguide width variations as large as ± 20 nm.

RESULTS

As a test case for our deep learning approach, we model the silicon SHFT spectrometer reported in [7], formed by an array of 32 MZIs with linearly increasing waveguide length imbalance up to 1.13 cm. Silicon waveguides are 450 nm wide and 260 nm thick to ensure single-mode operation and minimize scattering loss. We consider transverse magnetic (TM) polarization and propagation losses of 4 dB/cm. Our model relies on electromagnetic calculations of the phase propagation constant of the waveguides and the transfer matrix of the MZIs (i.e., the 2D calibration matrix comprising output power as a function of wavelength and MZI number) while artificially inducing waveguide width and temperature variations, alignment imperfections and noise. Simulations include chromatic dispersion and the thermo-optic coefficient of silicon silicon ($dn_{Si}/dT = 1.8 \times 10^{-4} \text{ K}^{-1}$). For each simulated realization of the SHFT spectrometer, the waveguide width of each MZI is randomly set within the 430 – 470 nm range. We also multiply all the transfer matrices by a random constant K that varies randomly in the 0.8-1 range. This constant, K , models the

alignment imperfections of the input beam that may occur during experimental characterization. We also add a white Gaussian noise with $\sigma = 0.05$ to the transfer matrix.

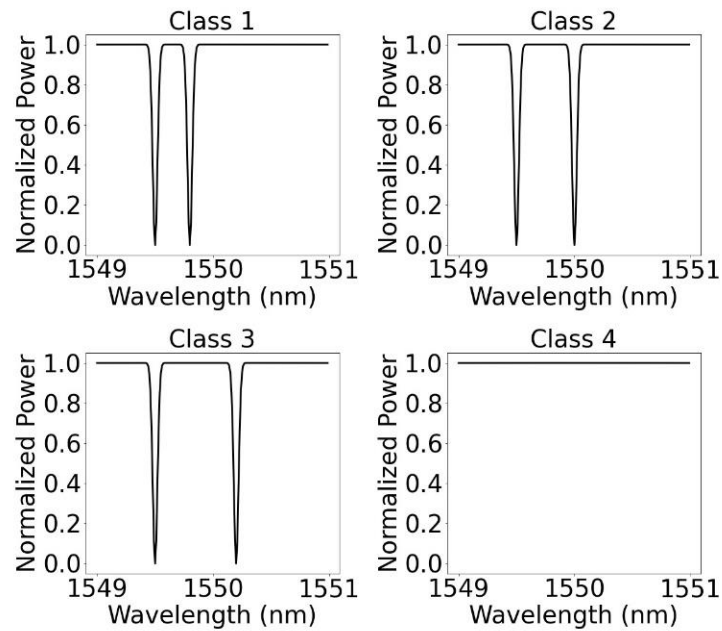


Fig. 1. Optical spectra of the four classes used for feature recognition on deep-learning algorithms

We consider a classification problem with four different classes (see Fig. 1). The first three classes have two absorption peaks with varying separations, whereas the last class presents no absorption peak. In the three first classes, there is one fixed peak at 1549.5 nm and other peaks at 1549.8 nm, 1550 nm, 1550.2 nm, respectively. This configuration with two peaks circumvents retrieval inconsistencies due to symmetry of the spectrum with respect to the Littrow wavelength. These retrieval inconsistencies can happen with wavelength shifts induced by temperature variation, which decrease the capacity of deep learning algorithm to differentiate two peaks. The fixed peak could be implemented with an optical wavelength filter in an experimental realization.

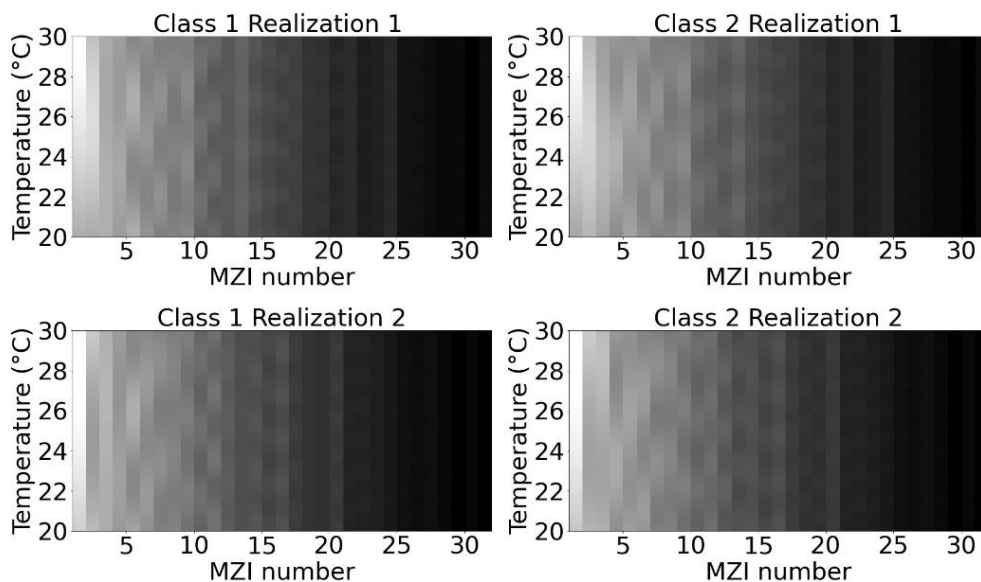


Fig. 2. Four examples of data points used for feature recognition with the deep learning algorithm. Each data point comprises a 2D matrix with the output of each MZI for a temperature variation between 20 and 30 °C, considering a single input spectrum and chip realization (i.e., a specific set of random and unknow fabrication imperfection)

For each SHFT realization, i.e., a given set of randomly distributed waveguide widths in each MZIs with alignment imperfection of the input beam and noise considered, the output interferogram is recorded as a function of the temperature. For the classification problem, each data point comprises a matrix with the output of the 32 MZI for temperature variation between 20°C and 30°C (see Fig. 2). We give no information about the temperature to the deep learning algorithm.

Recognizing the different classes from the analysis of the data matrices is a very similar problem to that solved in image recognition, leading to the decision of using convolutional neural network [8]. Our deep-learning model comprises two 3×3 convolutional layers and two dense layers with LeakyReLU as activation function. We use 2000 data points for training and 2000 data points for testing. Table 1 shows the confusion matrix for testing results. We obtain an accuracy detection of 92.6 %. These results show the potential of using deep learning algorithm for detecting specific absorption features directly on the output of the MZIs, even in presence of random and unknow fabrication imperfection.

	Class 1	Class 2	Class 3	Class 4
Class 1	456	1	52	0
Class 2	9	434	23	0
Class 3	55	4	460	2
Class 4	1	0	0	503

Tab.1. Confusion matrix

DISCUSSION

In conclusion, we proposed a new approach based on deep learning algorithms for improving the performance of integrated SHFT spectrometers against fabrication imperfections and environmental conditions. The first results on simulated data shows an accuracy detection exceeding 90%. This work opens interesting prospects for the use of artificial intelligence in integrated photonic circuits.

Acknowledgements: This work has been funded in part by the French Agence Nationale de la Recherche (ANR-MIRSPEC-17-CE09-0041), the Spanish Ministry of Science and Innovation (MICINN) under grants RTI2018-097957-B-C33, RED2018-102768-T, and PID2020-115353RA-I00, Horizon2020 (Marie Skłodowska-Curie grant No. 734331) and the Community of Madrid – FEDER funds (S2018/NMT-4326).

References

- [1] C. Burgess, P. Worsfold, C. Poole, A. Townshend, and M. Miró, Eds. Elsevier, "Optical spectroscopy: radiation sources," Encyclopedia of Analytical Science, vol. 8, pp. 103-109, 2019.
- [2] B. I. Akca and C. R. Doerr, "Interleaved silicon nitride AWG Spectrometers," IEEE Photonics Technol. Lett., vol. 31, pp. 90-93, 2019.
- [3] K. Ma, K. Chen, N. Zhu, L. Liu, and S. He, "High-resolution compact on-chip spectrometer based on an echelle grating with densely packed waveguide array," IEEE Photonics J., vol. 11, pp. 4900107, 2018.
- [4] J. Huang, J. Yang, H. Zhang, J. Zhang, W. Wu, and S. Chang, "Analysis of tunable flat-top bandpass filters based on graphene," IEEE Photonics Technol. Lett., vol. 28, pp. 2677-2680, 2016.
- [5] A. V. Velasco, P. Cheben, P. J. Bock, A. Delàge, J. H. Schmid, J. Lapointe, S. Janz, M. L. Calvo, D.-X. Xu, M. Florjanczyk, and M. Vachon, "High-resolution Fourier-transform spectrometer chip with microphotonic silicon spiral waveguides," Opt. Lett., vol. 38, pp. 706-708, 2013.
- [6] A. Herrero-Bermello, A. V. Velasco, H. Podmore, P. Cheben, J. H. Schmid, S. Janz, M. L. Calvo, D.-X. Xu, A. Scott, and P. Corredera, "Temperature dependence mitigation in stationary Fourier-transform on chip spectrometers," Opt. Lett., vol. 42, pp. 2239-2242, 2017.
- [7] A. Herrero-Bermello, J. Li, M. Khazaei, Y. Grinberg, A. V. Velasco, M. Vachon, P. Cheben, L. Stankovic, V. Stankovic, D.-X. Xu, J. H. Schmid, C. Alonso-Ramos, "On-chip Fourier-transform spectrometers and machine learning: a new route to smart photonic sensors," Opt. Lett., vol. 44, pp. 5840-5843, 2019.
- [8] Y. LeCun, P. Haffner, L. Bottou, and Y. Bengio. "Object recognition with gradient-based learning," In Shape, contour and grouping in computer vision, pp. 319-345. 1999.

On-chip silicon nitride ring resonator for background suppression in Brillouin spectroscopy

Giuseppe Antonacci^{1,*} Kareem Elsayad² and Dario Polli^{1,3}

¹Specto Srl, Via Caradosso 12, 20123 Milan, Italy

²Division of Anatomy, Center for Anatomy and Cell Biology, Medical University of Vienna, Waehringerstrasse 13, Vienna, A-1090, Austria

³Dipartimento di Fisica, Politecnico di Milano, Piazza L. da Vinci 32, 20133 Milan, Italy

*giuseppe@spectophotonics.com

Brillouin spectroscopy is an optical method to measure fundamental 3D material viscoelastic properties. The main challenge in Brillouin spectroscopy is the detection of the inelastic peaks as a consequence of the dominant elastic background light. Here, we demonstrate a silicon nitride ring resonator of ~ 10 dB extinction ratio and Q factor of $\sim 1.9 \times 10^5$ as an ultracompact notch filter to suppress the background light in Brillouin spectral measurements.

Keywords: silicon nitride, ring resonator, silicon photonics, Brillouin spectroscopy

INTRODUCTION

Characterization of the material mechanical properties is a primary task across several fields ranging from chemistry to material and life sciences. Unlike standard analytical approaches based on the application of contact forces, Brillouin spectroscopy is purely optical and provides access to 3D mechanical properties without the need of contact nor sample labelling [1]. In Brillouin spectroscopy, a narrowband monochromatic laser beam illuminates the sample and the scattered light is spectrally analyzed by a spectrometer with sub-GHz resolution. The frequency shift and the linewidth of the Brillouin spectral peaks arising from the light interaction with thermally-activated spontaneous acoustic waves of matter provide information about the individual elastic moduli that form the full material elastic tensor [2]. Combination of Brillouin spectroscopy with confocal microscopy has paved the way to a novel disruptive technology for mechanobiology and for biomedical diagnostics [1,3]. Yet, this optical method remains challenging as a consequence of the dominant elastic background light arising from both Rayleigh scattering and specular reflections. Several methods have been demonstrated in recent years in an attempt to suppress the elastic background light [4-6]. Despite a typical extinction ratio of >30 dB, these methods still rely on free-space optics that make them generally complex and expensive. Moreover, the long optical path makes these methods particularly sensitive to mechanical drifts and environmental temperature changes. To overcome these limitations, we demonstrate an ultracompact on-chip ring resonator working as a notch filter at $\lambda = 532$ nm central wavelength to attenuate the elastic background light in Brillouin spectroscopy measurements [7].

DEVICE FABRICATION

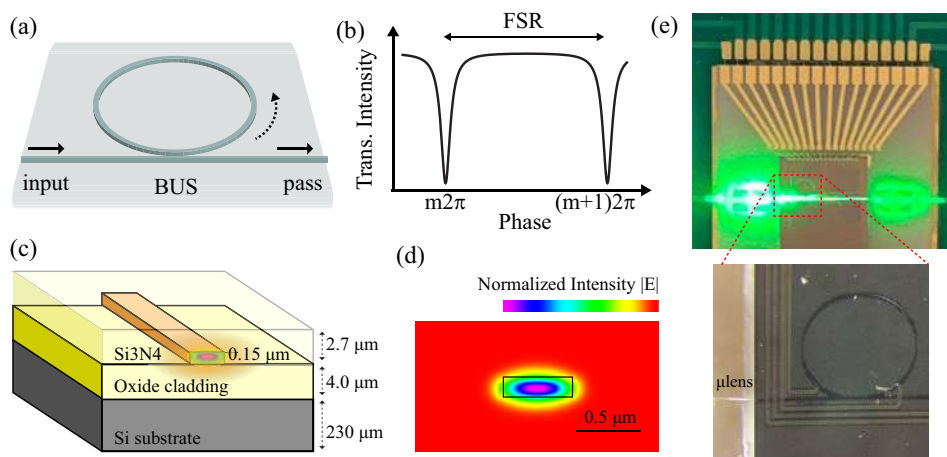


Fig. 1. All-pass ring resonator schematic (a) and transmission profile (b). Diagram of the PIC layers (c) providing a fundamental TE mode (d). The PIC was wire bonded on a PCB and optically coupled using μ -lensed fibers (e).

A standalone all-pass ring resonator (Fig. 1a) was designed to provide an almost flat transmission intensity profile with narrow resonance dips equally separated by a Free Spectral Range of $FSR = 40$ GHz (Fig. 1b). The photonic chip was fabricated in a silicon nitride platform by LPCVD process with a waveguide dimension of $600\text{ nm} \times 150\text{ nm}$ to confine the fundamental TE mode across the waveguide (Fig. 1c,d). To maximise the extinction ratio and thus the attenuation of the elastic background light, the ring was designed in an attempt to achieve critical coupling, a condition that we numerically estimated to be reached for a target ring power coupling of $k = 12.2\%$. Given the tight confinement of our propagating TE mode, the ring was designed in a racetrack configuration with a coupling length of $93.86\ \mu\text{m}$ and a gap size of 275 nm . Tuning of the ring resonance at the laser frequency was accomplished by means of a thermal phase shifter located above the ring structure. PIC packaging was performed to enable both electrical and optical coupling. To ease the electrical accessibility needed for the thermal tuning, the PIC was mounted and wire bonded on a custom printed circuit board (PCB), whose inputs and outputs were connected to a current supplier (Fig. 1e). Two μ -lensed single-mode fibers were used to compensate for the mode field diameter (MFD) mismatch between the input and output single-mode fibers in the visible range and our Si₃N₄ waveguides.

RESULTS

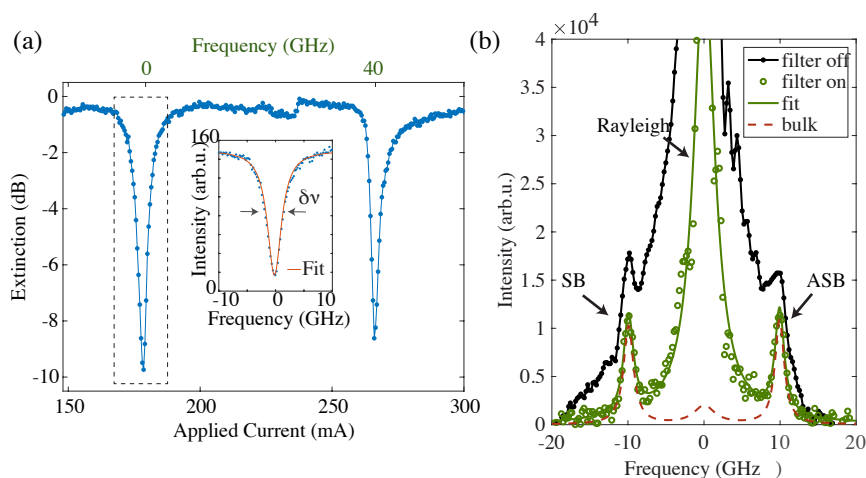


Fig. 2. Transmission intensity profile of the fabricated all-pass ring (a) with measured extinction ratio of ~ 10 dB and Q-factor of 1.9×10^5 . Brillouin spectra with the filter resonance off and at the laser frequency (b). Red dashed line shows a qualitative comparison of the spectrum achievable with conventional bulk filters.

The fabricated ring was characterized by direct coupling the light from a monochromatic single-longitudinal-mode laser (LaserQuantum Torus) working at $\lambda = 532\text{ nm}$ and tuning the input voltage applied to the phase shifter. Fig. 2a shows the transmission intensity profile of the ring obtained by detecting the light transmitted at the pass port and at each scanning phase step. From the transmission profile we measured an extinction ratio of ~ 10 dB and a linewidth of $\delta\nu = 3\text{ GHz}$, corresponding to a Q-factor of $\sim 1.9 \times 10^5$. A proof-of-concept of the capability of the integrated filter to attenuate the parasitic elastic background light was obtained in a custom Brillouin spectral system built in a 90-degree scattering geometry to avoid collection of specular reflections. The scattered light from a polystyrene sample was collected in confocal mode and delivered to the on-chip filter for background cleaning and to a single-stage VIPA spectrometer for spectral acquisition. The PIC insertion loss of 18 dB per facet obtained in the packaging process imposed a relatively long data acquisition time of 30 s with 150 mW optical power at the sample plane. Fig. 2b shows a comparison of the acquired Brillouin spectra of polystyrene with the filter off and with the resonance peak tuned at the laser frequency. By fitting the Rayleigh-attenuated spectrum, we obtained a measured Brillouin shift of $\nu_B \sim 9.9\text{ GHz}$, providing an acoustic velocity of $V = 2330\text{ m/s}$ in good agreement with expectations.

DISCUSSION

We demonstrated an ultracompact and fully integrated notch filter based on a racetrack all-pass ring resonator fabricated on a silicon nitride for visible light. While existing free-space filters for Brillouin spectroscopy provide a typically higher extinction ratio of >30 dB, our notch filter provides unprecedented robustness, dimension and ease of use. Fine tuning of the ring gap size as well as the integration of more rings in cascade can result in higher extinction ratio without compromising the system footprint. Our results demonstrate the opportunity to employ silicon photonics to develop novel integrated spectral devices for noncontact Brillouin spectroscopy.

References

- [1] Prevedel, R., Diz-Muñoz, A., Ruocco, G. and Antonacci, G., Brillouin microscopy: an emerging tool for mechanobiology. *Nature methods*, 16(10), pp.969-977, 2019.
- [2] Koski, K.J., Akhenblit, P., McKiernan, K. and Yarger, J.L., Non-invasive determination of the complete elastic moduli of spider silks. *Nature materials*, 12(3), pp.262-267, 2013.
- [3] Scarcelli, G. and Yun, S.H., Confocal Brillouin microscopy for three-dimensional mechanical imaging. *Nature photonics*, 2(1), pp.39-43, 2008.
- [4] Scarcelli, G. and Yun, S.H., Multistage VIPA etalons for high-extinction parallel Brillouin spectroscopy. *Optics express*, 19(11), pp.10913-10922, 2011.
- [5] Antonacci, G., Lepert, G., Paterson, C. and Török, P., Elastic suppression in Brillouin imaging by destructive interference. *Applied Physics Letters*, 107(6), p.061102, 2015.
- [6] Antonacci, G., De Panfilis, S., Di Domenico, G., DelRe, E. and Ruocco, G., 2016. Breaking the contrast limit in single-pass fabry-pérot spectrometers. *Physical Review Applied*, 6(5), p.054020.
- [7] Antonacci, G., Elsayad, K. and Polli, D., On-chip Brillouin notch filter on a silicon nitride ring resonator. *ACS Photonics* 2022 DOI: 10.1021/acsp Photonics.2c00005

Performance comparison of polarization rotator designs on 800 nm thick silicon nitride platform

(Student paper)

Georgios Patsamanis^{1,3*}, Dimitra Ketzaki^{2,3}, Dimitrios Chatzitheocharis^{1,3}, and Konstantinos Vyrsokinos^{1,3}

¹School of Physics, Aristotle University of Thessaloniki, A.U.Th. Campus, Thessaloniki, 54124, Greece

²Department of Informatics, Aristotle University of Thessaloniki, A.U.Th. Campus, Thessaloniki, 54124, Greece

³Center for Interdisciplinary Research and Innovation, Aristotle University of Thessaloniki, Thessaloniki, 57001, Greece

*email: gpatsama@auth.gr

This work numerically investigates two different polarization rotation concepts on the 800 nm thick Si₃N₄ platform through 3D-FDTD simulations. The explored rotation approaches rely on the mode-evolution and mode-hybridization mechanisms and the comparative study reveals a minimum polarization conversion efficiency of 90.7% and 98.2% across the entire 1500 - 1600 nm wavelength span, while the insertion losses remain below 0.1 dB for both layouts.

Keywords: Polarization rotator design, Silicon Nitride PIC, 3D-FDTD simulation method

INTRODUCTION

Photonic integrated circuits (PICs) that split or rotate polarization states are essential components of polarization diversity systems for applications in optical communications, data interconnects and quantum computing [1-3], with Si₃N₄ now gaining traction as the main choice over SOI due to lower propagation losses, the absence of nonlinearities as well as the higher fabrication yield [4]. However, polarization splitting and rotation is hard to achieve in Si₃N₄ based PICs due to the medium index contrast of the platform [5], with most layouts exploiting the mode evolution scheme for rotation, where the supported fundamental modes are twisted by the cross-sectional asymmetries of the waveguide. Even though there is plethora of such PICs recorded in the literature, there is a lack of performance comparison between well-established Polarization Rotation (PR) design approaches on Si₃N₄. Towards this direction this work presents a comprehensive numerical comparison of two photonic layouts, that include an asymmetric rib-type taper configuration that gradually converts the modes between the two polarization states based on mode evolution, and a rectangularly side-etched waveguide where the modes are hybridized by a symmetry break at the cross section of the waveguide [6-7]. The polarization conversion efficiency (PCE) is calculated with the use of three-dimensional finite-difference time-domain (3D-FDTD) electromagnetic simulations and two pure Si₃N₄ PR designs. The mode-evolution and mode-hybridization approaches feature minimum PCE values of 90.7% and 98.2%, respectively, across the 1500 - 1600 nm wavelength range, with calculated insertion losses (IL) remaining below 0.1 dB.

PRINCIPLE OF OPERATION, DESIGNS AND NUMERICAL RESULTS

The two polarization rotation mechanisms that will be investigated in this work are based on the mode evolution and mode hybridization mechanisms. The polarization rotation in a mode-evolution-based PR is induced by gradually twisting the waveguide using properly designed tapers that require two lithographic steps during fabrication. In this way, the initial polarization state of light in the transformation waveguide slowly undergoes an adiabatic 90° rotation. The length of mode-evolution-based PR devices is usually long and their main advantage is their large operation window. PRs relying on mode hybridization exhibit a break of symmetry at the cross section of the waveguide by applying a trench. This abrupt change across the waveguide enables polarization rotation through the interference between two orthogonal hybrid modes and complete conversion occurs at a length equal to the half of the beat length L_{π} of the two modes. The optical power is now exchanged between the two desired polarization states and more than one etching steps are required to realize the asymmetry.

The performance of a PR device is evaluated by calculating the PCE values for the conversion of one polarization state to the other based on the following equations:

$$PCE_{TE \rightarrow TM} = \frac{\text{Tr}(TE)}{\text{Tr}(TE) + \text{Tr}(TM)} \cdot 100\% \quad (1) \quad , \quad PCE_{TM \rightarrow TE} = \frac{\text{Tr}(TM)}{\text{Tr}(TM) + \text{Tr}(TE)} \cdot 100\% \quad (2)$$

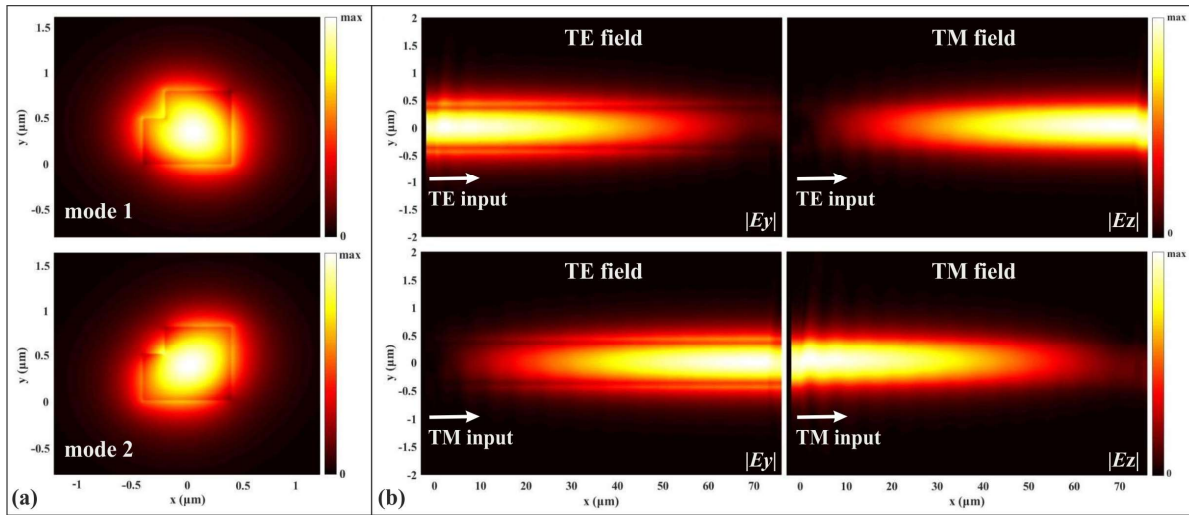


Fig. 1. a) Supported hybrid modes of an asymmetric waveguide at 1550 nm wavelength. b) Simulated electric field distributions of TE and TM polarized light across a PR device with very high PCE

where $T_r(E)$ and $T_r(M)$ are the percentages of the transmitted TE and TM polarized light, respectively, at the output port of the circuit. $PCE_{TE \rightarrow TM}$ refers to the conversion of the TE to TM light, while $PCE_{TM \rightarrow TE}$ to the conversion of TM to TE light, and their values usually have similar magnitude in PR devices.

In a mode-evolution-based rotator the asymmetry of the waveguide in the PR region gradually changes until the cross section of the waveguide becomes rectangular. As a result, two hybrid modes are supported having a varying TE / TM polarization fraction along the PR region and at a certain point their modal profiles are as the ones depicted in Fig. 1(a). On the contrary, in a mode-hybridization-based PR the cross-sectional geometry along the PR region is constant and the supported modes have a non-varying polarization fraction with modal fields as depicted in the same image Fig. 1(a). A large mode overlap between the two supported modes at the PR region enables exchange of power between them enhancing polarization rotation and therefore the PCE values. The rotation of the input modes along a PR with very high PCE is clearly depicted through the indicative simulated electric field distributions of Fig. 1(b), where the propagation of $|E_y|$ and $|E_z|$ components is presented as TE or TM polarized light is entering the device. When TE mode is launched, the E_y field is converted to E_z and TM mode is obtained, whereas the opposite is taking place where when TM mode is launched, the E_z field is converted to E_y and the TE mode is the dominant one.

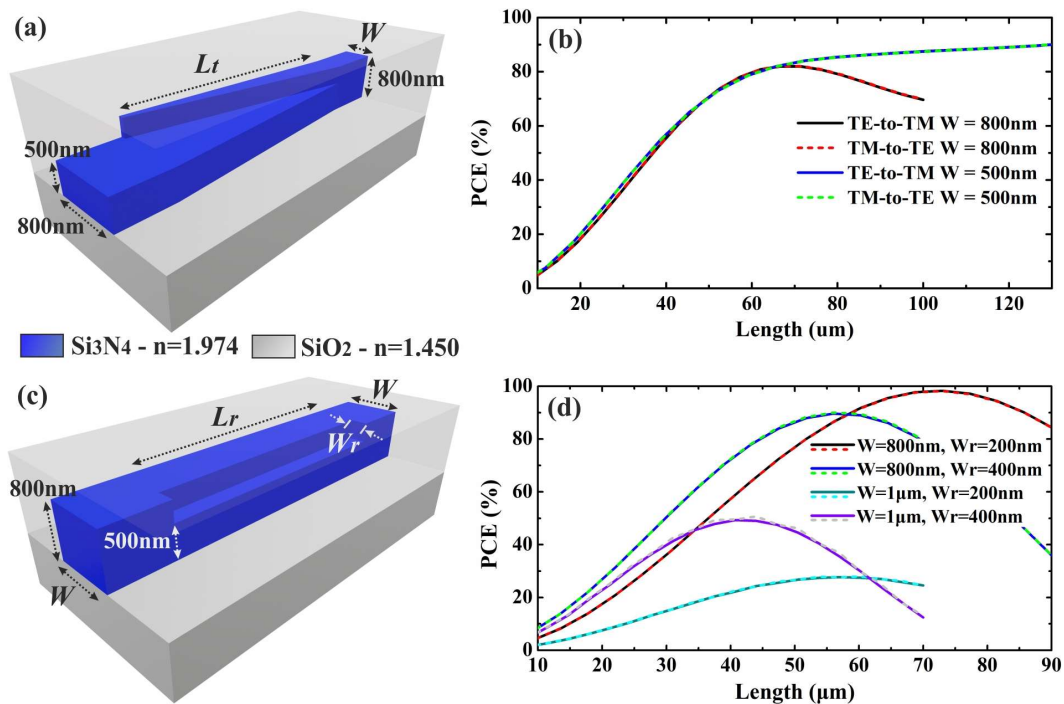


Fig. 2. a), c) 3D schematics of the two PR PIC layouts and b), d) their respective calculated PCE at 1550 nm wavelength versus the length of the polarization rotation stage

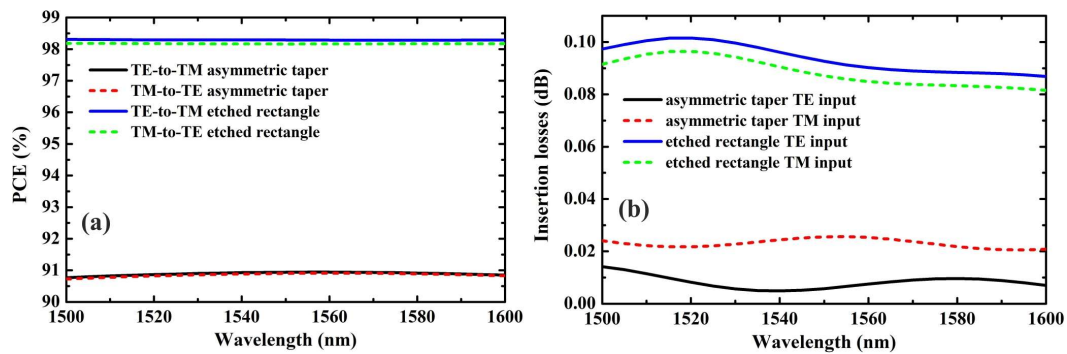


Fig. 3. a) Broadband performance of the two types of pure-SiN PR PICs and c) their corresponding insertion losses

The 3D schematics of the two investigated Si_3N_4 PR designs are shown in Fig. 2. The most well-known and explored scheme for rotation is the asymmetric rib-type taper configuration, shown in Fig. 2(a). Here the input waveguide of the structure has a 800 nm width and 500 nm thickness, the output has a width W and 800 nm thickness, while the rotation region has a length L_t and the tip of the linear taper is 100 nm wide. The refractive indices of the Si_3N_4 waveguide core and SiO_2 cladding at 1550 nm are 1.974 and 1.45, respectively. The PCE values are calculated at 1550 nm with varying L_t when W is 500 nm or 800 nm and Fig. 2(b) shows the corresponding performance curves. When $W = 800$ nm the maximum conversion achieved is 82% for $L_t = 68 \mu\text{m}$, but when $W = 500$ nm the base of the asymmetric rib taper is tapered down, the geometry of the waveguide mimics a 90° twist and the PCE progressively increases up to 91% at $L_t = 130 \mu\text{m}$. Moving on to the mode hybridization scheme, Fig 2(c) shows the PR design where a rectangular area with width W_r , length L_r and etched depth 300 nm has been removed from the side of a W wide waveguide. Four combinations with values $W = 800$ nm / $1 \mu\text{m}$ and $W_r = 200$ nm / 400 nm have been studied with varying L_r , where in each case the hybrid modes have different TE / TM polarization fractions. Figure 2(d) reveals a PCE of 98.2% for $W = 800$ nm, $W_r = 200$ nm and $L_r = 73 \mu\text{m}$, strongly indicating that the two supported hybrid modes in the PR region have TE / TM polarized fractions close to 50%. Rotation is also achievable when $W = 800$ nm and $W_r = 400$ nm with a PCE peak at 90%. On the other hand, the overlap between the two hybrid modes is very low when $W = 1 \mu\text{m}$ and therefore PCE values do not exceed 50%.

Concluding, Fig. 3 presents the broadband behavior of the Si_3N_4 designs with the highest PCE in the 1500 - 1600 nm wavelength region. As observed, the notable case of the simple mode-evolution-based PR featuring a waveguide twist of Fig. 2(a) exhibits the lowest PCE that scales between 90.7% and 91%. On the other hand, the design of Fig. 2(c) that induces polarization rotation based on orthogonal hybrid modes features the highest PCE and most solid response ranging between 98.2% and 98.3%. The calculated IL of both configuration when a TE or TM polarized mode is injected as input are shown in Fig. 3(b). The IL are below 0.03 dB for the asymmetric rib-taper-based PR and below 0.1 dB for the rectangularly etched waveguide for both input polarizations, granting the designs almost lossless properties. It is also worth to be noted that the PR performance of the devices can be further enhanced with fine tuning the cross section of the waveguides at the PR stage.

CONCLUSIONS

In this work, the concept of polarization rotation is numerically studied through 3D-FDTD electromagnetic simulations on two different rotator waveguide designs based on the 800 nm thick Si_3N_4 platform. The two layouts feature an asymmetric rib-type taper configuration and a rectangularly side-etched waveguide and achieve a minimum conversion efficiency of 90.7% and 98.2% respectively across the 1500 - 1600 nm span. The insertion losses are below 0.1 dB for both configurations in the same 100 nm region, confirming the robustness of the designs.

Acknowledgements: This work is supported by the European H2020 NEBULA (contract no. 871658) project.

References

- [1] H. Fakuda et. al., *Silicon photonic circuit with polarization diversity*, Opt. Exp., vol. 16, no. 7, pp. 4872-4880, 2008
- [2] Y. Yu et. al., *Intra-chip optical interconnection based on polarization division multiplexing photonic integrated circuit*, Opt. Exp., vol. 25, no. 23, pp. 28330-28336, 2017
- [3] A. Crespi et. al., *Integrated photonic quantum gates for polarization qubits*, Nature Communications, vol. 2, no. 566, 2011
- [4] D. J. Blumenthal et. al., *Silicon Nitride in Silicon Photonics*, Proc. of IEEE, vol. 106, no. 120, pp 2209-2231, 2018
- [5] M. R. Watts and H. A Haus, *Integrated mode-evolution-based polarization rotators*, Opt. Lett., vol 30, no. 2, 2005
- [6] A. Xie et. al., *Efficient silicon polarization rotator based on mode-hybridization in a double-stair waveguide*, Opt. Exp., vol 23, no. 4, pp. 3960-3970, 2015
- [7] A. Stroganov et. al., *Efficient Polarization Rotator for Thick-film Si_3N_4 Integrated Photonics Platform*, IPRSN, IM4A.5, 2021

Photonic chip based biosensing system with fully automatic alignment and parallel detection capability

L. Chang*, W.A.P.M. Hendriks, I. Hegeman, R.N. Frentrop, M. Dijkstra, J.P. Korterik, N.A. Schilder, H.A. Seubers and S.M. García-Blanco

Integrated Optical Systems, MESA+ Institute for Nanotechnology, University of Twente, P.O. Box 217, 7500 AE Enschede, The Netherlands

* l.chang@utwente.nl

We demonstrate a fully portable photonic chip based biosensing system. By a combination of chip design and a mechanical alignment system design, we demonstrate an affordable auto-align solution for biosensing applications.

Keywords: Optical connectivity, biosensing, invert waveguide taper

INTRODUCTION

In recent years, optical waveguide based biosensing has gained much interest. However, difficult optical alignment between the chip and the outside world has been one of the bottlenecks hindering the application of this technology outside the research lab [1]. In this study, we demonstrate a fully portable system, including chip design, input-output coupling automation, temperature control, and parallel detection. The input and output waveguides have inverted tapers with a mode size that matches the fiber mode. This largely reduces the alignment accuracy requirement and improves the coupling stability during sensing. Both input and output have been designed without any physical contact to prevent wear of optical surfaces. The system can fully automatically align the optical chips within 30 s.

OPTICAL SYSTEM DESIGN

The optical system design is shown in Fig. 1(a). We will introduce the design following the order from the chip input to the chip outputs.

The coupling between the input fiber and the chip has been designed through a lens system. This lens system re-images the fiber mode with 1:1 ratio, by using two identical aspherical lenses (Thorlabs F260APC-1064 – 1064 nm, $f = 15.43$ mm, NA = 0.16 FC/APC Fiber Collimation Pkg. and Thorlabs A260TM-B – $f = 15.29$ mm, NA = 0.16, Mounted Aspheric Lens, ARC: 650 – 1050 nm). This lens system provides ~ 14 mm working distance to the chip, which leads two key advantages in comparison with traditional end facet contact coupling. First, no wear-out of optical interfaces. This leads to significantly longer fiber lifetime. Second, no collision risk during the auto-alignment process. This leads to a simpler and faster auto-alignment procedure.

Inverted optical tapers are widely used to minimize the coupling loss between fiber and waveguide [2, 3]. The enlarged mode size in the inverted taper not only improves the coupling efficiency, but also improves the coupling stability during long sensing measurements. We design our waveguide taper by optimizing the coupling efficiency with the fiber mode, since our lens system re-images the fiber mode with 1:1 ratio. The waveguide cross section is shown in the insert of Fig. 1(b). The Al_2O_3 core thickness is 450 nm. Simulated coupling efficiency as a function of waveguide bottom width at different side wall angles θ for both TE and TM modes are shown in Fig. 1(b). Our e-beam lithography fabrication provides a side wall close to 90° , thus a waveguide bottom width of 150 nm has been chosen to achieve maximal coupling for both TE and TM modes at a wavelength of 1030 nm.

The input light is split by cascaded Y-splitters to 16 channels. In each channel, there is one microring resonator for sensing. The sensing principle is based on the resonance wavelength shift of a microring resonator when it experiences a refractive index change in its top cladding [4].

Both the Y-splitters and the chip input coupler are not 100% efficient, which results in stray light on the chip. In order to minimize the influence of the stray light, the output waveguides and the detector array are positioned 90° from the input to minimize unwanted background light. The output waveguides have the same inverted taper as the input waveguide. These enlarged modes have a smaller divergence angle compared to a normal waveguide, which allows for a larger distance ($< \sim 500$ μm) between the chip outputs and the detector array. This distance

ensures no collision risk exists during the auto-alignment process (only the chip is moving during an auto-alignment process.).

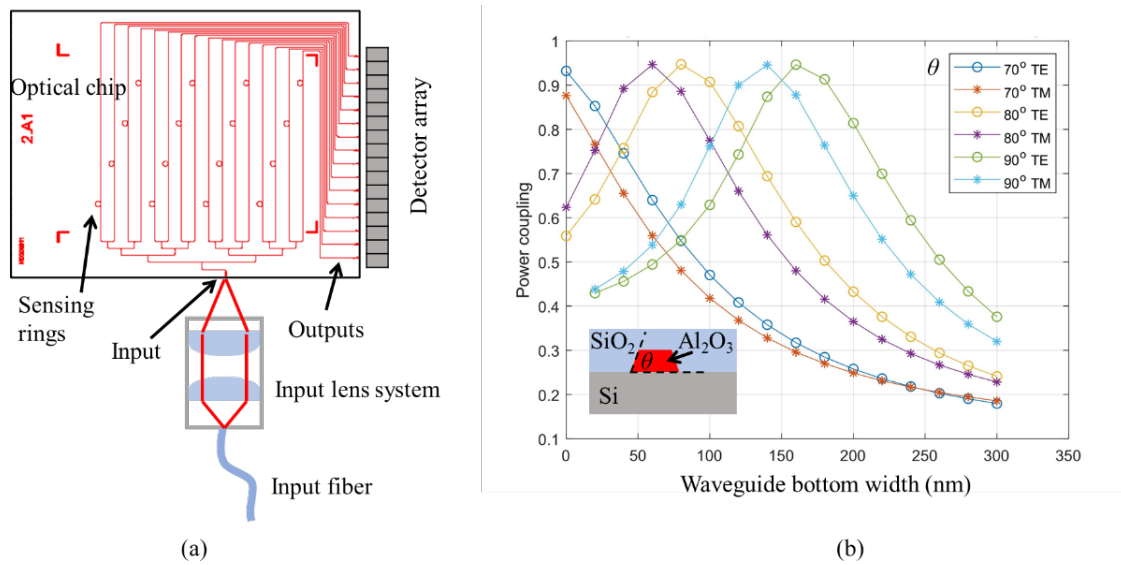


Fig. 1. (a) Optical system design. Both the input and output ports have no contact with the lens nor the detector array during the auto-alignment process. (b) Simulated input coupling efficiency.

OVERALL SYSTEM DESIGN

The full setup (except the laser source) is shown in Fig. 2 (a). It includes the alignment stages, stages control system, chip temperature control system, microfluidics system, 16 channel ADC system for signal readout, and a PC.

The alignment stages are shown in Fig. 2 (b). The input fiber, lens system, and the detector array (Hamamatsu, S4111-16Q with custom designed transimpedance amplifier array pcb) are mounted on two manual stages (Newport, MODEL: 9082-M). The manual stages are used during the first calibration alignment with the first chip. The chip is positioned in a chip holder on a 3-axis motorized stage (Thorlabs, MAX383/M - 3-Axis NanoMax Stage with custom built control system based on an Arduino Uno and 3 micro stepper drivers) for auto-alignment. The chip holder is shown in Fig. 2(c). The chip is inserted into the holder from the bottom left to the direction of the detector array. The chip holder has spring-based mechanical stops and clamps to hold the chip during sensing. At the bottom of the holder, a Peltier element with thermocouple is used for chip temperature control (custom built system using an Arduino Mega and Digilent Pmod AD5 ADC).

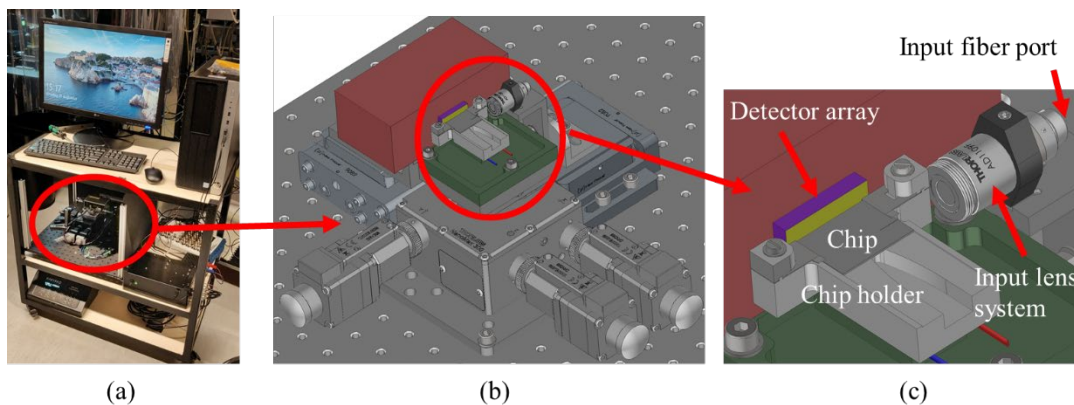


Fig. 2. (a) The full photonic chip based biosensing system is on a small trolley (except the laser source). (b) Solidworks model of the alignment stages. (c) Solidworks model around the chip area.

ALIGNMENT PROCESS

The alignment process has two main steps, namely, passive alignment and active alignment. The passive alignment consists of sliding the chip towards the mechanical stops in the chip holder. The alignment accuracy in this step is

limited by the outer dimensions of the chip, which are typically in the order of $\sim 20\text{-}30\ \mu\text{m}$. The beam waist of the input light is $\sim 5.5\ \mu\text{m}$, which is much smaller than the passive alignment error. This means normally a 2D scan is needed for the active alignment. However, a 2D scan is time consuming. Our approach is defocusing the input fiber to increase the spot size of the fiber on the end facet of the chip. This allows for more tolerant (albeit less efficient) coupling, thereby ensuring that a position where some light is coupled into the chips is always found. This limits the number of scans to 6 or 3 linear scans as shown in Fig. 3.

Prior to the scans, the chip is moved $300\ \mu\text{m}$ in the negative y direction to defocus the input light. This distance ensures the beam size on the chip facet is bigger than the typical passive alignment error mentioned above. Scan 1 (x), and 2 (z) are in the directions perpendicular to the input light propagation direction. The stage will move to the position of maximum intensity after the scan. The FWHM in these scans is significantly larger than the beam waist due to the defocused light. Scan 3 (y), is along the light propagation direction to find the focus. In principle, this should bring the chip to the best aligned position. However, in practice, we notice some angle between the y axis and the light propagation direction in our setup. Thus, we must repeat the three scans in a smaller range to reach the best coupling position. Scans 4 to 6 may be eliminated in the future with a better alignment between the stage y axis and the input light propagation direction.

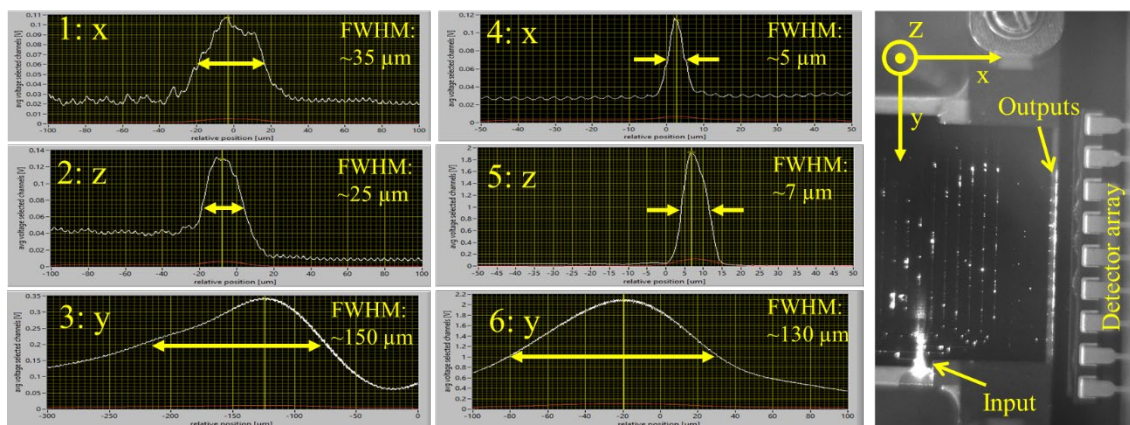


Fig. 3. The active alignment scans and a microscope image of the aligned chip. The y axis of the scans is the average readout from all 16 channels.

CONCLUSIONS AND OUTLOOKS

In this study, we have demonstrated a system capable of performing optical waveguide based biosensing outside a lab environment. The fully automatic alignment process is repeatable, reliable and can easily be used with minimal training. The alignment speed of the system could be further improved by optimizing the driving software and reducing the angle error between the stage y axis and the input light propagation direction. A cartridge could be introduced to prevent the user to work directly with the bare chip.

References

- [1] M. C. Estevez, M. Alvarez, and L. M. Lechuga, "Integrated optical devices for lab-on-a-chip biosensing applications," *LASER PHOTONICS REV*, vol. 6, no. 4, pp. 463-487, 2012.
- [2] J. Fernández, R. Baños, D. Doménech, C. Domínguez, and P. Muñoz, "Low-loss inverted taper edge coupler in silicon nitride," *IET Optoelectronics*, vol. 13, no. 2, pp. 62-66, 2019.
- [3] V. Nguyen *et al.*, "Silicon-based highly-efficient fiber-to-waveguide coupler for high index contrast systems," *Appl. Phys. Lett.*, vol. 88, no. 8, p. 081112, 2006.
- [4] M. de Goede *et al.*, "Al₂O₃ microring resonators for the detection of a cancer biomarker in undiluted urine," *Opt. Express*, vol. 27, no. 13, pp. 18508-18521, 2019/06/24 2019.

Integrated optical readout layer for ultrafast real-time delay reservoir computing

(Student paper)

Tigers Jonuzi^{1,2}, Mirko Goldmann², Apostolos Argyris², Ingo Fischer², Miguel C. Soriano² and David Doménech¹

¹VLC Photonics S.L., c/ Camino de Vera s/n -46022, Valencia, Spain

²Instituto de Física Interdisciplinar y Sistemas Complejos, IFISC (UIB-CSIC), Campus Universitat de les Illes Balears, Palma de Mallorca, E-07122, Spain

* tigers.jonuzi@vlcphotonics.com

Delay-based Photonic reservoir computing schemes offer fast, efficient and well performing options to implement machine learning techniques into hardware. So far, most of these time-multiplexing implementations still rely on electronics for digital post-processing of the output signal. We propose the implementation of an integrated all-optical readout layer for time-multiplexed reservoir computing. Our scheme promotes the potential of such all-optical systems for neuromorphic processors at GHz range and beyond.

Keywords: Reservoir computing, Readout layer, Machine learning, Neuromorphic computing

INTRODUCTION

Analog machine learning implementations offer promising opportunities to overcome the limitations of conventional computing. Therefore, an increasing amount of research has been directed to combine brain-inspired concepts with the advantages that computing with light offers. Photonic integration represents one of the biggest challenges towards wider applications. Reservoir computing (RC) [1] is one of the most promising schemes for hardware implementations. RC represents a conceptually simple, yet powerful method to train recurrent neural networks that do not require an optimization of the links between the input and the networks, and, among the network nodes'. This simplification allows reducing hardware complexity drastically and focusing on the optimization of only the output weights. RC is a method suitable for processing sequential data and there exist multiple electronic and photonic implementations that demonstrate excellence performance for time series prediction tasks. So far, in most of these hardware implementations, the output information is digitally post-processed, saving the output and applying the weighting and sum needed for RC offline, losing the fast real-time analog optical computation capabilities. Here, we propose an integrated readout layer for a photonic implementation of RC, which will be able to apply the weights and the summation in the optical analog domain and will allow for low latency and ultrafast real-time processing. We target the design of a readout layer suitable for delay-based reservoir computers. Delay-based reservoir computing is based on a single hardware node and a feedback delay loop [2]. The scheme and the steps of its functional operation are depicted in Fig. 1 and described in the following paragraph.

Firstly, in step 0, we use double modulation to create a different representation of each input by applying a random mask, $m(t)$, repeated for every value of the input $s(t)$. In step 1, we can appreciate the different states of the network's nodes over time, $x_i(t)$, with i denoting the different (virtual) nodes. The virtual nodes are separated by a time step ϑ , corresponding to an input period $T = N \cdot \vartheta$, with N being the total number of nodes. In step 2, we apply the weights to each node, e.g. by an amplitude modulation. Ultimately, in step 3, we apply an appropriate specific delay to each temporal node, in order to couple all the network nodes' relative to the same input k .

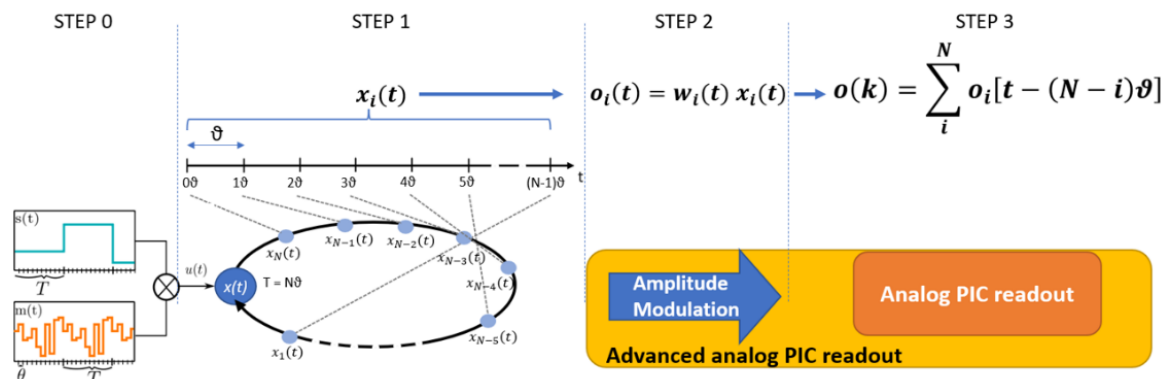


Fig. 1 Fundamental scheme of a delay-based reservoir network. Step 0) the input pre-processing. Step 1) The operation of the reservoir. Step 2) The output weights with an amplitude modulation. Step 3) Summation of the network nodes' contribution.

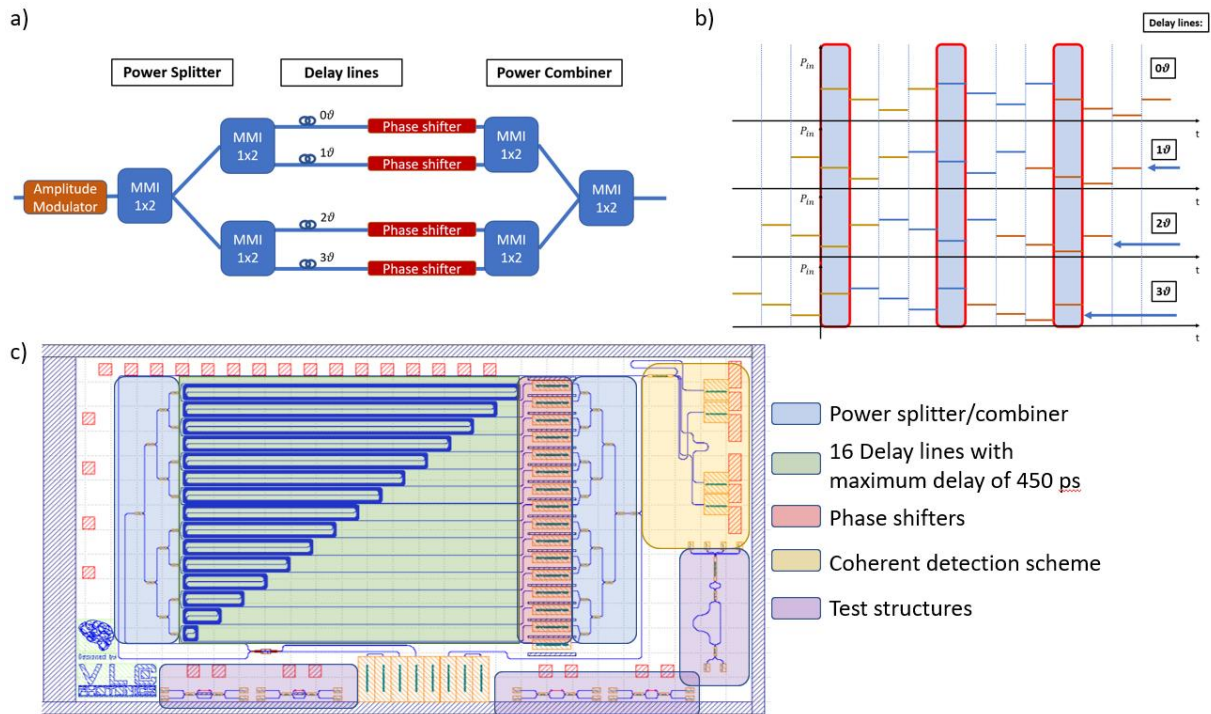


Fig. 2: a) Simplified scheme of the integrated optical readout layer. b) Optical signal flow of three inputs (orange, blue and yellow) over each branch after the delay line stage. We define a time slot (blue background) that correspond to the superposition of the virtual nodes. c) The real design of the 16 nodes integrated optical readout layer.

INTEGRATED CIRCUIT AND SYSTEM

Photonic integrated neural networks promise ultrahigh bandwidth, low power consumption and the inherent parallelism of light computation. Different schemes of integrated time-delay reservoir computing have been demonstrated, exploiting numerically the internal dynamics of micro-ring resonators [3] or experimentally a semiconductor laser, both, with and without an external feedback loop [4]. However, all these implementations require a digital post-processing of the output signal. Integrated photonics has reached a maturity level where different passive component can be designed to address the functionalities required by the machine learning techniques. In Fig. 2(a) we depict a simplified scheme of the building blocks required to perform, in real time, the operation of weighting and sum of the output signal for a delay-based reservoir (4 virtual nodes). The optical analog readout is composed of an amplitude modulator, used to apply the trained optical weight, a cascaded stage of multimode interferometer (MMI), utilized as splitting and combining stage, and delay lines to combine in time the delayed virtual nodes. In addition, phase shifters have been introduced for both matching the phase of the incoming signal for coherent summation in the combining stage and/or applying the weights in the phase domain. In Fig. 2(b) we are zooming into the optical signal after the delay lines of the scheme proposed in Fig. 2(a). The output signal is split in the various branches characterized by a delay line given by multiples of ϑ resulting in a temporal superposition of the various nodes in the time slot highlighted in blue. In Fig. 2(c) we show the designed integrated optical readout circuit optimized for combining 16 virtual nodes with a time separation $\vartheta = 30$ ps. In this first implementation, the optical weight will be applied with an external amplitude modulator at an operating frequency $f = 1/\vartheta \approx 33$ GHz, thus, supporting an input data rate of around 2 Gbit/s. The optical weighted signal is, then, injected in the circuit through edge couplers. A cascaded stage of 1x2 MMIs will split the signal in the delay line branches which will delay the various paths by multiples of 30 ps. Afterwards, phase shifters have been introduced to phase match the various tracks before entering in the optical combining stage of cascaded MMIs. Phase matching is an important condition to respect in case we deal with coherent input sources. However, the circuit topology can operate with incoherent sources at the cost of extra losses. In conclusion, all the components used for the design are available in the process design kit of most of the foundries, aiming for a good reproducibility.

SIMULATION AND RESULTS

To evaluate the performance of the introduced readout layer, we exploit a 3-bit-header recognition task, fed with a sequence of binary inputs (bits). The task is to classify the last three input signals towards eight different classes. The here simulated delay-based reservoir can be implemented with a Mach-Zehnder modulator for the non-linearity and an optical fiber for the delay. The dynamics of this setup are described by the Ikeda-equation [5]:

$$\dot{x}(t) = -x(t) + \beta \sin^2(x(t - \tau) + \gamma s_{in}(t) + b) \quad (1)$$

where $\beta = 0.77$ is the feedback gain, $\gamma = 1.53$ is the input gain, $b = 2.64$ is the phase offset of the sine-square non-linearity. The input period is defined by $T = N \cdot \vartheta$, where $N = 16$ is the number of nodes and $\vartheta = 1$ is the normalized temporal separation of the virtual nodes. The delay τ of the reservoir is set equal to the input period T . For the double modulation we use a random mask with values drawn from a uniform distribution $u[0,1]$. During the readout, Gaussian noise is added with an amplitude 10^{-3} . Fig. 3 depicts several steps of the signal processing using a delay-based reservoir with the proposed integrated readout layer. In Fig.3(a), we show the input signal for the 3-bit header recognition task. Each bit is double modulated by the same mask $m(t)$ and presented to the reservoir for a normalized input time $T=16$. In Fig.3(b), we display the response of the reservoir for the 10 consecutive input bits. The reservoir output is multiplied by the learned output weights $w(t)$ resulting in the weighted signal shown in c). The weighted states $w(t)x(t)$ enter the simulated integrated PIC and the nodes states are summed up to generate the continuous output signal $\hat{o}(t)$. Negative phase weights can be set by applying a π shift with the integrated thermal phase shifters in the PIC, surrounded with deep trenches to maximize the efficiency. Fig.3(e) shows the output sampled signal after summation, that indicates the reservoir prediction $\hat{o}(k)$ with respect the targeted signal $\tilde{o}(k)$. For this example, we obtain a bit error rate of 0.004, in line with the state of the art of Reservoir for 16 nodes.

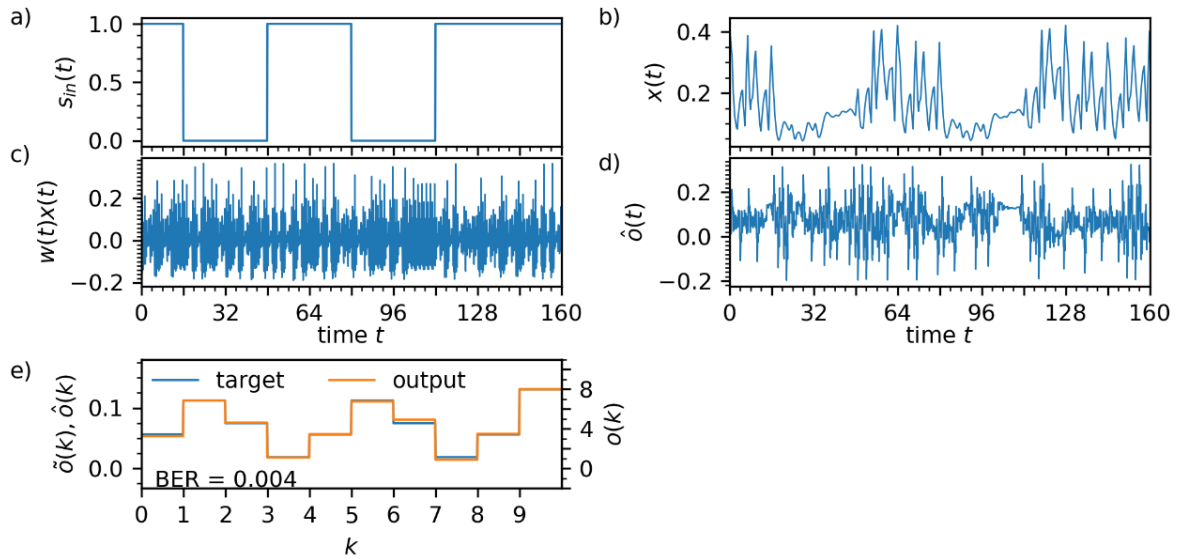


Fig. 3 Several steps in the signal processing using a delay-based reservoir and the proposed integrated optical readout layer. a) the input signal for a 3-bit-header recognition task. b) The reservoir response for 10 consecutive bits. c) The weighted states. d) The PIC output. e) The targeted signal (blue) and the reservoir prediction (orange).

DISCUSSION AND OUTLOOKS

The results based on numerical simulation show that the PIC readout supports the performance of the reservoir enabling real-time, low latency signal processing beyond GHz range. Future studies will focus on improving the scalability limited by the modulation bandwidth. Further improvements will be dedicated to replacing thermal phase shifters with optical MEMS or phase change materials to minimize power consumption.

Acknowledgements: Authors acknowledge the support of the European Union's Horizon 2020 research and innovation program under the Marie Skłodowska-Curie grant agreement No 860830 (POST DIGITAL).

References

- [1] G. Van der Sande, et al. "Advances in photonic reservoir computing." *Nanophotonics* 6.3, pp. 561-576, 2017.
- [2] L. Appeltant, et al. "Information processing using a single dynamical node as complex system." *Nature communications* 2.1, 468, 2011.
- [3] G. Donati, et al. "Microring resonators with external optical feedback for time delay reservoir computing." *Optics Express* 30.1, pp. 522-537, 2022.
- [4] K. Harkhoe, et al. "Demonstrating delay-based reservoir computing using a compact photonic integrated chip." *Optics Express* 28.3, pp. 3086-3096, 2020.
- [5] L. Larger, et al. "Ikeda-based nonlinear delayed dynamics for application to secure optical transmission systems using chaos." *Comptes Rendus Physique* 5.6, pp. 669-681, 2004.

Dynamic Labelling for Enhanced Biosensing with Microring Resonators

Student paper

P. Borga^{1*}, F. Milesi¹, N. Peserico², C. Groppi¹, A. Fincato³, R. Bertacco¹ and A. Melloni²

¹Dipartimento di Fisica, Politecnico di Milano, 20133 Milan, Italy

²Dipartimento di Elettronica, Informazione e Bioingegneria, 20133 Milan, Italy

³STMicroelectronics srl, 20864 Agrate Brianza, Italy

* piero.borga@polimi.it

A dynamic labelling technique for biosensing to be used in integrated optics with microring resonators is proposed. Analyte concentrations can be evaluated labelling the biomolecules with magnetic nanoparticles that are activated by time varying magnetic fields. The interrogation system extracts the information within few seconds and with a Limit of Detection improved by two orders of magnitude with respect the classical resonance tracking technique, tested on the same chip.

Keywords: labelled biosensing, microring resonators, diagnostics, optomagnetic biosensing

INTRODUCTION

Biosensing in integrated optics is a wide topic expected to increase its market potential in the near future and many platforms are evolving bringing improvement in performances such sensitivity, selectivity and reliability. Interferometric strategies, such with Mach-Zehnder interferometers and microring resonators (MRR), are showing a high technology readiness level [1]. The basic working principle is based on changing the refractive index of the waveguide cladding by binding molecules or nanoparticles on the chip surface. Changing the effective refractive index n_{eff} seen by the electromagnetic field affects its phase during light propagation, allowing to detect the biochemical modification by means of the interferometric scheme. A strong constrain to diagnostic applications is the time required for the molecular recognition and binding event to happen, that can be from some minutes to several hours depending on the molecular affinity between the analyte and the complementary receptor on the sensor and on the number of needed binding steps. Plus, the typical strategy [2] to quantify the analyte concentration with MRR consists in repeating transfer function scans (Figure 1a), from which the resonating wavelength shifts of functionalized and control sensors are extracted and compared over time to obtain the biomolecular recognition net shift (Figure 1b). To increase the effect, labels with large impact on the refractive index can be used, in this way it is possible to differentiate from label-free and passively-labelled approaches. Label-free assays are usually easier and faster but with a lower signal to noise ratio S/N, while labelled are more complex in sample preparation and slower but show a better S/N. Mechanical, thermal and other sources of noise over long times can hide the shifts, deteriorating the results at low concentrations. We conducted our tests on MRR with 60 base pair DNA strands and dextran-magnetite nanoparticles: following this classical technique the results (Figure 1c) show that the theoretical Limit of Detection (LOD) lays in the range 1-100nM for label-free and 0.1-1nM for labelled measurements, lasting over 2.5 hours of continuous tracking.

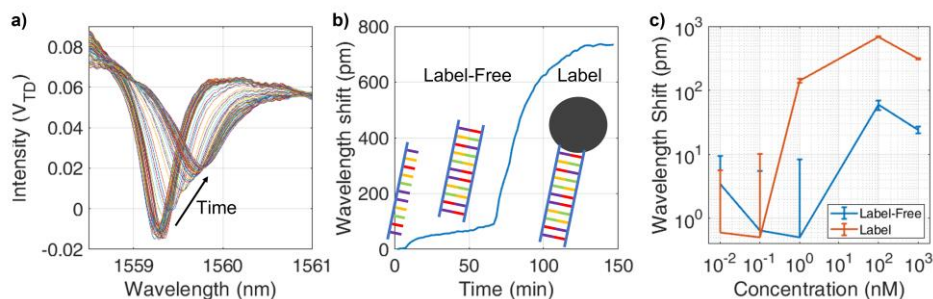


Fig. 1. Classical biosensing with MRR: a) transfer function repeatedly measured on sensing and control ring resonator; b) biomolecular binding resonance wavelength net shift over the necessary long time quantify the molecular recognition process, both with label-free and labelled approaches; c) analyte concentrations calibration curves, noise limits low concentration values

To overcome the issue of long-lasting measurements we propose a technique, named OptoMagnetic, that performs an active dynamic labelling approach to extract the information hours or even days after the molecular binding has happened, that requires no thermal stability, improves the limit of detection with respect of the classical method (tested with the same SiPh chips) and requires from few minutes down to few seconds for the interrogation process.

OPTOMAGNETIC CONCEPT

This method is meant to be performed after the molecular recognition already took place. The OptoMagnetic technique exploits magnetic nanoparticles (MNP) as labels. An external magnetic field generates an attractive force on the MNP, and the following displacement modifies the n_{eff} , thus shifting the resonance. Instead of attracting the MNP to speed up the binding process as in Ref. [3], with the use of an AC magnetic field the MNP oscillates between two positions thus modulating the n_{eff} in the cavity (Figure 2a). The periodically shifting resonance produces a modulation of the output optical power which intensity depends on the transfer function slope and on the resonance shift (Figure 2b) according to

$$\Delta P_0 = \frac{\delta T(\lambda)}{\delta \lambda} \Delta \lambda. \quad (1)$$

The optimal working point corresponds to the maximum transfer function's slope $dT/d\lambda$, where the signal ΔP_0 is maximized (Figure 2c). The output optical power, read by a photodiode (PD), can then be demodulated with a lock-in amplifier and together with the slope they are used to evaluate the resonance oscillation amplitude $\Delta \lambda$. This parameter depends on the number of MNP bind to the cavity waveguide, related to the analyte concentration.

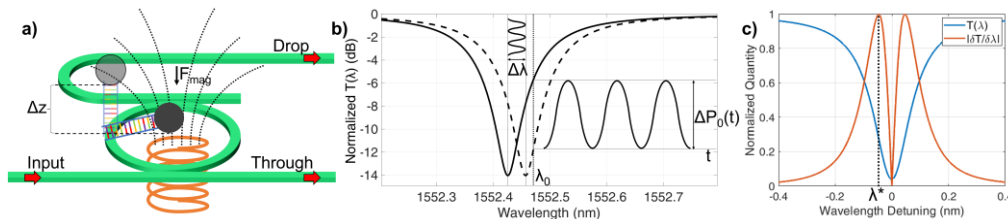


Fig. 2. OptoMagnetic technique concept: a) an external AC magnetic field forces the oscillation of the MNP on the MRR producing a n_{eff} modulation; b) the modulated resonance generates an oscillating optical power at the outputs, which intensity depends on the resonance modulation intensity and on the transfer function slope; c) technique's optimization suggests as working point the maximum slope of the transfer function.

SETUP AND RESULTS

To perform the OptoMagnetic measurements we used the setup showed in Figure 3a. The SiPh chip features 14 MRR with integrated PD at each output, provided by STMicroelectronics. The chip is glued and wire-bonded on a PCB to transfer the signals. The same PCB is used to mount and tightly fix a fluidic cell for liquid control, in Figure 3b. A detailed picture of the $80\mu\text{m}$ diameter MRR with Input, Through, Add and Drop waveguides is showed in Figure 3c. The 1550nm laser performs a wavelength ramp over a FSR of the MRR. The Through and Drop PD signals are amplified, then subtracted to maximize the slope $dT/d\lambda$ and the signal is brought to a lock-in amplifier. The signal generator drives at 80Hz the electromagnet placed under the chip and it is used as reference for the lock-in amplifier, which is devoted to demodulate the harmonics of the PD signal, with a bandwidth filter set to 5Hz.

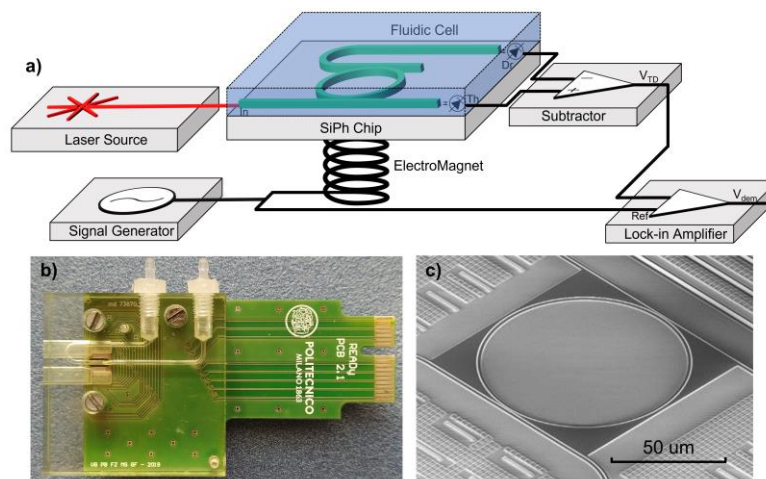


Fig. 3. OptoMagnetic technique setup: laser, chip with fluidic cell, electronics to subtract Through and Drop signals, signal generator with electromagnet under the MRR and lock-in amplifier; b) PCB holding the wire-bonded SiPh chip and the fluidic cell; c) detail of the $80\mu\text{m}$ diameter MRR.

The described setup is meant to perform measurements as showed in Figure 4a. The FSR laser scan allows to acquire the demodulator output V_{dem} and the transfer function of the MRR, from which the slope $dV/d\lambda$ is calculated. According to Equation (1), dividing these two quantities we extract the oscillation of the resonance wavelength $\Delta\lambda$. Repeating the process for different concentration and for both sensing and control MRR, we obtain a calibration curve indicating the relation between resonance oscillation magnitude and DNA concentration in the sample, Figure 4b. The reference measurements show an average wavelength shift $\mu=250\text{fm}$ and a standard deviation $\sigma=175\text{fm}$, and the LOD is expected to be in the range 10-100pM, at least one order of magnitude better than the classical technique. At a 10pm/s rate the scan will last from 1 up to 4 minutes, depending on the range of interest. At the lowest tested concentration of 10pM, sensing and reference responses are undistinguishable due to the low V_{dem} .

To improve the S/N ratio on low concentration measurements it is possible to follow this procedure: first perform a fast scan (a commercially available tunable laser source works at several nm/s) to extract the transfer function slope $dV/d\lambda$, then set the laser at the optimal working point (i.e. maximum slope), set the demodulator filter bandwidth to a smaller value (e.g. 0.1Hz) and finally switch on the AC magnetic field for few seconds to acquire the better filtered V_{dem} . The clean On-Off signals in Figure 4c, obtained with this procedure for 10pM DNA concentration, show a relevant difference between sensing and reference sensors. Over a 10s window on the plateau, the measurements return an average shift of $\mu_{sens}=55.5\text{fm}$ and a standard deviation $\sigma_{sens}=0.6\text{fm}$ for the sensing and $\mu_{ref}=12.3\text{fm}$ $\sigma_{ref}=0.35\text{fm}$ for the reference, indicating that we can still easily distinguish between the functionalized and the control sensors. Due to the low standard deviation, the limiting factor is represented by the reference signal, probably arising from residual free-floating MNP in the fluidic cell and electronic disturbances caused by the nearby electromagnet. A statistical crossing point between signal and reference should be below the lowest tested concentration of 10pM, pushing the LOD even lower by at least another order of magnitude.

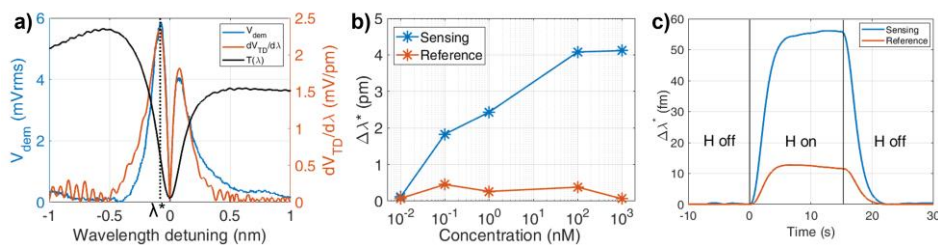


Fig.4. OptoMagnetic labelling results: a) typical scan with transfer function (no scale), its calculated slope and the demodulated signal from which the b) wavelength oscillation amplitudes are calculated for sensing and control sensors at different analyte concentrations; c) On-Off signal with narrow filtering to improve S/N at lower concentrations, here 10pM.

CONCLUSION

Biosensing and diagnostics with MRR is possible and already commercially available [4]. However, the classical resonance tracking technique requires high stability during the long biomolecular recombination time and at low analyte concentrations it becomes less reliable. To overcome the issue we propose the OptoMagnetic technique, a method to read the result after the molecular binding occurred. In this way the molecular recognition and the labelling process can be performed under the perfect biological conditions (e.g. shaking/stirring the sample, setting optimal temperature and humidity, ...), without worrying about electrical or optical access. When the biomolecule-label system is fully formed, a fast interrogation scheme extracts the needed information in few seconds and with high precision. With an optimized biochemistry process and the high sensitivity technique, we can expect to improve further the performances on refractive index based biosensing platforms.

Acknowledgements: Authors acknowledge CNR-SCITEC group for functionalization process, HTA srl for designing the fluidic cell, L. Livietti and S.V. Masci for technical support and wire-bonding. This work was partially performed at PoliFab, the micro- nano-fabrication facility of Politecnico di Milano.

References

- [1] J. Milvich, D. Kohler, W. Freude, C. Koos, *Integrated phase-sensitive photonic sensors: a system design tutorial*, Advances in Optics and Photonics, Vol. 13, Issue 3, pp. 584-642, 2021
- [2] P. Steglich, M. Hulsemann, B. Dietzel, A. Mai, *Optical biosensors based on silicon-on-insulator ring resonators: a review*, Molecules, 24, 3, 2019
- [3] E. Valera, M.S. McClellan, R.C. Bailey, *Magnetically-actuated, bead-enhanced silicon photonic immunosensor*, Analytical Methods, 7, 8539-8544, 2015
- [4] L. J. Donato, E. S. Theel, N. A. Baumann, A. R. Bridgeman, J. H. Blommel, Y. Wu, B. S. Karon, *Evaluation of the genalyte maverick SARS-CoV-2 multi-antigen serology panel*, Journal of Clinical Virology Plus, vol. 1, no. 3, 2021

Towards an integrated optic-electronic-optic interferometer

(Student paper)

Alexander Schindler^{1,2}, Felix Ganzer², Patrick Runge², Md Salek Mahmud³, Sebastian Randel³ and Martin Schell^{1,2}

¹Institute of Solid State Physics, Technische Universität Berlin, Berlin, Germany

²Fraunhofer Heinrich Hertz Institute, Berlin, Germany

³Institute of Photonics and Quantum Electronics, Karlsruhe Institute of Technology, Karlsruhe, Germany

* alexander.schindler@hhi.fraunhofer.de

An optic-electronic-optic interferometer has an optical opaque processing arm. Within this arm, the signal is coherently detected, electronically processed and re-modulated. We present a receiver module for a hybrid integrated optic-electronic-optic interferometer setup.

Keywords: *interferometer, coherent receiver, hybrid integration*

INTRODUCTION

Conventional all optical Mach-Zehnder interferometer (MZI) split light into an optical reference path and an optical processing path (Fig. 1 a)). Within the processing path, optical processing is applied before the arms are recombined to superpose the light from both arms. Optical processing is limited to quite simple linear operations as attenuation or phase shifting, which in turn limits the functionality of such conventional MZIs.

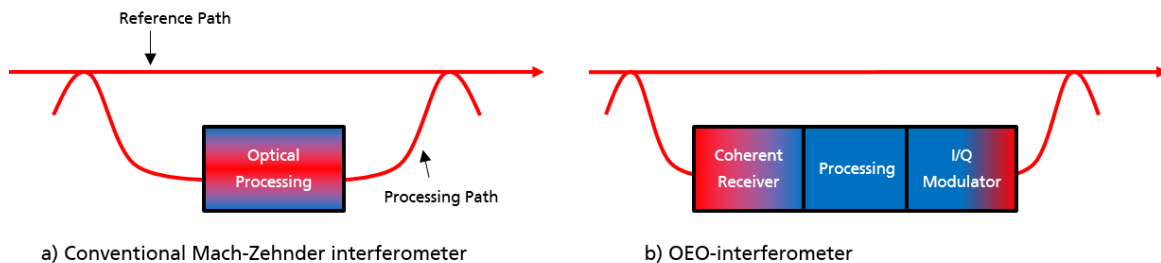


Fig. 1 Comparison of interferometer types

In contrast, the processing path of an optic-electronic-optic interferometer (OEO-interferometer) is optically opaque (Fig. 1 b)) [1]. A coherent receiver detects and converts the incoming light into the electronic domain. Digital signal processing manipulates the signal. Finally, an IQ modulator converts the processed electronic signal back into the optical domain. Due to the use of digital signal processing, the OEO-interferometer is flexible and nearly arbitrary complex operations are available to process the signal. The reference path has to compensate for the electronic digital signal processing (DSP) delay with an optical delay line. One particular use case is the subcarrier extraction in an optical orthogonal frequency division multiplexed (OFDM) signal [1]. Fig. 2 shows a detailed schematic of the OEO-interferometer for this use case.

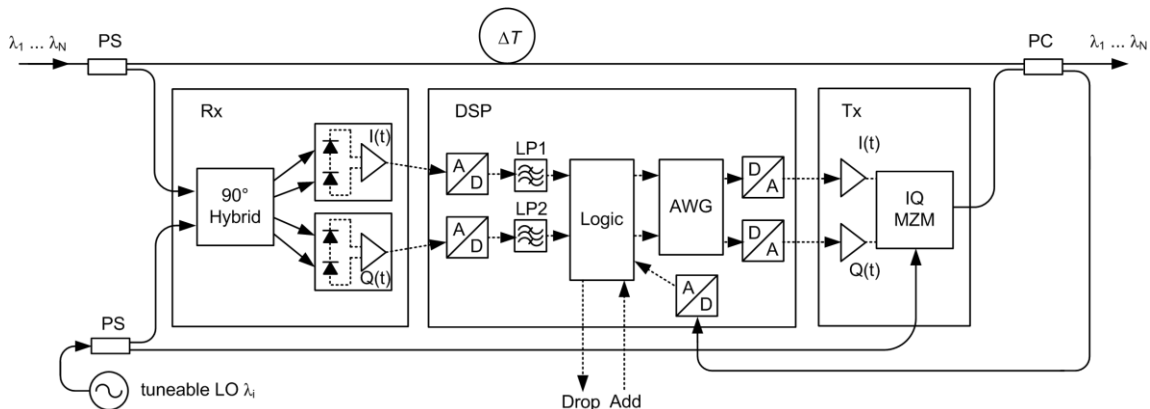


Fig. 2 Schematic OEO-interferometer (PS: power splitter; PC: power combiner; LP: low pass; LO: local oscillator; ΔT : delay line; AWG: arbitrary waveform generator).

In [2] a first experimental demonstration of an OEO-interferometer is presented using discrete components. Phase stability is crucial in the setup to realize proper interferometric recombination of the reference light and the modulated signal. Therefore, the goal of our work is to build a partially monolithically integrated OEO-interferometer module for improved phase and polarization stability. This means integrating coherent photodetector, IQ-MZM and LO on a chip. In this publication, we present an intermediate step, an interferometer receiver module, for a hybrid-integrated fiber-connected OEO-interferometer setup, which only integrates the coherent photodetector and the waveguide routing for the interferometer.

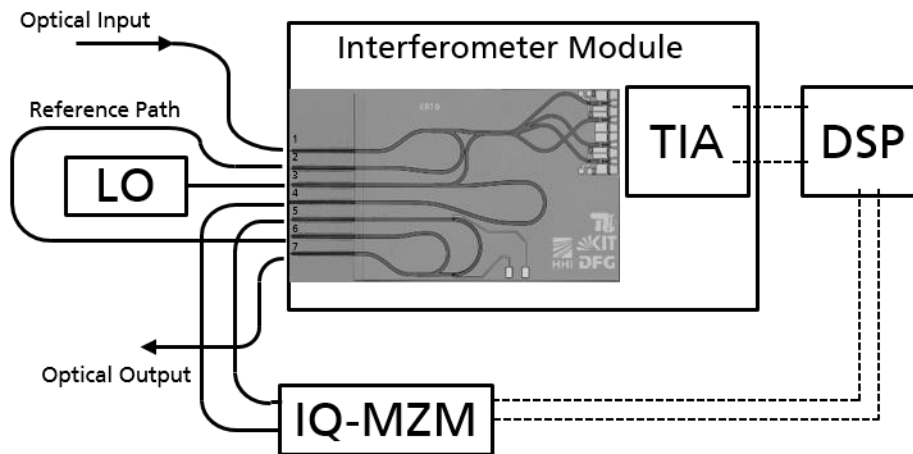


Fig. 3 OEO-interferometer setup using the presented module

CHIP RESULTS

The presented interferometer chip (Fig. 3) was manufactured on the same InP platform as in [3]. It combines a coherent photodetector and waveguide routing for the OEO-interferometer setup. The coherent photodetector consists of an optical 90° hybrid, which is based on a 2x4 multimode interference coupler, and four photodiodes. Since the compensation for the DSP delay would result in an optical delay line of several meters, the reference path will be an off-chip fiber. In order to compensate for phase shifts within the off-chip reference path, a thermal phase shifter is placed on the chip. Since the module will be used within a fiber-coupled setup, the processed chip comprises single mode fiber spot size converters as optical interfaces. Fig. 3 shows the configurations of these interfaces in an OEO-interferometer setup and an image of the processed chip.

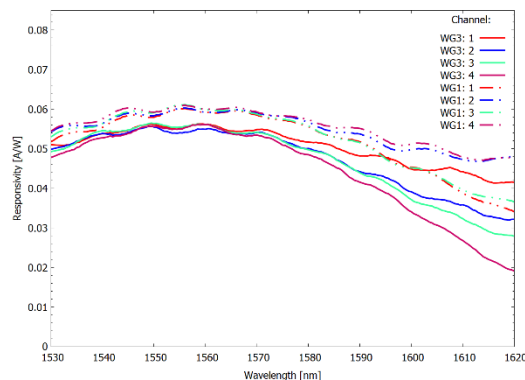


Fig. 4 Chip responsivity measurement

Fig. 4 shows a responsivity measurement of the coherent photodetector on the chip for the entire C- and L-band before assembly. It shows the results for TE polarized input light. The dashed lines refer to measurements optical interface 1 (Fig. 3) whereas the other refer to measurements using optical interface 3 (Fig. 3). The results show the center wavelength of the coherent photodetector is around 1550 nm as desired.

MODULE RESULTS

The assembled module setup consists of a module housing placed on an evaluation board (Fig. 5 b)). For the packaging a generic housing from the EU project PIXAPP has been used. Within the housing, an eight-channel fiber array is optically coupled to the facets of the chip. The interferometer chip and a TIA are placed on a ceramic substrate and the TIA is electrically connected via wire bonds to the pads of the coherent receiver part. DC and RF pads of the TIA are electrically connected with the corresponding connections of the housing. Within the setup in Fig. 3, the module serves as both the receiver part, which converts the optical signal into the electrical domain and the basis of the optical network of the OEO-interferometer setup optically connecting all components of the OEO-interferometer.

After assembling, a heterodyne bandwidth measurement of the module was performed using an electrical spectrum analyzer (ESA) (Fig. 5 a)). The presented results are for TE polarized input light. As seen in Fig. 5 a), the results of channel 1 to 3 agree well whereas channel 2 shows a different behavior for the measured frequencies.

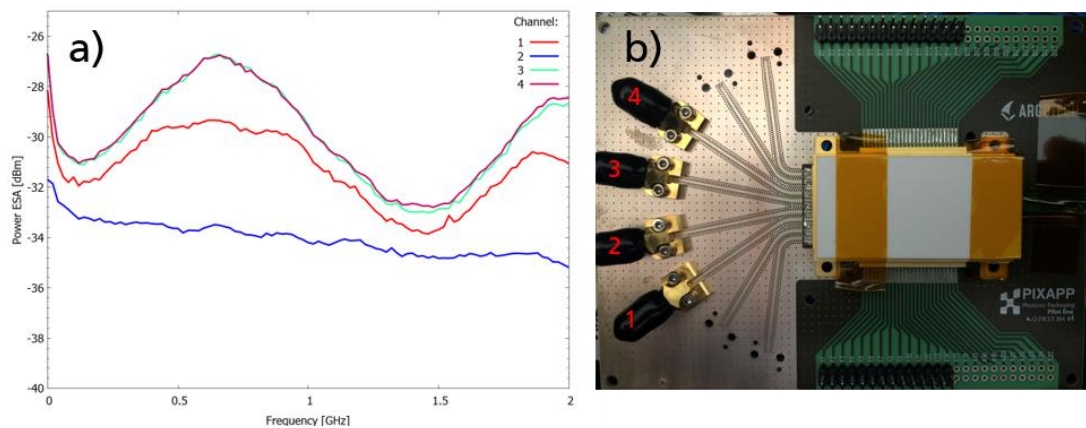


Fig. 5 a) Bandwidth measurement of all four channels of the assembled module; b) Assembled module with evaluation board

DISCUSSION

The presented OEO-interferometer module will be used within a fiber-connected hybrid setup together with an external IQ-MZM, an external laser source and a FPGA board (Fig. 3) to experimentally show the functionality of the hybrid integrated OEO-interferometer setup.

Further iterations of the module are planned with the final goal to present a monolithically integrated OEO interferometer module, monolithically integrating a coherent photodetector, an IQ MZM and a tuneable LO.

Acknowledgements: This work was funded by the Deutsche Forschungsgemeinschaft (DFG) within the SPP 2111 INTERFERE project.

References

- [1] P. J. Winzer, *An Opto-Electronic Interferometer and Its Use in Subcarrier Add/Drop Multiplexing*, JLT, vol. 31, no. 11, pp 1775-1776, 2013.
- [2] M.S. Mahmud et al., *Optic-Electronic-Optic Interferometer: A First Experimental Demonstration*, Conference on Lasers and Electro-Optics, OSA, paper SF1L1, 2020.
- [3] P. Runge et al., *Monolithic InP Receiver Chip With a Variable Optical Attenuator for Colorless WDM Detection*, in IEEE Photonics Technology Letters, vol. 26, no. 4, pp. 349-351, Feb.15, 2014.

Enhancing Sensitivity and Reducing Temperature Dependence of Contactless Light Sensors

(Student paper)

Vittorio Grimaldi, Francesco Zanetto, Fabio Toso, Francesco Morichetti, Andrea Melloni, Giorgio Ferrari and Marco Sampietro

Department of Electronics, Information and Bioengineering, Politecnico di Milano, piazza Leonardo da Vinci 32, Milano, Italy
* email: vittorio.grimaldi@polimi.it

Transparent photodetectors are fundamental components to unlock the potential of Silicon Photonics. This work presents an improved version of the CLIPP sensor, which shows a sensitivity unprecedented for this class of detectors, yet featuring a smaller footprint with respect to the traditional approach. A differential readout strategy is also discussed, allowing to reject thermal common-mode spurious effects.

Keywords: Transparent sensor, differential readout, Silicon Photonics, CLIPP

INTRODUCTION

Silicon Photonics is a promising technology to solve the power and bandwidth limitations imposed by traditional electronic interconnections. However, fabrication tolerances and the high thermo-optic coefficient of silicon has hindered the use of this technology in real-world applications. To solve this issue, it is necessary to develop control strategies to stabilize the working point of each device of interest. Integrated photodetectors are the key elements that enable this approach, allowing to locally monitor the photonic functionality. Transparent sensors are a promising class of on-chip detectors, since they introduce virtually zero losses and so they can be employed in many different points of the circuit without affecting the optical power budget. A transparent sensor developed in recent years is the Contact-Less Integrated Photonic Probe (CLIPP), that detects the optical power in the waveguide by measuring the light-induced conductance variations of the core [1]. In this paper, an enhanced version of the CLIPP is presented, that allows to reach record-high sensitivity for transparent detectors. A differential sensing approach is also shown, in order to reduce the dependency of the sensor on the global temperature and crosstalk phenomena.

CLIPP ELECTRICAL MODEL

The CLIPP sensor probes the conductance of the waveguide core in order to assess the quantity of light circulating inside the chip. To do so in a non-perturbative way, a direct contact to the waveguide is avoided and a capacitive access is preferred. To this aim, two metal pads are fabricated on top of the waveguide, typically around 700 nm from the core. The conductance measurement is then performed by stimulating one electrode (force) with an AC voltage and by collecting the resulting current with the other (sense), connected to a transimpedance amplifier (TIA). The equivalent electrical model of the sensor is depicted in fig. 1(a). The access capacitance C_A comes from the electrical coupling between the metal pads and the waveguide, while R_{WG} is the resistance of the portion of the core between the two electrodes. The two CLIPP pads are also connected by a direct stray capacitance, indicated as C_E , due to the coupling between the electrodes and the interconnections towards the electronic stimulation and readout system. This capacitance can range from few fF to hundreds of fF, depending on the strategies adopted to reduce its effect [2]. Another parasitic path of the sensor comes from the conductive silicon substrate of the photonic chip. Indeed, similarly to what happens with the waveguide, the pads of the CLIPP allow to probe the substrate resistance R_{SUB} through the capacitance C_B . Considering a box oxide thickness t_{BOX} of 2 μm , the value of C_B is in the order of 15 fF, similar to C_A .

CLIPP SENSOR WITH ENHANCED SENSITIVITY

The information probed by the CLIPP is the variation of the core electrical conductance. This can be expressed as:

$$G_{WG} = \frac{1}{R_{WG}} = q \mu p \frac{hW}{L} \rightarrow \Delta G_{WG} = q \mu \Delta p \frac{hW}{L} = \frac{\Delta p}{p} G_{WG}$$

where q is the electron charge, μ is the mobility of the carrier, p is the native doping of the waveguide (typically 10^{-15} cm^{-3}), h , W and L the height, width and length of the waveguide. It is possible to notice that if the dark conductance gets larger, its light-induced variations get larger as well. Consequently, any effort in increasing the waveguide conductance is directly mirrored in an increase of the sensitivity of the system. While the height, the

width and the doping of the waveguide are fixed by the technology, the length is only fixed by the distance between the two electrodes, which can be arbitrarily chosen in the design phase. This means that a shorter CLIPP can simultaneously achieve a better resolution while reducing its footprint. The only limitation comes from the fact that R_{WG} sets the access frequency for probing the core of the waveguide. Indeed, to properly bypass the access capacitance, the stimulation frequency should be around 10 times bigger than the access frequency set by the $\frac{C_A}{2} \cdot R_{WG}$ product. A high working frequency makes the readout more complex to handle and can ultimately worsen the sensitivity of the system [3]. To reduce R_{WG} while maintaining a low operating frequency, it's then necessary to increase the access capacitance as much as possible. While increasing the pads dimension is not a feasible approach, a possible solution comes from the use of rib waveguides. Indeed, the additional slabs can be used to increase the coupling area between the waveguide and the electric pads, leading to a bigger access capacitance. The layout of this improved CLIPP sensor is sketched in fig. 1(b) and fig. 1(c). Adiabatic transitions between the rib and the standard waveguides are realized in order to minimize the losses introduced. In fig. 1(d) a picture of the fabricated device in AMF passive technology is shown. The measured sensitivity is reported in fig. 1(e), showing how the short CLIPP is able to measure light signals down to -50 dBm, a 10-fold improvement with respect to standard CLIPP detectors [1], outperforming the resolution of other transparent sensors found in literature [4,5].

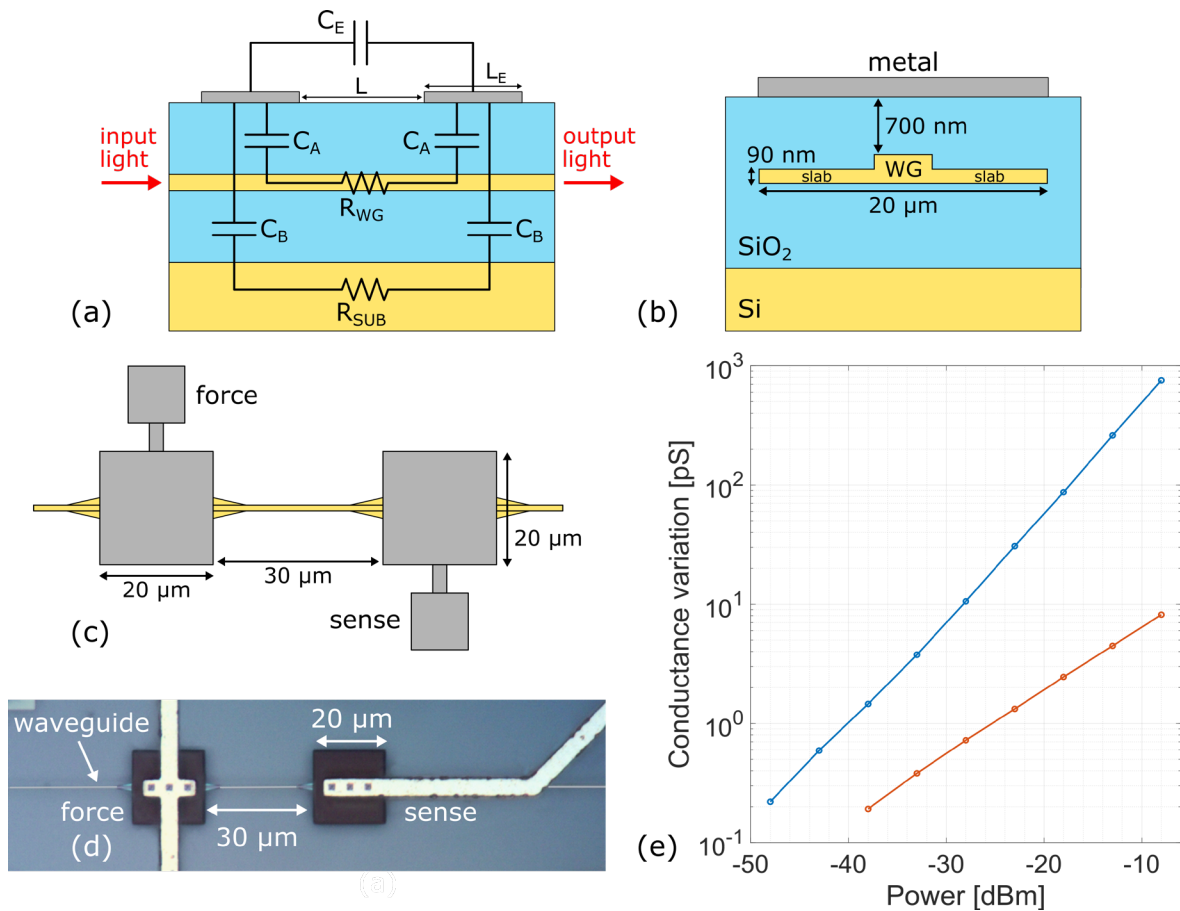


Fig. 1. a) Equivalent electrical model of the CLIPP. b) Cross-section and c) top view of the proposed layout. d) Microscope photograph of the fabricated sensor. e) Sensitivity curves of a standard (in orange) and a short CLIPP (in blue).

DIFFERENTIAL CLIPP

The mode of operation of the CLIPP sensor, although effective, can be improved by addressing two specific aspects. First, when an optical signal is injected into the photonic chip, especially through grating couplers, a fraction of the light fails to couple to the waveguide and scatters in the cladding oxide and chip substrate. This signal is detected by the CLIPP, through the C_B - R_{SUB} path, and it cannot be differentiated from the information of interest. As a result, crosstalk effects are observed between CLIPPs on different waveguides. Another issue comes from the fact that the light-induced conductance changes are superimposed to the dark conductance of the waveguide, that also depends on the local chip temperature. Any temperature variations during the operation of the CLIPP are therefore indistinguishable from light signals.

To reduce this parasitic contributions, some technological strategies can be employed. For instance, in order to

reduce the substrate effect, one could employ a photonic platform with thick box oxide or insulating substrate. Instead, to reduce the thermal crosstalk, the use of deep trenches could be exploited to thermally isolate the CLIPPs, since the largest temperature variations are usually caused by integrated heaters. Nonetheless, it's possible to envision a topological improvement of the CLIPP in order to reduce these issues regardless of the technology. The proposed solution here relies on the use of a dummy sensor on a blind waveguide that can be exploited to measure all the phenomena that are not light-induced, as sketched in fig. 2(a). By reading just the difference between the active CLIPP sensor and the dummy, only the information about the light is retained. This operation can be automatically done by connecting one electrode of the two CLIPPs together to the virtual ground of the readout TIA and by stimulating the others with two signals in counter-phase. In this way, any signal in common between the two devices is steered away from the virtual ground and does not contribute to create a signal at the output of the TIA.

A differential square CLIPP was thus designed and fabricated. To verify its effectiveness, a first experiments was conducted, in order to compare the CLIPP crosstalk between a standard and a differential device. To do so, a 5 dBm input signal was coupled into a waveguide and a CLIPP integrated in a different place was then read, first in a single-ended way and then differentially. Fig. 2(b) shows the measured variation of the conductance in the two cases, highlighting how the differential readout allows to strongly reduce the crosstalk effect.

To evaluate the robustness of the differential CLIPP to temperature variations, another experiment was conducted. No light was injected into the system, and the global temperature of the photonic chip was changed with an external thermo-electric cooler. The same device was once again measured both in a single-ended way and differentially. Fig. 2(c) shows that the differential approach allows to reduce of a factor 8 the sensitivity of the CLIPP also to temperature variations, increasing the reliability of the sensor without requiring any calibration.

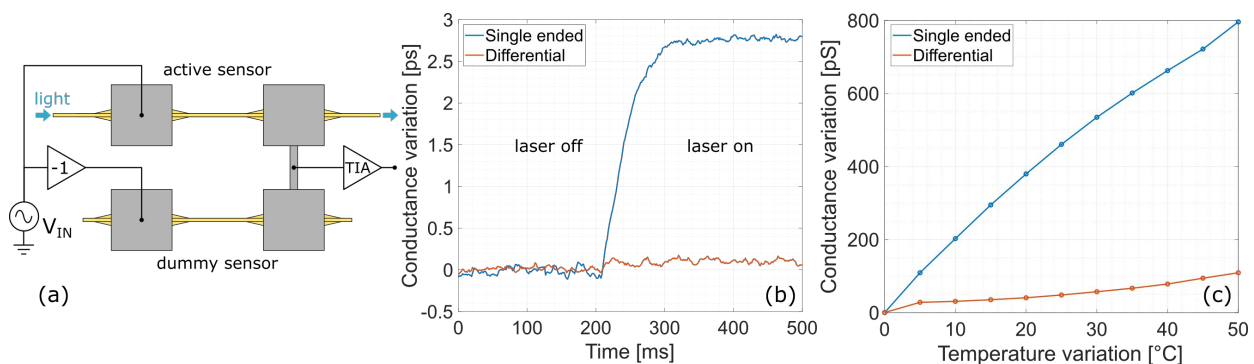


Fig. 2. a) Top view of the proposed differential readout scheme. b) Comparison of the crosstalk and c) the temperature dependence between single-ended and differential readout of the CLIPP.

CONCLUSIONS

Transparent detectors are key elements to enable closed-loop control of dense photonic circuits. An enhanced CLIPP sensor was here presented, that reaches an unprecedented sensitivity for transparent detectors with a smaller footprint compared to the standard structure. This result is further improved with the introduction of a differential readout scheme, that allows to reject the thermally-induced dark conductance variations and the crosstalk effects without requiring calibrations. The improved detector can be used to accurately and robustly monitor the operations of arbitrarily complex photonic systems, enabling new relevant architectures and applications.

Acknowledgements: part of the work was done at Polifab, the nanofabrication facility of Politecnico di Milano.

References

- [1] F. Morichetti et al., "Non-Invasive On-Chip Light Observation by Contactless Waveguide Conductivity Monitoring," in *IEEE Journal of Selected Topics in Quantum Electronics*, vol. 20, no. 4, pp. 292-301, July-Aug. 2014, Art no. 8201710, doi: 10.1109/JSTQE.2014.2300046.
- [2] M. Carminati et al., "Design Guidelines for Contactless Integrated Photonic Probes in Dense Photonic Circuits," in *Journal of Lightwave Technology*, vol. 35, no. 14, pp. 3042-3049, 15 July 2017, doi: 10.1109/JLT.2017.2710268
- [3] F. Zanetto et al., "Wide Dynamic Range Multichannel Lock-In Amplifier for Contactless Optical Sensors With Sub-pS Resolution," in *IEEE Solid-State Circuits Letters*, vol. 3, pp. 246-249, 2020, doi: 10.1109/LSSC.2020.3012920
- [4] Yu Li and Andrew W. Poon, "Active resonance wavelength stabilization for silicon microring resonators with an in-resonator defect-state-absorption-based photodetector," *Opt. Express* 23, 360-372 (2015)
- [5] Hasitha Jayatileka, Hossam Shoman, Lukas Chrostowski, and Sudip Shekhar, "Photoconductive heaters enable control of large-scale silicon photonic ring resonator circuits," *Optica* 6, 84-91 (2019)

Photonic time-delay reservoir computing based on an asymmetric Mach-Zehnder interferometer with reconfigurable memory capacity

(Student paper)

Mohab Abdalla^{1,2*}, Clément Zrounba¹, Raphael Cardoso¹, Guanghui Ren², Andreas Boes², Arnan Mitchell², Alberto Bosio¹, Ian O'Connor¹, and Fabio Pavanello¹

¹ Univ. Lyon, Ecole Centrale de Lyon, INSA Lyon, UCB Lyon, CPE Lyon, CNRS, INL, UMR5270, 69130 Ecully, France

² School of Engineering, RMIT University, Melbourne, Victoria, Australia

* mohab.abdalla@ec-lyon.fr

We present a novel photonic time-delay reservoir computing architecture based on an asymmetric reconfigurable Mach-Zehnder interferometer. Our simulation results show excellent performance on benchmark tasks such as NARMA10. We also explore a novel energy-efficient technique for reconfiguring the memory capacity of the system through coupling modulation, which may find application for performing tasks with different memory requirements using the same system, thus reducing complexity and footprint.

Keywords: reservoir computing, neuromorphic computing, integrated photonics

INTRODUCTION

The ever-growing computational demands in deep learning applications call for a paradigm shift in information processing. Reservoir computing aims to perform computations in an intertwined, brain-inspired manner, in contrast to traditional Von Neumann architectures. Due to the presence of feedback connections between the nodes, reservoir computing is especially well-suited to solve tasks which require the knowledge of previous inputs, such as time series prediction, speech recognition, and temporal bitwise operations [1]. Through a nonlinear, dynamical system (i.e., reservoir), the input is mapped onto a higher dimensional state space which can then be spatially and/or temporally sampled. The rich dynamics of the output response allows to solve non-linear, memory-dependent tasks through a linear combination of the read-out responses with output weights obtained by linear regression methods. Fortunately, only the output weights need be considered for training; the input weights, and internal weights of the reservoir, which constitute the connection strengths between the different nodes, are set and fixed to values which depend on the desired dynamical operating point and fabrication requirements of the system. Recently, it has become of great interest to implement reservoir computing architectures on photonic integrated circuits (PICs) thanks to their improved performance compared to electronic approaches in terms of power consumption and speed [2, 3]. Time-delay reservoir computing (TDRC) offers a footprint-friendly solution, requiring only a single physical non-linear node with feedback. The feedback line is sampled N times in the span of one input bit, such that the N samples can thus be viewed as the responses of N “virtual” nodes. A weighted linear combination of the output over every N samples constitutes one prediction made by the reservoir. In this work, we demonstrate a novel photonic architecture based on an asymmetric Mach-Zehnder Interferometer (MZI) for TDRC and suggest coupling modulation [4] as a means of reconfiguring the memory capacity of the system. This provides a more energy-efficient approach compared to approaches introducing a feedback attenuation block where a portion of the optical power is simply lost in the attenuation block rather than being re-routed to the read-out. Our approach also allows to shift the resonance wavelength, fine tune the resonator coupling condition to compensate for fabrication tolerances (e.g., to achieve critical coupling), and modify the memory capacity of the system with only one reconfigurable MZI.

RESERVOIR ARCHITECTURE

The reservoir architecture is based on an asymmetric MZI formed by two 3dB directional couplers and different arm lengths (1 mm and 3.88 mm) found through parametric sweeps, and a delay line, as shown in Fig. 1(a). In simulation, this difference in arm lengths has been found to enhance the richness of the output response by increasing the asynchronous character of the system i.e., the bit period versus the feedback loop duration. The bottom ports of the MZI are connected to each other by a delay line of length 13.12 cm chosen to almost match the bit period ($\tau \approx 1$ ns), thus allowing direct coupling (without relying on light recycling) of the nearest neighboring input bits. This architecture resembles an all-pass ring resonator, though the asymmetric MZI leads to different dynamics. In fact, it allows for the light to effectively propagate and interfere in multiple optical cavities, formed between the MZI arms and the feedback delay line. An integrated photonics platform based on thin-film lithium niobate on insulator [5] was considered for simulations to set the parameters as in Fig. 1(b).

The architecture is simulated using Photontorch [6] and trained on two well-known tasks in literature, first introduced in [7]:

- the NARMA10 (10th order Nonlinear Auto-Regressive Moving Average) task, which is a discrete-time nonlinear task with 10th order lag, and where the output series is generated through a recursive formula and the input is drawn from a uniform distribution. Due to non-linearity and long time lag, predicting the output of NARMA10 poses a challenge for classical computing systems
- the linear memory capacity task, which is a measure of how many past inputs the system can “remember”.

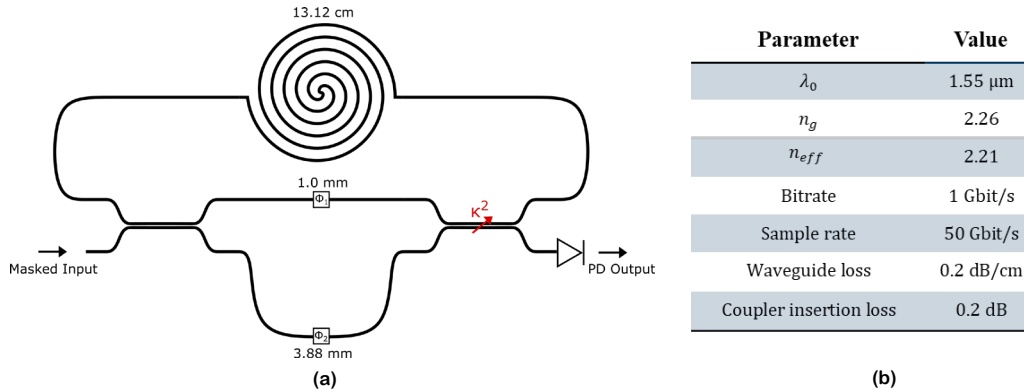


Fig. 1. (a) Asymmetric MZI-based reservoir; (b) Simulation parameters

TIME-SERIES PREDICTION

The 10th order NARMA (NARMA10) function is given by:

$$y[n + 1] = 0.3y[n] + 0.05y[n] \sum_{i=0}^9 y[n - i] + 1.5u[n]u[n - 9] + 0.1 \quad (1)$$

where $y[n]$ and $u[n]$ are the function output and input values, respectively, at discrete timestep n . The performance metric is the normalized mean square error (NMSE) between target and predicted values of the function, whereby a value of 1 refers to a constant prediction of the average value (i.e., containing no prediction of the function itself) and the desired value of 0 to a perfect prediction of the function. A training stream of 3000 samples is constructed from a uniform distribution of random numbers between 0 and 0.5. A mask based on random numbers from a uniform distribution is generated and applied to each input sample for the sample holding duration. This enables the reservoir to respond in a much richer way within the span of one input sample. In our case, the mask length is equal to the number of virtual nodes ($L_M = N = 50$). For validation, we used a different stream of similar length to the training stream. The NMSE obtained for 50 nodes is 0.13, which is close to the NARMA10 performance obtained in [8]. The non-linearity produced by the photodetector, by virtue of squaring the optical field, proves to be sufficient for this kind of task. The prediction results, along with a study of the effect of the number of virtual nodes on the NMSE, are shown in Fig.2.

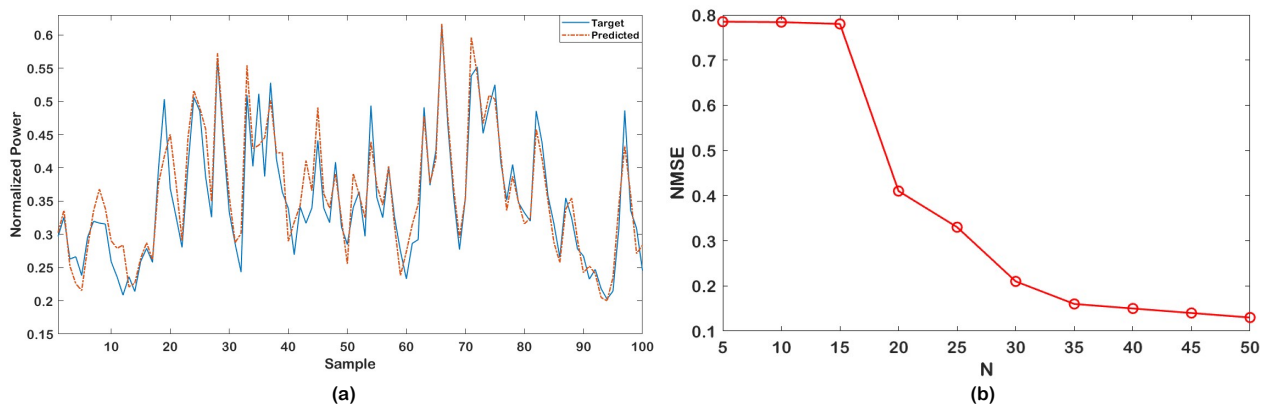


Fig. 2. (a) Target and predicted values for 100 samples; (b) NMSE as a function of number of virtual nodes N

TUNABLE MEMORY CAPACITY

The memory capacity MC_k of the system for an input shifted by k timesteps is given by:

$$MC_k = \frac{\text{cov}^2(u[n-k], y_k[n])}{\sigma^2(u[n])\sigma^2(y_k[n])}, \quad k = 1, 2, 3, \dots \quad (2)$$

where $y_k[n]$ is the prediction. In this task, the reservoir is trained to reconstruct the input $u[n]$ from a time-shifted version of it. An MC_k of 1 means a perfect memory of the k -shifted input stream and 0 means the opposite. The linear memory capacity of the system is given by $\sum_{k=1}^{k_{max}} MC_k$ where $k_{max} = N$.

For a 2x2 MZI, changing the phase difference between the two arms changes the portion of total power exiting the coupler at each port. In essence, one can view this as tuning the coupling to the resonator. By placing optical phase shifters on the MZI arms, we can obtain different linear memory capacities of the system, as shown in Fig. 3(a). For this task we used the same configuration and simulation parameters as shown in Fig. 1(b). The input stream was constructed out of 500 random numbers within a uniform distribution between 0 and 1. To calculate MC_k at $k = 50$ requires that at least the first 50 input points are removed.

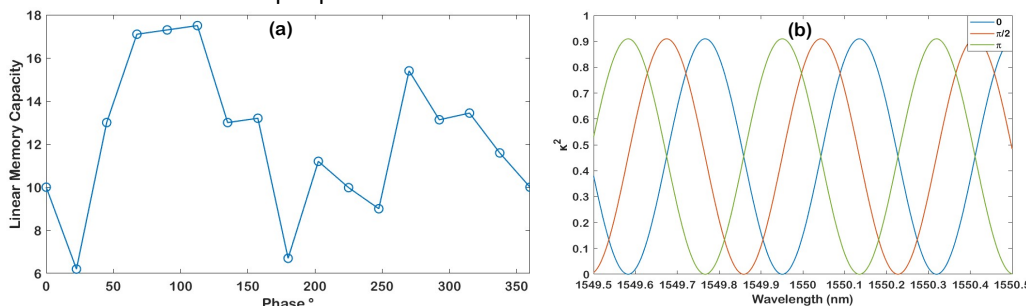


Fig. 3. (a) Memory capacity as a function of the phase difference between the MZI arms; (b) MZI power coupling coefficient (κ^2) for different values of phase difference between its arms

The results obtained show a change in linear memory capacity from 17.5 to 6.2, with the minimum value occurring around 22° and 180° phase shifts. This is analogous to changing the coupling coefficient of the all-pass resonator. The power coupled as a function of the applied phase shift is shown by a frequency domain simulation of the asymmetric MZI in Fig. 3(b). This approach allows the architecture to be adjusted for the optimal coupling coefficient after fabrication and to choose a specific feedback attenuation, while at the same time also tuning the resonance frequency. The power that is not coupled to the feedback delay line is routed to the read-out rather than being lost as in standard configuration where an attenuation block is used. The proposed architecture allows using just one active control element to achieve all these different functions and also takes into account fabrication tolerances, which can heavily affect coupling gaps in ring resonators as used in previous architectures [3].

CONCLUSION

We have shown a novel photonic reservoir computing architecture based on an asymmetric MZI allowing reconfigurable memory capacity at a system-level. Results show excellent performance on NARMA10 benchmark task. Furthermore, a new way of tuning the memory capacity is demonstrated achieving almost a threefold change. This could be used for training and optimizing a single system for tasks with different memory requirements.

ACKNOWLEDGEMENT

This work has been supported by the ECLAUSion program, which has received funding from the European Union's Horizon 2020 research and innovation programme under the Marie Skłodowska-Curie grant agreement No 801512.

References

- [1] G. Tanaka et al. *Recent advances in physical reservoir computing: A review*, Neural Networks, vol.115, pp. 100-123, 2014
- [2] Vandoorne et al, *Experimental demonstration of reservoir computing on a silicon photonics chip*, Nat Commun, 2014
- [3] G. Donati et al, *Microring resonators with external optical feedback for time delay reservoir computing*, Optics Express, vol. 30 issue 1, 2022
- [4] W. D. Sacher et al, *Coupling modulation of microrings at rates beyond the linewidth limit*, Opt. Express 21, 2013
- [5] A. Boes et al, *Status and Potential of Lithium Niobate on Insulator (LNOI) for Photonic Integrated Circuits*, Laser and Photonics Reviews, vol. 12, 2018
- [6] F. Laporte, J. Dambre, and P. Bienstman, *Highly parallel simulation and optimization of photonic circuits in time and frequency domain based on the deep-learning framework PyTorch*. Sci Rep 9, 5918, 2019
- [7] H. Jaeger, *Short term memory in echo state networks*, Technical Report GMD Report 152, 2002
- [8] Y. Paquot et al, *Optoelectronic Reservoir Computing*, Sci Rep 2, 2012

Experimental Characterization of sub-THz Wireless Communications Building Blocks on a Silicon Platform

(Student paper)

Kalliopi Spanidou¹, Robinson Guzmán¹, Luis Orbe², Luis González Guerrero¹ and Guillermo Carpintero¹

¹University Carlos III of Madrid, Av. de la Universidad, 30, Leganés, 28911, Spain

²Synopsys Photonics Solutions, Enschede, 7521, The Netherlands

* kspanido@ing.uc3m.es

In the evolution of RF photonics, silicon photonics is an important enabling technology providing high-performance devices. Here, we introduce key building blocks for a sub-THz prototype wireless transmitter utilizing Tower's PH18MA Silicon photonics platform including: single-ring resonators, 10x5 array waveguide grating and Mach-Zehnder modulators.

Keywords: Silicon Photonics (SiPh), RF Photonics, Array Waveguide Grating, Ring Resonators, Mach Zehnder Modulator

INTRODUCTION

Silicon Photonics (SiPh) technology is experiencing a rapid development in the past two decades, evolving to a mature photonic integration platform hosting multiple key building blocks onto a single silicon chip. It is expected to become an enabler for next-generation high-speed communications as well as sensor applications, such as light detection and ranging (LIDAR). One of SiPh's strongest features is its compatibility with industrial CMOS to unlock photonic-electronic convergence. Currently, a variety of SiPh technology platforms offer Multi-Project Wafer (MPW) services, which enables cost-effective access to the foundry services. The first MPW runs were offered through the ePIXfab service, which included IMEC and CEA-Leti foundries. TOWER Semiconductor, a silicon foundry specializing in Radio Frequency and High-Performance Analog and CMOS technology, introduced photonics into its platform, which has sparked high interest in RF Photonics applications.

Figure 1 depicts a schematic of the building blocks for a high-speed RF Photonics transmitter that is based on an external Optical Frequency Comb (OFC) offering phase-locked and constant mode-spacing, a high-speed photodiode, and a single SiPh chip as the key component of optical heterodyne RF Photonics transmission. The integrated components on the SiPh chip are optical wavelength selectors, optical modulators, and wavelength combiners. In this paper, we design and experimentally demonstrate the performance of SiPh key building blocks towards a monolithically integrated optical heterodyne system including:

- Optical filters, based in micro-ring resonators (MRRs), offering high wavelength selectivity to isolate individual wavelengths from an OFC, large free spectral ranges (FSRs) and high extinction ratios,
- Optical wavelength combiners, based on array waveguide grating (AWG) multiplexer/demultiplexer.
- Optical modulators, based on Mach-Zehnder Modulator (MZM) structures, which offer high-performance optical modulation enabling higher-order modulation formats reaching 100Gb/s.

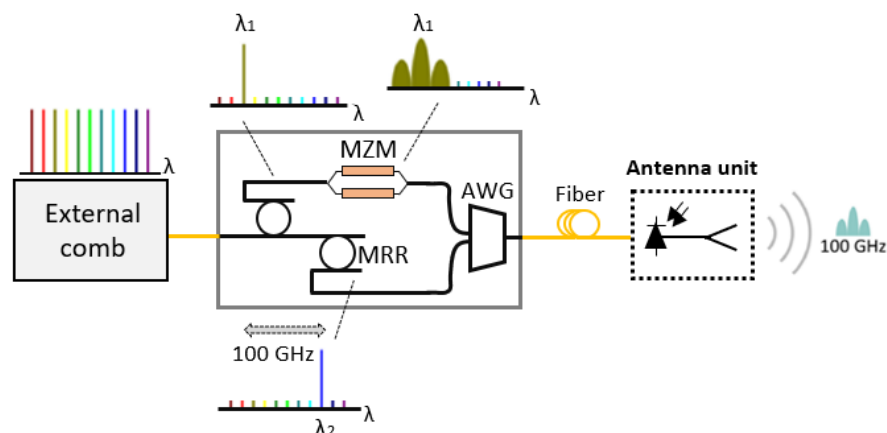


Figure 1 – An Illustration of the sub-THz wireless transmitter featuring MRR-based filtering, an AWG wavelength multiplexing and data modulation via MZM.

The Photonic integrated circuits (PICs) are integrated monolithically utilizing Tower's PH18MA Silicon photonics platform, which offers the 180 nm SOI process technology. The dimensions of the chips are 5 x 5 mm, resulting in an extremely compact optical circuit. The tested building blocks from this MPW submission were created and optimized using Synopsys OptoCompiler Platform and Photonic IC Design Flow.

DEVICE DESCRIPTIONS

Optical modulation and filtering are crucial functions in microwave photonics signal processing, important in optical heterodyne generation [5]. Considering this application, we demonstrate silicon ring resonators with an FSR at 100 GHz and AWG-based wavelength multiplexing structure with 50 GHz channel spacing. A ring resonator-based wavelength selector has a length of 713.8 μm and a phase-shifter (PS) of 266.68 μm on top of it, to ensure maximum tunability of the FSR. In addition, the tested AWG structure has 10 inputs and 5 outputs, with each input introduced in a phase shifter-based MZM, having a total length of 2000 μm , utilizing the electro-optic effect. Hence, relying on the plasma dispersion effect, the optical path can be altered via applied voltage. Also, grating couplers (GCs) of 18 μm diameter and maximum coupling angle at 8° are used in all the inputs and the outputs of the structures.

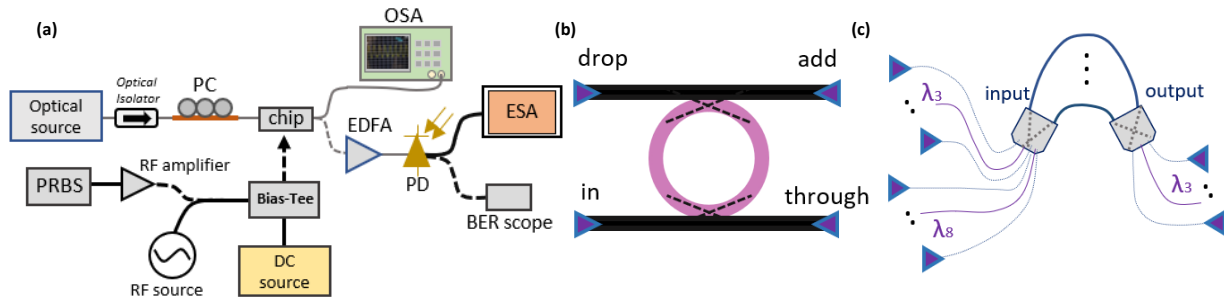


Figure 2- Illustration of the a) Experimental setup for the passive and active characterization of single-ring resonators, AWG and the MZM, respectively. b) single-MRR with GCs of 18 μm diameter (left), and c) 10x5 AWG structure utilizing the same GCs.

EXPERIMENTAL RESULTS

We report the spectral responses of the optical filtering based on the single-ring resonator structure and of the AWG-based multiplexing, operating in the C-band. Fig. 1(a) displays the characterization setup that has been deployed for the passive and active characterization of the optical components. The recording transmission spectra of the silicon RRs is recorded using an optical amplifier, Erbium-Doped Fiber Amplifier (EDFA) at the input and the Optical Spectrum Analyzer (OSA) to detect the spectral response at the drop port. Light is coupled and measured on the MRR structure through lensed fibers of 5 μm spot size in both input/output GCs. For the characterization of AWG structure, we conducted a die-scale test. The chip is placed on a copper chuck under temperature control close to 23°C . The optical testing was done manually using an 8° angled facet fiber array with a pitch of 250 μm . The fiber array is placed on a custom angled fiber array holder and mounted on a set of translation stages to form a 5-axis translation stage system.

Both of the spectral responses can be observed in Fig. 3(a). The response shaping of the micro-ring resonator at the drop port shows that the FSR is around 97 GHz, very close to the simulation value of 100 GHz. Also, the through transmission spectra of the resonator is measured and is reconciled well with the drop port. At the resonance wavelength of 1.55 μm , the following key parameters have been calculated for the assessment of MRR-based filters: FWHM is equal to 0.18 nm, the -3dB bandwidth is 16 GHz (0.1283 nm) and the Q-factor is $8.61 \cdot 10^3$. In the following step, the optical response of the AWG is measured for the two input center channels. Thus, measuring the response of the AWG's input centered channels 3 and 8, the maximum output optical power can be obtained from the center channel 3 at the output. As we can see in Fig. 3(a), there is a repetitive response from both of the channels with FSR of 463.5 GHz. Also, the channel spacing between channel 3 and 8 is 225 GHz, and the FWHM is 0.28 nm, which both are in good agreement with the simulated values. The generated side modes of each individual channel are caused probably from the internal reflections between GCs and AWG input/output and the chip facet. Therefore, it's under investigation to define precisely the origin of the noise between the resonant responses. Additionally, crosstalk between the waveguides can affect the performance, which depends on the quality of the fabrication process, device size, channels number and spacing, etc. However, waveguide fabrication imperfections are mainly responsible for the crosstalk increase.

Next, the electro-optic modulation response of the MZM is measured. Since the modulator has lumped electrodes as contact pads, a DC probe needles were used for RF signal injection. This is the reason why, as shown in Figure 3 (b), only a maximum data rate of 4 Gbit/s was successfully transmitted. For the testing of the MZM, 1550 nm light is coupled from an optical source of 10 dBm optical power into the GC. The MZM optical transmission response is captured by sweeping the DC voltage injected into one of the MZM arms from 0 to -14 V. We have recorded a RF π voltage (V_{π}) that is equal to -9 V and the quadrature transmission point at -3.6 V. Considering this, the voltage-length product is calculated at 1.8 V-cm, for a 2 mm modulation length. For the data transmission test, pseudo-random bit sequence (PRBS) with a length of 2^7-1 was used as the driving signal followed by an RF amplifier. The modulator is biased at quadrature transmission point. The optical output signal is amplified up to 10 dBm with an EDFA and then is detected by a single-ended photodiode (PD). Finally, a bit-error rate tester (BERT) is used for BER computing and eye-diagram analysis. The recorded eye-diagrams are shown in Fig. 3(b) for data rates of 1.5, 3, 4 and 4.5 Gbps. By optimizing the design of the MZM and by using traveling-wave electrodes instead of lumped electrodes, higher data rates can be achieved.

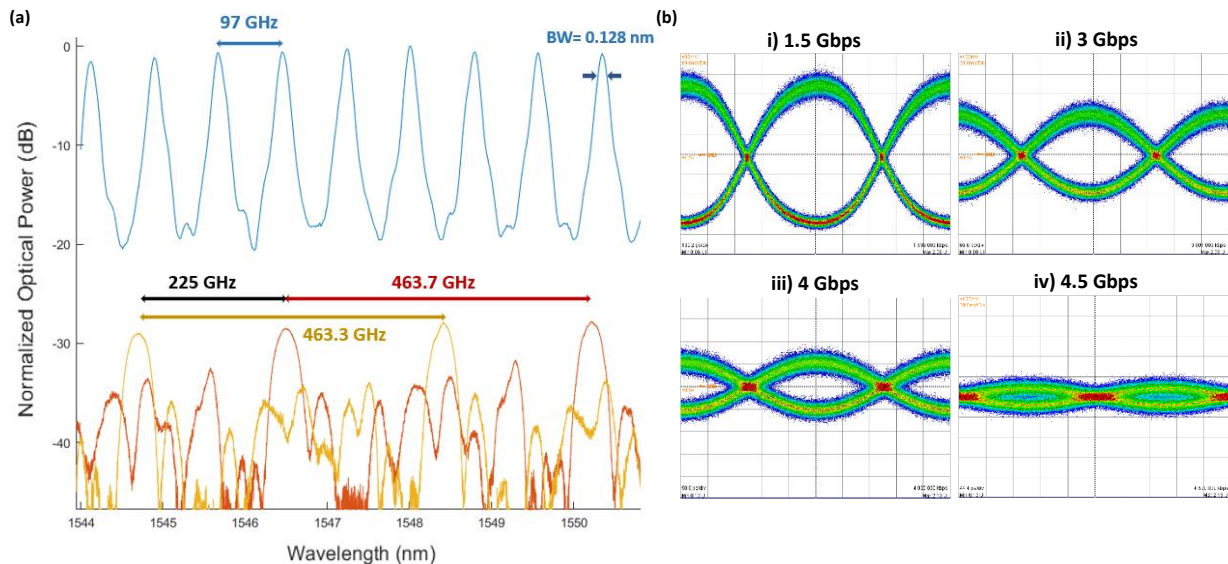


Figure 3 - a) Transmission spectra of the single-MRR at the drop port and of the AWG from the filtered center channels 3 and 8. b) Eye diagrams measured at a received power of -45 dBm for (i) 1.5 Gbps, (ii) 3 Gbps, (iii) 4 Gbps and (iv) 4.5 Gbps data transmission.

DISCUSSION

We have demonstrated a sub-THz wireless transmitter, achieving transmission data up to 4 Gbps. Monolithically integrated elements have recorded an FSR of almost 100 GHz from a micro-RR and a 225 GHz spacing between the AWG's center input channels. The reported performance of these building blocks proves that a complete optical processing fully-functional system can be miniaturized on-chip on the silicon platform.

Acknowledgements: Authors acknowledges TOWER Semiconductor for the fabrication of the chips and Synopsys Photonic Solutions support through the University Program. We acknowledge financial support by the TERAOPTICS project and TERAWAY project funded from the European Union's research and innovation programs under grant agreements No. 956857 and No 871668, respectively, the CONEX-Plus project funded by UC3M and the European Union under grant agreement No. 801538 and the European Space Agency (ESA) under Contract No. 4000135351/21/NL/GLC/my.

References

- [1] N. Margalit et. al, *Perspective on the future of silicon photonics and electronics*, Applied Physics Letters, vol. 118, no. 22, pp. 1-10, 2021
- [2] T. J. Kippenberg et. al, *Microresonator-Based Optical Frequency Combs*, Science, vol. 332, no.6029, pp. 555-559, 2011
- [3] A. Rahim et. al, *Taking silicon photonics modulators to a higher performance level: state-of-the-art and a review of new technologies*, Advanced Photonics, vol.3, no. 2, pp. 1-23, 2021

Modular and scalable photonic integrated multi-band wavelength-selective switch

Lorenzo Tunesi¹, Ihtesham Khan¹, Muhammad Masood¹, Enrico Ghillino²,
Andrea Carena¹, Vittorio Curri¹ and Paolo Bardella¹

¹Politecnico di Torino, Corso Duca degli Abruzzi 20, Torino, 10129, Italy

²Synopsys, Inc., 400 Executive Blvd Ste 101, Ossining, 10562, NY (USA)

* lorenzo.tunesi@polito.it

Photonic integrated solutions for signal switching and multiplexing in optical transport networks offer large bandwidth of operation, reduced costs and footprint, as well as low power consumption. In this context, we propose an architecture for a scalable and modular integrated wavelength-selective switch, operating on the S+C+L transmission windows.

Keywords: WSS, Photonic Integrated Circuits, WDM, Switching, Multi-Band.

INTRODUCTION

Today's optical transmission landscape is seeing a rapid increase in resource demand, due to bandwidth-intensive applications, emerging standards, such as 5G, as well as the expansion of the Internet-of-Things (IoT) paradigm. This requires an expansion of the current optical network infrastructure and capability, accommodating the increasing demand [1]. From the network operator standpoint, two main solutions are available: new infrastructure can be deployed, which represents the expensive solution, or the residual capacity of the existing network can be exploited through multi-band paradigms, which represents the more cost-effective solution [2].

To achieve the full utilization of the remaining available fiber spectrum, new technologies such as Band-Division Multiplexing (BDM) must be enabled on top of the already existing Wavelength-Division Multiplexing (WDM) based network. This requires switching and filtering elements suited for an ultra-wide bandwidth of operation, allowing consistent performances in the whole needed spectrum. For this purpose, photonic integrated circuits (PICs) represent an ideal solution, as they provide a large bandwidth of operation while maintaining low footprint, cost, and power consumption. To this end, we propose a fully integrated modular wavelength-selective switch (WSS), able to independently route each of the input signal channels towards the desired output port, operating on the S+C+L optical transmission windows.

Wavelength-selective switch architecture

The proposed WSS architecture achieves conflict-avoidance independent routing of the input channel by separating the switching and filtering operations into multiple stages, which are then cascaded into the desired configuration. This ensures the aforementioned modularity and scalability of the structure, as the design of each sub-stage can be tailored to the target implementation scenario.

The general structure of the proposed architecture can be seen in Fig.1a; in the first section the three bands of operation are filtered and routed to their respective channel filtering stage, which extracts the individual channels of the input WDM comb (Fig.1b). After the channel separation, each signal is then routed by an independent 1xN switching network, implemented as a cascade of fundamental 1x2 Optical Switching Elements (OSEs), depicted in Fig.1c. After the switching section, an interconnect crossing stage links the output of the switches to their target output fiber.

For our analysis, we designed and simulated the device through the Synopsys Photonic Circuit Design Suite, considering a target implementation with 30 total channels (10 channels per band), with 3 possible output fibers. The simulation and design of the components have been carried out through different methods, ranging from BPM, FDTD simulations, CMT, and analytical solutions: the waveguide and coupling simulations have been conducted in the Synopsys RSoft tool, allowing more detailed characterization of each sub-module, while the global simulation of the full device has been carried out in Optisim, which allows a block-oriented representation of the elements, and allowed the simulation of the whole structure at the transmission level, enabling a time-efficient and global evaluation of the implementation performance.

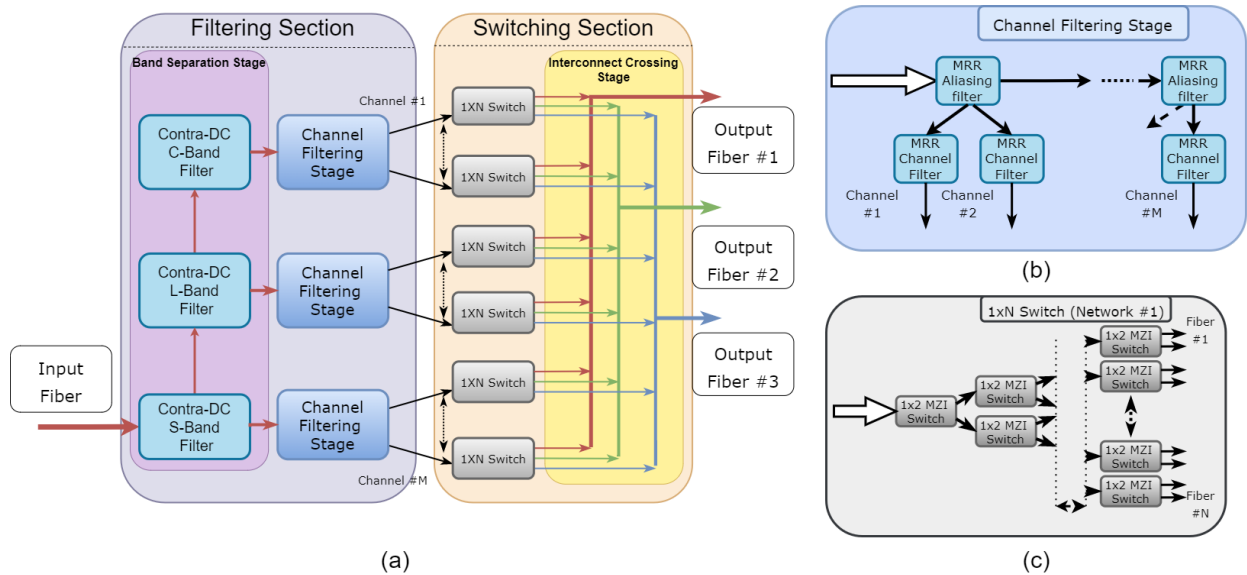


Fig. 1: (a) General structure of the proposed WSS. (b) Highlight of the channel filtering cascade. (c) 1xN Switching architecture

Device simulation and design

The devices have been designed considering the standard Silicon Photonic platform SOI, with reference Si on SiO₂ ridge waveguides with width $W=550\text{nm}$ and height $H=220\text{nm}$.

Three different devices have been used to achieve the WSS operation, with their circuit schematic and transmission performance depicted in Fig.2. Regarding the filtering section, Contra-Directional Couplers (CDC) have been used to achieve the S+C+L band separation, due to their flat wide-band of operation as well as the steep filtering roll-off. The CDCs have been designed as proposed in [3], using pitch chirp to extend and tailor the filtering bandwidth to the required regions. For our implementation the pitch of the three gratings (S, C and L band respectively) has been designed as $\Lambda = 289, 313, 325 \text{ nm}$, with the chirp $\Delta\Lambda = 20, 8, 18 \text{ nm}$. The two waveguides physical dimensions are equal in all three operating regions with $W_1=570 \text{ nm}$ $W_2=430\text{nm}$ $\Delta W_1=100 \text{ nm}$ $\Delta W_2=60 \text{ nm}$, with gap $G=200 \text{ nm}$. The lengths of the three devices are $L= 2.6, 1.2, 1 \text{ mm}$ respectively, with the resulting frequency response highlighted in the figure. For the following stage of filtering, a different filtering device is used, as to avoid the large footprint that CDCs introduce.

After the band separation, the channel extraction is carried out by a cascade of two-stage ladder MicroRing-Resonator (MRR) filters. The MRR radius is designed following [4], in order to obtain the desired frequency response for the target 100 GHz spaced WDM comb. One issue that arises from the use of resonator-based filtering elements is the channel aliasing, which would rapidly degrade the performance by introducing large insertion losses and crosstalk. This is mitigated by designing larger MRR based structure that act as anti-aliasing filters, as depicted

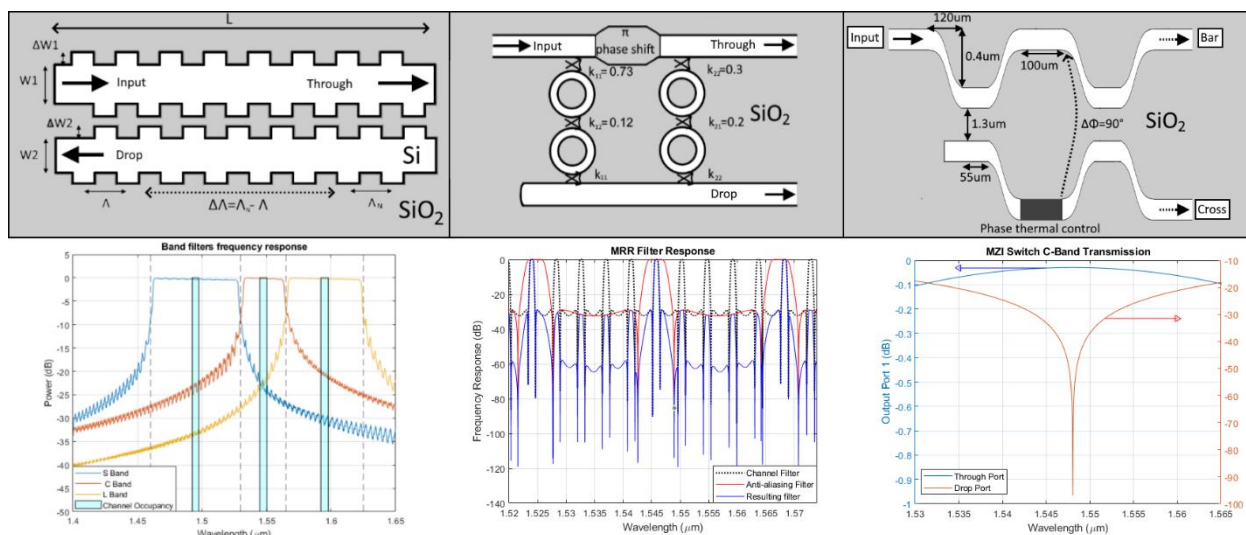


Fig. 2: Schematic (top) and corresponding simulated spectral response (bottom) of the fundamental blocks of the of the WSS (left to right: Contra-Directional Coupler, Two-stage ladder MRR filter, MZI thermally-controlled switch)

in the previous Fig.1c. By cascading these aliasing filters together with the appropriate channel cascade, the desired WDM comb can be extracted. In the implementation these anti-aliasing filters have been designed to handle two channels, although depending on the target implementation different trade-offs may be considered.

After the filtering stage, the OSEs have been implemented as MZI thermally controlled 1x2 switches. These elements provide a flat and large bandwidth for the desired application [5], depicted in Fig.2 for operation in the C-band. In each switching sub-network the MZI design can be tuned to provide the maximum transmission, while reducing the distortion and filtering penalties. The following interconnect crossing network has been modelled considering each waveguide crossing as a lossy element, introducing 0.04 dB of loss in the considered spectrum.

Results and conclusion

The structure has been simulated in a coherent transmission scenario, considering dual-polarization 16QAM modulation, with a symbol rate $R_s=60$ GBaud and spacing $FSR=100$ GHz. The Optical Signal-to-Noise Ratio (OSNR) added penalty has been considered as the performance metric to characterize the Quality-of-Transmission (QoT) impairment of the device. This metric has been evaluated by simulating the Bit-Error Rate (BER) for the different routings of all the possible channels, comparing it with the back-to-back BER of the transmitter-receiver system: the OSNR penalties have been extracted for a target BER of 10^{-3} .

The results of these simulations are depicted in Fig.3, which also highlights the crossing distribution encountered by the channels in each band: the histogram represents the distribution of the number of crossings considering every possible path for each channel. The penalties are depicted as a function of the number of encountered crossings, as to show the general trend and the penalty affecting the scalability: the waveguide crossings are the limiting factor for the scalability of such device, while the filtering and switching elements introduce a flat penalty which is not critical as the number of channels and output fibers increase.

Overall, the design strategy and the proposed architecture show promising results, with a large bandwidth of operation able to handle independently each channel of the WDM comb, without introducing severe filtering penalties on the channels.

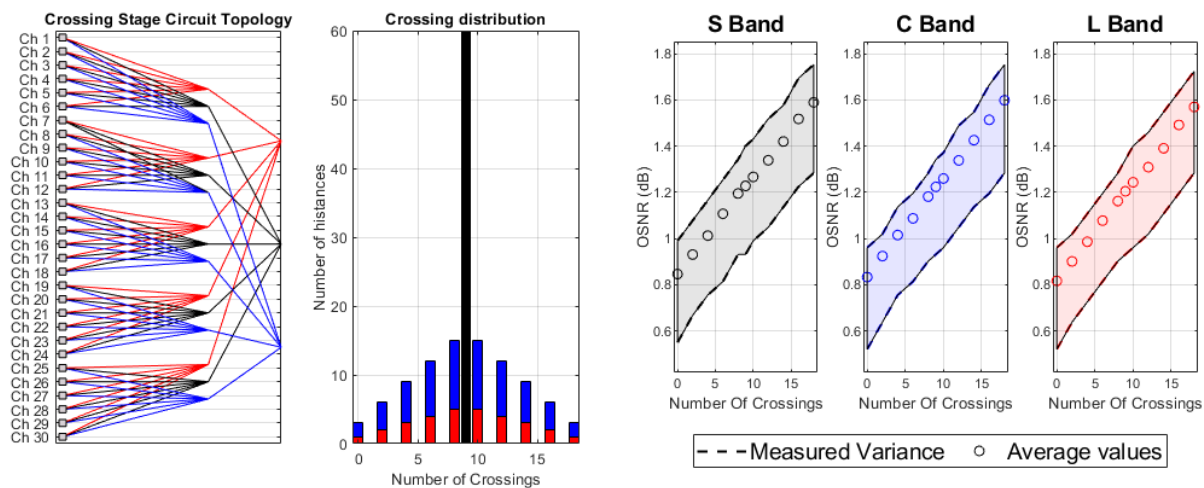


Fig. 3: Measured OSNR penalty for the different routing configurations of the thirty channels under analysis.

References

- [1] Cisco, "Cisco annual internet report (2018–2023) white paper," (2020).
- [2] V. Curri, "Multiband optical transport: a cost-effective and seamless increase of network capacity," in OSA Advanced Photonics Congress 2021.
- [3] M. Hammood *et al.*, "Broadband, silicon photonic, optical add-drop filters with 3 dB bandwidths up to 11 THz," *Opt. Lett.* 46, 2738-2741 (2021).
- [4] P. Masilamani *et al.*, "Design and realization of a two-stage microring ladder filter in silicon-on-insulator," *Opt. Lett.* 20, 24708–24713 (2012).
- [5] I. Khan *et al.*, "Performance evaluation of data-driven techniques for software-defined and agnostic management of N×N photonic switch," *Opt. Continuum* 1(2022).

Programmable Integrated Photonic Circuits: applications for 5G, Computing, Data Center and Sensing

Daniel Pérez-López¹

¹ ITEAM Research Institute, Universitat Politècnica de València, Spain,
iPronics programmable photonics S.L., Valencia, Spain

* dperez@iteam.upv.es, daniel.perez@ipronics.com

Multipurpose programmable circuits provide unlimited flexibility enabling dynamic system operation as an alternative to a custom fixed design. This work reviews the implications of the deployment of programmable hardware in microwave photonics, computing, sensing and data center.

Keywords: *Programmable, Photonic Integrated Circuits, sensing, smart transceiver*

INTRODUCTION

During the last decades, chip-assisted communications called for continuous improvement in high-speed, low latency, low power consumption and flexible signal processing and distribution. Photonic integrated circuits excelled as a great platform to provide high performance in a low form factor. In addition, emerging applications like RF-photonics signal processing, sensing and computing are benefiting from integrated photonics technology and generating considerable market traction. At the same time, the maturity of integrated photonics processes has enabled the incorporation of hundreds of on-chip phase actuators. This technological progress has permitted the development of complex reconfigurable circuits with more degrees of freedom and versatility, leading to the advent of a new class of devices called multipurpose programmable photonic circuits [1-2].

Programmable photonic circuits offer an optical alternative to process data in a flexible way and increase the density of functionalities per area. To do so, they rely on the large-scale integration of optical beam splitters and optical phase actuators into a central core, to which one can append a selection of high-performance building blocks to synthesize optical and electro-optical circuits on demand. The basic building block, the programmable unit cells, can be defined by a 4-port photonic unit cell that can perform either as a cross/bar switch, a tunable coupler, or as a phase shifter. Unlike conventional circuits, programmable photonic circuits are programmed after fabrication to implement multiple applications, tailoring their performance by setting phase and amplitude along arbitrary paths controlled by automated algorithms (Fig. 1a). Although most of the works have focused on the early-day demonstrations of small and medium scale circuits, applying the technology to practical demonstrations is one of the key pending challenges. In this work, we review the fundamentals of the technology and analyze the challenges to be addressed, with particular focus on the application of programmable photonic circuits to 5G, computing, data center communications and sensing.

2. Application focus: Microwave photonics

It is possible to reduce the existing barriers to the adoption of PIC technology (cost and development time) in many different scenarios by using programmable photonics. As a first example, Radiofrequency (RF) or microwave photonics explores the generation, transport, manipulation, and detection of high-speed RF signals [3]. An integrated RF photonics chip is composed of a laser light source, an optical modulator, an optical signal processor and a photodetector. A single programmable chip can integrate all the required devices with an extra degree of flexibility in terms of circuit topology, interconnection and design parameters (Fig 1 b). In addition to the miniaturization capabilities, the chip can perform basic functions like high-speed modulation and photodetection, spectral shaping, dispersion engineering. When combined, these functions can be applied to complex applications like arbitrary signal generation, filtering, equalization, distribution, beamforming and up/down conversion for fiber to the antenna systems and future 5G/6G station processing [4-6].

3. Application focus: Photonic computing

Another photonic-enabled application that can benefit from the versatile general-purpose processor is photonic computing. The generation of multi-mode linear processing has been demonstrated by integrating feedforward interferometric matrices, showing promising results for implementing matrix linear transformations useful in quantum computing, hardware accelerators for deep-learning applications, and general linear signal processing (Fig. 1b) [7] In addition, some works reported this functionality on hexagonal waveguide mesh arrangements [8]. The latter could also be exploited in computing applications benefiting from mixed feedforward and feed backward signal flows, like reservoir computing and future computing protocols.

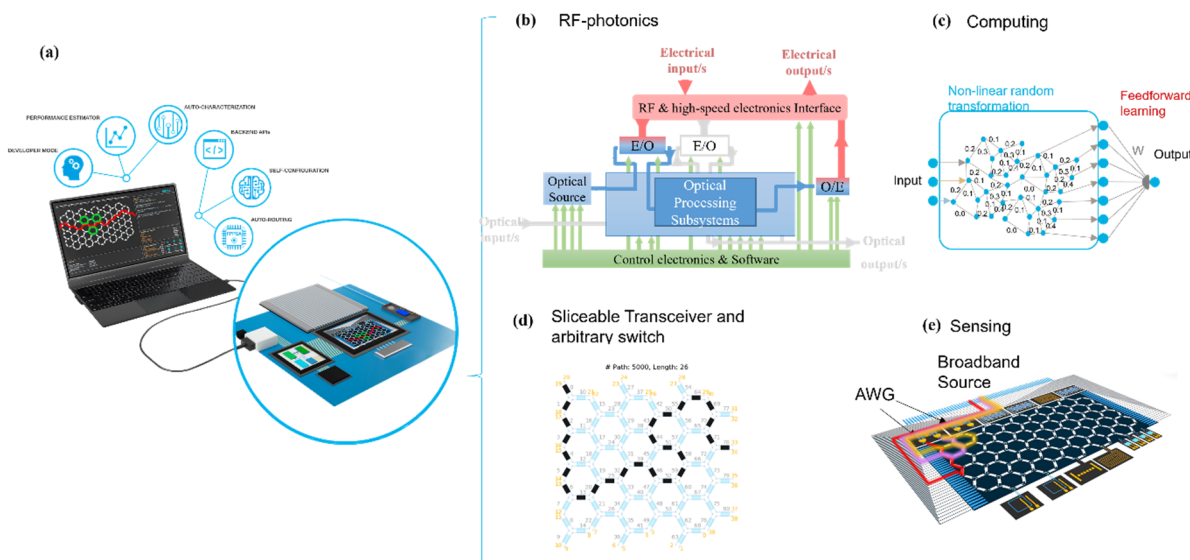


Fig. 1. (a) Diagram of a programmable photonic processor applied to: (a) RF-photonics, (b) photonic-assisted computing, (d) Sliceable transceivers and arbitrary switches, (e) sensing

To enable competitive and practical photonic-assisted applications, the processor demands extensively integrated and non-integrated components for signal preparation, optical monitoring, and electrical driving. Integrating these high-speed optoelectronic interfaces with many RF ports remains a critical challenge in the current photonic integration evolution.

On the software side, the scientific and industrial community is focused on efficient automated protocols and fault-tolerant reconfiguration routines. Although current experimental optical neural networks are mostly limited to small- and medium-scale integration proofs-of-concept and real-valued numbers, the evolution to large-scale integration could show the clear advantage of optical networks vs. electrical circuits, specifically in terms of bandwidth, and power consumption, a critical issue faced by electronic neural networks.

3. Application focus: Sliceable Transceiver and arbitrary switch

Programmable integrated circuits can be used to develop a high-capacity, scalable and smart DWDM sliceable bandwidth device, enabling workload-placing mechanisms by using reconfigurable bandwidth interconnections. The solution can be scalable by adding more lasers and modulators to the device externally, or by activating/deactivating the active components integrated on the chip allowing grow/pay-as-needed approaches that are economically efficient for the operators. In addition, the programmable photonic processors can integrate multiplexer subsystems controllable by the Software Defined Network (SDN) layer acting as a flexible ROADM (Reconfigurable optical add-drop multiplexer), the device can offload the DSP stage of simple tasks such as dispersion compensation and emulating the 2x4 hybrid for equalizing the imbalance in responsivities. This processing can take place in the optical domain using additional optical filtering over the analog lightwave prior to detection.

This configuration enables dynamic optical bandwidth allocation, providing an elastic bandwidth to serve the application/services components generating variable traffic volumes. In addition, this configuration enables point-to-multipoint transmission, broadcasting and multicasting as the programmable photonic core works as an interconnect, providing to the SDN control plane total flexibility to allocate resources (Fig. 1d). This reconfigurable network solution has the potential to circumvent the limitations of the static network solutions by reducing cabling costs or reducing the need to over-provision links.

4. Application focus: Sensing

Programmable photonics also finds application in the sensing field as central processor, able to process the light transmitted to and received from the sample. For example, chemical multisensing can be achieved by using a broadband laser and wavelength selection can be carried out in the programmable chip, transmitting to the sample different wavelengths corresponding to the fingerprints of the molecules to detect (see Figure 1). Other functions that programmable integrated circuits provide to the transmitter part are linewidth reduction and beam forming, enabling other applications like mapping LIDAR for gas detection. This central processor could switch between different functionalities and devices, processing signals coming from different type of sensors such as chemical and

fiber sensors and sending out the information through an antenna to the central, and being able to apply high-speed data processing and spectral pattern recognition (Fig. 1e).

3. Conclusions

Programmable photonic integrated circuits have a big potential to become a multipurpose technology that employs electrical signals to configure the performance of photonic chips on demand. Especially appealing for applications demanding dynamic and adaptative operations, we reviewed the opportunities in microwave photonics, photonic computing, communications and sensing.

Acknowledgments: This work was supported by the Spanish MINECO Juan de la Cierva Formación, Juan de la Cierva Incorporación program, ERC-ADG-2016-741415 UMWP-Chip, H2020-ICT-2019-021-871330 Neoteric, Generalitat Valenciana PROMETEO 2021/015 research excellency award, and Infraestructuras FEDER IDIFEDER/2018/031.

References

- [1] D. Pérez-López, et al., "Multipurpose self-configuration of programmable photonic circuits," *Nature Communications* 11, 6359, 2020.
- [2] D. Pérez-López, "Programmable Integrated Silicon Photonics Waveguide Meshes: Optimized Designs and Control Algorithms," in *IEEE Journal of Selected Topics in Quantum Electronics*, 26, 2, pp. 1-12, 2020.
- [3] D. A. I. Marpaung et al., "Integrated microwave photonics," *Laser Photon. Rev.*, vol. 7, pp. 1-33, 2013.
- [4] D. Pérez, et al., "Toward Programmable Microwave Photonics Processors," in *Journal of Lightwave Tech.*, 36, (2), pp. 519-532, 2018.
- [5] E. Sánchez et al., "Modeling amplified arbitrary filtered microwave photonic links and systems," *Optics Express*, 29(10), 2021.
- [6] G. Liu, et al., "Simultaneous Notch Filtering and Linearization in an Integrated Microwave Photonic Circuit," *IEEE Microwave Photonics*, 2021
- [7] L. De Marinis, et al., "Photonic neural networks: a survey." *IEEE Access*, 7, 175827-175841, 2019.
- [8] D. Pérez et al., "Silicon photonics rectangular universal interferometer," *Laser & Photonics Reviews*, 11(6), 1700219, 2017.

High-Performance CMOS Photonic Interfaces: From AI to IoT

(Plenary)

Rajeev J. Ram

Massachusetts Institute of Technology, Cambridge, MA, 02139, USA
* rajeev@mit.edu

Computing with reduced power and increased speed is required for the *ubiquitous data era*. While such advancements are increasingly hard to achieve with conventional CMOS logic, the CMOS ecosystem enables a host of devices beyond electronics – including *native* photonic components and heterogeneous integration. Here, we present photonic interfaces from data processing and sensing at the edge to high-performance classical and quantum computing.

Keywords: CMOS, Integrated Photonics, Silicon Photonics, High Performance Computing

INTRODUCTION

The last 36 years has seen a steady increase in the deployment of photonic integrated components. Over most of this history, the development of integrated photonic systems in both III-V and Group IV materials has been driven by the needs of fibre optic systems – from telecommunications, to LAN, to FTTH and data centre networks. In these applications, progress has been driven primarily by the properties of the transmission media (single-mode vs multi-mode fibre, fibre gain, etc). Today, photonic integration is increasingly driven by the unique properties of high-performance electronic-photonic interfaces. The low-capacitance, low-energy, high-bandwidth density of photonic integrated systems is now driving optical interconnection into board-scale, chip-scale, and intra-chip photonic systems.

Here, we consider new applications ranging from (1) deep learning systems and other data intensive classical compute applications, (2) optically addressed quantum computing fabrics – with tremendous progress being made today in the area of trapped-ion quantum computing, and (3) next-generation brain-computer interfaces where photonics may play an important role in the massively parallel signal detection.

DATA INTENSIVE COMPUTING

Today, deep learning algorithms are employed in an ever-expanding range of applications. They represent an important class of applications for compute systems from mobile phones to large-scale data centres. Recent, energy analysis on a range of representative deep learning neural networks (DNNs) has demonstrated that data movement represents a larger fraction of energy consumption than computation (multiplication-and-accumulation)[1]. While local (on-chip) memory access can be less expensive than accessing larger off-chip DRAM, together memory access is 2x (local) and 200x (DRAM) more energy intensive than computation resulting in as much as 90% of overall energy consumption devoted to data movement[1]. This memory bottleneck is well established in other data intensive computing applications and has motivated us to consider low-energy photonic interconnections[2]. CMOS photonic integration based on microring resonant modulators and detectors locked to arrays of DWDM light sources have been demonstrated as low-energy, high-bandwidth platforms for optical I/O [3]. As of 2019, CMOS photonic systems showed in-socket energy dissipation (<5pJ/bit) [4] comparable to in-package high bandwidth memory (HBM3 3.9 pJ/bit [5]). Continued innovation in the CMOS photonic platform – minimizing junction capacitance and increasing detector responsivity [6]– promises to further reduce energy consumption per bit by as much as 10x (<0.5 pJ/bit) – a reduction in GPU-to-memory access of this scale could dramatically reduce deep learning energy consumption. Optical I/O not only lower-energy access to larger memory resources but offers new networking possibilities. Recent analysis suggests that such terabit DWDM I/O could further reduce training times for deep learning by 1.9x [7].

OPTICALLY ADDRESSED QUANTUM COMPUTING

Trapped ion qubits enable high-fidelity quantum compute fabrics –these atomic qubits offer low decoherence over typical gate operation times. The performance of these systems is already competitive with superconducting, transmon based quantum compute architectures [8]and has motivated large investments by companies such as IonQ and Quantinuum/Honeywell. We proposed a photonic integrated architecture for scalable trapped-ion quantum computation. A visible waveguide platform employing focusing vertical grating couplers offers a path to

simultaneous addressing of large ensembles of trapped ion qubits[9]. The performance of each qubit can be improved because (1) the waveguide devices can be integrated directly into the surface electrode Paul trap hence eliminating beam pointing stability – an important source of technical noise and loss of fidelity and (2) the optical beams can be tightly focused allowing for faster gate operations (Rabi frequency). Since our initial proposal and demonstration of photonically addressed trapped ion qubits and CMOS Paul traps with integrated SPAD readout[10], several groups have made impressive progress. Mehta, et al. at ETH/Cornell have demonstrated multi-ion addressing with improved gate operation [11] and MIT Lincoln Lab has demonstrated fast readout of ion state using integrated SPADs [12]. Future embodiments of this platform can incorporate CMOS Paul traps, SPADs for readout, and visible waveguides in a single platform.

BRAIN-COMPUTER INTERFACES (BCI)

The platforms that have been developed for photonic integration in both high-performance computing and optically addressed quantum computing may also find a home in this most difficult of computing problems – the brain-computer interface. A closed-loop BCI couples automated detection of neural signals for behaviour with therapeutic neuromodulation [13] and has been proposed as a treatment for Parkinson's disease, epilepsy, chronic pain, and depression. The development of in vivo electrical and optical probes [14] for highly multiplexed recording and stimulation of neural circuits has been the focus of several international programs and commercial ventures. Integrated photonics may have an important role to play in both of these sensing and stimulation modalities.

Electrophysiological recording of biopotentials requires readout and processing of 1-10 mV signal levels (requiring $< 10\mu\text{V}$ noise). While these signals are relatively low bandwidth, the low electrical signal levels require amplification before analysis. Analog electrical amplification for each probe signal can require $5.2\ \mu\text{W}$ per pixel (excluding ADC) with a bandwidth of 27 kHz (190 pJ/bit) [15]. These links can be highly asymmetric as the temperature and power dissipation at the probe (brain) are critical whereas the machine terminal has relaxed energy and temperature requirements. Such low-energy, low-bandwidth optical links would not typically be feasible, however, recent improvements in silicon photonic technology has demonstrated low-optical insertion loss modulators that operate at mV-levels [16]. We have demonstrated photovoltaic modulators that harvest some of the energy lost due to background absorption to bootstrap a 10x voltage gain [17]. In this way, 1MHz bandwidth modulators with mV sensitivities have been realized with total (optical + electrical) power dissipation less than $8\ \mu\text{W}$ per channel. Further, improvements in device and system performance may enable 10-70x reductions in total power per channel.

Acknowledgements: The author acknowledges many years of fruitful collaboration with researchers in the Physical Optics and Electronics Group at MIT, Ayar Labs, UC Berkeley and Boston University.

References

- [1] Yang, T.J., Chen, Y.H., Emer, J. and Sze, V., *A method to estimate the energy consumption of deep neural networks*, Proceedings of 51st asilomar conference on signals, systems, and computers, pp. 1916-1920, 2017.
- [2] Batten, C., et al., *Building many-core processor-to-DRAM networks with monolithic CMOS silicon photonics*, IEEE Micro, vol. 29, no. 4, pp.8-21, 2009.
- [3] Sun, C., et al. *Single-chip microprocessor that communicates directly using light*, Nature, vol. 528 no. 7583, pp.534-538, 2015.
- [4] Wade, M., et al., *TeraPHY: a chiplet technology for low-power, high-bandwidth in-package optical I/O*. IEEE Micro, 40(2), pp.63-71, 2020.
- [5] O'Connor, M., Chatterjee, N., Lee, D., Wilson, J., Agrawal, A., Keckler, S.W. and Dally, W.J., *Fine-grained DRAM: Energy-efficient DRAM for extreme bandwidth systems*, Proceedings 2017 50th Annual IEEE/ACM International Symposium on Microarchitecture (MICRO), pp. 41-54, 2017.
- [6] Rakowski, M., et al., *45nm CMOS-silicon photonics monolithic technology (45CLO) for next-generation, low power and high speed optical interconnects*. Proceedings of Optical Fiber Communication Conference (pp. T3H-3). Optical Society of America, 2020.
- [7] Khani, M., Ghobadi, M., Alizadeh, M., Zhu, Z., Glick, M., Bergman, K., Vahdat, A., Klenk, B. and Ebrahimi, E., *SiP-ML: high-bandwidth optical network interconnects for machine learning training*, Proceedings of the 2021 ACM SIGCOMM 2021 Conference, pp. 657-675, 2021.
- [8] Linke, N.M., Maslov, D., Roetteler, M., Debnath, S., Figgatt, C., Landsman, K.A., Wright, K. and Monroe, C., *Experimental comparison of two quantum computing architectures*, Proceedings of the National Academy of Sciences, vol. 114, no. 13, pp.3305-3310, 2017.
- [9] Mehta, K.K., Bruzewicz, C.D., McConnell, R., Ram, R.J., Sage, J.M. and Chiaverini, J., *Integrated optical addressing of an ion qubit*, Nature nanotechnology, 11(12), pp.1066-1070, 2016.

- [10] R. J. Ram, *CMOS Photonic Circuits for Trapped Ion Quantum Computing and Molecular Sensing*, *Proceedings of Conference on Lasers and Electro-Optics (CLEO)*, 2018, pp. 1-2, 2018.
- [11] Mehta, K.K., Zhang, C., Malinowski, M., Nguyen, T.L., Stadler, M. and Home, J.P., *Integrated optical multi-ion quantum logic*, *Nature*, 586(7830), pp.533-537, 2020.
- [12] Reens, D., *et al.*, *High-Fidelity Ion State Detection Using Trap-Integrated Avalanche Photodiodes*, *arXiv:2202.01715*, 2022.
- [13] Zhang, Q., *et al.* *A prototype closed-loop brain-machine interface for the study and treatment of pain*, *Nature Biomedical Engineering*, pp.1-13, 2021.
- [14] Moreaux, L.C., *et al.*, *Integrated neurophotonic: toward dense volumetric interrogation of brain circuit activity—at depth and in real time*, *Neuron*, vol.108, no.1, pp.66-92, 2020.
- [15] Musk, E., *An integrated brain-machine interface platform with thousands of channels*, *Journal of medical Internet research*, vol.21, no.10, p.e16194, 2019.
- [16] de Cea, M., Wollman, E.E., Atabaki, A.H., Gray, D.J., Shaw, M.D. and Ram, R.J., *Photonic readout of superconducting nanowire single photon counting detectors*, *Scientific reports*, vol.10, no.1, pp.1-8, 2020.
- [17] de Cea, M., Atabaki, A.H. and Ram, R.J., *Energy harvesting optical modulators with sub-attojoule per bit electrical energy consumption*, *Nature communications*, 12(1), pp.1-9, 2021.

PIC Technologies for Quantum Secure Communications

Taofiq K. Paraiso*, Thomas Roger, Davide G. Marangon, Innocenzo De Marco, Mirko Sanzaro, Robert I. Woodward, James F. Dynes, Zhiliang Yuan & Andrew J. Shields

Toshiba Europe Ltd. Cambridge, UK

* taofiq.paraiso@crl.toshiba.co.uk

PICs offer unique opportunities for low-cost, highly-scalable quantum cryptographic systems. However numerous challenges such as packaging, power consumption and interfacing multiple chips in real-time, have for long impeded the demonstration of a standalone PIC-based QKD system. Here we show how we tackled these challenges to realize such a system with strong capabilities including autonomous operation without user intervention over multiple days and high secure key rates over all metropolitan distances.

Keywords: quantum communications; quantum key distribution; diode lasers; optical injection locking; direct modulation; photonic integrated circuits

INTRODUCTION

Quantum key distribution (QKD) systems based on discrete optics have been demonstrated in many scenarios and are now widely considered a mature technology. New approaches are now required to reduce the size, weight and power and to stimulate its wide-scale deployment. Integrated quantum photonics is an excellent candidate to address this question as it can easily interface with existing infrastructure [1]. Indeed, quantum communications is expected to be one of the first applications of integrated quantum photonics to reach maturity [2]. Quantum photonic chips have already been used to demonstrate a variety of QKD protocols [3-6]. However, these developments were all limited to proof-of-concept demonstrations, without presenting a fully deployable chip-based QKD system [7-9]. This challenging step requires one to overcome a range of shortcomings within the photonic design, the choice of integrated platform and from incorporation with bespoke high-speed electronics. In this paper we achieve this milestone by demonstrating a complete and viable real-time point-to-point QKD system based on integrated photonic circuits packaged into compact pluggable modules.

The photonic hardware comprises a quantum transmitter (QTx) chip, quantum receiver (QRx) chip and two quantum random number generator (QRNG) chips, co-designed to form a QKD system capable of operating at GHz clock rates. We implement a mix of different integrated photonic platforms, which best suit the specific requirements of the various components within the system. Quantum keys are phase encoded on the emitted attenuated laser pulses using the T12-BB84 protocol [10] for elevated efficiency. The protocol uses multiple fluxes (decoy intensities) to ensure security. We use 4 phase states produced in 2 non-orthogonal bases ($X [0, \pi]$ and $Z [\pi/2, 3\pi/2]$) and 3 pulse intensities (signal [u], decoy [v] and vacuum [w]). We demonstrate the stable system performance over multiple days of use with a feedback system acting only on the transmitter's phase.

The quantum transmitter chip is a directly phase-modulated light source that encodes photons via direct modulation and optical injection locking (OIL) [6]. The chip is built on the indium phosphide (InP) platform, which allows for integration of active components such as lasers and modulators. Fig. 1a shows an overview of the QKD system and the integrated photonic devices used within. The transmitter chip contains two distributed feedback (DFB) lasers, a Mach-Zehnder interferometer and an electro-absorption modulator (EAM). The direct-phase modulated light source scheme [12] has the advantage of producing phase-encoded pulses with high-fidelity, short duration and high repetition rate (2 GHz), without the need for electro-optic phase modulators, and therefore compact and power efficient for chip integration. The encoded pulses of light are then modulated in intensity using an EAM to produce decoy states. The selection probabilities used to encode the orthogonal bases and the pulse intensities are optimized to provide high secure key rates.

The quantum receiver includes a discrete optics high-speed phase modulator and a passive silicon-based photonic chip. The chip consists of an asymmetric Mach-Zehnder interferometer that has a relative temporal delay between the two arms of 500 ps. The interferometer measures the phase difference between consecutive pulses emitted by the transmitter. The phase modulator is used to choose the measurement basis. Photons exiting the interferometer outputs are detected via two avalanche photodiodes (APDs) and correspond to pulses measured in the two 'bit' values of each of the measurement bases (X, Z). The APDs are gated at 1 GHz and centered on the photon pulses carrying the encoded phase states.

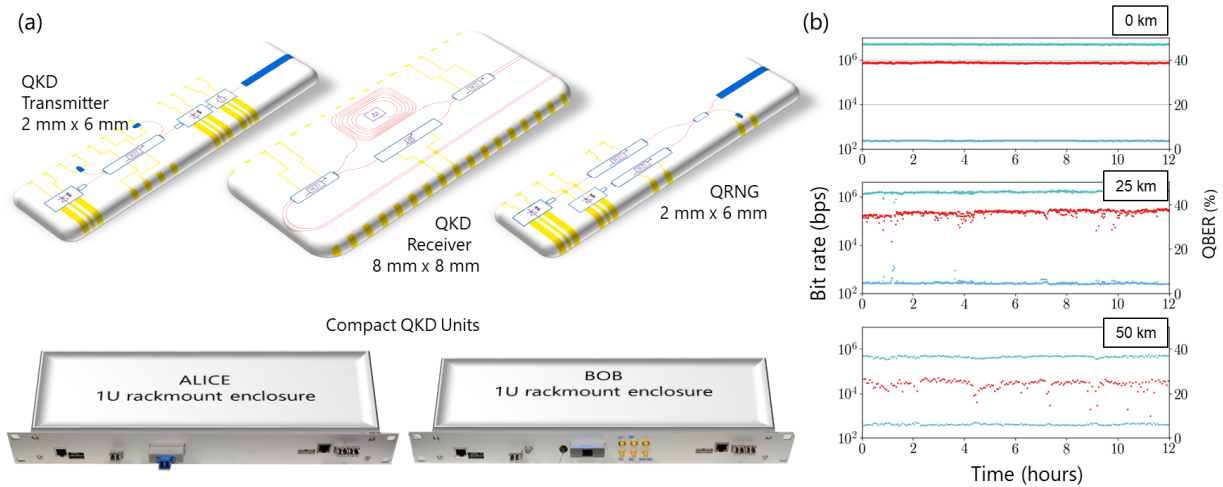


Fig. 1. (a) Photonic integrated quantum key distribution system. The system consists of a QTx unit and a QRx unit, each featuring a QRNG chip and a quantum communication chip. Random numbers generated continuously are used in real-time to encode and decode the quantum key information. Pluggable modules are used to package the QKD optics and the complete optoelectronics electronics is assembled in compact 1U rackmount enclosures. (b) Stable operation over extended periods of time is achieved over all metropolitan distances.

The QRNGs are also based on InP photonic chips, similar to the transmitter. These devices are typically omitted from QKD demonstrations, as sources of pseudo-random numbers can be used in their place as proof-of-concept. However, such omission is an important drawback for real QKD systems as the security of a QKD key directly relies on it being impossible to predict how the photons are encoded. We use QRNGs that exploit spontaneous emission phase noise in gain-switched laser diodes [9, 13]. Due to the typically low bit rates of these types of devices their implementation in QKD systems has been challenging. Here, we overcome this challenge by demonstrating QRNGs that produce verified random numbers at 4 Gb/s.

Table 1. Secure key rates achieved over different length quantum channels

Quantum channel length	SKR	QBER
0 km	726 kbps	3.72 %
10 km	470 kbps	4.50 %
25 km	235 kbps	4.66 %
50 km	28 kbps	6.15 %

RESULTS

The system capabilities were initially proven by connecting the transmitter and receiver with a short (few meters of single-mode fiber) quantum channel. QKD keys were generated with a sifted rate of 5.02 Mbps. Following error correction and privacy amplification algorithms, information theoretic secure keys are generated with a rate of 726 ± 35 kbps (see Fig. 1b). Measurements with 10 to 50 km of standard SMF-28e fiber were then acquired. The fibers spools were stored locally and connected between the two system units in the quantum channel. Table 1 reports the performance over different channel lengths. At 10 km, we found an average secure key rate of 470 ± 110 kbps.

To confirm the compatibility with real-life deployment, classical data encryption systems were connected to the system. The encryptors withdraw quantum keys from the units every minute. 352 bits of quantum key information are then used to form AES-256 keys (with a 96-bit initialization vector), which are capable of encrypting 100 Gb/s of data. These commercially available encryptors operate seamlessly with our chip-based QKD system, demonstrating its compatibility within existing optical communication infrastructure. We report continuous operation without user intervention over 11 days, at a rate sufficient to serve 1335 AES-256 keys per second and therefore to supply multiple encryptors simultaneously [14].

DISCUSSION

Our results establish the viability of quantum photonic integration for use in realistic quantum communications systems. This marks an important step for the practical deployment of quantum communication technologies based on quantum photonic chips. Reducing the cost and size of devices will allow for a significant increase in the manufacturability and reliability of these systems. As the fabrication processes for photonic integration continue to improve in terms of reproducibility, cost and volume, their use within commercial systems will become ubiquitous, allowing for easily upgradeable QKD systems, with reduced operational costs.

Acknowledgements: This work has been funded by the Innovate UK project AQUASEC, as part of the UK National Quantum Technologies Program.

References

- [1] J. Wang, F. Sciarrino, A. Laing & M. G. Thompson, “Integrated photonic quantum technologies,” *Nat. Photonics* **14**, 273–284 (2020).
- [2] N. Gisin, G. Ribordy, W. Tittel & H. Zbinden, “Quantum cryptography,” *Rev. Mod. Phys.* **74**, 145 (2002).
- [3] D. Bacco, Y. Ding, K. Dalgaard, K. Rottwitz & L. K. Oxenløwe, “Space division multiplexing chip-to-chip quantum key distribution,” *Sci Rep* **7**, 1–7 (2017).
- [4] C. Ma, *et al.* “Silicon photonic transmitter for polarization-encoded quantum key distribution. *Optica* **3**, 1274–1278 (2016).
- [5] C. Ma, *et al.* “Integrated Silicon Photonic Transmitter for Polarization-Encoded Quantum Key Distribution,” *Optica* Vol. 3 (2016).
- [6] T. K. Paraíso, *et al.* “A modulator-free quantum key distribution transmitter chip,” *NPJ Quant. Inf.* **5**, 1–6.
- [7] F. Xu, X. Ma, Q. Zhang, H.-K. Lo & J.-W. Pan, “Secure quantum key distribution with realistic devices,” *Rev. Mod. Phys.* **92**, 25002 (2020).
- [8] P. Sibson, *et al.* “Chip-based quantum key distribution,” *Nature communications* **8**, 13984 (2017).
- [9] T. Roger *et al.* “Real-time interferometric quantum random number generation on chip,” *JOSAB* **36**, B137-B142 (2019).
- [10] M. Lucamarini, *et al.* “Efficient decoy-state quantum key distribution with quantified security,” *Optics express* **21**, 24550–24565 (2013).
- [11] J. Qiu, “Quantum communications leap out of the lab,” *Nature News* **508**, 441 (2014).
- [12] Z. L. Yuan, *et al.* “Directly Phase-Modulated Light Source,” *Phys. Rev. X* **6**, 325 (2016).
- [13] C. Abellan, *et al.* “Quantum entropy source on an InP photonic integrated circuit for random number generation,” *Optica* **3**, 989 (2016).
- [14] T. K. Paraíso, *et al.* “A photonic integrated quantum secure communication system”, *Nature Photonics* **15**, 850-856 (2021).

Mid-infrared Ghost spectroscopy application using an entangled photons source in silicon

Matteo Sanna*, Davide Rizzotti**, Stefano Signorini** and Lorenzo Pavesi

Nanoscience Laboratory, Department of Physics, University of Trento, Via Sommarive 14,
38123, Trento, Italy

* matteo.sanna@unitn.it

**current address: ICFO-Institut de Ciències Fòniques, Av. Carl Friedrich Gauss 3, 08860 Castelldefels (Barcelona), Spain

We present two-photon state generation on an integrated platform using intermodal Spontaneous Four-Wave Mixing. The goal is to use this source for biphoton spectroscopy in the mid-infrared spectral region where the spectral fingerprints of molecules are contained. The technique of Ghost spectroscopy is able to achieve important advantages over classical absorption spectroscopy by allowing more detailed information to be obtained in the presence of environmental noise.

Keywords: *Nonlinear optics, Integrated photonics, Ghost spectroscopy*

INTRODUCTION

The mid-infrared (MIR) spectral region, which extends from 2 μm to 15 μm , is of interest to many areas of physics. Applications range from environmental monitoring [1] to LIDAR technology [2], from free space telecommunications [3] to applications in biology and medicine [4],[5]. The MIR region hosts the atmospheric window and the fingerprint of several molecular compounds [6]. This high and specific molecular response is of great interest to optical sensing. However, MIR optical technology is not mature, especially regarding detection, limited by low sensitivity devices. These limitations can be overcome by quantum photonics [7]. In particular, time-energy entangled photon pairs can be used to beat the shot noise limit [8] and to relax the technological constraints of MIR devices [7]. These photon pairs can be generated by non-linear optical processes, such as spontaneous parametric down-conversion (SPDC) or spontaneous four-wave mixing (SFWM) [9], [10].

In our work, we use an entangled photon source to implement quantum Ghost Spectroscopy (GS) for gas sensing [11], [12]. This spectroscopy method, in fact, uses time-energy correlated photons, where one photon interacts with the sample while the other is spectrally analyzed. In our case, the photon interacting with the gas belongs to the MIR, while the one spectrally analyzed is in the near infrared (NIR). Thanks to the spectral correlation between the photons, the gas spectral information probed by the MIR photon can be accessed by measuring the spectrum of the NIR photon, while the MIR one is detected with a bucket detector. In this way, this technique allows to use more efficient spectrometers with respect to MIR solutions. For this purpose, entangled photon pairs with a large spectral difference are required. By using spontaneous intermodal four-wave mixing (SFWM) [13], [14], we are able both to generate these photon pairs in a silicon integrated photonic device (SOI) and to apply this twin photon source for GS of CO_2 around 2 μm [15]. Specifically, using a continuous wave (CW) laser in the C-band, biphotons are generated one around 2 μm and the other around 1.3 μm . We are able to retrieve efficiently the CO_2 spectrum, demonstrating also a higher measurement visibility compared to classical spectroscopy.

RESULTS

The intermodal SFWM process involves the annihilation of two pump photons and the generation of a photon pair: an idler photon and a signal photon. The characteristic feature of intermodal is to use the chromatic dispersions of different spatial modes of an optical waveguide to achieve perfect phase matching [13]. We used an optical waveguide 1.5 cm long, with a channel cross-section of $(0.22 \times 2) \mu\text{m}^2$. We use a tunable pump CW laser at 1570 nm, injected on the TE0 and TE1 modes. The signal is generated around 2003 nm on TE1 and the idler around 1291 nm on TE0. To characterize the source, we detect the idler with an InGaAs single-photon detector (SPAD) and the signal, after being up-converted to the visible [16], with a Silicon SPAD. Due to the large detuning of the generated

photons from the pump and to their discrete bands, the pump can be easily rejected with short and long pass filters [17]. Fig. 1 shows the setup used for the coincidence measurement with details given in its description.

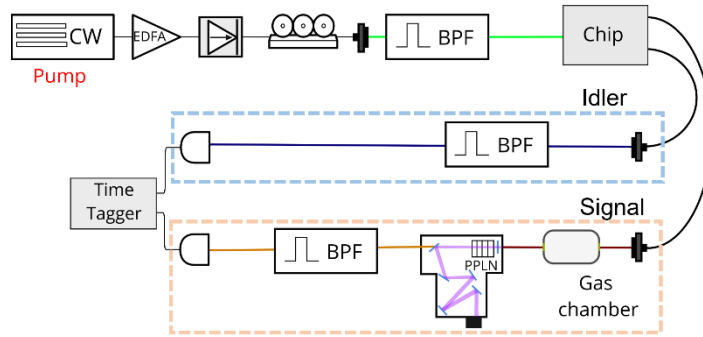


Fig. 1. Scheme of the experimental setup. A tunable continuous wave CW laser followed by its amplification and filtering stage. The chip where the SFWM is performed. After the generation of the two states, the idler channel (dashed blue line region) has a tunable band pass filter (BPF) and an InGaAs SPAD. The signal channel (orange dashed line region) has a Gas chamber followed by an upconverter system coupled to a silicon SPAD after a BPF.

To describe and compare the setups used for photon-pair generation and detection, the coincidence-to-accidental ratio (CAR) is used [18]. This parameter quantifies the probability of detecting a single-photon coincidence between signal and idler against noise and multi-pair events. The maximum CAR value is 114 ± 4 , obtained with an on-chip power of 7 mW, with (0.279 ± 0.007) Hz net coincidence rate (Fig. 2a). These results mark a 4-fold improvement with respect to the state of the art of integrated two-photon MIR sources [19]. The single-photon behavior of the source was demonstrated, measuring the heralded $g^{(2)}$ ($g_H^{(2)}$), with the signal as the heralded photon and the idler as the herald photon [18]. We measured a minimum $g_H^{(2)}(0) = 0.06 \pm 0.02$ at 10.5 mW, see Fig. 2b, demonstrating the antibunching regime of the generated photon in the MIR.

We subsequently used this source to perform quantum GS. For this application, it is useful to have a source whose

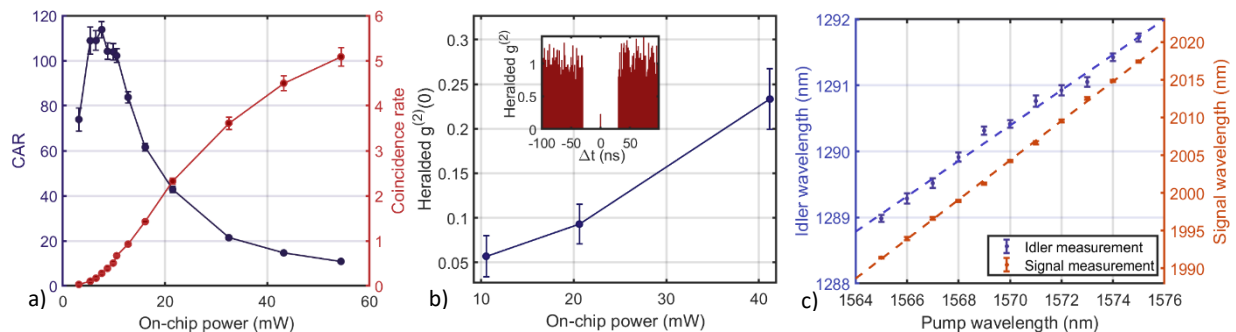


Fig. 2. a) CAR (dark blue) and net coincidence rate (dark red) as a function of pump power. b) $g_H^{(2)}(0)$ as a function of pump power. c) Signal (orange) and idler (purple) variation wavelengths as a function of pump wavelength.

wavelength can be tunable. Through the SFWM process, this can be easily achieved by simply tuning the wavelength of the pump. Fig. 2c shows the variation of the measured wavelength of the generated photons as a function of the wavelength of the pump. This is possible thanks to the energy conservation, which governs the spontaneous process used. In particular, the signal spans a range of more than 20 nm when the pump wavelength is changed by ± 5 nm, while the idler variation is less than ± 1.5 nm. In this way, the source can be used to perform broadband spectroscopy, while the idler can be easily filtered out and detected, all by shifting the pump laser wavelength by a few nanometers. The same tuning cannot be achieved with commonly used intramodal SFWM.

To compare GS with classical spectroscopy, we measured both the count rates of signal photons (classical spectroscopy) and the net coincidences between idler and signal photons (GS) as a function of pump wavelength. To perform this measurement and to emphasize the advantage of GS, an external environmental noise is inserted into the photon signal detection line, inducing a low signal-to-noise ratio (SNR) on the bare signal detection ($\text{SNR} \ll 1$). Fig. 3 shows the theoretical spectrum of the CO_2 (black line), compared with the CO_2 measured with

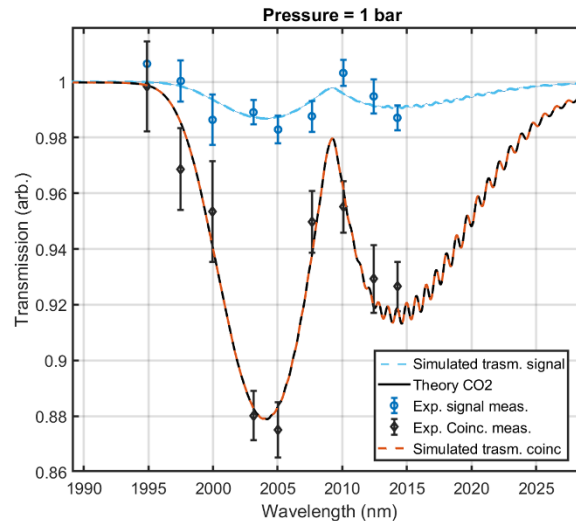


Fig. 3. Measurement with a cell filled with 1 bar CO_2 . The dark blue dots is the classical spectroscopy measurement, the blue dashed line the performed simulation. The black dots is the experimental GS measurements, the orange dashed line the performed simulation. The black line corresponds to the theoretical spectrum. The experimental count rates are recorded as a function of wavelength.

classical spectroscopy (dark blue dots) and with the GS technique (black dots) and the corresponding simulations (dashed lines). A significant reduction of the noise baseline is observed in the net coincidence spectrum, resulting in improved visibility of the spectral measurement.

With this measurement, we demonstrate that GS retrieves correctly the spectrum of CO_2 , providing at the same time higher visibility with respect to classical spectroscopy in the same noisy environment. The simulations perfectly match the trend of the experimental measurements obtained. This result paves the way to miniaturized quantum devices able to surpass classical limitations faced by MIR technologies.

DISCUSSION

In this work, we discussed the use of an integrated silicon entangled photon source for MIR ghost spectroscopy through the intermodal SFWM process. Using the GS technique, we demonstrate noise reduction in the presence of unknown environmental noise by coincidence measurements. This can be seen as a temporal filter, allowing us to retain all correlated photons and exclude all uncorrelated counts composed of the accidental counts and noise. The future perspective is to show a higher spectral resolution in the MIR by filtering only the beam in the NIR. This is possible by exploiting the spectral correlation that characterizes the CW-pumped SFWM.

Acknowledgements: This project has been supported by Q@TN, the joint lab between University of Trento, FBK-Fondazione Bruno Kessler, INFN-National Institute for Nuclear Physics and CNR-National Research Council.

References

- [1] Andreas Fix, et al. "Upconversion-based lidar measurements of atmospheric CO_2 ". In *Optics and Photonics for Energy and the Environment*, pages EM4A-5. Optical Society of America, 2016.
- [2] Petter Weibring, Hans Edner, and Sune Svanberg. "Versatile mobile lidar system for environmental monitoring". *Applied Optics*, 42(18):3583-3594, 2003.
- [3] Yulong Su et al. "10 GBPS DPSK transmission over free-space link in the mid-infrared". *Optics Express*, 26(26):34515-34528, 2018.
- [4] Giuseppe Bellisola and Claudio Sorio. "Infrared spectroscopy and microscopy in cancer research and diagnosis". *American journal of cancer research*, 2(1):1, 2012.
- [5] Kimberlee Potter, Linda H Kidder, Ira W Levin, E Neil Lewis, and Richard GS Spencer. "Imaging of collagen and proteoglycan in cartilage sections using fourier transform infrared spectral imaging". *Arthritis & Rheumatism*, 44(4):846-855, 2001.
- [6] Daniel Popa and Florin Udrea. "Towards integrated mid-infrared gas sensors". *Sensors*, 19(9):2076, 2019.
- [7] Rebecca Whittaker et al. "Absorption spectroscopy at the ultimate quantum limit from singlephoton states". *New Journal of Physics*, 19(2):023013, 2017.
- [8] Giorgio Brida, Marco Genovese, and I Ruo Berchera. "Experimental realization of sub-shot-noise quantum imaging". *Nature Photonics*, 4(4):227, 2010.
- [9] Prabhakar, Shashi, et al. "Two-photon quantum interference and entanglement at 2.1 μm ." *Science advances* 6.13 (2020): eaay5195.

- [10] Marco Fiorentino et al. "Spontaneous parametric down-conversion in periodically poled KTP waveguides and bulk crystals". *Optics express*, 15(12):7479–7488, 2007.
- [11] TB Pittman, YH Shih, DV Strekalov, and Alexander V Sergienko. "Optical imaging by means of two-photon quantum entanglement". *Physical Review A*, 52(5):R3429, 1995.
- [12] Kalachev, A. A., et al. "Biphoton spectroscopy of YAG: Er³⁺ crystal." *Laser Physics Letters* 4.10 (2007): 722.
- [13] Stefano Signorini et al. "Intermodal four-wave mixing in silicon waveguides". *Photonics Research*, 6(8):805–814, 2018.
- [14] Stefano Signorini et al. "Silicon photonics chip for inter-modal four wave mixing on a broad wavelength range". *Frontiers in Physics*, 7:128, 2019.
- [15] Signorini, S., et al. "A silicon source of heralded single photons at 2 μ m." *APL Photonics* 6.12 (2021): 126103.
- [16] Mattia Mancinelli et al. "Mid-infrared coincidence measurements on twin photons at room temperature". *Nature communications*, 8(1):1–8, 2017.
- [17] Paesani, Stefano, et al. "Near-ideal spontaneous photon sources in silicon quantum photonics." *Nature communications* 11.1 (2020): 1-6.
- [18] Signorini, S., and L. Pavesi. "On-chip heralded single photon sources." *AVS Quantum Science* 2.4 (2020): 041701.
- [19] Rosenfeld, Lawrence M., et al. "Mid-infrared quantum optics in silicon." *Optics Express* 28.25 (2020): 37092-37102.

Rethinking Sensing – Developing Next Generation Camera Technology

(Invited paper)

Johannes Bütow¹, Jörg S. Eismann^{1,2,3}, Varun Sharma¹, Dorian Brandmüller¹, and Peter Banzer^{1,2,3,*}

¹Institute of Physics, University of Graz, NAWI Graz, Austria

²Max Planck Institute for the Science of Light, Erlangen, Germany

³Institute of Optics, Information, and Photonics, University Erlangen-Nuremberg, Germany

*corresponding author, e-mail: peter.banzer@uni-graz.de

We discuss the utilization of reconfigurable photonic integrated circuits for the measurement of spatial phase, polarization, and intensity distributions of light beams. The fundamental principle as well as the main building blocks of this novel detector platform will be discussed.

Keywords: *silicon photonics, photonic integrated circuits, superpixels, structured light*

INTRODUCTION

Conventional detectors like cameras or photodiodes are usually ‘blind’ for parameters different than intensity or power. Additional optical elements, more complicated architectures, or completely different approaches are necessary to make them ‘see’, for instance, the phase and polarization of a light field or beam. All-integrated photonic circuits are also well suited for the aforementioned task of measuring (and shaping) light fields. They hold great potential as actively controllable on-chip detectors, inherently sensitive to intensity, phase and polarization, if constructed and calibrated appropriately.

DISCUSSION AND RESULTS

The structure of electromagnetic fields in general and light in particular plays a crucial role in many fields of research and applications, ranging from light steering and management at the nanoscale [1-3], (nano-)metrology [4-6], advanced spectroscopy [7,8], endoscopy [9] all the way to free-space (quantum) communications [10]. However, although very important, the direct and simultaneous measurement of light’s spatial degrees of freedom (intensity, phase, and polarization) is far from trivial. We now propose, implement and apply a novel route towards the spatially resolved measurement of said parameters. The corresponding novel detector consists of a reconfigurable photonic integrated circuit (PIC; see figure). Grating couplers, meshes of waveguides and Mach-Zehnder interferometers serve as an all-integrated platform – also referred to as Super-Pixels – for on-chip light processing [11-14]. After calibration of the system based on a known input field, the relative intensity and phase information between all pixels can be measured for arbitrary input beams [13]. The chosen architecture and layout of the input grating couplers (free-space interface) also provide for additional information about the polarization of input light fields. In addition, the PIC can also be ran in reverse to not only detect but also emit sculpted beams of light [14], with potential applications in beam steering, shaping, and optical communications.

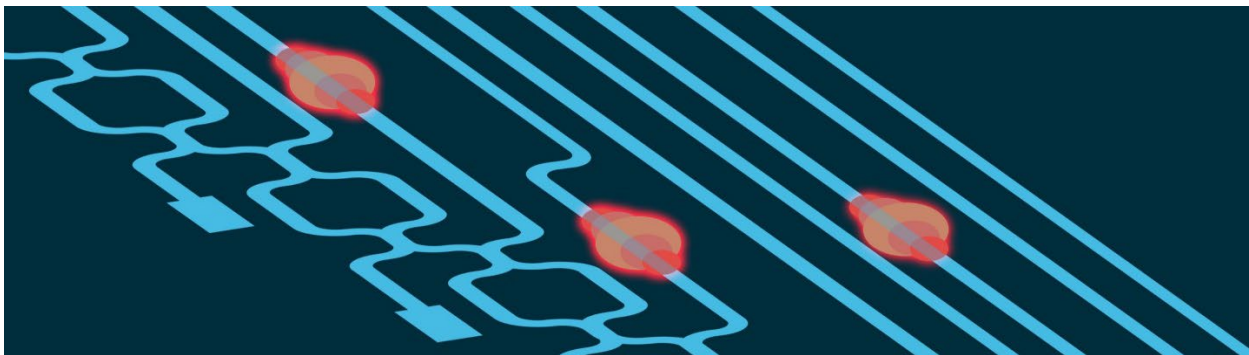


Fig. 1. Artistic impression of a photonic integrated circuit (PIC) consisting of silicon waveguides, on-chip interferometers, etc. Grating couplers arranged in a desired manner act as an input interface sampling a light beam in a spatially resolved manner (not shown). If combined with electronic phase-shifters (heaters), the waveguide modes can be manipulated selectively, eventually allowing for the retrieval of intensity, phase, and polarization information of the light field impinging on the PIC.

CONCLUSION

Novel integrated detectors capable of simultaneously measuring light's spatial intensity, phase and polarization distributions constitute a powerful addition to the existing detector toolbox. They pave the way towards intriguing applications in nano-optics, imaging, endoscopy, and optical communication. With their unique ability to also re-emit and shape the light field they are extremely versatile and flexible. In this presentation, we plan to introduce the corresponding photonic integrated architecture of superpixels, their building-blocks, and discuss selected applications.

Acknowledgement: We thank the Super-Pixels consortium for very valuable support and countless fruitful discussions. This project has received funding from the European Commission Horizon 2020 research and innovation programme under the Future and Emerging Technologies Open Grant Agreement Super-Pixels No. 829116.

References

- [1] S. Nechayev, J. S. Eismann, M. Neugebauer, P. Woźniak, A. Bag, G. Leuchs, P. Banzer, Huygens' dipole for polarization-controlled nanoscale light routing, *Phys. Rev. A* 99, 041801, 2019
- [2] M. F. Picardi, A. V. Zayats, F. J. Rodríguez-Fortuño, Janus and Huygens dipoles: near-field directionality beyond spin-momentum locking, *Phys. Rev. Lett.* 120, 117402, 2018
- [3] J. E. Vazquez-Lozano, A. Martinez, F. J. Rodriguez-Fortuno, Near-Field Directionality Beyond the Dipole Approximation: Electric Quadrupole and Higher-Order Multipole Angular Spectra, *Phys. Rev. A.* 12, 024065, 2019
- [4] M. Neugebauer, P. Wozniak, A. Bag, G. Leuchs, P. Banzer, Polarization-controlled directional scattering for nanoscopic position sensing, *Nature Commun.* 7, 11286, 2016
- [5] A. Bag, M. Neugebauer, P. Wozniak, G. Leuchs, P. Banzer, Transverse Kerker scattering for Angström localization of nanoparticles, *Phys. Rev. Lett.* 121, 193902, 2018
- [6] J. S. Eismann, M. Neugebauer, K. Mantel, P. Banzer, Absolute characterization of high numerical aperture microscope objectives utilizing a dipole scatterer, *Light: Science & Applications*, 10(1), 1-7, 2021
- [7] S. Grosche et al., Towards polarization-based excitation tailoring for extended Raman spectroscopy, *Optics Express* 28, 7, 2020
- [8] P. Woźniak and P. Banzer, Single nanoparticle real and k-space spectroscopy with structured light, *New Journal of Physics* 23, 10, 2021
- [9] P. Jákł et al., Endoscopic Imaging Using a Multimode Optical Fibre Calibrated with Multiple Internal References, *Photonics* 9, 1, 2022
- [10] M. P. J. Lavery et al., Free-space propagation of high-dimensional structured optical fields in an urban environment, *Science Advances* 3, 10, 2017
- [11] D. A. B. Miller, Self-aligning universal beam coupler, *Opt. Express* 21, 6360-6370, 2013
- [12] D. A. B. Miller, Self-configuring universal linear optical component, *Photonics Res.* 1, 1-15, 2013
- [13] J. Bütow, J. S. Eismann, M. Milanizadeh, F. Morichetti, A. Melloni, D. A. B. Miller, P. Banzer, Spatially resolving amplitude and phase of light with a reconfigurable photonic integrated circuit, Submitted, 2022
- [14] M. Milanizadeh, F. Toso, G. Ferrari, T. Jonuzi, D. A. B. Miller, A. Melloni, and F. Morichetti, Coherent self-control of free-space optical beams with integrated silicon photonic meshes, *Photon. Res.* 9, 2196-2204, 2021

Integrated Computer Generated Waveguide Hologram for Versatile Free-Space Beam Projection

(Student paper)

David De Vocht, Tianran Liu, Yuqing Jiao, Erwin Bente

Eindhoven University of Technology, 5612 AZ, Eindhoven, The Netherlands

e-mail: d.j.v.d.vocht@tue.nl

We present integrated Computer Generated Waveguide Hologram couplers that can emit or receive free-space optical beams at an ultra-long working distance. Single wavelength waveguide holograms for 1300, 1450 and 1600 nm have been designed, fabricated and characterized. We demonstrate the focusing of optical beams 10 mm above the optical chip's surface with beam waists closely approaching the diffraction limit in one dimension.

Keywords: *integrated photonics, free-space radiation, hologram, photonic-free-space coupling, sensing*

INTRODUCTION

Monolithically integrating a coupler on a photonic integrated circuit that can emit or receive free-space beams focussed at an ultra-long working distance, enables further miniaturization of optical devices by reducing the need for external optics such as lenses or gratings. Small area grating couplers ($\sim 10 \times 10 \mu\text{m}^2$) are widely used to couple light out to an optical fiber near the chip. For focusing at ultra-long distances ($\sim 1 \text{ cm}$), which is useful in e.g. optical sensing or free-space optical communication, diffraction makes that much larger couplers ($\sim 400 \times 400 \mu\text{m}^2$) are required. Furthermore, both the phase and intensity profile of the emitted beam - the coupler's near-field - need to be accurately controlled. Backlund et al [1] designed and demonstrated a Computer-Generated Waveguide Hologram (CGWH) consisting of a 2D array of grating lines. They engineered the offset of each grating line to obtain the required phase profile. Additionally, apodizing the filling factor of the grating lines allows to uniformly distribute the intensity over the surface of the coupler [2]. A limitation of the modelling used in [1-2] is the assumption that the optical behaviour of the pixels is independent of each other, i.e. changing the scattering properties of one pixel does not affect its neighbours. This limited the performance that could be demonstrated.

In previous work, we have shown that the neighbouring pixels do affect each other and that this has a large influence on the far-field pattern [3]. Therefore, we have developed a new model and design tool for waveguide holograms that incorporates the effects of neighbouring pixels [3]. By designing and demonstrating three single wavelength CGWH couplers for 1300, 1450 and 1600 nm with an ultra-long working distance of 1 cm, we prove that our model is highly flexible and suited for broadband applications. We have fabricated these couplers on the InP Membrane on Silicon (IMOS) platform that allows for dense monolithic integration of lasers and other building blocks [4]. In this paper, we present an overview of the design and the performance of the realised devices.

DESIGN

The conversion of the light field from the regular single-mode IMOS waveguide to free space occurs in three stages as shown in Figure 1. In the first stage, an 80 μm long taper expands the waveguide mode from 400 nm to 5 μm . In the second stage, the mode is expanded further in a 1 mm long slab waveguide. In the third stage, this wave enters the hologram, formed by a 2D array of subwavelength grating lines made in a Si_3N_4 layer above the InP slab waveguide. Each grating line scatters a small part of the light outward and induces a phase shift on the remaining propagating light in the slab waveguide.

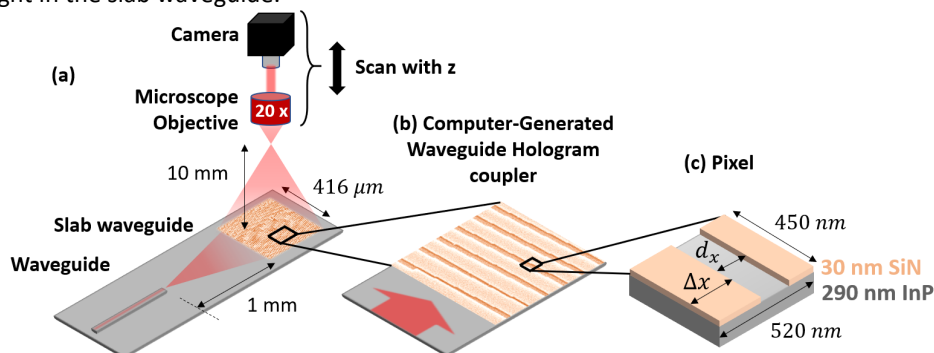


Fig. 1 (a) Schematic of the integrated chip and the measurement set-up. (b) Zoomed view of the CGWH and (c) one of its pixels.

We engineer the thickness of each grating line and its offset Δx from the edge of the pixel (i.e. the distance between them) to carefully control the upward coupling strength and phase shift at each pixel in the array. First, we linearly apodize the grating lines' thickness from 104 to 208 nm at $x = 0$ and $416 \mu\text{m}$, respectively. Then, we simulate using 2D FDTD in Lumerical the effects of neighbouring grating lines in the xz -plane on the far-field emission. This simulation includes an input beam confined in a waveguide, three consecutive grating lines etched in this waveguide and a field-profile monitor 700 nm above the grating lines. For different thicknesses and positions of the grating lines, we calculate the far-field profile of the monitor to determine which percentage of the scattered light will arrive at the target location. A 3D FDTD simulation can also analyse the effects from neighbouring pixels in the y -direction, however, this would highly increase the simulation time (currently 2-3 hours). Finally, we use a similar algorithm as described in [1] to optimize the offsets of the different grating lines [3].

To focus a $50 \mu\text{m}$ spot at an ultra-long distance of 10 mm, we need a large area coupler of at least $416 \mu\text{m}$ due to diffraction. Based on our algorithm, we have designed three single wavelength CGWH _{λ} couplers for wavelengths λ of 1300, 1450 and 1600 nm. We have fabricated the holograms monolithically in a 30 nm-thin Si₃N₄ layer deposited on top of a 290 nm-thick InP slab waveguide. By using a different material for the hologram, we can exploit the high dry etch selectivity between Si₃N₄ and InP. Our fabrication process is similar to [5], except that we do not use a metallic mirror and opt for Si₃N₄ instead of SiO₂ as it provides a higher coupling strength.

PERFORMANCE

In the experimental set-up, we use three fiber-coupled tunable lasers at 1300, 1450 and 1600 nm, respectively, and couple them via a side-fire fiber into on-chip grating couplers. A 20x microscope objective (Mitutoyo Plan APO NIR using a tube lens with a focal length of 200 mm) captures the light emitted by the CGWHs (Fig. 1). We mounted the objective and the camera on a motorized stage (CONEX-MFACC - Newport) to measure the far-field at different distances.

Figures 2(a-c) show the measured near- and far-field patterns of the different couplers. We notice that CGWH₁₃₀₀ already couples a large part of its light at the start of the hologram (Fig 2ab). This reduces the confinement of the light at the focusing plane in the x -direction (Fig. 2c).

The near-field pattern of CGWH₁₃₀₀ indicates that the current apodization is not strong enough as most of its light still couples out at the start of the coupler (Fig. 2a). Thus we need to reduce the thickness of the first grating line further. From the far-field pattern of CGWH₁₃₀₀, we notice that its strongest spot in the focal plane lies on a line with an angle of 0.02° from the normal. On the other hand, CGWH₁₄₅₀ and CGWH₁₆₀₀ both uniformly couple the light out of the hologram (Fig. 2b) and focus it with nearly an identical incident angle of -0.65° and -0.70° , respectively, at the focusing plane (Fig. 2a).

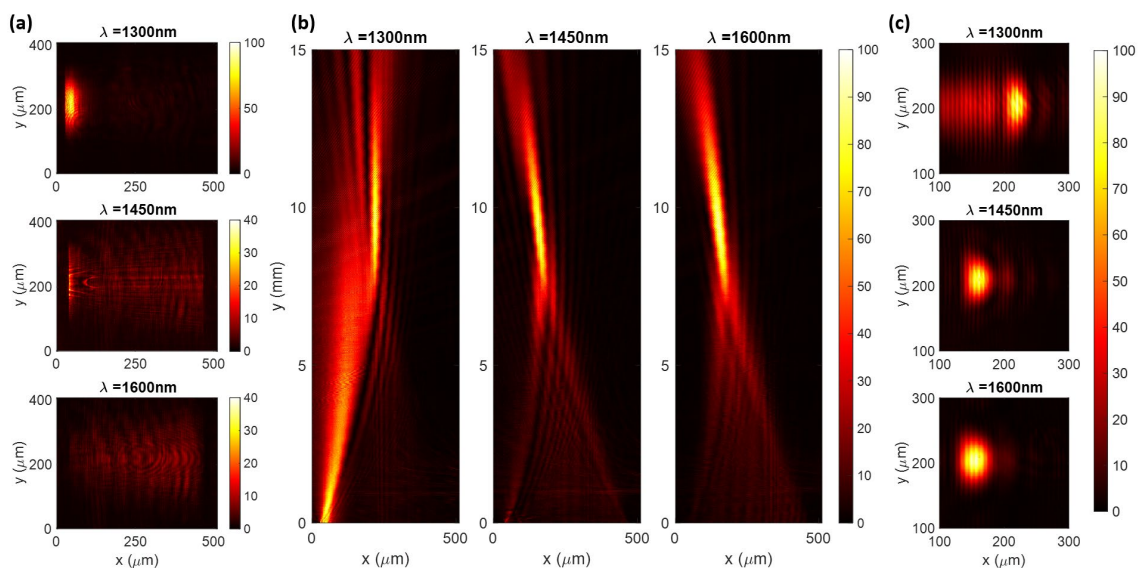


Fig. 2 (a) Measured near-field and (b) far-field intensity distributions in the axial and (c) focal plane of the different CGWH _{λ} operating at wavelengths of 1300, 1450 and 1600 nm. The colour bars indicate the normalized intensity for each CGWH _{λ} .

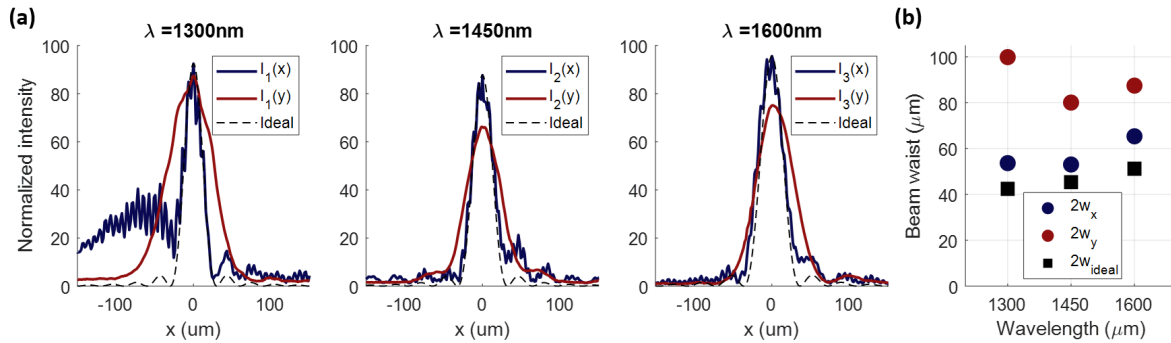


Figure 3 (a) Intensity of the x - (blue) and y -profile (red) across the measured focal spots of the different CGWH $_i$ operating at wavelengths of 1300, 1450 and 1600 nm compared to the diffraction-limited case of a uniformly illuminated flat-lens (ideal). The x -axis represents the relative position to the centre of the peak. (b) Beam waists ($1/e^2$) after fitting the measured intensity at the focal plane with a 2D Gaussian and for the diffraction-limited case without fitting (ideal).

Figure 3(a) shows the intensity profile of the horizontal $I_\lambda(x)$ and vertical cut $I_\lambda(y)$ of the measured focal spot of CGWH $_\lambda$ compared to the diffraction-limited case of a uniformly illuminated flat lens with focus $f = 10\text{ mm}$ having the same area as the coupler. We calculate the intensity profile of the diffraction-limited case to be proportional to

$$I_{\text{diff. limit}}(x, y) \sim \text{sinc}^2\left(\frac{\pi l_x x}{\lambda f}\right) \text{sinc}^2\left(\frac{\pi l_y y}{\lambda f}\right) \quad (1)$$

where l_x and l_y represent the dimensions of the coupler. We notice that the central peak of the different $I_\lambda(x)$ closely resembles with $I_{\text{diff. limit}}$. We observe strong sidelobes for $I_\lambda(x)$ as expected since they approach the diffraction limit. Even the location of the sidelobes matches with those of $I_{\text{diff. limit}}$. Moreover, we detect a fringe pattern for $I_\lambda(x)$ with a periodicity of several micrometres. Potentially, other functional devices or fabrication inaccuracies – e.g. particles or roughness – on the chip scatter part of the incident light which interferes with the coupler’s signal.

Figure 3(b) displays the beam waists after fitting the measured intensity at the focal plane with a 2D Gaussian fit and for $I_{\text{diff. limit}}$. While the beam waists in the x -direction are equal to 53-66 μm , they are 81-100 μm in the y -direction, an increase of 34 – 86%. The fact that the near-fields of CGWH $_{1450}$ and CGWH $_{1600}$ show a lower uniformity in the y -direction as opposed to the x -direction can explain this effect (Fig. 2b). This is not evidently noticeable for CGWH $_{1300}$. In general, apodizing the structures also in the y -direction will ensure higher uniformity of the near-field.

CONCLUSION

We have realized three monolithic integrated couplers that can focus light at an ultra-long working distance of 10 mm above the chip plane at respective wavelengths of 1300, 1450 and 1600 nm. The CGWH couplers achieve near-vertical focusing ($\theta < 0.7^\circ$) with beam waists ($1/e^2$) in the x -direction (53-66 μm) closely approaching the diffraction limit. Apodizing the structures in the y -direction will reduce these beam waists (81-100 μm) as well. Further research will focus on multiwavelength CGWH couplers and integration with other on-chip components to demonstrate its potential for gas sensing or compact position sensors.

Acknowledgements: This publication is part of NWO HTSM 2019 project 17971 which is (partly) financed by NWO. We thank professor Irwan Setija for the insightful discussions.

References

- [1] A. Larsson, C.-F. Carlström, J. Backlund, and J. Bengtsson, “Input waveguide grating couplers designed for a desired wavelength and polarization response,” *Applied Optics*, Vol. 41, Issue 15, pp. 2818-2825, vol. 41, no. 15, pp. 2818–2825, May 2002.
- [2] V. O. Smolski, O. v. Smolski, E. C. Browy, E. G. Johnson, and Z. A. Shellenbarger, “Design and experimental study of the controlled two-dimensional-intensity profile of the output beam from a broad-area laser diode using grating outcouplers,” vol. 51, no. 7, p. 074204, Jul. 2012.
- [3] T. Liu, Y. Jiao, and E. Bente, “Design of a computer-generated waveguide hologram for integrated free space sensing,” *Proceedings of the International Conference on Numerical Simulation of Optoelectronic Devices, NUSOD*, vol. 2021-September, pp. 95–96, Sep. 2021.
- [4] Y. Jiao et al., “Indium Phosphide Membrane Nanophotonic Integrated Circuits on Silicon,” *physica status solidi (a)*, vol. 217, no. 3, p. 1900606, Feb. 2020.

- [5] Y. Wang et al., "InP-Based Grating Antennas for High-Resolution Optical Beam Steering," IEEE Journal of Selected Topics in Quantum Electronics, vol. 27, no. 1, Jan. 2021.

Broadband optical beam steering over a wide field of view with a silicon quadratic metalens

Yang Liu^{1,2}, Jianhao Zhang¹, Xavier Le Roux¹, Cedric Villebasse¹, Eric Cassan¹, Delphine Marris-Morini¹, Laurent Vivien¹, Carlos Alonso-Ramos¹, and Daniele Melati^{1,*}

¹Centre de Nanosciences et de Nanotechnologies, Université Paris-Saclay, CNRS, 91120 Palaiseau, France

²Currently with DTU Fotonik, Technical University of Denmark, Ørsteds Plads 343, 2800 Kgs. Lyngby, Denmark

* daniele.melati@universite-paris-saclay.fr

Metasurfaces are a potential candidate to substitute bulk lenses in optical beam steering devices. However, off-axis and chromatic aberrations often limit their applicability. Here, we report on a single-layer, silicon metalens simultaneously providing a large field of view and broadband achromatic behaviour at optical communication wavelengths. The metalens features a quadratic phase profile, a numerical aperture of 0.83, and allows beam collimation and steering over a field of view of 86° and a bandwidth of 140 nm.

Keywords: beam steering, silicon on insulator technology, dielectric metalens, metasurface

INTRODUCTION

Photonic technologies such as light detection and ranging (lidar) and free-space optical communications have attracted a surging interest in the last few years, both from the academic and industrial point of view. This has ignited an intense research on compact solutions capable of generating, shaping, and steering optical laser beams. Integrated optical phased arrays are among the most vastly exploited devices that allow achieving these functionalities. By controlling the relative phase of the light emitted by an array of integrated antennas, it is possible to generate beams with divergence smaller than 0.1° and steer them over a field of view of a few tens of degrees [1,2]. However, phased arrays requires either the use of a laser with the emission wavelength tuneable over hundreds of nanometers or alternatively a very large number of integrated phase shifters.

A different approach to achieve beam steering relies on an array of antennas placed at the focal plane of a lens (focal plane array). Turning on one antenna at the time allows changing the position at which light arrives at the lens and hence the direction of the outgoing collimated beam [3,4]. A promising way to improve the compactness of such a system is to substitute the lens with a flat metasurface (metalens), i.e., a two-dimensional arrangement of subwavelength scattering elements [5]. While high optical performances have been demonstrated [6], metalenses often suffer from off-axis and chromatic aberrations. Simultaneously ensuring broadband operation and a wide field of view remains challenging [7], limiting the applicability of metalenses in the context of beam steering.

Here, we present the design and experimental demonstration of a silicon metalens at optical communication wavelengths overcoming this limitation. The use of a quadratic phase profile and a high numerical aperture of 0.83 allowed experimentally demonstrating a wide field of view of 86°, limited by our experimental setup. Additionally, this phase profile made the metalens inherently tolerant to chromatic aberrations, enabling an operational bandwidth of 140 nm.

RESULTS

Figure 1a schematically shows how beam steering can be achieved using a metalens and an array of antennas placed at its focal plane. If the antenna is aligned with the central axis of the lens, the emitted diverging beam propagating in the z direction is collimated and does not change direction upon crossing the metalens. When the antenna illuminates instead the metalens from an off-center position, for example with a displacement along the x axis, the collimated beam will be directed at a different angle in the far field, achieving beam steering. Reciprocally, when a plane wave illuminates the metalens at different incident angles, light is focused at different positions along x.

In order to achieve this behavior, we designed a metalens with a quadratic phase profile

$$\varphi(r) = -\omega r^2 / (2cf), \quad (1)$$

where ω is the frequency of the light, c is the speed of light, f is the focal distance of the metalens, and r is the radial distance from the central axis. The lens was designed to focus light in air. The choice of this phase profile was dictated by its particular characteristics. Compared to diffraction-limited metalenses, the use of a quadratic phase profile introduces spherical aberration which limits the resolution and gives the lens a rather long depth of focus

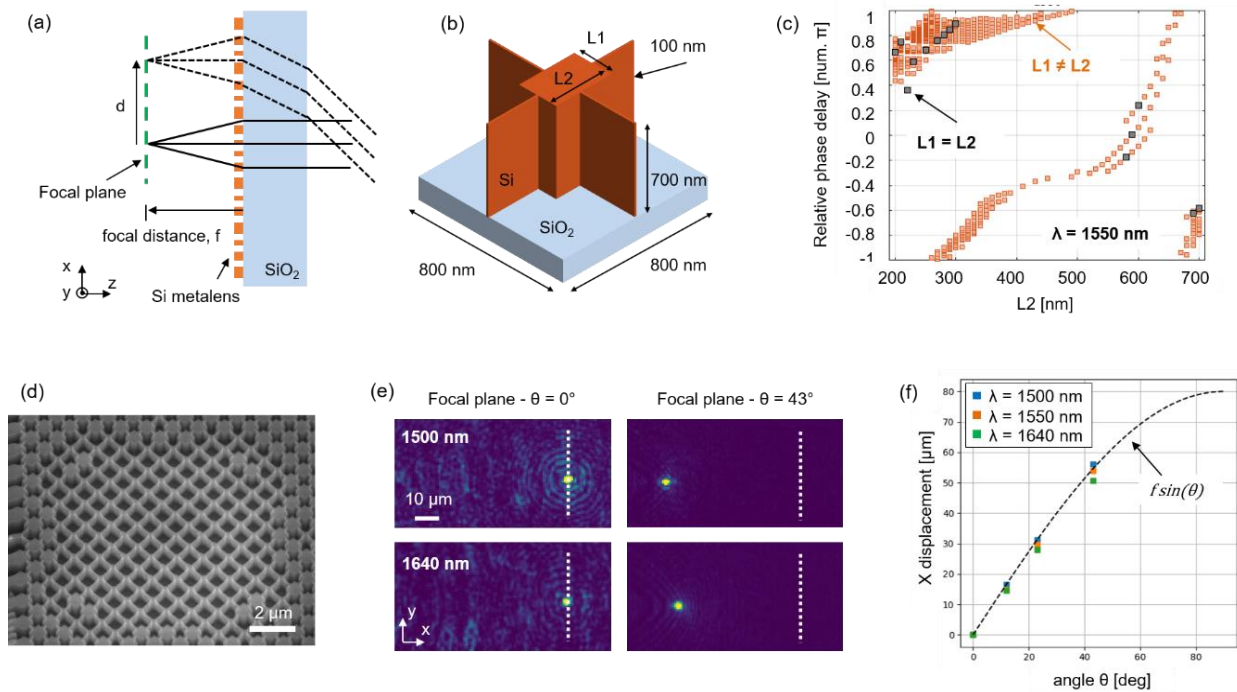


Fig. 1. (a) Sketch representing the metalens operation. Light incident at an angle is focused on the image plane at a distance d from the axis, virtually free of spherical aberrations. (b) Structure of the meta-atom used to realize the fishnet metalens. The dimensions $L1$ and $L2$ of the pillar are the design parameters. (c) Relative phase delay imparted by the meta-atom as a function of $L2$ for different values of $L1$ (orange marks) for $\lambda=1550$ nm. If $L1 = L2$, the range $[-\pi, \pi]$ cannot be properly sampled (black marks). (d) Scanning electron microscope (SEM) image of the center of the realized metalens. (e) Focal spot at the image plane with $\lambda=1500$ nm and $\lambda=1640$ nm for normal ($\vartheta=0^\circ$) and tilted incidence ($\vartheta=43^\circ$) in the x - z plane, as defined in (a). In the latter case, the focal spot remains undistorted and shifts along the x axis. (f) Focal spot displacement as a function of the incident angle ϑ for $\lambda=1500$ nm, $\lambda=1550$ nm, and $\lambda=1640$ nm. The dashed black line represents the expected displacement calculated using the metalens focal distance $f = 80 \mu\text{m}$.

[8]. At the same time, however, the lens properly focuses light also under tilted illumination. The focal spot remains undistorted and simply shifts in the focal plane by a quantity $d = f \sin(\theta)$, being θ the incident angle. The phase profile (1) hence represents an interesting choice for beam steering applications and allows achieving the behavior described in Fig. 1a. While limited resolution could be problematic for imaging applications, in the case of beam steering this is not necessarily a limiting factor since the optimal spot size would ultimately be determined by the size of the antenna. On the contrary, when used in combination with a focal plane array, a quadratic metalens would allow beam steering over an arbitrarily large field of view [9].

The described metalens was realized using a fishnet structure composed of the meta-atoms schematically represented in Fig. 1b. Silicon pillars have a height of 700 nm and are fabricated on top of a SiO_2 substrate. The lattice period is fixed at 800 nm. The width of the cross fins is fixed at 100 nm while $L1$ and $L2$ are varied between 200 nm and 700 nm. For each combination of $L1$ and $L2$ we computed the phase delay and amplitude modulation imparted by the meta-atom to an incident wavefront at $\lambda = 1550$ nm. We disregarded all meta-atoms with transmission lower than 0.5 in order to minimize losses. For the remaining set of pillars, the relative phase delay as a function of $L2$ is reported in Fig. 1c for different values of $L1$ with orange dots. As can be seen, the pillars produce a phase shift from $-\pi$ to π depending on the values of $L1$ and $L2$. It is worth noticing that this is not the case if the geometry of the pillars is constrained to $L1 = L2$ (square pillars, black dots in Fig. 1c).

The obtained library of meta-atoms was used to discretize the phase profile (1) considering a wavelength $\lambda = 1550$ nm, a lens diameter of 240 μm , and focal length of 80 μm , corresponding to a lens with numerical aperture $\text{NA} = 0.83$. The resulting structure was fabricated using electron beam lithography and dry etching (Fig. 1d). In order to characterize the behavior of the metalens we did not use it as a beam steering device but we illuminated it with a collimated laser beam and imaged the resulting focal spots in the x - y plane. We considered different illumination angles and also different wavelengths in order to also characterize the broadband performance of the lens.

Figure 1e reports on the results for $\lambda = 1500$ nm and $\lambda = 1640$ nm and illumination angles $\theta = 0^\circ$, i.e., normal incidence, and $\theta = 43^\circ$. All focal spots are imaged at a fixed distance along the z axis. As can be seen, the well-defined

spot remains almost unchanged in all the four considered cases. Under tilted illumination, its position on the focal plane shifts, as expected, along the x axis. The displacement of the focal spot as a function of the illumination angle is shown in Fig. 1f for sampled wavelengths across the 1500 nm - 1640 nm range. The measured displacements are in very good agreement with theoretical predictions, reported in Fig. 1f with a dashed line for $\lambda = 1550$ nm. These results confirm the proper functionality of the metalens across the entire wavelength range and the achievement of a wide field of view of at least $\pm 43^\circ$. Due to limitations of our experimental setup, we could not tilt the illuminating laser beyond this limit. It should be noticed, however, that full $\pm 90^\circ$ field of view has already been demonstrated using quadratic phase profiles [8].

In order to properly characterize the broadband behavior of the metalens, two chromatic aberrations should be considered. Longitudinal chromatic aberration causes the focal distance in the z direction to reduce at longer wavelengths. In the considered 140 nm wavelength range, the shift is limited to 4 μm . This chromatic focal shift is overcome by the large depth of focus of the lens that causes the fixed image plane to fall within the focal tolerance of the lens. This is confirmed by the results in Fig. 1e showing that the focal spot does not significantly enlarge or distort because of the wavelength change. Additionally, under tilted illumination, also the displacement of the focal spot in the x direction changes with wavelength (transverse chromatic aberration), as can be seen in Fig. 1f. For $\theta = 43^\circ$, the differential displacement between $\lambda = 1500$ and $\lambda = 1640$ nm is 3 μm . This difference is smaller than the full width at half maximum of the focal spot, measured as 3.5 μm independently of the wavelength or illumination angle. The rather large dimension of the focal spot (a diffraction limited spot would have a full width at half maximum of about 1 μm) allows compensating also the effect of transverse chromatic aberration, ensuring the broadband behavior of the metalens.

DISCUSSION

We have proposed and experimentally demonstrated a metalens exploiting a quadratic phase profile to simultaneously achieve a wide field of view and broadband achromatic behavior. The silicon metalens was realized in silicon using a fishnet structure and characterized in the 1500 nm - 1640 nm wavelength range. Under tilted illumination, the metalens remained free of off-axis aberrations up to an angle of $\pm 43^\circ$, limited by our experimental setup. Moreover, the relatively large depth of focus of the lens allowed compensating for longitudinal chromatic aberration. The shift of the focal spot due to transverse chromatic aberration under tilted illumination remained smaller than the full width at half maximum of the spot, ensuring a broadband achromatic behavior across the entire 140-nm wavelength range. These results demonstrate that the use of quadratic metalenses has a great potential for applications in optical beam steering.

Acknowledgements: The fabrication of the device was performed at the Plateforme de Micro-Nano-Technologie/C2N, which is partially funded by the Conseil General de l'Essonne. This work was partly supported by the French RENATECH network.

References

- [1] C. V. Poulton, A. Yaacobi, D. B. Cole, M. J. Byrd, M. Raval, D. Vermeulen, and M. R. Watts, 'Coherent solid-state LIDAR with silicon photonic optical phased arrays', *Optics Letters*, vol. 42, no. 20, p. 4091, Oct. 2017.
- [2] R. Fatemi, A. Khachaturian, and A. Hajimiri, 'A Nonuniform Sparse 2-D Large-FOV Optical Phased Array with a Low-Power PWM Drive', *IEEE Journal of Solid-State Circuits*, vol. 54, no. 5, pp. 1200–1215, May 2019.
- [3] C. Rogers, A. Y. Piggott, D. J. Thomson, R. F. Wiser, I. E. Opris, S. A. Fortune, A. J. Compston, A. Gondarenko, F. Meng, X. Chen, G. T. Reed, and R. Nicolaescu, 'A universal 3D imaging sensor on a silicon photonics platform', *Nature*, vol. 590, no. 7845, pp. 256–261, Feb. 2021.
- [4] C. Li, X. Cao, K. Wu, G. Qiu, M. Cai, G. Zhang, X. Li, and J. Chen, 'Blind zone-suppressed hybrid beam steering for solid-state Lidar', *Photon. Res., PRJ*, vol. 9, no. 9, pp. 1871–1880, Sep. 2021.
- [5] Y.-C. Chang, M. C. Shin, C. T. Phare, S. A. Miller, E. Shim, and M. Lipson, '2D beam steerer based on metalens on silicon photonics', *Opt. Express, OE*, vol. 29, no. 2, pp. 854–864, Jan. 2021.
- [6] M. Khorasaninejad, W. T. Chen, R. C. Devlin, J. Oh, A. Y. Zhu, and F. Capasso, 'Metalenses at visible wavelengths: Diffraction-limited focusing and subwavelength resolution imaging', *Science*, vol. 352, no. 6290, pp. 1190–1194, Jun. 2016.
- [7] F. Yang, S. An, M. Y. Shalaginov, H. Zhang, C. Rivero-Baleine, J. Hu, and T. Gu, 'Design of broadband and wide-field-of-view metalenses', *Opt. Lett., OL*, vol. 46, no. 22, pp. 5735–5738, Nov. 2021.
- [8] A. Martins, K. Li, J. Li, H. Liang, D. Contedua, B.-H. V. Borges, T. F. Krauss, and E. R. Martins, 'On Metalenses with Arbitrarily Wide Field of View', *ACS Photonics*, vol. 7, no. 8, pp. 2073–2079, Aug. 2020.
- [9] Y. Liu, X. L. Roux, E. Cassan, D. Marris-Morini, L. Vivien, C. Alonso-Ramos, and D. Melati, 'Silicon-based broadband metalens for wide-angle optical beam steering', *IEEE Group IV Photonic Conference*, Dec. 2021.

Carbon Dioxide Sensing with a Photonic Integrated Differential Absorption LiDAR Transmitter

A. Pérez-Serrano, C. Quevedo-Galán, V. R. Aguilera-Sánchez, J. M. G. Tijero and I. Esquivias

CEMDATIC-ETSI Telecomunicación, Universidad Politécnica de Madrid (UPM), Madrid, 28040, Spain.

* antonio.perez.serrano@upm.es

We have designed and characterized a differential absorption LiDAR transmitter based on an Indium Phosphide Photonic Integrated Circuit that has been fabricated through an open access generic integration platform using standard building blocks. We demonstrate its suitability for carbon dioxide sensing.

Keywords: *differential absorption LiDAR, carbon dioxide sensing, random-modulation continuous wave LiDAR, photonic integrated circuits, semiconductor lasers*

INTRODUCTION

Remote sensing of greenhouse gases, such as carbon dioxide (CO₂), methane (CH₄) or nitrous oxide (N₂O), is essential to control climate change. Differential Absorption LiDAR (DIAL) is the most implemented active technique for atmospheric greenhouse gases measurements. This technique consists in launching at least two laser signals tuned at different wavelength, one close to the center of a targeted gas absorption line and the other set away from the same line in a region of low absorption. In this way, the gas concentration along the light path can be obtained by measuring the different absorption that both signals have suffered.

DIAL systems are mainly based on solid state pulsed laser sources that can provide extremely high peak powers. However, Intensity-Modulated Continuous-Wave (IM-CW) techniques have gain interest due to their low peak power requirements which allow the use of semiconductor lasers [1]. Among these techniques, Random-Modulation Continuous-Wave (RM-CW) technique [2] has already been implemented using discrete semiconductor lasers [3]. It consists in modulating the intensity of both signals with a pseudorandom sequence or M-sequence, with a delay between them. These signals are launched, and after traveling and interacting with the gas, are backscattered by a hard target and detected at the receiver. Due to the M-sequence correlation properties, performing the cross correlation of the received signals with the original M-sequence allows to determine the absorption that each wavelength has suffered and, in consequence, the gas concentration and the distance to the target. These relatively complex DIAL systems can benefit from the advantages shown by Photonic Integrated Circuits (PICs) in terms of multiple device integration, power efficiency, small footprint and weight, low cost and radiation hardness. Recently, a dual laser Indium Phosphide (InP) PIC operated in pulsed regime has been proposed for carbon dioxide sensing [4].

In this contribution, we demonstrate an InP PIC as the transmitter of a RM-CW DIAL system by measuring a carbon dioxide gas cell in a fiber setup. The PIC has been fabricated through an open access generic integration platform using standard building blocks. We discuss its design and the performance of the different integrated devices as well as the PIC as a whole.

DESIGN AND FABRICATION

Fig.1 shows a photograph of the fabricated device as well as its schematic. The PIC consists of three identical 4-section DBR lasers. All lasers are designed to emit close to 1572 nm and include an internal photodiode (PD) (not indicated) to monitor their output power. Lasers 1 and 2 are used to perform the DIAL measurement and are tuned to λ_1 and λ_2 , respectively. Laser REF is used together with fast PDs, PD1 and PD2, to tune and stabilize the emission wavelength of lasers 1 and 2 by measuring their beating notes while keeping the Laser REF wavelength tuned to the CO₂ absorption line through an electro-optical loop in the same way as in [3]. Therefore, the PIC contains not only the transmitter for the DIAL system but also the optical part of the stabilization unit. The pseudorandom modulation of each signal is implemented with electro-absorption modulators EAM1 and EAM2, respectively. Five Semiconductor Optical Amplifiers (SOAs) are integrated to provide gain to the outputs of the PIC and to control the output power of the different lasers. The chip has two optical outputs, one for the DIAL signals and the other for the reference signal, denoted as OUTPUT and OUTPUT REF, respectively. On the electrical side, the PIC has twenty DC electrical pads for providing current and voltage to the different blocks and measuring the internal PDs. In the lower part of the PIC, four RF ground-signal-ground pads are used for modulating the EAMs and getting the beating note signals from the fast PDs. The backside of the chip is the common ground for all DC blocks.

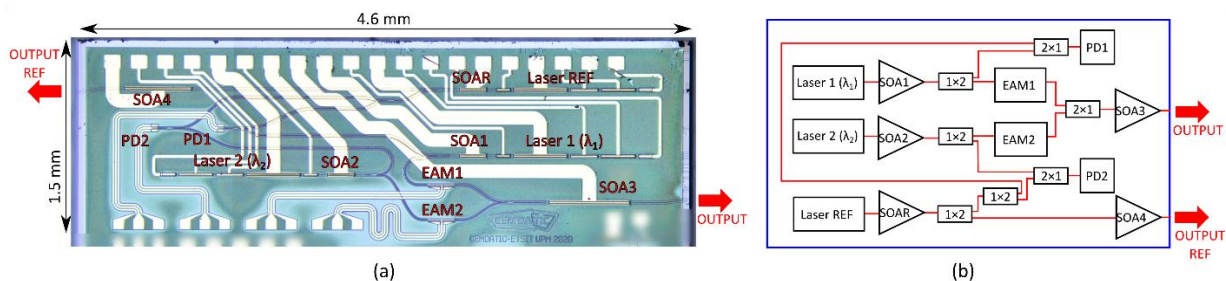


Fig. 1. (a) Photograph of the developed PIC transmitter for RM-CW DIAL with a size of 4.6×1.5 mm. (a) Schematic of the PIC.

The PIC has been fabricated by SMART Photonics through the open access platform JePIX (Joint European Platform for Photonic Integration of Components and Circuits). The initial design and simulations were performed using VPIphotonics Design Suite while the final design and layout was created with Nazca Design.

EXPERIMENTAL RESULTS

We have experimentally characterized the different blocks and devices that are integrated in the PIC. The DBR lasers are single-mode and show some degree of tunability by adjusting the current through the DBR, phase and active sections. The full PIC is also tuned by controlling its temperature. Fig. 2 (a) shows the power-current (P-I) and voltage-current (V-I) curves and their corresponding optical spectra map obtained using a 6 GHz resolution Optical Spectrum Analyzer (OSA). In the upper part of Fig. 2 (a) we can observe the behavior of Laser 1 when its current is swept. Its threshold is around 25 mA and some discontinuities and kinks are shown around 40 and 70 mA that correspond to modal jumps. In spite of this, Laser 1 shows single mode operation in almost the complete lasing range with a Side-Mode Suppression-Ratio (SMSR) of 40 dB. All DBR lasers behave similarly when operated individually. When this measurement is repeated with Laser 2 switched-on, both P-I curve and spectra change considerably as shown in the lower part of Fig. 2 (a). The Laser 1 threshold is maintained but the modal jumps sequence has changed. We attribute this to the low isolation of the DBR lasers, due to the small reflectivity of the front DBR sections, together with the amplified spontaneous emission from outer SOAs and residual reflectivity at the integrated couplers. However, a detailed exploration of the different parameters unveils regions where the whole system is stable and robust.

Fig. 2 (b) illustrates the performance of the EAMs by showing the optical spectra recorded with a high resolution (10 MHz) Brillouin Optical Spectrum Analyzer (BOSA). The wavelength difference between both lasers is 0.13 nm (15.8 GHz). We have noticed a linewidth increase in Laser 1 due to the current injection in the mirror sections that have applied to tune Laser 1 respect to Laser 2. The estimated linewidth of Laser 1 is around 700 MHz, while for Laser 2 is around 100 MHz. The extinction ratio induced by the EAMs is around 15 dB in both signals and no changes in the wavelengths are observed.

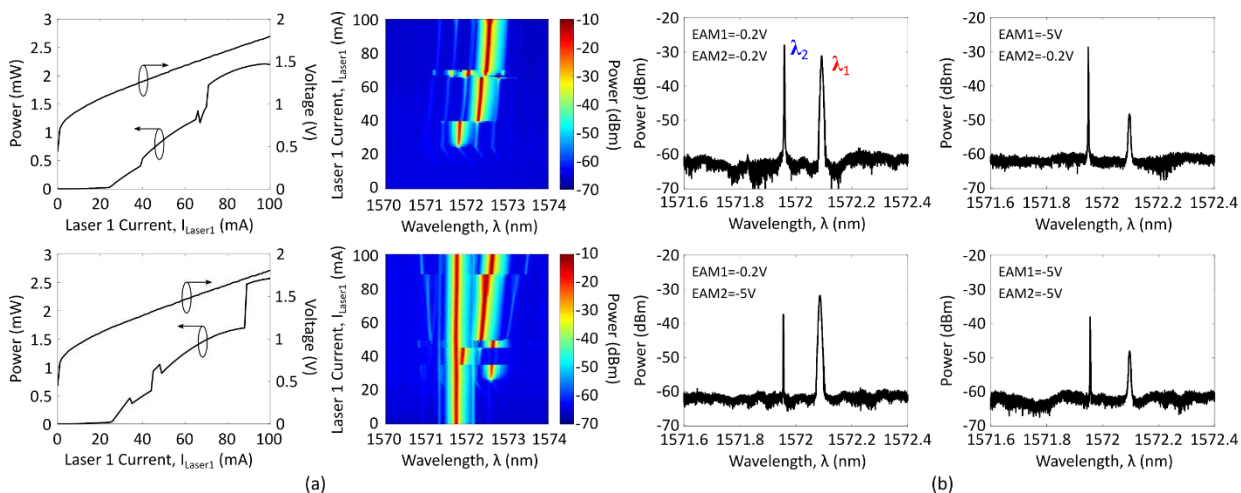


Fig. 2. (a) DBR lasers performance. Left: Power-current and voltage-current curves. Right: Their corresponding optical spectra map. Upper: Only Laser 1 switched-on and sweeping its current. Lower: Laser 2 switched-on and sweeping Laser 1 current. (b) EAMs performance. Optical spectra measured for different EAM voltages.

Fig. 3 (a) shows the experimental setup used to demonstrate the fabricated PIC for carbon dioxide sensing. The output signals from the OUTPUT port are gathered using a lensed fiber, then the light is divided in two paths, one goes directly to the receiver and the other is directed using a circulator to a path which includes the carbon dioxide gas cell and a fiber spool ended with a fiber reflector. After being reflected, the light follows the path back to the circulator which directs it to the receiver. The receiver is a PIN PD with a 200 MHz bandwidth transimpedance amplifier. The M-sequences are generated using a System-on-Chip Field Programmable Gate Array (SoC FPGA) that have fast ADC and DAC converters (100 MSA/s). It also digitizes the received signals and sends the data to a PC that performs the cross-correlation. Fig. 2 (b) shows the correlation results using a 12.5 Mbit/s 8-bit M-sequence. For this measurement, λ_2 is tuned to the peak of the chosen carbon dioxide absorption line (1572.02 nm) while λ_1 is tuned off the line (1572.2 nm). The first two peaks in the cross-correlation, E_1 and E_2 , correspond to the signals that have travelled the short path, while the two peaks, R_1 and R_2 , correspond to the signals that have travelled the path with the gas cell. From the correlation, the Differential Absorption Optical Depth (DAOD) [3], i.e. the absorption due to the gas, the Signal-to-Noise ratio (SNR) for the lowest intensity signal, the path optical losses difference (α) and the path length difference (L) can be obtained. In this case, DAOD = -0.51 dB, SNR = 13.2 dB, α = 7.6 dB and L = 1044 m, that are in agreement with the values obtained by tunable laser absorption spectroscopy performed with the BOSA and an optical time domain reflectometer.

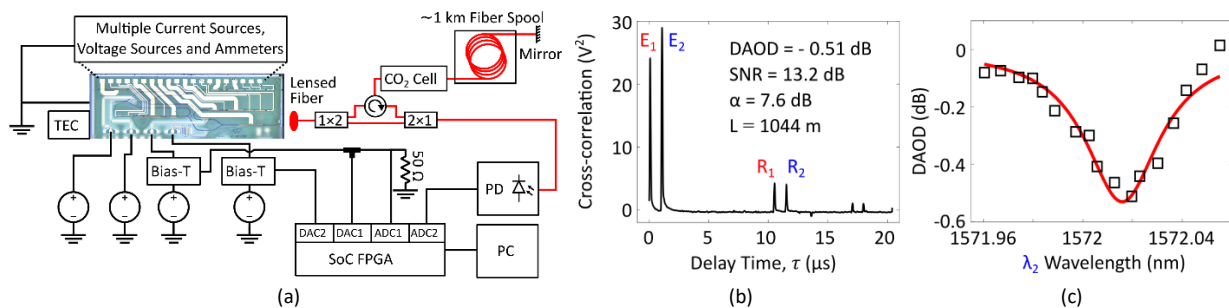


Fig. 3. (a) Experimental setup for the carbon dioxide gas cell measurement that emulates a LiDAR configuration. (b) Cross-correlation obtained averaging 50 single-sequence cross-correlations from the received signals. (c) Carbon dioxide absorption line at 1572.18 nm measured with the PIC while changing its temperature and consequently the tuning of the pair of signals.

CONCLUSIONS AND OUTLOOK

We have designed and characterized a RM-CW DIAL transmitter based on an InP PIC that has been fabricated through an open access generic integration platform using standard building blocks. We have characterized the individual integrated blocks and devices as well as the performance of the PIC as a whole. Carbon dioxide sensing with our PIC has been demonstrated by measuring a gas cell in a fiber setup. Next steps include implementing the wavelength stabilization unit and performing a real scenario measurement of atmospheric carbon dioxide.

Acknowledgements:

This work was supported by the Ministerio de Economía y Competitividad of Spain (LIDERA, RTI2018-094118-B-C21), Universidad Politécnica de Madrid and Comunidad de Madrid (MULTI-GAS-PIC, APOYO-JOVENES-KXHJ8C-16-VCKM78) and Comunidad de Madrid and FEDER Program (SINFOTON2-CM, P2018/NMT-4326).

References

- [1] J.F. Campbell, et al., *Field evaluation of column CO₂ retrievals from intensity-modulated continuous-wave differential absorption lidar measurements during the ACT-America campaign*, Earth and Space Science, vol. 7, e2019EA000847, 2020.
- [2] N. Takeuchi, N. Sugimoto, H. Baba, and K. Sakurai, *Random modulation cw lidar*, Applied Optics, vol. 22, no. 9, pp. 1382--1386, 1983.
- [3] M. Quatrevalet, et al., *Atmospheric CO₂ sensing with a random modulation continuous wave integrated path differential absorption lidar*, IEEE Journal of Selected Topics in Quantum Electronics, vol. 23, no. 2, pp. 157--167, 2017.
- [4] J. Fridlander, et al., *Dual laser indium phosphide photonic integrated circuit for integrated path differential absorption lidar*, IEEE Journal of Selected Topics in Quantum Electronics, vol. 28, no. 1, 6100208, 2022.

Low-noise frequency-agile photonic integrated lasers for coherent ranging

(Student paper)

Grigory Lihachev¹, Johann Riemensberger¹, Wenle Weng¹, Junqiu Liu¹, Hao Tian², Anat Siddhart¹, Viacheslav Snigirev², Vladimir Shadymov¹, Andrey Voloshin¹, Rui Ning Wang¹, Jijun He¹, Sunil A. Bhave², and Tobias J. Kippenberg^{1*}

¹Laboratory of Photonics and Quantum Measurements, Swiss Federal Institute of Technology Lausanne (EPFL), CH-1015 Lausanne, Switzerland

²OxideMEMS Lab, Purdue University, 47907 West Lafayette, IN, USA

*tobias.kippenberg@epfl.ch

We demonstrate a hybrid photonic integrated laser that exhibit intrinsic linewidth of 25 Hz, while offering megahertz actuation bandwidth with the tuning range larger than 1 GHz, attained by a DFB laser self-injection locking to a high-Q Si₃N₄ microresonator with high confinement waveguides and AlN piezoelectrical actuator, allowing both single line operation and microcomb generation. We develop a compact FMCW LiDAR laser with triangular chirp optical signals at a rate up to 1 MHz and perform optical ranging in lab environment without requiring any linearisation.

Keywords: FMCW LiDAR, hybrid integrated lasers, silicon nitride, self-injection-locking

INTRODUCTION

Low-noise lasers are of central importance in a wide variety of applications, including high-spectral-efficiency coherent communication protocols, long-distance coherent light detection and ranging (LiDAR) and distributed fibre sensing. In addition to low phase noise, the ability to achieve high bandwidth actuation of the laser frequency is imperative for carrier recovery in coherent communications and triangular chirping for frequency-modulated continuous-wave (FMCW) based ranging. While there has been major progress in the development of heterogeneously integrated silicon based lasers – now commercially employed in data centres – that leverage CMOS wafer scale manufacturing, integrated lasers with lowest phase noises are based on optical feedback from components that do not possess fast frequency tunability, thus resulting in the lack of frequency agility. Applying the technique of self-injection locking to ultra low loss Si₃N₄ photonic integrated circuits has enabled hybrid integrated lasers with Hz-level Lorentzian linewidth, that have showed steady improvements. A particularly interesting application for integrated photonics based low noise lasers is coherent FMCW LiDAR. Recently, autonomous driving and areal mapping has increased the interest in such sources and a fully hybrid integrated low-noise, high and frequency agile source could hence unlock further applications of coherent FMCW LiDAR. Laser phase noise limits the maximum operating distance and ranging precision in FMCW LiDAR. However, a key requirement for FMCW at long range is in addition to low phase noise, frequency agility, i.e to achieve fast, linear and hysteresisfree tuning.

RESULTS

The hybrid laser system comprises a laser chip with a distributed feedback (DFB) structure and a Si₃N₄ photonic chip in which a microring resonator and an AlN piezoelectrical actuator are integrated (Fig. 1(a-c)). The Si₃N₄ microresonator and the bus waveguide are fabricated with the photonic Damascene reflow process [1], showing an intrinsic quality factor of $Q_0 > 20$ millions. Made from polycrystalline AlN (Fig 1 (d)) as the main piezoelectric material, the piezoelectric actuator has molybdenum (Mo) and aluminium (Al) as the bottom electrode (ground) and the top electrode, respectively [2]. The DFB laser diode that is directly butt-coupled to the photonic chip is operating at central wavelength of 1556 nm with output power of 40 mW in free running regime. The gap between the laser chip and the microresonator is adjusted for optimal feedback phase [3], yielding the maximum locking range and the highest noise suppression rate of more than 35 dB. Figure 1(e) shows the frequency noise spectra of the laser in free-running regime and self-injection-locking to resonators with distinct FSRs of 190, 10 and 2 GHz, respectively. At frequencies above 1 MHz, the laser frequency noises reaches under 8 Hz²/Hz, and the optical cross-correlation-based characterisation allows us to confirm the laser intrinsic linewidth is below 25 Hz.

The frequency noise power spectral density was found to be in good quantitative agreement with fundamental thermo-refractive noise (TRN) limit of the microresonator at mid range offsets from 5 to 100 kHz. Thus, we demonstrate using high confinement Si_3N_4 platform the laser performance limited by thermorefractive noise, which has only been shown in Si_3N_4 low confinement waveguides. We note that this intrinsic linewidth can be further reduced by using microresonators with even larger optical mode volume and therefore reduced TRN.

By tuning the voltage applied to the AlN actuator we tune the cavity resonance. By maintaining diode current at fixed value corresponding to the center of the self-injection locking range, we sweep the laser frequency. With the AlN actuators engineered based on novel contour mode cancellation and differential drive schemes, the microresonator resonance can be frequency-modulated via the stress-optical effect with a flattened bandwidth up to 1 MHz. We demonstrate optical carrier that is triangularly chirped with frequency excursion 1.2 GHz at rates up to 800 kHz with a deviation from a linear chirp less than 1 % (Fig.1 (f)). The versatility permitted by the outstanding optical and mechanical properties of the system allows us to demonstrate low-cost FMCW LiDAR engine with 12.5 cm resolution and 100 kpixel/s rate and perform an optical ranging experiment in the lab.

We investigate the reduction of tuning voltage requirement by introducing an integrated piezoelectric actuator based on lead zirconium titanate (PZT).

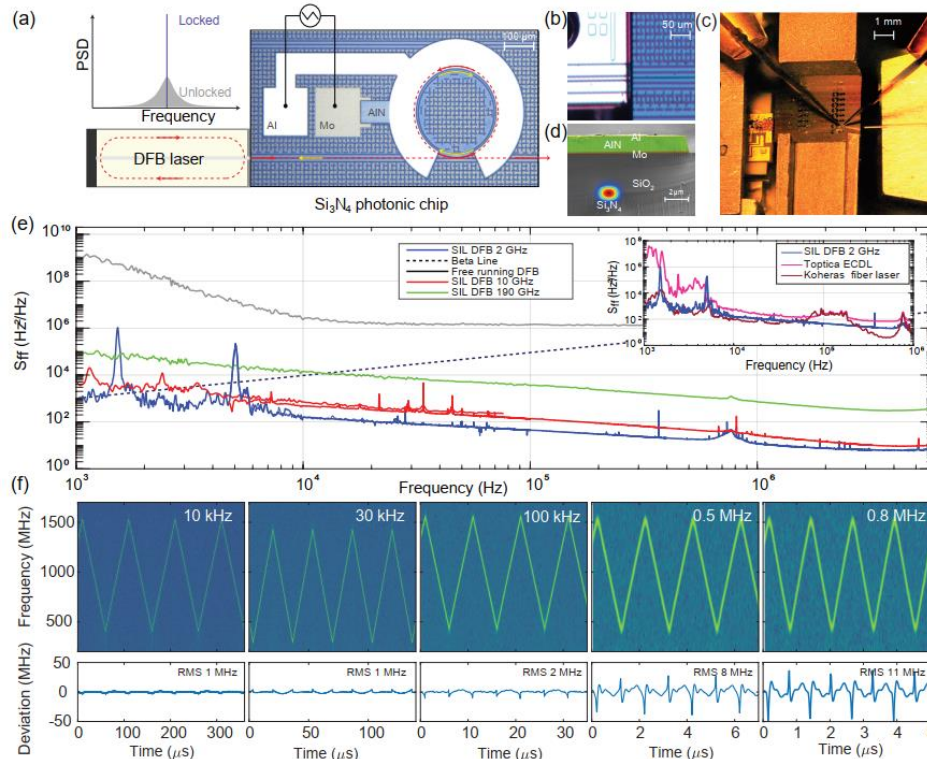


Fig. 1. (a) Principle of laser linewidth narrowing via laser self-injection locking. The laser frequency tuning is realised by applying a sweeping electrical signal on the AlN actuator that is monolithically integrated on the Si_3N_4 microresonator. (b) Optical micrograph showing the DFB laser butt-coupled to the Si_3N_4 photonic chip. (c) Material stack of the device. (d) Photo of the hybrid laser. (e) Frequency noise spectra of the hybrid integrated laser system using microresonators with different FSRs. Inset: comparison to commercial ECDL and fiber lasers. (f) Time-frequency spectrograms of the heterodyne beatnotes for different chirp frequency. Bottom row: Residual of least squares fitting of the experimental time-frequency traces with a lineartriangular chirp pattern.

As an actual demonstration of the potential of the hybrid integrated laser, we perform optical FMCW LiDAR mapping in the laboratory environment. Importantly, we can - due to the excellent linearity, low hysteresis, and narrow linewidth - perform ranging without any adaptive clock sampling and without pre-distortion linearization.

DISCUSSION

The approach is based on foundry-ready processes that include photonic integrated circuits based on Si_3N_4 as well as AlN and PZT MEMS processing, and is therefore amenable to large-volume manufacturing. The combination of narrow linewidth (kHz level) along with the fast and flat actuation response, makes the

source ideally suited for medium to long-range coherent LiDAR, as required for autonomous driving, drone navigation, or industrial and terrain mapping. The combination of low noise and fast on chip tuning, alleviates the need for external components such as AOMs or single sideband modulators for fast frequency actuation, and may also find use in other areas such as locking of lasers to reference cavities, or atomic transitions - where a tight lock is required, and can be achieved with a high actuation bandwidth as demonstrated here. In addition, while our lasers were demonstrated at 1556 nm, the center wavelength can be readily extended to other ranges, including the near IR and mid-infrared, due to the transparency of Si₃N₄.

Acknowledgments: This work was supported by funding from the European Union H2020 research and innovation programme under FET-Open grant agreement no. 863322 (TeraSlice) and the Marie Skłodowska-Curie IF grant agreement No. 846737 (CoSiLiS). This material is based upon work supported by the Air Force Office of Scientific Research under award number FA9550-19-1-0250. This work was supported by funding from the Swiss National Science Foundation under grant agreement No.176563 (BRIDGE). This work was supported by funding from the European Union H2020 research and innovation programme under HOT: FET-Proactive grant agreement No. 732894. This work was also supported by the United States' National Science Foundation under Award 18- 39164 and QIS DCL 20-063. The chip samples were fabricated in the EPFL center of MicroNanoTechnology (CMi), and in the Birck Nanotechnology Center at Purdue University. AlN deposition was performed at OEM Group Inc. PZT layer was fabricated at Radiant Technologies Inc.

References

- [1] Junqiu Liu et al., "Ultralow-power chip-based soliton microcombs for photonic integration," *Optica* **5**, 1347–1353 (2018)
- [2] Hao Tian et al., "Hybrid integrated photonics using bulk acoustic resonators," *Nature Communications* **11**, 1–8 (2020).
- [3] N.M Kondratiev et al., "Self-injection locking of a laser diode to a high-q wgm microresonator," *Optics Express* **25**, 28167–28178 (2017)

Impact of the saturable absorber on the linewidth enhancement factor of hybrid silicon quantum dot comb lasers

(Student paper)

Thibaut Renaud^{1*}, Heming Huang¹, Geza Kurczveil², R.G. Beausoleil² and Frédéric Grillot^{1,3}

¹LTCI, Télécom Paris, Institut Polytechnique de Paris, 19 place Marguerite Perey, 91120 Palaiseau, France

²Large-Scale Integrated Photonics Lab, Hewlett Packard Labs, Hewlett Packard Enterprise, Milpitas, CA 95035, USA

³Center for High Technology Materials, University of New-Mexico, 1313 Goddard SE, Albuquerque, USA

*correspondence to: thibaut.renaud@telecom-paris.fr

This work investigates the effects of the saturable absorber on the linewidth enhancement factor of hybrid silicon quantum dot comb lasers, which is a key parameter involved in frequency comb generation. Experiments have been performed on two carefully chosen laser devices sharing the same gain material and cavity design, with and without saturable absorber. The results unveil that the increase of the reversed bias on the absorber drives up the linewidth enhancement factor, which gives birth to the comb spectrum. This paper brings insights on the fundamental aspects of comb lasers and provides concepting guidelines of future on-chip light sources for integrated wavelength-division multiplexing applications.

Keywords: Quantum dots, frequency combs, linewidth enhancement factor, silicon photonics

INTRODUCTION

The recent years have seen a great increase in data transfer for smaller and smaller distances, in particular for High Performance Computing (HPC) systems where it reaches several petabits per second between the memory and the different compute nodes¹. These optical interconnects rely on on-chip wavelength-division multiplexing (WDM) to transmit the data through multiple separately modulated channels at once, in order to vastly improve the transfer speed. Although this approach can be achieved using one single-wavelength laser per channel, it is not very suitable for silicon based integrated photonics circuits (PICs) as it results in a larger footprint and energy consumption. On top of that, it is also associated to a lower stability since WDM requires all modes frequencies to stay equally spaced. Therefore, a better solution consists in using a single laser with a quantum dot (QD) active region producing an efficient optical frequency comb (OFC) wherein the phase of each line cannot shift independently from the others². Furthermore, the ultimate carrier quantization within the QDs provides lasers with an exceptional thermal stability, along with a large gain bandwidth and a narrow linewidth³ which is desired in OFC. On the first hand, the linewidth of each comb line is linked to the phase noise and can be reduced through the linewidth enhancement factor (α_H -factor), while on the other hand, the operating comb bandwidth directly scales with the magnitude of α_H -factor^{4,5}. As a consequence of that, the optimization of the comb properties requires a careful understanding of the α_H -factor in particular, when a saturable absorber (SA) is incorporated in the device. In this work, we are experimentally looking at this concern in two hybrid silicon InAs/GaAs QD comb lasers. The lasers share the same gain material, but possess slightly different cavity designs hence one has a SA section and the other does not. We believe that this paper brings further insights on comb lasers which is of paramount importance for future on-chip light sources for integrated WDM applications in data centers and in supercomputers.

LASER STRUCTURE

The multi-section cavity design of the devices is shown schematically in Figure 1(a). The structure consists of a 2.6-mm-long cavity that has mirrors with 50% reflectivity on one side and 100% on the other, and a 1.4-mm-long active region is placed in the center. The semiconductor optical amplifier (SOA) section incorporates 8 layers of QDs, and one of the two lasers has a 176- μm -long SA positioned in the middle in order to favor the frequency comb operation. Mode converters ensure the optical mode transfer from active waveguide down to the passive Si waveguide and the output light is coupled out through a grating coupler (GC).

The integration on silicon is realized by wafer-bonding an unpatterned InAs/GaAs QD wafer to a Silicon-on-Insulator (SOI) wafer already patterned with the Si passive devices. The QD material is then etched and the p- and n-contacts are deposited, using standard III-V processing techniques. More information about the epitaxial structure can be found elsewhere^{6,7}.

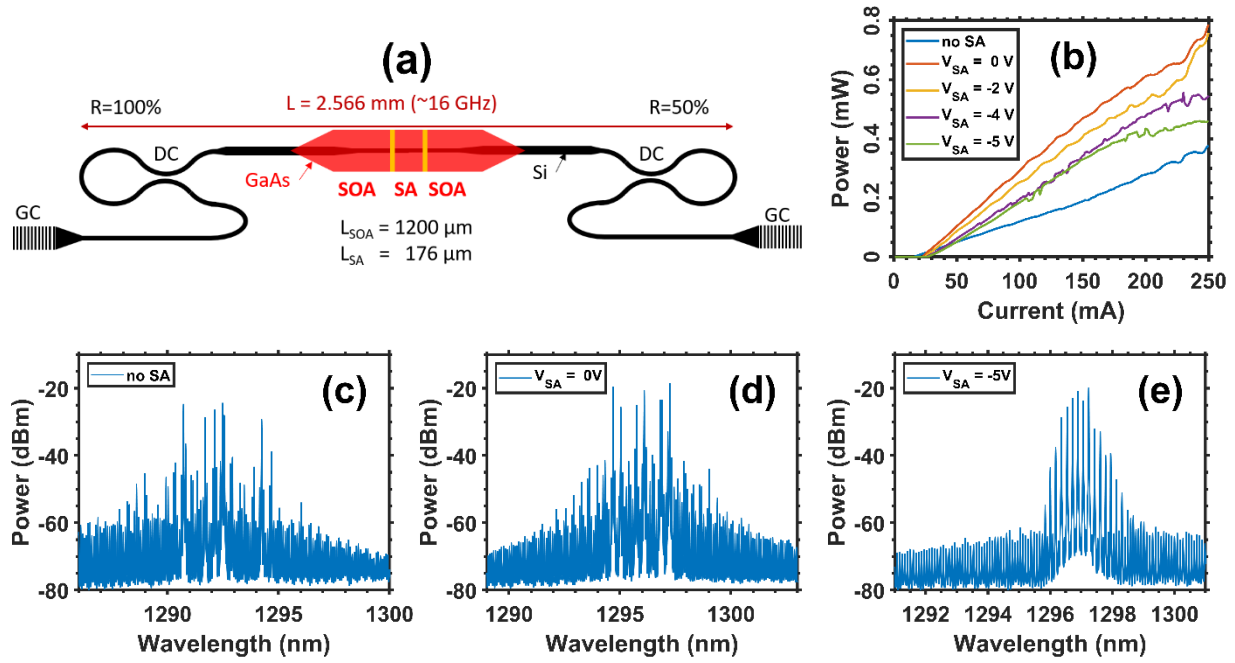


Fig. 1. (a) Schematics of the laser design. SOA: semiconductor optical amplifier; SA: saturable absorber; GC: Grating Coupler; DC: directional coupler. (b) LI characteristics of the two lasers at 20°C . (c)(d)(e) Optical spectra of the two lasers at $2 \times I_{th}$ and 20°C .

Figure 1(b) shows the LI characteristics of both lasers at room temperature (20°C), with applied voltages of $V_{SA} = 0\text{V}$, -2V , -4V and -5V for the SA. The threshold current I_{th} increases from 23 mA to 27 mA when the SA voltage goes from 0V to -5V , while the laser without SA has a threshold at 16 mA. The higher threshold is due to the increased internal loss coefficient in the SA. The optical spectra depicted in Figure 1(c), (d) and (e) show the evolution of the frequency comb at room temperature (20°C) for the laser without SA and for the other one at $V_{SA} = 0\text{V}$ and -5V . Both lasers are pumped at $2 \times I_{th}$. Under these conditions, the emission wavelength is centered around 1292 nm, 1296 nm and 1297 nm, respectively. At a -5V reverse voltage condition, the comb spectrum takes place with 15 lines above noise floor, and with 6 lines within the -10 dB bandwidth.

RESULTS AND DISCUSSION

The impact of the SA on the α_H -factor of the laser can be better understood by tracking the modal wavelength shift below threshold. The α_H -factor has often been measured in mono-section devices under straightforward biased condition whereas for reverse biased SAs it has not been extensively studied or measured despite the importance to understand its magnitude in SAs. The α_H -factor is measured from the Amplified Spontaneous Emission (ASE)⁸⁻¹¹. Its extraction is performed by capturing a set of optical spectra below and above the laser's threshold with a high-resolution (10 pm) optical spectrum analyzer (OSA), and then by calculating the differential gain $\Delta g/\Delta I$ and the wavelength shift $\Delta\lambda/\Delta I$ for each longitudinal mode. A correction for the thermal red-shift is taken into account using the above threshold spectra¹⁰. Finally, the α_H of each comb line is retrieved through the expression^{8,10,11}

$$\alpha_H = -\frac{4n\pi}{\lambda^2} \frac{\Delta\lambda/\Delta I}{\Delta g/\Delta I} \quad (1)$$

where n is the effective group index, λ the photon wavelength, and g the net modal gain.

Figure 2(a) shows the wavelength shift $\Delta\lambda$ with respect to the normalized current I/I_{th} for one mode in each laser. Without SA, the wavelength is found slightly blue-shifted below threshold and red-shifted above due to thermal effects. However, when the SA is included (assuming $V_{SA} = 0\text{V}$), the wavelength is found redshifted with increasing the pump current even from below threshold. This thermal load is also retrieved at any other reverse voltage conditions. Therefore, the saturation of the absorber is connected with the thermal heating of the device.

Figure 2(b) displays the threshold value of the linewidth enhancement factor for each condition on the SA studied in this work. This value is taken as the mean of the α_H -factors of a few modes around the first lasing mode, which is to say the mode with the highest intensity just above threshold. As the two lasers have the same design, the difference in the α_H -factor is only due to the presence of the SA. First, the orange triangle represents the laser

without SA. Therefore, the measured value at 0.9 reflects the α_H of the sole nominal gain section. In the open circuit (OC) configuration, the laser with SA exhibits a α_H -factor of around 1, hence slightly higher than the one without. At higher reverse voltages, it slightly goes up monolithically until a sharp increase occurs around -4V, up to ~ 2.5 for $V_{SA} = -5V$. This threshold effect is concomitant with the birth of the comb lines displayed in Figure 1(c). Note that this phenomenon has already been observed in other similar devices⁴. This result somewhat illustrates the interplay between this device parameter governing many coherent processes in semiconductor lasers, and the frequency comb operation.

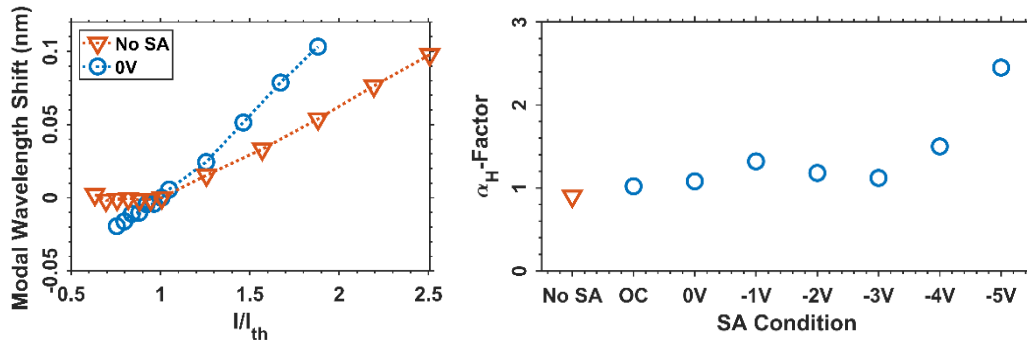


Fig. 2. (a) Wavelength shift $\Delta\lambda$ with respect to the normalized current I/I_{th} for the laser without SA and for the laser with SA at $V_{SA} = 0V$. (b) The mean value of the α_H -factor for a few modes around the first lasing mode at different SA conditions. OC: open circuit.

CONCLUSION

In this work, the influence of the SA on the linewidth enhancement factor is studied in multi-section hybrid silicon QD lasers. The experiments unveil that, the introduction of the SA enhances the α_H -factor of the device especially when the comb spectrum is formed at higher reverse bias conditions. Here, we present an experimental demonstration of a QD comb laser, confirming the predicted key role of the α_H -factor in the formation of the frequency comb dynamics. These results gained deeper insights on the underlying physics of multi-section comb lasers and thus provide further guidelines for the conception of future on-chip multi-wavelength light sources in integrated WDM applications.

Acknowledgements: This work is supported by Hewlett Packard Enterprise (HPE) and the Institut Mines Telecom.

References

- [1] D. Dai and J. E. Bowers, *Silicon-based on-chip multiplexing technologies and devices for peta-bit optical interconnects*, *Nanophotonics* **3**(4-5), pp. 283–311, 2014.
- [2] L. Lundberg, M. Karlsson, A. Lorences-Riesgo, M. Mazur, V. Torres-Company, J. Schröder, and P. A. Andrekson, *Frequency comb-based wdm transmission systems enabling joint signal processing*, *Applied Sciences* **8**(5), 2018.
- [3] J. Duan, H. Huang, Z. G. Lu, P. J. Poole, C. Wang, and F. Grillot, *Narrow spectral linewidth in inas/inp quantum dot distributed feedback lasers*, *Applied Physics Letters* **112**(12), p. 121102, 2018.
- [4] B. Dong, H. Huang, J. Duan, G. Kurczveil, D. Liang, R. G. Beausoleil, and F. Grillot, *Frequency comb dynamics of a 1.3 μm hybrid-silicon quantum dot semiconductor laser with optical injection*, *Opt. Lett.* **44**, 5755-5758, 2019.
- [5] F. Cappelli, G. Villares, S. Riedi, and J. Faist, *Intrinsic linewidth of quantum cascade laser frequency combs*, *Optica* **2**, 836-840, 2015.
- [6] G. Kurczveil, A. Descos, D. Liang, M. Fiorentino, and R. Beausoleil, *Hybrid silicon quantum dot comb laser with record wide comb width*, in *Frontiers in Optics / Laser Science*, p. FTu6E.6, Optical Society of America, 2020.
- [7] G. Kurczveil, D. Liang, M. Fiorentino, and R. G. Beausoleil, *Robust hybrid quantum dot laser for integrated silicon photonics*, *Opt. Express* **24**, pp. 16167–16174, 2016.
- [8] H. Huang, K. Schires, P. J. Poole, and F. Grillot, *Non-degenerate four-wave mixing in an optically injection-locked InAs/InP quantum dot Fabry–Perot laser*, *Appl. Phys. Lett.* **106**, p. 143501, 2015.
- [9] C. Wang, F. Grillot, F. Y. Lin, I. Aldaya, T. Batte, C. Gosset, E. Decerle, and J. Even, *Nondegenerate Four-Wave Mixing in a Dual-Mode Injection-Locked InAs/InP(100) Nanostructure Laser*, *IEEE Photonics Journal*, vol. **6**, no. 1, pp. 1-8, 2014.
- [10] B. Zhao, T. R. Chen, S. Wu, Y. H. Zhuang, Y. Yamada, and A. Yariv, *Direct measurement of linewidth enhancement factors in quantum well lasers of different quantum well barrier heights*, *Appl. Phys. Lett.* **62**, 1591-1593, 1993.
- [11] R. Raghuraman, N. Yu, R. Engelmann, H. Lee and C. L. Shieh, *Spectral dependence of differential gain, mode shift, and linewidth enhancement factor in a InGaAs-GaAs strained-layer single-quantum-well laser operated under high-injection conditions*, in *IEEE Journal of Quantum Electronics*, vol. **29**, no. 1, pp. 69-75, 1993.

Low Noise 2.6 to 26 GHz Tenfold Frequency Multiplication by an InP Broadly Tunable Optical Comb

Nicola Andriolli¹, Eduardo Saia Lima², Evandro Conforti³, Giampiero Contestabile^{4*} and Arismar Cerqueira Sodré Junior²

¹ CNR-IEIIT, Via Caruso 16, 56122 Pisa, Italy

² Lab. WOCA, INATEL, Santa Rita do Sapucaí, Brazil

³ DECOM - University of Campinas, Brazil

⁴ Scuola Superiore Sant'Anna, Via Moruzzi 1, 56124 Pisa, Italy

* corresponding author e-mail: giampiero.contestabile@santannapisa.it

We report low phase noise tenfold frequency multiplication based on an InP monolithically integrated optical frequency comb (OFC) generator, made by a DFB laser and cascaded optical modulators. The tenfold multiplied signal at 26 GHz, useful for 5G New Radio applications, provides a remarkably low phase noise, equivalent to the radio frequency generator used as an electrical source for the OFC at the same RF power.

Keywords: mm-waves, optical frequency comb generation and InP monolithic integration.

INTRODUCTION

Millimeter-wave signals with high spectral purity and low phase noise (PN) are mandatory in several scenarios, such as wireless communications, radar, and spectroscopic sensing [1]. In these applications, electronic synthesized radio frequency (RF) generators are used, especially for generating signals in the mm-waves range, even if they are typically bulky and expensive. To overcome these issues, several techniques for the generation of low-phase-noise and frequency-tunable mm-waves implemented in the optical domain have been proposed, such as external modulation, optical injection locking, and optical phase-lock loop [2]. In particular, external modulation based on phase modulators (PMs) and Mach-Zehnder modulators (MZMs) has demonstrated potential to provide generation and frequency multiplication with low phase noise, offering large flexibility in terms of selection of both wavelength and frequency repetition rate [3]. In this context, a photonic integrated optical frequency comb (OFC) generator based on cascaded modulators monolithically integrated in an Indium phosphide (InP) platform has been recently reported [4, 5]. In this contribution, we experimentally demonstrate low-phase-noise mm-waves generation based on the integrated optical frequency comb. More in detail, we show that the OFC-based tenfold multiplied signal obtained at 26 GHz is suitable for 5G New Radio (NR) wireless transmission, providing remarkably low phase noise, equivalent to the one generated by the commercially available RF generator used as comb driving source.

DEVICE DESCRIPTION, EXPERIMENTAL SETUP AND RESULTS

Fig. 1(a) shows a schematic of the InP photonic integrated circuit characterized in [4, 5] and implementing the optical frequency comb generator. The device has been integrated in an Indium Phosphide multi-project wafer run exploiting a generic integration platform. An on-chip distributed Bragg reflector laser diode (DBR-LD) is used as a continuous-wave (CW) light source, while an external laser coupled to the PIC input waveguide through a spot-size converter (SSC) can also be employed. The CW signal from either source enters a 2×2 multi-mode interference (MMI) splitter, which sends the divided signals to a monitor output or toward a dual-drive Mach-Zehnder modulator. In detail, the MZM is composed of a 1×2 MMI splitter, two 1-mm-long PMs, and a 2×1 MMI employed as an optical combiner. The phase modulators, exploiting the quantum-confined Stark effect, have a 3-dB bandwidth of about 7 GHz and a V_{π} of about 5 V. The signal then crosses a series of two further 1-mm-long PMs. Finally, the signal is amplified by a 500- μ m-long multi quantum-well SOA and then, coupled to the output fiber through another SSC. A high numerical aperture fiber array is aligned at the chip edge by means of a micro-positioner, minimizing coupling losses due to misalignment. The PIC has been mounted on a metal chuck and connected through wire bonds to a custom-designed printed circuit board (PCB) where four RF ports drive the phase modulators and five DC ports feed the DBR sections and the SOA. The chip on the metal chuck surrounded by the PCB is depicted in Fig. 1(b): the footprint is around 4.5×2.5 mm², limited by design constraints concerning the orthogonal placement of PMs and gain sections. The PCB with SMA RF interfaces and the general purpose input/output (GPIO) DC interfaces is shown in Fig. 1(c).

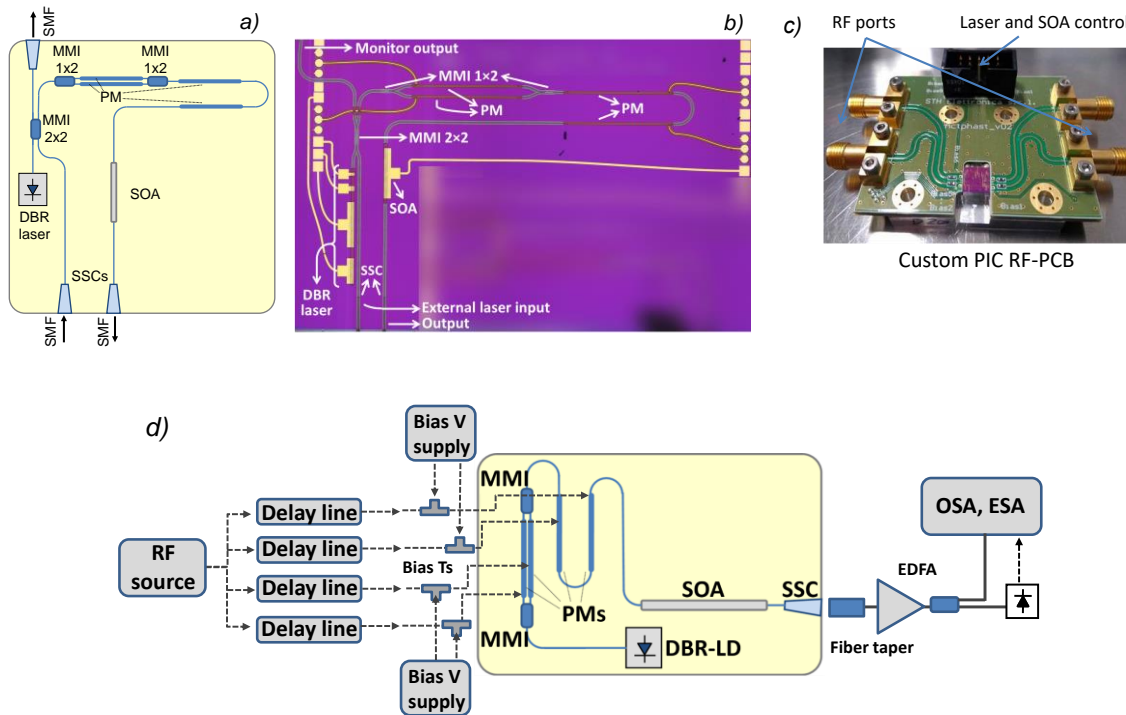


Fig. 1. a) Integrated comb generator PIC schematic. b) Picture of the fabricated PIC (Footprint: $4.5 \times 2.5 \text{ mm}^2$). c) PIC-PCB assembly. d) Experimental setup for comb generation test.

Fig. 1(d) reports the block diagram of the proposed low-phase-noise tenfold frequency multiplication based on an integrated OFC. A 43-GHz RF generator (Keysight E8267D PS) provides a 25 dBm electrical carrier centered at 2.6 GHz, which is equally divided in four by means of an electrical splitter. The phase of each branch is controlled by mechanical delay lines, enabling a proper adjustment on the temporal phase alignment among the PMs, which directly impacts the OFC spectral flatness. Afterward, bias tees have been used for combining the electrical carriers with the required DC bias voltage, feeding the PMs through SMA connectors. In order to achieve a large number of comb lines and enhance the comb flatness, the PMs have been driven with V_π multiples, whereas the MZM has been polarized around V_π . The integrated DBR laser and the SOA currents have been set to 70 mA and 55 mA, respectively. At the PIC output, the power of the optical frequency comb was about -6 dBm. The signal has been then split in two ways: 1% optical power was monitored by an optical spectrum analyzer (OSA), whereas the remaining optical power (99%) reached an Erbium-doped fiber amplifier (EDFA) and then a high-speed photodetector. The EDFA has been used to monitor and control the optical power, ensuring 2 dBm optical power at the photodetector input. Since conventional optical spectrum analyzers cannot resolve the comb spectrum, we have used a heterodyne detection technique to reconstruct the optical spectrum. Results are reported in Fig. 2(a), where the 2.6 GHz spaced optical frequency comb centered at 193.5 THz is shown. The optical tones extend from 193.4 THz up to 193.6 THz. More in detail, there are 19 tones within a 10 dB intensity range from the maximum optical power level, characterized by an optical signal-to-noise ratio (OSNR) larger than 40 dB. Considering the whole comb and the noise floor around -60 dBm, 49 tones show an OSNR larger than 20 dB, whereas 36 tones present an OSNR beyond 30 dB. Therefore, the OFC is suitable for generating mm-waves signals on a wide spectral range.

The phase-stabilized optical frequency comb lines have been converted into a set of electrical tones by means of a 74-GHz bandwidth photodetector and measured by a 43-GHz electrical spectrum analyzer (ESA). A stable electrical comb with 2.6 GHz repetition rate can be appreciated over the entire frequency range, as shown in Fig. 2(b). In addition, a high signal-to-noise ratio (SNR) can be observed for all generated harmonics. Therefore, after the photodetection process, the electrical carriers can be properly separated and employed in specific applications, depending on the desired frequency range. Considering a tenfold frequency multiplication, a high spectral purity mm-wave electrical carrier can be noted at 26 GHz. We have used a 1-dB insertion loss band-pass filter (BPF) with 1-GHz bandwidth centered at 26 GHz for isolating the single harmonic and improving the spectral purity, as presented in the inset of Fig. 2(b), since this frequency range has been standardized for 5G mm-wave applications. As expected, the electrical filter selected only the 26 GHz signal, demonstrating a high spectral purity and a significant electrical power of -34 dBm.

Phase noise measurements are essential in communication systems, enabling to precisely characterize the frequency stability of systems and oscillators. In order to validate the low-phase noise tenfold frequency multiplication based on an integrated OFC, we have measured the OFC-based signal phase noise and compared with the one of the low-noise electrical RF generator used to generate the optical frequency comb. Fig. 2(c) reports the phase noise measurements at 2.6 GHz and 26 GHz for both the electrical RF generator and the optical one. The monolithically integrated OFC source provides phase-stabilized optical lines and, as a consequence, frequency multiplication with low phase noise. Considering the 26 GHz signals, measured phase noise is around -50 dBc/Hz and -80 dBc/Hz for 10 Hz and 1 kHz offset, respectively. This remarkably low phase noise is comparable to the one of commercially available electrical RF generator for the same RF power. Regarding the fundamental frequency (2.6 GHz), a similar phase noise response can be appreciated, with -70 dBc/Hz and -90 dBc/Hz for 10 Hz and 1 kHz offset, respectively. Therefore, it is noteworthy that the InP integrated OFC is suitable for implementing, in a compact and low power device, RF frequency multiplication up to mm-waves, with a phase noise equivalent to the one of the low noise bulk electric RF generators i.e., without adding any significant phase distortion.

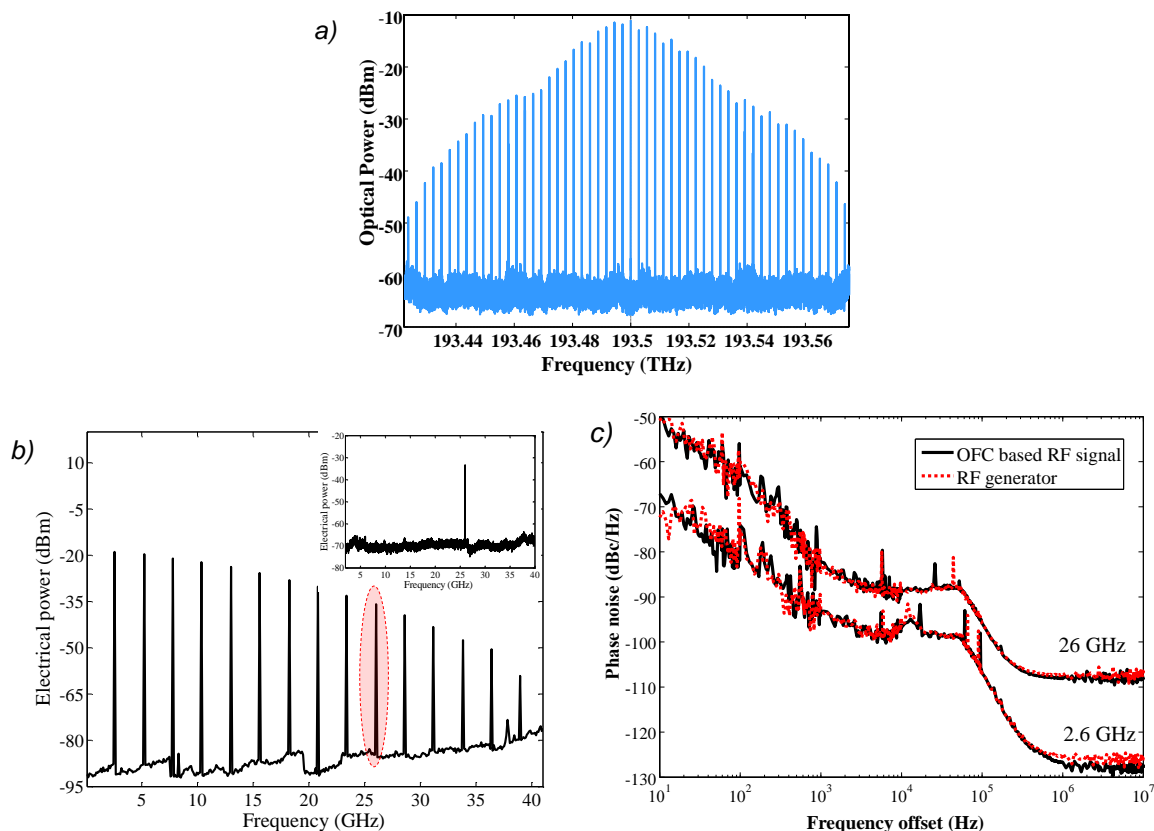


Fig. 2. a) 2.6 GHz optical frequency comb at the PIC output b) 2.6-GHz electrical comb at the photodetector output; in the inset the filtered tone at 26 GHz. c) 2.6 GHz and 26-GHz phase noise comparison between OFC-based signals and the commercial RF generator.

Acknowledgements: This work was supported by RNP-MCTIC Grant No. 01245.010604/2020-14, under the Brasil 6G project, CNPq, CAPES, FINEP and FAPEMIG. Fapesp Contracts #21/06569-1 and #15/24517-8; CNPq #402471-2021-0. Dr. Marco Chiesa is gratefully acknowledged for the support in PIC mounting.

References

- [1] I. Degli-Eredi, P. An, J. Drasbæk, H. Mohammad Hosseini, L. Nielsen, P. Tønning, S. Rommel, I. T. Monroy, and M. J. Heck, "Millimeter-wave generation using hybrid silicon photonics," *Journal of Optics*, vol. 23, no. 4, p. 043001, 2021
- [2] V. Torres-Company et al. "Optical frequency comb technology for ultra-broadband radio-frequency photonics" *Laser Photonics Rev.* 8, No. 3, 368–393 (2014)
- [3] W. Li and J. Yao, "Investigation of photonic assisted microwave frequency multiplication based on external modulation," *IEEE Transactions on Microwave Theory and Techniques*, vol. 58, no. 11, pp. 3259–3268, 2010
- [4] N. Andriolli, T. Cassese, M. Chiesa, C. de Dios, and G. Contestabile, "Photonic integrated fully tunable comb generator cascading optical modulators," *Journal of Lightwave Technology*, vol. 36, no. 23, pp. 5685–5689, 2018
- [5] F. Bontempi, N. Andriolli, F. Scotti, M. Chiesa, and G. Contestabile, "Comb line multiplication in an InP integrated photonic circuit based on cascaded modulators," *IEEE Journal of Selected Topics in Quantum Electronics*, vol. 25, no. 6, pp. 1–7, 2019

Heterogeneously integrated low-loss lithium niobate photonic platform

(Student paper)

M. Churaev^{1,*}, A. Riedhauser², R. N. Wang¹, C. Möhl², T. Blésin¹, M. H. Anderson¹, V. Snigirev¹, A. Siddharth¹, Y. Popoff^{2,3}, U. Drechsler², D. Caimi², S. Hönl², J. Riemensberger¹, J. Liu¹, P. Seidler², and T. J. Kippenberg¹

¹ Institute of Physics, Swiss Federal Institute of Technology Lausanne (EPFL), CH-1015 Lausanne, Switzerland

² IBM Research Europe, Zurich, Säumerstrasse 4, CH-8803 Rüschlikon, Switzerland

³ Integrated Systems Laboratory, Swiss Federal Institute of Technology Zurich (ETH Zürich), CH-8092 Zürich, Switzerland

*mikhail.churaev@epfl.ch

We demonstrate a hybrid LiNbO₃-Si₃N₄ photonic integrated platform with a propagation loss of 8.5 dB/m at wafer-scale for various devices. The platform exhibits low fiber-to-chip insertion loss, high power handling, and precise lithographic control.

Keywords: hybrid integration, thin-film lithium niobate, silicon nitride, electro-optics, microresonators, nonlinear photonics

INTRODUCTION

Recent breakthroughs in thin-film lithium niobate on insulator (LNOI) have enabled low-loss photonic integrated circuits (PICs) based on LiNbO₃ [1-2]. Excellent physical properties together with commercial availability have made this material extremely compelling for the photonics community. Despite the achievements to date, widespread adoption of LiNbO₃ integrated photonics is still impeded by several key issues such as CMOS compatibility, wafer-scale yield, and edge fiber-to-chip coupling [3]. As an alternative to conventional bulk LiNbO₃ and ridge waveguide-based photonic devices, hybrid platforms emerged recently, combining thin-film LiNbO₃ with waveguides made of Si, Si₃N₄, or Ta₂O₅ [4-5]. However, direct wafer bonding at the wafer-level was not achieved (only small chiplets were used), and the approaches could not retain the ultra-low propagation losses of Si₃N₄. Here we overcome the challenges mentioned above and demonstrate a high-yield, low-loss, integrated LiNbO₃ photonic platform with efficient edge coupling that harnesses the mature Si₃N₄ PDK and endows the platform with selective electro-optic functionality.

RESULTS

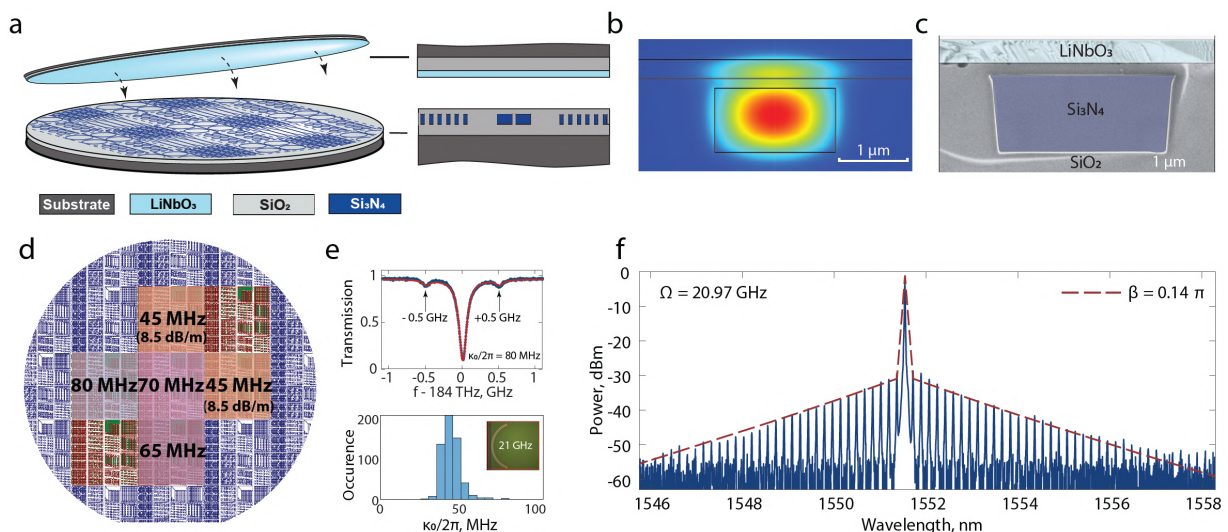


Fig. 1. (a) Full wafer bonding approach illustration. (b) Optical mode profile in the hybrid structure. (c) SEM cross-section of a resulting hybrid waveguide. (d) Wafer map of microresonator resonance linewidth distribution. (e) Examples of one resonance fit and statistical analysis of more than 500 resonances linewidth. (f) Electro-optical frequency comb generation in a hybrid microresonator.

The process flow of our hybrid PIC starts with the fabrication of Si₃N₄ PIC based on the photonic Damascene process [6]. As depicted on Figure 1(a), all the photonic designs are imprinted on the Si₃N₄ layer and therefore the process does not depend on the LiNbO₃ etching. The photonic Damascene process used for the donor silicon nitride wafer, has several particular advantages, in particular a flat wafer surface planarized with CMP for heterogeneous

integration. After planarization, a commercially available LNOI wafer is bonded with subsequent substrate removal. The resulting waveguide cross-section and optical mode distribution are depicted on Figure 1 (b)-(c). The mode is partially confined in the slab LiNbO₃ layer, while the Si₃N₄ layer serves for guiding the optical signal. In the current configuration, we use 300 nm LiNbO₃ layer bonded to 950 nm thick silicon nitride layer with a silica interlayer of approximately 100 nm between two materials. The silica layer is used to maintain homogeneous and flat surface of the donor wafer for the wafer-scale bonding. With the waveguide width of 1.8 μm, this configuration gives approximately 12% of the optical mode in lithium niobate. One of the advantages of lithium niobate heterogeneous integration is that fiber to chip coupling can be achieved via the Si₃N₄ layer, which offers low insertion loss. In order to increase the coupling efficiency, we remove lithium niobate from the chip facet regions and achieve in total 18% fiber-to-fiber transmission.

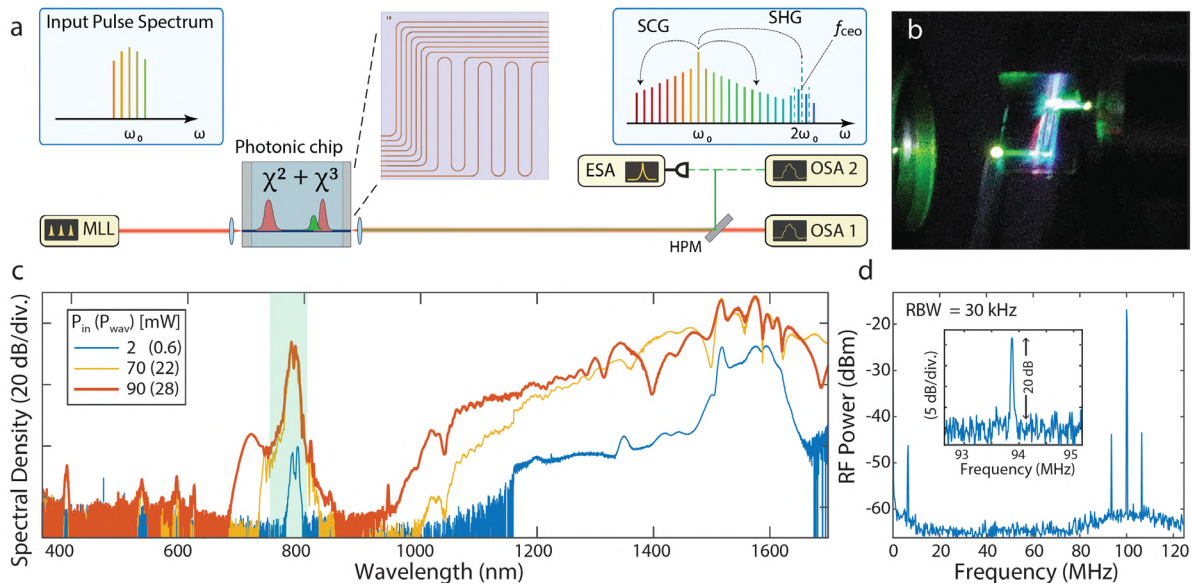


Fig. 2. (a) Experimental schematic for supercontinuum generation in a $\chi(2)$, $\chi(3)$ LiNbO₃ waveguide. (b) Photo of the supercontinuum process in experiment. Blue and Green light corresponds to higher harmonic generation. (c) Total output spectrum for different incident (in waveguide) power levels P_{in} (P_{wav}). (d) f_{ceo} beatnote and $f_{rep}=100$ MHz repetition rate beatnote, detected at $P_{wav}=28$ mW.

To illustrate the versatility, lithographic precision, and yield of our process, we fabricate a reticle with a variety of devices. We study optical losses by measuring intrinsic linewidth of hybrid microresonators with 1 mm radius. The wafer map of mean linewidth values is depicted in Fig. 1(d). Some of the wafer areas show 45 MHz linewidth, which corresponds to quality factors of $Q = 3 \times 10^6$ and approximately 8.5 dB/m linear optical loss value. Importantly this corresponds to not a single isolated resonance, but to a statistical ensemble of more than 500 resonances (cf. Fig 1(e)). We also use the same microring resonators combined with metal electrodes for electro-optic frequency comb generation [7]. Even though the electro-optic coupling is limited in our case by the mode participation in lithium niobate (around 12% in this experiment), we observe a broad comb with 60 sidebands within a 25 dB span (cf. Figure 1(f)). This is achieved due to ultra low losses of our structure combined with flat integrated dispersion. With a further geometry optimization, there is only a minor reduction in electro-optic efficiency ($2 \times V_{\pi}L$ product) in comparison to approaches using ridge waveguides, while enabling lower propagation losses on wafer-scale, independent on quality of the LiNbO₃ etching [8].

Besides electro-optics, the low loss of our platform is also a key for nonlinear photonics applications. We demonstrate supercontinuum generation with combined $\chi^{(2)}$ and $\chi^{(3)}$ nonlinear optical processes using the hybrid waveguides, as shown in Fig. 2(a). We observe octave-spanning supercontinuum generation mediated by the $\chi^{(3)}$ nonlinearity, together with simultaneous second harmonic generation (SHG) due to optical field in LiNbO₃ [9]. As shown in Fig. 2(d), we obtain the fundamental repetition rate of the supercontinuum as well as the f_{ceo} in the RF spectrum, which shares similar laser noise as the seed mode-locked laser input.

DISCUSSION

To sum up, we demonstrate a novel, hybrid LiNbO₃ and Si₃N₄ photonic integrated circuit using direct wafer bonding. The high yield and wafer-scale nature of the process enables complex photonic architectures relying on low optical loss and high-speed optical modulation, and enables LiNbO₃ to be confined in regions of interest on the chip (e.g. as modulators).

Acknowledgements

his work was supported by funding from the European Union Horizon 2020 Research and Innovation Program under the Marie Skłodowska-Curie grant agreement No. 722923 (OMT) and No. 812818 (MICROCOMB), as well as under the FET-Proactive grant agreement No. 732894 (HOT). This work was also supported by the Swiss National Science Foundation under grant agreement No. 176563 (BRIDGE) and 186364 (QuantEOM), as well as by Contract HR0011-20-2-0046 (NOVEL) from the Defense Advanced Research Projects Agency (DARPA), Microsystems Technology Office (MTO).

References

- [1] D. Zhu et al. "Integrated photonics on thin-film lithium niobate", *Adv. Opt. Photon.* **13**, 242–352 (2021).
- [2] C. Wang et al. "Monolithic lithium niobate photonic circuits for kerr frequency comb generation and modulation" *Nature Communications* **10**, 978 (2019).
- [3] L. He et al., "Low-loss fiber-to-chip interface for lithium niobate photonic integrated circuits", *Optics Letters* **44**, 2314 (2019)
- [4] P. O. Weigel et al., "Lightwave Circuits in Lithium Niobate through Hybrid Waveguides with Silicon Photonics", *Scientific Reports* **6**, pp. 1–9 (2016)
- [5] N. Boynton et al., "A heterogeneously integrated silicon photonic/lithium niobate travelling wave electro-optic modulator", *Optics Express* **28**, 1868 (2020)
- [6] J. Liu et al., "High-yield, wafer-scale fabrication of ultralow-loss, dispersion-engineered silicon nitride photonic circuits", *Nature Communications* **1**, 12 (2021)
- [7] M. Zhang et al., "Broadband electro-optic frequency comb generation in a lithium niobate microring resonator", *Nature* **568**, pp. 373–377 (2019)
- [8] M. He et al., "High-performance hybrid silicon and lithium niobate Mach–Zehnder modulators for 100 Gbit s⁻¹ and beyond" *Nature Photonics* **13**, 1, pp. 359–364 (2019)
- [9] D. D. Hickstein et al. "Ultrabroadband supercontinuum generation and frequency-comb stabilization using on-chip waveguides with both cubic and quadratic nonlinearities", *Physical Review Applied* **8**, 014025 (2017).

Mid-Infrared Supercontinuum Generation in a Tapered SiGe/Si Waveguide for Multi-Species Gas Spectroscopy

Alberto Della Torre^{1,*}, Rémi Armand¹, Milan Sinobad¹, Kokou Firmin Fiaboe^{1,2}, Barry Luther-Davies³, Stephen Madden³, Arnan Mitchell², Thach Nguyen², David J. Moss⁴, Jean-Michel Hartmann⁵, Vincent Reboud⁵, Jean-Marc Fedeli⁵, Christelle Monat¹ and Christian Grillet¹

¹ Université de Lyon, Institut des Nanotechnologies de Lyon, UMR CNRS 5270, Ecully, 69131, France

² School of Engineering, RMIT University, Melbourne, VIC 3001, Australia

³ Quantum Science and Technology, The Australian National University, Canberra, ACT 2600, Australia

⁴ Optical Sciences Centre, Swinburne University of Technology, Hawthorn, VIC 3122, Australia

⁵ Université Grenoble Alpes, CEA-Leti, Grenoble, 38054, France

* alberto.della-torre@ec-lyon.fr

We report the experimental generation of a broadband and flat mid-infrared supercontinuum in a silicon-germanium-on-silicon inverse tapered waveguide. The supercontinuum extends from 2.4 to 5.5 μm , only limited by the long wavelength detection limit of our spectrum analyzer. We exploit the enhanced flatness of our supercontinuum for a proof-of-principle demonstration of gas spectroscopy of water vapor and carbon dioxide.

Keywords: Mid-infrared, nonlinear optics, supercontinuum, spectroscopy

INTRODUCTION

Mid-infrared (MIR, from 3 to 13 μm) supercontinuum (SC) sources are of great interest for high precision and high throughput spectroscopy [1,2]. The MIR band is known as the molecular fingerprint region. Many important molecules (e. g. pollutants and greenhouse gases) have fundamental roto-vibrational modes absorbing in the MIR region. Therefore, molecule detection and spectroscopy in the MIR can have orders of magnitudes higher sensitivity than in the near-infrared and visible regions, where only weak overtones of the fundamental absorption lines are present. However, commercial MIR technology is still relatively bulky and expensive. The last ten years have seen a quest to develop compact and cheaper sensing and spectroscopic devices with high performances. An integrated MIR SC is an ideal source for such devices, since it can provide broadband, fast, and high resolution measurements.

Germanium-based waveguides are particularly interesting for integrated MIR SC generation, since they combine a wide transparency window in the MIR (up to 8.5-13 μm , depending on the germanium content) [3], and high nonlinearity [4]. In addition, the use of group IV materials is particularly important for future commercial applications, since it allows to leverage the well-developed microfabrication technologies of the electronic industry for cost-effective mass production of the final devices. In the last years, we have demonstrated SC generation in silicon-germanium and pure germanium waveguides [5,6], as well as the ability to control the properties of the generated SC [7–9]. SC generation in silicon-germanium waveguides covering the entire molecular fingerprint region has also been demonstrated [10]. The properties of the generated SC strongly depend on the group velocity dispersion profile of the underlying waveguide. Typically, a waveguide pumped in the anomalous dispersion region generates a broader SC with, however, low spectral flatness and poor coherence. On the other hand, high spectral flatness and coherence can be achieved in a waveguide operating in the all-normal dispersion regime, but at the cost of reducing the SC bandwidth. High resolution, multi-species parallel absorption spectroscopy would greatly benefit from a SC that combines high spectral flatness and a broad spectral coverage, i.e. from a design that allows to overcome this trade-off.

Here, we employ an air-clad silicon-germanium on silicon (SiGe/Si) two-stages inverse-tapered waveguide to enhance the efficiency, the spectral flatness, and the spectral coverage of our SC. We harness the spectral quality of our SC for a proof-of-principle demonstration of parallel free-space spectroscopy of water vapor and carbon dioxide.

RESULTS

Our waveguide consists of a 3.3 μm thick air-clad $\text{Si}_{0.6}\text{Ge}_{0.4}$ core on a silicon substrate (fig. 1a). At the input side, the waveguide is 3.25 μm wide and has a 3 mm long straight section, followed by an inverse-tapered section which increases the waveguide width up to 9 μm at the output side. The small cross straight section at the input enhances

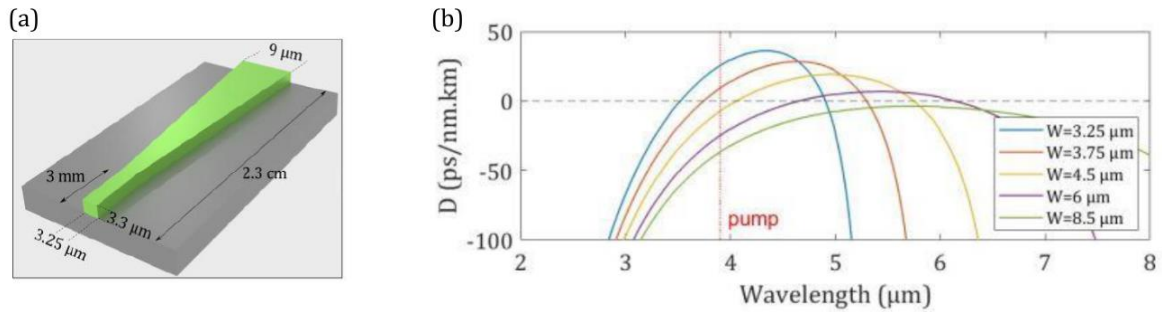


Fig. 1. (a) Schematic of the tapered SiGe/Si waveguide. (b) Dispersion profile for selected waveguide widths.

the efficiency of the nonlinear spectral broadening, which is maximized by the anomalous dispersion profile (fig. 1b, blue curve). The inverse-tapered section enables to continuously shift the position of the two zero dispersion wavelengths (fig. 1b), and therefore the spectral location of the generated dispersive waves, resulting in a flat and broadband spectrum.

Figure 2a shows a schematic of the free-space experimental setup. We pumped the waveguide at $3.9 \mu\text{m}$, in the anomalous dispersion regime (fig. 1b, blue curve), with 200 fs TE polarized pulses at 63 MHz repetition rate and 60 mW average power, delivered by a tunable Optical Parametric Amplifier (OPA, Hotlight Systems MIROPA-fs). We used a set of two polarizers and a half wave-plate to control the input power and polarization. Light was coupled to the waveguide and the output was collected with the help of two MIR lenses, a visible camera (Dino-lite) and a MIR camera (Lynred). The top part of figure 2b shows the generated SC, recorded using an Optical Spectrum Analyzer (OSA, Thorlabs OSA205) sensitive from $<2 \mu\text{m}$ to $5.5 \mu\text{m}$. The SC extends over more than an octave, from 2.4 to $5.5 \mu\text{m}$. The extension at the long wavelength side is limited by the detection band of our spectrum analyzer. Numerical simulations show that the SC could reach $7.8 \mu\text{m}$ wavelength. The continuous spectral shift of the zero dispersion wavelengths, and therefore of the dispersive waves, given by the waveguide tapering results in the filling of the 2.4 - $3 \mu\text{m}$ and 6 - $7.8 \mu\text{m}$ spectral regions, leading to a flatter SC in the tapered than in waveguides with constant width (the spectra recorded for the latter are not shown here).

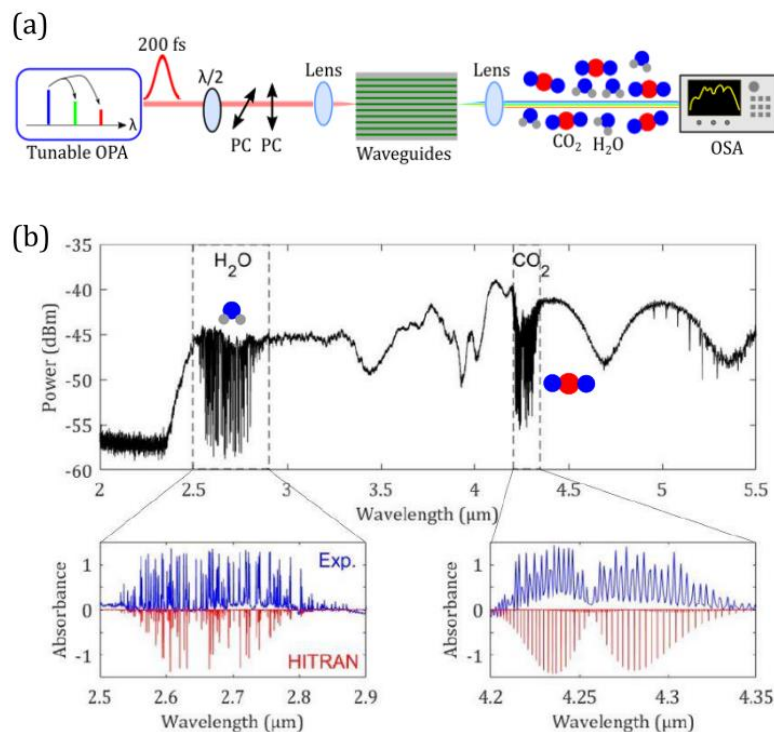


Fig. 2. (a) Schematic of the experimental setup. (b) Experimental SC (top), absorbance of water vapor (bottom left) and carbon dioxide (bottom right) as retrieved from the measured spectrum (blue) and from the HITRAN database (red). The latter was inverted for clarity.

The absorption from water vapor and carbon dioxide in the 55 cm long free-space path between the waveguide output and the spectrum analyzer (see fig. 2a) are clearly visible in the spectrum. In particular, the increased flatness given by our tapered design at the blue end of the spectrum leads to better resolution of the dips due to water absorption at around $2.7 \mu\text{m}$. Similar dips are also visible at around $4.2 \mu\text{m}$ due to the absorption from CO_2 . The bottom part of figure 2b shows the absorbance of water (left) and carbon dioxide (right) as retrieved from our measurements (blue) and compared to the HITRAN database (red). The agreement is relatively good, and it is limited by the resolution, of our spectrum analyzer. We can notice that, in the case of CO_2 , we obtain the double branch absorption spectrum typical of roto-vibrational modes in linear molecules. In the case of water, which is not a linear molecule, the absorption lines have a more complex pattern.

CONCLUSION

In conclusion, we have demonstrated efficient MIR SC generation in a SiGe/Si waveguide. The waveguide was designed to generate a broadband and flat spectrum. We harnessed the spectral quality of our SC for a proof-of-principle demonstration of multi-species parallel gas spectroscopy.

Acknowledgements: We acknowledge the support of the International Associated Laboratory in Photonics between France and Australia (LIA ALPhFA), the Agence Nationale de la Recherche (MIRSICOMB, ANR-17-CE24-0028), the Horizon 2020 research and innovation programme under the Marie Skłodowska-Curie Actions (MSCA) (ECLAUSion, grant agreement No 801512), and the European Research Council (ERC) under the European Union's Horizon 2020 program (GRAPHICS 648546). We also gratefully acknowledge Lynred® for lending us the MIR camera.

References

- [1] M. Vainio and L. Halonen, *Mid-infrared optical parametric oscillators and frequency combs for molecular spectroscopy*, Phys. Chem. Chem. Phys., vol. 18, pp. 4266-4294, 2016
- [2] E. Tagkoudi *et al.*, *Parallel gas spectroscopy using mid-infrared supercontinuum from a single Parallel gas spectroscopy using mid-infrared supercontinuum from a single Si_3N_4 waveguide*, Opt. Lett., vol. 45, pp. 2195, 2020
- [3] R. Soref, *Mid-infrared photonics in silicon and germanium*, Nat. Photonics, vol. 4, pp. 495-497, 2010
- [4] N. K. Hon, R. Soref, and B. Jalali, *The third-order nonlinear optical coefficients of Si, Ge, and $\text{Si}_{1-x}\text{Ge}_x$ in the midwave and longwave infrared*, J. Appl. Phys., vol. 110, pp. 011301, 2011
- [5] M. Sinobad *et al.*, *Mid-infrared octave spanning supercontinuum generation to $8.5\mu\text{m}$ in silicon-germanium waveguides*, Optica, vol. 5, pp. 360-366, 2018
- [6] A. Della Torre *et al.*, *Mid-infrared supercontinuum generation in a low-loss germanium-on-silicon waveguide Mid-infrared supercontinuum generation in a low-loss germanium-on-silicon waveguide*, APL Photonics, vol. 6, pp. 016102, 2021
- [7] M. Sinobad *et al.*, *Dispersion trimming for mid-infrared supercontinuum generation in a hybrid chalcogenide/silicon-germanium waveguide*, J. Opt. Soc. Am. B, vol. 36, pp. A98, 2019
- [8] M. Sinobad *et al.*, *High coherence at f and $2f$ of mid-infrared supercontinuum generation in silicon germanium waveguides*, IEEE J. Sel. Top. Quantum Electron., vol. 26, pp. 1-8, 2019
- [9] M. Sinobad *et al.*, *Mid-infrared supercontinuum generation in silicon-germanium all-normal dispersion waveguides*, Opt. Lett., vol. 45, pp. 5008-5011, 2020
- [10] M. Montesinos-Ballester *et al.*, *On-Chip Mid-Infrared Supercontinuum Generation from 3 to $13 \mu\text{m}$ Wavelength*, ACS Photonics, vol. 7, pp. 3423-3429, 2020

High performance photonic devices based on photonic crystal bimodal interferometer

Invited paper

Jaime García-Rupérez

Nanophotonics Technology Center, Universitat Politècnica de València, Camino de Vera s/n, 46022
Valencia, Spain
* jaigarru@ntc.upv.es

The use of photonic crystal (PhC) structures for the creation of single-channel bimodal interferometric structures allows using the interesting dispersive properties of these periodic structures to improve the performance and to reduce the final footprint of the devices. These structures have been validated for modulation, sensing and switching applications.

Keywords: *photonic crystals, bimodal interferometry, slow-wave, modulator, sensor, switch*

INTRODUCTION

Interferometers are key elements for the development of a wide range of optical components such as modulators, switches or sensors comprising today's photonic integrated circuits (PICs). Their operation is based on their ability to convert refractive index changes occurring either within the structure itself or in its surroundings into a relative phase change between the modes propagating along the interferometer's paths. An interesting property of these structures is that their performance can be improved simply by increasing their length; however, this also implies that they might have a large footprint that hinders their final integration level. An alternative approach to reducing the footprint of an interferometer is by using a bimodal scheme [1], where a single optical waveguide is properly designed in order to simultaneously support two propagating modes having a different propagation constant as well as a different interaction with the structure and with its surroundings. These bimodal waveguides allow reducing the footprint of the device simply due to the fact that only a waveguide is required to perform the interferometry instead of two separated paths as happens in typical interferometric configurations. However, long structure lengths will still be required in order to obtain a good performance.

An alternative approach that has been recently proposed in order to significantly reduce the total footprint of interferometric devices consists on creating photonic crystal (PhC) based bimodal structures. By properly designing a PhC waveguide, several propagating modes can be excited on it for the wavelength region of interest. But more interestingly, the structure can be tuned for these modes to work in the so-called slow-wave regime appearing at the edges of the photonic bandgaps (PBGs) of the structure. The dispersion properties of these regions, where the group velocity of the propagating mode tends to zero, will be translated into a significantly higher phase change when a variation of the refractive index is produced, thus significantly improving the performance of the interferometer and reducing the required length. Additionally, we can also act on the dielectric distribution of the PhC structure in order to control the field distribution of each propagating mode, thus leading to an optimal interaction of the modes with the regions where the refractive index change is expected to be produced.

PhC-BASED BIMODAL INTERFEROMETER FOR MODULATION AND SENSING APPLICATIONS

We have designed a 1D PhC structure having a bimodal behavior for the spectral range corresponding to the vicinities of the PBG created due to the anti-crossing produced between the first and the second TE modes with in-plane even symmetry in the structure (see Fig. 1a) [2]. By properly designing the PhC structure, a very high group index difference between both excited modes can be obtained if one of them is in the slow-wave regime (in this case, the second order mode), thus leading to a dramatic increase in the phase sensitivity. The interferometric response of this bimodal PhC configuration has been experimentally confirmed (see Fig. 1b and 1c), also observing that the interference fringes get closer and narrower as we move towards the slow-wave region of the second order mode due to the increase of its group index (see Fig. 1d).

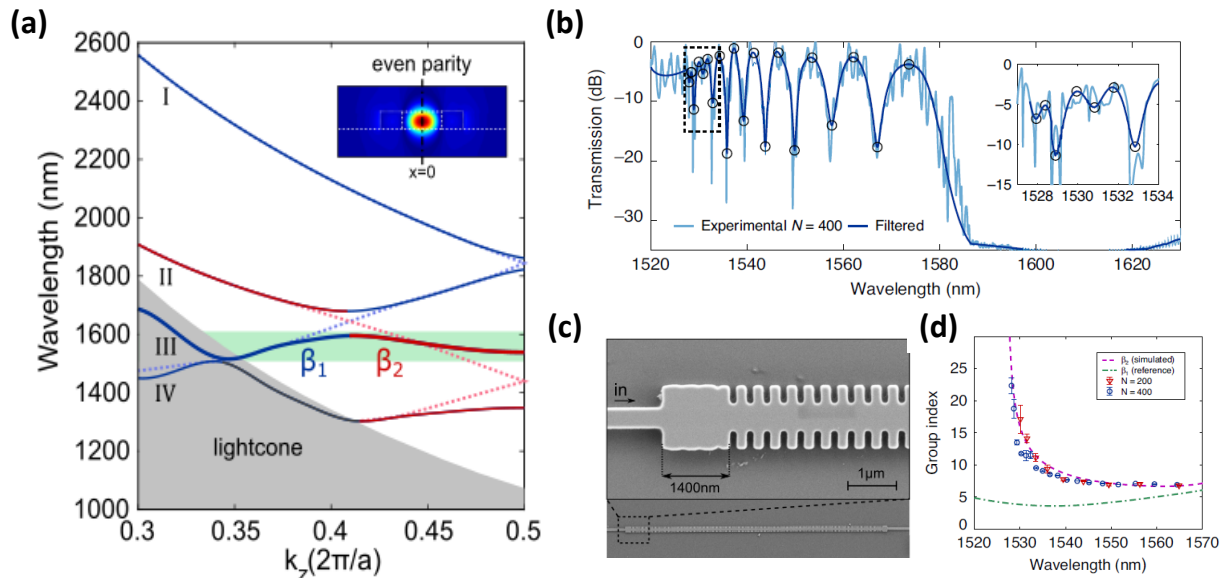


Fig. 1. (a) Dispersion diagram of the 1D PhC structure for the in-plane even parity bands of TE polarization (blue - first order mode / red - second order mode). The green shaded area depicts the bimodal region, where two modes with two different propagation constants are excited. (b) Experimental transmission spectrum for one of the fabricated bimodal 1D PhC interferometric structures comprising $N=400$ periods (length $148\ \mu\text{m}$). (c) Scanning electron microscope (SEM) image of the fabricated bimodal 1D PhC interferometric structure, where an access rectangular taper is created to properly excite both modes. (d) Group index of the second order mode experimentally obtained from the interference fringes observed in the measured spectrum.

This bimodal 1D PhC interferometer structure has been experimentally validated both for modulation and sensing applications, confirming the performance improvement that is obtained when working in the slow-wave region of the second order mode (see Fig. 2). Regarding modulation experiments, it was possible obtaining a phase shift variation of π at the output by only changing the temperature by $13.2\ ^\circ\text{C}$ for a bimodal 1D PhC interferometric structure being $148\ \mu\text{m}$ long. Regarding sensing experiments, normalized phase sensitivity values even above $10^4\ 2\pi\ \text{rad}/\text{RIU}\cdot\text{cm}$ have been obtained, which means an improvement greater than 10x with respect to traditional Mach-Zehnder interferometers and around 7.5x for silicon nitride bimodal waveguides not based on PhC structures.

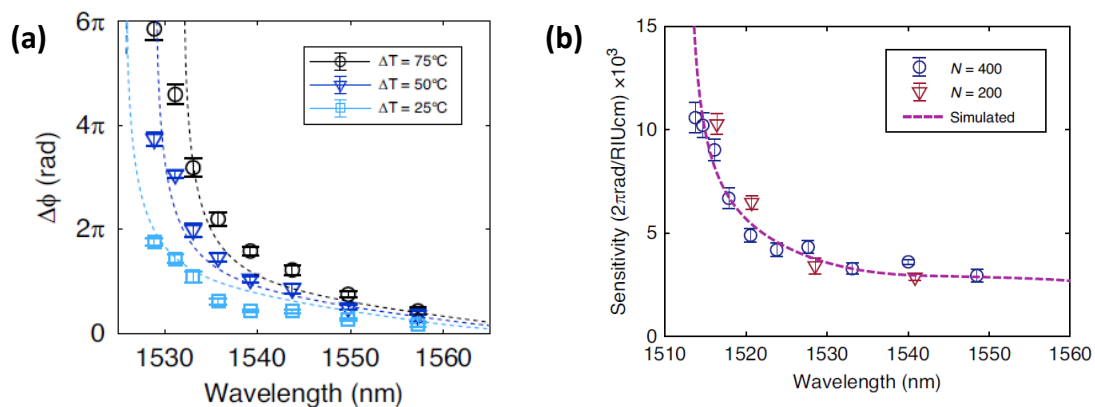


Fig. 2. (a) Experimental phase shift variation measured for different temperature changes of a bimodal 1D PhC interferometric structure of length $148\ \mu\text{m}$ ($N=400$ periods). (b) Experimental length-normalized phase sensitivity obtained for two bimodal 1D PhC interferometric sensors having a different number of periods ($N=200$ and $N=400$). For both plots, dashed lines represent theoretical calculations. In both cases, a significant sensitivity increase is observed as we move into the slow-wave region.

PhC-BASED BIMODAL INTERFEROMETER FOR SWITCHING APPLICATIONS

In this case, the design of the bimodal 1D PhC interferometric structure is modified in order to be able to operate as a 2×2 switch. To this aim, instead of exciting the structure using a single access waveguide aligned with the axis of the 1D PhC, two access waveguides whose position is shifted with respect to this axis are used for the excitation (see Fig. 3a). In this way, both even and odd in-plane symmetry modes can be excited to obtain the bimodal

interferometric response (see Fig. 3b). One of the advantages of this configuration is that both even and odd modes can be designed independently because of symmetry conditions and thereby a flat spectral region of high group index contrast can be engineered.

This structure has been fabricated including titanium heaters on top of the bimodal interferometric structures. By changing the voltage applied to these heaters, it is possible to switch the response of the structure (see Fig. 3c). By properly designing the 1D PhC interferometer, it has been possible to demonstrate switching using a structure with a footprint of only $63 \mu\text{m}^2$ (length of $37 \mu\text{m}$) and applying a voltage of 3V (power consumption of 19.5 mW).

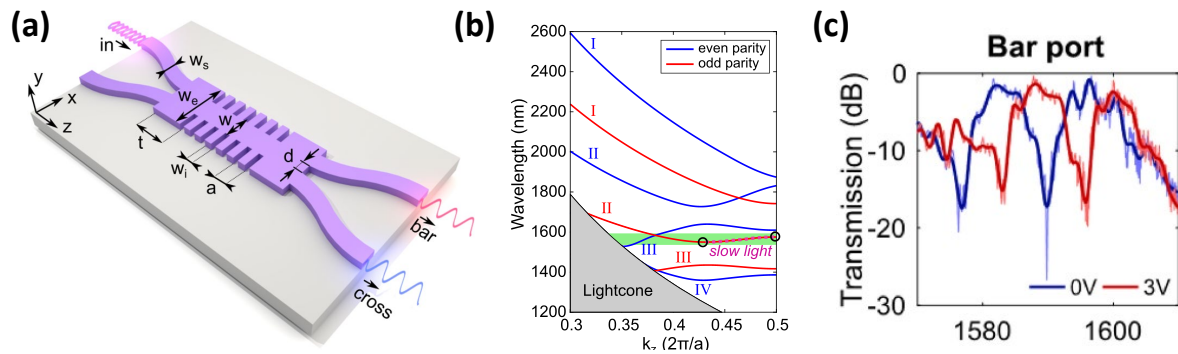


Fig. 3. (a) Scheme of the proposed 2×2 switch-like bimodal 1D PhC interferometric structure. (b) Band structure of the designed 1D PhC structure for the TE bands with even and odd in-plane symmetry. The green shaded area indicates the bimodal region of interest, where the odd parity band becomes slow light. (c) Experimental transmission spectrum at the bar output port for one of the fabricated structures, showing the switching operation when the voltage applied to the heaters is changed.

Acknowledgements: Authors acknowledge the support from the Spanish MCIN/AEI /10.13039/501100011033 through the PID2019-106965RB-C21 project and by the European Union through the operational program of the European Regional Development Fund (FEDER) of the Valencia Regional Government 2014-2020.

References

- [1] K. E. Zinoviev, et al., *Integrated Bimodal Waveguide Interferometric Biosensor for Label-Free Analysis*, J. Light. Technol., vol. 29, pp. 1926-1930, 2011
- [2] L. Torrijos-Morán, et al., *Slow light bimodal interferometry in one-dimensional photonic crystal waveguides*, Light Sci Appl., vol. 10, pp. 16, 2021
- [3] L. Torrijos-Morán, et al., *Ultra-compact optical switches using slow light bimodal silicon waveguides*, J. Light. Technol., vol. 39, pp. 3495-3501, 2021

Curved waveguide grating demultiplexer (CWG) with a flattened response via bimodal output waveguides

(Student paper)

Abdelfettah Hadij-ElHouati,^{1,*} Robert Halir,¹ Alejandro Ortega-Moñux,¹ J. Gonzalo Wangüemert-Pérez,¹

Jens H. Schmid,² Pavel Cheben,² and Iñigo Molina-Fernandez¹

¹Telecommunication Research Institute (TELMA), Universidad de Málaga, CEI Andalucía TECH, Louis Pasteur 35, 29010 Málaga, Spain

²National Research Council Canada, Ottawa, Ontario K1A 0R6, Canada

* abdel@uma.es

We demonstrate a compact wavelength demultiplexer for the silicon-on-insulator platform based on the curved waveguide grating (CWG) architecture. The proposed device uses bimodal output waveguides to achieve a low-loss flattened spectral response. The device shows insertion loss as low as 1.2 dB and crosstalk below -20 dB.

Keywords: WDM demultiplexer, curved waveguide grating, SOI, SWG, flat-top

INTRODUCTION

Silicon photonics (SiPh) has become the leading integrated photonics technology [1]. It brings together high integration density while being compatible with the already established microelectronic CMOS process allowing low-cost mass production. Datacom is an important application area of SiPh [2]. Wavelength division multiplexing (WDM) data links are used to achieve high aggregated data rates without increasing the symbol rates, which are limited by the modulator and demodulator bandwidths. The wavelength (de)multiplexer is a key component in WDM systems. Various WDM demultiplexing schemes have been proposed for the SiPh platform including ring resonator filters, lattice-form filters, arrayed waveguide gratings (AWGs) and echelle gratings (EGs) [3]. Flattened spectral response is highly desired for demultiplexers as it reduces the spectral stability requirements of the laser, hence reducing the laser cost and avoiding the need for thermal control.

The curved waveguide grating (CWG) demultiplexer was proposed by Hao et al. as a promising alternative to the conventional architectures [4] and was later demonstrated for the silicon-on-insulator (SOI) platform at the National Research Council Canada [5], [6]. We recently demonstrated a low-loss CWG demultiplexer that achieves state-of-the-art performance [7]. In that work, we use the single-beam condition [8] to suppress the off-chip radiation that causes optical loss [9]. For doing so, we judiciously design the diffractive grating period and the lateral subwavelength grating (SWG) slab metamaterial to frustrate phase-matching in the silica while allowing it in the SWG slab. Figure 1 shows a schematic of the proposed CWG demultiplexer comprising: a curved waveguide grating placed along a circular path, SWG a slab, a free propagation region (FPR) slab and output receiving waveguides positioned on the so-called Rowland circle. The SWG slab is a periodic structure that synthesizes an artificial metamaterial with a properly designed effective refractive index [10], [11].

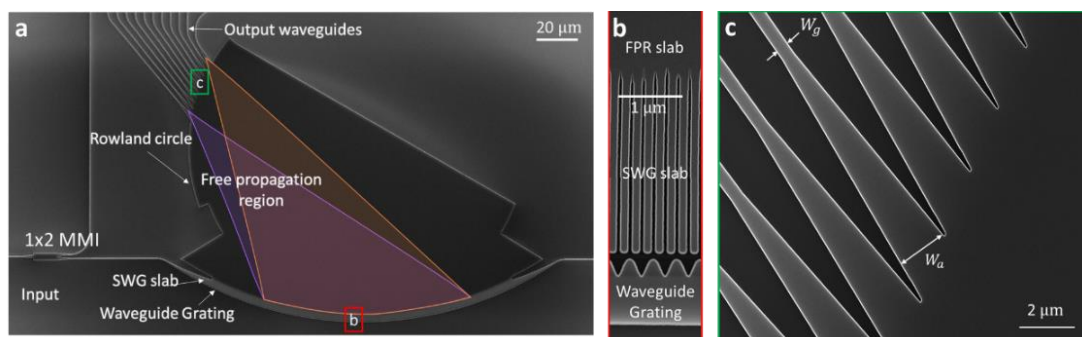


Fig. 1. Curved waveguide grating demultiplexer schematic (a), detail of the sinusoidal waveguide grating (b) and detail of the receiving waveguides and tapers (c).

Here, we present a low loss CWG demultiplexer with a flattened response that uses the first two modes of the output waveguides to achieve a low loss flattop response [3]. The device efficiently separates 5 channels spaced 10nm within C-band with an insertion loss as low as 1.2 dB and crosstalk better than -20 dB.

FUNDAMENTALS AND DESIGN

The TE polarized light entering the device from the input waveguide is progressively diffracted by the waveguide grating. The SWG region guides the diffracted light into the FPR. The light propagates through the FPR and is focused on the Rowland circle where is captured by the receiving apertures of width W_a that are tapered to the output waveguides of width W_g (see Fig. 1c). The dispersive nature of the waveguide grating produces the demultiplexing functionality since the diffraction angle θ varies with the wavelength as described by the grating equation:

$$\theta(\lambda) = \text{asin}((n_{FB} - \lambda/\Lambda)/n_S) \quad (1)$$

where, n_{FB} is the waveguide grating Floquet-Bloch mode effective index, λ is the free-space wavelength, Λ is the waveguide grating period and n_S is the effective index of the FPR slab. To fulfil the single beam condition [8], output waveguides are placed at an angle $\theta \approx -35^\circ$ from the grating normal.

The CWG demultiplexer was designed following the same procedure as the Gaussian-shaped device reported in [7]. The grating radius was set to $R = 230 \mu\text{m}$ to enforce a channel separation of 10 nm. To limit the grating length to $\pi/3$ rad along the grating circle, the illumination spot at the focal plane was set to a Gaussian with a mode field radius (MFR) of $0.75 \mu\text{m}$, which corresponds to the fundamental mode of a $2.15\text{-}\mu\text{m}$ width waveguide. For this illumination, we have evaluated the transmission response as a function of the spectral shift normalized to the 25-dB bandwidth (shown in Fig. 2) for both the monomodal (grey curve) and bimodal output waveguides cases (coloured curves). We observe that the response is flattened for the bimodal case as the taper width W_a is increased. We also include, for reference, the response when a mono-mode output is used with a taper width matched to the illumination ($W_a = 2.15 \mu\text{m}$).

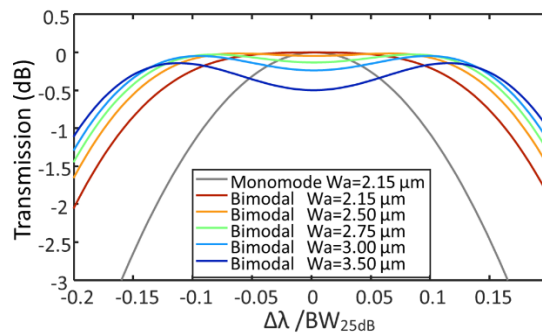


Fig. 2. Channel response for mono-mode (grey) and bimodal outputs (colour) for various widths of the receiving tapers W_a .

Figure 3 shows the response characteristics as a function of the taper width W_a . To measure flatness, we used the ratio of 25-dB and 1-dB bandwidths, shown in Fig. 3.a. We see that by increasing the taper width W_a , the flatness improves when using bimodal outputs (purple) and stays unaltered for the mono-mode outputs (grey). However, this also raises the ripple (Fig. 3.b) and loss (Fig. 3c). We use $W_a = 2.75 \mu\text{m}$ as a compromise value to attain twice the flatness while incurring a negligible impact on the loss (<0.2 dB) and ripple (<0.2 dB). The output waveguides width W_g was set to 700 nm, ensuring low-loss propagation for the two first TE modes while frustrating higher-order modes propagation.

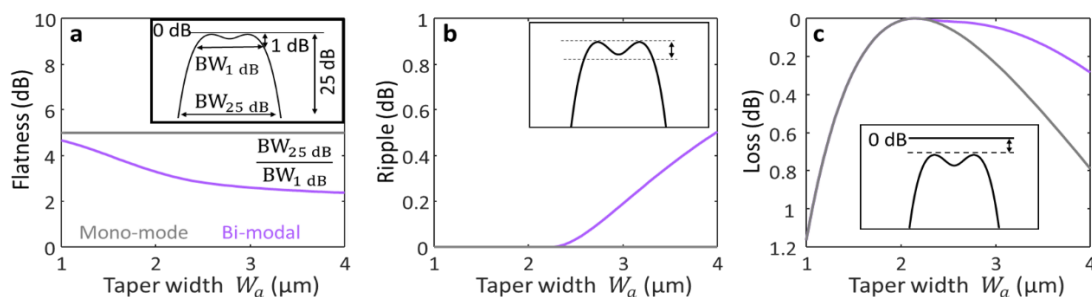


Fig. 3. Response characteristics for a bimodal output CWG (purple) compared with a mono-mode output (grey). a) Flatness, b) ripple and c) loss when the CWG focuses a $0.75\text{-}\mu\text{m}$ -MFR Gaussian illumination at the receiving tapers versus their width W_a .

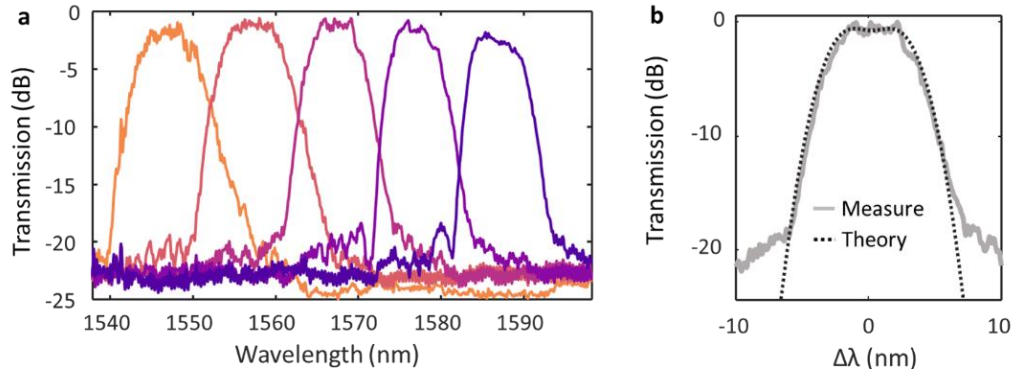
EXPERIMENTAL VERIFICATION


Fig. 3. a) Measured spectra for the fabricated CWG demultiplexer with flat-top response. b) Comparison of a selected channel response with the designed theoretical response shape.

The device was fabricated in a standard SOI platform wafer using electron beam lithography patterning and reactive ion etching.

The characterization was done by injecting a monochromatic, TE-polarized signal from a tuneable laser and measuring the signal power at the output waveguides with a photodetector. An on-chip 3dB power splitter was used at the device input to extract a reference signal to determine the device transmittance (see Fig. 1a). Figure 4 shows the measured transmission spectra for the device. The response shape matches the theoretical flat-top response as shown in Fig. 4.b. The measured losses range from 1.2 dB to 2 dB and the crosstalk is lower than -20 dB for all channels.

CONCLUSIONS

We have demonstrated a low-loss flat-top 5-channel curved waveguide grating wavelength demultiplexer for the SOI platform. The off-chip radiation was virtually suppressed by enforcing the single beam condition on the grating waveguide using metamaterial refractive index engineering while flat-top response was achieved via bi-modal output waveguides. The experimental device exhibits flattened spectral response while maintaining low loss (1.2-2 dB) and crosstalk (<-20 dB).

Acknowledgements: Universidad de Málaga; Ministerio de Educación, Cultura y Deporte (MECD) (FPU16/03401), Ministerio de Ciencia, Innovación y Universidades (MCIU) (PID2019-106747RBI00), Consejería de Economía, Conocimiento, Empresas y Universidad (CECEU) (UMA18-FEDERJA-219, P18-RT1453, P18-RT-793).

References

- [1] D. Thomson *et al.*, 'Roadmap on silicon photonics', *J. Opt.*, vol. 18, no. 7, p. 073003, Jul. 2016.
- [2] Z. Zhou, R. Chen, X. Li, and T. Li, 'Development trends in silicon photonics for data centers', *Optical Fiber Technology*, vol. 44, pp. 13–23, Aug. 2018.
- [3] K. Okamoto, 'Wavelength-Division-Multiplexing Devices in Thin SOI: Advances and Prospects', *IEEE J. Select. Topics Quantum Electron.*, vol. 20, no. 4, pp. 248–257, Jul. 2014.
- [4] Y. Hao *et al.*, 'Novel dispersive and focusing device configuration based on curved waveguide grating (CWG)', *Opt. Express*, vol. 14, no. 19, p. 8630, 2006.
- [5] J. H. Schmid *et al.*, 'Refractive Index Engineering With Subwavelength Gratings in Silicon Microphotonic Waveguides', *IEEE Photonics J.*, vol. 3, no. 3, pp. 597–607, Jun. 2011.
- [6] P. J. Bock *et al.*, 'Demonstration of a curved sidewall grating demultiplexer on silicon', *Opt. Express*, vol. 20, no. 18, p. 19882, Aug. 2012.
- [7] A. Hadij-Elhouati *et al.*, 'Low-loss off-axis curved waveguide grating demultiplexer', *Opt. Lett.*, vol. 46, no. 19, p. 4821, Oct. 2021.
- [8] A. Hadij-Elhouati *et al.*, 'High-efficiency conversion from waveguide mode to on-chip beam using a metamaterial engineered Bragg deflector', *Opt. Lett.*, vol. 46, no. 10, pp. 2409–2412, May 2021.
- [9] A. Hadij-Elhouati *et al.*, 'Distributed Bragg deflector coupler for on-chip shaping of optical beams', *Opt. Express*, vol. 27, no. 23, pp. 33180–33193, Nov. 2019.
- [10] P. Cheben *et al.*, 'Subwavelength integrated photonics', *Nature*, vol. 560, no. 7720, pp. 565–572, Aug. 2018.
- [11] J. M. Luque-González *et al.*, 'A review of silicon subwavelength gratings: building break-through devices with anisotropic metamaterials', *Nanophotonics*, vol. 10, no. 11, pp. 2765–2797, Aug. 2021.

Subwavelength metamaterials for broadband mode multiplexing and power splitting in silicon waveguides

Aitor V. Velasco¹, David González-Andrade², Raquel Fernández de Cabo¹, Jaime Vilas³, Irene Olivares³, Antonio Dias³, José Manuel Luque-González⁴, J. Gonzalo Wangüemert-Pérez⁴, Alejandro Ortega-Moñux⁴, Íñigo Molina-Fernández^{4,5}, Robert Halir^{4,5} and Pavel Cheben⁶

¹Instituto de Óptica Daza de Valdés, Consejo Superior de Investigaciones Científicas (CSIC), Madrid 28006, Spain

²Centre de Nanosciences et de Nanotechnologies, CNRS, Université Paris-Saclay, Palaiseau 91120, France

³Alcyon Photonics S.L., Madrid 28004, Spain

⁴Universidad de Málaga, Departamento de Ingeniería de Comunicaciones, ETSI Telecomunicación, 29071 Málaga, Spain

⁵Bionand Center for Nanomedicine and Biotechnology, Parque Tecnológico de Andalucía, Málaga 29590, Spain

⁶National Research Council Canada, 1200 Montreal Road, Bldg. M50, Ottawa K1A 0R6, Canada

*a.villafranca@csic.es

Subwavelength metamaterials provide a powerful tool for the realization of compact and high-performance integrated photonic devices. In this work, we apply subwavelength metamaterials to novel devices for mode multiplexing and power splitting in silicon on insulator. We experimentally demonstrate ultra-broad operational bandwidths over 245 nm in both applications.

Keywords: Silicon photonics, subwavelength, mode multiplexing, power splitting

INTRODUCTION

Mode-division multiplexing (MDM) in integrated silicon photonics is emerging as a fundamental technology to address the challenge of ever-increasing global data traffic and data center demand.^[1] High-performance mode converters and multiplexers/demultiplexers (MUX/DEMUX) are the fundamental building blocks at the core of MDM technologies, with current architectures including asymmetric directional couplers (ADC), asymmetric Y-junctions, adiabatic tapers, and topologies based on inverse design, among others.^[2-5] In particular, MDM architectures based on multimode interference (MMI) couplers have reported good performance over a relatively wide wavelength range^[6-7], although further bandwidth enhancements are still sought after. Auxiliary devices beyond MUX/DEMUX are also required in MDM systems, such as multimode power splitters. A broad range of power splitters has been proposed, including topologies based on symmetric Y-junctions, MMIs, inverse and adiabatic tapers, directional couplers, slot waveguides or photonic crystals.^[8-11] In particular, symmetric Y-junctions^[8] are one of the most common alternatives given their ease of design, simply consisting of a stem waveguide ramifying into two arms of the same width. However, finite resolution of fabrication processes results in deviations from the nominal design at the junction tip, and degrade the performance of the fabricated devices.

Subwavelength grating (SWG) metamaterials provide a powerful tool for improving the performance of MUX/DEMUX and power splitters, among other photonic devices.^[12] SWG structures are arrangements of dielectric materials with a scale substantially smaller than the operating wavelength, hence suppressing diffractive effects and enabling dispersion engineering.^[13] In the MDM field, SWGs have been applied to adiabatic couplers^[14], ADCs^[15] or MMI couplers^[16,17]; whereas in the field of power splitting, SWG engineering has also been applied to asymmetric directional couplers^[18], MMI devices^[19], or Y-junctions^[20], among others.

In this work, we review our latest SWG-based MUX/DEMUX and power splitter^[17,20], expand on the experimental characterization of both devices, and present enhanced topologies for improved performance and additional features such as higher-order mode support. In particular, we experimentally demonstrate ultra-broad operational bandwidths over 245 nm in both SWG-enhanced mode multiplexer and power splitter.

MODE MULTIPLEXING

Our SWG MUX/DEMUX is based on the combination of a MMI, a 90° phase shifter and a symmetric Y-junction (Fig. 1). Both the MMI and the phase shifter are implemented with SWG metamaterials for enhanced bandwidth.^[17] When operating as MUX, the fundamental transverse electric modes (TE₀) in ports 1 (blue) and 2 (green) are equally divided by the metamaterial-based MMI, while inducing a 90° phase shift between MMI output ports. The phase shifter delays the mode propagated through the upper arm an additional 90°, which either compensates the MMI phase shift (blue), or results in a total phase shift of 180° (green). As a result of the phase relations of the modes at the Y-junction arms, their conversion results in TE₀ (blue) or TE₁ (green) at port 3.

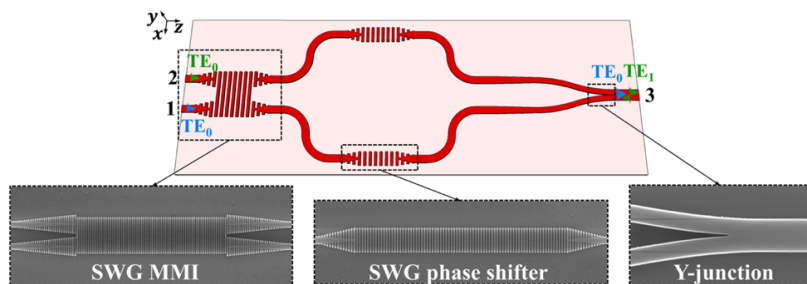


Fig. 1. Mode converter and multiplexer based on an SWG MMI, an SWG phase shifter and a symmetric Y-junction.

The SWG MUX/DEMUX was fabricated in a commercial foundry using silicon-on-insulator (SOI) wafers with a silicon thickness of 220 nm, a buried oxide (BOX) layer of 2 μm , and a 2.2 μm thick SiO_2 upper cladding oxide. SWG edge couplers were incorporated for high-efficiency input and output coupling.^[21] Experimental characterization of a full MUX/DEMUX link (i.e. devices connected back-to-back), presented in Fig. 2., shows insertion losses of 2 dB and crosstalk better than -17.2 dB for the full link over a 245 nm bandwidth (1427 – 1672 nm). These results entail a 100 nm bandwidth expansion when compared to the device with a non-SWG phase shifter.^[16]

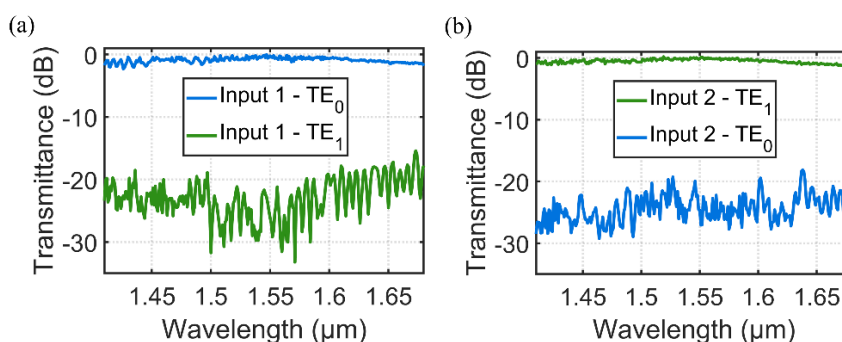


Fig. 2. Experimental transmittance measurements for the proposed mode converter and multiplexer for output modes TE_0 and TE_1 , when using input 1 (a) and input 2 (b).

POWER SPLITTING

Our power splitter is based on a SWG-engineered symmetric Y-junction for reduced mode confinement at the junction tip (Fig. 3). This topology circumvents minimum feature size (MFS) limitations at the junction tip and significantly improves TE_0 excess loss (EL), at the expense of a slight increase in TE_1 loss. Arm width was optimized to minimize effective index mismatch at the interface between the stem (i.e. multimode input waveguide) and the arms.^[21] The device was optimized considering two target minimum feature sizes, namely 50 nm and 100 nm. Conventional Y-junctions with the same MFS limitations were also fabricated for comparison.



Fig. 3. Scanning electron microscope image of the proposed subwavelength Y-junction

The SWG power splitter was fabricated in the same 220 nm SOI platform as the MUX/DEMUX devices. Cascaded splitters were included for accurate characterization of TE_0 loss, whereas a dual-core adiabatic taper MUX^[5] was incorporated for TE_1 loss measurement. Fig. 4 shows the excess loss under 0.3 dB over a 260 nm bandwidth for TE_0 in the high resolution lithography (MFS = 50 nm), and EL less than 1 dB for TE_1 within a 100 nm bandwidth.

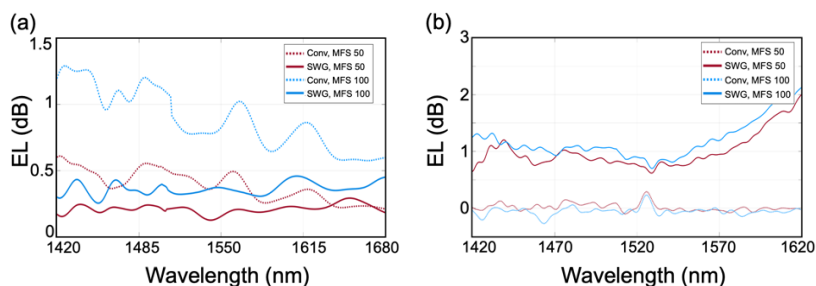


Fig. 4. Experimental excess loss of the proposed subwavelength Y-junction (solid) and a conventional Y-junction (dotted), with minimum feature sizes of 50 nm (red) and 100 nm (blue), for TE_0 (a) and TE_1 (b) modes.

CONCLUSIONS

We have presented a mode multiplexer/demultiplexer and a multimode power splitter based on SWG metamaterials. Experimental characterization of the fabricated devices demonstrates bandwidths over 245 nm in both applications.

Acknowledgements: This work has been funded in part by the Spanish Ministry of Science and Innovation (MICINN) under grants RTI2018-097957-B-C33, RED2018-102768-T and PID2020-115353RA-I00; by MICINN, the Spanish State Research Agency (AEI) and the European Union – NextGenerationEU, through the Recovery, Transformation and Resilience Plan (IND2020/TIC-17510, DIN2020-011488); the Community of Madrid – FEDER funds (S2018/NMT-4326, STARTUP2020\L2550); and by Horizon 2020 (Marie Skłodowska-Curie grant No. 734331).

References

- [1] C. Li, D. Liu, and D. Dai, "Multimode silicon photonics," *Nanophotonics*, vol. 8, no. 2, pp. 227–247, 2019.
- [2] J. Wang, Y. Xuan, M. Qi, H. Huang, Y. Li, M. Li, X. Chen, Z. Sheng, A. Wu, W. Li, X. Wang, S. Zou, and F. Gan, "Broadband and fabrication-tolerant on-chip scalable mode-division multiplexing based on mode-evolution counter-tapered couplers," *Opt. Lett.*, vol. 40, no. 9, pp. 1956–1959, 2015.
- [3] H. Li, P. Wang, T. Yang, T. Dai, G. Wang, S. Li, W. Chen, and J. Yang, "Experimental demonstration of a broadband two-mode multi/demultiplexer based on asymmetric Y-junctions," *Opt. Laser Technol.*, vol. 100, pp. 7–11, 2018.
- [4] W. Chang, L. Lu, X. Ren, D. Li, Z. Pan, M. Cheng, D. Liu, and M. Zhang, "Ultra-compact mode (de) multiplexer based on subwavelength asymmetric Y-junction," *Opt. Express*, vol. 26, no. 7, pp. 8162–8170, 2018.
- [5] D. Dai, C. Li, S. Wang, H. Wu, Y. Shi, Z. Wu, S. Gao, T. Dai, H. Yu, and H.-K. Tsang, "10-channel mode (de)multiplexer with dual polarizations," *Laser Photonics Rev.*, vol. 12, p. 1700109, 2018.
- [6] Y. Li, C. Li, C. Li, B. Cheng, and C. Xue, "Compact two-mode (de)multiplexer based on symmetric Y-junction and multimode interference waveguides," *Opt. Express*, vol. 22, no. 5, pp. 5781–5786, 2014.
- [7] L. Han, S. Liang, H. Zhu, L. Qiao, J. Xu, and W. Wang, "Two-mode de/multiplexer based on multimode interference couplers with a tilted joint as phase shifter," *Opt. Lett.*, vol. 40, no. 4, pp. 518–521, 2015.
- [8] C. Sun, J. Zhao, Z. Wang, L. Du, and W. Huang, "Broadband and high uniformity Y junction optical beam splitter with multimode tapered branch," *Optik*, vol. 180, pp. 866–872, 2019.
- [9] S. Hassan and D. Chack, "Design and analysis of polarization independent MMI based power splitter for PICs," *Microelectronics J.*, vol. 104, p. 104887, 2020.
- [10] Z. Lu, H. Yun, Y. Wang, Z. Chen, F. Zhang, N. A. F. Jaeger, and L. Chrostowski, "Broadband silicon photonic directional coupler using asymmetric-waveguide based phase control," *Opt. Express*, vol. 23, no. 3, pp. 3795–3806, 2015.
- [11] D. González-Andrade, C. Lafforgue, E. Durán-Valdeiglesias, X. Le Roux, M. Berciano, E. Cassan, D. Marris-Morini, A. V. Velasco, P. Cheben, L. Vivien, and C. Alonso-Ramos, "Polarization- and wavelength-agnostic nanophotonic beam splitter," *Sci. Rep.*, vol. 9, p. 3604, 2019.
- [12] P. Cheben, R. Halir, J. H. Schmid, H. A. Atwater, and D. R. Smith, "Subwavelength integrated photonics," *Nature*, vol. 560, no. 7720, pp. 565–572, 2018.
- [13] P. Cheben, P. J. Bock, J. H. Schmid, J. Lapointe, S. Janz, D.-X. Xu, A. Densmore, A. Delâge, B. Lamontagne, and T. J. Hall, "Refractive index engineering with subwavelength gratings for efficient microphotonic couplers and planar waveguide multiplexers," *Opt. Lett.*, vol. 35, no. 15, pp. 2526–2528, 2010.
- [14] L. Xu, Y. Wang, D. Mao, J. Zhang, Z. Xing, E. El-Fiky, M. G. Saber, A. Kumar, Y. D'Mello, M. Jacques, and D. V. Plant, "Ultra-broadband and compact two-mode multiplexer based on subwavelength-grating-slot-assisted adiabatic coupler for the silicon-on-insulator platform," *J. Lightw. Technol.*, vol. 37, no. 23, pp. 5790–5800, 2019.
- [15] Z. Jafari, A. Zarifkar, and M. Miri, "Compact fabrication-tolerant subwavelength-grating-based two-mode division (de)multiplexer," *Appl. Opt.*, vol. 56, no. 26, pp. 7311–7319, 2017.
- [16] D. González-Andrade, J. G. Wangüemert-Pérez, A. V. Velasco, A. Ortega-Moñux, A. Herrero-Bermello, I. Molina-Fernández, R. Halir, and P. Cheben, "Ultra-broadband mode converter and multiplexer based on sub-wavelength structures," *IEEE Photon. J.*, vol. 10, no. 2, p. 2201010, 2018.
- [17] D. González-Andrade, R. Fernández de Cabo, J. Vilas, I. Olivares, A. Dias; J. M. Luque-González, J. Gonzalo Wangüemert-Pérez, A. Ortega-Moñux, I. Molina-Fernández, R. Halir, P. Cheben, and A. V. Velasco, "Mode converter and multiplexer with a subwavelength phase shifter for extended broadband operation," *IEEE Photonics Technol. Lett.*, vol. 33, no. 22, pp. 1262–1265, 2021.
- [18] C. Ye and D. Dai, "Ultra-compact broadband 2×2 3 dB power splitter using a subwavelength-grating-assisted asymmetric directional coupler," *J. Lightw. Technol.*, vol. 38, no. 8, pp. 2370–2375, 2020.
- [19] H. Shiran, G. Zhang, and O. Liboiron-Ladouceur, "Dual-mode broadband compact 2×2 optical power splitter using sub-wavelength metamaterial structures," *Opt. Express*, vol. 29, no. 15, pp. 23864–23876, 2021.
- [20] R. Fernández de Cabo, D. González-Andrade, P. Cheben, and A. V. Velasco, "High-performance on-chip silicon beamsplitter based on subwavelength metamaterials for enhanced fabrication tolerance," *Nanomaterials*, vol. 11, no. 5, p. 1304, 2021.
- [21] P. Cheben, J. H. Schmid, S. Wang, D.-X. Xu, M. Vachon, S. Janz, J. Lapointe, Y. Painchaud, and M. J. Picard, "Broadband polarization independent nanophotonic coupler for silicon waveguides with ultra-high efficiency," *Opt. Express*, vol. 23, no. 17, pp. 22553–22563, 2015.

Metamaterial-engineered silicon devices fabricated with deep UV immersion lithography

Daniele Melati^{1,*}, Vladyslav Vakarin^{1,†}, Thi Thuy Duong Dinh¹, Xavier Le Roux¹, Warren Kut King Kan², Cécilia Dupré², Bertrand Szlag², Stéphane Monfray³, Frédéric Boeuf³, Pavel Cheben^{4,5}, Eric Cassan¹, Delphine Marris-Morini¹, Laurent Vivien¹ and Carlos Alonso-Ramos¹

¹Centre de Nanosciences et de Nanotechnologies, Université Paris-Saclay, CNRS, 91120 Palaiseau, France

²LETI, University Grenoble Alpes and CEA, 38054 Grenoble, France

³STMicroelectronics SAS, 850 rue Jean Monnet, 38920 Crolles, France

⁴National Research Council Canada, 1200 Montreal Road, Ottawa, ON K1A 0R6, Canada

⁵Center for Research in Photonics, University of Ottawa, Ottawa, ON K1N 6N5, Canada

[†]Current address: III-V Lab, a Joint Lab of Nokia Bell Labs, Thales Research and Technology and CEA LETI, 91767 Palaiseau, France.

* daniele.melati@universite-paris-saclay.fr

Subwavelength grating (SWG) metamaterials have enabled the realization of silicon photonic devices with unprecedented performance. However, most successful SWG realizations relied on electron-beam lithography, compromising the scalability of the approach. Here, we report SWG metamaterial engineered devices fabricated with deep-ultraviolet immersion lithography in a 300-mm silicon-on-insulator technology.

Keywords: subwavelength grating; metamaterial; silicon photonics; multi-mode interference coupler; beam splitter; ring resonator; immersion deep-UV lithography

INTRODUCTION

The use of subwavelength grating (SWG) metamaterials opened a powerful degree of freedom in the development of silicon photonic devices, offering the possibility to control the effective refractive index of the material. This is achieved because dielectric structures arranged at a distance substantially smaller than the wavelength of the propagating light effectively acts as a homogeneous material whose optical properties (e.g., effective index, dispersion, and anisotropy) are determined by the geometry of the unit cells [1,2]. Since their initial introduction, SWGs enabled the demonstration of a vast number of silicon photonic devices with record performance, e.g., edge couplers, surface gratings, resonators, filters, and multi-mode interference (MMIs) couplers, to name a few [3-6]. The use of a graded index SWG metamaterial has also been recently proposed for devices realized in III-V membranes on silicon [7].

The fabrication of SWG metamaterials uses the same process of conventional waveguides and can hence be easily implemented in established platforms. However, the need to maintain the grating period smaller than the wavelength of light often creates small features that may be challenging to fabricate in a reliable and reproducible way using dry deep-ultraviolet (DUV) lithography [8]. One possibility is to constrain the minimum feature size above the resolution limit of dry DUV lithography, typically in the order of 120 nm. However, this constraints the available design space and the range of achievable properties of the effective material, ultimately impacting the performance of the devices. Alternatively, electron-beam lithography offers higher resolution but at the expense of a vastly reduces throughput mostly compatible with research or small volume productions.

In order to overcome this limitations, we explore here the use of immersion DUV lithography for the fabrication of photonic devices based on SWG metamaterials. Immersion DUV lithography is compatible with high-volume production and, compared to dry lithography, allows achieving a three-fold improvement in device size reproducibility, reduced line edge roughness, and sufficient resolution to pattern feature with sizes close to 60 nm [9]. We take advantage of the significant quality improvement offered by immersion DUV lithography by exploiting a 300-mm silicon-on-insulator (SOI) fabrication platform to experimentally demonstrate two SWG-engineered devices with high performance, i.e., a broadband integrated beam splitter and ring resonator with low thermal sensitivity. Both devices have a silicon thickness of 300 nm and nominal minimum feature sizes of 75 nm for the splitter and 100 nm for the ring, below the resolution capabilities of dry DUV lithography. The beam splitter is based on an SWG engineered multi-mode interference (MMI) coupler [10] and exhibits low excess losses below 1 dB with negligible power imbalance and phase errors over a bandwidth of 186 nm near $\lambda = 1550$ nm. The ring resonators operate for transverse-magnetic polarization at a wavelength near 1310 nm, with a measured thermal shift of the resonant wavelength of only ~ 30 pm/°C, a two-fold reduction compared to standard silicon ring resonators [11].

RESULTS

MMIs exploit multi-mode interference in a large waveguide section to achieve beam splitting. Since interference is defined by the wavelength-dependent relative phase delays between the modes, bandwidth is typically limited to about 100 nm to ensure an insertion loss penalty smaller than 1 dB in 2×2 MMIs with solid silicon cores [12]. Here we used an SWG metamaterial to realize the multi-mode waveguide section in order to exploit its anisotropy, as first proposed by Halir et al. [10]. By controlling the dispersion of the effective material index, it is possible to reduce the wavelength dependence of the difference between the propagation constants of the modes and increase the MMI bandwidth. We consider in particular a TE polarized light in a silicon core thickness of 300 nm with 2 μm buried oxide (BOX), and 2 μm upper cladding. The period of the metamaterial is $\Lambda = 150$ nm and the duty cycle $DC = 0.5$, resulting in minimum feature size of 75 nm. The width of the multi-mode section is chosen as 3.5 μm and the length 18 μm (120 periods for the SWG). The width of the access waveguides is 1.7 μm while the 0.4- μm -wide silicon wire waveguides are widened to 1 μm and adiabatic transitions are used between the solid core waveguides and the SWG access waveguides. The distance between the access waveguides is 2.17 μm . Figure 1a shows an SEM picture of the realized MMI before deposition of the SiO_2 upper cladding. The device was characterized using asymmetric Mach-Zehnder interferometers and a reference waveguide for transmission normalization. The experimental results are shown in Figs. 1b-d. Insertion losses and power imbalance remain smaller than 1 dB in the entire wavelength range between 1490 nm and 1680 nm. Regarding phase error measurements, an increased noise can be observed for $\lambda < 1500$ nm. Despite this, phase errors smaller than $\pm 6^\circ$ are obtained for $\lambda > 1494$ nm. Our sources do not extend beyond $\lambda = 1680$ nm, preventing measurements at longer wavelengths. Aiming for excess losses and imbalance below 1 dB and phase error smaller than 6° , these results yield an experimentally measured bandwidth of at least 186 nm.

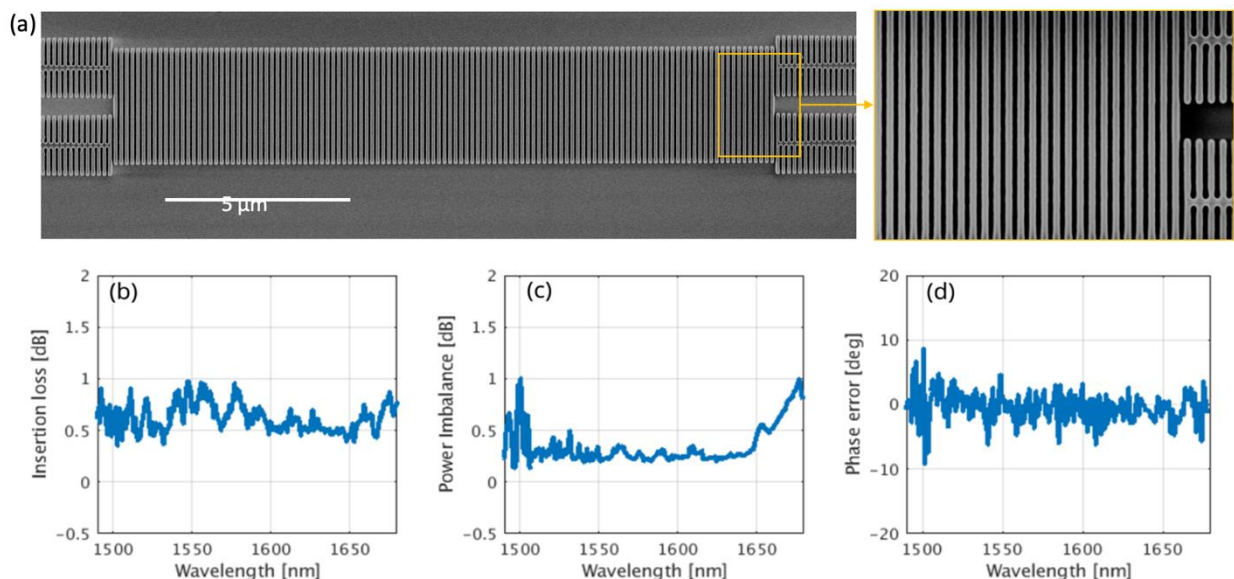


Fig. 1. Experimental characterization of the SWG-engineered beam splitter fabricated on a 300-nm SOI platform using immersion DUV lithography. (a) SEM image before the deposition of the upper cladding, showing the quality of the fabrication. (b) Measured insertion loss, (c) power imbalance, and (d) phase error of the beam splitter. The fabricated MMI shows high performance over a 186-nm bandwidth, with losses and imbalance smaller than 1 dB and phase error less than 6° .

Ring resonators are key components for applications, including optical modulators, communications, and sensing. The position of the resonance wavelength is highly sensitive to temperature variations due to the comparatively high thermal coefficient of silicon ($dn_{\text{Si}}/dT = 1.9 \times 10^{-4} \text{ }^\circ\text{C}^{-1}$), hampering stable operation. Here, we exploit the ability of SWG-engineered waveguides to delocalize the optical mode, reducing the overlap with silicon and hence the thermally-induced resonance wavelength shift [13]. The ring resonators are optimized for TM polarization near 1310 nm wavelength. Figure 2a shows the SEM image of a fabricated SWG ring with a period of 200 nm and a duty cycle of 0.5 and a waveguide width of 750 nm. Figure 2b shows the measured transmittance spectra for different temperatures between 20 $^\circ\text{C}$ and 30 $^\circ\text{C}$. The quality factor of the resonator is $Q \sim 5000$ and extinction ratio exceeding 15 dB. From the resonance wavelength shift, we estimate a thermal dependence of ~ 30 pm/ $^\circ\text{C}$. For comparison, in Fig 2c we show the measured resonance shift of a ring resonator implemented with a conventional strip waveguide (400 nm width and 300 nm thickness) and our SWG resonator, both for TM polarization and 1310 nm wavelength. The SWG approach yields a two-fold reduction of the thermally-induced resonance shift.

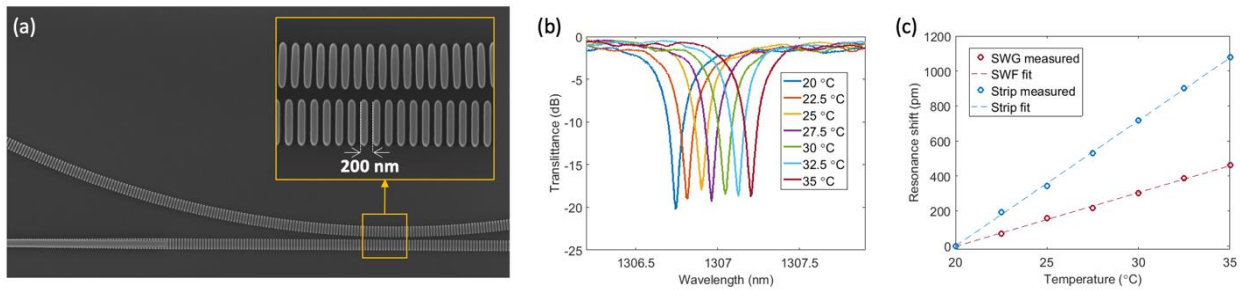


Fig. 2. Experimental characterization of the SWG-engineered ring resonator fabricated on a 300-mm SOI platform using immersion DUV lithography. (a) SEM image before the deposition of the upper cladding. (b) Measured transmittance spectra for different temperatures (c) Comparison of measured thermally-induced shift of the resonance for ring resonators implemented with conventional strip waveguide and SWG waveguide.

DISCUSSION

We have reported on the implementation of SWG metamaterial-engineered devices using a 300-mm SOI fabrication platform with DUV immersion lithography. The high resolution of immersion lithography allowed designs with nominal feature size down to 75 nm. These results show the feasibility of the implementation of SWG metamaterials with a fabrication process compatible with high-volume production, with excellent prospects for bringing the potentialities of metamaterial refractive index engineering toward commercial exploitation. This opens a new path for the fabrication of high-performance devices such as fiber-to-chip couplers, power and polarization splitters, and spectral filters, to name a few, for a wide range of applications, including coherent communications, quantum photonics, sensing, and spectrometry.

Acknowledgements: This work was partially supported by Technological Research Institute (IRT) Nanoelectronics Nano 2022 and Important Project of Common European interest (IPCEI).

References

- [1] Cheben, P.; Halir, R.; Schmid, J.H.; Atwater, H.A.; Smith, D.R. Subwavelength Integrated Photonics. *Nature* 2018, 560, 565.
- [2] Halir, R.; Bock, P.J.; Cheben, P.; Ortega-Moñux, A.; Alonso-Ramos, C.; Schmid, J.H.; Lapointe, J.; Xu, D.X.; Wangüemert-Pérez, J.G.; Molina-Fernández, Í.; et al. Waveguide Sub-Wavelength Structures: A Review of Principles and Applications. *Laser Photonics Rev.* 2015, 9, 25–49.
- [3] Cheben, P.; Xu, D.-X.; Janz, S.; Densmore, A. Subwavelength waveguide grating for mode conversion and light coupling in integrated optics. *Opt. Express* 2006, 14, 11, 4695–4702.
- [4] Cheben, P.; Bock, P. J.; Schmid, J. H.; Lapointe, J.; Janz, S.; Xu, D.-X.; Densmore, A.; Delâge, A.; Lamontagne, B.; Hall, T. J. Refractive index engineering with subwavelength gratings for efficient microphotonic couplers and planar waveguide multiplexers. *Opt. Lett.* 2010, 35, 15, 2526–2528.
- [5] Barwicz, T.; Peng, B.; Leidy, R.; Janta-Polczynski, A.; Houghton, T.; Khater, M.; Kamapurkar, S.; Engelmann, S.; Fortier, P.; Boyer, N.; et al. Integrated Metamaterial Interfaces for Self-Aligned Fiber-to-Chip Coupling in Volume Manufacturing. *IEEE J. Sel. Top. Quantum Electron.* 2019, 25, 1–13.
- [6] Halir, R.; Ortega-Moñux, A.; Benedikovic, D.; Mashanovich, G.Z.; Wangüemert-Pérez, J.G.; Schmid, J.H.; Molina-Fernández, Í.; Cheben, P. Subwavelength-Grating Metamaterial Structures for Silicon Photonic Devices. *Proc. IEEE* 2018, 106, 2144–2157
- [7] Puts, L.; Leijtens, X.; Cheben, P.; Schmid, J.; Reniers, S.; Melati, D. Anti-Reflection Subwavelength Gratings for InP-Based Waveguide Facets. *Opt. Lett.* 2021, 46, 3701–3704.
- [8] Siew, S.Y.; Li, B.; Gao, F.; Zheng, H.Y.; Zhang, W.; Guo, P.; Xie, S.W.; Song, A.; Dong, B.; Luo, L.W.; et al. Review of Silicon Photonics Technology and Platform Development. *J. Light. Technol.* 2021, 39, 4374–4389
- [9] Selvaraja, S.K.; Heyn, P.D.; Winroth, G.; Ong, P.; Lepage, G.; Cailler, C.; Rigny, A.; Bourdelle, K.K.; Bogaerts, W.; Thourhout, D.V.; et al. Highly Uniform and Low-Loss Passive Silicon Photonics Devices Using a 300mm CMOS Platform. In *Optical Fiber Communication Conference (2014)*, Paper Th2A-33; Optical Society of America: San Francisco, CA, USA, 2014; p. Th2A.33
- [10] Halir, R.; Cheben, P.; Luque-González, J. M.; Sarmiento-Merenguel, J. D.; Schmid, J. H.; Wangüemert-Pérez, G.; Xu, D.-X.; Wang, S.; Ortega-Moñux, A.; Molina-Fernández, Í Ultra-broadband nanophotonic beamsplitter using an anisotropic sub-wavelength metamaterial. *Laser & Photonics Reviews* 2016, 10, 6, 1039–1046.
- [11] Lee J.-M.; Kim D.-J.; Ahn H.; Park S.-H.; Kim G. Temperature Dependence of Silicon Nanophotonic Ring Resonator with Polymer Overlayer. *J. Light. Technol.* 2007, 25, 2236–2243
- [12] Maese-Novo, A.; Halir, R.; Romero-García, S.; Pérez-Galacho, D.; Zavargo-Peche, L.; Ortega-Moñux, A.; Molina-Fernández, I.; Wangüemert-Pérez, J.G.; Cheben, P. Wavelength Independent Multimode Interference Coupler. *Opt. Express* 2013, 21, 7033.
- [13] Schmid, J. H.; Ibrahim, M.; Cheben, P.; Lapointe, J.; Janz, S.; Bock, P. J.; Densmore, A.; Lamontagne, B.; Ma, R.; Ye, W. N.; Xu, D.-X. Temperature-Independent Silicon Subwavelength Grating Waveguides. *Opt. Lett.* 2011, 36, 2110–2112

Design of autocorrective interferometers using the Bloch sphere

Matteo Cherchi

VTT – Technical Research Centre of Finland
matteo.cherchi@vtt.fi

The Bloch sphere is a very powerful tool to design two-path interferometric systems, providing superior physical insight into the working principle of autocorrective devices like broadband 50:50 splitters or flat-top interleavers, also enabling the derivation of simple analytical design formulas. I will first introduce a few examples of design applications to then present experimental realisations of the same on our silicon photonics platform.

Keywords: *integrated interferometers, Bloch sphere, autocorrective photonic devices, flat top filters, wavelength insensitive splitters, photonic integrated circuits*

GEOMETRIC REPRESENTATION OF TWO-PATH INTERFEROMETRIC SYSTEMS

Two-path interferometric devices are ubiquitous in photonic integrated circuits. They are simply built out of just two basic building blocks: power splitters – including directional couplers and multimode interferometer (MMI) splitters – and phase shifters – including imbalanced waveguide lengths or waveguide tapering [1]. These systems can be treated analytically based on a transfer matrix formalism, but significant physical insight can be gained when representing them on the so-called Bloch sphere [1]. All possible combinations of power splitting ratio and relative phase can be mapped on the sphere as depicted in Fig. 1. Therefore, any state is unequivocally determined by two angles: ϑ representing the phase shift and 2α corresponding to the splitting ratio $\sin^2(\alpha)/\cos^2(\alpha)$. The three Stokes parameters S_1 , S_2 , and S_3 correspond to the three orthogonal axes. The intersections of S_1 with the sphere represent the single uncoupled waveguide modes E_1 and E_2 , the intersections of S_2 represent the eigenmodes of synchronous directional couplers, i.e., the symmetric and anti-symmetric modes E_S and E_A , whereas the intersections of S_3 represent the superpositions in quadrature and anti-quadrature E_R and E_L . Noticeably, the sphere is not only a tool to show the states as static points, but also a powerful way to show their evolution under the action of power splitters and phase shifters, which operate as simple rotations on the sphere. A synchronous directional coupler acts as a rotation around S_2 , which is the axis of its eigenmodes, i.e., the symmetric and anti-symmetric modes E_S and E_A . Similarly, a phase shifter acts as a rotation around S_1 , which is the axis of its eigenmodes, i.e., the single waveguide modes E_1 and E_2 . More in general, an asynchronous coupler acts as a rotation about the axis of its eigenstates [1], i.e., an axis laying in the equatorial plane somewhere between S_1 and S_2 .

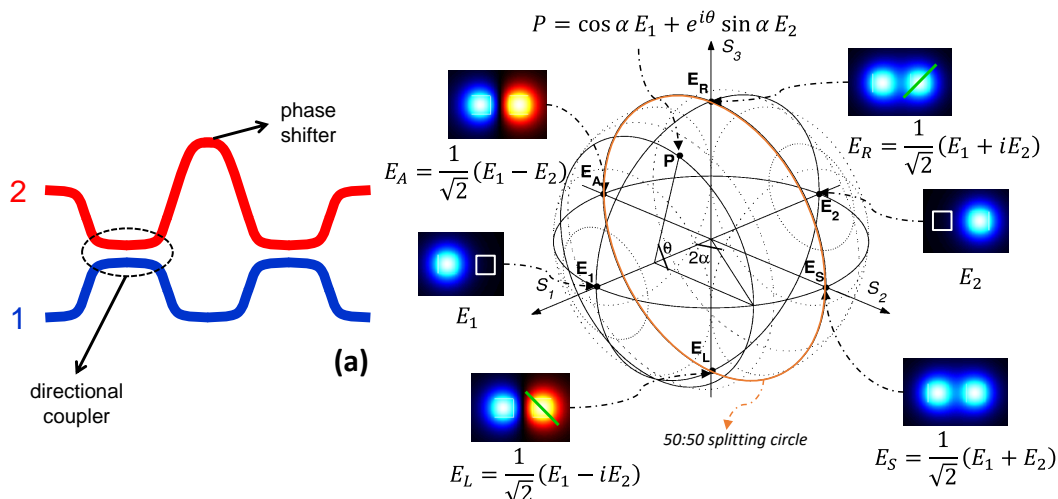


Fig. 1 a) Schematic layout of a simple 2-path interferometer; b) the Bloch sphere as a geometric representation of all possible states of a two-path system, showing the eigenmodes corresponding to the axes S_1 , S_2 and S_3 and the two angles α and ϑ associated with a generic point P on the sphere. The angle α indicates the power fractions $\cos^2\alpha$ and $\sin^2\alpha$ in the single waveguide modes E_1 and E_2 respectively, whereas ϑ shows the relative phase between the two paths.

FLAT-TOP 50:50 SPLITTERS

Little and Murphy [2] have reported a maximally flat 50:50 splitter in the form of a generalised Mach-Zehnder interferometer (MZI) composed by a 50:50 (“half”) coupler and a 100:0 (“full”) coupler (the first number representing the percentage in the cross port) with a 120° phase shifter in between them (see Fig. 2), but their

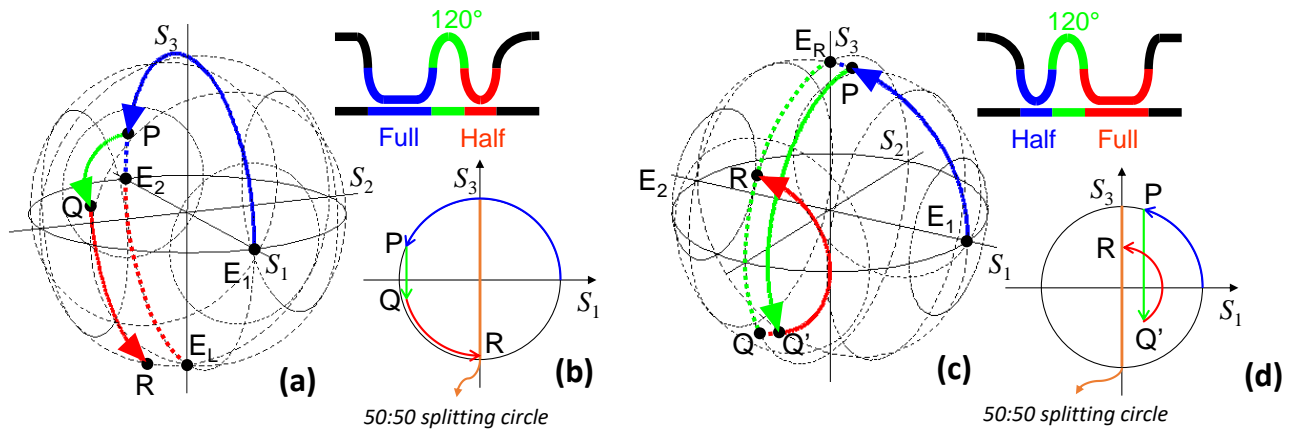


Fig. 2. a) FH configuration and its trajectory on the Bloch sphere. The dashed lines correspond to the nominal case, whereas continuous lines show the autocorrective action when the coupling angles are reduced by 10%; b) projection of the same trajectory on the S_1S_3 plane c) and d) same as a) and b) but for the HF configuration.

paper did not disclose how the result had been derived. The working principle of the flattened MZI 50:50 splitter can be easily understood using the geometrical representation. Let's first consider the configuration where the full coupler comes first, which we will call the FH configuration (Fig. 2a). At the nominal wavelength, the full coupler will simply switch all the power to the cross port, i.e., rotate the state by 180° from E_1 till the antipodal E_2 . In this particular case, the phase shifter rotation corresponds to no changes (E_2 lies on S_1 or, in other words, it is an eigenstate of the phase shifter), and the last 50:50 directional coupler simply rotates the state by 90° to reach the south pole state E_L , i.e., perfect 50:50 splitting (see dashed trajectory in Fig. 2a). Things become more interesting off the nominal wavelength, for example at the shorter wavelength corresponding to a reduction of 10% in the coupling angle. In this case, the full coupler will reach only till the point P, just above E_2 (blue continuous line in Fig. 2a). This time the 120° phase shifter brings P to Q that, by construction, has a distance from the equatorial plane that is half the distance of P, but with opposite sign. This compensates exactly for the 10% reduction in the last coupling rotation, given that the reduction of a half coupler must be half that of a full coupler. Therefore, the ending point R belongs to the circle in the S_2S_3 plane, which is the locus of all the 50:50 states. This ensures a flat 50:50 amplitude response. Nevertheless, R departs from the south pole E_L by an angle proportional to the departure of the coupling angle from its nominal value, resulting in a linear variation of the relative phase. In a similar fashion, we can appreciate the working principle of a HF configuration, where the half coupler comes first (Fig. 2c).

In this case the nominal trajectory reaches the north pole E_R first, then point Q in the southern hemisphere (with -150° phase shift) and finally point R (with 150° phase shift). All points E_R , R and Q belong to the 50:50 circle. At a shorter wavelength corresponding to, e.g., 10% reduction of the coupling angle, the trajectory changes, but the end point R remains substantially the same. This is because the 120° phase shift ensures that the red rotation occurs on a circle with half the radius of the blue rotation. As a result, the blue arc and the red arc are shortened exactly by the same length because the coupling angle changes proportionally to the angle itself and, by construction, the coupling angle of the full coupler is twice the angle of the half coupler. Therefore, this configuration ensures flat response for amplitude and phase at the same time. This difference between the HF and FH configuration becomes very important when designing integrated Michelson interferometers [3].

FLAT-TOP FILTERS

The geometrical representation can also easily explain the working principle of two-stage generalised lattice filters that are cascades of couplers and phase shifters where the imbalance between the two arms doubles at each stage. The usual design approach is based on numerical optimization algorithms to determine the coupling coefficients of the splitters. Let's consider one of the examples reported by Madsen and Zhao [4], with couplers of 0.500, 0.7143, and 0.9226, and phase shifters of order +1 and +2. We sketch in (a) a possible physical realisation of the filter. The transfer matrix response of the filter is plotted in Fig. 3(e). Central wavelengths of transmission bands in the cross-port correspond to a $\pi+2k\pi$ (k integer) phase shift in the first phase shifter, whereas for the bar port, central wavelengths correspond to $2m\pi$ (m integer) phase shift in the first phase shifter. For wavelengths slightly off the central wavelengths, the phase shift will depart from multiples of π , which, in the case of simple MZIs, leads to reduced transmission and extinction ratio, i.e., to non-flat response. Instead, the 2-stage filter is designed such that the phase offset in the first stage is compensated by the offset in the second stage, resulting in autocorrective behaviour and consequent flat response. In fact, the angular offset in the second stage is, by construction twice as the angular offset in the first stage, but it occurs on a circle that has about half the radius, and in the opposite

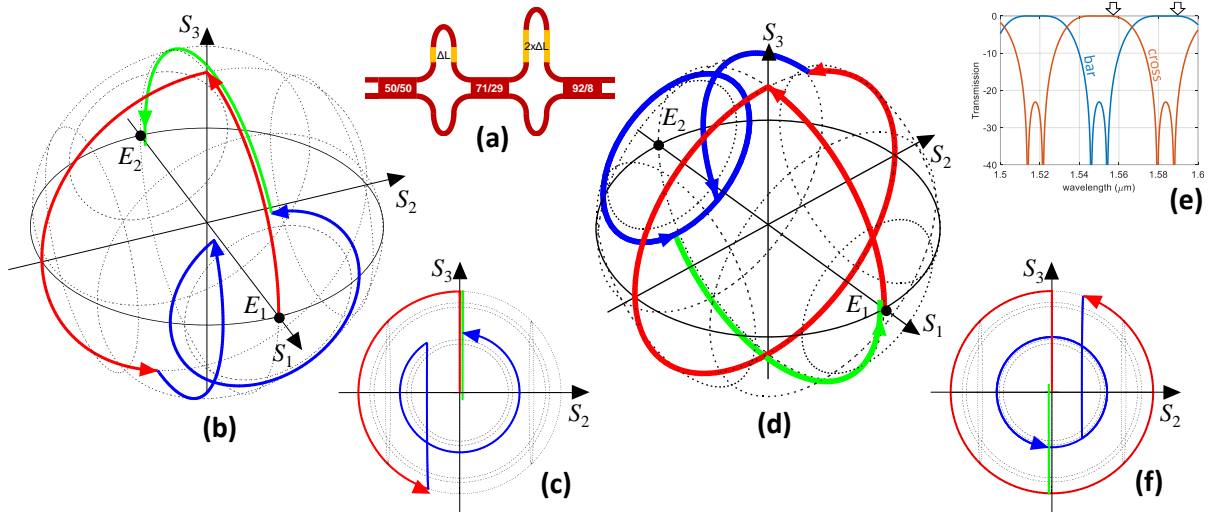


Fig. 3. a) two-stage filter under study, b) and d) show the autocorrective trajectories ensuring the flat-top response simulated in (e). c) and f) show the projections on the S_2S_3 plane, highlight the autocorrective behaviour.

direction. This is shown in Fig. 3 for the cross port and bar port respectively. The half radius is guaranteed by having chosen a 71:29 splitter, i.e., very close to 75:25 that would correspond to exactly 120° rotation. This way, the physical offsets cancel out, having same magnitude and opposite sign. More in general, thanks to the geometric representation one can derive analytic expression to identify all possible working configurations. If, like in the previous example, we want $\pi+2k\pi$ phase shifts and $2m\pi$ phase shifts to correspond to the cross state and to the bar state respectively, the rotation angles on the sphere ϕ_1 , ϕ_2 , and ϕ_3 corresponding to the three splitters must obey the simple system of linear equations

$$\begin{cases} \phi_1 + \phi_2 + \phi_3 = 2m\pi \\ \phi_2 - \phi_1 + \phi_3 = (2k+1)\pi \\ |\sin\phi_1| = 2|\sin(\phi_2 - \phi_1)| \end{cases} \quad \text{with solution} \quad \begin{cases} \phi_1 = \frac{\pi}{2} + p\pi \\ \phi_2 = \frac{-3\pm 1}{6}\pi + q\pi, \\ \phi_3 = \mp \frac{\pi}{6} + t\pi \end{cases}$$

where p , q and t are integers. In particular, the solution $\phi_1 = \pi/2$, $\phi_2 = 2\pi/3$, and $\phi_3 = 5\pi/6$ corresponds to the filter in Fig. 3. Some solutions require phase shifters with same sign and other ones with opposite sign. Another set of solutions can be also derived assuming that the cross (bar) state correspond to even (odd) phase shifts.

Eventually, in Fig. 4 we show the measured flat-top spectral response of similar devices designed using the Bloch sphere based on single multimode interferometers [5], and fabricated on VTT thick SOI platform.

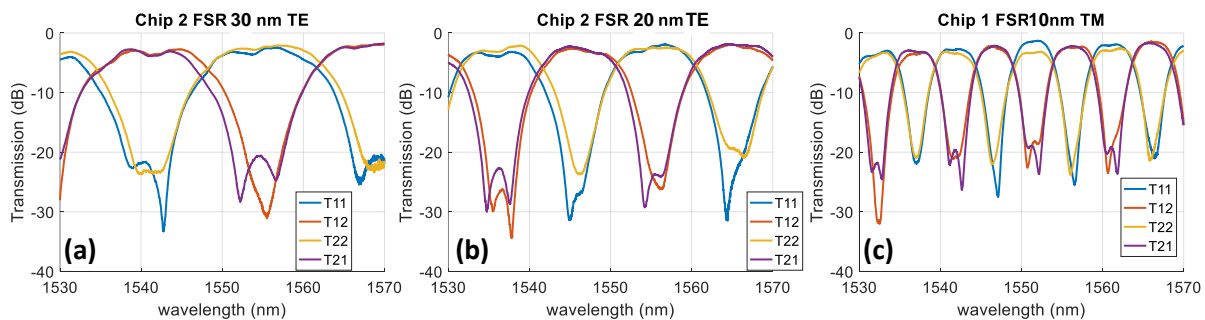


Fig. 4. Measured spectral response of three different two-stage interleavers with different FSR.

Acknowledgements: This work has been supported by the Academy of Finland [PREIN](#), decision number 320168.

References

1. M. Cherchi, "Wavelength-Flattened Directional Couplers: A Geometrical Approach," *Appl. Opt.* **42**, 7141 (2003).
2. B. E. Little and T. Murphy, "Design rules for maximally flat wavelength-insensitive optical power dividers using Mach-Zehnder structures," *IEEE Photonics Technol. Lett.* **9**, 1607–1609 (1997).
3. M. Tormen and M. Cherchi, "Wavelength-flattened directional couplers for mirror-symmetric interferometers," *J. Light. Technol.* **23**, 4387–4392 (2005).
4. C. K. Madsen and J. H. Zhao, *Optical Filter Design and Analysis: A Signal Processing Approach* (Wiley, 1999).
5. M. Cherchi, F. Sun, M. Kapulainen, M. Harjanne, and T. Aalto, "Flat-top interleavers based on single MMIs," in *Silicon Photonics XV* (International Society for Optics and Photonics, 2020), Vol. 11285, p. 112850G.



Topological control of light spectrum using dynamically modulated optical waveguides

Francesco Sergio PICCIOLI^{1,2*}, Alexander SZAMEIT², Iacopo CARUSOTTO²

¹INO CNR - BEC Center and Department of Physics - University of Trento, via Sommarive 14, Povo (TN) 28133, Italy

²Institute of Physics - University of Rostock, Albert-Einstein-Str. 23, Rostock, 18059, Germany

* Francesco.piccioli@unitn.it

The control of the frequency spectrum of light is a ubiquitous problem in physics and engineering. Fast telecommunication protocols rely on frequency multiplexing, and the indistinguishability of photons, strictly related to their spectral properties, is a necessary requirement for the entanglement in photonic quantum technologies. Most of the available protocols for the modification of the spectral properties of a classic light signal or single photon wave-packets are based on non-linear wave mixing, which is intrinsically stochastic and strongly dependent on the nonlinear susceptibility of the employed material. Most recently, dynamical modulation has emerged as an alternative platform to manipulate the frequency of light trapped in resonating structures [1] or travelling in isolated waveguides [2]. In this work, we theoretically inspect the dynamical modulation of homogeneous 1D arrays of optical waveguides using a refractive index perturbation caused by a sound wave travelling in a material with strong acousto-optic response. With respect to previous works, the model presented here is based on cavity-less design that allows to work with arbitrarily broadband signals. Moreover, the study of 1D chains enables the observation of topological phenomena unavailable in isolated waveguides such as disorder protected unidirectional conversion of light frequency.

DYNAMICAL MODULATION OF AN OPTICAL WAVEGUIDE

We consider paraxial light propagation in a weakly guiding optical waveguide such as the ones fabricated on fused silica substrate using femtosecond direct laser writing technique [3]. Considering a reasonably small frequency range, the waveguide supports single mode propagation over a continuous frequency spectrum ω with dispersion relation $\kappa_l(\omega)$. We now include, as depicted in fig. 1a, a monochromatic travelling-wave refractive index perturbation $\Delta n(z, t) = 2b \cos(\mathbf{k}_m \cdot \mathbf{r} - \Omega_m t)$, that can be generated by a sound wave propagating in a material with strong acousto-optic response. To gain control with respect to the longitudinal wavevector of the perturbation, we consider the sound propagating with an angle θ with respect to the optical waveguide axis so that the longitudinal wavevector can be written as $k_m^z = k_m \cos(\theta)$. This condition could be put in practice by enforcing a specific phase relation between individual sound emitters distributed in an array. Employing a linear expansion of $\kappa_l(\omega)$ around a carrier frequency ω_0 (figure 1b), the equation describing the evolution of the spectral components of an impinging light wave packet can be expressed [4] in the form of a Schrodinger-like equation in a continuous 1D frequency space with long-range interactions between frequency components separated by the dynamical modulation frequency Ω_m :

$$i\partial_z E(z, \omega) = V_s \omega E(z, \omega) - \beta E(z, \omega \mp \Omega_m). \quad (1)$$

In equation (1), the hopping amplitude $\beta = k_0 b$ is proportional to the refractive index perturbation and the diagonal term $V_s = \Delta k / \Omega_m$ is proportional to the phase mismatch $\Delta k = k_m^z - \Omega_m \partial \kappa_l / \partial \omega$ between the z -component of the refractive index perturbation and the light mode and represents a (static) scalar potential along the frequency dimension. Assuming a monochromatic light input at frequency ω_0 the symmetry of the problem allows to restrict the study to a discrete set of frequencies $\{\omega_n\} = \omega_0 + n\Omega_m$ and equation (1) can be fully discretized into the following

$$i\partial_z a_n(z) = \Delta k n a_n(z) - \beta a_{n\mp 1}(z). \quad (2)$$

In the case of phase matching $\Delta k = 0$ both eqn. (1) and (2) represent a system in which the dynamical modulation induces a coupling between different frequencies which ultimately modifies the spectral property of a signal travelling in the modulated waveguide. If we consider a narrowband input spectrum the dynamics in the synthetic space is well described by eq. (2) in which only one component $a_n(z) \neq 0$ for $z = 0$. As illustrated in figure 1c the diffraction pattern obtained is typical of a discrete system. On the contrary, if the spectrum of the input signal is much broader than the dynamical modulation frequency Ω_m , equation (1) describes a continuous 1D space with short range interactions and the diffraction pattern is typical of propagation in a continuous space.

In this regime the time duration of the input signal is much shorter than the period of the dynamical modulation and, as we discuss in [4], the arrival time of the light pulse with respect to the dynamical modulation can be used to control the dynamics in the frequency dimension. Indeed when the spectrum of the input light pulse encompasses several sites of the synthetic space lattice, the phase relation between these frequency components (the so-called frequency momentum) plays the same role of the momentum for a quantum particle, or the transverse wavevector for light in waveguide arrays. As the reciprocal space of frequency is time, frequency momenta can be realistically excited with a simple time delay of the light pulse.

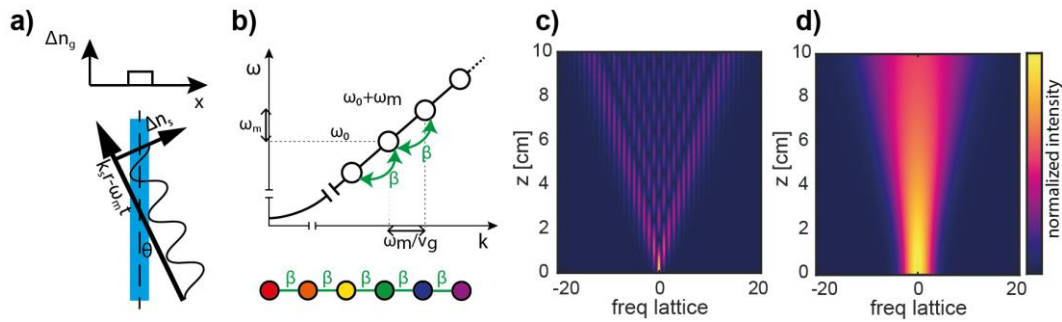


Fig. 1.(a) schematic of an optical waveguide with a travelling wave refractive index modulation. (b) spectral lattice induced in the continuous dispersion relation of the waveguide fundamental mode. (c,d) Spectral power density as a function of the propagation distance for (c) a narrowband ($\Delta\omega = 0.3\omega_m$) and (d) a broadband ($\Delta\omega = 3\omega_m$) light input in a dynamically modulated waveguide

TOPOLOGICAL EFFECTS IN A DYNAMICALLY MODULATED 1D HOMOGENEOUS CHAIN

To fully exploit the potential of our model in terms of topological robustness it is necessary to increase the dimensionality of the system. To this aim we consider an array of identical, equally spaced, optical waveguides placed at positions $x_\ell = \ell d$ subject to the same dynamical modulation propagating with an angle θ with respect to the z -axis $\Delta n(x, z, t) = 2b \cos(k_m^z z + k_m^x x - \Omega_m t)$, where $k_m^z = k_m \cos(\theta)$ and $k_m^x = k_m \sin(\theta)$ are, respectively, the longitudinal and transverse components of the modulation wavevector. Under tight binding approximation for the isolated waveguide modes, the equation describing the evolution of the spectral components of light travelling in the ℓ -th waveguide of the array can be written as:

$$i\partial_z E_\ell(z, \omega) = V_s \omega E_\ell(z, \omega) - \beta e^{\pm i\Phi_\ell} E_\ell(z, \omega \mp \Omega_m) - \xi E_{\ell \pm 1}(z, \omega), \quad (3)$$

Where ξ represents the coupling coefficient between closely placed waveguides and $\Phi = k_m^x \sin(\theta) d$ is proportional to the transverse component of the modulation wavevector. As already mentioned in the previous section, a full discretization of the frequency space leads to a lattice version of equation (3)

$$i\partial_z a_{\ell, n}(z) = n\Delta k a_{\ell, n}(z) - \beta e^{\pm i\Phi_\ell} a_{\ell, n \mp 1}(z) - \xi a_{\ell \pm 1, n}(z), \quad (4)$$

Equation (4) describes a rectangular lattice in a synthetic 2D space composed by a spatial dimension (the waveguide index) and a synthetic dimension associated with the light frequency. As illustrated in figure 2a, the nonreciprocal phase factor in the coupling term along the frequency dimension provides a linear gauge field that, under Peierls substitution, is analogous to a magnetic field perpendicular to the 2D plane. As a result, eq. (4) is analogous to a Harper Hofstadter model characterized by a flux-per-plaquette of Φ .

A well-known property of the Harper Hofstadter lattice is that, whereas the flux takes rational values $\Phi = p/q$, with p and q co-prime integers, the spectrum is divided into exactly q well separated bands with topologically nontrivial properties. As a result, topological states appear within each bandgap that can be used to transport light in a unidirectional fashion. As an example, we consider a $\Phi = 1/4$ Harper Hofstadter model. In figure 2b we plot the dispersion relation of such lattice by considering a truncation along the real space and an infinite extension along the frequency space. The states in fig 2b are color coded accordingly to their localization in the spatial dimension, as highlighted in figure 2a. At each bandgap only one couple of states with well-defined and opposite group velocities exist, with exponential localization at opposite spatial terminations of the waveguide array. Counterpropagating states cannot scatter into one another because of opposite edge localization therefore elastic backscattering is inhibited and, once excited, these states can be used to shift the light frequency in a unidirectional and topologically protected way, as depicted in figure 2c. Crucially, for each value of the *frequency momentum* k_ω only one topological mode exists at each spatial termination. Therefore, it is possible to excite a desired red(blue)-shifting topological mode by simply injecting a light pulse in the proper edge waveguide with the right time delay. Of particular interest for applications, we note that each edge waveguide supports both blue and red-shifting topological modes with a relative difference in the frequency momentum of $\Delta k_\omega = \pi/\Omega_m$. If a train of pulses with a time difference equal to Δk_ω is injected into an edge waveguide, the even and odd pulses will excite, respectively blue- and red-shifting topological modes leading to spectrally separated pulses at the output of the device. This mechanism can have several applications in telecommunication technology for the realization of time-frequency (de)multiplexing devices or in quantum technologies for manipulating the entanglement between the time, frequency and spatial variables of photons

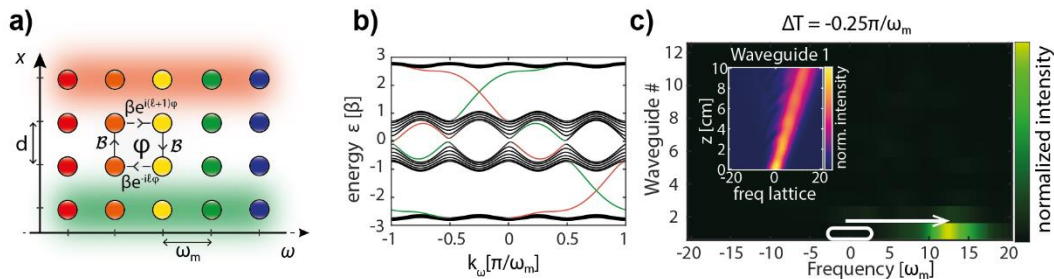


Fig. 2. a) Schematic representation of the synthetic 2D position-frequency space emerging from a dynamically modulated 1D Waveguide array. b) dispersion relation of a $1/4$ Harper Hofstadter lattice. Topological edge states are color-coded accordingly to their localization in the synthetic 2D space as in (a). c) Robust frequency up-conversion mediated by a topological state in the synthetic space

References

- [1] T. Ozawa, H. M. Price, N. Goldman, O. Zilberberg, and I. Carusotto, *Synthetic dimensions in integrated photonics: From optical isolation to four-dimensional quantum hall physics*, PRA, vol. 93, 043827, 2016.
- [2] C. Qin, L. Yuan, B. Wang, S. Fan, and P. Lu, *Effective electric-field force for a photon in a synthetic frequency lattice created in a waveguide modulator*, PRA. Vol. 97, 063838, 2018.
- [3] A. Szameit and S. Nolte, *Discrete optics in femtosecond-laser-written photonic structures*, Journal of Physics B, vol. 43, 163001, 2010.
- [4] F.S. Piccioli, A. Szameit and I. Carusotto, *Topologically protected frequency control of broadband signals in dynamically modulated waveguide arrays*, arXiv:2111.13574, 2021
- [5] T. Ozawa, H. M. Price, A. Amo, N. Goldman, M. Hafezi, L. Lu, M. C. Rechtsman, D. Schuster, J. Simon, O. Zilberberg, and I. Carusotto, *Topological photonics*, Rev.Mod. Phys. Vol. 91, 015006, 2019.

Bound States in the Continuum in LiNbO₃ Waveguides: An Assessment

Jiří Čtyroky^{1*}, Jiří Petráček^{2,3}, Vladimír Kuzmiak¹ and Ivan Richter⁴

¹Institute of Photonics and Electronics of the CAS, Chaberská 1014/57, 18251 Prague 8, Czech Republic

²Faculty of Mechanical Engineering, Brno University of Technology, Technická 2896/2, 61669 Brno, Czech Republic

³Central European Institute of Technology, Brno University of Technology, Purkyňova 656/123, 61200 Brno, Czech Republic

⁴Faculty of Nuclear Sciences and Physical Engineering, Czech Technical University in Prague, Břehová 7, 11519 Prague 1, Czech Republic

*ctyroky@ufe.cz

Several types of integrated photonic waveguides based on LiNbO₃ crystal support propagation of modes which can be classified as bound states in the continuum. Their properties are discussed from the point of view of their suitability for implementation in photonic devices.

Keywords: Bound states in the continuum, LiNbO₃ waveguides

INTRODUCTION

The concept of the bound state in the continuum (BIC) was introduced nearly 90 years ago in quantum physics by von Neumann and Wigner [1] as a theoretical construction. Recently it was shown that it has interesting applications also in photonics [2]. Different kinds of BICs have been found in various photonic structures – gratings, photonic crystals, etc. Such BICs are represented by standing waves characterized by the quality factors approaching infinity. On the other hand, propagating BICs are confined guided modes with suppressed coupling to the continuum of radiation modes into which they are embedded. The coupling can be suppressed, e.g., by destructive interference of two or more radiation channels due to particular device symmetry, or by polarization properties. In the case that the coupling is not completely suppressed, the modes propagate with nonzero radiation loss and can then be considered as quasi-BICs (q-BICs). In the traditional guided-wave terminology, they are known as leaky modes [3].

BICs or q-BICs can be identified in several kinds of waveguide structures containing LiNbO₃ crystal. At first we show that the traditional and most widely used titanium in-diffused (Ti:LiNbO₃) waveguides [4] and annealed proton exchanged (APE) LiNbO₃ waveguides [5] fall into this category. Then we turn our attention to dielectric-loaded waveguides [6] based on lithium niobate on insulator (LNOI) platform [7], and finally, to the proton-exchanged LNOI waveguides [8]. The properties of BIC or q-BIC modes in these structures will be shown, and the suitability of their implementation in integrated photonic devices for real-world applications will be briefly discussed.

Ti:LiNbO₃ AND APE LiNbO₃ WAVEGUIDES

Lithium niobate is an optically negative anisotropic crystal with the birefringence $n_o - n_e \approx 0.08$. The titanium in-diffusion results in (slightly different) increases of both ordinary and extraordinary refractive indices by the amount typically smaller than the LiNbO₃ crystal birefringence. In the APE process, only the extraordinary refractive index is increased by a similar amount, while the ordinary refractive index remains nearly unchanged or even slightly decreased. An example of the refractive index profiles of a Z-cut Ti:LiNbO₃ planar waveguide and effective indices of the TE and TM modes are shown in Fig. 1a).

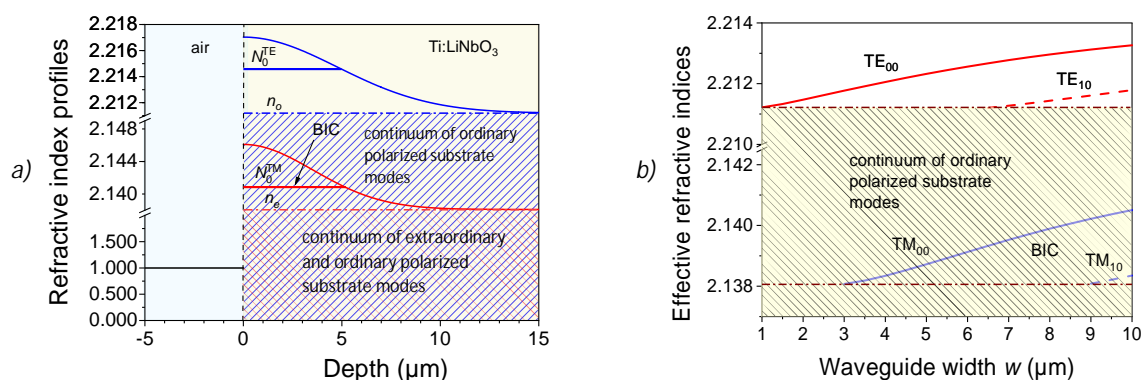


Fig. 1. a) Refractive index profiles of planar Z-cut Ti:LiNbO₃ waveguide; b) Dispersion curves of a channel waveguide. Refractive index changes due to Ti diffusion are $\Delta n_e = 0.005 \left[\operatorname{erf} \left(\frac{w/2+x}{D_x} \right) + \operatorname{erf} \left(\frac{w/2-x}{D_x} \right) \right] e^{-(y/D_y)^2}$, $\Delta n_o = (0.010834 \cdot \Delta n_e)^{0.55}$, $D_x = 4 \mu\text{m}$, $D_y = 5 \mu\text{m}$ [9].

In this (essentially 2D) case, there is no coupling between the extraordinary polarized TM mode with the ordinary polarized TE radiation modes, the effective indices of which span the whole interval between zero and n_0 . The electric field intensity vectors of guided TM and radiation TE modes are namely mutually orthogonal. Thus, such a mode can be classified as a *pure BIC propagating state*. Since the modes of *channel* waveguides are, as a rule, hybrid, having all electric field components nonzero, one might expect some coupling of (quasi-)TM modes with the ordinary polarized continuum, which would result in radiation loss. However, no such losses have been reported in literature, despite the fact that such waveguides are already for decades indispensable components of integrated photonic devices of key importance. Our numerical simulations of Ti:LiNbO₃ channel waveguides using COMSOL Multiphysics found extremely low radiation losses, lower than 10^{-4} dB/cm. This is by several orders of magnitude lower value than experimentally measured losses on real waveguides, which are typically close to 0.1 dB/cm. Thus, the TM modes of channel waveguides are BICs, too. The dispersion curves of simulated channel waveguides are shown in Fig. 1b). The refractive index profiles used for simulations are given in the figure caption. The TM modes of APE waveguides behave similarly, they are thus also BICs, while the TE modes are not supported.

LOW-INDEX DIELECTRIC-LOADED LNOI WAVEGUIDES

Recent availability of a novel high refractive index contrast platform, LNOI, has stimulated a new wave of interest in LiNbO₃ integrated photonic devices. Lateral confinement is typically ensured by etching a ridge in the LiNbO₃ layer. A Z-cut LNOI structure behaves as a planar waveguide in which the waveguide birefringence is enhanced by the natural birefringence of the LiNbO₃ crystal. The TE modes of this planar waveguide, propagating in any direction in the plane, represent the continuum of radiation modes, into which the lower-index TM modes of shallow ridge waveguides can couple [10]. To suppress radiation, an optimum ridge width is to be chosen [11]. Such waveguides thus support propagation of TM q-BICs. In deep enough ridge or even rib waveguides, both TE and TM modes are fully guided. An interesting approach to avoid uneasy etching of the LiNbO₃ layer has been recently described in [6]. A low-index electron beam resist ($n_{poly} = 1.5429$) was used as a dielectric load for lateral confinement of modes on Z-cut LNOI. The low-loss TM modes of properly chosen widths of the polymer loading stripe are q-BICs or BICs while the TE modes propagate without radiation as ordinary guided modes.

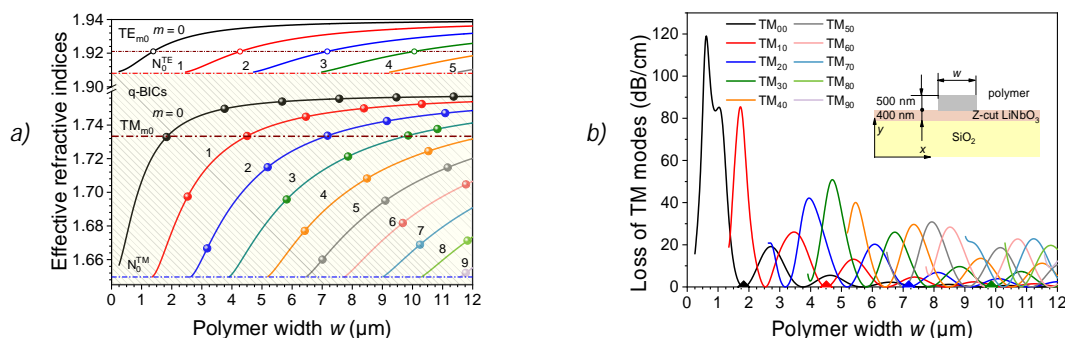


Fig. 2. a) Effective refractive indices of TE and TM modes and b) radiation loss of TM modes of the polymer loaded LNOI waveguides as a function of the polymer stripe width w . Waveguide cross-section is shown in the inset of Fig. 2b). Full dots in Fig. 2a) indicate minimum radiation loss.

As it is indicated in Fig. 2a) by the dash-dot line, the effective refractive indices of the four lowest-order TM modes are nearly identical, $N_{eff} \approx 1.733$, just for stripe widths corresponding to minimum radiation loss. This interesting feature was utilized in [12] for design of four-channel mode de/multiplexor based on directional couplers. Note, however, that the same principle can be applied to the design using ordinary TE modes, too, as it is indicated by open circles on the dispersion curves of TE modes in Fig. 2a). In this case, radiation losses are absent, so that they do not play any restrictive role. Moreover, for TE modes, the electrooptic modulation using laterally placed electrodes as in [6] is much more efficient.

PROTON EXCHANGED LNOI WAVEGUIDES

Lateral confinement can be created in LNOI waveguides also by proton exchange (PE) [8]. The cross-section of the waveguide is shown in Fig. 3a). We numerically simulated the structure with the thickness of the LiNbO₃ layer of 500 nm. The depth refractive index profile was approximated by the Gaussian function with the diffusion coefficient $D_y = 2 \mu\text{m}$, lateral diffusion was neglected. The extraordinary refractive index variation due to PE at the surface

was $\Delta n_e = 0.08$. Calculated effective indices of TM modes versus the width of the PE section are plotted in Fig. 3b). The radiation losses were found negligible for any width of the PE section. (The measured losses reported in [8] were by orders of magnitude higher, but they could be assigned to waveguide imperfections, not to radiation.)

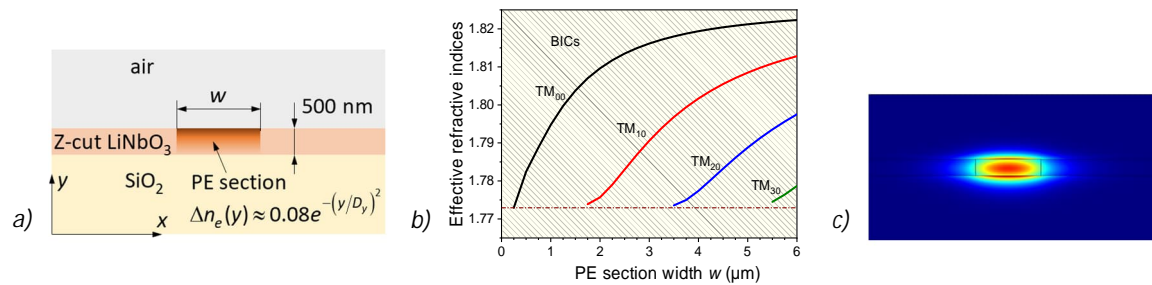


Fig. 3. a) Cross-section of the proton exchanged channel waveguide in Z-cut LNOI, b) dispersion curves of TM modes, c) electrical mode field distribution of the TM_{00} mode for $w = 2 \mu\text{m}$.

The propagation constants of the TM modes belonging to the channel PE waveguide are embedded in the continuum of the omnidirectionally propagating planar TE_0 modes supported by the lithium niobate slab. However, because of negligible radiation, the TM modes can be also considered as BIC states. Since their electric field is well localized in the lithium niobate slab, see Fig. 3c), they can be also utilized for efficient electro-optic modulation.

CONCLUSIONS

All three kinds of LiNbO_3 waveguide structures considered are capable of supporting BICs, or low-loss q-BICs. While the Ti:LiNbO_3 and APE LiNbO_3 waveguides have already proved their nearly unrivalled usefulness in a number of commercial applications (decades before the concept of BICs was introduced into photonics!), the polymer-loaded LNOI structure seems to be an interesting example of implementation of q-BIC rather than a competitive candidate for realistic applications; employing the q-BIC here is neither necessary nor advantageous. The real applicability of PE LNOI structure would require considerable improvement in the fabrication technology in order to reduce the waveguide loss while keeping the refractive index change high enough for sufficient lateral mode localization.

More types of waveguide structures, including those based on X-cut LiNbO_3 , will be discussed during the presentation at the conference, too.

Acknowledgements: This work was supported by the Czech Science Foundation under Project 1900062S.

References

- [1] J. v. Neumann and E. P. Wigner, *Über merkwürdige diskrete Eigenwerte*, Phys. Z., vol. 30, pp. 465-467, 1929
- [2] S. I. Azzam and A. V. Kildishev, *Photonic Bound States in the Continuum: From Basics to Applications*, Advanced Optical Materials, vol. 9, no. 1, art. n. 2001469, 2020
- [3] R. Sammut and A. W. Snyder, *Leaky modes on a dielectric waveguide: orthogonality and excitation*, Appl. Opt., vol. 15, no. 4, pp. 1040-1044, 1976
- [4] R. V. Schmidt and I. P. Kaminow, *Metal-diffused optical waveguides in LiNbO_3* , Appl. Phys. Lett., vol. 25, no. 8, pp. 458-460, 1974.
- [5] J. L. Jackel, C. E. Rice, and J. J. Veselka, *Proton exchange for high-index waveguides in LiNbO_3* , Appl. Phys. Lett., vol. 41, p. 607, 1982
- [6] Z. J. Yu, X. Xi, J. W. Ma, H. K. Tsang, C. L. Zou, and X. K. Sun, *Photonic integrated circuits with bound states in the continuum*, Optica, vol. 6, no. 10, pp. 1342-1348, 2019
- [7] A. Boes, B. Corcoran, L. Chang, J. Bowers, and A. Mitchell, *Status and Potential of Lithium Niobate on Insulator (LNOI) for Photonic Integrated Circuits*, Laser & Photonics Reviews, vol. 12, no. 4, art. n. 1700256, 2018
- [8] L. Cai, S. L. H. Han, and H. Hu, *Waveguides in single-crystal lithium niobate thin film by proton exchange*, Opt. Express, vol. 23, no. 2, pp. 1240-1248, 2015
- [9] P. Ganguly, D. C. Sen, S. Datt, J. C. Biswas, and S. K. Lahiri, *Simulation of refractive index profiles for titanium indiffused lithium niobate channel waveguides*, Fiber and Integrated Optics, vol. 15, no. 2, pp. 135-147, 1996
- [10] S. T. Peng and A. A. Oliner, *Guidance and leakage properties of a class of open dielectric wave-guides .1. Mathematical formulations, 2. New physical effects*, IEEE Trans. Microwave Theory Tech., vol. 29, no. 9, pp. 843-855, 855-869, 1981
- [11] T. G. Nguyen, R. S. Tummidi, T. L. Koch, and A. Mitchell, *Rigorous Modeling of Lateral Leakage Loss in SOI Thin-Ridge Waveguides and Couplers*, IEEE Phot. Tech. Lett., vol. 21, no. 7, pp. 486-488, 2009
- [12] Z. Yu, Y. Tong, H. K. Tsang, and X. Sun, "High-dimensional communication on etchless lithium niobate platform with photonic bound states in the continuum," *Nat Commun*, vol. 11, no. 1, p. 2602, 2020

Spontaneous polarization reversal induced in α -phase lithium niobate channel waveguides by proton exchange

Alicia Petronela RAMBU, Vasile TIRON, Eugen ONICIUC and Sorin TASCU*

Research Center on Advanced Materials and Technologies, Department of Exact and Natural Science, Institute of Interdisciplinary Research, Alexandru Ioan Cuza University of Iasi, Blvd. Carol I, No. 11, 700506 Iasi, Romania
*sorin.tascu@uaic.ro

The α -phase waveguides are well known for preserving both the excellent nonlinear properties and the ferroelectric domains orientation of lithium niobate substrates. However, by using the piezoresponse force microscopy (PFM), we present a coherent study on ferroelectric dipoles switching induced by the one step fabrication process of α -phase waveguides on Z-cut congruent lithium niobate (CLN) substrates.

Keywords: α -phase lithium niobate waveguides; piezoresponse force microscopy; spontaneous polarization reversal; piezoelectric coefficient

INTRODUCTION

It is already known that waveguides fabricated on periodically poled lithium niobate (PPLN) substrates are one of the most widely used devices for many nonlinear optical applications based on the quasi-phase matching (QPM) process. However, an efficient nonlinear process such as second harmonic generation (SHG), spontaneous parametric down conversion (SPDC) or different variants of optical frequency conversion, requires, among others, waveguide fabrication techniques that allow preserving both the nonlinear coefficient and the domains orientation of the substrate. Despite the large number of articles that have proven the efficiency of α -phase channel waveguides for optical frequency conversion in PPLN devices, it has been observed that even α -phase waveguides in PPLN can exhibit uncontrollable nanodomains switching, which can be harmful to the initial periodic structure and obstruct the (QPM) process. Having in mind this idea, we performed, a coherent study of ferroelectric dipoles switching that occurred during the fabrication of α -phase channel waveguides on Z-cut congruent lithium niobate (CLN) substrates, by using the piezoresponse force microscopy (PFM).

The α -phase waveguides were fabricated by using High Vacuum Proton Exchange (HiVacPE) technique [1]. The proton exchange process was performed in a hermetically sealed hourglass tube. A mixture composed of Benzoic Acid (BA) and Lithium Benzoate (LB) was used as proton source. The waveguides were fabricated using different LB concentrations ranging from 2.5% up to 3% incremented by 0.1%, at $T=300^\circ\text{C}$ for $t=72$ hours. In this concentration range, the major difference between the HiVacPE and Soft Proton Exchange (SPE) is the very high reproducibility and control of the index contrast obtained by HiVacPE technique [2]. As expected, the α -phase waveguides exhibit an exponentially decreasing index profile and low values of the index contrast [1]. These kind of profiles and the calculated values of index contrast are the signature of lower $\text{H}^+ \leftrightarrow \text{Li}^+$ substitution ratio ($<10\%$) [3, 4].

RESULTS

The PFM investigations were carried out on the xy plane by respecting the geometry of the samples as depicted in Fig 1. The topography and piezoresponse of the sample surface were simultaneously probed, the PFM microscope software providing three overlaid images namely, topography (exactly like a classical atomic force microscope),

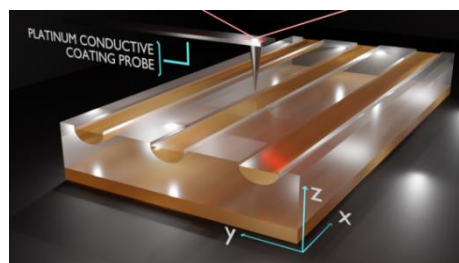


Fig. 1. Experimental setup for PFM investigations of α -phase channel waveguides. Cantilever movements are in x-y plane with the respect of samples geometry allowing scanning both waveguides and virgin CLN regions in a single scan.

PFM magnitude, and PFM phase, respectively, all of them associated to the same investigated area. Therefore, Fig. 2 shows 2D images recorded on α -phase channel waveguides fabricated with $\rho_{\text{LB}}=2.5\%$ in the bath. The images

correspond to: (a) topography, (b) PFM magnitude, (c) PFM phase, and (d) is the corresponding line profiles extracted at the same location of the images triplet.

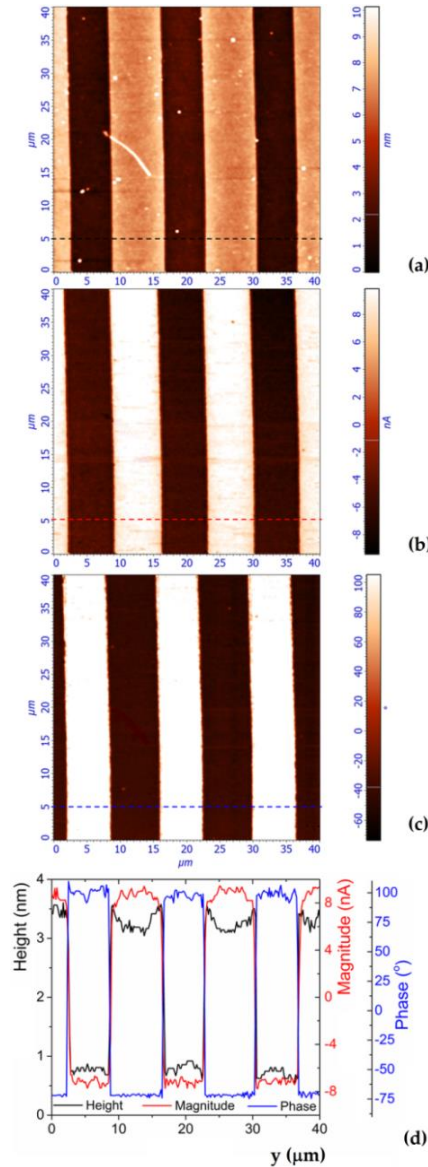


Fig. 2. Images triplet (topography, PFM magnitude and PFM phase) of CLN sample protonated with 2.5% LB: (a) topography of the sample, (b) 2D of PFM magnitude mapped in the same location as topography, (c) PFM phase of the piezoresponse mapped in the same location as topography and (d) line profiles extracted at the same location of the images triplet.

For quantitative assessments of the piezoelectric-like response of protonated regions (waveguides), we carried out the surface displacement calibration procedure of the piezoresponse signal [5]. Since this procedure depends on the quality of the calibration of the z-scanner itself, we have used a test PPLN sample with a known piezoelectric coefficient. Doing so, we were able to identify the conversion factor (ν_{AFM}) linking the amplitude of the vibration of the surface and the PFM response of the surface, respectively. Therefore, from the amplitude value h of the piezoresponse signal measured in a given point of the sample surface and knowing the amplitude V_{DC} of the probing DC voltage, the local piezoelectric coefficient d_{33} was determined from the slope of the plot of Eq. (1) [5].

$$h = \nu_{AFM} d_{33} V_{DC} \quad (1)$$

The reduction in the piezoelectric coefficient d_{33} induced by the proton exchange compared with the virgin CLN is ranged between 18.3% for 2.5% LB in the bath and 8.8% for 3% in the bath. We found a very good agreement between index contrast (optical investigation) and d_{33} reduction (PFM investigations) being proof of a clear connection between the increasing of the refractive index (Δn_e) and the decreasing of the magnitude of spontaneous polarization (ΔP_s) in protonated regions.

Having a high interest towards nonlinear performances of photonics devices based on PPLN substrates, we have also investigated how deep the spontaneous polarization reversal induced by proton exchange takes place inside the α -phase channel waveguides. Therefore, in order to evaluate this depth, all the samples were subjected to a

clever surface engineering. The surface containing the channel waveguides was polished at a small angle ϑ with the respect of the xy surface plane. The angle, measured under optical microscope setup is less than $\vartheta=0.10^\circ\pm 0.05^\circ$. This allows the observation by PFM of the evolution of spontaneous polarization reversal as the waveguide thickness decreases from the surface down into the substrate. Fig. 3 provides a sketch of the experimental configuration and geometrical details. After scanning of a $50\times 50\mu\text{m}^2$ area, the sample has moved in x -axis direction so that the next scan imagines the same waveguides but with decreasing thickness as the scan progresses.

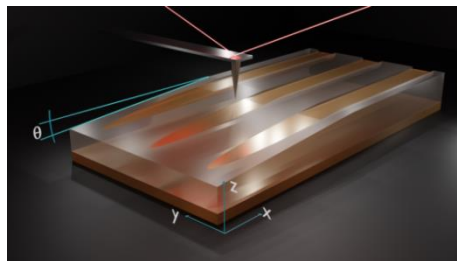


Fig. 3. α -phase waveguides polished with the respect to the xy surface for revealing the deepness of polarization reversal.

Our investigations reveal that the whole deepness of spontaneous polarization reversal induced by proton exchange is 5 ± 0.2 nm. All investigated samples exhibit, in the limit of measurements errors, the same deepness of spontaneous polarization reversal.

DISCUSSION

By corroborating PFM investigation and optical characterizations of α -phase protonated regions and virgin CLN on $\pm Z$ surfaces of the samples, we find a very good agreement between index contrast (optical investigation) and d_{33} reduction (PFM investigations). We clearly showed that the increase in the in-diffused proton concentration (increase in index contrast) in protonated zones decreases the piezoelectric coefficient d_{33} values. We estimated a decrease between 18.5% and 9% depending on the acidity of the bath. This fact was experimentally demonstrated only for high $\text{Li}^+\leftrightarrow\text{H}^+$ substitution ratio ($>70\%$) in the so-called β -phase waveguides [6]. To the best of our knowledge, this is the first time that such a study has been conducted on α -phase waveguides for which the substitution ratio is less 10%. Also, we have assessed that the spontaneous polarization reversal takes place only in a 5 ± 0.2 nm very thin subsurface layer. This result is important for any devices using α -phase channel waveguides in PPLN. In such a case, the 5 ± 0.2 nm subsurface layer of the waveguide can no longer assure the QPM process. In this case, two scenarios can appear. First, if the propagation of different optical modes (associated to pump, signal, and idler, respectively) takes place mainly towards the surface of the waveguides, which is the case for waveguides exhibiting very low index contrast $<1.5\times 10^{-2}$, the QPM is disturbed and the devices will exhibit poor performance of the SHG process. Second, if the propagation of different optical modes takes place mainly in the middle of the waveguides, which is the case for waveguides exhibiting index contrast $>1.5\times 10^{-2}$, the QPM is not disturbed and SHG or SPDC processes can proceed successfully.

Therefore, beyond basic research aspects, our work contributes to the applied research effort on frequencies conversion in waveguides fabricated on LN platforms, where generation and manipulation of photons are crucial since real-world implementations demand high efficiency devices.

Acknowledgements: This work was supported by a grant of the Romanian Ministry of Education and Research, CNCS—UEFISCDI, Project number PN-III-P4-ID-PCE-2020-0239, Contract number PCE 142/2021, within PNCDI III.

References

- [1] A.P. Rambu, A.M. Apetrei, F. Dautre, H. Tronche, M. De Micheli, S. Tascu, *Analysis of high-index contrast lithium niobate waveguides fabricated by High Vacuum Proton Exchange*, Journal of Lightwave Technology, vol. 36, no. 13, pp 2675–2684, 2018.
- [2] A.P. Rambu, A.M. Apetrei, S. Tascu, *Role of the high vacuum in the precise control of index contrasts and index profiles of LiNbO_3 waveguides fabricated by High Vacuum Proton Exchange* Optics and Laser Technology vol. 118, pp 109–114, 2019.
- [3] Y.N. Korkishko, V.A. Fedorov, *Structural phase diagram of $\text{H}_x\text{Li}_{1-x}\text{NbO}_3$ waveguides: The correlation between optical and structural properties*, IEEE Journal of Selected Topics in Quantum Electronics, vol. 2, no. 2, pp 187–196, 1996.
- [4] Y.N. Korkishko, V.A. Fedorov, M.P. De Micheli, P. Baldi, K. El Hadi, A. Leycuras, *Relationships between structural and optical properties of proton-exchanged waveguides on Z-cut lithium niobate*, Applied Optics vol. 35, no. 36, pp 7056–7060, 1996.
- [5] A.P. Rambu, V. Tiron, E. Oniciuc S. Tascu *Spontaneous polarization reversal induced by proton exchange in Z-Cut lithium niobate α -phase channel waveguides* Materials vol. 14, no. 23, pp 7127, 2021.
- [6] M. Manzo, D. Denning, B.J. Rodriguez, K. Gallo, *Nanoscale characterization of β -phase $\text{H}_x\text{Li}_{1-x}\text{NbO}_3$ layers by piezoresponse force microscopy*, Journal of Applied Physics, vol. 116, no. 6, pp 066815, 2014.

Optimization of Brillouin Gain in Subwavelength Silicon Membrane Waveguides using a Genetic Algorithm

(Student paper)

Paula Nuño Ruano^{1,*}, Jianhao Zhang¹, Daniele Melati¹, David Goanzález-Andrade¹, Xavier Le Roux¹, Eric Cassan¹, Delphine Marris-Morini¹, Laurent Vivien¹, Norberto Daniel Lanzillotti-Kimura¹, and Carlos Alonso-Ramos¹

¹Centre de Nanosciences et de Nanotechnologies, Université Paris-Saclay, CNRS, 91120 Palaiseau, France

*corresponding author, paula.nuno-ruano@universite-paris-saclay.fr

Brillouin optomechanics has a great potential for applications in communications, quantum and sensing. Here, we propose a new approach based on a combination of genetic algorithm optimization and subwavelength structuration in silicon waveguides to achieve a Brillouin gain of $3300 \text{ W}^{-1}\text{m}^{-1}$ for a mechanical mode of frequency 14.79 GHz.

Keywords: Brillouin scattering, subwavelength, genetic optimization

INTRODUCTION

Brillouin scattering (BS) refers to the nonlinear interaction between optical and mechanical fields inside a material. BS has generated a great scientific interest due to its numerous applications in communications, sensing and quantum technologies [1]. In nanometric-scale geometries, BS is mediated by the complex interplay between electrostrictive forces and the radiation pressure on the boundaries of the structure [2-4]. As a result, Brillouin gain can be greatly enhanced. However, efficient Brillouin interactions require simultaneous confinement of optical and mechanical modes. Such optomechanical confinement is challenging in silicon-on-insulator (SOI) waveguides due to a strong phonon leakage towards the silica cladding [5-7]. A successful strategy to overcome this drawback is to isolate the silicon optomechanical waveguide by removing the silica cladding. Based on this concept, several membrane designs have been shown to exhibit large Brillouin gain [8-11]. Pedestal waveguides yield a Brillouin gain of $3000 \text{ W}^{-1}\text{m}^{-1}$ [10], but the need for narrow width pedestals to optimize the Brillouin gain complicates the fabrication process and may compromise mechanical stability. On the other hand, the Brillouin gain in silicon membrane rib waveguides is limited to $1000 \text{ W}^{-1}\text{m}^{-1}$ due to the very different confinement of optical and mechanical modes [9]. Photonic crystals with simultaneous photonic and phononic bandgaps have been proposed to maximize the Brillouin gain in silicon, achieving calculated values up to $8000 \text{ W}^{-1}\text{m}^{-1}$ [12]. Nevertheless, the narrow bandwidth and high optical propagation loss, typically linked to bandgap confinement, may compromise the performance of these devices.

Subwavelength structuration represents a promising tool to control photonic and phononic modes in suspended silicon waveguides. Forward Brillouin scattering (FBS), which exhibits the highest gain in silicon nano-structures, relies on longitudinally propagating photons and transversally propagating phonons [5-7]. Hence, engineering the longitudinal and transversal subwavelength geometries would allow independent control of photonic and phononic modes. The exploitation of subwavelength geometries has been proposed to optimize Brillouin gain in suspended silicon waveguides [13,14]. Still, they require several etch steps for the silicon layer, complicating device fabrication. Here, we propose a novel approach that yields high Brillouin gain by using subwavelength-structured Si membranes requiring a single-etch step of silicon, illustrated in Figure 1. We develop an optimization method to design the waveguide geometry, combining multi-physics optical and mechanical simulations with a genetic algorithm (GA) capable of handling a large parameter-space [15]. The optimized geometry yields a calculated Brillouin gain of $3300 \text{ W}^{-1}\text{m}^{-1}$, with minimum feature size of 50 nm, compatible with electron-beam lithography.

RESULTS

The proposed optomechanical waveguide geometry, depicted in Figure 1, comprises a suspended central strip of width $w_g = 400 \text{ nm}$, anchored to the lateral silicon slabs by a lattice of arms with a longitudinal period of $\Lambda = 300 \text{ nm}$, shorter than half of the optical wavelength, ensuring optical operation in the subwavelength regime. The whole waveguide has a fixed silicon thickness of $t = 220 \text{ nm}$, allowing for single-etch step fabrication. The anchoring arms are segmented in several sections of width (W_i) and length (L_i), where the index $i = 1$ refers to the section contiguous to the waveguide core and the index $i = 5$, to the outermost section.

We implement an optimization method to design the waveguide geometry, combining multiphysics optical and mechanical simulations with a GA capable of dealing with a large parameter space [15]. For FBS, the optical and mechanical mode equations decouple and can be solved separately [7] using here COMSOL Multiphysics® software. We reduce the 3D structure to an equivalent 2D geometry by considering the effective index method and the in-plane stress approximation to compute the optical and mechanical modes, respectively. The Brillouin gain is computed afterwards using MATLAB® [6]. Based on the optomechanical calculations, the GA performs a process of fitness-based selection and recombination to produce a successor population, the next generation. Throughout the optimization process, the dimensions of the sections 1 to 4 are subject to variations within fabrication-oriented limits, while the dimensions of the outermost section remain fixed ($W_5 = 500$ nm, $L_i = 50$ nm) to ensure proper optical guidance.

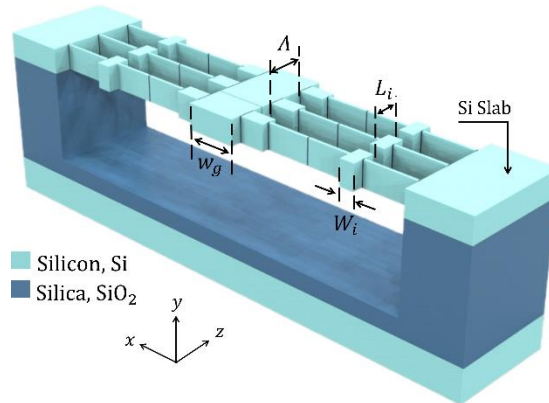


Figure 1: Proposed optomechanical waveguide. The width of the waveguide core ($w_g = 400$ nm), the period ($\Lambda = 300$ nm) and the dimensions of the outermost section ($W_5 = 500$ nm, $L_5 = 50$ nm) remain fixed throughout the optimization process. The thickness of the silicon slab is set to $t = 220$ nm.

The obtained Brillouin gain G_B as function of the number of generations is shown in Figure 2a. The convergence criterion is defined in terms of the difference in performance between the best design and the average of the whole population, $G_B(\text{best}) - G_B(\text{average}) < 10$ $W^{-1}m^{-1}$ over at least 10 generations. The calculated field distribution for the x-component of the optical field (mode effective index is 2.36 and wavelength in vacuum of $\lambda = 1556$ nm) as well as the mechanical displacement are depicted in Figure 2b for the optimized 2D geometry. This structure exhibits a calculated Brillouin gain of $G_B = 3461$ $W^{-1}m^{-1}$ for a mechanical mode with frequency 14.35 GHz and quality factor $Q = 3200$. Additionally, a full 3D simulation of the optimized geometry was carried out to verify the performance of the optimized geometry. The field distributions of the optical (mode effective index is 2.36 and wavelength in vacuum of $\lambda = 1549$ nm) and mechanical modes are presented in Figure 2c. The calculated Brillouin gain provided by this structure reaches $G_B = 3278$ $W^{-1}m^{-1}$ for a mechanical mode of frequency 14.79 GHz and quality factor $Q = 4000$. These results show a good agreement between the simulations of the approximated 2D and the 3D geometries.

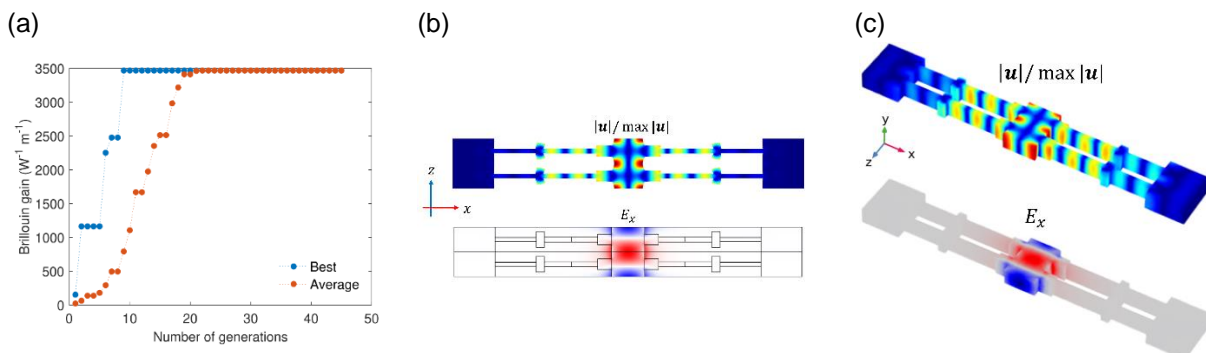


Figure 2: (a) Best (in blue) and average (in orange) Brillouin gain as function of the generation number during the optimization with genetic algorithm. (b) Optical and mechanical modes of the optimized 2D geometry. Normalized mechanical displacement for the mode with frequency 14.35 GHz (up) and x-component of the optical field at $\lambda = 1556$ nm in vacuum (down). (c) Optical and mechanical modes of the optimized 3D geometry. As before, normalized mechanical displacement for the mode with frequency 14.79 GHz (up) and x-component of the optical field at $\lambda = 1549$ nm in vacuum (down) are shown.

For comparison, previously reported silicon periodic waveguides achieved a calculated Brillouin gain of $8000 \text{ W}^{-1}\text{m}^{-1}$ with a frequency of 5 GHz for photonic crystal approach (photonic and phononic bandgap) [12], a gain of $1750 \text{ W}^{-1}\text{m}^{-1}$ with a frequency between 3.21 and 3.48 GHz for hybrid subwavelength (for MIR optical mode) and phononic crystal (for mechanical mode) [13] and a gain of $2000 \text{ W}^{-1}\text{m}^{-1}$ with a frequency of 9.1 GHz for subwavelength waveguide (for optical and mechanical modes) [14]. Our approach yields a gain of $3300 \text{ W}^{-1}\text{m}^{-1}$ with a frequency of 14.79 GHz. This result improves previous reported geometries based also on subwavelength structuration both in gain and mechanical frequency. Additionally, while it does not reach the gain provided by phoxonic crystal approach, our geometry may be more feasible in terms of optical propagation loss.

CONCLUSION

In conclusion, we propose a novel strategy to optimize Brillouin gain in subwavelength-structured silicon membranes requiring only one etch step. Based on this approach combining optomechanical simulations and a genetic algorithm optimizer, we present a original design that yields a Brillouin gain up to $3300 \text{ W}^{-1}\text{m}^{-1}$ for a mechanical mode of frequency 14.79 GHz. This result compares favourably to previously reported subwavelength-based Brillouin waveguides, requiring several etching steps [13]. Additionally, our results illustrate the potential of optimization for obtaining novel designs with improved performance in the context of Brillouin Scattering. Moreover, they show the reliability of computationally efficient optimizations based on approximated 2D simulations.

Acknowledgements: the authors want to thank the Agence Nationale de la Recherche for supporting this work through BRIGHT ANR-18-CE24-0023-01 and MIRSPEC ANR-17-CE09-0041. P.N.R. acknowledges the support of Erasmus Mundus Grant: Erasmus+ Erasmus Mundus Europhotonics Master program (599098-EPP-1-2018-1-FR-EPPKA1-JMD-MOB) of the European Union.

References

- [1] E. Garmire, *Perspectives on stimulated Brillouin scattering*, New J. Phys., vol. 19, no. 1, p. 011003 (2017)
- [2] P. T. Rakich *et al.*, *Giant Enhancement of Stimulated Brillouin Scattering in the Subwavelength Limit*, Phys. Rev. X, vol. 2, no. 1, p. 011008 (2012)
- [3] W. Qiu *et al.*, *Stimulated Brillouin scattering in nanoscale silicon step-index waveguides: a general framework of selection rules and calculating SBS gain*, Opt. Express, vol. 21, no. 25, pp. 31402-31419 (2013)
- [4] C. Wolff *et al.*, *Stimulated Brillouin scattering in integrated photonic waveguides: Forces, scattering mechanisms, and coupled-mode analysis*, Phys. Rev. A, vol. 92, no. 1, p. 013836 (2015)
- [5] B. J. Eggleton *et al.*, *Brillouin integrated photonics*, Nat. Photonics, vol. 13, no. 10, pp. 664–677 (2019)
- [6] G. S. Wiederhecker *et al.*, *Brillouin optomechanics in nanophotonic structures*, APL Photonics, vol. 4, no. 7, p. 071101 (2019)
- [7] A. H. Safavi-Naeini *et al.*, *Controlling phonons and photons at the wavelength scale: integrated photonics meets integrated phononics*, Optica, vol. 6, no. 2, pp. 213-232 (2019)
- [8] H. Shin *et al.*, *Tailorable stimulated Brillouin scattering in nanoscale silicon waveguides*, Nat. Commun., vol. 4, no. 1, 2013
- [9] E. A. Kittlaus *et al.*, *Large Brillouin amplification in silicon*, Nat. Photonics, vol. 10, no. 7, pp. 463-467 2016
- [10] R. van Laer *et al.*, *Interaction between light and highly confined hypersound in a silicon photonic nanowire*, Nat. Photonics, vol. 9, no. 3, pp. 199–203 (2015)
- [11] R. van Laer *et al.*, *Net on-chip Brillouin gain based on suspended silicon nanowires*, New J. Phys., vol. 17, no. 11, p. 115005 (2015)
- [12] R. Zhang *et al.*, *Design of silicon phoxonic crystal waveguides for slow light enhanced forward stimulated Brillouin scattering*, J. Light. Technol., vol. 35, no. 14, pp 2917–2925 (2017)
- [13] M. K. Schmidt *et al.*, *Suspended mid-infrared waveguides for Stimulated Brillouin Scattering*, Opt. Express, vol. 27, no. 4, pp. 4976-4989 (2019)
- [14] J. Zhang *et al.*, *Subwavelength engineering for Brillouin gain optimization in silicon optomechanical waveguides*, Opt. Lett., vol. 45, no. 13, pp. 3717-3720 (2020)
- [15] J. Håkansson *et al.*, *Generating novel waveguides for stimulated Brillouin scattering with genetic algorithms*, APL Photonics, vol. 4, no. 1, p. 010803 (2019)

Nonlocal Fourier Modal Method

Pavel Kwiecien*, Milan Burda, and Ivan Richter

Department of Physical Electronics, Faculty of Nuclear Sciences and Physical Engineering, Czech Technical University in Prague, Břehová 7, 11519 Prague 1, Czech Republic

* pavel.kwiecien@fjfi.cvut.cz

We have developed a methodology to incorporate nonlocal optical responses, described with a simple hydrodynamic model, into the numerical Fourier modal method (FMM) technique, to enable broadening of simulation portfolio of such physical phenomena in plasmonic nanostructures.

Keywords: *Nonlocal optical response, Fourier modal method, plasmonics*

INTRODUCTION

Approximation of the local response of the material is a common approach in the analysis of the resonant behavior of the interaction of light with plasmonic nanostructures. However, as the characteristic dimensions of such structures decrease (in the order of nm), as has recently been shown, models based on nonlocal response (or even quantum interaction) are needed to describe such plasmonic systems [1]. These new models then provide an explanation of effects such as new types of resonances and their blue spectral shifts. In reality, in microscopic descriptions of light-matter interactions, such nonlocal optical response reveals due to the quantum mechanical uncertainties in material excitations. Up-to-date, there are several nonlocal models existing, based on different starting conditions, and predicting not always consistent and equivalent phenomena. Selected nonlocal models have already been successfully implemented in a number of numerical methods such as finite element method [2], finite-difference time-domain method, integral methods, Mie theory, and others. However, successful and effective implementation [3,4] using modal methods is missing.

NONLOCAL FOURIER MODAL METHOD

We have relied on our previous profound experience with both periodic (for one-dimensional - 1D and two-dimensional - 2D cases) and aperiodic version (i.e. isolated structures - for 2D and three-dimensional - 3D cases) of the FMM technique (or traditionally called rigorous coupled wave analysis, RCWA [5]), applied extensively in various rather complex problems, including, e.g. plasmonic gratings, periodic arrays exhibiting the extraordinary optical transmission (EOT) effects, plasmonic metasurfaces, etc., with traditional local-response approximation (LRA), and several important technical extensions implemented, such as proper Fourier factorization, adaptive spatial resolution, and symmetrization techniques [6-8]. Here, based on this experience, we have incorporated newly the nonlocal-response approximation (NRA) into the periodic FMM technique, described with a proper hydrodynamic model. In modifying the FMM method for these effects, our approach is based on [3]. We consider Maxwell's equations in the frequency domain with linearized hydrodynamic correction [2]. This model of nonlocal phenomena is one of the simpler (compared to more complex or quantum models) but it can well describe many experimental results.

Consider a one-dimensional diffraction grating with a grating period Λ (see Fig. 1a). A plane wave with a wavelength of λ is incident upon the diffraction grating at an angle θ (we consider only planar diffraction), due to the nonlocal effect in metals, we can focus only on TM polarization here. The FMM method is based on the evolution of the electromagnetic field and material parameters (within one layer) into a Fourier series. Because we have limited ourselves to TM polarization here, Maxwell's equations (frequency domain) contain only 3 electromagnetic field components: E_x , E_z , and H_y . The algorithm consists of two basic steps. First, the eigenvalue equation is solved, due to the non-locality, however, the electric intensity E_x is connected with the divergence of current density J . In the second step, the S matrix propagation algorithm is solved. Compared to the non-local variant, one equation for boundary conditions of J_z has to be added.

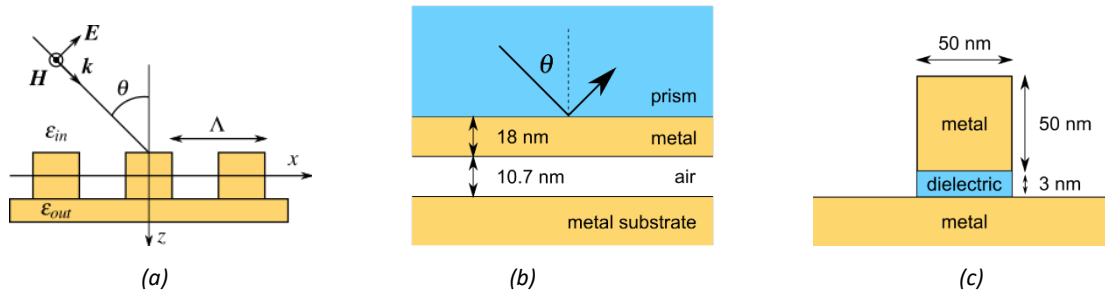


Fig. 1.: (a) Basic geometry and notation of a periodic diffraction grating, Λ represents the grating period, θ is the incident angle of the TM polarized plane wave, ϵ_{in} is the permittivity of a input medium, and ϵ_{out} is the permittivity of the output medium (substrate); (b) Schematic of the multilayer structure, parameters: $\lambda=543$ nm (TM polarization), prism is given with TiO_2 ($n=2.5489-0.0003i$), metal layer and metal substrate are made of silver ($n=0.1442-3.1365i$); (c) one period of the resonant diffraction grating, similar to (a), used for non-local simulations. The grating period is 200 nm.

RESULTS

A first example is a simple multilayer structure (see Fig. 1b), for simplicity, we applied the structure from the article [9] and here we checked the results of our novel non-local code with the Moosh program [9] (see also: <https://github.com/AnMoreau/Moosh>), applicable for nonlocal layers. The input TM polarized plane wave @ $\lambda=543$ nm propagates through a TiO_2 prism ($n=2.5489-0.0003i$), a plasmon mode is then generated on a silver layer with a thickness of 18 nm. The propagation properties of the plasmon mode are further influenced by a thin layer of air with a width of 10.7 nm. Below the air layer is a silver substrate. Since the metal layer is 18 nm thick (+ possible resonant effects), non-local effects are already expected here which was confirmed. Figure 2a shows the dependence of the reflectivity R on the incident angle θ , again, there is a comparison of our code with the program Moosh shown. Due to the fact that the condition for the generation of the plasmon mode is fulfilled for a certain angle, there is a decrease in reflection around $\theta=80^\circ$. If we take into account the nonlocal properties of silver, represented with the β parameter, $\beta=1.35 \times 10^6$ m/s, there is a further decrease in reflection and there is a small shift of the peak towards a smaller angle of incidence. In both cases, we can see very good agreement between our nonlocal tool and the software Moosh. Similarly, figure 2b shows the spectral dependence of the reflectivity R . The blue line shows the local behavior and the red line the nonlocal behavior. The angle of incidence is set to $\theta=82.61^\circ$.

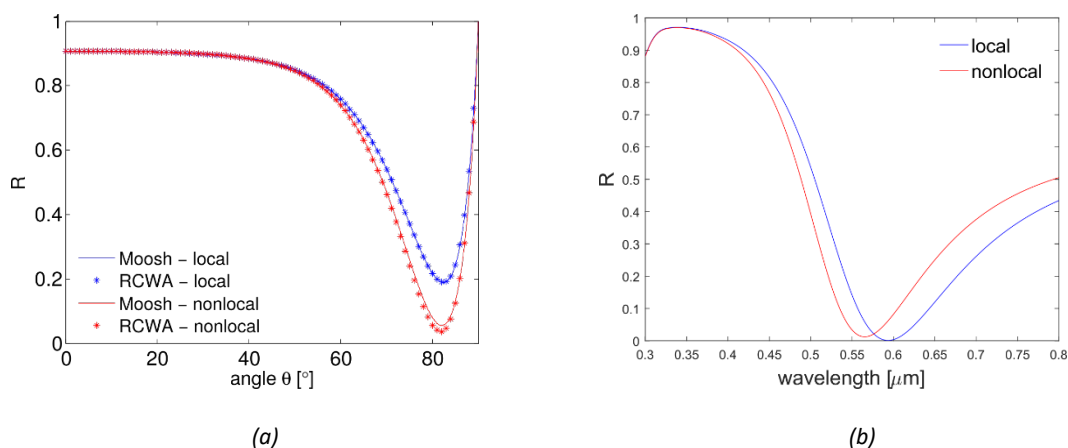


Fig. 2.: (a) Dependence of the reflectivity R on the incident angle θ : comparison of our new implementation with the program Moosh. Local solutions are shown in blue, nonlocal solutions (for $\beta=1.35 \times 10^6$ m/s) are shown in red; (b) Dependence of the reflectivity R on the wavelength λ ($\theta=82.61^\circ$). Again, local solution is shown in blue, nonlocal solution (for $\beta=1.35 \times 10^6$ m/s) is shown in red.

A second example given here is a resonant diffraction grating (see Fig. 1c), this example is taken from [10]. An incoming plane wave (TM polarization) propagates perpendicularly to the 1D diffraction grating with a period of 200 nm. A silver rod with dimensions 50 nm x 50 nm is separated from the metal substrate (silver) by a thin dielectric layer ($n=1.33$) with a thickness of 3 nm. Figure 3a shows a comparison of the zero-order reflectivity spectra for different number of orders N showing a very good convergence behavior. Next, figure 3b shows the spectral dependence of the reflectivity. Clearly, there is a resonant peak present around the wavelength of 900 nm. To check

the performance of the nonlocal version of the FMM method, there is first a local calculation using the standard version of the FMM (blue line) shown, together with a local calculation using the non-local version of the FMM (blue dots, here, the nonlocality is just switched off). As can be seen, the results obtained are identical. Further, the red line shows a rather artificial (but numerically appreciative) case of switching on only the nonlocality of the substrate, while the black line represents the more realistic case where each metal component is considered nonlocally. Clearly, the expected blue shift of the resonance towards shorter wavelengths has gradually manifested itself, for the red and black lines, respectively. Finally, the applicability and flexibility of our nonlocal FMM have been shown, making it a useful tool for further investigations in the field of nanoplasmonics.

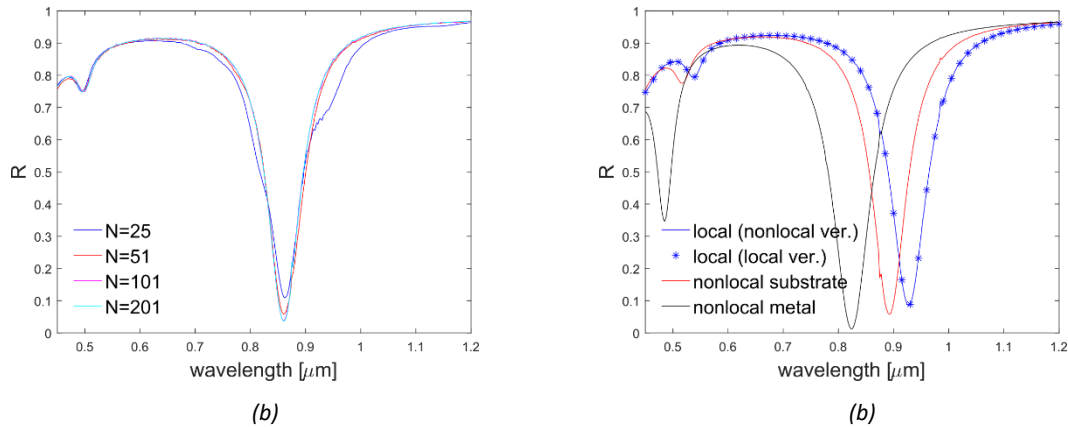


Fig. 3.: (a) Comparison of the zero-order reflectivity spectra for different number of orders N ; (b) Spectral dependencies of zero-order reflectivity efficiency. The blue curve represents the local calculation using the algorithm given here, which is checked (blue dots) by the standard RCWA algorithm, the red line shows the calculation of only nonlocal substrate, while the black curve shows the calculation where all metal components are considered nonlocally.

Acknowledgements: This work was financially supported by the Czech Science Foundation under Project 1900062S and by the Project Center of Advanced Applied Sciences CZ.02.1.01/0.0/0.0/16_019/0000778 –European Structural and Investments Funds – Operational Programme Research, Development, and Education.

References

- [1] S. Raza, G. Toscano, A.P. Jauho, M. Wubs, N.A. Mortensen, *Unusual resonances in nanoplasmonic structures due to nonlocal response*, Physical Review B, vol. 84, p. 121412, 2011
- [2] K. Hiremath, L. Zschiedrich, and F. Schmidt, *Numerical solution of nonlocal hydrodynamic Drude model for arbitrary shaped nano-plasmonic structures using Nedelec finite elements*, J. Comput. Phys., vol. 231, pp. 5890–5896, 2012
- [3] A. Yanai, N. Mortensen, and U. Levy, *Absorption and eigenmode calculation for one-dimensional periodic metallic structures using the hydrodynamic approximation*, Phys. Rev. B, vol. 88, p. 205120, 2013
- [4] Ch. David, J. Christensen, *Extraordinary optical transmission through nonlocal holey metal films*, Appl. Phys. Lett., vol. 110, p. 261110, 2017
- [5] M. G. Moharam, Drew A. Pommet, Eric B. Grann, and T. K. Gaylord, *Stable implementation of the rigorous coupled-wave analysis for surface-relief gratings: enhanced transmittance matrix approach*, J. Opt. Soc. Am. A, vol. 12, 1pp. 077–1086, 1995
- [6] B. Maes, J. Petráček, S. Burger, P. Kwiecien, J. Luksch, and I. Richter, *Simulations of high-Q optical nanocavities with a gradual 1D bandgap*, Opt. Express, vol. 21, pp. 6794–6806, 2013
- [7] P. Kwiecien, I. Richter, V. Kuzmiak, and J. Čtyroký, *Nonreciprocal waveguiding structures for THz region based on InSb*, J. Opt. Soc. Am. a-Optics Image Sci. Vis., vol. 34, pp. 892–903, 2017
- [8] Lifeng Li, *Use of Fourier series in the analysis of discontinuous periodic structures*, J. Opt. Soc. Am. A, vol. 13, pp. 1870–1876, 1996
- [9] J. Benedicto, R. Polles, C. Ciraci, E. Centeno, D. Smith, and A. Moreau, *Numerical tool to take nonlocal effects into account in metallo-dielectric multilayers*, J. Opt. Soc. Am. a-Optics Image Sci. Vis., vol. 32, pp. 1581–1588, 2015
- [10] A. Moreau, C. Ciraci, and D. R. Smith, *Impact of nonlocal response on metallo-dielectric multilayers and optical patch antennas*, Phys. Rev. B, vol. 87, p. 045401, 2013

Nonlocal interactions in planar metal layers

Milan Burda, Pavel Kwiecien, and Ivan Richter*,

Department of Physical Electronics, Faculty of Nuclear Sciences and Physical Engineering, Czech Technical University in Prague, Břehová 7, 11519 Prague 1, Czech Republic

* ivan.richter@fjfi.cvut.cz

Nonlocal interactions of plasmonic nanostructures are currently being intensively investigated. It is generally accepted that nonlocal interactions are most pronounced on metallic structures with nanometre unit sizes and affect the shape of spectral functions of characterizing quantities in the resonance region. Since the numerical analysis of nonlocal phenomena is quite complicated in general. Clearly, it is advantageous to use it for the analysis of geometrically more complex structures. However, for some structures with simpler morphology, it is possible and beneficial to find (quasi)analytical solutions which can then be applied to build semi-analytical approaches for the analysis of more complex structures. Therefore, this contribution is focused on the analytical description of nonlocal manifestations of planar metal layers using the hydrodynamic model. Our aim is to present here the possibilities of constructing an efficient nonlocal model for 1D metal layers.

Keywords: Hydrodynamical model, nonlocal plasmonics, metal layer, transfer matrix

INTRODUCTION

So-called non-local phenomena in metallic structures are currently being intensively investigated. These phenomena are more pronounced on metal structures whose at least one dimension is usually nanometer-sized [1]. In very general terms, the nonlocal medium disrupts the relationship between the electric field vector and the electric induction vector in the form $\mathbf{D}(\mathbf{r}, \omega) = \varepsilon(\omega)\mathbf{E}(\mathbf{r}, \omega)$, which applies to dielectric materials. This deviation is caused by induced current density waves which are associated with a longitudinal electric field that does not exist in dielectric materials. In order to be able to more accurately simulate the behavior of metallic nanostructures with an incident electromagnetic wave, it is necessary to extend the classical models by an equation including the relationship between the electric field and the induced current density. The most commonly used non-local model is the so-called hydrodynamic model (HDM) which already has a number of applications and modifications [2]. For our purposes, however, a standard version of HDM in the form of equations (1) and (2) will suffice. The first HDM equation is de facto Maxwell's wave domain equation assuming that the electromagnetic wave propagates in the environment of positively charged metal ions [3] of permittivity $(\varepsilon_t - \varepsilon_{eg})$, where ε_t denotes the total permittivity of the material and ε_{eg} is the permittivity of the free electron gas. The symbol $k_0 = \omega/c$ denotes the wave number in vacuum. Equation (2) represents a linearized form of equation for the electron gas motion in the EM field in the frequency domain.

$$\nabla \times (\nabla \times \mathbf{E}) - k_0^2(\varepsilon_t - \varepsilon_{eg})\mathbf{E} = i\omega\mu\mathbf{J}, \quad (1)$$

$$\beta^2\nabla(\nabla \cdot \mathbf{J}) + \omega(\omega + i\gamma)\mathbf{J} = i\omega\omega_p^2\varepsilon_0\mathbf{E}. \quad (2)$$

The values of the important constants of the HD model (Fermi velocity, plasmonic frequency, nonlocal

parameter, damping coefficient) for silver and gold are given in Table 1.

constant	units	gold	silver
v_f	$10^6 m \cdot s^{-1}$	1.39	1.39
ω_p	$10^{16} Hz$	13673	13627
β	$10^6 m \cdot s^{-1}$	$0.774 * v_f$	$0.774 * v_f$
γ	$10^{16} Hz$	$\omega_p/127$	$\omega_p/360$

Tab. 1 Table of HD model parameters (Fermi velocity, plasmonic frequency, nonlocal parameter, damping)[3].

MODEL FOR NONLOCAL METALLIC LAYERS

One of the simplest and also the easiest structures to fabricate is a structure composed of planar metal-dielectric layers. The analysis of these structures is very valuable both for the examination of the deviations and limits of classical local theory and also for the knowledge that could help in the analysis of more complex structures in the future. Recently, some numerical simulation methods have been developed [4], but our interest here is to find a (quasi)analytical solution, specifically using the formalism of transfer matrices [5] which is a suitable tool for the analysis of planar layered structures. In addition to the advantages of simple implementation and calculation speed, analytical methods have clearly other positives, such as a relatively easy possibility of finding extremes of selected quantities or a possibility of adapting to some modifications of the HDM or boundary conditions for the current density. Our goal was to create a simple simulation tool enabling the analysis of both single metal layers and metal bilayers, surrounded by dielectrics, see Fig. 1. We focused exclusively on the description of the interaction of the TM polarized plane wave with the metallic gold or silver layer because in the case of TE polarization, the existence of nonlocal

effects does not manifest. The interaction of the TM plane wave with the nonlocal environment can be schematically illustrated in Figure 1.

As indicated in Figure 1, a TM polarized wave propagates into a metal layer at the angle of incidence α_0 . The plane of incidence is determined by the X and Y axes. The first medium is a dielectric defined by the refractive index n_0 and the impedance $z_0 = \sqrt{\mu/\varepsilon}$, where μ and ε denote relative permeability and permittivity of the first medium, respectively. The parameters of surrounding media are marked analogously. The numbers in the subscript of the quantity are assigned to the surrounding medium, the lowercase letters r, s, t, i represent quantities of the reflected, scattered, transmitted, and incident fields, capitals letters T and L indicate transversal and longitudinal waves. The additional superscripts (+) and (-) of the wave number are tied to the direction of propagation along the Z axis. Tangent fields in the y -axis direction at the first interface are denoted as \mathbf{E}_{01} and \mathbf{H}_{01} , similarly tangent fields at the second interface are denoted as \mathbf{E}_{12} and \mathbf{H}_{12} .

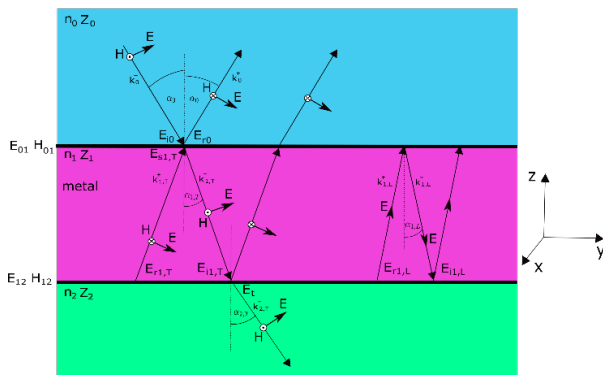


Fig. 1 Scheme of nonlocal interaction of metal layer with TM-polarized plane wave.

All the characteristic properties of a considered metal layer can be determined by solving the boundary conditions of the continuity of tangential components of \mathbf{E} and \mathbf{H} at both boundaries together with the conditions $\mathbf{J}_n = \mathbf{0}$, i.e. the zero normal components of the current density. From equations (1) and (2), it is possible to determine the wave numbers for the transverse and longitudinal fields and a specific form of the boundary conditions can be determined from the geometric concepts, see Fig. 1. In further relatively laborious steps, it is possible to obtain relationships between the magnitudes of the tangential fields at both interfaces of the metal layer and thus obtain a transfer matrix, expressed with a general expression (3) (the symbol η_0 means the vacuum impedance):

$$\begin{pmatrix} E_{01} \\ \eta_0 H_{01} \end{pmatrix} = M_1 \begin{pmatrix} E_{12} \\ \eta_0 H_{12} \end{pmatrix}. \quad (3)$$

The transfer matrix of the resulting multilayer structure, i.e. the structure with isolated metal layers, can be expressed using the transfer matrices of the individual layers as

$$M_{tot} = M_1 * M_2 \dots \dots M_n. \quad (4)$$

The index numbering of the layers and their transfer matrices is considered ascending in the direction of propagation of the incident wave. The situation is much more complicated in the case of two bounded metal layers. The boundary condition for the normal components of the current density at the joint interface of the two metals no longer applies and even relation (4) for the total transfer matrix cannot be used. However, in general, if the total transfer matrix of a given multilayer is already known, then the individual characteristic quantities of the whole structure can be determined as an analytical function of the components of the total transfer matrix.

RESULTS

We have built an analytical method based on the above-mentioned principles, which can analyze the non-local effects of both metal layers and metal bilayers. Our research has so far been limited to finding the parameters of the structure and the incident TM plane wave in which the nonlocal response is more pronounced. Fig. 2 shows two cases of analyzed structures: (a) a single metal layer and (b) a metal bilayer which we investigated.

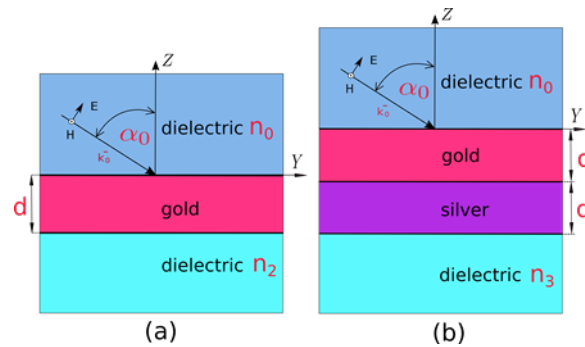


Fig. 2 Illustration of structure and main parameters of (a) single metal layer and (b) double metal layer.

In order to assess the effect of the nonlocal response, we chose the deviation between reflectances ($R_{HD} - R$), where R_{HD} is the reflectance calculated using the HD nonlocal model while R is the reflectance determined in the standard (local) way. Below we present selected calculations of the reflectance deviation for the gold metal layer (see Figs. 3 and 5) and their analogues (see Figs. 4 and 6) for the metal bilayer (for simplicity selected here as: the upper layer as gold, lower layer as silver, same thickness). From our extensive simulations, it turns out that a more significant deviation due to nonlocal behavior can

be expected mainly for the sliding angles of incidence (the angle 85.5 degrees chosen as the optimal value).

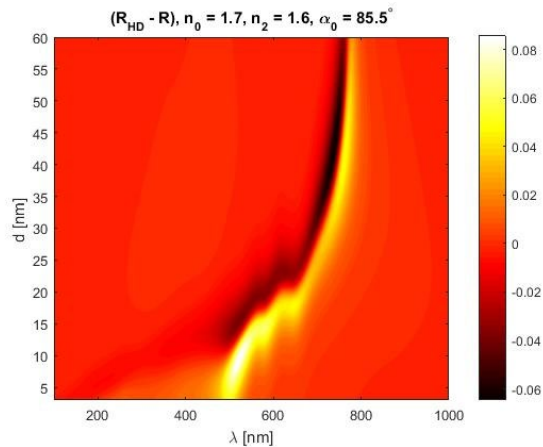


Fig. 3. Reflectance deviation between HD and local model as dependence on gold layer thickness d and wavelength λ .

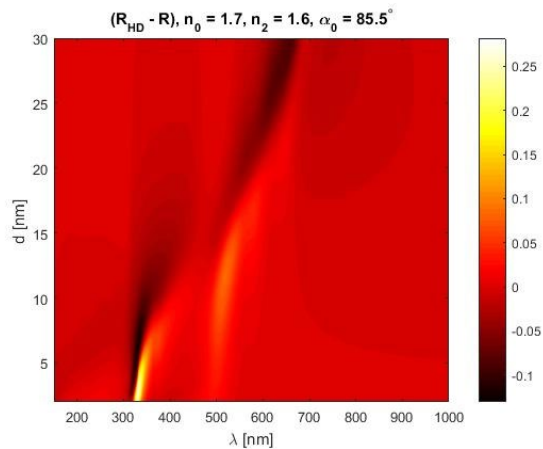


Fig. 4. Reflectance deviation between HD and local model as dependence on total gold-silver layer thickness d_{tot} and wavelength λ .

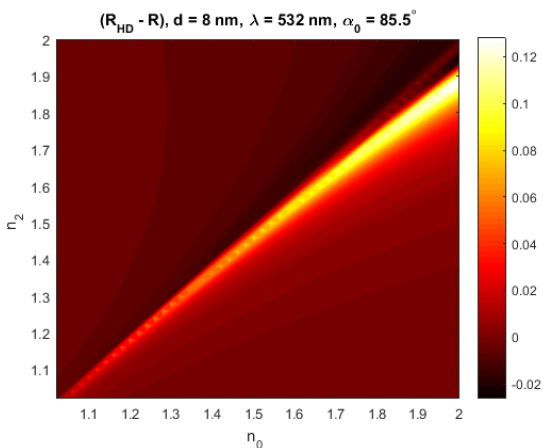


Fig. 5. Reflectance deviation between HD and local model for gold layer at wavelength $\lambda = 532 \text{ nm}$ as dependence on upper n_0 and bottom n_2 refractive indices.

Figs. 3 and 4 show the dependence of the reflectance deviation on the wavelength of the incident wave and the thickness d of the gold layer (d_{tot} for the gold-silver bilayer in Fig. 4), for the refractive indices of the media of $n_0 = 1.7$ and $n_2 = 1.6$ (or n_3 , respectively).

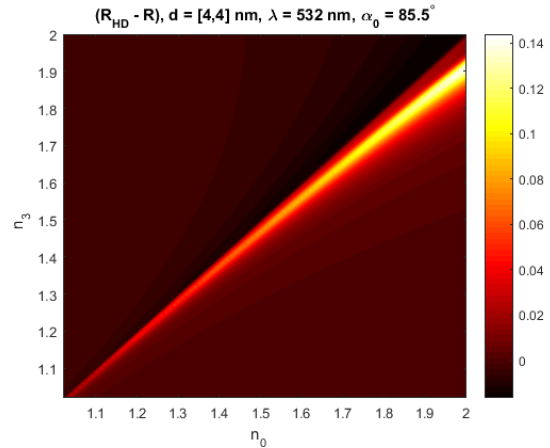


Fig. 6. Reflectance deviation between HD and classic model for gold-silver bilayer at wavelength $\lambda = 532 \text{ nm}$ as dependence on upper n_0 and bottom refractive index n_3 .

The deviation of the reflectance is fundamentally influenced by the refractive indices of the external environment, such dependence at a fixed thickness of the gold layer and the total thickness of the bilayer at 8 nm (@ wavelength of 532 nm) is shown in Figs. 5 and 6, respectively. From the analysis presented here, it is evident that in specific situations, for certain parameters, non-local effects can manifest themselves in a significant way for thin metal layers and bilayers.

Acknowledgements: This work was financially supported by the Czech Science Foundation under Project 1900062S and Project Center of Advanced Applied Sciences CZ.02.1.01/0.0/0.0/16_019/0000778.

References

- [1] N. Mortensen, "Nonlocal formalism for nanoplasmonics: Phenomenological and semi-classical considerations", *Photonics and Nanostructures - Fundamentals and Applications*, vol. 11, no. 4, pp. 303-309, 2013
- [2] N. Mortensen, S. Raza, M. Wubs, T. Søndergaard and S. Bozhevolnyi, "A generalized non-local optical response theory for plasmonic nanostructures", *Nature Communications*, vol. 5, no. 1, 2014
- [3] S. Raza, S. Bozhevolnyi, M. Wubs and N. Asger Mortensen, "Nonlocal optical response in metallic nanostructures", *Journal of Physics: Condensed Matter*, vol. 27, no. 18, p. 183204, 2015
- [4] J. Benedicto, R. Pollès, C. Ciraci, E. Centeno, D. Smith and A. Moreau, "Numerical tool to take nonlocal effects into account in metallo-dielectric multilayers", *Journal of the Optical Society of America A*, vol. 32, no. 8, p. 1581, 2015
- [5] M. Born and E. Wolf, *Principles of optics*. Cambridge: Cambridge University Press, 1999.

Comparative performance evaluation of transparent conducting oxides with moderate mobility for all-optical switching in silicon

Juan Navarro-Arenas¹, Jorge Parra¹, Pablo Sanchis^{1,*}

¹Nanophotonics Technology Center, Universitat Politècnica de València, Camino de Vera s/n, 46022 Valencia, Spain

* corresponding author e-mailpabsanki@ntc.upv.es

All-optical switching is an appealing approach for signal processing, optical communications or sensing systems. In this paper, we compare the performance of aluminium doped zinc oxide (AZO) and indium tin oxide (ITO) as epsilon-near-zero materials in thin-film configuration integrated in a hybrid silicon photonic waveguide. Our results reveal the best operational parameters for enabling compact, ultrafast and energy-efficient operation.

Keywords: *epsilon-near-zero, nonlinear optics, silicon photonics, all-optical, switching*

INTRODUCTION

Nonlinear optical effects enable a wide variety of photonic applications in the fields of telecommunications and information technology [1]. These effects can be utilized to control all-optically the amplitude, phase and frequency of light. Furthermore, with the arrival of new computational demands such as artificial intelligence, all-optical signal processing may become a key technology to enable the next generation of computation and communication devices. However, such technologies are fundamentally limited by the weak optical nonlinearity exhibited by most CMOS compatible materials [2]. This leads to high power consumption and long propagation lengths, making the integration of compact and efficient nanophotonic devices a challenging task. In view of these considerations, recent studies have demonstrated that epsilon-near-zero (ENZ) materials can be leveraged to perform large ultrafast modulations of their complex refractive indices, enabling highly efficient all-optical switching in ultra-compact devices[3]. An interesting subset of ENZ materials are low-loss ENZ materials, also known as near-zero index (NZI) materials, in which the real index is less than unity. Such materials allow an enhancement of nonlinear processes due to strong light confinement effects, especially in hybrid silicon photonic waveguide architectures[3]. In this regard, transparent conductive oxides (TCOs) can be considered CMOS compatible NZI materials that operate in the near infrared (NIR), thereby offering great potential for integrated photonic applications. Indeed, when TCOs permittivity becomes close to zero the materials induces an extraordinary enhancement of local electric field[4] and extreme optical nonlinear effects [3], [5], [6]. In 2016 Alam et al. showed that indium tin oxide (ITO) exhibits unity order nonlinear response linked to its ENZ resonance upon optical pumping. This effect was understood as a consequence of the change in effective mass due to the non-parabolic electron dispersion [7]. Similar nonlinear response has been observed in other TCOs such as doped zinc oxides [8] and cadmium oxide (CdO) [9]. To date, all-optical switching with CdO hybrid waveguides has been proposed in the form of ENZ absorption modulators [6], switching between a low loss dielectric state and the lossy ENZ state of the TCO film. Electro-optical ENZ based phase modulators has also been proposed [10]. These articles converge in pointing out the importance high mobility TCOs as a requisite to design efficient modulators, signalling CdO as an ideal candidate. However, future perspectives on TCOs such as CdO are limited due to their scarcity or toxicity. In this regard, more eco-friendly alternatives such as AZO are investigated in this article to bridge the gap between current TCO research and their future applicability as optical switches and modulators. Here we present an ENZ-based all-optical amplitude switch built on a TCO/Si hybrid waveguide operating near the third telecom window with ultrafast switching time—tens of femtoseconds—and picojoule energy consumption. The impact of the TCO's carrier density and mobility on the performance of the switch, including energy consumption arguments, is investigated by selecting two TCOs with different properties (ITO and AZO) and calculating a suitable figure of merit (FOM) to gain insight into the underlying physical mechanisms as well as to predict the optimal material and experimental requirements to design efficient devices.

RESULTS

Near resonant values of the TCO refractive index need to be considered in the design for an efficient operation. The relative permittivity of TCOs in the NIR region under intraband excitation can be described by a Drude model with a nonparabolic electron band. The nonparabolicity introduces electron effective mass dependence on energy, defining an electron temperature-dependent effective-mass contribution that can be used to interpret the cause of the nonlinearity and to provide functional relationships between the refractive index, the wavelength and the excitation energy. Such relationships are numerically calculated for ITO and AZO with reported parameters [11] and

the expression of the nonparabolic Drude model [12] taken from literature. From the perspective of design, the two most important parameters of a TCO described by a Drude model are carrier concentration N and mobility μ . Here N is taken as a variable. Thus, the selected materials will be defined by their mobility, having a value of $15 \text{ cm}^2 \text{ V}^{-1} \text{ s}^{-1}$ for ITO and $50 \text{ cm}^2 \text{ V}^{-1} \text{ s}^{-1}$ for AZO. While N controls the position of the ENZ (temperature and wavelength), μ has an effect on the shape of the resonance.

Then, the permittivity values are used to calculate the first TM mode of the ultra-thin TCO film/Si hybrid waveguide shown in Figure 1(a). All-optical phase switching is attained by employing a pulsed pump and a continuous wave (CW) probe configuration that, upon pump absorption, raises the electron temperature up to several thousands of Kelvins and, in this way, switches the device's state from a low loss state to a high loss state (tuned at the ENZ temperature). High losses are produced by the strong modal confinement withing the lossy TCO film. In general, switch's ON-state is activated at the ENZ temperature (T_e^{ENZ}) and its value depends on TCO's carrier concentration and wavelength. In the contour maps of Figure 1(b-c) the color bar values of ER are defined as the OFF-state losses ($T_e = 300 \text{ K}$) minus the ON state losses (*i.e.* $ER = Loss(300\text{K}) - Loss(T_e)$ in $\text{dB}/\mu\text{m}$ units). The maps were calculated at a fixed wavelength of 1550 nm . In such plots the position of the ENZ resonance as a function of carrier concentration N is shown as a dotted line. In the case of AZO, the room temperature ENZ ($T_e = 300 \text{ K}$) is located at $N = 0.9 \times 10^{21} \text{ cm}^{-3}$. This means that losses are maximal at 1550 nm for this particular value of N and T_e and that, upon absorption of pump power, the system would detune from being resonant at the ENZ as temperature rises, therefore decreasing losses (this is the reason why ER is negative around this region). To operate the device inversely (ER positive) the value of N should be increased to detune the ENZ resonance from $T_e = 300 \text{ K}$. It follows that, the higher the value of N the greater the ER of the device and the lower the insertion losses ($IL = Loss(300\text{K})$). However, the required value of ΔT_e also scales and, consequently, the energy consumption of the switch. In this context, the $FOM = ER/\Delta T_e$ can be introduced to compare the performance of both materials. This results in the maps of Figure 1(d-e). Such maps reveal a fivefold difference between ITO and AZO materials (see maximum FOM values in Table 1), implying the superior switching performance of AZO in terms of energy efficiency. Another metric that can be obtained is the bandwidth of the device. Figure 1(f-g) was calculated by sweeping the wavelength for a given value of N and T_e (in this case, the pair of values that maximizes the FOM) revealing that the hybrid waveguide loaded with ITO has a much broader response.

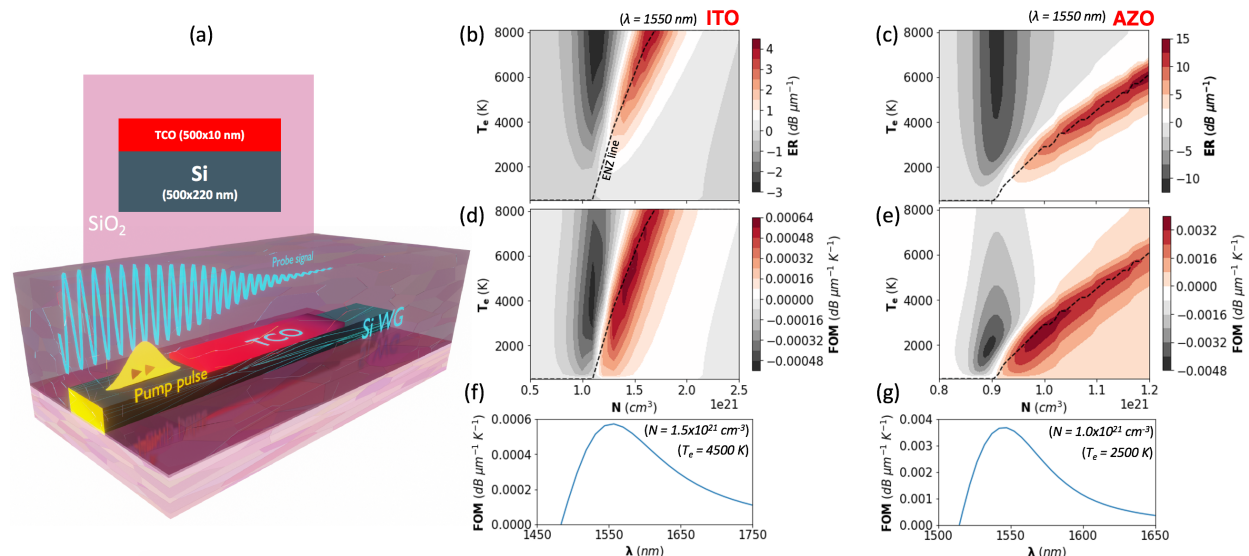


Fig. 1. (a) Cross section and sketch of the all-optical switch based on a hybrid TCO/Si waveguide. (b), (c), (d), (e) Contour maps of the ER and FOM as a function of T_e and N calculated at a fixed wavelength of 1550 nm . (f), (g) Dependence of FOM with wavelength for a given value of N and T_e .

Another important analysis that can be performed with our device is to balance the energy requirements and optical losses of the switching process. The transient evolution of the TCO can be described through a Two-Temperature Model (TTM). Such models are typically used to evaluate the energy transfer following ultrafast photoexcitation. In our case, the FOM can be redefined as $FOM = ER/E_s$. Here E_s is the switching energy required to produce the increment ΔT_e . In Table 1 the FOM with energy units was calculated with a pump pulse of 100 fs . Required powers were of 3 W and 0.5 W to reach $\Delta T_e = 4500 \text{ K}$ in the case of ITO and $\Delta T_e = 2500 \text{ K}$ in the case of AZO. All modelling parameters and equations were taken from [7] and [9].

	ER (dB/ μm)	IL (dB/ μm)	FOM (dB $\mu\text{m}^{-1} \text{K}^{-1}$)	FOM (dB $\mu\text{m}^{-1} \text{pJ}^{-1}$)	Bandwidth (nm)
AZO/Si	4	1	0.0006	5	80
ITO/Si	15	2	0.0032	130	180

Tab. 2. Maximum values of the FOM and ER, IL corresponding to maximum ER point and optical bandwidth.

DISCUSSION

Through analysis of nonparabolic Drude model equations the large nonlinear response TCOs under ENZ regime has been explored. We calculate a FOM that compares TCOs at their peak performance. For moderate mobility ranges, $15 - 50 \text{ cm}^2 \text{ V}^{-1} \text{ s}^{-1}$, large values of ER can be obtained (up to $15 \text{ dB}/\mu\text{m}$ in the case of AZO, Table 1). The IL associated with the maximum ER configuration are also reported in Table 1. When compared with ultrahigh mobility materials such as CdO ($>300 \text{ cm}^2 \text{ V}^{-1} \text{ s}^{-1}$) on similar hybrid Si waveguide switching devices, having a maximum ER of $20 \text{ dB}/\mu\text{m}$ [9], we can therefore conclude that pursuing exceptionally low loss ENZ materials is not pivotal in the design of efficient amplitude switches. On the contrary, device performance should be balanced with energy consumption. Indeed, when FOM takes into account the energy consumption argument, the comparison between high mobility TCOs ($200 \text{ dB } \mu\text{m}^{-1} \text{ pJ}^{-1}$ for CdO [9]) and moderate mobility TCOs ($130 \text{ dB } \mu\text{m}^{-1} \text{ pJ}^{-1}$ for AZO in Table 1) become less prominent. Still, TCOs with even lower mobilities present huge performance gaps that renders materials such as ITO unfeasible to develop efficient all-optical integrated devices ($5 \text{ dB } \mu\text{m}^{-1} \text{ pJ}^{-1}$ for ITO in Table 1). Another relevant consideration is optical bandwidth because as mobility is increased the value of bandwidth decreases (Table 1). In this scenario, high mobility TCOs might offer worst performance depending on the application.

In conclusion, TCO are materials with tremendous potential for integrated photonics. To date, all-optical switching between high-low loss ENZ modes exhibit the highest switching efficiency in current literature [9]. Apart from their remarkable nonlinear response due to their NZI condition, TCOs can be readily integrated into current nanophotonic circuitry without costly fabrication procedures and their optical properties can be flexibly tuned during fabrication time or even electro-optically during run time. However, such flexibility requires the development of computational tools and predictive knowledge to tackle the many possibilities that arise during design. That is the reason why comparative analysis such as the one conducted on this paper may help to pave the road towards next generation all-optical switches based on TCOs.

Acknowledgements: This work is supported by grants PID2019-111460GB-I00, ICTS-2017-28-UPV-9F, and FPU17/04224 funded by MCIN/AEI/10.13039/501100011033, by "ERDF A way of making Europe" and "ESF Investing in your future". Funding from Generalitat Valenciana (PROMETEO/2019/123) is also acknowledged.

References

- [1] K. Ikeda, K. Suzuki, R. Konoike, S. Namiki, and H. Kawashima, *Large-scale silicon photonics switch based on 45-nm CMOS technology*, *Opt. Commun.*, vol. 466, p. 125677, 2020.
- [2] V. Yoshioka, J. Lu, Z. Tang, J. Jin, R. H. Olsson, and B. Zhen, *Strongly enhanced second-order optical nonlinearity in CMOS-compatible Al_{1-x}Sc_xN thin films*, *APL Mater.*, vol. 9, no. 10, p. 101104, Oct. 2021.
- [3] J. Wu, Z. T. Xie, Y. Sha, H. Y. Fu, and Q. Li, *Epsilon-near-zero photonics: infinite potentials*, *Photonics Res.*, vol. 9, no. 8, pp. 1616–1644, 2021.
- [4] I. V. A. K. Reddy, J. M. Jornet, A. Baev, and P. N. Prasad, *Extreme local field enhancement by hybrid epsilon-near-zero--plasmon mode in thin films of transparent conductive oxides*, *Opt. Lett.*, vol. 45, no. 20, pp. 5744–5747, Oct. 2020.
- [5] N. Kinsey, C. DeVault, A. Boltasseva, and V. M. Shalaev, *Near-zero-index materials for photonics*, *Nat. Rev. Mater.*, vol. 4, no. 12, pp. 742–760, 2019.
- [6] O. Reshef, I. De Leon, M. Z. Alam, and R. W. Boyd, *Nonlinear optical effects in epsilon-near-zero media*, *Nat. Rev. Mater.*, vol. 4, no. 8, pp. 535–551, 2019.
- [7] M. Z. Alam, I. De Leon, and R. W. Boyd, *Large optical nonlinearity of indium tin oxide in its epsilon-near-zero region*, *Science (80-)*, vol. 352, no. 6287, pp. 795–797, 2016.
- [8] N. Kinsey, C. DeVault, J. Kim, M. Ferrera, V. M. Shalaev, and A. Boltasseva, *Epsilon-near-zero Al-doped ZnO for ultrafast switching at telecom wavelengths*, *Optica*, vol. 2, no. 7, pp. 616–622, Jul. 2015.
- [9] E. Li and A. X. Wang, *Femto-Joule All-Optical Switching Using Epsilon-Near-Zero High-Mobility Conductive Oxide*, *IEEE J. Sel. Top. Quantum Electron.*, vol. 27, no. 2, pp. 1–9, 2021.
- [10] I. C. Reines, M. G. Wood, T. S. Luk, D. K. Serkland, and S. Campione, *Compact epsilon-near-zero silicon photonic phase modulators*, *Opt. Express*, vol. 26, no. 17, pp. 21594–21605, Aug. 2018.
- [11] R. Secondo, J. Khurgin, and N. Kinsey, *Absorptive loss and band non-parabolicity as a physical origin of large nonlinearity in epsilon-near-zero materials*, *Opt. Mater. Express*, vol. 10, no. 7, pp. 1545–1560, Jul. 2020.
- [12] H. Wang et al., *Extended Drude Model for Intraband-Transition-Induced Optical Nonlinearity*, *Phys. Rev. Appl.*, vol. 11, no. 6, p. 64062, Jun. 2019.

Supercontinuum generation in ultra-low loss silicon nitride waveguides

(Student paper)

Yijun Yang^{1,*}, Christian Lafforgue¹, Quentin Wilmart², Thibaut Sylvestre³, Sylvain Guerber², Xavier Le Roux¹, Eric Cassan¹, Delphine Marris-Morini¹, Carlos Alonso-Ramos¹, Bertrand Szlag² and Laurent Vivien¹

¹ Université Paris-Saclay, CNRS, Centre de Nanosciences et de Nanotechnologies (C2N), 91120 Palaiseau, France

² Univ. Grenoble Alpes, CEA, LETI, Grenoble, 38000, France

³ Institut FEMTO-ST, Université Bourgogne Franche-Comté CNRS UMR 6174, 25000, Besançon, France

* yijun.yang@c2n.upsaclay.fr

In this paper, we present the generation of supercontinuum in ultra-low loss silicon nitride waveguides fabricated in 200mm wafer. The waveguide was pumped at its maximum group velocity dispersion wavelength. Both experimental and simulation results are presented and compared. We observed a rather flat and symmetric spectrum expansion over 1.3 octave from visible to near IR wavelength range with a pump pulse energy lower than 65pJ.

Keywords: *silicon photonics, nonlinear optics, supercontinuum, integrated optics*

INTRODUCTION

Nonlinear optics has paved a way to many integrated photonics applications including optical communications, sensing and quantum technology. Among all nonlinear mechanisms, supercontinuum generation (SCG) taking advantage of third order nonlinearity (optical Kerr effect) is an interesting effect to largely expand the spectrum covering over one octave. Indeed, the wide spectrum expansion is essential for f-2f interferometry [1]. For applications like optical tomography and spectroscopy, we wish spectra to be as wide as possible [2]. In our research, we focus on SCG in ultra-low-loss silicon nitride waveguide. Silicon nitride is currently used for its good compatibility to silicon platform and low propagation loss behavior. Our SiN waveguides were fabricated by CEA Leti using a wafer-scale process to achieve ultra-low loss property, as low as a few dB/m [3]. Such low loss can compete with the performance obtained with Damascene process [4]. Besides, this material has a negligible nonlinear loss (two photon absorption, TPA) in visible and near IR wavelength range. We pumped the waveguide in anomalous dispersion area around its maximum group velocity dispersion (GVD) wavelength. We have obtained a relatively symmetric spectrum broadening over 1.3 octave due to its quasi-parabolic group velocity dispersion profile [5].

RESULTS

- WAVEGUIDE DESIGN

The device is implemented on the silicon nitride on insulator (SiNOI) platform with a geometry reported in Fig.1(a). The cross section has a 40° bevel on the corner attributed to encapsulation step in the fabrication process. The length of the waveguide is 2cm. We harness soliton fission and dispersion wave (DW) generation from dispersion engineering to largely extend bandwidth [6].

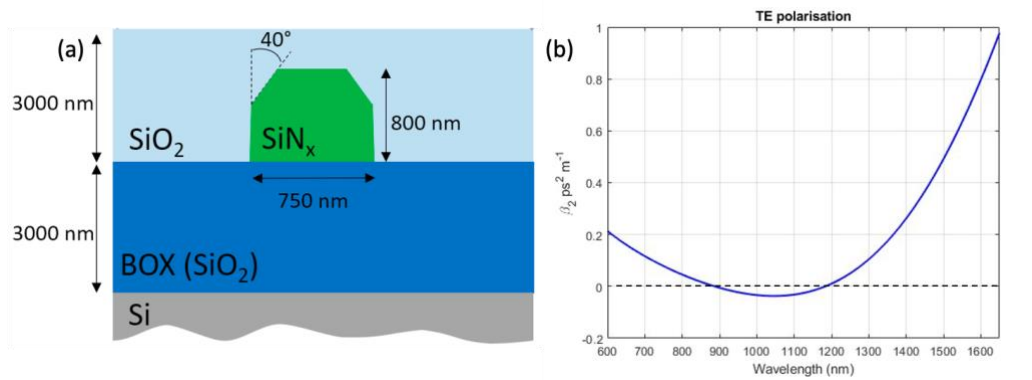


Fig. 1.(a) Waveguide cross section geometry. (b) Group velocity dispersion curve at TE polarization.

The waveguide presents a linear loss below 20dB/m and a group velocity dispersion (GVD) property showed in Fig.1(b). From the integrated dispersion curve reported in Fig.3(b), two dispersive waves are predicted around 645nm and 1465nm, which results in a spectrum expansion around 1.3 octave.

- CHARACTERISATION

To predict the spectrum of supercontinuum, numerical simulations have been investigated. In the simulation, we numerically solved the generalized nonlinear Schrodinger equation (GNLSE), see Eq.1, in which the noise has also been taken into account in simulations. We have neglected Raman effect in our simulations because of the short Raman shock time and short waveguide length. The material index dispersion of SiN_x was measured by ellipsometry method and has been taken into account in the simulations. A nonlinear refractive index of $n_2 = 2.4 \cdot 10^{-19} \text{ m}^2/\text{W}$ was used which is a common value for stoichiometric Si₃N₄.

$$\frac{\partial A}{\partial z} = -\frac{\alpha}{2}A + i \sum_{k \geq 2} \beta_k \frac{i^k}{k!} \frac{\partial^k A}{\partial t^k} + i\gamma(1 + i\tau_{shock} \frac{\partial}{\partial t})|A|^2 A \quad (1)$$

Experimental characterizations were carried out using a femtosecond laser (FWHM 190fs, repetition rate 1Mhz) which is tunable by using optical parametrical amplifier Fig.2.

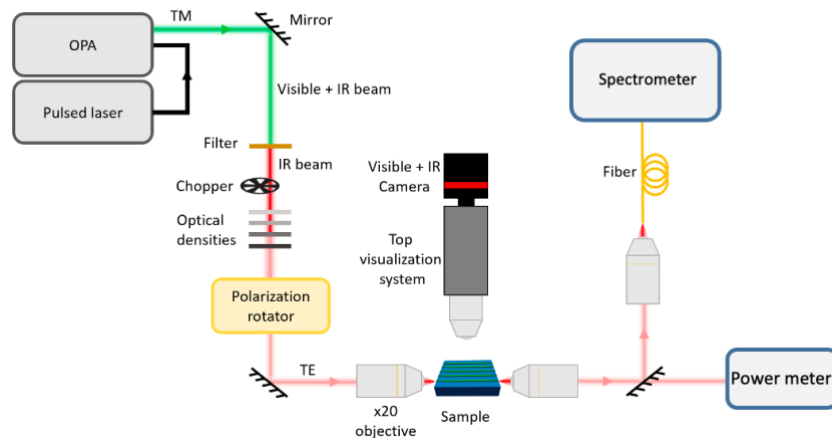


Fig. 2. Schematic view of our tunable femtosecond laser set-up.

We pumped the waveguide around its maximum GVD in the anomalous dispersion region. The coupled peak power varied from 69W to 695W for pump at a wavelength of 1060nm. The coupled powers are measured from a broadband power meter and are also determined from simulation results. The output spectra of the device exhibit an extensive broadening of the input pulse from 630nm to 1500nm at -30dB level with a pump peak power of about 300W (single pulse energy 65pJ). The spectra become quite flat if we continue increasing the pump power. The numerical simulations also show a good agreement with experimental results.

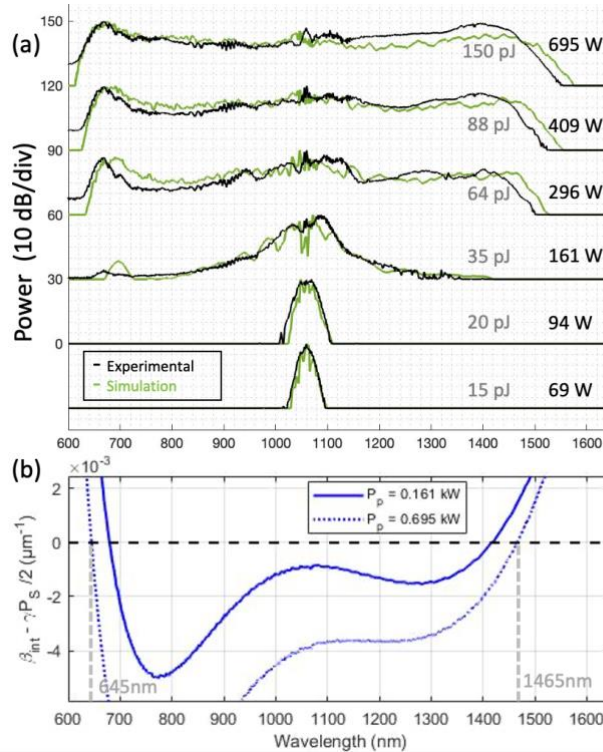


Fig. 3. (a) Experimental (black line) and simulation (green line) spectra of the waveguide in function of coupled peak power from femtosecond laser pumped at 1060nm. The pulse energies are also shown on the graph in grey. (b) Dispersive waves phase-matching conditions are shown in two different peak pump power (161W and 695W). The positions of DW correspond well with experimental characterizations.

DISCUSSION

We used femtosecond pulses to generate supercontinuum in the soliton fission regime caused by higher order dispersion. Comparing to previous work on nitrogen-rich SiN waveguide [7] and Ge-rich graded SiGe waveguide [8], the experimental results show a rather symmetric and flat spectrum broadening. The depletion of pump power indicates a good conversion efficiency. The slight difference between experimental characterizations and simulations could origin from inaccuracy in dispersion simulation since supercontinuum is very sensitive to dispersion curve. We have proved that the wafer-scale ultra-low-loss SiN_x platform developed by CEA Leti is interesting for supercontinuum generation under low input power. The broadened spectrum from visible to near-IR is suitable for applications like optical tomography and sensing. More works in the future will be carried out to reduce the power demand toward using a compact on-chip source to trigger this complex nonlinear effect.

References

- [1] D. R. Carlson *et al.*, "Self-referenced frequency combs using high-efficiency silicon-nitride waveguides," *Opt. Lett.*, vol. 42, no. 12, p. 2314, Jun. 2017, doi: 10.1364/OL.42.002314.
- [2] L. Froehly and J. Météau, "Supercontinuum sources in optical coherence tomography: A state of the art and the application to scan-free time domain correlation techniques and depth dependant dispersion compensation," *Optical Fiber Technology*, vol. 18, no. 5, pp. 411–419, Sep. 2012, doi: 10.1016/j.yofte.2012.08.001.
- [3] H. El Dirani *et al.*, "Ultralow-loss tightly confining Si₃N₄ waveguides and high-Q microresonators," *Opt. Express*, vol. 27, no. 21, p. 30726, Oct. 2019, doi: 10.1364/OE.27.030726.
- [4] M. H. P. Pfeiffer, J. Liu, A. S. Raja, T. Morais, B. Ghadiani, and T. J. Kippenberg, "Ultra-smooth silicon nitride waveguides based on the Damascene reflow process: fabrication and loss origins," *Optica*, vol. 5, no. 7, p. 884, Jul. 2018, doi: 10.1364/OPTICA.5.000884.
- [5] J. M. Dudley and J. R. Taylor, Eds., *Supercontinuum Generation in Optical Fibers*. Cambridge: Cambridge University Press, 2010. doi: 10.1017/CBO9780511750465.
- [6] H. Guo *et al.*, "Mid-infrared frequency comb via coherent dispersive wave generation in silicon nitride nanophotonic waveguides," *Nature Photon*, vol. 12, no. 6, pp. 330–335, Jun. 2018, doi: 10.1038/s41566-018-0144-1.
- [7] C. Lafforgue *et al.*, "Broadband supercontinuum generation in nitrogen-rich silicon nitride waveguides using a 300 mm industrial platform," *Photon. Res.*, vol. 8, no. 3, p. 352, Mar. 2020, doi: 10.1364/PRJ.379555.
- [8] M. Montesinos-Ballester *et al.*, "On-Chip Mid-Infrared Supercontinuum Generation from 3 to 13 μm Wavelength," *ACS Photonics*, vol. 7, no. 12, pp. 3423–3429, Dec. 2020, doi: 10.1021/acsp Photonics.0c01232.

Intersubband Absorption in p-type Ge Multiple Quantum Wells for Mid-IR Sensing Applications

Andrea Barzaghi^{1*}, Virginia Falcone¹, Stefano Calcaterra¹, Raffaele Giani¹, Andrea Ballabio¹, Daniel Christina¹, Giovanni Isella¹ and Jacopo Frigerio¹

¹L-NESS, Dipartimento di Fisica, Politecnico di Milano, Polo Territoriale di Como, Via Anzani 42, Como, 22100, Italy
* andrea.barzaghi@polimi.it

High-quality p-type Ge multiple quantum wells structures were grown, and mid-IR absorption spectra have been measured by FTIR spectrometry. Clear absorption peaks were observed for different values of the quantum well thickness and were attributed to intersubband transitions by k-p simulations backed by XRD measurements.

Keywords: Ge MQW, QWIP, intersubband

INTRODUCTION

Detection in the mid-IR wavelength range is of great interest to enable gas sensing and biological spectroscopic detectors, which require an absorbing material in the 3-5 and 8-13 μm windows [1]. Commercial detectors employ either mercury-cadmium-telluride (MCT) or InSb as sensing material, but they're fragile, difficult to process and integrate on silicon, resulting in a very high cost [2, 3].

Cost effective mid-IR detectors may be fabricated by exploiting intersubband transitions in high-quality Ge multiple quantum wells nanostructures, thanks to the possibility of integration in standard CMOS processes. Moreover, the absorption of such quantum well infrared photodetectors (QWIP) can be tuned by varying the quantum well width and strain level, therefore shifting the transition energy to the desired value.

n- and p-type SiGe QWIPs, which present a weaker absorption compared to pure Ge MQW structures, have already been demonstrated in the past [4,5], and germanium QWIPs have only been demonstrated by exploiting intersubband transitions in the conduction band [6]. Here p-type Ge MQWs structures are investigated as a platform for the fabrication of QWIPs which, thanks to the non-parabolicity and band-mixing effects in the valence band, present both TE and TM absorption and can therefore be employed in both vertical illuminated and waveguide geometries, while having a larger absorption coefficient compared to SiGe designs.

RESULTS

Three different Ge MQW designs, each with a different quantum well width, were grown by LEPECVD on high-resistivity Si wafers. Moreover, a second set of samples was grown with the same quantum well thickness to investigate the effect of different doping levels. A virtual substrate with a linearly graded concentration profile from pure Si to SiGe 80% was used as a buffer layer to achieve high quality QW superlattices with a low density of defects.

High resolution x-ray diffraction (XRD) reciprocal space maps were then acquired and the relevant parameters (i.e. quantum well thickness, superlattice period, average Ge content of the MQW stack) and used as the starting point of the **k**·**p** simulations. The theta scan of the three samples are shown in Fig. 1 together with the fitted curves.

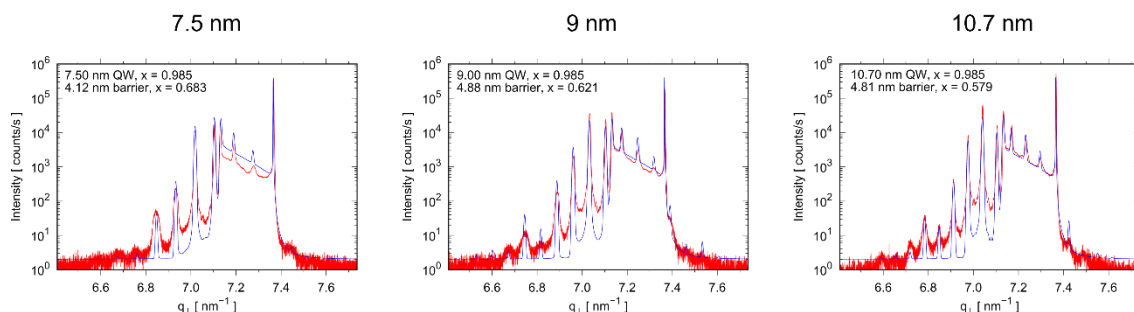


Fig. 1 Theta scan of the samples with different MQW design, showing the goodness of the fitted curves and the extracted parameters.

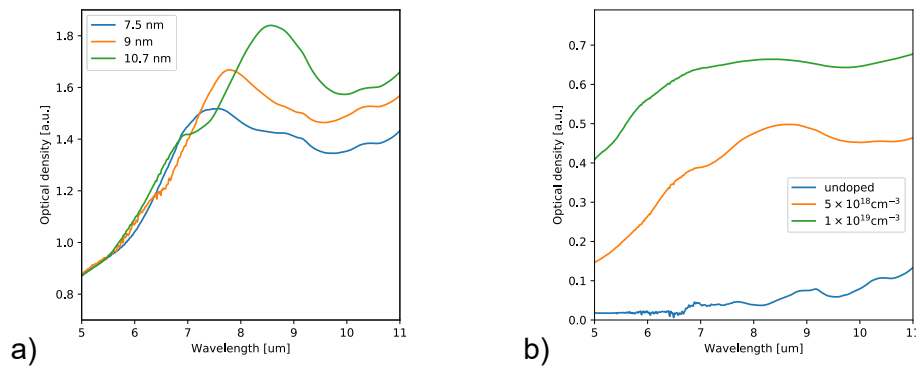


Fig. 2 FTIR room-temperature absorption spectra of MQW designs with a) different quantum well thickness for a $5 \times 10^{18} \text{ cm}^{-3}$ p-type doping, superimposed to $\mathbf{k}\cdot\mathbf{p}$ simulations (dashed lines), and b) different p-type doping levels of the 10.7 nm quantum well.

Room-temperature absorption spectra of the MQW stacks were obtained by measuring the transmittance and reflectance spectra at normal incidence with a FTIR spectrometer and a LN_2 -cooled MCT detector, and the resulting spectra are shown in Fig. 2 for the two sets of samples.

Finally, 8-band $\mathbf{k}\cdot\mathbf{p}$ simulations were performed to attribute the experimental peaks to an intersubband transition, using the structural parameters extracted from the XRD data.

DISCUSSION

Clear absorption peaks can be observed in the spectra in Fig. 2a in the 7-9 μm wavelength range, which is the desired one for many sensing applications. Moreover, it can be clearly seen that the absorption peak shifts to longer wavelengths (i.e. lower energies) as the quantum well width increases, thus reducing the spacing between the confined energy levels. The $\mathbf{k}\cdot\mathbf{p}$ simulations confirm that this peak is related to the LH1-LH2 and show the same experimental shift due to the different quantum well widths.

The absorption spectra for a 10.7 nm QW design with different doping levels in Fig. 1b shows that p-type doping is indeed needed to move the Fermi level in the valence band and populate the LH1 energy level. Further increase of the doping is not beneficial as more transitions toward weakly or non-confined states become available, leading to a very wide peak compared to the $5 \times 10^{18} \text{ cm}^{-3}$ sample. Moreover, free carrier absorption is also expected to be stronger.

Therefore, it can be concluded that p-type doped Ge MQWs structures are a promising platform for the fabrication of inexpensive QWIPs, and that their optical properties can be tuned by changing the quantum well width.

Acknowledgements: The authors acknowledge Francesco Rusconi and Paolo Biagioni for access to the FTIR spectrometer and constructive discussions about the measurements. This work has been supported by Fondazione Cariplo, grant n° 2020-4427.

References

- [1] R. Soref, *Toward silicon-based longwave integrated optoelectronics (LIO)*, Proc. SPIE, 6898, 689809, 2008
- [2] A. Rogalski, *Quantum well photoconductors in infrared detector technology*, J. Appl. Phys. 93, 4355, 2003
- [3] B. W. Jia, K. H. Tan, W. K. Loke, S. Wicaksono, K. H. Lee, S. F. Yoon, *Monolithic Integration of InSb Photodetector on Silicon for Mid-Infrared Silicon Photonics*, ACS Photonics, 5 (4), 1512-1520, 2018
- [4] R. P. G. Karunasiri, J. S. Park, Y. J. Mii, K. L. Wang, *Intersubband absorption in Si_{1-x}Ge_x/Si multiple quantum wells*, Appl. Phys. Lett. 57, 2585-2587, 1990
- [5] J. S. Park, R. P. G. Karunasiri, and K. L. Wang
- [6] M. De Seta, G. Capellini, Y. Busby, F. Evangelisti, M. Ortolani, M. Virgilio, G. Grosso, G. Pizzi, A. Nucara, S. Lupi, *Conduction band intersubband transitions in Ge/SiGe quantum wells*, Appl. Phys. Lett. 95, 051918, 2009

Static and Dynamic Nonlinear Effects in Silicon Micro-Rings: Impact of Trap Assisted Shockley Read Hall Carrier Recombination

(Student paper)

Marco Novarese¹, Stefania Cucco¹, Sebastian Garcia Romero², Jock Bovington³, Rongqing Hui⁴, Mariangela Giannini¹

¹Dipartimento di Elettronica e Telecomunicazioni, Politecnico di Torino, Torino, 10129, Italy

²Cisco Optical GmbH, Nuremberg, Germany

³Cisco Systems, San Jose, CA 95134, USA

⁴The University of Kansas, Lawrence, KS 66045

* marco.novarese@polito.it

We present a new model for the analysis of non-linear effects in silicon micro-ring resonators based on the Shockley Read Hall model for carrier recombination in the silicon core. We can reproduce both measured ring transmission spectra varying input power and measured ring oscillating regimes. We report also pump-probe experiments for extracting the recovery dynamics of the effective loss and refractive index change.

Keywords: SRH, Non-linear effects, ring resonator, FCA, TPA, self-heating, pump-probe

INTRODUCTION

It is well known that silicon waveguides and rings experiment important non-linear effects that often hinder the use of these devices in silicon photonic integrated circuits dealing with power in the order of a few tens of milliwatts. This is in particular true in ring resonators, where high circulating power can be reached. As a result, in order to efficiently design silicon based micro-ring resonator, an accurate model is needed. Models in the literature, developed to fit experiments, are based on empirical expressions for the carrier lifetime[1],[2] and thermodynamic modelling of self-heating [3]. We present a new model that is based on the Shockley-Read-Hall (SRH) theory to predict the carrier lifetime of free carriers (FC) generated in the silicon waveguide core. We show that, by properly defining values for the energy of traps and surface trap density, we are able to reproduce experimental measurements in both steady state and in time domain when the ring output power presents periodic oscillation even with CW injection. This oscillating regime is due to the interplay between FC generation and self-heating. We also propose pump-probe experiments for measuring the time evolution of the ring transmission spectrum and then retrieve the time recovery of the non-linear absorption and refractive index change.

MODEL

Our theory is based on the well-established model of Two Photon Absorption (TPA), Free Carrier Absorption (FCA), Free Carrier Dispersion (FCD) and self-heating [2] in silicon. The inclusion of the SRH non radiative recombination of the free carriers is performed with the introduction of the rate equations for trap assisted recombination processes [4] which allows us to calculate the excess electron (n_e) and hole (p_e) generated by TPA. The electron and holes SRH rate equations can be decoupled in steady state making it possible to solve them analytically. The self-heating is included by calculating the temperature increase due to the power absorbed in the silicon core. For fixed input bus power P_{bus} and wavelength λ_{in} we solve a non-linear system that returns the power circulating in the ring (P_c), the excess carriers, the effective waveguide loss, the variation of refractive index and the temperature increase. Sweeping λ_{in} , we can then compute the transmission coefficient of the ring and compare it with the experiments. To simulate the ring dynamics and oscillating behaviour, the model is also extended to the time domain by naturally solving the SRH rate equations coupled with the dynamic equation for the circulating optical electric field in the ring. In this framework the temperature variation in time is modelled in Comsol Multiphysics and thermal time constants are derived in accord with [3]. This model can be also used to interpret the and probe experiments discussed in the following.

RESULTS

We consider a racetrack ring of total length of 80 μm . The ring waveguide has a width of $W = 450 nm$ and height $h = 215 nm$. Steady state measurements were performed by a forward wavelength sweep from blue to red around

a selected cold resonance wavelength $\lambda_0 \approx 1540.2 \text{ nm}$ using an Agilent 8168A and a N7714A tunable lasers. The measured spectra were then fitted with the theoretical model to reproduce the shift of resonant wavelength and the variation of the transmission coefficient at resonance as a function of P_{bus} . The energy level of traps E_t and the related surface trap densities were set as the fitting parameters, the first was varied around the middle of the band gap while the second is expected to be in the range $10^{10} - 10^{12} \text{ cm}^{-2}$ [5]. Fig. 1 (a) and (b) shows the fitting results in the case $E_t = 0.69 \text{ eV}$, $N_s = 7.4 \cdot 10^{10} \text{ cm}^{-2}$. Fig. 1(c) reports the comparison between measured and simulated transmission spectra at low input power (almost linear regime) and high power when strong non-linear effects and self-heating are excited. The larger error bars in Fig. 1(a) and (b) refers to the precision of the high power tunable laser employed in measurements, whereas the error bar in Fig. 1(c) refers to output power oscillations observed at high input power.

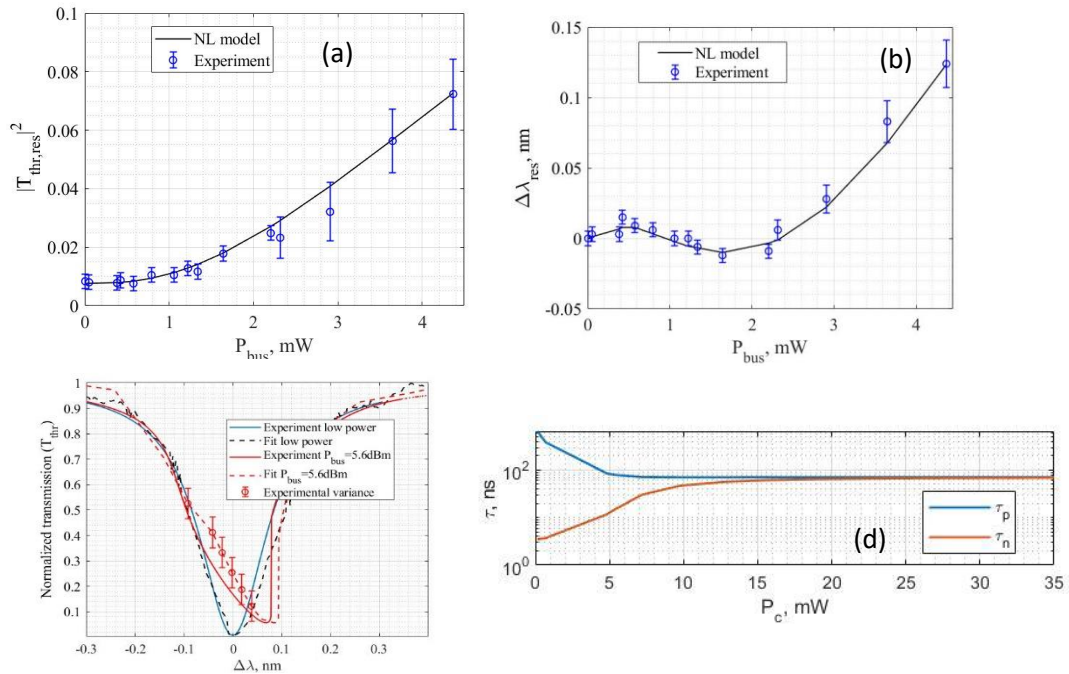


Fig. 1. Shift of resonant frequency (a) and variation of transmission at the through port at resonance (b), blue dots represent values extracted from measured spectra. From the fitting procedure we have $E_t = 0.69 \text{ eV}$, $N_s = 7.4 \cdot 10^{10} \text{ cm}^{-2}$. (c) Low power (blue) and high power (red) transmission coefficient, dashed line are measured transmission coefficients, the red error bar indicate the oscillatory behaviour caused by the interplay of FC and self-heating with CW input power. (d) Holes and electron lifetime as a function of the calculated circulating power.

Fig. 1 (d) shows the calculated hole and electron lifetimes, defined as $\tau_{p,n} = \frac{(n_e p_e)}{G_{TPA}}$, as a function of P_c . Both lifetimes exhibit a non linear behaviour as they are function of the circulating power and this dependence is essential to reproduce the experimental results. We note that for bus power higher than 1.5 mW , corresponding to $P_c = 15 \text{ mW}$, both holes and electrons lifetime tend to a constant value equal to $\tau_\infty \approx 70 \text{ ns}$, meaning that all traps are saturated by captured carriers. In this case electrons and holes dynamics can be approximated as equal, which justifies the assumption considered in other works [1,2,3]. Nonetheless thanks to our SRH model we can calculate the lifetimes without the need of any empirical expression. With the fitting parameters retrieved from the steady state analysis and measurements, we proceeded in reproducing periodic oscillations of the ring observed by measuring the time trace of the output power at the through port of the racetrack resonator. Fig. 2 (a) shows the superposition of the normalised output signal recorded with an oscilloscope and the prediction from the model in the time domain when we inject CW $P_{bus} \approx 11 \text{ dBm}$ at $\lambda_{in} \approx \lambda_0$. We can see that the model is able to follow the measured signal very well and can predict the periodicity of the oscillations. By analysing the simulated time evolution of excess carriers and circulating power in Fig. 2(b) and the variation of effective refractive index due to FCD and self-heating in Fig. 2(c) we are able to explain the origin of these self-oscillations as the interplay between the FC dynamics and the thermal transient which causes the resonant wavelength to oscillate with time (blue curve in Fig. 3c). We conclude by proposing a pump-probe experiment whose principal steps are summarised in Fig. 4. We set an high energy pulsed pump signal ($P_{pump}(t)$) with pulse width equal to 200 ps and a period of $130 \text{ }\mu\text{s}$ at a

ring resonance $\lambda_{0,pump} = 1547.1 \text{ nm}$, whereas the CW probe wavelength λ_{probe} is swept around the cold nearest resonance at $\lambda_{0,probe} = 1540.2 \text{ nm}$, as sketched in Fig. 4 (a).

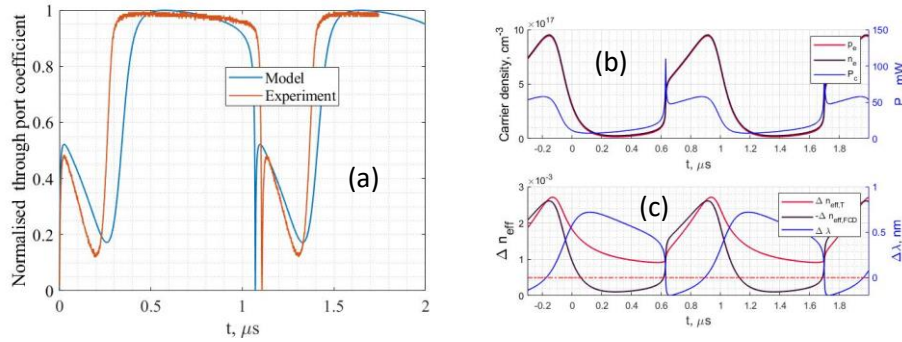


Fig. 3. (a) superposition of the normalized through port signal recorded on an oscilloscope and simulated through port coefficient for (b) Simulated holes and electron carrier densities (left) and circulating power (right) as a function of time. (c) Variation of refractive index due to temperature and FCD (left) and resonant wavelength (right) in time.

Generated free carriers by the pump pulse force a refractive index change that causes a blue shift of the resonance. The variation of the probe power depends therefore on the relative position of λ_{probe} with respect to the cold resonance wavelength $\lambda_{0,probe}$. By recording many different pump traces at different wavelengths λ_{probe} , we can reconstruct the ring spectral response at different time instants after the pump pulse. By fitting the time resolved transmission spectra we can extract the variation of effective refractive index due to FCD ($\Delta n_{eff,FCD}$) and the nonlinear loss as a function of time as shown in Fig. 4(e). The model we developed will then be applied to understand these recovery dynamics.

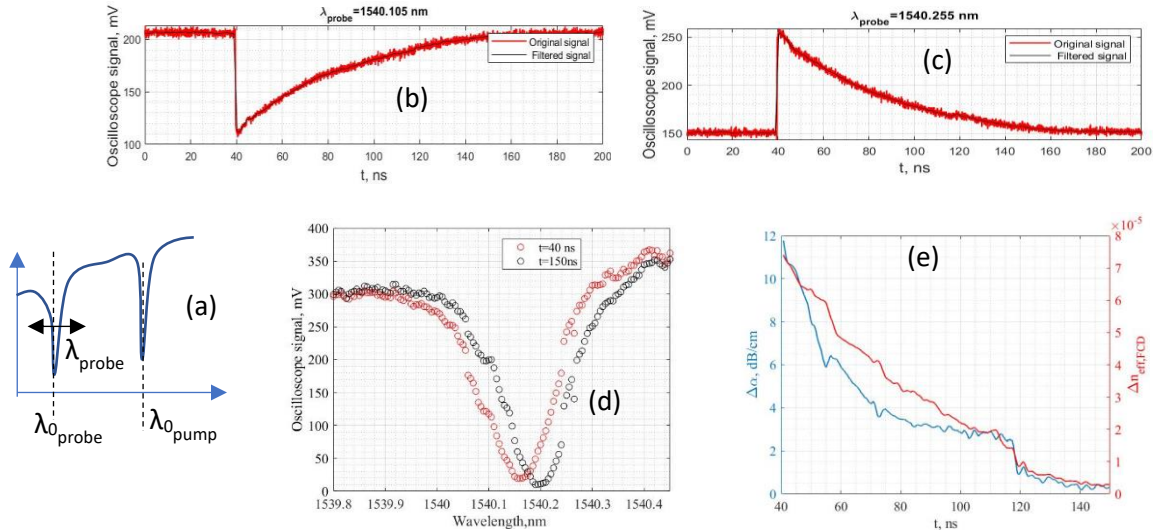


Fig. 4. (a) Schematic of the pump-probe experiment. (b) and (c) show probe powers traces signals recorded at the through port for probe wavelength below (b) and above (c) the cold resonance. (d) Time resolved spectral response of the ring around $\lambda_{0,probe}$ at $t = 40 \text{ ns}$ (just after the pump pulse) and at $t = 150 \text{ ns}$ (when the non-linear transient is concluded and the ring is in linear regime). (e) Extracted variation of effective refractive index due to FCD and non-linear loss in the ring versus time.

References

- [1] P. E. Barclay, K. Srinivasan, and O. Painter, "Nonlinear response of silicon photonic crystal microresonators excited via an integrated waveguide and fiber taper," *Opt. Express* 13, 801–820 (2005).
- [2] G. Priem, P. Dumon, W. Bogaerts, D. V. Thourhout, G. Morthier, and R. Baets, "Optical bistability and pulsating behaviour in silicon-on-insulator ring resonator structures." *Opt. Express* 13, 9623–9628 (2005)
- [3] M. Borghi, D. Bazzanella, M. Mancinelli, and L. Pavesi, "On the modeling of thermal and free carrier nonlinearities in silicon-on-insulator microring resonators," *Opt. Express* 29, 4363–4377 (2021)
- [4] J. Blakemore, *Semiconductor Statistics*, Dover Books on Physics Series (Dover, 2002).

Integrated electro-optical modulator operating in the long-wave infrared spectral range

(Student paper)

Thi Hao Nhi Nguyen¹, Natnicha Koompai¹, Miguel Montesinos-Ballester¹, Lucas Deniel¹, Jacopo Frigerio², Andrea Ballabio², Virginia Falcone², Xavier Le Roux¹, Carlos Alonso-Ramos¹, Laurent Vivien¹, Adel Bousseksou¹, Giovanni Isella², and Delphine Marris-Morini¹

¹ Centre de Nanosciences et de Nanotechnologies, Université Paris-Saclay, CNRS, 91120 Palaiseau, France

² L-NESS, Dipartimento di Fisica, Politecnico di Milano, Polo di Como, Via Anzani 42, 22100 Como, Italy

e-mail: thi-hao-nhi.nguyen@universite-paris-saclay.fr

Abstract: Free carrier plasma dispersion effect has been exploited to obtain an integrated electro-optical modulator operating in a broad spectral range of the mid-infrared regime. This modulator is based on a Schottky diode used to modulate free carrier concentration in a graded Silicon Germanium (SiGe) optical waveguide and to obtain modulation of the optical transmission. In the first experimental demonstration, operation was obtained from 6.4 to 10.7 μm wavelength with a single device. The dynamic characterization was performed up to 225 MHz. The work now focuses on the design of electrical access and RF electrodes to achieve high speed operation. Interestingly electro-optical bandwidth of a few tens of GHz is expected. © 2022

Keywords: Electro-optical modulator, silicon photonics, mid-IR wavelength, silicon, germanium,

INTRODUCTION

Mid-infrared (mid-IR) spectroscopy is of a great importance to detect the traces related to environmental and toxic vapors. The on-chip integration of spectroscopic system is promising for the development of sensors with high efficiency and compactness. Due to their vibrational and rotational resonances, many molecules can be detected in the mid-IR spectral range, especially for the wavelengths from 5 μm to 11 μm [1-3]. Integrated electro-optical modulator (EOM) operating in this wavelength range is interesting for many applications, such as sensitivity enhancement via on-chip synchronous detection. Recently, we have demonstrated the first integrated modulator based on a silicon germanium (SiGe) graded-index platform operating from 6.4 to 10.7 μm wavelength [4]. This modulator exploits free carrier concentration variations in a Schottky diode to obtain absorption coefficient variations. In this work, we evaluate the possibility to improve the device performance to achieve high speed operation.

RESULTS

a. Experimental results

The schematic view of the integrated modulator is depicted in Fig. 1a. It relies on a graded SiGe waveguide in which the concentration of Germanium linearly increases from 0 to 100%, which is responsible for a linear increase of the refractive index in the waveguide. The 6 μm -thick graded layer is grown on a highly n-doped Silicon substrate with doping concentration of $2 \times 10^{19} \text{ cm}^{-3}$, which allows for electrical access from the backside of the sample. The graded epi layer is non-intentionally doped, with a residual n-doped concentration estimated to be in the order of 10^{15} - 10^{16} cm^{-3} . The waveguide width and etching depth are 5.5 μm and 6.8 μm , respectively. The electric field profile of the TE mode at the wavelength of 8.5 μm is shown in Fig. 1b, showing a light confinement at the top of the waveguide. Electrical contacts are deposited on the backside of the sample and on the top of the waveguide, forming a vertical Schottky diode at the top of the waveguide. When tuning the voltage applied to the device, the variation of free carriers in depletion or injection regimes is thus responsible for variation of the absorption coefficient of the guided mode, and for modulation of the optical transmission. Fig. 1c shows a SEM image of the fabricated sample with 2.6 mm-long modulators.

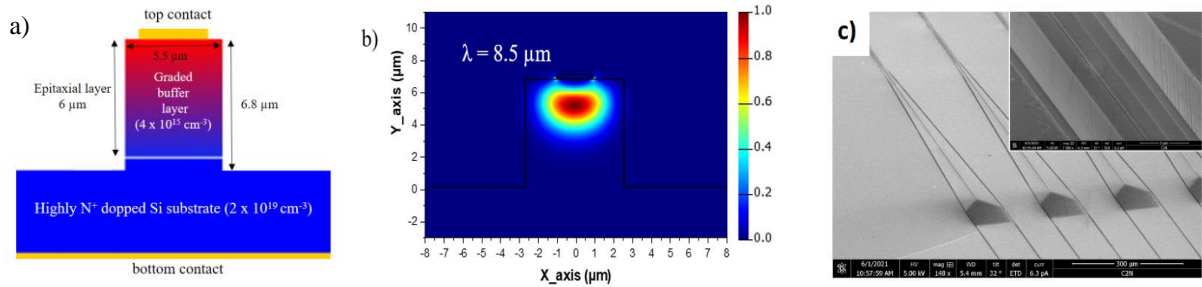


Fig. 1. (a) Schematic view of the modulator. (b) Electric field profile of the TE mode at 8.5 μm . (c) SEM picture of the fabricated device. The optical taper used to enlarge the waveguide and the top contact layer, to apply the electrical probe can be seen.

First, the modulation has been characterized in terms of modulation efficiency. In the injection regime, the concentration of free charge carriers in the optical waveguide increases by applying a direct voltage on the diode. Thus, the relative optical transmission gradually decreases when the current increases. The highest extinction ratio obtained in this configuration is 1.3 dB at the wavelength of 10.7 μm (Fig. 2a). In the depletion regime, free carriers are extracted out of the depletion region, thus the relative optical transmission increases when the reverse bias voltage increases (Fig. 2b).

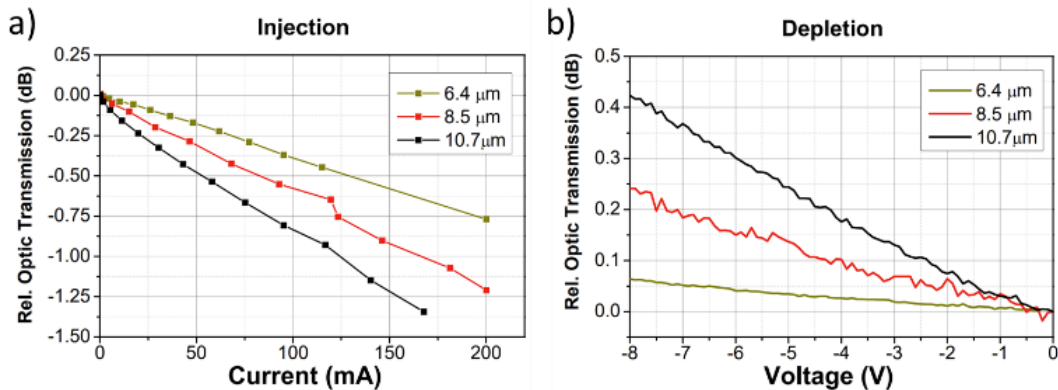


Fig. 2. Electro-optical modulation in TE polarization (a) in the injection regime and (b) in the depletion regime.

Dynamic characterization has also been performed. To this end, the light coming out from the output of the device is sent to a fast mid-IR detector operating up to 600 MHz. An RF electrical signal is applied to the modulator, and an electrical spectrum analyzer is used to measure the photodetected signal as a function of the RF frequency that is applied. Fig. 3 shows the photodetected signal as a function of the RF frequency in both injection and depletion schemes. As observed in injection regime, the signal linearly decreases when the electrical frequency is larger than 50 MHz, which is attributed to the effect of free carrier recombination lifetime. In depletion regime, the modulated signal is almost flat up to frequency of 225 MHz, while measurement at higher frequency is limited by the noise.

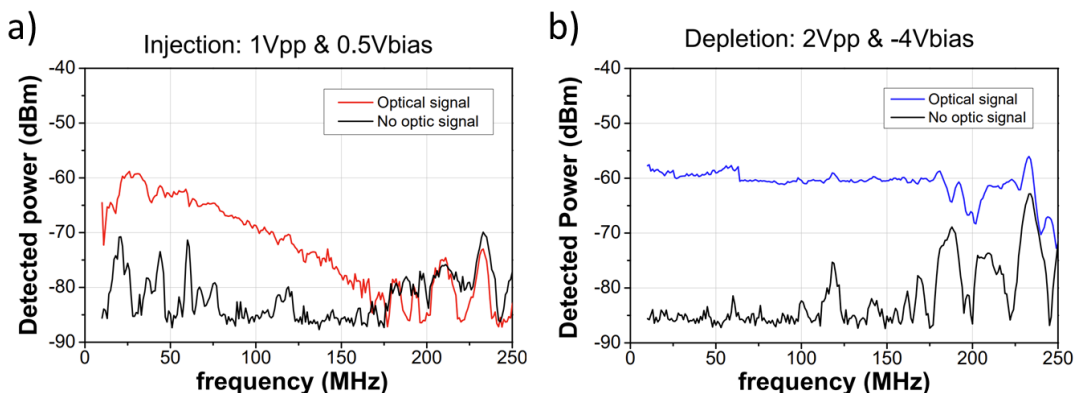


Fig. 3. Amplitude of the photodetected signal as a function of the RF frequency in (a) carrier injection regime and (b) carrier depletion regime.

b. Design for high-speed operation

While the achieved performances are already compatible with applications such as on-chip synchronous detection, it is highly interesting to investigate the possibility to reach higher frequency operation. To this end, the focus will be given on the depletion regime, where few tens of GHz of electro-optical bandwidths are expected. A careful design of the electrical access and the RF electrodes is then needed, in order to: (i) ensure that the equivalent RC product is compatible with high-speed operation; (ii) achieve impedance matching with the equipment used for the electro-optical characterization (50 ohms) to avoid high RF signal reflection; (iii) reduce the speed difference between electrical and optical signals propagating along the modulator.

The use of grounded coplanar waveguide (CPWG) electrodes is investigated to that end. A distributed model considering both light and electrical signal propagation is considered and used to evaluate the electrical S parameters and the 3 dB electro-optical bandwidth. The equivalent electrical circuit of the Schottky diode is implemented, both in terms of equivalent capacitance (obtained from simple electrical modelling) and access resistance (based on experimental results). Finally, the parameters of the electrodes, such as the width of the signal line path and the distance between the signal and the ground are optimized by numerical calculations. Interestingly, it will be shown that electro-optical bandwidth of a few tens of GHz can be expected.

CONCLUSION

This work focuses on an integrated electro-optical modulator based on a Schottky diode embedded in a graded SiGe optical waveguide. This modulator can operate in a wide wavelength range of the mid-IR spectrum (6.4 - 10.7 μm). While the first experimental results were limited to modulating frequencies below 250 MHz, the design of the electrical contacts and RF electrodes has been carried out to optimize the electro-optical bandwidth. Interestingly, by using grounded coplanar waveguide electrodes, electro-optical bandwidth of a few tens of GHz are expected.

Acknowledgements

This work was supported by Light-up Project (ANR-19-CE24-0002-01). This work was partly supported by the French RENATECH network.

References

- [1] J.-M. Ramirez *et al.*, "Graded SiGe waveguides with broadband low-loss propagation in the mid infrared", *Opt. Express* 26, p. 870 (2018).
- [2] H. Lin *et al.*, "Mid-infrared integrated photonics on silicon: a perspective," *Nanophotonics* 7(2), p. 393 (2018).
- [3] D. Marris-Morini *et al.*, "Germanium-based integrated photonics from near- to mid-infrared applications", *Nanophotonics* 7(11), p. 1781 (2018).
- [4] M. Montesinos-Ballester *et al.*, "Ge-rich graded SiGe waveguides and interferometers from 5 to 11 μm wavelength", *Opt. Express* 28 (9), p. 12771 (2020).

1×5 reconfigurable optical wireless routers for on-chip interconnection

Loredana Gabriele¹, Gaetano Bellanca^{2*}, Jacopo Nanni³, Marina Barbiroli³, Franco Fuschini³, Velio Tralli², Davide Bertozzi², Giovanni Serafino⁴, Vincenzo Petruzzelli¹, and Giovanna Calò¹

¹Department of Electrical and Information Engineering, Polytechnic University of Bari, Via Orabona, 4, Bari 70125, Italy

²Department of Engineering, University of Ferrara, Via Saragat, 1, Ferrara 44122, Italy

³Department of Electrical, Electronic and Information Engineering “G. Marconi”, University of Bologna, Viale del Risorgimento, 2, Bologna 40136, Italy

⁴Scuola Superiore Sant’Anna, TeCIP Institute, via G. Moruzzi 1, 56124 Pisa, Italy

* gaetano.bellanca@unife.it

In this paper we report the design of 1×5 wireless routers, based on transmitting and receiving integrated Optical Phased Arrays (OPA), which allow on-chip optical wireless interconnections. The proposed devices aim at achieving high-bandwidth and reconfigurable links between multiple nodes. The general design criteria of these routers are reported and performance increase in terms of insertion loss and crosstalk, obtained by increasing the number of antennas in each OPA, are demonstrated.

Keywords: wireless optical interconnects, optical antennas, optical phased arrays.

INTRODUCTION

Chip Multiprocessors (CMPs) exploiting the potentialities of parallel computing are the state-of-the-art solution to face the constant need of increasing computing system efficiency. As the number of cores in chip multiprocessors continues to scale up, the efficient interconnection of these cores is becoming a major challenge to avoid communication bottleneck and to meet the high bandwidth, low-power and low-latency requirements which, actually, cannot be matched by traditional point-to-point connections through dedicated electrical links [1].

The realization of efficient on-chip interconnections is one of the most important challenges in developing new computing architectures based on heterogeneous multichip integration. In order to overcome the communication bottleneck of these multichip systems, in this work we propose a new approach based on the use of optical wireless routers. These routers can be integrated with an existing Optical Network on Chip as an alternative to ring-based routing matrices, with the aim to increase the overall efficiency of the network. Different configurations of on-chip 1×5 optical wireless interconnections are proposed. These configurations exploit transmitting and receiving Optical Phased Arrays (OPAs) made of taper antennas [2, 3]. We report the wireless router design criteria as well as the results of three-dimensional Finite Difference Time Domain (FDTD) simulations. The effect of the multipath propagation in the on-chip multi-layered medium is also taken into account.

RESULTS

A conceptual scheme of a 1×5 Optical Wireless Interconnection Block (OWIB) is shown in Fig. 1 (a), while the cross section of the on-chip multilayer structure is illustrated in Fig. 1 (b) [4]. In this scenario, the transmitting OPA can illuminate five different receivers, provided that suitable phase shifts are applied at the different antennas in each OPA. The phase shift of the optical signal applied at the input of the different antennas, allows tilting the radiated beam toward the selected receiving OPA. To guarantee the interconnection between the transmitter and the addressed receiver, a suitable phase shift must be applied also at the receiving OPA, to virtually steer the radiation diagram of the receiving array.

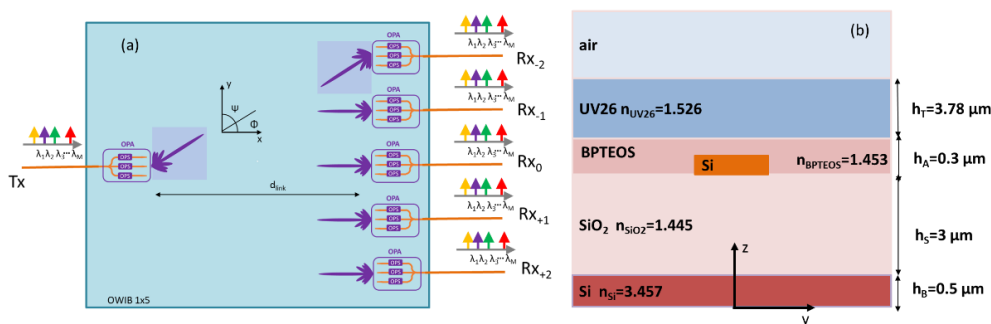


Fig. 1. (a) Scheme of a 1×5 OWIB. OPA: Optical Phase Array; OPS: Optical Phase-Shifter; (b) On-chip multilayer structure (yz-cross section), highlighting the multiple interfaces in the vertical plane.

The phase shift necessary for the OWIB operation can be achieved in Si waveguides by using Optical Phase Shifters (OPs) based either on thermo-optic or plasma-optic effect [5]. In the scheme of Fig. 1 (a), the antennas are integrated with standard waveguides and they radiate a wavelength-division multiplexed (WDM) signal with parallel and simultaneous transmission of different data channels. The wireless propagation of the optical signal occurs in the on-chip multilayered structure shown in Fig. 2 (b), which was already analyzed by the authors in [3, 4, 6].

The transmitting and receiving OPAs schematized in Fig. 1 (a) are made by aligning some antennas along the y-axis; each antenna is made by inversely tapering a standard SOI waveguide, with cross-section height $h = 220$ nm and width $w = 450$ nm. The taper, having length $L_T = 2$ μm , is terminated on a small tip with length $l = 1$ μm , and width $w_T = 130$ nm. The guided mode becomes evanescent while propagating in the inverse taper and, therefore, it is radiated in the surrounding dielectric.

Two different 1×5 OWIB configurations are analyzed, namely: 1) a 1×5 OWIB exploiting $N = 3$ antennas for each OPA with distance $d_a = 2\lambda/n_{UV26}$ (where λ/n_{UV26} is the wavelength in the cladding medium) between adjacent antennas, and 2) a 1×5 OWIB exploiting $N = 5$ antennas for each OPA, having one half of the distance ($d_a = \lambda/n_{UV26}$) between the adjacent elements.

Figs. 2 show the calculated radiation diagrams of the two analyzed OPA configurations as a function of the angle Φ on the horizontal plane with (a) $N = 3$ and (b) $N = 5$ antennas, for different applied phase shifts. The radiation diagram of the single taper antenna is also reported in Figs. 2 (black curve), for the sake of comparison. To calculate the radiation diagrams, the antenna arrays were modeled through the FDTD method. Standard near-to-far field projections of the fields recorded on a closed box, surrounding the antenna and the SOI waveguides, were calculated after the Fourier transformation of the time-domain electromagnetic fields [3, 7]. As can be seen in Figs. 2, both configurations allow addressing 5 receivers. In the first configuration (Fig. 2 (a)), the distance between the $N = 3$ antennas is $d_a = 2\lambda/n_{UV26}$. As expected from antenna theory, distances d_a between adjacent radiators greater than the wavelength in the propagation medium, lead to having multiple main lobes in the visible space. This feature can be exploited in the design of the OPA to address multiple receivers.

As an example, when a phase shift equal to $\alpha = \pm 360^\circ/N = \pm 120^\circ$ is applied to the array elements of the transmitter, it is possible to steer the maxima of the radiation diagram to the positions of the radiation nulls of the broadside array ($\alpha = 0$, yellow curve). In this way, either $Rx_{\pm 1}$ or $Rx_{\pm 2}$ can be illuminated. To minimize crosstalk, the five receivers Rx_i (with $i = 0, \pm 1, \pm 2$) should be placed in correspondence of the radiation peaks/nulls.

In the second configuration (Fig. 2 (b)), the distance between the $N = 5$ antennas is halved ($d_a = \lambda/n_{UV26}$). In this case, the antenna gain exhibits a single main lobe for every phase shift considered. When the phase shifts $\alpha = \pm 360^\circ/N = \pm 72^\circ$ and $\alpha = \pm 2 \cdot 360^\circ/N = \pm 144^\circ$ are applied to the array elements of the transmitter, it is possible to steer the maxima of the radiation diagram to the positions of the radiation nulls of the broadside array ($\alpha = 0$, yellow curve).

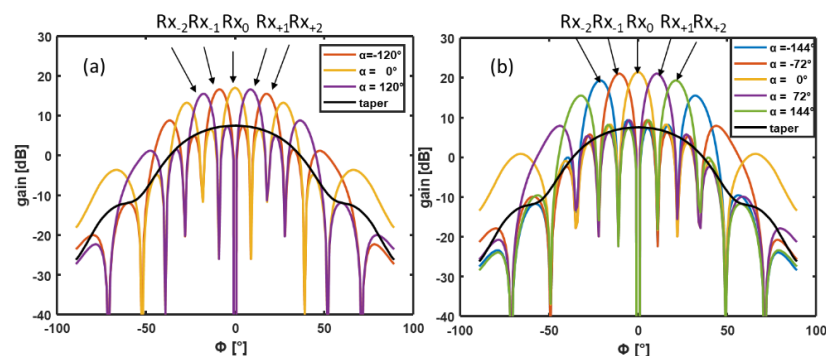


Fig. 2. Gain as a function of the angle Φ for different values of the phase shift α calculated for: (a) an array of $N = 3$ taper antennas with antenna distance $d = 2\lambda/n_{UV26}$, and (b) an array of $N = 5$ taper antennas with antenna distance $d = \lambda/n_{UV26}$. The taper length is $L_T = 2$ μm and the gain of the taper antenna is also reported (black curve). The wavelength is 1550 nm.

In order to evaluate the performances of the two OWIB configurations, the full devices (made of 1 transmitting and 5 receiving OPAs) were simulated by FDTD considering the propagation in the multilayered medium schematized in Fig. 1 (b). The transmittances of every link, computed as the total power coupled into the receiver waveguides divided by that at the transmitter, were calculated for the different phase-shift values. In both configurations, the distance d_{link} between the transmitters and the receivers, and the distance between the different receiving OPAs, were optimized to minimize crosstalk and multi-path attenuation [4].

Figs. 3 show the transmittance in dB, calculated as a function of the wavelength, at the receiving OPAs, i.e. Rx_0 , $Rx_{\pm 1}$ and $Rx_{\pm 2}$, with three taper antennas for each array; the taper length is $L_T = 2$ μm , the antenna distance is $d = 2\lambda/n_{UV26}$ and the link distance is $d_{\text{link}} = 55$ μm . The receivers (a) Rx_0 , (b) $Rx_{\pm 1}$, and (c) $Rx_{\pm 2}$ are addressed by applying the indicated phase shifts at the transmitting and at the receiving OPAs. The transmittances pertaining to the links

between the transmitter and either Rx₋₁ and Rx₋₂ are not reported since, for the symmetry of the device, they are similar to Figs. 3 (b) and (c).

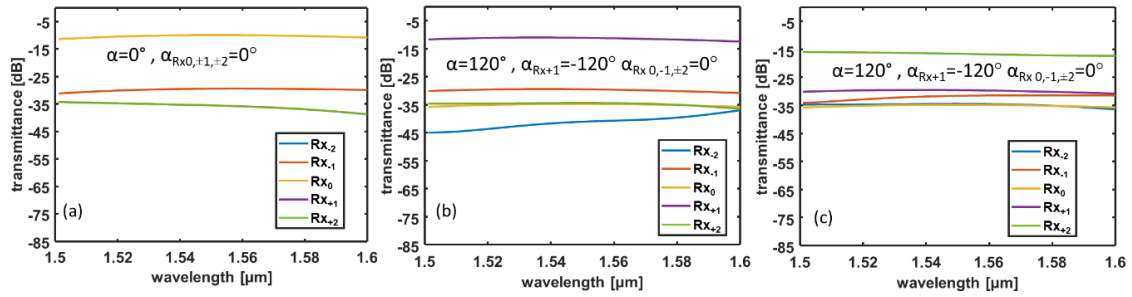


Fig. 3: Transmittance (in dB), calculated as a function of the wavelength, at the receiving OPAs, i.e. Rx₀, Rx_{±1} and Rx_{±2}, with three taper antennas for each array (taper length $L_T = 2 \mu\text{m}$, antenna distance $d = 2\lambda/n_{UV26}$ and link distance $d_{\text{link}} = 55 \mu\text{m}$). The receivers (a) Rx₀, (b) Rx_{±1}, and (c) Rx_{±2} are addressed by applying the indicated phase shifts at the Tx and at the Rx OPAs.

Similarly, Figs. 4 show the performances at the receiving OPAs, i.e. Rx₀, Rx_{±1} and Rx_{±2}, with five taper antennas for each array. In this case, the taper length is $L_T = 2 \mu\text{m}$, the antenna distance is $d = \lambda/n_{UV26}$, and the link distance is $d_{\text{link}} = 65 \mu\text{m}$. As before, the receivers (a) Rx₀, (b) Rx_{±1}, and (c) Rx_{±2} are addressed by applying the indicated phase shifts at the transmitting and at the receiving OPAs.

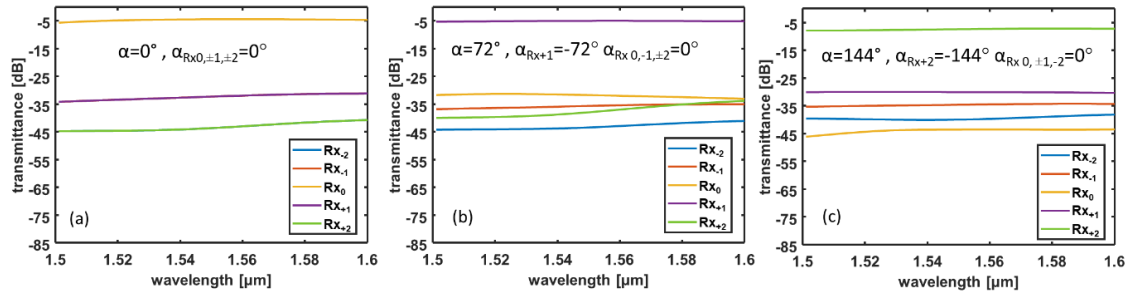


Fig. 4: Transmittance (in dB), calculated as a function of the wavelength, at the receiving OPAs, i.e. Rx₀, Rx_{±1} and Rx_{±2}, with five taper antennas for each array (taper length $L_T = 2 \mu\text{m}$, antenna distance $d = \lambda/n_{UV26}$, and link distance $d_{\text{link}} = 65 \mu\text{m}$). The receivers (a) Rx₀, (b) Rx_{±1}, and (c) Rx_{±2} are addressed by applying the indicated phase shifts at the Tx and at the Rx OPAs.

DISCUSSION

From Figs. 3 we can infer that, for the OWIB exploiting OPAs with $N = 3$ antennas, the worst-case insertion loss $IL \approx -15$ dB occurs when the receivers Rx_{±2} are addressed. Moreover, the crosstalk between the different ports can be determined as $XT_{ij} = 10 \log_{10}(T_{Rxi}/T_{Rxj})$, where T_{Rxj} is the transmittance of the addressed port and T_{Rxi} is the transmittance of a non-addressed one. For the OWIB exploiting OPAs with $N = 3$ antennas, the worst-case crosstalk $XT_{21} \approx -12$ dB occurs for the links $Tx \rightarrow Rx_{+2}$ and between the nodes Rx₊₁ and Rx₊₂. Similarly, from Figs. 4 we can observe that, for the OWIB exploiting OPAs with $N = 5$ antennas, the worst-case insertion loss occurs, again, when the receivers Rx_{±2} is addressed. However, thanks to the higher gain of the OPA, the worst-case insertion loss is lower $IL \approx -7.5$ dB. Also, the crosstalk is improved with a worst-case value $XT_{21} \approx -22$ dB for the link $Tx \rightarrow Rx_{+2}$ and between the receivers Rx₊₁ and Rx₊₂. Therefore, increasing the number of antennas in the OPA improves the OWIB performances. As a counterpart, this increases device footprint and complexity of the phase-shifting circuitry.

References

- [1] J. Flich and D. Bertozzi, Designing Network-on-Chip Architectures in the Nanoscale Era (CRC Press, 2019).
- [2] C. García-Meca, et Al., "On-chip wireless silicon photonics: from reconfigurable interconnects to lab-on-chip devices," Light Sci Appl 6(9), e17053 (2017).
- [3] G. Calò, et Al., "Design of reconfigurable on-chip wireless interconnections through optical phased arrays," Optics Express, vol. 29, no. 20, pp. 31 212–31 228, 2021.
- [4] J. Nanni et al., "Multi-path propagation in on-chip optical wireless links," IEEE Photonics Technology Letters, vol. 32, no. 17, pp. 1101–1104, 2020.
- [5] W.N. Ye and Y. Xiong, "Review of silicon photonics: history and recent advances," J. Mod. Opt. 60(16), 1299–1320, (2013).
- [6] B. Alam, et al., "Numerical and experimental analysis of on-chip optical wireless links in presence of obstacles," IEEE Photonics Journal, vol. 13, no. 1, pp. 1–11, 2020.
- [7] G. Calò et al., "Double Vivaldi antenna for wireless optical networks on chip", Optical and Quantum Electronics, Vol. 50, n. 6, Article number 261, 2018

Compact and Alignment-Tolerant Vertical Coupler for Heterogeneous Photonic Integration

(Student paper)

Chunhui Yao, Qixiang Cheng* and Richard V. Penty

Centre for Photonic Systems, Electrical Engineering Division, Department of Engineering, University of Cambridge,
9 JJ Thomson Avenue, Cambridge, CB3 0FA, U.K.

* qc223@cam.ac.uk

We present a generic design method of compact and alignment-tolerant vertical coupler for III-V-on-silicon photonic integrated circuits. Based on a multi-segmented tapered structure, our coupler (87 μm long) is almost 3-fold shorter than the state-of-the-art adiabatic couplers but still outperforms with a < 0.3 dB coupling loss (i.e., $> 94\%$ efficiency) with ± 1.0 μm misalignment, making it suitable for commercially available assembly tools, such as micro-transfer printing and flip-chip bonding.

Keywords: Heterogeneous integration, vertical coupler, compact, alignment-tolerant.

INTRODUCTION

III-V-on-silicon heterogeneous integration enables a variety of active photonic devices, such as SOAs and lasers, to be integrated with Si photonics circuits. Among diverse integration techniques, flip-chip bonding and die/wafer bonding are widely used thanks to their high technical maturity. The former allows the III-V devices to be pre-processed/tested yet suffers from limited integration densities and strict coupling requirements, while the latter supports dense integration but demands modifications on the silicon photonics back-end flow [1]. Recently, micro-transfer-printing (μTP) arose as a newcomer in the field. By parallelly transfer printing III-V coupons onto silicon platforms, it combines the advantages of flip-chip bonding and die/wafer bonding without disturbing the process on the silicon photonics side [2].

The vertical coupler is a key building block for heterogeneous integration as it enables the power transition between the III-V and silicon layers. The tolerance to lateral misalignment is essential for vertical couplers. For example, the 3σ alignment accuracy for current μTP tools ranges from ± 0.5 to ± 1.5 μm , which, with further development, is expected to be ± 1.0 μm for large-array transfer printing, setting a benchmark for the coupler design [3]. The compactness of vertical coupler is also of great importance, especially for applications like optical switches and optical processors where massive III-V components are densely integrated at chip-level. However, it is non-trivial to achieve both metrics. Based on different working principles, vertical couplers can be classified as resonant couplers or adiabatic couplers. Utilizing the periodic interference phenomena between the coupled waveguides, resonant couplers can be rather short but always sensitive to alignment/fabrication variations [4]. Adiabatic couplers, in contrast, rely on gradual changes in the device structure to slowly transfer the power into target waveguide, which relaxes the alignment/fabrication control but requires hundreds of microns in length to ensure the adiabatic condition [5]. To solve this dilemma, we propose a compact and alignment-tolerant vertical coupler with multiple tapered segments on the basis of resonant coupling mechanism. The device is 87 μm long and has a < 0.3 dB coupling loss even when ± 1.0 μm misaligned, which, to our best knowledge, is a new record for heterogeneous III-V-on-silicon vertical couplers.

RESULTS

Our design is demonstrated based on an example III-V-on-silicon heterogeneously integrated system (detailed layer information can be found in [5]), where the III-V component is located on top of a 400 nm silicon rib waveguide with a lateral misalignment Δm , as shown in Fig. 1(a). The mode propagation and interaction in such coupled-waveguide system can be described by the coupled mode theory, as [6]:

$$\frac{d}{dz} \begin{bmatrix} a_1 \\ a_2 \end{bmatrix} = \begin{bmatrix} -i\beta_1 & -i\kappa \\ -i\kappa & -i\beta_2 \end{bmatrix} \begin{bmatrix} a_1 \\ a_2 \end{bmatrix}, \quad (1)$$

where a_1 and a_2 represents the the mode amplitudes in the uncoupled III-V and Si waveguides, while β_1 and β_2 are their propagation constants, respectively. z denotes the propagation direction. κ is the mode coupling coefficient, defined as:

$$\kappa_{ij} = \frac{k_0^2}{2\beta} \iint (n^2 - n_j^2) \psi_i \psi_j^* dx dy, \quad (2)$$

where ψ_i and ψ_j are the normalized eigenmodes in each uncoupled waveguide, β is the mode propagation in the coupled waveguide, k_0 is the free-space propagation constant, and n , n_i , and n_j are the refractive index profiles of the coupled waveguide and two uncoupled waveguides, respectively. It can be derived from Eq.(1) that the optical mode beats periodically between the two waveguides (assuming κ to be constant) and reaches its first maximum at $z = \pi/2\kappa\sqrt{1+\gamma^2}$, where $\gamma \equiv (\beta_2 - \beta_1)/2\kappa$, with a transferred power of $1/(1+\gamma^2)$. Hence, to design a conventional resonant coupler with no coupling loss, its length should be set as half the mode beating period, while the waveguide widths need to be well chosen to make sure that γ is 0 (i.e., β_2 should be equal to β_1 , known as the phase matching condition). Nevertheless, misalignments can significantly weaken the coupling strength (i.e., reduce the value of κ) so that the coupler no longer cuts off at the point of maximal power transition. To mitigate such sensitive dependence on the coupling length, one viable way is to use tapered structures to break the periodical resonant behavior, as reported in [7]. Thus, in our case, we first propose a vertical coupler based on sharp linear tapers, and then extend it to a multi-segmented tapered structure to enhance the performance, as shown in Fig. 1(b-c). Detailed analysis of the two designs are presented successively as follow.

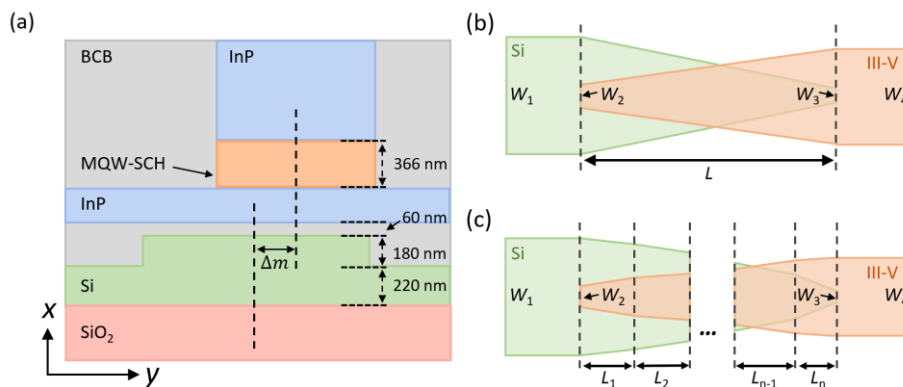


Fig. 1. (a) Cross-section schematic of a III-V-on-silicon vertically coupled-waveguide system [5]. (b-c) Top view of the proposed vertical couplers with linearly tapered structure and multi-segmented tapered structure, respectively.

The geometry of the linearly tapered structure is determined by the widths W_1 to W_4 and length L , where the tip widths W_2 and W_3 are set to be $0.5 \mu\text{m}$ and $0.2 \mu\text{m}$, respectively, considering the fabrication limitations on critical dimensions. Our optimization strategy is firstly to select the combination of widths W_1 and W_4 , and then sweep the length L to search for the best alignment tolerance. As there are only three parameters, this process can be done via a brute-force search that the optimal combination of W_1 and W_4 is found to be $3.35 \mu\text{m}$ and $2.95 \mu\text{m}$, respectively. Figure 2(a) shows the calculated map of γ for different width combinations of the III-V and silicon waveguides when misalignment is $1.0 \mu\text{m}$, in which the width combination of the optimized linearly tapered structure is illustrated by the white-dashed line. Figure 2(b) shows the simulated efficiencies versus length L at different misalignment levels. Under perfect alignment, the coupling efficiency reaches the peak when L is $52 \mu\text{m}$ and keeps high with increasing taper length, illustrating the suppression of the periodic coupling phenomenon. While as the misalignment increases, a longer taper length is required, e.g., L needs to be $93 \mu\text{m}$ to achieve a < 0.4 dB loss when $0.6 \mu\text{m}$ misaligned, which indicates that a better alignment tolerance can be realized by properly lengthening the taper. However, when the misalignment increases further, the coupling efficiency dramatically deteriorates even with a longer taper length. This can be explained by the simple fact that there is only one point in the linearly tapered structure that is perfectly phase matched ($\gamma = 0$) while all other parts are mismatched, especially at the beginning and the end where the absolute value of γ is on the order of ten, as shown in Fig. 2(a).

Thus, to obtain better performance, a tapered structure with varying slopes is proposed that the slopes at its central region where the phase matching can be reasonably satisfied is designed to be gentler than those phase-mismatched peripheral regions. In practice, we adopt a multi-segmented tapered structure. The design procedure also starts with selecting the width combinations for each segment, shown by the red dots in Fig. 2(a) that each two adjacent dots correspond to one specific segment. Most dots are selected around the phase-matched point, following the distribution of the optimal result of the linearly tapered coupler (i.e., the white-dashed line), while at both ends, the dots are adjusted to have smaller values of γ to attain a higher efficiency. As for the lengths of each segment, since it involves a global optimization of multiple parameters, we employ the particle swarm optimization (PSO) algorithm, targeting for the best alignment tolerance with as high efficiency as possible. Note that here, the number of segments is set to be 10 to avoid an overlarge searching space for the algorithm. Figure 2(c) shows the optimized device geometry, which is $87 \mu\text{m}$ long. As intended, the segments around the central part are more gradual than those on the two sides. Figure 2(d) presents the FDTD simulated results for the multi-segmented

coupler with different misalignments. The coupling loss is only 0.09dB when perfectly aligned, remains < 0.3 dB even with a 1.0 μm misalignment, and drops to 3 dB when 1.2 μm misaligned.

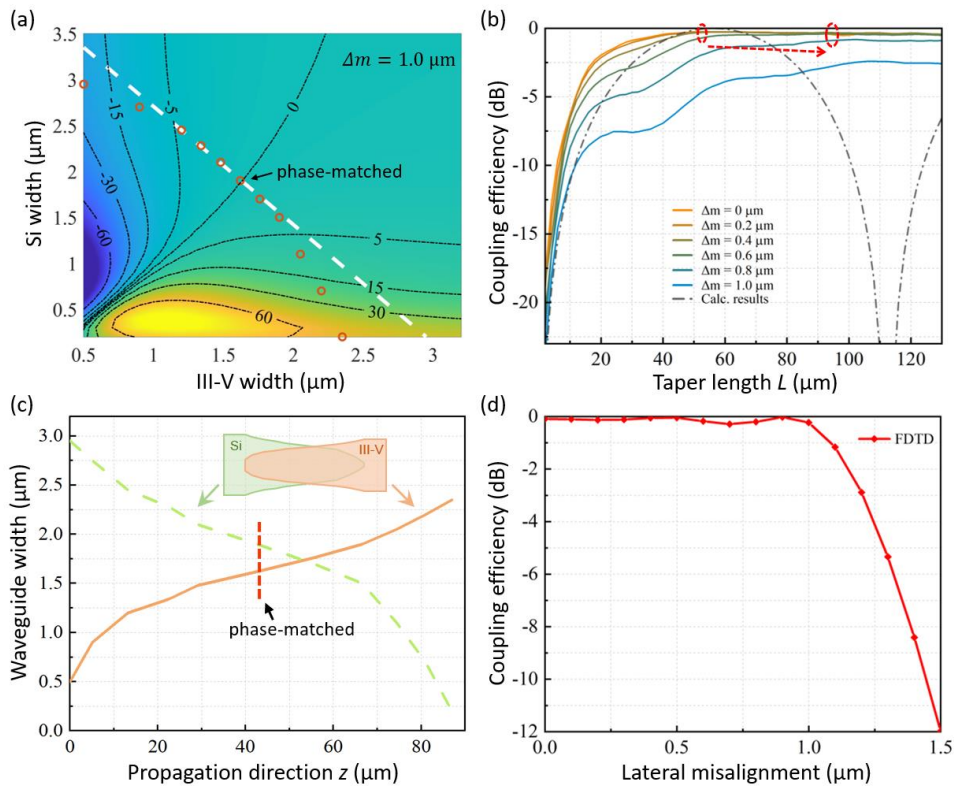


Fig. 2. (a) Map of γ for different waveguide width combinations when Δm is 1.0 μm . (b) Coupling efficiency vs. taper length for the linearly tapered coupler, with a theoretical calculation of conventional resonant coupler plotted for reference. (c) Width variations of the multi-segmented coupler. (d) Coupling efficiency vs. misalignment for the multi-segmented coupler.

CONCLUSION

In this paper, we present a design of a compact and alignment-tolerant vertical coupler based on the resonant coupling mechanism for heterogeneously integrated III-V-on-silicon photonic systems. The coupler structure contains multiple tapered segments, of which the width combinations are carefully selected based on the coupled mode theory, while the lengths are optimized using the PSO algorithm. The device length is 87 μm , nearly 3 times shorter than the state-of-the-art alignment-tolerant adiabatic couplers [5]. Simulation results show that our coupler achieves < 0.3 dB coupling loss even when $\pm 1.0 \mu\text{m}$ misaligned, which makes it particularly applicable for those commercially available assembly tools with potential alignment deviations, e.g., micro-transfer printing and flip-chip bonding. The proposed design method can also be applied to different material systems, therefore is expected to find wide applications in various heterogeneous or monolithic integration platforms.

References

- [1] G.-H. Duan *et al.*, 'New advances on heterogeneous integration of III-V on silicon', *J. Lightwave Technol.*, vol. 33, no. 5, pp. 976–983, 2015.
- [2] J. Yoon, S.-M. Lee, D. Kang, M. A. Meitl, C. A. Bower, and John. A. Rogers, 'Heterogeneously Integrated Optoelectronic Devices Enabled by Micro-Transfer Printing', *Advanced Optical Materials*, vol. 3, no. 10, pp. 1313–1335, Oct. 2015.
- [3] 'InP on SiN Photonic Integrated circuits REALized through wafer-scale micro-transfer printing | INSPIRE Project | Fact Sheet | H2020 | CORDIS | European Commission'. <https://cordis.europa.eu/project/id/101017088> (accessed Feb. 16, 2022).
- [4] A. He, X. Guo, H. Wang, L. Sun, and Y. Su, 'Ultra-Compact Coupling Structures for Heterogeneously Integrated Silicon Lasers', *J. Lightwave Technol.*, pp. 1–1, 2020.
- [5] B. Haq *et al.*, 'Micro-Transfer-Printed III-V-on-Silicon C-Band Semiconductor Optical Amplifiers', *Laser & Photonics Reviews*, vol. 14, no. 7, p. 1900364, Jul. 2020.
- [6] W.-P. Huang, 'Coupled-mode theory for optical waveguides: an overview', *J. Opt. Soc. Am. A*, vol. 11, no. 3, p. 963, Mar. 1994.
- [7] C. Liu, G. Zhao, F. Yang, Q. Lu, and W. Guo, 'Design of Compact but Fabrication-Tolerant Vertical Coupler for Active–Passive Integration', *J. Lightwave Technol.*, vol. 36, no. 3, pp. 755–762, Feb. 2018.

Lithium-niobate-based frequency-agile integrated laser sources

(Student paper)

V. Snigirev^{1,*}, A. Riedhauser², G. Likhachev¹, J. Riemensberger¹, R. N. Wang¹, C. Moehl², M. Churaev¹, A. Siddharth¹, G. Huang¹, Y. Popoff^{2,3}, U. Drechsler², D. Caimi², S. Hoel², J. Liu¹, P. Seidler², and T. J. Kippenberg¹

¹ Institute of Physics, Swiss Federal Institute of Technology Lausanne (EPFL), CH-1015 Lausanne, Switzerland

² IBM Research Europe, Zurich, Säumerstrasse 4, CH-8803 Rüschlikon, Switzerland

³ Integrated Systems Laboratory, Swiss Federal Institute of Technology Zurich (ETH Zürich), CH-8092 Zürich, Switzerland

* viacheslav.snigirev@epfl.ch

We demonstrate narrow linewidth ultrafast tunable photonic integrated lasers based on heterogeneously integrated thin-film lithium niobate on ultra-low loss silicon nitride integrated photonic circuits. Using self-injection locking of a hybrid microresonator, we achieve a tuning speed of > 10 peta-Hertz-per-second over a bandwidth of 0.5 GHz. We show the utility of this approach by demonstrating coherent FMCW LiDAR ranging.

Keywords: *thin-film lithium niobate, Damascene silicon nitride, frequency-agile lasers, FMCW LiDAR*

INTRODUCTION

Rapid progress in the domain of thin-film lithium niobate integrated photonics resulted in demonstration of CMOS-compatible electro-optic modulators [1, 2], electro-optic frequency combs generation [3] and microwave-optical quantum transduction [4]. Photonic circuitry based on lithium niobate can also find its application in the domain of integrated tuneable lasers [5]. Ultra-low noise lasers have been demonstrated based on self-injection locking of diode lasers to integrated [6] and whispering gallery mode [7] optical microresonators with ultra-low loss. We have recently demonstrated that by using an optical microresonator with piezo-electrical actuation and stress optical tuning, we can endow such a laser with MHz tuning bandwidth and GHz frequency excursion, ideal for coherent laser based ranging [8].

Although high tuning linearity and efficiency were observed, the frequency bandwidth of laser wavelength modulation is inherently limited by the excitation of mechanical modes by the actuator. Thus, additional stringent phononic engineering is required to reach high modulation frequencies (up to 10 MHz [8]). In contrast electro-optical actuation does not strongly excite mechanical modes of the chip and supports GHz bandwidths [1]. Therefore, we designed an electro-optically tuneable laser source based on the heterogeneously integrated lithium niobate on Damascene silicon nitride (LNOD) platform [9], endowing ultra-low-loss circuits [10] with electro-optic tunability and demonstrate its potential for applications such as frequency modulated continuous-wave (FMCW) LiDAR.

RESULTS

A conceptual representation of the proposed tunable laser is given in Fig. 1(a). A distributed-feedback (DFB) indium phosphide laser is self-injection-locked to an external LNOD microring resonator mode, and the output frequency is changed by applying voltage to electrodes placed along the resonator circumference. The structure of the LNOD waveguide (see Fig. 1(b)) leads to a hybrid optical mode that partially penetrates the layer of lithium niobate making possible electro-optic modulation. A high quality factor for the LNOD mode is important for achieving wide locking bandwidth and pronounced linewidth narrowing [11]. Because of the low-loss Damascene silicon nitride circuits underneath, median intrinsic coupling rate (Fig. 1(c)) is 100 MHz. That is equivalent to a quality factor of 2×10^6 . The self-injection-locked state of the laser is characterized by locking bandwidth of 1.1 GHz, 30 dB suppression of the phase noise spectrum and intrinsic frequency noise of 3 kHz (see Fig. 1(e)).

The frequency tuning potential of the laser can be inferred from Fig. 1(d), where the electro-optic response curve is measured it by positioning a reference laser on the flank of a selected resonance and applying a voltage to the electrodes with a vector network analyzer. The small-signal frequency response is flat, showing no degradation of modulation efficiency with the modulation frequency from 10 kHz to 100 MHz. For frequency-modulated continuous wave (FMCW) LiDAR [12], linear ramp wavelength tuning plays the central role. Thus, we characterize this tuning pattern by applying a triangular voltage waveform to the microresonator electrodes (see Fig. 1(f)). Using

a 10 MHz of modulation frequency, we achieve a laser wavelength tuning rate of 12 PHz/s. The chirp nonlinearity at 100 kHz is $< 1\%$, and the tuning efficiency is 30 MHz/V.

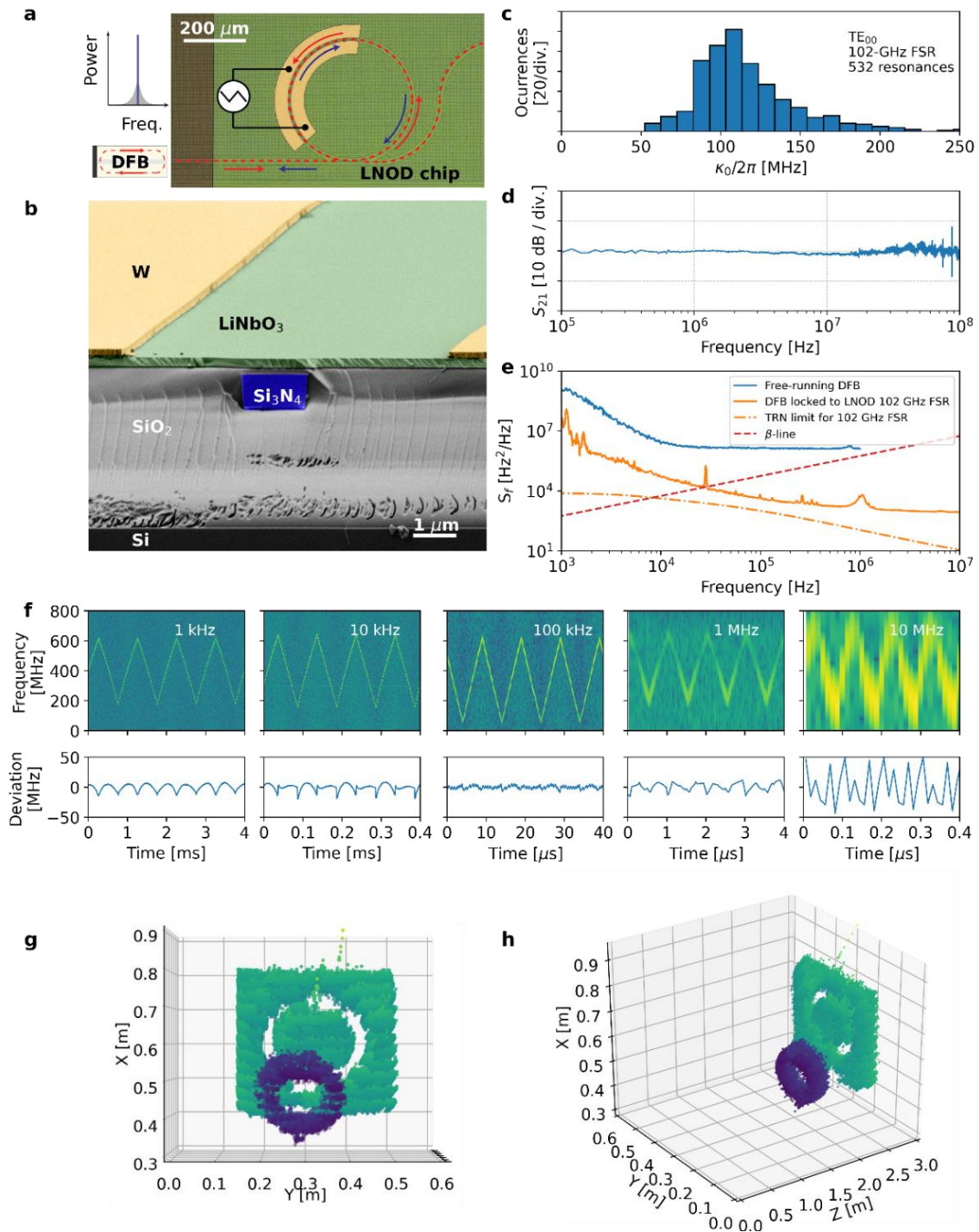


Fig. 1. (a) Schematic of the integrated tunable laser source. A DFB laser diode is self-injection locked to a high-Q optical mode of a LNOD microring resonator via butt-coupling. Rayleigh scattering from inhomogeneities in the microring provide the feedback to the DFB. The laser frequency is modulated by applying a voltage from an arbitrary waveform generator to integrated tungsten electrodes. (b) False-colored scanning electron microscope image of a LNOD waveguide cross-section. (c) Histogram indicating intrinsic decay rate distribution of 532 resonances of a LNOD microring with a free spectral range (FSR) of 102 GHz. The median of the distribution is 100 MHz, which corresponds to a quality-factor of 2×10^6 . (d) Frequency-dependent electro-optic modulation efficiency of the optical microresonator. (e) Laser frequency noise spectra of the free-running DFB laser (blue line), of the DFB locked to a LNOD microring with 102-GHz FSR (solid orange line), its simulated thermorefractive noise limit (dash-dotted line), and β -line (dashed red line) [15]. (f) (Top row) Time-frequency analysis of triangular laser frequency chirps measured via the heterodyne beatnote between the tunable laser and a CW reference laser. (Bottom row) Deviation of measured laser frequency from ideal triangular chirp. (g-h) Point clouds representing a scene composed of a polystyrene donut-like shape and a plastic plane behind, obtained in FMCW LiDAR experiments with the tunable laser source.

As proof-of-principle demonstration, we perform FMCW LiDAR measurements in laboratory environment. For scene elements, we selected a donut-like polystyrene shape and a plastic instrument box. The collected data, after processing, is presented as the point clouds in Fig. 1(g, h). The evaluated resolution of these experiments is 15 cm.

DISCUSSION

By increasing the quality factor of fabricated LNOD microresonators and the amount of back-reflection, it should be possible to increase the locking bandwidth and decrease the linewidth. Thus, a finer resolution in FMCW ranging experiments would be expected. The reflection could be increased, for instance, by introducing tapers on the lithium niobate layer to enable adiabatic transition of the mode of Damascene silicon nitride integrated waveguide into the one of a LNOD integrated waveguide. This would improve the coupling efficiency of light coming back to the laser. The tuning efficiency could also be improved by optimizing the hybrid LNOD waveguide geometry to achieve a higher confinement factor in the lithium niobate layer. Beyond FMCW LiDAR, the tunable laser source demonstrated here could be utilized for optical coherence tomography [13] and trace gas sensing [14].

Acknowledgements

The samples were fabricated at the EPFL Center of MicroNanoTechnology (CMi) and the Binnig and Rohrer Nanotechnology Center (BRNC) at IBM Research. We thank the cleanroom operations team of the BRNC, especially Diana Davila Pineda and Ronald Grundbacher, for their help and support. This work was supported by contract HR0011-20-2-0046 (NOVEL) from the Defense Advanced Research Projects Agency (DARPA), Microsystems Technology Office (MTO), by funding from the European Union Horizon 2020 Research and Innovation Program under the Marie Skłodowska-Curie grant agreements No. 722923 (OMT) and No. 812818 (MICROCOMB) and under the FET-Proactive grant agreement No. 732894 (HOT), and by funding from the Swiss National Science Foundation under grant agreements No. 176563 (BRIDGE) and No. 186364 (QuantEOM).

References

- [1] C. Wang et al., *Nature*, **562**, 7725 (2018)
- [2] M. Heet al., *Nature Photonics*, **13**, 5 (2019)
- [3] M. Zhang et al., *Nature*, **568**, 7752 (2019)
- [4] Y. Xu et al., *Nature Communications*, **12**, 4453 (2021)
- [5] C. Op de Beeck et al., *Optica*, **8**, 10 (2021)
- [6] W. Jin et al., *Nature Photonics*, **15**, 346 (2021)
- [7] M. Soltani et al., *Opt. Lett.* **41**, 4375 (2016)
- [8] G. Lihachev et al., arXiv: 2104.02990 (2021)
- [9] M. Churaev et al., arXiv: 2112.02018 (2021)
- [10] J. Liu et al., *Nature Communications*, **12**, 2236 (2021)
- [11] N. M. Kondratiev et al., *Optics Express*, **25**, 23 (2017)
- [12] D. Uttam et al., *Journal of Lightwave Technology*, **3**, 5 (1985)
- [13] X. Li et al., *APL Photonics*, **4**, 090803 (2019)
- [14] G.-W. Truong et al., *Nature Photonics*, **7**, 532 (2013)
- [15] G. D. Domenico et al., *Appl. Opt.*, **49**, 4801 (2010)

A Monolithically Integrated Tunable Comb Source and Filter

(Student paper)

John McCarthy^{1,2}, Maryam Shayesteh³, Mohamad Dernaika⁴, Jack Mulcahy^{1,2} and Frank Peters^{1,2,4}

¹Tyndall National Institute, Lee Maltings, Cork, Ireland

²Physics Department, University College Cork, College Road, Cork, Ireland

³University of Southampton, Southampton, Hampshire, UK

⁴Rockley Photonics Ireland, Lee Mills House, Lee Maltings, Cork, Ireland

* john.mccarthy@tyndall.ie

A tunable comb source and filter is demonstrated on a monolithically integrated Photonic Integrated Circuit (PIC). The tunable comb source is created by gain switching a slave Fabry-Pérot laser that is injection locked to a master slotted Fabry-Pérot laser. The master section of the PIC produces a single mode spectra with a tunable range of 1557nm – 1573nm. A ring laser is also integrated with the on-chip device to filter the individual comb lines and is tuned using current injection.

Keywords: Frequency comb, gain switching, de-multiplexing

INTRODUCTION

Optical frequency comb sources (OFCS) show significant promise in many modern day applications such as spectroscopy [1], spaced based instruments [2] and high speed telecommunications [3]. OFCS generate equally spaced spectral carriers with a known phase relation between adjacent carriers. Due to their precise and stable frequency and relative phases, they can be used in wavelength division multiplexing (WDM) communications to create coherent optical superchannels, where guardbands between neighbouring WDM signals are no longer required [4]. One method of generating a frequency comb in a PIC (which is the method described in this paper) is by injection locking a slave laser to a single mode master laser and gain switching the slave laser by applying a high power radio frequency (RF) signal.

A comb based coherent superchannel would require the optical source to be integrated with a de-multiplexer, which would filter out individual lines into separate waveguides with separate modulators before being recombined and transmitted. Monolithically integrated comb sources with frequency spacing of 4 - 9 GHz have been demonstrated with InP devices [5]. However, typical methods of de-multiplexing these narrow lines on a PIC have not been feasible [6], due to the difficulty of de-multiplexing the comb while retaining relative coherence between the optical carriers.

In this paper we focus on an injection locked ring laser as a tunable filter element that can be used as part as a full de-multiplexer, which is monolithically integrated with a tunable comb source. The comb source itself is demonstrated by injection locking a single mode master laser into a gain switched slave laser. Injection locking using an external master laser has been demonstrated to reduce phase noise and linewidth in gain switched lasers [7]. These two lasers are monolithically integrated in a strongly coupled master/slave configuration [5], whereby the slave laser is optically phase locked to the master laser. The single mode characteristics of the slave laser have been known to improve by on-chip optical phase locking, particularly with increasing the side mode suppression ratio (SMSR) of the slave [8]. The master laser is more heavily biased than the slave and so the two lasers are operating in an asymmetric bias regime. So while no isolator exists between the two lasers, the asymmetry of the operation has been shown to allow for injection locking [9]. The slave laser is then gain switched using a high power RF signal generator to generate the optical combs. The generated comb is injected into a monolithically integrated ring laser which acts as an integrated laser filter (ILF). Using current injection, this ILF filters out a single comb line. The output of the device is analysed by an ANDO AQ6317B optical spectrum analyser (OSA), which has a resolution of 0.02 nm, and so the comb lines and their spacings can be observed.

DEVICE DESIGN

The device was fabricated with commercially available material designed for the emission at 1550 nm, purchased from IQE. This lasing material consists of 5 compressively strained 6 nm wide AlGaInAs quantum wells on an n-doped InP substrate. The upper p-doped cladding consists of a 0.2 μm InGaAs cap layer, which is followed by 0.05 μm of InGaAsP, lattice matched to 1.62 μm of InP. The ridge and slot features are defined using standard lithographic techniques, with a ridge width of 2.5 μm and a height of 1.7 μm , and a slot width of 1 μm , with the ridge etch stopping above the quantum wells. The slots were used as both optical reflection as well as electrical

isolation between different sections of the PIC. A ground-signal-ground (GSG) contact was added to the slave section to allow for the gain switching of the device.

The master section of the device is made up of the gain section, 600 μm in length, and mirror section. The mirror section is made up of 8 slots etched into the ridge with an interslot separation of 108 μm . These slots act as reflective defects along the ridge by creating regions of lower effective refractive index, effectively creating a master section that is both single mode and tunable [5], [10]. This master laser is integrated with a 2x2 multimode interferometer (MMI) which splits light equally into both slave lasers. At this point, either slave laser could be used to generate the comb. The upper slave is injection locked to the master and is gain switched, generating a comb while the lower slave is unused. This comb is reflected back into the 2x2 MMI and is split equally into the master laser and into the lower waveguide coupling with the ring laser. The ring laser is used to filter a single line from the comb by injecting the comb into the ring [11]. The individual comb lines are filtered using current injection and are detected through Port D. The addition of multiple ring laser filters would facilitate the full de-multiplexing of the comb.

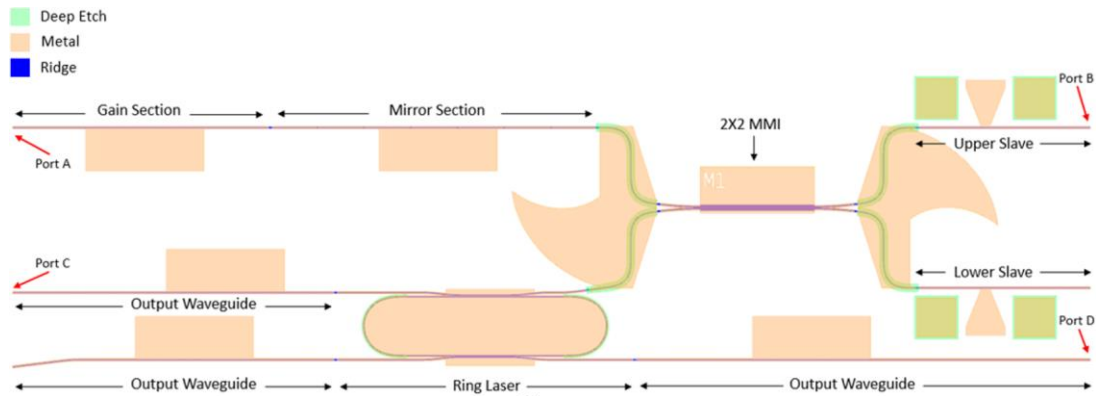


Fig. 1. Schematic of the PIC design.

RESULTS

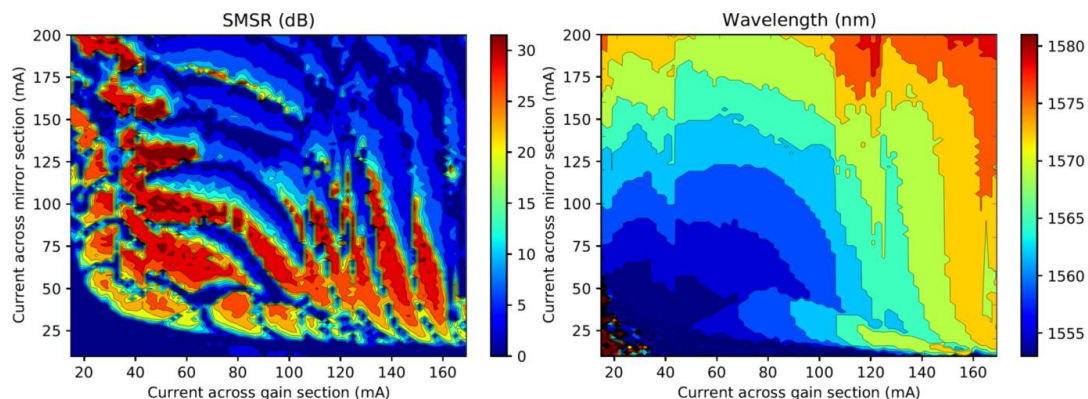


Fig. 2. (left) SMSR and (right) lasing wavelength of the Master Laser.

The master laser was initially characterised by biasing the gain and mirror sections of the device independently, sweeping the current through both sections and measuring the spectra through Port A at each interval. The SMSR and lasing wavelength were recorded and plotted as shown in Fig. 2.

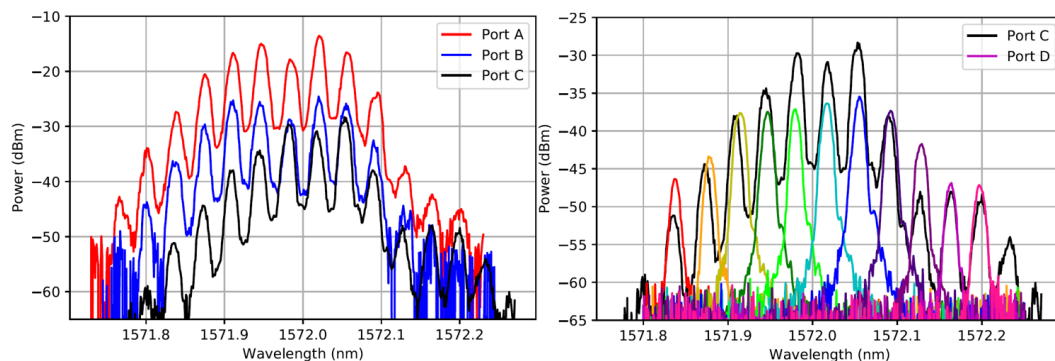


Fig. 3. (left) Generated comb detected through Port A, B and C and (right) the individual comb lines detected through Port D.

When the single mode nature of the master laser was determined, the MMI section was biased at 180 mA, the upper slave laser was biased just above threshold current and the spectra of slave laser was optically phase locked to that of the master. A strong RF signal was applied to the slave section to allow for gain switching to occur and a comb to be generated. Due to the design of the PIC, the generated comb was detected through Port A, B and C as shown in Fig. 3 (left).

Once this was achieved, the ring was biased and the resulting spectra was detected through Port D. By varying the current through the ring laser, different peaks were attained, and plotting these against the comb detected through Port C (Fig. 3.) it is clear that these peaks are a result of the different comb lines being filtered by the ring laser. The colour plot in Fig. 4 illustrates the growth and suppression of the individual comb lines as the current across the ring laser is varied.

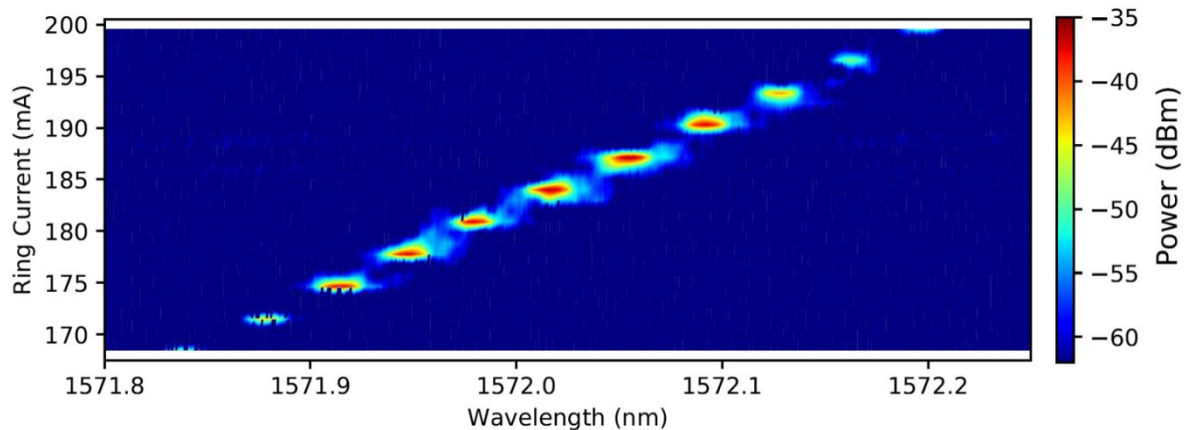


Fig. 4. Colour plot depicting the power of the spectra detected through Port D as the current through the ring laser changes.

CONCLUSION

This PIC demonstrates how a coherent optical comb can be created and de-multiplexed. An optical frequency comb was obtained from the PIC by gain switching a slave laser that has been injection locked with a single mode master laser. Due to the reflective defects caused by the slots used in the mirror of the master, the master laser was shown to have a tunable wavelength. The integrated ring laser allowed for the injection locking of the individual comb lines and therefore the selective or tunable filtering of the comb.

ACKNOWLEDGMENTS

This work was supported by Science Foundation Ireland under grants 12/RC/2276 (IPIC), and SFI/13/IA/1960.

References

- [1] I. Coddington, W. Swann, and N. Newbury, "Coherent multiheterodyne spectroscopy using stabilized optical frequency combs," *Phys. Rev. Lett.* 100(1), 013902 (2008).
- [2] X. Wang, S. Takahashi, K. Takamasu, and H. Matsumoto, "Space position measurement using long-path heterodyne interferometer with optical frequency comb," *Opt. Express* 20(3), 2725-2732 (2012).
- [3] A. Ellis and F. Gunning, "Spectral density enhancement using coherent WDM," *IEEE Photon. Technol. Lett.* 17(2), 504-506 (2005).
- [4] R. Zhou, P. M. Anandarajah, D. G. Pascual, J. O'Carroll, R. Phelan, B. Kelly, and L. P. Barry, "Monolithically integrated 2-section lasers for injection locked gain switched comb generation," *Optical Fiber Communications Conference and Exhibition* (2014).
- [5] J. K. Alexander, P. E. Morrissey, H. Yang, P.J. Marraccini, B. Corbett, and F. H. Peters, "Monolithically integrated low linewidth comb source using gain switched slotted fabry-perot lasers," *Opt. Express* 24, 7960-7965 (2016).
- [6] W. Cotter, P. E. Morrissey, H. Yang, J. O'Callaghan, B. Roycroft, B. Corbett, and F. H. Peters, "Integrated demultiplexing and amplification of coherent optical combs," *Opt Express* 27, 16012-16023 (2019).
- [7] L. Barry, P. Anandarajah, and A. Kaszubowska, "Optical pulse generation at frequencies up to 0 GHz using external-injection seeding of a gain switched commercial fabry-perot laser," *IEEE Photonics Technol. Lett.* 13, 1014-1016 (2001).
- [8] A. Tauke-Pedretti, G. A. Vawter, E. J. Skogen, G. Peake, M. Overberg, C. Alford, W. W. Chow, Z. S. Yang, D. Torres, and F. Cajas, "Mutual injection locking of monolithically integrated coupled-cavity DBR lasers," *IEEE Photonics Technol. Lett.* 23, 908-910 (2011).
- [9] A. H. Perrott, L. Caro, M. Dernaika, and F.H. Peters, "A comparison between off and on-chip injection locking in a photonic integrated circuit," *Photonics* 6 (2019).
- [10] Q. Y. Lu, W. H. Guo, R. Phelan, D. Byrne, J. F. Donegan, P. Lambkin, and B. Corbett, "Analysis of slot characteristics in slotted single-mode semiconductor lasers using the 2-D scattering matrix method," *IEEE Photonics Technol. Lett.* 18, 2605-2607 (2006).
- [11] K. Shortiss, M. Shayesteh, W. Cotter, A. H. Perrott, M. Dernaika, and F. H. Peters, "Mode suppression in injection locked multi-mode and single-mode lasers for optical demultiplexing," *Photonics* 6 (2019).

Silicon photonic mode demultiplexer enabled by on-chip beamforming

David González-Andrade^{1,*}, Xavier Le Roux¹, Thi Thuy Duong Dinh¹, Dorian Oser^{1,2}, Diego Pérez-Galacho³, Eric Cassan¹, Delphine Marris-Morini¹, Laurent Vivien¹ and Carlos Alonso-Ramos¹

¹Centre de Nanosciences et de Nanotechnologies, CNRS, Université Paris-Saclay, 10 Bd. Thomas Gobert, Palaiseau, 91120, France

²QuTech and Kavli Institute of Nanoscience, Delft University of Technology, Delft, 2600 GA, The Netherland

³ITEAM Research Institute, Universitat Politècnica de València, Camino de Vera s/n, Valencia, 46022, Spain

* david.gonzalez-andrade@c2n.upsaclay.fr

Mode-division multiplexing has a great potential to increase the bandwidth and data rates of emerging communication systems. Here, we propose a novel silicon photonic mode multiplexer exploiting on-chip free-space-like propagating optical beams to achieve TE₀ and TE₁ mode demultiplexing with a 1 dB bandwidth of 100 nm and crosstalk lower than -42 dB in a 200 nm bandwidth for both fundamental and first-order modes.

Keywords: silicon photonics, silicon-on-insulator, mode-division multiplexing, leaky mode, slab waveguide

INTRODUCTION

Silicon photonic devices are becoming a cornerstone of modern communication systems. The possibility to integrate multiple components on a single chip allows a significant reduction in the size, energy consumption and cost of optical modules and interconnects [1]. Among the different material platforms, silicon-on-insulator provides a high refractive index contrast and compatibility with complementary metal-oxide-semiconductor (CMOS) processes, resulting in cost-effective mass production [2]. Optical interconnects based on SOI have attracted much attention as a solution to address the ever-increasing demand for broader bandwidth and higher data rates of new services. Different advanced multiplexing technologies have been employed to scale the transmission capacity, such as wavelength-, polarization- and time-division multiplexing [3-5]. Recently, mode-division multiplexing (MDM) has been proposed to further increase aggregate bandwidth and data rates by transmitting information encoded in different spatial modes at the same wavelength and polarization [6].

The mode multiplexer/demultiplexer (MUX/DEMUX) is the fundamental device at the core of any MDM system. Its main function is to convert fundamental modes into higher-order modes and combine them into a single multimode waveguide (MUX operation), or vice versa (DEMUX operation). Several SOI device configurations have been reported for MDM, including asymmetric Y-junctions [7], tapered or adiabatic couplers [8], asymmetric directional couplers [9], ring resonators [10], multimode interference (MMI) couplers [11] and topology-optimized devices [12]. However, in all these photonic devices light is guided within a spatially bounded structure, restricting both the region and the field distribution with which light propagates (i.e., propagation of light wave is limited to a set of modes confined to a waveguide). Radiation of electromagnetic fields within a chip offers interesting opportunities to overcome the stringent design rules and limited on-chip reconfigurability of fixed layout-guided interconnects, opening new venues for on-chip wireless optical communications [13,14]. Contrary to diffractive gratings, of which a considerable number have been demonstrated for out-of-plane light coupling [15], only a few works have addressed radiation from a channel waveguide into an adjacent slab [14,16]. Still, these devices are intended for wavelength-division multiplexing as they rely on frequency-scanning focus of the beam within the slab.

In this work, we expand on this concept and propose a silicon photonic mode demultiplexer based on in-slab beam forming. Optical tunneling effect is exploited in order to couple the fundamental and first-order transverse-electric (TE) modes from a waveguide to an adjacent slab. The slab acts as a free-space-like propagation region where the different beams are vertically confined and focused on a specific position. Our simulation results show coupling efficiencies of 97%, and 83%, as well as 1 dB bandwidths of 124 nm and 107 nm, for TE₀ and TE₁ mode demultiplexing, respectively.

RESULTS

Figure 1 illustrates the geometry and operation principle of the proposed device, which comprises a tapered waveguide that is placed in close proximity to a slab. The light propagates through the input multimode waveguide (width W_1) in the form of fundamental and first-order TE modes. As the light propagates along the taper (length L_T), it progressively couples to the adjacent slab via optical tunneling effect [14]. The angle at which the vertically confined beam propagates within the slab, defined with respect to the y axis, is given by:

$$\theta = \sin^{-1} \left(\frac{n_{eff,W}^i}{n_{eff,S}} \right), \quad (1)$$

where $n_{eff,W}^i$ is the effective index of the i -th order mode in the waveguide and $n_{eff,S}$ is the effective index of the slab. The separation between waveguide and slab allows to tailor the leakage rate and thus the field profile of the in-slab beam. The DEMUX is designed for SOI with 220-nm-thick silicon, a 3- μ m-thick buried oxide (BOX) layer and a 2- μ m-thick polymethyl methacrylate (PMMA) upper cladding. The input waveguide has a width of $W_I = 710$ nm to support both fundamental and first-order TE modes within the design wavelength range, i.e., 1450 – 1650 nm. The separation between input waveguide and slab varies from $G_I = 340$ nm to $G_E = 40$ nm to achieve a near-Gaussian field profile. Finally, the width of the input waveguide is reduced from $W_I = 710$ nm to $W_E = 250$ nm along the 20 μ m long taper to ensure that all the optical power is radiated from the input waveguide into the slab.

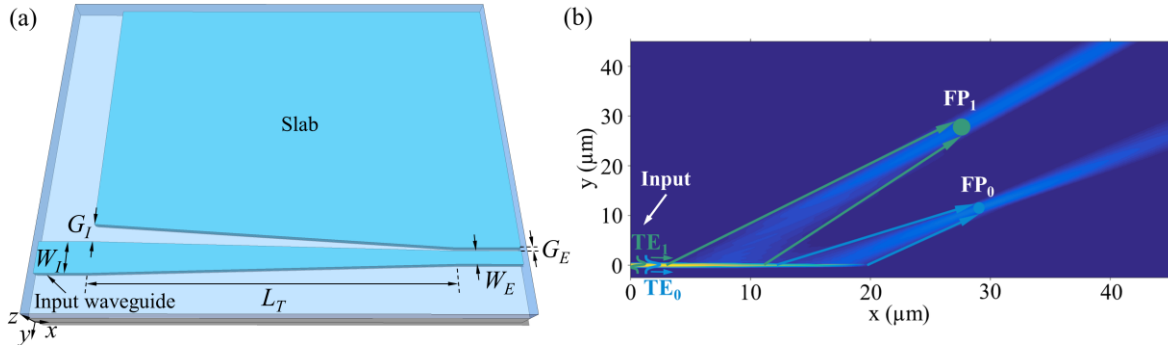


Fig. 1. (a) Schematic representation of the free-space mode multiplexer and its geometrical design parameters. (b) Illustration of the operation principle working as demultiplexer: electric field magnitude (normalized to the maximum) in the XY plane in the middle of the Si layer at 1550 nm. The fundamental and first-order transverse-electric modes that propagate through the input waveguide are coupled into the slab producing two in-slab beams that are focused on different points (i.e., FP_0 and FP_1).

The mode DEMUX was simulated with a three-dimensional finite-difference time-domain (3D FDTD) solver. Figure 1b shows an illustration of the electric field magnitude in the middle of the silicon layer at the center wavelength (i.e., $\lambda_0 = 1550$ nm). It is observed that the TE_1 mode is radiated along the first half of the taper, while the TE_0 mode is radiated towards the end. In this case, the lower modal confinement of TE_1 compared to TE_0 results in a greater evanescent interaction with the slab and, therefore, in a stronger radiation strength at the beginning of the taper. When TE_0 is injected through the input waveguide, the in-slab beam focus on point FP_0 with an angle of 48° . Conversely, when TE_1 is injected, the beam focus on FP_1 with an angle of 36° .

The figure of merit used to evaluate the performance of the device is the coupling efficiency (CE), which is defined similarly to the coupling efficiency employed in fiber-chip grating couplers: $CE = (1 - \rho_R) \cdot \eta_U \cdot \eta_{OL}$, where ρ_R is the reflection coefficient, η_U is the ratio between the power injected in the input waveguide and the power radiated into the slab, and η_{OL} is the overlap integral between the radiated field and a Gaussian-like mode field. For TE_0 mode demultiplexing, a high overlap of 98.7% is achieved between the radiated field and a Gaussian field with $\sigma = 4.7$ μ m at FP_0 . On the other hand, for TE_1 mode demultiplexing, the overlap is 92.7% between the radiated field and a Gaussian field with $\sigma = 5.9$ μ m at FP_1 .

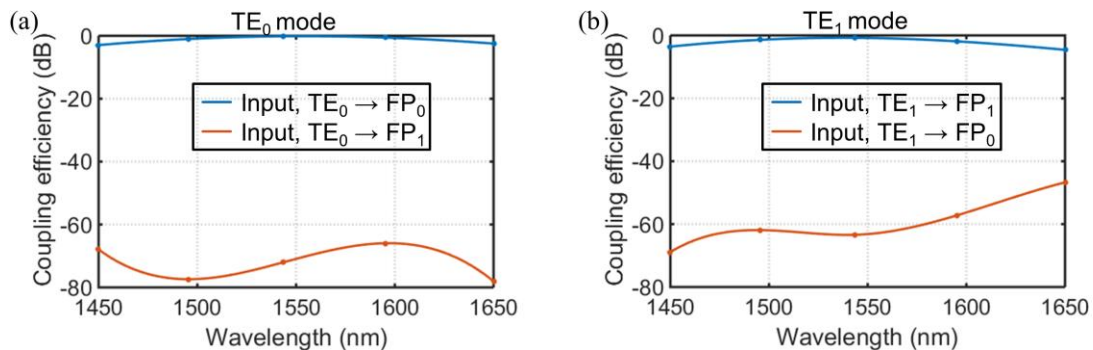


Fig. 2. Calculated coupling efficiency as a function of the wavelength for the mode demultiplexer when (a) TE_0 and (b) TE_1 modes are injected through the input waveguide. Blue curves correspond to the coupling efficiency at desired positions, while orange curves correspond to the coupling efficiency at undesired positions.

The performance of our proposed device is shown in Fig. 2. Blue curves indicate the CE at desired positions, i.e., calculated at FP_0 and FP_1 for TE_0 and TE_1 mode demultiplexing, respectively. In this case, the mode DEMUX yields efficiencies of 97.1% (-0.13 dB) and 82.8% (-0.82 dB) at 1550 nm when TE_0 and TE_1 modes are injected through the input waveguide, respectively. Notably, the device exhibits broad 1 dB bandwidths of 124 nm for TE_0 and 107 nm for TE_1 . Orange curves, on the contrary, indicate the CE at undesired positions. The CE at FP_1 is as low as -66 dB when the TE_0 mode is injected through the input waveguide and below -47 dB at FP_0 when the TE_1 mode is injected, both within the entire simulated wavelength range. The crosstalk is, therefore, below -42 dB for both modes in the entire 200 nm simulated bandwidth.

DISCUSSION

In this work, we propose a novel two-mode multiplexer that leverages optical tunneling between a tapered waveguide and an adjacent slab. The device was designed for the silicon-on-insulator platform considering a standard silicon thickness of 220 nm and a PMMA cladding. First-order and fundamental TE modes injected through the input waveguide are radiated sequentially from the taper into the slab due to their different evanescent field interaction. Full 3D FDTD simulations show efficiencies of 97.1%, and 82.8% for TE_0 and TE_1 mode demultiplexing, respectively, at 1550 nm. In addition, a remarkable 1 dB bandwidth of 124 nm is achieved for TE_0 , while the 1 dB bandwidth for TE_1 is 107 nm. The proposed device also exhibits a high isolation between the beams in the slab, with values lower than -47 dB for both modes within the 1450 – 1650 nm wavelength range. We believe that these results open promising prospects for emerging applications such as on-chip wireless optical communications.

Acknowledgements: This work has been partially funded by the French Industry Ministry (Nano2022 project under IPCEI program); and the Agence Nationale de la Recherche (ANR-MIRSPEC-17-CE09-0041). The fabrication of the device was performed at the Plateforme de Micro-Nano-Technologie/C2N, which is partially funded by the Conseil General de l'Essonne. This work was partly supported by the French RENATECH network.

References

- [1] L. Vivien, L. Pavesi, *Handbook of silicon photonics*, Taylor & Francis, 2016.
- [2] D. Thomson, A. Zilkie, J. E. Bowers, T. Komljenovic, G. T. Reed, L. Vivien, D. Marris-Morini, E. Cassan, L. Virost, J.-M. Fédéli, J.-M. Hartmann, J. H. Schmid, D.-X. Xu, F. Boeuf, P. O'Brien, G. Z. Mashanovich, M. Nedeljkovic, *Roadmap on silicon photonics*, *J. Opt.*, vol. 18, no. 7, pp. 073003, 2026.
- [3] Z. Liu, J. Zhang, X. Li, L. Wang, J. Li, C. Xue, J. An, B. Cheng, *25 × 50 Gbps wavelength division multiplexing silicon photonics receiver chip based on a silicon nanowire-arrayed waveguide grating*, *Photon. Res.*, vol. 7, no. 6, pp. 659-663, 2019.
- [4] C. R. Doerr, P. J. Winzer, Y.-K. Chen, S. Chandrasekhar, M. S. Rasras, L. Chen, T.-Y. Liow, K.-W. Ang, G.-Q. Lo, *Monolithic polarization and phase diversity coherent receiver in silicon*, *J. Lightwave Technol.*, vol. 28, no. 4, pp. 520-525, 2009.
- [5] Y. Ding, H. Hu, M. Galili, J. Xu, L. Liu, M. Pu, H. C. H. Mulvad, L. K. Oxenløwe, C. Peucheret, P. Jeppesen, X. Zhang, D. Huang, H. Ou, *Generation of a 640 Gbit/s NRZ OTDM signal using a silicon microring resonator*, *Opt. Express*, vol. 19, no. 7, pp. 6471-6477, 2011.
- [6] C. Li, D. Liu, D. Dai, *Multimode silicon photonics*, *Nanophotonics*, vol. 8, no. 2, pp. 227-247, 2019.
- [7] W. Chen, P. Wang, T. Yang, G. Wang, T. Dai, Y. Zhang, L. Zhou, X. Jiang, and J. Yang, *Silicon three-mode (de)multiplexer based on cascaded asymmetric Y junctions*, *Opt. Lett.*, vol. 41, no. 12, pp. 2851-2854, 2016.
- [8] D. Guo, T. Chu, *Silicon mode (de) multiplexers with parameters optimized using shortcuts to adiabaticity*, *Opt. Express*, vol. 25, no. 8, pp. 9160-9170, 2017.
- [9] J. Wang, P. Chen, S. Chen, Y. Shi, D. Dai, *Improved 8-channel silicon mode demultiplexer with grating polarizers*, *Opt. Express*, vol. 22, no. 11, pp. 12799-12807, 2014.
- [10] B. A. Dorin, N. Y. Winnie, *Two-mode division multiplexing in a silicon-on-insulator ring resonator*, *Opt. Express*, vol. 24, no. 4, pp. 4547-4558, 2014.
- [11] D. González-Andrade, J. G. Wangüemert-Pérez, A. V. Velasco, A. Ortega-Moñux, A. Herrero-Bermello, I. Molina-Fernández, R. Halir, P. Cheben, *Ultra-broadband mode converter and multiplexer based on sub-wavelength structures*, vol. 10, no. 2, pp. 2201010, 2018.
- [12] L. F. Frellsen, Y. Ding, O. Sigmund, L. H. Frandsen, *Topology optimized mode multiplexing in silicon-on-insulator photonic wire waveguides*, *Opt. Express*, vol. 24, no. 15, pp. 16866-16873, 2016.
- [13] C. García-Meca, S. Lechago, A. Brimont, A. Griol, S. Mas, L. Sánchez, L. Bellieres, N. S. Losilla, J. Martí, *On-chip Wireless silicon photonics: from reconfigurable interconnects to lab-on-chip devices*, *Light Sci. Appl.*, vol. 6, no. 9, pp. e17053, 2017.
- [14] D. Headland, W. Withayachumnankul, M. Fujita, T. Nagatsuma, *Gratingless integrated tunneling multiplexer for terahertz waves*, *Optica*, vol. 8, no. 5, pp. 621-629, 2021.
- [15] D. González-Andrade, D. Pérez-Galacho, M. Montesinos-Ballester, X. Le Roux, E. Cassan, D. Marris-Morini, P. Cheben, N. Vulliet, S. Monfray, F. Boeuf, L. Vivien, A. V. Velasco, C. Alonso-Ramos, *Dual-band fiber-chip grating coupler in a 300 nm silicon-on-insulator platform and 193 nm deep-UV lithography*, *Opt. Lett.*, vol. 46, no. 3, pp. 617-620, 2021.
- [16] A. Hadij-Elhouati, A. Ortega-Moñux, J. G. Wangüemert-Pérez, R. Halir, S. Wang, J. H. Schmid, P. Cheben, Í. Molina-Fernández, *Low-loss off-axis curved waveguide grating demultiplexer*, *Opt. Lett.*, vol. 46, no. 19, pp. 4821-4824, 2021.

Plasmonic slot ferroelectric MZIR modulator on Si₃N₄ in the O-band

(Student paper)

Dimitrios Chatzitheocharis^{1,2}, Dimitra Ketzaki^{2,3}, Georgios Patsamanis^{1,2}, and Konstantinos Vyrsoinos^{1,2}

¹School of Physics, Aristotle University of Thessaloniki, A.U.Th. Campus, Thessaloniki, 54124, Greece

²Center for Interdisciplinary Research and Innovation, Aristotle University of Thessaloniki, Thessaloniki, 57001, Greece

³Department of Informatics, Aristotle University of Thessaloniki, A.U.Th. Campus, Thessaloniki, 54124, Greece

*email: dchatzit@auth.gr

Herein, we present the performance analysis of a ferroelectric plasmonic Mach-Zehnder in a Ring (MZIR) modulator on Si₃N₄ for gold (Au), silver (Ag) and copper (Cu) based phase shifters targeting O-band interconnects. The Cu based MZIR featuring a 5μm long slot, exhibits Insertion Losses of 6.85dB, an Extinction Ratio of 9dB for a differential applied voltage of 2.74V_{pp} and a Comparison Factor of 0.7x vs. a symmetric MZI with equal phase shifter length.

Keywords: MZI-Ring Modulator, Silicon Nitride, Plasmonic Slot, Coupling Interface

INTRODUCTION

Silicon nitride (Si₃N₄), with its low propagation losses, low cost, and high compactness, has emerged as a very promising platform for photonic integrated circuits (PICs) over the last few years. One of the key components missing from the Si₃N₄ library though is a CMOS compatible modulator, eliminating in this way the main advantage currently possessed by SOI based PICs. Towards this direction many studies have focused on the co-integration of Si₃N₄ with ferroelectric materials and as such in [1] a hybrid lithium niobate (LiNbO₃) allowed operation with sub-volt half-wave voltage (V_{π}), a half-wave voltage-length product ($V_{\pi}L$) of 2.11 V*cm, and 5.4dB insertion losses (IL). In [2] a Si₃N₄ loaded LiNbO₃ modulator exhibited a $V_{\pi}L$ of 2.24 V*cm, and an extinction ratio (ER) up to 20dB. The evolution of PICs in terms of compactness has brought on surface the development of hybrid photonic-plasmonic PICs and in this direction miniaturized CMOS compatible modulators have been demonstrated [3], featuring though Si as the basic underlying material platform [4]. In this paper we numerically demonstrate a ferroelectric Mach-Zehnder in Ring (MZIR) modulator for the O-band in Si₃N₄ that requires as low as 0.44x voltage for maximum extinction ratio versus symmetric MZIs [5]. The performance analysis investigates two low loss noble metals well known in the plasmonics literature, Au [6], Ag [7] and CMOS compatible Cu [8] for the formation of the plasmonic waveguide. Simulation results reveal that Ag presents the best performance, followed by Au and then by Cu. The Cu based MZIR modulator exchanges performance for CMOS compatibility and for a 5μm phase shifter features insertion losses of 6.85dB with an extinction ratio of 9dB for 2.74V_{pp} applied voltage to the arms of the MZI.

NUMERICAL RESULTS

The proposed plasmonic slot ferroelectric MZIR configuration is shown in a 3D-schematic in Fig. 1(a). The basis of the integrated optical device is Si₃N₄ waveguide, supporting a fundamental TE-mode with an effective index close to $\text{Re}(n_{\text{eff}}) = 1.773$ and 0.2dB/cm propagation losses. The two 2x2 O-Band MMIs that form the MZI of the MZIR are assumed to induce 0.2dB/MMI according to 3D-FDTD simulations at $\lambda = 1310\text{nm}$. The MZIR cavity is formed by directly connecting one of the output MMI ports to the one input port of the input MMI. The loop length includes approximately 300μm from the two MMIs, 186μm from the two Si₃N₄ to plasmonic coupling interfaces and the variable length L_{slot} of the plasmonic phase shifter. Fig. 1(b) presents in detail the cross section of the phase shifter that is based on a plasmonic slot formed by two metals with the gap filled by barium titanate (BaTiO₃ or BTO) material. The metal for the plasmonic waveguide in this work is either Au, or Ag targeting low loss with a noble material or Cu for CMOS compatibility. To bridge the two platforms, an amorphous silicon intermediate waveguide vertically transfers light in a multi-layer fashion where, initially, an adiabatic coupler with a coupling length of 90μm transfers the TE-mode from the Si₃N₄ waveguide to a 350nm x 220nm aSi waveguide featuring a TE mode of $\text{Re}(n_{\text{eff}}) = 2.45034$. In the next step, a directional coupling step transfers the light from aSi to the plasmonic slot. The SiO₂ gaps between SiN and aSi and between aSi and BTO are 100nm.

The performance analysis of the three MZIRs layouts starts from the extraction of the propagation characteristics in the plasmonic slot waveguides for the three metals via 2D eigenvalue calculations. Fig. 2(a) shows that the effective index $\text{Re}(n_{\text{eff}})$ is similar for Cu, Au, and Ag for increasing slot widths w_{slot} with only small differences observed between the three. The plasmonic slots are almost phase-matched with the aSi waveguide mode for $w_{\text{slot}} = 90\text{nm}$ for Ag and for 100nm for Au/Cu, allowing in this way efficient directional vertical coupling between the

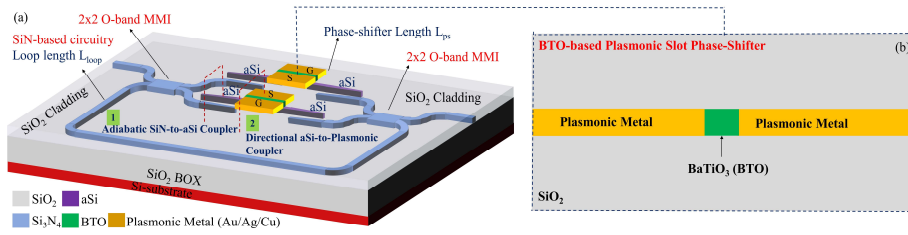


Fig. 1. 3D-schematic of the proposed ferroelectric plasmonic slot MZI-Ring configuration

two waveguides. Fig. 2(b) reveals the propagation losses of the three slot waveguides for widths between 25nm and 200nm. The Ag-based slot in symphony with theory and other experimental works [7] exhibits the lowest propagation losses of the three with $0.33\text{dB}/\mu\text{m}$ for $w_{\text{slot}} = 90\text{nm}$, while for Au with $w_{\text{slot}} = 100\text{nm}$ this value is slightly increased to $0.5\text{dB}/\mu\text{m}$. For Cu on the other hand the losses are now more than doubled versus Ag to $0.78\text{dB}/\mu\text{m}$, but now there is CMOS compatibility for low-cost mass scale fabrication. Fig. 2(c) illustrates that the power confinement is almost exclusively determined by the slot width with values ranging between 80% and 45%, while the metal type has almost negligible effect on the confinement factor of the electric field. For the calculation of the electro-optic characteristics of the plasmonic slot phase-shifters, Poisson's equation was solved in a 2D-FEM eigenvalue solver for applied voltage between 0V and 5V for slot widths of 90nm for Ag and 100nm for Au/Cu. The E-field components of the FEM solution were interpolated and fed to 2D-FDE optical eigenvalue simulations at 1310nm wavelength to extract the modified effective index for each voltage. Fig. 2(d) shows that the trend is almost linear as expected for all three metals. The Ag-based slot has the largest effective index difference vs. applied voltage due to a higher overlap between the RF and optical fields. From the relation $\Delta\phi = (2\pi/\lambda_0)\Delta\text{Re}(n_{\text{eff}})L$, the half-wave voltage product was calculated to $25.51\text{V}\cdot\mu\text{m}$ for Ag, $28.06\text{V}\cdot\mu\text{m}$ for Au, and $27.33\text{V}\cdot\mu\text{m}$ for Cu. The effective electro-optic coefficient for the BTO is assumed to be $300\text{pm}/\text{V}$.

In terms of coupling interfaces, the numerical simulations indicate that the adiabatic coupler transfers the light from the Si_3N_4 to the aSi efficiently with only 0.06dB losses. Fig. 2(e) showing the sideview of the electric field $|E|$ verifies this result with the very smooth transition between the two layers. For the next step a directional coupler has been designed for each metal, with the coupling length calculated by detailed 3D-FDTD simulations. For Ag the optimum value is $2.78\mu\text{m}$, for Au $2.71\mu\text{m}$ and for Cu $2.67\mu\text{m}$, with the close proximity expected from the almost identical $\text{Re}(n_{\text{eff}})$ values of Fig. 2(a). Fig. 2(f) shows the sideview of the electric field $|E|$ from aSi to the Cu-based slot, indicating efficient and seamless light transfer to the slot. Similar graphs are produced for the other two metals. The coupler exhibits coupling losses calculated at $x = 3\mu\text{m}$ from the initiation point of the slot waveguide in the x-axis ($x=0$) as 0.71dB for Ag, 0.86dB for Au and 1.23dB for Cu.

All the above simulation parameters were inserted in our in-house scattering-matrix based model for the DC-analysis of the MZIR modulator. A length difference $\Delta L = L_{\text{FSR}}/2 = \lambda_0/(2\text{Re}\{n_{\text{eff}}(\text{SiN})\})$ has been inserted between the two arms of the MZIR, so as to set the initial state of the MZIR at minimum insertion losses. The calculated relation providing the transmission spectrum at the output of the MZIR is the following:

$$\left| \frac{b_1}{a_1} \right|^2 = A_{\text{Lop}}^2 \frac{A_{\text{TOT}}^2 + \cos^2\left(\frac{\Delta\phi}{2}\right) - 2A_{\text{TOT}} \cos\left(\frac{\Delta\phi}{2}\right) \cos(\beta_0 L_{\text{OPT}})}{1 + A_{\text{TOT}}^2 \cos^2\left(\frac{\Delta\phi}{2}\right) - 2A_{\text{TOT}} \cos\left(\frac{\Delta\phi}{2}\right) \cos(\beta_0 L_{\text{OPT}})} \quad (1)$$

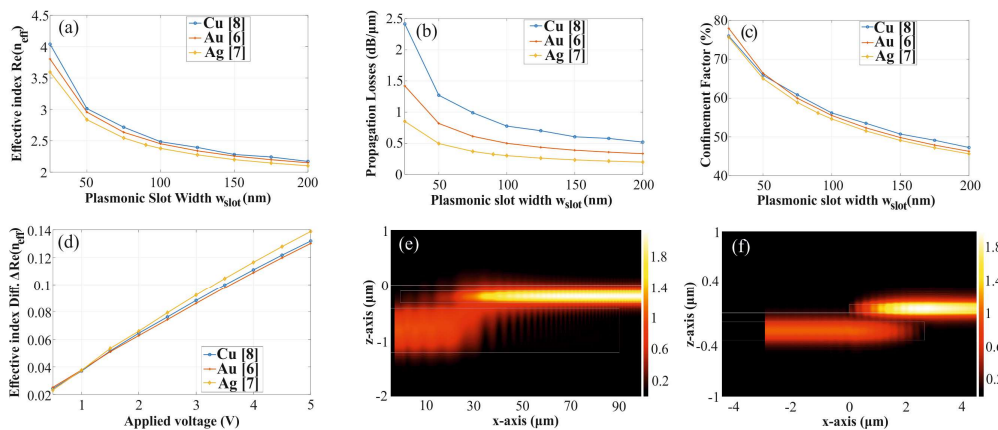


Fig. 2. (a) Effective index $\text{Re}(n_{\text{eff}})$, (b) Propagation Losses ($\text{dB}/\mu\text{m}$), and (c) Confinement factor (%) for increasing plasmonic slot width, (d) Effective index difference $\Delta\text{Re}(n_{\text{eff}})$ for increasing applied voltage V , (e) Sideview of $|E|$ field distribution for the transition from SiN to aSi, (f) Sideview of $|E|$ field distribution for the transition from aSi to Cu-based plasmonic slot

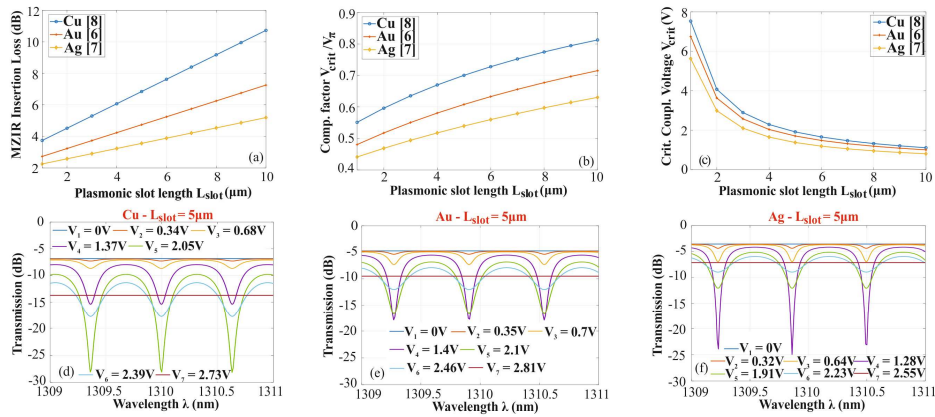


Fig. 3. (a) MZIR Insertion losses IL (dB), (b) Comparison factor $CF = V_{crit}/V_{\pi}$ and (c) Critical coupling voltage V_{crit} (V) for increasing plasmonic slot phase shifter length L_{slot} (μm), (d) Power transfer functions of the MZIR for Cu-based slot, (e) Au-based slot and (f) Ag-based slot with $5\mu\text{m}$ length for various applied voltages at the two arms

where A_{LOP} is the coefficient related with the efficiency coming from the transition through one MZI branch, A_{TOT} is the coefficient containing the coupling efficiency coming from the transition through the whole cavity, β_0 is the wavenumber $\beta_0 = 2\pi/\lambda_0$, L_{OPT} is the total optical path length of the whole MZIR cavity, and $\Delta\phi$ is the phase difference between the two MZI branches of the MZIR. The IL come directly out of the MZIR transfer function. The Comparison factor $CF = V_{crit}/V_{\pi}$ can be calculated at resonance as $CF = 2\cos^{-1}(A_{TOT})/\pi$, signifying the fraction of voltage needed for the maximization of the ER in an MZIR vs a symmetric MZI. The voltage for critical coupling in the MZIR modulator is $V_{crit} = V_{\pi}\cos^{-1}(A_{TOT})/\pi$. The results for the three plasmonic metals can be seen in Fig. 3(a)-(c). Fig. 3(a) indicates that the best in terms of performance is Ag providing IL values below 5dB for slot lengths between $1\mu\text{m}$ and $10\mu\text{m}$. For Au the IL lie between 2.7dB and 7.3dB, while Cu provides IL between 3.7dB and 11dB. Fig. 3(b) shows the performance improvement of the MZIR over a symmetric MZI. The Ag based MZIR requires 0.44x the voltage V_{π} needed to achieve maximum ER in the MZI for a $1\mu\text{m}$ long slot, while this value is 0.63x for slot lengths up to $10\mu\text{m}$. For Au these values are between 0.48x and 0.72x, while for Cu are between 0.55x and 0.81x. Finally, as seen in Fig. 3(c) V_{crit} becomes sub-volt for Ag for slot lengths higher than $7\mu\text{m}$, for Au higher than $9.5\mu\text{m}$ and close to 1.1V for a $10\mu\text{m}$ Cu based plasmonic phase shifter. Fig. 3(d)-(f) illustrate the transmission spectra for various voltages applied for Cu, Au, and Ag plasmonic slots with $5\mu\text{m}$ phase shifter length, respectively. For the Cu-based MZIR shown in Fig. 3(d) the IL are close to 6.85dB, with an ER of 9dB for an applied voltage of $2 \times 1.37\text{Vpp}$ and a CF of 0.7. The Au-based MZIR exhibits IL of 4.74dB, a 13.04dB ER for a $2 \times 1.4\text{Vpp}$ differential voltage and a CF of 0.61. Finally, the Ag-based MZIR has the best performance with 3.56dB IL only, an ER of 21.4dB for $2 \times 1.28\text{Vpp}$ differential voltage and a 0.54x required voltage for maximum ER in comparison with the symmetric MZI.

CONCLUSIONS

This paper presents the performance improvement of a plasmonic slot ferroelectric MZIR modulator design on the Si_3N_4 photonic vs. a symmetric plasmonic MZI, for Au, Ag and Cu as metals for the plasmonic phase shifter. The optimum CMOS compatible device is based on Cu, achieving IL of 6.85dB, ER as high as 9dB for 2.34Vpp differential applied voltage and a 0.7x required voltage for critical coupling compared with the V_{π} of a symmetrical MZI.

Acknowledgements: This work is supported by the European H2020 NEBULA (contract no. 871658) project.

References

- [1] A. N. R. Ahmed, et al., *Subvolt electro-optical modulator on thin-film lithium niobate and silicon nitride hybrid platform*, Optics letters, vol. 45, no. 5, pp. 1112-1115, 2020
- [2] P. Zhang, et al., *High-speed electro-optic modulator based on silicon nitride loaded lithium niobate on an insulator platform*, Optics letters, vol. 46, no. 23, pp. 5986-5989, 2021
- [3] V. E. Babicheva, et al., *A plasmonic modulator based on metal-insulator-metal waveguide with barium titanate core*, Photonics Letters of Poland, vol. 5, no. 2, pp.57-59, 2013
- [4] A. Messner, et al., *Plasmonic ferroelectric modulators*, Journal of Lightwave Technology, vol. 37, no. 2, pp.281-290, 2018
- [5] W. D. Sacher, et al., *Coupling modulation of microrings at rates beyond the linewidth limit*, Optics express, vol. 21, no. 8, pp. 9722-9733, 2013
- [6] W. M. Haynes, et. al., *CRC handbook of chemistry and physics*, CRC press, Boca Raton, 2016
- [7] P. B. Johnson et. al., *Optical constants of the noble metals*, Physical review B, vol. 6, no. 12, pp. 4370, 1972
- [8] J.-C. Weeber, et al., *Characterization of CMOS metal based dielectric loaded surface plasmon waveguides at telecom wavelengths*, Optics Express, vol. 25, no. 1, pp.394-408, 2017

Integrated Wavelength Filter on thin-film Lithium Niobate for a Photonic-enabled Radiometer

(Student paper)

Jessica César Cuello¹, Robinson C. Guzmán¹, Alberto Zarzuelo¹, Jeffrey Holzgrafe², Marko Lončar², Gabriel Santamaria³, Luis E. García¹ and Guillermo Carpintero¹

¹ University Carlos III of Madrid, Av. Universidad 30, Leganes, 28911, Spain

² Harvard University, 29 Oxford Street, Cambridge, 02138, USA

³ University of Colorado at Boulder, Boulder, CO 80309, USA

*jecesarc@ing.uc3m.es

This paper presents the first results in the development of a monolithically integrated photonic-based millimetre-wave radiometer for satellite payload weather monitoring sensor. Key photonic components to be integrated in a thin-film Lithium Niobate (LN) platform have been designed and fabricated. In this paper we present our results for an asymmetric Mach-Zehnder Interferometer (AMZI) for required optical wavelength filtering functionality. The AMZI Free Spectral Range (FSR), defined by a path length imbalance of 250 μm , is around 5 nm (625 GHz).

Keywords: Lithium Niobate, Asymmetric Mach-Zehnder Interferometer, Wavelength Filter

INTRODUCTION

Recent interest in the study of the Cosmic Microwave Background (CMB) and earth observation for weather monitoring has motivated the development of space missions capable of detecting signals at millimetre and sub-millimetre wavelengths [1][2]. However, the weak intensity of those signals (comparable to the thermal radiation generated by the receiver itself) makes it necessary to use very low-noise receivers. Conventional low-noise receivers require cryocooling, which increases the size, power consumption and cost of the receiver.

A novel photonic-based millimetre and sub-millimetre receiver architecture, capable of operating at room temperature, was recently presented [3][4]. In this photonic-based radiometer, the millimetre wave signal is upconverted into the optical domain modulating an optical wavelength in a low-loss nonlinear crystal [5][6] where detectors are less susceptible to thermal noise at room temperature.

Our goal is to develop such architecture into a Photonic Integrated Circuits (PIC), achieving size and weight reduction critical for the intended satellite payload application. In this paper, we present the design and characterization of a key component for this application, an integrated wavelength filter based on an asymmetric Mach-Zehnder interferometer (AMZI). Due to the need of nonlinear characteristics of the chip, this has been fabricated on a thin-film Lithium Niobate (LN) substrate, which unlocks high-Q resonators.

Thin-film LN-on-insulator has proven to be an integration technology that offers large Pockels electro-optic efficiency [7], low propagation loss and high Q-factor ring resonators [8]. The devices studied here are realized by direct etching by 325 nm into the 600 nm LN layer and cladding with 1.4 μm of silicon dioxide as describe in [7] and are characterized by a large index contrast and strong mode confinement. Losses of 2.7 ± 0.3 dB/m for straight waveguides and 9.3 ± 0.9 dB/m were demonstrated in [8].

RESULTS and DISCUSSION

We report the characterization of 4 different AMZIs designs, all with the same optical path length imbalance between the arms (250 μm), but different waveguide gap in the directional couplers (DC) of the AMZIs. The goal of this work is to determine the directional coupler parameters, and determine the fabrication specifications to achieve 50/50 splitting ratio. The different values for the DC gap that have been tested are 0.65 μm (AMZI 1), 0.55 μm (AMZI 2), 0.45 μm (AMZI 3) and 0.35 μm (AMZI 4). The structures under test are presented in Fig. 1(a), which has been characterized using the Component Analyzer feature of the High-Resolution Optical Spectrum Analyzer from Aragón Photonics. The light is injected and collected through edge coupled optical waveguides, using lensed fibers as shown Fig. 1(b).

The device characterization was performed injecting the Component Analyzer source into the top arm of the AMZI and collecting the light from the top (BAR port) and bottom (CROSS port) arms of the output directional coupler. Then, the input fiber is moved to the bottom arm of the input directional coupler and the light is again collected from the two corresponding output waveguides of the AMZI under test. The results from these measurements are shown in Fig. 2.

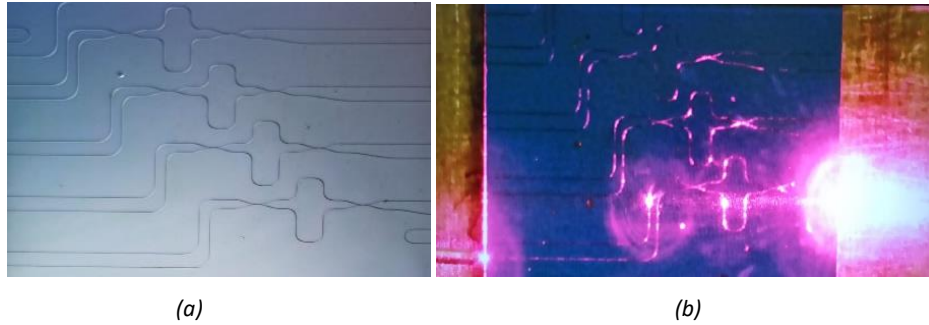


Fig. 1. Microscope image of (a) the 4 AMZIs structures (b) AMZI #4 during fiber-to-chip coupling.

Each graph in Fig. 2 contains the results for the four different AMZI (each with different spacing at the directional couplers). The wavelength axis has been normalized, representing the wavelength offset to the value where the absolute minimum in the optical response is achieved. The insertion loss measured at each facet, working with a lensed fiber of 2 μm spot diameter and 1.8 μm wide waveguides, was found to be around 5.5 dB.

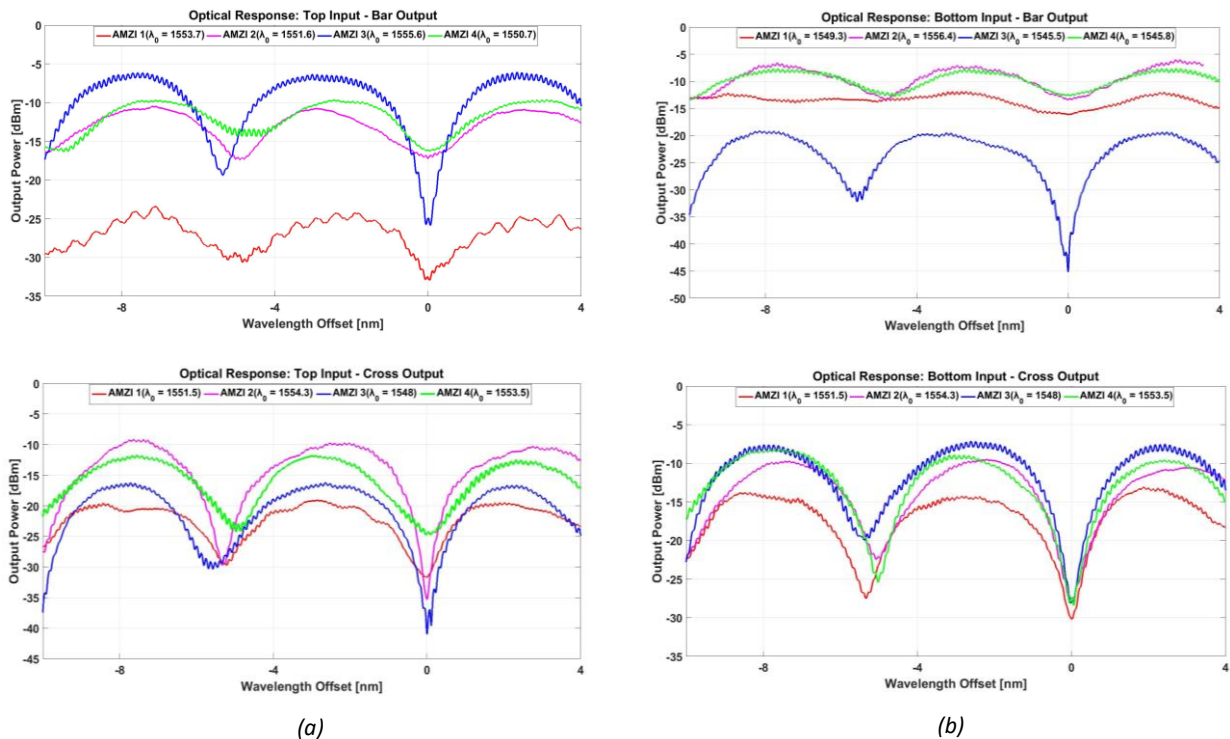


Fig. 2. Optical Spectrum of the response of each structure when (a) light is injected for the Top input waveguide of the DC, (b) light is injected for the Bottom input waveguide of the DC.

When light was injected to the top arm of the input directional couplers, the optical extinction ratio that we achieved at the bar output waveguide of the different samples was 8.5 dB for AMZI 1, 6.5 dB for AMZI 2, 19.5 dB for AMZI 3 and 6.5 dB for AMZI 4. This seems to point to AMZI 3 as being closer to the desired 50/50 splitting ratio. If we now turn to the cross output, the results that we obtain give an extinction ratio of 12.5 dB for AMZI 1, 25.3 dB for AMZI 2, 25 dB for AMZI 3 and 13 dB for AMZI 4 [Fig. 2(a)]. These results are in line with the conclusion from the bar measurements.

If we now turn to the bottom arm of the input directional couplers, the results for the corresponding outputs were: 4 dB for AMZI 1, 6.5 dB for AMZI 2, 25 dB for AMZI 3 and 5 dB for AMZI 4, while for the cross output the results were 17 dB for AMZI 1, 18 dB for AMZI 2, 20.6 dB for AMZI 3 and 19 dB for AMZI 4 [Fig. 2(b)].

The wavelength spacing between the maximum and the minimum transmittance is defined by the path length imbalance (ΔL) between the two arms of the AMZI as:

$$\Delta\lambda = \frac{\lambda_1\lambda_2}{2 * \eta * \Delta L} \quad (1)$$

where η is the refractive index of the waveguides. The Free Spectral Range (FSR) is then given as $2 * \Delta\lambda$. For all four AMZI structures, as they were designed with the same ΔL , the FSR was found to be around 5 nm (625 GHz).

As mentioned before, the different structures were designed and fabricated for the calibration of the directional couplers splitting ratio as function of the different gaps to find the optimum gap for the 50/50 DC. The suppression of the unwanted signal at each output port will be higher as closer to 50/50 is the splitting ratio of the DC and, from the results presented in Fig. 2. It can be observed that AMZI 3 is the structure that provides the maximum suppression at both output ports when light is coupled to any arm of its input DC.

CONCLUSION

In this paper we presented a monolithically integrated wavelength filter that forms part of a novel radiometer architecture for space applications that eliminates the need for cryostats, reducing the impact of the payload in the satellite. A maximum 25 dB of suppression was achieved with AMZI 3 when injecting light in either of the two arms of the input directional coupler. Therefore, we can also conclude that the DC gap that offers the splitter ratio closer to the desire 50/50 is 0.45 μm . The FSR of the filter can be adjusted by changing the path length imbalance of the AMZI. Furthermore, from the results we can also infer that the highest level of suppression with each structure is obtained when the output is collected at the cross arm of the output directional coupler with respect to the arm of the input directional coupler where light is injected. More extensive work will be carried out to study this behavior.

Acknowledgements: This work was supported by the Comunidad de Madrid through grant S2018/NMT-4333 MARTINLARA-CM project (<https://martinlara3.webnode.es/>) within the Programa de Actividades de I+D entre grupos de investigación de la Comunidad de Madrid en Tecnologías 2018, as well as by Spanish Ministerio de Ciencia e Innovación through Programa Estatal de Generación de Conocimiento y Fortalecimiento Científico y Tecnológico del sistema de I+D+i orientada a los Retos de la Sociedad convocatoria 2019 (grant PID2019-109984RB-C42)

References

- [1] PRISM collaboration, "Prism (polarized radiation imaging and spectroscopy mission): an extended white paper," J. Cosmol. Astropart. Phys. 2014
- [2] A. R. Cooray and Origins Space Telescope Study Team, "Origins Space Telescope," in American Astronomical Society Meeting Abstracts #229, 2017
- [3] G. S. Botello, L. E. G. Muñoz, et al., "Sensitivity limits of millimeter-wave photonic radiometers based on efficient electro-optic upconverters," Optica 5, pp. 1210-1219, 2018
- [4] L. E. G. Muñoz, G. S. Botello, et al., "Room temperature radiometer based on an up-conversion process for CubeSats applications", invited paper, Proc. SPIE 11348, Terahertz Photonics, 2020
- [5] A. Rueda, D. V. Strekalov, et al., "Efficient microwave to optical photon conversion: an electro-optical realization," Optica 3, pp. 597-604, 2016
- [6] G. S. Botello, Z. Popovic, L. E. G. Muñoz, et al., "Sensitivity and noise in THz electro-optic upconversion radiometers", Scientific Reports 10, 2020
- [7] C. Wang, M. Lončar, et al., "Nanophotonic lithium niobate electro-optic modulators," Opt. Express 26, pp. 1547-1555, 2018
- [8] M. Zhang, Marko Lončar, et al., "Monolithic ultra-high-Q lithium niobate microring resonator," Optica 4, pp. 1536-1537, 2017

Thermally tunable Silicon polarization rotator based on mode hybridization

(Student paper)

Theoni Prousalidi^{1,2}, Giannis Pouloupoulos¹, Carmelo Scarcella², Harry Zervos¹, Daisy Bergin^{2,3}, Anthony Bulling², Stéphane Detraz², Milana Lalović^{2,4}, Leonardo Marcon², Lauri Olanterä², Ulrik Sandven², Christophe Sigaud², Csaba Soos², Jan Troska² and Hercules Avramopoulos¹

¹School of Electrical and Computer Engineering, National Technical University of Athens, 15780 Zografou, Athens, Greece

²CERN, Esplanade des Particules 1, 1211 Geneva, Switzerland

³University of Bath, Claverton Down, Bath BA2 7AY, UK

⁴School of Electrical Engineering, University of Belgrade, Belgrade, Serbia

* theoni.prousalidi@cern.ch

A novel thermally tunable polarization rotator based on mode hybridization, is presented. The proposed component features a compact device footprint of 15.5 μm , insertion loss of 2.25 dB, and PER value above 13 dB across the entire C-band. By exploiting a thermal tuning mechanism, PER higher than 30.5 dB over 15 nm range is achieved with 3.5 mW/nm tuning efficiency.

Keywords: Silicon Photonics, polarization rotator, thermal tuning, mode hybridization

INTRODUCTION

Silicon Photonics platform (SiPh) is playing an important role in optical communications due to its compatibility with complementary metal oxide semiconductor (CMOS) fabrication processes [1] and the availability of multi-project wafer (MPW) services [2], while enabling highly integrated circuits with compact footprint and low power consumption. However, the high index contrast of SiPh induces strong birefringence and, thus, polarization dependent waveguiding. On-chip polarization diversity circuits can be exploited to overcome the polarization dependence [3]. In addition, they enable polarization division multiplexing (PDM) schemes that can be used to double link capacity [4]. A key component to enable on-chip polarization diversity is the polarization rotator (PR). PRs can be based on different techniques, such as mode coupling, mode evolution [5],[6] and mode hybridization [7], while other more advanced configurations, such as plasmonic [8] or subwavelength structures [9], can achieve increased performance. However, such solutions suffer from high insertion loss and low polarization extinction ratio (PER), or require complex integration and fabrication processes, respectively.

In this work, we propose a thermally tunable polarization rotator, based on mode hybridization, which features a compact device length of 15.5 μm with insertion loss of 2.25 dB and PER > 13 dB across the C-band. By exploiting the thermal tuning mechanism, PER higher than 30.5 dB over 15 nm range is achieved with 3.5 mW/nm tuning efficiency. The tuning mechanism presented requires low power and enables the integration of a high PER polarization rotator component in flex-grid DWDM systems, and in circuits with varying temperature operational requirements. The component is compatible with MPW services and is highly tolerant against fabrication variations.

SIMULATIONS AND DESIGN

The polarization rotator consists of an intermediate rotator segment, shaped as a single-stair waveguide, connecting an input and an output wire waveguide (Figure 1 (a)). By breaking the symmetry of the waveguide cross-section, the supported propagation modes are hybridized, whereas by changing the rotator segment length (L) the state of the polarization at the output waveguide can be selected. The rotator segment supports two hybrid modes (Figure 1 (b),(c)) with their optical axes perpendicular to each other. The optical axis is calculated in Eq.(1) [10]:

$$\tan \theta = \frac{\iint_{\Omega} n^2(x,y) \cdot H_x^2(x,y) dx dy}{\iint_{\Omega} n^2(x,y) \cdot H_y^2(x,y) dx dy} \quad (1)$$

where $n(x,y)$ is the refractive index distribution profile, while $H_x(x,y)$ and $H_y(x,y)$ are the x- and y- components, respectively, of the magnetic field of the hybrid mode.

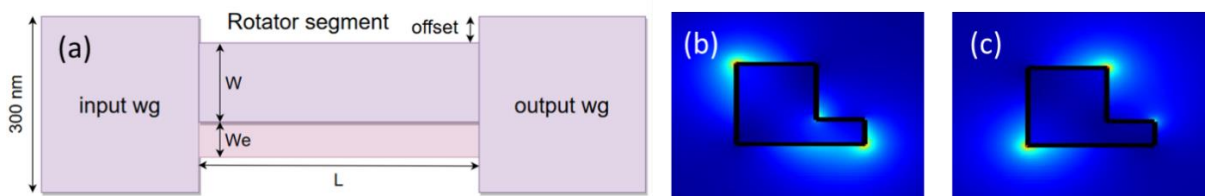


Figure 1: (a) Top View of the geometry of the proposed polarization rotator, (b) first hybrid mode, and (c) second hybrid mode.

Since the hybrid modes have different effective refractive indices and therefore different propagation constants (β_1 and β_2), while they propagate in the rotator segment they accumulate a phase difference. For π rad phase difference polarization rotation is achieved. This condition is fulfilled for rotator segment length equal to the conversion length, given by Eq. (2):

$$L_\pi = \frac{\pi}{\beta_1 - \beta_2} \quad (2)$$

The rotator segment can be characterized by the polarization conversion efficiency (PCE), given by Eq. (3) in [10]:

$$PCE = 4 \sin^2 \theta \cos^2 \theta \sin^2 \left(\frac{\pi L}{2L_\pi} \right) \times 100\% \quad (3)$$

where θ is the optical axis of the first hybrid mode, L_π is the conversion length and L the actual length of the rotator segment. To achieve maximum PCE three requirements must be met. Firstly, the hybrid modes should be equally TE and TM polarized, thus their optical axes need to be near 45° . Secondly, both hybrid modes are targeted to be equally excited by the input modes and finally the actual length L of the segment must be equal to L_π . Considering these, simulations were performed to determine the optimal geometrical parameters of the rotator segment. A topview of the rotator is shown Figure 1(a) which was simulated in the 220 nm SOI with 3 μm BOX integration platform. The rotator segment single step is formed via etching part of the waveguide as shown in Figure 1(a), where W is the width of the unetched part, and W_e the width of the etched part of the waveguide (150 nm etch depth). Finite Difference Eigenmode (FDE) simulations varying a set of (W, W_e) pairs were performed, to optimize the intermediate segment rotation efficiency. Calculated hybrid mode profiles are shown in Figures 1(b) and (c). In Figure 2, the calculated results regarding theta (θ) angle and PCE, are plotted varying (W, W_e) pair values. The set of pairs for which the optical axis is close to 45° and the PCE near 100% is shown in dark red in the PCE plot (Figure 2(b)).

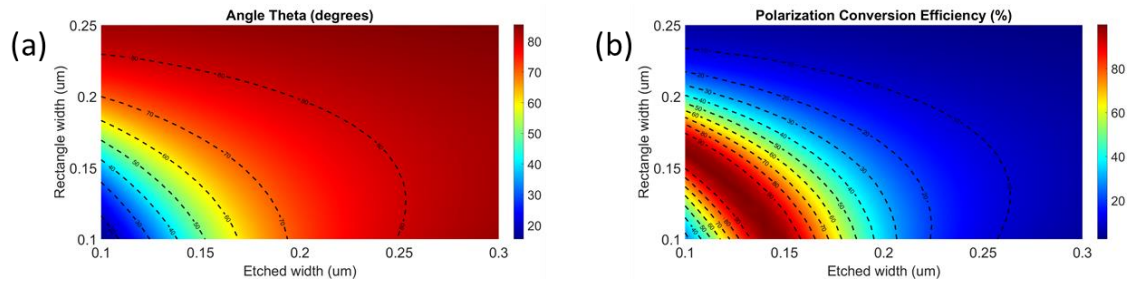


Figure 2: Calculated (a) angle theta and (b) PCE values of the rotator segment, for $L = L_\pi$, varying (W, W_e) pairs.

To calculate the overall component's efficiency, a set of EigenMode Expansion (EME) propagation simulations are carried out considering the rotator segment and input/output waveguides. In these simulations, input/output waveguides width value as well as the lateral offset between them and the intermediate segment (Figure 1(a)), are optimized to achieve equal excitation of the two hybrid modes, and minimise the interface insertion losses. Having defined the optimum lateral offset and input/output waveguides width (300 nm - 450 nm), for each pair of (W, W_e) values, the TE efficiency (TM mode excited at input) and Polarization Extinction Ratio (PER) values are presented in Figure 3(a), and (b), respectively, calculated via 3D-EME simulations.

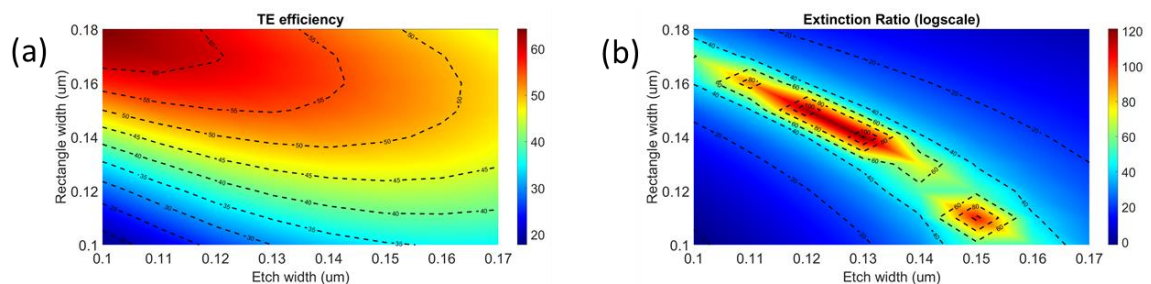


Figure 3: Calculated (a) TE efficiency and (b) PER at rotator output varying (W, W_e) values, for optimized lateral offset and $L=L_\pi$.

W and W_e values that result in maximum TE efficiency, and the corresponding values of lateral offset, can be identified. Optimum geometrical characteristics can be found with dark red in these plots (Figure 3)), while the final design parameters deduced are $W=170$ nm, $W_e=100$ nm, and *lateral offset*=-60 nm. A tolerance study was then carried out, investigating the effect of $\pm 10\%$ variation in the etch depth and waveguide height, around 150 nm and 220 nm, respectively. TE efficiency remains above 53% for up to ± 15 nm etch depth variation (Figure 4 (a)), and 50% for up to ± 10 nm silicon waveguide height variation (Figure 4 (b)), showcasing relaxed fabrication requirements of the component and full compatibility with fabrication in Silicon Photonics MPW services.

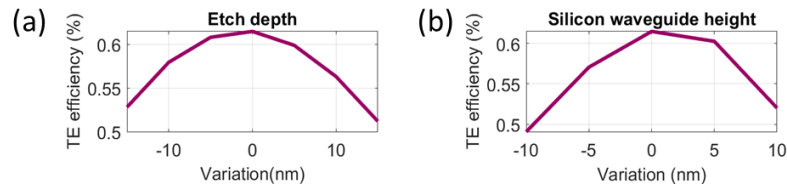


Figure 4: Rotator efficiency versus (a) etch depth variation and (b) Si waveguide height variation for $L=L\pi$.

The spectral performance of the rotator, calculated with 3D-EME and validated with 3D-FDTD simulations, is shown in Figure 5(a). TE efficiency, TM efficiency and PER value (right axis), reveal broadband operation centred around 1550 nm, where 62% TE efficiency and 30.5 dB PER is achieved. Over the entire C-band, TE efficiency > 59.5% and PER > 13 dB is achieved.

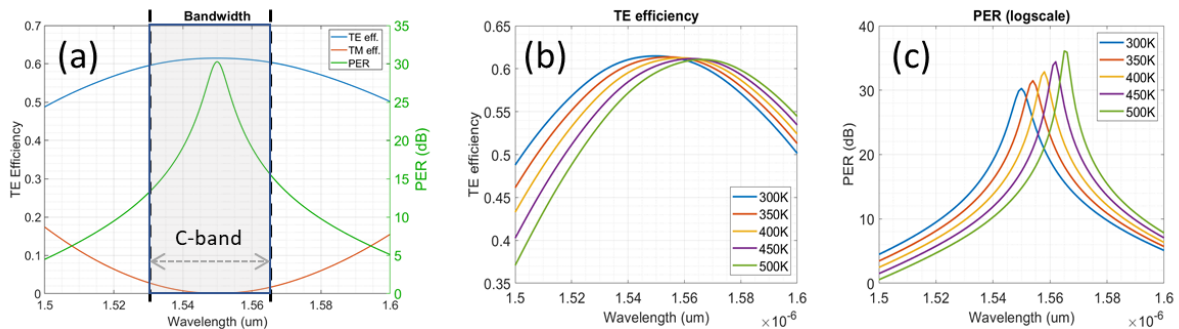


Figure 5: (a) Proposed rotator spectral performance. (b) TE efficiency and (c) PER values for different temperatures.

Thermal tuning of the component is achieved through a 1.5 μm wide metal heater wire placed 1 μm above the rotator segment waveguide. By applying DC voltage, the rotator segment temperature can be adjusted thusly tuning the refractive index exploiting the thermo-optic effect. The thermo-optic coefficients used for Si and SiO₂ were 1.8×10^{-4} and 1×10^{-5} respectively, with reference temperature of 300 K. EME simulation results for TE efficiency and PER values, varying temperature from 27 °C to 227 °C (300 K to 500 K) are shown in Figure 5(b) and (c), respectively. A 0.075 nm/°C central wavelength redshift is calculated for both TE efficiency and PER values, resulting in a 3.5 mW/nm power tuning efficiency. This low-power thermal tuning mechanism allows this polarization rotator to be used in applications under changing temperature environments where thermal tuning is necessary to ensure maximum PER in a specific wavelength. In addition, it can be deployed as a key element in elastic optical networks where wavelength tunability and high PER are indispensable requirements.

CONCLUSIONS

We presented a novel broadband polarization rotator element designed for 220-nm top SOI integration platform. It is characterized by a short length of 15.5 μm , insertion loss of 2.25 dB and PER value above 13 dB across the entire C-band. By exploiting the thermal tuning mechanism, PER value higher than 30.5 dB over 15 nm range is achieved with 3.5 mW/nm tuning efficiency. Its low fabrication complexity and low power consumption enable its adoption across many polarization diversity photonic integrated circuits and elastic optical network deployments.

ACKNOWLEDGMENTS

This work was supported by the European Commission, through H2020-QAMELEON project (780354).

References

- [1] W. Bogaerts and L. Chrostowski, "Silicon photonics circuit design: methods, tools and challenges," *Laser & Photonics Rev.*, vol. 12, no. 4, p. 1700237, 2018.
- [2] M. Pantouvaki *et al.*, "50Gb/s silicon photonics platform for short-reach optical interconnects," in *Optical Fiber Communication Conference*, 2016, pp. Th4H--4.
- [3] H. Fukuda *et al.*, "Silicon photonic circuit with polarization diversity," *Opt. Express*, vol. 16, no. 7, pp. 4872–4880, 2008.
- [4] C. Li, D. Liu, and D. Dai, "Multimode silicon photonics," *Nanophotonics*, vol. 8, no. 2, pp. 227–247, 2019.
- [5] Y. Yin, Z. Li, and D. Dai, "Ultra-broadband polarization splitter-rotator based on the mode evolution in a dual-core adiabatic taper," *J. Light. Technol.*, vol. 35, no. 11, pp. 2227–2233, 2017.
- [6] R. Bustamante *et al.*, "A compact and highly efficient SOI polarization splitter and rotator based on a bow-tie structure," in *SBMO/IEEE MTT-S International Microwave and Optoelectronics Conference (IMOC)*, 2019, pp. 1–3.
- [7] A. Xie, L. Zhou, J. Chen, and X. Li, "Efficient silicon polarization rotator based on mode-hybridization in a double-stair waveguide," *Opt. Express*, vol. 23, no. 4, pp. 3960–3970, 2015.
- [8] S. Kim and M. Qi, "Plasmonic mode-evolution-based polarization rotator and coupler," in *2015 Conference on Lasers and Electro-Optics (CLEO)*, 2015, pp. 1–2.
- [9] Z. Yu *et al.*, "Subwavelength-structure-assisted ultracompact Polarization-handling Components on Silicon," *J. Light. Technol.*, 2021.
- [10] Z. Wang and D. Dai, "Ultrasmall Si-nanowire-based polarization rotator," *JOSA B*, vol. 25, no. 5, pp. 747–753, 2008.

Demonstration of self-spiking neuron behavior in a monolithically integrated two-section laser

Lukas Puts¹, Kevin Williams¹, Daan Lenstra¹ and Weiming Yao¹

¹Photonic Integration Group, department of Electrical Engineering,
Eindhoven University of Technology, P.O. Box 513, Eindhoven 5600MB, The Netherlands
*l.puts@tue.nl

An integrated two-section laser with saturable absorber and gain section fabricated in an InP technology platform is analysed. Bistability and a voltage depending self-spiking behaviour are demonstrated. Additional simulations show that the self-spiking behaviour is likely triggered by noise, and that the pulse density can be controlled by the absorber voltage. This makes the proposed device a most promising encoder in a photonic spiking neural network.

Keywords: optical neuron, spiking neuron, bistable laser, photonic integrated laser

INTRODUCTION

Due to the development of novel artificial intelligence (AI) algorithms and neural network modelling, big data and the predictions of the end of Moore's Law, research into AI has grown exponentially [1]. The efficiency and speed of large neural networks in conventional hardware is limited due to the Von Neumann bottleneck, and thus new ways to implement neural networks in hardware are being explored [2]. One specific type of neural network is a spiking neural network (SNN), which comprises artificial neurons in multiple layers that closely mimic the dynamics of its biological counterpart, and thus attracted significant research interest. In an SNN, input data can be encoded using a temporal based or a rate based encoding scheme. In the latter, the input data is translated to a density of pulses at the input layer [3]. After this input layer, very short pulses are generated by individual neurons and transmitted as an optical trigger to consecutive neurons. The next neuron then either fires a spike or remains in its rest state. In an all-optical photonic spiking neuron (PSN), these optical spikes can potentially be very fast and short in time, and consequently an SNN based on photonic components can offer high operational speed at potentially low power consumption. To achieve this, various strategies to attain a photonic spiking neuron were recently proposed. For example, an integrated optical neuron based on a VCSEL [4] or a fiber laser [5] have been investigated. However, a fully integrated and scalable excitable spiking neuron for spike processing and data encoding has not yet been demonstrated.

A saturable absorber next to the gain section in a laser cavity introduces rich dynamics such as excitability, also observed in biological neurons, due to the different carrier lifetimes in the gain and absorber sections [6]. From previous work it is well understood that such a device can be bistable and has three operation regimes: cw, self-pulsation or an excitable regime [6]–[8]. In the two latter operation regimes spikes can be generated. Due to bistability, this device exhibits a hysteresis in the L-I characteristics and a negative differential resistance in the saturable absorber [8]. When the device is biased close to but below the hysteresis, an excitable response is expected when a perturbation above a threshold is applied [5]. Such non-linear response is the basic functionality of a neuron. Here, we demonstrate the bistability (i.e. the hysteresis and negative differential resistance) of an integrated two-section laser, fabricated in a multi-project wafer (MPW) InP platform, by measuring its L-I characteristics and the saturable absorber I-V curve. We also show how this laser exhibits noise-triggered self-spiking output (i.e., without any intentionally applied optical perturbation) with voltage controlled relative spike densities. We believe the self-spiking output could be useful to implement a rate-based encoding scheme in the input layer of an SNN, where the input data in such a network is translated to a spike density.

DEVICE AND EXPERIMENTAL SETUP

To experimentally observe a pulsed laser output, we fabricated two-section lasers, each consisting of a gain and a saturable absorber section on a commercial active-passive generic integration platform on InP [9]. Due to the maturity of this platform and the use of generic building blocks, future upscaling to an SNN containing multiple neurons is feasible. The device under investigation is a linear Fabry-Pérot type laser, comprising an 80 μm saturable absorber (SA) and 500 μm gain element (SOA), a 350 μm distributed Bragg reflector (DBR) optimized for reflections at 1550 nm, and a multimode interference reflector (MIR) (see the top laser in Fig. 1 (a)). The measurement setup for optical and electrical characterization is schematically shown in Fig. 1 (b). Light is coupled out of the chip using a lensed fiber coupler, and amplified using a low-noise EDFA. An optical isolator prevents reflections from the measurement equipment to interfere with the laser dynamics. An ILX Lightwave 3900 controller was used to pump

the gain section with current. To collect time traces a 6 GHz LeCroy Wavemaster 8600A real time oscilloscope was used.



Figure 1: (a) Micrograph of the fabricated PIC showing three lasers with different gain section lengths. (b) Overview of the measurement setup used to characterize the fabricated PIC. SMU: source measure unit, RTS: real time oscilloscope, PD: photodiode, PM: powermeter, EDFA: amplifier, ISO: optical isolator.

EXPERIMENTAL RESULTS

As mentioned in the introduction, the saturable absorber makes our two-section laser a bistable device. This bistability is experimentally confirmed by measuring the laser L-I and saturable absorber I-V characteristics, as shown in Fig. 2 (a) and (b). In case (a), a small positive current was applied to the saturable absorber to decrease the absorption. When the gain pump current is swept from 0 to 100 mA, denoted by the blue curve, a sudden stepwise increase of the optical output is seen at approximately 60 mA. By sweeping the gain current in the reverse direction, this step shifted to a lower current by approximately 10 mA. From similar measurements it was observed that this hysteresis width and step height can be tuned by changing the absorber current. In case (b), a negative differential resistance in the saturable absorber observed in the I-V characteristics. In this experiment, the gain section was first pumped at a relatively low current of 35 mA. The voltage at the saturable absorber was then swept from 0.0 to 1.0 V in steps of 0.01 V, while the current through the saturable absorber was monitored. This procedure was repeated for 10 different gain pump currents. At a saturable absorber voltage of 0 V, the absorption is strong and stimulated emission in the cavity is suppressed. Increasing the saturable absorber voltage decreases the absorption, which increases stimulated emission and the photon density in the cavity and as a result a larger negative photo current in the absorber is generated. This is observed in Fig. 2 (b) between approximately 0.5 V and 0.8 V for gain currents between 35 and 70 mA. In this case, the saturable absorber is bleached and the laser is turned on. When the voltage is further increased to a value above 0.8 V, the typical exponential diode characteristic becomes dominant [8].

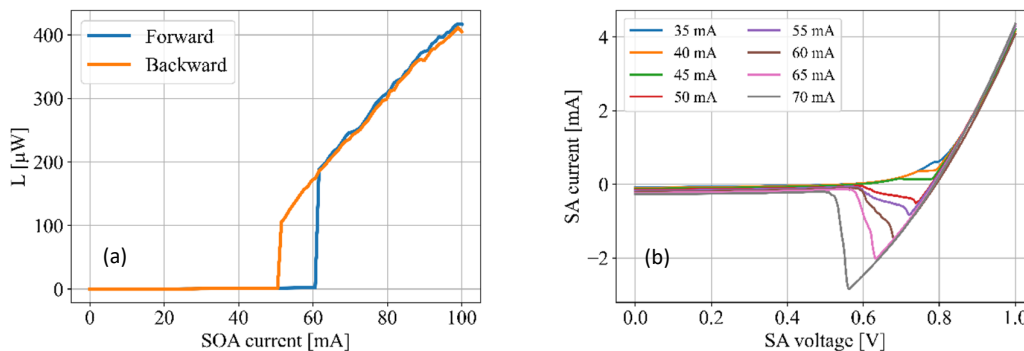


Figure 2: (a) Measured L-I laser characteristics for a small current applied at the saturable absorber. (b) Measured I-V saturable absorber characteristics for different gain currents as indicated.

In the next experiment, the gain section is biased at 50.11 mA, very close but slightly below the hysteresis. The optical output is analysed over 50 ms using the real time oscilloscope for three saturable absorber voltages, which are all located in the region of negative differential resistance shown in Fig. 2 (b). Fig. 3 (a), (b), and (c) show the oscilloscope time traces in case of a saturable absorber voltage of 0.720, 0.727, and 0.730 V, respectively. For all biasing conditions, pulses are observed in the time traces although the pulse densities are different. Note that in (b) and (c) the pulses do not show a fixed repetition rate, which would be expected for pulses generated in the self-pulsating operating regime. From this and given that the timescale is in the order of milliseconds, we conclude the observed pulses are not generated by the self-pulsating mechanism and relaxation oscillations but that these pulses likely are triggered by external noise. Note that because of the limited bandwidth of the real time oscilloscope, the temporal pulse width cannot be extracted from these time traces. However, as the generation of the pulses is directly related to the absorber and gain carrier lifetimes, which are in the order of hundreds and tens of picoseconds for this platform [10], we expect a sub-nanosecond pulse width.

SIMULATIONS

From previous numerical simulations, it was shown that in the region of excitability, injected noise can be strong enough to excite the laser and produce a pulse train [11]. To verify that the pulses in our experiment originate from injected noise, we simulated the two section laser using the normalized Yamada rate equations in the excitable regime [2]. This model describes the gain, absorber and optical intensity dynamics of a two section laser, where we added an extra term in the intensity equation to account for injected noise. We found that under reasonable normalized noise levels, the noise is indeed strong enough to perturb the laser and produce pulses. Similar to our experimental observations, the simulated pulse density increases when the absorption decreases.

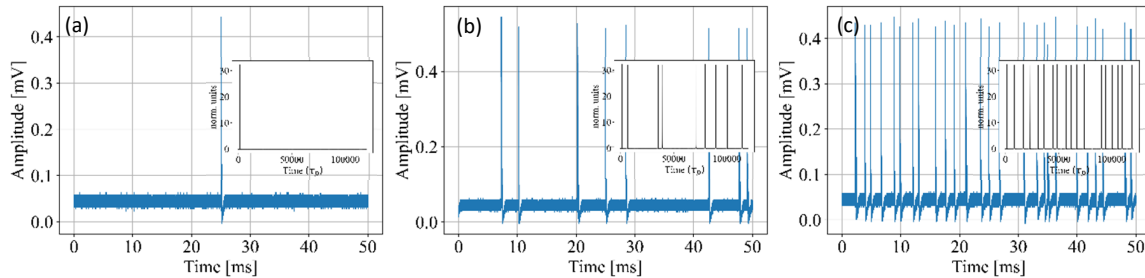


Figure 3: Time traces showing different pulse densities for $V_{SA} = 0.720$ V, 0.727 V, and 0.730 V, respectively. The gain section was pumped with a current of 50.11 mA. The insets show examples of the noise simulations with similar pulse densities.

CONCLUSION

We demonstrated bistability and voltage-dependent pulse densities when a two-section laser is biased close to this bistability. Simulations show that these pulses do not originate from self-pulsating mechanisms, but are likely triggered by external noise. We believe this is a successful first step towards a photonic SNN in an InP technology platform, since the proposed design can be used to encode data by controlling the pulse densities. Future work is aimed at achieving excitable pulse behaviour in the proposed structure, and realization of an all-optical photonic neuron as building block of a photonic SNN.

ACKNOWLEDGEMENT

We would like to thank Ruud van Sloun and Lizeth Gonzalez Carabarin for discussing the measurement results.

REFERENCES

- [1] C. Huang *et al.*, "Prospects and applications of photonic neural networks," *ArXiv210509943 Phys.*, May 2021, Accessed: Aug. 25, 2021. [Online]. Available: <http://arxiv.org/abs/2105.09943>
- [2] M. A. Nahmias, B. J. Shastri, A. N. Tait, and P. R. Prucnal, "A Leaky Integrate-and-Fire Laser Neuron for Ultrafast Cognitive Computing," *IEEE J. Sel. Top. Quantum Electron.*, vol. 19, no. 5, pp. 1–12, Sep. 2013, doi: 10.1109/JSTQE.2013.2257700.
- [3] M. Hejda, J. Robertson, J. Bueno, J. A. Alanis, and A. Hurtado, "Neuromorphic encoding of image pixel data into rate-coded optical spike trains with a photonic VCSEL-neuron," *APL Photonics*, vol. 6, no. 6, p. 060802, Jun. 2021, doi: 10.1063/5.0048674.
- [4] Y. Zhang, J. Robertson, S. Xiang, M. Hejda, J. Bueno, and A. Hurtado, "All-optical neuromorphic binary convolution with a spiking VCSEL neuron for image gradient magnitudes," *Photonics Res.*, vol. 9, no. 5, p. B201, May 2021, doi: 10.1364/PRJ.412141.
- [5] R. Otupiri, B. Garbin, N. G. R. Broderick, and B. Krauskopf, "Excitability in an all-fiber laser with a saturable absorber section," *J. Opt. Soc. Am. B*, vol. 38, no. 5, p. 1695, May 2021, doi: 10.1364/JOSAB.420204.
- [6] R. Otupiri, B. Krauskopf, and N. G. R. Broderick, "The Yamada model for a self-pulsing laser: bifurcation structure for non-identical decay times of gain and absorber," *Int. J. Bifurc. Chaos*, vol. 30, no. 14, p. 2030039, Nov. 2020, doi: 10.1142/S0218127420300396.
- [7] L. Puts, W. Yao, and D. Lenstra, "Modeling a Spiking Optical Neuron using Normalized Yamada Rate Equations," in *25th Annual Symposium of the IEEE Photonics Benelux*, Mons, Belgium, Nov. 2021, p. 4.
- [8] C. Harder, Kam Lau, and A. Yariv, "Bistability and pulsations in semiconductor lasers with inhomogeneous current injection," *IEEE J. Quantum Electron.*, vol. 18, no. 9, pp. 1351–1361, Sep. 1982, doi: 10.1109/JQE.1982.1071711.
- [9] M. Smit *et al.*, "An introduction to InP-based generic integration technology," *Semicond. Sci. Technol.*, vol. 29, no. 8, p. 083001, Jun. 2014, doi: 10.1088/0268-1242/29/8/083001.
- [10] V. Moskalenko, *Extended cavity passively mode-locked lasers in indium phosphide generic integration technology*. Technische Universiteit Eindhoven, 2016.
- [11] J. L. A. Dubbeldam, B. Krauskopf, and D. Lenstra, "Excitability and coherence resonance in lasers with saturable absorber," *Phys. Rev. E*, vol. 60, no. 6, pp. 6580–6588, Dec. 1999, doi: 10.1103/PhysRevE.60.6580.

Compact, spatial-mode-interaction-free, ultralow-loss, nonlinear photonic integrated circuits

(Student paper)

Xinru Ji¹, Junqiu Liu¹, Jijun He¹, Rui Ning Wang¹,
Zheru Qiu¹, Johann Riemensberger¹ and Tobias J. Kippenberg¹

¹ Institute of Physics, Swiss Federal Institute of Technology Lausanne (EPFL), CH-1015 Lausanne, Switzerland

* Email: xinru.ji@epfl.ch

We implement Euler bends to build compact high- Q Si_3N_4 racetrack microresonators, featuring a small footprint of only 0.21 mm^2 for 19.8 GHz free spectral range. We demonstrate that these multi-mode microresonators can be operated in the single-mode regime and generate a single soliton microcomb.

Keywords: Compact high- Q Si_3N_4 microresonator, single-mode operation

INTRODUCTION

For Kerr nonlinear photonics, anomalous GVD is required, which is realized via geometric dispersion engineering using multi-mode waveguides. However, uncontrollable spatial mode coupling in highly over-moded waveguides is undesired, as it yields spectrally distributed avoided mode crossings (AMXs) with random strengths, prohibiting soliton formation [1] and significantly distorting soliton spectra [2].

Microring resonators are used to avoid mode mixing. Single solitons with repetition rates in the microwave X- and K-band are generated [3], however the devices suffer from significant footprints and constrained device density. Alternatively, mode filtering elements [5] can be used to suppress mode mixing, yet at the same time limit the Q -factor.

Here, we demonstrate single mode operation in multi-mode Si_3N_4 racetrack microresonators with two symmetric Euler π -bends [6, 7], which have a curvature (k , the inverse of radius) varying linearly with its path length (s),

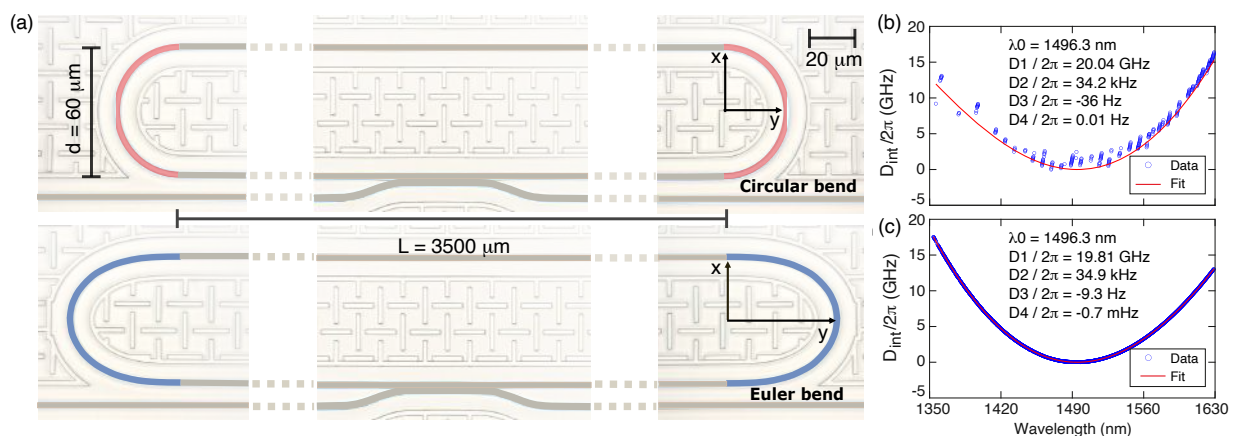


Fig. 1. Microscope image and integrated dispersion of Si_3N_4 racetrack microresonators with Euler bends and circular bends.

(a) Optical microscope images showing fabricated Si_3N_4 racetrack microresonators with Euler bends and circular bends. Both racetrack microresonators have the same span of $d = 60 \mu\text{m}$ for the π -bends, and length of $L = 3500 \mu\text{m}$. The device footprint is approximately 0.21 mm^2 . (b)-(c) Integrated dispersion characterization of racetrack microresonators with circular bends and Euler bends, fitted with $D_{\text{int}}(\mu) = D_2 \mu^2/2 + D_3 \mu^3/6 + D_4 \mu^4/24$

i.e. $k(s) = \alpha \cdot s$. The racetrack microresonators consist of two straight waveguides measuring $L = 3500 \mu\text{m}$ in length, and two π -bends spanning $d = 60 \mu\text{m}$. The resulted footprint is only 0.21 mm^2 for 19.8 GHz free spectral range (FSR), which is considerably smaller than the footprint of microring resonators of the same FSR that cover an area of more than 4 mm^2 in Ref. [3]. Such a size reduction allows for the integration of 30 devices on a $5 \times 5 \text{ mm}^2$ chip. It also benefits devices that have capacitance dependence on area, e.g. piezoelectric modulators [4], where a small footprint allows to reduce the time constant and increase the modulation speed.

RESULTS

We fabricated Si_3N_4 racetrack microresonators using the photonic Damascene reflow process [8]. The Si_3N_4 waveguide has a cross-section of $2.2 \mu\text{m}$ width and $0.90 \mu\text{m}$ height, featuring 10 transverse eigenmodes. To characterize resonance linewidths (i. e. microresonator loss) and microresonator dispersion, we use frequency-comb-assisted, cascaded diode laser spectroscopy, to cover the entire telecommunication E- to L-band (1350 to 1630 nm) [9]. We quantitatively characterize the strength of spatial mode interaction by studying the microresonator dispersion, and investigate AMXs. Figure 1(b,c) show the measured integrated microresonator dispersion with 4-th order fitting.

For the racetrack microresonator with Euler bends, AMXs are not observable in the dispersion profile. They are only revealed when D_2 and D_3 terms are both removed. While for the racetrack microresonator with circular bends, the missing resonances and exaggerated AMXs prohibit to fit D_{int} in Figure 1(c), leading to infeasibility to extract D_3 and D_4 values.

Finally, we demonstrate single soliton generation of 19.8 GHz repetition rate in the racetrack microresonator with Euler bends. We observe a soliton step length of $\sim 0.5 \text{ ms}$, on par with the previously reported value in a 100-GHz FSR microresonator [10]. Due to the suppressed AMXs, the soliton step is sufficiently long, allowing for direct access to the single soliton state using simple laser piezo frequency tuning, without any other complex tuning schemes or auxiliary lasers. An erbium-doped fiber amplifier (EDFA) is used to increase the on-chip pump power to approximately 55.7 mW to seed soliton formation. Figure 2(a) shows the single soliton spectrum, which does not show prominent dispersive wave features caused by AMXs. The single soliton spectrum fit shows a 3-dB bandwidth of 16.3 nm , corresponding to a pulse duration of 156 fs .

Further single-sideband (SSB) phase noise measurement of the soliton repetition rate shows a weak quiet point effect [11], indicating inhibited dispersive wave generation, due to suppressed spatial mode interaction and avoided-mode crossings.

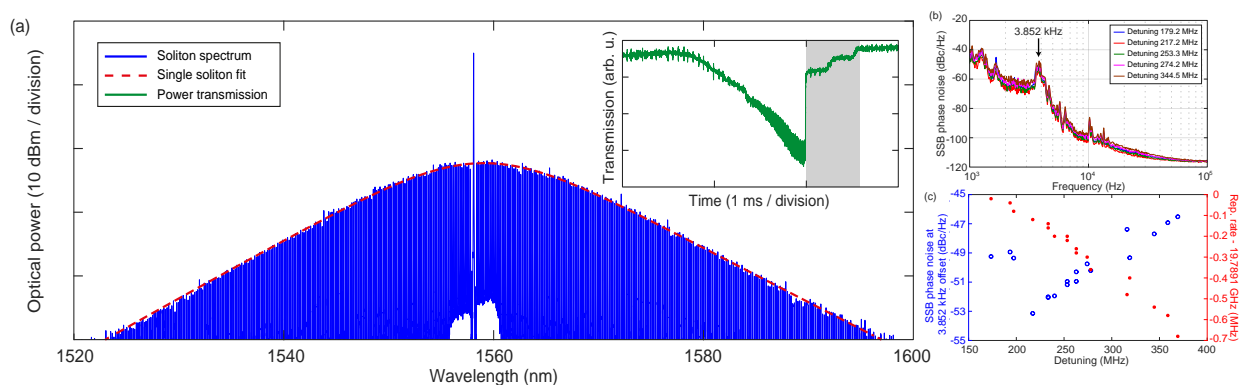


Fig. 2. Single soliton generation in the racetrack microresonator with Euler bends, and the phase noise characterization of soliton repetition rate. (a) Single soliton spectra of 19.8 GHz repetition rate. No prominent dispersive wave features caused by AMXs are observed. Inset: When the pump laser scans across the resonance, a soliton step of $\sim 0.5 \text{ ms}$ length in the microresonator transmission is seen (marked in the gray zoom). (b) SSB phase noise measurement with different soliton detuning values. No prominent phase noise change due to the quiet point operation is observed. The feature at 3.852 kHz Fourier offset frequency is caused by the diode laser pump [3]. (c) SSB phase noise at 3.852 kHz Fourier offset frequency and measured repetition rate shift with different soliton detuning values. The absence of strong quiet point is likely due to the inhibited dispersive wave generation that is caused by the suppressed spatial mode interaction and avoided-mode crossings.

Acknowledgements: This work was supported by the Air Force Office of Scientific Research (AFOSR) under Award No. FA9550-19-1-0250, by Contract HR0011- 20-2-0046 (NOVEL) from the Defense Advanced Research Projects Agency (DARPA), Microsystems Technology Office (MTO), by the Swiss National Science Foundation under grant agreement No. 176563 (BRIDGE), and by the EU H2020 research and innovation programme under grant agreement No. 965124 (FEMTOCHIP). The Si₃N₄ chips were fabricated in the EPFL center of MicroNanoTechnology (CMi).

References

- [1] T. Herr *et al.*, Phys. Rev. Lett. 113, 123901 (2014)
- [2] S. Ramelow *et al.*, Opt. Lett. 39, 5134 (2014)
- [3] J. Liu *et al.*, Nat. Photonics 14, 486–491 (2020)
- [4] J. Liu *et al.*, Nature 583, 385–390 (2020)
- [5] A. Kordts *et al.*, Opt. Lett. 41, 452 (2016)
- [6] T. Fujisawa *et al.*, Opt. Express 25, 9150 (2017)
- [7] F. Vogelbacher *et al.*, Opt. Express 27, 31394 (2019)
- [8] J. Liu *et al.*, Nature Communications 12, 2236 (2021)
- [9] J. Liu *et al.*, Opt. Lett. 41, 3134 (2016).
- [10] J. Liu *et al.*, Optica 5, 1347 (2018).
- [11] Yi, X. *et al.*, Nat Commun 8, 14869 (2017)

Ultra-broadband polarization beam splitter with a gradual anisotropy engineered subwavelength metamaterial

(Student paper)

José Manuel Luque-González^{1*}, Robert Halir^{1,2}, J. Gonzalo Wangüemert-Pérez^{1,2}, Jens H. Schmid³, Pavel Cheben³,
Íñigo Molina-Fernández^{1,2}, Alejandro Ortega-Moñux¹

¹Telecommunication Research Institute (TELMA), Universidad de Málaga, CEI Andalucía TECH, Louis Pasteur 35, 29010 Málaga, Spain

²Bionand Center for Nanomedicine and Biotechnology, Parque Tecnológico de Andalucía, 29590 Málaga, Spain

³National Research Council Canada, 1200 Montreal Road, Bldg. M50, Ottawa K1A 0R6, Canada

*jmlg@ic.uma.es

Polarization management is a key requirement in highly birefringence photonic platforms such as silicon-on-insulator. Many on-chip solutions to handle polarization leverage subwavelength grating metamaterials, as they provide control over material birefringence. Here we show the design of a polarization beam splitter based on an advanced SWG topology which controls the propagation of multiple TE and TM modes at the same time. The proposed device achieves a simulated insertion loss <1 dB and extinction ratio >20 dB over a 400 nm bandwidth.

Keywords: Photonic integrated devices, polarization management, subwavelength gratings.

INTRODUCTION

Silicon photonics is leading the landscape of integrated photonics, with the Silicon-On-Insulator (SOI) having important commercial applications specially on the data/telecom industry [1]. The huge success of SOI principally comes from its high integration density and the compatibility with CMOS fabrication processes of SOI chips with the CMOS fabrication process. However, the CMOS compatibility comes with the drawback of restricting the available materials to those compatible with the fabrication process, hindering the design of high-performance devices. Moreover, the high index contrast between silicon in the waveguide core ($n_{Si}=3.476$) the silicon dioxide cladding ($n_{SiO_2}=1.444$), combined with the usually rectangular waveguide geometries lead to an extremely a high polarization birefringence. However, polarization independent operation is often desired to handle the random changes in the polarization state that usually occurs in optical fibers. A usual method to achieve polarization transparency is by using polarization diversity schemes which require polarization beam splitters (PBS), polarization rotators (PR) and polarizations filters (PF). Many state-of-the-art polarization management devices in SOI are designed by using SWG metamaterials because they provide lithographic control over optical material properties, including modal birefringence [2,3]. In this work, a polarization beam splitter based on a gradual index (GRIN) lens is proposed. We use an SWG topology with a variable duty cycle [4] and with gradual shifting [5], as shown in Fig. 1, enabling the control of both polarizations almost independently. In a gradual SWG (see Fig. 1a), the duty cycle of the periodic structure is gradually modulated along the transversal direction, $DC(x)$, enabling the synthesis of a gradual material. In a bricked-modulated SWG (see Fig. 1b), a conventional SWG periodic structure is transversely divided in periodic segments, alternatively shifting the resulting blocks a length, $\Delta z(x)$, providing control over the TE modes. The combination of both topologies (See Fig. 1c) provides control over both polarization by first setting the TM modes with the gradual index profile and then adjusting the TE modes with the shifting. By using this strategy, a GRIN lens-based PBS has been designed, obtaining $IL < 1$ dB with an $ER > 20$ dB in a bandwidth over 400 nm. To the best of our knowledge this is one of the polarization splitters with broadest bandwidth reported to date.

WORKING PRINCIPLE OF A GRIN LENS BASED POLARIZATION BEAM SPLITTER

In a conventional isotropic GRIN lens, the refractive index profile follows a parabolic distribution (see Fig. 2a):

$$n_{GRIN}(x) = n_{max} \sqrt{1 - \alpha^2 x^2}, \quad \text{with} \quad \alpha = \frac{1}{w_{GRIN}/2} \sqrt{1 - \left(\frac{n_{min}}{n_{max}}\right)^2}, \quad (1)$$

where n_{max} and n_{min} are the refractive indices at the center and the edge of the lens and w_{GRIN} is the width of the lens. A paraxial ray at the input of GRIN lens with the profile given by Eq. (1) is collimated at a distance equal to the

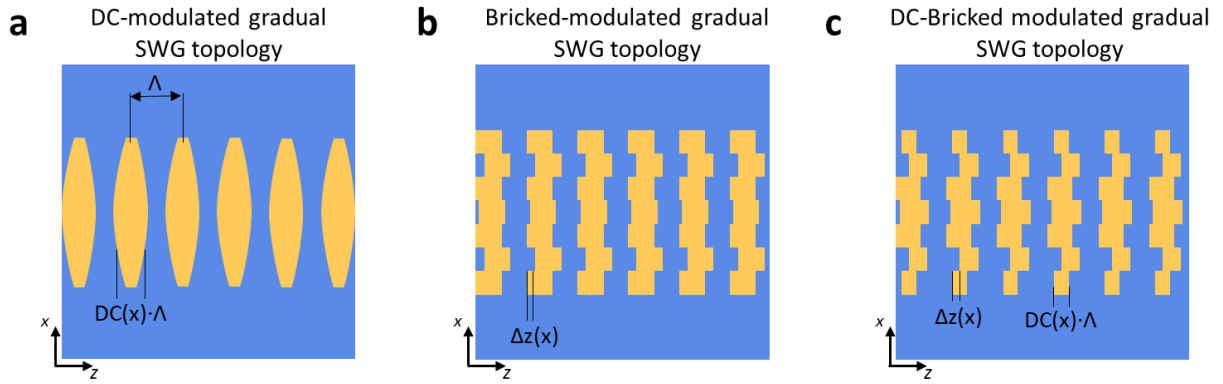


Figure 1. Schematic representation of SWG topologies allowing to implement a GRIN profile, including a) a DC-modulated gradual SWG topology, b) a bricked-modulated gradual SWG topology and c) a combination of the SWG topologies shown in (a) and (b), the DC-bricked modulated gradual SWG topology.

focal length, $f = \pi/(2\alpha)$, and then it is focused again at a distance $2f$ on the symmetrical point [See Fig. 2b, red line]. This behavior can be used to design a polarization beam splitter by achieving that the focus length for both polarizations, f_{TE} and f_{TM} , verify the condition:

$$L/2 = mf_{TE} = nf_{TM}, \quad (2)$$

where L is the device length and m and n are integers, with $|m - n|$ being an odd number, typically $m = 2$ and $n = 1$. By doing so, the input polarization will be split as schematically shown in Fig. 2b, where the blue line represents the TE polarization and the red line the TM polarization.

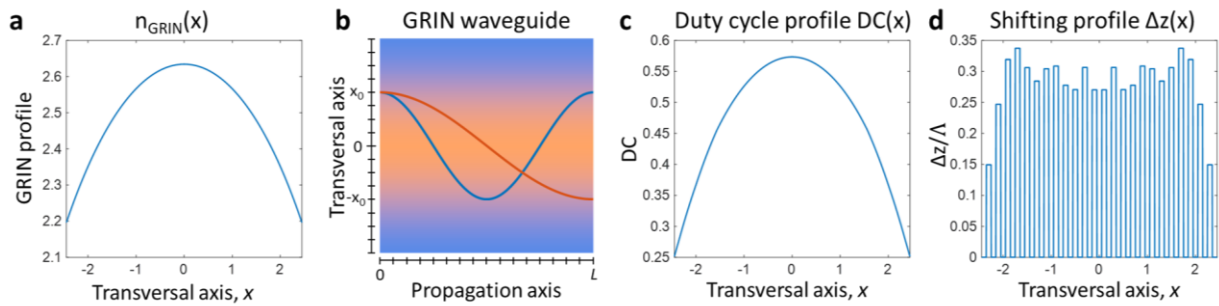


Figure 2. a) Parabolic index profile required to implement a GRIN lens. b) Schematic of the trajectory of an input TE/TM ray (blue/red line) in a GRIN waveguide. c) Duty cycle profile to implement the desired GRIN profile by using a duty cycle modulated gradual SWG metamaterial. d) Shifting profile to correct the focal length of the TE polarization ensuring the polarization splitting condition [Eq. (2)].

DESIGN OF THE GRIN LENS WITH SWG METAMATERIAL

A $5 \mu\text{m}$ wide SWG metamaterial waveguide is used to implement the GRIN lens PBS. By using the design process described in [4], the required duty cycle $DC(x)$ to implement the index profile given in Eq. (1) is obtained (see Fig. 2c). This GRIN profile has a simulated focal length $f_{TM} = 8.22 \mu\text{m}$ for the TM polarization and $f_{TE} = 5.45 \mu\text{m}$ for TE polarization. This focus lengths are calculated with the Floquet mode simulations as $f = \lambda_0/[4(n_{\text{eff}1} - n_{\text{eff}2})]$, where $n_{\text{eff}1}$ and $n_{\text{eff}2}$ are the effective indices of the first and second mode of the GRIN metamaterial waveguide. To satisfy the splitting condition given by Eq. (2), the focal length of the TE polarization has to be decreased to $\sim 4.11 \mu\text{m}$. For this purpose, the SWG metamaterial is bricked to engineer the TE polarization while virtually unaffacting the TM modes. By using a perturbational method [6], the shifting profile, $\Delta z(x)$, which set the desired focus length is obtained (see Fig. 2d).

DEVICE PERFORMANCE

The resulting DC-bricked SWG structure is shown in Fig 3a, including the input transitions tapers. To calculate the device performance, a 3D-FDTD simulator is used, calculating the insertion loss and the polarization extinction ratio as:

$$IL^{TE} = \frac{P_{\text{bar}}^{TE}}{P_{\text{in}}^{TE}}; \quad IL^{TM} = \frac{P_{\text{cross}}^{TM}}{P_{\text{in}}^{TM}}; \quad \text{and} \quad ER^{TE} = \frac{P_{\text{cross}}^{TE}}{P_{\text{bar}}^{TE}}; \quad ER^{TM} = \frac{P_{\text{bar}}^{TM}}{P_{\text{cross}}^{TM}}; \quad (3)$$

where $P_{\text{bar}}^{TE/TM}$ and $P_{\text{cross}}^{TE/TM}$ is the power in the fundamental TE/TM mode in the bar and cross ports, and $P_{\text{in}}^{TE/TM}$ is the power of the fundamental TE/TM mode the input port [See Fig. 3b and 3c]. The proposed device has a simulated insertion loss lower than 1 dB and extinction ratio larger than 20 dB over a 400 nm bandwidth.

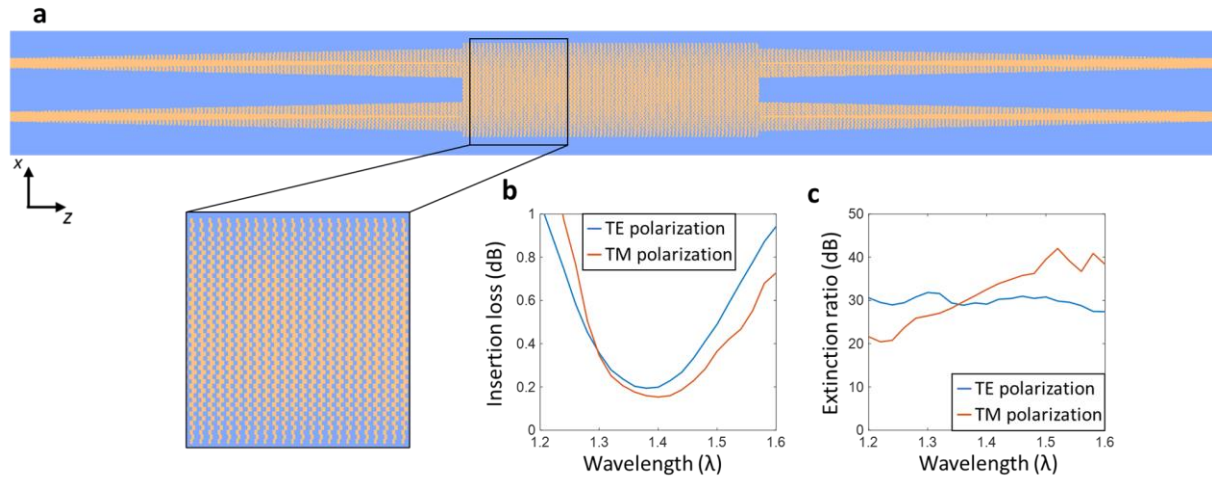


Figure 3. a) Schematic representation of the designed GRIN lens polarization beam splitter. b) Simulated insertion loss and c) extinction ratio of the TE and TM polarization.

CONCLUSION

In this talk, a new polarization beam splitter which uses the combination of two SWG topologies to control light propagation is presented. The proposed device not only exhibits an impressive performance but also shows the potential of this advanced SWG topology, enabling the precise manipulation of multiple modes of both polarizations at the same time. This capability opens new venues for the control of the light propagation on integrated chips.

Acknowledgements: Universidad de Málaga; Ministerio de Educación, Cultura y Deporte (MECD) (FPU16/06762), Ministerio de Ciencia, Innovación y Universidades (MCIU) (PID2019-106747RB-I00), Consejería de Economía, Conocimiento, Empresas y Universidad (CECEU) (UMA18-FEDERJA-219, P18-RT-1453, P18-RT-793),

References

1. S. Y. Siew, B. Li, F. Gao, H. Y. Zheng, W. Zhang, P. Guo, S. W. Xie, A. Song, B. Dong, L. W. Luo, C. Li, X. Luo, and G.-Q. Lo, "Review of Silicon Photonics Technology and Platform Development," *J. Light. Technol.* **39**, 4374–4389 (2021).
2. P. Cheben, R. Halir, J. H. Schmid, H. A. Atwater, and D. R. Smith, "Subwavelength integrated photonics," *Nature* **560**, 565–572 (2018).
3. J. M. Luque-González, A. Sánchez-Postigo, A. Hadij-ElHouati, A. Ortega-Moñux, J. G. Wangüemert-Pérez, J. H. Schmid, P. Cheben, Í. Molina-Fernández, and R. Halir, "A review of silicon subwavelength gratings: building break-through devices with anisotropic metamaterials," *Nanophotonics* **10**, 2765–2797 (2021).
4. J. M. Luque-González, R. Halir, J. G. Wangüemert-Pérez, J. De-Oliva-Rubio, J. H. Schmid, P. Cheben, Í. Molina-Fernández, and A. Ortega-Moñux, "An Ultracompact GRIN-Lens-Based Spot Size Converter using Subwavelength Grating Metamaterials," *Laser Photon. Rev.* **13**, 1900172 (2019).
5. J. M. Luque-González, A. Ortega-Moñux, R. Halir, J. H. Schmid, P. Cheben, Í. Molina-Fernández, and J. G. Wangüemert-Pérez, "Bricked Subwavelength Gratings: A Tailorable On-Chip Metamaterial Topology," *Laser Photon. Rev.* **15**, 2000478 (2021).
6. Í. Molina-Fernandez, A. Ortega-Moñux, and J. G. Wangüemert-Pérez, "Improving Multimode Interference Couplers Performance Through Index Profile Engineering," *J. Light. Technol.* **27**, 1307–1314 (2009).

Stokes-vector receivers on an indium phosphide membrane

Sander Reniers¹, Jos van der Tol¹, Kevin Williams¹ and Yuqing Jiao¹

¹Eindhoven University of Technology, De Groene Loper 19, Eindhoven, 5612 AP, The Netherlands
* s.f.g.reniers@tue.nl

Initial experimental results of a Stokes-vector receiver on an integrated indium phosphide membrane platform are presented. The ability to detect polarization states with a minimal absolute distance of 34° on the Poincaré sphere is achieved, which can be further improved by optimization of the polarization rotator section lengths.

Keywords: Photonic integrated circuit, membrane, indium phosphide, polarization converter

INTRODUCTION

Short-reach optical links are still relying on intensity modulation or direct detection formats due to the relatively high cost of coherent modulation format solutions. To add extra dimensions to these single dimensional solutions, the polarization space can be exploited by using Stokes-vector modulation (SVM). These modulation schemes have been demonstrated experimentally in several systems [1]–[3]. We demonstrate a compact (310 μm by 180 μm for the characterization structures) SVM receiver, realized on the InP-membrane-on-silicon (IMOS) platform, which is able to detect 32 polarization states. The realized structures include a fully passive approach to demonstrate the potential of this solution. Integration with high-speed photodiodes can result in a fast fully integrated opto-electronic SVM receiver. In this work we will introduce the SVM receiver design and demonstrate the ability to detect polarization states with these circuits.

DESIGN

A Stokes-vector receiver (SVR) needs to be able to distinguish between polarization states of the incoming signal. The passive circuit consists of input and output grating couplers, multimode interference couplers (MMIs) and polarization converters (PCs). On the IMOS platform, the photodiodes absorb TE polarized light, with high extinction ratio (typically >10 dB) towards the TM polarization. As a result, the S_1 component of the Stokes vector $\mathbf{S} = (S_1, S_2, S_3)$ can be directly measured. To measure the other components, polarization rotation is required.

For the polarization converters in the SVRs, optimal tilt angles of the hybrid modes are either 22.5° or 45°, since these would project the S_2 (22.5°) or the S_3 (45°) component onto the S_1 component, which can then be directly measured. An example of the case with a 22.5° tilt angle is shown in Fig. 1. The S_2 component is projected onto the S_1 component with a section length of $L_\pi = \frac{\pi}{\beta_1 - \beta_2}$, where $\beta_{1,2}$ are the propagation constants of the two hybrid modes in the triangular PC-section. The projection of S_3 onto S_1 requires an intermediate step of projecting S_3 onto S_2 , which is realized by a $\frac{\pi}{2}$ phase shift between the TE and TM parts of the mode in a rectangular waveguide: $L_r = \frac{\pi}{2(\beta_{1,r} - \beta_{2,r})}$, where $\beta_{1,r}$ and $\beta_{2,r}$ are the propagation constants of the quasi-TE and quasi-TM modes. Then it is projected again onto S_1 with a PC.

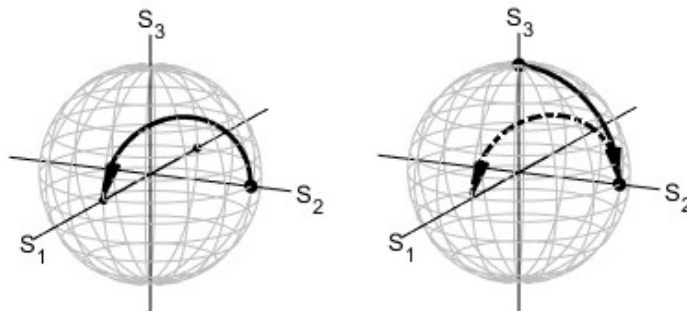


Fig. 1 - Poincaré spheres showing the projection of S_2 onto S_1 (left) and S_3 onto S_1 (right).

A schematic of the ideal passive receiver circuit is shown in Fig. 2. Cascaded 1x2 MMIs are used to split the input, since these are inherently symmetric. In the top arm, the S_1 component of the input signal is directly measured. In the second arm, a PC with a length of L_π (introduced above) is included, which will project S_2 onto S_1 . This can then be measured with the TE/TM output grating couplers. In the third arm an offset with respect to the PC in the second

arm is included, to first project S_3 onto S_2 , after which an identical PC to the one in the second arm is included. In this way, S_3 is projected onto S_1 and can be measured. In the bottom arm, which is redundant, a PC with double the length of the middle arms is included. If the length is chosen correctly, the output measured in this arm should be the same as the top arm, except with the insertion loss and propagation loss of the PC with double length included.

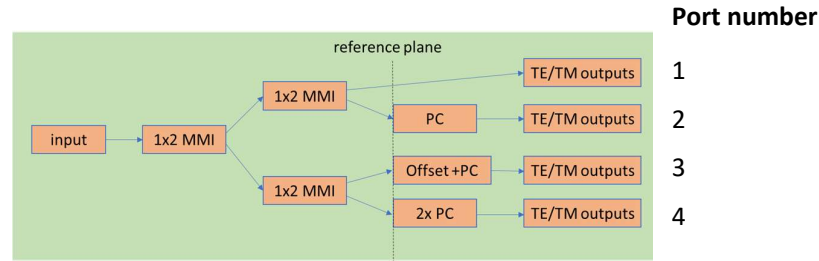


Fig. 2 - Schematic of passive Stokes-vector receiver circuit. The reference plane for determination of the polarization state is chosen just before the PC section in the second and fourth arm.

In our circuits, the PC that is used is shown in Fig. 3 [4]. The waveguides are 300 nm thick and 400 nm wide, and the PC is 460 nm high, with a sloped side with a 35° angle with respect to the wafer. To rotate the polarization from the S_2 and S_3 components to S_1 , a single section device will suffice, since the tilt angle of the hybrid modes in the triangular sections is around 26° .

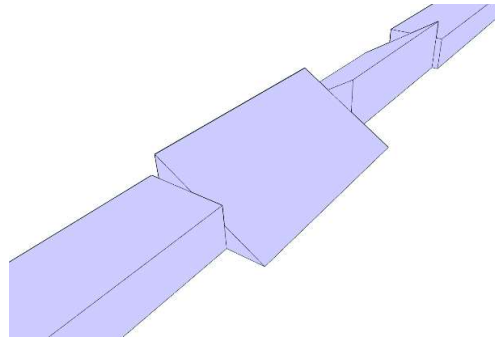


Fig. 3 - 3D mock of a double section polarization converter on IMOS before wafer bonding.

Since the PC on our platform has tilt angles of the hybrid modes that are not exactly 22.5° or 45° , some digital signal processing of the measured values will be required to obtain the original components. In [5], it has been shown that any tilt angle of the hybrid modes between 22.5° and 67.5° is suitable to convert a Stokes-vector on the S_2 - S_3 plane to a TE polarization state.

RESULTS

The circuit as depicted in Fig. 2 has been realized on the IMOS-platform [6]. Added to it is an extra polarization rotator in the input, in order to test the detection for various input SOPs. A series of SVRs has been made with the following parameter variations:

- The length of the PC added to the input, varying from 0.6 to 1.4 μm .
- The length of the PCs in the detection branches, running from 0.2 to 0.8 μm .
- Two values for the offset in the 3rd branch: 2.55 and 2.95 μm .

Before the SVR-performance can be analyzed several basic parameters have to be determined from the measurements. This can be done by comparing the TE and TM output for different lengths of input PC on the upper branch (i.e., the " S_1 " port). This should reflect the conversion of the input TE-mode for all circuits. The TM/TE ratio from the outputs is shown in Fig. 4. Due to polarization dependent phase and loss variations, related to the long paths between the input PC and the reference plane, only the averaged values can be analyzed. From these three parameters are obtained: the coupling ratio between the TE and TM output gratings (the TM-grating has 1.9 dB higher loss, which agrees with characterization of other structures in the same realization), the conversion length L_π , which is found to be 2.1 μm , and the mode tilting angle of the PC, 26.1° . These values are used in the rest of the analysis. Note however that the conversion length found is much larger than the values used in the circuits. This means that the PCs do not give the intended operation as described in the section "DESIGN". An inverted matrix operation to convert the measured S_1 -parameters at the three upper branches to the SOP of the reference plane

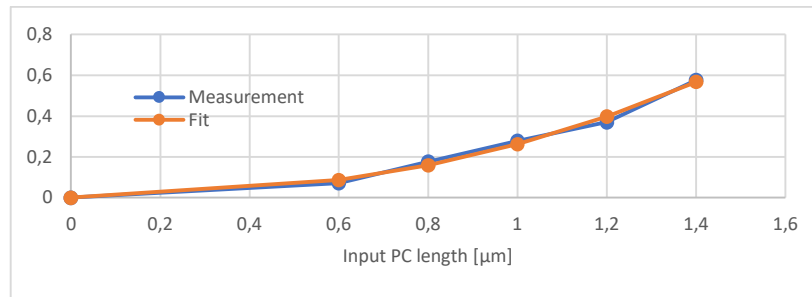


Fig. 4 - Average TM/TE ratio for all circuits (the point at 0 μm length is added for completeness).

can be constructed, but the mathematical problem turns out to be poorly defined (the determinant of the inverted matrix is much smaller than 1, which means the projection is far from ideal). This combined with the observed scattering on the results gives large errors and different points cannot be distinguished. Instead, a different approach was followed, which also considers the fourth branch with the double length PC. For a set of circuits with the same assumed polarization state at the reference plane (i.e., with the same input PC-length) a least square fit is performed to find S_1 , S_2 and S_3 at that reference plane. To determine if the SOPs determined in this way are distinguishable from each other we analyze the inner product of every pair of Stokes vectors. If polarization states are identical, this will yield "1", if they are orthogonal, it will be "-1". If a statistically significant difference between two pairs can be detected by the SVR-circuits, the polarization states are distinguishable, and can be used in a polarization modulation scheme. Fig. 5 shows the inner product of the SOP resulting from the shortest input PC (with 0.6 μm length; there are two sets of these, with different offsets in the third branch) with those from all the other lengths.

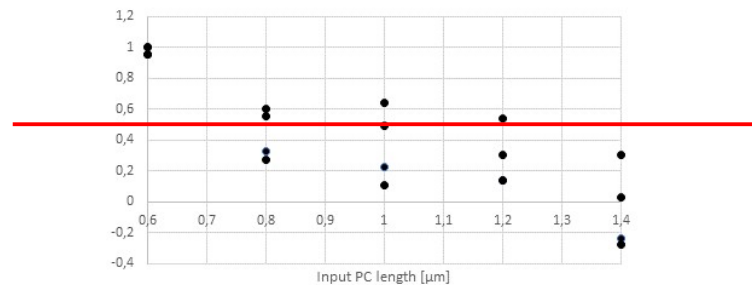


Fig. 5 - Stokes vector inner products for SOPs from different input PC lengths. The red line indicates a decision threshold between two points.

It can be seen that the only unambiguous difference is found between the SOPs from the shortest and the longest input PCs. For the other lengths the scatter on the data is too much to distinguish the states. The length difference of 0.8 μm implies a rotation over the Poincaré sphere of about 34° . With this separation of polarization states at least 32 of them can be positioned on the sphere, allowing 5 bits of information in one symbol, and thus a 5-fold increase of transmission capacity. However, if the length of the PCs in the branches is adjusted to 2.1 μm , and if the variation in transmission is reduced with shorter waveguide paths, even more distinguishable states will become possible.

References

- [1] T. Tanemura and Y. Nakano, "Compact InP Stokes-Vector Modulator and Receiver Circuits for Short-Reach Direct-Detection Optical Links," *IEICE Trans. Electron.*, vol. E101.C, no. 7, pp. 594–601, Jul. 2018.
- [2] S. Ghosh, Y. Kawabata, T. Tanemura, and Y. Nakano, "Polarization-analyzing circuit on InP for integrated Stokes vector receiver," *Opt. Express*, vol. 25, no. 11, p. 12303, May 2017.
- [3] K. Kikuchi and S. Kawakami, "Multi-level signaling in the Stokes space and its application to large-capacity optical communications," *Opt. Express*, vol. 22, no. 7, p. 7374, Apr. 2014.
- [4] J. Pello *et al.*, "High-efficiency ultrasmall polarization converter in InP membrane," *Opt. Lett.*, vol. 37, no. 17, pp. 3711–3713, Sep. 2012.
- [5] T. Suganuma, S. Ghosh, M. Kazi, R. Kobayashi, Y. Nakano, and T. Tanemura, "Monolithic InP Stokes Vector Receiver With Multiple-Quantum-Well Photodetectors," *J. Light. Technol.*, vol. 36, no. 5, pp. 1268–1274, Mar. 2018.
- [6] S. F. G. Reniers, "Integration of a polarization converter on the active-passive IMOS platform," PhD thesis, Eindhoven University of Technology, Eindhoven, 2022.

Ge/Si Electrically Tunable VIS/SWIR Photodetector

Andrea Ballabio¹, Andrea De Iacovo², Jacopo Frigerio¹, Andrea Fabbri³, Giovanni Isella¹ and Lorenzo Colace²

¹LNESS- Dipartimento di Fisica, Politecnico di Milano, Como, Italy

²Dipartimento di Ingegneria, Università degli Studi Roma Tre Roma, Italy

³INFN, Università degli Studi Roma Tre, Roma, Italy

* andrea.ballabio@polimi.it

We report on a epitaxial Ge-on-Si dual-band photodetector grown on a Si p-n junction, to form two photodiodes connected in a back-to-back configuration. The device responsivity can be tuned, with an external bias, to cover wavelengths within the visible and near-infrared spectral regions.

Keywords: Ge epitaxy, Ge-on-Si photodetectors, dual band.

INTRODUCTION

This Ge-on-Si photodiodes have been firstly reported more than twenty years ago [1] opening the way for the integration of IR photodetectors on Si. A tremendous development has been done, moving from vertically illuminated, stand-alone devices, to waveguide integrated arrays of photodetectors [2] and CMOS integrated imagers [3]. Usually, the Ge epilayer act as the absorbing material for the SWIR radiation, while Si acts only as a substrate. Here we report on a dual-band Ge-on-Si photodetector where light detection can take place both within the Ge epilayer and the underlying Si substrate: the device responsivity can thus be tuned from the VIS to the SWIR spectral range by means of an external bias. Therefore, the presented device can be implemented as a VIR-NIR-SWIR CMOS compatible imager.

WORKING PRINCIPLE AND DESIGN

A schematic representation of the dual-band photodetector is shown in in Fig. 1. Two photodiodes in a back-to-back configuration are formed by p-doping the back side of a high resistivity Si wafer and by epitaxially growing a p-i-n heterojunction Ge-on-Si layer on the front side (Fig. 1a)). An external bias can be applied to the whole layer stack be means of ohmic contacts formed on the top Ge layer and on the wafer backside (see Fig. 1b)). When a positive bias is applied between the top and bottom contact, the Ge diode is forward biased while the Si diode is reversed biased. In such a configuration the photocurrent generated within the Si substrate by back illuminating the device, will flow through the external circuit and be detected. By reversing the bias polarity, still maintaining a backside illumination, the detected photocurrent will be that generated within the Ge epilayer: in this way it is possible to tune the device responsivity simply by controlling the external bias.

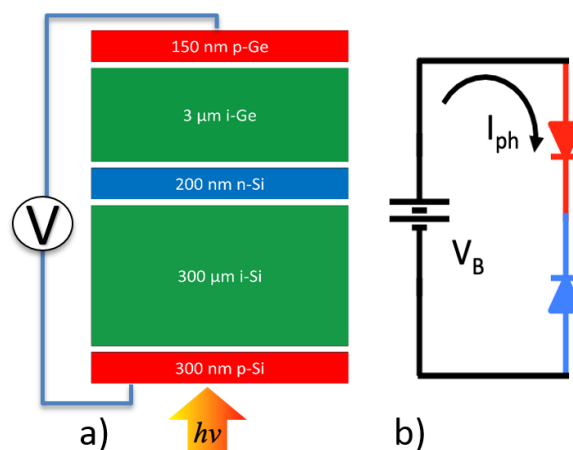


Figure 1: a) Schematic representation of the layer stack resulting in a Si p-n junction and Ge-on-Si p-i-n junction connected back to back as sketched in panel b).

EPITAXIAL GROWTH AND DEVICE FABRICATION

A TCAD model has been set up to optimize doping levels, in particular that of the Si substrate, determining the most effective position the p-n junction within the Si photodiode (at the bottom surface or at the Ge/Si interface) and investigate the role played by substrate thickness [4]. The layer stack reported in Fig. 1a) represents the outcome of such optimization procedure. A p-type layer has been formed on the backside of an intrinsic Si wafer by spin-on-dopant obtaining a boron-doped layer with an average concentration of $2 \times 10^{19} \text{ cm}^{-3}$ and a thickness of $\approx 300 \text{ nm}$. The epitaxial growth has been performed by low-energy plasma-enhanced chemical vapor deposition (LEPECVD)[6]. Firstly a 200 nm thick phosphorous-doped Si layer has been deposited at 760°C followed by $3 \mu\text{m}$ thick nominally undoped Ge, grown at 500°C . Six thermal annealing cycles have been performed in-situ to reduce threading dislocation density. As a final step 150 nm of boron-doped Ge have been deposited.

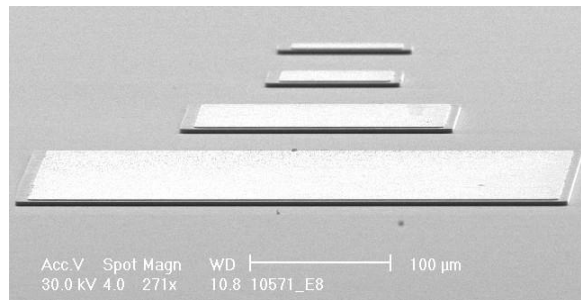


Figure 2: SEM view of the Ge mesa and top contact.

Prior to fabrication the Si wafer has been diced into square $1 \times 1 \text{ cm}^2$ chips. Square mesas with dimensions ranging between $100\text{-}500 \mu\text{m}$ have been realized by standard UV lithography and dry etching on the Ge-on-Si epitaxial layer. The mesas have been etched down to the intrinsic Si surface to electrically isolate the different devices on the same chip. The top ohmic contacts have been realized by e-beam deposition of a Ti/Al metal stack (100 nm Ti and 1000 nm Al) and lift-off. The bottom ohmic contact has been fabricated by depositing two rectangular stripes of Ti/Au (10 nm Ti, 150 nm of Au) on the backside of the chip. An SEM image of the fabricated device is shown in Fig. 2.

DEVICE CHARACTERIZATION

Optical characterization was performed by means of lamp-monochromator set-up. The bias dependent dual-band operation of the device is demonstrated in Fig. 3, where the spectral responsivity is shown for two different applied voltages. The VIS/NIR operation of the device is clearly demonstrated. For $V_B = +1 \text{ V}$, the Si photodiode is reverse biased giving a photoresponse in the $400\text{-}1200 \text{ nm}$ spectral range. When the bias voltage is reversed to $V_B = -1 \text{ V}$, the Ge photodiode is reverse biased and a photoresponse in the $1000\text{-}1650 \text{ nm}$ spectral range is obtained. Its short wavelength cut-off is due to the absorption of Si.

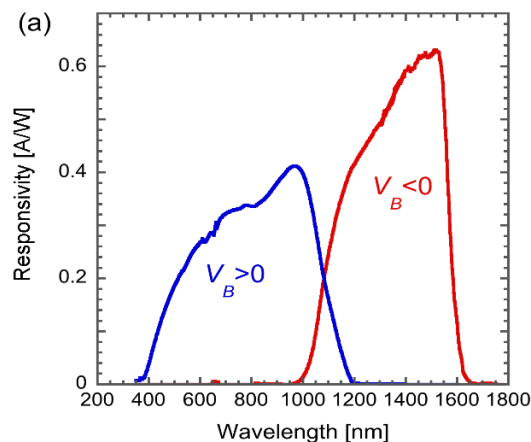


Figure 3: Spectral responses measured at $V_B = +1 \text{ V}$ (blue) and at $V_B = -1 \text{ V}$ (red).

The peak responsivities of the two bands are 0.41 A/W and 0.63 A/W at 960nm and 1520 nm, respectively. The overall performance of a photodetector has been evaluated by estimating the specific detectivity D^* of the device, which, thanks to its low voltage operation has been found to be $7 \cdot 10^{11} \text{cmHz}^{1/2}/\text{W}$ and $2 \cdot 10^{10} \text{cmHz}^{1/2}/\text{W}$ in the VIS and NIR, respectively [7].

VIS-NIR single-pixel imaging was performed by mounting the chip on a rastering system comprising a three-axis stage. In this way the pixel can scan the image plane behind a plano-convex lens. Two images, one in the VIS and one in the NIR, can be obtained by repeating the scanning and changing the polarity of the applied bias at the device. A coloured VIS image has been obtained by repeating the measurements three times with three different optical bandpass filters (450nm, 550nm and 650nm) resulting in three images with R, G, and B components, which have been combined to obtain the final VIS image.

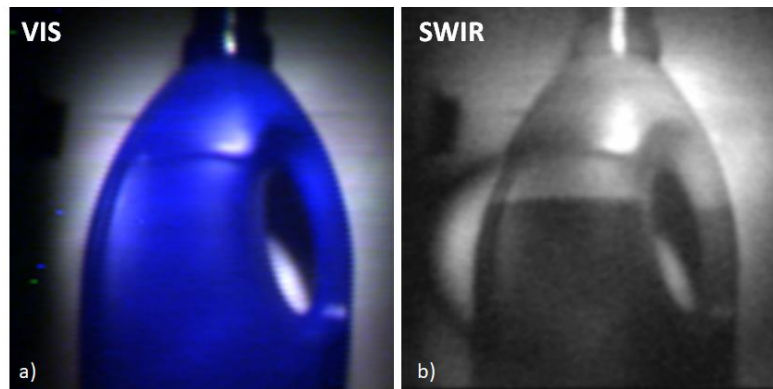


Figure 4 Images obtained with the rastering system a) RGB image obtained with the Si part of the device and b) SWIR image obtained with the Ge part of the device.

CONCLUSION

In conclusion, we have designed and fabricated a voltage-tunable dual-band photodetector operating in the VIS and NIR range. The device is based on a couple of p-i-n photodiodes connected back-to-back formed within a Ge-on-Si epitaxial structure. The device operates between 400 and 1600 nm and its architecture enables to electronically select the shorter (400-1100 nm) or longer (1000-1600 nm) wavelength range with a relatively low applied voltage. VIS-NIR single-pixel imaging has been performed.

ACKNOWLEDGMENT

This work has been supported by SEGREDIFESA of the Italian Ministry of Defence under the National Military Research Plan R&T Project, the TEINVEIN project funded by POR FESR 2014-2020 (ID: 242092) and the EU Horizon 2020 FET project microSPIRE (ID: 766955). The Acoustoelectronics Laboratory (ACULAB) of the Università degli Studi Roma Tre is acknowledged for device packaging. The Authors would like to acknowledge Fulvio Mancarella - IMM CNR for the spin-on-dopant processing.

References

- [1] L. Colace, G. Masini, F. Galluzzi, G. Assanto, G. Capellini, L. Di Gaspare and F. Evangelisti, *Solid State Phenom.* 54, 55–58 (1997).
- [2] D. Ahn, C. Hong, J. Liu, W. Giziewicz, M. Beals, L. Kimerling, J. Michel, J. Chen, and F. Kärtner, *Opt. Express* 15, 3916-3921 (2007)
- [3] R. Kaufmann, G. Isella, a. Sanchez-Amores, S. Neukom, a. Neels, L. Neumann, a. Brenzikofer, a. Dommann, C. Urban, and H. von Känel, *J. Appl. Phys.* 110, 023107 (2011)
- [4] A. De Iacovo, A. Ballabio, J. Frigerio, L. Colace and G. Isella. *Journal of Lightwave Technology*, 37 (14), 3517 (2019).
- [5] M. Young, *The Technical Writer's Handbook*. Mill Valley, CA: University Science, 1989.
- [6] C. Rosenblad, H. R. Deller, A. Dommann, T. Meyer, P. Schroeter, and H. von Känel *J. Vac. Sci. Technol. A* 16 (5) 2785--2790 (1998)
- [7] E. Talamas Simola, A. De Iacovo, J. Frigerio, A. Ballabio, A. Fabbri, G. Isella, L. Colace, *Opt. Express* 27, 8529-8539 (2019)

Mode Overlap Simulations for Quantification of Bend Loss in Silicon Nitride Strip Waveguides for Sensing

Anton Buchberger^{1*}, Desiree Rist¹, Jakob Hinum-Wagner^{1,2}, Samuel Hörmann^{1,2}, Jochen Kraft¹ and Alexander Bergmann²

¹ams-OSRAM AG, Tobelbader Str. 30, 8141 Premstaetten, Austria

²Institute of Electrical Measurement and Sensor Systems, Graz University of Technology, Inffeldgasse 33/I, 8010 Graz, Austria

* anton.buchberger@ams-osram.com

Bent waveguides are not just essential for the connection of functional building blocks in photonic integrated circuits (PIC), but can be used to increase the sensitive area of a sensor based on optical waveguides. The bend loss of the investigated silicon nitride strip waveguides without top oxide cladding is about 2-4 times lower than with cladding. Such waveguide bends can be used for environmental or bio sensor PIC designs with increased sensitivity.

Keywords: Silicon nitride, waveguide, bend, mode simulation, photonic sensors

INTRODUCTION

Bent and straight waveguides are an important photonic element for connecting functional building blocks in a photonic integrated circuit (PIC). Unlike electrical connections with 90° corners, light cannot be transmitted in this Manhattan routing style. The radius of such bent connectors plays an important role in terms of losses. In addition, the loss for bent strip waveguides depends on essential parameters such as height and width. Another important function of waveguide bends can be found in many sensor applications. Silicon nitride strip waveguides are commonly covered with a top oxide cladding in order to prevent interference with the surrounding environment. In case of a sensor, this very interaction with the environment is the basis for most sensor effects and therefore the top cladding is removed within a dedicated area. The sensitivity of such photonic sensors is dependent on the interaction length with the analytes. Bent waveguides are used to increase the sensitive surface within the cladding-free area and exploit it as much as possible. For example, bent waveguides have been used in previous work to increase the interaction probability of a particle detector based on optical waveguides [1]. However, the total number of bends that can be integrated in a PIC is limited by the loss introduced by the bends. Besides roughness induced propagation loss along the bend, a major source of bend loss is mode mismatch between the straight and bent part of the waveguide [2][3]. Numeric simulations were carried out for 250 nm thick silicon nitride strip waveguides with and without top oxide cladding in order to determine the mode profiles and calculate the corresponding overlap for several bend radii and waveguide widths. The simulation results are compared with comprehensive measurements of dedicated test structures fabricated with a PECVD silicon nitride technology presented in previous work [4].

METHODS

We investigated the bend loss of silicon nitride strip waveguides with a height of 250 nm and widths from 450 nm to 750 nm for bend radii from 10 μm to 35 μm at a wavelength of 850 nm and TE polarization. The propagation loss of these waveguides was demonstrated previously to be as low as 1 dB/cm for the case with and 2-4 dB/cm without top oxide cladding [5]. Due to the short path length of the investigated waveguide bends and these low losses, propagation loss could be neglected. Lumerical MODE was used to compute the modal fields of the straight and the bent waveguide and an overlap integral was calculated to quantify the modal mismatch (cf. Figure 1).

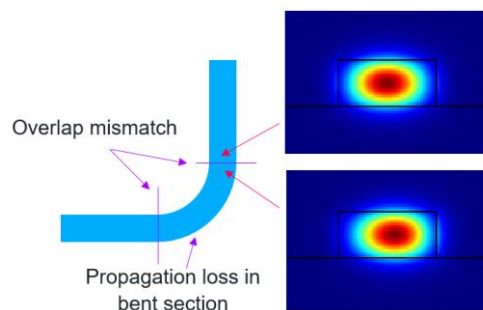


Figure 1: Sketch depicting loss sources of waveguides bends including mode overlap mismatch and propagation loss and two exemplary mode profiles.

Dedicated test structures were designed to compare the bend loss simulations with measurements. In order to compensate for the propagation loss of the entire test structure, a concept with spirals of identical total length but different bend radii was chosen. All measurements are referred to a spiral where the bend radius is such that the mode mismatch and thus the bend loss are negligible. Preliminary measurements have shown that a radius of $70\ \mu\text{m}$ leads to negligible bend loss and can therefore be used as a reference. The losses of all other spirals refer to this reference spiral with the same waveguide width. Thus, it is a relative measurement, which provides good reproducibility as long as the coupled laser power remains constant during the measurement of a group of test spirals. Figure 2 shows an exemplary test structure for the bend loss measurement of one radius and one waveguide width. Grating couplers were implemented on each test structure to couple a power meter and a diode laser providing TE-polarized light at $850\ \text{nm}$ wavelength. A dedicated set of spirals is required for each waveguide width with one spiral for each radius of interest.

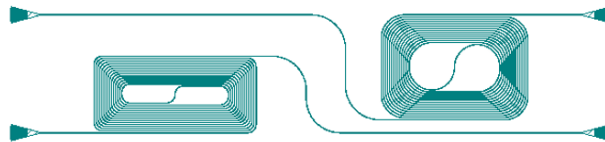


Figure 2: Layout of an exemplary test structure for the measurement of bend loss on a test wafer with the reference spiral implemented on the right.

The total loss per spiral is defined by the number of bends and matches with the dynamic range of the applied power meter. The bend loss for a 90° bend BL is derived for each waveguide width with the following formula

$$\text{BL} = \frac{P_x}{P_0 n_{\text{bends}}} \quad (1)$$

containing the transmitted power P_x of each spiral with bend radius x , normalized to the transmitted power of its corresponding reference spiral P_0 and divided by the number of 90° bends n_{bends} . An automatic wafer prober system was used to measure all dies on two test wafers, which lead to about 100 measurement values for each test structure.

RESULTS

Measurements for four different waveguide widths and eight different radii per width were performed and compared with the simulation in Lumerical MODE. Figure 3(a) and 3(b) show the result for a 90° silicon nitride strip waveguide bend with and without top oxide cladding, respectively, together with the corresponding waveguide cross section.

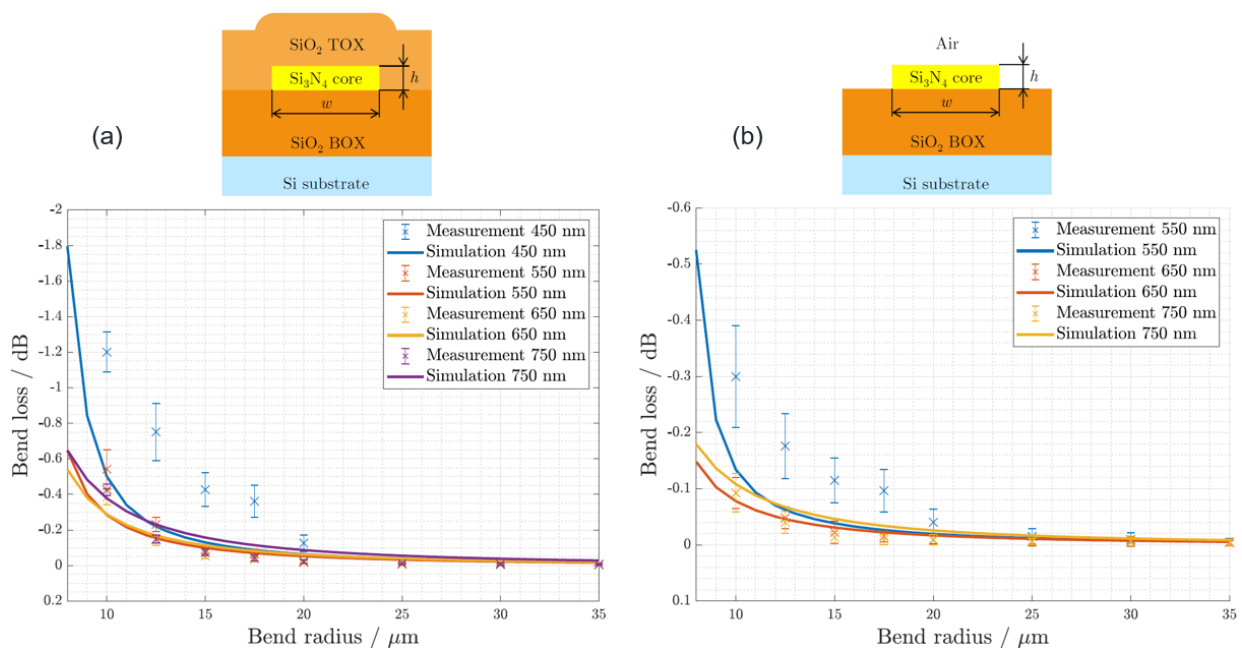


Figure 3: Measurement and simulation results of the loss of $250\ \text{nm}$ thick strip waveguides (a) with and (b) without top oxide cladding (cross section on top) for a 90° bend at $850\ \text{nm}$ wavelength dependent on bend radius for four and three waveguide widths w , respectively.

There are no results for the 450 nm wide waveguide without top oxide cladding, since there are no propagation modes in the bend. The trend of measurement and simulation is comparable and shows an increase of the bend loss at smaller bend radii up to -1.2 dB and -0.3 dB for a 90° bend with and without top oxide cladding, respectively.

DISCUSSION

The simulation results for the narrowest waveguide widths (450 nm with and 550 nm without top oxide) are significantly lower than the measured values. Presumably, for very small bend radii, the propagation loss along the waveguide bend is much larger than for the straight waveguide and is not negligible, because the mode field is pushed closer to the sidewall where it is scattered more by the rough surface. However, since the typical roughness size parameter is in the order of a few nanometers it is very difficult to take it into account in the simulation and will be explored in a future publication, currently in preparation. Hence, modal mismatch simulations are not suitable for very narrow waveguides close to the lower cut-off of the propagation condition.

Figure 3 shows another very interesting phenomenon for both configurations with and without top oxide cladding. Apparently, there is an optimum waveguide width, which provides the lowest bend loss. This is also confirmed by the measurements, although the difference is within the measurement uncertainty. Obviously, wider waveguides are more susceptible regarding mode field displacement, which correspondingly increases modal mismatch and bend loss.

A comparison between the two waveguide configurations shows that the bend loss for the waveguide without top oxide cladding is about 2-4 times lower than with top oxide cladding, which is also confirmed by the simulation. This is remarkable because, the propagation loss is about 2-3 times greater compared to the waveguide with top oxide [5]. Supposedly, the lack of the top oxide cladding is beneficial in terms of mode overlap and therefore reduces the bend loss significantly. This may be caused by the higher index contrast of the waveguide without top oxide cladding, which confines the modes in the bend region more to the silicon nitride waveguide core and reduces therefore the mode mismatch. These findings are very valuable for optimized designs of environmental or bio sensors based on optical waveguides with a large sensitive area and low limits of detection (LOD).

References

- [1] A. Buchberger *et al.*, "Silicon Nitride Photonic Particle Detector—Experiments and Model Assessment," *IEEE Sens. J.*, vol. 21, no. 17, pp. 18829–18836, Sep. 2021, doi: 10.1109/JSEN.2021.3087633.
- [2] L. Chrostowski and M. Hochberg, *Silicon Photonics Design: From Devices to Systems*. Cambridge: Cambridge University Press, 2015.
- [3] A. Sakai, H. Go, and T. Baba, "Sharply bent optical waveguide silicon-on-insulator substrate," in *Physics and Simulation of Optoelectronic Devices IX*, 2001, vol. 4283, no. July 2001, p. 610, doi: 10.1117/12.432614.
- [4] M. Sagmeister *et al.*, "Monolithically Integrated, CMOS-Compatible SiN Photonics for Sensing Applications," in *Euroensors 2018: Proceedings*, 2018, doi: 10.3390/proceedings2131023.
- [5] A. Buchberger, J. Pulko, D. Morecroft, O. Basso, J. Kraft, and A. Bergmann, "Modelling Propagation Loss of PECVD Silicon Nitride Strip Waveguides: Evaluation and Assessment of Width Dependency," in *Conference on Lasers and Electro-Optics*, 2021, p. JTh3A.84, doi: 10.1364/CLEO_AT.2021.JTh3A.84.

In-line photo-thermal plasmonic detectors integrated in TiO₂ optical waveguides

(Student paper)

Andres Martinez¹, Vittorio Grimaldi¹, Deepak Kumar Sharma², Christian De Vita¹, Francesco Morichetti¹, Alexandre Bouhelier², Marco Sampietro¹

¹Dipartimento di Elettronica, Informazione e Bioingegneria, Via Colombo 81, Milan, 20133, Italy

²Laboratoire Interdisciplinaire Carnot de Bourgogne CNRS UMR 6303, 9 avenue Alain Savary, Dijon, 21078, France

*corresponding author: andresivan.martinez@polimi.it

We demonstrate a compact in-line surface plasmon photo-thermal detector integrated on a TiO₂ photonic platform. The detector is only 1.6 μm long and shows a sensitivity of -20 dBm with a bandwidth of more than 100 kHz and an insertion loss of 2.3 dB.

Keywords: Photo-thermal detector, plasmonic, waveguides

INTRODUCTION

Photonic Integrated Circuits (PICs) are evolving towards architectures with an ever-increasing scale of integration, which implement more and more complex functionalities. To develop PICs that can be reconfigured reliably, on-chip photodetectors must be integrated to locally monitor the optical power and closed-loop control systems have to be designed to set and stabilize their working point. Semiconductor photodetectors are widely employed in the near infrared-range because of their small size, fast detection speed, high detection efficiency [1] and monolithic integration on silicon and III-V photonic platforms. This family of transducers includes photodiodes [2], photoconductors [3] and sub-band-gap detectors based on surface state absorption [4]. However, these approaches cannot be deployed onto dielectric waveguide platforms, such as silicon nitride or oxide waveguides. We propose here a solution to this problem by integrating an in-line photo-thermal detector. The device consists of a metal strip placed underneath the waveguide sustaining surface plasmons polaritons (SPP). SPPs favor the absorption of optical power and from the temperature-dependent change of the metal resistivity it is possible to monitor the transmitted optical power by measuring the voltage drop across the metal [5,6,7]. Different configurations have been proposed for photo-thermal detectors such as a Wheatstone bridge [6] and the use of hybrid plasmonic waveguides [5].

In this work, we designed an in-line Surface Plasmon Detector (SPD) integrated in a TiO₂ platform that exploits the photo-thermal effect to monitor the optical power inside the waveguides. To maximize the responsivity of the device, we investigate the effect of the metal strip size in the coupling between the dielectric and plasmonic modes, the power dissipated in the metal, and the equivalent thermal resistance of the structure. We use a 3D Field Element Method multi-physics study including an optical, thermal, and electrical analysis. Experimental results show a sensitivity of -20 dBm and a bandwidth of about 100 kHz in an SPD with a length of only 1.6 μm.

DESIGN AND NUMERICAL ANALYSIS

The waveguide used for this work is realized with an air cladded 1.2 μm-wide and 370 nm-high titanium dioxide (TiO₂) core above a 2 μm-thick silicon dioxide (SiO₂) layer thermally grown of Si wafer. The SPD consists of a 30 nm-thick gold (Au) strip [see Fig. 1(a) and (b)] realized by a first step of e-beam lithography prior to the deposition of a TiO₂ layer. The layer is then structured by a second e-beam lithography combined with reactive ion etching to produce waveguides and grating input and output couplers. The waveguide and the detector are optimized to work at 1550 nm. A top view photograph of a fabricated SPD device is shown in Fig. 1(c).

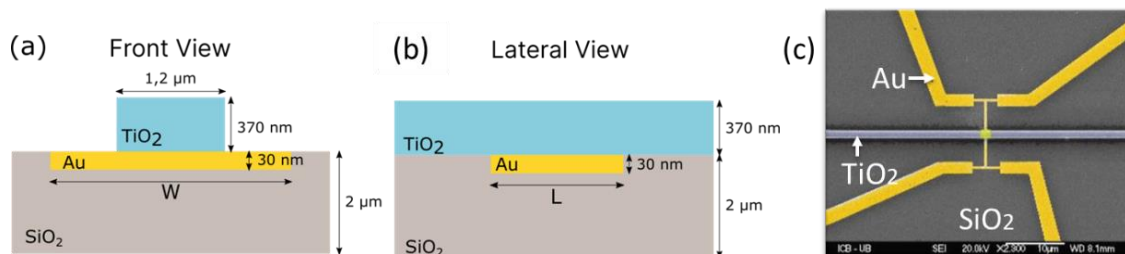


Fig. 1. Surface Plasmon Detector (SPD) geometry. (a) Front view of the SPD. The waveguide is made of TiO₂ (turquoise), the detector is Au (yellow), and the cladding is SiO₂ (tan). (b) Lateral view of the SPD. (c) Scanning electron micrograph of the fabricated device showing the sensing section underneath the waveguide and the access microscopic electrodes.

Surface plasmon modes are influenced by the thickness of the metal over which they propagate. For thick strips the evanescent component of the field penetrates more into the metal. However, the rapidly decaying SPP mode profile makes this contribution too small to dominantly affect the SPP mode propagation loss α [8]. Furthermore, if the gold is too thick, the large discontinuity of the propagation medium at the edges of the Au strip would severely increase backreflections and scattering and reduce the coupling to the detector. We find that α depends mostly on the field intensity adjacent to the Au strip, which increases for thinner strips. Thus, for sensing applications, the metal thickness should be maintained thin enough to reduce losses and increase the gold absorptance. The length of the detector L is the fundamental design parameter as it determines the amplitude of the transmitted optical wave and the gold absorbed power. For this structure, the SPD has a numerically determined fundamental SPP mode with a complex-refractive index $n_{eff} = 2.096 - i0.019$ which corresponds to a propagation loss of $0.67 \text{ dB}/\mu\text{m}$.

The simulated normalized transmittance P_{tx} versus the detector length is shown in Fig. 2(a). If the dielectric mode is TM polarized (orange) two independently propagating SPP modes are excited [9]. These modes propagate along the top and bottom surfaces of the metal with different speed and, depending on L , they will interfere constructively or destructively at the end of the strip. For this reason, the TM P_{tx} follows a decaying sinusoid with an oscillation period of $2.4 \mu\text{m}$. For $L = 1.1$ and $3.5 \mu\text{m}$, the SPP modes are out of phase and P_{tx} is almost zero. Instead, for $L = 2.3$ and $4.6 \mu\text{m}$, the SPP modes are in-phase and P_{tx} is maximum, although not equal to P_{in} due to coupling losses and gold absorption. On the other hand, the TE mode cannot excite the SPP modes and therefore it has an almost flat P_{tx} . The small fluctuations are caused by a Fabry-Perot cavity effect. Yet as the detector length increases, this effect reduces due to the absorption of the gold. As a result, the TE transmittance flattens after $L = 3 \mu\text{m}$. The cavity effect is also present in the TM mode but the beating between the two SPP modes remains the dominant effect.

The losses efficiency η defined as the ratio between the actual power dissipated in the gold P_d and overall losses P_l gives a direct measurement of the capacity of the gold to transform all the lost power into heat. In Fig. 2(b), the simulated losses efficiency is shown, highlighting how the TM mode (orange) exhibits both the oscillations mentioned previously: the fast fluctuations (500 nm period) due to the Fabry-Perot cavity are superimposed to the wide oscillations ($2.4 \mu\text{m}$ period) due to the coupling of the SPP propagating modes. For short lengths, P_l is dominated by the coupling mismatch and η is low. As the length increases the coupling losses remain constant but P_d increases and so does η . An efficiency of 42.5% is achieved for the TM mode at $L = 2.3 \mu\text{m}$ and 50.4% at $L = 4.7 \mu\text{m}$, which coincide with the transmittance peaks. This is a remarkable result since there are lengths for which the transmitted optical power and gold absorptance are maximum. The low efficiency (below 55%) is caused by the coupling losses and the mismatch between the waveguide mode and the SPPs modes, and it can be significantly improved by introducing a mode adapter at the input/output sections of the plasmonic waveguide.

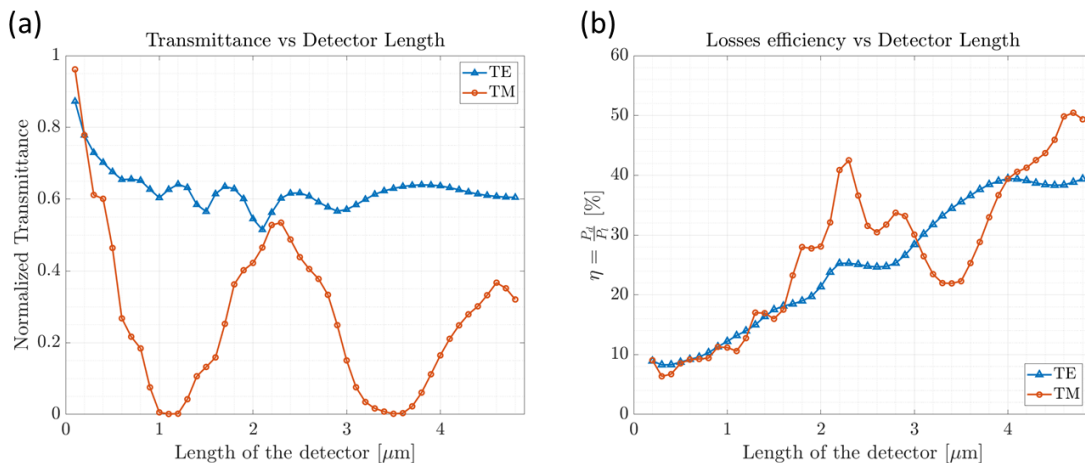


Fig. 2. (a) Normalized transmittance vs the length of the SPD. The TM excites two SPP modes that interfere constructively ($L = 2.3 \mu\text{m}$ and $4.7 \mu\text{m}$) or destructively depending on L . (b) Losses efficiency of the SPD. The maximum efficiency coincides with the maximum transmittance shown in (a).

DEVICE FABRICATION AND CHARACTERIZATION

Straight waveguides integrating a different number of cascaded detectors with the same length ($L = 1.6 \mu\text{m}$) were fabricated to assess the excess loss and the back reflections of the SPD. The TiO_2 waveguides are 1200 nm -wide, 370 nm -high and 1.5 mm -long. Light coupling into the chip was achieved by using grating couplers designed to operate on TM polarization. The metal layer of the detector has a thickness of 37 nm (3 nm Cr adhesion layer + 34 nm Au) and a width of $3 \mu\text{m}$ and it was deposited directly on top of the SiO_2 layer below the TiO_2 core of the waveguide.

By measuring the transmitted optical power, over a wavelength range from 1520 nm to 1580 nm, an insertion loss IL of about $2.3 (\pm 0.3)$ dB was observed, which is very close to the 2.0 dB estimated from electromagnetic simulations. To obtain the reflected power of the SPD, a circulator was added before the input fiber to collect the back reflected signal from the waveguide. A coherent optical frequency domain reflectometry (OFDR) [10] technique was employed to obtain the reflection coefficient of each SPD amounting to -17 dB.

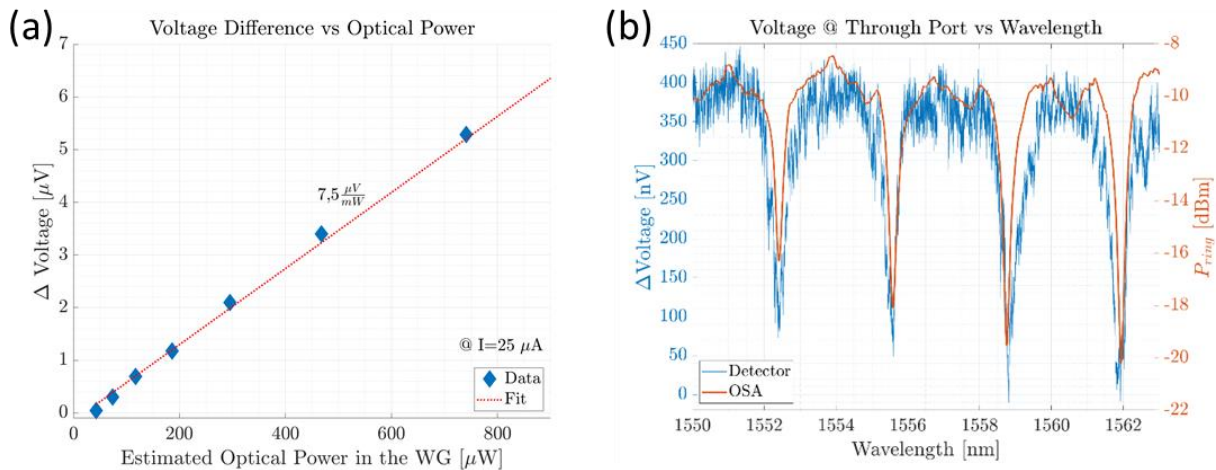


Fig. 3. (a) Measured responsivity of the SPD for $I_{bias} = 25 \mu A$. (b) Spectral response of a ring resonator acquired with the SPD.

Figure 3(a) shows the light-dependent change of the voltage drop across the gold strip of the SPD, as measured by a lock-in scheme, for increasing power in the waveguide, when a bias current $I_{bias} = 25 \mu A$ is applied. The voltage is linear versus the optical power and the responsivity R_d , which is given by the slope of the linear fit (red), equals $7.5 \mu V/mW$. The SPD can operate over a 15 dB dynamic range with a minimum detectable power of $P_{in} = -20$ dBm. These values can be improved by increasing the I_{bias} . The response time of the SPD was measured by modulating the input light with a square wave at 20 kHz and reading the detector voltage with an oscilloscope triggered by the modulating signal. The resulting time constant was $1.2 (\pm 0.07) \mu s$, that corresponds to a bandwidth of 132 kHz.

SPDs were also integrated at the output port of a microring resonator to monitor the wavelength response of the device. An example is reported in Fig.3(b), where the blue curve is the SPD measurement, while the reference curve (in orange) is acquired with an external optical spectrum analyser. The good agreement demonstrates the possibility of monitoring the working point of PICs by the proposed SPD in order to implement a closed-loop control system.

CONCLUSION

In conclusion, we demonstrated the possibility of monitoring in-line the light intensity in TiO_2 waveguides by exploiting photo-thermal effect in a surface plasmon based detector. The fabricated devices are very compact ($1.6 \mu m$ long) and their performance in terms of sensitivity (-20 dBm) and speed (>100 kHz) make SPDs good candidate for implementing monitor and control operations in dielectric waveguide platforms, where monolithic integration of semiconductor photodetectors is not a viable approach.

Acknowledgments: The work has been supported through H2020 grant number 871658 (Nebula).

References

- [1] R. Hui, *Introduction to Fiber-Optic Communications*, Chapter 4 - Photodetectors, Academic Press, 125-154, (2020)
- [2] D. Logan et al., *IEEE Photonics Technology Letters*, vol. 24, no. 4, pp. 261-263, (2012)
- [3] R. Kingston, *Optical Detectors*, Encyclopedia of Physical Science and Technology (III Edition), Academic Press, 237-253, (2003)
- [4] F. Morichetti et al., *IEEE Journal of Selected Topics in Quantum Electronics* 4, Vol. 20, 292-301, (2014).
- [5] H. Wu et al., *Nanophotonics*, vol. 6, no. 5, pp. 1121-1131, (2017).
- [6] J. Gosciniaik et al., *Opt. Express* 21, 5300-5308, (2013)
- [7] M.-M. Mennemanteuil et al., *Nanophotonics* 7, 1917 (2018)
- [8] H. Okda, S. Rabia, and H. Shalaby, *Opt. Soc. Am. B* 38, 1405-1415, (2021)
- [9] J. Homola, *Springer Series on Chemical Sensors and Biosensors*, Vol. 4, 2006
- [10] F. Morichetti et al., *Phys. Rev. Lett.* 104, 033902, (2010)

Numerical Analysis of Digital Pulse Modulation of Strongly Injection-Locked Whistle-Geometry Microring Lasers

Gennady A. Smolyakov¹ and Marek Osinski^{1,*}

¹Center for High Technology Materials, University of New Mexico, 1313 Goddard SE, Albuquerque, New Mexico 87106-4343, USA

*osinski@chtm.unm.edu

The potential of strongly injection-locked whistle-geometry semiconductor ring lasers for digital pulse modulation is investigated. Pulse modulation with up to 50 GHz repetition rate and substantially suppressed transient behaviour is demonstrated in numerical modelling.

Keywords: semiconductor ring laser, injection locking, ultrafast modulation

INTRODUCTION

Directly modulated laser sources with very high modulation bandwidths exceeding 100 GHz are highly desirable for the rapidly growing applications of RF optical fibre links. Optical injection locking has been actively researched for its potential to improve ultrahigh frequency performance of semiconductor lasers and to reach beyond the record values of modulation bandwidth achieved for free-running devices [1]. We have proposed an optical injection-locking scheme for modulation bandwidth enhancement, involving a distributed-Bragg-reflector (DBR) master laser monolithically integrated with a strongly injection-locked unidirectional whistle-geometry microring laser (WRL), illustrated in Fig. 1 [2]. Enhanced ultra-high-speed performance of that scheme in response to small-signal sinusoidal modulation has been confirmed in numerical modelling [2]. Large-signal analogue modulation has also been investigated and advantages of strong injection locking for high-fidelity large-signal modulation have been confirmed through numerical modelling by comparing high-speed performance of a strongly injection-locked WRL with that of a free-running ring laser [3]. In this work, we investigate the potential of strongly injection-locked WRLs for digital pulse modulation. Specifically, we address the question of potential optical output signal distortion due to transient behaviour of the laser in response to picosecond input pulses of injection current.

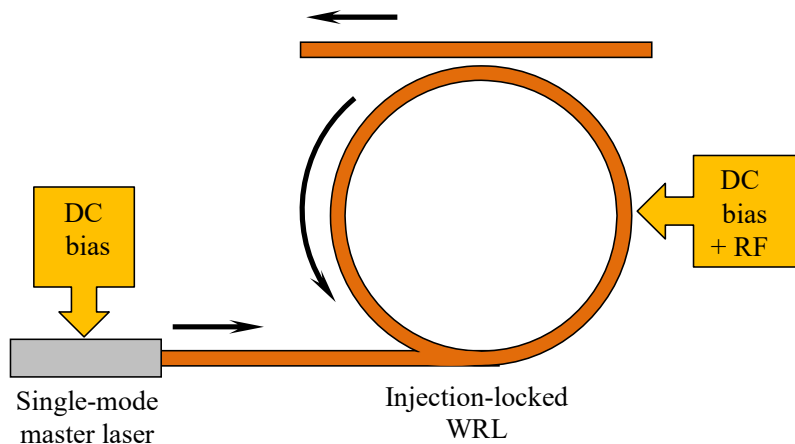


Fig. 1. Schematic diagram of a strongly optically injection-locked whistle-geometry semiconductor ring laser (WRL) monolithically integrated with a single-mode master laser.

APPROACH

Optical response of strongly injection-locked WRL to triangular injection current pulses of picosecond duration was investigated. The dynamic response of the WRL was modeled by a system of first-order rate equations written in terms of the photon densities, phases, and carrier densities in the single-frequency master and microring slave lasers. Parameters used for simulation were calculated for both the 50- μm long master DBR and the 2- μm -diameter ring lasers based on a deeply etched ridge-waveguide laser structure optimized for single-mode operation,

assuming a 1.55- μm GaInAs/AlGaInAs/InP multiple-quantum-well epitaxial structure of [4] with 7, rather than 6, quantum wells. The power reflectivity of the back DBR mirror was assumed to be 100%, whereas that of the front injecting DBR mirror was calculated at 1.55 μm wavelength to be $\sim 82.5\%$ for the front mirror consisting of two quarter-wave layers of benzocyclobutene (BCB) and one quarter-wave layer of semiconductor (refractive index equal to n_{eff}) in between, separating the identical ridge waveguide structures of the master laser and the injecting waveguide. We neglected the bending radiation losses under the assumption that the 2- μm -diameter WRL will eventually be implemented in a photonic-crystal-waveguide-based platform.

RESULTS

Special conditions have been determined in terms of the frequency detuning and injection current pulse duration for controlling the optical response in order to suppress transients. Pulse modulation of a 2- μm -diameter strongly injection-locked WRL with up to 50 GHz repetition rate with substantially suppressed transient emission tails and sufficiently high signal-to-noise ratio (S/N) has been demonstrated in numerical modeling for a sequence of triangular injection current pulses of picosecond duration (Fig. 2).

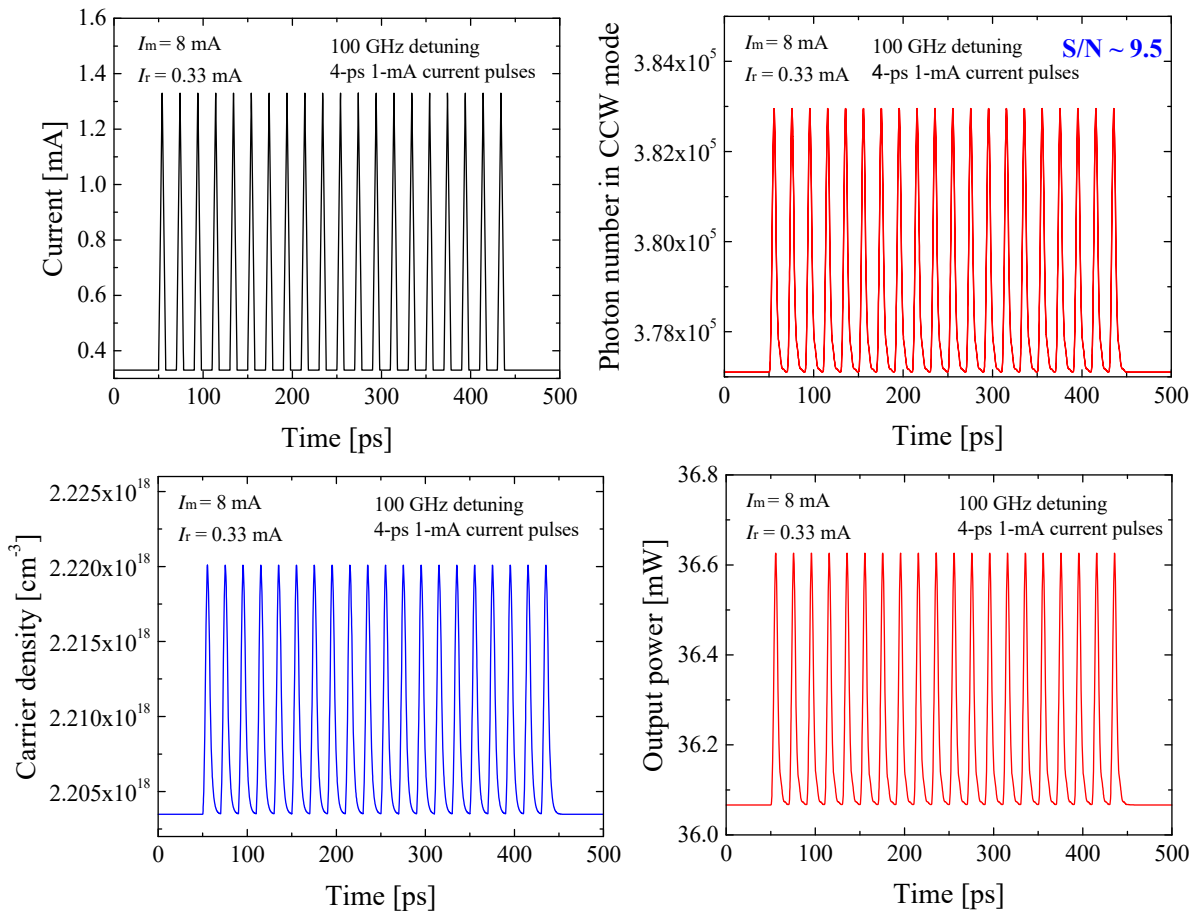


Fig. 2. Calculated optical and carrier density response of a strongly injection-locked WRL to a sequence of “one” bits, each bit represented by a triangular 4-ps injection current pulse of 1-mA amplitude, with the repetition rate of 50 GHz.

CONCLUSION

In conclusion, rate equation analysis has been performed of digital pulse modulation in a strongly injection-locked 2- μm -diameter whistle-geometry semiconductor ring laser. Digital data transmission rate of, at least up to 50 Gb/s has been predicted. Further improvement of S/N ratio and, therefore, higher repetition rates are possible for WRLs with higher differential gain (e.g., in strained QW laser structures).

Acknowledgements: This work was supported by the Office of Naval Research Grants N00014-17-1-2416 and N00014-21-1-2683.

References

- [1] E. K. Lau, L. H. Wong, and M. C. Wu, *Enhanced modulation characteristics of optical injection-locked lasers: A tutorial*, IEEE Journal of Selected Topics in Quantum Electronics, vol. 15, no. 3, pp. 618-633, 2009
- [2] G. A. Smolyakov and M. Osiński, *High-speed modulation analysis of strongly injection-locked semiconductor ring lasers*, IEEE Journal of Quantum Electronics, vol. 47, no. 11, pp. 1463-1471, 2011.
- [3] G. A. Smolyakov and M. Osiński, *Large-signal analysis of directly-modulated strongly-injection-locked whistle-geometry ring lasers*, Physics and Simulation of Optoelectronic Devices XXV (B. Witzigmann, M. Osiński, and Y. Arakawa, Eds.), SPIE International Symposium on Integrated Optoelectronic Devices OPTO 2017, San Francisco, CA, 30 Jan. – 2 Feb. 2017, Proc. SPIE 10098, Paper 100980L (12 pp.).
- [4] H. Y. Wong, M. Sorel, A. C. Bryce, J. H. Marsh, and J. M. Arnold, *Monolithically integrated InGaAs-AlGaInAs Mach-Zehnder interferometer optical switch using quantum-well intermixing*, IEEE Photonics Technology Letters, vol. 17, no. 4, pp. 783-785, 2005.

Characterization of Passively Mode-Locked lasers and Saturable Absorbers based on an InP quantum well amplifier suitable for active-passive integration at 1300 nm

Joel Hazan¹, Aser Nassar¹, Steven Kleijn², Kevin A. Williams¹, Erwin A.J.M. Bente¹

¹Photonic Integration Group, Electrical Engineering department, Eindhoven University of Technology, Groene Loper, Eindhoven, 5600 MB, The Netherlands

²Smart Photonics B.V., High Tech Campus, Eindhoven, 5600 MB, The Netherlands

We present the characterization of a two-section Fabry-Perot passively mode-locked laser, with 20 GHz repetition rate, and measurement of the unsaturated absorption of the saturable absorber. The devices have been realized using a new monolithic quantum-well based InP amplifier designed to be included in a photonic integration platform at 1300 nm. Q-switching and mode-locking regimes have been investigated as function of injected current and reverse bias voltage. RF peak power 40 dB over the noise floor and a 12nm broad frequency comb were observed for . The unsaturated absorption of a 100 μm long absorber revealed more than 300 cm^{-1} absorption losses at 1300 nm for -4V of applied reverse bias voltage.

Keywords: InP, Monolithic Integration, Quantum Wells, Passive Mode-Locking, Semiconductor Lasers, Saturable Absorber,

INTRODUCTION

The generation of short optical pulses is a key technology in developing ultrafast optoelectronics, and microwave photonics [1], but presents also applications in the distance metrology [2] and in high resolution imaging [3]. Passive mode-locking of laser diodes has been used widely to generate picosecond pulses in the 1300 nm and the 1550 nm wavelength regime [2],[3]. Monolithic passive Mode-Locked lasers (PMLLs) at 1300 nm are often base on quantum dot (QD) laser technology [6], which allows to obtain high pulse power and sub-picosecond pulse durations inside fully active laser systems [7]. The introduction of a new quantum well (QW) based semiconductor optical amplifier (SOA) at 1300 nm, suitable for a generic technology with a butt-joint monolithic active/passive integration scheme [8], leads to the development of QW based extended cavity Mode-locked laser in the 1300 nm wavelength range. Extended cavity designs can lead to higher coherent optical bandwidth and shorter pulse durations [9] due to the possibility to decouple the amplifier and the absorber lengths to the length of the laser cavity which determines the laser repetition rate. In this work we discuss the use of the amplifier developed by us [8] in a fully active Fabry-Perot PMML. The results obtained from the characterization of a PMLL with 20.3 GHz repetition rate are described. Signal to noise ratio of the RF beat signal from the laser of over 40 dB was measured together with a 20 nm wide frequency comb around 1340 nm. Unsaturated absorption measurements to investigate the behaviour of the amplifier under the reverse bias condition and no laser light are also presented. This is intended to be a first step in the realization of extended cavity PMLLs at 1300 nm with active/passive integration capabilities.

PASSIVE MODE-LOCKING

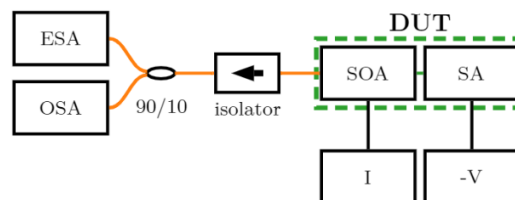


Fig. 1. Schematics of the experimental setup used to characterize the Passively Mode-Locked Lasers

Fully active Fabry-Perot cavity lasers are tested to evaluate the Mode-Locking operation of the quantum well active layers. The longer section that is used as an SOA and is forward biased with a current between 1 and 10 kA/cm^2 , while the shorter section is used as a saturable absorber (SA) when reverse biased. The two electrodes are separated by a 20 μm long isolation section where a 1 μm of p-doped InP was removed from the waveguide cross section to ensure an electrical resistance between the two electrodes [10]. The chip's uncoated facets reflections are calculated to be 31.7% from simulations. The chip length is 2 mm, which lead to a 20.4 GHz cavity free spectral range. PMLLs with SA lengths of 100 μm and 150 μm have been tested. A schematics of the setup used for the measurements is highlighted in Fig. 1 and briefly described as follows. The light is coupled out from the chip's facet with a lensed single mode optical fiber. After traveling through an optical isolator, which prevents the presence of

any external feedback into the laser cavity, the optical power is detected with an optical (OSA) and an high frequency electrical spectrum analyzer (ESA) connected to a high frequency photodiode (50 GHz). Passive mode-locking (PML) is demonstrated when the SA is reversely biased, and the SOA is forward bias with current injection. Fig. 2. A) shows the radiofrequency (RF) power from the photodiode as a function of current and reverse bias voltage applied to the two-section device. We can notice how the PML at 20.4 GHz happens at higher currents ranging from 100 mA to 115 mA when we increase the SA reverse bias from 0 to -0.7 V. In Fig. 2 b) the PMLL behaviour is depicted as a function of SOA current for a fixed reverse bias voltage of -0.5V. it is possible to identify different operating regimes as function of the injected current between 50 and 200 mA. Above threshold the two section laser operates in a Q-switching regime, i.e. low-frequency self-modulation of the cavity losses [11]. From the 2D map in Fig. 2 b) it is possible to identify the presence of harmonics spaced by 300 MHz around the fundamental frequency of the laser. As we increase the current, those harmonics are translated to sidebands centered to the mode-locking frequency. Further increasing of SOA current above 110 mA leads to mode-locked operation. Fig. 2 c) illustrates the repetition rate frequency tuning to lower frequencies with the current. The tuning of the repetition rate is found to originate from the gain/absorption saturation effects from the cavity's roundtrip frequency in passively mode-locked lasers [1]. We can see how the mode-locking frequency shifts from 20.4 to 20.23 GHz between 110 and 300 mA. At 300 mA, the output optical power on the SA is derived to be as high as 40 mW after subtracting the leakage current from the electrical isolation.

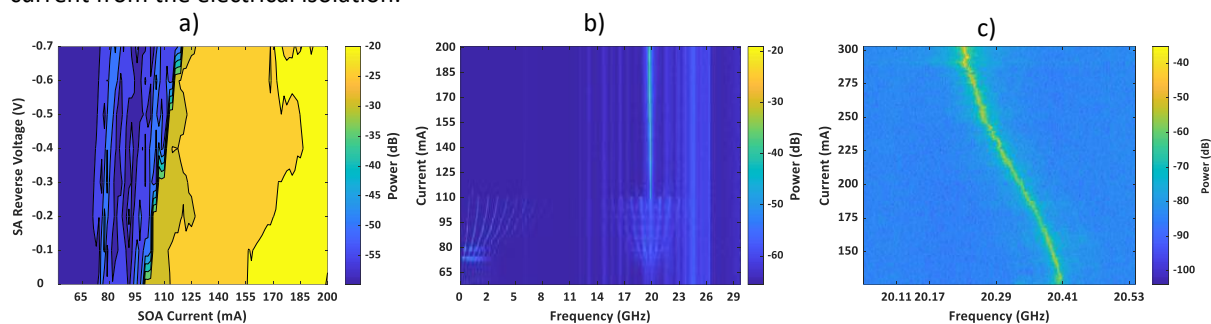


Fig. 2. A) RF Peak Power as function of SOA ($L_{SOA} = 1880 \mu\text{m}$) current and SA ($L_{SA} = 100 \mu\text{m}$) reverse bias voltage. b) 30 GHz RF spectra behaviour as function of SOA current for $V_{SA} = -0.5\text{V}$. c) Details of the RF peak tuning with the SOA current.

The mode-locking behaviour is analysed taking RF spectra with 30 GHz span and 3 MHz resolution as shown in Fig. 3 a). A clear resonance at 20.2 GHz, for an injected current of 270 mA, is shown together with a 40 dB signal to noise ratio. In Fig. 3 b) a 50 KHz resolution scan around 20.3 GHz with a 500 MHz span is presented. The RF linewidth is 4 MHz at -20 dB. A 3 dB linewidth is extracted to be 200 kHz from the linear power scale. Fig. 3 c) depicts an optical spectrum for an operating point of ML operation. It is possible to observe a broadband frequency comb, which is 12 nm within 20 dB below the maximum power, with a full width half maximum (FWHM) of 3 nm around 1340 nm. The frequency comb is shown at higher wavelength compare to the center of the gain spectra of the SOA, (1300 nm at 1 kA/cm²) as reported in [8], due to the very long SOA and SA sections. Long SOAs allow to have sufficient gain to bleach the SA at around 1340 nm, due to the relatively low absorption of 50 cm⁻¹ as shown in Fig. 4 b). This can also explain why in Fig. 2a) the mode-locking threshold current does not vary with the SA reverse bias voltage.

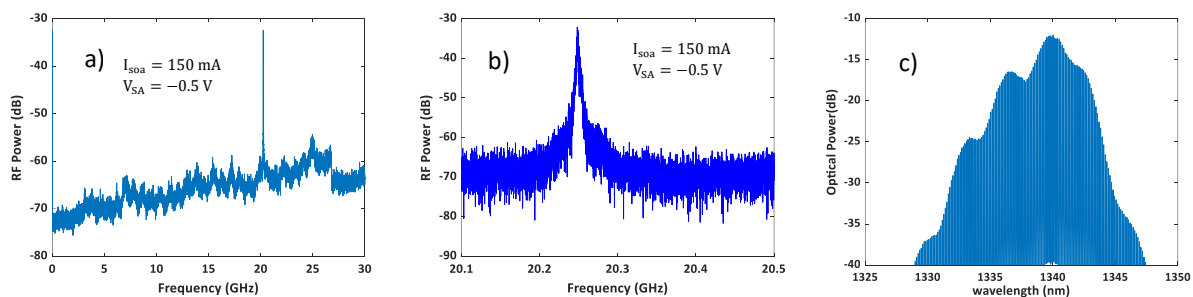


Fig.3. a) RF spectra obtained for a 2 mm long fully active device with $L=150 \mu\text{m}$ absorber reversely biased at $V=-0.5\text{V}$. b) Detail of the RF spectrum around the ML peak. The frequency resolution used in those RF spectra are 3 MHz (a) and 5 kHz (b) respectively. c) Optical spectrum obtained for $I_{soa} = 170 \text{ mA}$ and $V_{SA} = -0.7 \text{ V}$ with a resolution of 1 GHz.

ABSORPTION MEASUREMENTS

The saturable absorber is characterized through unsaturated absorption measurements of the SOA spontaneous emission. The absorption spectrum of a reversely bias SA is calculated from the transmitted power to the SA according to Beer's law as [12]. An anti-reflection (AR) coating is applied to the chip's facets to avoid any lasing behaviour from the two section devices. Fig 4 a) shows the schematics setup used in the absorption measurements.

The optical spectra of the ASE are recorded from both the two edges of the optical chip. We assume that the ASE spectrum generated by the SOA is the same in both directions. So in this way both the input power and the output power which is transmitted through the absorber are recorded. The amplified spontaneous emission is used as input reference power. To ensure an equal amount of coupling losses between the two facets, automated alignment routines are performed to maximize the output power as function of a piezo-controller movement [13]. In Fig. 4 b) the absorption spectra as function of reversely bias applied voltage between -1 and -6V, for a 100 μm long absorber, are plotted. As expected from theory, the absorption decreases at higher wavelengths due to the quantum confined stark effect [14]. Increasing the reverse bias voltage the absorption amplitude increases over the full range due to the voltage dependent carrier extraction from the absorber active region. The increase in the reverse bias induces a frequency shift of the absorption spectra towards shorter wavelength as a result of the electro-absorption. The second decrease in the amplitude of the absorption at low wavelengths (1250 nm) is under investigation. Measurements of polarization resolved absorption are planned to allow us to discriminate between the absorption from an excited state of the quantum wells or from the TM-polarized light absorption, which is shifted in frequency with respect to the TE-polarized light absorption, due to the presence of compressive strain inside the quantum wells, which removes the degeneracy of the light and heavy holes valence energy bands.

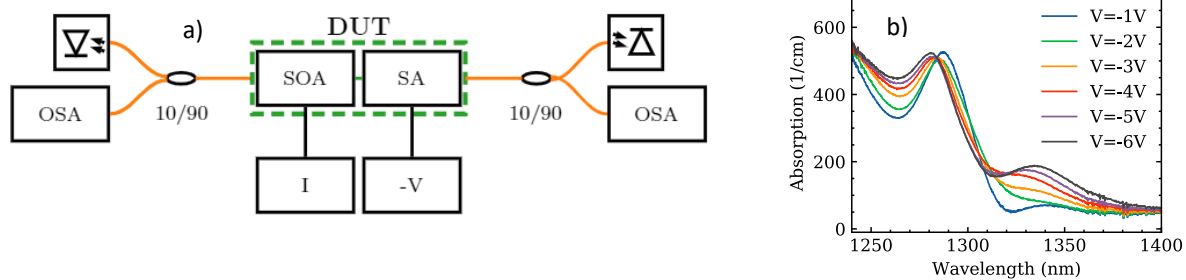


Fig. 4 a) Schematics of the experimental setup used in the optical absorption measurements. b) Absorption spectra for a 100 μm long absorber as function of the reversely bias voltage applied to its contact.

ACKNOWLEDGEMENTS

This publication is part of the project “An integrated Optical Coherence Tomography system for medical imaging at 1300nm” (project number 16251) of the research program HTSM2017 which is (partly) financed by the Dutch Research Council (NWO).

References

- [1] S. Arahira and Y. Ogawa, “Repetition-frequency tuning of monolithic passively mode-locked semiconductor lasers with integrated extended cavities,” *IEEE J. Quantum Electron.*, vol. 33, no. 2, pp. 255–264, 1997, doi: 10.1109/3.552266.
- [2] K. Hei *et al.*, “Distance Metrology with Integrated Mode-Locked Ring Laser,” *IEEE Photonics J.*, vol. 11, no. 6, pp. 1–10, 2019, doi: 10.1109/JPHOT.2019.2940068.
- [3] W. Drexler, “Ultrahigh-resolution optical coherence tomography,” *J. Biomed. Opt.*, vol. 9, no. 1, p. 47, 2004, doi: 10.1117/1.1629679.
- [4] G. Carpintero, M. G. Thompson, R. V. Penty, and I. H. White, “Low noise performance of passively mode-locked 10-GHz quantum-dot laser diode,” *IEEE Photonics Technol. Lett.*, vol. 21, no. 6, pp. 389–391, 2009, doi: 10.1109/LPT.2008.2011918.
- [5] K. A. Williams, M. G. Thompson, and I. H. White, “Long-wavelength monolithic mode-locked diode lasers,” *New J. Phys.*, vol. 6, pp. 1–30, 2004, doi: 10.1088/1367-2630/6/1/179.
- [6] V. F. Olle, M. G. Thompson, K. A. Williams, R. V. Penty, and I. H. White, “20 GHz picosecond pulse generation by a 1300nm mode-locked quantum dot master oscillator power amplifier,” *Conf. Opt. Fiber Commun. Tech. Dig. Ser.*, pp. 2–4, 2009, doi: 10.1364/ofc.2009.owj2.
- [7] E. U. Rafailov, M. A. Cataluna, and W. Sibbett, “Mode-locked quantum-dot lasers,” *Nat. Photonics*, vol. 1, no. 7, pp. 395–401, 2007, doi: 10.1038/nphoton.2007.120.
- [8] J. Hazan, S. Andreou, D. Pustakhod, S. Kleijn, K. Williams, and E. Bente, “1.3 μm InGaAsP / InP semiconductor optical amplifier compatible with an active / passive integration technology,” pp. 5–6, doi: 10.1109/3.283797.A.
- [9] V. Moskalenko, S. Latkowski, S. Tahvili, T. de Vries, M. Smit, and E. Bente, “Record bandwidth and sub-picosecond pulses from a monolithically integrated mode-locked quantum well ring laser,” *Opt. Express*, vol. 22, no. 23, p. 28865, 2014, doi: 10.1364/oe.22.028865.
- [10] J. Hazan, K. A. Williams, and E. A. J. M. Bente, “Gain spectra and saturation power measurements in a two-section InGaAsP / InP semiconductor optical amplifier at 1.3 μm ,” *Proc. IEEE Photonics Benelux Symp.*, p. 4, 2021.
- [11] E. Bente and M. Smit, “Ultrafast InP optical integrated circuits,” *Optoelectron. Integr. Circuits VIII*, vol. 6124, p. 612419, 2006, doi: 10.1117/12.660399.
- [12] M. Born and E. Wolf, “Principles of Optics - M.Born, E. Wolf.pdf.” 1986.
- [13] S. Latkowski, D. Pustakhod, M. Chatzimichailidis, W. Yao, and X. J. M. Leijtens, “Open Standards for Automation of Testing of Photonic Integrated Circuits,” *IEEE J. Sel. Top. Quantum Electron.*, vol. 25, no. 5, pp. 1–8, 2019, doi: 10.1109/JSTQE.2019.2921401.
- [14] L. A. Coldren, “Diode Lasers and Photonic Integrated Circuits,” *Opt. Eng.*, vol. 36, no. 2, p. 616, 1997, doi: 10.1117/1.601191.

Freeform optical arrays for free-space coupling into photonic integrated circuits

(Student paper)

Rakan E. Alsaigh¹, Martin P.J. Lavery¹

¹James Watt School of Engineering - University of Glasgow, Glasgow G12 8QQ, United Kingdom
e-mails: r.alsaigh.1@research.gla.ac.uk, martin.lavery@glasgow.ac.uk

Photonic integrated circuits are versatile technology to transport and process light. However, one challenge for these chips is the effective optical coupling from external environments, especially in free-space settings. We have designed a freeform optical array that can focus and tilt normally incident free-space beam to efficiently couple into grating couplers at 12° with a gain factor of 3.14 over normal coupling using a traditional plano-convex lens.

Keywords: Freeform optics, free-space optics, optical interface

INTRODUCTION

Photonic integrated circuits (PIC) are an emerging technology that have drawn wide attention over the past years due to their ability to transport and process light in a compact, versatile, and programmable form. These circuits have a vast potential to be exploited in a wide range of applications such as communication, sensing, nanophotonics, and quantum information processing [1]. One long-standing challenge for photonic integrated circuits is the optical interface between the chip and the external world, mainly due to the requirement of the incident field to be matched to that accepted by the chip, where multiple coupling mechanisms have been explored over the years to facilitate such coupling [2]. Grating coupler is perhaps the most preferred solution to bridge the coupling gap in photonic chips due to their increased design flexibility, integration density, and testing feasibility [2–4]. However, one common challenge for these grating couplers is the efficient optical coupling from external sources. This is mainly due to the fact that grating couplers are usually optimised to collect and radiate optical fields at a specific angular tilt that fulfils the diffraction directionality requirement for a maximum transmission and minimum back-reflection [5].

The diffraction directionality in grating couplers require the incident beam to be tilted, e.g. be optimised for 10° tilt [6] off vertical, to minimise back reflection and break the grating bidirectional symmetry [3]. This requirement is attributed to the second-order diffraction back reflections and the fact that normally incident light onto the grating would symmetrically couple and split into both diffraction directions along the grating, resulting in only 50% of the coupled light being radiated toward the waveguide. This is usually addressed by tilting the incident field (or the chip) to break such symmetry. Additionally, there have been considerable investigations to enhance true vertical coupling [7–9], however, such alignment would generally induce additional losses and result in relatively lower coupling efficiency than the tilted geometries [3]. Even though the use of tilted optical fibres have been sufficient for many static applications, the desire to exploit photonic integrated circuits in future deployable, dynamic, and readily packaged platforms, such as imaging and sensing technologies, raise a considerable demand for solutions that allow efficient vertical coupling.

In this work, we present the design of a compound freeform element that can potentially be interfaced with photonic chips for efficient vertical free-space optical coupling. This element consists of a lens on one side and freeform surface on the other to readily focus and tilt normally incident beam at an angle of 12° for use on top of standard angle-sensitive grating couplers. The novelty of this design is not only due to its optical compound, but also due to the freeform structure, see Figure. 1(a), that was numerically optimised to allow for mode match the field to that accepted by on-chip surface gratings. Through the modelling of this design on top of standard grating coupler at normal incidence, we expect a coupling efficiency that is 3.14 times greater than a beam normally coupled through traditional plano-convex lens at a central wavelength of 1550 nm. This element can readily be arranged in an array to allow a seamless mapping of a single input field onto an array of couplers for chips with higher dimensionality and improved resolution, see Figure. 1(b).

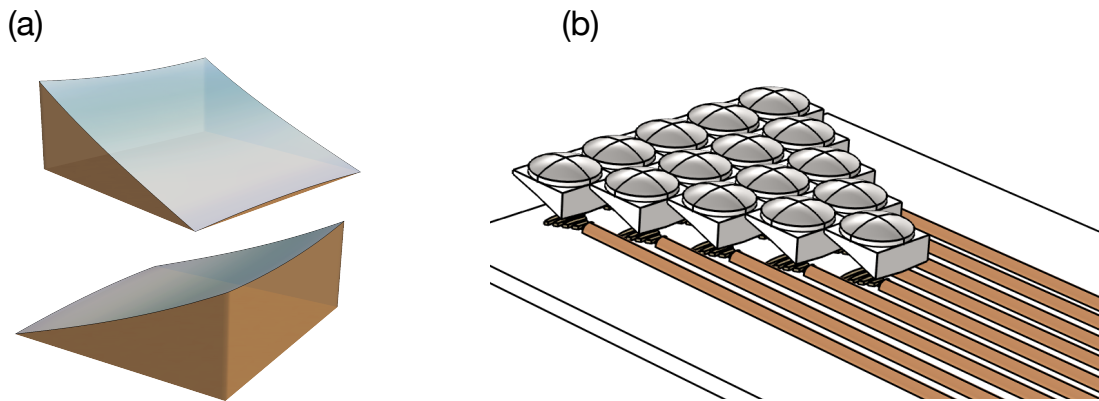


Figure. 1 (a) Illustrations of a prism-like freeform surface that can tilt the focused beam while accounting for the phase variations of the focused beam for equivalent deflection (b) Illustration of an array of our freeform element on top of an array of grating couplers, where such approach could potentially allow efficient free-space interface with integrated photonic circuits and facilitate their use in various optical applications.

Freeform Element Design and Modelling with Grating Coupler

Given the requirement for incident fields to match the numerical aperture and angular tilt accepted by grating coupler for efficient beam coupling, the first design step to address these optical requirements was to model the optical fields accepted by the grating couplers and subsequently optimise an optical surface to meet these requirements. For a standard grating couplers with a grating pitch of 630 nm, etch length of 315 nm, and etch depth of 70 nm; we modelled the field that can be efficiently collected by these grating couplers to have an optimum angular tilt of 12° in free-space. To match such optical field and address the challenge of performing two optical functions with minimum optical losses, a compound freeform element was derived through numerical optimisation to simultaneously focus and tilt normally incident field using a plano-convex lens and a wedge-like freeform surface. This was initially derived using a lens only, where the expected ray positions and distributions at its focal plane were calculated. These positions are then compared to the positions of a beam transmitted through a wedge prism only with a deflection angle that matches the tilt of standard grating couplers of 12° in free-space, providing the associated radial ray displacement for the given angular shift and allow for 2D mapping from the initial spots position to the 'target' tilted position. This is a crucial step to create a geometrical map to optimise the prism surface from a wedge to a freeform surface that accounts for phase shifts induced by the lens and closely map the beam to the desired target positions. Once this map is calculated, a finite number of evenly spaced hexahedrons, with initial overall dimensions similar to the 12° wedge prism, are attached to the two central axes of the flat surface of the lens. These hexahedrons are then optimised using a gradient-free Nelder-Mead algorithm in Comsol Multiphysics to map the incident rays from the initial to the target positions. Using this optimisation method, a control constraints function was applied to ensure that each adjacent hexahedrons have at least two connected points at the edge to avoid any surface discontinuity that can reduce surface quality and ensure seamless surface manufacturability. The final design of this freeform surface have an overall side thicknesses of 3 μm and 19.2 μm with its flat surface bonded to a convex lens with an NA of 0.3, radius of curvature of 46.3 μm , equivalent focal length of 91 μm ; where this single element can be formed in triangular array for use with a triangle array of grating couplers with an increased effective fill factor of over 95%, see Figure. 1(b).

Upon the design and optimisation of the freeform element, theoretical modelling of its performance was investigated in terms of transmission efficiency and coupling efficiency into grating couplers. The first transmission efficiency model looked into how much of the optical power is transmitted through the compound element, which results in transmission efficiency of 91.8% at normal incidence, which is almost consistent with the traditional 4% back-reflection losses per surface for uncoated elements, see Figure. 2(a). As the incident beam might vary from a perfect normal incidence, we further examined the angular acceptance of this lens over 20° field of view and the transmission efficiency is expected to fall to a minimum of 89.7% at -10° , see Figure. 2(a). Although this is still relatively high coupling efficiency, the mode profile at such angles is expected to not be maintained due to off-axis distortion and the axial symmetry in the element. To further investigate the functionality of our optical design that potentially satisfies the focus and tilt requirements of grating couplers with minimum optical losses, we utilised numerical modelling based on a finite element method (FEM) to quantify the free-space coupling performance onto a standard surface coupler. We simulated both the freeform element and grating design in a single modelling environment to quantify the percentage of power that can be directed by the element and coupled by the grating

toward the waveguide, and potentially onto the chip. With our freeform element placed one focal length away from the grating coupler, an excitation port was used to release a Gaussian beam in free-space to be normally incident onto the full aperture of our element and then propagated and inputted onto the grating coupler. The transmitted power by this grating is then computed using a detection port located along the direction of the waveguide for c-band wavelengths between 1520-1570 nm in steps of 5 nm, see Figure. 2(b). To directly compare the coupling efficiency of our freeform element to traditional vertical coupling techniques, a normally incidence beam propagating from a fibre port as well as a normally incidence beam focused by the plano-convex lens in free space were modelled in place of our element and the power coupled by the grating for both cases was also calculated, see Figure. 2(b). These numerical results show that our freeform element outperforms the other normally incident reference optics and improve the coupling efficiency onto the grating coupler, with a coupling efficiency increase factor of 3.14 and 55 times greater than a beam normally coupled through traditional plano-convex lens and an optical fibre at a central wavelength of 1550 nm, respectively. This is expected to largely be due to the angular tilt induce by our element that matches the NA and angle of the grating. It is important to note that such coupling efficiency is dependent on the position of illuminating beam with respect to the grating coupler, where such position was optimised in our model for maximum coupling.

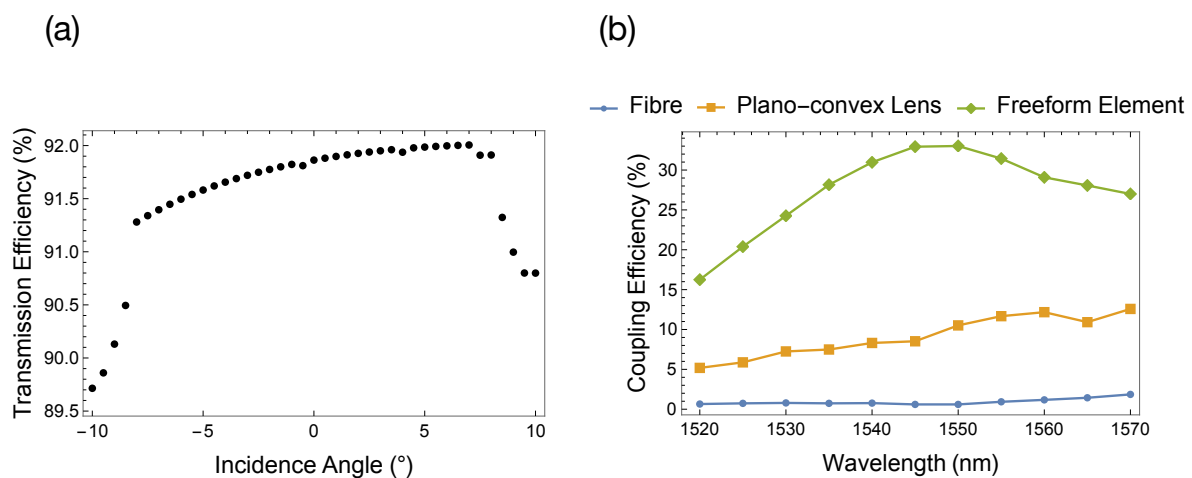


Figure. 2 (a) Simulation of the angular transmission efficiency of the freeform element for incident angles of $\pm 10^\circ$. The difference in efficiency between the minus incidence angles and the plus incidence angles is due to the asymmetrical behaviour of the freeform surface along one of its geometrical axis. (b) Simulation of the coupling efficiency of a grating coupler when our freeform element is placed on top of the coupler for different wavelengths with a normal incident beam. This model is compared to the use of a plano-convex lens or optical fibre instead of our element for different wavelengths with normally incident beams.

Discussion

We designed a novel freeform element that can simultaneously focus and deflect a normally incident beam to match the coupling requirements of standard surface grating couplers. This element consists of three compounded elements; convex lens to focus the light and a freeform prism-like structure to mode match to the angled couplers on photonic chip. Although our design is optimised for 12 degrees tilt angle that matches the free-space incident angle of standard grating couplers and increases the effective fill factor to almost over 95%, this method provides a ray mapping process that can be applied to develop different angular specs, transformations, and functions.

References

- [1]. J. Capmany and D. Perez, *Programmable Integrated Photonics* (Oxford University Press, 2020).
- [2]. W. Bogaerts and D. Vermeulen, "Off-Chip Coupling," in *Handbook of Silicon Photonics* (CRC Press, 2013).
- [3]. L. Cheng, et al., "Grating Couplers on Silicon Photonics: Design Principles, Emerging Trends and Practical Issues," *Micromachines* 11, (2020).
- [4]. F. Van Laere, et al., "Focusing polarization diversity grating couplers in silicon-on-insulator," *J. Light. Technol.* 27, 5 (2009).
- [5]. R. Marchetti, et al., "Coupling strategies for silicon photonics integrated chips [Invited]," *Photonics Res.* 7, 2 (2019).
- [6]. X. Chen, et al. "Apodized Waveguide Grating Couplers for Efficient Coupling to Optical Fibers," *IEEE Phot. Technol. Lett.* 22, 1156–1158 (2010).
- [7]. G. Roelkens, et al., "High efficiency grating coupler between silicon-on-insulator waveguides and perfectly vertical optical fibers," *Opt. Lett.* 32, 1495–1497 (2007).
- [8]. X. Chen, C. Li, and H. K. Tsang, "Fabrication-Tolerant Waveguide Chirped Grating Coupler for Coupling to a Perfectly Vertical Optical Fiber," *IEEE Photonics Technol. Lett.* 20, 1914–1916 (2008).
- [9]. Z. Zhang, et al., "High-efficiency apodized bidirectional grating coupler for perfectly vertical coupling," *Opt. Lett.* 44, 5081–5084 (2019).

Inverse Design of Nanophotonic Circuitry Components based on Reinforcement Learning

(Student paper)

Marco Butz^{1,2,4}, Alexander Leifhelm^{1,2}, Marlon Becker³, Benjamin Risse³ and Carsten Schuck^{1,2,*}

¹Institute of Physics, University of Münster, Wilhelm-Klemm-Str. 10, 48149 Münster, Germany

²Center for Soft Nanoscience, Busso-Peus-Str. 10, 48149 Münster, Germany

³Institute for Computer Science, University of Münster, Einsteinstr. 62, 48149 Münster, Germany

⁴marco.butz@uni-muenster.de, *carsten-schuck@uni-muenster.de

We introduce a reinforcement learning-based method for solving the pixel-discrete inverse-design problem. The approach is capable of producing highly efficient, yet compact photonic circuit components of any desired linear optical functionality. We apply the algorithm to design a nanophotonic waveguide-mode converter ($TE_{00} \rightarrow TE_{20}$) with a conversion efficiency of more than 85% and compact footprint of only a few vacuum wavelengths.

Keywords: *Inverse-Design, Reinforcement Learning, Nanophotonic Circuits*

INTRODUCTION

The complexity of photonic integrated circuits is increasing steadily as optical functionalities are replacing electronic integrated circuits and open new information processing capabilities, e.g. in quantum photonics. To sustain the growth of nanophotonic applications, novel device functionalities and compact footprints will be required. Currently, photonic integrated circuit components are predominantly designed following a bottom-up approach, where the designer aims to exploit intuitive physical effects in combination with brute-force methods for device optimization purposes. The layout for a nanophotonic waveguide mode converter, for instance, would be based on evanescent wave coupling and hybrid mode effective refractive index matching [1]. In consequence, the resulting devices suffer from large footprints and are limited in the number of possible functionalities as complex phenomena, such as multi-wave-interference effects cannot be considered, because they are not accessible by physical intuition. Consequently, the overwhelming part of the vast design space that is available with modern nanofabrication techniques, in particular those featuring sub-wavelength dimensions, is not accessible. This method is opposed by top-down approaches, where the device is seen as a pixel-discretized black-box, which is the subject of an optimization problem where known inputs and desired outputs are defined as boundary conditions. Here, the limitations mentioned above do not exist and – given a suitable computational routine – complex devices with sub-wavelength features may be found that realize previously inaccessible functionalities and smaller device footprints [2].

Generally, photonic black-box optimization problems are of non-convex nature. Thus, following inverse-design approaches that rely on gradient techniques to produce efficient device layouts on computationally feasible timescales is not a trivial task. Previously, numerous computational methods employing convex optimization or direct search methods have been demonstrated. All of them suffer from drawbacks such as exponential runtime scaling with increasing design space, solutions featuring continuous permittivity distributions that cannot be produced with common nanofabrication methods, or failure to consider stochastic processes due to their dependency on calculated gradient fields [3].

In this work we show how to phrase the nanophotonic black-box optimization problem as a reinforcement learning (RL) application. Our method overcomes previous limitations by leveraging a distributed and highly parallel computational architecture, showing stable learning behavior that scales well with increasing design space dimensionality. The direct application of general reward-based reinforcement learning algorithms enables us to optimize any pixel-discrete nanophotonic device accessible by electromagnetic simulations. We can manipulate the dataflow in different stages of the algorithm, allowing us to implement arbitrary geometry constraints, e.g. for observing limitations imposed by nanofabrication capabilities.

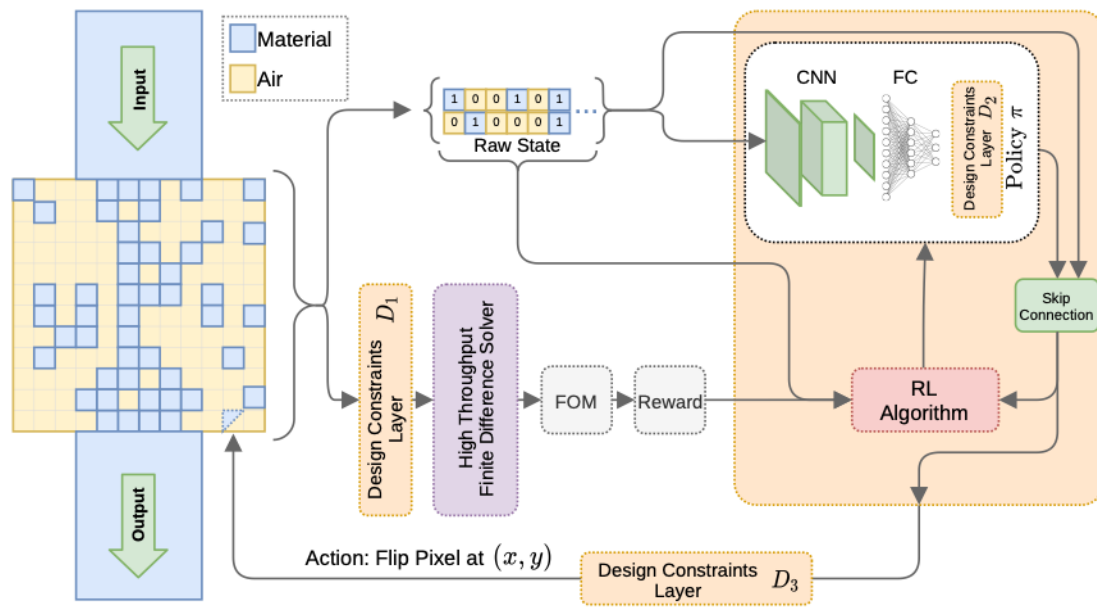


Fig. 1. Data-flow in a RL-worker. The device shown on the left is the numerical representation of the optimization problem as specified by parameters such as pixel-size, device-dimensions and the waveguide-modes under consideration. The agent (orange box) interacts with the environment while the actions and observations are processed and possibly altered in between.

METHOD AND APPLICATION

Reinforcement learning is a biology-inspired domain of artificial intelligence where an autonomously acting entity referred to as the agent explores an environment by taking a series of actions. These actions change the state of the environment, and a reward is reported back to the agent. The reward is a measure for the improvement in device performance achieved by the action, such that an optimal behavior of the agent can be obtained by maximizing the cumulative reward following a policy, understood as a mapping from states to actions. Fig. 1 shows how this concept is applied to the pixel-discrete nanophotonic inverse-design problem. The device shown on the left represents the environment, where we define the state to be the two-dimensional pixel-configuration encoding the presence of material or air as logic values ,1' or ,0', respectively. We refer to this representation as the „raw state“, which is further processed in the policy-determining convolutional neural network (CNN) and fully connected layers (FC). To suppress the common problem of reward-hacking through repetitive behavior, we combine the network's output with the initial raw state using a specifically tailored skip connection, which bypasses the convolutional processing layers. Finally, a soft-max function is applied to the output to determine the next action from the corresponding probability distribution, i.e. the coordinates of a pixel which is to be flipped from material to air or vice versa. To calculate the associated reward, the device performance is evaluated under consideration of the surrounding waveguide geometry and involved input- and output-modes using a customized high-throughput Finite Difference Frequency Domain (FDFD) solver. The results of the simulation are used to calculate a figure of merit, which in turn is used as an input for the reward calculation, while both functions can be specified by the user in order to account for special requirements of specific devices. The resulting tuple of state, action and reward is subsequently processed by a reinforcement learning algorithm adjusting the weights in the neural network to optimize the current policy.

The workflow depicted in Fig. 1 is implemented in an isolated instance, which we refer to as a „worker“. Multiple workers can be employed on remote machines, communicating with a central instance [4], thus granting scalability of our approach ranging from single desktop-PCs to whole HPC-clusters. Multiple levels of parallelism here enable us to optimize devices in large and complex environments.

In Fig. 2 we show an exemplary application of our method on a nanophotonic waveguide-mode converter, which is supposed to convert the fundamental quasi-transverse electric (TE_{00}) to the higher order quasi- TE_{20} waveguide-mode at a wavelength of 775 nm. We configure the device to have a length of 3.2 μm and a width of 1.6 μm discretized in 80 and 40 pixels, respectively, realized in 200 nm thin silicon-nitride-on-insulator. The pixels are quadratic with a side-length of 40 nm and the optimization, including all involved simulations, are conducted in full 3D. Through one of the design-constraint-layers depicted in Fig. 1, namely D_3 , we enforce a symmetric layout. The final device is shown in Fig. 2 (left), while the corresponding evolution of the maximum figure of merit, as calculated by 8 parallel workers, are shown in Fig. 2 (right). The learning behavior is strong, stable and reproducible, resulting in successful mode conversion with an efficiency of 85.5% (-0.68 dB) and low crosstalk into the TE_{00} -mode of 2.8% (-15.53 dB). Our implementation is sufficiently versatile to allow for biasing the results in order obey fabrication constraints, if necessary.

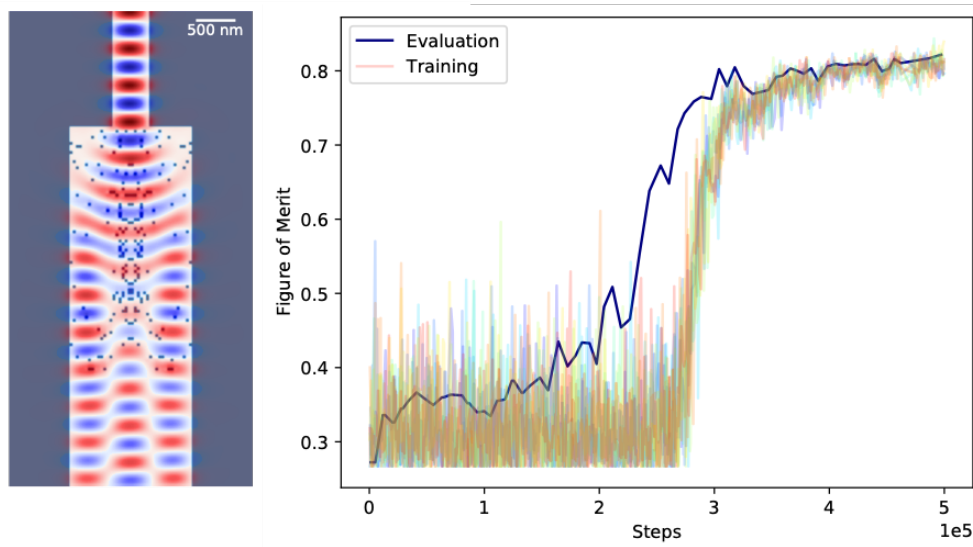


Fig. 2. Optimization of a nanophotonic waveguide-mode converter. The final device with the electric field overlay (E_y -component, perpendicular to the direction of propagation) excited by a distribution corresponding to the fundamental waveguide-mode is depicted on the left. Dark blue and white background indicate the presence of air and material, respectively. The figure of merit, which is representative of the conversion efficiency, plotted against the total number of steps taken by all workers is shown on the right.

CONCLUSION AND OUTLOOK

In this work, we apply RL, as one of the most promising approaches in artificial intelligence, to nanophotonic inverse-design. Our method is highly flexible as it allows for the optimization of any device accessible by electromagnetic simulations. Theoretical advances in the field of reinforcement learning will be directly applicable to this approach and thus we expect to immediately benefit from recent findings such as sophisticated approaches to handle delayed- or sparse-reward environments or novel and more accurate neural-network architectures to derive the current state-action-policy.

Acknowledgements: C.S. acknowledges support from the Ministry for Culture and Science of North Rhine-Westphalia (No. 421-8.03.03.02-130428).

References

1. LW. Luo, N. Ophir, C. Chen et al. *WDM-compatible mode-division multiplexing on a silicon chip*, Nature Communications 5, 3069, 2014
2. S. Molesky, Z. Lin et al. *Inverse design in nanophotonics*, Nature Photonics 12, pp. 659–670, 2018
3. Jesse Lu, Jelena Vučković, *Objective-first design of high-efficiency, small-footprint couplers between arbitrary nanophotonic waveguide modes*, Opt. Express 20, pp. 7221-7236, 2012
4. M. Volodymyr, A. P. Badia et al. *Asynchronous Methods for Deep Reinforcement Learning*, Proceedings of The 33rd International Conference on Machine Learning, PMLR 48:1928-1937, 2016

Polarization mode converter based on hybrid integration of nanowires on a silicon waveguide

A. Emre Kaplan¹, Valerio Vitali^{2,*}, Francesco Rossella³, Valeria Demontis³, Andrea

Fontana⁴, Periklis Petropoulos², Vittorio Bellani⁵, Cosimo Lacava^{1,2} and Ilaria Cristiani¹

¹Department of Electrical, Computer and Biomedical Engineering, University of Pavia, Pavia, IT27100, Italy

²Optoelectronics Research Centre, University of Southampton, SO17 1BJ, United Kingdom

³NEST, Scuola Normale Superiore and Istituto Nanoscienze-CNR, Pisa, IT56126, Italy

⁴Istituto Nazionale Fisica Nucleare (INFN)-Pavia Section, Pavia, IT27100, Italy

⁵Department of Physics, University of Pavia, Pavia, IT27100, Italy

*v.vitali@soton.ac.uk

We present a novel technique to realize polarization mode conversion in silicon waveguides via hybrid integration of InP nanowires. A total TE to TM polarization conversion can be achieved by a proper selection of the nanowire dimensions, whose impact on the conversion efficiency, bandwidth and insertion losses is discussed. The proposed approach allows post fabrication trimming and opens the way to reconfigurable polarization-controller circuits.

Keywords: nanowires, polarization, silicon waveguides

INTRODUCTION

The precise and dynamic control of the state of polarization of light is essential for the development of complex integrated photonic circuits (PICs). Several demonstrations on polarization manipulation in integrated waveguides have been reported in the literature, for example, based on asymmetric waveguide geometries, tapered waveguides, plasmonic effects, metamaterials and grating-assisted structures [1-7]. Even though these devices show relatively low insertion losses (typically <1 dB) and relatively high polarization extinction ratios (>15 dB), they typically require complex fabrication processes such as multiple lithography steps. Furthermore, the degree of polarization conversion is a priori determined by the initial design and fabrication processes and it cannot be modified or tailored at a post-processing stage. In this paper, we report on a new approach for polarization conversion in integrated devices, based on hybrid integration of semiconductor nanowires (NWs) on standard silicon waveguides. The proposed scheme allows both full TE-TM polarization conversion and an easy reconfiguration of polarization manipulation functions after fabrication. Indeed, NWs can be placed, moved or removed according to the designer needs, as previously reported in [8], enabling post-fabrication trimming and ultimately leading to a novel approach for the realization of reconfigurable polarization-coded integrated circuits. We note that such a hybrid approach can be extended to a vast range of 2D materials that can be deposited on PICs after fabrication.

RESULTS

Polarization conversion in integrated waveguides can be achieved by introducing a periodical variation of the waveguide effective birefringence [9]. In our design, this effect is obtained by placing an array of NWs on the top of a silicon waveguide, in a configuration able to periodically break the waveguide symmetry. We numerically studied the polarization rotation induced by an InP NW array integrated on top of a standard single mode silicon on insulator (SOI) waveguide (cross section of 450 nm x 220 nm), as shown in Fig. 1. Device performance in terms of polarization conversion efficiency was simulated by 3D Finite-Difference Time-Domain (FDTD) simulations using a commercial solver. The input beam was set to the linear TE polarization state at the input of the waveguide.

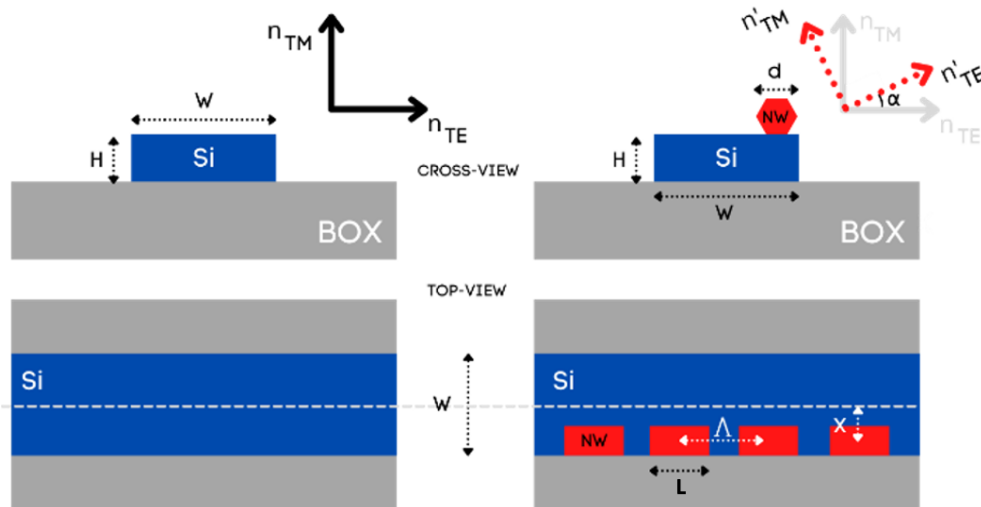


Figure 1: Cross- and top-view of a silicon waveguide being integrated with an array of NWs. The insertion of a NW results in a rotation of the waveguide effective principal axes of birefringence by an angle α . Parameters definition: W : waveguide width; H : waveguide height; d : NW diameter; Λ : NW period; L : NW length; x : offset position between waveguide and NW centres.

In the waveguide section without the NW (see Fig.1 (left panel)), the waveguide birefringence is essentially determined by the structure geometry. Therefore, the birefringence principal axes corresponded to the TE and TM directions and the effective refractive indices were equal to $n_{\text{eff, TE}} = 2.35$ and $n_{\text{eff, TM}} = 1.73$ respectively, as calculated at $\lambda = 1550$ nm for a waveguide with $W = 450$ nm and $H = 220$ nm. As qualitatively shown in Fig. 1 (right panel), the insertion of a NW on top of the silicon waveguide induces the propagation of two hybrid quasi-TE and quasi-TM modes, with a rotation of the effective principal polarisation axes of the waveguide by an angle α . This results in coupling of the optical power in the unperturbed structure from the TE to the TM mode. The overall polarization conversion efficiency along the waveguide is determined by a phase matching (PM) condition that depends on the NW dimensions, array period and on the effective birefringence along the principal axes exhibited by the structure without or with the NWs. In simple periodic structures, this effect can be modeled by a sequence of identical waveplates with a fixed and alternate rotation of the principal axes. In this case, the PM condition can be easily calculated by imposing the period of the birefringence variation to be equal to $\lambda/(\Delta n)$, where Δn is the effective refractive index difference of the two hybrid modes.

The NW radius and length are critical to the conversion process, since they determine both the angle of rotation of the principal axes and the amount of birefringence perturbation. Fig. 2 shows the results of our numerical simulations. The polarization conversion efficiency is plotted as a function of the number of NWs and the NW length L for different values of the NW radius R . As can be seen from Fig. 2 (left panel), the use of larger NWs allows achieving a 100% TE-TM polarization conversion efficiency using a lower number of elements compared to the case of smaller NWs, suggesting that the NW radius has a significant impact on the effective angle of rotation α . On the other hand, NWs with larger radius require a longer interaction length L to get a complete polarisation conversion from the TE to the TM mode (see Fig. 2 (right panel)). Overall, this results in a greater device insertion loss, since the optical propagation losses increase as a function of the NW length L , essentially due to a stronger light scattering, as is shown in Fig. 2 (right panel). Another aspect worth noting is the bandwidth of the polarization conversion efficiency. As a result of our simulations, we observed that the use of NWs with larger radius allow achieving a broader operational bandwidth, with an almost-flat 100% TE-TM polarization conversion efficiency across the C band.

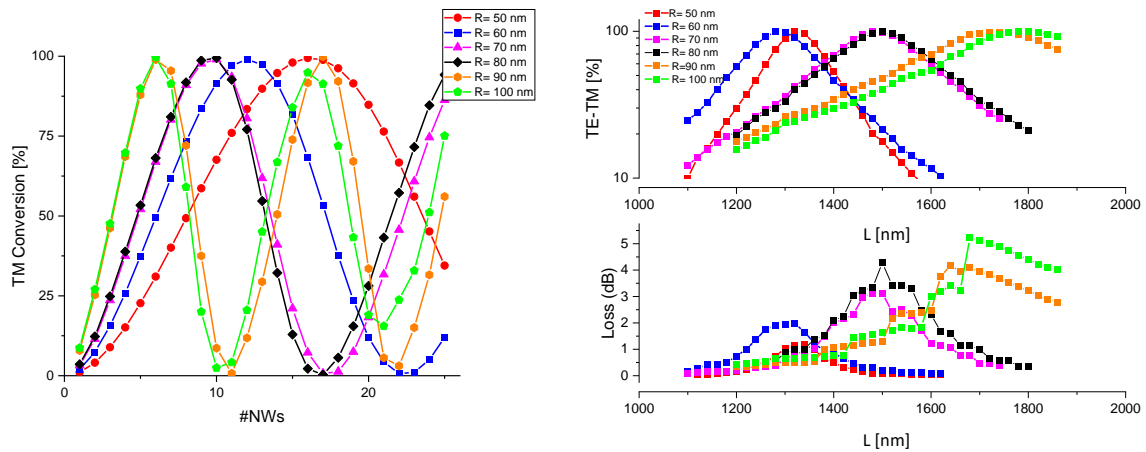


Figure 2: Left panel: TE-TM polarization conversion efficiency as a function of the number of NWs, calculated considering different NWs radius; Right panel: TE-TM polarization conversion efficiency (top) and device total insertion losses (bottom) as a function of the NWs length L .

DISCUSSION

In this paper, we report on a novel technique to realize polarization manipulation in integrated waveguides via hybrid integration of semiconductor NWs. Our results showed that TE-TM full polarization conversion can be achieved by using an array of InP NWs placed on a standard silicon waveguide. The impact of the different NW parameters was numerically investigated. The use of NWs with larger radius leads to a broader conversion bandwidth and full TE-TM polarization conversion with a smaller number of elements compared to NWs with lower radius, resulting in a reduced device footprint. However, the use of larger NWs increases the overall device insertion losses. Therefore, depending on the specific applications and their associated requirements, the NW parameters can be selected to obtain a proper balance between conversion efficiency, bandwidth, insertion losses and device footprint. The feasibility of such a scheme is already demonstrated by post-fabrication protocols [8] which allow for precise NW placing and physical manipulation onto a Si-photonics platform. Additionally, we note that the hybrid NW-waveguide integration approach can be generalized and applied to a variety of advanced photonic applications: NWs can be functionalized to perform advanced optical processing, therefore their integration to silicon devices is promising for the development of advanced integrated circuits.

References

- [1] A. V. Velasco, M. L. Calvo, P. Cheben, et al., Í. Molina Fernandez, J. Lapointe, M. Vachon, S. Janz, and D. Xia Xu, *Ultracompact polarization converter with a dual subwavelength trench built in a silicon-on-insulator waveguide*, Opt. Lett. Vol. 37, pp. 365-367, 2012
- [2] W. Chang, S. Xu, M. Cheng, D. Liu, and M. Zhang, *Inverse design of a single-step-etched ultracompact silicon polarization rotator*, Opt. Express Vol. 28, pp. 28343-28351, 2020
- [3] D. Dai and H. Wu, *Realization of a compact polarization splitter-rotator on silicon*, Opt. Lett. Vol. 41., pp. 2346-2349, 2016
- [4] L. Gao, Y. Huo, Y., K. Zang, K. et al., *On-chip plasmonic waveguide optical waveplate*, Sci Rep Vol. 5, 15794, 2015
- [5] H. Xu and Y. Shi, *Subwavelength-grating-assisted silicon polarization rotator covering all optical communication bands*, Opt. Express Vol. 27, pp. 5588-5597, 2019
- [6] A. Majumder, B. Shen, R. Polson, and R. Menon, *Ultra-compact polarization rotation in integrated silicon photonics using digital metamaterials*, Opt. Express Vol. 25, pp. 19721-19731, 2017
- [7] Y. Xu, J. Xiao, *Ultracompact and high efficient silicon-based polarization splitter-rotator using a partially-etched subwavelength grating coupler*, Sci Rep Vol. 6, 27949, 2016
- [8] Chen, B., Wu, H., Xin, C. et al. Flexible integration of free-standing nanowires into silicon photonics. Nat Commun Vol. 8, 20 (2017).
- [9] Y. Shani, R. Alferness, T. Koch, U. Koren, M. Oron, B. I. Miller, and M. G. Young, *Polarization rotation in asymmetric periodic loaded rib waveguides*, Applied Physics Letters Vol. 59, pp. 1278-1280, 1991

Numerical Calculation of Active Waveguide Bragg Gratings Amplification Dependences

Ángel Sanz-Felipe¹, Manuel Macias-Montero², Rocío Ariza², Juan A. Vallés³, and Javier Solís²

¹Centro Universitario de la Defensa (AGM), Ctra. de Huesca s/n, Zaragoza 50090, Spain

²Grupo de Procesado por Láser, Instituto de Óptica "Daza de Valdés" (IO,CSIC), Serrano 121, Madrid 28006, Spain

³Departamento de Física Aplicada & I3A, Universidad de Zaragoza, C/ Pedro Cerbuna 12, Zaragoza 50009 Spain

* corresponding author: angel_sf@unizar.es

A numerical study of active WBG is made in this work. First, a numerical method is implemented to consider the reflective behaviour of a Bragg grating written within an active Er³⁺/Yb³⁺ doped waveguide. Second, the WBG response is analysed as a function of the grating properties and pumping conditions. A significant gain in the WBG reflected signal is obtained, which represents a promising result for potential active waveguide photonic applications.

Keywords: *waveguide Bragg grating, active waveguide, grating coupling coefficient, reflectivity*

INTRODUCTION

A distributed waveguide Bragg grating (WBG) consists of a periodic perturbation of the refractive index of the light guiding region inside a bulk material. The perturbations lead to an interference behaviour so that when a light wave enters the grating, some particular wavelengths can be efficiently reflected if they satisfy the Bragg condition [1,2]. This property can serve as the basis for many photonic devices such as optical band filters, optical sensors or external cavity lasers [1].

Besides, rare earths doped waveguides present an active character when light of a particular wavelength is guided, so that a light amplification can overcome the attenuation losses and therefore a power gain can be obtained [3,4]. The combination of both remarkable behaviours would be useful for potential photonic applications such as monolithic lasing and amplifying structures. However, it also represents a challenge to model and optimize its design and performance.

In this work, both aspects are addressed together as an initial approach. First, a numerical program has been developed to complementarily simulate the active behaviour of an Er³⁺/Yb³⁺ doped waveguide and the reflective characteristics of a distributed Bragg grating written within the waveguide. Second, a numerical study has been carried out in order to analyse the WBG gain capability and its dependences on the main grating parameters and working conditions. As a consequence, this work aims to be the basis for further theoretical-experimental studies that fully characterize and optimize the WBG response for potential active waveguide photonic applications.

METHODOLOGY

A numerical program has been implemented in order to simulate the light power propagation evolution within an active Er³⁺/Yb³⁺ co-doped waveguide working at its maximum amplification wavelength (1534 nm) [4]. At the same time, a uniform Bragg grating structure written within the guiding core is simulated. In order to numerically simulate its response, the WBG is divided in N uniform sections and an iterative calculation is employed. The propagated power in each of these sections and its derivative are used by a Runge-Kutta method, so that their evolution along the waveguide propagation direction z can be determined. For this aim, the next equation is calculated by the program in each i section to determine the signal and pump power propagation:

$$\frac{dP_i(z)}{dz} = \left[A(\eta, \sigma, z) - \alpha + \frac{\ln(t_i)}{\Delta z} \right] P_i(z) \quad (1)$$

Three terms are distinguished within the brackets. The first one, A , represents a function which determines the waveguide active behaviour along the propagation direction depending on the overlapping factors between the mode intensity and population density distributions, η , and the levels transition cross section, σ . More details of this function can be found in [4]. The second term is the power attenuation constant of the media. The third term is included in order to consider the reflective characteristic of the uniform Bragg grating.

Consider a N -sections grating of total transmissivity T . Then, the transmission coefficient associated to every i -th Δz -length section, t_i , is related to the total grating transmissivity as $T = t_i^N$. Obviously, the t_i coefficient and Δz depend on the number of sections N in which the grating is divided. Nevertheless, in order to better understand the Bragg grating dependences and contribution to the active WBG response, the two main grating characteristics can be broken down and isolated. It is well known that the maximum passive WBG reflectivity is described by [2]:

$$R = \tanh^2(\kappa L) \quad (2)$$

where L is the grating length and κ its coupling coefficient (attenuation loss not considered). The grating coupling depends on many writing parameters (grating period, refractive index modulation amplitude, duty cycle, etc.) [1] which can be adequately selected at the WBG manufacturing process to optimize its properties [2]. However, this is not the specific aim of this work but the active WBG dependence on this parameter. Then, the t_i coefficient is related to both parameters since the grating transmissivity can be simply described by $T = 1 - R$.

Once all these considerations are implemented to the code, the copropagating power evolution along the z direction is calculated using equation (1) from the grating entrance towards its end. Then, the counterpropagating power is calculated backwards analogously. The adequate boundary conditions (injected signal and pump powers) at both grating ends are taken into account for these calculations. All this process is considered as a complete iteration. Then, both co- and counterpropagating powers are used as starting values for a new iteration, and a converged solution is achieved in typically 4-6 iterations, when the iterative process is interrupted. A previous study has been done to verify the adequate numerical program set-up: simple active waveguide ($t_i = 1$) and passive WBG responses have been checked [2,4]. In addition, the adequate number N of sections is properly selected to reach a compromise between minimal computational times and accurate calculation results.

RESULTS

Several simulations have been carried out to study the fundamental dependences of the WBG amplification properties. As an initial approach, two tuneable parameters in the WBG manufacturing process such as the grating's coupling coefficient and length are analysed. In addition, a fundamental working condition such as the pump power injected to the WBG to stimulate the amplification behaviour of the rare earth doped waveguide is also studied.

First, the reflectivity of a 5 mm WBG has been calculated as a function of the grating coupling constant. Three pump power conditions have been considered: 200 mW copropagating, 300 mW bidirectional and zero pumping. Simulations have been carried out using a signal wavelength of 1534 nm (100 μ W signal power). The pumping wavelength used is 976 nm. An attenuation loss factor $\alpha = 0.03 \text{ mm}^{-1}$ has been considered, which represents a typical value for these media. The results of the WBG reflectivity are shown in Figure 1.

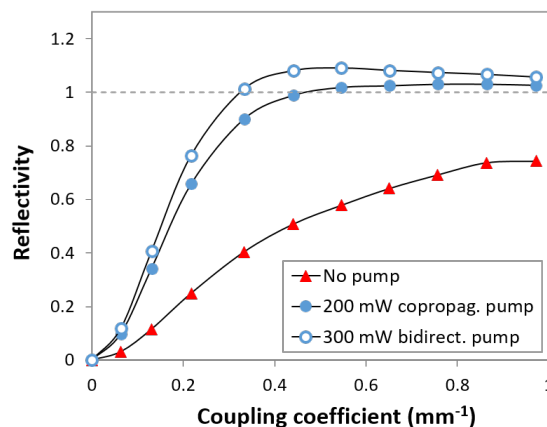


Fig. 1. Reflectivity of a 5 mm long WBG as a function of the grating coupling coefficient. Three pumping conditions are considered.

When pumping is not injected, the reflected signal is similar to that expected for a non-amplified Bragg grating. However, when the pump is considered, the reflectivity clearly increases. First, when only the copropagating pump is employed, the attenuation losses are balanced by the active waveguide behaviour even to obtain a reflected signal slightly greater than the one injected to the grating. Second, when a bidirectional pump is employed, a maximum gain of 9% is detected with grating coupling coefficients around $\kappa = 0.55 \text{ mm}^{-1}$, which represents a considerable value to be manufactured [2]. Although the pump power in both cases is not exactly the same value,

it is observed that calculations lead to a saturation of the amplified response when coupling coefficients tends to 1 mm^{-1} , that is to say, when the grating is much more efficient. This result is consistent: the signal is more efficiently reflected and, therefore, less amplification can occur along the active waveguide. The same simulation has been carried out with two others grating lengths of 3 and 10 mm in order to study the relevance of this characteristic parameter. Results with copropagating and bidirectional pumping are shown in Figure 2.

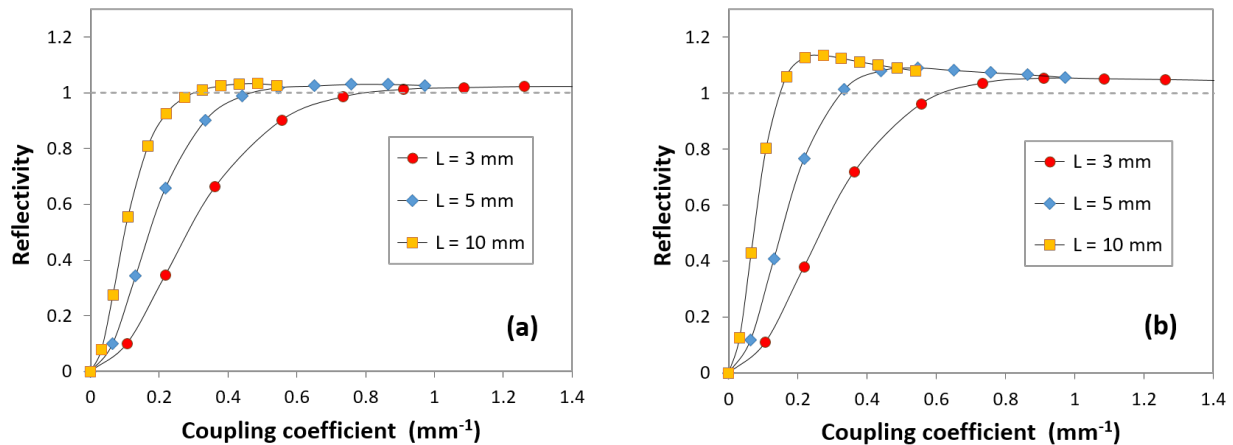


Fig. 2. Reflectivity obtained with WBG lengths of 3, 5 and 10 mm as a function of the grating coupling coefficient. Pumping conditions employed are (a) 200 mW copropagating pump power and (b) 300 mW bidirectional pump power.

Results using the copropagating pump, Figure 2(a), confirm the already mentioned behaviour: the attenuation losses of the three grating lengths are compensated by the WBG amplification, leading to an effective grating which reflects a signal power equal to that injected, even with a slight gain. On the other hand, Figure 2(b) reveals again that a peak of effective gain is detected, which clearly depends on the grating length: the longer the grating, the greater the gain peak observed (at least in this three grating lengths). A 13.4% gain is obtained with a 10 mm WBG of coupling coefficient $\kappa = 0.27 \text{ mm}^{-1}$, higher than the 9% obtained with the 5 mm WBG with a more efficient grating ($\kappa = 0.55 \text{ mm}^{-1}$). As observed in these results, the longer the length, the smaller the coupling coefficient is needed, that is to say, the less effective the Bragg grating must be. These results show up the importance of properly characterizing and selecting the grating and working conditions.

DISCUSSION

A numerical method to simulate the power propagation of light along a $\text{Er}^{3+}/\text{Yb}^{3+}$ doped waveguide Bragg grating has been implemented successfully. This has allowed to study the interesting combination of efficient reflective Bragg gratings embedded in an amplifying medium. As a result, an effective gain has been numerically observed in the reflected signal power depending on the grating writing parameters and working conditions such as the pumping employed. The results present a very interesting approach to these structures and their potential for amplifying and lasing applications. A deeper study must be developed in order to adequately design and optimize the WBG grating parameters and working conditions, as well as a theoretical-experimental comparison.

Acknowledgements: This work was partially supported by the Spanish Ministry of Science and Innovation under the PID2019-108598GB-I00 and PID2020-112770RB-C21 projects, and by the Department of Industry and Innovation (Government of Aragón) through the research group Grant E44-20R (cofinanciado con Feder 2014-2020: Construyendo Europa desde Aragón). M.M. acknowledges the postdoctoral Juan de la Cierva Incorporación grant (IJC-2017-33317) of the Spanish Ministry of Research and Innovation.

References

- [1] M. Ams, P. Dekker, S. Gross and M.J., *Fabricating waveguide Bragg gratings (WBGs) in bulk materials using ultrashort laser pulses*, *Nanophotonics*, vol. 6, no. 5, pp. 743-763, 2017.
- [2] Á. Sanz-Felipe, M. Macías-Montero, J.A. Vallés and J. Solís., *Waveguide Bragg gratings fabrication and optimization as a function of the duty cycle*, in *Proceedings of the Conference "XII Reunión Española de Optoelectrónica, OPTOEL'21"*, pp. 59-64, 2021. ISBN: 9788418471759.
- [3] R. Osellame *et al.*, *Femtosecond writing of active optical waveguides with astigmatically shaped beams*, *J. Opt. Soc. Am. B*, vol. 20, no. 7, pp. 1559-1567, 2003.
- [4] D. Benedicto *et al.*, *Characterization of multicore integrated active waveguides written in an $\text{Er}^{3+}/\text{Yb}^{3+}$ codoped phosphate glass*, *J. Light. Technol.*, vol. 39, no. 15, pp. 5061-5068, 2021.

SiP Waveguide-Embedded Electronic Devices controlled by Substrate/Gate Potential Tuning

(Student paper)

Alessandro Perino, Francesco Zanetto, Matteo Petrini, Francesco Morichetti, Andrea Melloni, Giorgio Ferrari and Marco Sampietro

Department of Electronics, Information and Bioengineering, Politecnico di Milano, Milano, Italy
* email: alessandro.perino@polimi.it

Electrical properties of waveguide-embedded optoelectronic devices in Silicon Photonics chips are affected by the chip substrate potential, that can compensate the effect of electric charges in the cladding oxide. By properly tuning the substrate voltage, we demonstrate the control of a waveguide-embedded heater and the photoconductivity enhancement of a transparent photoconductor, that can be used to detect light intensities down to -60dBm.

Keywords: silicon photonics, integrated photodetectors, substrate voltage tuning

INTRODUCTION

The positive charges in the oxide surrounding a Silicon Photonic (SiP) waveguide (WG) and the trap energy states at the Si/SiO₂ interface have influence on the electronic behaviour of WG-integrated devices. As reported in [1], these charges affect in particular the free-carrier concentration of low-doped WGs, that does not correspond anymore to the nominal doping value at fabrication (10^{15} cm^{-3} , p-doped), and degrade the electrical conductivity of their core.

Figure 1a illustrates the cross-section of the device we studied in this work, fabricated in a commercial SiP technology. The device is embedded in a rib-waveguide with $500 \times 220 \text{ nm}$ core, $900 \times 90 \text{ nm}$ slabs and a total length of $100 \mu\text{m}$. The device has been designed with a p-i-p structure: the silicon waveguide (WG) core and the optical slabs have the same 10^{15} cm^{-3} p-type doping of the original SOI wafer, while the external slab regions (named Drain and Source) are heavily p-doped (10^{20} cm^{-3}) to ensure ohmic electrical contacts. The 900 nm distance of the electrical contacts from the WG core guarantees that no additional propagation losses are introduced. The box oxide is $3 \mu\text{m}$ thick. As we demonstrated in [1], the device tends to be naturally depleted from free carriers due to the effect of oxide charges, thus showing a transversal resistance (between V_s and V_d terminals in the figure) that is about four orders of magnitude higher ($G\Omega$) than what expected from the doping level (tens of $k\Omega$) if surface phenomena are not considered.

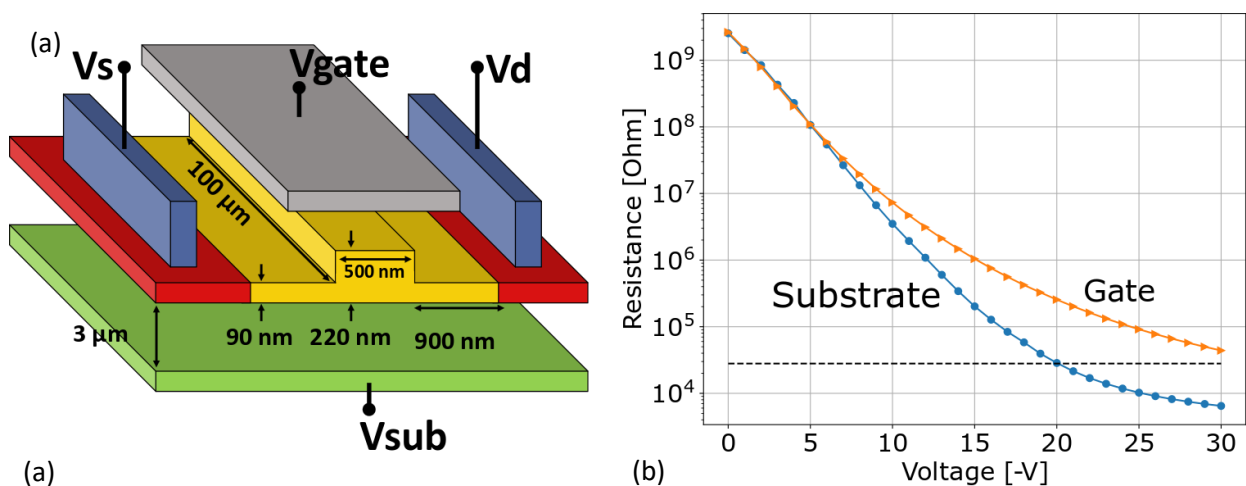


Figure 1: a) Schematic structure of the measured device. b) Measured resistance as function of the control voltage applied to the Gate electrode (orange) or to the chip substrate (blue).

However, the surface effects can be compensated by applying a voltage to the chip substrate or to a gate electrode placed over the waveguide by using one of the available metal layers of the technology. Fig. 1b shows how the device resistance can be tuned by the substrate/gate potential. When V_{SUB} is around -20V the effect of oxide charges

is compensated and the device resistance is brought back to its nominal value ($28\text{k}\Omega$). The control over the effect of oxide charges by means of an external potential is of fundamental importance to tune and set the free carrier concentration of the WG core to the desired level. In this way, we can not only operate the WG-embedded electronic devices in their optimal working point, but also conceive new functionalities of interest.

HEATER WITH LINEAR BEHAVIOUR

Heaters actuators are commonly used to control the behaviour of SiP fabrics. They are resistances placed close to the WG or embedded in it [2], driven by an external voltage. When power is dissipated through the heater, the local temperature increases, modifying the WG effective refractive index (n_{eff}) according to the thermo-optic coefficient of silicon. The quadratic dependence of the controlled quantity (n_{eff}) on the control variable (heater voltage) can be problematic when using the heater as actuator in a feedback loop to lock the working point of photonic structures, like Mach-Zehnder interferometers or ring-resonators. Instead, by taking advantage of the relation between the WG resistance and substrate voltage [1], it is possible to have a linear dependence between the new control variable (V_{SUB}) and n_{eff} . This is well demonstrated by the experiments in Fig.2. The figure shows the linear variation of the resonance peak of a ring resonator as a function of the substrate potential when a constant voltage ($V_{\text{ds}} = 12\text{V}$) is applied across the device. The figure also reports the quadratic behaviour that is obtained when the actuator is operated in the standard way.

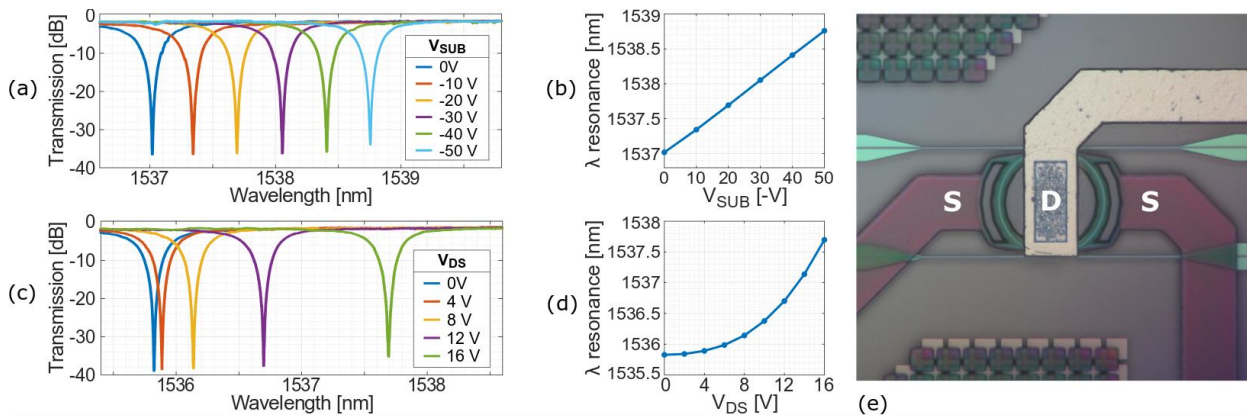


Fig. 2. a) Transfer function of a ring resonator for different values of the substrate voltage ($V_{\text{ds}} = 12\text{V}$). b) Linear variation of the resonance wavelength of the microring resonator as a function of the substrate voltage. c) Transfer function of the ring resonator for different values of V_{ds} voltage ($V_{\text{sub}} = -20\text{V}$). d) Quadratic dependence between the resonance peaks and the voltage applied across the device. e) Microscope photograph of the device.

PHOTOCONDUCTOR SENSITIVITY ENHANCEMENT

Oxide charges greatly affect the performance of the p-i-p device also when used as in-line photoconductor [3]. Indeed, the WG depletion causes an oddly distributed electric field in the WG core and induces longer transit times and smaller photoresistive gains [4] for the photo-generated carriers. Compensation of this effect is therefore essential. Figure 3a shows the variation of photo-current obtained by tuning the substrate voltage from 0V to -30V. The photo-generated current is greatly amplified as the substrate voltage goes negative. Thanks to this amplification, light intensities as low as -60dBm can be easily measured with a standard electronic readout. To highlight the extraordinary performance that can be achieved with a low doped photoconductor, we have compared it with a commonly doped device [5] and with a p-i-n photodiode. The three devices differ just for the doping type and level of WG and slab regions while they all have the same geometry. The doped photoconductor has a $n^+n^-n^+$ structure: n^+ -doped slabs with a doping concentration of 10^{20} cm^{-3} and n^- -doped core with a doping concentration of 10^{17} cm^{-3} , leading to a resistance around 60Ω . Its sensitivity curve is shown in Fig. 3a in green at the same V_{ds} voltage of 1V. It is clearly seen that the produced photocurrent is lower by more than one order of magnitude with respect to the low-doped device, thus resulting in a light intensity detection capability limited to about -35 dBm. The same figure also reports the photodiode sensitivity as a reference for the primary current (red) directly generated in the WG without the amplification mechanism of the photoconductors.

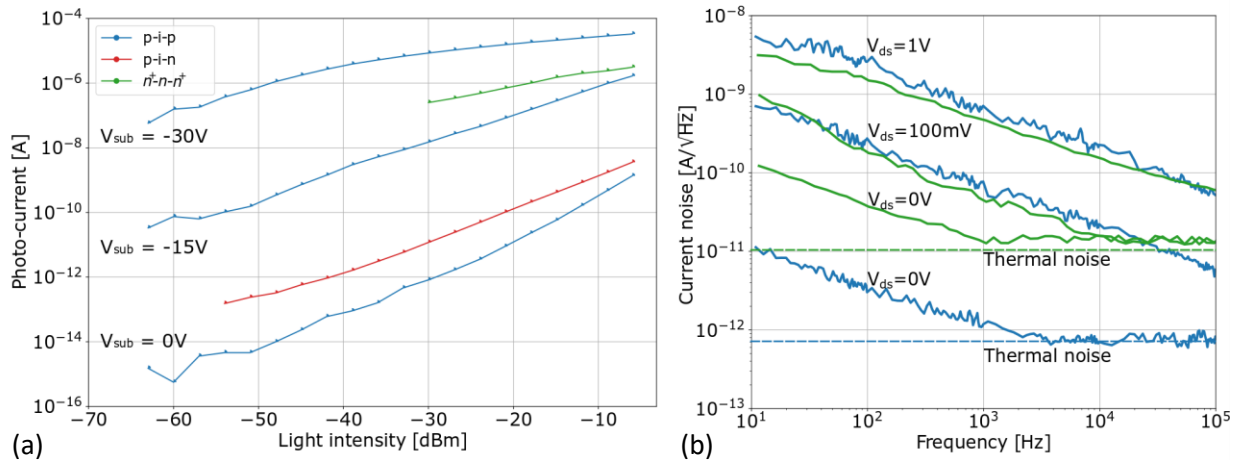


Fig. 3. a) Photo-generated current for the three measured WG-embedded sensors. The sensitivity curve of the low doped photoconductor (blue curves) varies with the substrate voltage, while that of the doped photoconductor (green) and the p-i-n photodiode (red) does not depend on it. b) Current noise power spectral densities of the two photoconductors when V_{ds} is 0V, 100mV and 1V, revealing a bias dependent $1/f$ component ($V_{sub} = -30V$ for the low-doped device).

PHOTOCONDUCTOR NOISE

As a final aspect in the comparison between the two types of photoconductor, their noise behaviour has been investigated. Figure 3b shows the current noise power spectral density measured at V_{ds} bias voltages of 0V, 100mV and 1V in both devices [6]. The measurements confirm that, when $V_{ds}=0V$, the noise of both photoconductors agrees with their thermal noises, with the low-doped device showing a much lower current noise than the high-doped one, in proportion to their resistances (the residual $1/f$ noise measured at very low frequencies is in this case attributed to the measuring instrument). However, as soon as the devices are biased, they both show an unexpected yet comparable bias-dependent $1/f$ component. This $1/f$ component follows Hooge's law [7] and the corner frequency is proportional to the square of the current in the device. Because of this, the two photoconductors are equivalent in terms of noise when operated at the same bias voltage, unless a readout frequency larger than the noise corner of the doped device is targeted. The better performance in terms of sensitivity of the low-doped sensor should thus be attributed only to its higher photoconductive gain.

CONCLUSIONS

We demonstrated that oxide charges can impair the behaviour of waveguide-embedded electronic devices and showed how to compensate their effect by properly acting on the voltage of the chip substrate or by using a gate electrode. As two applications, we reported the use of the substrate/gate voltage to linearly change the power dissipation of a waveguide-embedded heater and enhance the photoconductivity of transparent photoconductors. To demonstrate the effectiveness of this approach, the performance of the obtained sensor has been compared to other transparent detectors, showing a much better sensitivity (-60 dbm) and the same noise behaviour.

Acknowledgements: part of the work was done at Polifab, the nanofabrication facility of Politecnico di Milano.

References

- [1] F. Zanetto et al., "Electrical conductance of silicon photonic waveguides", *Optics Letters*, vol. 46, n. 1, pp. 17-20, 2021.
- [2] A. Gazman et al., "Tapless and topology agnostic calibration solution for silicon photonic switches," *Optics Express*, vol. 26, no. 25, pp. 32662–32674, 2018.
- [3] L. Zhou et al., "Photoconductive effect on p-i-p micro-heaters integrated in silicon microring resonators," *Optics Express*, vol. 22, no. 2, pp. 2141–2149, 2014.
- [4] R. H. Bube, "Photoconductivity of solids", Wiley, New York, USA, 1960.
- [5] H. Jayatilika et al., "Photoconductive heaters enable control of largescale silicon photonic ring resonator circuits," *Optica*, vol. 6, no. 1, pp. 84–91, 2019.
- [6] G. Ferrari and M. Sampietro, "Correlation spectrum analyzer for direct measurement of device current noise", *Review of scientific instruments*, vol. 73, n. 7, pp. 2717-2723, 2002.
- [7] F. N. Hooge, "1/f noise is no surface effect", *Physics Letters A*, vol. 29, n. 3, pp. 139-140, 1969.

Low loss SiN optical modulator for kHz-rate switching applications

Alessandro Brugnoli^{1,*}, Ali Emre Kaplan¹, Michele Re², Cosimo Lacava¹ and Ilaria Cristiani¹

¹Photonics Group, Department of Computer and Biomedical Engineering, University of Pavia, 27100 Pavia, Italy

²Huawei Technologies Italia S.r.l., centro direzionale Milano 20054, Segrate, Italy

* Alessandro.brugnoli01@universitadipavia.it

In this paper we present the design and characterization of a low loss, kHz rate, silicon nitride modulator. By minimizing the linewidth of channel transmission thanks to low loss waveguide propagation (0.2 dB/cm), the presented thermally tuned microring resonator in add/drop configuration shows 10dB ER at 1kHz modulation and has a static insertion loss of 2dB.

Keywords: *Microring resonators, silicon nitride, optical modulators*

INTRODUCTION

In the last 10 years, silicon photonic circuits have played a fundamental role in the development of many applications fields, ranging from telecommunications and sensing, touching also frontier research themes such as those related to optical computing and advanced non-von Neumann machines [1]–[3]. The main target of these research efforts has always been related to the operational speed, targeting to improve the pJ/bit figure of merit, leading to the development of 100G+ optical modulators, with compact footprints and high integration capabilities. Differently, frontier and emerging applications related to quantum processing and machine learning require modulators (either phase or amplitude) with different requirements: here extremely low optical loss, low optical power consumption and thermal stability are the main requested ingredients, operating at modest speed values (kHz range). For such applications, modulation utilizing the thermo-optic effects is an effective option [4]. In this context SiN has emerged as a very attractive option for large-volume and low-cost fabrication, thanks to its CMOS compatibility and availability in all major foundries. Despite the low refractive index contrast that implies a larger footprint with respect to Si, SiN offers a larger transparency bandwidth (bandgap $\sim 5\text{eV}$) and very low linear propagation losses that can be two orders of magnitude less with respect to Si providing new opportunities for the design and development of complex integrated circuits.

Here we present the design and experimental characterization of a thermally tunable ring resonator modulator based on SiN offering extremely low optical loss and low power consumption operating at telecom wavelengths.

DESIGN AND EXPERIMENTAL RESULTS

We present the design of a SiN intensity modulator based on low loss, high Q-factor microring resonator. Modulation is achieved via a local change of the refractive index through thermo-optics effect that, in turns, allows shifting the resonance frequencies of the device. Intensity modulation can be achieved if a continuous wave laser is placed at the initial resonance frequency and a driving voltage is applied to the integrated heater. Here, the required power to achieve a deep ($>10\text{ dB}$) on-off keying (OOK) modulation is related to the capability to design MRR exhibiting a sharp and narrow (in frequency) resonances: in this way a small amount of applied voltage will result in an enhanced modulation performance of the MRR. The main requirement to achieve such behaviour is related to the waveguide optical loss. We initially compared the attainable performance of the two main silicon photonic-based platforms: silicon on insulator (SOI) and SiN. The outcomes of the comparison of figures of merit of MRRs in these two platforms are reported in Table 1. For such comparison we have assumed the ideal case: coupling and bend sections are lossless and MRRs fulfill the theoretical critical coupling condition. Typical propagation loss values for SOI and SiN platforms were considered as 3dB/cm and 0.1dB/cm and modest minimum radii were chosen as 20 μm and 70 μm , respectively. The main output of our modelling is the required temperature change to achieve 10 dB ER modulations with MRR size as a free parameter. Our results show that, despite the lower thermo-optics effect of SiN compared to the one of SOI, thanks to the low losses of SiN waveguides, the required temperature change to achieve the desired modulation can be lower than in the case of SOI.

Technology and Design parameters	Si	SiN
Loss [dB/cm]	3	0.1
T/O coefficient [1/K] @ 1550 nm	2.08×10^{-4}	2.45×10^{-5}
Bending radius [μm]	20	70
Results of the analytical model	Si	SiN
FWHM [pm] (minimum)	31.8	1.87
Q-factor (maximum)	48×10^3	820×10^3
Temperature Increase needed for modulation	2 °C	1.4 °C

Table 1: Comparison of figures of merit according to typical technology parameters of Si and SiN MRRs with given propagation loss and bend radius. In the analytical model, couplers and bends are assumed to be lossless and the MRR is in the critical coupling regime.

The designed MRR was fabricated by Ligentec using standard MPW fabrication platform. The layer stack of the deep etched Si_3N_4 waveguide with SiO_2 cladding is depicted in Fig. 1a. The propagation loss of the single mode waveguide was 0.2 dB/cm with a fibre to chip coupling coefficient of 1.7 dB. An image of the fabricated SiN microring resonator in add/drop configuration is shown in Fig. 1b. The MRR was designed with a 60 μm of radius and 500 nm gap between the ring and the bus waveguide. Numerical simulations were performed in to feed the analytical model. The power coupling coefficient for 500 nm of gap through the 3D FDTD simulation was calculated to be 0.025 which corresponds to 3.5 dB of the bandwidth of drop port channel at $\lambda=1.55\mu\text{m}$. By using the obtained effective refractive indices and group index of the TE mode within the C-band in the analytical model, we set the Free-Spectral-Range (FSR) to be 375 GHz.

Subsequently, we performed preliminary static and dynamic characterizations of the device. The transmission of the Through and Drop ports of the MRR and the used characterization set-up are shown in Fig.1c-d. For the static transmission characterization, only the output of the EDFA was used without the tunable laser source (TLS) since the EDFA output was broadband enough to cover the C-band. The drop port transmission of the EDFA was fed to the fibre-based Polarization Beam Splitter (PBS). The slow-axis port of the PBS was then adjusted to the TE polarization which was used as the input for the Device Under Test (DUT). The signals between the PBS and DUT were transferred by a PM fibre. The measured FSR and 3dB bandwidth of the drop channel are 376 GHz and 5GHz, respectively. Resonance wavelengths with Q- factor of $3.9 \cdot 10^4$ at 1.55 μm has the Extinction Ratio (ER) larger than 30 dB. Since the incoming lights from EDFA were unpolarized, the secondary peaks that appear with lower transmissions confirmed high polarization extinction (~ 20 dB) provided by input PM fibre alignment in the set-up. The obtained experimental results show extremely good agreement with the expected parameters in terms of FSR and BW.

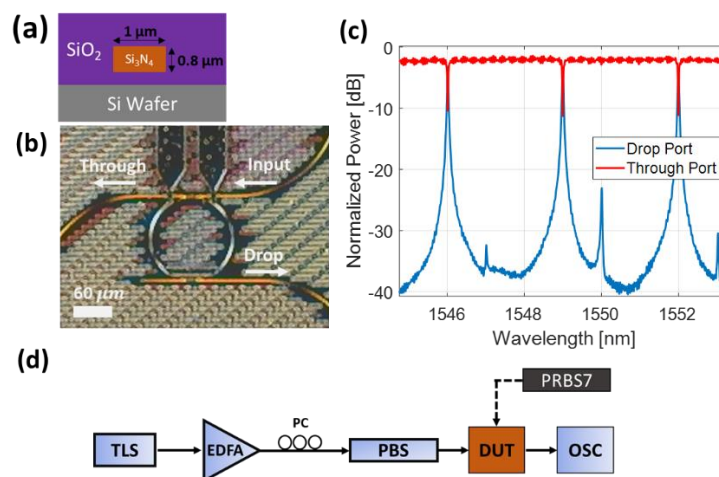


Figure 1. (a) Layer stack of the deep etched SiN waveguide. (b) a photograph of the fabricated MRR. (c) Static transmission of the drop port (blue) and through port (red) of the MRR modulator. (d) The experimental setup.

Dynamic behaviour was evaluated using the modulator to synthesize OOK signals (PRBS7) at a rate of 1 kHz. To carry out modulation operations, the output wavelength of a CW laser output was first tuned to reach the resonance wavelength and then modulated by thermal tuning. Preliminary results of the obtained eye diagrams at 1 kbps OOK modulation with different applied voltages and measured ER values with respect to applied powers are shown in Fig. 2. Average power consumption of ones and zeros of the bit patterns, when 1, 1.5 and 2 applied volts have been measured as 3.5 mW, 19.5 mW and 29 mW, respectively. As shown in Fig. 2b, the ER obtained from the eye diagrams exceeds 10 dB with 29 mW of the applied power.

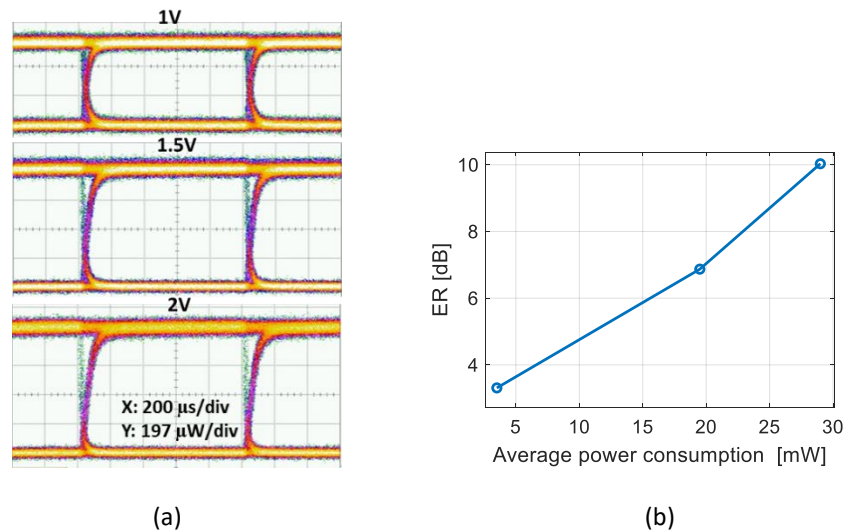


Figure 2. Eye diagrams at 1kbps OOK modulation with different voltage levels (a) and corresponding extinction ratios as a function of average power consumption (b).

Overall, it has been shown that the modulation performance of the thermally-tuned MRR fabricated in SiN has been evaluated in terms of required modulation power and ER at kHz rate.

CONCLUSIONS

In this work we reported the design and the preliminary characterization of a silicon nitride kHz- rate thermo-optical modulator. By using a proper design approach based on both numerical simulations and the analytical model, an excellent agreement between the expected and obtained parameters has been achieved. The device was operated with a maximum of 29 mW of electrical power for an OOK modulation signal that showed a maximum of 10 dB of ER. The insertion loss of the device was 2dB. This modulator can be employed as a basic switching component for more complex architectures where low speed and power efficient modulators are needed.

Acknowledgements: authors acknowledge Huawei Technologies Italia, Milan RC for the support.

References

- [1] H. J. Caulfield and S. Dolev, "Why future supercomputing requires optics," *Nat. Photonics*, vol. 4, no. 5, pp. 261–263, 2010, doi: 10.1038/nphoton.2010.94.
- [2] A. Samani, V. Veerasubramanian, E. El-Fiky, D. Patel, and D. V. Plant, "A silicon photonic PAM-4 modulator based on dual-parallel Mach-Zehnder interferometers," *IEEE Photonics J.*, vol. 8, no. 1, 2016, doi: 10.1109/JPHOT.2015.2512105.
- [3] S. Azzini *et al.*, "From Classical Four-Wave Mixing to Parametric Fluorescence in Silicon micro-ring resonators," *Opt. Lett.*, vol. 37, no. 18, pp. 3807–3809, 2012, doi: 10.1364/OL.37.003807.
- [4] S. Chung, M. Nakai, and H. Hashemi, "Low-power thermo-optic silicon modulator for large-scale photonic integrated systems," *Opt. Express*, vol. 27, no. 9, p. 13430, 2019, doi: 10.1364/oe.27.013430.

Miniaturization of 90-degree hybrid optical couplers

Alessio Miranda¹, Weiming Yao¹, Jos van der Tol¹ and Kevin Williams¹

¹Eindhoven University of Technology, De Zaale, Eindhoven, 5612 AZ, The Netherlands
* a.m.d.miranda@tue.nl

Here we explore the limits of miniaturization of an efficient 90-degree hybrid coupler on the InP photonic integration platform, working in the L, C and S bands, with respect to their figures of merit. We investigate the main effects responsible for the degradation of the performance of the devices, and establish the minimal dimension that such devices can have without significant degradation for photonic applications. The miniaturized device has a footprint of only $2200\mu\text{m}^2$, more than 5 times smaller than the conventional device used as reference.

Keywords: multimode interferences MMI, 90-degree hybrid coupler, quadrature hybrid coupler, balanced detector, miniaturization, scaled device, interference

INTRODUCTION

Multi-mode interferometers (MMI), are a fundamental type of photonic components, whose main function is to distribute the incoming light over several output ports, each with a well-defined power ratio and phase difference with respect to the input [1,2]. The working principle is based on self-imaging caused by internal interference of the modes excited and propagating in it. 90-degree hybrid couplers are a subclass of MMIs, which finds applications in coherent detection systems, where they are used for demodulating optical signals with quadrature phase shift keyed (QPSK) modulation format and in balanced detection [3, 4].

Its structure, depicted in figure 1a, is designed in such way that by applying the received signal S , and a local oscillator (LO) at its input ports, the power at the four outputs is equally distributed, and the phase differences between signal and local oscillator are 0° , $\pm 90^\circ$, $\mp 90^\circ$ and 180° degrees for each port respectively. In this case, the phase difference between the output channels 1 and 4 (in-phase component) is 0° for the signal and 180° for the local oscillator, while that for the channels 2 and 3 (quadrature component) is 180° and 0° respectively. The in-phase and quadrature components can be used for balanced detection, allowing for suppression of common mode distortions and improvement of the signal-to-noise ratio.

For large scale integrated circuits, it is required that these devices fit within a densely packed chip. It is thus important to implement strategies for the miniaturization of these devices without compromising their performance. However, the miniaturization of an MMI presents three main challenges: the first is that a reduced size in the input waveguides increases the diffraction effects when the input signals enter the MMI. The second is that crosstalk between input and output waveguides may appear if these are too close. The third is that a reduction of the width of the MMI implies a reduced number of excited and propagating modes inside the MMI which leads to reduced imaging quality. The purpose of this paper is to explore the limits of miniaturization of a working 90-degree hybrid coupler with respect to these challenges and to establish the minimal dimension for which such devices can operate without significant degradation for photonic applications.

DISCUSSION

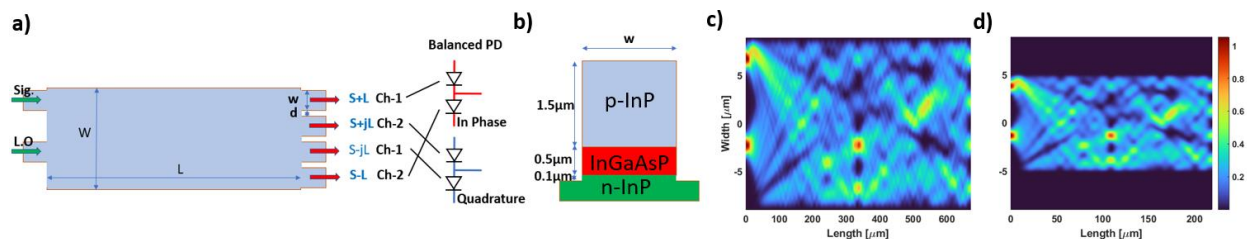


Fig. 1. a) Top view of the hybrid, with output channels and their role in balanced photodetection, b) vertical cross section of the device, c) the intensity distribution in the reference MMI ($W=17.8\mu\text{m}$, $L=671\mu\text{m}$, $w=3.5\mu\text{m}$, $d=1\mu\text{m}$) with a footprint of almost $12000\mu\text{m}^2$ and d) in a miniaturized MMI ($W=10.2\mu\text{m}$, $L=219\mu\text{m}$, $w=2\mu\text{m}$, $d=570\text{nm}$) with a footprint of around $2200\mu\text{m}^2$.

The vertical structure of the waveguides and the MMIs in this study, depicted in figure 1b, is a deeply etched rib-waveguide, with a top cladding of 1500nm p-InP ($n_u=3.17$), a waveguide thickness of 500nm InGaAsP ($n_w=3.38$), a

lower layer of 100nm of n-InP ($n_0=3.163$) on the same substrate [5]. The device is surrounded by a layer of polyamide ($n=1.5$). All the simulations are performed using an Eigenmode Expansion Solver (Lumerical MODE-EME), the results refer to the principal TE mode.

The device we chose as reference avoids the restrictions mentioned above: all the waveguides have a width $w=3.5\mu\text{m}$, to avoid diffraction at the working wavelength ($\lambda=1550\text{nm}$), the fixed distance between the edges of the output waveguides is $d=1\mu\text{m}$ to avoid cross talking. the Signal and LO input waveguides are indicated in figure 1a. In order to have a correctly working 90 degree hybrid coupler the size of the MMI is chosen to have a $W=18\mu\text{m}$ and $L \approx \frac{4n_{eff}W^2}{3\lambda} \approx 671\mu\text{m}$ as calculated in accordance to the literature [1, 2]. By taking into account the effect of the evanescent fields, neglected in [1], we find that the optimal device has a width of $W=17.8\mu\text{m}$, the other parameters remaining the same as described above. To evaluate the performance of our devices we use four figures of merit at 1550m: the minimum of the moduli of the common mode rejection ratios $|CMRR|$ (as defined in [5]), the maximum of the moduli of the phase errors $|\varepsilon|$ (also defined in [5]), the maximum of the moduli of the excess losses $|\text{loss}|$, and the minimum $|Imb|$ between the moduli of the imbalances in phase and quadrature which we define as $Imb_I = 10 \log(|S_{4S}|^2 - |S_{1S}|^2 - |S_{4LO}|^2 + |S_{1LO}|^2)$ and $Imb_Q = 10 \log(|S_{3S}|^2 - |S_{2S}|^2 - |S_{3LO}|^2 + |S_{2LO}|^2)$.

We consider a miniaturized device as suitable for photonic applications if $|CMRR| > 20\text{dB}$, $|\varepsilon| < 5^\circ$, $|\text{loss}| < 1\text{dB}$ and $|Imb| > 10\text{dB}$, at the operation wavelength. These conditions are stricter than those which normally apply for a 90-degree hybrid for to be used for balanced detection [6]. For the reference structure, whose images are shown in figures 1c the four figures of merit are $|CMRR|=40.2\text{dB}$, $|\varepsilon| = 0.1^\circ$, $|\text{loss}| = 0.08\text{dB}$, $|Imb|=24\text{dB}$.

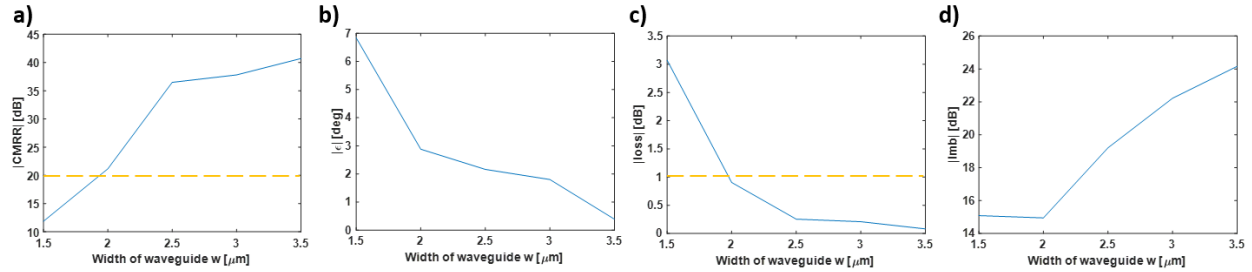


Fig. 2. Comparison of the figures of merit for a) modulus of CMRR, b) modulus of phase error, c) modulus of insertion loss, and modulus of absolute imbalance for devices consisting of the MMI of dimensions ($671\mu\text{m} \times 17.8\mu\text{m}$) and waveguides scaling from $3.5\mu\text{m}$ to $1.5\mu\text{m}$ (the dashed line, when present, indicates the thresholds we set for a suitable device).

In order to explore the effect of diffraction by shrinking the width of the input and output waveguides, we shrink all the waveguides in the reference device, from $3.5\mu\text{m}$ to $1.5\mu\text{m}$ by leaving all other dimensions unchanged. As can be seen in figure 2, the device has low degradation for all the figure of merit till a waveguide of $2\mu\text{m}$ width.

The effect of crosstalk was studied by analysing the S_{12} of two $100\mu\text{m}$ long waveguides of width from $1.5\mu\text{m}$ to $3.5\mu\text{m}$ separated by 200nm , the minimal distance in the simulation. The length of $100\mu\text{m}$ is more than sufficient to allow the waveguides to depart from a parallel configuration in a real integrated circuit. In all the examined configurations the calculated cross talk was found to be less than -20dB , which is negligible.

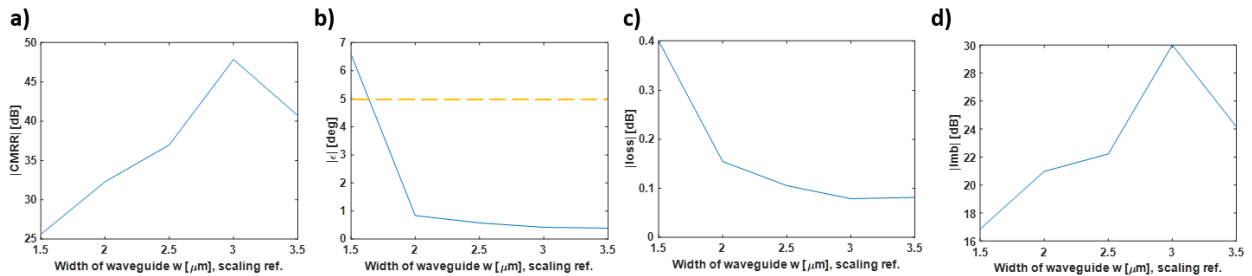


Fig. 3. Comparison of the figures of merit for a) modulus of CMRR, b) modulus of phase error, c) modulus of insertion loss, and modulus of absolute imbalance for devices with waveguides scaling from $w_{min}=3.5\mu\text{m}$ to $1.5\mu\text{m}$, and other dimensions scaling accordingly.

Thirdly, we study the dependency of the quality on the number of TE modes excited and propagating in the shrinking MMI. For our devices the number of modes N propagating in the MMI scales as $N = [1.1 W[\mu\text{m}] - 0.48]$.

Because of the geometry of the hybrid, a scaling of the width of the device cannot be independent from the scaling of the waveguides, which must be fully contained in it. Thus we adopt the approach to scale the width of the

waveguides w , their relative distance d and width of the MMI W by the same factor α , and to scale the length of the MMI L by α^2 in order to maintain the same proportions as the reference for image formation [1]. This means that the footprint of the MMI scales by α^3 . In figure 3 we compare the figures of merit for the miniaturized device depending on the scaling of the waveguide width w_{min} , to which we link the scaling factor of the device as $\alpha = w_{min}/w_{ref}$, where $w_{ref}=3.5\mu m$ is the width of the waveguide of the reference. We observe that a scaling to $w_{min} = 2\mu m$, corresponding to $\alpha = 0.57$, preserves all the four figures of merit. This corresponds to a miniaturized device with dimensions $W=10.2\mu m$, $L=219\mu m$, $w=2\mu m$, $d=570nm$ and a footprint of only $2200\mu m^2$.

The intensity distribution, depicted in figure 1d looks very similar to the one of the reference device depicted in figure 1c.

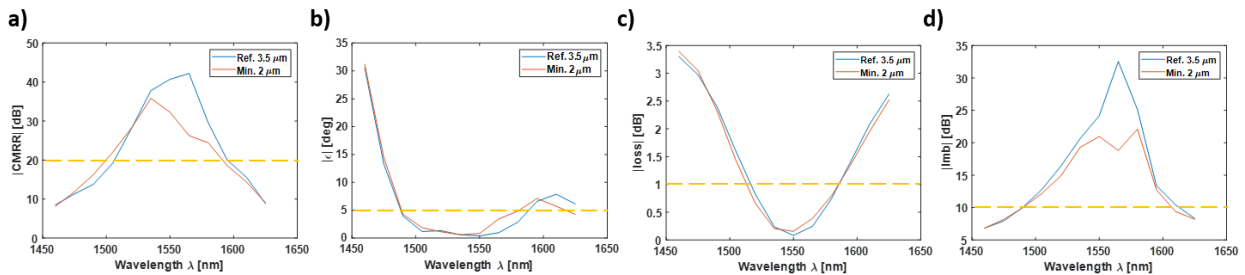


Fig. 4. Comparison of the figures of merit for a) modulus of CMRR, b) modulus of phase error, c) modulus of insertion loss, and modulus of absolute imbalance, in the C, L, S bands.

Finally, in figure 4 we compare the performance of the reference hybrid ($w_{ref}=3.5\mu m$, $\alpha = 1$) to the miniaturized one ($w_{min}=2\mu m$, $\alpha = 0.57$) for L, C and S band. It can be observed that the devices behave similarly with optimal performance at the working wavelength $\lambda = 1550nm$, and excellent performance from $1520nm$ to $1580nm$ which is the whole C band and part of the L and S bands.

CONCLUSION

In conclusion, we have demonstrated that a standard 90-degree hybrid couple can be scaled from a footprint of $12000\mu m^2$ to one of only $2200\mu m^2$ maintaining a sufficient performance. We compared the principal figures of merit and the behavior in the C, L and S bands for this device and the reference one. This result can prove useful for the integration of these components densely packed photonic circuits.

Acknowledgements: AM would like to thank Ozan Çirkinoglu, Marco Gagino and Dr. Xaveer Leijens for fruitful discussion.

References

- [1] L. B. Soldano, E. C. M. Pennings, M, *Optical Multi-Mode Interference Devices Based on Self-Imaging : Principles and Applications*, JOURNAL OF LIGHTWAVE TECHNOLOGY, VOL. 13, NO. 4, pp. 615-627,(1995)
- [2] K Cooney, FH Peters, *Analysis of multimode interferometers*, Optics express 24 (20), 22481-22515, (2016)
- [3] Y. Painchaud, M. Poulin, M. Morin, and M. Têtu, *Performance of balanced detection in a coherent receiver*, Optics Express Vol. 17, Issue 5, pp. 3659-3672 (2009)
- [4] B. Zhang, Ch. Malouin, and Th. J. Schmidt, *Design of coherent receiver optical front end for unamplified applications*, Optics Express Vol. 20, Issue 3, pp. 3225-3234 (2012)
- [5] E. Kleijn, *Passive components in indium phosphide generic integration technologies*. PhD Thesis, Technische Universiteit Eindhoven, (2014)
- [6] OIF-DPC-RX-01.1: Implementation Agreement for Integrated Dual Polarization Intradyn Coherent Receivers, Optical Internetworking Forum Std., April (2010)

Advances on 5G, research directions and role of optical technologies - An industry view

Renato Lombardi

Huawei Fellow, Chairman of ETSI ISG mWT
Milan, Italy
renato.lombardi@huawei.com

SUMMARY

One important aspect of 5G, compared to previous generations, is the prominent role of a diverse set of usage scenarios with applications above and beyond the traditional high-speed connection. Even though enhanced mobile broadband (eMBB) is still an important use case for mobile operators around the world, emergence of other usage scenarios such as those classified under massive machine type communications (mMTC) and ultra-reliable/low-latency communications (URLLC) enabled by 5G NR has opened the door for a myriad of non-traditional applications.

In this context 5G is targeting unprecedented improvements over the previous generations of mobile networks such as a 1000-times increase in system capacity, 100-times improvement in energy efficiency, down to milliseconds end-to-end network latency and massive machine type connectivity for numerous devices.

Notwithstanding 5G is in its deployment phase industry is already researching what is coming beyond 5G with a further new set of challenges to satisfy the envisaged applications that are going to require even more bandwidth, extremely precise positioning, real-time and up-link centric broadband, integration of communication and sensing.

In order to implement this vision, millimeter-wave spectrum, new solutions and new network topology will be necessary posing challenges to the research not only for the wireless domain but also for optical technologies, expected to play a key role for innovative base stations architectures and above all in the backhaul to transport and route the enormous quantity of data.

Envisioned 5G to 6G communication architecture scenario

5G to 6G key requirements driving evolution of mobile access and wireless x-haul to millimeter-wave and sub-millimeter ranges

Research directions for optical technologies in the backhaul and innovative base station architectures

Analysis of the most important requirements of 5G to drive optical technologies

- Free Space Optical links both in Near InfraRed and Mid InfraRed ranges
- RoF or MWoF technologies
- Microwave Photonics for sub-TeraHz signal generation

Towards passive hybridization of high-power and high-speed InP transmitters

(Invited paper)

Hélène Debrégeas¹, François Lelarge¹, Suresh Vankatesan²

¹Almae Technologies, Route de Nozay, 91460 Marcoussis, France

²POET Technologies, 1107-120 Eglinton Ave E, Toronto, ON M4P1E2, Canada
helene.debregeas@almae-technologies.com

We present a versatile InP technology, applied for lasers, laser-modulators and semiconductor optical amplifiers, particularly adapted for hybrid integration with silicon photonics. In particular we show examples of passive hybridization of high power lasers for silicon photonics modulators, 100Gb/s PAM4 laser-modulators with fiber for datacom, and reflective SOAs in tunable external cavity lasers.

Keywords: photonic integration, hybridisation, semiconductor lasers

INTRODUCTION

In order to face the permanent increase of optical data rates and the reduction of transmitter costs, photonic integration has been the focus of many researchers, either by monolithic integration on InP [1], or by hybrid integration with the active material in InP and other passive optic functionalities integrated in Silicon (SiPho) with waveguides constructed in different materials such as Silicon, SiN, SiO₂, Thin film LiNbO₃ etc. The hybrid integration approach benefits from low propagation losses, and utilizes a mature and low-cost technology platform compatible with electronics. Moreover, the hybrid integration approach is particularly adapted for wafer scale integration, and for transmitters with intensity and phase modulation.

Different integration techniques have been developed in recent years:

- Micro-packaging using 3D-printing directly on the components to transform and guide the optical mode between InP and SiPho platform [2, 3].
- Hybridization that butt-joints the InP chip in front of SiPho waveguides with precise alignment. Transfer printing with automatic InP chip placement is an emerging approach aiming at industrial quasi-automatic hybridization [4].
- Heterogeneous integration that positions InP material directly onto SiPho waveguides before final processing, the optical wave propagating locally in the InP gain region by evanescent coupling. This technologically complex approach, which requires a very specific process, has been the subject of numerous works over the last twenty years, and has finally led to excellent performances [5]. The direct epitaxy of InP on Si is also a promising way [6].

In this paper, we present our InP technology based on Semi-Insulating Buried Heterostructure waveguide (SIBH) which allows to reach excellent performances for several types of devices, and is particularly adapted to the hybridization method with SiPho.

InP TECHNOLOGY OPTIMUM FOR HYBRIDIZATION

Our SIBH technology, the result of many years of research and optimizations, presented in detail in [7], allows us to develop various optical components mainly for telecom applications: Distributed FeedBack (DFB) lasers, possibly integrated with electro-absorption modulators (DFB-EAM), as well as Semiconductor Optical Amplifiers (SOAs). After etching the waveguide, it is buried into semi-insulating iron-doped InP by selective Metal-Organic Vapor Phase Epitaxy (MOVPE), then the SiO₂ mask is removed, and the structure is buried again by p-doped InP. A lateral H⁺ proton implantation allows to limit the diode capacitance, and possibly to electrically separate the different sections (fig.1a). This technology, a little more complex than the ridge waveguide, brings many advantages such as excellent thermal dissipation and mechanical robustness. But most important for hybridization, the optical mode is quasi-circular. And by a simple reduction of the waveguide width, it can be progressively enlarged for an optimal and tolerant optical coupling, reaching for example, with a waveguide at 0.35 μ m, a 1/e² mode diameter of 3.4 μ m x 4.5 μ m (divergence of 17° x 11°) as illustrated fig.1b.

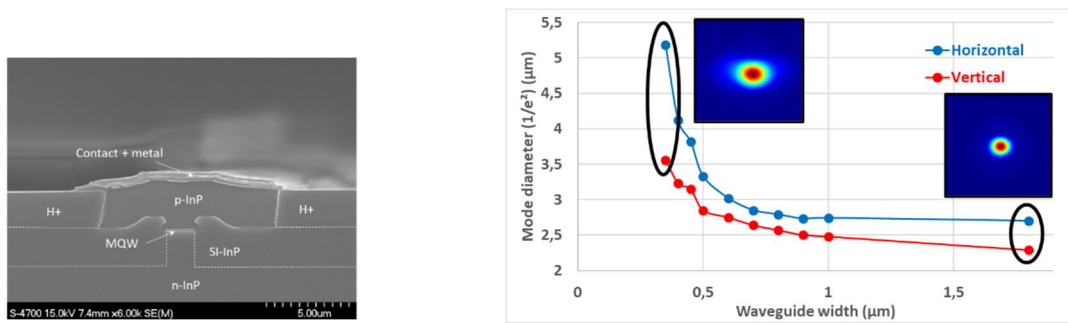


Fig. 1: (a) SEM photograph of a SIBH waveguide at facet, (b) experimental measurements of $1/e^2$ mode diameters versus waveguide width (near field profiles in insert for $0.35\mu\text{m}$ and $1.8\mu\text{m}$ waveguide widths)

Moreover, Almae Technologies has the specificity to use both MOVPE epitaxy for selective SI-InP growth, but also Gas Source Molecular Beam Epitaxy (GSMBE) for all other growths, thus combining the advantages of the two techniques. The multi-quantum well structures, for example, are grown by GSMBE, and integrated by butt-joint to optimize independently the different sections. And the p-InP regrowths in GSMBE use the Beryllium p-dopant rather than the Zinc p-dopant of MOVPE. Since Beryllium diffuses much less than Zinc, this avoids any risk of electrical leakage through the SI-InP, and allows to efficiently and homogeneously apply the electric field in the electro-absorption modulators, leading to very steep extinction curves and reduced the modulation voltage swing V_{pp} .

Finally, we use an e-beam technology for the definition of Bragg gratings of the DFBs, allowing a perfect control of emission wavelength, and the possibility of realizing DWDM transmitter arrays [8].

This technological mastery has allowed us to develop a wide range of components, and to develop hybrid InP / SiPho subsystems in the framework of partnerships, with a co-design of the InP chip and the SiPho platform.

HYBRIDISATION OF INP DEVICES ON SIPHO PLATFORMS

High-power DFBs: we have developed high power DFBs lasers, in O-band (25 to 85°C) and C-band, either as power source for coherent SiPho modulators or for LIDAR applications (fig 2a). We are developing with POET Technologies a visually assisted passive assembly with an interposer including SiN guides (figure 2b). The simultaneous optimization of mode converters in the InP laser and in the SiN guides allows an excellent mode overlap, alignment tolerance compatible for passive alignment, reaching coupling rates around 1dB.

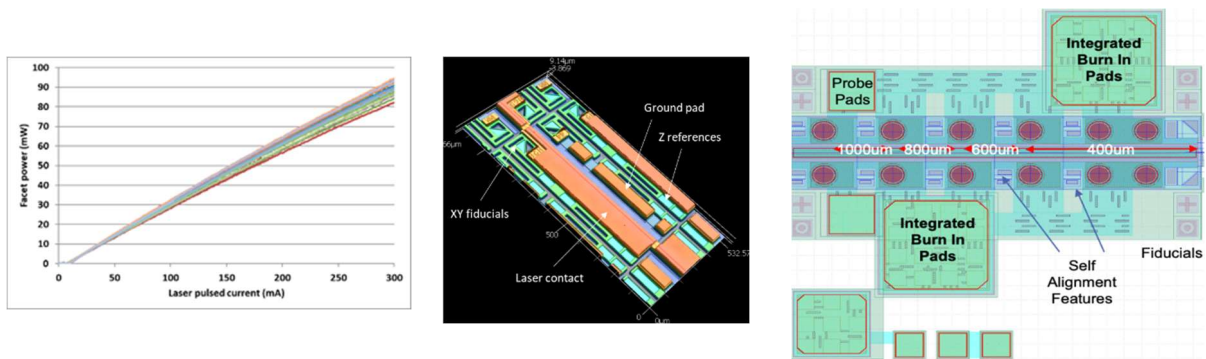


Fig.2: (a) facet power versus pulsed laser current of high-power C-band DFB lasers at 25°C, (b) 3D photography of DFB laser with mechanical fiducials, (c) scheme of the SiPho interposer for coupling into SiN waveguides and SiPho coherent modulators.

400Gb ethernet transmitter for datacom: within European ECSEL project APPLAUSE, we aim to demonstrate a low-cost industrial assembly solution for 400Gb Ethernet, using our uncooled (20-70°C) 100Gb/s PAM4 DFB-EAMs in O-band (fig.3a). The chip implements a metallization compatible for flip-chip, Z stoppers aligned with the quantum wells, and X-Y stoppers defined at the same time as the waveguide (fig.3b). The Silicon submount developed by IZM Fraunhofer includes AuSn bumps for flip-chip and HF lines for high-speed EAM driving. Plus, trenches for a lens and isolator, and a V-groove for a fiber are defined at the same stage as stoppers in X, Y and Z, that will face those of the InP chip (fig.3c). During the flip-chip, the InP chip is automatically translated during soldering by capillarity, until the InP chip and SiPho stoppers come to stall together. The InP waveguide, lens, isolator and fiber in the V-groove are then automatically self-aligned.

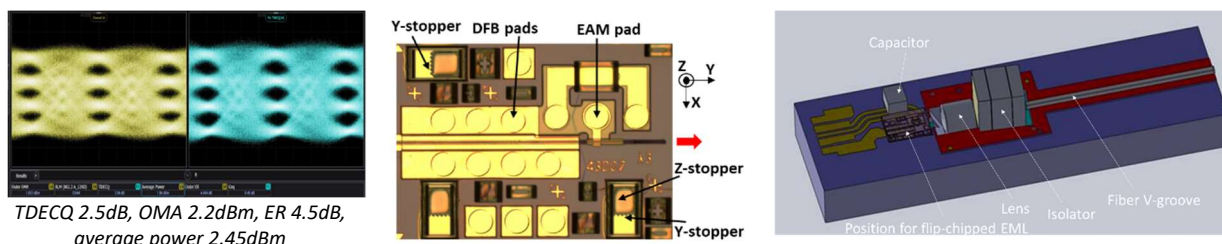


Fig. 3: (a) DR4 module experimental results at 100Gb/s (53GBaud PAM4) at 60°C, (b) photograph of DFB-EAM for self-alignment, (c) scheme of the SiPho submount with HF lines, lens, isolator and V-groove

External cavity tunable laser: we also develop SOAs or reflective SOAs which integrate under the quantum wells a sole material with a slightly higher index, allowing to reduce losses, increase saturation power and obtain an ultra-wide optical mode. These RSOAs, are particularly suitable for tunable lasers with external cavity by butt-joint coupling with a tunable passive filter in SiPho [9], or as boosters at the exit of photonic circuit.

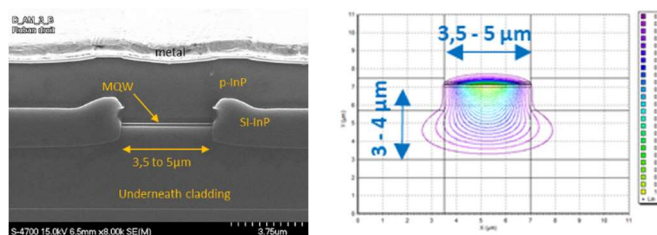


Fig. 4: (a) SEM photograph of an SOA facet with broad waveguide and underneath layer, (b) simulated ultra-broad optical mode

CONCLUSION AND PERSPECTIVES

The integration of InP and SiPho platforms seems to be the key solution for many applications. Heterogeneous integration now provides excellent performance, and is reaching sufficient maturity to become open source, which suggests significant developments in the coming years. But this requires complex and specific technology, very large investments, and only few actors can master it. Therefore it seems essential to us to develop hybridization in parallel because it is a flexible approach, which allows an independent optimization of the different components. It provides economic autonomy with a multiplicity of possible collaborations, and the rapid implementation of new components.

We have developed a SIBH technology particularly suitable for hybridization, and are studying different approaches (passive alignment with fiducials or self-alignment). The key factor for success will be performance, but also industrialization with the possibility of achieving large quantities, automation, yields, costs.

Authors acknowledge the European Commission for their support in the project APPLAUSE, and in particular Charles-Alix Manier and Hermann Oppermann from IZM Fraunhofer Institute for self-aligned assembly.

References

- [1] K.Lawniczuk, "Photonic ICs in a generic foundry", IPRM 2014.
- [2] M.Thiel et al., "3D printing of polymer optics", CLEO 2017.
- [3] C.Koos et al., "Photonic wire bonding and 3D nanoprinting in photonic integration – from lab demonstrations to production", ECOC 2018.
- [4] G.Roelkens, "III-V/Si PICs based on micro-transfer printing", OFC 2019.
- [5] C.Xiang et al., "High-performance silicon photonics using heterogeneous integration", IEEE J. of Sel. Topics in Quantum Electronics, Vol.28, no.3, May-June 2022.
- [6] C.Besançon et al., "Comparison of AlGaInAs-based laser behavior grown on hybrid InP-SiO₂/Si and InP substrates", IEEE Photonics Technology Letters, Vol.32, no.8, 2020.
- [7] X.Dai et al., "Versatile externally modulated lasers technology for multiple telecommunication applications", IEEE J. of Sel. Topics in Quantum Electronics, Vol.27, no.3, 2021.
- [8] H.Debrégeas et al., "High-performance 100Gb/s DWDM transmitter through fully passive assembly of a single-chip array of directly modulated lasers with SiO₂ AWG", ISLC 2014
- [9] A.Verdier et al., "Ultrawideband wavelength-tunable hybrid external-cavity lasers", Journal of Lightwave Technology, Vol.36, no.1, 2018.

Micro-Transfer-Printed III-V-on-Si Laser with 120nm tuning range

(Student paper)

Emadreza Soltanian^{1,2*}, Grigorij Muliuk³, Sarah Uvin⁴, Dongbo Wang^{1,2}, Guy Lepage³, Peter Verheyen³, Joris Van Campenhout³, Stefan Ertl⁵, Johanna Rimböck⁵, Nicolas Vaissiere⁶, Delphine Néel⁶, Joan Ramirez⁶, Jing Zhang^{1,2} and Gunther Roelkens^{1,2}

¹Photonics Research Group, INTEC, Ghent University - IMEC, Ghent, Belgium

²Center for Nano- and Biophotonics, Ghent University - IMEC, Ghent, Belgium

³IMEC, Kapeldreef 75, 3001 Heverlee, Belgium

⁴Brolis Sensor Technology BV, Bollebergen 2B/Box 11, 9052 Zwijnaarde, Belgium

⁵EV Group E.Thallner GmbH, DI Erich Thallner Str. 1, 4782 St. Florian am Inn, Austria

⁶III-V Lab, Avenue Augustin Fresnel 1, F91767 Palaiseau, France

* emadreza.soltanian@ugent.be

Many integrated photonics applications require miniaturized on-chip sources over a wide wavelength range, such as coherent optical communication and spectroscopy. In this work, we demonstrate for the first time a 120nm tuning range (1495nm-1615nm) widely-tunable III-V-on-Si laser realized using micro-transfer printing technology.

Keywords: Silicon Photonics, Widely Tunable Lasers, Micro-Transfer Printing, Heterogeneous Integration

INTRODUCTION

Silicon photonics (SiPh) enables the realization of photonic integrated circuits (PICs) on 200mm or 300mm Silicon-on-Insulator (SOI) wafers with high uniformity and yield by leveraging the CMOS fabrication infrastructure [1]. Since Si does not provide optical gain, III-V semiconductors have to be introduced to enable SiPh providing complex PICs for a wide range of applications, such as optical communication, sensing and spectroscopy. Various heterogeneous III-V-on-Si integration methods have been intensively investigated in the past, such as flip-chip integration, die-to-wafer bonding, and even hetero-epitaxial growth [2]. However, these methods suffer from drawbacks like a dedicated III-V process flow and modified back-end process on 200mm wafers in the case of bonding, limited throughput for the flip-chip method and III-V material quality for hetero-epitaxial growth. Here, we use micro-transfer-printing (μ TP) [3] for the realization of a 120nm III-V-on-Si widely tunable laser (WTL). The technique allows for high-throughput & wafer-scale III-V integration, minimal disruption to the SiPh process flow, no singulation and handling of individual III-V chips and the possibility of densely integrating different non-native components on the SiPh platform.

DESIGN and FABRICATION

The III-V-on-Si laser structure is based on the μ TP of pre-fabricated InP-based semiconductor optical amplifiers (SOAs) as the gain section in a SiPh external cavity. The PICs are fabricated in imec's SiPh pilot line on 200mm SOI wafers with a 400nm thick silicon device layer and a 2 μ m thick buried oxide layer (BOX), including a back-end stack incorporating the heaters and metal tracks. The μ TP process is based on the use of an elastometric polydimethylsiloxane (PDMS) stamp to pick-up the pre-fabricated InP-based SOA (which is undercut by selectively etching the release layer) from its native III-V source wafer and to print it on the target substrate, which has recesses in the back-end down to the 3 μ m wide Si-waveguide. A spray-coated DVS-BCB adhesive bonding layer enables a high-yield printing process. The schematic of μ TP of pre-fabricated III-V SOAs on the imec's 400nm SOI platform is shown in Fig. 1.

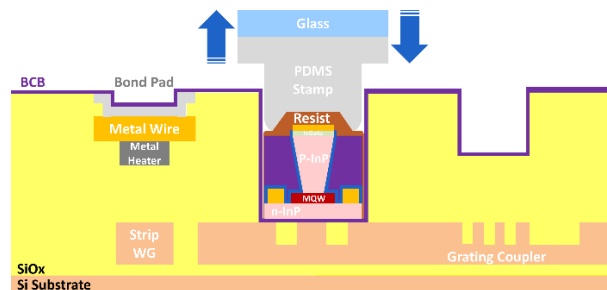


Fig. 1. Schematic of μ TP of a pre-fabricated III-V SOA on imec's 400nm SOI platform (not-to-scale).

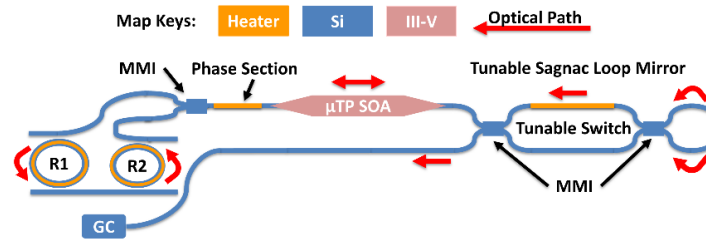


Fig. 2. Schematic layout of the laser cavity design of the individual tunable lasers.

The widely tunable laser is realized by combining two laser cavities in a single mode waveguide, each laser with a different SOA gain peak wavelength. The individual devices are formed by a linear cavity, shown in Fig. 2. The cavity consists of a tunable Sagnac loop mirror, a deep recess to print the pre-fabricated SOA (Fig. 1), a phase section based on thermo-optic tuning, a pair of thermally tunable micro-ring resonators (MRRs), and a grating coupler (GC) as the output of the laser. The tunable Sagnac loop mirror enables the optimization of out-coupling mirror reflectivity. The tunable MRRs with a slightly different radius ($27\mu\text{m}$ and $29.3\mu\text{m}$) are used to form a Vernier filter, which enables wavelength selection. The free spectral range (FSR) of each ring is around 4nm and the combined FSR of the Vernier filter is around 45nm in the envisioned wavelength range. 65mW of electrical power is required to tune a single ring over one FSR. The length of the III-V SOAs (fabricated by III-V Lab) are 1mm , including a pair of $180\mu\text{m}$ long adiabatic tapers for an efficient coupling between the III-V SOA and the underlying Si-waveguide. An additional pair of adiabatic $50\mu\text{m}$ long Si tapers is used to couple the optical mode between the $3\mu\text{m}$ wide Si-waveguide underneath the III-V SOA and the single-mode rib waveguide. The design and fabrication of the III-V SOAs is similar to what is described in detail in Ref. [4].

Prior to the μTP a combination of dry-etch (by RIE) and wet-etch (by BHF) was firstly applied to the SiPh chip to remove the back-end stack, to form the recess where the InP-based SOA will be integrated. The locally opened recess is slightly longer and wider than the pre-fabricated III-V SOA. Next, a thin DVS-BCB adhesive layer with a thickness of about 100nm was spray-coated to enhance the bonding strength between the III-V SOA and the underlying Si-waveguide. A short soft bake of spray-coated sample at 150°C was done before the μTP . The μTP was done by using a X-Celeprint $\mu\text{TP-100}$ lab-scale printer, followed by an oxygen-plasma etch to remove the photoresist encapsulation on the III-V SOA. The post-processing finishes by electrically connecting the devices to the silicon photonics back end. Fig. 3 shows a microscope image of two fabricated lasers with the two transfer-printed SOAs, both combined in a single output waveguide using a 3dB combiner. The SOA printed on the first laser (Laser 1) has a gain peak around 1575nm and the other one around 1525nm (Laser 2).

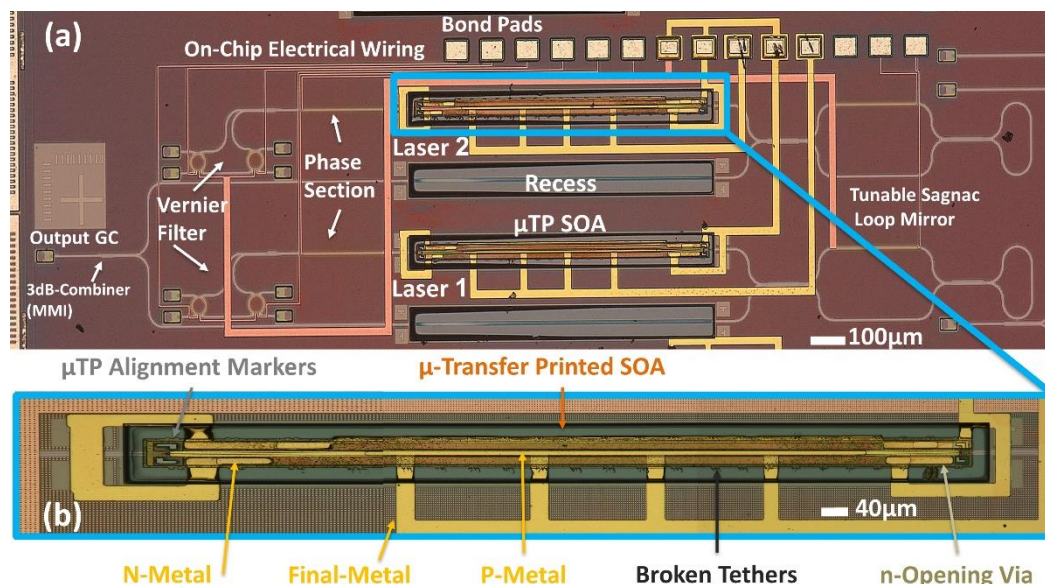


Fig. 3. (a) Microscope image of the combined widely tunable laser. (b) micro-transfer-printed III-V amplifier in the recess (after final metallization).

CHARACTERIZATION

To characterize the combined widely tunable laser, the sample is placed on a temperature-controlled stage stabilized at 15°C. The μ TP III-V SOAs of both lasers had a differential resistance of about 10 Ω biased at 140mA. The threshold current of both the lasers is around 60mA. Fig.4 shows the discrete wavelength tuning by thermally tuning one of the micro-rings and phase section of each laser, which resulted in a tuning range of 120nm. The phase section is used to adjust the phase of the laser cavity to be matched with the tuned filter. Fine-tuning is achieved by thermally tuning both the micro-rings and the phase section simultaneously, as shown in the inset.

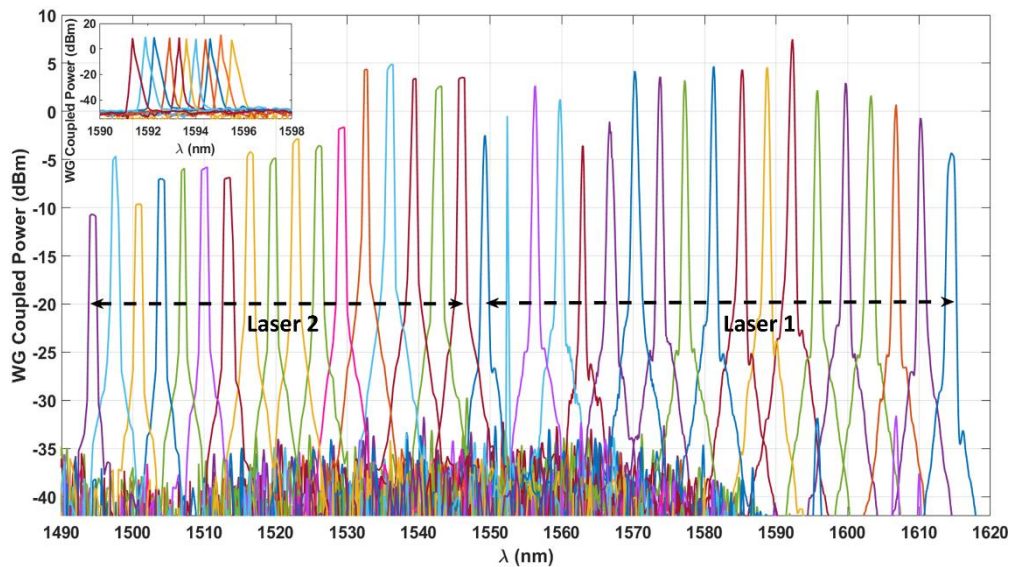


Fig. 4. Wavelength tuning behavior of the combined widely tunable laser (Fine-tuning is done in 10 steps over a range of 4nm, which is equal to the FSR of one ring).

CONCLUSION

For the first time, we demonstrate a 120nm III-V-on-Si widely tunable laser by micro-transfer printing pre-fabricated InP-based SOAs on a SiPh platform. This is a stepping stone towards the realization of complex PICs with integrated lasers and semiconductor optical amplifiers over a wide range of wavelengths for applications such as sensing, spectroscopy and optical communication.

Acknowledgements: This work was supported by the European Union's Horizon 2020 research and innovation programs under agreement No. 871345 (MedPhab) and No. 814276 (ITN-WON).

References

- [1] C. Xiang et al., "High-Performance Silicon Photonics Using Heterogeneous Integration", IEEE Journal of Selected Topics in Quantum Electronics, vol. 28, no. 3, pp. 1-15, 2022
- [2] Wang, Z. et al., "Novel Light Source Integration Approaches for Silicon Photonics", Laser & Photonics Reviews, vol. 11, pp. 63, 2017
- [3] J. Zhang et al., "III-V-on-Si Photonic Integrated Circuits Realized Using Micro-Transfer-Printing", APL Photonics (invited), vol. 4, pp. 110803-1108013, 2019
- [4] B. Haq et al., "Micro-Transfer-Printed III-V-on-Silicon C-Band Semiconductor Optical Amplifiers", Lasers & Photonics Reviews, vol. 14, 1900364, 2020

CW emission and self-pulsing in III/V SiN hybrid laser with narrowband mirror

Cristina Rimoldi¹, Lorenzo Columbo¹, Sebastian Romero-García², Jock Bovington³ and Mariangela Gioannini¹

¹Dipartimento di Elettronica e Telecomunicazioni, Politecnico di Torino, Corso Duca degli Abruzzi 24, Torino, IT-10129, Italy

²CISCO Optical, Nuremberg, Germany

³CISCO Systems, San José, CA, USA

*cristina.rimoldi@polito.it

We investigate the CW stability of a III-V SiN hybrid laser. By detuning the lasing frequency with respect to the narrowband mirror reflectivity peak, we observe regimes of ultra-damped relaxation oscillations, turbulence, and self-pulsing, caused by the interplay of four-wave mixing, the non-null linewidth enhancement factor, and the narrowband reflectivity. The laser tolerance to optical feedback is also investigated, for the purpose of providing indications on isolator-free operation.

Keywords: Silicon photonics, hybrid lasers, optical feedback, self-pulsing

INTRODUCTION

Laser sources integrated in Silicon Photonic (SiPh) platforms are essential for the realization of low-cost optical transmitters for optical interconnects, for sensing and LIDAR applications. These lasers usually consist of a III-V gain material for light generation and amplification coupled to the rest of the silicon photonic chip, providing the laser mirror facet and extending the laser cavity. The design of the SiPh mirror can include several components, such as micro-rings, delay lines, Mach-Zehnder interferometers, and DBR reflectors, all providing very narrow band (a few GHz bandwidth) dispersive reflectors [1], which allow to obtain long external cavity narrow linewidth lasers with wide tunability [2,3]. While much effort has been dedicated to the experimental and theoretical study of the laser linewidth reduction, few works have been focused on the study of other dynamical characteristics. Alongside narrow linewidth and CW emission, generation of self-pulsing and chaotic regimes was also reported [2,3]. In this work, we theoretically investigate the impact of the dispersive narrow band reflector in the dynamical performance of the laser. First, we consider the dynamics of the solitary laser and we analyze when and why CW emission can turn into a multimode regime. We demonstrate that several dynamical regimes can be observed, ranging from CW ultra-stable (where the laser relaxation oscillations are strongly damped) to self-pulsing or turbulent. These regimes have been experimentally observed [2,3] via the tuning of the lasing frequency, however they lack, to the best of our knowledge, a theoretical description able to explain the reasons behind their occurrence. Our work proves that these regimes are due to the interplay between the non-null linewidth enhancement factor and four-wave mixing in the reflective semiconductor optical amplifier and depend on the narrow bandwidth of the SiPh mirror and on the laser effective length. In the second part we discuss how the external optical feedback (due to spurious back-reflections coming from the other components of the SiPh circuit or from the output optical fiber) destabilize the CW emission. In the framework of investigating laser design for isolator-free operation [4,5], we study the laser tolerance to optical feedback and we highlight regions of ultra-stability, with tolerance to optical feedback up to -10 dB. The presented work provides a versatile tool for the analysis of external cavity hybrid lasers and our results can potentially be extended to other laser configurations.

METHODS

We consider the hybrid laser illustrated in Fig 1(a). This laser consists of an off-the-shelf III-V MQW 1mm long HR/AR RSOA edge-coupled to a silicon photonic circuit based on two coupled Si₃N₄ micro-rings, which provide narrowband dispersive reflectivity through Vernier effect. The ring radii are chosen in order to maximize the tuning range and minimize the overlap of the ring resonance peaks near the lasing one. The ring coupling coefficients are chosen as equal to obtain maximum mirror reflectivity in the critical coupling regime. This configuration has been analyzed in [5]. The overall effective reflectivity of the SiPh mirror ($|r_R(\nu)|^2$ in Fig.1(a)) has an FWHM bandwidth of 6 GHz (unless otherwise specified), obtained through ring design. The peak of $|r_R(\nu)|^2$ is 3% and the output power is collected through the output coupler $T_{c,out}=73\%$ [5]. Detuning of the lasing frequency with respect to the effective reflectivity peak is obtained via tuning of the phase $\Delta\phi$ of the control section PS. To account for spurious optical back-reflection, we include the possibility of an external reflector (r_{ext}) at a distance L_{ext} from the output coupler; based on the origin of the back reflection, we assume that the external optical feedback can range from -40 dB to -10 dB and L_{ext} can vary from a few millimeters to a few centimeters. The numerical model applied in our analysis

is based on [6] and consists in a set of time-delayed algebraic differential equations at the reference plane of the AR-coated facet of the RSOA. The model accounts for the frequency-selective mirror and assumes a Lorentzian response for the rings around the reference frequency. In particular, an integral equation for propagation of the optical electric field in the RSOA is coupled to the delayed differential equations accounting for the response of the rings and to the rate equation for the average carrier density of the RSOA. A linear stability analysis (LSA) of the CW solutions of the laser [6] allows to address the impact of the dispersive mirror bandwidth, the tuning of the phase control section, and the external cavity on the laser dynamics. In particular, the main complex roots of the determinant of the linearized system for the CW perturbations result associated to the relaxation oscillation (RO) and the photon-photon resonance (PPR) and give the frequency (real part of the roots, f_{pert}) and damping (imaginary part of the roots, γ_{pert}) of these resonances. Numerical simulations of the dynamical equations give the temporal evolution of the laser in terms of output power versus time, RIN spectra, integrated RIN, and optical spectra.

RESULTS AND DISCUSSION

In Fig. 1(b) we show the map of the integrated RIN (over a bandwidth of 25 GHz) computed for different values of RSOA bias current and detuning $\Delta\nu$ of the lasing frequency with respect to the effective reflectivity $|r_R(\nu)|$ peak. The blue region of low RIN (< -160 dBc/Hz) corresponds to a stable single-mode regime, while the red region of high RIN (> -130 dBc/Hz) corresponds to a multimode regime (which we will characterize as self-pulsing or turbulent in the following). The white dashed line is obtained through LSA and highlights the border beyond which single mode emission becomes unstable (i.e., when the imaginary part of the RO root becomes negative, leading to undamped RO).

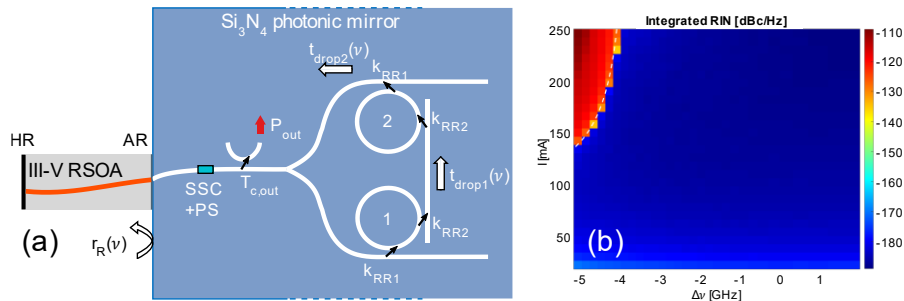


Fig. 1. Schematics of the III-V/SiN hybrid laser (a) and integrated RIN for different detuning $\Delta\nu$ of lasing frequency and RSOA bias current (b). $\Delta\nu=0$ corresponds to lasing at the reflectivity peak which is centered at 1310 nm.

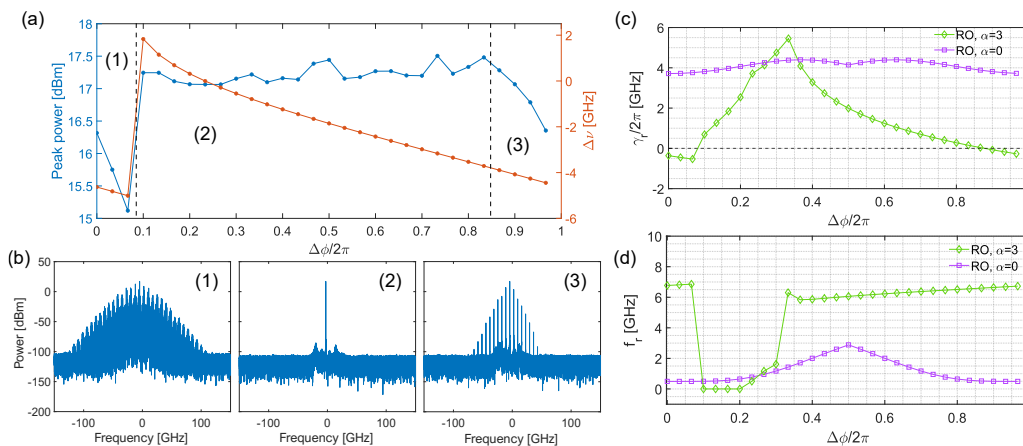


Fig. 2. Simulated lasing frequency and output power obtained through tuning of the phase section PS (a), optical spectra for the three dynamics regimes (b), damping (c) and frequency (d) of the roots associated to ROs for varying $\Delta\phi$. The RSOA bias current is fixed at 230 mA.

Figure 2(a) shows the lasing frequency (in orange) and the average output power (in blue) for varying $\Delta\phi$ and fixed RSOA bias current of 230 mA. In Fig. 2(b) we report the optical spectra related to region 1 (turbulent regime), region 2 (stable single-mode emission), and region 3 (self-pulsing regime). In order to interpret the transition between single mode and multimode regimes, we consider the results of LSA, reported in Fig. 2(c,d), where we show, in green, the frequency (c) and damping rate (d) of the roots associated to ROs for different $\Delta\phi$: when the perturbation frequency becomes resonant with the beating between neighboring longitudinal modes, the damping becomes negative and we enter a CW unstable regime, characterized by undamped relaxation oscillations and consequent

multimode regime. In particular, for negative detuning of the lasing frequency $\Delta\nu$, the phase noise, caused by spontaneous emission and the α -parameter, turns into intensity noise due to the narrow band reflector and may cause another longitudinal mode to reach the lasing threshold. When the beating frequency between the competing modes is resonant with the RO, the latter becomes undamped and the laser typically enters in a self-pulsing regime. This effect tends to decrease for smaller (but still negative) detuning because of the contrasting effect of detuned loading [7], until an optimal maximum RO damping point is reached. The following reduction of the damping through further increase of $\Delta\phi$ is then due to the progressive reduction of the detuned loading effect. Note that, when the effect of the linewidth enhancement factor is neglected (purple curves in Fig. 2 (c,d)), this scenario is completely altered because of the reduced phase noise effect and self-pulsing and turbulent regimes are unachievable. The results in Fig. 2 are in accordance with experimental findings in [2,3] and can exemplify a valuable approach to interpret experimental results. As a general trend, we show in Fig. 3(a) that through proper design of effective mirror, narrow bandwidths can give higher damping factors in comparison with the case of a broad band reflector. The longer cavity effective length implies the emergence of a second peak in the IM response, associated to PPR, which plays an important role in the laser tolerance to optical feedback.

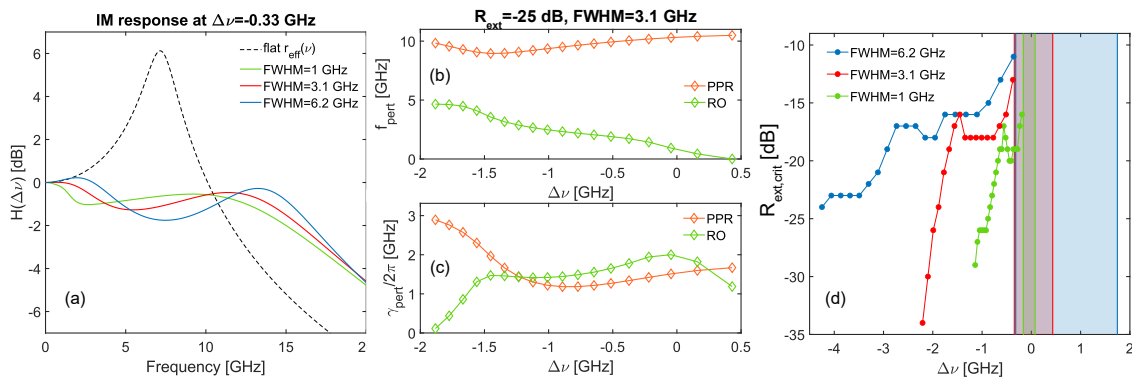


Fig. 3. Intensity-Modulation response for different reflectivity FWHMs at the RSOA bias current of 104 mA, corresponding to a power output of 20 mW (a), frequency (b) and damping (c) of the main roots for FWHM=3.1 GHz and $R_{ext}=-25$ dB versus detuning $\Delta\nu$, and (d) critical feedback level versus detuning $\Delta\nu$.

To study the effect of spurious back-reflections, we place e.g. the external reflector at $L_{ext}=0.5$ cm from the output coupler in Fig. 1(a). In Fig. 3(b,c), we show (for the case of FWHM=3.1 GHz and $r_{ext}^2 = R_{ext} = -25$ dB) the main roots of the perturbations as a function of the detuning $\Delta\nu$, associated to RO (in green) and PPR (in orange). Here, while the laser is still stable, PPR has become less damped in comparison to ROs and will eventually trigger instability. This is shown in Fig. 3(d), where we report the critical feedback level (i.e., the value of R_{ext} for which the laser becomes CW unstable) as a function of the detuning for the three FWHMs. The shaded areas of matching colors identify regions of ultra-stability, where the laser is particularly resilient to optical feedback up to $R_{ext}=-10$ dB. In all cases, near the ultra-stable region, instability is triggered by PPR: smaller FSR for narrow mirror bandwidth favor longitudinal mode coupling and this leads to a lower tolerance to optical feedback, an effect that is not possible to capture through a standard single-mode Lang-Kobayashi approach [5].

In conclusion, while narrow mirror bandwidths are effective in suppressing ROs, the emergence of a second resonance due to PPR is not to be neglected and leads to lower laser feedback tolerance. Consequently, proper design of the SiPh mirror is necessary to guarantee the laser feedback tolerance while reducing the mirror bandwidth, which is important in light of enabling isolator-free operation.

References

- [1] C. Xiang et al., *Widely tunable Si₃N₄ triple-ring and quad-ring resonator laser reflectors and filters*, 2018 IEEE 15th International Conference on Group IV Photonics (GFP), pp. 1–2 2018.
- [2] D. Huang et al., *High-power sub-kHz linewidth lasers fully integrated on silicon*, *Optica*, vol. 6, pp. 745-752, 2019
- [3] J. Mak et al., *Linewidth narrowing via low-loss dielectric waveguide feedback circuits in hybrid integrated frequency comb lasers*, *Opt. Express*, vol. 27, pp. 13307-13318, 2019
- [4] Z. Zhang et al., *Linewidth enhancement factor in InAs/GaAs quantum dot lasers and its implication in isolator-free and narrow linewidth applications*, *IEEE J. Sel. Top. Quantum Electron.* Vol. 25, pp. 1–9, 2019.
- [5] L. Columbo et al., *Efficient and optical feedback tolerant hybrid laser design for silicon photonics applications*, *IEEE J. Sel. Top. Quantum Electron.*, vol. 26, pp. 1-10, 2020
- [6] E. Detoma, *The complex way to laser diode spectra: example of an external cavity laser with strong optical feedback*, *IEEE J. Quantum Electron.*, vol. 41, pp. 171-182, 2005.
- [7] M. A. Tran et al., *Tutorial on narrow linewidth tunable semiconductor lasers using Si/III-V heterogeneous integration*, *APL Photonics*, vol. 4, pp. 111101, 2019.

Integration of Quantum Dot Lasers with SOI Waveguides using Micro-Transfer Printing

(Student paper)

Ali Uzun¹, Fatih Atar¹, John Justice¹, Ruggero Loi², Alex Farrell², Peter Ossieur³, Jing Zhang⁴, Gunther Roelkens⁴, Igor Krestnikov⁵, Johanna Rimböck⁶, Stefan Ertl⁶, Marianna Pantouvaki⁷, Guy Lepage⁷, Joris Van Campenhout⁷, Brian Corbett¹

¹Tyndall National Institute, University College Cork, Ireland.

²X-Celeprint Ltd, Lee Maltings, Dyke Parade, Cork, Ireland.

³imec-IDLab and Ghent University, Ghent, Belgium.

⁴Photonics Research Group, INTEC, Ghent University—imec, 9052 Ghent, Belgium.

⁵Innolume GmbH, Konrad-Adenauer-Allee 11; 44263 Dortmund, Germany.

⁶EV Group E.Thallner GmbH, DI Erich Thallner Str. 1, 4782 St. Florian am Inn, Austria.

⁷imec, Kapeldreef 75, Leuven, Belgium.

email: ali.uzun@tyndall.ie

We demonstrate the integration of long (2.4 mm) 1.3 μm etched facet quantum dot (QD) laser diodes into 7 μm deep recesses on an SOI wafer by micro transfer printing (μTP). Inverse tapered waveguide couplers were used to edge-couple the light from the QD laser to the 220 nm thick Si waveguide layer. Characterization exhibits that the QD lasers with 2 mm cavity length have threshold currents ~ 20 mA with output powers above 10 mW at 80 mA. A waveguide-coupled power of ~ 1 mW was obtained.

Keywords: Butt Coupling, Quantum Dot Laser Diodes, Silicon Photonics, transfer printing

INTRODUCTION

Si-based photonic integrated circuit (PIC) platforms provide a powerful route to scaling the performance (bandwidth, energy consumption) of optical transceivers while reducing the manufacturing cost [1]. These circuits require integrated light sources which introduces co-integration challenges. Several integration approaches have been explored including wafer/die bonding [2-3], flip chip technique [4] and micro-transfer-printing (μTP) [5-6] for wafer level integration of devices such as laser diodes, modulators, and photodetectors. Each technique has its own advantages and drawbacks. We achieve integration through edge-coupling the laser via μTP inside recesses to the waveguide, which offers high throughput, parallel device integration and the opportunity of pre-integration testing.

The target recesses are 120 μm wide and 2.5 mm long on a silicon-on-insulator (SOI) wafer, Fig. 1(a). 7 μm deep trenches are formed with two etch steps. The receiving Si waveguides with single inverse tapered tip (Fig.1(a) inset) are designed and fabricated on the imec 220 nm silicon photonics platform with a 2 μm buried oxide and a 5 μm SiO₂ over-cladding (Fig. 1(b)). An edge coupling efficiency of above 60% (-2 dB) for the quantum dot waveguide is simulated for the laser mode with a lateral and vertical misalignment tolerance of ± 1.3 μm and ± 0.5 μm respectively, for a -3 dB coupling penalty as shown in Fig. 2(a). The vertical tolerance is rather smaller than that in the horizontal direction as a result of the strong vertical mode confinement in the QD region. In addition, the longitudinal spacing between the laser facet and receiving Si waveguide has a 5 μm -3 dB coupling tolerance with an in-fill refractive index of 1.5 as given in Fig. 2(b).

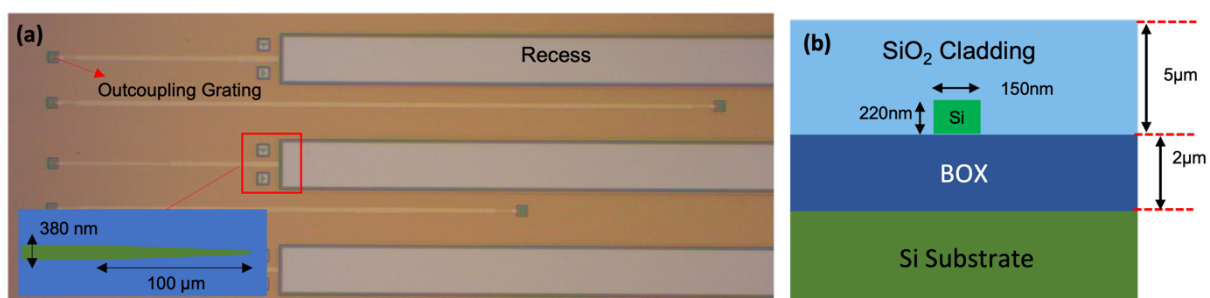


Fig. 1. a) 2.5 mm long and 120 μm wide recess on SOI wafer (Inset: schematic of Si waveguide coupler inverse tapered from 150 nm to 380 nm over 100 μm distance) and b) Cross section of a single tip inverse taper coupler design.

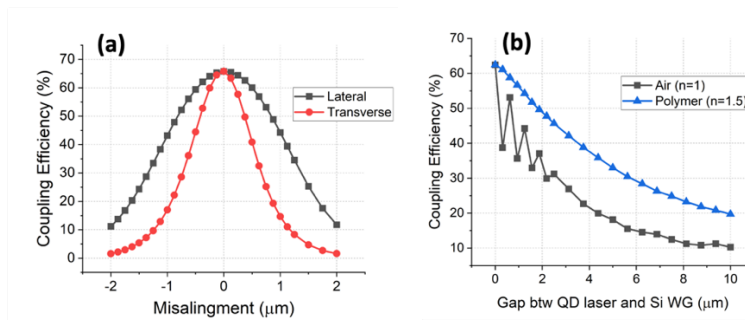


Fig. 2.a) Lateral and transverse misalignment tolerance simulation for an inverse single tapered waveguide, and b) Longitudinal tolerance as a function of spacing and refractive index of filling material.

The GaAs QD laser coupons were designed to be 65 μm wide with physical lengths of 1.5 mm, 1.8 mm, and 2.4 mm (corresponding laser cavity lengths in these coupons are 1 mm, 1.5 mm, and 2 mm, respectively) including bond pads for probing the devices. Laser devices were fabricated based on an epitaxial structure grown by Innolume that contains an active region comprising of a stack of 14 InAs QD layers separated by GaAs spacers. The waveguide is clad by 1.2 μm thick p- and n- doped AlGaAs layers. After device formation, encapsulation and tether definition, laser coupons were released using diluted HCl by selectively etching an $\text{Al}_{0.95}\text{Ga}_{0.05}\text{As}$ sacrificial layer which was added to the epitaxial structure in between the substrate and the n-GaAs layer in order to permit the release of the device from the native wafer. The suspended QD laser coupons then were transfer-printed into the deep recess containing 100 nm spray-coated Benzocyclobutene (BCB) by EVG prior to printing. The fabrication and integration flow is depicted in Fig. 3.

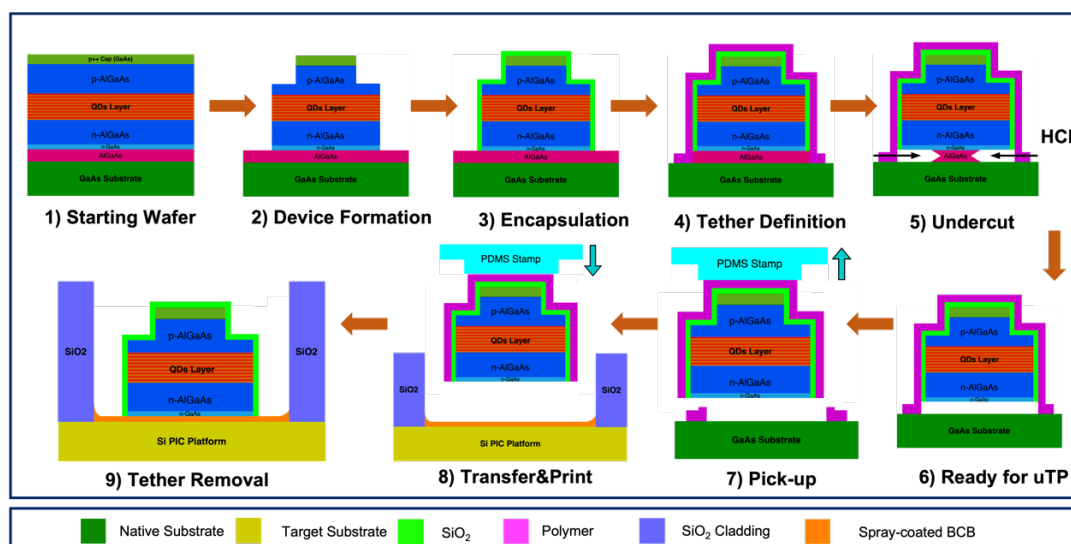


Fig. 3. Device fabrication flow on an epitaxial structure including an AlGaAs release layer (1-2). Coupons were encapsulated by SiO_2 for facet and epitaxial structure protection during release etch (3). A polymer (resist) anchor system (4) keeps coupons in place during sacrificial layer etch by HCl:DI (5). Then, devices are picked-up by a PDMS (Polydimethylsiloxane) stamp (7) and transfer-printed into 7 μm deep Si recess (8). Finally, the resist tethers were removed for electrical connection (9).

RESULTS and ANALYSIS

QD laser coupons up to 2.4 mm long were transfer printed with high yield (>90%) on both flat Si substrates and in the trenches on the SOI target, Fig. 4(a). In order to evaluate the device performance after release and transfer, laser diodes printed on flat Si coated with 1 μm Intervia were characterized under continuous wave (CW) conditions. Light-Current-Voltage (LIV) characteristics showed that laser can deliver an output power > 10 mW at 80 mA with an 18 mA threshold current, Fig. 5(a), which confirms that there is no degradation (i.e. threshold current) after printing. At 150 mA more than 20 mW is obtained. The emission wavelength is measured to be 1290 nm, Fig. 5(a) inset. The waveguide coupled edge-emitting transfer-printed lasers were characterized under CW using the setup depicted in Fig. 4(c). Up to 250 μW light coupling to the receiving single mode fiber is measured from the waveguide with single tip inverse taper design (Fig. 5(b)) with a 1.8 mm long laser coupon with threshold current 25 mA. The slight increase in the threshold current is because of the polymer in-fill between the QD laser and Si coupler which reduces the facet reflectivity. As the coupling loss due to the grating and fibre is ~ 6 dB, a waveguide power of 1 mW is estimated. Considering the amount of power that the laser is capable of producing, waveguide coupled light

suffers from misalignments due to tight tolerance of edge-coupling in lateral, longitudinal and transverse direction. The main reason for the low power is the longitudinal misalignment of $> 5\mu\text{m}$ as measured in SEM image (Fig. 4(b)).

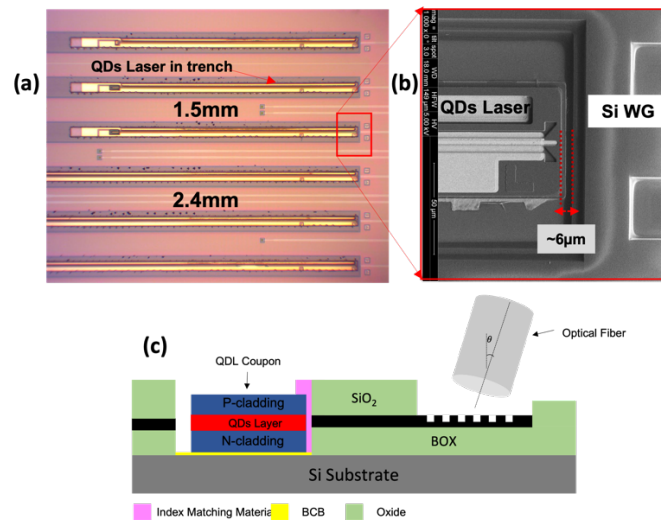


Fig. 4. a) Optical image that shows QD laser coupons >1.5 mm length transfer-printed into a deep trench on SOI, b) SEM image of a laser coupon inside a recess next to a Si waveguide coupler and c) Edge coupling schematic describing light coupling from laser to Si waveguide and from Si grating to fiber.

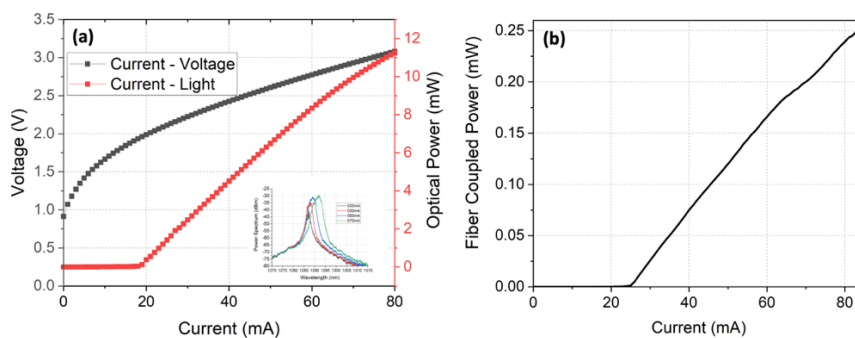


Fig. 5. a) LIV plots of a transfer printed 1.8 mm QD laser on $1\mu\text{m}$ Intervia on Si (Inset: spectrum at different bias current) and b) Current versus coupled light into the Si waveguide from a 1.8 mm long laser coupon.

CONCLUSION

Integration and waveguide coupling of low threshold and high efficiency edge-emitting QDs laser coupons was demonstrated. QD laser devices longer than 1.5 mm showed a threshold current of 20 mA with output power above 10 mW at 80 mA. $250\mu\text{W}$ of light is measured from the outcoupling grating to a single mode fiber and it is expected that much higher powers in the Si waveguide are achievable with optimum positioning of the laser.

Acknowledgements: This work has been supported by the CALADAN project, grant agreement No 825453 and Science Foundation Ireland 12/RC/2276_P2.

References

- [1] D. Thomson et al., "Roadmap on silicon photonics," J. Opt., vol. 18, no. 7, 2016.
- [2] G. Roelkens et al., "III-V/silicon photonics for on-chip and intra-chip optical interconnects," Laser Photon. Rev., vol. 4, no. 6, pp. 751–779, 2010.
- [3] B. Song et al., "3D integrated hybrid silicon laser," Opt. Express, vol. 24, no. 10, pp. 10435–10444, 2016.
- [4] T. Shimizu et al., "Optical Characteristics of a Multichannel Hybrid Integrated Light Source for Ultra-High-Bandwidth Optical Interconnections, Photonics," vol. 2, no. 4, pp.1131-1138, 2015.
- [5] R. Loi et al., "Edge-Coupling of O-Band InP Etched-Facet Lasers to Polymer Waveguides on SOI by Micro-Transfer-Printing," in IEEE Journal of Quantum Electronics, vol. 56, no. 1, pp. 1-8, Feb. 2020.
- [6] J. Zhang et al., "Transfer-printing-based integration of a III-V-on-silicon distributed feedback laser," Opt. Express, vol. 26, no. 7, pp. 8821–8830, 2018.

Long cavity hybrid mode-locked laser with improved modulation efficiency

(Student paper)

Yasmine Ibrahimi^{1,3}, Sylvain Boust¹, Quentin Wilmart², Jean-François Paret², Alexandre Garreau¹, Karim Mekhazni¹, Catherin Fortin¹, François Duport¹, Ghaya Baili⁴, Corrado Sciancalepore², Stéphanie Garcia², Laurent Vivien, and Frédéric van Dijk¹

¹III-VLab, a joint laboratory between Nokia Bell Labs, Thales Research and Technology, and CEA-LETI, 91767, Palaiseau, France

²CEA-LETI University Grenoble Alpes, 38000, Grenoble, France

³C2N University Paris-Saclay, 91767, Palaiseau, France

⁴Thales Research and Technology, RD 128 91767 Palaiseau Cedex, France

* yasmine.ibrahimi@3-5lab.fr

In this work, we highlight the enhancement of the performances of our hybrid InP/Si₃N₄ mode-locked laser under active and harmonic mode locking. To this end, we use a two-section R-SOA with a dedicated section for modulation. This configuration provides 3 times the modulation efficiency, which not only improves the overall performances of active mode locking but also allows for harmonic mode locking up to the 10th harmonic.

Keywords: Mode-locked lasers, R-SOA modulation, Silicon nitride extended cavity, Active mode locking

INTRODUCTION

Optical frequency combs (OFC) provide an effective solution for many applications that requires accuracy and precision such as metrology, spectroscopy and frequency banks generation in the microwave domain for RADAR and LIDAR systems [1-2]. OFC is a coherent source made of a train of equidistant lines in the frequency domain and can be generated using different methods such as ring resonators [3] or mode-locked Fabry-Perot laser oscillators. In this work, we present active and harmonic mode locked laser on the InP/Si₃N₄ hybrid platform based on low FSR and high quality factor extended cavity. The Si₃N₄ (silicon nitride) chips provides low propagation losses (< 10 dB/m) and low bend losses allowing for compact waveguides and very long cavities which is suitable for very low FSR (Free Spectral Range) mode-locked lasers. Our laser cavity is made of an R-SOA (Reflective Semiconductor Optical Amplifier) on InP which provides the gain source (>20 dB) and the back mirror of the cavity, butt-coupled to an Si₃N₄ chip that contains a delay line (~28 cm) and a Bragg grating used as the filter and the second cavity mirror. The cavity FSR is of 364 MHz. The passive Si₃N₄ chips are using a 90 nm thick, 2.9 μm wide stoichiometric Si₃N₄ buried in silica [4].

R-SOA RF MODULATION

The R-SOA chip provides a compact optical gain source with a large modulation bandwidth. For our application, the gain from the R-SOA allows to compensate the losses in the extended Si₃N₄ cavity. The R-SOA chips are also used for their electro-optical modulation ability [5] that allowed us to achieve active mode locking via electrical modulation.

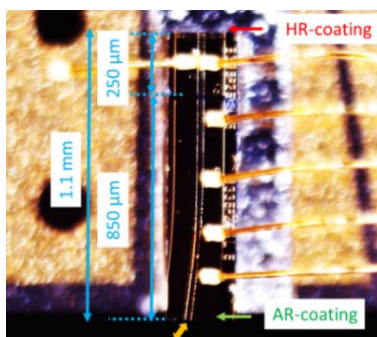


Figure 1 Two-section R-SOA with 250 μm section for modulation access and a 850 μm section for DC current access

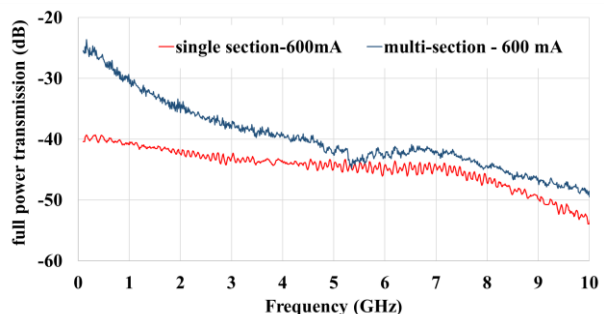


Figure 2 : Comparison of the RF power transmission with a two-section R-SOA (dark blue) and a mono-section R-SOA (red)

In this work, we used a two-section R-SOA. The 1.1mm waveguide is divided into two sections: the first section has a length of 250 μm , it has an RF access that allows for modulation, while the second section has a length of 850 μm and is only DC biased (*Figure 1*). Using a dedicated section for electrical modulation allows for a higher modulation efficiency [6]. We investigated this hypothesis by measuring the RF power transmission of the two section R-SOA and compare it with a 1100 μm long single section R-SOA from the same fabrication run used in our previous work [4]. The power transmission is measured using a VNA (Vector Network Analyser) and measurement results can be found in *Figure 2*. The modulation section was biased at 50mA and the second section at 600 mA. The single section R-SOA was biased at 600 mA. We can see that the power transmission achieved using two-section R-SOA is more than 14 dB higher than that of a single-section R-SOA at 364 MHz and more than 4 dB higher at 3.64 GHz, the mode-locked laser's 10th harmonic. We concluded that using a two-section R-SOA could improve active and harmonic mode locking efficiency.

ACTIVE AND HARMONIC MODE LOCKING RESULTS

We used a dynamic alignment setup to align the two-section R-SOA to the Si_3N_4 passive chip. For active mode-locking, we used an RF source which provides up to 30 dBm RF power to the R-SOA via the modulation section. The butt-coupling setup is illustrated in *Figure 3*.

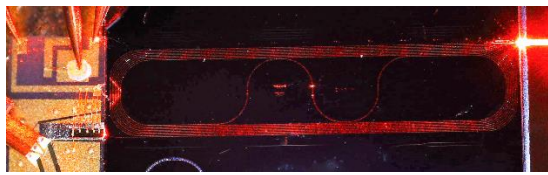


Figure 3: Photograph of R-SOA butt-coupled to the Si_3N_4 chip. The waveguide illuminated with a red laser to make it visible

Figure 4 and *Figure 5* show the optical and the electrical spectrum of the mode-locked laser (MLL) in active mode-locking configuration at 364 MHz. The results are similar to those obtained in our last work [4], but we've applied significantly less RF power to achieve it (14 dBm instead of 23 dBm), this shows that the modulation efficiency is indeed higher when using a two-section R-SOA. We can see that the electrical spectrum measurement shows that the mode at 364 MHz is 20 dB higher than the higher frequency tones (above 2 GHz).

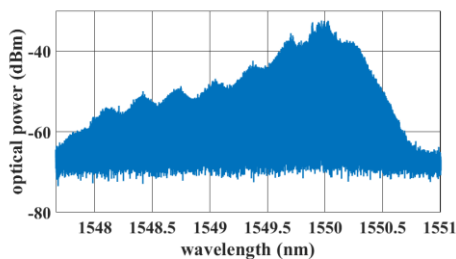


Figure 4: Active mode locking optical spectrum acquired using a high resolution optical spectrum analyzer

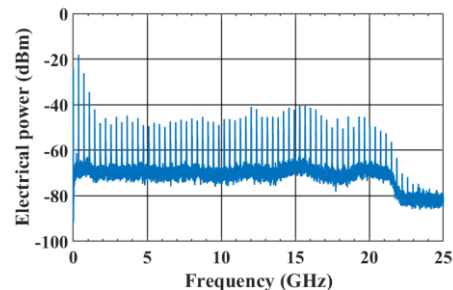


Figure 5: Active mode locking electrical spectrum

We operated the MLL in the harmonic mode-locking configuration. *Figure 6* and *Figure 7* show the results obtained with a modulation frequency at the 10th harmonic (3.64 GHz) when applying 30 dBm of RF power.

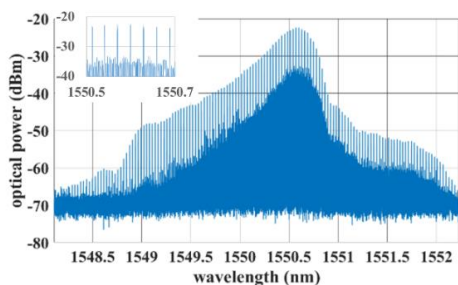


Figure 6 : harmonic mode-locking optical spectrum with $f_{RF} = 3.64$ GHz. Insert gives a zoom on the center of the spectrum

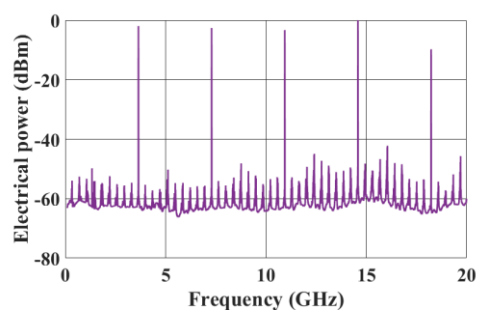


Figure 7: corresponding electrical spectrum detected with a 20GHz BW photodiode, showing a SMSR of more than 50 dB

We obtain an electrical SMSR (side mode rejection ratio) of more than 50 dB Figure 7. On the optical spectrum (Figure 6), we can see the modes with a 3.64 GHz spacing, and an optical SMSR of more than 10 dB. In our previous work [4], we were able to achieve harmonic mode locking up to the 6th harmonic only and at very low R-SOA bias currents (around 120 mA). In this case, however, the current was set at 450 mA for the DC current supply section and at 16mA for the modulation section. We were hence able to achieve harmonic mode locking at a higher frequency while operating the MLL at almost twice the current used previously. Biasing the laser at a higher current, as far as possible from its threshold, allows to have a better rejection of spontaneous emission noise and leads to more gain in the cavity which means a higher output power.

To complete our study, we performed phase noise measurements on the MLL in the harmonic mode locking regime. Figure 8 6 shows the MLL phase noise at 3.64 GHz. For this measurement, we used the phase noise measurement option of a Rohde&Schwarz FSU 67 electrical spectrum analyser. Figure 8 shows also the phase noise measurement of the synthesizer used for the electrical injection locking, the measurement floor here is mainly due to the electrical spectrum analyser limits. We obtain a phase noise level of the mode-locked laser below -120 dBc/Hz for an offset frequency above 1 kHz. We observe noise excess above 1MHz due to the laser large cut-off frequency (> 10's of MHz). This noise can be filtered with longer cavities. We observe also noise excess at harmonics of the laser FSR due to spontaneous emission located at non-lasing modes frequencies.

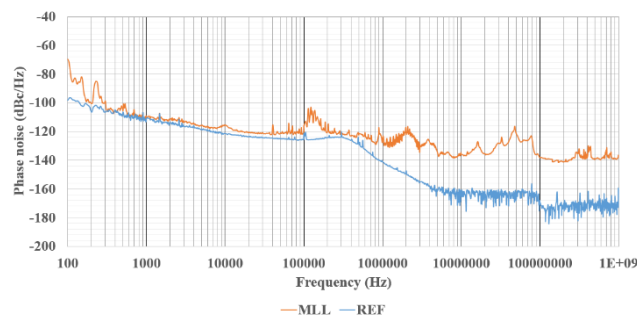


Figure 8 6 Phase noise measurement in harmonic mode locking configuration

DISCUSSION

We demonstrated that separating the modulation section from the current supply section in an R-SOA improves the modulation efficiency in our extended hybrid mode-locked laser cavity. Harmonic mode locking up to the tenth harmonic has been obtained with a good phase-noise level considering the dynamically butt-coupled laser cavity configuration. Packaging of this laser should lead to a better mechanical stability of the laser cavity and even better phase noise performances.

ACKNOWLEDGEMENT

This work has been achieved with the support of the Direction Générale pour l'Armement (DGA). The authors thank the European Defense Agency (EDA) for the support to this work in the context of the project entitled "Photonic integrated circuits for multiband RF transceiver in arrayed systems (PICTURE)" funded by France and Italy and coordinated by Leonardo S.p.a. in the frame of the Project n°B-1487-IAP1-GP of the European Defense Agency. The authors thank the staff of the LETI silicon platform for the Si₃N₄ process optimization.

REFERENCES

- [1] Schiller, S. "Spectrometry with frequency combs." *Optics letters* 27.9 (2002): 766-768.
- [2] Gaeta, Alexander L., Michal Lipson, and Tobias J. Kippenberg. "Photonic-chip-based frequency combs." *nature photonics* 13.3 (2019): 158-169.
- [3] Kippenberg, Tobias J., Ronald Holzwarth, and Scott A. Diddams. "Microresonator-based optical frequency combs." *science* 332.6029 (2011): 555-559.
- [4] Y. Ibrahim et al., "Low FSR Mode-Locked Laser Based on InP-Si₃N₄ Hybrid Integration," in *Journal of Lightwave Technology*, vol. 39, no. 24, pp. 7573-7580, 15 Dec.15, 2021, doi: 10.1109/JLT.2021.3089322.
- [5] G. Stathi, Z. V. Rizou and K. E. Zoiros, "Simulation of directly modulated R-SOA," 2017 International Conference on Numerical Simulation of Optoelectronic Devices (NUSOD), 2017, pp. 145-146, doi: 10.1109/NUSOD.2017.8010033
- [6] F. Duport et al., « Directly modulated high power semiconductor optical amplifier », in 2018 International Topical Meeting on Microwave Photonics (MWP), Toulouse, oct. 2018, p. 1-4.

GaSb/SOI flip-chip integrated DBR laser at 2 μm wavelength region

(Student paper)

Nouman Zia, Jukka Viheriälä, Heidi Tuorila, Samu-Pekka Ojanen, Eero Koivusalo, Joonas Hilska, Mircea Guina

Tampere University, Korkeakoulunkatu 3, Tampere, 33720, Finland

*nouman.zia@tuni.fi

Integrated photonics is rapidly progressing towards addressing the needs of a wider range of applications, owing to its potential for mass manufacturability and miniaturization. This development trend requires novel laser sources compatible with silicon photonics technology and operating at wavelengths beyond the traditional telecom window. In particular, novel applications in gas sensing or medical diagnosis require operation at 2–3 μm range. To this end, the first flip-chip integrated hybrid laser comprising a cavity formed by a GaSb gain element and a distributed Bragg reflector (DBR) grating realized in a silicon photonics platform is demonstrated. The laser emitted slightly more than 6 mW at room temperature with a narrow spectral linewidth.

Keywords: SOI, GaSb, flip-chip, DBR

INTRODUCTION

Photonics Integrated Circuits (PICs) technology has seen prodigious growth since its advent, powered by penetration to an increasing number of volume applications, such as datacom, sensing, or lab-on-chip biophotonics. In this context, silicon photonics (SiPhs) and InP-based PICs have become already mature technology with major commercial deployment in datacom applications, operating around 1.3 μm and 1.55 μm wavelength regions [1,2]. However, many other emerging applications, for example, sensing of atmospheric pollutants [3] or real-time monitoring of biomarkers [4], such as glucose, lactates, or ethanol would require wavelength extension of PIC platforms beyond 2 μm . While the heterogeneous integration of InP light-emitting material and SiPhs have enabled the wavelength extension slightly beyond 2 μm [5], the further wavelength increase is limited by the inherent bandgap engineering of InP. To this end, GaInAlAsSb/GaSb-based laser diodes can reach an emission wavelength up to 3.5 μm [6], which then can be leveraged to SiPhs applications.

Hybrid extended cavity lasers based on GaSb reflective semiconductor optical amplifiers (RSOA) and SiPhs PICs have been already demonstrated near 2 μm [7] and more recently at 2.6 – 2.7 μm window [8]. However, these demonstrations are based on butt-coupling GaSb and SiPhs chips on different carriers hence lacking essential integration features of PICs, like compactness and the ability to combine different types of chips on the same PIC. Here we demonstrate for the first an on-chip hybrid distributed Bragg reflector (DBR) laser comprising GaSb RSOA and a 3 μm thick silicon-on-insulator (SOI) circuit waveguide for wavelength locking. The integration method is based on “flip-chip” bonding. Specifically, we are deploying the μm -scale SOI waveguide technology, which we have shown to exhibit low loss at 2.65 μm [9]. In general, the μm -scale SOI waveguides exhibit lower loss at mid-IR compared to more conventional submicron waveguides. This is because of the strong mode confinement in the Si waveguide, which minimizes the cladding loss and scattering loss. Moreover, the optical mode size for propagation in μm -scale SOI waveguides matches the mode size of III-V waveguides enabling high coupling efficiency between the two platforms. This demonstration opens an attractive perspective towards wavelength versatility by integrating broadband GaSb-based gain chips for the detection of multiple gas or biophotonics.

DESIGN AND FABRICATION

The detailed hybrid DBR laser cavity architecture used in this work is shown in Figure. 1. It comprises a J-shaped ridge waveguide RSOA [10] end-fire coupled to a tilt-facet DBR on SOI. The tilt angle of the RSOA, θ , was 7° and was optimized for the minimum back reflection. The RSOA ridge waveguide (RWG) width and epitaxially grown waveguide thickness were optimized to maximize simultaneously the coupling efficiency between the two waveguides (mode overlap) and RSOA modal gain. The simulation results for the mode mismatch

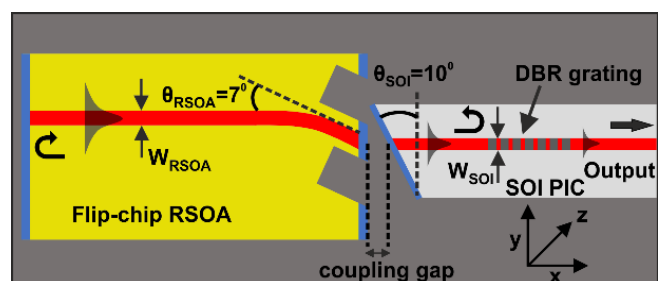


Fig. 1. Schematic of the hybrid integrated DBR laser based on flip-chip integration of RSOA and SOI waveguides.

loss and quantum well confinement (QWC) factor are shown in Figure 2. The ridge width and waveguide thickness were chosen to be $3\mu\text{m}$ or $5\mu\text{m}$, and 130nm respectively. These values ensured a mode mismatch loss of $\sim 0.6\text{dB}$ and quantum well confinement (QWC) factor of $\sim 2.4\%$.

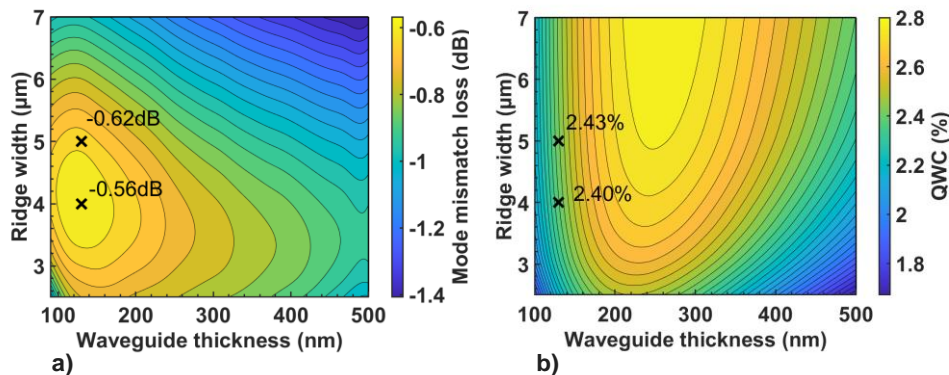


Fig. 2. Simulated mode mismatch loss (dB) between the RSOA and SOI waveguides, assuming perfect alignment, and b) quantum well confinement factor (%) in RSOA, for varying RSOA epitaxial waveguide thicknesses and ridge widths. The markers indicate the parameters used in the fabrication.

The epitaxial structure was grown by molecular beam epitaxy (MBE) using similar parameters as previously reported for the state-of-the-art superluminescent diodes [10]. The RWG width and the etch depth were optimized to ensure operation with the transverse electric single-mode profile. The RWG was defined by UV photolithography and dry-etched with an inductively coupled plasma reactive ion etch system (ICP-RIE). Additional ICP steps etch were done to etch a trench, which was used to fine-tune the optical axis vertical alignment, as well as grooves along the RSOA front facet. This last step was essential in minimizing the gap between RSOA and SOI waveguide, as shown in Figure.1. For current confinement, SiN_x was deposited and a contact window was etched at the center of the RWG employing photolithography and RIE-etching. The p-side contact consisted of Ti/Pt/Au-layers that were deposited with an e-beam evaporator. The sample was thinned to allow the subsequent cleaving of high-quality facets and on the n-side of the sample, a Ni/Au/Ge/Au stack was evaporated to form the n-contact. The wafer was cleaved into bars and the rear and front facets were coated with high-reflection (HR) and anti-reflection (AR) coatings, respectively. Individual devices were tested under continuous wave (CW) current injection before the flip-chip bonding.

RESULTS AND DISCUSSION

The hybrid integrated DBR lasers were tested under controlled temperature and continuous wave (CW) operation. The output power as a function of the injection current at 23°C is shown in Figure. 3. The maximum output power of 6.12 mW was achieved for an injection current of 352 mA where the laser emits around 1984 nm . Thermal tuning was also measured to be $0.14\text{ nm}/^\circ\text{C}$. The oscillations in the power-current curve are caused by the laser locking to the DBR mirror, i.e. at the peaks the cavity mode overlaps with the resonance peak of the DBR, and in the dips, there is minimal overlap between the cavity mode and DBR resonance. In addition, the output power is saturated at larger currents due to increased thermal and carrier-induced losses in the RSOA.

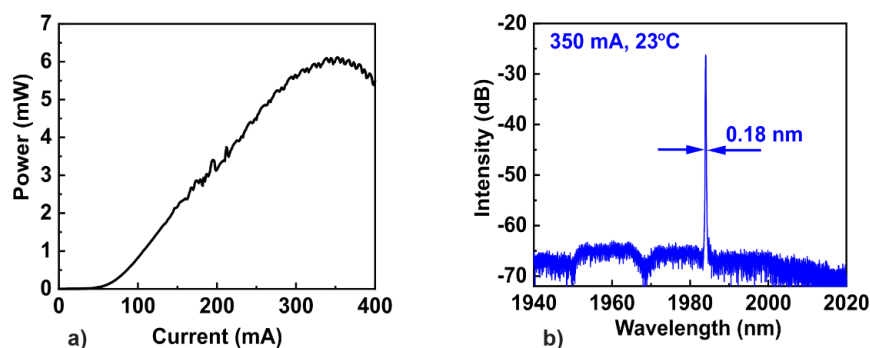


Fig. 3: a) The light-current characteristic curve of the hybrid laser at 23°C , and b) the spectrum of same laser at 23°C for an injection current of 350 mA . The maximum wavelength was 1984 nm with a full-width at half-maximum of 0.18 nm .

CONCLUSION

A GaSb/SOI hybrid DBR laser based on the flip-chip integration technique was demonstrated. A GaSb RSOA was based on a double quantum well with a J-shaped waveguide provided gain at around 2 μm . The use of μm -scale SOI enables a mode mismatch loss as low as 0.6 dB assuming perfect alignment. The hybrid DBR laser generated a CW output power up to 6.12 mW at 23°C. Further work is aimed at the wavelength extension beyond 3 μm wavelength, and demonstrating advanced tuning capability, so far realized only using but-coupling between GaSb and SOI chips mounted on different carriers.

Acknowledgments: The research was funded by EU Business Finland projects RAPSI (decision 1613/31/2018) and PICAP (decision 44761/31/2020). The work is also part of the Academy of Finland Flagship Programme PREIN #320168.

References

- [1] M. Smit, K. Williams, and J. Van Der Tol, "Past, present, and future of InP-based photonic integration," *APL Photonics*, vol. 4, no. 5, p. 050901, May 2019.
- [2] R. Soref, "The past, present, and future of silicon photonics," *IEEE J. Sel. Top. Quantum Electron.*, vol. 12, no. 6, pp. 1678–1687, Nov. 2006
- [3] A. Hänsel and M. J. R. Heck, "Opportunities for photonic integrated circuits in optical gas sensors," *JPhys Photonics*, vol. 2, no. 1. IOP Publishing Ltd, p. 12002, Jan. 23, 2020.
- [4] P. T. Lin *et al.*, "Label-Free Glucose Sensing Using Chip-Scale Mid-Infrared Integrated Photonics," *Adv. Opt. Mater.*, vol. 4, no. 11, pp. 1755–1759, Nov. 2016.
- [5] G. Boehm, G. Roelkens, M.-C. Amann, R. Baets, R. Wang, and S. Sprengel, "Broad wavelength coverage 2.3 μm III-V-on-silicon DFB laser array," *Opt. Vol. 4, Issue 8*, pp. 972–975, vol. 4, no. 8, pp. 972–975, Aug. 2017.
- [6] K. Vizbaras, A. Vizbaras, A. Andrejew, C. Grasse, S. Sprengel, and M.-C. Amann, "Room-temperature type-I GaSb-based lasers in the 3.0 - 3.7 μm wavelength range," in *Novel In-Plane Semiconductor Lasers XI*, Feb. 2012, vol. 8277, p. 82771B.
- [7] R. Wang, A. Malik, I. Šimonytė, A. Vizbaras, K. Vizbaras, and G. Roelkens, "Compact GaSb/silicon-on-insulator 20x μm widely tunable external cavity lasers," *Opt. Express*, vol. 24, no. 25, p. 28977, Dec. 2016.
- [8] S.-P. Ojanen *et al.*, "GaSb diode lasers tunable around 2.6 μm using silicon photonics resonators or external diffractive gratings," *Appl. Phys. Lett.*, vol. 116, no. 8, 2020.
- [9] J. Viheriälä *et al.*, "Building blocks for mid-IR programmable light source based on GaSb-based amplified spontaneous emission sources and μm -scale Silicon-on-Insulator waveguide photonics," in *Proceedings of the Conference ECIO, 2019*, Accessed: Aug. 14, 2020.
- [10] N. Zia, J. Viheriälä, E. Koivusalo, and M. Guina, "High-power single mode GaSb-based 2 μm superluminescent diode with double-pass gain," *Appl. Phys. Lett.*, vol. 115, no. 23, p. 231106, Dec. 2019.

Mid-infrared Fourier-transform spectrometer based on suspended silicon metamaterial waveguides

(Student paper)

Thi Thuy Duong Dinh^{1,*}, Xavier Le Roux¹, Natnicha Koumpai¹, Daniele Melati¹, Miguel Montesinos-Ballester¹, David González-Andrade¹, Pavel Cheben^{2,3}, Aitor V. Velasco⁴, Eric Cassan¹, Delphine Marris-Morini¹, Laurent Vivien¹ and Carlos Alonso-Ramos¹

¹Centre de Nanosciences et de Nanotechnologies, CNRS, Université Paris-Saclay, 10 Bd. Thomas Gobert, Palaiseau, 91120, France

²National Research Council Canada, 1200 Montreal Road, Bldg. M50, Ottawa, Ontario K1A 0R6, Canada

³Center for Research in Photonics, University of Ottawa, Ottawa, Ontario K1N 6N5, Canada

⁴Instituto de Óptica Daza de Valdés, Consejo Superior de Investigaciones Científicas (CSIC), Madrid 28006, Spain

* thi-thuy-duong.dinh@c2n.upsaclay.fr

Integrated mid-infrared micro-spectrometers hold great potential for environmental monitoring and aerospace applications. The use of silicon-on-insulator in the mid-infrared is limited by the absorption of the buried oxide layer beyond 4 μm wavelength. We overcome this limitation by using metamaterial-cladded suspended silicon waveguides to implement a Fourier-transform spectrometer operating near 5.5 μm wavelength.

Keywords: Fourier-transform spectroscopy, mid-infrared, metamaterial, silicon photonics

INTRODUCTION

The mid-infrared (mid-IR), spanning wavelengths from 2 to 20 μm , is a crucial wavelength range for spectroscopic applications because it comprises the absorption fingerprints of many chemical and biological compounds. Mid-IR optical spectrometers are employed in a wide variety of applications, including food safety, medical diagnostics, indoor air quality monitoring, astronomy, and resource exploitation [1]. Integrated spectrometers that can provide high sensitivity and real-time monitoring within ultra-compact and low-cost chips are highly sought after in mid-IR applications. Spatial heterodyne Fourier-transform spectrometers (SHFTS) have significant benefits in terms of optical throughput, resolution, and resilience against manufacturing imperfections [2]. The compatibility of SHFTS with passive calibration techniques enables software correction of amplitude and phase errors, as well as machine-learning algorithms for enhanced resilience against environmental instabilities [3].

Silicon photonics holds great potential for the implementation of compact and low-cost integrated spectrometers in the mid-IR, especially SHFTS [4]. Mid-IR SHFTS based on SiGe technology have recently been reported to reach 8.5 μm wavelength with a resolution of 15 cm^{-1} [5]. However, demonstrations of SHFT spectrometers based on silicon-on-insulator (SOI) technology are restricted to 3.75 μm wavelength (2 cm^{-1} resolution) due to the strong absorption of the buried oxide (BOX) layer for wavelengths above 4 μm [6]. Since their first demonstration in silicon photonics [7,8], subwavelength-grating (SWG) metamaterials [9] have been used as a powerful tool for refractive index engineering, overcoming performance limitations of conventional silicon photonic devices. Suspended silicon membrane waveguides with SWG cladding have been recognized as a potential solution to exploit the full silicon transparency window (1.1-8 μm wavelength range) [10]. This type of waveguide allows for the selective removal of the BOX layer underneath the waveguide core while benefiting from the high index contrast of silicon waveguides.

In this work, we demonstrate a SHFTS implemented with suspended silicon waveguides based on SWG metamaterial (see Fig. 1), effectively circumventing operational wavelength limits induced by BOX absorption. We demonstrate SHFTS operation near a wavelength of 5.5 μm , with a spectral resolution of approximately 13 cm^{-1} .

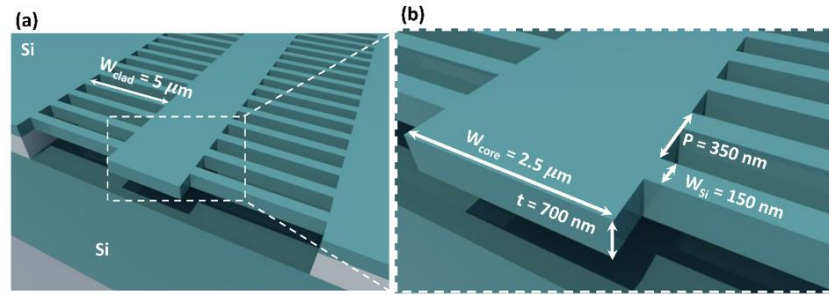


Fig. 1: (a) Schematic of a suspended silicon waveguide with metamaterial lateral cladding; (b) detailed view showing the main geometrical parameters.

RESULTS

We implemented the SHFTS as an array of 19 Mach-Zehnder interferometers (MZIs) with different optical path lengths ranging from $20\ \mu\text{m}$ to $\Delta L_{Max} = 200\ \mu\text{m}$. These parameters yield a theoretical resolution of $13\ \text{cm}^{-1}$, and a free spectral range (FSR) of $120\ \text{cm}^{-1}$. Figure 1 shows the schematic of the suspended silicon waveguide with metamaterial cladding used for the implementation of the MZIs. The metamaterial cladding offers mechanical stability and necessary effective lateral index contrast to confine the optical mode, while still requiring manufacture with a single Si etch step. The suspended SWG waveguides were implemented on the SOI platform with a silicon thickness of $700\ \text{nm}$, and a buried oxide layer thickness of $3\ \mu\text{m}$. The waveguide core width is $2.5\ \mu\text{m}$, and the cladding width is $5\ \mu\text{m}$. The lateral cladding grating has a period of $350\ \text{nm}$. To allow the penetration of hydrofluoric (HF) acid vapor for substrate removal, we select a gap length of $200\ \text{nm}$. Figure 2a presents the optical image of the fabricated spectrometer with a total footprint of $18\ \text{mm} \times 7.1\ \text{mm}$. Scanning electron microscopy (SEM) images of the suspended SWG waveguide and a Y-junction splitter are shown in Fig. 2c and 2b, respectively.

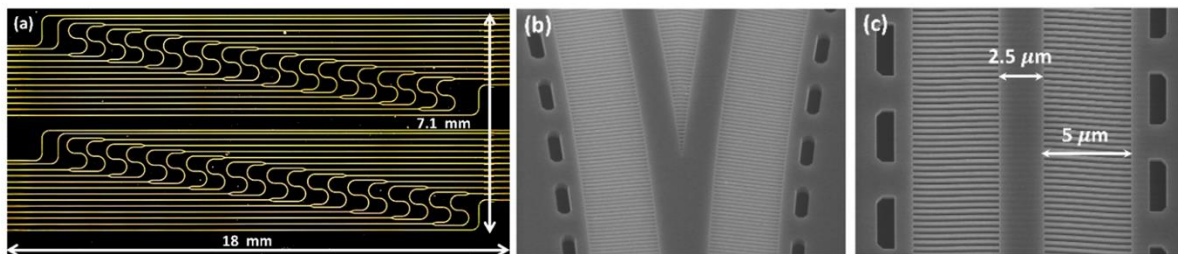


Fig. 2: (a) Optical image of the fabricated SHFTS. (b) SEM images of Y-junction splitter, and (c) metamaterial-cladded suspended waveguide.

Light from a tunable quantum cascade laser was injected and extracted from the chip using aspheric ZnSe lenses to measure the device's performance. A mercury-cadmium-tellurite (MCT) photodetector was used to measure the output signal. To determine the propagation losses of the suspended waveguides, we used the cut-back method by sampling the optical transmission of four waveguides with different lengths ranging from $1.4\ \text{cm}$ to $2.58\ \text{cm}$. Our suspended waveguides show propagation losses of $1\text{-}2\ \text{dB/cm}$ between 5.2 and $5.7\ \mu\text{m}$ wavelengths. We applied the pseudo-inverse matrix approach to calibrate the SHFT spectrometer and retrieve the input spectrum [2]. The pseudo-inverse retrieval approach is beneficial for correcting amplitude and phase errors caused by manufacturing imperfections. The input spectrum B is retrieved by the product between the output spectrum I and the calibration matrix T , which comprises the transmittance spectra of 19 MZIs. Figure 3a shows the measured calibration matrix T . For signal retrieval, we chose a bandwidth of $100\ \text{cm}^{-1}$, which corresponds to the theoretical calculation of the FSR. Figures 3b-3d present the retrieved spectra for monochromatic and doublets signals for wavelengths near $5.44\ \mu\text{m}$, $5.5\ \mu\text{m}$, and $5.6\ \mu\text{m}$, respectively. Correct doublet retrieval demonstrates a spectral resolution of approximately $13\ \text{cm}^{-1}$.

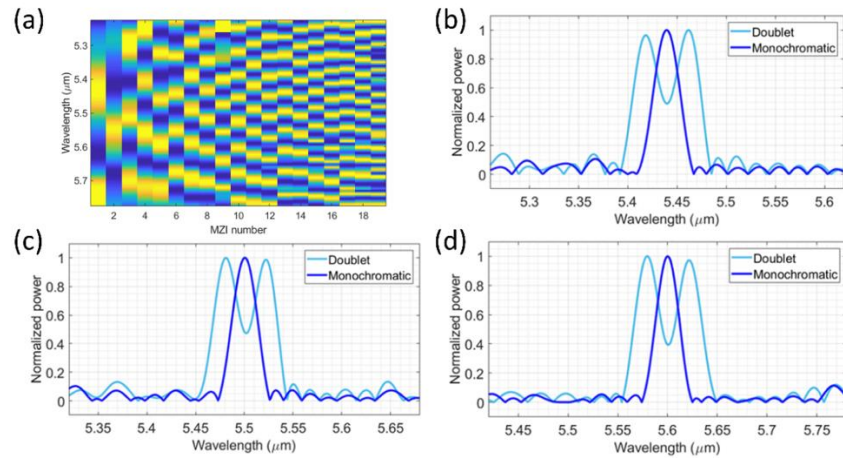


Fig. 3: (a) Calibration matrix of a SHFT with 19 MZIs. Retrieved spectrum of monochromatic and doublet inputs with peak-to-peak spacing of 13 cm^{-1} in the bandwidth of 100 cm^{-1} , for wavelengths around (a) $5.44 \mu\text{m}$, (b) $5.5 \mu\text{m}$, and (c) $5.6 \mu\text{m}$.

DISCUSSION

In conclusion, we presented an integrated mid-IR SHFTS chip implemented with suspended silicon waveguides with metamaterial grating cladding. This device overcomes the major limitation of the SOI technology in the mid-IR by circumventing the absorption of the silica BOX for wavelengths above $4 \mu\text{m}$. Fabricated waveguides present propagation loss of $\sim 2 \text{ dB/cm}$ near $5.5 \mu\text{m}$ wavelength. The SHFTS chip yields a measured resolution of 13 cm^{-1} and a bandwidth of 100 cm^{-1} . To the best of our knowledge, this is the longest wavelength reported for an integrated silicon SHFT spectrometer. These findings pave the way for the development of integrated spectrometers with high throughput and resistance to manufacturing imperfections while taking advantage of the whole silicon transparency range.

Acknowledgements: This work has been funded in part by the Agence Nationale de la Recherche (ANR-MIRSPEC-17-CE09-0041). The fabrication of the device was performed at the Plateforme de Micro-Nano-Technologie/C2N, which is partially funded by the Conseil General de l'Essonne. This work was partly supported by the French RENATECH network, the Spanish Ministry of Science and Innovation (MICINN) under grants RTI2018-097957-B-C33, RED2018-102768-T, and PID2020-115353RA-I00, Horizon2020 (Marie Skłodowska-Curie grant No. 734331) and the Community of Madrid – FEDER funds (S2018/NMT-4326).

References

- [1] L. Zhang, J. Chen, C. Ma, W. Li, Z. Qi, and N. Xue, *Research Progress on On-Chip Fourier Transform Spectrometer*, Laser Photonics Rev., vol. 15, pp. 2100016, 2021.
- [2] A. V. Velasco, P. Cheben, P. J. Bock, A. Delàge, J. H. Schmid, J. Lapointe, S. Janz, M. L. Calvo, D.-X. Xu, M. Florjanczyk, and M. Vachon, *High-resolution Fourier-transform spectrometer chip with microphotonic silicon spiral waveguides*, Opt. Lett., vol. 38, pp. 706-708, 2013.
- [3] D. M. Kita, B. Miranda, D. Davela, D. Bono, J. Michon, H. Lin, T. Gu, and J. Hu, *High-performance and scalable on-chip digital Fourier transform spectroscopy*, Nat. Commun., vol. 9, pp. 4405, 2018.
- [4] R. Soref, *Mid-infrared photonics in silicon and germanium*, Nat. Photonics, vol. 4, pp. 495-497, 2010.
- [5] Q. Liu, J. M. Ramirez, V. Vakarin, X. Le Roux, C. Alonso-Ramos, J. Frigerio, A. Ballabio, E. Talamas Simola, D. Bouville, L. Vivien, G. Isella, and D. Marris-Morini, *Integrated broadband dual-polarization Ge-rich SiGe mid-infrared Fourier-transform spectrometer*, Opt. Lett., vol. 43, pp. 5021-5024, 2018.
- [6] M. Nedeljkovic, A. V. Velasco, A. Z. Khokhar, A. Delàge, P. Cheben, and G. Z. Mashanovich, *Mid-Infrared Silicon-on-Insulator Fourier-Transform Spectrometer Chip*, IEEE Photonics Technol. Lett., vol. 28, pp. 528-531, 2016.
- [7] P. Cheben, D.-X. Xu, S. Janz, and A. Densmore, *Subwavelength waveguide grating for mode conversion and light coupling in integrated optics*, Opt. Express, vol. 14, pp. 4695-4702, 2006.
- [8] P. Cheben, P. J. Bock, J. H. Schmid, J. Lapointe, S. Janz, D.-X. Xu, A. Densmore, A. Delàge, B. Lamontagne, and T. J. Hall, *Refractive index engineering with subwavelength gratings for efficient microphotonic couplers and planar waveguide multiplexers*, Opt. Lett., vol. 35, pp. 2526-2528, 2010.
- [9] P. Cheben, R. Halir, J. H. Schmid, H. A. Atwater, and D. R. Smith, *Subwavelength integrated photonics*, Nature, vol. 560, pp. 565-572, 2018.
- [10] J. Soler Penades, A. Sánchez-Postigo, M. Nedeljkovic, A. Ortega Moñux, J. G. Wangüemert-Pérez, Y. Xu, R. Halir, Z. Qu, A. Z. Khokhar, A. Osman, W. Cao, C. G. Littlejohns, P. Cheben, I. Molina-Fernández, and G. Z. Mashanovich, *Suspended silicon waveguides for long-wave infrared wavelengths*, Opt. Lett., vol. 43, pp. 795-798, 2018.

Germanium quantum wells for mid-infrared integrated photonics

Andrea Barzagli¹, Virginia Falcone¹, Stefano Calcaterra¹, Raffaele Giani¹, Andrea Ballabio¹, Giovanni Isella¹, Daniel Chrastina¹, Michele Ortolani², Michele Virgilio³ and Jacopo Frigerio¹

¹L-NESS Dipartimento di Fisica, Politecnico di Milano, Via Francesco Anzani 42, Como, I-22100, Italy

²Dipartimento di Fisica, Sapienza Università di Roma, Piazzale Aldo Moro 5, I-00185 Rome, Italy

³Dipartimento di Fisica "E. Fermi", Università di Pisa, Largo Pontecorvo 3, I-56127 Pisa, Italy

* jacopo.frigerio@polimi.it

Ge/SiGe quantum wells grown on Si substrates can be used to explore new functionalities in mid-infrared integrated photonics. In such structures, intersubband optical transitions in the valence band can be leveraged to realize wavelength converters.

Keywords: mid-infrared photonics, quantum wells, nonlinear optics

INTRODUCTION

In recent years, mid-infrared integrated photonics has raised an increasing interest due to the envisioned applications in molecular sensing, environmental monitoring and security [1]. The Silicon-on-insulator (SOI) based technology, operating at wavelengths $\lambda < 3.2 \mu\text{m}$ has already reached a significant technology readiness level. By leveraging the maturity of the SOI technology, and taking advantage of the high index contrast between Si and SiO₂ many functionalities such as low-loss waveguiding, modulation and frequency comb generation have already been demonstrated. [1] Nevertheless, extending the operational wavelengths toward the long-wave infrared region (LWIR) ($8 \mu\text{m} - 12 \mu\text{m}$) present many challenges. First of all, the SOI technology cannot be used above $3.2 \mu\text{m}$ because of the strong absorption in SiO₂. In order to address these challenges, many material platforms including III-V semiconductors, halides, chalcogenides have been investigated. In this framework, the SiGe-on-Si material platform seems particularly promising. First of all, by taking advantage of the wide transparency range of Ge, low-loss waveguides operating up to $\lambda = 11 \mu\text{m}$ have been recently demonstrated, as well as a whole set of passive photonic components including Mach-Zehnder interferometers, resonators and spectrometers [2]. Also electro-optic modulation based on the plasma effect has been recently reported [3]. Nevertheless, key functionalities such as wavelength conversion, photodetection and high speed optical modulation are still missing. In this framework, Ge/SiGe quantum wells (QW) could be exploited to fill this gap. Intersubband optical transitions in the valence band of such heterostructures can be used for light detection, for high-speed modulation through the quantum confined Stark effect (QCSE), and for wavelength conversion through second harmonic generation. Ge/SiGe QWs can be easily grown on top of SiGe buffers, making them fully compatible with the existing SiGe-on-Si material platform. In this work, we show an experimental demonstration of second harmonic generation at mid-infrared frequencies [4,5] and a preliminary study for waveguide integration of the QW stack.

MID-INFRARED SECOND HARMONIC GENERATION

Group IV semiconductors, such as Si and Ge, feature a vanishing second-order optical linearity $\chi^{(2)}$ due to their centrosymmetric crystal structure. Nevertheless, such symmetry can be broken by creating an asymmetric potential profile for carriers, a condition that can be easily achieved in asymmetric coupled quantum wells (ACQW). Interestingly, the $\chi^{(2)}$ arising from intersubband dipole moments in ACQWs can reach values of 10^4 - 10^5 pV/cm, orders of magnitudes higher with respect to the best nonlinear crystals. Such giant optical nonlinearities have been investigated in III-V semiconductors, but only in recent years the SiGe epitaxial technology has reached a sufficient level of maturity for growing these heterostructures. The bandstructure of the sample has been designed with a semi-empirical first-neighbor $sp^3d^5s^*$ tight-binding Hamiltonian which includes spin-orbit interaction (fig 1a) and it has been used to calculate the absorption spectrum (fig 1b) and the second order nonlinear susceptibility (fig 1c).

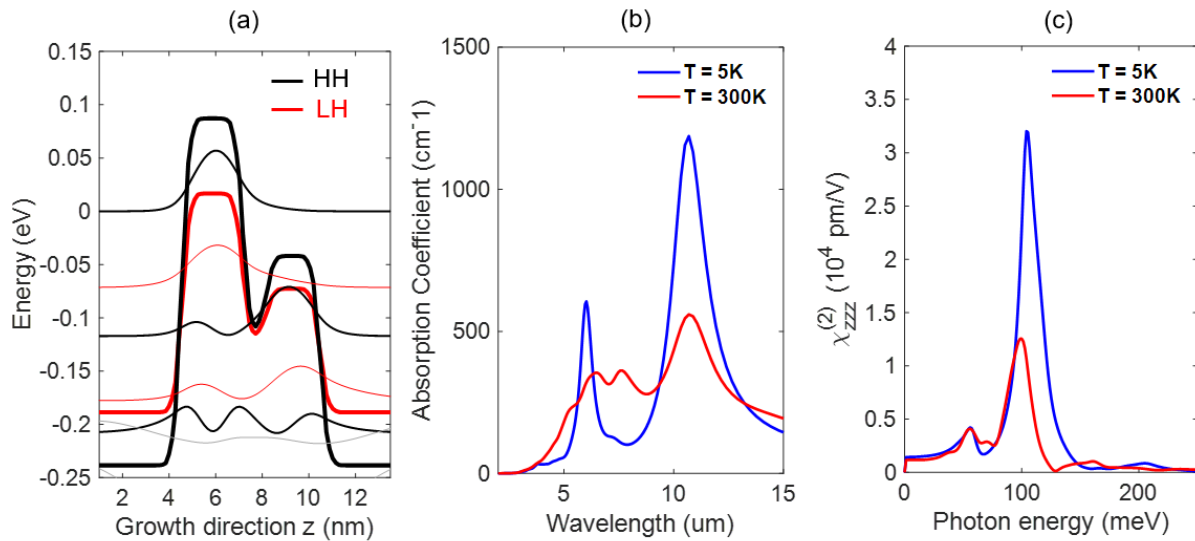


Figure 1: Valence band profile and wavefunctions (a), calculated absorption spectrum (b) and second order nonlinear susceptibility of the ACQW for TM polarization at $T = 5\text{ K}$ (blue) and at room temperature (red).

The sample (see fig. 2a) has been grown by low-energy plasma enhanced chemical vapor deposition (LEPECVD) on a (100) Si-substrate. The first part of the structure consists in a $1\ \mu\text{m}$ thick $\text{Si}_{0.8}\text{Ge}_{0.2}$ buffer followed by a $1\ \mu\text{m}$ thick $\text{Si}_{0.3}\text{Ge}_{0.7}$ virtual substrate. Then 20 periods of the ACQW (well/barrier thickness $2.4/1.0/2.7/3.9\ \text{nm}$, and Ge content $x_{\text{Ge}} = 0.96/0.67/0.93/0.52$) have been deposited at a rate of $0.1\ \text{nm/s}$ at a growth temperature of $T = 350^\circ\text{C}$. The main well has been p-doped with a 2D concentration of $4.1 \times 10^{11}\ \text{cm}^{-2}$. The sample has been structurally characterized by high-resolution X-Ray diffraction (HR-XRD). The reciprocal space map (RSM) relative to the (224) Si reflection is reported in Fig. 2b. From the RSM it is possible to notice the very high quality of the ACQW stack and its coherence with respect to the virtual substrate.

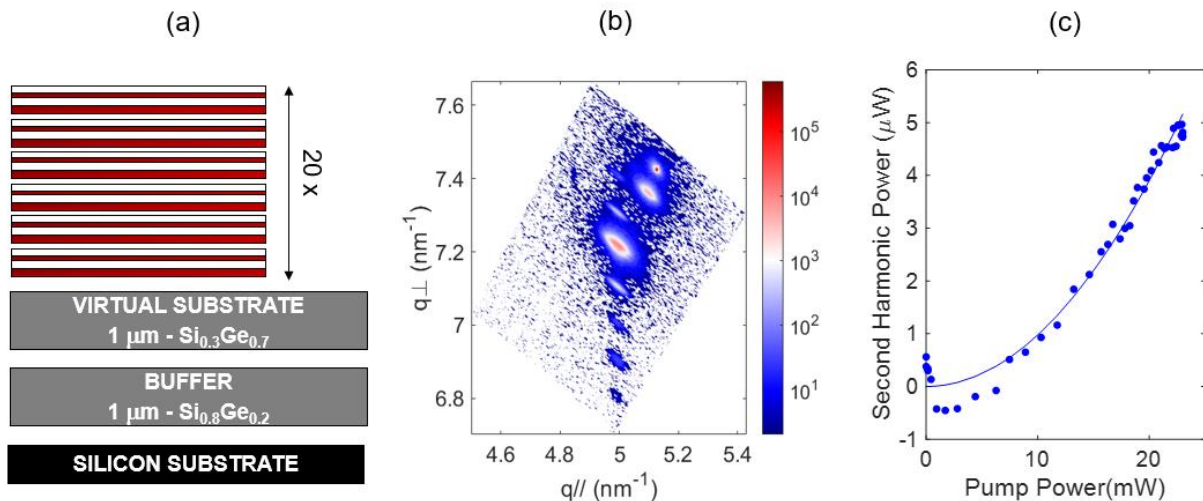


Figure 2: Schematic of the ACQW stack (a), 224 RSM of the sample (b). Second harmonic emission as a function of the pump power (c).

For the optical measurements, samples were cut in a $2\ \text{mm}$ single-pass surface-plasmon waveguide with the side facets shaped to 70° with respect to the growth plane and the top facet close to the ACQWs region coated by a Ti/Au layer. Then the samples (cooled at $10\ \text{K}$) have been pumped with a CW quantum cascade laser emitting at $\lambda = 10.3\ \mu\text{m}$. The light coming out from the samples have been then filtered and collected by an MCT detector. The second harmonic emission has been recorded as a function of the input power (see fig. 2c). A $\chi^{(2)} = 6 \times 10^4\ \text{pm/V}$ has been extracted from the measurement.

Finally, we have theoretically investigated the possibility to integrate the ACQW in waveguides. Since these “artificial nonlinearities” involve real quantum states, as opposite to the virtual quantum states employed in standard nonlinear crystals, optical absorption at the pump and second harmonic wavelengths must be taken into account. Some studies [6,7], by solving the coupled wave equations in presence of absorption, show that the second harmonic emission has a peak for an optimal wavelength length (assuming perfect phase matching), and then decays for the combined effect of pump depletion and second harmonic re-absorption. Preliminary calculations show that such optimal length, in the case of Ge/SiGe ACQW, is of a few hundreds of μm . For this reason, we are considering the design sketched in fig. 3a for ACQW integration. In this concept, the light coming from a $\text{Si}_{0.3}\text{Ge}_{0.7}$ waveguide is injected in a second waveguide, integrating the ACQW stack, through an adiabatic taper. The pump and the second harmonic mode are fairly overlapped in the ACQW region, as shown in fig 3a and 3b, where we calculated the distribution of the first TM mode by the Lumerical software package. The waveguide integrating the ACQW is periodically etched to achieve phase matching.

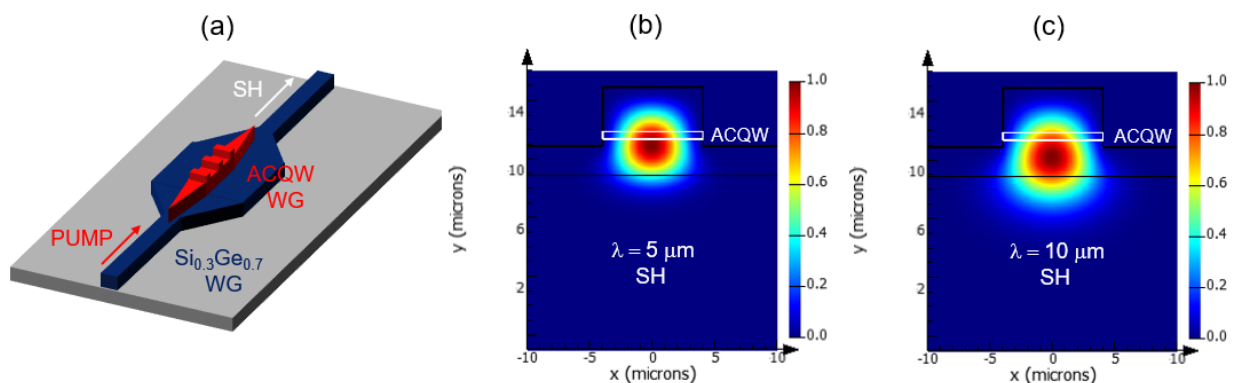


Figure 3: Sketch of the envisioned waveguide integrated wavelength converter (a), First TM mode at $\lambda = 5 \mu\text{m}$ (SH) (b) and at $\lambda = 10 \mu\text{m}$ (PUMP) (c) in the ACQW waveguide.

In conclusion, Ge/SiGe ACQW are very promising to expand the functionalities available in MIR integrated photonic circuits, especially in the important LWIR spectral region. In particular, the experimental data obtained from the material characterization, as well as the preliminary studies of waveguide integration show that Ge/SiGe ACQW has the potential to realize integrated wavelength converters.

Acknowledgments: This work has been supported by Fondazione Cariplo, grant n° 2020-4427.

References

- [1] R. Soref, Toward silicon-based longwave integrated optoelectronics (LIO), Proc. SPIE, 6898, 689809, 2008.
- [2] M. Montesinos-Ballester et al., *Ge-rich graded SiGe waveguides and interferometers from 5 to 11 μm wavelength range*, Opt. Exp. 28, 12771 (2020).
- [3] M. Montesinos-Ballester et al, *Mid-infrared Integrated Electro-optic Modulator Operating up to 225 MHz between 6.4 and 10.7 μm Wavelength*, ACS Photonics 9, 249 (2022).
- [4] J. Frigerio et al., *Modeling of second harmonic generation in hole-doped silicon-germanium quantum wells for mid-infrared sensing*, Opt. Expr. 26, 31861 (2018).
- [5] J. Frigerio et al., *Second harmonic generation in germanium quantum wells for nonlinear silicon photonics*, ACS Photonics 8, 3573 (2021).
- [6] G. Almyog and A. Yariv, *Second harmonic generation in absorptive media*, Opt. Lett. 19, 1828 (1994).
- [7] D. Neuschafer et al, *Second-harmonic generation using planar waveguides with consideration of pump depletion and absorption*, J. Opt. Soc. Am. B, 11, 649 (1994).

Mid-Infrared High Q Factor Silicon-Germanium Ring Resonator

(Student paper)

Marko Perestjuk^{1,2,*}, Rémi Armand¹, Alberto Della Torre¹, Milan Sinobad¹, Arnan Mitchell², Andreas Boes², Jean-Michel Hartmann³, Jean-Marc Fedeli³, Vincent Reboud³, Christelle Monat¹ and Christian Grillet¹

¹Université de Lyon, Institut des Nanotechnologies de Lyon (INL, UMR-CNRS 5270), Ecole Centrale de Lyon, 69130 Ecully, France

²School of Engineering, RMIT University, Melbourne, VIC 3001, Australia

³Université Grenoble Alpes, CEA-Leti, 38054 Grenoble Cedex 9, France

*email: marko.perestjuk@ec-lyon.fr

We demonstrate a ring resonator with high Q-factor in the mid-infrared in a silicon-germanium on silicon chip-based platform. The side-coupled ring exhibits a loaded Q-factor of 90,000 at the operating wavelength around 4.18 μm . This is the highest Q-factor achieved on this material platform.

Keywords: Mid-infrared, Cavities, Ring Resonators, Silicon Germanium

INTRODUCTION

The mid-infrared (MIR) wavelength range (between 3 and 13 μm) has shown a large potential for sensing applications, as many molecules have strong fundamental absorption lines in this range [1]. However, the high cost and bulky MIR technology has prevented a real breakthrough so far. The integration of MIR components on-chip can provide a crucial step towards large scale applications.

Several on-chip devices were implemented in the MIR [2-4], especially ring (and racetrack) resonators are expected to play a crucial role in on-chip integrated sensing schemes. As was first demonstrated in the near-IR, they can be used to generate frequency combs [5], and could thus provide a broadband MIR light source, a key element of sensing devices that can operate in a wide spectral range. Resonators with a high Q-factor can also enhance the interaction between light and molecules and hence boost the sensitivity [4, 6]. Several ring resonators have been demonstrated in the MIR [7-12]. High Q-factors have been achieved predominantly on silicon-on-insulator (SOI, [7]) and silicon-on-sapphire (SOS, [8]) platforms, which, however, have high losses beyond $\sim 3.5 \mu\text{m}$ and $\sim 6.5 \mu\text{m}$, respectively [1]. They were also used to demonstrate frequency combs at this wavelength range [13-15], for example one state-of-the-art demonstration at 2.4-4.3 μm in a silicon microring was shown in [13]. At the long wavelength end the power was quite low though due to the absorption. High-Q ring resonators in the MIR have been realized also with chalcogenide glass [16], although the material photosensitivity could translate in a low temporal device stability. In addition, group IV materials are preferable for cost-effective large scale fabrication. Silicon-germanium (SiGe) is a promising material, thanks to its CMOS compatibility and transparency window up to 15 μm [1]. Low-loss SiGe waveguides operating in the MIR have been already demonstrated [17], and their nonlinear properties were exploited for supercontinuum generation [18]. So far, however, only one SiGe ring resonator demonstration has been reported, with a moderate 3,200 Q-factor around 8 μm wavelength [9]. Here, we report a SiGe ring resonator coupled to a bus waveguide, which exhibits a loaded Q-factor of 90,000 at 4.18 μm .

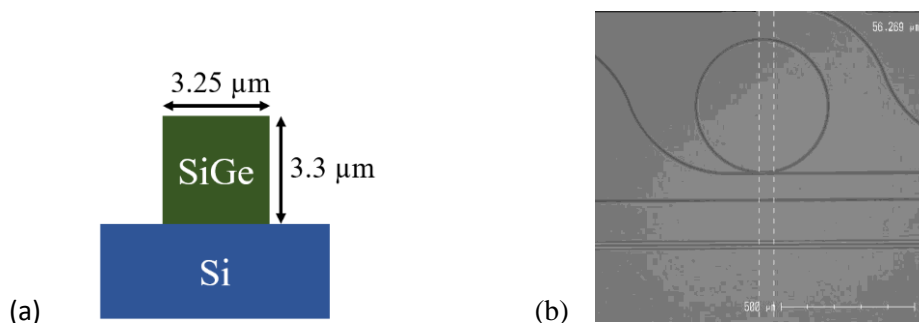


Fig. 1. (a) SiGe platform used for the ring resonator. (b) SEM picture of the ring resonator.

FABRICATION AND RING RESONANCE MEASUREMENT

Our platform consists of an air-cladded $3.3 \mu\text{m}$ thick and $3.25 \mu\text{m}$ wide $\text{Si}_{0.6}\text{Ge}_{0.4}$ core waveguide on a silicon substrate (Fig. 1a). The resonators were fabricated on a 200 mm CMOS pilot line at CEA-Leti using deep ultraviolet photolithography and deep reactive ion etching. A ring radius of $R = 250 \mu\text{m}$ (Fig. 1b) was chosen to target a free spectral range (FSR) of 53 GHz. The coupling gap between ring and bus waveguide is 250 nm .

Fig. 2 shows a scheme of our measurement setup. The ring resonance characterization was done using an Adtech $4.18 \mu\text{m}$ distributed feedback quantum cascade laser (QCL) providing cw light. The out-coupled light was recorded by a Thorlabs Fourier transform optical spectrum analyzer (OSA). We did not utilize the spectral mode of the OSA but rather used it as a photodetector through the interferometry between the two delay beams to have less noise than with a normal photodetector. The emission wavelength of the QCL was modulated between 4177.27 nm and 4177.89 nm by applying a periodic triangular current modulation. The optical pump power was 20 mW (measured directly before the input coupling lens).

Fig. 3a shows one period of the modulation recorded by the interferogram mode of the OSA. Over the whole wavelength range there are pronounced Fabry-Perot resonances, which result from the cavity formed by the two end-facets of the access bus waveguide. Nonetheless, the ring resonance can be clearly distinguished on this plot: it manifests as an additional dip occurring twice, during the wavelength ramp up and the ramp down, respectively. Fig 3b shows a zoom-in of the ring resonance. From this resonance we could retrieve a total (loaded) quality factor of $Q = 90,000$. We did not determine yet if we are at critical coupling. In any case, for the intrinsic quality factor a value much higher than 105 is expected.

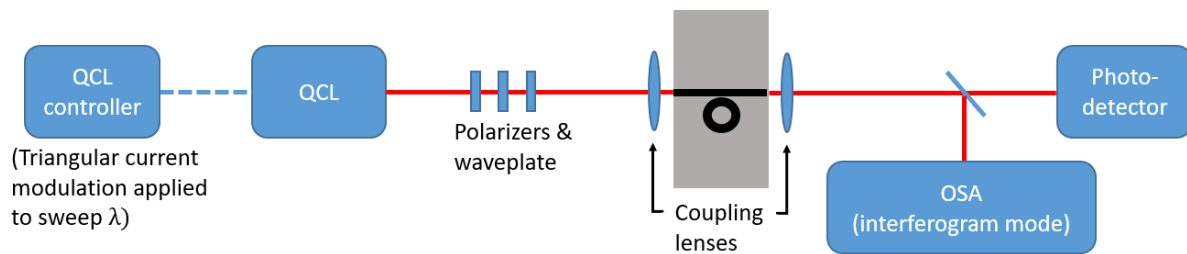


Fig. 2. Measurement setup.

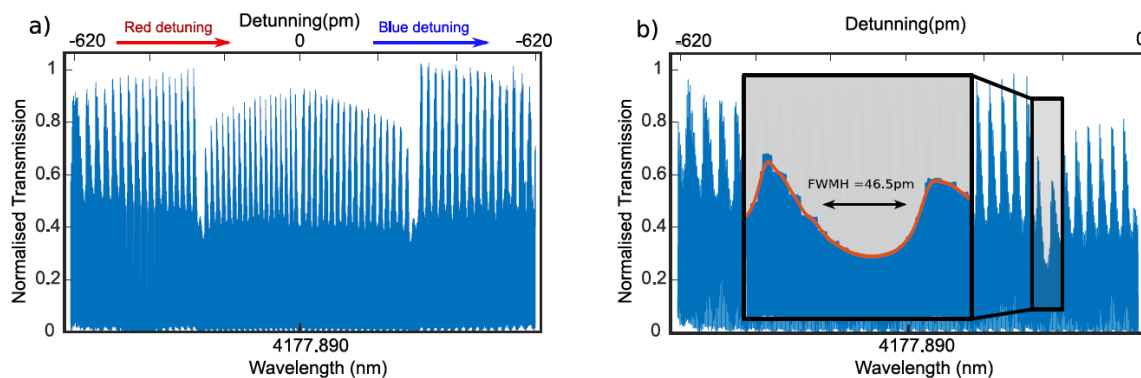


Fig. 3. (a) Wavelength scan (ramp up and ramp down) of the ring resonance with a cw QCL. The ring resonance at one specific wavelength can be clearly distinguished from the Fabry-Perot resonances, which occur due to the waveguide facet at input and output coupling. (b) Zoom-in on the ring resonance.

CONCLUSION

To conclude, we have reported a SiGe ring resonator operating around 4.18 μm , with a loaded Q-factor of 90,000. This is the highest Q-factor achieved on this material platform and among the highest achieved around this wavelength range on a CMOS-compatible platform in general. These results set the basis for generating frequency combs in the MIR spectral range. The operation at 4.18 μm was only limited by the availability of the QCL while SiGe allows for much longer wavelengths, so we expect to be able to demonstrate similar Q-factors deeper into the MIR.

Acknowledgements: We acknowledge the support of the International Associated Laboratory in Photonics between France and Australia (LIA ALPhFA) and the Agence Nationale de la Recherche (MIRSIComb, ANR-17-CE24-0028). The ECLAUSion project has received funding from the European Union's Horizon 2020 research and innovation program under the Marie Skłodowska-Curie grant agreement No 801512.

References

- [1] R. Soref, *Mid-infrared photonics in silicon and germanium*, Nature photonics, vol. 4, no. 8, pp. 495-497, 2010
- [2] Y. Zou, *et al.*, *Mid-infrared silicon photonic waveguides and devices [Invited]*, Photonics Research, vol. 6, no. 4, pp. 2018
- [3] H. Lin, *et al.*, *Mid-infrared integrated photonics on silicon: a perspective*, Nanophotonics, vol. 7, no. 2, pp. 393-420, 2017
- [4] T. Hu, *et al.*, *Silicon photonic platforms for mid-infrared applications [Invited]*, Photonics Research, vol. 5, no. 5, pp. 2017
- [5] T. J. Kippenberg, *et al.*, *Microresonator-based optical frequency combs*, Science, vol. 332, no. 6029, pp. 555-559, 2011
- [6] P. Ma, *et al.*, *High Q factor chalcogenide ring resonators for cavity-enhanced MIR spectroscopic sensing*, Opt Express, vol. 23, no. 15, pp. 19969-19979, 2015
- [7] S. A. Miller, *et al.*, *Low-loss silicon platform for broadband mid-infrared photonics*, Optica, vol. 4, no. 7, pp. 2017
- [8] R. Shankar, *et al.*, *Integrated high-quality factor silicon-on-sapphire ring resonators for the mid-infrared*, Applied Physics Letters, vol. 102, no. 5, pp. 051108, 2013
- [9] J. M. Ramirez, *et al.*, *Broadband integrated racetrack ring resonators for long-wave infrared photonics*, Opt Lett, vol. 44, no. 2, pp. 407-410, 2019
- [10] D. A. Kozak, *et al.*, *Germanium-on-silicon waveguides for long-wave integrated photonics: ring resonance and thermo-optics*, Opt Express, vol. 29, no. 10, pp. 15443-15451, 2021
- [11] B. Troia, *et al.*, *Germanium-on-silicon Vernier-effect photonic microcavities for the mid-infrared*, Opt Lett, vol. 41, no. 3, pp. 610-613, 2016
- [12] S. Radosavljevic, *et al.*, *Mid-infrared Vernier racetrack resonator tunable filter implemented on a germanium on SOI waveguide platform [Invited]*, Optical Materials Express, vol. 8, no. 4, pp. 2018
- [13] M. Yu, *et al.*, *Mode-locked mid-infrared frequency combs in a silicon microresonator*, Optica, vol. 3, no. 8, pp. 2016
- [14] K. Luke, *et al.*, *Broadband mid-infrared frequency comb generation in a Si(3)N(4) microresonator*, Opt Lett, vol. 40, no. 21, pp. 4823-4826, 2015
- [15] A. G. Griffith, *et al.*, *Silicon-chip mid-infrared frequency comb generation*, Nat Commun, vol. 6, no. 6299, 2015
- [16] H. Lin, *et al.*, *Demonstration of high-Q mid-infrared chalcogenide glass-on-silicon resonators*, Opt Lett, vol. 38, no. 9, pp. 1470-1472, 2013
- [17] L. Carletti, *et al.*, *Nonlinear optical response of low loss silicon germanium waveguides in the mid-infrared*, Opt Express, vol. 23, no. 7, pp. 8261-8271, 2015
- [18] M. Sinobad, *et al.*, *Mid-infrared octave spanning supercontinuum generation to 85 μm in silicon-germanium waveguides*, Optica, vol. 5, no. 4, pp. 2018

Ge micro-crystals photodetectors with enhanced infrared responsivity

(Student paper) / (Invited paper)

Virginia Falcone¹, Andrea Ballabio¹, Andrea Barzagli¹, Carlo Zucchetti¹, Luca Anzi¹, Federico Bottegoni¹, Jacopo Frigerio¹, Roman Sordan¹, Paolo Biagioni² and Giovanni Isella¹

¹L-NESS Dipartimento di Fisica, Politecnico di Milano, Via Francesco Anzani 42, Como, I-22100, Italy

²Dipartimento di Fisica, Politecnico di Milano, Piazza Leonardo da Vinci 32, Milano, I-20133, Italy

* virginia.falcone@polimi.it

Ge-on-Si micro-crystals grown on Si patterned substrates can be used as absorbing elements for photodetection in the near-infrared. In such microstructures light confinement effects, due to crystal faceting and pattern periodicity, enhance light absorption in the near-infrared as compared to conventional epitaxial layers. The fabricated devices, with graphene as top contact, feature a responsivity exceeding that of planar devices with comparable thickness.

Keywords: *Microcrystal, photodetector, graphene, near-infrared enhancement*

INTRODUCTION

The direct epitaxial growth of germanium on silicon (Ge-on-Si) has fostered the development of near infrared detectors for telecom and imaging applications [1]. The long wavelength responsivity of these devices is limited to approximately 1550 nm corresponding to the direct energy gap of Ge $E_{gI} = 0.8$ eV. Indeed, the absorption coefficient at the indirect gap $E_{gI} = 0.66$ eV ($\lambda \approx 1800$ nm) is roughly two orders of magnitudes lower than that above the direct gap threshold. A sizable absorption within the 1550-1800 nm windows would, therefore, require exceedingly thick epilayers which would lead to wafer bowing and crack formation. An extended infrared absorption would be beneficial for imaging applications since long wavelength radiation is less affected by Rayleigh and Mie scattering limiting visibility in fog and dusty conditions.

A viable route to enhance the responsivity of Ge-on-Si photodetectors in the 1550-1800 nm region might be exploiting the micro-structuring of the absorbing layer to increase the effective volume of interaction between light and matter.

In this work we report on a new type of detector, obtained from Ge micro-crystals epitaxially grown on a patterned Si substrate [2]. The faceted morphology and relatively high aspect ratio of the microcrystals is seen to enhance the detector responsivity in the wavelength region comprised between the direct ($\lambda \approx 1550$ nm) and indirect ($\lambda \approx 1800$ nm) gap of Ge, as compared to conventional planar devices.

EPITAXIAL GROWTH, MODELLING AND DEVICE FABRICATION

The epitaxial growth has been performed by means of Low-Energy Plasma-Enhanced CVD (LEPECVD). Microcrystal formation is based on the self-assembly of Ge crystals on a Si substrate, deeply patterned by optical lithography and reactive ion etching. 3D microcrystals, several micrometer tall and characterized by a limited lateral expansion, are obtained by using optimized growth parameters [3]. Due to crystal faceting and pattern periodicity, enhanced light absorption as compared to conventional epitaxial layers, is expected. This makes Ge micro-crystals interesting building blocks for optoelectronic devices, able to operate in the near-infrared spectral region.

Modeling of the near-IR absorption properties of the Ge-on-Si micro-crystals has been performed by finite difference time domain (FDTD) simulations [4]. The ratio between the calculated fraction of absorbed power of an array of Ge-on-Si micro-crystals and a planar Ge-on-Si epilayer is represented in Figure 1. The absorbed power ratio is always higher than one, with a relevant increase in the indirect gap wavelength range.

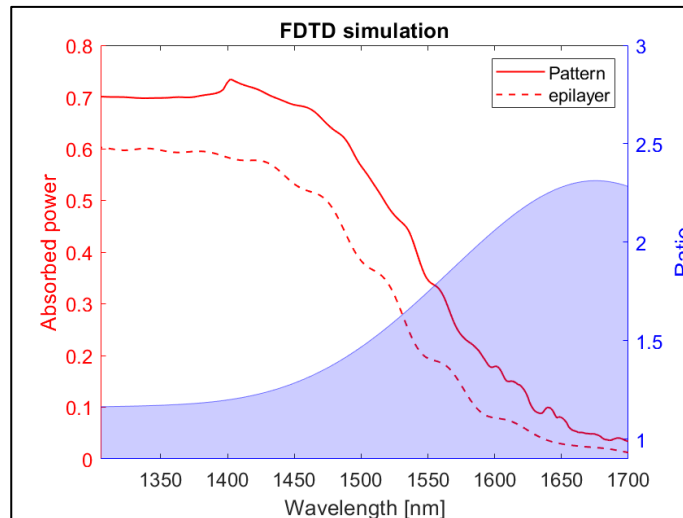


Fig.1 Fraction of absorbed power of Ge- on-Si microcrystals (continuous red line) and Ge epilayer (dashed red line). Ratio between the calculated fraction of absorbed power of Ge-on-Si micro-crystals and the fraction of absorbed power of an equivalent planar epilayer (blue curve).

The main challenge in realizing vertically illuminated photodiodes based on Ge-on-Si microcrystals is the formation of a top transparent contact that can adapt to the 3D-morphology of the surface and bridge the 100-200 nm gap between adjacent microcrystals. To this purpose, graphene can be used as a suspended continuous top contact, with an absorption that does not exceed 2.4%. The fabrication process consists in the deposition of a SiO_2 layer and a subsequent opening of a window on the patterned area by means of optical lithography and HF wet etch. In this way the graphene layer will establish an electrical contact with the Ge micro-crystals and be isolated from the unpatterned area. A second step of optical lithography and evaporation allow the generation of the metal contact, Au/Ti, on the unpatterned region. In the last fabrication step a wet-transfer process is used to form the graphene top contact, as schematically shown in Figure 2. After the wet transfer of a single graphene layer observation by SEM revealed the presence of cracks leading to a not continuum top contact over the patterned area, generating a “spider web” effect. The reason behind this could be capillary forces that play an important role for this type of patterned substrate in which the distance between the pillars is the order of a hundred nanometers.

Different strategies have been tried to solve this issue. Eventually, the number of suspended graphene layers was increased and a graphene bilayer was obtained by modifying the transfer process. The absorption due to such graphene bilayer, is estimated to be around 5% and therefore will not significantly affect the efficiency of the optoelectronic device.

PHOTOCURRENT MESUARUMENTS

The fabricated devices have been characterized by electrical and optical measurements that confirm the near- IR photoresponse [5].

A confocal microscope with a supercontinuum laser source (1300 - 1800 nm), has been used to obtain the photodetector responsivity. The spot size is smaller than the patterned area ($100 \mu\text{m} \times 100 \mu\text{m}$) thus enabling the illumination of a few Ge-on-Si micro-crystals.

Responsivity measurements experimentally confirm the enhanced absorption close to the germanium indirect gap. Fixing the reverse bias at -2V the responsivity of the micro- crystals is substantially larger than that of the epitaxial layer in the 1550- 1800 nm wavelength range (Fig.3). This responsivity enhancement in the near-infrared region is linked to light-trapping effects taking place within the micro-crystals array. The responsivity ratio trend confirms the trend observed in the simulation (Fig.1). The detailed dependence of the photoresponse spectra shape on the pattern geometry and micro-crystals morphology, are still under investigation.

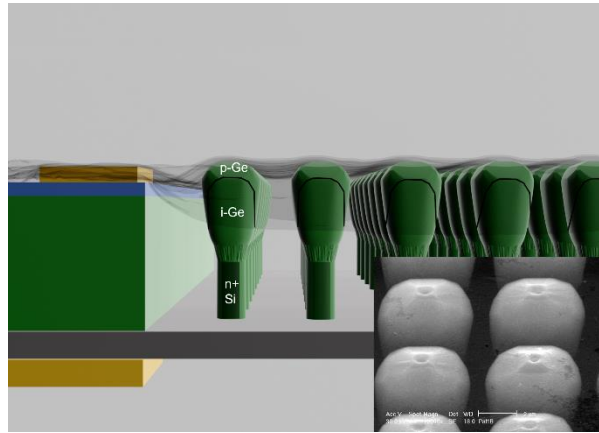


Fig.2 Schematic view and SEM image (inset) of the fabricated device. Graphene is used as a transparent top contact to extract the photocurrent generated within the Ge-on-Si microcrystals.

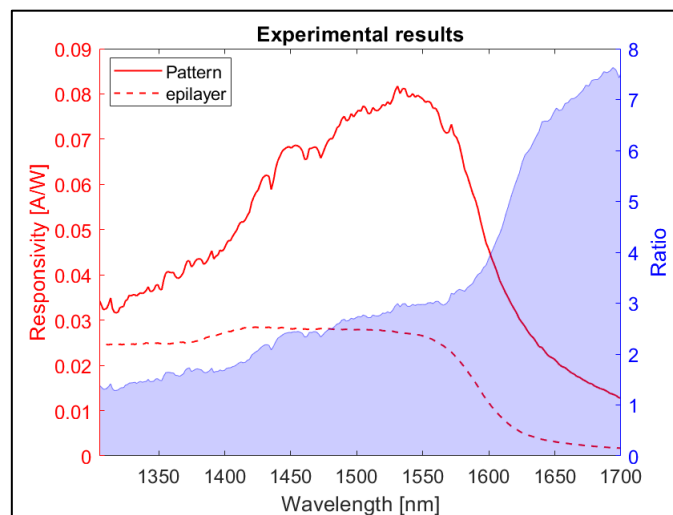


Fig.3 Responsivity at a reverse bias of $-2V$: of a Ge epitaxial layer (dashed red line) on Si substrate and Ge/Si micro-crystal (continuous red line); The blue curve is the ratio of these two quantities.

Acknowledgements: This work has been funded by the EU Horizon-2020 projects microSPIRE Grant No. 766955 and Graphene Flagship Core 3 Grant No. 881603. The authors acknowledge F. Mancarella for the microfabrication of patterned substrates and Polifab for the access to the facility for the device fabrication.

References

- [1] J. Michel, J. Liu, and L. C. Kimerling, *High-performance Ge-on-Si photodetectors*, Nat. Photonics, vol. 4, no. 8, pp. 527–534, Jul. 2010, doi: 10.1038/nphoton.2010.157.
- [2] C. V. Falub et al., *Scaling Hetero-Epitaxy from Layers to Three-Dimensional Crystals*, Science (80-.), vol. 335, no. 6074, pp. 1330–1334, Mar. 2012, doi: 10.1126/science.1217666.
- [3] R. Bergamaschini et al., *Self-aligned Ge and SiGe three-dimensional epitaxy on dense Si pillar arrays*, Surf. Sci. Rep., vol. 68, no. 3–4, pp. 390–417, 2013, doi: 10.1016/j.surfrep.2013.10.002.
- [4] J. Pedrini et al., *Broadband control of the optical properties of semiconductors through site-controlled self-assembly of microcrystals*, Opt. Express, vol. 28, no. 17, p. 24981, Aug. 2020, doi: 10.1364/OE.398098.
- [5] V. Falcone, et al., *Graphene/Ge microcrystal photodetectors with enhanced infrared responsivity*, APL Photonics, under review

Etchless Pedestal Chalcogenide Waveguides for Mid-IR On-Chip Sensing and Spectroscopy Applications

(Student paper)

Vasileios Mourgelas, Ben D. Rowlinson, James S. Wilkinson and Ganapathy Senthil Murugan

Optoelectronics Research Centre, University of Southampton, Southampton, SO17 1BJ, UK

* v.mourgelas@soton.ac.uk

Etchless pedestal waveguides are demonstrated with confirmed long-wave IR transparency up to 12 μm . Direct etching of the chalcogenide layers is avoided by using Si micropatterning and thermal evaporation. Losses as low as 0.5 dB/cm were estimated, making the platform a promising candidate for on-chip sensing and spectroscopy.

Keywords: Mid-IR, Waveguides, Chalcogenides, Spectroscopy, on-chip

INTRODUCTION

The mid-infrared (mid-IR) spectral region (2.5-25 μm) is of great interest due to the unique molecular absorptions present predominantly between wavelengths of 2.5 and 15 μm . The close study of these absorptions can provide extremely useful information about a specimen of interest. Optical spectrometers are used to extract and study these absorptions, and these are typically bulky and expensive making them unattractive for widely-deployable on-site molecular analysis applications.

One of the most important performance considerations for integrated optical sensors and waveguide based on-chip spectrometers is low propagation loss across the desirable wavelength band of operation. The range of materials that can be used in the mid-IR and more specifically for long-wave IR applications, is quite limited. The reason behind this is usually the strong material absorptions emerging at longer wavelengths (oxygen related, phonon or free carrier absorption). Glasses are used in optics very extensively, with the most common glass family being the oxides. Oxides have good optical properties; however, they absorb light very strongly above $\sim 4 \mu\text{m}$. Chalcogenide glasses are not characterised by such absorptions and have shown to possess excellent properties such as wide infrared transparency (sometimes up to 20 μm), large refractive index (usually between 2 and 3) and high optical non-linearity [1,2].

Regardless of their huge potential, chalcogenide glasses have proven to be very delicate and as a result special care is required during their processing. More specifically, chalcogenides tend to be prone to chemically induced damage. Such chemicals include alkaline solutions used in photolithographic developers as well as ionised gases used in dry etching [3]. Nonetheless, several examples of chalcogenide waveguide platforms have been reported in the literature [3-6]. In these works, various methods of fabrication have been presented such as hot embossing [3], photolithography and etching [4], photodarkening [5] and micro-transfer moulding [6]. Even though low propagation losses of less than 0.5 dB/cm are estimated in [3] and [4], there are serious drawbacks associated with the high temperatures used in hot embossing as well as with the complex process tailoring required for waveguide layer etching of these materials. Therefore, there remains a great deal of potential for the development of new fabrication approaches for integrated chalcogenide waveguides.

As mentioned above, low waveguide propagation losses are considered a necessity when it comes to design an efficient on-chip spectrometer. In integrated waveguides, reducing sidewall roughness plays a major role in reducing the propagation losses. Rib waveguides are usually utilised when limited interaction between the propagating mode and the sidewall is necessary. However, this geometry is not suitable for applications where interaction between the mode and the outer medium is essential (i.e sensing). In such applications a ridge geometry is required. Furthermore, in devices relying on the use of very tight bends such as spiral waveguide spectrometers, the use of ridge waveguides is essential for keeping the radiation losses low while maintaining as small device footprint as possible.

In order to reduce the propagation loss induced by sidewall roughness, the post deposition processing of the chalcogenide layers must be completely eliminated. Instead of using lift-off which still requires a lift-off resist pattern removal step, we utilised a similar etchless process to that described in [7]. In this process, pedestals are formed on a Si wafer using standard photolithography and etching methods. The optical layers are then deposited on these pedestals. In that way, waveguides are formed without the need for etching the optical layers.

In this study, we fabricate and test a chalcogenide waveguide platform which will subsequently be implemented on an on-chip spectrometer that will operate in the long-wave IR spectral region.

FABRICATION

The proof of principle on-chip spectrometer we are developing is using a simple and efficient thermo-optically tuneable spiral armed interferometer. The novel combination of materials used for the core and claddings in this work is GeAsSeTe (IG3) and GeAsSe (IG2), respectively. Example respective refractive index values for these layers at $\lambda=1553$ nm are 2.99 and 2.65, providing a respectable index contrast of 0.34. For the fabrication of simple straight waveguides that can be used in a variety of applications ranging from biomedical sensing to non-linear optical processing, a simple wet etching method was utilised which consisted of buffered oxide etch and KOH etch. By using [110] Si wafers and exposing them to a KOH solution after proper mask alignment, completely vertical sidewall Si pedestals were fabricated. With subsequent evaporation of the optical layers, ridge waveguides were defined as we have also reported in [8]. Since the sidewall angle is dictated by the Si plane directions in the wet etching method, this method is not suitable for devices with structures that cross multiple planes/directions such as bends, spirals and splitters and a dry etching method is required. We have exploited a dry etching to create waveguide-based components such as splitters and spirals required for our on-chip spectrometer. To minimise the sidewall deposition of waveguide materials during the evaporation, we required negative (re-entrant) sidewalls during dry etching. For the patterning of pedestals with such characteristics we studied and used a Bosch process and a pseudo-Bosch process. Example waveguides fabricated using the wet (Fig. 1 a-c) and dry (Fig. 1 d-f) etch methods are presented below.

RESULTS AND DISCUSSION

The propagation loss was estimated for the wet etched pedestal waveguides using the scattering streak fitting method. An infrared camera collected the scattered light emanating from the top surface of the waveguides (Fig. 1 g and by exploiting the decaying nature of the light streak, the propagation loss was estimated for two different waveguides (1 and 2), for TE and TM polarisations between $\lambda = 7$ and $11 \mu\text{m}$ and is shown in Fig.1 i. The overall loss is showing a decreasing trend with wavelength which agrees with reduced scattering at longer wavelengths. The peak observed at $\lambda = 8 \mu\text{m}$ for TE polarisation was attributed to Ge-O related vibrations. Similar absorption bands have also been reported in GeAsSeTe fibres [9].

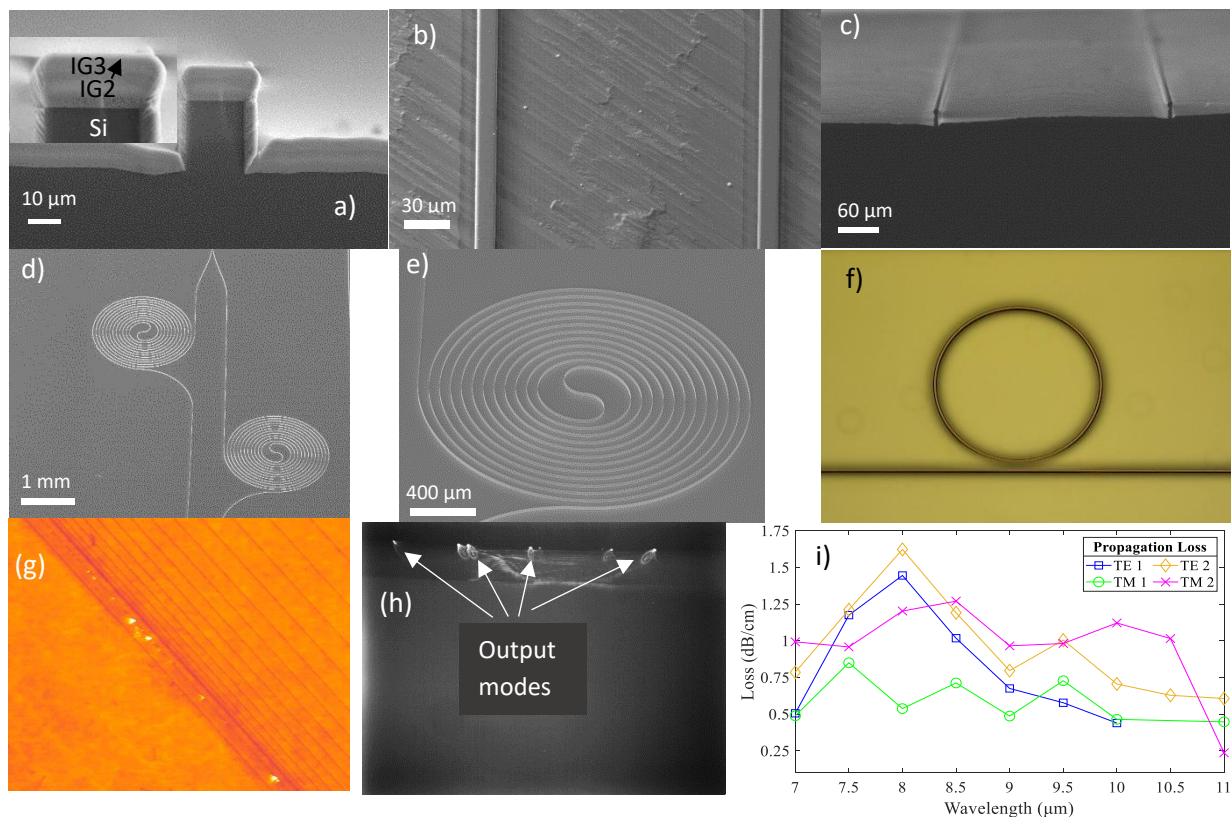


Fig. 1. a) Cross-section of $26.5 \mu\text{m}$ wide wet etched waveguide (IG3 core: $\sim 3.6 \mu\text{m}$, IG2 cladding $\sim 7 \mu\text{m}$, IG2 capping layer ~ 250 nm), b/c) top /tilted view of wet etched waveguides, d) dry etched spiral Mach-Zehnder interferometer (MZI), e) close view of

dry etched spiral, f) dry etched ring resonator, g) scattering on the surface of a wet etched waveguide at $\lambda = 9 \mu\text{m}$, h) output modal spots of dry etched splitter, i) propagation loss estimation

As can be seen in Fig. 1 a-c, the fabricated pedestal waveguides have very smooth surfaces with no observable interfacial cracks or large grain structure. This is also reflected in the low estimated propagation losses which according to our estimations, average about 0.9 dB/cm in the long-wave IR spectral region.

The dry etched pedestal waveguide platform presented above is employed on our on-chip spectrometer design which is currently under fabrication. With the insight provided by our current characterisation results, we believe that the platform has huge potential for use in on-chip spectrometers as well as integrated sensor devices. As discussed before, our spectrometer design is based on a simple thermo-optically tuneable MZI. For such a device to be efficient, the waveguide materials should possess good thermo-optic properties. Using the thermo-optic coefficient values of the bulk chalcogenide glasses and after a quick estimation we predict that the thermo-optic performance of the spectrometer will be similar to that of a Si based one.

CONCLUSION

The low optical losses demonstrated here coupled with the ease and straightforwardness of the fabrication of this waveguide platform, could pave the way for wider use of chalcogenides in integrated mid-IR waveguide applications. We have shown propagation losses as low as 0.5 dB/cm in the long-wave IR which are among the lowest reported for integrated chalcogenide waveguides. In addition, the novel material combination of the optical layers used in this work, not only is characterised by low losses, good index contrast and wide transparency up to 12 μm , but it is also expected to perform very efficiently as a thermo-optic medium for on-chip spectrometer application due to its good thermo-optic coefficient as well as inherently low thermal conductivity.

Acknowledgements: This work was supported by "The Future Photonics Hub" (UK EPSRC grant EP/N00762X/1).

References

- [1] J. L. Adam and X. Zhang, *Chalcogenide glasses. Preparation, Properties and Applications*, Electronic and Optical Materials, Woodhead Publishing, Cambridge, UK, 2014
- [2] G.S. Murugan, *Photonic glasses and glass-ceramics*, Research Signpost, Kerala, India, 2010
- [3] T. Han, S. Madden, S. Debbarma, and B. Luther-Davies, *Improved method for hot embossing As₂S₃ waveguides employing a thermally stable chalcogenide coating*, Opt. Express 19, 25447-25453, 2011
- [4] Y. Ruan, W. Li, R. Jarvis, N. Madsen, A. Rode and B. Luther-Davies, *Fabrication and characterization of low loss rib chalcogenide waveguides made by dry etching*, Opt. Express 12, 5140-5145, 2004
- [5] D.A. Turnbull, J.S. Sanghera, V.Q. Nguyen and I.D. Aggarwal, *Fabrication of waveguides in sputtered films of GeAsSe glass via photodarkening with above bandgap light*, Materials Letters 58, 51-54, 2003
- [6] C. Tsay, Y. Zha and C. B. Arnold, *Solution-processed chalcogenide glass for integrated single-mode mid-infrared waveguides*, Opt. Express 18, 26744-26753, 2010
- [7] J. H. Sierra, R. C. Rangel, R. E. Samad, N. Dias Vieira Jr., M. I. Alayo, and D. O. Carvalho, *Low-loss pedestal Ta₂O₅ nonlinear optical waveguides*, Opt. Express 27, 37516-37521, 2019
- [8] V. Mourgelas, N. P. Sessions, J. S. Wilkinson, and G. Senthil Murugan, *Etchless Pedestal Chalcogenide Waveguide Platform for Long-Wave IR Applications*, Optical Materials Express Vol. 12, No. 3, 1154-1162, 2022
- [9] Su, J., Dai, S., Jiang, L., Lin, C., Yang, C., Zhang, N. and Yuan, Y., *Fabrication and bending strength analysis of low-loss Ge₁₅As₂₅Se₄₀Te₂₀ chalcogenide glass fiber: a potential mid-infrared laser transmission medium*, Optical Materials Express, 9(7), 2859, 2019

Integrated microwave photonics

Invited paper

Antonella Bogoni^{1,2}, Manuel Reza¹, Giovanni Serafino¹, Antonio Malacarne², Mirco Scaffardi², Claudio Porzi¹, Paolo Ghelfi²

¹ Sant'Anna School of Advanced Studies, Via Moruzzi 1, 56124, Pisa, Italy

² CNIT, via Moruzzi 1, 56124 Pisa, Italy

* Antonella.bogoni@cnit.it

In this paper the main integrated photonic building blocks for microwave applications are described, with emphasis to the open issues concerning the device performance and the subsystem co-packaging. A first prototype of IMWP-based radar transceiver is also presented.

Keywords: integrated microwave photonics, radar and 5G, hybrid integration

INTRODUCTION

Our society must evolve into a fully connected world. This change passes through two technological revolutions: the connectivity beyond 5G and the Industry 4.0. Both of them are based on extended use of virtual reality (VR) for a plethora of applications, such as remote surgery, emergency operations using drones, smart industry automation. This needs an increasing number of smart sensors and a wider communication bandwidth for VR representation and transmission. In this scenario, microwave photonics (MWP), i.e., the use of photonics in radiofrequency (RF) applications, has been recently demonstrated to overcome the intrinsic limitations of RF electronics such as narrow bandwidth, reduced and slow reconfigurability, sensitivity to electro-magnetic interferences, and high transmission losses [1]. MWP systems have the potential to revolutionize the connectivity and sensing paradigms providing wideband and frequency flexible operations [1]-[3], real time RF signal processing (e.g. faster, more precise and multibeam RF beamforming [5]) and distribution [6]-[9] (through low loss and low distortion optical links with extremely high coherence), as it has been demonstrated by few research groups [2],[3].

In this framework, MWP based on photonic integrated circuits (PICs), the so-called integrated MWP (IMWP), is mandatory to reduce size and consumption [10] as requested by compact platforms (e.g., drones and robots) or harsh environments (i.e., satellites). Few innovative solutions [4], [11]-[14] have been proposed. However, since photonics integration technologies have been driven by the requirements of optical communications, the IMWP systems implemented so far demonstrated specific limits preventing their use [12], mainly related to unaffordable RF loss of the PIC, frequency limitations due to the chip packaging, and thermal management issues in interfacing photonics and electronics.

Therefore, the full exploitation of IMWP potentials is partially limited by the current available technologies.

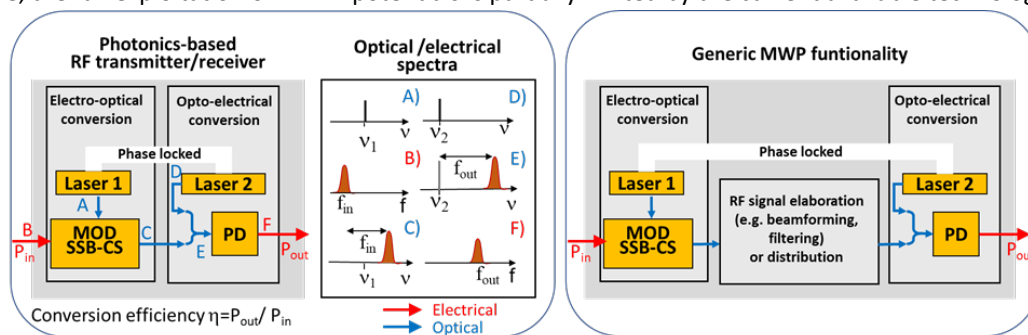


Fig. 1. Left: Electro-optical & opto-electrical conversion blocks cascaded to implement photonic-based RF transceivers; right: scheme for a generic MWP function. SSB-CS MOD: single sideband suppressed carrier modulator; PD: photodiode.

IMWP BUILDING BLOCKS

The two main building blocks of a MWP system are the electro-optical (EO) and opto-electrical (OE) conversion blocks (Fig. 1 left), implemented respectively through an EO modulator (MOD) (in single-sideband carrier-suppressed (SSB-CS) or in dual-sideband (DSB) configuration) and a photodiode (PD). These implement the conversion from intermediate frequency (IF) or RF to the optical domain, and vice versa. Their cascade realizes a

photonics-based RF transmitter or receiver. If an additional functional block is inserted between them, further MWP functionalities can be implemented such as RF beamforming, filtering, or distribution (Fig. 1 right).

A recent implementation of a photonics-based integrated RF transceiver in silicon-on-insulator (SOI) [12] technology has highlighted the main critical parameter in IMWP systems: the conversion efficiency η , which is the power ratio between the output RF (or IF) and the input IF (or RF) (Fig. 1 left). That implementation has reported $\eta \approx -55\text{dB}$, which is sensibly lower than that of RF electronics systems ($\eta > -20\text{dB}$). This limitation arises from: the relatively large propagation losses of silicon waveguides, the limited input optical power (limited by silicon nonlinear absorption), the lack of pure phase modulation in SOI [15], the high MOD $V\pi$ (the voltage necessary to induce a π phase shift), the limited maximum input power of the PD. Moreover, optical gain can not be implemented in SOI technology for compensating the optical losses. Other established monolithic technological platforms do not offer a better scenario: III-V platforms (e.g., Indium Phosphide, InP) allows for implementing good-quality optical sources and amplifiers and PDs [16], [17] although MODs typically suffer from high losses and nonlinear effects and passive waveguides are also lossy, whereas the Silicon Nitride (SiN) platform which provides the minimum waveguide propagation loss does not allow implementing high-speed modulation at all.

The best technology so far for implementing MOD is the bulk lithium niobate (LN) that dominated the telecom industry scene for decades, thanks to the Pockels effect that ensures pure and linear phase modulation (also useful for beamforming functionalities), allowing the implementation of high-quality SSB-CS modulation in a low-index contrast platform [18]. Very recently, strong field confinement in LN waveguide has been achieved with the development of the LN-on-insulator (LNOI) platform [19],[20], which enables on-chip manufacturing of LN modulators with potentially much lower $V\pi$ per unit length and substantially reduced size [21],[22], besides other standard functional passive components such as optical splitters/couplers and tunable filters [23]. The latter are particularly important in IMWP for implementing complex microwave functions in the optical domain. However, some of the LNOI components developed so far still do not have the required performance for MWP applications (i.e., narrow and steep filters, very low- $V\pi$ MODs). Moreover, LNOI as well does not have optical gain for lasers and amplifiers. Consequently, a hybrid approach (i.e., the combination of components realized from different materials) is necessary to meet the requirements for IMWP applications.

IMWP ELECTRO-OPTICAL CO-PACKAGING

The interface between the PIC and its input/output RF ports or RF electronics driving circuits is one of the main bottlenecks of IMWP, in particular for applications requiring very large bandwidth, since it may cause attenuation, distortions and crosstalk. The performance of such interfacing is dictated by the coupling approach between photonics and electronics at packaging level, which includes wire bonding [24] or flip-chip bonding [25]. Wire-bonding is the most common and affordable approach, but it suffers from parasitic effects induced by the bonding wires, limiting the operation bandwidth and performance. In contrast, the flip-chip bonding of high-speed digital electronics on top of PICs is boosting the market of optical communications and data centers [26],[27]. Unfortunately, this approach is not suitable for IMWP where high-frequency analog RF signals must be routed from the input to the output of the system. Therefore, a more suitable co-packaging approach has to be pursued.

CASCADED BUILDING BLOCKS FOR THE REALIZATION OF A FREQUENCY-AGILE RADAR TRANSCEIVER: FIRST PROTOTYPE

RADAR systems are remote sensing apparatuses that transmit radio frequency (RF) signals and measure the back scattered energy in order to estimate the distance and the velocity of a target. Depending on the application, different waveforms and frequencies are preferred, in a tradeoff between the observable distance, the resolution, the robustness to weather conditions, and so on. Multi-band systems can gain performance by taking advantage of the peculiarities of each different frequency band, e.g. the low atmospheric attenuation of the lower frequencies or the high fractional bandwidth available at higher carrier frequencies. However, multi-band radars are not quite common due to the complexity of the required circuitry. Here, we report the first implementation of a radar system based on integrated photonics. The architecture of the photonics-based multiband radar system is sketched in Fig.1. A PIC has been fabricated with SOI platform and packaged for allowing an agile utilization in a whole radar system setup. A two-tone analysis, in case of down-conversion from S and X band (3.43 GHz and 9.9 GHz) to an intermediate frequency (IF) of 100 MHz, allowed to verify the performance in terms of spurious free dynamic range (SFDR) (97 & 95 dBHz^{2/3}) and signal-to-noise ratio (SNR) (55 & 51 dB/1MHz). The phase noise has been also confirmed to coincide with the theoretical expected value, while the conversion loss has been confirmed to exceed the 60 dB. As described above, this latter feature represents the main open issue of the developed radar transceiver and is mainly due to the relatively high losses of silicon guides and the low efficiency of silicon optical modulators. Possible approaches

for reducing these criticalities are (i) introducing amplification stages to reduce losses in the photonic circuit (e.g., hybrid III-V/SOI integration); (ii) reducing the nonlinearities and the V_{π} -voltage of the modulator. Despite the existing limitations, the developed radar transceiver has been very recently tested in a real dual-band radar system in a maritime field trial, confirming all the requirements of the considered scenario (e.g. in terms of resolution, sensitivity, linearity).

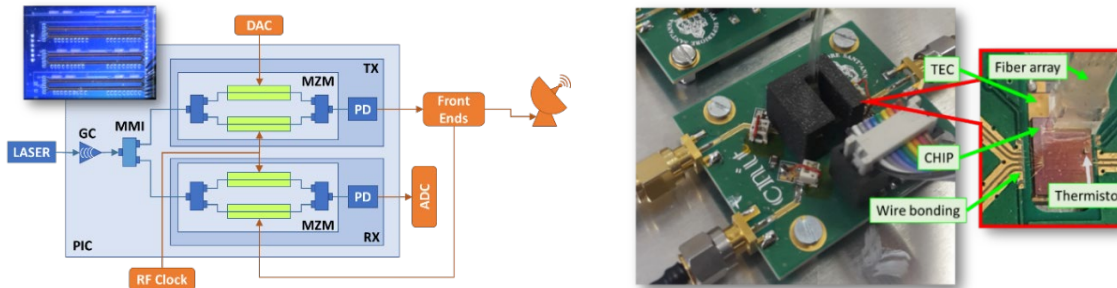


Fig. 2. Left: Architecture of the photonics-based multiband radar system. The PIC picture is also shown; MMI: multimode interference splitter, GC: grating coupler Right: Packaged chip on the control board.

References

- [1] J. Capmany, & D. Novak, "Microwave photonics combines two worlds". Nature Photon Vol. 1, pp. 319–330 2007 9
- [2] P. Ghelfi, et al., "A fully photonics-based coherent radar system," Nature, Vol. 507, 2014
- [3] G. Serafino et al, "Microwave Photonics for Remote Sensing: From Basic Concepts to High-Level Functionalities", IEEE Journal of Lightwave Technology, Vol. 38, n. 19, 2020
- [4] Y. Liu "Ultra-Low-Loss Silicon Nitride Optical Beamforming Network for Wideband Wireless Applications", IEEE Journal of Selected Topics in Quantum Electronics, Vol. 24, n. 4, 2018
- [5] C. Tsokos "Analysis of a Multibeam Optical Beamforming Network Based on Blass Matrix Architecture", IEEE Journal of Lightwave Technology Vol. 36, n. 16, 2018
- [6] S. Rommel et al., "Towards a Scaleable 5G Fronthaul: Analog Radio-over-Fiber and Space Division Multiplexing", IEEE Journal of Lightwave Technology Vol. 38, n. 19, 2020
- [7] D.F. Paredes-Palaz, "Radio over Fiber: An Alternative Broadband Network Technology for ...", Electronics, Vol. 9, n. 11, 2020
- [8] T. Umezawa, "Radio Over FSO Communication Using High Optical Alignment Robustness 2D-PDA and its Optical Path Switching Performance", IEEE Journal of Lightwave Technology Vol. 39, n. 16, 2021
- [9] A. Malacarne, et al., "Coherent Dual-Band Radar-Over-Fiber Network With VCSEL-Based Signal Distribution", IEEE Journal of Lightwave Technology Vol. 38, n. 22, 2020
- [10] D. Marpaung, et al., "Integrated microwave photonics". Nature Photon Vol. 13, pp. 80-90, 2019
- [11] C. Porzi et al. "Silicon Photonics High-Order Distributed Feedback..", IEEE Journal of Quantum Electronics, Vol. 56, n. 1, 2020
- [12] F. Falconi et al., "A Combined Radar & Lidar System based on Integrated Photonics in Silicon-on-Insulator", IEEE Journal of Lightwave Technology, Vol. 39, n.1, 2021
- [13] G. Serafino et al., "Photonic approach for on-board and ground radars in automotive applications", IET Radar, Sonar & Navigation, Vol. 12, n. 10, 2018
- [14] C. Porzi et al., "Broadband and High-Capacity Silicon Photonics Single-Sideband Modulator," IEEE Journal of Lightwave Technology, vol. 40, no. 2, 2022"
- [15] D. Thomson et al., "Roadmap on silicon photonics", Journal of Optics, vol. 18, n. 7, 2016
- [16] L.A. Coldren et al., "Diode Lasers and Photonic Integrated Circuit" Wiley Online Library, DOI:10.1002/9781118148167
- [17] Y. Li et al, "High Linearity InP-Based Phase Modulators Using a Shallow Quantum-Well Design," in IEEE Photonics Technology Letters, vol. 22, no. 18, pp. 1340-1342, Sept.15, 2010
- [18] T. Kawanishi and M. Izutsu, "Linear single-sideband modulation for high- SNR wavelength conversion," Photon. Technol. Lett., vol. 16, pp. 1534–1536, 2004
- [19] D. Pohl, et al. "An integrated broadband spectrometer on thin-film lithium...", Nature Photonics Vol. 14, pp. 24–29 2020
- [20] K. Luke, et al., "Wafer-scale low-loss lithium niobate photonic integrated circuits", Optics Express Vol.28, n.17, 2020
- [21] M. Loncar et al., "An Integrated Low-Voltage Broadband Lithium Niobate Phase Modulator", IEEE Photonics Technology Letters Vol. 31, n. 11, 2019
- [22] M. Xu, et al., "High-performance coherent optical modulators based on thin-film lithium niobate platform", Nature Communications Vol. n. 11, 2020
- [23] X. Liu et al., "Highly efficient thermo-optic tunable micro-ring resonator based on an ...," Opt. Lett. 45, 6318-6321 (2020)
- [24] K. Li et al., "Co-design of electronics and photonics components for Silicon Photonics transmitters", in European Conference on Optical Communication (ECOC), 2018
- [25] M. Raj et al., "Design of a 50-Gb/s Hybrid Integrated Si-Photonic Optical Link in 16-nm FinFET", IEEE Journal of Solid-State Circuits Vol. 55, n. 4, 2020
- [26] K. Li, et al., "Electronic–photonic convergence for silicon photonics transmitters beyond 100 Gbps on–off Keying", Optica, Vol. 7, n. 11, 2020
- [27] K. Patel, "Rapid growth of IP traffic is driving adoption of silicon photonics in data centers", Design, Automation & Test in Europe Conference & Exhibition (DATE), 2017

Microwave-optical transduction using high overtone bulk acoustic resonances

(Student paper)

Terence Blésin¹, Anat Siddharth¹, Hao Tian², Rui Ning Wang¹, Alaina Attanasio², Sunil A. Bhawe² and Tobias J. Kippenberg^{1*}

¹Laboratory of Photonics and Quantum Measurements
Swiss Federal Institute of Technology Lausanne (EPFL), Lausanne, CH-1015, Switzerland

²OxideMEMS Laboratory, Purdue University, West Lafayette, Indiana 47907, USA

*tobias.kippenberg@epfl.ch

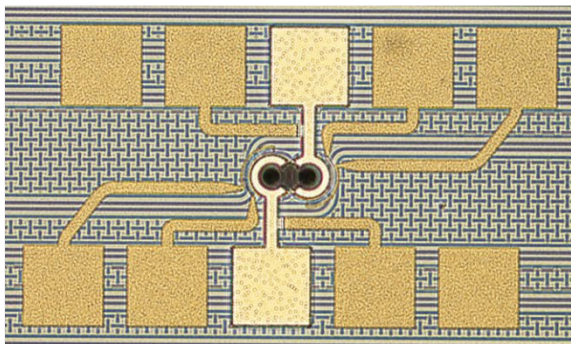
We demonstrate efficient microwave-optical frequency conversion using a released HBAR-on-photonic damascene platform. Thermal tuning of coupled optical ring cavities with integrated heaters allows to operate in the triply resonant transduction scheme.

Keywords: bulk acoustic resonators, integrated photonics, microwave-optical transduction, silicon nitride, aluminum nitride

INTRODUCTION

Microwave photonics is an interdisciplinary field that encompasses the generation, transmission and processing of microwave signals using integrated photonics technologies usually used at optical frequencies. Shifting the window of operation to optical frequencies provides the advantages of a wider operations frequency range, low loss and frequency independent noise transmission in optical fibers, and even size reduction. To date, important demonstrations include the generation of ultra-broadband signals, programmable filters, and photonics enhanced radars [1]. Thanks to the efforts of the scientific community towards the development of efficient transducers [2], [3], applications of microwave photonics can now be envisioned in the quantum coherent regime, for example with the generation of entangled photons pair in the microwave and optical domains, which would provide advanced tools for quantum sensing [4].

a



b

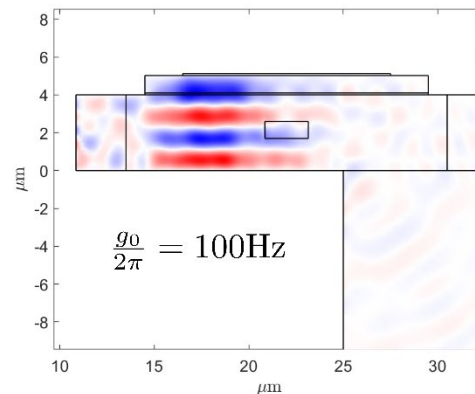


Fig. 1. (a) Optical microscope photograph of coupled optical cavities, showing the AlN actuators as well as heaters for tuning the optical resonance frequency. Each of the optical ring cavity can be modulated by a AlN actuator as well as by a Mo heater. (b) Finite element simulation of the HBAR mode illustrating the HBAR mode at 2.685 GHz, with a simulated single photon optomechanical coupling rate of $\frac{g_0}{2\pi} = 100\text{Hz}$.

RESULTS

In this context, we have recently proposed and comprehensively analyzed a new kind of transducer [5] harnessing the strong piezoelectric coupling of microwave signals to a mechanical excitation, a high overtone bulk acoustic resonance (HBAR), parametrically interacting with optical supermodes of optically coupled ring cavities to realize a coherent microwave-optical conversion. This device takes advantage of the high quality factors of Si_3N_4 waveguides fabricated using the photonic damascene process [6]. The integration of MEMS actuators on top of these waveguides allows for modulation using stress-optical phenomena, namely the moving boundaries and

photoelastic effects [7]. These effects are exacerbated by releasing the Si substrate below the actuators, leaving a thin acoustic cavity mainly consisting of the SiO_2 cladding embedding the Si_3N_4 waveguides, which led to the demonstration of optical isolation via angular momentum biasing [8], [9].

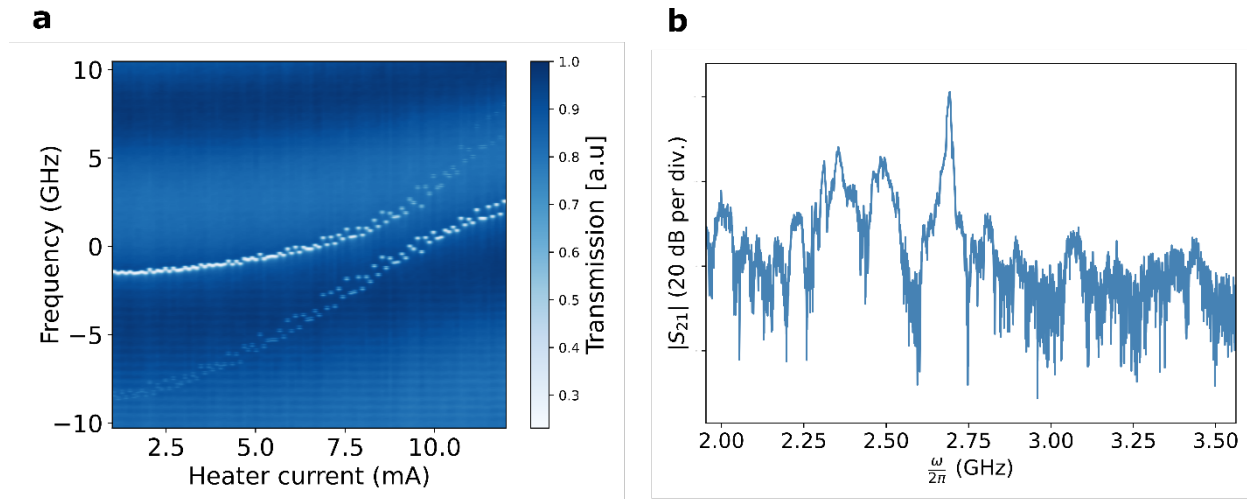


Fig. 2: (a) Contour plot showing the optical transmission through the coupled optical ring cavities for varying bias current through the heater. The small splitting corresponds to scattering due to defects in the waveguides, which can easily be removed in future devices. (b) Microwave-optical transmission, where the peak at 2:685 GHz indicates the frequency of the strongest cladding HBAR mode, which can be used for transduction.

DISCUSSION

Fig. 1 (a) shows the cross section of the structure. The mechanical resonator is formed by the electrodes, the piezoelectric (here AlN) and the SiO_2 substrate. The stress pattern, obtained using finite element simulations, shows that a large volume of the acoustic wave interacts with the optical waveguide. The small aspect ratio of the released structure enables to tightly confine the acoustic wave in the region where it interacts with the optical waveguide. The resulting enhanced optomechanical coupling enables to see prominent peaks in the microwave-optical transmission spectrum on Fig. 1 (b). This phenomenon has already led to the demonstration of optical isolation using momentum biasing [9].

We now demonstrate microwave-optical conversion using pairs of coupled optical modes created by evanescent coupling between adjacent optical ring cavities. The integration of heaters on near the optical waveguides enables controlling the resonance frequency of the ring cavities, compensating for the intrinsic detuning between adjacent cavities in order to benefit from the intracavity power enhancement of the triply resonant scheme. The actuators, heaters and compensation of the optical detuning are illustrated on Fig. 2. Improvement of this device, such as grounding for cryogenic compatibility and optimization of the release process, are expected to enable experiments showing the quantum coherence of this interface between the optical and microwave frequencies.

Acknowledgements:

This material is based upon work supported by the Air Force Office of Scientific Research under numbers FA8655-20-1-7009 and FA9550-21-1-0047 (Quantum Accelerator), as well as NSF QISE-Net under grant DMR 17-47426. This work was further supported by funding from the European Union H2020 research and innovation program under grant agreement No. 732894 (FET-Proactive HOT)), and the European Research Council (ERC) under grant agreement No. 835329 (ExCOM-Cceo). Samples were fabricated in the EPFL Center of MicroNanoTechnology (CMi), and Birck Nanotechnology Center at Purdue University.

References

- [1] D. Marpaung, J. Yao, and J. Capmany, "Integrated microwave photonics," *Nature Photonics*, vol. 13, no. 2, Art. no. 2, Feb. 2019, doi: 10.1038/s41566-018-0310-5.
- [2] A. P. Higginbotham *et al.*, "Harnessing electro-optic correlations in an efficient mechanical converter," *Nature Physics*, vol. 14, no. 10, Art. no. 10, Oct. 2018, doi: 10.1038/s41567-018-0210-0.

- [3] L. Fan *et al.*, “Superconducting cavity electro-optics: A platform for coherent photon conversion between superconducting and photonic circuits,” *Sci. Adv.*, vol. 4, no. 8, p. eaar4994, Aug. 2018, doi: 10.1126/sciadv.aar4994.
- [4] S. Barzanjeh, S. Pirandola, D. Vitali, and J. M. Fink, “Microwave quantum illumination using a digital receiver,” *Science Advances*, vol. 6, no. 19, p. eabb0451, May 2020, doi: 10.1126/sciadv.abb0451.
- [5] T. Blésin, H. Tian, S. A. Bhave, and T. J. Kippenberg, “Quantum coherent microwave-optical transduction using high-overtone bulk acoustic resonances,” *Phys. Rev. A*, vol. 104, no. 5, p. 052601, Nov. 2021, doi: 10.1103/PhysRevA.104.052601.
- [6] J. Liu *et al.*, “High-yield, wafer-scale fabrication of ultralow-loss, dispersion-engineered silicon nitride photonic circuits,” *Nat Commun*, vol. 12, no. 1, p. 2236, Apr. 2021, doi: 10.1038/s41467-021-21973-z.
- [7] J. Liu *et al.*, “Monolithic piezoelectric control of soliton microcombs,” *Nature*, vol. 583, no. 7816, pp. 385–390, Jul. 2020, doi: 10.1038/s41586-020-2465-8.
- [8] H. Tian *et al.*, “Hybrid integrated photonics using bulk acoustic resonators,” *Nature Communications*, vol. 11, no. 1, Art. no. 1, Jun. 2020, doi: 10.1038/s41467-020-16812-6.
- [9] H. Tian *et al.*, “Magnetic-free silicon nitride integrated optical isolator,” *Nat. Photon.*, vol. 15, no. 11, pp. 828–836, Nov. 2021, doi: 10.1038/s41566-021-00882-z.

Widely Tunable Flat-Top Integrated Microwave Photonic Passband Filter

Claudio Porzi^{1*}, Manuel Reza¹, Paolo Ghelfi², Marc Sorel^{1,3}, and Antonella Bogoni^{1,2}

¹TeCIP Institute, Scuola Superiore Sant'Anna, Via Moruzzi 1, Pisa, 56124, Italy

²PNTlab, CNIT, Via Moruzzi 1, Pisa, 56124, Italy

³School of Engineering, University of Glasgow, Glasgow, G128LT, UK

* claudio.porzi@santannapisa.it

A microwave photonic filter is realized in silicon-on-insulator technology featuring flat top passband width, large out-of-band rejection of 40 dB and wide tuning range from DC to 70 GHz in a compact footprint of less than 2 mm².

Keywords: Microwave photonics, silicon photonics, optical filters, waveguide Bragg gratings

INTRODUCTION

Microwave photonic (MWP) filters have been proposed as agile front-end processors for broadband RF signals [1]. On-chip integration of such functionality brings the required compactness and stability for practical applications, along with the possibility of cutting down fabrication costs. Current wireless mobile and satellite communications systems as well as radar sensors networks make use of widely different frequency bands centred around carriers ranging from few GHz to several tens of GHz, with continuous exploration toward higher carrier frequencies for improving the system throughput capacity. Simultaneous detection of these multiple bands through ultrawideband antennas is nowadays possible [2], and a MWP bandpass filter able to dynamically select specific broadband (i.e., multi-GHz bandwidth) channels over such a wide frequency range would increase the flexibility and service coverage of a single RF receiver. The solutions so far reported for integrated (I-) MWP bandpass filters suffered however by either limited tuning range below 20 GHz, maximum out-of-band rejection of about 20 dB, non-flat passband width, or a combination of all these issues [3-5]. A silicon photonics (SiP) IMWP flat-top passband filter with a tuning range over 70 GHz, and an out-of-band rejection of up to more than 40 dB is here demonstrated.

OPERATION PRINCIPLE AND CIRCUIT IMPLEMENTATION

The proposed scheme exploits optical-to-RF mapping of a narrowband optical filter (OF), as illustrated in the schematic operation of Fig. 1. An optical carrier at the frequency ν_0 (i) from a laser source is launched into the photonic integrated circuit (PIC) and split into two paths by a variable optical splitter (VOS). On one path, a phase modulator (PM) driven by the received RF signals comprising several modulated carriers (ii) and having an overall power well below the modulator half-wave voltage, produces an optically-upconverted dual-sideband replica of the input electrical spectrum around ν_0 (iii). At the output of the PM, a passband OF with central frequency ν_{OF} properly detuned from ν_0 (iv) selects a portion of one sideband containing the desired channel, while strongly suppressing all the other spectral components (v). After the OF, the selected channel is re-coupled with the laser carrier emerging from the other branch of the VOS (vi) through an optical coupler (OC). The composite signal at the output of the OC is then routed to a photodiode (PD) that down-converts back to the electrical domain the selected channel sideband spectrum (vii) for being delivered to an electrical amplifier (EA) at the circuit output. By acting on the VOS, the optical carrier-to-selected channel sideband power ratio can be finely adjusted for optimizing the performances of the IMWP filter, and changing the laser-OF detuning allows selecting different RF channels.

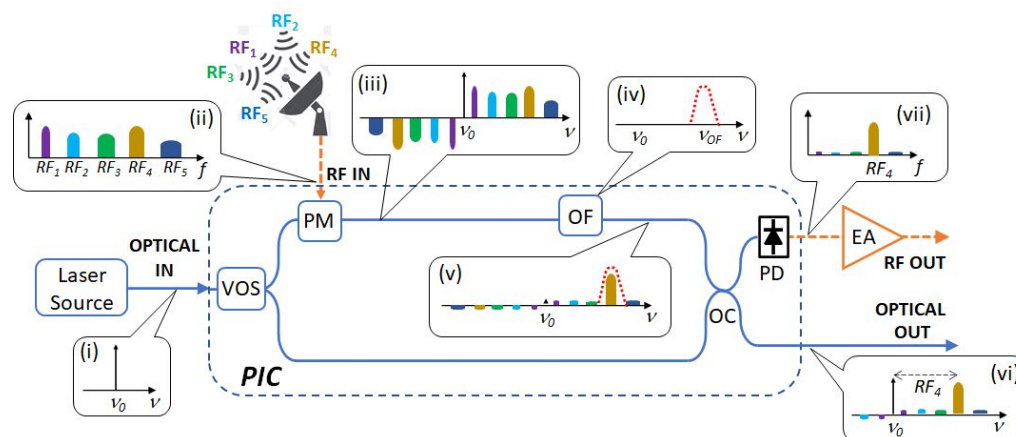


Fig. 1. Integrated microwave photonic filter operation principle.

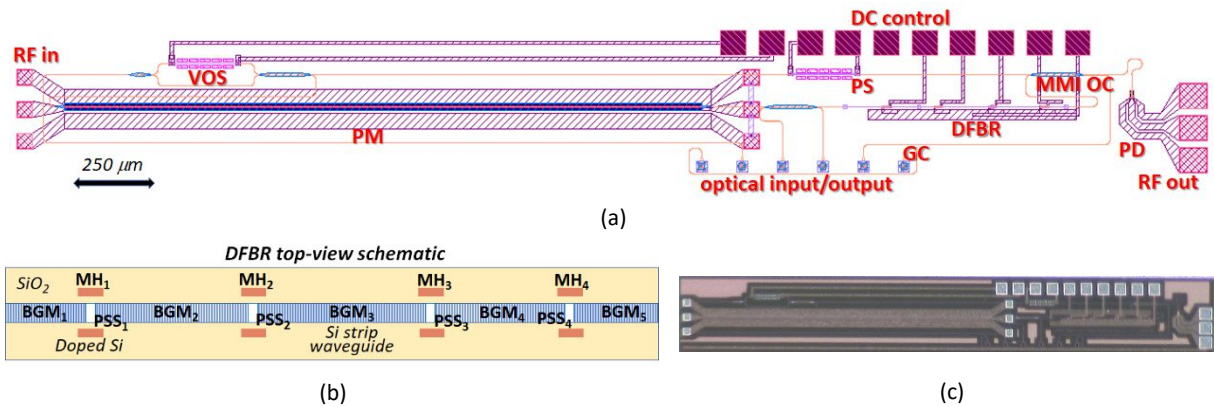


Fig. 2. (a): Mask layout for PIC fabrication in SOI technology. (b): Schematic top-view layout of the DFBR tunable optical filter. (c): Picture of fabricated PIC.

The circuit has then been realized in silicon-on-insulator (SOI) technology, and the produced mask layout for device fabrication using standard DUV lithography through a multi-project wafer service [6] is shown in Fig. 2(a). The PM is a 2-millimetre-long carrier-depletion-based device, and the integrated OF is implemented in a 4th-order multi-cavity distributed feedback resonator (DFBR) architecture, which is particularly suitable for realizing narrow passband windows in a compact wire-like waveguide geometry [7]. The VOS is realized using a symmetric balanced Mach Zehnder interferometer with thermal phase control onto its arms. The output OC is a 2×2 multimode interference (MMI) device, with a SiP Ge PD connected to one of its output ports. The second port of the MMI OC provides the optical output of the PIC, and an additional MMI splitter is used for signals monitoring. Grating couplers (GCs) provide access to the optical input/output ports through a fiber array, and metal routes and pads are used for contacting the heaters controlling the DFBR filter and the VOS. The overall layout footprint is ~1.7 mm². The tuning mechanism of the DFBR, whose schematic structure is also shown in Fig. 2(b), relies on controlling the optical path of the coupled cavities created by four phase shift section (PSSs) comprised between five strip waveguide Bragg grating mirrors (BGMs) using doped-Silicon micro-heaters (MHs) symmetrically placed at the sides of the PSSs.

DEVICE CHARACTERIZATION AND RESULTS

The spectral characterization of the DFBR filter is reported in Fig. 3(a) and is obtained by scanning the output of a tunable laser source (TLS) with steps of 1 pm and recording the transmitted filter power from a PIC monitor output port on an optical spectrum analyser. Two different filter tuning settings corresponding to a 50 GHz frequency shift of the passband window are shown in the long-span spectral response. The filter insertion loss is below 4 dB, and the passband details reveals a -3 dB bandwidth of 4.2 GHz and an attenuation of 28 dB at 5 GHz from the filter central frequency. These values can be tailored at design stage, and passband widths down to 2 GHz have been previously demonstrated in similar structures [7]. The small-signal modulation bandwidth of the SiP PM is also characterized using the set-up of Fig.3(b). A 67-GHz bandwidth vector network analyser (VNA) sweeps the modulator driving frequency at the RF input port of the PIC in the range between 10 MHz and 70 GHz and collects the signal detected by a 70 GHz-bandwidth external PD which is connected to the optical output port of the PIC.

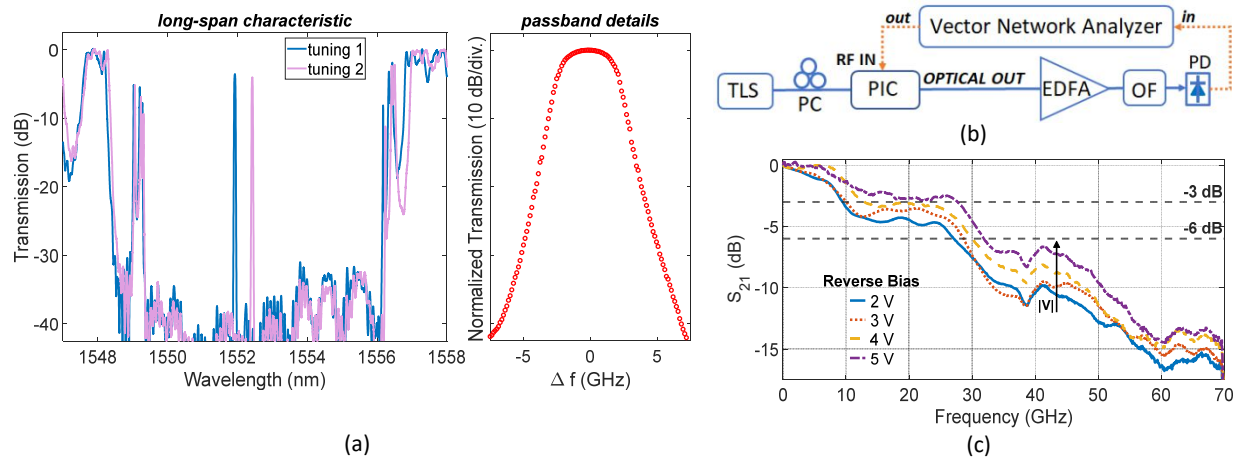


Fig. 3. (a): DFBR optical transmission spectra. (b): Experimental set-up. (c): SiP PM small-signal modulation bandwidth at different reverse bias voltage levels.

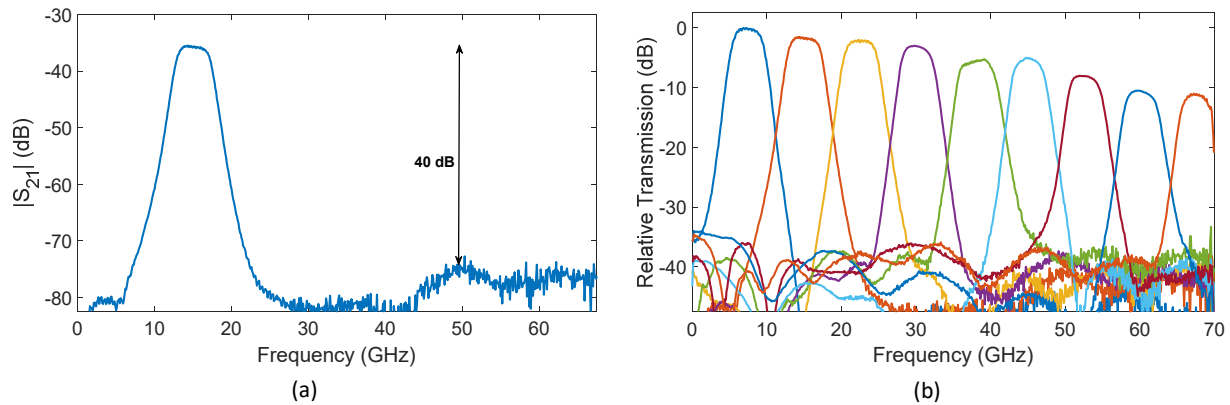


Fig. 4. (a): Measured power transmission for a laser carrier-DFBR filter detuning of 15 GHz (b): IMWP filter response at different tuning of the central frequency in the range 0-70 GHz.

A polarization controller (PC) is used to maximize the injected optical power into the circuit from a tunable laser source (TLS) through the GCs, and at the PIC output an erbium-doped fiber amplifier (EDFA) followed by an OF raises the signal level at the PD input to about 3 dBm. In the measurement, the output wavelength from the TLS is matched to the central frequency of the DFBR filter passband window and the optical power entering the circuit is evenly split onto the two output branches of the VOS, thus making the scheme of Fig. 1 acting as a Mach-Zehnder interferometer which is then biased at quadrature using a thermal phase shifter (PS) placed on the carrier path (see Fig. 2(a)). The measured normalized magnitude of the S_{21} parameters from the VNA for different reverse bias values of the modulator pn-junction are shown in Fig. 3(c). Although the maximum 3 dB cut-off modulation frequency stays below 30 GHz under any bias condition, a slow roll-off of the small-signal response down to about 15 dB below the low-frequency value is observed at the maximum driving frequency of 70 GHz.

In this preliminary characterization, due to the lack of a wideband RF amplifier boosting the signal after the Ge PD, the tuning capability of the proposed IMWP filter is also evaluated using the set-up of Fig. 3(b). The trace in Fig. 4(a) shows the measured magnitude of the IMWP filter S_{21} parameter when the detuning between the optical carrier and DFBR filter is 15 GHz. As shown, the out-of-band rejection is well above 40 dB over the considered frequency range of more than 60 GHz. The measured -6 dB bandwidth of 4.8 GHz well agrees with the observed value for the DFBR filter bandwidth, and the IMWP filter roll-off is larger than 7 dB/GHz over an excursion of more than 30 dB in its transition band. The results relative to the tuning of the IMWP filter central frequency with 7.5 GHz steps are shown in Fig. 4(b), where the relative transmissions with respect to the normalized filter response at the low-frequency tuning are displayed, and the carrier-to-sideband level at the PD input is adjusted in each measurement through the VOS for maximizing the filter rejection. For the sake of simplicity, the IMWP filter tuning is obtained by changing the TLS output wavelength, while keeping fixed the DFBR filter central wavelength. The measurements indicate that a minimum out-of-band rejection of 35 dB is preserved over the full 70 GHz span when tuning the IMWP filter central frequency up to 45 GHz. At larger detuning between the TLS carrier and DFBR passband window the drop in the PM frequency response causes a reduction of the IMWP filter rejection, which is nevertheless about 25 dB for the maximum central frequency tuning of 67.5 GHz.

Acknowledgements: This work has been supported by the project COSMOS: Photonics-based COherent SAR constellation for Multistatic and multispectral satellite Earth ObServation” funded by the Ministry of Education, Universities and Research-FISR program (special supplementary fund for research)

References

- [1] J. Capmany et al, A tutorial on microwave photonic filters, IEEE J. Lightw. Technol., vol. 24, no. 1, pp. 201-229, 2006
- [2] S. Dey, M. S. Arefin and N. Karmakar, Design and Experimental Analysis of a Novel Compact and Flexible Super Wide Band Antenna for 5G. IEEE Access, vol 9, pp. 46698-46708, 2021
- [3] J. Fandiño et al., A monolithic integrated photonic microwave filter, Nature Photon. Vol. 11, pp. 124–129, 2017
- [4] W. Zhang and J. Yao, Integrated Frequency-Tunable Microwave Photonic Bandpass Filter on a Silicon Photonic Chip, Optical Fiber Communications Conference and Exposition (OFC), pp. 1-3, 2018
- [5] Z. Zhu, et al., Positive link gain microwave photonic bandpass filter using Si3N4-ring-enabled sideband filtering and carrier suppression, Opt. Expr., vol. 27, no.,22/28, pp. 31727-31740, 2019
- [6] <https://compoundtek.com>
- [7] C. Porzi, G. J. Sharp, M. Sorel and A. Bogoni, Silicon Photonics High-Order Distributed Feedback Resonators Filters, IEEE J. Quantum Electron., vol. 56, no. 1, pp. 1-9, 2020

Integrated THz-photonics transceivers by all-dielectric phonon-polariton nonlinear nanoantennas

(Invited paper)

Unai Arregui Leon¹, Davide Rocco^{2,3}, Luca Carletti^{2,3}, Marco Peccianti⁴, Stefano Maci⁵, Giuseppe Della Valle^{1,6}, and Costantino De Angelis^{2,3}

¹Politecnico di Milano, Department of Physics, Piazza Leonardo da Vinci 32, Milano 20133, Italy

²University of Brescia, Department of Information Engineering, via Branze 38, 25123 Brescia, Italy

³National Institute of Optics, Consiglio Nazionale delle Ricerche, via Branze 45, 25123 Brescia, Italy

⁴University of Sussex, Emergent Photonics Lab (EPic), Dept. of Physics and Astronomy, Brighton, BN1 9QH, United Kingdom

⁵University of Siena, Department of Information Engineering and Mathematics, 53100 Siena, Italy

⁶Institute for photonics and nanotechnologies, CNR, Piazza Leonardo da Vinci 32, Milano 20133, Italy

* corresponding author: e-mail davide.rocco@unibs.it

The THz spectrum offers the potential of a plethora of applications, ranging from the imaging through non transparent media to wireless-over-fiber communications and THz-photonics. The latter framework would greatly benefit from the development of optical-to-THz wavelength converters. Exploiting Difference Frequency Generation in a nonlinear all dielectric nanoantenna, we propose a compact solution to this problem. The approach is completely transparent with respect to the modulation format and can be easily integrated in a metasurface platform for simultaneous frequency and spatial moulding of THz beams.

Keywords: photonic metasurfaces, THz photonics

INTRODUCTION

The terahertz (THz) region of the electromagnetic spectrum has gained increasing attention in the last decades and today it is one of the fundamental emerging branches of research for the broad photonics community.

Astrophysics, communications, imaging, spectroscopy, biotechnology and security are among the huge plethora of applications where THz technology can provide ground-breaking devices and systems, also thanks to the particular features of a wide range of media in the THz spectral range [1, 2, 3]. Research is thus today focused on overcoming or bypassing difficulties in the advancement of this technology, such as the scarcity of transmitters and receivers and the, sometimes, poor availability of components able to manipulate THz radiation (lenses, polarizers, mirrors, beam splitters, etc.). Noteworthy, metasurfaces are today identified as the framework where all the above approaches can be conveniently unified to provide a compact and integrable solution to a variety of different beam forming needs. For example, in Fig. 1 the THz surface wave is beam formed into the far-field (FF) THz radiation by a modulated THz metasurface, providing gain and directionality.

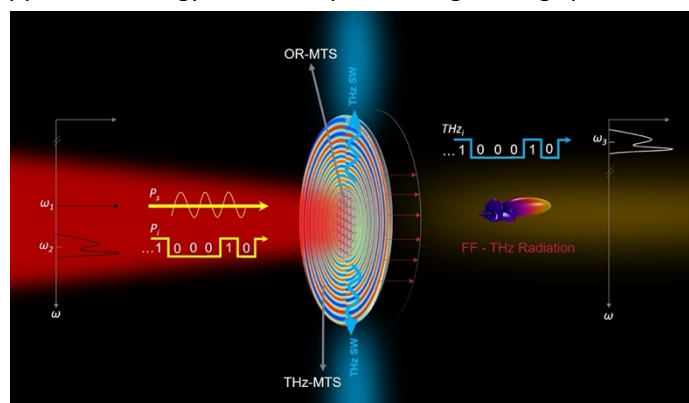


Figure 1: The wavelength converter: the information message, with power P_i , mixes with the incident signal, power P_s , both in the IR region. DFG in the all-dielectric nanoantennas emitting the THz information signal, THz, to produce a THz surface wave (SW) which propagates in the surrounding THz metasurface where it is converted into the desired THz radiation in the far-field (FF).

As far as transmitters are concerned, modulated THz generation is needed with high repetition rate in different spectral regions. Despite the fact that THz sources are still lacking in some spectral regions, photoinduced THz generation is today obtained by various mechanisms. Recently, in order to get the highest performance per unit volume via resonant, nanoscale, compact platforms, THz generation by optical rectification in plasmonic Split-Ring Resonators (SRRs) has been reported [4]; the THz signal is produced from nanoscale SRRs by exciting magnetic-dipole modes in the infrared regime. A thorough study of THz pulse generation using a 40 nm thin metasurface based on plasmonic SRRs excited with a laser oscillator emitting nanojoule femtosecond pulses has been reported

in [5], measuring a conversion efficiency as high as that of a 0.1 mm thick ZnTe crystal. Despite these pioneering results, a breakthrough in the field demands for a substantial improvement of the conversion efficiency at the nanoscale.

One promising alternative to plasmonic THz emitters is represented by all-dielectric THz antennas. Such a structure has already gained a lot of attention in nonlinear optics as a building block for second and third harmonic generation in dielectric metasurfaces. As schematically depicted in Fig. 1, exploiting DFG driven by second-order nonlinearities in a nonlinear all dielectric nanoantenna, we have proposed this wavelength converter in [6]. As a prototype example, for an AlGaAs nanoantenna, we calculate a strong conversion efficiency around 11 THz for an optimized structure. Moreover, we also stress that the same approach can be applied also using different materials with second-order nonlinearity, such as LiNbO₃, to access different spectral regions.

RESULTS

Let us imagine a scenario in which a dielectric metasurface generates a THz signal through DFG process when excited with pumps in the infrared regime, see Fig. 1. The optical-rectifying metasurface (OR-MTS) can be encapsulated at the center of a THz metasurface. In this context, the OR-MTS represents a THz launcher that has the scope to excite a THz surface wave on the THz-MTS. By properly optimizing the THz-MTS it is possible to generate a broadside radiation at THz by modulating the THz MTS through the heights of the nanopillars. To this end, the radial period of the modulation should match the wavelength of the surface wave excited at terahertz, thus providing an energy conversion into a leaky-mode. The first and fundamental step in this design, which also coincides with the main results presented here, is the engineering of the single nanoresonator that directly converts light from Infra-Red (IR) to the THz with high efficiency.

To demonstrate this statement, we aim to exploit nonlinear DFG process in an all-dielectric nanoantenna of AlGaAs crystalline structure. Indeed, starting from two intense laser beams in the infra-red, the DFG nonlinear generated field can have a frequency of few THz, thus laying within the THz gap window. Although there exist other compounds that possess zincblende structure, the choice of AlGaAs is rather advantageous for our purpose, due to its low loss and dispersion in the optical region, high refractive index, large nonlinear susceptibility of the second-order as well as a well-established fabrication techniques.

Let us consider an AlGaAs nanocylinder free-standing in air, with radius r equal to 200 nm and height h of 400 nm. The geometrical parameters of the nanodisk are selected in order to fulfill a magnetic dipolar resonance around the fundamental wavelength. We consider two incident pump beams that excite the proposed nanodisk in the infra-red range. The two incident signals, which logically correspond to the IR pump beam and information signal, are modeled as plane waves linearly polarized at 45° (L45). Thus, two spectrally close components of the input optical pulses are mixed via the DFG process, so that the terahertz component is generated.

To perform simulations of the DFG process in Comsol, the knowledge of the AlGaAs nonlinear susceptibility in the THz region is mandatory. Far away from the material resonances, Miller's (empirical) rule is an interesting tool for determining the second-order nonlinear susceptibility from the material linear properties. However, the presence of phonon resonances in the THz region, prevents the exploitation of Miller's rule in our case. Instead, the so-called Faust-Henry model can be used.

A critical computational aspect of the DFG process under study is that it comprises physical problems with extremely different characteristic length scales. To avoid an extremely high memory requirement for the model execution, we thus implement a geometry (and related mesh) based on two different components: one for the optical problems and a second one for the THz problem in which the domain is bigger. This allows us to significantly relax the minimum mesh element size in the host medium (air) when solving the THz simulation, but still maintain the same finer mesh as that at the near-IR inside the nanocylinder. In details, a General Extrusion coupling operator is used to connect the nanocylinders of both components.

The role of localized surface phonon-polaritons (SPhP) can be investigated by resorting to a reduced quasi-static model of the THz generation process. This is based on the assumption that the efficiency of the process is proportional to the quality factors Q_1 and Q_2 of the IR resonances interacting with the two pumps, to the quasi-static linear extinction cross-section, and, of course, to the modulus of the nonlinear coefficient. This way, one can estimate the DFG efficiency according to a simple semi-analytical formula.

A fair qualitative agreement with the extinction efficiency evaluated from FEM numerical analysis (blue trace in Fig. 2) is retrieved. Note that if one considers non-resonant extinction from the Rayleigh background, the estimated DFG efficiency would drop by almost two orders of magnitude on the efficiency peaks (red curve in Fig. 2). This ascertains the key role of SPhP in the THz generation from all-dielectric nonlinear nanoantennas.

Lastly, to further highlight the potential of the proposed structure for THz applications, we perform a comparison with state-of-the-art configurations, based on a plasmonic structure. We consider an isolated gold split-ring resonator with similar geometrical parameters as the one reported in [5]. Such THz generation efficiency simulations retrieve 7 orders of magnitude lower than what is attained with the proposed single AlGaAs nanopillars. Hence, using high-refractive index dielectric materials not only strongly enhances the DFG process thanks to the bulk nonlinear coefficient and THz SPhP oscillations, but also provides, from a simple cylindrical geometry of the antenna, a configuration of the nonlinear radiation pattern that is suitable for launching surface waves in THz metasurfaces.

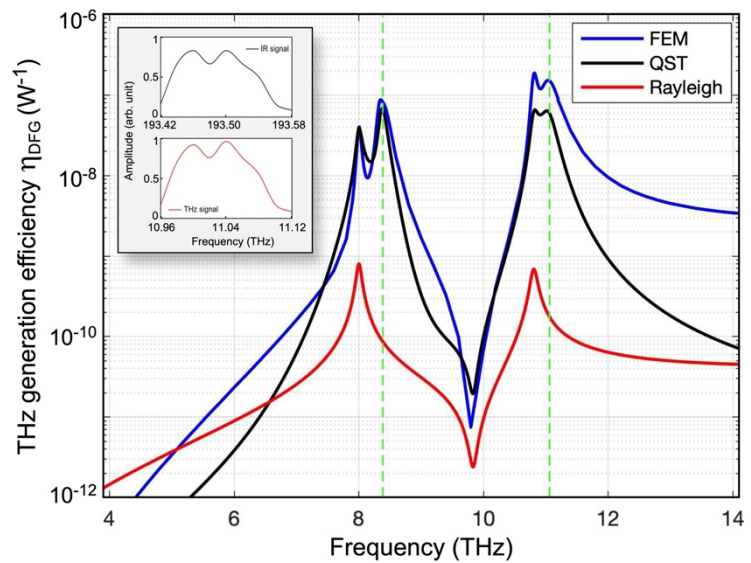


Figure 2: Conversion efficiency for THz generation by DFG in the proposed AlGaAs nanoantenna, evaluated from FEM numerical analysis (blue), and reduced model with (black) or without (red) contribution from phonon permittivity. The inset shows the negligible spectral distortion introduced by the proposed transceiver.

Acknowledgements: The authors acknowledge fruitful discussions with Professor Giuseppe Leo. This work was supported by the European Commission Horizon 2020 H2020-FETOPEN2018-2020 (899673); the National Research Council, Joint Laboratories program (SAC.AD002.026); the Italian Ministry of University and Research (PRIN 2017MP7F8F and PRIN2020EY2LJ).

References

- [1] Yang, X. et al. Trends in biotechnology 34, 810–824 (2016).
- [2] Peters, L., Tunesi, J., Pasquazi, A. & Peccianti, M., Sci. reports 7, 1–9 (2017).
- [3] Faenzi, M., Gonzalez-Ovejero, D. & Maci, S., IEEE Transactions on Antennas Propag. 69, 1942–1951 (2020).
- [4] Fang, M. et al., Opt. express 26, 14241–14250 (2018).
- [5] Tal, M., Keren-Zur, S. & Ellenbogen, T., ACS photonics 7, 3286–3290 (2020).
- [6] Leon, U.A. et al, Sci Rep 12, 4590 (2022).

3D printed on-chip parabolic mirror for chip-to-fiber and chip-to-chip coupling

Y. Kong, H.L. Offerhaus, M. Dijkstra, S.M. García Blanco, L. Chang*

Optical Sciences Group, MESA+ Institute for Nanotechnology, University of Twente, 7500 AE Enschede, The Netherlands
*l.chang@utwente.nl

Reflection of light by a 3D printed aluminum coated micro parabolic mirror overcomes the in-plane limitation of waveguide end facet coupling between two photonic devices. Its application includes broad wavelength range wafer-level testing and inter-chip coupling. Design, fabrication and preliminary characterization of 3D printed micro-mirrors on optical waveguide chips will be described in this work.

Keywords: *Optical connectivity, 3D print, micro mirror, wafer-level photonic packaging*

INTRODUCTION

Wafer-level testing of optical waveguide devices is an important enabling technology to reduce cost. It is also a great tool to reduce testing time in comparison with die-level testing, which leads to faster developing cycle. In the Si waveguide platform, grating couplers have been used to couple the light out of the wafer plane for wafer-level testing [1]. However, it is challenging to use grating coupler in lower contrast waveguide material platforms due to the relative small bandwidth (i.e., typically spanning only a few tens of nanometers) [2]. In this preliminary study, a reflection-based micro-mirror is proposed to reflect the light out of the wafer plane. Depending on the applied coating, a parabolic mirror can work over a very large wavelength range (e.g., from the UV to the infrared for an aluminum coating) compared to a grating coupler. A metal coated reflection layer is an interesting alternative to the previously proposed total internal reflection based mirrors[3], especially in certain applications in which air cavities need to be removed during packaging. The technology proposed in this work has the potential to be used with many material platforms since it has low dependency to the substrate. Structure design, 3D printing, and the aluminum coating process will be discussed in detail in this paper.

PARABOLIC MICRO MIRROR FABRICATION

There are two main steps to fabricate the parabolic micro mirrors, namely, 3D printing of the mirror structure and aluminum coating forming the reflecting surface. 3D printing is based on two-photon lithography (2PL), which is a powerful way for manufacturing prototypes of micro size optical components [4]. Most structural materials fabricated by 2PL are photopolymers. The 3D printer (Photonic Professional GT) developed by Nanoscribe is used in this project. The photoresist, IP-S, is used to produce a smooth surface quality and dimensional accuracy [5]. Aluminum coating is chosen in this project due to its high reflectivity over a large spectrum range (i.e., from UV to IR). A ~200 nm thick Al coating is fabricated by e-beam evaporation (BAK600) directly on the 3D printed mirror. A SEM image of a coated mirror is shown in Fig. 1.

MIRROR CHARACTERIZATION WITH A BARE FIBER

In order to test the mirror performance without the complexity of a waveguide mode, standalone mirrors (i.e., without waveguide) have been fabricated on a flat Si wafer. The mirror is then tested with a bare fiber at a wavelength of 976 nm. The testing schematic is shown in Fig. 1. The optical mode profile of a cleaved bare fiber is measured, without the micro mirror, with a beam profiler (Thorlabs BP209IR1(/M)) at location 1. By inserting the micro mirror into the beam path, the light is reflected vertically up. The corresponding beam profile is then measured by moving the beam profiler to location 2. A side view camera image is shown to indicate the relative position between the bare fiber and the micro mirror. Since the entire wafer surface acts itself as a mirror, the mirrored image of the micro mirrors and the fiber is clearly visible in the picture.

The reflected beam profile (i.e., shape and size) depends on the alignment between the bare fiber tip and the micro mirror. The reflected beam profile shown in Fig. 1 corresponds to the case in which the fiber tip is positioned close to the mirror focal point. The nice beam profile indicates that the parabolic mirror surface works as expected.

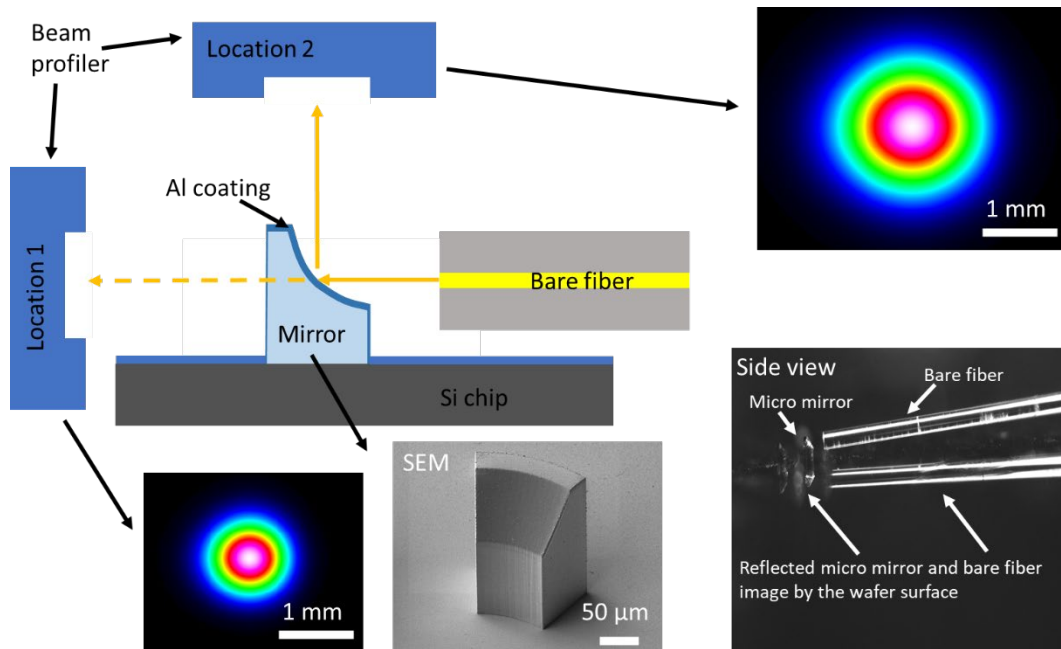


Fig. 1. Schematic of the setup utilized to test the standalone mirrors. A bare fiber is used in order to bring the fiber tip close enough to the printed mirror. The reflected beam profile is measured by the beam profiler at location 2. It has a similar shape as the profile measured in the case of no mirror (i.e., lowering the chip and moving the beam profiler to location 1). A SEM image of the printed and aluminum coated mirror is shown. A side view indicates the relative position between the fiber tip and the mirror.

PRINTED MIRROR ON A WAVEGUIDE CHIP

In this section, we first describe the additional fabrication processes needed to combine the mirror on a Si_3N_4 waveguide chip. Then present the fabrication result and preliminary optical characterization.

There are three main steps during the fabrication. First, in order to align the mirror focal point to the waveguide end facet, a deep reactive ion etched platform is needed as shown in Fig. 2(a). The detailed etching process is described in our early work [6]. Second, both the parabolic mirror as well as a cover above the waveguide end facet are 3D printed. The cover is used to prevent deposition of aluminum on the waveguide end facet in the next step. If an aluminum layer forms at the waveguide end facet, it will prevent light exiting or entering the waveguide. Third, an aluminum layer is deposited by e-beam evaporation. This deposition is very directional. The chip surface normal is pointed to the Al target. Thus the area under the cover will not be coated. A SEM image of fabricated mirrors is shown in Fig. 2(b).

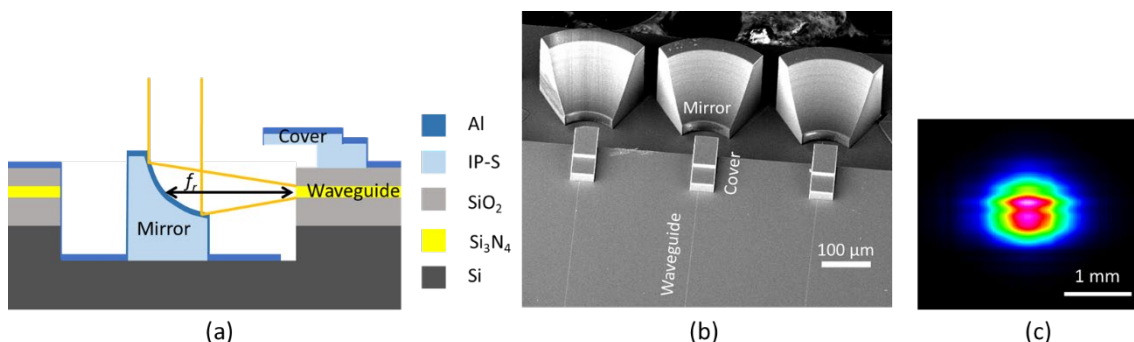


Fig. 2. (a) Printed mirror on a waveguide chip schematic. (b) SEM image of 3 fabricated mirrors aligned with corresponding waveguides. (c) Measured beam profile of light exit from a waveguide and reflected by the corresponding mirror at 976 nm.

For testing purposes, the other end of the waveguide, not shown in Fig. 2(b), has been diced for butt coupling before steps 2 and 3. Thus, that end facet has a thin layer of Al coating. This Al layer is removed by dipping this end facet (half of the diced chip) into aluminum etchant. The sample is then measured by butt coupling the light from a fiber

into the waveguide. The light exit the waveguide, is reflected by the mirror and then is measured by a beam profiler located on top of the chip. A measured beam profile is shown in Fig. 2(c). It matches our expectation except the horizontal features. This mainly due to the waveguide end facet roughness in the horizontal direction. Therefore, a optimization of a deep reactive ion etch process is needed to improve the end facet.

CONCLUSIONS AND OUTLOOKS

In this work, we demonstrate the fabrication process and preliminary characterization results of 3D printed micro parabolic mirror on a Si_3N_4 waveguide chip. It shows the potential to be used for wafer-level testing and inter-chip optical connections.

In the future, further fabrication development is needed to remove the aluminum coating on the locations from which is not needed.

References

- [1] A. Mekis et al., "A grating-coupler-enabled CMOS photonics platform," *IEEE J. Sel. Top. Quantum Electron.*, vol. 17, no. 3, pp. 597-608, 2010.
- [2] C. R. Doerr, L. Chen, Y.-K. Chen, and L. L. Buhl, "Wide bandwidth silicon nitride grating coupler," *IEEE PHOTONIC TECH L*, vol. 22, no. 19, pp. 1461-1463, 2010.
- [3] S. L. Yu, H. J. Zuo, X. C. Sun, J. F. Liu, T. Gu, and J. J. Hu, "Optical Free-Form Couplers for High-density Integrated Photonics (OFFCHIP): A Universal Optical Interface," (in English), *J. Lightwave Technol.*, vol. 38, no. 13, pp. 3358-3365, July1, 2020.
- [4] T. Gissibl, S. Thiele, A. Herkommer, and H. Giessen, "Two-photon direct laser writing of ultracompact multi-lens objectives," *Nat. Photonics*, vol. 10, no. 8, pp. 554-560, 2016.
- [5] M. Schmid, D. Ludescher, and H. Giessen, "Optical properties of photoresists for femtosecond 3D printing: refractive index, extinction, luminescence-dose dependence, aging, heat treatment and comparison between 1-photon and 2-photon exposure," *Opt. Mater. Express*, vol. 9, no. 12, pp. 4564-4577, 2019.
- [6] L. T. Chang et al., "Waveguide-coupled micro-ball lens array suitable for mass fabrication," (in English), *Opt. Express*, vol. 23, no. 17, pp. 22414-22423, Aug 24 2015.



Demonstration of an on-chip optical circulator for TE mode light

RUI MA^{1*}, SANDER RENIERS¹, YUYA SHOJI², TETSUYA MIZUMOTO², KEVIN WILLIAMS¹, YUQING JIAO¹, JOS VAN DER TOL¹

¹Institute for Photonic Integration (IPI), Eindhoven University of Technology, PO Box 513, 5600 MB Eindhoven, The Netherlands

²Department of Electrical and Electronic Engineering/FIRST, Tokyo Institute of Technology, Tokyo, Japan
* r.ma@tue.nl

Abstract

An on-chip optical circulator on an InP membrane on Silicon (IMOS) platform, operating for TE mode input light, is demonstrated. The circulator is composed of two multi-mode interferometers (MMIs), four polarization converters (PCs), and a Cerium-doped Yttrium Iron Garnet (Ce:YIG) die. The Ce:YIG die is adhesively bonded on the InP membrane via a 70-nm thin Benzocyclobutene (BCB) layer. Non-reciprocal phase shift (NRPS) is employed in the presence of a transverse magnetic field. The device works as a 4-port optical circulator with a maximum optical isolation of 27.0 dB and a minimum optical isolation of 18.6 dB for TE mode input light.

Introduction

The IMOS platform is promising for the integration of nano-photonics with high performance active devices [1]. In the IMOS platform, various of active and passive devices, like lasers, photodiodes, modulators, and polarization converters (PCs), are demonstrated [2]. For the next level up with single chip implementations for fibre sensor interrogators, optical imaging systems and PON transceivers, optical circulators are needed in the IMOS platform. In recent years, on-chip optical non-reciprocal devices, like optical isolators and circulators, based on heterogeneous integration of Ce:YIG on the silicon-on-insulator (SOI) platform have been investigated [3]. Four approaches are used to integrate Ce:YIG with SOI: i) Pulsed laser deposition (PLD), ii) Sputtering deposition, iii) Direct bonding and iv) Adhesive bonding. Among them, the last approach is the most suitable for the IMOS platform. The Ce:YIG layer needs over 800 °C annealing temperature to crystallize [4], and this would destroy the InP-material. Direct bonding [5] on the other hand is not reliable for the IMOS platform, due to the presence of surface topology[1]. Therefore, in this paper, an on-chip optical circulator is realized by adhesive bonding of a Ce:YIG die on an IMOS wafer.

Device design

The schematic of the on-chip optical circulator is shown in Fig. 1. The device is based on a Mach-Zehnder interferometer (MZI), including two MMIs, four polarization converters [6] and a Ce: YIG layer. For the forward direction, the input signal coupled into port 1 is split into two branches by a 2x2 MMI. If the input is TE mode, it will be converted to TM mode after passing through PC 1 in the upper branch. The evanescent wave of the TM mode will interact with the Ce: YIG layer, which will provide a non-reciprocal phase shift (NRPS) of $\pi/2$ when a transverse magnetic field is applied. Afterwards, the TM mode will be converted back to TE mode after PC 2.

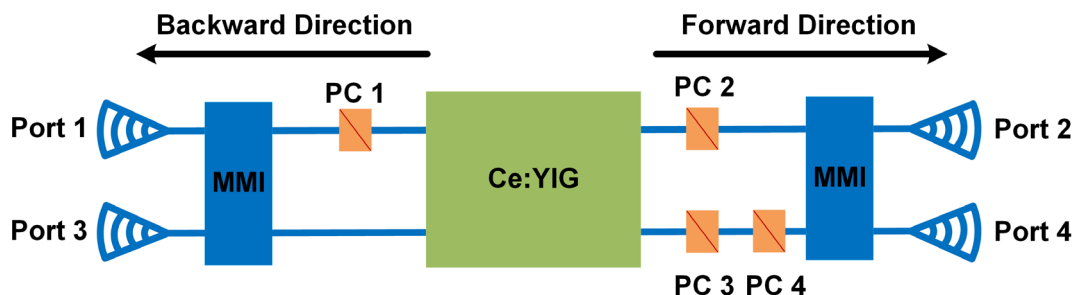


Fig. 1. Schematic of the on-chip optical circulator



In the lower branch, the TE mode will not be affected by the NRPS effect. The TE mode signal in the lower branch will be converted to TM mode after PC 3 and be converted back to TE mode after PC 4. PC 3 and PC 4 are used to balance the optical powers in the two branches before they enter the second 2x2 MMI. The birefringence in the two branches causes an additional $\pi/2$ phase shift but this is reciprocal. When both signals are combined in the output MMI, a total phase difference of π is presented. Thus, the output signal will emerge in port 2. Similarly, inputs from port 3 will appear from port 4. For the backward direction, the NRPS has the opposite sign. Therefore, the TE input signal launched in port 2(4) will emerge in port 3(1) by cancelling the phase difference between the two branches. Hence, the device works as a 4-port optical circulator for TE input.

Fabrication

In our design, the Ce:YIG die is 4 mm x 4 mm and has a thickness of 500 nm, which is sputtered on a substituted Gadolinium Gallium Garnet (SGGG) substrate [5]. The amount of NRPS depends on the thickness of the bonding layer between the InP waveguides and the Ce:YIG layer. Simulation shows that the thickness of the bonding layer should be 120 nm (50 nm SiO₂ and 70 nm BCB) at a wavelength of 1550 nm (3-D Finite Difference Time Domain (FDTD) solver [7]) to reach $\pi/2$ NRPS. However, thicknesses obtained with the commercial BCB solutions are over 1 μm . In order to reach the required thickness of the BCB bonding layer, mesitylene can be added to BCB to reduce the viscosity of the solution, resulting in a smaller spin-coated layer thickness [8].

The process flow is shown in Fig. 2. The device is fabricated on the IMOS platform [2]. The surface of the IMOS wafer is cleaned using an oxygen plasma process. Immediately afterwards, a 50 nm thick SiO₂ layer is deposited on the IMOS wafer to increase the adhesion of BCB.

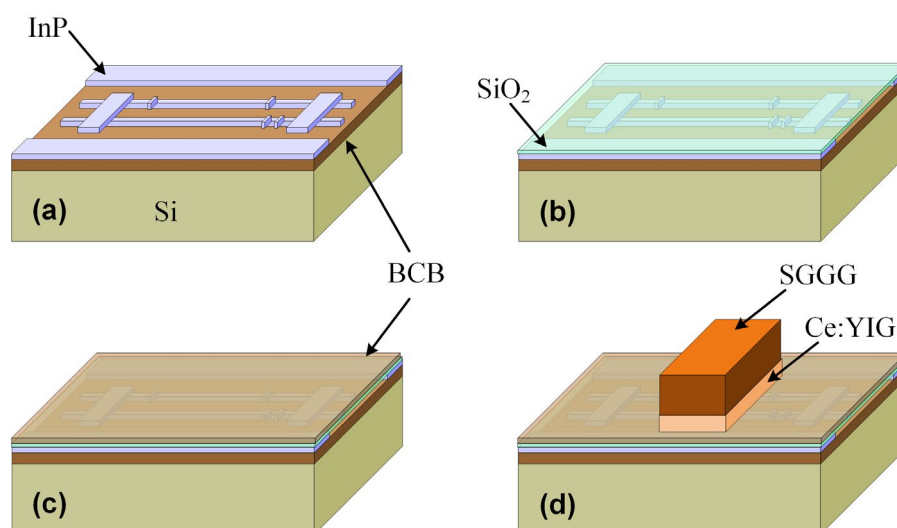


Fig. 2. Schematic of the bonding process (a) Processed IMOS wafer (b) SiO₂ deposition (c) BCB spinning (d) Ce:YIG bonding

Diluted BCB (Cyclotene 3022-46: Mesitylene 1:5 v/v) is spin-coated at 4000 rpm for 30 seconds. Then, the IMOS wafer is kept on a hot plate for 15 minutes to evaporate the remaining mesitylene. The temperature is increased up to 135 °C, with a ramp of 5 °C/min. This results in a 70 nm thick BCB bonding layer.

The Ce:YIG die is cleaned using Acetone and Isopropylalcohol (IPA), for 15 minutes each. Then, the die is aligned and attached manually on top of the IMOS waveguides. The Ce:YIG die is bonded on the IMOS wafer in an EVG bonder under a pressure of 1.6 MPa at a temperature of 280 °C for 1 hour, while ramping the temperature with 2 °C/min in a N₂ environment.

Characterization

This device is characterized on a polarization-maintaining system at room temperature. Four grating-couplers are designed at the four ports to couple light into or out of the device to the fibers (see fig. 1). The transmission spectra of the device are measured using a tunable laser and a power meter. A Nd-Fe-B magnet is placed about 5 cm away from the Ce:YIG die to provide a transverse magnetic field. The magnitude of this field at the Ce:YIG



die is strong enough to saturate the magnetization of the Ce:YIG layer. The transmission spectra are recorded from the four grating couplers for forward and backward propagation.

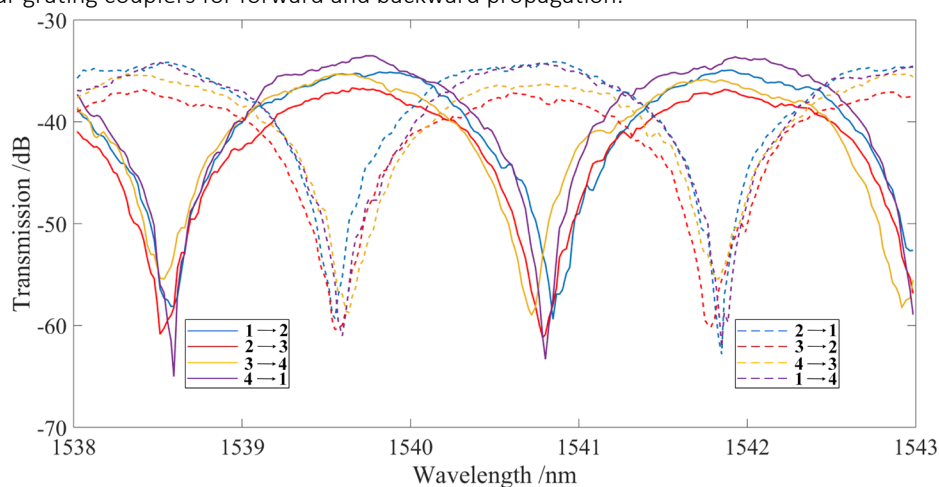


Fig. 3. Transmission spectra between different ports for TE mode input (Drawn lines: clockwise direction. Dashed lines: counterclockwise direction).

The measured transmission between two ports on opposite sides of the circulator are presented in Fig. 3. The non-reciprocal circulator functionality is clearly visible. The transmittance for the clockwise direction at a wavelength of 1539.6 nm is between -36.9 dB and -34.0 dB, and for counterclockwise direction between -61.0 dB and -54.5 dB. The isolation ratio computed between two opposite ports reaches a maximum value of 27.0 dB, while a minimum isolation of 18.6 dB is found.

The transmittance differences among the port pairs are attributed to unintentional power ratio imbalanced in the 2x2 MMI. Excess losses are attributed to optical absorption in Ce:YIG, and to scattering and reflection at the boundaries between BCB and Ce:YIG cladding regions. In addition, the relatively high propagation loss of the waveguide in this realization brings extra insertion loss due to sidewall roughness.

Conclusion

In this work, a 4-port on-chip optical circulator for TE mode light is demonstrated, realized with an adhesively bonded Ce: YIG die to a MZI-based structure, fabricated on the IMOS platform. A Ce:YIG-die-to-IMOS-wafer adhesive bonding procedure is reported. An ultra-thin (70 nm) BCB bonding layer is achieved. The device shows a maximum optical isolation of 27.0 dB and a minimum optical isolation of 18.6 dB for TE mode light. Sources of the insertion losses are also studied. The device can be integrated with other photonic components, like lasers and amplifiers. It provides a step forward towards a multi-functional PIC.

Reference

- [1] J. J. G. M. Van Der Tol, Y. Jiao, J. Van Engelen, V. Pogoretskiy, A. A. Kashi, and K. Williams, InP Membrane on Silicon (IMOS) Photonics, IEEE J. Quantum Electron. vol. 56, no. 1, pp. 1-7, 2020.
- [2] Y. Jiao, N. Nishiyama, J. J. G. M. Van Der Tol, J. p. Van Engelen, V. Pogoretskiy, S. Reniers, and S. Arai, InP membrane integrated photonics research, Semicond. Sci. Technol. vol. 36, no.1, pp. 1-26, 2020.
- [3] W. Yan, Y. Yang, W. Yang, J. Qin, L. Deng and L. Bi, On-Chip Nonreciprocal Photonic Devices Based on Hybrid Integration of Magneto-Optical Garnet Thin Films on Silicon. IEEE J. Sel. Top. Quantum Electron. vol. 28, no. 3, pp. 1-15, 2022.
- [4] W. Yan, Y. Yang, S. Liu, Y. Zhang, S. Xia, T. Kang, and L. Bi, Waveguide-integrated high-performance magneto-optical isolators and circulators on silicon nitride platforms, Optica, vol. 7, no. 11, pp. 1555-1562, 2020.
- [5] Y. Shoji and T. Mizumoto, Magneto-optical non-reciprocal devices in silicon photonics, Sci Technol Adv Mater, vol. 15, no. 1, pp. 1-10, 2014.
- [6] J. Pello, J. J. G. M. Van Der Tol, S. Keyvaninia, R. van Veldhoven, H. Ambrosius, G. Roelkens, and M. K. Smit, High-efficiency ultrasmall polarization converter in InP membrane, Opt. Lett. vol. 37, no. 17, pp. 3711-3713, 2012.
- [7] R. Ma, S. Reniers, Y. Shoji, T. Mizumoto, K. Williams, Y. Jiao and J. J. G. M. Van Der Tol, Integrated polarization-independent optical isolators and circulators on an InP membrane on silicon platform. Optica, vol. 8, no. 12, pp. 1654-1661, 2021.
- [8] S. Keyvaninia, M. Muneeb, S. Stanković, P. J. Van Veldhoven, D. Van Thourhout and G. Roelkens, Ultra-thin DVS-BCB adhesive bonding of III-V wafers, dies and multiple dies to a patterned silicon-on-insulator substrate. Opt. Mater. Express, vol. 3, no. 1, pp. 35-46, 2013.

Assessment of electro- and thermo-optics response of thin film lithium niobate with phase shifted Bragg gratings

(Student paper)

Alessandro Prencipe^{1*}, Katia Gallo¹

¹ Department of Applied Physics, KTH Royal Institute of Technology, Roslagstullsbacken 21, Stockholm SE-106 91, Sweden
* prenc@kth.se

We report a comparative study of the performance of electro-optic (EO) and thermo-optic (TO) devices in lithium niobate on insulator (LNOI) exploiting the high sensitivity of phase shifted Bragg gratings in 300nm-high rib waveguides etched in 500nm-thick X-cut LNOI. We determined the EO and TO tunability of the TE₀₀-mode effective index to be $3 \times 10^{-5}/V$ and $3.6 \times 10^{-3}/W$ respectively and address the temporal response and its stability for both cases.

Keywords: Lithium Niobate on Insulator, integrated Bragg filter, Electrooptics, Thermooptics.

INTRODUCTION

Photonic integrated circuits are used in a wide variety of applications ranging from light generation, detection, filtering and routing and allow to get an important advantage with respect to their tabletop optics counterparts in terms of stability and scalability. Lithium niobate on insulator (LNOI) is a promising material for on-chip quantum optics and ultrafast signal modulation relying on its second-order nonlinearity and electro-optic properties [1]. LN allows to use both electro-optic (EO) and thermo-optic (TO) effects to implement device reconfiguration. EO grants speed, low operating voltages thanks to the recently developed LNOI waveguide technology, and operation also at cryogenic temperatures with low power consumption, extremely important for quantum optics applications [1]. However, LN EO waveguide devices suffer from low-frequency drift [2], a well-known issue for conventional modulators, requiring active stabilization of their operational bias. The thermo-optic properties of LN provide a complementary route to achieve device tunability and switching, in a similar way to devices implemented in silicon photonics [3]. EO and TO effect can be complementary and provide optimal performance depending on the specific application. For this purpose, a careful assessment and comparison of their tunability, temporal response and stability is of utmost importance.

Here we present a systematic study of TO and EO tunability in the LNOI integrated nanophotonic platform. The performances of the two approaches are compared by performing measurements under identical conditions and with high resolution. The latter is achieved using the high sensitivity to refractive index changes afforded by integrated Bragg grating devices, namely phase-shifted Bragg grating (PSBG). These structures, known for being excellent sensors in fiber integrated configuration [4], guarantee an extremely good sensitivity in LNOI too [5].

RESULTS

Figure 1 shows the SEM image of a fabricated LN Bragg grating, schematics of the TO and EO devices and the typical spectral responses for a transmission measurement.

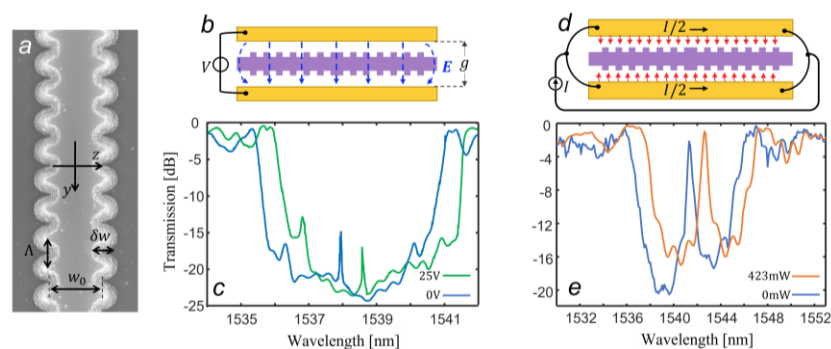


Fig. 1. a: SEM image of a Bragg grating. b: schematic of the device tuned via EO. c: EO, measured transmission spectra when applying 0V (blue line). By applying 25 V (green line) the peak, featuring a BW of 60 pm at around 1538 nm, is shifted of 0.63 nm d: schematic of the device tuned via TO. e: TO, measured transmission spectra without tuning (blue line). By dissipating 0.423W (orange line) the peak, featuring a bandwidth of 296 pm at around 1540 nm, is shifted of 1.31 nm.

The devices were fabricated on a 500nm thick X-cut LNOI wafer (NANOLN). A single pass electron beam lithography was used to structure a negative tone resist (maN2400) spun on a Cr layer which had been formerly evaporated on the LN. The pattern was then transferred to the metal by Cl_2/O_2 reactive ion etching and from the Cr to the LN by Ar^+ milling. The optical measurements were performed by using a tunable laser (Yenista T100S) synchronized with a power meter (Newport 2931-C). The details about the fabrication and the characterization can be found in reference [5]. The nano-waveguides are aligned with the Y-axis of the LN crystal and are characterized by an etching depth of 300 nm and an average width $w_0 \sim 700$ nm, a period $\Lambda \sim 420$ nm and a modulation depth δw ranging between 100 and 200 nm. The transmission peak for a PSBG is located at wavelength $\lambda_B = 2\Lambda n_{eff}$ where n_{eff} represents the average effective refractive index of the TE_{00} guided mode in the grating structure section, polarized along the extraordinary axis (Z). Hence, a refractive index change can be measured very precisely through the wavelength shift experienced by the transmission peak in the spectrum: $\frac{\partial n}{\partial \lambda} = \frac{1}{2\Lambda}$. Taking advantage of the narrow transmission bandwidth (BW) it is possible to detect changes in n_{eff} in the order of $\sim 10^{-6}$. Figure 1b shows the device configuration used to study the EO effect in LN. When a voltage difference is applied to electrodes placed on either sides of the waveguide, an electric field E is generated along the Z-axis of the crystal, accessing the highest EO coefficient of LN, i.e. $r_{33} = 33$ pm/V. The change in the effective refractive index of the waveguide can be quantified as follows:

$$\delta n_{eff} = \frac{1}{2} n_{eff}^3 r_{33} \Gamma \frac{V}{g} \quad (1)$$

Where Γ is the overlap between the guided optical mode and the static electric field [5], V is the applied voltage and g the separation along Z between electrodes. From equation (1) it is possible to estimate the refractive index change for the waveguide mode to be $\frac{\partial n}{\partial V} \approx 10^{-5}$, for typical values of g (i.e. g between 3.5 and 7 μm). Figure 1c displays the measured spectra when implementing EO tuning. By applying a voltage of 25V, the peak is shifted by 630 pm yielding a wavelength tunability of $\frac{\partial \lambda}{\partial V} = 25.2$ pm/V. This corresponds to a refractive index change per unit volt $\frac{\partial n}{\partial V} = 3 \times 10^{-5}/V$, consistent with the above theoretical estimation. Figure 1d shows the configuration for tuning the same PSBG structure through TO effect. Here the control parameter is the electrical power \mathcal{P} dissipated by means of Joule's effect in heaters in the vicinity of the waveguide. The filter in Figure 1d is perfectly analogous to the one of Figure 1b: the main difference between the two approaches is the wiring of the electrodes. In the case of TO effect, the refractive index change can be estimated through the temperature dependent Sellmeier equations [6] as $\frac{\partial n}{\partial T} \approx 5 \times 10^{-5}$. Figure 1e presents the measured transmission spectrum of a fabricated device with and without TO tuning. The PSBG spectrum features a peak centered at 1541.3 nm with a 3dB bandwidth of 296 pm that is shifted by 1.31 nm when $\mathcal{P} = 0.423$ W. This corresponds to a wavelength tunability $\frac{\partial \lambda}{\partial \mathcal{P}} = 3.1$ nm/W. Hence the index change per unit power amounts to $\frac{\partial n}{\partial \mathcal{P}} = 3.6 \times 10^{-3}/W$. The heater resistance, when no current is flowing, amounts to 60 Ω . These results were assessed when the gap between the electrodes is $g = 4$ μm .

Figure 2 shows the results about thermal cross talk, dependance of the tunability on the gap size for both the EO and TO effect and the stability over time for the two approaches.

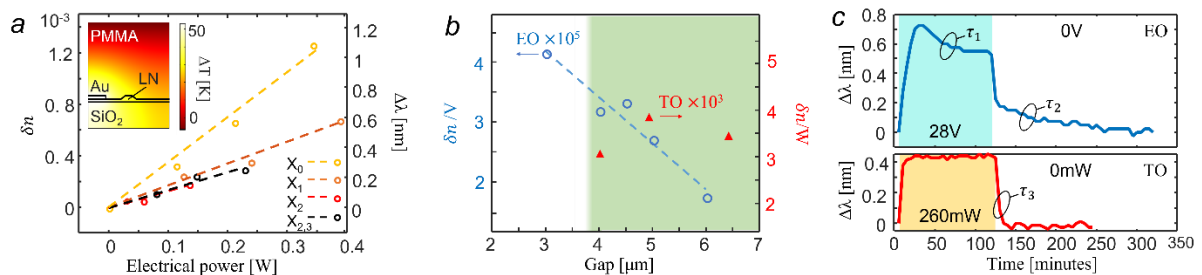


Fig. 2.a: measurement of thermal Cross-talk. When tuning a neighbouring waveguide (curves $X_{1,2,3}$ for first, second and third nearest neighbour respectively), the induced $\Delta\lambda$ is approximately half the one obtained when heating up the device measured (X_0). The inset shows the simulation for the TO effect. b: tunability (blue circles for EO and red triangles for TO) as a function of the gap between the electrodes. When the background is green, extra losses due to the electrodes are negligible. c: wavelength shift as a function of time. In the case of EO tunability, the effect of a DC drift affects the stability of the measured $\Delta\lambda$. In the TO case, instead, the $\Delta\lambda$ is stable after a few minutes of thermalization. The noise in the plots is mainly due to coupling instability.

In the case of EO no cross talk was observed among adjacent devices (spaced by 65 μm). When using the TO effect, instead, the same kind of structures shows a non-negligible cross talk as shown in Figure 2a. X_0 represent the wavelength shift (or, equivalently, the refractive index variation) as a function of the power dissipated directly on

the device under test. X_0 has a slope of 3.1nm/W. X_1 , X_2 , X_3 display the unwanted wavelength shift (or index change) on that same optical device when tuning via TO effect the adjacent waveguides at distance 65, 130 and 195 μm respectively. In the three cases, the slope is $\left(\frac{\partial\lambda}{\partial P}\right)_{X\text{-talk}} \sim \frac{1.5\text{ nm}}{W}$, i.e. approximately half the one of the direct TO tunability. Figure 2b shows a study of the device response with respect to the size of the gap between the electrodes g . In the case of EO the experimental data (blue circles) show the trend predicted by equation (1): the refractive index change induced by virtue of the EO effect increases as the gap gets smaller. However, the g cannot be decreased indefinitely because of the extra losses induced by the electrodes on the guided mode. This is illustrated in the figure by the background color: in the green region, the extra loss is negligible. A minimum gap size of $g = 4\ \mu\text{m}$ is needed to avoid non negligible extra losses. The value for EO waveguide tunability quoted above ($\frac{\partial\lambda}{\partial V} = 25.2\ \text{pm/V}$) corresponds to the case of this minimum gap size. At variance with EO tunability, in the case of TO effect there is no marked dependence of the response on the gap size (the red triangles show the experimental data). Hence the TO approach allows a larger gap size without worsening the tunability. Figure 2c compares the two approaches in terms of stability. The horizontal axis shows the time in minutes and the vertical axis the wavelength shift $\Delta\lambda$ in nm. The latter was sampled every 5 minutes, the purpose being to investigate the slow dynamics of the DC drift in the EO tuning. In both cases a static control signal was applied constantly for the first two hours of measurement (highlighted area). In the EO device the wavelength shift was obtained by applying a voltage of 28 V. Even if the latter was kept constant, the $\Delta\lambda$ reached a peak before experiencing a progressive blue shift (characterized by a time constant $\tau_1 \approx 26$ minutes). After 120 minutes the voltage is turned off and the $\Delta\lambda$ drops at $\sim 200\ \text{pm}$, then slowly converges to zero ($\tau_2 \approx 74$ minutes). In the case of TO tuning a power of 260 mW was dissipated. A $\Delta\lambda = 400\ \text{pm}$ is reached with no oscillation and constantly maintained for 120 minutes. When the external current is switched off, $\Delta\lambda$ decays to zero after a few minutes ($\tau_3 \approx 3.3$ minutes).

CONCLUSION

We reported a comparative study of EO and TO tunability in LNOI using PSBG operating at telecom wavelength. Thanks to the intrinsically high sensitivity to changes in the refractive index of Bragg grating structures, a precise analysis of the tunability performance and stability could be performed. We measured a wavelength tunability of 25.2 pm/V and of 3.1 nm/W for EO and TO devices respectively under comparable conditions. These values correspond to an index tunability of $\frac{\partial n}{\partial V} = 3 \times 10^{-5}/V$ for the EO effect and of $\frac{\partial n}{\partial P} = 3.6 \times 10^{-3}/W$ for the TO effect. The experiments show that the TO offers a better stability over time with respect to the EO approach where the DC-drift strongly affects the measured shift $\Delta\lambda$. On the other hand, the TO effect suffers from a non-negligible thermal crosstalk. This study provides useful knowledge for choosing the optimal solution to achieve tunability in LNOI weighting considerations on power consumption, device footprint, response speed and stability according to the needs of the many possible applications of this platform ranging from nonlinear optics, frequency converters, modulators and switches to filters for both classical and quantum applications.

We acknowledge financial support from the Knut and Alice Wallenberg Foundation through grant nr. 2017.099 and from the Wallenberg Center for Quantum Technology (WACQT), as well as from the Swedish Research Council through grant no. 2018-04487 and the research environment Optical Quantum Sensing (OQS, grant nr. 2016-06122)

References

- [1] D. Zhu, L. Shao, M. Yu, R. Cheng, B. Desiatov, C. Xin, Y. Hu, J. Holzgrafe, S. Ghosh, A. Shams-Ansari, E. Puma, N. Sinclair, C. Reimer, M. Zhang, M. Lončar, *Integrated photonics on thin-film lithium niobate*, Adv. Opt. Photon. 13, 242-352, 2021
- [2] J. P. Salvestrini, L. Guilbert, M. Fontana, M. Abarkan, S. Gille, *Analysis and Control of the DC Drift in LiNbO₃-Based Mach-Zehnder Modulators*, J. Light. Technol., 29, 1522-1534, 2011
- [3] N. C. Harris, G. R. Steinbrecher, M. Prabhu, Y. Lahini, J. Mower, D. Bunandar, C. Chen, F. N. C. Wong, T. Baehr-Jones, M. Hochberg, S. Lloyd, D. Englund, *Quantum transport simulations in a programmable nanophotonic processor*, Nat. Photonics, 11, 447-452, 2017
- [4] R. Kashyap, *Fiber Bragg Gratings*, Academic Press, 2009
- [5] A. Prencipe, M. A. Baghban, K. Gallo, *Tunable Ultranarrowband Grating Filters in Thin-Film Lithium Niobate*, ACS Photonics, 8, 2923-2930, 2021
- [6] G.J. Edwards, M. Lawrence, *A temperature-dependent dispersion equation for congruently grown lithium niobate*. Opt. Quant. Electron. 16, 373-375, 1984

Enhanced all-optical reading of subwavelength magnetic bits on a photonic integrated device using magneto-plasmonic effects

Hamed Pezeshki^{1,2*}, Figen Ece Demirer¹, Reinoud Lavrijsen¹, Jos van der Tol², and Bert Koopmans¹

¹Department of Applied Physics, Eindhoven University of Technology, Eindhoven, 5612 AZ, Netherlands
²Institute of Photonic Integration, Eindhoven University of Technology, Eindhoven, 5600 MB, Netherlands
 *h.pezeshki@tue.nl

We present a device for all-optical reading of magnetic bits, consisting of a plasmon-assisted reading module and a polarization rotator (PR). Localized enhancement of light by plasmonics can enable detection of the magnetization, using the polar magneto-optical (MO) Kerr effect, in targeted bits in a magnetic racetrack medium toward $\sim 100 \times 100 \text{ nm}^2$. Finally, we show how the PR provides MO read-out by transforming the MO phase into an intensity variation.

Keywords: Magneto-plasmonics, Plasmonics, Photonic integrated circuits, Spintronics, Localized surface plasmons, Polar magneto-optical Kerr effect, Indium phosphide.

INTRODUCTION

With the increase in demand for high bit-rate data transfer in the fields of telecommunication and quantum information, the need for new technologies for high speed and reliable data reading/writing is foreseen. Advancements in the field of photonics have enabled wide bandwidth optical data transmission on photonic integrated circuits, while spintronics has empowered high bit-rate data storage [1]. So far, magnetic tunnel junction spintronic devices have proved their effectiveness in reading magnetic bits with conversion into electric signals [2]. However, it is expected that a combination of photonics and spintronics on a single photonic integrated circuit, without any intermediate controlling high-frequency electronics, can bring higher bit-rate data transfer, energy efficient reading and writing, as well as higher data storage capability [3].

In this paper we propose an integrated device for enhanced all-optical reading of magnetic bits by taking advantage of magneto-plasmonic effects. The targeted functionality is to read out data, which are stored in the up/down magnetization of ferromagnetic bits of a racetrack, placed on top of a photonic waveguide. This uses the polar magneto-optical Kerr effect (PMOKE). The intrinsically weak PMOKE, which introduces a small change in the polarization state of the light propagating through the waveguide, depending on the magnetization direction, is enhanced by hybridizing a plasmonic nanoantenna (PNA) with the racetrack. To detect the magnetic bits, the resultant phase change by PMOKE is transformed into an intensity variation using our proposed hybrid plasmonic-photonic polarization rotator (PR). Based on numerical simulations, it is expected that the presented technology device (namely, the PNA device) can enable the detection of the magnetization direction in targeted bits in a magnetic racetrack medium toward a footprint of $\sim 100 \times 100 \text{ nm}^2$. In contrast, for the waveguide without the PNA, i.e. the bare waveguide (BW) device, this is not possible. Moreover, by using the PR, we show that the memory state in a magnetic bit with the size of $200 \times 120 \text{ nm}^2$ can be read-out all-optically with an intensity contrast of more than 0.2 % only with using the PNA device. The proposed device is a generic model which can be used in other areas as well, such as in a lab-on-a-chip biosensing platform for conducting surface-enhanced Raman/fluorescence spectroscopy [4].

RESULTS

The schematic diagram of the proposed integrated device for all-optical reading of magnetic bits is shown in Fig. 1. As depicted, the device consists of two sections: the reading module and the PR. The whole device is based on the indium phosphide (InP) membrane on silicon (IMOS) technology [5]. The reading module is composed of a magnetic racetrack coupled with a PNA as top-cladding of the waveguide. A current pulse is injected through the racetrack to move magnetic domains along it and over the magneto-optical reading area. The PR section operates based on an integrated hybrid plasmonic-photonic quarter-wave plate functionality, which basically creates a $\pi/2$ phase shift between the two beating modes through the waveguide, i.e. the transverse electric and magnetic (TE_0 and TM_0) modes.

The device operates by coupling an incident continuous wave into the TE_0 waveguide mode. Upon interaction between the waveguide mode and the PNA under resonance condition, localized surface plasmons of the PNA get excited and enhance the electric field at the nanoscale hot spot of the PNA, where the magnetic racetrack is

coupled. The concentrated electric field proliferates the absorption cross section of the racetrack and its polarizability, which consequently leads to an enhanced PMOKE and the rotation in the polarization of light (see Fig. 1 (a)). Changing the magnetization direction reverses the rotation angle due to PMOKE and consequently creates a small phase difference. To detect this small phase change as shown in Fig. 1 (a), the propagating wave is transmitted through the PR from which the phase difference is transformed to an intensity difference (see Fig. 1 (b, c)), due to partial conversion of the TE_0 mode to TM_0 mode - resulting in interference with the TM -part from PMOKE.

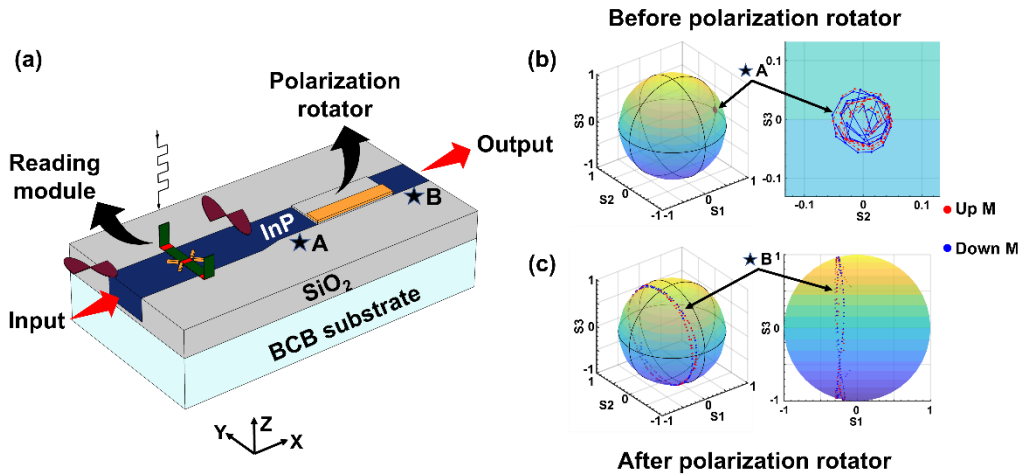


Fig. 1. The concept of the integrated device for all-optical reading of magnetic bits. (a) The schematic diagram of the device illustrating the operation principle. The visualization of the polarization state of the waveguide mode using Poincaré sphere before (b) and after (c) the polarization rotator. The markers 'A' and 'B' indicate the Stokes parameters before and after the polarization rotator. Up and Down M: upward and downward magnetization directions.

The device's performance is calculated using Lumerical, as shown in Fig. 2. Figures 2 (a, b) show the change in the magnitude and phase of the Kerr rotation of light, before the PR, in terms of the targeted magnetic domain width (DW, shown by red in the inset of Figs. 2 (a, b)) in the presence of the oppositely magnetized (blue) rest of the linear racetrack. According to Fig. 2 (a), by varying the DW from 60 to 570 nm, there is a minimum in the magnitude of the Kerr rotation at DW = 120 nm (200) for the PNA (BW) device, for which a jump in the phase of the Kerr rotation happens as shown in Fig. 2 (b). The drop and jump in the magnitude and phase of the Kerr signal is because of the destructive interference between the PMOKE signals of the blue and red magnetic domains (see the inset in Figs. 2 (a, b)). In other words, for DW < 150 (< 240 nm) in the PNA (BW) device, the PMOKE signal from the superposition of the two blue magnetic domains is larger than the PMOKE signal from the targeted red magnetic domain. In this way, the magnetic signal is dominated by the 'down' magnetization in the blue magnetic domains. However, for DW ≥ 140 nm (≥ 240 nm) in the PNA (BW) device, the magnitude of the PMOKE signal from the red domain with the 'up' magnetization dominates the sum of the PMOKE signals of the blue domains. Thus, the targeted magnetic domain with the 'up' magnetization can be unambiguously determined for DW ≥ 140 nm (≥ 240 nm) in the PNA (BW) device, independent of the bit pattern outside the targeted area. The reason for the difference in minimum resolvable DW between the BW and PNA device is related to the strong excitation of localized surface plasmons of the PNA which enhance the polarizability of the targeted magnetic bit. To elaborate on the variation in the magnitude and phase of the Kerr signal, we show the development of the Kerr rotation for the PNA device along the propagation direction of light through the waveguide in the absence of the PR for DWs of 60, 200, and 570 nm as shown in Fig. 2 (c). Based on this figure, for the DWs of 200 and 570 nm, where the phase of the Kerr rotation is positive, the Kerr rotation oscillation is reversed compared to that of the DW = 60 nm. In other words, for the DW = 60 nm, the Kerr rotation is determined by the magnetization in the blue domains, whereas for the DWs of 200 and 570 nm, the Kerr rotation is determined by the magnetization in the targeted red domain as mentioned earlier. This sign reversal in the oscillation of the Kerr signal alongside its phase indicate that for DW ≥ 140 nm in the PNA device, the magnetization within the targeted domain can be detected.

As shown in Figs. 1 (b, c), to read the magnetic state all-optically, we transform the phase change of the input TE_0 mode to the intensity change of the TM_0 mode, which is generated by the PR. Based on the resultant intensity change, we defined the relative contrast figure of merit as:

$$\Delta C (\%) = \frac{|I_{TM}^{\uparrow M} - I_{TM}^{\downarrow M}|}{I_{TM}^{\uparrow M} + I_{TM}^{\downarrow M}} \times 100, \quad (1)$$

where $I_{TM}^{\uparrow M}$ and $I_{TM}^{\downarrow M}$ are the intensities of the forward power density of TM_0 mode for 'up' and 'down' magnetization

directions, respectively. To illustrate the impact of the PNA on the read-out functionality, the result for the magnetic DW of 200 nm for the BW and PNA devices is shown in Fig. 2 (d). As the intensity contrast is generated by the PR, we showed ΔC for the PR section. According to this figure, as light propagates through the PR, the TE_0 mode partially converts to the TM_0 mode. In this case, the resultant phase change caused by PMOKE starts to transform to the TM_0 intensity contrast (ΔC). When the partial TE_0 to TM_0 conversion completes at the end of the PR, ΔC becomes more than 0.2 % with oscillation through the rest of the waveguide due to the mode beating between the TE_0 and TM_0 modes. In contrast, for the BW device with the same DW, the relative contrast is almost zero – meaning that the targeted magnetic state cannot be read. This is in agreement with the Kerr results based on which, the magnitude of the Kerr rotation is almost zero for the BW device.

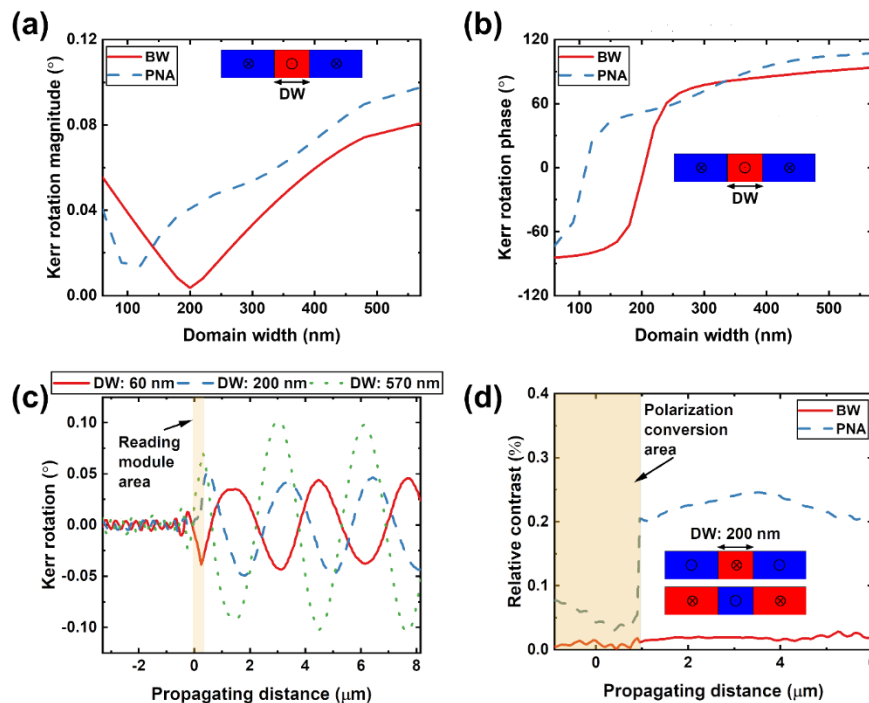


Fig. 2. All-optical reading of the magnetic bits. (a, b) Magnitude and phase of the Kerr rotation in terms of the targeted magnetic domain width (DW), shown red in the inset. (c) Kerr rotation in terms of the propagating distance along the waveguide for three different DWs of 60, 200, and 570 nm. (d) Intensity contrast between the memory states of a magnetic bit with the size of $200 \times 120 \text{ nm}^2$ in the BW and PNA devices.

DISCUSSION

We showed the concept of an integrated magneto-plasmonic device for all-optical reading of memory states. The device is composed of a reading module based on a PNA and a PR based on a plasmonic quarter-wave plate. By taking advantage of localized enhancement of light at the nanosized gap of the PNA, we numerically showed the possibility of detecting the magnetization direction in magnetic bits down to $\sim 100 \times 100 \text{ nm}^2$ with the aid of PMOKE. Moreover, we illustrated that the integrated PR can transform the phase change (caused by PMOKE) to an intensity change of the TM_0 mode, allowing the read-out of a 200×120 with an intensity contrast of $> 0.2\%$. In contrast, using the BW device, detecting such a small magnetic bit is not possible. Further enhancement in the intensity contrast is expected by improving the reading module. The proposed device is generic and can be used for other applications including biosensing. We believe this device can offer an alternative method for reading magnetic bits and is a promising future technology of memory read-out devices.

References

- [1] M. L. M. Lalieu, *et al.*, *Integrating all-optical switching with spintronics*, Nat. Commun., vol. 10, no. 1, pp. 1-6, 2019
- [2] S. S. P. Parkin, *et al.*, *Magnetic domain-wall racetrack memory*, Science, vol. 320, no. 5873, pp. 190-194, 2008
- [3] Y. van Hees, *et al.*, *Deterministic all-optical magnetization writing facilitated by non-local transfer of spin angular momentum*, Nat. Commun., vol. 11, no. 1, pp. 1-7, 2020
- [4] H. Pezeshki, *Lab-on-a-chip technology platform for biophotonic applications*, Doctoral dissertation, University of Nottingham, 2021
- [5] J. J. G. M. van der Tol, *et al.*, *Indium Phosphide Integrated Photonics in Membranes*, IEEE J. Sel. Top. Quantum Electron., vol. 24, no. 1, pp. 1-9, 2017

Beyond Interconnects Applications using a 300mm Silicon Photonics Technology

F. Boeuf¹, S. Monfray¹, C. Barrera^{1,2}, A. Fincato¹, H. Tang⁴, S. Guerber², S. Ohno⁴, D. Fowler², I. Charlet^{1,2}, L. Maggi³, M. Shaw³, K. Toprasertpong⁴, S. Takagi⁴ and M. Takenaka⁴

¹STMicroelectronics, Technology & Design Platform ²CEA-LETI Université Grenoble Alpes, ³STMicroelectronics Agrate, ⁴The University of Tokyo

I. Introduction

Experimentally investigated for more than 40 years, silicon photonics (SiPho) finally reached the CMOS fab in the late 2000s and was available in state-of-the-art 300mm CMOS fab in the early 2010s [1]. This technology was originally developed for data transmission and found its first products development a time where lower cost 100G interconnect for intermediate reach (2km) in mega-datacenter was needed. Nevertheless, until now the volume of production is lower than for other CMOS technologies and the diversification of application is mandatory to ensure long term sustainability of Silicon Photonics. In the recent years, several works in academic world demonstrated the interest of using silicon photonics for chip-to-chip interconnects, programmable photonics, 3D-sensing, quantum computing, bio-sensing etc. In this paper we discuss about the evolution of our 300mm silicon photonics platform toward “beyond interconnects” applications. We are taking the example of 3D-sensing and neuromorphic applications to discuss the future evolution of our process technology.

II. Industrial Silicon Photonics Platform

Our SiPho process relies on 310nm thick SOI wafers with 1.5 μ m BOX. Triple SOI etching steps allows defining various combinations of waveguides heights and slab thicknesses for rib waveguide definition: 310nm/150nm, 310nm/50nm, 150nm/50nm, as well as 310nm-thick strip waveguides. After patterning and lateral SiO₂ isolation, implantations are realized to define modulators, followed by Ge photodetector fabrication. PECVD Silicon Nitride (SiN) is then deposited and patterned to define strip and rib SiN waveguides. After dielectric deposition and planarization contact level followed by 4 Cu-interconnect levels are deposited. Once Aluminum pads are patterned an optional localized dielectric patterning is done to access the SiN waveguide layer. Fig.1 is showing a cross section of the process. At 1.31 μ m, Si and SiN single mode waveguide (SMW) propagation losses are respectively 0.9dB/cm and 0.6 dB/cm. Various types of PN junction modulator have been demonstrated using different combinations of Silicon slabs and SMW thicknesses. Performances are summarized on fig.2. Fiber coupling is relying on surface grating coupler (~1.5dB peak loss) and adiabatic coupling through the use of an external interposer adiabatically coupled to SiN waveguides. In this last scheme, fiber to chip loss is about 2dB for TE/TM modes over an 80nm optical bandwidth [2].

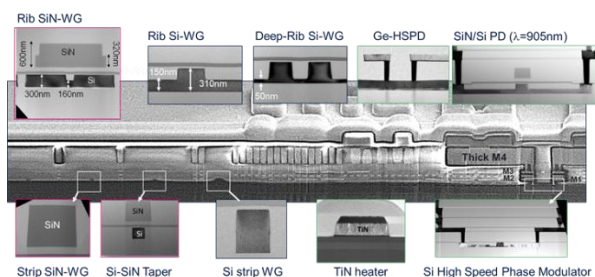


Fig.1 : SiPho platform cross-section

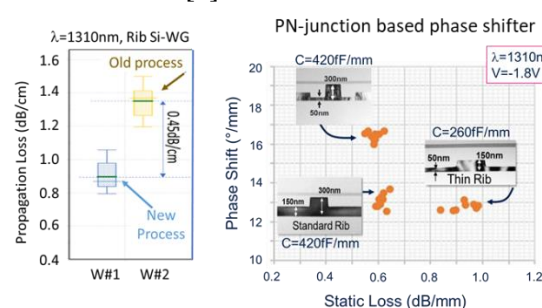


Fig 2 :SMW loss and Phase shifter performance

III. Optical Phased Array for Beam Scanning and Beam Forming applications

Using this SiPho platform we designed 16 channels Optical Phased Array (OPA) using both Si and SiN layers. Principle of operation is summarized on Fig. 2a. Si-based OPA are operating at $1.55\mu\text{m}$, whereas SiN-based OPA are operating at 905nm . For Si-OPA we used both thermal- phase -shifter (TPS) and opto-electronic phase (PiN diode) controls [3]. In the first case the $P_{\pi}=50\text{mW}$ Si-based heaters lead to a high-power consumption, whereas in the second case PiN diodes allow to reach less than 2mW per channel for 2π phase shift. Thanks to a genetic algorithm to control each of the individual channels [4] both beam forming and beam scanning have been demonstrated (fig.3), nevertheless due to the measurement setup limitation, only $\pm 5^\circ$ beam steering is measured. Operation of SiN-OPA relying on TPS is also achieved with a $\pm 10^\circ$ scanning angle (also limited by experimental setup). A network of 4 SiN-OPAs, addressed through a thermo-optical switch, allows to demonstrate a 2D scanning of $\pm 3^\circ$ in the vertical direction [5].

Although optical losses are higher with PiN (carrier injection) or PN junction (carrier depletion) than with TPS, using TPS lead to a few W of overall power consumption when several hundreds of channels are needed to achieve a high angular resolution. Therefore, to address low power application ($\ll 1\text{W}$), a low loss, efficient modulator would be needed to reach at the same time low power and low optical losses. Hybrid III-V/Si SISCAP modulator demonstrated a very high efficiency [6] and could be good candidates for integration with OPA. We estimated that the additional insertion loss due to use of SISCAP could be $<1\text{dB}$ in optimal conditions.

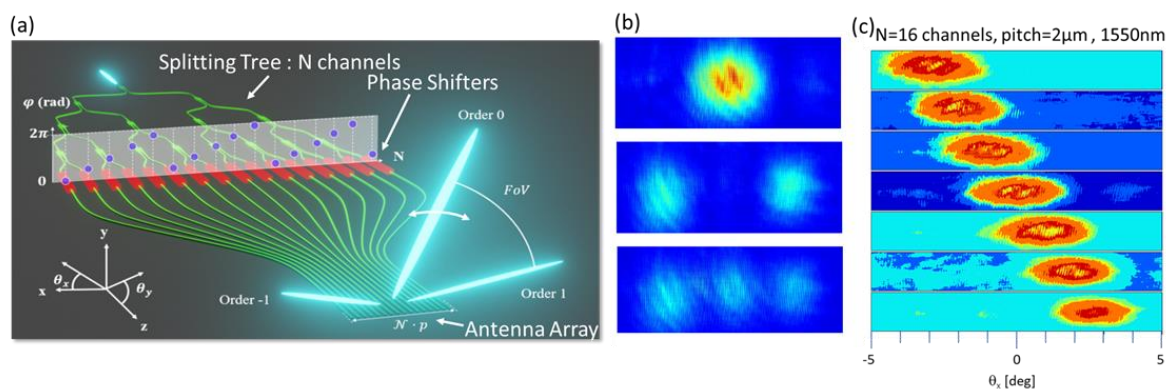


Fig 3 : (a) Optical Phased Array principle (b) example of beam forming (c) beam scanning

IV. III-V / Si heterogeneous integration

Integration of III-V on Silicon for the fabrication of monolithic light-source started in the late 2000s [7]. Since then, numerous demonstrations have been made, such as the integration of laser and optical modulator in a single chip [8] or integrated source with Optical phased array [9]. Nevertheless, it was proposed by Han *et al.* [6] to use III-V layer in SISCAP structure to improve modulator efficiency, thanks to the higher plasma dispersion effect of n-doped InP or InGaAsP layers. Using our SiPho platform we fabricated micro-ring-resonators (MRR) and Mach-Zehnder interferometer (MZI) Silicon base wafers on which III-V layers were bonded at laboratory. Fig. 4a is showing a TEM cross section of a hybrid InP/Si MRR. The InP layer is 25nm which allows a coupling between Si and III-V layers without any taper. This device can be used in a low power switching system, such as a cross bar array for multiply-and-accumulate functionality [10]. A $500\mu\text{m}$ long Linear MZI based on 200nm thick InGaAsP layer with a 15nm Al_2O_3 layer was also fabricated, showing $V_{\pi L \pi} = 0.3\text{V}\cdot\text{cm}$, that is an 8 times improvement over our regular rib-waveguide PN junction modulator.

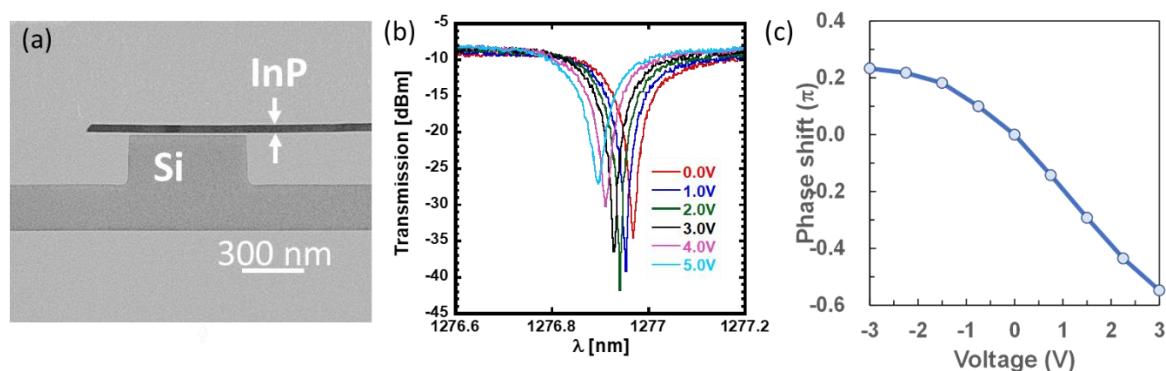


Fig 4 (a) TEM cross section of hybrid InP/SOI MRR (b) hybrid InP/SOI MRR transmission spectra for various reverse polarization (c) phase-shift vs voltage for InGaAsP/SOI MZI device

V. Conclusion

Our Industrial Si-Photonics platform originally designed for data-communication is now used to investigate beyond interconnects applications. Thanks to its versatility a wide range of applications can be addressed. We took the example of 3D-sensing for LiDAR applications and heterogenous integration of III-V materials for low power modulator integration as potential axis of development.

References:

- [1] F. Boeuf et al., "A multi-wavelength 3D-compatible silicon photonics platform on 300mm SOI wafers for 25Gb/s applications," 2013 IEEE International Electron Devices Meeting, 2013, pp. 13.3.1-13.3.4.
- [2] F. Boeuf et al., "A Silicon Photonics Technology for 400 Gbit/s Applications," 2019 IEEE International Electron Devices Meeting (IEDM), 2019, pp. 33.1.1-33.1.4
- [3] C. Barrera, S. Guerber, D. Fowler, S. Monfray, A. Montagne, A. Myko, P. Grosse, K. Ribaud, P. Lemaitre, S. Cremer, I. Charlet, L. Vivien, F. Bœuf, "Fast optical phased array on a 300-mm silicon platform", Proceedings Volume 11690, Smart Photonic and Optoelectronic Integrated Circuits XXIII; 1169007 (2021)
- [4] Sylvain Guerber, Daivid Fowler, Ismael Charlet, Philippe Grosse, Kim Abdoul-Carime, Jonathan Faugier-Tovar, Bertrand Szelag, "Development, calibration and characterization of silicon photonics based optical phased arrays", Smart Photonic and Optoelectronic Integrated Circuits XXIII, SPIE Photonics West 2021
- [5] S.Monfray, S.Guerber, A.Montagné, D.Fowler, P.Grosse, J.Planchot, D.Ristoiu, F.Baron, M.Brihoum, L.Babaud, A.Taute, E.Kempf, K.Rovayaz, P.Chantraine, S.Delmedico1, F.Leverd, L.Balme, D.Pellissier, K.Haxaire, M.Guillermot, S.Mermoz, M.Hello, S.Jan, P.Chevalier, F.Boeuf, Proceeding of OFC 2022
- [6] Han, JH., Boeuf, F., Fujikata, J., Takahashi, S., Takagi, S., Takenaka, T. Efficient low-loss InGaAsP/Si hybrid MOS optical modulator. Nature Photon 11, 486–490 (2017).
- [7] Alexander W. Fang, Hyundai Park, Oded Cohen, Richard Jones, Mario J. Paniccia, and John E. Bowers, "Electrically pumped hybrid AlGaInAs-silicon evanescent laser," Opt. Express 14, 9203-9210 (2006)
- [8] Thomas Ferrotti, Benjamin Blampey, Christophe Jany, Hélène Duprez, Alain Chantre, Frédéric Boeuf, Christian Seassal, and Badhise Ben Bakir, "Co-integrated 1.3 μ m hybrid III-V/silicon tunable laser and silicon Mach-Zehnder modulator operating at 25Gb/s," Opt. Express 24, 30379-30401 (2016)
- [9] H. Byun et al., "Single-Chip Beam Scanner LiDAR Module for 20-m Imaging," 2021 IEEE International Electron Devices Meeting (IEDM), 2021, pp. 20.4.1-20.4.4 [8]
- [10] S. Ohno, K. Toprasertpong, S. Takagi and M. Takenaka, "Demonstration of Classification Task Using Optical Neural Network Based on Si Microring Resonator Crossbar Array," 2020 European Conference on Optical Communications (ECOC), 2020, pp. 1-4

Automatic Testing of Silicon Photonic Add/Drop Multiplexer

Student paper

Matteo Petrini^{1*}, Rita Baldi¹, Moritz Seyfried², Francesco Morichetti¹ and Andrea Melloni¹

Dipartimento di Elettronica, Informazione e Bioingegneria

¹Politecnico di Milano, Piazza Leonardo da Vinci 32, Milano, 20133 Italy

²Ficontec Service GmbH, Rehland 8, 28832 Achim, Germany

* matteo.petrini@polimi.it

We present a novel approach to perform electrical and optical testing of complex photonic integrated circuits (PICs). The proposed techniques exploits a probe card to simultaneously measure the I-V curves of several electrical devices embedded in the photonic chip and enables fast automatic tuning of the PIC spectral response. The effectiveness of the technique is demonstrated on a silicon-photonic microring resonator tuneable add-drop multiplexer.

Keywords: Silicon Photonics, Photonic Testing, Control and Calibration

INTRODUCTION

With the continuous improvement of technological processes in commercial foundries and the advance of knowledge, expertise and pervasiveness, Photonic Integrated Circuits (PICs) are increasing their integration density and complexity. Reconfigurability and programmability are becoming common features as well as the need for calibration. For these reasons, photonic testing is one of the most urgent needs of the field [1].

Testing the optical circuit at wafer level, unlike single die characterization, should be flexible, effective but also fast and accurate [2]. The nature of photonic testing is twofold. On one side the functionality of the electrical and electronic elements (heaters, photodetectors, pn-junctions, etc.) embed inside the PIC should be checked, on the other side its optical behaviour has to be validated. Typically, to access the electrical elements of the PIC, wire bondings are employed. While providing stable and reliable connection, obviously this approach is not suitable for large volume and wafer level testing purposes. Concerning optical domain, coupling through surface grating or edge coupling are the two typical options. The optical validation, however, requires the tuning or calibration of the PIC through electrical signals until the desired behaviour is obtained. One of the methods to tune a PIC (frequency selective, for example) is the minimization of the Mean Squared Error between a desired frequency mask and the spectral response of device itself. This can be reasonable performed during the calibration and/or the characterization phase, but due to its inherent time and resource consumption, it is hardly feasible during volume testing.

In this work, we propose the use of an electrical probe head to simultaneously contact all the 56 pads of a reconfigurable PIC. At the moment the 12 optical I/Os are contacted with a separate fiber block. Thanks to the fast and reliable electrical access, we are able to demonstrate and automatically execute a novel technique to replicate the wavelength response of a tuneable photonic filter as copycat of a reference golden sample.

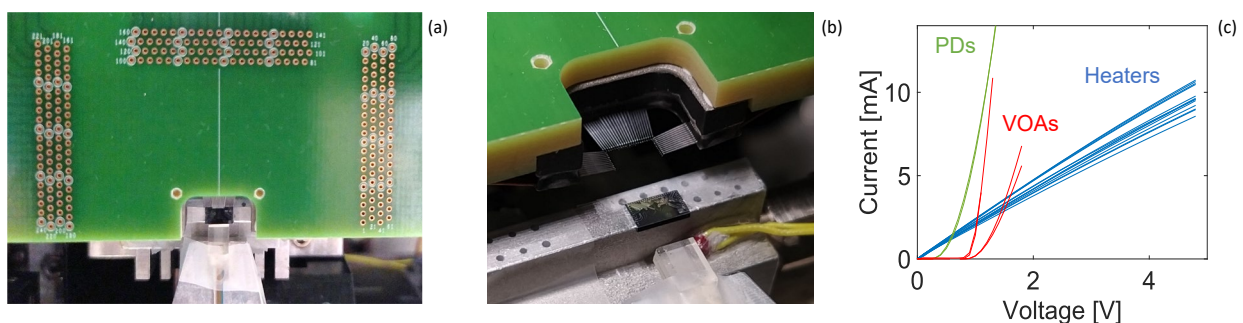


Fig. 1. (a) Top view of the probe card contacting the photonic chip. (b) Detail of the 56 cantilevers over the PIC. (c) IV curves of the electrical devices embedded in the PIC, simultaneously acquired

ELECTRICAL TESTING

A 4 channels silicon photonic add drop multiplexer is considered. Given its own reconfigurable nature, many sensors and actuators are directly integrated, such as heaters, Variable Optical Attenuators (VOAs) and Photodetectors (PDs). To sense the optical power and to drive actuators, we electrically contact all the pads (56),

simultaneously, by means of a Probe Head (shown in fig. 1(a)). This device has been mechanically designed in such a way that its cantilever needles are matched (with a precision of around $6\ \mu\text{m}$) with the photonic chip pads (square-shaped $90\ \mu\text{m}$ by $90\ \mu\text{m}$). Tungsten Rhenium Alloy [W(R)] cantilevers ensure good coupling with electrical contacts (made from aluminum), showing a parasitic resistance of hundreds of $\text{m}\Omega$ per connection (always below $1\ \Omega$) when the pushing force is between 224 g and 560 g, considering a unitary contact force of $98.5\ \text{g}/\text{mm}/\text{pad}$ and an overtravel distance between $40\ \mu\text{m}$ and $100\ \mu\text{m}$. Each needle handles a maximum current of around 30mA, a fair amount to drive Si-photonics thermo-optic and electro-optic actuators. A detailed picture of electrical needles over the chip is reported in fig. 1(b).

Through PCB tracks, electrical signals are routed from the needles to a standard flat cable, which is connected to a custom (and multichannel) Sense and Measurement Unit (SMU). The SMU generates a voltage staircase, from 0 to 5V, characterized by steps of 100 mV (ΔV), whose duration is 5 ms (with transitions duration shorter than $10\ \mu\text{s}$). At the same time, the instrumentation is able to read and store the value of the current provided to the load, by means of a proper sensor (together with analog filtering stage, ADC stage and digital filtering stage). 16 different IV curves are measured in parallel, for all the electrical devices embedded in the PIC. These plots are reported in fig. 1(c). The duration of the electrical testing is 250 msec, and many useful information can be inferred, for example if a device is faulty or not, if it is compliant with design specification or not, evaluating important design parameters such as the equivalent resistances of heaters, threshold voltages of p-i-n junctions (implementing VOAs) or dark currents of PDs and their statistical distributions.

OPTICAL TESTING

Once the chip has been fully electrically characterized, optical functionalities have to be considered. The PIC used for this demonstration is a 4-channel Tuneable Optical Add/Drop Multiplexer (TOADM). Every channel is implemented through a 4th order Microring Resonator (MRR) based filter, whose schematics is shown in fig. 2(a). Its design relies on a novel Vernier scheme, to make it FSR-free, over an operational wavelength interval larger than 100 nm (i.e., covering the whole C+L band) [3]. Spectral features of this filter include a 40 GHz 3dB-bandwidth and around 17 dB Return Loss (averaged in the bandwidth), as it can be deduced by nominal transfer functions, reported in fig. 2(b). Full reconfigurability of the device is obtained by means of thermo-optic actuators, placed above each MRR and by tuneable couplers between the chain of rings and bus waveguides. Further details about this kind of device can be found in [3]. Such a complex device requires its own control system to be effectively

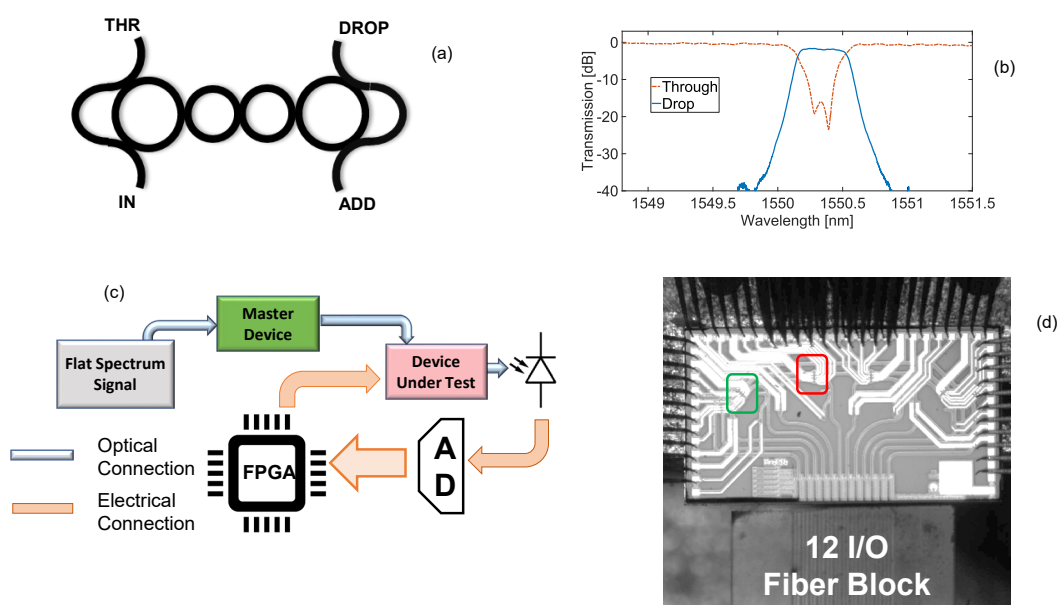


Fig. 2. (a) Topology of the single channel filter of the TOADM and (b) its own tuned spectral response (for both Through and Drop ports). (c) Schematic of the control loop to tune the PIC, with a master filter used as reference. (d) Whole chip (Optical Add Drop Multiplexer) hosting the reference filter and the tuneable one, optically accessed by means of fiber block and electrically accessed with a probe card.

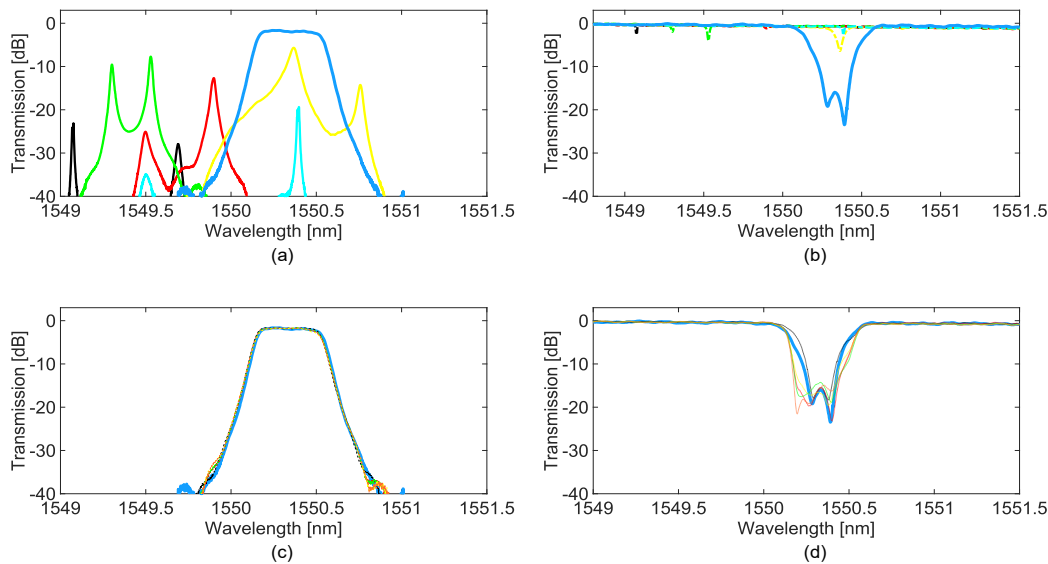


Fig. 3. (a) and (b) Drop and Through port spectral responses of the reference device (cyan curves), when the Device Under Test is in its own natural condition (red curves) or randomly perturbed. (c) and (d) Drop and Through port spectral responses of the Device Under Test tuned achieving cloning of the reference one.

tuned, to recover its nominal frequency response. In this work we propose a calibration technique which is flexible, fast and robust, compliant with the demanding requirements for volume testing. It has been implemented through the block scheme reported in fig. 2(c). A flat and broadband spectrum signal -for example the Amplified Spontaneous Emission (ASE) noise outcoming from Erbium Doped Fiber Amplifier (EDFA)- is filtered by a reference device, that acts as a frequency shaper. The obtained Power Spectral Density (PSD), is coupled to the Device Under test (DUT), equipped with its own control loop, which works as follows. The power outcoming from Through port is sensed by a photodetector, and the collected signal, after data acquisition chain is delivered to a FPGA, that executes the calibration strategy. It relies on a simple gradient descent algorithm, whose purpose is the maximization of the rejection at the Through port. To achieve this aim, the working point of every single heater (i.e., its driving current/voltage) is recursively changed, till reaching convergence, that generally occurs in few tens of milliseconds (physically limited by thermo-optic time constant and by the minimum number of iterations). According to [4] using this method to tune a filter, its transfer function should be tailored onto the PSD coupled to the DUT. In this work we used, as a master filter, the MRR sub-device surrounded by the green box in fig. 2(d), tuned in its nominal condition, around 1550 nm by using a pre-computed LookUp Table. Its spectral responses, for both Through and Drop ports, are shown in fig. 3(a) and 3(b), respectively (cyan curves). In these figures, the other curves represent the frequency responses of the DUT [in the red box in fig. 2(d)], in its natural condition (red plot) and four randomly perturbed cases. Results of the control procedure execution are shown in fig. 3(c), for Drop port, and in fig. 3(d), for Through port. An almost perfect overlap, in frequency domain, can be observed. This has been also a-posteriori assessed by the computation of the MSE between the passband of the reference device and the passband of every converged sample.

Acknowledgements: The authors acknowledge the staff of Polifab (www.polifab.polimi.it), the microelectronic facility of Politecnico di Milano, for the support in the assembly of photonic chips. The authors also acknowledge ficonTEC GmbH for the support throughout the whole testing activity. The work has been performed within the JRC T3 (Techniques and Tooling for Photonic Testing) between PoliMi and ficonTEC.

References

- [1] S. Latkowsky, D. Pustakhod, C. M., Y. Weiming and J. M. Leijtens, «Open Standards for Automation of Testing of Photonic Integrated Circuits,» IEEE Journal of Selected Topics in Quantum Electronics, vol. 25, n. 5, pp. 1-8, 2019.
- [2] R. Polster, L. Y. Dai, M. Oikonomou, Q. Cheng, S. Rumley and K. Bergman, «Challenges and solutions for high-volume testing of silicon photonics,» in Proc. SPIE 10537, Silicon Photonics XIII, San Francisco, 2018.
- [3] F. Morichetti, M. Milanizadeh, M. Petrini, F. Zanetto, G. Ferrari, D. Aguiar, E. Guglielmi, M. Sampietro and A. Melloni, «Polarization-transparent silicon photonic add-drop multiplexer with wideband hitless tuneability,» Nature Communications, vol. 12, n. 4324, 2021.
- [4] M. Milanizadeh, S. Ahmadi, M. Petrini, D. Aguiar, R. Mazzanti, F. Zanetto, E. Guglielmi, M. Sampietro, F. Morichetti and A. Melloni, «Control and Calibration Recipes for Photonic Integrated Circuits,» Journal of Selected Topics in Quantum Electronics, vol. 26, n. 5, pp. 1-10, 2020.

Micro transfer printing of electronic integrated circuits on Silicon photonics substrates

Ruggero Loi^{1*}, Prasanna Ramaswamy¹, Alex Farrell¹, Antonio Jose Trindade¹, Alin Fecioru¹, Johanna Rimböck², Stefan Earthl², Marianna Pantouvaki³, Guy Lepage⁴, Joris Van Campenhout⁴, Tinus Pannier⁵, Ye Gu⁵, David Gomez¹, Patrick Steglich⁶ and Peter Ossieur⁵

¹X-Celeprint Ltd., Lee Maltings, Dyke Parade, Cork, Ireland.

²EV Group E. Thallner GmbH, DI Erich Thallner Str. 1, 4782 St. Florian am Inn, Austria.

³Formerly with imec, , Kapeldreef 75, Leuven, Belgium.

⁴imec, Kapeldreef 75, Leuven, Belgium.

⁵Ghent University, iGent, Technologiepark 126, 9052 Ghent, Belgium.

⁶IHP – Leibniz-Institut für innovative Mikroelektronik, Im Technologiepark 25, Frankfurt (Oder), 15236 , Germany.

* rloi@x-celeprint.com

Electronic integrated circuits with 230x330 μm^2 foot-print were heterogeneously integrated for the first time onto silicon photonics substrates by micro transfer printing. The devices were fabricated with a 0.13 μm SiGe BiCMOS technology and released from the original substrate with a TMAH:DI (1:4) solution. A spray coated BCB 25-200 nm thick adhesive layer provided a >90% high yield bonding of the devices. The preparation of the devices for transfer printing, the release technology and the transfer printing process are discussed in this work.

Keywords: *Heterogeneous Integration, micro transfer printing, Electronic Integrate Circuits, Silicon Photonics.*

INTRODUCTION

Optical transceivers built around e.g. silicon photonic integrated circuits (PICs) require the integration of the optical functions such as modulation, wavelength (de-)multiplexing, detection and routing with high-speed electronic integrated circuits [1]. State of the art packaging strategies for electronics rely on flip-chip-bonding or wire-bonding [2], which may introduce significant parasitic phenomena reducing bandwidth and increasing energy consumption. As a consequence, thermal and signal integrity issues arise when operating at high frequency [3]. One possible solution to shorten the electrical connections is to integrate the electronics directly onto the PIC, i.e. closer to the optical components. From a production cost point-of-view, note that the wire-bonding and flip-chip processes are partially or fully sequential, i.e. they cannot be executed at the wafer-level and in parallel. One solution to address all the aforementioned requirements is Micro-Transfer-Printing (μTP) as it allows flexible and scalable integration of micron scale discrete components on different substrates, with high placement accuracy capability of $<1.5 \mu\text{m}$ 3σ [4]. μTP has been extensively applied to the integration of a variety of optical components and materials onto Silicon photonics (SiPh) [5 - 8]. Similarly, μTP can be used for the heterogenous integration of electronic integrated circuits (EICs) with small metal pads directly onto a PIC platform. The metal pads can be further processed by electroplating, which reduces the chip size, the length of electrical connections and the total size of the packaged interposer. This strategy aims to reduce thermal and capacitance issues that arise at high frequency operation of the EICs. In this work we present the first transfer printed EICs fabricated in a SiGe BiCMOS pilot line and heterogeneously integrated in dedicated spots on a SiPh substrate.

EXPERIMENTAL METHODS

The process for making the EICs transfer printable was developed on 25x25 mm² dies of a dummy material consisting of 1 μm thick SiGe front end of line (FEOL) on a 1 μm thick buried oxide (BOX) material seating on top of a $\langle 100 \rangle$ Si substrate. Moreover, two types of back end of line (BEOL) layer stacks of 10 μm (reduced BEOL) and 15 μm (standard BEOL) total thickness were fabricated on top of the FEOL. The μTP preparation process included the singulation of 200x300 μm^2 coupons, an encapsulation patio of 15 μm width around each coupon, and the definition of a dielectric tether structure to anchor the devices to the substrate [Fig. 1]. The total foot print of the EICs was 230x335 μm^2 if we consider the tether breakage might leave a $<5 \mu\text{m}$ long flap on one end of the coupon. All the components and metal pads for each EIC device were arranged inside the 200x300 μm^2 rectangular area. In order to singulate each coupon a resist mask defined by lithography protected the coupon rectangular area during a C₄F₈/H₂/He based induced coupled plasma (ICP) dry-etching, the etching areas around each coupon in the BEOL were kept free from metal layers. Next a second ICP dry-etch with an SF₆/C₄F₈ based chemistry went through the FEOL layer and it stopped half way in the 1 μm thick BOX layer. Next, a lithography defined the patio around each

coupon and another $C_4F_8/H_2/He$ based ICP dry-etch removed the BOX to the top of the Si substrate; a BOE 5:1 diluted wet etch of few seconds permit to clean the top of the Si substrate of any BOX remnant. Then, a PECVD of a dielectric double layer structure of 500-1000 nm SiO_2 and 1.5-2 μm SiN_x , a lithography step and another $C_4F_8/H_2/He$ based ICP dry-etch to the Si substrate served to define the tethers. Finally a wet etch undercut in TMAH:DI (1:4) at 70 °C and 40 °C towards the end of the step, released the coupons from the Si substrate [Fig. 2a,b], the result was a pattern of suspended coupon ready for μTP [Fig. 2c].

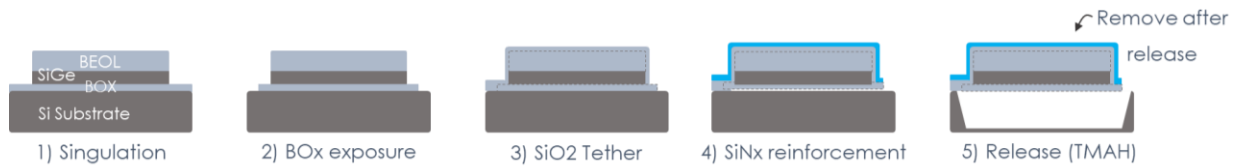


Fig. 1. Main fabrication steps for the preparation of transfer printable EICs anchored with a dielectric tether.

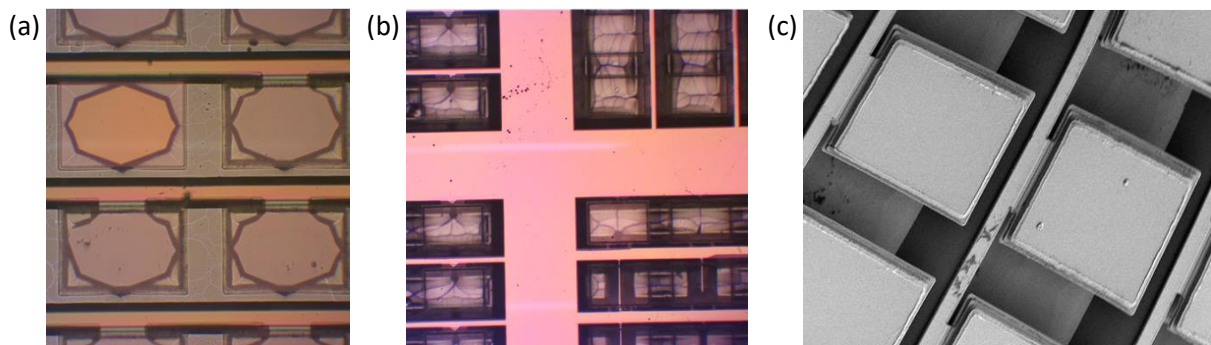


Fig. 2. (a) Wet etch undercut of the SiGe BiCMOS test coupons in TMAH (5%) at 70°C, after 1h, it is possible to observe the etch front progress on the $\langle 100 \rangle$ Si substrate used as a sacrificial layer. (b) Same coupons at the end of the undercut (etch at 40 °C). (c) Released EIC material coupons ready for μTP .

RESULTS AND DISCUSSION

Following the preparation steps, the coupons were picked-up from the original substrate at the μTP tool with up to 100% pick-up yield depending on the tether design used. Next, the coupons were integrated with single post transfer on different Si and glass substrates spray coated with BCB of different thickness in the range 25nm to micron scale. The print yield reached up to 100% on $>25nm$ thick BCB layer, defective coupons or landing site with defects or debris showed lower print yield. Moreover, it was noticed that any stress coming from the encapsulation and tethers dielectric layers could reduce the coupon flatness consequently reducing the print yield, especially on thinner coupons (reduced BEOL) and when printing on $<75 nm$ thin BCB layers.

The μTP process developed on dummy material was then applied successfully to the heterogenous integration of EICs fabricated on $3 \times 3 mm^2$ areas defined on $25.88 \times 31.70 mm^2$ dies coming from diced multi project wafers (MPW) [Fig. 3a]. The pick-up and print yield was found at 100% over flat Si and glass substrates spray coated with a BCB layer of thickness ranging from 25-200 nm [Fig. 3b, c]. The presence of debris in the printing spots has to be avoided as much as possible in order to keep the adhesion of the coupons to the substrate complete [Fig. 3c].

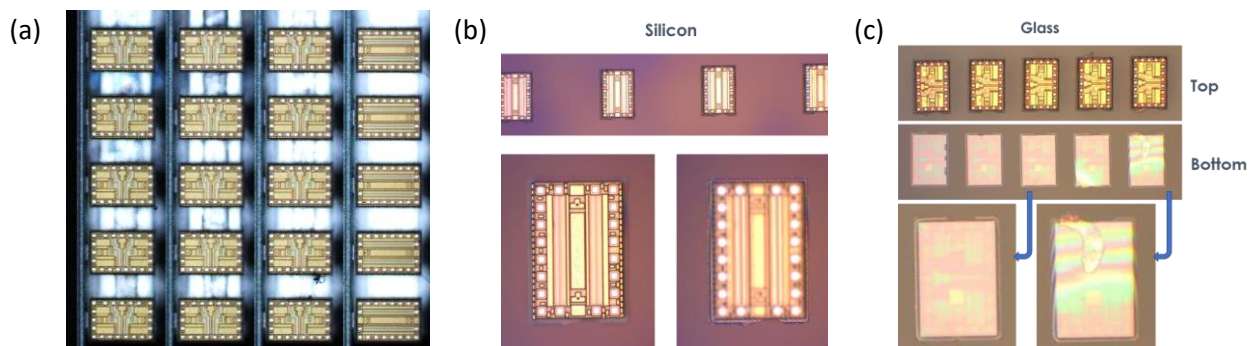


Fig. 3. (a) EICs fabricated on a $3mm^2$ area on the MPW dies, were released and transfer printed to (b) a Si substrate and (c) to a glass substrate coated with 75nm BCB and. As shown in the inset (c) defects can interfere with the quality of the bonding.

As a further step in the development, EIC coupons were transfer printed with >90% print yield onto a SiPh interposer [Fig. 4a, b]. The landing spots on the interposer being covered with metal tracks for electrical connections were planarized with a $\sim 3 \mu\text{m}$ thick BCB spin coated layer.

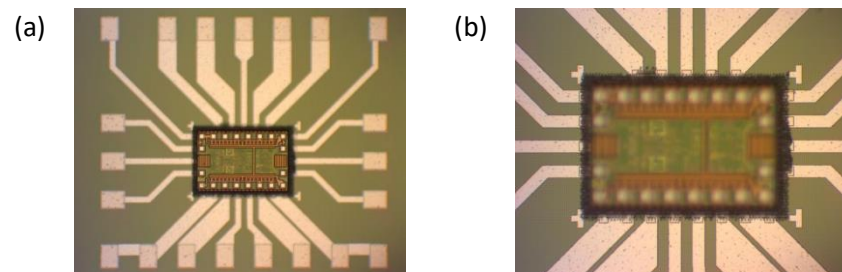


Fig. 4. (a) EICs were integrated on a SiPh interposer. (b) zoom of the integrated EIC on the landing spot.

CONCLUSION

A process to make transfer printable SiGe BiCMOS EICs has been developed using dielectric tethers and the SOI substrate as sacrificial layer for the release of the devices from the original substrate. The undercut with TMAH:DI (1:4) solution has confirmed excellent release properties with smooth and flat surfaces suitable for full contact print. A >90% integration yield was achieved on Silicon Photonic substrates coated with >25 nm thick BCB adhesive layers.

This strategy enables the integration of EIC components on dedicated spots on the Silicon PIC paving the way towards the creation of very densely integrated optical engines.

Next steps in this work are the electrical connection of the devices to the Silicon PIC and the optical devices integrated in it and their performance analysis. Further development of the heterogenous integration process will be made to demonstrate the scalability of the process by integrating arrays of EICs through μTP .

ACKNOWLEDGEMENTS

This work is funded under EU H2020 CALADAN project, grant agreement n. 825453.

References

- [1] A. Rahim, et al., "Taking silicon photonics modulators to a higher performance level: state-of-the-art and a review of new technologies," *Adv. Photon.* 3(2) 024003, 2021.
- [2] P. E. Morrissey, et al., "Packaging of silicon photonic devices: from prototypes to production", *Proc. SPIE 10537, Silicon Photonics XIII*, 105370L, 2018.
- [3] J. S. Lee, et al., "Meeting the Electrical, Optical, and Thermal Design Challenges of Photonic-Packaging," in *IEEE Journal of Selected Topics in Quantum Electronics*, vol. 22, no. 6, pp. 409-417, 2016.
- [4] D. Gomez, et al. "Process capability and elastomer stamp lifetime in micro transfer printing." 2016 IEEE 66th Electronic Components and Technology Conference (ECTC). IEEE, 2016.
- [5] B. Corbett, et al., "Transfer print techniques for heterogeneous integration of photonic components," *Prog. Quantum Electron.*, vol. 52, pp. 1-17, 2017.
- [6] J. Justice, et al., "Wafer-scale integration of group III-V lasers on silicon using transfer printing of epitaxial layers," *Nature Photon.*, vol. 6, no. 9, pp. 610-614, 2012.
- [7] R. Loi, et al., "Edge-Coupling of O-Band InP Etched-Facet Lasers to Polymer Waveguides on SOI by Micro-Transfer-Printing," in *IEEE Journal of Quantum Electronics*, vol. 56, no. 1, pp. 1-8, 2020.
- [8] I. Mathews, et al. "Microtransfer Printing High-Efficiency GaAs Photovoltaic Cells onto Silicon for Wireless Power Applications." *Advanced Materials Technologies* 5.8, 2020.

Integrated Electronic Control of Silicon Mach-Zehnder Interferometers

Student paper

Fabio Toso¹, Francesco Zanetto¹, Maziyar Milanizadeh¹, Andrea Melloni¹, Marco Sampietro¹, Francesco Morichetti¹ and Giorgio Ferrari¹

¹Politecnico di Milano, Piazza Leonardo da Vinci 32, Milano, 20133, Italy

* fabio.toso@polimi.it

The control and stabilization of a 4-inputs binary-tree mesh of Mach-Zehnder interferometers on a Silicon Photonics platform by means of an integrated electronic controller is presented. The designed multichannel ASIC can control up to 4 independent interferometers, with a power consumption of 20mW each, a closed-loop control bandwidth of 50Hz and residual oscillations of the output optical power lower than 1dB.

Keywords: *Mach-Zehnder interferometer, CMOS, analog feedback, integrated photonics*

INTRODUCTION

Integrated Mach-Zehnder interferometers (MZIs) are being used to build programmable photonic circuits, with applications in the field of information processing, artificial intelligence and sensing [1]. These circuits are usually designed as meshes of MZIs [2], where each interferometer needs to be controlled in real time to steer the incoming light to a single output of the optical circuit. A particular case is a so-called diagonal mesh, with just one row of Mach-Zehnder interferometers, which can be used as a self-aligning universal beam coupler [3]. This device offers several modes of operation, with applications in free-space optical communication and sensing. These applications require an external control system to maximize or minimize the light at the output of each MZI and to stabilize the required working point against changes in the input light or environmental variations. Previously proposed control systems are implemented with discrete electronic components and rely on digital processors, like micro-controllers [4] or FPGAs [5,6], to perform their control action. Although this approach guarantees maximum flexibility, the area occupation and the power dissipation of the control electronics are much higher than those of the photonic circuit. In this scenario, we developed an integrated controller with a simpler and more specific control strategy, but scalable on a large number of channels and with a reduced power consumption.

CONTROLLER ARCHITECTURE

Large MZI meshes can be conveniently controlled by individual control loops acting on single MZIs, without requiring a complex multi-input multi-output optimization [6]. Around a stable working point, the individually controlled MZI cells are independent and their local control loops work in parallel. Instead, after a significant perturbation, the cells adjust their working point sequentially, starting from the one closer to the input. To overcome the limitation to the number of interferometers that can be controlled in parallel, which is given by the power consumption and area occupation of the proposed discrete-components implementations, we designed a fully integrated controller based on the same control strategy proposed in [6]. The high-level structure of the multichannel ASIC is shown in Figure 1a. Each of the four channels of the controller is able to monitor the working point of a single MZI through a CLIPP detector (C1) integrated at the output of the interferometer [7]. The sensor is read-out by a low-noise lock-in front-end (amplifier A1 and lock-in demodulator at f_{CLIPP}) operating at frequencies between 100kHz and 4MHz and with a resolution between -40dBm and -50dBm, depending on the design of the specific CLIPP sensor. The control strategy is based on the use of two orthogonal dithering signals (f_{DITH1} , f_{DITH2}), which are superimposed to the bias voltage applied to the two thermal actuators present in the interferometer (H1, H2). The oscillation of the output optical power caused by the two dithering signals is monitored by de-modulating the CLIPP output separately at f_{DITH1} and f_{DITH2} . The correct working point to be applied to the MZI is determined by integrating (analog integrators A2 and A3) the two extracted output dithering signals. The integral control action enables to minimize the residual output dithering oscillations, thus locking the MZI to a maximum or a minimum of its optical transfer function, depending on the sign of the integrators. The driving voltages are applied to the two thermal actuators by two integrated driving stages with an output range of 0V to 5V. Figure 1b shows a photomicrograph of the realized ASIC controller, designed and fabricated using AMS CMOS 0.35 μ m technology.

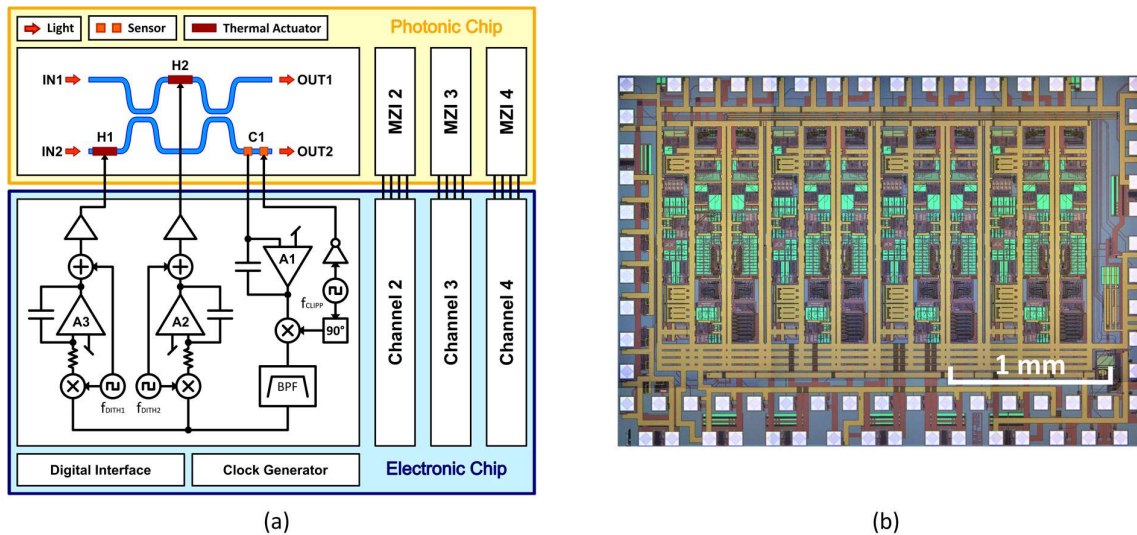


Fig. 1. (a) Schematic representation of the designed 4-channel integrated ASIC controller, showing connections to the controlled Mach-Zehnder interferometers. Each MZI is controlled separately by a different channel of the ASIC. (b) Photomicrograph of the fabricated ASIC.

STABILIZATION OF A 4x1 MZI MESH

The proposed ASIC controller was used to stabilize a 4-inputs binary tree MZI mesh designed using AMF passive Silicon Photonics technology (Figure 2a and 2b). The electronic and the photonic chips were designed to allow direct wire-bonding between them for optimal performances. Figure 2a shows the test setup with the two circuits mounted on a custom-designed holder PCB and connected together. An additional heater was included in each MZI of the mesh (H3 in Figure 2a) for test purposes, in order to allow to inject phase disturbs between the optical inputs of the circuit.

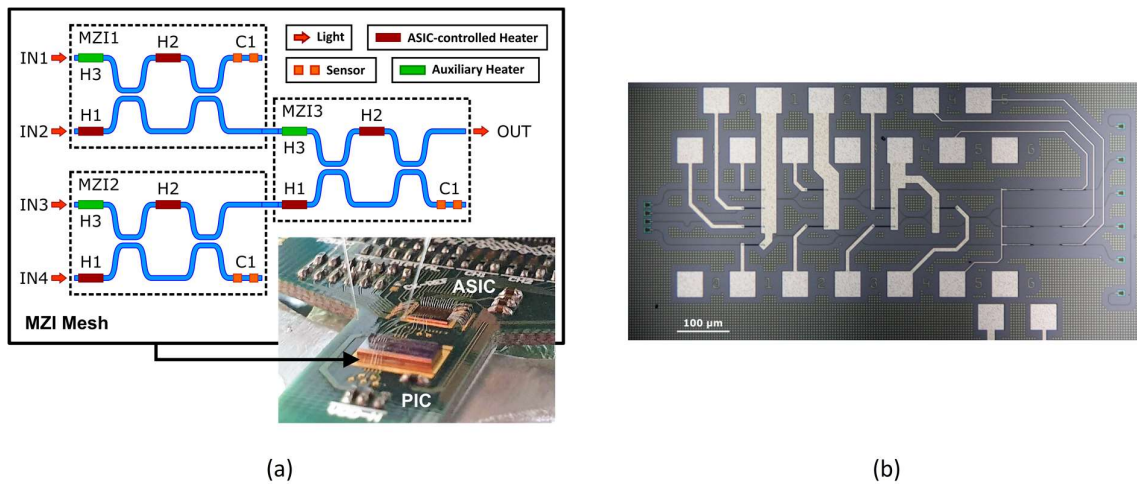


Fig. 2. (a) Schematic representation of the target binary-tree mesh and experimental setup with PIC and controlling ASIC glued on the same PCB and connected together with chip-to-chip wire-bonds. (b) Photomicrograph of the realized photonic circuit.

The capability of the ASIC to control individual interferometers was tested by injecting light at inputs IN3 and IN4 of the mesh and by introducing a sinusoidal phase disturb at 2Hz through H3 of MZI2. The signal applied to the heater had an amplitude of 400mV. Results are shown in Figure 3a. With the control system disabled, a 10dB disturb was present at the optical output. When the system was turned on at $t = 5s$ and set to maximize the output optical power, it began to adjust the voltage of the heater on the input branch of the controlled interferometer in order to compensate for the disturbance. The output optical power was correctly stabilized at its maximum value, with residual oscillations of less than 1dB given by noise and by fluctuations of the input power. The voltage applied to

the second heater of the interferometer was kept constant by the controller to the value required to correctly route the input light to the desired output.

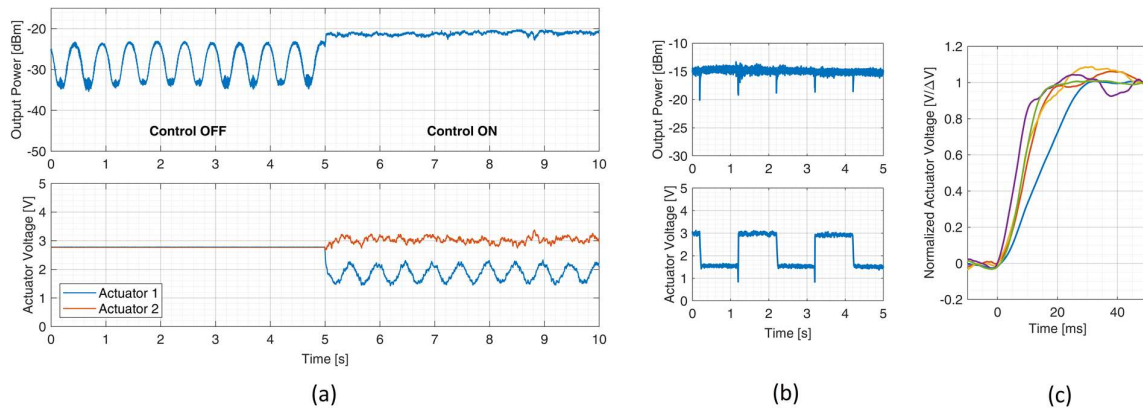


Fig. 24. (a) Rejection of a sinusoidal phase disturb injected in the system through Heater3 of MZI2. While the control system was off ($t < 5s$), the disturb caused the power at the output of the PIC to oscillate of more than 10dB. After the control system was activated ($t > 5s$), the controlled heater voltage started tracking the disturbance and the power at the output was stabilized. (b) Response of the control system to a square wave phase perturbation. (c) Normalized time responses of the system to step input phase variations.

BANDWIDTH OF THE CONTROL LOOP

The bandwidth of the proposed control system was assessed by introducing a small square wave perturbation at 0.5Hz to H3 and by observing the transient response of the system after the input phase step changes (Figure 3b). Results for different working points and step amplitudes are shown in Figure 3c. The measured time constant of the system varies between 2ms and 8ms, indicating a bandwidth between 20Hz and 80Hz with the selected settings of the system, which were chosen to optimize noise performances in the readout of the CLIPP detector. This speed is suitable to effectively compensate thermal instabilities of the mesh and safeguard its operations, demonstrating the correct functionality of the controller.

CONCLUSION

We presented a fully integrated electronic CMOS controller for meshes of Mach-Zehnder interferometers. The device includes all the circuitry necessary to control 4 interferometers in parallel, with a power consumption of 20mW/MZI. The controller has a closed-loop bandwidth of 50Hz and can stabilize the working point of the controlled interferometers in real time against optical input variations, with residual oscillations lower than 1dB. By increasing the ASIC channels number or by using multiple chips simultaneously, we envision that meshes of relevant complexity can be controlled in a very power- and area-efficient way, enabling new relevant applications.

Acknowledgements: This work was supported by the EU H2020 project Super-Pixels (grant no. 829116)

References

- [1] W. Bogaerts et al., *Programmable photonic circuits*, Nature, vol. 586, no. 7828, pp. 207–216, 2020.
- [2] D. A. B. Miller, *Self-configuring universal linear optical component*, Photonics Research, vol. 1, no. 1, pp. 1–15, 2013.
- [3] D. A. B. Miller, *Self-aligning universal beam coupler*, Optics express, vol. 21, no. 5, pp. 6360–6370, 2013.
- [4] Y. Li and A. W. Poon, *Active resonance wavelength stabilization for silicon micro-ring resonators with an in-resonator defect-state-absorption-based photodetector*, Optics express, vol. 23, no. 1, pp. 360–372, 2015.
- [5] A. Gazman, C. Browning, Z. Zhu, L. R. Barry, and K. Bergman, *Automated thermal stabilization of cascaded silicon photonic ring resonators for reconfigurable WDM applications*, 2017 European Conference on Optical Communication, pp. 1–3.
- [6] F. Zanetto, et al., *Dithering-based real-time control of cascaded silicon photonic devices by means of non-invasive detectors*, IET Optoelectronics, vol. 15, no. 2, 2021.
- [7] F. Morichetti, et al., *Non-invasive on-chip light observation by contactless waveguide conductivity monitoring*, IEEE Journal of Selected Topics in Quantum Electronics, vol. 20, no. 4, pp. 292–301, 2014.

Optical modulation based on DC Kerr effect in silicon waveguide

Student paper

Jonathan Peltier^{1,2*}, Leopold Virost², Christian Lafforgue¹, Lucas Deniel¹, Delphine Marris-Morini¹, Guy Aubin¹, Farah Amar¹, Dehn Tran³, Callum G. Littlejohns³, David J. Thomson³, Weiwei Zhang^{3*}, Laurent Vivien¹

¹University Paris Saclay, CNRS, Centre for Nanoscience and Nanotechnology (C2N), Palaiseau, 91120, France

²Univ. Grenoble Alpes, CEA, LETI, Grenoble, 38000, France

³ Optoelectronics Research Centre, Zepler Institute for Photonics and Nanoelectronics, Faculty of Engineering and Physical Sciences, University of Southampton, Southampton SO17 1BJ, UK

*corresponding author: Weiwei.Zhang@soton.ac.uk and jonathan.peltier@c2n.upsaclay.fr

DC Kerr effect was experimentally and theoretically studied for light modulation in silicon waveguide. A clear linear behavior of the dynamic electro-optic response has been demonstrated under a reverse bias applied across a PIN junction. A modulation at twice the RF frequency applied is also shown and assigned to Kerr effect.

Keywords: Kerr effect, DC Kerr, electro-optic modulation, silicon photonics

INTRODUCTION

Integrated modulators are key components for communications, quantum, spectroscopy and LIDAR. These applications require high speed and low power consumption characteristics. Silicon modulators, which are mainly based on the plasma dispersion effect [1], consume a lot of power and are limited in bandwidth [2]. To overcome those limitations, such modulators can also rely on Pockels effect, an inherently fast and pure phase modulation effect. Since silicon does not have a natural $\chi^{(2)}$ due to its centrosymmetric structure, pure phase modulators cannot be achieved directly with silicon waveguides. Nevertheless, pure phase modulation in silicon can be realized either by straining silicon [4], by associating materials with high $\chi^{(2)}$ such as polymer, BTO, PZT, lithium niobate [3], or by using DC Kerr effect [5] to electrically induce an effective $\chi^{(2)}$. The latter is studied in this paper, in a silicon Mach-Zehnder modulator (MZM) based on PIN junctions. This effect, also known as electrical field induced Pockels effect, arises from the third-order nonlinear susceptibility tensor in presence of an electrical static field. This induced Pockels effect is proportional to the DC field inside the waveguide.

DC KERR MODULATION

DC Kerr effect comes from the third-order nonlinear susceptibility tensor $\chi^{(3)}$ of silicon. Its corresponding refractive index changes with an applied electrical field $F(t)$ is [6]:

$$\Delta n(t) = \frac{3\chi^{(3)}}{2n} F(t)^2 \quad (1)$$

Considering $F(t) = F_{DC} + F_{AC} \cos \Omega t$, with Ω the angular frequency of the RF signal, the refractive index variation is:

$$\Delta n(t) = \frac{3\chi^{(3)}}{2n} \left[(F_{DC}^2 + \frac{1}{2}F_{AC}^2) + 2F_{DC}F_{AC} \cos \Omega t + \frac{1}{2}F_{AC}^2 \cos 2\Omega t \right] \quad (2)$$

We can see from Eq. (2) that the amplitude of Ω spectral component grows linearly with both DC and RF fields. Furthermore, a 2Ω Kerr component is also expected and depends only on the RF field squared.

The Ω signal at 5 GHz is applied to the PIN structure of a MZM. Indeed, the MZM branches consist of PIN junctions to evacuate free carriers from the intrinsic region and induce a strong electric field inside the core of the waveguide. A simplified schematic view of the experimental set-up used to characterize the electro-optic (EO) modulation is provided in figure 1 (a). DC and RF biases are swept to observe the Ω signal evolution. The phase shift $\Delta\theta = \frac{2\pi}{\lambda} n_g \Delta L$ induced by the extra length (ΔL) of one arm of the MZM is used to set the operating point by tuning the laser wavelength around 1550 nm. Applying a DC bias on both arms and using a push-pull configuration allows DC and RF voltage to be swept without shifting the operating point of the transfer characteristics.

Considering the transfer function of the MZM:

$$\frac{P(t)}{P_0} = \frac{1}{2} [1 + \cos(\Delta\phi(t) + \Delta\theta)] \quad (3)$$

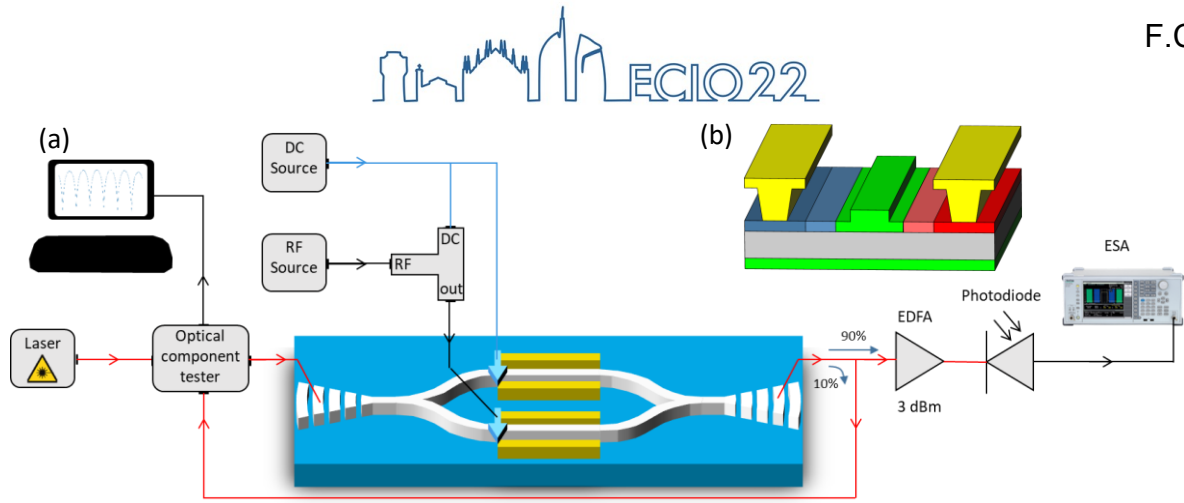


Figure 1: (a) Simplified experimental set-up used to measure the electro-optical modulation of the Mach-Zehnder modulator. DC is applied on both arms, RF is either applied in single-drive or push-pull configuration. (b) PIN junction depiction.

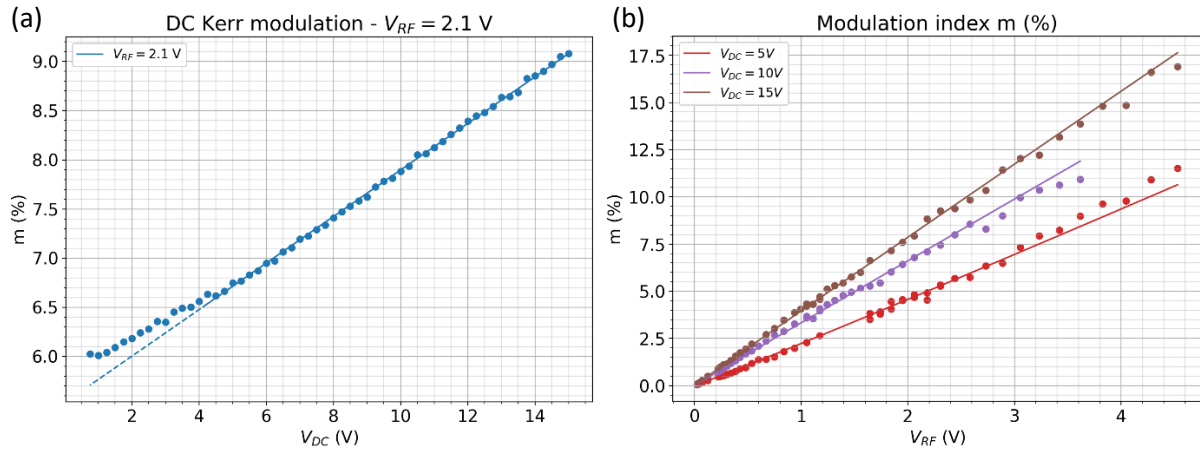


Figure 2: Modulation index measured in push-pull configuration function of (a) the applied reverse bias, (b) the applied RF bias at different DC biases. The difference of m value in both curves is mainly due to a difference of input optical power which do not induce a difference of the linearity of the results.

The EO modulation can be approximated at the quadrature point ($\Delta\theta = \frac{\pi}{2}$) as $P_{\Omega}(t) \approx \frac{P_0}{2} \Delta\phi(t)$ when $\Delta\phi(t) = m \cos \Omega t$ is the weak applied RF modulation signal and m is the modulation index.

A linear enhancement of the modulation index m with the applied DC and RF bias is observed (figure 2), which is identified to a clear signature of a DC Kerr modulation. The non-zero intersection of m at DC=0V (figure 2 (a)) indicates that carriers also contributed to the modulation in addition to the DC Kerr effect.

Next, the EO signal observed at twice the applied RF frequency is measured to confirm the DC Kerr modulation. Because the Kerr signal is proportional to the square of the field, it can only be observed in single-drive configuration. In addition, the applied RF signal is filtered out of the generator to remove the second harmonic which would mask any EO modulation at twice the applied frequency. Finally, the MZM operating point is swept by changing the input wavelength allowing to distinguish the origin effect of the 2Ω signal between the MZM distortion and the Kerr signal.

The phase shift induced by the carriers and the Kerr effect can be written as follows:

$$\Delta\phi(t) = m \cos \Omega t + m_2 \cos 2\Omega t \quad (4)$$

With $m = m_k + m_c$, m_k the DC Kerr contribution $m_k = \frac{2\pi}{\lambda} L \frac{3\chi^{(3)}}{n} F_{DC} F_{AC}$, m_c the carrier's contribution and $m_2 = \frac{2\pi}{\lambda} L \frac{3\chi^{(3)}}{4n} F_{AC}^2$ which is the Kerr effect recorded at 2Ω .

The optical signals can be written - after inserting (4) in (3), performing a Jacobi-Anger expansion and neglecting intermodulation - as follows:

$$\frac{P_{\Omega}(t)}{P_0} = \sin(\Delta\theta) J_1(m) \cos \Omega t \quad (5)$$

$$\frac{P_{2\Omega}(t)}{P_0} = [-\cos(\Delta\theta) J_0(m_2) J_2(m) + \sin(\Delta\theta) J_0(m) J_1(m_2)] \cos 2\Omega t \quad (6)$$

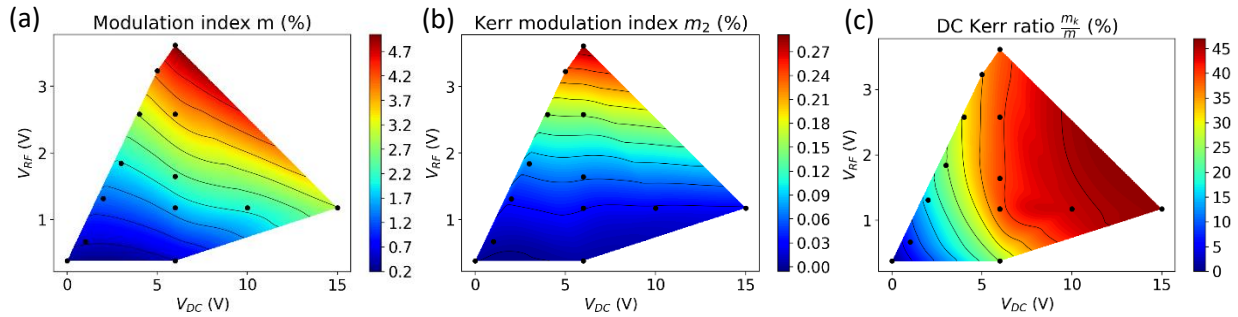


Figure 3: Map of the modulation index (a) m including both Kerr and carrier contributions (b) m_2 only induce by Kerr effect recorded at 2Ω , and (c) DC Kerr ratio in the modulation behavior at an angular frequency of Ω as a function of the applied DC and RF biases. Maps are cubic interpolation based on the experimental data represented with black dots.

With $J_n(m)$ the Bessel function of the first kind. Note that $J_n(m) = \frac{1}{n!} \left(\frac{m}{2}\right)^n$, $m \rightarrow 0$. This means that for small m : $J_0(m) \approx 1$, $J_1(m) \approx \frac{m}{2}$ and $J_2(m) \approx \frac{m^2}{8}$.

Using Eq. (6), the 2Ω signal dependency with the operating point gives information about its origin. At quadrature ($\Delta\theta = \frac{\pi}{2}$), $\frac{P_{2\Omega}}{P_0} = J_0(m)J_1(m_2) \approx \frac{m_2}{2}$ gives the Kerr signal modulation index. But to obtain a more robust measurement, the modulation indices m and m_2 are determined by fitting the experimental data using equations (5) and (6). Results are displayed in Fig. 3, and shows that m_2 increases quadratically with the RF signal amplitude and is independent of the DC bias (Fig. 3 (b)), as expected with a Kerr signal.

Moreover, the Kerr signal can be used to estimate the DC Kerr contribution to the modulation at Ω using:

$$m_k = \frac{4F_{DC}}{F_{AC}} m_2 \quad (7)$$

As a first hypothesis, the relation between the AC field and the AC voltage is supposed to be the same as the one of DC field and DC bias, resulting in $\frac{F_{DC}}{F_{AC}} = \frac{V_{DC}}{V_{AC}}$ and allowing to calculate $m_k = \frac{4V_{DC}}{V_{AC}} m_2$. The DC Kerr contribution is found to be larger for higher DC biases and has a small variation with the RF voltage (figure 3 (c)).

CONCLUSION

The DC Kerr effect has been here observed in a Si PIN junction-based MZM with a linear behavior of the modulation index with both DC and RF biases.

The resulting 2Ω spectral component from Kerr effect was used to quantify the carriers and DC Kerr contributions at an angular frequency of Ω , showing that carriers play a significant role for small reverse DC biases and DC Kerr effect becomes dominant for high reverse DC biases.

Acknowledgements: The authors acknowledge CORNERSTONE team of University of Southampton for the device fabrication and Quentin Chateiller and Bruno Garbin for developing Autolab, a Python library used to perform the measurements.

References

- [1] A. Rahim *et al.*, "Taking silicon photonics modulators to a higher performance level: state-of-the-art and a review of new technologies," *Adv. Photonics*, vol. 3, no. 02, Apr. 2021, doi: 10.1117/1.AP.3.2.024003.
- [2] G. Sinatkas, T. Christopoulos, O. Tsilipakos, and E. E. Kriezis, "Electro-optic modulation in integrated photonics," *J. Appl. Phys.*, vol. 130, no. 1, p. 010901, Jul. 2021, doi: 10.1063/5.0048712.
- [3] M. He *et al.*, "High-performance hybrid silicon and lithium niobate Mach-Zehnder modulators for 100 Gbit s⁻¹ and beyond," *Nat. Photonics*, vol. 13, no. 5, pp. 359–364, May 2019, doi: 10.1038/s41566-019-0378-6.
- [4] M. Berciano *et al.*, "Fast linear electro-optic effect in a centrosymmetric semiconductor," *Commun. Phys.*, vol. 1, no. 1, p. 64, Dec. 2018, doi: 10.1038/s42005-018-0064-x.
- [5] E. Timurdogan, C. V. Poulton, M. J. Byrd, and M. R. Watts, "Electric field-induced second-order nonlinear optical effects in silicon waveguides," *Nat. Photonics*, vol. 11, no. 3, pp. 200–206, Mar. 2017, doi: 10.1038/nphoton.2017.14.
- [6] P. Steglich *et al.*, "Electric Field-Induced Linear Electro-Optic Effect Observed in Silicon–Organic Hybrid Ring Resonator," *IEEE Photonics Technol. Lett.*, vol. 32, no. 9, pp. 526–529, May 2020, doi: 10.1109/LPT.2020.2983034.

Quantifying Hidden Noise in Integrated Nonlinear Sources

(Student paper)

Ben M. Burridge^{1,2,*}, Imad I. Faruque¹, John G. Rarity¹, Jorge Barreto¹

¹Quantum Engineering Technology Laboratories, University of Bristol, Bristol, United Kingdom.

²Quantum Engineering Centre for Doctoral Training, Centre for Nanoscience & Quantum Information, University of Bristol, Bristol, United Kingdom.

* ben.burridge@bristol.ac.uk

Using quantum mechanical modelling techniques, we quantify the often-overlooked levels of noise due to parasitic single-photon generation within auxiliary components of an integrated photonic circuit. We verify our model using experimental observations and compare these results to an identical model without noise. Modelling in this way identifies the bottlenecks in current designs of integrated photonic circuits and can be used to correct impacted results.

Keywords: Noise, Filters, Nonlinear Optics, Quantum, Photon Generation

INTRODUCTION

Filtering out intense pump light is of staggering importance for conventional probabilistic photon generation strategies in the regime of single-photon counting [1, 2]. Removing the pump prevents the generation of spurious photon pairs via spontaneous four-wave mixing (SFWM) in unintended parts of the circuit and prevents linear noise from reaching the detectors. Therefore, it makes sense that experiments employing heralded single-photon sources (HSPs) should filter after the source [3] to remove the pump from the remaining circuitry, more so for sources producing pure photons. Regardless, there are many examples of benchmark and hero experiments that do not remove the pump on-chip [4, 5, 6], most assuredly resulting in contamination and loss throughout the most sensitive regions of the circuit.

It is generally assumed that photon sources are "bright enough" to sufficiently increase the signal-to-noise ratio beyond any background generated in the adjoining components by filtering or de-multiplexing the pump after a

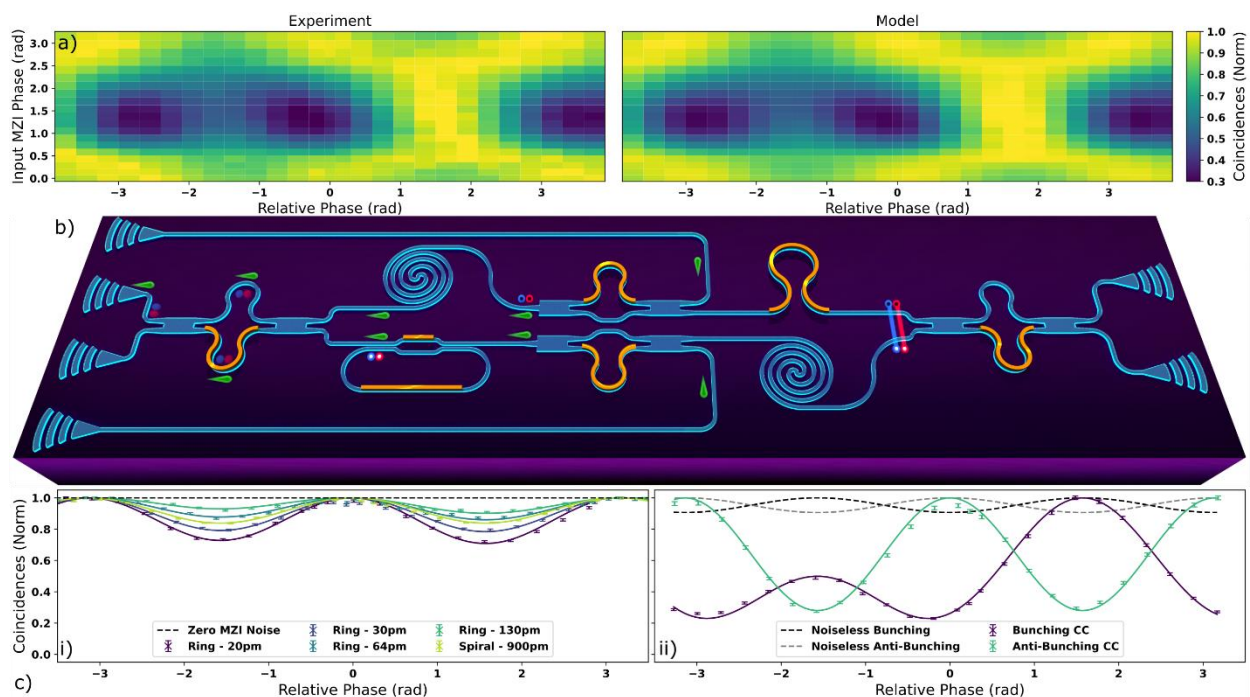


Fig. 1.a) Comparing the interference pattern of the experiment, with that of the fitted model. b) A computer-generated image of the experiment. The pump (green) is input through a grating coupler on the left. It generates photon-pairs everywhere that it is present (represented by the red and the blue spheres). The cores of the red/blue spheres represent the origin of the photon-pair, clear: spurious pairs from waveguides not designed to be a photon source, white: from the ring, and black: from the spiral. The pairs are brought together on a final MZI programmed to be a beam splitter. c) Fitted interference patterns where either i) a single source is pumped, or ii) both sources are pumped. In the case of i) the source and its bandwidth are shown in the legend. In the case of ii) this is the maximum observed interference. Dashed lines are models with noise terms zeroed.

pure-photon source [4, 6, 7]. However, as we move towards increasingly pure photon sources [8], bottlenecks in the surrounding photonic circuitry have the potential to become the most prominent sources of noise. Spurious photons generated outside of a pure photon source will only degrade the purity of the outgoing quantum state.

Here, we present results that quantify the contamination of a pure HSPS, even in the presence of filtering after the source. We measure and subsequently model the quantum interference of two different sources and highlight the need to alter future designs of integrated photonics circuits.

CIRCUIT DESIGN AND EXPERIMENTAL SETUP

Our experimental device has been fabricated on the silicon-on-insulator (SOI) platform, and we have used it previously for other investigations [9]. We use vertical grating couplers (VGCs) to couple light between fibre and Silicon waveguides. The circuit itself (Fig 1b.) uses a combination of multi-mode interference regions in addition to thermo-optic phase modulators to define tuneable Mach-Zehnder interferometers (MZI). These MZIs are then used to divide light into two paths according to its internal tuneable phase ($\Delta\theta$), which connect to distinctly different HSPSs. Our sources of choice are a long waveguide and a micro-racetrack resonator with a tuneable coupling region in the form of an MZI. Following the sources, we use asymmetric MZIs (AMZIs) to preferentially filter pump light off-chip and direct the remaining light towards phase-shifting elements ($\Delta\phi$), path-matching, and a final MZI configured as a 50:50 beam splitter. The outputs of this MZI terminate in VGCs that direct light towards superconducting nanowire single-photon detectors (SNSPDs) of >90 % detection efficiency. We used band-pass (900 pm bandwidth) filters to isolate our pump, signal, and idler wavelengths and record two-fold coincidences between pairs of detectors. Our pump is a pulsed laser with a bandwidth of 340 pm, centered at 1546 nm. With this setup, we measure the on-chip interference of our two distinct sources and model the circuit numerically to validate our findings.

RESULTS AND DISCUSSION

We have modelled the interference produced between single photons at specific wavelengths as output by our experimental device using a numerical model that simulates the biphoton wavefunctions. In the ideal case, all photons are generated at either of our two different sources according to their bandwidth. Our model validation comes from the measured interference of these sources, seen when scanning $\Delta\theta$ for a brightness set by $\Delta\phi$ (Fig. 1a, c). In our model, we account for all sources of spurious SFWM, resulting in an accurate reproduction of the interference we observe.

Our methodology allows us to accurately quantify the contributions of non-source elements to the photon channels. These "noise contributions" fall into two main categories, those from waveguides designed for light transport and generation, respectively. We can isolate these contributions if their states are separable in some way. For example, we can numerically disentangle contributions from the input waveguide and MZI but cannot do so for light generated in the resonant ring structure and adjoining waveguides. Luckily, their biphoton wavefunctions are sufficiently distinct such that we can extract this information by fitting experimental data.

In addition to fitting our experimental data, we can extrapolate our model to remove this noise from the data and, as a result, observe perfectly uncontaminated interference (Fig. 1c). Without noise, stark differences in visibility emerge between the interference with and without noise.

It is generally expected that resonant sources will be less affected by spurious pair generation [6, 10]; here, this is not the case. Consequently, we aim to establish a design rule that cites the need to filter out spurious pairs before the source and the pump immediately afterwards. We draw this conclusion for two main reasons: Tellingly, we observe quantum interference for all values of $\Delta\theta$ (Fig. 1a,c), which indicates the presence of SFWM outside of the two sources. In parallel, our model fits the interference pattern using the strength of all sources of SFWM and suggests significant contributions beyond the two designated sources. In our case, photons generated inside the first MZI exit through both its outputs, regardless of $\Delta\theta$, because the two arms of the MZI are themselves small HSPSs [10]. This numerical analysis is extremely useful for estimating the noise floor of a similarly designed photonic circuit and highlights a fundamental bottleneck of this kind of filter arrangement. In our case, photons generated inside the first MZI exit through both its outputs, regardless of $\Delta\theta$, because the two arms of the MZI are themselves small HSPSs [10].

As a result, creating a pure HSPS on the SOI platform is difficult because SFWM happens in the Si waveguides that we use to route pump light to our sources, painting the picture of a pure and parasitic source integrated on top of each other. Previously, this has not demanded much attention due to the purity of existing sources [8], but as we push towards higher purity sources, this noise becomes the bottleneck. In particular, the only part of an integrated photonic circuit that should generate photons is the photon source itself; this can take the form of an "effective"

nonlinearity. By isolating the HSPS inside a filter network, it is possible to reduce the number of photons generated spuriously which reach the source and prevent their generation afterwards. We should also question the design of these filters. Any spurious noise generated inside a filter must not contaminate its output, as is the case with the commonly used AMZI, suggesting that AMZIs should either be as small as possible or not used at all where SFWM is likely to occur.

Acknowledgements: This work was supported by EPSRC Grant No. EP/L015730/1.

References

- [1] Husko, Chad A., et al. "Multi-photon absorption limits to heralded single photon sources." *Scientific reports* 3.1 (2013): 1-8.
- [2] Harris, Nicholas C., et al. "Integrated source of spectrally filtered correlated photons for large-scale quantum photonic systems." *Physical Review X* 4.4 (2014): 041047.
- [3] Paesani, Stefano, et al. "Generation and sampling of quantum states of light in a silicon chip." *Nature Physics* 15.9 (2019): 925-929.
- [4] Llewellyn, Daniel, et al. "Chip-to-chip quantum teleportation and multi-photon entanglement in silicon." *Nature Physics* 16.2 (2020): 148-153.
- [5] Wang, Jianwei, et al. "Multidimensional quantum entanglement with large-scale integrated optics." *Science* 360.6386 (2018): 285-291.
- [6] Faruque, Imad I., et al. "On-chip quantum interference with heralded photons from two independent micro-ring resonator sources in silicon photonics." *Optics express* 26.16 (2018): 20379-20395.
- [7] Silverstone, Joshua W., et al. "Qubit entanglement between ring-resonator photon-pair sources on a silicon chip." *Nature communications* 6.1 (2015): 1-7.
- [8] Moody, Galan, et al. "Chip-scale nonlinear photonics for quantum light generation." *AVS Quantum Science* 2.4 (2020): 041702.
- [9] Silverstone, Joshua W., et al. "On-chip quantum interference between silicon photon-pair sources." *Nature Photonics* 8.2 (2014): 104-108.
- [10] Faruque, Imad I., et al. "Phase tomography of spontaneously emitted photon-pairs." *CLEO: QELS_Fundamental Science*. Optical Society of America, 2021.

Strong Pump Rejection Filter for Polarization-Diverse Silicon Platforms

Jérôme Michon^{1,3}, Xavier Le Roux¹, Alexandre Huot de Saint-Albin¹, Dorian Oser¹, Sébastien Tanzilli², Laurent Labonté², Eric Cassan¹, Laurent Vivien¹, and Carlos Alonso-Ramos^{1,*}

¹Centre de Nanosciences et de Nanotechnologies (C2N), Université Paris-Saclay, UMR CNRS 9001, 10 Boulevard Thomas Gobert, 91120 Palaiseau, France

²Université Côte d'Azur, CNRS, Institut de Physique de Nice (INPHYNI), Parc Valrose, 06108 Nice Cedex 2, France

³Current address: InSpek SAS, 73 Rue Léon Bourgeois, 91120 Palaiseau, France

*Corresponding author: carlos.ramos@c2n.upsaclay.fr

We propose a new approach for high-rejection filters in polarization-diverse platforms by combining cascaded Bragg filters and anisotropy-engineered metamaterial bends. Based on this strategy, we experimentally demonstrate optical rejection exceeding 60 dB in 300 nm-thick, cladded silicon waveguides that support both a TE and a TM mode.

Keywords: *Bragg filter, metamaterial, polarization*

INTRODUCTION

Integrated high-rejection wavelength filters have been a standing need in integrated photonics to enable a wide variety of applications such as quantum computing. Amongst the numerous designs for high-rejection integrated filters in silicon platforms, non-coherent cascading of Bragg filters stands as a promising solution that can provide remarkable optical rejections even in the presence of imperfections. It allowed the experimental demonstration of optical rejection exceeding 80 dB in an all-passive implementation [1]. Still, optical rejection may be limited by residual power carried by the orthogonal polarization that propagates unperturbed through the filter. This limitation has been solved using 220 nm-thick silicon waveguides without top cladding, that do not propagate transverse magnetic (TM)-polarized modes. However, the increasing level of integration in silicon photonics has driven the use of silicon thicknesses different from the standard 220 nm widely offered by foundries [2]. Thick silicon-on-insulator (SOI) platforms then present the challenge of additional modes that may not be accounted for in components designed for thinner platforms. For non-coherent cascaded Bragg filters which rely on modal engineering of the TE₀ mode, any power in the TM mode, such as residual power from the grating couplers or roughness-induced backscattering (typically around -40 dB to -20 dB compared to the TE mode [3]), propagates unperturbed through the filters and limits the overall rejection. We propose to solve this issue by combining non-coherent cascaded Bragg filters with polarization filters that remove the residual TM mode.

RESULTS

Compared to adiabatic directional couplers, plasmonic couplers, and Bragg filters, which are limited either in fabrication tolerances, excess loss, and footprint, using a 180° metamaterial waveguide bend [4] is preferred as it combines a low excess loss (EL), a high extinction ratio (ER), a broad bandwidth, tolerance to fabrication deviations, and doesn't add to the footprint of cascaded Bragg filters. This design relies on the difference between the ordinary and extraordinary effective indices induced by the subwavelength ridges, leading to the TE mode being well-guided and experiencing low bending loss, whereas the TM mode is leaky and shows a high bending loss. To improve the performances in the case of a low birefringence, e.g. a 300 nm-thick cladded waveguide, we modified the design in two ways illustrated on Fig. 1(a). First, instead of gradually decreasing the metamaterial duty cycle, it is kept constant at the value that maximizes the effective index difference, to minimize the confinement of the TM mode. Second, instead of diffracting the TM mode into free space, a slab region is added after the metamaterial region to extract the TM mode more efficiently, as can be seen on the right plot of Fig. 1(b). This extraction mechanism also presents the benefit of avoiding the TM mode interference which reduces the PER of the diffraction-based design.

The design parameters of the slab-based filter were optimized by simulating the polarization filter using 3D finite-difference time-domain software (Lumerical FDTD). The mode propagation profiles [Fig. 1(b)] for the optimized filter with a bending radius of 5.5 μm, 5 subwavelength periods of 340 nm, and a duty cycle of 0.61, show that the incident TE remains well confined in the waveguide and can propagate through the bend with low loss, while the TM mode is delocalized into the metamaterial and eventually the slab, with little power remaining in the waveguide. This yields an EL of 0.18 dB and a ER of 18.4 dB at λ=1550 nm. While this ER would not be sufficient for rejection of the residual TM mode, the low EL allows for the cascading of these polarization filters and the addition of the ERs, thereby enabling an ER of over 80 dB while maintaining the EL below 1 dB.

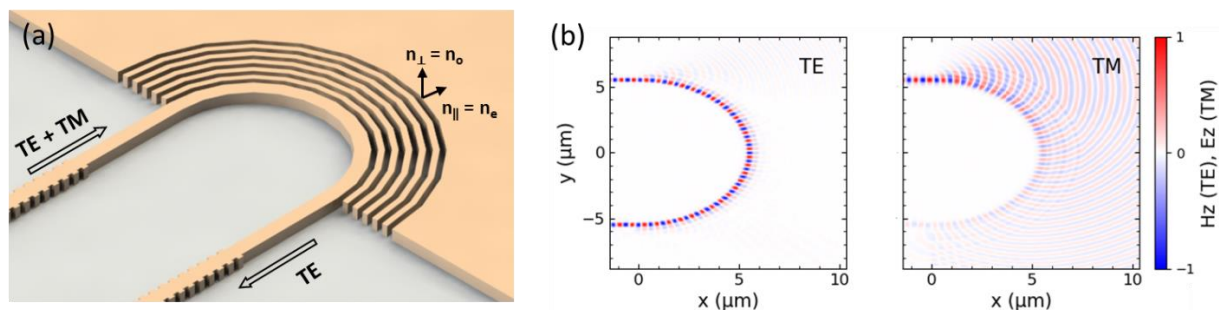


Fig. 1. (a) 3D schematic rendering of the proposed filter design (not to scale). (b) Simulated TE (left) and TM (right) light propagation profiles for the optimized polarization filter at $\lambda=1550$ nm.

The optimized polarization filters were then integrated with cascaded Bragg filters. As the working principle of the non-coherent Bragg filter requires waveguide bends between sections of the filter to radiate out the reflected TE_1 mode, the polarization filters can be placed in these bends without adding to the device's overall footprint, as can be seen on Fig. 2(a). The overall device comprising Bragg filters and polarization filters was fabricated on SOI wafers with 300 nm silicon and 2 μm buried oxide. The device was measured using a tunable laser source (Yenista) providing 10 dBm of power and a detector (Yenista CT400) with a noise floor of about -75 dBm.

Comparing the spectra obtained for a reference waveguide, a single Bragg filter a cascaded Bragg filter without polarization filter, and a cascaded Bragg filter with polarization filters [Fig. 2(b)] highlights the features of the proposed overall filter. We can first observe that the single Bragg filter presents a 30 dB rejection with negligible EL. It then appears that the rejection of the cascaded Bragg filter without polarization filter does not follow the law of accumulated rejection expected from cascaded non-coherent filters. Instead of over 150 dB of rejection, the cascaded filter presents a rejection of 45 dB. This is explained by the presence of residual power in the TM mode due to imperfect grating couplers and roughness-induced scattering. Finally, the spectrum of the cascaded Bragg filter with polarization filters highlights the benefits of integrating the polarization filters. First, the polarization filters do not increase the EL outside of the rejection. Second, the rejection ratio of the overall device is increased until the noise floor of the detector. This confirms that the power observed in the rejection band of the cascaded filter without polarization filter is propagating in the TM mode, and that the polarization filters efficiently remove it.

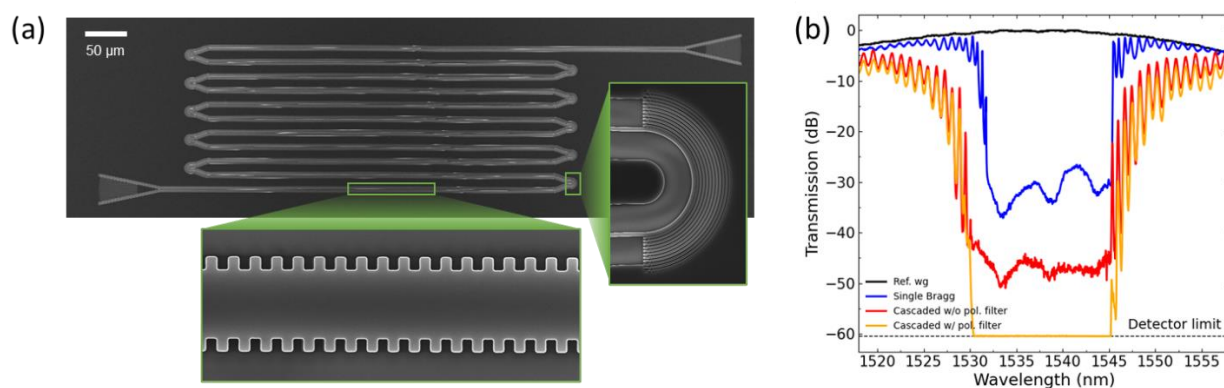


Fig. 2. (a) Scanning electron microscope top-view image of the fabricated device, with 10 cascaded Bragg filters (in the straight sections) and 10 polarization filters (in the 180° bends). (b) Measured transmission spectra of (black) a 550 μm -long reference waveguide, (blue) a single Bragg filter, (red) 10 cascaded Bragg filters without polarization filter, (orange) 10 cascaded Bragg filters with 10 polarization filters.

DISCUSSION

We have proposed and experimentally demonstrated a filter design allowing for high-rejection wavelength filtering in low-birefringence silicon waveguides that support both TE and TM modes. Our design overcomes the rejection limitation of non-coherent cascaded Bragg filters by integrating low-loss, high-rejection, compact-size polarization filters to remove the residual TM mode and restore the Bragg filters' high rejection. We have implemented the proposed device in a 300 nm-thick SOI platform and showed that the integration of the polarization filters allowed to recover a rejection ratio exceeding 60 dB. This work represents the first demonstration of an all-passive pump rejection filter with over 60 dB rejection in a polarization-diverse platform [5].

Acknowledgements: The fabrication of the device was performed at the Plateforme de Micro-Nano-Technologie/C2N, which is partially funded by the Conseil Général de l'Essonne. This work was partly supported by the French RENATECH network and ANR SPHIFA.

References

- [1] D. Oser, F. Mazeas, X. Le Roux, D. Pérez-Galacho, O. Alibart, S. Tanzilli, L. Labonté, D. Marris-Morini, L. Vivien, É. Cassan, and C. Alonso-Ramos, "Coherency-Broken Bragg Filters: Overcoming On-Chip Rejection Limitations", *Laser & Photonics Rev.* **13**, 1800226 (2019).
- [2] D. X. Xu, J. H. Schmid, G. T. Reed, G. Z. Mashanovich, D. J. Thomson, M. Nedeljkovic, X. Chen, D. Van Thourhout, S. Keyvaninia, and S. K. Selvaraja, "Silicon photonic integration platform-Have we found the sweet spot?" *IEEE J. on Sel. Top. Quantum Electron.* **20** (2014).
- [3] F. Morichetti, A. Canciamilla, C. Ferrari, M. Torregiani, A. Melloni, and M. Martinelli, "Roughness induced backscattering in optical silicon waveguides", *Phys. Rev. Lett.* **104**, 033902 (2010).
- [4] H. Xu, D. Dai, and Y. Shi, "Anisotropic metamaterial-assisted all-silicon polarizer with 415-nm bandwidth," *Photonics Res.* **7**, 1432 (2019).
- [5] J. Michon, X. Le Roux, A. Huot de Saint-Albin, D. Oser, S. Tanzilli, L. Labonté, E. Cassan, L. Vivien, and C. Alonso-Ramos, "Strong pump rejection filter for polarization-diverse silicon platforms," *Opt. Lett.* **47**, 341-344 (2022).

Fully Integrated, Scalable Quantum Entropy Source at 1 Gbps

(Student paper) / (Invited paper)

Miquel Rudé¹, Domenico Tulli¹, Waldimar Amaya¹, Carlos Abellán¹

¹Quside Technologies, Carrer Esteve Terradas 1, Castelldefels, 08860, Spain

* mrude@quside.com

We introduce a fully integrated, high speed quantum entropy source (QES) based on an InP photonic integrated circuit (PIC). The QES is integrated in a 5x5 mm² standard IC package with all electrical inputs/outputs and can generate up to 1 Gbps quantum random numbers by modulating 2 DFB lasers in gain switching (GS) and detecting the random phase of their beat note.

Keywords: Quantum random number generation, Integrated Photonics, PIC Packaging

INTRODUCTION

Nowadays, we are witnessing a proliferation of cyberattacks, and an emerging greater awareness of their negative impact on the economy and on society. Moreover, the technological evolution driven by IoT and 5G networks has posed the priority in implementing stronger cryptographic systems, raising the need for security at the edge. The development of products and infrastructure offering long-term security guarantees and stronger computational capabilities is a global priority to ensure the socio-economic growth. Near-term, quantum technologies provide a radically new toolset to realize stronger encryption systems.

Quantum entropy sources (QES) are a fundamental building block for cryptography and many other areas as high-performance computing, Monte Carlo simulations, scientific research, etc. This technology harnesses the laws of quantum physics to provide true randomness in contrast to deterministic chaotic systems and pseudo random number generators (PRNGs) based on deterministic dynamics or computationally complex algorithms. To date, several QESs either based on commercial of the shelf (COTS) or PICs are commercially available ranging from a few Mb/s entropy generation rate to Gb/s rates, as those demonstrated with phase diffusion (PD) in semiconductor lasers [1].

Quside exploits phase diffusion technology and photonic integrated circuit (PIC) to build reliable high-speed and scalable quantum random number generators. The device is made possible by a design using two-laser interference and heterodyne detection, allowing QES rates in the Gb/s regime. The proprietary technology based on Indium Phosphide PIC makes use of standard manufacturing processes to assure cost-effectiveness and scalability. Moreover, its small dimensions make the device the perfect candidate to secure mobile and IoT devices.

RESULTS

Figure 1 shows a schematic and picture of the QES. The device is based on an InP PIC (2.5x1 mm²) containing two single mode DFB lasers ($\lambda \sim 1270$ nm) with integrated metallic heaters to tune the individual wavelength of each laser. The optical fields of the 2 lasers are coupled to single mode waveguides and combined in a 2x2 multimode interferometer (MMI) before being sent to 2 photodetectors (PDs) to detect the random amplitudes of the beating signal. The device is packaged in a standard QFN (5x5 mm²; 32 pins) using 25 μ m Au wire-bonds.

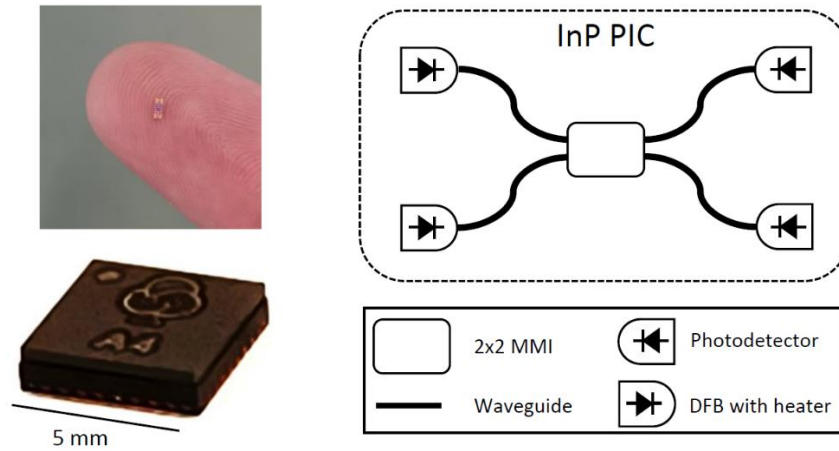


Fig. 1. Left: Picture of a fully packaged QES in an open cavity QFN32 (5x5 mm²;32 pins) and optical microscope image of the InP PIC inside. Right: Schematic of the photonic circuit in the PIC used to generate quantum random numbers at high-speed.

The operating principle behind the QES is phase-diffusion in 2 gain-switched DFB lasers [1]. When the 2 lasers are modulated above and below threshold ($I_{th} = 15 \text{ mA}$) at $f_m=1 \text{ GHz}$ the initial phase of each pulse is random. By interfering the pulses of each laser one obtains a beating signal (Ω_b) given by the difference of their optical frequencies $\Omega_b(t) = \omega_1(t) - \omega_2(t)$ and a random initial phase for each modulation cycle. After interference in the 2x2 MMI the intensity reaching the photodetector is given by:

$$i_{PD}(t) = i_{L1}(t) + i_{L2}(t) + 2\sqrt{i_{L1}(t)i_{L2}(t)}\cos(\Omega_b t + \Delta\theta) \quad (1)$$

where $i_{L_i}(t)$ is the intensity of each laser, Ω_b is the beating frequency and $\Delta\theta = \theta_1 - \theta_2$ is the difference of the initial random phases of each laser, which for large phase diffusion follows an approximately uniform distribution between 0 and 2π , and encodes all the randomness originating from this process. Note that in general the optical frequency (and thus the beating frequency) of modulated lasers can be strongly chirped and evolves over the modulation cycle ($\omega_i(t) \approx \omega_i^0 + \beta_i t$) due to carrier induced changes in the refractive index. However, by modulating the two lasers, which have similar chirp $\Delta\beta_i \approx 0$, this effect can be compensated, obtaining an approximately single frequency beat note $\Omega_b = \Delta\omega_i^0 + \Delta\beta_i t \approx \Delta\omega_i^0$. Finally, in order to recover the beating signal one must tune the beat note to be smaller than the PD response time $\Omega_b < 1/\tau_{PD}$. Experimentally, we can tune the wavelength to be within the response time of the PD by injecting current into one of the integrated metallic heaters of the lasers.

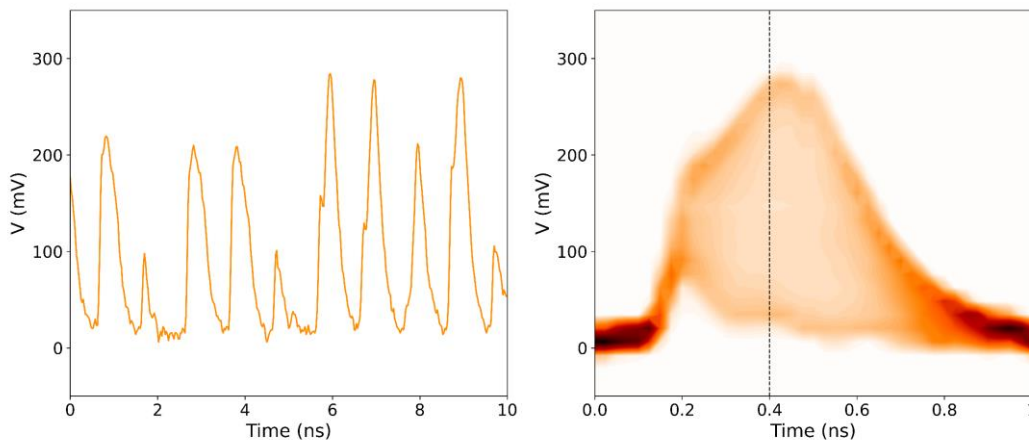


Fig. 2. Left: Interference trace at $f_m=1 \text{ GHz}$, showing random amplitude pulses. Right: Accumulated traces generated with 25000 pulses.

Figure 2 shows both a single and accumulated (25000 pulses) interference traces at $f_m=1$ GHz, where the random amplitudes of each cycle are clearly visible. The beating frequency is tuned to be around $f_b=1.5$ GHz by injecting ≈ 7 mA into one of the integrated heaters. As f_b is comparable with f_m , a full oscillation of the beat note cannot be resolved within the modulation cycle.

Finally, we have analyzed the histogram and autocorrelation of the interference signal at a sampling point inside the pulse. For a phase-diffusion QES the histogram of amplitudes at a fixed sampling point should follow a smoothed arcsine distribution [2], as shown in Figure 3. Small imbalances in the arcsine can be present, due to a combination of envelope slope, jitter and bandwidth effects.

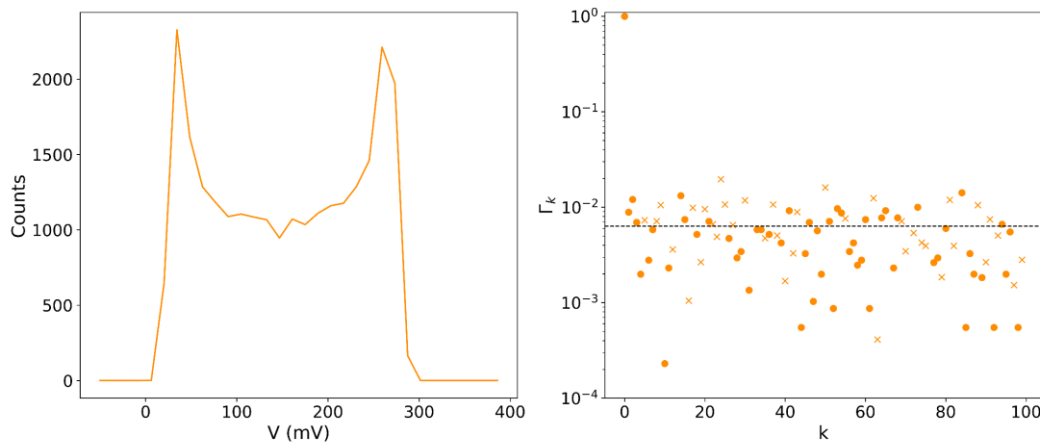


Fig. 3. Left: Histogram at a sampling point inside of the pulse (dashed vertical line in Figure 2 right), showing a smoothed arcsine distribution. Right: Absolute value of autocorrelation of the digitized interference trace at the same sampling point.

For each sampling point we have also digitized the interference trace with a 1-bit digitizer and analyzed the autocorrelation up to a shift of $k=100$, using $N=25000$ bits. All obtained values lie within the statistical noise (dashed line in Figure 3 right). Larger datasets will be analyzed in future work.

CONCLUSION

We have introduced a fully integrated and fully packaged QES based on phase-diffusion in gain switched DFB lasers. The device is implemented using an heterodyne detection scheme in a small size InP PIC. By strongly modulating the two DFB lasers and fine tuning their optical frequencies one can generate up to 1 Gbps quantum random numbers.

The device has a small footprint and is designed for high scalability and low-cost, paving the way towards the use of QRNGs for cybersecurity in a wide range of applications, from data centers to IoT markets.

References

- [1] C. Abellán et al., *Quantum entropy source on an InP photonic integrated circuit for random number generation*, Optica, vol. 3, no. 1 pp., 989-994, 2016
- [2] C. Abellán et al., *Ultra-fast quantum randomness generation by accelerated phase diffusion in a pulsed laser diode*, Opt. Express, vol. 22, no. 2, pp. 1645-1654, 2014

Sub-milliwatt and tunable optical power limiters using vanadium dioxide in ultra-compact silicon waveguides

(Student paper)

Jorge Parra¹, Juan Navarro-Arenas¹, Jean Pierre-Locquet² and Pablo Sanchis^{1*}

¹Nanophotonics Technology Center, Universitat Politècnica de València, Camino de Vera s/n, 46022 Valencia, Spain

²Department of Physics and Astronomy, KU Leuven, Celestijnenlaan 200D, 3001 Leuven, Belgium

*pabsanki@ntc.upv.es

In this work, we report ultra-compact optical limiters with tunable performance on silicon photonics using vanadium dioxide (VO₂). Our experimental device features a threshold power of only ~3.5 mW in 15 nm of bandwidth using a 20-μm-long VO₂/Si waveguide. Through numerical simulations, we prospect sub-milliwatt threshold powers. Our work could serve for developing on-chip activation functions in photonics-based neural networks applications.

Keywords: optical limiter, vanadium dioxide, silicon photonics

INTRODUCTION

Silicon photonics encompasses a wide variety of passive and active building blocks [1]. However, to date, there is no clear approach to implementing optical limiting devices. Optical limiters are devices that exhibit a clipped-like input-output power response. Below a certain threshold, the device has a linear response, whereas for higher values becomes nonlinear and saturates the output [2]. In the field of integrated optics, the applications of optical limiters can range from protecting optical devices against hazardous high-port signals and provide stability from fluctuations in high-Q resonant structures, to provide activation functionalities [3] in emerging areas such as artificial intelligence or neuromorphics [4].

Optical limiting is readily observable in silicon waveguides owing to silicon nonlinearities such as two-photon absorption (TPA) or free carrier absorption (FCA) [5]. However, the nonlinear properties of silicon are very inefficient, requiring thus resonant structures to enhance the nonlinear processes, but at the expense of a dramatic reduction in the operational optical bandwidth. To overcome the trade-offs imposed by silicon, integrating new active materials into the silicon photonics platform is a subject of current interest. In this context, vanadium dioxide (VO₂) is a complementary metal-oxide-semiconductor (CMOS)-compatible phase transition oxide exhibiting a unity order change on both real and imaginary parts of its refractive index. Such appealing optical properties stem from the insulator-metal transition (IMT) at around 65 °C and have been leveraged on many nanophotonic devices [6].

In the present work, we experimentally demonstrate an ultra-compact VO₂/Si optical limiter on silicon photonics featuring low-threshold power and tunability over a broad spectral response. Through numerical simulations, we show that a sub-milliwatt operation could be achieved by optimizing the distance between the VO₂ and the silicon waveguide.

RESULTS

Optical limiting is achieved when the induced optical losses match the increase of the optical power when this exceeds the threshold power. Thereby, the output is constant regardless of the input value. For a hybrid VO₂/Si waveguide with in-plane excitation, such a condition is satisfied when [7]:

$$\eta(\alpha_m - \alpha_i) = 1 \quad (1)$$

where η stands for the thermo-optical efficiency of the hybrid waveguide relating the length of VO₂ that changes from insulating to metallic to the optical power, and $\alpha_{m/i}$ is the propagation loss in the metallic/insulating state.

Fig. 1(a) shows a micrograph of the fabricated optical limiter. Our optical limiter is based on a 20-μm-long single-mode 480 nm × 220 nm Si waveguide with a 40-nm-thick VO₂ layer on top separated by a 60 nm spacer formed by a 10-nm-thick silicon oxide layer plus a 50-nm-thick SiN hardmask. The chip was covered with 700 nm of SiO₂ by plasma-enhanced chemical vapor deposition (PECVD). The optical limiter works for the transverse electric (TE) polarization. The TE optical modes in the hybrid waveguide for the insulating and metallic states are shown in Figs. 1(b) and 1(c), respectively. At 1550 nm, the propagation loss in the insulating (metallic) state is 0.91 dB/μm (1.61 dB/μm), and the photothermal efficiency is 1.06 μm/dB [8]. These values yield $\eta(\alpha_m - \alpha_i) \approx 0.74$, which is near the optimal limiting condition of Eq. (1).

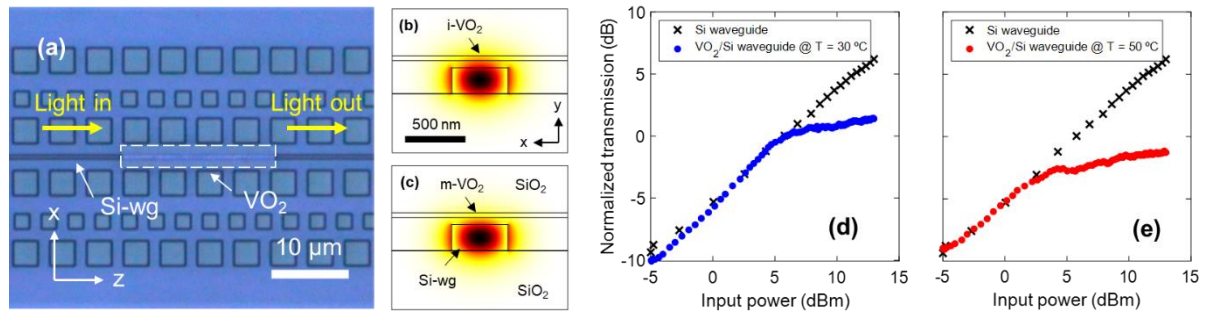


Fig. 1. (a) Optical image of the fabricated VO_2/Si optical limiter. (b,c) Simulated optical modes (E_x) of the hybrid waveguide with VO_2 in the (b) insulating ($i\text{-VO}_2$) and (c) metallic ($m\text{-VO}_2$) states at $\lambda=1550$ nm for TE polarization. (d,e) Experimental optical response of the VO_2/Si waveguide acting as an optical limiter and the silicon reference waveguide at (d) 30 °C and (e) 50 °C. Measurements were carried out at $\lambda=1565$ nm.

The power limiting response was characterized for a fixed wavelength (1565 nm) and by increasing the optical power. Fig. 1(d) shows the experimental optical response of a reference silicon waveguide without VO_2 and the hybrid waveguide. Input optical power values are given on-chip, and transmission is normalized arbitrarily for the sake of comparison. Nonlinear effects from silicon are discarded because the reference waveguide exhibits a linear response. Hence, the optical limiting response of the VO_2/Si waveguide owns to the gradual change of the VO_2 path from insulating to metallic, which is induced by photothermal effect.

Near room temperature (30 °C), our device features a low threshold power of ≈ 5.4 dBm (≈ 3.5 mW). Since the IMT is photothermally triggered, our optical limiter also provides the possibility of tuning its response. Biasing the temperature of the VO_2 near the IMT reduces the threshold power. In such a way, the temperature of the chip was increased to 50 °C, near the IMT (≈ 65 °C), with a Peltier device. Consequently, the threshold power was reduced down to ≈ 3 dBm (≈ 2 mW) since a smaller increase of temperature was required to trigger the IMT [see Fig. 1(e)]. On the other hand, we measured an optical limiting response in 15 nm of bandwidth (1550-1565 nm). However, it should be mentioned that this value was restricted by our setup and not by the device. The non-resonant response of the device and low dispersion of VO_2 at telecom wavelengths can cover both C- and L-band [8].

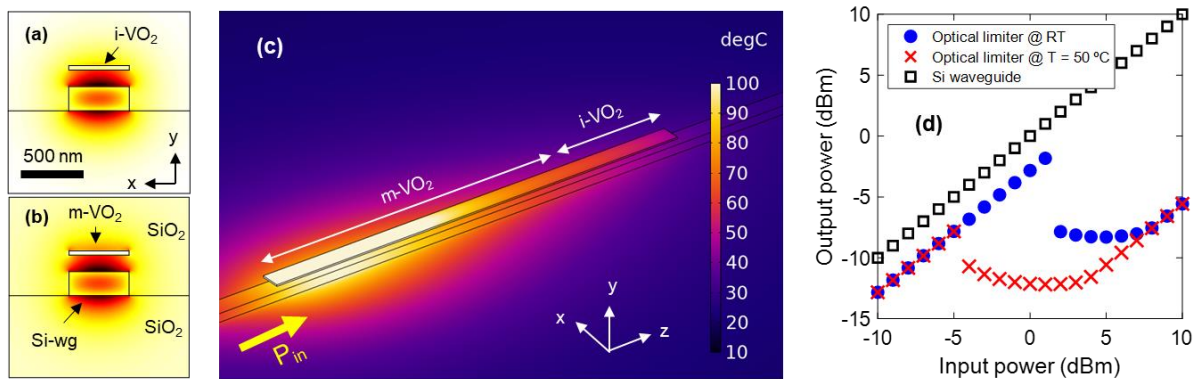


Fig. 2. (a,b) Simulated optical modes (E_y) of the hybrid waveguide with VO_2 in the (a) insulating ($i\text{-VO}_2$) and (b) metallic ($m\text{-VO}_2$) states for TM polarization. (c) Temperature distribution of the 11- μm -long optimized optical limiter under a 2 mW continuous wave signal. (d) Simulated optical response of the optical limiter. Simulations are given at $\lambda=1550$ nm.

The insertion loss of the optical limiter can be significantly reduced by engineering the hybrid waveguide structure. Through numerical simulation, we obtained a significant reduction of the propagation loss in the insulating state, down to 0.26 dB/ μm , by increasing the gap between the silicon waveguide and the VO_2 layer to 150 nm and using TM polarization. For the sake of simplicity, we consider that the upper cladding is comprised only of SiO_2 , and the width of the VO_2 patch equals the silicon waveguide. The optical modes of the optimized hybrid waveguide in the insulating and metallic state are shown in Figs. 2(a) and 2(b), respectively. The propagation loss in the metallic state is 1.42 dB/ μm , and the photothermal efficiency is 0.64 $\mu\text{m}/\text{dB}$. This latter was obtained by heat transfer simulations using COMSOL.

Considering the non-uniform heating of the VO_2 patch along the propagation direction, we restrict the length of the optical limiter to 11 μm to avoid ablation on the VO_2 . Figure 2(c) shows the temperature distribution of the optical limiter in the steady-state under a 2 mW continuous wave signal and at room temperature. Based on our optical and thermal simulations, we obtained the output-input response of the optical limiter at room temperature and 50

°C as shown in Fig. 2(d). The linear response of the silicon waveguide is also shown as a reference. Compared to the experimental device, the insertion loss is reduced to 2.8 dB. The kink on the response of the optical limiter is attributed to the high difference on the propagation losses between both states of the VO₂ and its nonlinear behaviour. On the other hand, a threshold power below the milliwatt could be achieved by biasing the temperature of the VO₂ to 50 °C.

DISCUSSION

In summary, we have experimentally demonstrated ultracompact optical limiters on silicon photonics with tunable performance and broadband response harnessing the photo-induced IMT of VO₂. Through numerical simulations we have optimized the device by reducing the insertion loss down to 2.8 dB together with a threshold below the milliwatt by locally heating the hybrid waveguide near the IMT temperature. Since VO₂ is a CMOS-compatible material, our study opens up opportunities to include such a building block onto dense and low power consumption photonic integrated applications.

Acknowledgements: This work is supported by grants PID2019-111460GB-I00, ICTS-2017-28-UPV-9F, and FPU17/04224 funded by MCIN/AEI/10.13039/501100011033, by "ERDF A way of making Europe" and "ESF Investing in your future". Funding from Generalitat Valenciana (PROMETEO/2019/123) is acknowledged. We thank Mariela Menghini and Maria Recaman for their help with the deposition of VO₂.

References

- [1] S. Y. Siew et al., "Review of Silicon Photonics Technology and Platform Development," *J. Light. Technol.*, vol. 39, no. 13, pp. 4374-4389, 2021.
- [2] L. W. Tutt and T. F. Boggess, "A review of optical limiting mechanisms and devices using organics, fullerenes, semiconductors and other materials," *Prog. Quantum Electron.*, vol. 17, no. 4, pp. 299-338, 1993.
- [3] C. Nwankpa, W. Ijomah, A. Gachagan, and S. Marshall, "Activation Functions: Comparison of trends in Practice and Research for Deep Learning," *arXiv*, pp. 1–20, 2018.
- [4] B. J. Shastri et al., "Photonics for artificial intelligence and neuromorphic computing," *Nat. Photonics*, vol. 15, no. 2, pp. 102-114, 2021.
- [5] R. M. Osgood, Jr. et al., "Engineering nonlinearities in nanoscale optical systems: physics and applications in dispersion-engineered silicon nanophotonic wires," *Adv. Opt. Photonics*, vol. 1, no. 1, p. 162, 2009.
- [6] S. Cuffet et al., "VO₂ nanophotonics," *APL Photonics*, vol. 5, no. 11, p. 110901, 2020.
- [7] J. Parra, J. Navarro-Arenas, M. Menghini, M. Recaman, J. Pierre-Locquet, and P. Sanchis, "Low-threshold power and tunable integrated optical limiter based on an ultracompact VO₂/Si waveguide," *APL Photonics*, vol. 6, no. 12, p. 121301, 2021.
- [8] J. Parra, T. Ivanova, M. Menghini, P. Homm, J.-P. Locquet, and P. Sanchis, "All-Optical Hybrid VO₂/Si Waveguide Absorption Switch at Telecommunication Wavelengths," *J. Light. Technol.*, vol. 39, no. 9, pp. 2888-2894, 2021.

Does the world need general-purpose programmable photonics?

(Invited paper)

Wim Bogaerts

Ghent University – IMEC, Technologiepark-Zwijnaarde 126, 9052 Gent, BELGIUM
Wim.bogaerts@ugent.be

General-purpose programmable can provide an easily accessible technology for prototyping new photonic functions on chip, enabling innovations in new applications without the steep entry cost of full-custom photonic integrated circuits.

Keywords: Programmable photonics

Programmable photonics is the emerging research field of photonic chips where the flow of light can be reconfigured through an electronics and software layer [1]. This contrasts with traditional photonic chips, which usually have a fixed connectivity and are designed for one particular application. To assess the potential of such reconfigurable circuits, we draw a comparison between the field of integrated photonics and the field of integrated electronics.

Silicon electronics has become pervasive in most aspects of our lives. Our technologically advanced society relies on electronic chip technology for data processing, computation, communication, and sensing. The versatility of electronic chips has even made them more cost-effective for many simple management and control tasks than traditional mechanical or hydraulic systems. It would be impossible to imagine our society without electronics. The economies of the semiconductor industry have enable the fabrication of massive amounts of electronic chips.

Photonics is slowly assuming a similar role. We already know that the ubiquitous internet communications are supported by a hidden network of high-bandwidth fiber-optic links, but we also use light for diverse functions in sensing, data storage and manipulation of our environment. Like in electronics, these optical functions are being integrated on chips, which often make use of similar fabrication technologies as electronic chips, especially when it comes to so-called ‘silicon photonics’ [2].

Even though many of the critical building blocks of photonics and electronics originated in the same period between 1945 and 1960 (most notably the laser and the transistor) one can argue that the ecosystem of photonic chips is lagging several decades behind that of their electronic counterparts. This can be observed through various metrics:

- The diversity of technologies:** While one can argue that photonic chips today use a much wider range of material systems (Silicon, III-V semiconductors, silica, polymers, LiNbO₃, silicon nitride) compared to electronics (99.9% silicon), there is an enormous diversity in industrial electronic chip platforms, covering 2-3 orders of magnitude in transistor gate length (so-called ‘technology nodes’), with flavors for high-voltage, low-power, high-speed or radiation hardened circuits, with both analog and digital functions. For most electronic chip designers, it is much easier to find a platform with the desired characteristics than it is for a photonics designer. For photonics designers, there is of course the additional complication that different use cases might require different optical wavelengths, which limits the materials that can be used.

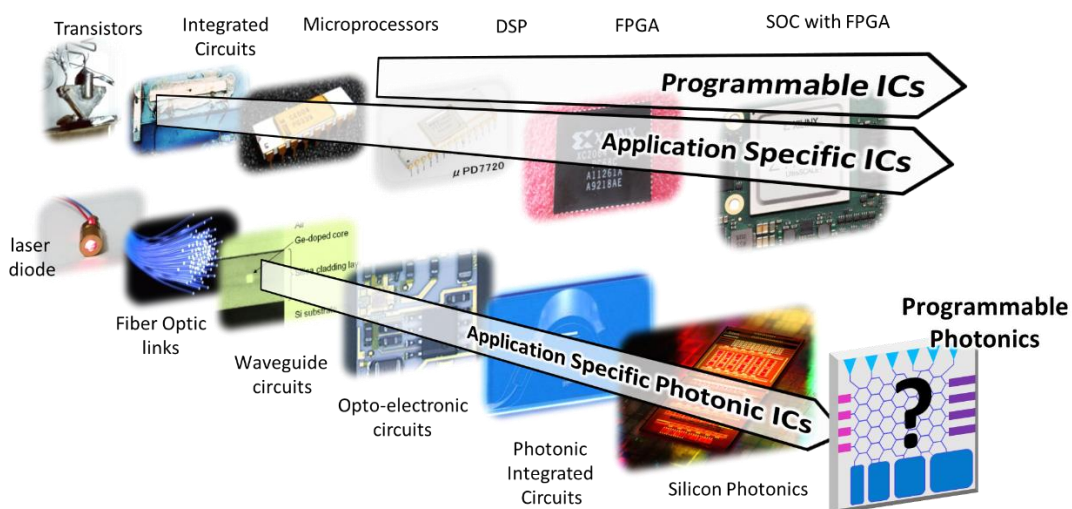


Figure 1: Photonics and electronics follow the same scaling path in circuit complexity, but the success of electronics has been multiplied by programmable hardware, which today is missing in the field of photonics

- **The manufacturing volumes:** The numbers of chips being churned out by a single modern electronic foundry dwarf the total worldwide production volume of photonic chips. As a result, the benefits of scale are often not large enough to really bring down the cost of photonic chip production, even in situations where the photonics is fabricated in the same fab facilities as electronics. As a result, the maturity of fabrication processes for photonic chips is often much lower.
- **Diversity in applications:** today, we find electronics in applications well beyond the field of “computing”. The applicability of electronics to make traditional hardware ‘smart’ has played in tandem with the economies of wafer-scale fabrication to make it possible for product developers to incorporate electronic chips in even the cheapest consumer goods.
- **Design and prototyping:** One of the aspects that allowed the widespread proliferation of electronics is the capability to design a complex chip with many analog and digital functions, and accurately predict how this chip will behave after fabrication. The rapid evolution of electronic design automation (EDA) tools in the 1990s and 2000s, together with the introduction of reusable ‘IP blocks’, has enabled first-time-right design, lowering the threshold for new designers to use the technology. This, in turn, has accelerated the prototyping of new electronic functions for new applications. In photonics, the evolution of the design tools is rapidly evolving in the same direction, but the lack of standards and the lower maturity of the fabrication processes make first-time-right design for photonic chips an elusive goal [3]. While the prototyping time of a new photonic chip is similar as a new electronic chip (1-2 years), the photonic chip will often require multiple iterations.
- **Programmability and Software:** One of the most prominent features of many electronic chips is their programmability, which makes it possible to adjust, modify or redefine the functionality of the hardware after fabrication [4]. This can be as ‘programmable hardware’ like field-programmable gate arrays (FPGA), specialist chips (e.g. digital signal processors – DSP) or general-purpose microprocessors. Most photonic chips today are designed for specific functions and cannot be reconfigured after fabrication. True, many chips include electro-optic tuning mechanisms to finetune the chip response, or can be used to switch optical signals, but they are still built to perform specific functions. In contrast with electronic FPGAs and microprocessors, new photonic functionality will require the design and fabrication of a new photonic chip.
- **Education and Community:** the success of electronics has, over the past decades, led to widespread educational programs in electronics engineering, but also in computer and Software Engineering. This has created an enormous worldwide community to innovate in these technologies, create new applications, drive standards and overall push the field forward. The well-known Moore’s law can be seen as both a cause and a consequence of this widespread adoption. While optics as a field is much older than electronics, it has not seen this rapid growth, and it turns out that there is also a considerable gap between traditional optics and the newer chip based ‘photonics’. Today, for every engineer that can design a photonic chip, there are at least 100 electronic chip designers, and probably 1000 software engineers to program their functionality.

If we look at the above metrics, we can clearly see that many of those are correlated, and mutually reinforcing. Today, we see that the field of integrated photonics is rapidly growing, but it lacks several enablers that have been crucial for the widespread adoption of electronics. One of the key factors that made electronics successful as a driver of innovation, including the emergence of a large “Maker” community, is its programmability. Programmable electronics makes it possible to experiment, develop and prototype many new applications without the prohibitively expensive design-fabricate-test cycles of custom electronic chips. Even though programmable electronics are generally larger, slower, and consume more power than optimized application-specific integrated circuits (ASICs), they are in many cases good enough, and can be more cost-effective in low to moderate volumes.

Today, this low-threshold model for developing new application is completely absent in integrated photonics. There is simply no photonic equivalent for general-purpose FPGAs or microprocessors. Because of this, every new idea for a photonic innovation that could be implemented on a chip, and that could lead to new applications and products, has to go through numerous design-fabrication-test cycles. This is a costly and cumbersome process, and as a result the spread of photonic chip technologies is progressing at a slow pace, except in the few fields where it is already successful, in particular fiber-optic communications.

Programmable photonics, or more precisely general-purpose programmable photonic chips could dramatically lower this adoption threshold. If such chips are available as off-the-shelf components at a modest price point (because they can be fabricated in much higher volumes than application specific chips) the lead time for experimenting with this technology is reduced from a months/years to mere days. This is conducive for agile product development and innovation, as new ideas can be prototyped through software development and iteratively tested with actual users. Just like with electronics, there might be many use cases where the performance of these programmable chips is adequate. In other cases, they could help to identify the performance gap, and if the market drive is strong enough, the design could be converted into a custom-designed chip. In all these scenarios, it will stimulate experimentation, and boost the adoption.

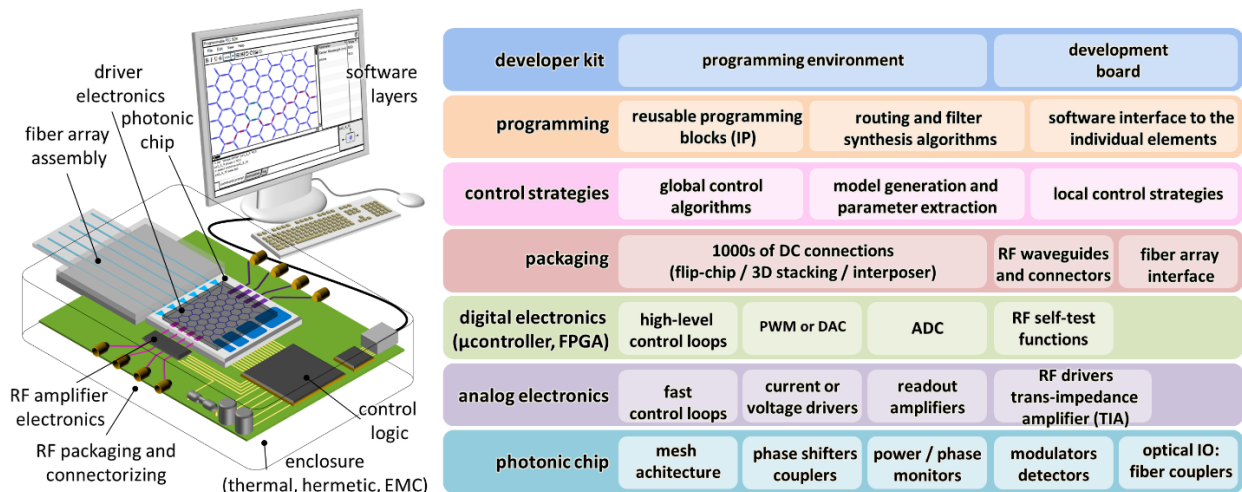


Figure 2: Technology stack for programmable photonic circuits. Apart from the photonic and electronic chip, connected with packaging technology, there is a need for multiple layers of driver, control, configuration algorithms and programming tools.

Of course, a first requirement is that this technology becomes available. To realize the promise of such programmable photonic chips, the entire technology stack must be accessible to the users [5]. Like application-specific photonic circuits this requires a photonic chip, but also the electronic drivers, fiber connections and packaging technologies (including high-speed electronics if needed). But on top of that, programmable photonics needs additional software layers, starting with low-level management of the individual actuators and detectors in the circuit, to control and calibration routines (all elements in these circuits are analog and susceptible to fabrication variations). Users of these programmable chips will need synthesis algorithms to implement custom functionality such as wavelength filters, and define connectivity between building blocks and subcircuits (similar to placement and routing in electronic FPGAs). Also, like with programmable electronics, these design activities should be supported by a solid development kit that allows the users to inspect and debug the behavior of their photonic system. While the first hardware demonstrations are slowly taking shape, the software elements today are in an embryonic or even nonexistent state, and it will be interesting to observe their emergence and evolution in the coming years.

To conclude, we can go back to the question whether the world will need general-purpose programmable photonics? If we want to reap the same benefits of scale as with on-chip electronics, the answer is a definite Yes. The world needs photonic integration for the functionality it can provide (at a fundamental lower cost and power consumption), but to reach the same critical mass as integrated electronics, we need a much larger community that can innovate based on this technology. Photonic chips with a higher-level design interface, in the form of programmable software layers, can open up this technology to the much wider group of electronics and software engineering professionals, and even put photonic chips in the hands of the maker community.

Acknowledgements

The author is supported by the European Union through the ERC Consolidator Grant PhotonicSWARM (725555) and the H2020 project MORPHIC (780283), as well as by the Flemish Research Foundation through grant G020421N

References

- [1] W. Bogaerts *et al.*, "Programmable photonic circuits," *Nature*, 586(7828), 207–216, (2020).
- [2] S. Y. Siew *et al.*, "Review of Silicon Photonics Technology and Platform Development," *J. Light. Technol.*, 1–1, (2021).
- [3] W. Bogaerts *et al.*, "Silicon Photonics Circuit Design: Methods, Tools and Challenges," *Laser Photonics Rev.*, 1700237, 1–29, (2018).
- [4] S. M. Trimberger, "Three ages of FPGAs: A retrospective on the first thirty years of FPGA technology," *Proc. IEEE*, 103(3), 318–331, (2015).
- [5] W. Bogaerts *et al.*, "Programmable Photonics: An Opportunity for an Accessible Large-Volume PIC Ecosystem," *IEEE J. Sel. Top. Quantum Electron.*, 26(5), 1, (2020).

Multi-channel free-space optical communication between self-configuring silicon photonics meshes

(Student paper)

SeyedMohammad SeyedinNavadeh¹, Maziyar Milanizadeh¹, Francesco Zanetto¹, Vittorio Grimaldi¹, Christian De Vita¹, Giorgio Ferrari¹, David A.B. Miller², Andrea Melloni¹, Francesco Morichetti¹

¹ Department of Electronics, Information and Bioengineering, Politecnico di Milano, via Ponzio 34/5, 20133, Milano, Italy

²Ginzton Laboratory, Stanford University, Spilker Building, Stanford, CA 94305, USA

*corresponding author e-mail: francesco.morichetti@polimi.it

Two reconfigurable meshes of Mach-Zehnder Interferometers (MZIs) are employed to automatically establish pairs of orthogonal free-space communication links between two photonic chips. The meshes adjust to preserve more than 30 dB mutual rejection between the channels even after a partial obstruction is introduced in the path.

Keywords: Programmable Photonic Circuits, Free-Space Optics, Orthogonal Communication Channels, Silicon Photonics

INTRODUCTION

Photonic Integrated Circuits (PICs) consisting of generic architectures that can be reconfigured during operation are emerging as a promising approach for advanced processing of optical signals. Applications span from widely reconfigurable wavelength-selective devices to analog photonic processors, quantum information processing and artificial neural networks, and optical beamforming and sensing [1]. Recently, we demonstrated that a silicon photonic mesh of Mach-Zehnder Interferometers (MZIs), through controlling an array of imperfect optical antennas, can self-configure to generate perfectly shaped free-space optical beams and to image a desired field pattern through obstacles [2].

In this work, we show that a pair of self-configuring MZI meshes, used respectively at the transmitter (Tx) and receiver (Rx) side, can be used to establish chip-to-chip Free-Space Optical (FSO) links on multiple orthogonal beams. The system automatically finds the best FSO communication channels by iteratively optimizing the configuration of the two meshes. We demonstrate that two orthogonal FSO beams can be separated with more than 30 dB of mutual isolation even after a partially obstructing mask is introduced in the free-space path.

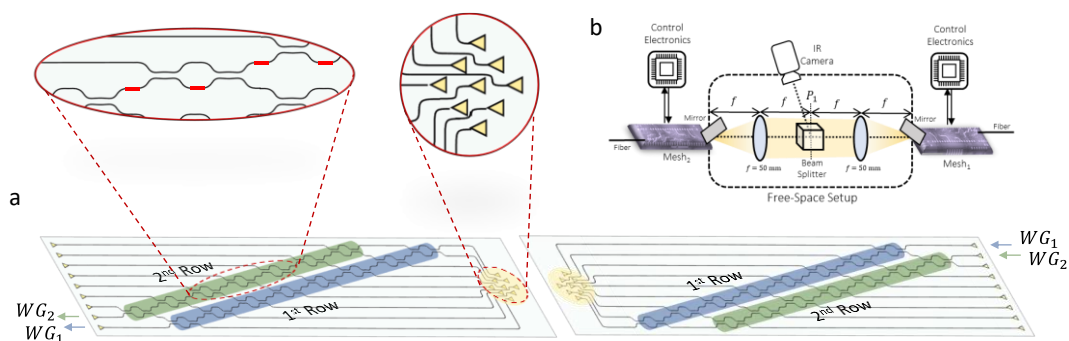


Fig. 1. (a) Schematic of the bi-diagonal meshes of MZIs, indicating the grating coupler array and integrated MZI blocks; (b) schematic of the free-space setup used for establishing communication channels between two photonic chips.

SELF-CONFIGURING PHOTONIC MESH CIRCUIT

We use two identical reconfigurable MZI mesh PICs, each fabricated in 220 nm thick standard silicon photonics technology and operating at 1.55 μm wavelength. The “bi-diagonal” mesh topology consists of two “diagonal rows” of MZIs – a 1st and a 2nd row – including 8 and 7 diagonally cascaded MZIs, respectively (Fig. 1a). The PICs each terminate at one side with 9 vertically radiating grating couplers, arranged in a 3x3 square array, which are used as a 2D optical antenna array to couple the light into free space (or vice versa); at the other end of each mesh, two input/output waveguides, labelled as $WG_i, i = \{1,2\}$, couple the light to optical fibres. The spacing between the elements in the square array is much larger than half a wavelength ($\sim 32\lambda$), so that higher orders appear in the far-

field diffraction pattern; these orders are basically replicas of the main central beam radiating out of the array. Each MZI is controlled by using two thermo-optic phase shifters, integrated on top of the waveguides of the interferometer.

The free-space optical setup is schematically illustrated in Fig. 1(b). Two biconvex lenses with focal length $f = 50$ mm are used in a Fourier transforming configuration to give a collimated far field at plane P_1 , and then to transform (and hence converge) the beam back to the grating coupler array of the 2nd mesh. The far-field beam shapes are acquired using an IR camera focused on plane P_1 , making use of a beam splitter. Two fixed turning mirrors on top of the photonic chips reflect the light beam, vertically emitted by the grating couplers, to horizontal propagation.

ESTABLISHING TWO ORTHOGONAL CHANNELS AUTOMATICALLY

The two bi-diagonal meshes of MZIs in this free-space optical setup are used to establish two orthogonal communication channels between the photonic chips, making use of two automatically optimized orthogonal spatial modes (Fig. 2a). As discussed in [3], the optimization process can consist of injecting the light iteratively back and forward in the corresponding “input” WGs of meshes on both sides and setting up the rows of MZIs in the receiving mesh using a simple local feedback loop for zeroing the bottom output of each single MZI block. Here, we exploited the dithering signal technique [4] and one external PD at the corresponding output WG_i to maximize the output power.

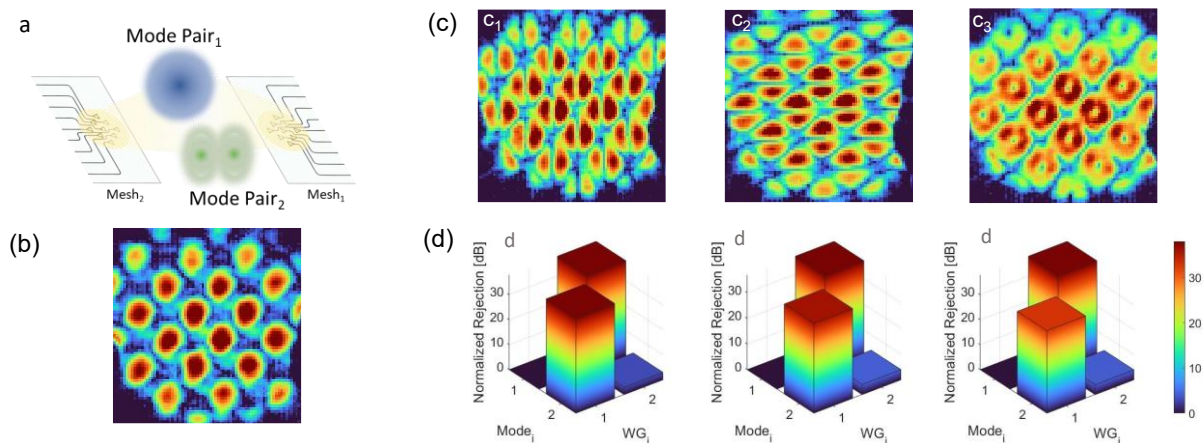


Fig. 2. (a) Establishing two orthogonal communication channels between photonic chips, (b) far-field beam acquired for automatically optimized mode of 1st rows of MZIs, (c) possible beam shapes for 2nd optimized mode, (d) bar charts showing normalized power extracted and rejected for different solutions in (c).

Figure 2(b) shows the shape of the beam that is automatically obtained using the optimization process for the 1st rows of MZIs in both meshes. This beam shape can be considered as the shape of the most strongly coupled mode (1st mode), since with this optimization method, the system automatically performs a physical implementation of multiple-channel Singular Value Decomposition (SVD) between the source and receiver spaces [3]. If we run the same process also for the 2nd rows of MZIs in both meshes, the 2nd most strongly coupled mode is found; this can have any of the beam shapes in Fig. 2(c). Each of these shapes are acquired with a slightly different condition of the physical channel (e.g., alignment of the mirrors), but if the channel is left unchanged, this power-optimized solution always converges to the same shape, which is the orthogonal mode with the second-strongest coupling strength.

Note that the same beam shapes are obtained if we run the system from “left to right” or from “right to left” by injecting the light into the corresponding WG_i of each row i of either the mesh on the left or the mesh on the right; by the symmetry of the problem, the same forms of the vector of source and receiver amplitudes are generated in both cases on both sides [5]. Mode rejection for each solution (Fig. 2c) is shown in bar charts in Fig. 2(d). As can be seen, if we consider the extracted powers normalized to the 1st mode (at WG_1 of Rx mesh), the 2nd mode can be extracted with a (slightly) lower power (at WG_2 of Rx mesh). The rejection obtained between the 1st and 2nd modes is more than 30 dB for all the beam shapes in Fig. 2(c), demonstrating the mutual orthogonality between these solutions.

To further examine the possibility of automatically establishing orthogonal channels, a partially obstructing mask is inserted in the free-space path between the two chips (Fig. 3a). This mask is a pattern of obstructing spots, each $\sim 75\%$ of the size of the main spot, and with approximately the same period as the radiation diffraction pattern (Fig. 2b). It is inserted at the far-field (Fourier) plane between the two lenses in the setup. The initial beam shapes

for 1st and 2nd modes (same as solution of Fig. 2c₃), along with the initial (reference) mode rejection are shown in Fig. 3(b₁- b₃). The mask is then aligned to partially obscure the beam spots (Fig. 3c₁-c₂). Note that after insertion of the mask, both the coupled power and the mutual rejection of the modes are degraded (bar chart of Fig. 3c₃). Now, if we perform the optimization process described previously on the MZI rows of both meshes, two (new) orthogonal channels can be obtained automatically, with almost the same initial mode power extraction and more than 30 dB of rejection, as shown in Fig. 3(d). Note that the new beam shapes, as optimized by the meshes, do not obviously belong to any particular standard family of modes, yet they are still mutually orthogonal, as shown by the good rejection.

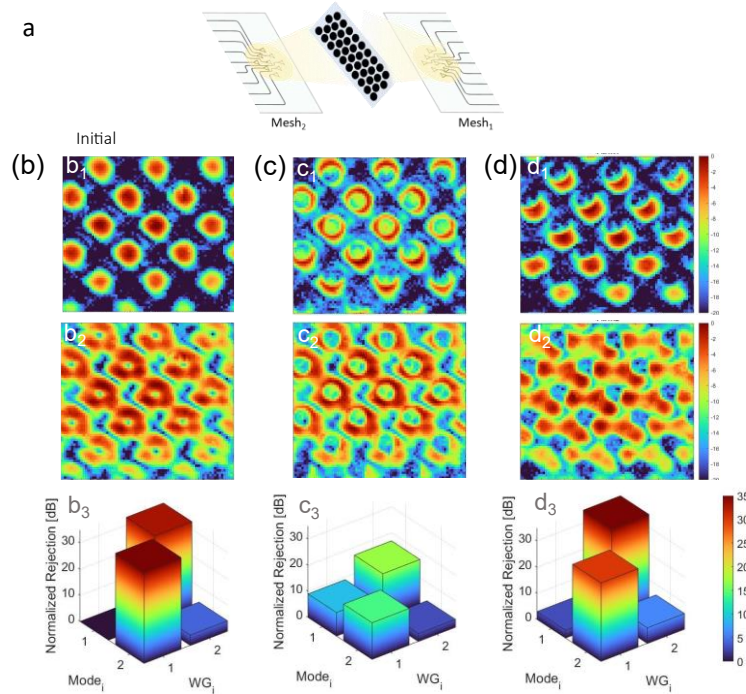


Fig. 3. (a) An obstacle made of a spatially periodic lossy mask is inserted in the FSO path between the two chips. (b) Initial beam shapes (no mask) for 1st and 2nd modes along with power extraction/rejection. (c) Inserting the mask into the FSO path gives a high degradation for both extracted power and mutual mode rejection. (d) After automatic configuration of the MZI mesh at the Tx and Rx sides, two orthogonal channels are generated automatically, with high mutual rejection.

CONCLUSION

We demonstrated automatic establishment of chip-to-chip multiple FSO links by using a pair of self-configuring MZI meshes. These automatically configure to find the best FSO communication channels, physically implementing the SVD of the wave coupling between source and receiver spaces, with neither knowledge of the transmission matrix nor calculation of the channel eigenmodes, and even after partially obstructing the path. Separation of orthogonal modes is achieved without any fundamental excess loss and more than 30 dB rejection. The approach is readily scalable to more than two orthogonal channels if architectures with more MZI rows are used.

Acknowledgements: This work was supported by the European Commission through the H2020 project SuperPixels (grant 829116), and by the Air Force Office of Scientific Research (AFOSR) under award number FA9550-17-1-0002. Part of this work was carried out at Polifab, Politecnico di Milano, Milan, Italy.

References

- [1] W. Bogaerts, D. Pérez, J. Capmany, et al., "Programmable photonic circuits," *Nature* 586, 207–216, 2020.
- [2] M. Milanizadeh, F. Toso, G. Ferrari, et al. "Coherent self-control of free-space optical beams with integrated silicon photonic meshes," *Photon. Res.* 9, 2196-2204, 2021.
- [3] D. A. B. Miller, "Establishing Optimal Wave Communication Channels Automatically," *Journal of Lightwave Technology*, vol. 31, no. 24, pp. 3987-3994, 2013
- [4] F. Zanetto, V. Grimaldi, F. Toso, et al., "Dithering-based real-time control of cascaded silicon photonic devices by means of non-invasive detectors," *IET Optoelectron.*, 15: 111-120, 2021
- [5] D. A. B. Miller, "Waves, modes, communications, and optics: a tutorial," *Adv. Opt. Photon.* 11, 679-825, 2019

6-mode Universal Photonic Processor fabricated by Femtosecond Laser Writing

(Student paper)

Ciro Pentangelo^{1,2*}, Francesco Ceccarelli^{2,1}, Simone Piacentini^{1,2}, Riccardo Albiero^{1,2}, Simone Atzeni^{1,2}, Andrea Crespi^{1,2} and Roberto Osellame^{2,1}

¹Dipartimento di Fisica - Politecnico di Milano, piazza Leonardo da Vinci 32, 20133 Milano, Italy

²Istituto di Fotonica e Nanotecnologie - Consiglio Nazionale delle Ricerche (IFN-CNR), piazza Leonardo da Vinci 32, 20133 Milano, Italy

*ciro.pentangelo@polimi.it

Universal photonic processors (UPPs) are integrated circuits able to implement arbitrary unitary transformations on a light signal. Femtosecond laser writing (FLW) is a versatile technology for the rapid and cost-effective fabrication of low-loss waveguides and micromachining in glass-based substrates. An efficient implementation of reconfigurable Mach-Zehnder interferometers (MZIs) in the FLW platform allowed the fabrication of a 6-mode UPP featuring a total of 15 MZIs in a rectangular mesh geometry.

Keywords: Femtosecond Laser Writing, Photonic Integrated Circuits, Universal Photonic Circuits, Thermo-optic Phase Shifters, Thermal Crosstalk.

INTRODUCTION

Integrated photonics provides many advantages when compared to bulk optic implementations, among them we have the ability to implement a large number of devices on the same monolithic chip while guaranteeing high stability and miniaturization. Photonic integrated circuits (PICs) enable applications in fields such as broadband optical communications and quantum information processing [1,2]. One of their main features is their reconfigurability, which is achieved through the use of thermo-optic actuators commonly referred to as thermal shifters. Thermal shifters are microheaters which induce phase shifts through the thermo-optic effect without introducing additional losses in the circuit. Reconfigurable PICs can implement a large number of different transformations on the same circuit, similarly to electronic FPGAs.

Recently, there has been a growing research interest towards the development of universal photonic processors (UPPs), which can implement any arbitrary unitary transformation on the input signal. UPPs can be obtained in a number of ways, for example through a triangular or rectangular mesh of reconfigurable MZIs [3,4]. Such interferometric meshes have been demonstrated in integrated photonics platforms such as silicon nitride [5,6], silica-on-silicon [7] and femtosecond laser writing (FLW) [8]. FLW is a versatile fabrication technique which allows the fabrication of low-loss and low-birefringence [9] waveguides (< 0.3 dB/cm in the visible and NIR) in glass-based substrates. Furthermore, FLW allows for the micro-structuring of glass, which can be exploited for the fabrication of thermal isolation trenches which have been shown to drastically reduce the power dissipation and thermal crosstalk of thermal shifters [10]. In the following we exploit this technology to demonstrate a 6-mode UPP in the rectangular mesh configuration featuring a total of 15 MZIs and 30 thermal shifters, along with 60 isolation trenches.

FABRICATION PROCESS AND PRELIMINARY CHARACTERIZATION

The waveguides of the 6-mode circuit have been written in alumino-borosilicate glass (Corning EAGLE XG) at a depth of $30\ \mu\text{m}$ and have been optimized for single-mode operation at a wavelength of $\lambda = 785\ \text{nm}$. An inter-waveguide pitch of $80\ \mu\text{m}$, bending radius of $30\ \text{mm}$ and interferometer arms long $1.5\ \text{mm}$ yield a total circuit length of around $8\ \text{cm}$, including fan-in and fan-out for coupling to standard fiber arrays with $127\ \mu\text{m}$ pitch. The final circuit (shown schematically in Fig. 1) features a total $2.7\ \text{dB}$ insertion losses. Thermal isolation trenches have been fabricated by water-assisted laser ablation [11] on either side of each thermal shifter. They measure $300\ \mu\text{m}$ in depth and $60\ \mu\text{m}$ in width.

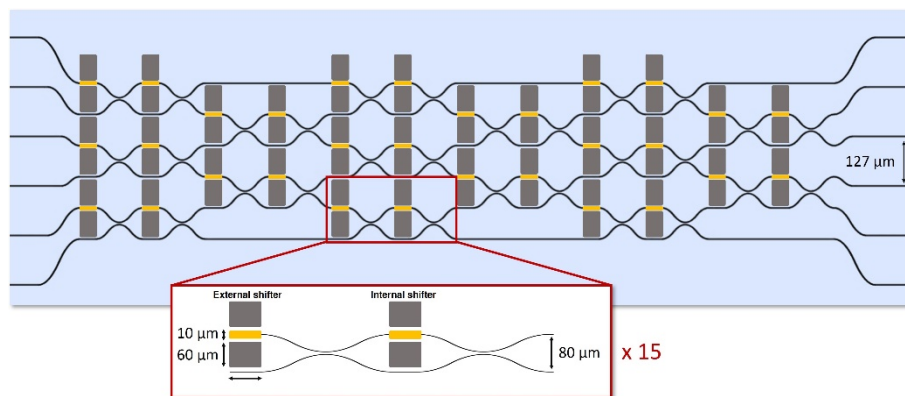


Fig. 1. Conceptual scheme of the 6-mode UPP circuit. Gray rectangles represent trenches, yellow rectangles represent thermal shifters. A single reconfigurable MZI is highlighted at the bottom, featuring two thermal shifters (external on the left, internal in the center) and two balanced directional couplers.

Finally, thermal shifters have been fabricated starting from a 100 nm thick gold film which is annealed and subsequently ablated by a femtosecond laser to form 10 μm thin and 1.5 mm long resistive strips and large conductive contact pads. A picture of the final device complete with electrical packaging is shown in Fig. 2.

The two rightmost MZIs of the circuit have been characterized in both air and vacuum to evaluate the thermal shifter performance. We investigated two parameters: power dissipation and thermal crosstalk. Power dissipation is the electrical power required to obtain a given phase shift, in particular we evaluate this factor in terms of the power $P_{2\pi}$ required for a full phase shift. Thermal crosstalk is evaluated as the phase shift induced on a static MZI at a certain distance from the actuated MZI as a percentage of the phase induced on the actuated MZI itself. At ambient pressure the power dissipation $P_{2\pi}$ is on average 32 mW, while the average crosstalk is 18%. The value of $P_{2\pi}$ decreases to 11 mW when the device is operated in a vacuum chamber at a pressure of 2.5×10^{-3} mbar, while thermal crosstalk drops to 2%. The significant improvement in performance when the device is being operated in a vacuum environment is explained by a reduction in thermal conduction through the air inside of the trenches, which can aid the transport of heat to nearby waveguides [10].

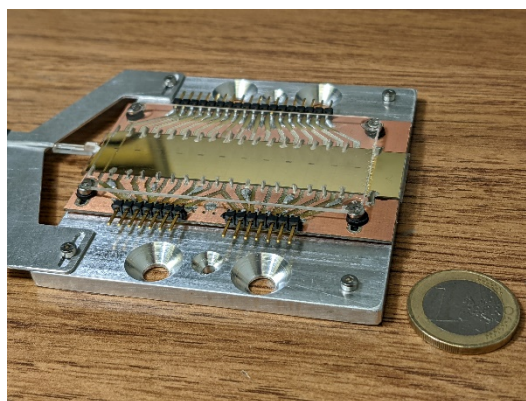


Fig. 2. Picture of the 6-mode UPP complete with electrical packaging and pigtailed fiber array at its input.

CALIBRATION AND UNITARY IMPLEMENTATION

The calibration procedure for the rectangular mesh UPP has been adapted from literature [4,7]. It is divided in two steps. First, the 15 'internal' phase shifters that control the transmissivity of each individual MZI are calibrated by sweeping the power dissipated on them, routing light in various paths through the circuit. In the second step the 'external' phase shifters are characterized by forming interferometric rings around them thanks to the previously characterized 'internal' shifters. This calibration is required due to the fact that the static phase contribution of each phase shifter is unpredictably distributed due to the fabrication process, as is the case for other platforms. Finally, we compensate crosstalk by measuring the phase shift induced by each thermal shifter on neighboring shifters on the same vertical column, neglecting thermal crosstalk between shifters on different columns. This assumption has been verified experimentally and is justified by the fact that shifter columns are millimeters apart from each other, while vertically each shifter is separated of only 160 μm from its neighbors.

A preliminary performance evaluation of the UPP has been carried out by implementing and measuring two unitaries: the identity matrix and the Pauli X^3 gate. These two measurements are shown in Fig. 3. The fidelity of these implementations has been calculated as:

$$F(M_{exp}, M) = \frac{1}{6} \text{Tr}(M_{exp}^\dagger M), \quad (1)$$

yielding 0.9968 and 0.9967 respectively for identity and Pauli X^3 .

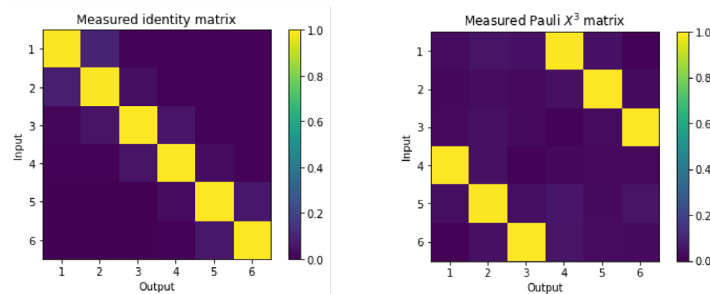


Fig. 3. Measured identity and Pauli X^3 gate implemented in the 6-mode UPP.

CONCLUSION

In this work we have presented a demonstration of a 6-mode UPP with a total of 30 thermal shifters, the largest to date in the FLW platform. The circuit features a total of 60 thermal isolation trenches which allow for a drastic reduction in both power dissipation and thermal crosstalk of the processor. Furthermore, we have presented a preliminary calibration of the device and benchmarked it by implementing two unitary matrices with state of the art fidelity. This demonstration indicates how FLW can be a valuable platform for the fabrication of UPPs.

Acknowledgements: This work is supported by the European Union's Horizon 2020 research and innovation programme under the PHOQUSING project GA no. 899544. R.O. further acknowledges funding from the European Research Council (ERC) under the European Union's Horizon 2020 research and innovation programme (project CAPABLE – Grant agreement No. 742745). A.C. and S.A. acknowledge funding by the Italian Ministry of University and Research (PRIN 2017 programme, QUSHIP project-id. 2017SRNBRK). Fabrication of the resistive heaters for the femtosecond laser-written devices was performed at PoliFAB [12], the micro and nano-fabrication facility of Politecnico di Milano. The authors would like to thank the PoliFAB staff for the valuable technical support.

References

- [1] Y. A. Vlasov, *Silicon CMOS-integrated nano-photonics for computer and data communications beyond 100G*, IEEE Commun. Mag. **50**(2), s67-s72, 2012
- [2] J. L. O'Brien et al., *Photonic quantum technologies*, Nat. Photon. **3**, 687-695, 2009
- [3] M. Reck et al., *Experimental realization of any discrete unitary operator*, Phys. Rev. Lett., **73**, 58-61, 1994
- [4] W. R. Clements et al., *Optimal design for universal multiport interferometers*, Optica **3**, 1460-1465, 2016
- [5] C. Taballione et al., *8x8 reconfigurable quantum photonic processor based on silicon nitride waveguides*, Opt. Express **27**, 26842-26857, 2019
- [6] C. Taballione et al., *A universal fully reconfigurable 12-mode quantum photonic processor*, Mater. Quantum. Technol. **1**(3), 035002, 2021
- [7] J. Carolan et al., *Universal linear optics*, Science **349**(6249), 711-716, 2015
- [8] I. V. Dyakonov et al., *Reconfigurable photonics on a glass chip*, Phys. Rev. Appl. **10**, 044048, 2018
- [9] G. Corrielli et al., *Symmetric polarization-insensitive directional couplers fabricated by femtosecond laser writing*, Opt. Express **26**, 15101-15109, 2018
- [10] F. Ceccarelli et al., *Low power reconfigurability and reduced crosstalk in integrated photonic circuits fabricated by femtosecond laser micromachining*, Laser Photonics Rev. **14**(10), 2000024, 2020
- [11] R. Murakami et al., *Water-assisted laser drilling for miniature internal thread in a glass and evaluation of its strength*, J. Laser Micro Nanoeng. **12**, 203-205, 2017
- [12] <http://www.polifab.polimi.it/>

A high-index SiON integrated photonic-electronic platform for quantum technologies

M. Ghulinyan^{1,*}, M. Bernard¹, G. Piccoli^{1,2}, M. Sanna², M. Borghi^{2,3}, S. Azzini², F. Acerbi¹, G. Paternoster¹, A. Gola¹, L. Pavesi² and G. Pucker¹

¹Sensors and Devices, Fondazione Bruno Kessler, via Sommarive, 18, Trento, 38123, Italy

²Department of Physics, University of Trento, via Sommarive, 14, Trento, 38123, Italy

³Department of Physics, University of Pavia, via Agostino Bassi, 6, 27100, 27100, Italy

* ghulinyan@fbk.eu

We present a low-loss dielectric platform based on high-refractive index silicon oxynitride (SiON) material which offers excellent characteristics for linear and non-linear optics applications in a wide range of red/near-infrared wavelengths. The SiON photonic circuitries, which include integrated photon sources and thermo-optically reconfigurable waveguide architectures are coupled directly to the Si substrate-integrated photodetectors and SPAD arrays. First devices, operating at room-temperatures, show up to 44% external quantum efficiency at 850 nm. The developed platform is the cornerstone technology of H2020 EPIQUS project, aiming to demonstrate a cheap, easy-to-use, performant Quantum Simulator based on full integration of silicon oxynitride photonics with silicon electronics.

Keywords: Silicon oxynitride, photonic-electronic integration, optical nonlinearities, photon detection

INTRODUCTION

The simulation of quantum mechanical systems using conventional computers, requires resources, which grow exponentially with the system size. Quantum Simulators (QS) – devices that operate according to the laws of quantum mechanics – are able to simulate a broad range of quantum phenomena beyond the classical computer capabilities [1]. The ascent of the Second Quantum Revolution has triggered intensive effort towards development of miniaturized, integrated quantum photonic technologies [2].

While partial integration of different functionalities required for a QS has been tested, a stand-alone quantum/classical processor has still to be realized. Sources of single photons and active control of optical qubits, the potential for source scalability in silicon [3] and silica integrated devices [4], as well as waveguide-coupled high-efficiency single photon detectors [5] have been demonstrated in the past years. Nevertheless, single photon sources and detectors, operating at room-temperatures, have not been integrated together on the same chip due to a number of technological challenges.

Within the [EPIQUS](#) project, we are developing a portable QS based on a photonic chip-integrated scalable platform, operating at ambient temperatures. The QS chip will include all necessary components – scalable sources of near-infrared (NIR) photon pairs, quantum interference photonic reconfigurable circuitries coupled to scalable arrays of single photon avalanche diodes (SPADs), analog control and readout of the QS. All these will be fully interfaced to a classical computer via specifically developed quantum codes and algorithms (Fig. 1).

RESULTS

Our quantum photonic chip is based on a low-loss (≤ 1 dB/cm) Silicon Oxynitride (SiON) platform, which operates at NIR wavelengths (750-850 nm) and enables a monolithic integration of the quantum photonic circuits with Si single photon avalanche diodes (SPADs) on the same chip.

Linear properties – The SiON material is realized via plasma-enhanced chemical vapor deposition (PECVD) at a temperature of 300 °C using SiH₄, N₂O and NH₃ gas precursors. The material has a refractive index of ~ 1.665 at 800 nm and an optical bandgap $E_g \sim 3.8$ eV ($\lambda_g \sim 325$ nm) allowing for a sufficiently high modal confinement, small footprint and low material absorption through entire VIS-NIR spectral range. The reconfigurability of SiON-based photonic circuitry relies on a moderate thermo-optical coefficient of $\frac{dn}{dT} \sim 1.8 \times 10^{-5} \text{ K}^{-1}$ [6].

Non-linear optical properties – The Kerr nonlinearity n_2 of our SiON material has been investigated by analyzing the dispersion-induced pulse broadening of ps-long laser pulses due to the phenomenon of Self-phase Modulation. The

experiments, carried out on cm-long spiral waveguides, revealed systematically increasing n_2 values from $5.5(0.4) \times 10^{-20} \text{ m}^2/\text{W}$ to $14.1(0.7) \times 10^{-20} \text{ m}^2/\text{W}$ with reducing the wavelength from 840 nm to 740 nm, in accordance with the predictions that the maximum in the nonlinear Kerr coefficient is located close to the two-photon absorption (2PA) edge at $E_g/2$ [7].

The knowledge of the linear and non-linear properties of the SiON platform enables the design of all the necessary components of the quantum photonic circuitries, from single photon sources, based on intermodal spontaneous Four Wave Mixing [8], to quantum interference circuits (Fig. 2a).

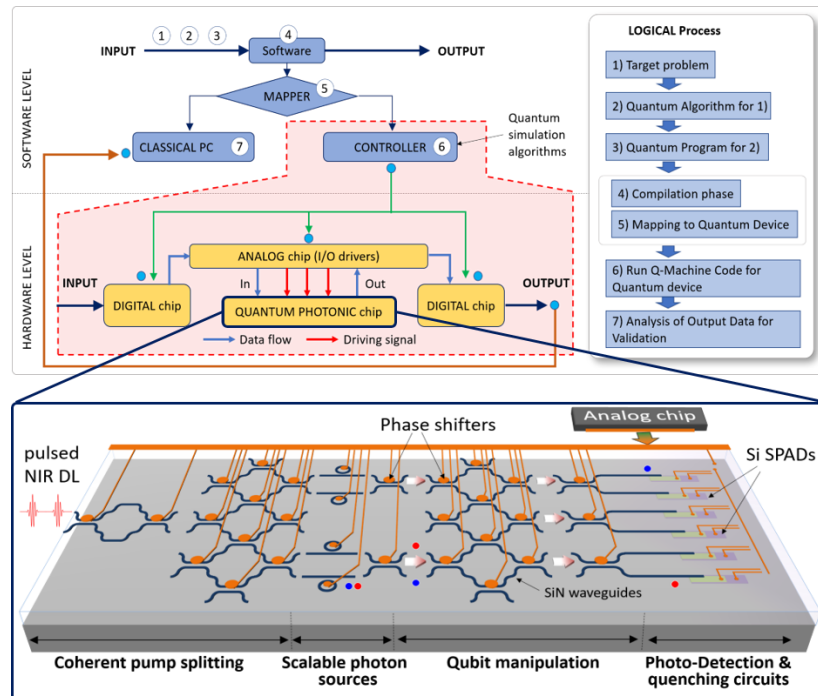


Fig. 1. The vision of EPIQUS aiming to develop a Photonic Quantum Simulator (QS), where all necessary components photon pair sources, quantum interference circuit, single photon detectors and driving electronic circuit are integrated together. User programs run via software level components (compiler, mapper and controller). The quantum hardware (photonic chip) will merge SiON-based optically transparent quantum photonic circuits with Silicon SPADs within a unique top-down technological approach in order to realize an integrated QS device.

Photonic-electronic coupling – The challenges to integrate directly single photon resolving devices with quantum photonic circuitries have been stimulated by the recent advances in quantum technologies.

Our approach to this problem consists in realizing the photonic-electronic monolithic coupling by shaping the bottom cladding of the photonic circuit into an adiabatic, shallow-angled wedge form (Fig. 2b) [9]. Far from the detector's region, light propagates within the SiON circuitry without photon loss towards the substrate (see the electromagnetic field intensity distributions in lower panels of Fig. 2b). At the vicinity of the detectors, the SiON waveguides follow the wedge-profile of the bottom cladding and approach the substrate at the photodetector locations. Here, the optical modes leak into the Silicon substrate and get absorbed within the epitaxial-Si layer. The generated electron-hole pairs are then collected efficiently through the p-n junctions.

The first fabricated devices with coupling to conventional photodetectors showed external quantum efficiencies as high as 44% against a 46% of theoretical prediction [10]. The detection characteristics of SPAD devices, coupled to SiON waveguides are currently under investigation.

We envision that the developed photonic-electronic coupling efficiency can be improved significantly upon an optimization of the current technology. Our preliminary simulations predict an improvement of the coupling efficiency up to 90% both for conventional Si photodiode and SPAD devices operating at NIR wavelengths.

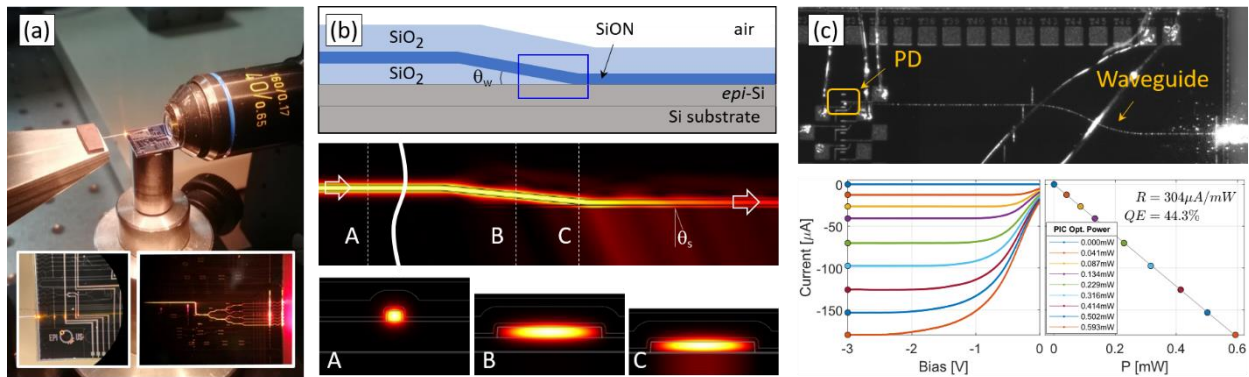


Fig. 2. (a) Optical images of the first generation of SiON-based integrated sources of entangled photon pairs. (b) The schematics of direct refractive coupling of SiON photonic circuitry to substrate-integrated Si photodiodes. (c) The generated photocurrent as a function of input optical power and the responsivity curve showing a 44% of external Quantum Efficiency of the device.

DISCUSSION

We have presented a high-refractive index silicon oxynitride platform for the realization of quantum integrated photonic architectures, operating at NIR range of wavelengths. The latter choice enables the monolithic, top-down convergence of NIR photonics with substrate-integrated Silicon photon-resolving devices, operating at ambient temperatures. These developments target to integrated quantum photonic applications based on silicon micro/nanofabrication technologies.

Acknowledgements: This work has been supported by the European Commission under GA No. 899368. We acknowledge the support of Q@TN, the joint laboratory between University of Trento, FBK – Fondazione Bruno Kessler, INFN – National Institute for Nuclear Physics and CNR – National Research Council.

References

- [1] A. Aspuru-Guzik and P. Walther, "Photonic quantum simulators." *Nature Physics*, vol. 8, no. 4, pp. 285-291, 2012
- [2] A. de Touzalin, C. Marcus, F. Heijman, I. Cirac, R. Murray, and T. Calarco, "Quantum Manifesto for Quantum Technologies", <http://guoep.eu/manifesto>
- [3] D. Grassani *et al.*, "Micrometer-scale integrated silicon source of time-energy entangled photons." *Optica*, vol. 2, no. 2, pp. 88-94, 2015; J.W. Silverstone *et al.*, "Qubit entanglement between ring-resonator photon-pair sources on a silicon chip." *Nature Communications*, vol. 6, no.1, pp. 1-7, 2015; Ch. Ma *et al.*, "Silicon photonic entangled photon-pair and heralded single photon generation with CAR > 12,000 and $g(2)(0) < 0.006$." *Optics Express*, vol. 25, no. 26, pp. 32995-33006, 2017.
- [4] Justin B. Spring *et al.*, "Chip-based array of near-identical, pure, heralded single-photon sources." *Optica*, vol. 4, no. 1, pp. 90-96, 2017
- [5] W.H. Pernice *et al.*, "High-speed and high-efficiency travelling wave single-photon detectors embedded in nanophotonic circuits." *Nature Communications*, vol. 3, no. 1, pp. 1-10, 2012
- [6] A. Trenti *et al.*, "Thermo-optic coefficient and nonlinear refractive index of silicon oxynitride waveguides." *AIP Advances*, vol. 8, no. 2, p. 025311, 2018
- [7] M. Sheik-Bahae *et al.*, "Dispersion and band-gap scaling of the electronic Kerr effect in solids associated with two-photon absorption." *Physical Review Letters*, vol. 65, no. 1, pp. 96-99, 1990
- [8] S. Signorini *et al.*, "Intermodal four-wave mixing in silicon waveguides." *Photonics Research*, vol. 6, no. 8, pp. 805-814, 2018
- [9] M. Ghulinyan *et al.*, "Formation of Mach angle profiles during wet etching of silica and silicon nitride materials." *Applied Surface Science*, vol. 359, pp. 679-686, 2015
- [10] M. Bernard *et al.*, "Top-down convergence of near-infrared photonics with silicon substrate-integrated electronics." *Optica*, vol. 8, no. 11, pp. 1363-1364, 2021

A Universal 20-mode Quantum Photonic Processor

(Student paper)

Caterina Taballione^{1,*}, Malaquias Correa Anguita², Michiel de Goede¹, Pim Venderbosch¹, Ben Kassenberg¹, Henk Snijders¹, Narasimhan Kannan¹, Devin Smith¹, Jorn Epping¹, Reinier van der Meer², Pepijn W. H. Pinkse², Hans van den Vlekkert¹ and Jelmer J. Renema^{1,2}

¹QuiX Quantum BV, 7521 AN Enschede, The Netherlands

²Mesa+ Institute for Nanotechnology, University of Twente, 7522 NB Enschede, The Netherlands

* corresponding author e-mail

Universal, phase-stable, reconfigurable quantum photonic processors enable manipulation of photonic quantum states and are one of the main components of photonic quantum computers in various architectures. In this paper, we report the realization of the largest quantum photonic processor to date.

Keywords: *quantum, reconfigurable photonics, silicon nitride*

INTRODUCTION

With the recent experimental results demonstrating a quantum advantage^{1,2}, photonics has become one of the most attractive approaches to quantum computing. The strengths of photonics as quantum computing platform are, for example, its inherent low decoherence due to the weak interaction of quantum states of light with their environment and the operation at room temperature. Photonic quantum computing can also exploit the high maturity of existing classical integrated photonics technologies making it a scalable and phase-stable approach to large-scale quantum computing.

Quantum computational models based on photonics range from non-universal approaches, such as Boson Sampling³, which forms the basis of the recent quantum advantage experiments^{1,2}, to universal ones based on a variety of different encodings⁴⁻⁶. Applications of non-universal photonic quantum computing have been proposed, such as quantum chemistry^{7,8} and graph properties⁹.

A quantum photonic processor^{7,10-12}, or linear optical interferometer, is one of the essential components of photonic quantum computing and is the main player in applications such as quantum neural networks¹³, quantum metrology¹⁴, PUFs¹⁵, witnesses of bosonic interference^{16,17} and for benchmarking multi-photon light sources^{18,19}.

Of the available integrated platforms, silicon nitride (Si₃N₄) is the most promising platform for photonic quantum computing. It provides an optimal combination of low loss and high optical mode confinement²⁰, enabling the scaling up of low-loss fully-reconfigurable linear optical interferometers for quantum computing and information processing.

In this paper, we present the largest universal quantum photonic processor to date, with 20 input/output modes. Our processor is based on silicon nitride waveguides. The device has losses of 2.9 dB/mode and enables arbitrary linear optical transformations, making it compatible with all linear optical models of quantum computation. We validate the processor performances over more than 1000 experiments showing high-fidelity operations.

RESULTS

Our 20-mode quantum photonic processor consists of three parts: the Si₃N₄ photonic chip, the peripheral system which includes the control electronics, and the dedicated control software¹².

The Si₃N₄ photonic chip (Fig. 1a) contains a total of 380 thermo-optic tunable elements, arranged in a universal square interferometer²¹ where the unit cell comprises a tunable beam splitter (TBS) followed by a phase shifter (PS). Propagation losses as low as 0.07 dB/cm at 1562 nm are measured across the entire photonic chip, obtained by a higher-temperature annealing process compared to our previous chip¹². The peripheral system comprises the control electronics and an active cooling module. The thermo-optic tunable elements can be switched at kHz rate²⁰, setting the limit for the switching speed between different configurations of the processor. To precisely control the temperature of the photonic chip, it is actively cooled. The cooling module consists of a Peltier element attached

to a water-cooling module providing a maximum heat reduction rate of 200 W. The dedicated control software performs both the decomposition of any unitary matrix transformation into the phase settings of each unit cell and their assignment to the corresponding tunable elements. The control software takes also into account the imperfections of the processor, such as crosstalk of individual tunable elements and compensates for those.

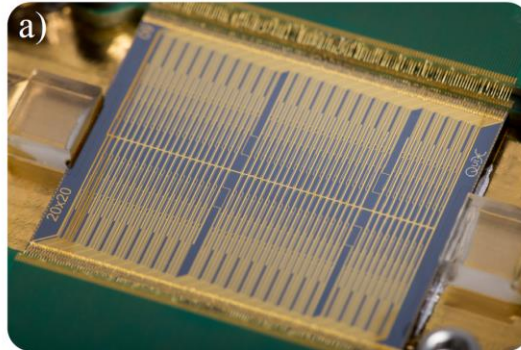


Figure 1 Photograph of the 20-mode processor chip 22×30 mm. The chip is optically packaged to an input/output fiber array and it is wire-bonded to the control PCB enabling the addressing of each individual tunable element.

The characterization of the 380 tunable elements shows that they all have a phase tuning range exceeding 2π , allowing for full control of the unitary transformation implemented within the interferometer. The insertion loss of the photonic processor is measured to be 2.9 ± 0.2 dB: this is the overall loss experienced by light going in and out of the processor, from input to output fiber, through all the tunable MZIs and phase shifters. Coupling losses are measured at 0.9 dB/facet, which is derived from measuring the insertion loss on the on-chip alignment loops, i.e., paths consisting of a very short length section with negligible propagation loss which therefore only have fiber-to-chip coupling losses.

We verify the reconfigurability and control of the processor by generating and implementing 190 permutation and 1000 Haar-random matrices on the device. For each input mode of each matrix, the output intensity distribution is measured, from which a fidelity measure $F = \frac{1}{20} (|U^+| \cdot |U_{exp}|)$ of the unitary optical transformations on the input light is determined. We obtain fidelities as high as $F = (99.5 \pm 0.2)\%$ and $F = (97.4 \pm 0.5)\%$ for the permutations and the Haar-random transformations, respectively (see also Fig.2 a and b).

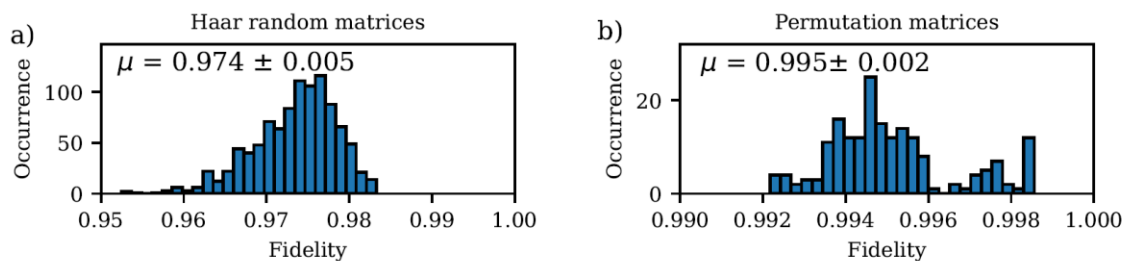


Figure 2 Distribution of the measured amplitude fidelities for, respectively, 1000 Haar-random matrices (a) of average fidelity $(97.4 \pm 0.5)\%$ and for 190 Permutation matrices (b) of average fidelity $(99.5 \pm 0.2)\%$.

Measuring the visibility of quantum interference²² at every location on the processor provides quantum validation of the device. The photons are then injected into pairs of input modes are routed to interfere at each on-chip TBS, set to a 50:50 splitting ratio. The output modes are connected to superconducting nanowire single-photon detectors (SNSPDs), whose coincidence rate is measured using a standard time-tagger. To route the two photons to every on-chip TBS, and to the connected outputs, the entire interferometer is used. TBSs are set to full reflection or transmission to create optical paths, which contain no intersections other than the TBS of interest. The spatial distribution of the 190 HOM visibilities over the rows and columns of the network, as shown in Fig. 3, is quite random, confirming that there are no systematic errors within the processor. Furthermore, the visibility of the HOM interference appears to be limited by the quality of the source used for the characterization.

In conclusion, we have demonstrated a record universal quantum photonic processor with 20 input/output modes, which is the largest processor to date. Thanks to its low loss and high-fidelity operations, it locates itself at the top of all ever demonstrated universal quantum photonic processors.

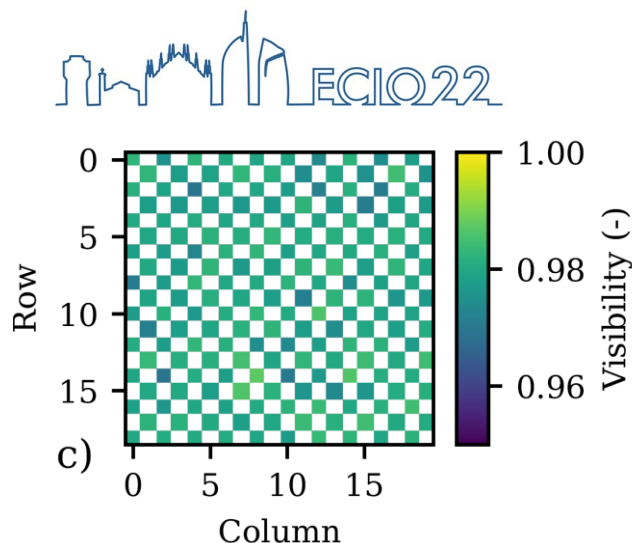


Figure 3 HOM visibilities of all TBS for each network row and column. The checkerboard pattern reflects the alternating pairwise coupling of neighbouring channels as layed out in Fig. 1b.

Acknowledgements: Funding is acknowledged from the Nederlandse Organisatie voor Wetenschappelijk Onderzoek (NWO) via QuantERA QUOMPLEX (Grant No. 680.91.037), NWA (Grant No.40017607), and Veni (grant No. 016.Veni.192.121).

References

1. Zhong, H.-S. *et al.* Phase-Programmable Gaussian Boson Sampling Using Stimulated Squeezed Light. *Phys. Rev. Lett.* **127**, 180502 (2021).
2. Zhong, H.-S. *et al.* Quantum computational advantage using photons. *Science* **370**, 1460–1463 (2020).
3. Aaronson, S. & Arkhipov, A. The Computational Complexity of Linear Optics. in *Proceedings of the Forty-Third Annual ACM Symposium on Theory of Computing* 333–342 (Association for Computing Machinery, 2011). doi:10.1145/1993636.1993682.
4. Kok, P. *et al.* Linear optical quantum computing with photonic qubits. *Rev. Mod. Phys.* **79**, 135–174 (2007).
5. Takeda, S. & Furusawa, A. Toward large-scale fault-tolerant universal photonic quantum computing. *APL Photonics* **4**, 060902 (2019).
6. Larsen, M. V., Guo, X., Breum, C. R., Neergaard-Nielsen, J. S. & Andersen, U. L. Deterministic multi-mode gates on a scalable photonic quantum computing platform. *Nature Physics* **17**, 1018–1023 (2021).
7. Sparrow, C. *et al.* Simulating the vibrational quantum dynamics of molecules using photonics. *Nature* **557**, 660–667 (2018).
8. Banci, L., Fingerhuth, M., Babej, T., Ing, C. & Arrazola, J. M. Molecular docking with Gaussian Boson Sampling. *Science Advances* **6**, eaax1950 (2020).
9. Bromley, T. R. *et al.* Applications of Near-Term Photonic Quantum Computers: Software and Algorithms. *arXiv:1912.07634* (2019).
10. Carolan, J. *et al.* Universal linear optics. *Science* **349**, 711 (2015).
11. Harris, N. C. *et al.* Quantum transport simulations in a programmable nanophotonic processor. *Nature Photonics* **11**, 447–452 (2017).
12. Taballione, C. *et al.* A universal fully reconfigurable 12-mode quantum photonic processor. *Materials for Quantum Technology* **1**, 035002 (2021).
13. Steinbrecher, G. R., Olson, J. P., Englund, D. & Carolan, J. Quantum optical neural networks. *npj Quantum Information* **5**, 60 (2019).
14. Matthews, J. C. *et al.* Towards practical quantum metrology with photon counting. *npj Quantum Information* **2**, 16023 (2016).
15. Smith, A. M. & Jacinto, H. S. Reconfigurable Integrated Optical Interferometer Network-Based Physically Unclonable Function. *J. Lightwave Technol.* **38**, 4599–4606 (2020).
16. van der Meer, R. *et al.* Experimental demonstration of an efficient, semi-device-independent photonic indistinguishability witness. *arXiv [quant-ph]* (2021).
17. Brod, D. J. *et al.* Witnessing Genuine Multiphoton Indistinguishability. *Phys. Rev. Lett.* **122**, 063602 (2019).
18. Tiedau, J., Engelkemeier, M., Brecht, B., Sperling, J. & Silberhorn, C. Statistical Benchmarking of Scalable Photonic Quantum Systems. *Phys. Rev. Lett.* **126**, 023601 (2021).
19. Pont, M. *et al.* Quantifying n-photon indistinguishability with a cyclic integrated interferometer. *arXiv [quant-ph]* (2022).
20. C. G. H. Roeloffzen *et al.* Low-Loss Si₃N₄ TriPLeX Optical Waveguides: Technology and Applications Overview. *IEEE Journal of Selected Topics in Quantum Electronics* **24**, 1–21 (2018).
21. Clements, W. R., Humphreys, P. C., Metcalf, B. J., Kolthammer, W. S. & Walmsley, I. A. Optimal design for universal multiport interferometers. *Optica* **3**, 1460–1465 (2016).
22. Hong, C. K., Ou, Z. Y. & Mandel, L. Measurement of subpicosecond time intervals between two photons by interference. *Phys. Rev. Lett.* **59**, 2044–2046 (1987).

Integrated distributed feedback (DFB) perovskite lasers in SiN waveguide platform

(Student paper)

Federico Fabrizi^{1,2}, Piotr Cegielski¹, Manuel Runkel³, Saeed Goudarzi², Cedric Kreuzel³, Bartos Chmielak¹, Lyudmila Staroduptceva^{1,2}, Dmitry Dirin⁴, Viktoriia Morad⁴, Maksym Kovalenko⁴, Thomas Riedl³, Max Lemme^{1,2}

¹AMO GmbH, Otto-Blumenthal-Straße 25, Aachen, 52074, Germany

²RWTH Aachen University, Templergraben 55, Aachen, 52062, Germany

³Bergische Universität Wuppertal, Gaußstraße 20, Wuppertal, 42119, Germany

⁴ETH Zürich, Vladimir-Prelog-Weg 1-5/10, Zürich, 8093, Switzerland

* fabrizi@amo.de

In this work we present first-order distributed feedback (DFB) lasers based on solution processed CsPbBr₃ perovskite thin films and FAPbBr₃ nanocrystals integrated into silicon nitride waveguide platform.

Keywords: On-chip laser, perovskite, integrated photonic

INTRODUCTION

Lead halide perovskite thin films and nanocrystals are solution processed semiconductors promising for integration of lasers into silicon nitride nanophotonic circuits [1]. Unlike established compound semiconductors, perovskites do not require expensive epitaxy growth processes at high temperatures on crystalline substrates with matching lattice constants [2] or bonding to the waveguide wafer [3] and can emit in the so called green-orange gap [4], where III-V emitters are not available. Perovskites can be deposited by spin coating and annealing at temperature of only 100° C [5]. This makes them a promising material for on-chip laser integration. Perovskites, however, have refractive indices much higher than that of typical waveguide materials such as SiN. This makes it very difficult to extract light from perovskite lasers into such waveguides in a well-controlled way. In this work, this problem is addressed by using SiN waveguides interacting with the perovskite gain medium via evanescent field instead of using perovskite both for waveguiding and light amplification ([1], [6]).

LASER DESIGN

The design of the integrated perovskite laser is presented in Fig. 1. Two versions of the laser have been designed and fabricated with different laser gain media: I) based on a 30 nm thick film of FAPbBr₃ nanocrystals (Fig. 1(a)) and II) based on approx. 90 nm thick film of CsPbBr₃ (Fig. 1(b)). The distributed feedback (DFB) laser consists of a 200 nm SiN rib waveguide, with a quarter wavelength shifted (QWS) first order grating structure etched directly into the waveguide as shown in Fig. 1 (c). Having QWS first- order grating facilitates single mode emission [7]. Refractive index of halide perovskites ($n=2.3-2.6$) is higher than that of SiN ($n=2$), therefore the cross-section of SiN waveguide has been chosen to maximize the effective refractive index of the waveguide mode. This combined with the low thickness of the perovskite film ensures that the mode is guided in the SiN and that the interaction with perovskite occurs via the evanescent field of that mode. For the film thickness of 30 nm the mode overlap between SiN waveguide mode and the perovskite film is 2.6 % (Fig. 1(a)) and in case of 90 nm thick film it is 24 % (Fig. 1 (b)). The grating periods are varied from 136 nm to 141 nm. The grating etch depth is only 25 nm, to obtain low scattering losses in the distributed resonator.

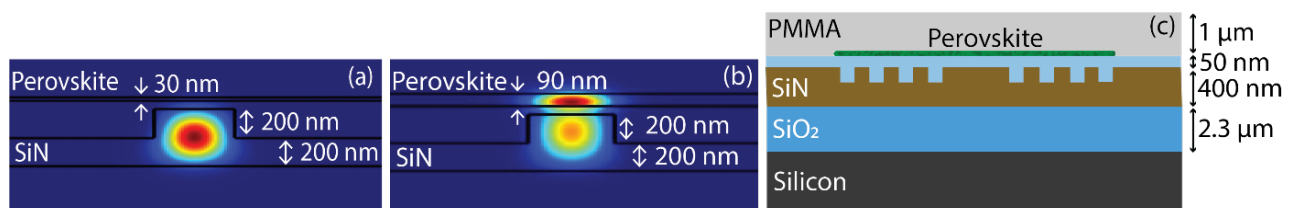


Fig. 1. (a) and (b) TE waveguide mode with perovskite film thickness of 30 nm and 90 nm respectively. (c) Side-view of the DFB perovskite laser.

FABRICATION

PICs (photonic integrated circuits) were fabricated using 6" silicon handle wafers with 2.3 μm of thermally grown SiO_2 . 200 nm of Si_3N_4 was deposited by low-pressure chemical vapor deposition (LPCVD). Next, the gratings were patterned using electron beam lithography (Vistec EBPG 5200) and dry etching. This step was performed first on perfectly flat wafers to ensure high quality of the lithography process. Next, the waveguides were patterned using projection lithography (Canon FPA 3000 i5r i-line stepper) and dry etching. This was followed by the deposition of 1 μm of LTO (low temperature oxide) in an LPCVD furnace. Dry etching was used to planarize the layer and to maintain only 50 nm of SiO_2 on top of the waveguides. This step was followed by dicing of wafers into individual chips. A CsPbBr_3 solution was prepared, and spin coated on the chips. The as-deposited layer was recrystallized by a thermal imprint process using a flat silicon stamp [8]. The resulting flattened perovskite thin film was patterned by photolithography and dry etching by the process reported in [6] (Fig. 2(a)). Finally, perovskite was encapsulated by 1 μm thick layer of PMMA. Finished devices are shown in Fig. 2(b). For the fabrication of the nanocrystal integrated laser, a photoresist mask with openings in the active device area was patterned. Next, FAPbBr_3 nanocrystals were spin coated onto the chips using a solvent orthogonal to the photoresist. This was followed by dissolving the photoresist in a solvent orthogonal to the nanocrystals, which lifted the excess nanocrystals preserving them only in the active areas of the DFB lasers. Finally, perovskite was encapsulated by 1 μm thick layer of PMMA.

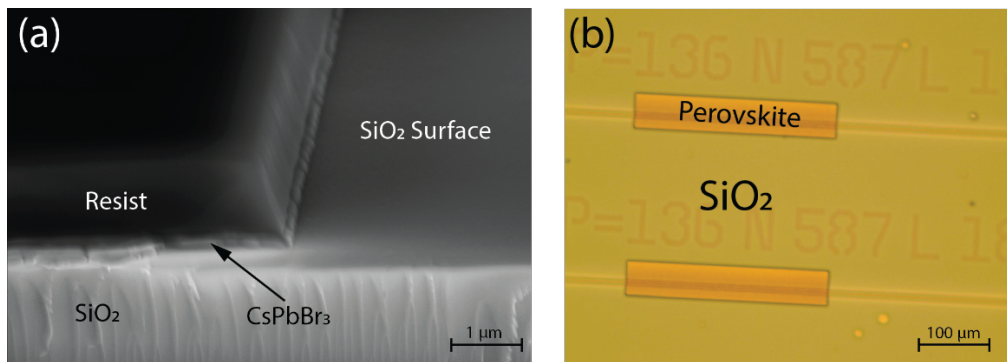


Fig. 2. (a) Optical microscope image of DFB lasers after the perovskite etching process and the resist stripping. The perovskite layer remains only on top of the grating forming the laser's active area. (b) SEM cross-section picture of the etched CsPbBr_3 film before resist stripping.

LASER CHARACTERIZATION

The schematic illustration of the characterization setup is illustrated in Figure 3. The integrated lasers were pumped from the top with 300 ps laser pulses at a wavelength of 355 nm and 1 kHz repetition rate, which were focused onto the devices to a spot with a diameter of 0.7 mm. The PICs were cleaved in order to obtain high quality facets needed for edge coupling of the optical output. Laser emission was measured by an optical fiber aligned with the SiN output waveguide, which was connected with a spectrometer.

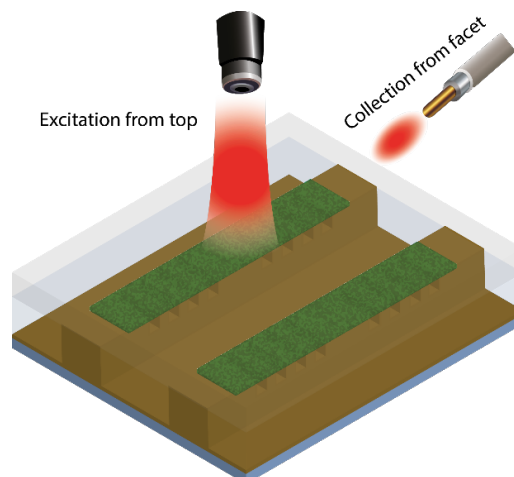


Fig. 3. Schematic illustration of the measurement setup.

At low excitation fluence a weak photoluminescence signal was observed. When the pump power was increased to $195 \mu\text{J}/\text{cm}^2$ for the nanocrystal lasers and $775 \mu\text{J}/\text{cm}^2$ for CsPbBr₃ lasers a single narrow peak appeared in the spectra (Fig. 4 (a)-(b)) with a threshold in the emission intensity vs pump pulse fluence curve (Fig. 4(a)-(b) insets), which is a clear sign of lasing. The lower threshold of of nanocrystal based lasers results from better morphology of the nanocrystal film and higher quantum yield (95%) compared to the CsPbBr₃ film (68%, [8]).

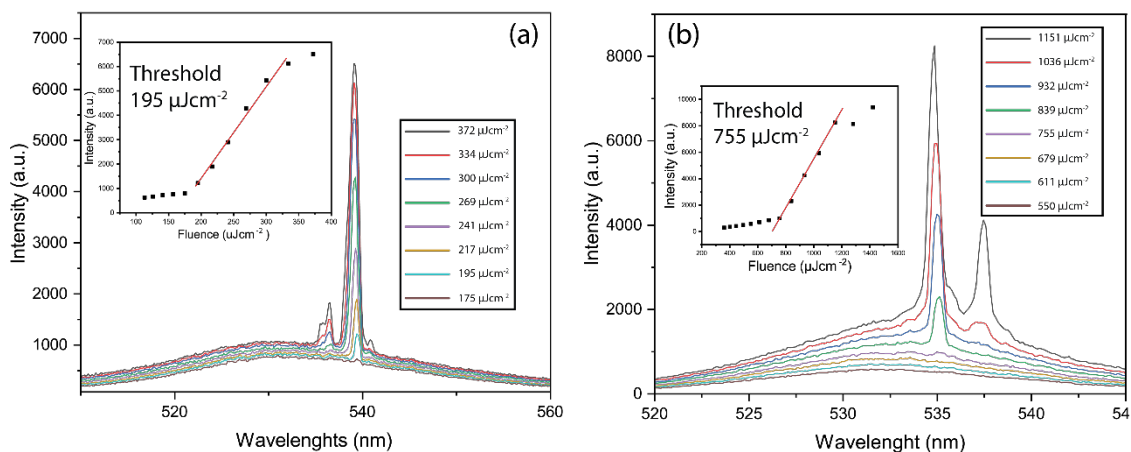


Fig. 3. (a) Spectra of the laser with FAPbBr₃ nanocrystal. (b) Spectra of the laser with CsPbBr₃ thin film.

CONCLUSIONS

In summary, the first perovskite first-order grating DFB lasers integrated into silicon nitride waveguide platform have been demonstrated. In these devices, light is guided in SiN and amplified by evanescent field interaction with perovskite medium. This gives much better control over the spectral characteristics of emission and enables output power scaling compared to previously reported integrated perovskite lasers, in which the perovskite was acting both as the active medium and the resonator ([1], [6]). Because of that, this work is an important step towards development of perovskite laser diodes relevant for commercial use.

Acknowledgements: European Union's Horizon 2020 research and innovation programme under the Marie Skłodowska-Curie grant agreement No 956270 (PERSEPHONE) and LeitmarktAgentur.NRW grant PerovskET (EFRE-0801 508).

References

- [1] P. J. Cegielski et al., "Integrated perovskite lasers on a silicon nitride waveguide platform by cost-effective high throughput fabrication," *Opt. Express*, vol. 25, no. 12, p. 13199, 2017.
- [2] K. E. Moselund et al., "Monolithic integration of III-V nanostructures for electronic and photonic applications," in *Low-Dimensional Materials and Devices*, p. 19, 2017.
- [3] N. Daix et al., "Towards large size substrates for III-V co-integration made by direct wafer bonding on Si," *APL Mater.*, vol. 2, no. 8, 2014.
- [4] T. Langer et al., "Origin of the "green gap": Increasing nonradiative recombination in indium-rich GaInN/GaN quantum well structures," *Phys. Status Solidi C*, 8: 2170-2172, 2011.
- [5] N. J. Jeon, J. H. Noh, Y. C. Kim, W. S. Yang, S. Ryu, and S. Il Seok, "Solvent engineering for high-performance inorganic-organic hybrid perovskite solar cells," *Nat. Mater.*, vol. 13, no. July, pp. 1-7, 2014.
- [6] P. J. Cegielski et al., "Monolithically Integrated Perovskite Semiconductor Lasers on Silicon Photonic Chips by Scalable Top-Down Fabrication," *Nano Letters* 18 (11), 6915-6923, 2018.
- [7] S. Wang, "Principles of distributed feedback and distributed Bragg-reflector lasers," *IEEE J. Quantum Electron.*, 10, 413-427, 1974.
- [8] N. Pourdavoud et al., "Room-Temperature Stimulated Emission and Lasing in Recrystallized Cesium Lead Bromide Perovskite Thin Films," *Adv. Material*, 31, 1903717, 2019.

TiO₂ channel waveguides with 0.5 dB/cm propagation losses

(Student paper)

A. Aguirre Fontenla¹, W.A.P.M. Hendriks¹, M. Dijkstra¹, and S.M. García-Blanco^{1*}

¹Integrated Optical Systems, University of Twente, P.O. 217, 7550 AE, Enschede, Netherlands

* s.m.garciablanca@utwente.nl

Scattering represents a major contribution to the optical propagation losses of channel waveguides. By optimization of the reactive sputtering deposition process, volume scattering can be minimized. In this work, we focus on the reduction of surface scattering by applying a chemical mechanical polishing step following reactive sputter deposition of TiO₂ layers. Propagation losses below 0.1 dB/cm at 980 nm of wavelength were experimentally characterized for TiO₂ slabs on oxidized silicon wafers. The propagation loss increases to 0.5 dB/cm at 1550 nm of wavelength for fully etched channel waveguides. Such low propagation loss paves the way for the utilization of TiO₂ in advanced integrated photonics circuits.

Keywords: Titanium Dioxide, Amorphous, Chemical Mechanical Polish, Optical Propagation Loss, Reactive Sputtering

INTRODUCTION

TiO₂ is a promising material for integrated photonics. Its high linear (i.e., 2.3 at 633 nm [1]) and non-linear (i.e., 2.3×10^{-18} m²/W [2][3]) refractive indices together with its negative dn/dT [4] and the possibility of doping with rare-earth ions [5] make TiO₂ very interesting for the realization of non-linear, athermal and/or active integrated optical devices, in combination with more established platforms such as Si₃N₄ [6] and Al₂O₃ [7]. Four wave mixing (FWM) [8] [9] [10], supercontinuum generation [11] and athermal devices [12][13][14] have been recently demonstrated in TiO₂ waveguides.

However, high propagation losses (~3-8 dB/cm at 1550 nm [9][11][13][15]) have prevented TiO₂ from reaching mainstream applications. Both absorption and scattering losses contribute to the final performance of the device. TiO₂ exhibits a bandgap of 3 eV [16], which leads to optical transparency down to visible wavelengths. Absorption in the material can originate from insufficient oxygen in the layer [17] and the incorporation of hydrogen bonds, which introduce absorption bands at different locations in the near-IR. Optimization of the reactive sputtering deposition process leads to layers where the main contributor to losses is surface scattering [18][19].

In this work, we introduce a chemical mechanical polishing (CMP) step after reactive sputter deposition of the TiO₂ layers to reduce the effect of surface scattering on the propagation losses. A reduction in the propagation loss of ~0.3 dB/cm is observed at 978 nm of wavelength in the layers studied, with losses below 0.1 dB/cm at 978 nm on a 131 nm thick TiO₂ slab. Losses after reactive ion etching of the channel waveguides increased by ~0.2 dB/cm for a 277 nm thick polished waveguide.

RESULTS

Two TiO₂ thin films of different thicknesses (i.e., wafers 20211014-A, and 20211014-B) were deposited by DC reactive sputtering in the MESA+ Nanolab TCOater sputtering system. During both deposition processes, the process pressure was kept at 6E-3 mBar and the base pressure at 1E-6 mBar. The temperature of the substrate during the deposition was 25 C. The substrate was rotated at 5 rpm. Gas flows of 80 sccm of argon and 9.8 sccm and 9.6 sccm of oxygen for wafers 20211014-A and 20211014-B respectively, which lead to a relative discharge voltage of 97.5% [17][18], were added to the sputtering chamber. A DC power of 500 W was applied to the titanium target. The thickness of the samples was characterized by ellipsometry. Wafer 20211014-A had an as-deposited thickness of 152 nm while the thickness of wafer 20211014-B was 291 nm. The surface roughness of the as-deposited wafers was characterized by atomic force microscopy (AFM). The two deposited wafers exhibited a surface roughness of 1.3 nm and 1.5 nm RMS respectively after deposition. Table 1 shows a summary of the characterization data of the two deposited wafers.

	Sample #	Thickness	Roughness	Loss@978 nm
Unpolished	20211014-A	152 nm	1.4 nm	0.2±0.1 dB/cm
Unpolished	20211014-B	291 nm	1.6 nm	0.7±0.4 dB/cm

Polished	20211014-A	131 nm	0.3 nm	-----
Polished	20211014-B	277 nm	0.3 nm	0.4±0.4 dB/cm

Table 1. Thickness, roughness and optical propagation loss of the two wafers of this study before and after the CMP step.

To reduce the roughness of the films and improve the optical propagation losses, we developed a chemical mechanical polishing process on the thin films using a Mecapol E460 CMP instrument. A solution of Semi Sperse 25 (SS25) slurry in 1 to 2 ratio with DI water with silica nanoparticles of 20 nm diameter was utilized. The pH was controlled to be 7. The details of the process are summarized in Table 2. As shown in Table 1, the surface roughness of the thicker as-deposited TiO₂ layer (20211014-B) was higher than that of the thin wafer (20211014-A). Such increase of RMS roughness with thickness is expected. After polishing, the RMS roughness of both wafers is drastically reduced to ~0.3 nm. Figure 1(left) shows the AFM images of the two wafers before and after CMP step.

Step	Duration	Pad Rotation Speed	Polishing head Rotation Speed	Polishing head Pressure
1. Landing	0 sec.	55 rpm	55 rpm	0.40 mbar
2. Polishing	30 sec.	55 rpm	55 rpm	0.50 mbar
3. Rinsing	60 sec.	55 rpm	55 rpm	0.40 mbar

Table 2. Chemical mechanical polishing process steps at the Mecapol E460 for TiO₂ thin films. A solution of Semi Sperse 25 (SS25) slurry in 1 to 2 ratio with DI water was utilized.

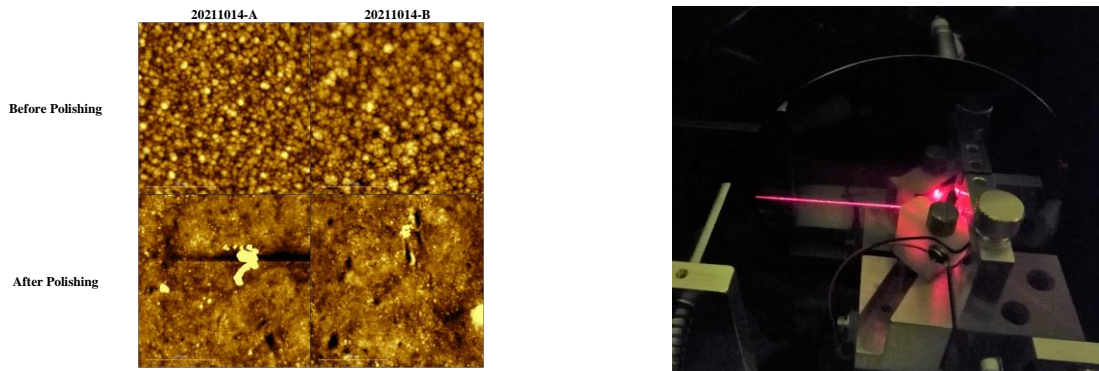


Figure 1. Image of the AFM scans at the center of the two wafers(20211014-A and 20211014-B) before and after CMP (Left); Light strike propagation at 633 nm. Wafer 20211014-B before polishing (right) showing propagation till the end of the wafer.

The propagation losses of the films before and after polishing were measured using a commercial prism coupler instrument (Metricon 2010/M) with a fiber-based propagation loss measurement module. Figure 1(right) shows the light strike at 633 nm as it propagates through the length of the 20211014-B wafer (before polishing). Figure 2 shows the intensity decay of the light strike (978 nm of wavelength) detected by the fiber before and after polishing. By fitting the intensity decay with an exponential model, a value for the propagation losses can be obtained and are summarized in Table 1. In both cases, the propagation losses decreased by ~0.3 dB/cm upon polishing. The thicker TiO₂ layer exhibits higher losses even after polishing, when a similar surface roughness is observed. This effect is attributed to the structure of the TiO₂ during the growth of a thicker layer, as reported by us in an earlier work [17].

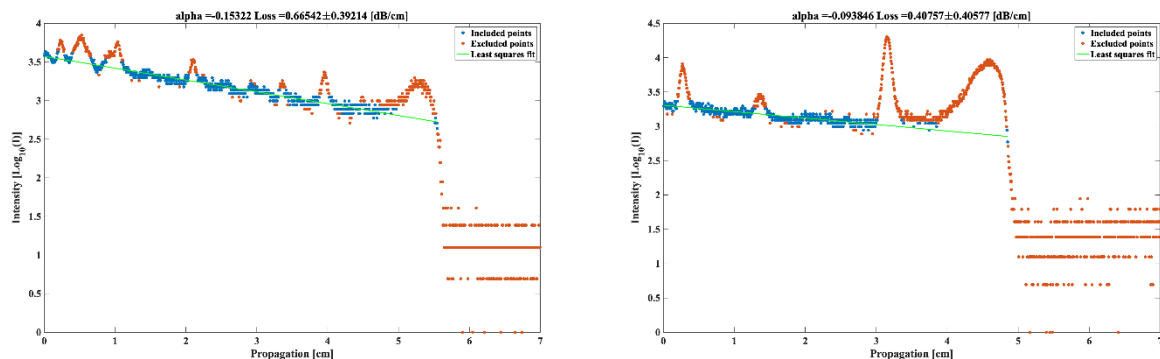


Figure 2. Metricon intensity plot of the scattered light from the light strike as a function of propagation distance for wafer 20211014-B before (left) and after (right) CMP process. The propagation losses extracted from the fit are shown as well as the data points included in the fit. Measurement wavelength 978 nm.

Microring resonator devices with coupling gaps varying between 300 nm and 700 nm and channel waveguides of width 1.1 μm were patterned by electron-beam lithography and reactive ion etching on the polished wafer 20211014-B. A 1 μm thick cladding of PMMA was then deposited over the singulated chips for characterization. The same characterization setup as described in more detail in [19] was utilized, which consists of a tunable laser source around 1550 nm (i.e., Agilent 8164B) and a PM500 nano-positioning stage. Details on how to extract the propagation losses from the measured microring resonator resonances are given in [19]. Using this methodology, propagation losses of ~ 0.5 dB/cm were measured on waveguides of cross-section 277 nm \times 1.1 μm at a wavelength of 1550 nm. Such losses are comparable to the propagation losses on other integrated photonic platforms and therefore renders the TiO₂ technology as useful platform for the realization of more complex integrated photonic devices or to be combined with other low-loss platforms.

CONCLUSIONS

The application of a chemical mechanical polishing (CMP) step to the fabrication process flow of TiO₂ waveguides permitted to achieve slab losses as low as 0.1 dB/cm at 978 nm of wavelength and channel propagation losses of 0.5 dB/cm in thick channel waveguides of 277 nm \times 1.1 μm of cross-section. Further improvements on the deposition and etching of the devices could lead to further reduction of the propagation losses, which are however already comparable to the losses reported for other integrated photonic platforms.

Acknowledgements: Authors thanks are due to Marion Nijhuis for supporting the development of the CMP process for TiO₂ thin films and collaborations with MESA+ Institute and colleagues from the Optical Science group from the University of Twente.

References

- [1] E. D. Palik, Handbook of Optical Constants of Solids (Academic, 1985).
- [2] M. Fu, Y. Zheng, G. Li, W. Yi, J. Qi, S. Yin, X. Li, and X. Guan, "Ultra-compact titanium dioxide micro-ring resonators with sub-10- μm radius for on-chip photonics," *Photon. Res.* 9, 1416-1422 (2021).
- [3] X. Guan, H. Hu, L. K. Oxenløwe, and L. H. Frandsen, "Compact titanium dioxide waveguides with high nonlinearity at telecommunication wavelengths," *Opt. Express* 26, 1055-1063 (2018).
- [4] O. Reshef, K. Shtyrkova, M. G. Moebius, S. Griesse-Nascimento, S. Spector, C. C. Evans, E. Ippen, and E. Mazur, "Polycrystalline anatase titanium dioxide microring resonators with negative thermo-optic coefficient," *J. Opt. Soc. Am. B* 32, 2288-2293 (2015).
- [5] A. Bahtat, M. Bouazaoui, M. Bahtat, J. Mugnier, "Fluorescence of Er³⁺ ions in TiO₂ planar waveguides prepared by a sol-gel process," *Opt. Commun.* 111, 55-60 (1994).
- [6] J. Liu, G. Huang, R.N. Wang, et al. "High-yield, wafer-scale fabrication of ultralow-loss, dispersion-engineered silicon nitride photonic circuits," *Nat Commun* 12, 2236 (2021).
- [7] W. A. P. M. Hendriks, L. Chang, C. I. van Emmerik, J. Mu, M. de Goede, M. Dijkstra, S. M. Garcia-Blanco, "Rare-earth ion doped Al₂O₃ for active integrated photonics," *Adv. Phys. X* 6, 1833753 (2021).
- [8] M. Fu, Y. Zheng, G. Li, H. Hu, M. Pu, L. Katsuo Oxenløwe, L. Hagedorn Frandsen, X. Li, and X. Guan, "High-Q titanium dioxide micro-ring resonators for integrated nonlinear photonics," *Opt. Express* 28, 39084-39092 (2020).
- [9] M. Fu, Y. Zheng, G. Li, W. Yi, J. Qi, S. Yin, X. Li, and X. Guan, "Ultra-compact titanium dioxide micro-ring resonators with sub-10- μm radius for on-chip photonics," *Photon. Res.* 9, 1416-1422 (2021).
- [10] X. Guan, H. Hu, L. K. Oxenløwe, and L. H. Frandsen, "Compact titanium dioxide waveguides with high nonlinearity at telecommunication wavelengths," *Opt. Express* 26, 1055-1063 (2018).
- [11] K. Hammani, L. Markey, M. Lamy, B. Kibler, J. Arocas, J. Fatome, A. Dereux, J. C. Weeber, and C. Finot, "Octave Spanning Supercontinuum in Titanium Dioxide Waveguides," *Appl. Sci.* 8(4), 543 (2018).
- [12] F. Qiu, A. Spring, and S. Yokoyama, "Athermal and high-Q hybrid TiO₂-Si₃N₄ ring resonator via an etching-free fabrication technique," *ACS Photonics* 2(3), 405-409 (2015).
- [13] O. Reshef, K. Shtyrkova, M. Moebius, S. Griesse-Nascimento, S. Spector, C. Evans, E. Ippen, and E. Mazur, "Polycrystalline anatase titanium dioxide microring resonators with negative thermo-optic coefficient," *J. Opt. Soc. Am. B* 32(11), 2288-2293 (2015).
- [14] L. He, Y. Guo, Z. Han, K. Wada, J. Michel, A. M. Agarwal, L. C. Kimerling, G. Li, and L. Zhang, "Broadband athermal waveguides and resonators for datacom and telecom applications," *Photonics Res.* 6(11), 987-990 (2018).
- [15] G. Li, M. Fu, Y. Zheng, and X. Guan, "TiO₂ microring resonators with high Q and compact footprint fabricated by a bottom-up method," *Opt. Lett.* 45(18), 5012-5015 (2020).
- [16] M. Landmann, E. Rauls, and W. G. Schmidt, "The electronic structure and optical response of rutile, anatase and brookite TiO₂," *J. Phys.: Condens. Matter* 24(19), 195503 (2012).
- [17] I. Hegeman, M. Dijkstra, F. B. Segerink, W. Lee, and S. M. Garcia-Blanco, "Development of low-loss TiO₂ waveguides," *Opt. Express* 28(5), 5982-5990 (2020).
- [18] A. A. Fontenla, I. Hegeman, W. A. P. M. Hendriks, M. Dijkstra and S. M. G. Blanco, "Low-loss reactive sputter deposited titanium oxide waveguides," 2021 IEEE 17th International Conference on Group IV Photonics (GFP), 2021, pp. 1-2
- [19] A. A. Fontenla, I. Hegeman, W. A. P. M. Hendriks, M. Dijkstra, C. E. O. Martínez and S. M. G. Blanco, "Propagation Loss Measurements in Sputter Coated Titanium Oxide Waveguides," *Proc. SPIE Photonics West* (2022).

Integrated amorphous-silicon photodetector on Silicon nitride waveguide

Student paper

Christian De Vita^{1*}, Fabio Toso¹, Natale Giovanni Pruiti², Charalambos Klitis², Giorgio Ferrari¹,
 Marc Sorel^{2,3}, Andrea Melloni¹, Francesco Morichetti¹

¹ Department of electronics, information and bioengineering (DEIB), Politecnico di Milano, 20133 Italy

² University of Glasgow, Rankine Building, Oakfield Avenue, Glasgow G12 8LT, UK

³TeCIP, Sant'Anna School of Advanced Studies, Via Moruzzi 1, 56127 Pisa, Italy

*christian.devita@polimi.it

A compact in-line power monitor for visible light integrated photonics is presented. The photodetector is integrated onto Si_3N_4 waveguides, operates in the red-light wavelength range (660 nm) and has a footprint of few tens of microns. Experimental results show a responsivity of 30 mA/W, a sensitivity of -45 dBm and a sub- μs time response.

Keywords: Photodetector, Visible, Integration

INTRODUCTION

Visible spectrum is becoming more and more attracting in the last years, with applications that varies from biosensing [1] to virtual reality [2]. Silicon nitride is the leading platform due to its high-index-contrast and especially for its low propagation losses. As for the near-infrared spectrum, also in visible the market is moving toward the request of complex and programmable integrated circuits [3]. This high level of integration requires a monolithical approach for the implementation of light sources and detectors on a single chip. On-chip detectors play a key role, since they are necessary to monitor the working point of the PIC and to realize a closed-loop control of the system. Amorphous-silicon is renowned for its photoconductive properties, enabling the realization of compact integrated detectors with high sensitivity and a reduced impact on the light propagating in the waveguides [4]. In this work, we exploit the photoconductivity of an a-Si film additively deposited on top of a Si_3N_4 waveguide to realize a weakly invasive light monitor in a closed loop control system.

FABRICATION

The 200-nm thick Si_3N_4 waveguides are fabricated by using Low Pressure Vapor Chemical Deposition (LPCVD) on a 4 μm thermal oxide layer over a Si carrier wafer and then buried in a 600 nm thick hydrogen silsesquioxane (HSQ) upper cladding cured for 72 h at 180 °C. The waveguides have a width in the range 300 to 450 μm to operate in the single mode or slightly multimode regime and are accessed by edge coupling. Both waveguides and tapers have been patterned by using electron beam lithography. A 3D qualitative representation of the device is reported in fig. 1(a), while a top view photograph of the manufactured detector is presented in figure 1(b).

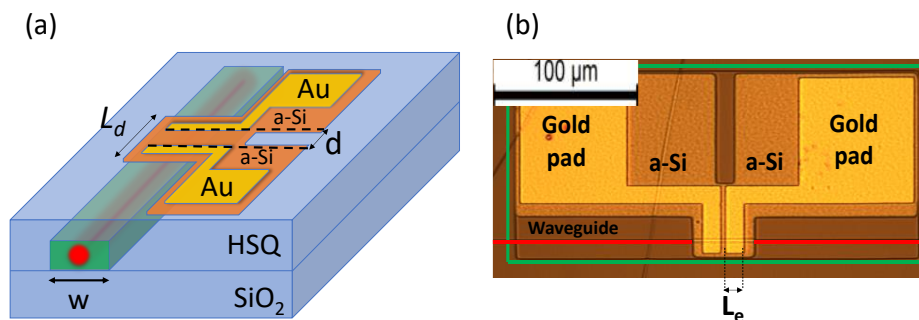


Figure 1. (a) False scale 3D schematic of the device. (b) Top view photo of the realized photodetector.

The HSQ cover is selectively thinned in an area which is large enough ($350 \times 150 \mu\text{m}$, green box in fig. 1b)) to accommodate also the contact pads. A 200 nm thick layer of a-Si:H was deposited by PECVD using SiH_4 as a gas precursor for suitable hydrogenation of the film [5] and then patterned over the waveguide to a length $L_d = 50 \mu\text{m}$ to reduce the interaction with the optical mode. This size provides a satisfactory tradeoff between detector sensitivity and attenuation of the optical field. The two gold electrodes have a thickness of 150 nm, a width $L_e = 15 \mu\text{m}$ and are spaced by a distance $d = 4 \mu\text{m}$. Due to the limited resolution of the fabrication process, the length $L_d = 50 \mu\text{m}$ of the a-Si region is intentionally longer than the region covered by the electrodes, $2L_e + d = 34 \mu\text{m}$.

ELECTRO-OPTIC BEHAVIOR OF THE PHOTODETECTOR

For the assessment of the photoconductor response, the photonic chip was glued with a steel-based glue onto a thermally-stabilized printed circuit board (PCB). Electrical connections were established through chip-to-board wire-bonds. Figure 2a) shows the measured light-dependent current of the sensor for increasing values of the optical power P_{opt} at the input, when a constant voltage $V_{bias} = 8\text{ V}$ is applied between the two electrodes. The dark current of the device, measured when no light is applied, is about 50 pA, corresponding to a resistance of 160 G Ω between the electrodes. Since the transversal width of the a-Si film between the electrodes is 70 μm , this results in a conductivity of 18 nS/cm for the a-Si:H film.

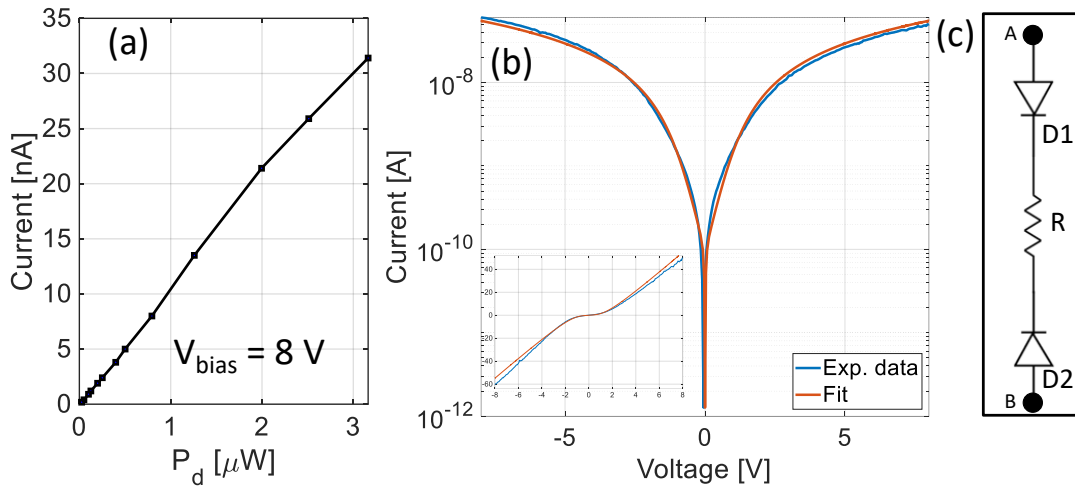


Figure 2. a) Current behaviour varying the optical power P_{opt} reaching the detector b) Measured I-V curve (blue) of the device with its fit (red) in logarithmic scale, the linear scale is presented in the inset. (c) Model used for the fitting of the contacts, where D1 and D2 model the metal contacts, and R the photoresistor, $V_{bias} = V_{AB}$.

The dark current limits the sensitivity of the device to a lower limit of 31 nW. Above the sensitivity threshold, we observe a change of the photocurrent versus the optical power P_{opt} across a dynamic range of more than two orders of magnitude (20 dB), with a maximum power limit of 3.2 μW given by the overall losses of the measurement setup. By defining the absorbed power as $P_{abs} = \eta P_{opt}$, where $\eta = 1 - \exp(-\alpha L_d)$ is the fraction of guided light absorbed by the amorphous silicon, we can call R_d the responsivity of the device, defined as the ratio between the measured current and the absorbed power P_{abs} , resulting in $R_d = 30\text{ mA/W}$.

As already reported in other works, the metal-amorphous silicon barrier presents a non-ohmic behavior [6]. Usually, a metal/semiconductor junction can be modeled either as an ohmic contact, presenting a linear current-voltage (I-V) characteristic, or as a rectifying contact (i.e. a diode) controlled by a potential barrier. In our specific case, we modelled the two contacts of the device as two diodes with opposite polarity, with the photo-resistance of the detector in between them (figure 2c). According to Rhoderick [7], image-force effects always result in a voltage dependence of the energy barrier

$$\Phi_{Bi} = \Phi_{B0i} + qV \left(1 - \frac{1}{n_i}\right) \quad (1)$$

where Φ_B is the energy barrier, V the applied bias and n_i the non-ideality factor. We can then define the current as

$$I = I_0 e^{\frac{\beta V}{n}} (1 - e^{-\beta V}) \quad (2)$$

With $\beta = \frac{q}{k_b T}$ and $I_0 = SAT^2 e^{-\beta \Phi_{B0}}$, being A the effective Richardson constant, S the contact surface and T the temperature in K. From literature, $A = 197\text{ A/cm}^2\text{K}^2$ for amorphous-silicon [8]. The I-V curve of our devices is reported in figure 2b as blue curve and its fitting in red. The fitting is pretty good and provides $I_{01}=I_{02}=100\text{ pA}$ and the two non-ideality factors $n_1=n_2=1.1$. This brings to a barrier, given by the reverse Richardson-Dushman equation, $\Phi_{B1} = \Phi_{B2} = 0.716\text{ eV}$. In the model, the two contacts are assumed identical, as they are fabricated together, and hence the red fitting curve is perfectly symmetrical, with the same barrier energy on both sides, while in reality a small asymmetry is observed.

TIME RESPONSE MEASUREMENT

To measure the time response behavior of the sensor, a pulsed optical signal is obtained by modulating the driving current of the laser with a square wave at 100 Hz, with a rise and fall time of 1 μs . The same time constant is observed on the laser intensity modulation, reported in Fig. 3 as reference (blue line), measured with a fiber pigtailed commercial fast silicon photodiode (110 MHz bandwidth). The time behavior of the electrical signal detected by the amorphous-silicon integrated photodetector, acquired with a transimpedance amplifier FEMTO DHPCA-100, providing a gain of 10^8 A/V and a bandwidth of 220 kHz, is reported in Fig. 3. The output, that refers to $P_{\text{opt}} = -25$ dBm and $V_{\text{bias}} = 10$ V, was collected by an oscilloscope, triggered by the same electrical signal used to drive the laser source.

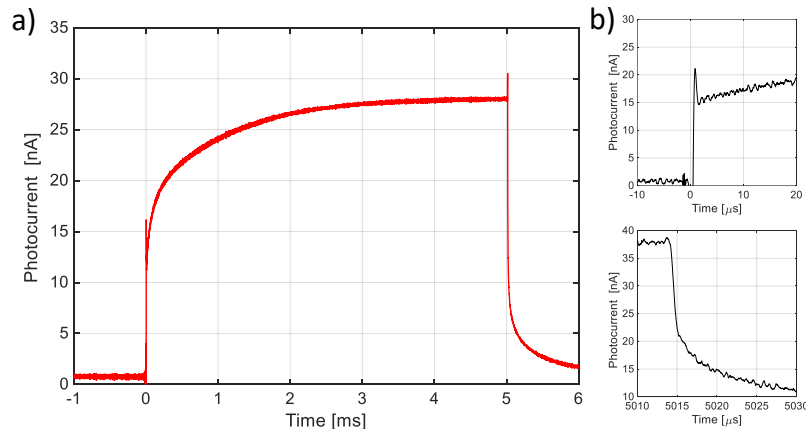


Figure 3. a) Measured time response of the photodetector. $P_{\text{opt}} = -25$ dBm, $V_{\text{bias}} = 10$ V. b) detail of the rise and fall time edges.

Two-time constant responses are experimentally observed: a rapid rise and fall time of about 1 μs , followed by a slower behavior, in the range of several hundreds of μs . This slow response can be explained by the dynamic of the carriers trapped in the intragap states of a-Si [9]. The leading and trailing fast transients are due to the effective lifetime of free carriers τ_{eff} , expected to be in the order of several ns. In our setup, the measurement of the faster time response is limited by the rise-time response of the laser (~ 1 μs) and the bandwidth of the TIA., that is responsible for the damping at the fast transitions of the measured current signal. Considering that more than half of the dynamic happens in the first few μs , even if the full transition occurs in several ms, this device can be exploited to implement very fast control systems, up to hundreds of kHz.

CONCLUSION

We presented a-Si in-line photodetector operating in the 660-nm wavelength range that is monolithically integrated with standard Si_3N_4 waveguides. The device, made with a CMOS compatible fabrication, has a sensitivity of -45 dBm, a responsivity of 30 mA/W and a good linearity across a dynamic range of more than 20 dB (limited by setup losses). Considering the absorption region of amorphous silicon, the working principle of this device can be extended to shorter wavelengths, operating over the full RGB spectrum that can be guided in Si_3N_4 waveguides.

Acknowledgment. This work was partially performed at Polifab, the micro- and nanofabrication facility of Politecnico di Milano (<https://www.polifab.polimi.it/>) within the EU project Superpixel (829116).

References

- [1] C. A. A. Franken et al., Opt. Lett. 46, 4904-4907 (2021).
- [2] A. Nakao et al., Proceedings of the International Display Workshops, p. 649, (2020).
- [3] W. Bogaerts et al., Nature 586, 207-216 (2020).
- [4] B. Desiatov and M. Loncar., Appl. Phys. Lett. 115, 121108 (2019).
- [5] A.T.M. Wilbers et al., Thin Solid Films, Vol. 204, Issue 1 (1991).
- [6] C. R. Wronski et al., Appl. Phys. Lett. 29, 602-605 (1976).
- [7] Rhoderick E. H., "Metal Semiconductor Contacts" (Oxford:Clarendon), (1988).
- [8] I. A. Niaz et al., J. Light. Technol., vol. 37, 19, 5056–5066 (2019).
- [9] K. A. Conrad and E.A. Schiff, Solid State Communications 60: 291-294, (1986).

Low-noise near-ultraviolet photonic integrated lasers

(Student paper)

Anat Siddharth¹, Thomas Wunderer², Grigory Lihachev¹, Andrey S. Voloshin¹, Camille Haller³, Rui Ning Wang¹, Mark Teepe², Zhihong Yang², Junqiu Liu¹, Johann Riemensberger¹, Nicolas Grandjean³, Noble Johnson², and Tobias J. Kippenberg^{1*}

¹Laboratory of Photonics and Quantum Measurements, Swiss Federal Institute of Technology Lausanne (EPFL), CH-1015 Lausanne, Switzerland

²Palo Alto Research Center, Palo Alto, CA 94304 USA

³Laboratory of Advanced Semiconductors for Photonics and Electronics, Swiss Federal Institute of Technology Lausanne (EPFL), CH-1015 Lausanne, Switzerland

*tobias.kippenberg@epfl.ch

We demonstrate for the first time a hybrid integrated low-noise laser composed of a gallium nitride (GaN) based laser diode and a silicon nitride photonic chip-based microresonator operating at record low wavelengths as low as 410 nm. By self-injection locking of the Fabry-Pérot diode laser to a high Q (0.4×10^6) photonic integrated microresonator, we reduce the optical phase noise at 461 nm by a factor greater than 100×, limited by the device quality factor and back-reflection.

Keywords: visible integrated photonics, hybrid integrated lasers, silicon nitride, injection-locking

INTRODUCTION

Photonic integrated lasers that operate in the visible to ultraviolet (UV) spectral regime featuring narrow emission linewidth and low phase noise are required for the miniaturization of photonic systems. Applications for such systems range from quantum metrology and sensing based on laser-cooled neutral atoms and ions [1], precision atomic clocks [2], underwater laser range-finding [3], interferometric biophotonics [4] or visible spectroscopy [5].

The wide bandgap group III-Nitride semiconductor material family is ideally suited as active materials platform for next-generation integrated photonics covering operation wavelengths in the UV and visible spectral regime. High power III-N laser sources (i.e. GaN and its alloys) are commercially available today and can be found in various products such as Blu-ray players or modern car headlamps, for example. For many of the aforementioned applications, however in particular for neutral atom and ion-based Quantum Information Science and Metrology, conventional III-N laser diodes cannot meet the requirements in terms of emission linewidth (i.e. phase noise) and longitudinal mode stability (i.e. drift) during operation. Integrating compact III-N laser gain elements with high-performance Si₃N₄-based photonic circuits for single-frequency laser operation with narrow emission linewidth and the prospect for tunability and stable operation has not been explored in great detail so far. Si₃N₄ is an ideal material for visible to UV lasers due to the 5 eV bandgap and low propagation loss [6].

RESULTS

Figure 1a depicts the experimental setup with a custom AlGaInN-based Fabry-Perot laser diode chip directly butt-coupled to a Si₃N₄ photonic chip to realize laser self-injection locking [7]. Custom AlGaInN near-UV laser diodes were fabricated on low-defect density native GaN substrates using Metal-Organic Vapor Phase Epitaxy (MOVPE) [8]. The laser diode showed a characteristic laser threshold of about 70 mA and can produce more than 100 mW of optical output power at a wavelength of 410 nm. The laser is mounted on a thermo-electric cooler for stabilizing its temperature and is operated at 21°C. The Si₃N₄ waveguides and microresonators are fabricated using a subtractive process and have a uniform height and width of 50 nm and 600 nm, respectively. Stoichiometric Si₃N₄ thin films are grown with low-pressure chemical vapor deposition (LPCVD) and etched in a Fluorine chemistry. The waveguides are fully buried in SiO₂ cladding (bottom cladding is made of thermal oxide whereas, the top cladding is composed of TEOS and low-temperature oxide) of 5.4 μm thickness. The entire device sits on a 230 μm-thick Si substrate. The radius of the microring resonator is 200 μm, corresponding to a free spectral range of approximately 107.08 GHz. Development of a low-loss photonic platform in the blue and near-ultraviolet spectral regime is challenging as Rayleigh-like scattering scales with λ^{-4} and material loss also increases as wavelengths approach the Si₃N₄ bandgap. Figure 1b presents a linewidth measurement of our microresonator carried out at 461 nm, which reveals a loaded linewidth $\kappa/2\pi = 2.33$ GHz and an intrinsic linewidth $\kappa_0/2\pi = 1.69$ GHz, corresponding to an intrinsic quality factor of $\sim 0.4 \times 10^6$.

Figure 1c demonstrates self-injection locked lasing in the near-ultraviolet (410 nm), as well as in the visible (blue and green wavelength range) using the same Si_3N_4 photonic chip. Coupling the custom AlGaInN near-UV laser diodes for light emission at 410 nm (nominal output power of ca. 3.5 mW), we achieve laser self-injection locking at a diode current of 130 mA with fiber-coupled output powers up to 0.185 mW. As shown in Figure 1c, we achieve single-frequency lasing at 410.3 nm with a side-mode suppression ratio greater than 20 dB.

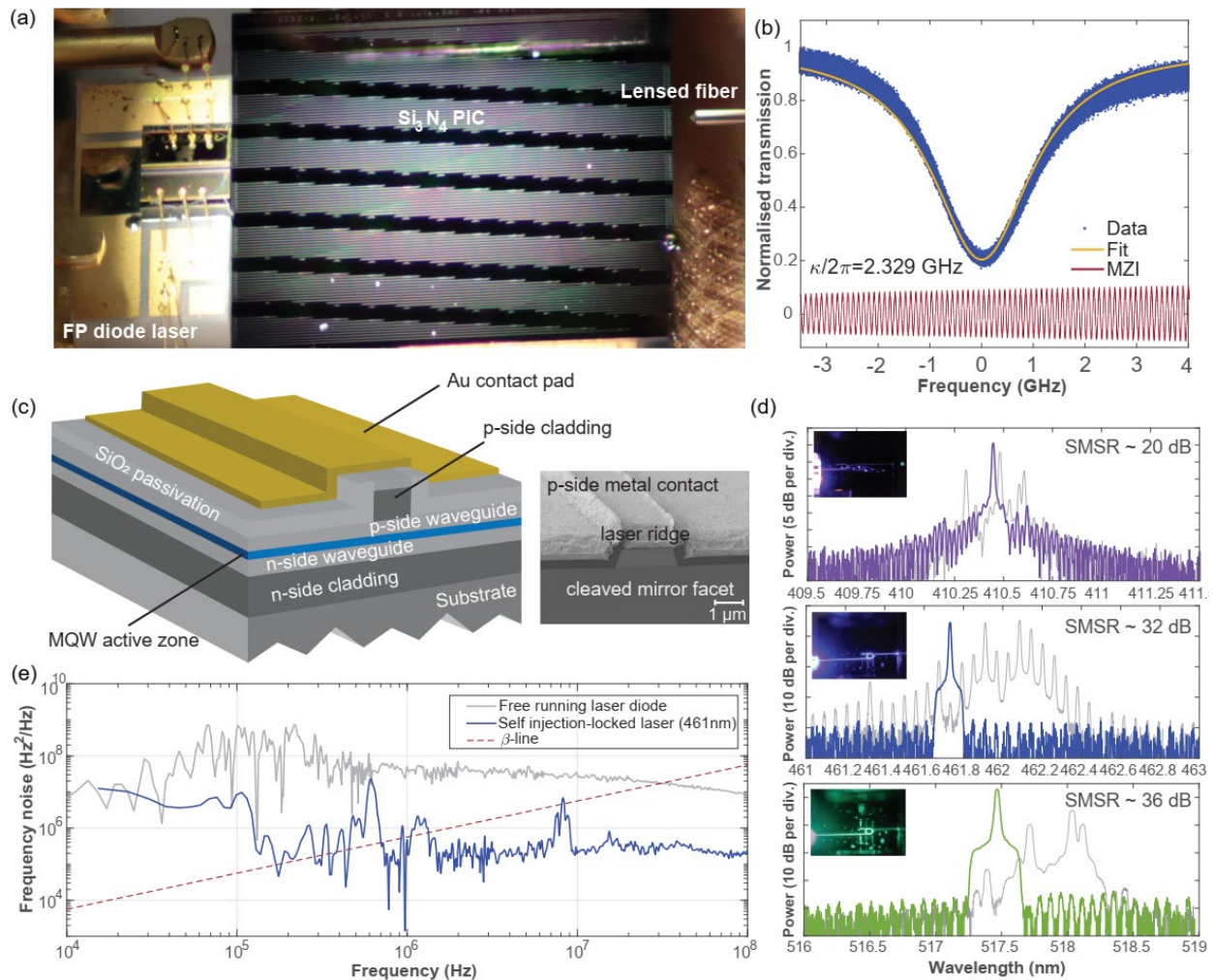


Fig. 1. (a) Photo of the experimental setup showing the Fabry-Perot laser diode butt-coupled to the Si_3N_4 photonic chip, along with a lensed fiber. (b) Measured transmission spectra of a mode using a tunable laser at 461 nm calibrated by a fiber MZI with free spectral range of 100.12 MHz. (c) Schematic showing the laser diode structure that emits laser light near-UV wavelengths (410 nm) with SEM image of the sample cross-section showing the laser ridge. (d) Optical spectra of self-injection locked state (single frequency) and multimode state (dashed grey lines) at different wavelengths (near-ultraviolet, blue and green) using the same Si_3N_4 photonic chip. (e) Frequency noise spectra of the self-injection locked hybrid integrated laser system at 461.5 nm.

DISCUSSION

This constitutes the shortest wavelength hybrid integrated laser-based on Si_3N_4 . We also show operation in the visible and attain single-frequency lasing at blue (461.8 nm) and green wavelengths (518.6 nm) via self-injection locking. The fiber-coupled output powers were 1.1 mW and 1.9 mW with respective side-mode suppression ratios of 24 dB and 28 dB. In summary, we show successful integration of an AlGaInN laser gain element coupled to a Si_3N_4 Photonic Integrated Circuit (PIC) platform featuring narrow laser emission intrinsic linewidth of ~ 1.15 MHz with more than $100\times$ frequency noise reduction via self-injection locking.

Acknowledgments: This material is based on research sponsored by Army Research Laboratory under agreement number W911NF-19-2-0345, by the Army Research Office under Cooperative Agreement number W911NF-20-2-0214, and by the Air Force Office of Scientific Research under award number FA9550-21-1-0063. This work was further supported by the Swiss National Science Foundation under grant agreement No. 176563 (BRIDGE). A.S. acknowledges support from the European Space Technology Centre with ESA Contract No. 4000135357/21/NL/GLC/my and J.R. acknowledges support from the Swiss National Science Foundation under grant no. 201923 (Ambizione). The U.S. Government is authorized to reproduce and distribute reprints for Government purposes notwithstanding any copyright notation thereon. The views and conclusions contained herein are

those of the authors and should not be interpreted as necessarily representing the official policies or endorsements, either expressed or implied, of Army Research Laboratory (ARL) or the U.S. Government.

References

- [1] R. J. Niffenegger et al., “Integrated multi-wavelength control of an ion qubit,” *Nature*, vol. 586, pp. 538–542, Oct. 2020.
- [2] A. D. Ludlow et al., “Optical atomic clocks,” *Rev. Mod. Phys.*, vol. 87, no. 2, pp. 637– 701, Jun. 2015.
- [3] L. J. Mullen, A. J. C. Vieira, P. R. Herezfeld, and V. M. Contarino, “Application of RADAR technology to aerial LIDAR systems for enhancement of shallow underwater target detection,” *IEEE Transactions on Microwave Theory and Techniques*, vol. 43, no. 9, pp. 2370–2377, Sep. 1995, doi: 10.1109/22.414591.
- [4] A. B. T. Ghisaidoobe and S. J. Chung, “Intrinsic Tryptophan Fluorescence in the Detection and Analysis of Proteins: A Focus on Förster Resonance Energy Transfer Techniques,” *International Journal of Molecular Sciences*, vol. 15, no. 12, Art. no. 12, Dec. 2014, doi: 10.3390/ijms151222518.
- [5] D. A. Kalashnikov, A. V. Paterova, S. P. Kulik, and L. A. Krivitsky, “Infrared spectroscopy with visible light,” *Nature Photon*, vol. 10, no. 2, pp. 98–101, Feb. 2016, doi: 10.1038/nphoton.2015.252.
- [6] J. Liu et al., “High-yield, wafer-scale fabrication of ultralow-loss, dispersion-engineered silicon nitride photonic circuits,” *Nat Commun*, vol. 12, no. 1, p. 2236, Apr. 2021, doi: 10.1038/s41467-021-21973-z.
- [7] G. Lihachev et al., “Ultralow-noise frequency-agile photonic integrated lasers,” arXiv:2104.02990 [physics], Apr. 2021, Accessed: Apr. 16, 2021. [Online].
- [8] M. Kneissl et al., “Performance and degradation of continuous-wave InGaN multiple-quantum-well laser diodes on epitaxially laterally overgrown GaN substrates,” *Appl. Phys. Lett.*, vol. 77, no. 13, pp. 1931–1933, Sep. 2000.

Low-loss chemical mechanically polished Al₂O₃ thin films for UV integrated photonics

(Student paper)

S. Mardani, M. Dijkstra, W.A.P.M. Hendriks, M.P. Nijhuis - Groen, S.M. Garcia-Blanco

MESA+ Institute, University of Twente, P.O. Box 217, 7550 AE, Enschede, The Netherlands

In this work, we report low-loss aluminum oxide (Al₂O₃) thin films for integrated photonics in the near ultra-violet using a reactive sputtering process. The Al₂O₃ film is polished by chemical mechanical polishing (CMP). We obtain layers with a surface roughness of 0.3 nm and propagation losses of 0.6 ±0.3 dB/cm for the fundamental slab mode at 377 nm.

Keywords: UV-waveguides, Propagation loss, Aluminum oxide, Optical waveguide

INTRODUCTION

Aluminum oxide (Al₂O₃) is a dielectric material that is an excellent candidate for integrated photonic devices, especially in the near-UV and mid-infrared due to its large transparency window expanding from 150 nm to 5500 nm[1–5]. Low loss sputtered Al₂O₃ thin films for integrated photonic devices have been demonstrated with losses down to 1.8 dB/cm at 407 nm[6], where it is hypothesized that a significant fraction of the losses originates from surface roughness scattering. Chemical mechanical polishing (CMP) is a well-established process for the reduction of surface roughness scattering in waveguide structures[7]. In this work, we show our advancements towards low loss high confinement Al₂O₃ waveguides for photonic integrated circuits in the UV. First, a 170 nm thick Al₂O₃ layer is deposited by reactive sputter coating and the surface and optical properties are characterized. Next, the surface roughness is reduced by CMP, again followed by surface and optical characterization. Finally, the obtained improvement is discussed.

EXPERIMENTAL AND RESULTS

The Al₂O₃ layers are deposited using an AJA ATC 15000 RF reactive co-sputtering system [8] on 10 cm diameter silicon wafers with 8 μm thick thermal oxide. The system can host three 2 inch RF guns, one of which was installed with an aluminium target (Al, 99.9995 % purity). The depositions are performed with a constant RF power of 200 W applied to the aluminium target. All parameters used for the deposition of the Al₂O₃ layer with a thickness of 170 nm are given in Table 1.

Table 1 Optimized Rf reactive sputtering process parameters

Parameter	Value	Unit
Argon flow	30	sccm
Oxygen flow	3.1	sccm
Relative bias voltage	4.6	%
Pressure	3.9	mTorr
Substrate set temperature	760	°C
Target-substrate distance	15.2	cm
Power	200	W

The deposited layer is polished using a CMP Mecapol E460 polishing system. The slurry used was Semi-Sperse 25 from Semi-Sperse CO. The parameters as used for the polishing of the Al₂O₃ layer are shown in Table 2.

Table 2 CMP setting parameters

Preconditioning	Yes
Slurry	Semi-Sperse 25
Slurry PH	11
Slurry:Water	1:2
Polishing head speed (tr/min)	55
Polishing table speed (tr/min)	55

Work pressure	0.5
Time (s)	20

The surface and optical analysis are performed before and after polishing. First, the thickness and refractive index are measured using an Woollam M-2000UI ellipsometer. Given the 8 μm oxide layer a fitting range from 600 to 1600 nm is used to determine the layer properties with a Cauchy model of the layer. The found Cauchy model is extrapolated to the near UV region of interest and the result before and after polishing are presented in figure 2 (A). The surface roughness of the layers is measured using an Bruker Fast Scan AFM in scan assist mode. The propagation loss of the layer is measured using a Metricon 2010/M prism coupler with propagation loss module. The propagation loss is determined at 377 nm, 407 nm and 451 nm.

The surface morphologies of the Al_2O_3 thin film before and after polishing are presented in Figure 1. The scanned area was $500 \times 500 \text{ nm}^2$. The surface roughness before polishing was 1.5 nm RMS. After polishing, the determined RMS is 0.3 nm, where it should be noted that the attainable resolution with the given AFM configuration and available tip was insufficient to accurately determine the roughness. We can however confidently conclude that the polishing significantly reduces the surface roughness.

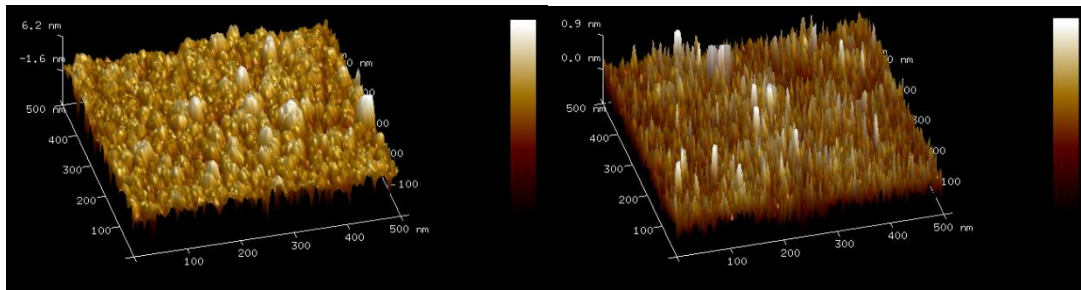


Figure 1 Surfaces of Al_2O_3 thin films (left) before and (right) after polishing measured with AFM.

The removal rate of the CMP process is determined by ellipsometry to be 0.4 nm/s, which allows for accurate control of the final layer thickness. Figures 2 (A) and (B) show the effect of the polishing process on the refractive index and propagation losses as determined by the ellipsometer and prism coupling measurements respectively. The reduction in refractive index observed is a consequence of the inherent gradient in the refractive index caused by the deposition process[9]. therefore as the top layer is removed, the average refractive index of the layer is reduced. The reduced surface roughness, as expected, significantly reduces the propagation losses from $1.5 \pm 0.3 \text{ dB/cm}$ to $0.6 \pm 0.3 \text{ dB/cm}$ for the fundamental slab mode at 377 nm. Another noteworthy feature is the significantly larger reduction in propagation losses for shorter wavelengths, indicative of the obtained reduction being caused by the reduced surface roughness and thus surface scattering.

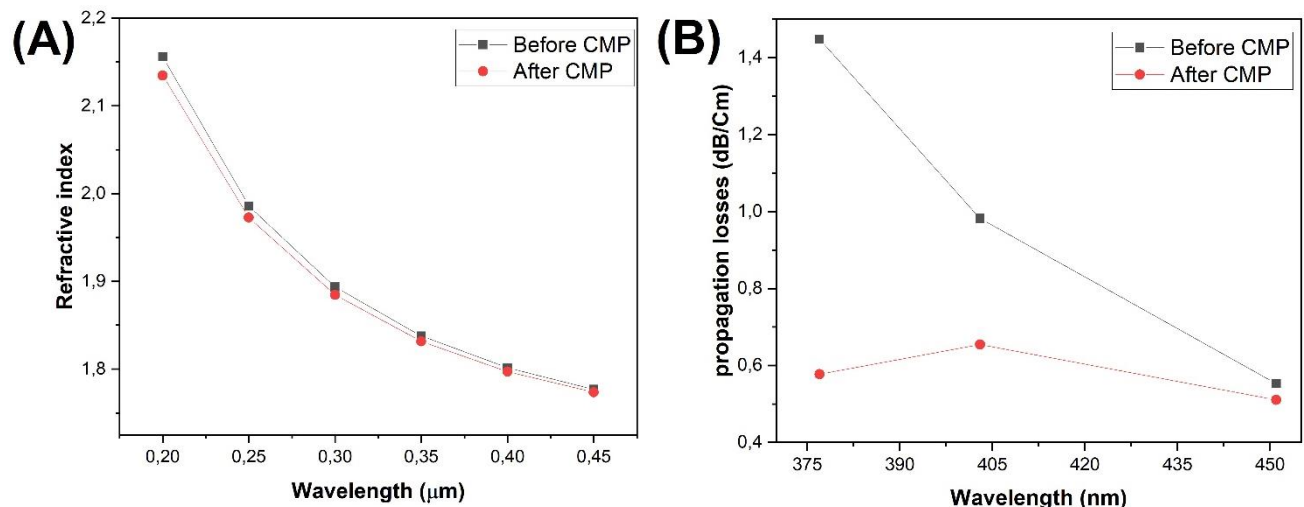


Figure 2 (A) Refractive index, and (B) propagation losses at different wavelengths before and after polishing

Figure 3 shows a picture of the fundamental 377 nm mode propagating through the layer. This propagation qualitatively and visually corroborates the previously discussed quantitative measurements of low propagation loss in our polished Al_2O_3 films. These experimental results confirm the ability of the sputter deposition and CMP process to produce low-loss optical layer operating in the near-UV.

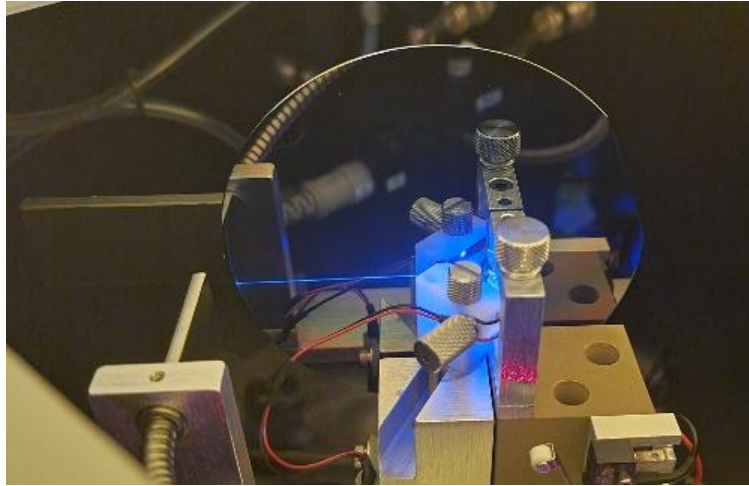


Fig. 3. Picture of the guided UV light (377 nm) showing that the optical beam has propagated 8 cm inside the Al_2O_3 thin-film.

SUMMARY

In summary, we report the fabrication and characterization of Al_2O_3 layers with low propagation losses in the near-UV and visible wavelength range. Silicon wafers with 8 μm thick thermal oxide buffer were sputter coated with an Al_2O_3 layer of thickness 170 nm. The roughness of the layer measured by AFM was 1.46 nm RMS which, after polishing, reduced to 0.3 nm. The measured propagation losses show that the CMP process can reduce the propagation losses for the Al_2O_3 layer. These results enable the fabrication of photonic integrated circuits for UV applications.

References

- [1] J. D. Bradley, R. Stoffer, L. Agazzi, F. Ay, K. Wörhoff, and M. Pollnau, "Integrated $\text{Al}_2\text{O}_3\text{:Er}^{3+}$ ring lasers on silicon with wide wavelength selectivity," *Opt. Lett., OL*, vol. 35, no. 1, pp. 73–75, Jan. 2010, doi: 10.1364/OL.35.000073.
- [2] L. Agazzi *et al.*, "Monolithic integration of erbium-doped amplifiers with silicon-on-insulator waveguides," *Opt. Express, OE*, vol. 18, no. 26, pp. 27703–27711, Dec. 2010, doi: 10.1364/OE.18.027703.
- [3] S. A. Vázquez-Córdova *et al.*, "Erbium-doped spiral amplifiers with 20 dB of net gain on silicon," *Opt. Express, OE*, vol. 22, no. 21, pp. 25993–26004, Oct. 2014, doi: 10.1364/OE.22.025993.
- [4] N. Li *et al.*, "Broadband 2- μm emission on silicon chips: monolithically integrated Holmium lasers," *Opt. Express, OE*, vol. 26, no. 3, pp. 2220–2230, Feb. 2018, doi: 10.1364/OE.26.002220.
- [5] E. R. Dobrovinskaya, L. A. Lytvynov, and V. Pishchik, "Application of Sapphire," in *Sapphire: Material, Manufacturing, Applications*, V. Pishchik, L. A. Lytvynov, and E. R. Dobrovinskaya, Eds. Boston, MA: Springer US, 2009, pp. 1–54. doi: 10.1007/978-0-387-85695-7_1.
- [6] W. a. P. M. Hendriks, M. Dijkstra, C. I. van Emmerik, I. Hegeman, and S. M. G. Blanco, "High refractive index low-loss aluminium oxide waveguides," presented at the 22nd European Conference on Integrated Optics, ECIO 2020, Jun. 2020. Accessed: Mar. 01, 2022. [Online]. Available: <https://research.utwente.nl/en/publications/high-refractive-index-low-loss-aluminium-oxide-waveguides>
- [7] M. H. P. Pfeiffer, J. Liu, A. S. Raja, T. Morais, B. Ghadiani, and T. J. Kippenberg, "Ultra-smooth silicon nitride waveguides based on the Damascene reflow process: fabrication and loss origins," *Optica, OPTICA*, vol. 5, no. 7, pp. 884–892, Jul. 2018, doi: 10.1364/OPTICA.5.000884.
- [8] K. Wörhoff, J. D. B. Bradley, F. Ay, D. Geskus, T. P. Blauwendraat, and M. Pollnau, "Reliable Low-Cost Fabrication of Low-Loss $\text{Al}_2\text{O}_3\text{:Er}^{3+}$ Waveguides With 5.4-dB Optical Gain," *IEEE Journal of Quantum Electronics*, vol. 45, no. 5, pp. 454–461, May 2009, doi: 10.1109/JQE.2009.2013365.
- [9] A. Anders, "A structure zone diagram including plasma-based deposition and ion etching," *Thin Solid Films*, vol. 518, no. 15, pp. 4087–4090, May 2010, doi: 10.1016/j.tsf.2009.10.145.

Femtosecond Laser Micromachining of Integrated Hollow-core Waveguides for High-order Harmonic Generation and XUV Filtering

Pasquale Barbato^{1,2*}, Gabriele Crippa^{1,2}, Anna G. Ciriolo², Michele Devetta², Caterina Vozzi², Salvatore Stagira^{1,2}, Valer Tosa³, Roberto Osellame² and Rebeca Martínez Vázquez²

¹ Politecnico di Milano, Physics Department, Piazza Leonardo da Vinci 32, Milano, 20133, Italy

² Institute for Photonics and Nanotechnologies, National Research Council, Piazza Leonardo da Vinci 32, 20133, Milano, Italy

³ National Institute for R&D of Isotopic and Molecular Technologies, Donat Str., Cluj-Napoca, 400293, Romania

* pasquale.barbato@polimi.it

We report on the realisation, by femtosecond laser micromachining in fused silica, of integrated hollow waveguides for efficient high-order harmonic generation and near infrared rejection from the generated XUV pulses. This work represents an important step in the miniaturization of XUV beamlines.

Keywords: *Femtosecond Laser Micromachining, Waveguides, High-order Harmonic Generation, Integrated Optics*

INTRODUCTION

High-order Harmonic Generation (HHG) represents today a well-known approach to deliver XUV/soft-X ray attosecond pulse trains [1]. This phenomenon relies on the interaction between ultrashort near - and mid - infrared pulses and noble gas samples, resulting in a burst of coherent radiation in the form of high-order, odd harmonics of the fundamental wavelength, with frequencies ranging from extreme ultraviolet (XUV) to the soft-X rays. Such sub-femtosecond pulses are of central interest for a wide spectrum of technological applications and fundamental research [2] but are currently mostly provided by expensive laboratories or large facilities such as synchrotrons and free-electron lasers.

In this work, we exploit Femtosecond Laser Irradiation followed by Chemical Etching (FLICE) to fabricate integrated devices, based on the principle of hollow waveguiding, to confine the driving field, to generate high order harmonics and subsequently to separate them from the residual driving field. Taking advantage of FLICE unique capabilities we aim to integrate the generation and filtering system within the same device, thus pushing towards the concept of "lab-on-a-chip", i.e., the embedding of different functionalities in the same small-scale photonic platform.

RESULTS

Although first demonstrations of HHG were performed on gas-jet systems, the gas-filled hollow waveguide scheme is now broadly used as it assures higher conversion efficiencies thanks both to the confinement of the fundamental pulses in the interaction region and to the high gas densities achievable in the small waveguide volume. Therefore, it is possible to reach conversion efficiencies up to 10^3 times better than the ones obtained in gas-jet setups, but still of the order of 10^{-5} of the driving field in the best conditions. For this reason, there is still a strong presence of the fundamental field after the HHG region, which should be filtered to isolate the emitted XUV pulses.

Our device is schematically represented in Fig. 1a. A first chip, called "generation stage", includes a cylindrical hollow waveguide filled with a noble gas: the driving field is coupled inside the waveguide and due to its interaction with the gas, the XUV radiation is generated. The output radiation will be then collected by a second device called "filtering stage" that rejects the residual IR from the XUV radiation. As schematically shown in Fig. 1a, the waveguiding effect of the main channel, which has a smooth radius of curvature, can spatially separate the near-infrared radiation from the generated XUV.

The integrated waveguides are fabricated by FLICE, a well-established technique for the realization of micrometric hollow buried structures inside fused silica substrates [3]. When femtosecond laser pulses carrying an adequate amount of energy are focused inside a fused silica sample, nonlinear processes occur [4] that lead to an energy transfer from the field to the material and eventually to permanent modifications in a micrometric volume around the focus, in a controllable and reproducible way. By moving the laser focus with respect to the silica substrate, it is possible to build complex three-dimensional paths. With an appropriate choice of the exposure parameters, this

modification leads to a local higher etching speed when treated with a wet chemical agent like HF [5]. To date, numerous lab-on-a-chip devices have been produced with FLICE technique for manipulating fluids or hosting the interaction between strong laser fields and gaseous molecules.

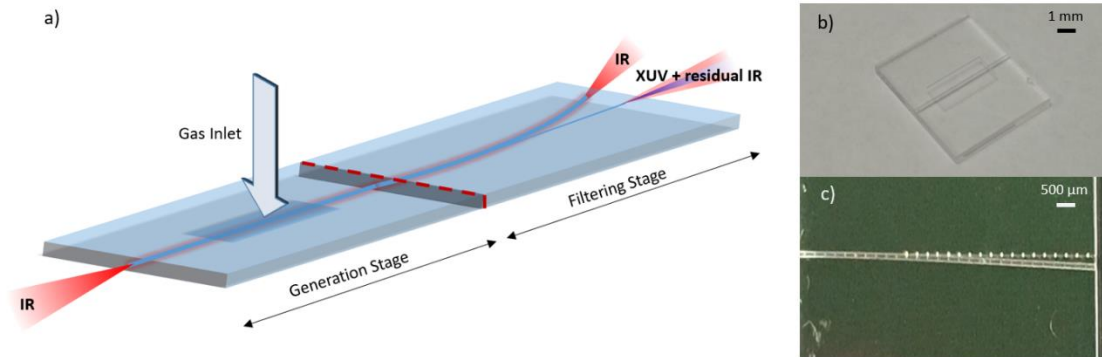


Fig. 1. a) A schematic representation of the device integrating waveguides for HHG and IR rejection, b) a picture of the HHG chip and c) an image of the curved waveguide for IR filtering and XUV channeling.

The two devices were fabricated separately (Fig. 1b and 1c) and then optically characterized before their utilization in the HHG setup. The generation section, shown in Fig. 1b, consists of a 130 μm -diameter 8 mm long hollow waveguide and a rectangular gas inlet that guarantees a uniform gas distribution. The filtering stage is composed of a small straight channel for XUV transmission and of a bent 15 mm-long hollow waveguide for IR rejection, which has the same diameter as the waveguide in the generation stage. A curvature radius of 300 mm is impressed to this waveguide for IR rejection. Different diameters of the XUV channel were investigated to obtain the best IR rejection-XUV attenuation combination.

For the micromachining of both devices, the second harmonic (515 nm) of a femtosecond laser beam (Satsuma, Amplitude Systemes, 230fs, 300 nJ, 1 MHz) is focused inside a fused silica sample by a 63x microscope objective, with the sample which is moved by a high-resolution translational stage. Subsequently, the sample is immersed in an ultrasonic bath of a 20% aqueous solution at 35 $^{\circ}\text{C}$ for about 2 h. As a final step of the fabrication, the device is thermally annealed to smooth the surface of the hollow waveguide.

For a preliminary optical characterization of the waveguides, the light beam from a laser with a central frequency at 780 nm was coupled to them to get the near field images of the output modes and to measure insertion losses. For the generation hollow waveguide, we were able to observe the mode with lowest attenuation (Fig. 2a), which is expected to be an EH_{11} [6], and measure the insertion losses, which were found to be 0.77 dB. The device is ultimately tested for HHG. The driving pulses are provided by an amplified Ti:Sapphire laser system at 800 nm, with a repetition rate of 1 kHz, a pulse energy of 400 μJ and a duration of 25 fs. Figure 2b shows a typical harmonic spectrum generated in the chip filled with 90 bars of Argon. In these conditions, we measured efficient XUV generation in the spectral range from 40 to 60 eV, with photon flux on the order of 10^{12} photons/s at 40 eV, corresponding to a very high conversion efficiency of almost 10^{-5} .

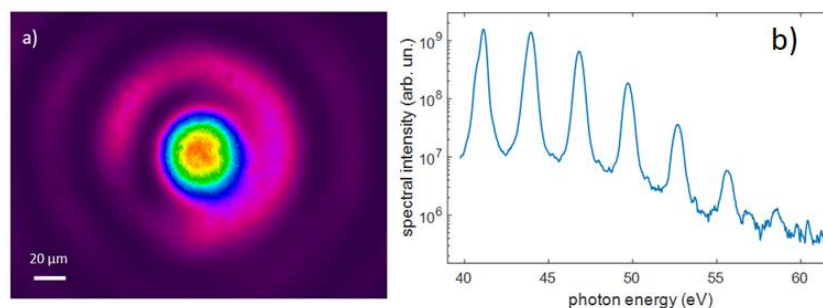


Fig. 2. (a) The near field image of the HHG waveguide's fundamental mode and (b) High-order harmonic spectrum generated in the microfluidic device filled Argon at a backing pressure of 90 mbar

When coupling the filtering device with the laser beam, we saw a highly multimode behaviour and higher insertion losses that depend on the dimensions of the XUV channel (fig. 3a).

The filter is then inserted into the HHG beamline to characterize its performance in rejecting the driving field compared with the attenuation of the XUV. Preliminary characterization demonstrates that with a 20- μm diameter XUV channel the driving IR field is rejected by a factor 10^{-2} from the XUV path, while the harmonics were attenuated by a factor 4 due to the presence of the filter, as shown in Fig. 3b.

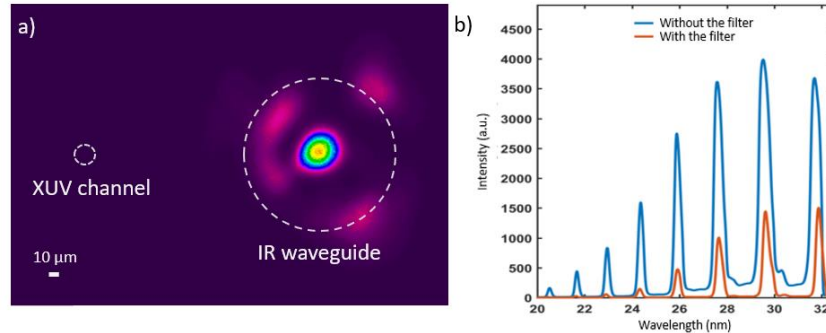


Fig. 3. a) Near field image of the multimodal waveguide for IR rejection and b) intensity of high-order harmonic generated in Argon at 90 mbar with (orange) and without (blue) the filtering stage

DISCUSSION

In conclusion, we demonstrated that it is possible to employ an integrated hollow-core waveguide to generate high-order harmonics with efficiencies comparable to other techniques. Moreover, the same waveguide can act like a filter to reject IR from the generated attosecond pulses. This approach provides some clear advantages with respect to standard thin metallic films commonly adopted to attenuate IR in HHG experiment, although the rejection performances are not yet comparable. In fact, there is in principle no bandwidth limitation in the frequencies which can be filtered; glass devices are less prone to optical damage than metallic films and, furthermore, the IR beam is preserved from absorption and can be possibly used for other experimental or diagnostic purposes.

We are currently performing investigations, assisted by numerical simulations, to enhance the performance of this already reliable device and to move in the direction of integrating more functionalities in a new compact design for coherent XUV platforms.

References

- [1] F. Krausz and M. Ivanov, *Attosecond physics*, *Reviews of Modern Physics*, vol. 81, Iss.1, 163-234, 2009
- [2] Francesca Calegari et al., *Advances in attosecond science*, *Journal of Physics B: Atomic, Molecular and Optical Physics*, vol. 49, iss. 06, 2016
- [3] R. Osellame, H.J.W.M. Hoekstra, G. Cerullo, M. Pollnau, *Femtosecond laser microstructuring: an enabling tool for optofluidic lab-on-chips*, *Laser and Photonics Reviews*, vol. 5, iss. 3, pp. 442-463, 2011
- [4] R.R. Gattass, E. Mazur, *Femtosecond laser micromachining in transparent materials*, *Nature Photonics*, vol. 2, pp. 219-225, 2008
- [5] R. Taylor, C. Hnatovsky, E. Simova, *Applications of femtosecond laser induced self-organized planar nanocracks inside fused silica glass*, *Laser and Photonics Reviews*, vol. 2, iss. 1-2, pp. 26-46, 2008
- [6] E. A. J. Marcatili; R. A. Schmeltzer, *Hollow Metallic and Dielectric Waveguides for Long Distance Optical Transmission and Lasers*, *The Bell System Technical Journal*, vol. 43, iss. 4, pp. 1783-1809, 1964

History and perspectives of an InP-based generic foundry approach

Invited paper

Meint K. Smit

Up to the 1990 the complexity of Photonic Integrated Circuits was low, most emphasis was on development of high-quality components, like lasers in InP and modulators in Lithium Niobate.

During the nineties a Moore's law-like complexity increase, driven by the requirements of WDM-technology, started and lasted for almost 25 years when a complexity of 1700 components in a single chip was reported by Infinera for a coherent WDM transceiver. The highest complexities were reported in InP-technology, which supported the integration of lasers, optical amplifiers, modulators and a broad class of passive components. It was followed by silicon photonics, which supported integration of huge numbers of components, but was limited in complexity by the fact that the technology did not support monolithic integration of lasers and optical amplifiers.

Using the classical approach of optimizing the technology for every application, development of complex Photonic Integrated Circuits (PICs) for commercial applications was only affordable for big companies which served large markets. Inspection of the architecture of the reported PICs showed, however, that most of them were composed of a fairly small set of basic components: lasers, optical amplifiers, modulators, detectors and passive waveguide components. Because the lasers could be constructed from optical amplifiers many applications could be served, in principle, by a technology that supported integration of optical amplifiers, phased modulators, detectors and a number of passive waveguide components.

In the first decade of the 21st century a consortium of research institutes cooperating the European Network of Excellence ePIXnet, started exploring the possibility of foundry model for providing shared excess to a standardized technology that supported integration of a small set of high-quality basic components (a generic foundry approach). In the early years there was a lot of skepticism whether such a standardized technology could compete with technology that was optimized for specific applications, but in the second decade it was demonstrated that for many applications the performance of generic foundry technology could come close to application-specific technology. And through the cost-sharing in so-called Multi-Project Wafer (MPW) runs, the development costs were much lower and came within reach also for small and medium-size enterprises.

In the third decade of our century the generic foundry approach has become widely accepted, both in InP-based and silicon photonics technology. Businesses are using dedicated wafers with the same generic foundry technology to fine tune their designs for volume production. In the presentation the history of the InP-based generic foundry approach will be described and its perspectives will be discussed.